THE
PHYSICAL REVIEW

A journal of experimental and theoretical physics established by E. L. Nichols in 1893

SECOND SERIES, VOL. 98, No. 6 JUNE 15, 1955

Pressure-Volume Isotherms of He^3 between 1.5 and 3.8°K*

WILLIAM E. KELLER
University of California, Los Alamos Scientific Laboratory, Los Alamos, New Mexico
(Received March 7, 1955)

PV isotherms of He^3 gas have been measured at 3.786, 2.991, 2.161, 1.818, and 1.516°K. Values of the second virial coefficient, B, derived from the data, are, respectively, −65.37, −86.25, −117.9, −142.3, and −168.0 cc/mole. For only the isotherms of 3.786 and 2.991°K was the third virial coefficient found to be significant. These values are 1132 and 1718 $cc^2/mole^2$, respectively. The measured B's are shown to be in satisfactory agreement with those calculated using a modified Slater-Kirkwood type potential, with constants chosen to give a good fit to the measured He^4 B's below 4°K.

I. INTRODUCTION

HERETOFORE no experimental data have been reported on the equation of state of He^3 gas, although several calculations[1–3] have been made of the second virial coefficient, B. The purposes of the present investigation of the P–V–T properties of He^3 gas in the interesting temperature region below 4°K were (1) to provide experimental values of B for comparison with the calculated B's, and (2) to determine the total gas imperfection—the extent that higher virial coefficients are important—knowledge of which is often necessary in other experiments with He^3 vapor and liquid. The isotherms also, as expected, furnish information on the density of the saturated vapor and, from the values of RT obtained, on the thermodynamic temperature scale below 4°K.

II. EXPERIMENTAL PROCEDURE

In almost every respect the experimental procedure followed in the present work duplicated that used in measuring the isotherms of He^4 described in a previous paper.[4] Also the apparatus, except for minor modifications in the gas-handling system, remained unchanged. We therefore are concerned here principally with the deviations from the former procedure.

The gas-handling operations were altered so that all the He^3 gas used was recovered. Replacement of forepumping by Toepler-pumping in several steps of the procedure required additional time for a given run, so that the maximum number of points that could be conveniently obtained for one filling of the cell was reduced from four to three.

Below the λ point of the He^4 bath, there is no danger of nonequilibrium of gas in the cell resulting from temperature gradients in the bath. Therefore for the three He^3 isotherms below 2.18°K the exchange gas was allowed to remain in the space between the inner and outer cans. Also, in this way thermal equilibrium was attained more rapidly.

One exception was made to the usual way of measuring the gas temperature. For the isotherm at 2.1605°K, He^3 was used in the vapor pressure thermometer. Since the He^3 contained a small amount of He^4, the thermometer was not used as the temperature standard for this isotherm, but was used for determining the correction to the raw PV/N product. Temperatures of the thermometer on the Kistemaker[5] scale were determined using the vapor pressure data of Abraham, Osborne, and Weinstock.[6] Experiments with He^4 in the thermometer at this temperature had shown that the bath and the thermometer were at exactly the same temperature; therefore the bath pressure as read on a dibutyl sebacate manometer was used as the temperature standard for this isotherm. All primary temperature measurements for the four remaining isotherms were

* Work done under the auspices of the U. S. Atomic Energy Commission.
[1] De Boer, van Kranendonk, and Compaan, Physica **16**, 545 (1950).
[2] Kilpatrick, Keller, Hammel, and Metropolis, Phys. Rev. **94**, 1103 (1954).
[3] Kilpatrick, Keller, and Hammel, Phys. Rev. **97**, 9 (1955).
[4] W. E. Keller, Phys. Rev. **97**, 1 (1955).
[5] J. Kistemaker, Physica **12**, 272 (1946).
[6] Abraham, Osborne, and Weinstock, Phys. Rev. **80**, 366 (1950).

TABLE I. Experimental data for the isotherms of He^3.

Exp. No.	P, mm Hg	$10^4(N/V)$ cc/mole	$T_{Vap(\alpha)}$°K	$(PV/N)_{Corr.}$ cc-mm/mole	δ
		$T_\alpha = 3.7860$°K			
γ-1-1	173.55	7.7467	3.7854	224 069	−9
γ-1-2	85.11	3.6970	3.7869	230 156	22
γ-2-1	309.39	14.4562	3.7845	214 113	1
γ-2-2	135.60	5.9794	3.7854	226 815	−96
γ-3-1	223.33	10.1266	3.7861	220 532	−28
γ-3-2	105.36	4.6005	3.7884	228 866	−60
γ-4-1	470.86	23.3981	3.7856	201 264	−31
γ-4-2	274.97	12.6845	3.7871	216 708	9
γ-4-3	160.21	7.1136	3.7912	224 893	119
γ-6-1	423.94	20.6638	3.7880	205 036	91
γ-6-2	251.53	11.5143	3.7881	218 320	125
γ-7-1	390.72	18.7808	3.7868	207 992	−161
γ-7-2	211.58	9.5595	3.7852	221 380	−31
γ-7-3	36.197	1.5514	3.7847	233 405	52
γ-8-1	356.67	16.9544	3.7837	210 512	−40
γ-8-2	157.72	6.9998	3.7862	225 308	−126
γ-9-1	415.46	20.1782	3.7884	205 745	77
γ-9-2	203.77	9.1821	3.7875	221 827	85
		$T_\alpha = 2.9910$°K			
δ-1-1	271.89	16.9576	2.9912	160 323	−60
δ-1-2	182.04	10.7264	2.9905	169 743	−3
δ-1-3	95.58	5.3664	2.9908	178 121	−30
δ-2-1	315.59	20.3205	2.9910	155 306	−55
δ-2-2	162.02	9.4317	2.9920	171 720	20
δ-3-1	83.34	4.6489	2.9894	179 368	−135
δ-4-1	455.08	33.3347	2.9910	136 518	22
δ-4-2	330.84	21.5843	2.9902	153 328	58
δ-4-3	171.20	10.0233	2.9904	170 838	−13
δ-5-1	371.68	25.0435	2.9937	148 246	89
δ-5-2	247.18	15.1707	2.9907	162 952	3
δ-5-3	135.77	7.7893	2.9906	174 329	−36
δ-6-1	421.77	29.7769	2.9903	141 688	−141
δ-6-2	288.40	18.1900	2.9932	158 412	5
δ-6-3	137.87	7.9202	2.9898	174 149	−60
δ-7-1	362.64	24.2819	2.9908	149 357	83
δ-7-2	213.63	12.8392	2.9907	166 408	90
δ-7-3	37.382	2.0407	2.9908	183 195	171
		$T_\alpha = 2.1605$°K			
α-1-1	128.37	10.9918	2.1470[a]	116 787	64
α-1-2	86.39	7.0141	2.1486	123 065	51
α-2-1	99.76	8.2052	2.1550	121 082	−49
α-2-2	35.100	2.6909	2.1559	129 884	33
α-3-1	42.147	3.2674	2.1472	129 979	39
α-3-2	18.106	1.3733	2.1481	131 771	−165
α-4-1	146.37	12.8568	2.1487	113 740	−34
α-4-2	68.84	5.4812	2.1496	125 431	−8
α-5-1	165.95	15.0350	2.1477	110 332	3
α-5-2	111.62	9.3488	2.1489	119 277	−45
α-5-3	24.298	1.8485	2.1495	131 295	111
		$T_\alpha = 1.8180$°K			
ϵ-2-1	89.82	9.1099	1.8178	98 608	−10
ϵ-2-2	37.668	3.4986	1.8194	107 577	66
ϵ-3-1	71.75	7.0558	1.8147	101 895	14
ϵ-3-2	23.322	2.1257	1.8158	109 852	4
ϵ-4-1	63.85	6.2017	1.8132	103 254	31
ϵ-4-2	15.980	1.4412	1.8154	111 043	−84
ϵ-5-1	83.40	8.3637	1.8166	99 803	−3
ϵ-5-2	28.778	2.6387	1.8184	109 038	−9
ϵ-6-1	100.66	10.4175	1.8196	96 526	−36
ϵ-6-2	41.952	3.9146	1.8216	106 944	28
		$T_\alpha = 1.5156$°K			
β-2-1	28.006	3.1370	1.5108	89 614	−34
β-2-2	13.988	1.5222	1.5132	92 080	64
β-3-1	42.141	4.8730	1.5108	86 815	7
β-3-2	22.346	2.4735	1.5108	90 678	−44
β-4-1	36.579	4.1764	1.5114	87 883	46
β-4-2	16.791	1.8384	1.5102	91 708	−66
β-5-1	39.022	4.4784	1.5108	87 470	−21
β-5-2	20.237	2.2291	1.5132	90 974	48

[a] The temperatures for this isotherm were determined from the vapor pressure of He^3, see text.

made with the vapor pressure thermometer filled with He^4, while the bath pressure was used as a monitor.

Gas-imperfection corrections for the number of moles of He^3 in the volume-manometer were made on the assumption that B for He^3 at these temperatures (about 300°K) has the same value as for He^4, chosen as 11.4 cc/mole. Even if the error in B is as great as 50 percent, an extremely generous tolerance, the error introduced by this in determining the number of moles would never be greater than 0.015 percent.

The gas used for the present measurements had a helium composition of 99.75 percent He^3, 0.25 percent He^4. Analyses determined with a Consolidated Nier type isotope ratio mass spectrometer were performed before and after the complete experiment with no significant difference in results.

III. RESULTS AND DISCUSSION

A. Experimental Data

A summary of the experimental data for five PV isotherms of He^3 gas is given in Table I. The symbolism used in this table is identical to that of Table I of reference 4, with two exceptions: (1) the order of the Greek letters designating an isotherm in the present table indicates the order in time in which the isotherms were measured; and (2) the δ heading the last column refers to the residuals (calculated minus observed values of PV/N) computed from the accepted analytical expression for each isotherm—as we shall see below, the latter is not always the linear form as in reference 4.

Figure 1 displays the isotherm data graphically with the dimensionless quantity PV/NRT plotted against the molar density.[7]

B. Virial Coefficients

As in the case of He^4, it was found for He^3 that the isotherm data can be more reliably analyzed using the inverse-volume virial expansion rather than the pressure expansion. All of the information collected from the He^3 isotherms appearing in Table II has been derived employing the expansion in N/V. We present in Table II the virial coefficients as the constants which are obtained when the isotherm data are fitted by using the method of least squares to both a linear and a quadratic equation. It can be seen that except for isotherm α there is a significant difference between the values of B obtained with the two equations. The choice of which expression better represents the measurements is made on the basis of the criterion given by Eq. (3) of reference 4; i.e., if we calculate $Q>1$ we have an indication that the introduction of a quadratic term is significant in that the curvature is effectively greater than the scatter of the data. The virial coefficients chosen in this way (with the exception of isotherm ϵ) are shown in Table II. No correction was made to

[7] In the similar plot for He^4, Fig. 3 of reference 4, the labeling of the abscissa should be "N/V, moles/cc" and not "N/V, cc/mole."

TABLE II. Summary of data derived from isotherms of He^3.

Isotherm T_{48}°K	γ 3.7860	δ 2.9910	α 2.1605	ϵ 1.8180	β 1.5156
Results using two-constant equation					
1. $A=RT$, cc-mm/mole	235 524	185 948	134 108	113 282	94 562
2. B, cc/mole	−62.59	−80.65	−117.9	−142.3	−168.0
3. P.e. of a measured point, percent	0.040	0.106	0.038	0.027	0.036
4. $\Sigma\delta_2^2/(n-2)=E_2$	17 704	74 515	6049	2476	2742
Results using three-constant equation					
5. $A=RT$, cc-mm/mole	235 842	186 638	134 090	113 392	94 427
6. B, cc/mole	−65.37	−86.25	−117.4	−146.8	−157.9
7. C, cc²/mole²	1132	1718	−328	3975	−16 124
8. P.e. of a measured point, percent	0.026	0.032	0.038	0.017	0.035
9. $\Sigma\delta_3^2/(n-3)=E_3$	7566	7143	6685	1106	2979
10. $Q=E_2/E_3$	2.340	10.432	0.905	2.239	0.920
Data derived from accepted virial coefficients (boxed figures)					
11. $T_{48}-T_{\text{isotherm}}$°K	0.0042	−0.0018	0.0101	0.0015	−0.0007
12. $T_{48}-T_{\text{mag}}$°K, reference 10	0.0051	0.0019	0.0100	0.0070	0.0040
13. $(N/V)_{\text{sat}}$, g/cc—from isotherm data	···	0.01849	0.00572	0.00337	0.00187
14. $(N/V)_{\text{sat}}$, g/cc—from Eq. (4), reference 8	···	0.01780	0.00565	0.00335	0.00194
15. $(N/V)_{\text{sat}}$, g/cc—from ideal gas equation	···	0.00991	0.00444	0.00284	0.00169

either the B or C values for the small percentage of He^4 in the experimental gas; in the worst case (isotherm β) the correction in B amounts to only 0.125 percent.

For isotherm ϵ the two-constant representation has been selected in spite of the fact that the computed value of Q is considerably greater than unity. It is inconsistent for Q to be <1 for isotherms α and β and >1 for isotherm ϵ; the same is true concerning the values of C computed for these three isotherms in that C is positive for ϵ while negative for α and β. In other words there is sufficient uncertainty in the values of C for these three isotherms to justify the conclusion that addition of the square term does not improve the *over-all* fit to the data.

On the other hand, for isotherms γ and δ it is felt that the values of C given are significant. Whereas there is yet no theoretical basis for predicting the temperature dependence of C for a quantum gas, one may roughly guess the behavior of C for He^3 from that of He^4, even though experimental results[4,8] for the latter are not free from ambiguity. C probably passes through a maximum slightly above the critical point, C positive; proceeding to lower temperatures from there, C diminishes and passes through zero somewhere below the boiling point, remaining negative, at least down to 1°K. Because isotherm γ is at a temperature above the critical temperature, it is possible that the smaller value of C for this isotherm than for δ indicates that C possesses a maximum between 3.0° and 3.8°K. However, another possible interpretation is that higher virial coefficients are becoming important and because we have terminated the series with C it includes the corrections due to higher terms—the value of B might also be affected by premature termination of the series, but to a very greatly reduced degree. The presence of this ambiguity in the meaning of the value of C for isotherm γ prompts us to warn that with the virial coefficients given here extrapolation of this isotherm to pressures or densities higher than those measured may yield misleading results.

Use of the virial coefficients given for isotherms α, β, δ, and ϵ is considered to give reliable equation of state information over the whole range up to saturation. Evidence for this is found by comparison of the densities of the saturated vapor as computed from the virial

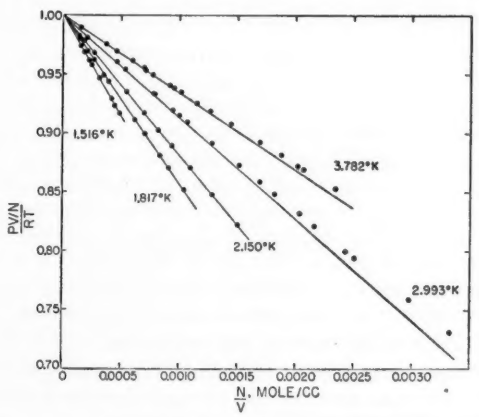

FIG. 1. Plot of PV/NRT *vs* N/V for five isotherms of He^3. Values of RT used are those appearing on the boxes of Table II. Solid circles represent the experimental data while the solid straight lines are drawn with the slopes given by the values of B in the boxes of Table II.

[8] W. H. Keesom, *Helium* (Elsevier Publishing Company, Inc., Amsterdam, 1942), p. 36.

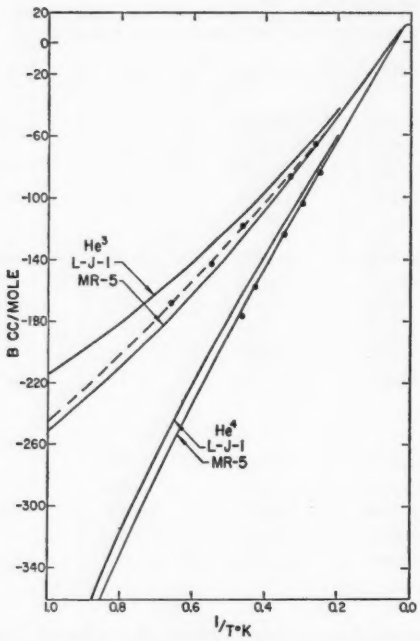

FIG. 2. Comparison of experimental and calculated second virial coefficients of He^3 and He^4 as a function of reciprocal temperature. Solid circles represent experimental points; the dashed curve is drawn from Eq. (2).

coefficients with those found experimentally by Kerr[9] (lines 13 and 14 of Table II). Between 1.6°K and 3.1°K Kerr estimates that his Eq. (4) gives densities reliable to 2 percent. For isotherm δ the agreement between the two methods is within 3.8 percent; but an error of only 1 cc/mole in B could account for this discrepancy, so the correspondence is considered very satisfactory. Added significance is given to the value of C of isotherm δ by this comparison, for imaginary values of $(N/V)_{sat}$ are obtained if calculated using only the second virial coefficient in the inverse volume expansion. In the middle temperature range, isotherms α and ϵ, there is excellent agreement between the two methods. As we proceed to lower temperatures the value of $(N/V)_{sat}$ obtained from the isotherms becomes much less sensitive to the value of B, e.g., for ϵ, the 0.6 percent difference between the two methods could be accounted for by a value of B 3 percent (4.3 cc/mole) less negative than the one chosen. Kerr states[9] that below 1.6°K his Eq. (4) gives values too high; this is borne out by the data derived from isotherm β. At this temperature the 3.7 percent difference in the two values of $(N/V)_{sat}$ corresponds to a value of B 16 percent more negative than the value obtained. We conclude that the isotherm data are the more reliable at this temperature.

[9] E. C. Kerr, Phys. Rev. **96**, 551 (1954). The value of C of Kerr's Eq. (4) used in computing entries to line 14, Table II, was 2.3015×10^{-6} rather than the value given in the paper erroneously as 3.3015×10^{-6}.

C. Comparison of Experimental and Calculated B's

Recent calculations[3] of the second virial coefficients of He^4 and He^3 have been made using a modified Slater-Kirkwood type interaction potential. The three constants for the potential (referred to as MR-5) considered to give the best over-all fit to the experimental data were determined from the measured values[4] of B for He^4 below 4°K. (It is to be re-emphasized that once the form of the potential is chosen, variations in potential constants do not alter the shape of the B *vs* T curve; and in principle a value of B at a single temperature is sufficient to determine two of the three constants—the third is fixed by a fit with high-temperature gas viscosity data.) With these constants the B *vs* T relation was predicted for He^3.

In Fig. 2 we present for both He^3 and He^4 graphical comparison of the experimental B's with those calculated from MR-5 and from a Lennard-Jones potential[2] with constants given by de Boer and Michels[10] ($L-J-1$). B is plotted against $1/T$ rather than T in order to emphasize some of the interesting differences in the behavior of He^3 and He^4.

A glance at Fig. 2 discloses immediately that the He^4 experimental B's fall on the MR-5 curve whereas the He^3 data lie between the MR-5 and $L-J-1$ curves. Yet there is clear indication that the He^3 points are closer to MR-5 than to $L-J-1$. Also one notes that in the temperature region 1°K to 5°K the splitting between $L-J-1$ and MR-5 is about 1.5 times greater for He^3 than for He^4, from which one concludes that the calculated He^3 second virial coefficients in this range are much more sensitive to the changes in the potential constants than are those for He^4. In other words we would expect a better fit to all the data if the He^3 B's were used to determine the potential constants rather than the He^4 B's. On the other hand, since we are aware that MR-5 is only a rough approximation to the true He-He interaction potential, we are inclined to feel that the He^3 fit to the MR-5 curve is altogether satisfactory.

It is often useful to have an interpolation formula for experimental data; and the nature of the B *vs* $1/T$ plot reveals that for He^3 and He^4 simple equations will suffice. For He^4 it is seen that B is practically linear in $1/T$ between 2° and 5°K. A straight line was arbitrarily passed through the MR-5 values at these two points resulting in the following equation:

$$B, \text{ cc/mole} = 23.05 - 421.17/T. \quad (1)$$

The nature of agreement between B's calculated from Eq. (1) ($B_{\text{int eq}}$) and those obtained from MR-5 and from measured isotherms is given in the upper half of Table III. For He^3 a three-constant least-squares fit was made to the experimental B's:

$$B, \text{ cc/mole} = 10.26 - 299.90/T + 44.27/T^2. \quad (2)$$

[10] J. de Boer and A. Michels, Physica **5**, 945 (1938).

This curve is represented as the dashed line in Fig. 2. No great amount of faith should be placed in the extrapolation of this formula, but it is shown to indicate the reasonableness of the form of the equation. Comparisons similar to those given for Eq. (1) are given for Eq. (2) in the lower half of Table III. It is interesting to note that although the probable errors obtained for the He^3 isotherms (lines 3 and 8, Table II) are about half as large as for the He^4 isotherms, the points for He^3 on the B *vs* $1/T$ curve show considerable more scatter than the points for He^4.

D. Thermodynamic Temperatures from the Isotherm

It was found[4] for He^4 that from the experimental values of $A=RT$ one obtains values of the thermodynamic temperatures in good agreement with temperatures measured magnetically.[11] These temperatures are conveniently expressed as deviations from the 1948 or "agreed" temperature scale.[12] Deviations derived from the He^3 isotherms are shown on line 11 of Table II; line 12 of this table gives the corrections obtained from magnetic data (Fig. 4, reference 10) at the corresponding temperatures.

If we let $\Delta=T_{\text{isotherm}}-T_{\text{mag}}$, it is seen that Δ is excessively large for β and ϵ, the order of 0.005°K. It is believed that this discrepancy can be explained in terms of evaporation and recondensation of the He^4-II film in the vapor pressure thermometer tube. A plausible picture of the process can be constructed with reference to the diagram of the cell (Fig. 1, reference 4). The He^4-II film forms on the tube walls and extends some considerable distance up the tube above the level of the bath, until at some point at which $T=T_\lambda$ most of the film is evaporated. The gas from the evaporated film travels downward and is mostly recondensed at the coldest portion of the tube. It is highly probable that the coldest spot is located in the vicinity of where the tube passes through the copper inner can; heat absorbed at this point is rapidly distributed over the cell, which presents a large surface for ready transfer of the heat by convection to the outer can (the space between the cans is filled with exchange gas). There is, however, still considerable resistance to the transfer of heat from the film to the copper can offered by the wall of the monel tube, even though this wall is only 0.0075 cm thick—if it is assumed that all the heat from the film condensation is transferred across a section of tubing 1 cm long one calculates a thermal gradient of the order of 0.01°K. Assuming Poiseuille flow of the gas returning down the tube, it can be easily shown that the pressure gradient associated with this flow is entirely negligible. We therefore expect the pressure read on the thermometer to be that at the coldest spot, which in turn is still warmer than the gas in the cell. We would be more certain of the correctness of this picture if we could quantitatively show that the convection process between cans is rapid compared with the transfer across the walls, but this is a very difficult problem.

An alternate cause of the large value of Δ for isotherms β and ϵ might lie in the occurrence of Taconis oscillations, but we feel that the former explanation is more satisfactory.

We conclude therefore that the temperatures derived from the two lowest isotherms are not significant in determining corrections to the 1948 scale; this in no way detracts from the validity of other results obtained from these isotherms. Furthermore, if the recondensation hypothesis is correct, the effect of recondensation would be negligible for the isotherm at 2.15°K. Here the film flow rate is less than 5 percent of what it is at 1.5°K and 1.8°K, and the temperature gradient across the tube wall is directly proportional to this rate (assuming the same area of the tube for recondensation).

For isotherm δ the value of $\Delta=0.0037$°K is moderately large—about three times as great as would be expected from the precision of the data—but still acceptable. Δ for isotherms α and γ shows excellent agreement between the two methods of measuring temperature.

TABLE III. Comparison of calculated and experimental values of the second virial coefficient for He^4 and He^3.

	T°K	B_{meas}	$B_{\text{int eq}}$	B_{MB-s}
He^4	3.960	−83.7	−83.3	−82.8
	3.341	−103.4	−103.0	−102.1
	2.859	−123.6	−124.3	−123.2
	2.321	−157.7	−158.4	−157.5
	2.148	−176.4	−173.0	−172.4
He^3	3.782	−65.4	−65.9	−66.8
	2.993	−86.3	−84.9	−87.8
	2.150	−117.9	−119.5	−125.4
	1.817	−142.3	−141.3	−148.5
	1.516	−168.0	−168.1	−176.3

ACKNOWLEDGMENTS

The author wishes to thank Mr. M. Goldstein and his group for performing the least-squares calculations reported in this paper; also Dr. S. G. Sydoriak for much helpful discussion.

[11] R. A. Erickson and L. D. Roberts, Phys. Rev. 93, 957 (1954).
[12] H. van Dijk and D. Shoenberg, Nature 164, 151 (1949).

Retrograde Motion in Gas Discharge Plasmas

K. G. HERNQVIST AND E. O. JOHNSON
RCA Laboratories, Princeton, New Jersey
(Received March 4, 1955)

It has been discovered that the glow region of the ball-of-fire mode in a hot-cathode discharge exhibits retrograd motion like the cathode spot of a mercury pool arc. The dependence of the velocity of motion on magnetic field, gas pressure, and current has been studied. Measurements have been made on tubes simulating the geometry and flow conditions of the ball-of-fire mode of discharge. A mechanism for retrograde motion is proposed. An expression for the velocity of motion is derived based on the stability criterion for a space charge sheath connecting two plasmas. Conclusions from a possible analogy with the mercury pool arc are made.

1. INTRODUCTION

RETROGRADE motion[1] is well known as a phenomenon of motion of the mercury pool cathode spot, when subjected to a transverse magnetic field; the direction of motion is opposite to the electromagnetic force on the moving charges. This effect has been assumed to be characteristic of "cold cathode" arcs in contrast to thermionic arcs.[2] Although several possible explanations for retrograde motion have been suggested, no completely satisfactory analysis of the phenomenon has previously been made.

This report deals with a similar effect observed in externally heated hot-cathode gas-discharges of the ball-of-fire mode.[3] Experimental studies of the retrograde motion and measurements on analog tubes are first described. A mechanism for retrograde motion is proposed and an expression for speed of the motion is developed. Conclusions based on the possible analogy with the mercury pool arc are made.

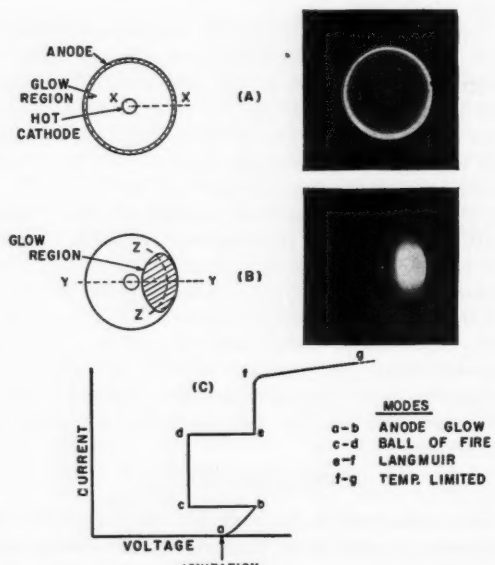

FIG. 1. Schematic drawing and photograph of cylindrical diode operating in (A) anode glow mode and (B) ball of fire mode, together with idealized volt-ampere characteristic (C).

II. HOT-CATHODE GAS-DISCHARGE MODES

Hot-cathode gas-discharges have recently been investigated by Johnson, Malter, and Webster.[3-5] A summary of some of the results from these investigations will be given here.

Studies of externally heated hot cathode gas-discharges in noble gases have shown that such discharges can exist in any one of four different modes. These are characterized by different glow patterns and potential distributions. For example, consider the cylindrical diode whose cross-section is shown in Fig. 1(A). If this tube is connected in series with a source of dc potential and a limiting resistor, the discharge for relatively low anode currents will be characterized by a glow which appears solely in a thin layer on the anode surface. Because of its unique appearance this mode has been termed the "anode glow." When the tube current has been increased beyond a certain critical value, which depends upon both gas and tube parameters, the discharge suddenly changes over into another mode wherein the glow takes a sphere-like form as shown in Fig. 1(B). This mode has been termed the "ball-of-fire." As the tube current is increased the glow region increases in size. When the current is approximately half the emission capability of the cathode the glow fills the entire tube except for a thin layer surrounding the cathode. Since numerous discharges answering this latter description were extensively studied by Langmuir, this mode has been termed the "Langmuir" mode. Finally, when the tube current becomes equal to the emission capabilities of the cathode, the glow fills the entire tube and the discharge operates in what is termed the "temperature-limited" mode. An idealized volt-ampere characteristic of a hot-cathode discharge is shown in Fig. 1(C); the sections of the characteristic corresponding to the different modes are as noted. The

[1] R. M. St. John and J. G. Winans, Phys. Rev. **94**, 1097 (1954). (This paper contains a fairly complete list of references to the subject.)
[2] C. G. Smith, Phys. Rev. **73**, 543 (1948).
[3] Malter, Johnson, and Webster, RCA Rev. **12**, 415 (1951).
[4] Webster, Johnson, and Malter, RCA Rev. **13**, 163 (1952).
[5] E. O. Johnson and W. M. Webster, RCA Rev. (to be published).

following descriptions are restricted to the first two modes, since only these are of interest in the present studies.

The anode glow mode has the potential distribution shown in Fig. 2(A). Electrons from the cathode enter the dark plasma against a small retarding potential V_c (~0.5 volt) and drift, by virtue of density gradients and weak electric fields, to the edge of the anode sheath. The plasma electron temperature is approximately equal to the temperature of the cathode. The electrons gain energy in the anode sheath and excite as well as ionize neutrals. The ions created in this sheath flow into the dark plasma and sustain its density against diffusion losses to the end plates. Because of the potential barriers at both the cathode and anode, the ions are discouraged from leaving the dark plasma at these boundaries. Because of cathode nonuniformities, however, the situation at the cathode is not the ideal one portrayed in the figure and a significant ion current escapes at this surface. This situation is aggravated either by an increase in the tube current or by a decrease in cathode temperature. The ratio of ion to electron current density in the anode sheath is

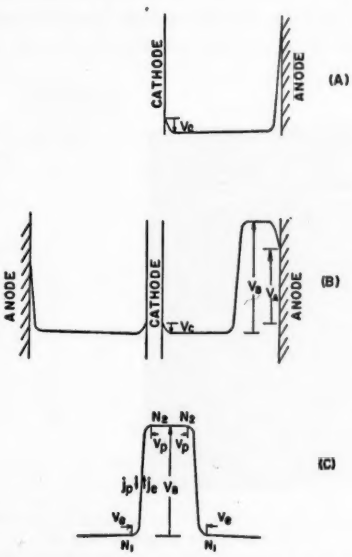

FIG. 2. Potential distributions (A) for anode glow mode along XX of Fig. 1(A) and for ball of fire mode, (B) along YY of Fig. 1(B) and (C) along ZZ of Fig. 1(B).

$$j_p/j_e=\alpha(m_e/m_p)^{\frac{1}{2}},$$

where m_p is the ion mass, m_e is the electron mass and α a factor, usually of the order of 0.1 or less.

As the discharge current is increased, the anode sheath gets thinner, and consequently, the dark plasma gets thicker and so requires a larger ion current for its maintenance. This, in addition to the increased ion losses at the cathode, causes the factor α to increase.

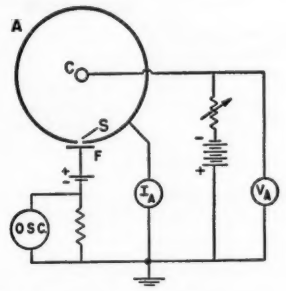

FIG. 3. Schematic diagram of tube and circuit.

When α reaches a value of about 0.7, sheath instability sets in and the current ratio rapidly rises to the limiting value $(m_e/m_p)^{\frac{1}{2}}$. The sheath instability arises from a complex relationship between ion generation, ion and electron flow in the sheath, and the sheath voltage distribution. When α reaches the value 1, both electron and ion currents are space charge limited and the electric field at each end of the sheath is essentially zero. The glow region now is a regular plasma at a high potential. Due to the increase in size of the region for ionization, the ionization would be too large if the whole anode current were to pass through the glow region. Therefore, this region can no longer cover the whole anode area but must only occupy a limited part of the cathode-anode region as shown in Fig. 1(B). Stroboscopic observations have shown that this transition from anode glow to ball-of-fire mode of discharge does not occur in the sequence described above, but rather that the glow region of the ball-of-fire mode seems to "grow" out from some spot at the anode surface.

Although the details of the transition are not known, it is reasonably certain that the final location of the sheath boundary between the two plasmas, as exemplified in the potential diagram of Fig. 2(B) and 2(C) is subject to the following dictates:

(1) Sheath stability requires that the ratio of ion to electron current density must everywhere along the boundary between the dark plasma and the glow region be equal to the limiting value,

$$j_p/j_e=(m_e/m_p)^{\frac{1}{2}}. \quad (1)$$

(2) The sheath boundary must be situated in a region of the dark plasma where the electron current-carrying capability is a minimum.

(3) The size and character of the new plasma, wherein all ions are generated, must be such that the ion requirements of the dark plasma are satisfied.

The following two important features of the ball-of-fire mode of discharge have been verified both theoretically and experimentally:

(1) The potential V_B of the glow region may be equal to, or less than, the ionization potential of the gas, but is usually higher than the anode potential V_A.

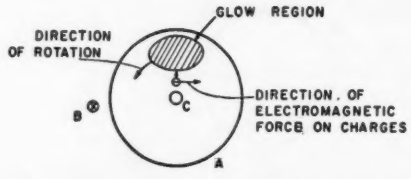

FIG. 4. Diagram showing direction of motion of glow region. Direction of magnetic field B is in toward the plane of the paper.

(2) An anomalously high scattering of electrons takes place in the glow region. The effect of this scattering is the establishment of a nearly perfect Maxwellian velocity distribution. For typical parameter values, the electron temperature is usually found to be about 10 000°K.

III. EXPERIMENTAL OBSERVATIONS OF THE RETROGRADE MOTION OF THE "BALL-OF-FIRE" MODE DISCHARGE

The construction of the tube and circuit used in the tests is shown schematically in Fig. 3. The tube is a cylindrical diode with an oxide-coated indirectly-heated cathode C of 0.050-in. diameter and a nichrome anode A of 1-in. diameter. The tube structure is 1-in. long and has mica insulators covering the ends. A 0.010-in. wide slit S is cut along the entire anode length parallel to the cathode. Behind this slit is placed a collector F. The anode is grounded and the cathode is connected through a limiting resistor and a dc voltage source to ground. The collector is biased slightly positive relative to ground. The collector current is monitored by an oscilloscope. An adjustable magnetic field parallel to the cathode is obtained by a coil surrounding the tube structure.

When operated in the ball-of-fire mode, the glow region is usually at rest at some preferred place in the cathode-anode region, presumably determined by irregularities in the tube structure. If a magnetic field is applied parallel to the cathode, the glow region is found to rotate around the cathode in a direction opposite to the electromagnetic forces on the charges flowing between cathode and anode as indicated in Fig. 4. Stroboscopic observations using a toothed wheel indicated a true motion of the glow region. The shape of the glow region was practically undisturbed during the rotation.

In Fig. 5 is shown a typical oscillogram of the current to F. When the glow region passes by the slit S, the current rises sharply to about ten times its value when the dark plasma is adjacent to the slit. It is also seen

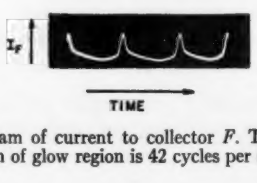

FIG. 5. Oscillogram of current to collector F. The frequency of rotation of glow region is 42 cycles per second.

that the current through the dark plasma is somewhat lower at the leading edge than at the trailing edge of the glow region. Figure 6 shows this more clearly and also that this dissymmetry increases with magnetic field strength.

From oscillograms such as that of Fig. 5, the frequency of rotation of the glow region can be measured. Figures 7 shows the frequency of rotation f as a function of magnetic field strength B for a tube filled with helium. In these curves the gas pressure p is a parameter, and the anode current I_A is a constant. For magnetic fields higher than those shown in Fig. 7, the discharge becomes unstable and no consistent measurements can be made. A frequency of rotation of 100 cycles per second corresponds to an average velocity of about 6 meters per second. It was found that the frequency of rotation is practically independent of the anode current I_A except for high currents under which conditions the glow region occupies almost half of the

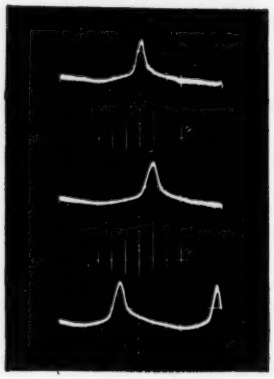

FIG. 6. Oscillograms of current to collector F for three different values of the magnetic field B.

cathode-anode space. Figures 8–10 show the result of measurements for neon, argon, and xenon.

From these measurements it is seen that for low values of the magnetic field B, the frequency of rotation is roughly proportional to B, decreases with pressure, and is practically independent of the cathode current. No definite conclusions can be drawn as to the dependence on the nature of the gas.

IV. MEASUREMENTS ON "BALL-OF-FIRE" ANALOG TUBES

The flow conditions in a plasma in the presence of a magnetic field have been treated by several investigators.[6,7] For low values of the magnetic field the direct influence on the ions is negligible. The influence of the magnetic field on the electrons is essentially equivalent to that of an electric field transverse to the

[6] L. Tonks, Phys. Rev. **56**, 360 (1939).
[7] L. G. H. Huxley, Phil. Mag. **23**, 210 (1937).

path traveled by electrons between collisions. The continuity equations (see Appendix) show that the perturbation caused by the magnetic field is some function of the product of electron mobility and magnetic field strength. A rigorous solution of the flow conditions in the presence of a magnetic field [i.e., a solution of Eqs. (17) and (18) of the Appendix] is very difficult to obtain due to the complicated and uncertain boundary conditions. It is possible, however, to obtain a qualitative solution from measurements on tubes simulating the geometry and flow conditions of the ball-of-fire mode of discharge.

The construction of an analog tube for studying the flow conditions in the dark plasma is shown schematically in Fig. 11. This tube structure is similar to the one shown in Fig. 4 except for the anode A which has a diameter of 0.800 in. and has the part behind the six electrodes B_1–B_6 cut away. The electrodes B_1–B_6 are

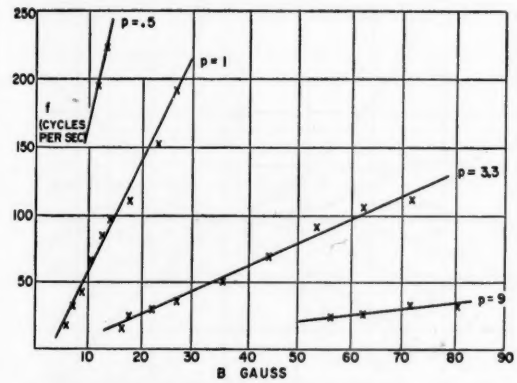

FIG. 7. Variation of the frequency of rotation f of the glow region with magnetic field B. Parameter is the pressure p of helium gas in mm of mercury. $I_A=70$ milliamperes.

of the same length as the tube structure and form part of a cylinder 0.500 in. in diameter with the center at the anode. Thus they simulate geometrically the boundary of a cylindrically shaped glow region. An adjustable magnetic field parallel to the cathode is obtained by a coil surrounding the tube structure.

When operated in the anode glow mode, the electrodes B_1–B_6 are uniformly covered by a thin layer of glow and the rest of the cathode-anode region is dark. The potential of A with respect to C can be varied and is actually held below the ionization potential of the gas. Operated in this manner, the tube simulates quite well the flow conditions in the dark plasma of the ball-of-fire mode of discharge. The main difference is that the ratio of ions leaving and electrons arriving at the boundary of the glow region is about ten times higher for the case of the actual ball-of-fire mode of discharge. However, since the influence of the magnetic field on the ion flow is negligible this difference should not qualitatively violate the similarity.

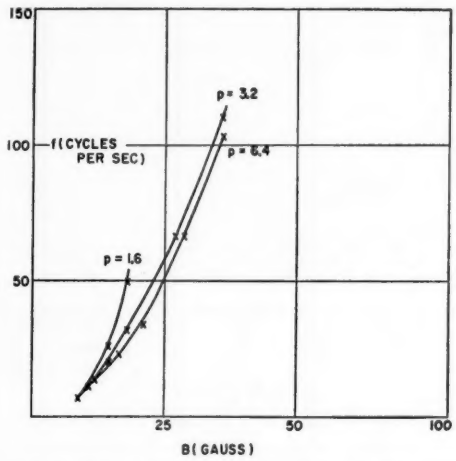

FIG. 8. Variation of frequency of rotation f with magnetic field B. Parameter is the pressure of neon gas in mm of mercury. $I_A=50$ milliamperes.

The currents to the six electrodes B_1–B_6 were recorded as the magnetic field B parallel to the cathode was varied. Figure 12 shows the relative change of current to each electrode as a function of magnetic field. The magnetic field B is defined as positive when its direction relative to the tube structure is as shown in Fig. 11. It is seen that the electron flow from C to B_1–B_6 is bent by the magnetic field in the same direction as the electromagnetic forces on the electrons. Figure 13 shows the relative change (or perturbation) of current to the electrode B_1 as a function of magnetic field with the helium gas pressure as parameter. Figure 14 shows the same functional dependence but with the voltage V_A between A and C as parameter. It is seen from Fig. 14 that as V_A approaches V_B the perturbation for

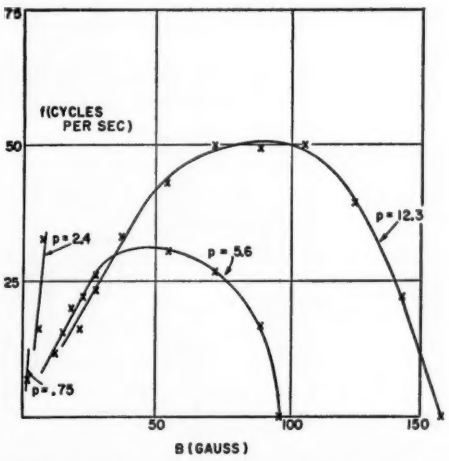

FIG. 9. Variation of the frequency of rotation f with magnetic field B. Parameter is the pressure p of argon gas in mm of mercury. $I_A=50$ milliamperes.

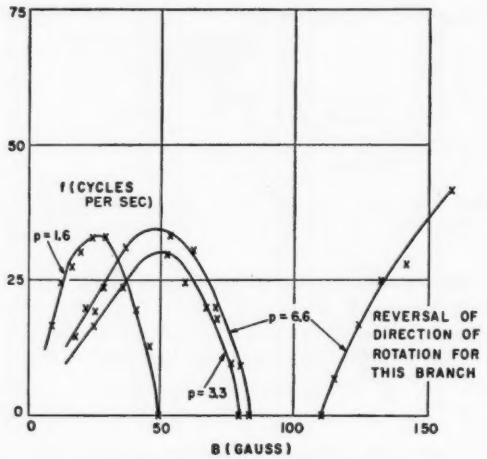

FIG. 10. Variation of the frequency of rotation f with magnetic field B. Parameter is the pressure of xenon gas in mm of mercury. $I_A=50$ milliamperes.

a certain magnetic field decreases, and even changes sign as V_A becomes equal to V_B. This effect is caused by the changing current distribution between A and B_1–B_6 as V_A approaches V_B. In the actual ball-of-fire mode of discharge, the potential of the glow region corresponding to V_B always exceeds the anode potential corresponding to V_A.

In general, it is seen that the magnitude of the perturbation depends on magnetic field and gas pressure in a way similar to that in which the frequency of rotation of the glow region depends on these parameters. Significant is also the strong dependence of the perturbation on the ratio between V_A and V_B.

These observations are consistent with probe current oscillograms for the rotating glow region as seen in Fig. 6. This shows that retrograd motion corresponds to motion of the glow region into a region of decreased density and away from a region of increased density of the dark plasma.

The magnetic field will also influence conditions in the glow region. However, because of the high electron temperature and the anomalously high scattering of the electrons in the glow region, the electron mobility in this region will be much lower than in the dark plasma. The perturbation on the flow conditions in the glow region will thus be smaller than that in the dark plasma. Also, because of the long mean free path for ionization, ion formation in the glow region will be quite insensitive to small displacements of the electron flow entering from the dark plasma. Thus, it may be anticipated that the relative density perturbation caused by the magnetic field will be much lower in the glow region than in the dark plasma. Figure 15 shows schematically a tube built for checking this postulate experimentally. The tube structure is similar to the one shown in Fig. 4 except for the addition of a cylindrically shaped mesh grid G, which is welded on to part A_2 of the anode. If G and A_2 are left floating and A_1 is connected to the cathode through a source of dc potential and a limiting resistor, the tube will operate in the ball-of-fire mode, having an anchored glow region. The dark plasma occupies the region limited by C, A_2, and G. The glow completely fills the region between G and A_1. Since the grid is an ion sink, the space charge sheath joining the two plasmas is securely anchored at the grid.[8] Four probes, P_{D1}, P_{D2}, P_{G1}, and P_{G2} are located close to the sheath boundaries in respective plasmas. These probes are biased negatively with respect to the cathode and record the change in plasma density as a magnetic field B is applied parallel to the cathode.

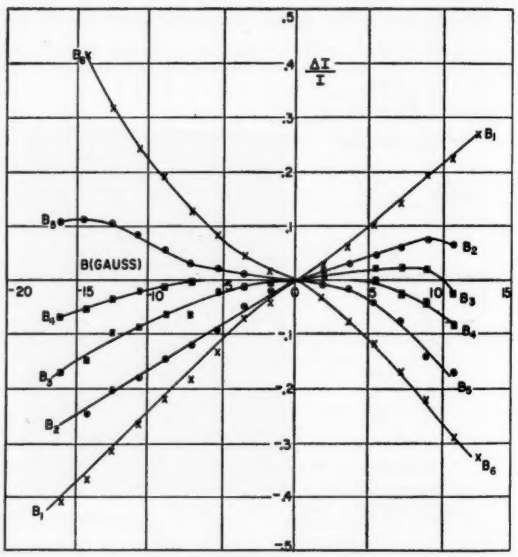

FIG. 12. Variation of relative change of current with magnetic field B. $V_B=26$ volts, $V_A=6$ volts. Helium gas at $p=1.25$ mm mercury.

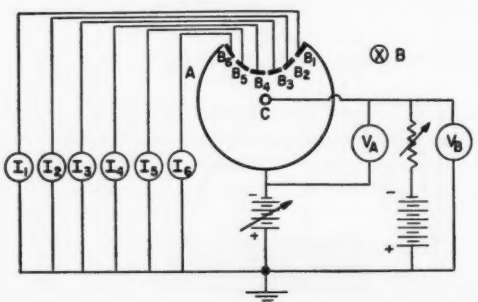

FIG. 11. Schematic diagram of analog tube and circuit. Positive magnetic field B is in the direction in toward the plane of the paper.

[8] E. O. Johnson, "Studies of the low voltage arc," presented at 1954 Gaseous Electronics Conference, New York, New York (to be published in RCA Rev.).

Figure 16 shows the relative change in probe currents as functions of B. It is seen that the perturbation is always greater in the dark plasma than in the glow region. Based on visual observations of the glow pattern is can be assumed that this behavior is even more exaggerated in the case of a nonanchored glow region. Thus it appears to be justified, as a first approximation, to assume that the conditions in the glow region are uninfluenced by the magnetic field.

V. STABILITY OF A MOVING SPACE CHARGE SHEATH AS CRITERION FOR RETROGRADE MOTION[9]

The mechanism for retrograde motion that will be proposed in this section will be valid only for *low* values of the magnetic field strength. As the magnetic field is increased the perturbation introduced on the flow conditions will finally be such as to change the whole nature of the discharge.

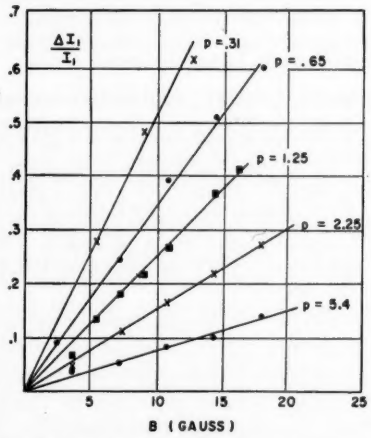

FIG. 13. Variation of relative change in current to B_1 with magnetic field B. Parameter is the pressure of helium gas in mm of mercury. $V_B=26.5$ volts, $V_A=6$ volts.

As discussed in Sec. II, when the glow region is at rest the ratio of ion to electron current density in the sheath boundary between the dark plasma and the glow region must satisfy Eq. (1). The effect of an applied magnetic field is primarily to bend the electron flow in the dark plasma. Thus the density of the dark plasma is increased on one side of the glow region and decreased on the other side. Since conditions in the glow region are practically undisturbed by the magnetic field, Eq. (1) will no longer be satisfied along the boundary. The conditions arising from this perturbation are quite complicated. From experience, however, it may be expected that the main result of the violation of Eq. (1) is the appearance of an electric field at the boundary of that plasma which has an insufficient space current to satisfy Eq. (1). This electric field will cause a decay of plasma density at the boundary, or in other words, the space charge sheath will seek to travel into the plasma deficient in density. Since the bending of the electron flow in the dark plasma is in the direction of electromagnetic force, the glow region will travel in the retrograde direction.

[9] It has been suggested (reference 8) that striations of the positive column constitute plasmas at different potentials joined by space charge sheaths. In accordance with this theory the basic ideas and results presented in this section should also be applicable to moving striations.

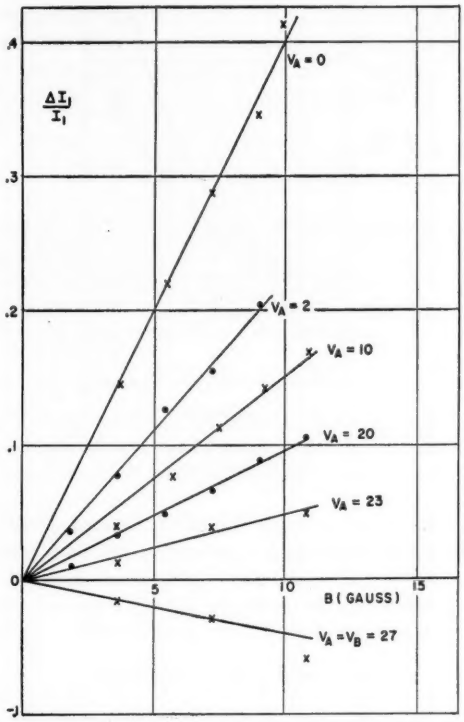

FIG. 14. Variation in relative change in current to B_1 with magnetic field B. Parameter is the voltage of A. Helium gas at a pressure of 1.6 mm of mercury.

Instead of treating the mechanism of motion in detail one can try to find a moving system in which the cri-

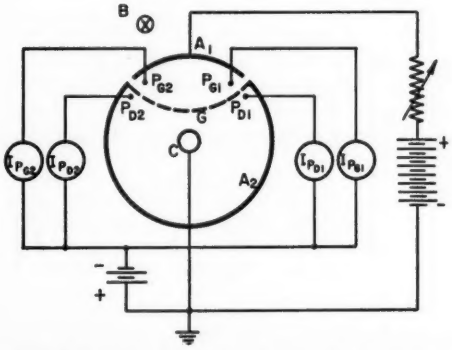

FIG. 15. Schematic diagram of tube having an anchored glow region. Positive magnetic field is in direction in towards the plane of the paper.

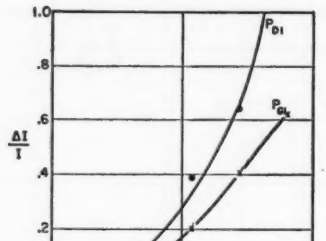

FIG. 16. Variation of relative change in probe current with magnetic field B.

terion for sheath stability is fulfilled. Assume conditions to be symmetrical with a density of the dark plasma equal to N_1 and of the glow region equal to N_2 at the sheath boundary as shown in Fig. 2(C).

For sheath stability according to Eq. (1)

$$j_p/j_e = N_2 v_p/N_1 v_e = (m_e/m_p)^{\frac{1}{2}}, \tag{2}$$

where v_p is the average velocity of ions entering the sheath from the glow region and v_e is the average velocity of electrons entering the sheath from the dark plasma. Now suppose the density of the dark plasma is perturbed by an amount $-\Delta N_1$ on one side of the glow region and $+\Delta N_1$ on the other side. Further, assume that the sheaths travel through the neutral gas with velocities v_{I} and v_{II} in direction toward the plasma deficient in density as shown in Fig. 17(a). The new condition for sheath stability will then be for sheath I:

$$\frac{N_2(v_p - v_{\mathrm{I}})}{(N_{\mathrm{I}} - \Delta N_{\mathrm{I}})(v_e + v_{\mathrm{I}})} = \left(\frac{m_e}{m_p}\right)^{\frac{1}{2}}, \tag{3}$$

and for sheath II:

$$\frac{N_2(v_p + v_{\mathrm{II}})}{(N_1 + \Delta N_1)(v_e - v_{\mathrm{II}})} = \left(\frac{m_e}{m_p}\right)^{\frac{1}{2}}. \tag{4}$$

Thus the sheath velocities are given by

$$v_{\mathrm{I}} = \frac{\Delta N_1 v_e}{N_2\left(\frac{m_p}{m_e}\right)^{\frac{1}{2}}\left[1 + \frac{N_1}{N_2}\left(\frac{m_e}{m_p}\right)^{\frac{1}{2}} - \frac{\Delta N_1}{N_2}\left(\frac{m_e}{m_p}\right)^{\frac{1}{2}}\right]}, \tag{5}$$

and

$$v_{\mathrm{II}} = \frac{\Delta N_1 v_e}{N_2\left(\frac{m_p}{m_e}\right)^{\frac{1}{2}}\left[1 + \frac{N_1}{N_2}\left(\frac{m_e}{m_p}\right)^{\frac{1}{2}} + \frac{\Delta N_1}{N_2}\left(\frac{m_e}{m_p}\right)^{\frac{1}{2}}\right]}. \tag{6}$$

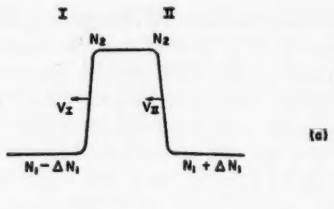

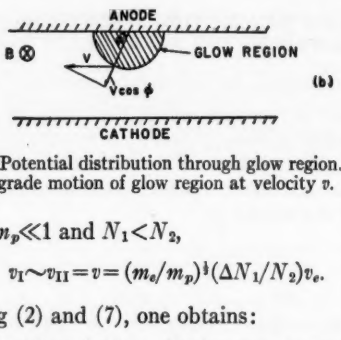

FIG. 17. (a) Potential distribution through glow region. (b) Retrograde motion of glow region at velocity v.

Since $m_e/m_p \ll 1$ and $N_1 < N_2$,

$$v_{\mathrm{I}} \sim v_{\mathrm{II}} = v = (m_e/m_p)^{\frac{1}{2}}(\Delta N_1/N_2)v_e. \tag{7}$$

Combining (2) and (7), one obtains:

$$v = 36.4(\Delta N_1/N_1)(T_p/M)^{\frac{1}{2}} \text{ meters/second}, \tag{8}$$

where T_p is the ion temperature in the glow region in °K and M is the molecular weight of the ions.

When the sheath travels at the velocity given by (8), the field at the plasma boundary, which is the physical cause of the sheath motion, is cancelled. The actual velocity may be expected to be somewhat less than that given by Eq. (8).

To demonstrate the sheath stability criterion in a case of retrograde motion, assume as shown in Fig. 17(b) a plane parallel cathode-anode structure with a glow region in the shape of half a sphere. (Such a shape can actually be observed experimentally.) Further, assume that the perturbation introduced by a magnetic field on the dark plasma is of the form

$$-(\Delta N_1/N_1)_0 \cos\phi$$

along the boundary. This is in qualitative agreement with the measurements described in Sec. IV. If the glow region travels parallel to the anode with a velocity v, the velocity perpendicular to the boundary is $v\cos\phi$. Thus sheath stability is insured if the glow region remains unchanged in shape and travels in the direction of retrograde motion with a velocity given by Eq. (8).

As shown in the appendix, the perturbation $\Delta N_1/N_1$ is a function of the product of electron mobility μ^- in the dark plasma and the magnetic field B. The experiments described in Sec. IV show that this functional relationship is a nearly linear one. Then the velocity of motion of the glow region v_B can be written as

$$v_B = 36.4 G\mu^- B(T_p/M)^{\frac{1}{2}} \text{ meters/sec}. \tag{9}$$

Here G is a geometrical factor which can only be determined from a complete solution of the flow conditions in the dark plasma.

The mechanism of retrograde motion proposed here is not a motion of the individual charges constituting the plasma but a motion relative to the neutral gas of the boundary between two plasmas. Thus, the glow region would remain at rest relative to the tube structure if a wind of velocity v blew in the neutral gas in a direction opposite to the direction of retrograde motion.

In order to see that Eq. (8) gives a velocity of the right order of magnitude we note from Fig. 7 for helium that at a pressure of 1 mm of mercury, the frequency of rotation f is equal to 55 cycles per second for a magnetic field B of 10 gauss. This corresponds to a velocity of about 3.3 meters per second. With $M=4$ and $T_p=300°\text{K}$, Eq. (8) gives a relative density perturbation

$$\Delta N_1/N_1=0.011.$$

From Fig. 14 it is seen that this perturbation is of the right order of magnitude to be expected for V_A slightly below the ionization potential of 24.5 volts.

VI. CONCLUSIONS FROM POSSIBLE ANALOGY WITH THE MERCURY POOL ARC

Comparison between the retrograde motion of the ball-of-fire mode of discharge and that of the mercury pool arc[1] shows that the functional dependence of the two phenomena on gas pressure, current, and magnetic field are quite similar. This suggests very strongly that the mechanisms of the two phenomena are similar. If this is so, and if the mechanism for retrograde motion proposed in Sec. V is the correct one, the following conclusions can be made about the nature of the mercury pool arc: (1) The mercury pool arc operates in the ball-of-fire mode; the glow region is very small in size and is situated close to the mercury pool cathode. (2) Electron emission from the cathode occurs into a dark plasma which is at a much lower potential than the glow region. Thus, the distance between the cathode surface and the glow region cannot be obtained from a calculation based on space charge sheath considerations, nor can the electric field at the cathode surface be estimated on the same basis.

APPENDIX

Plasma Flow Conditions in Presence of Magnetic Field

The effect of a weak magnetic field $\mathbf{B}$ on the charge flow of a plasma is primarily to introduce a fictitious electric field $\mathbf{v}^-\times\mathbf{B}$ which is experienced only by the electrons ($\mathbf{v}^-$ is the electron velocity). Thus, for charge flow in a plane perpendicular to a magnetic field $\mathbf{B}=(0,0,B)$, one can write the flow equations.

$$\mathbf{v}^-=-\mu^-\mathbf{E}-D^-(1/N)\,\text{grad}N-\mu^-\mathbf{v}^-\times\mathbf{B}, \tag{10}$$

$$\mathbf{v}^+=\mu^+\mathbf{E}-D^+(1/P)\,\text{grad}P, \tag{11}$$

where $\mathbf{v}^-$ and $\mathbf{v}^+$ are electron and positive ion velocities, respectively, μ^- and μ^+ are mobilities, D^- and D^+ the diffusion coefficients, N and P particle densities, and $\mathbf{E}$ the electric field. N, P, and $\mathbf{E}$ are determined by the boundary conditions, by the Poisson equation

$$\nabla\cdot\mathbf{E}=1.81\times10^{-8}(P-N), \tag{12}$$

and by the continuity equations. For a plasma where no charges are generated and no volume recombination occurs, the continuity equations are

$$\text{div}(N\mathbf{v}^-)=0, \tag{13}$$

$$\text{div}(P\mathbf{v}^+)=0. \tag{14}$$

With the usual assumption $N=P$ and introducing

$$\mathbf{b}=-\frac{\mu^-}{D^-}\mathbf{E}-\frac{1}{N}\,\text{grad}N, \tag{15}$$

$$\mathbf{a}=\frac{\mu^+}{D^+}\mathbf{E}-\frac{1}{N}\,\text{grad}N, \tag{16}$$

we can write (13) and (14) as

$$\text{div}\mathbf{b}-\frac{1}{1+T^-/T^+}\mathbf{a}\cdot\mathbf{b}-\frac{1}{1+T^+/T^-}\mathbf{b}\cdot\mathbf{b}$$

$$-\frac{1}{1+T^-/T^+}(0,0,\mu^-B)\cdot(\mathbf{b}\times\mathbf{a})=0, \tag{17}$$

$$\text{div}\mathbf{a}-\frac{1}{1+T^+/T^-}\mathbf{a}\cdot\mathbf{b}-\frac{1}{1+T^-/T^+}\mathbf{a}\cdot\mathbf{a}=0, \tag{18}$$

where T^- and T^+ are the electron and ion temperature respectively. The last term of Eq. (17) represents the perturbation caused by the magnetic field on the flow conditions. This perturbation is thus a function of the product of electron mobility and magnetic field strength.

Self-Focusing Streams

WILLARD H. BENNETT
Naval Research Laboratory, Washington, D. C.

(Received September 30, 1953; revised manuscript received November 10, 1954)

Streams consisting of a mixture of ions and electrons in which the average velocity of the electrons in the direction of the stream is different from the average stream velocity of the ions can be magnetically self-focusing. The random velocities of the electrons and ions about their respective average stream velocities do not need to be Maxwellian. The only condition which must be met is that the total electric current in stream must exceed a critical value which can be calculated in terms of the stream velocities and the average kinetic energies of the particles due to components of velocity transverse to the axis of the stream. Streams containing both slow and fast particles of like kind tend to eject the slow particles and keep the fast ones. Streams of particles of one kind only, entering an ionized or ionizable region can be self-focusing. Axial asymmetries grow in arcs but disappear in low-density self-focusing streams.

SINCE the original publication[1] of the basic theory applicable to magnetic self-focusing in streams consisting of mixtures of charged particles of opposite polarities, a number of experiments have been reported on magnetic self-focusing.[2–4] Theoretical papers have also appeared[5–8] which were written apparently in ignorance of the original work and which failed to recognize the more important physical properties of such streams. For this reason it would be desirable at this time to present the theory of magnetic self-focusing in a somewhat more general form in order to point out these properties more clearly and to assist in presenting some new applications of the theory which have recently been recognized.[9] The theory will be developed in a relativistically invariant form and it will be shown: (1) that whether or not mixed low-density ion and electron streams have Maxwellian velocity distributions, there is a critical current which must be exceeded if the stream is to be magnetically self-focusing; (2) that in the evolution of any such stream, the first things to happen are the permanent loss from the stream of some of its components and the rapid attainment of cylindrical symmetry by the remainder of the stream; (3) that such streams are not subject to the "kink" instability of arcs; (4) that the application of a sustained emf to the stream, as done in all reported experiments, makes published theories wholly inadequate to explain those experiments; and (5) that this theory explains magnetic self-focusing in interplanetary proton streams.

The kind of stream considered consists of a stream of ions most of which move in one direction mixed with a stream of electrons most of which move in the opposite direction. Each kind of particle in the stream is assumed to have a distribution in velocity and in radial distance from the axis which is approximately uniform along the stream at any instant and which is symmetric about the same axis at all times. No restrictions will be imposed on the radial variations of these distributions with time. It will be supposed that the ions and electrons may initially each have any distribution in velocity component parallel with the axis, and that each such distribution may be divided into a a large number of subdistributions each of which consists of all the particles of one kind in the stream having velocity component parallel with axis in a small interval of such velocity component. The various subdistributions are mixed with each other in space but not necessarily in uniform proportions because each subdistribution may have a distribution in radial distance from the axis which initially is different from that of the other subdistributions. Each subdistribution is supposed to continue to be symmetric about the axis while its radial distribution may vary with time.

It is essential at the outset to distinguish clearly between "low-density streams" in which the effects of collisions are small during the mean time of travel of charged particles between their positions farthest from and nearest to the axis, and "high-density streams" where the effects of collisions during such a time are large making it necessary that a sustained emf be applied in the direction of the stream to maintain a current or in other words to have any stream at all. The first part of this paper will relate to low-density streams to which no emf is applied in the direction of the stream, after which high-density streams will be discussed.

LOW-DENSITY STREAMS

The force exerted on any particle with charge e_1 and velocity $\mathbf{v}_1$ by any other charge e_2 with velocity $\mathbf{v}_2$ located at a displacement $\mathbf{r}$ from the first particle is

$$\mathbf{E}+(1/c^2)\mathbf{v}_1\times[\mathbf{v}_2\times\mathbf{E}], \qquad (1)$$

[1] W. H. Bennett, Phys. Rev. **45**, 890 (1934).
[2] S. W. Cousins and A. A. Ware, Proc. Roy. Soc. (London) **64**, 159 (1951) and A. A. Ware, Trans. Roy. Soc. (London) **243**, 197 (1951).
[3] Bostick, Levine, and Coombes, Gaseous Electronics Conference, Princeton, New Jersey (September 6, 1952) (unpublished).
[4] Thoneman, Cowhig, and Davenport, Nature **169**, 34 (1952).
[5] L. Tonks, Phys. Rev. **56**, 360 (1939).
[6] P. C. Thoneman and W. T. Cowhig, Nature **166**, 903 (1950); Proc. Roy. Soc. (London) **64**, 345, 618 (1951).
[7] M. Blackman, Proc. Roy. Soc. (London) **64**, 1039 (1951).
[8] A. Schlüter, Z. Naturforsch. **6A**, 73 (1951).
[9] For one of these, see W. H. Bennett and E. O. Hulburt, Phys. Rev. **95**, 315 (1954) and J. Atmos. Terrest. Phys. **5**, 211 (1954).

where the first term is the Coulomb electrostatic force between the two charged particles in the direction of **r** and the second term is the magnetic force[10] not generally in the direction of **r**. By resolving the force on any one charged particle into radial, tangential and axial components and integrating over all the other particles in the assumed radially symmetric and longitudinally uniform stream, it is found that the force on each particle in the stream in which the transverse components of velocity are a lower order of magnitude than the axial components of velocity of at least some of the particles in the stream is approximately the same as it would be if all particles in the stream had velocities equal to only their components of velocity parallel with the axis (axial components of velocity).

If e_α is the charge on each particle in the αth subdistribution, ρ_α is the numerical density of particles in that subdistribution and is a function of radial distance r from the axis, and u_α is the axial component of velocity of the particles in that subdistribution, then the force (radially away from the axis) which the particles in the αth subdistribution exert on any particle, say one in the κth subdistribution, having charge e_κ and axial component of velocity u_κ, is given by

$$\frac{2e_\kappa e_\alpha}{r}\left(1-\frac{u_\kappa u_\alpha}{c^2}\right)\int_0^r \rho_\alpha 2\pi r dr,$$

and the total force acting on any particle is

$$F_\kappa=\frac{2e_\kappa}{r}\sum_\alpha e_\alpha\left(1-\frac{u_\kappa u_\alpha}{c^2}\right)\int_0^r \rho_\alpha 2\pi r dr, \qquad (2)$$

which is obtained by summing over all the subdistributions in the stream.

In the radially symmetric and longitudinally uniform streams considered here, the forces acting on each particle are radial, that is, the forces are cylindrically central. Except for the effects of collisions, the angular momentum of each particle about the axis is conserved. If the particles have random distribution in angular momentum and in total energy, they will have correspondingly random distributions in period of motion between the positions nearest to and farthest from the axis and they will have random rates of precession about the axis. In a low-density stream, these spreads in periods and in rates of precession produce a mixing in radial distribution approaching a nearly steady state early in the evolution of the stream and long before collisions within each subdistribution have produced Maxwellian velocity distributions within each of the various subdistributions.

The stream will be said to be in its first phase from the time it is first set up with its non-Maxwellina distributions until each subdistribution has become approximately Maxwellian, and will be in its second phase while the kinetic energies due to transverse momenta are slowly increasing due to conversions of axial momenta into transverse momenta.

[10] M. Mason and W. Weaver, *The Electromagnetic Field* (Dover Publications, New York, 1952), p. 299.

FIRST PHASE

The virial of Clausius in cylindrical coordinates can be used for finding the directions of radial acceleration in a stream prior to the arrival of the stream at the quasi-steady state produced by the mixing mentioned above. The virial is derived in Appendix A, and the second time derivative of the moment of inertia per unit length of the stream is obtained:

$$\frac{1}{2}\frac{d^2I}{dt^2}=2N\psi+\frac{i^2}{c^2}-q^2.$$

In this equation, the moment of inertia per unit length of stream,

$$I=\sum_\alpha \int_0^\infty m_\alpha r^2 \rho_\alpha(r) 2\pi r dr,$$

may be used as a measure of the radial spread of the stream without implying that there will be any rotation of the stream about the axis, which of course there cannot be if the velocity distributions are symmetrical about the axis; N is the total number of particles per unit length of stream; ψ is the mean kinetic energy per particle due to components of velocity transverse to the direction of the axis;

$$i=\sum_\alpha e_\alpha u_\alpha \int_0^\infty \rho_\alpha(r) 2\pi r dr$$

is the total electric current in the stream; and

$$q=\sum_\alpha e_\alpha \int_0^\infty \rho_\alpha(r) 2\pi r dr$$

is the total charge per unit length of stream. For the stream to concentrate towards the axis, dI/dt must be negative and for this reason, a negative value of d^2I/dt^2 is used as the criterion for self-focusing. This criterion can be written in the form

$$i_c=c(2N\psi+q^2)^{\frac{1}{2}} \qquad (3)$$

for the critical current which the stream must exceed in order to be self-focusing. In a stream in which there is zero net charge per unit length of stream ($q=0$), all subdistributions of positive charges moving in the direction opposite to that of the net current, i, and all negative charges moving with the net current are magnetically repelled everywhere and permanently lost from the stream. Such losses increase the net current, i, in the stream and increase the value of "transverse" kinetic energy ψ which the remainder of the stream may have and still be self-focusing. As will be shown in the

following, the changes in the velocity and density distributions produced by mixing and more slowly by collisions do not at any time violate the aforementioned criterion for self-focusing.

Boltzmann's equation can be used in deriving the quasi-steady state equation which must be satisfied by each subdistribution as soon as radial redistributions have been arrested by the mixing specified earlier. The quasi-steady state equation is derived in Appendix B, Eq. (20):

$$e_\kappa \sum_\alpha e_\alpha \left(1-\frac{u_\kappa u_\alpha}{c^2}\right)\int_0^r \rho_\alpha(\xi)2\pi\xi d\xi+\theta_\kappa-\phi_\kappa - \frac{r}{\rho_\kappa}\frac{d}{dr}(\rho_\kappa\phi_\kappa)=0, \quad (4)$$

where θ_κ is the mean kinetic energy at radial distance r of the κth kind of particle due to tangential components of velocity, and ϕ_κ is the mean kinetic energy at r of the same particles due to radial components of velocity. This equation is useful for deriving relationships, which will not be detailed here, for the first-phase steady-state stream prior to the attainment of Maxwellian velocity distributions, and it will also be needed in deriving the equations for the second phase with its Maxwellian distributions in the following.

SECOND PHASE

The effects of collisions in systems consisting principally or entirely of charged particles can most easily be found by applying the equations derived by Thomas.[11] Where a charged particle is moving among charged particles there is no definite mean free path but time rates of change of mean kinetic energy can be calculated. Thomas' equation (4.33) can be rewritten to give the rate of change of mean kinetic energy of a particle with charge e and mass m_1 moving with a velocity v_1 through a density N_2 of particles each with charge e, mass m_2 and root mean square velocity v_2. When $v_1>v_2$ the rate of change of mean kinetic energy ψ due to components of velocity transverse to the direction of v_1 (which multiplied by $\frac{3}{2}$ equals the rate of increase of mean thermal energy of the particle) is given approximately by

$$\frac{d\psi}{dt}=\frac{4\pi e^4 N_2}{m_1 v_1}\log\left(\frac{2A}{\log A}\right), \quad (5)$$

where

$$A=\frac{3m_1^3 m_2^3 v_1^6}{4\pi e^6(m_1+m_2)^3 N}.$$

In this Eq. (5), the N_2 is the density of the particles of the second kind whose mean thermal velocity is less than the velocity of the particle of the first kind relative to the mean velocity (vectorial) of the particles of the second kind. As the particle of the first kind approaches thermal equilibrium with the particles of the second kind, the portion which N_2 is of the density of all the particles of the second kind diminishes and so the expression (5) for $d\psi/dt$ finally approaches zero as it approaches mean random velocity of the particles of the second kind. The value of (5) is comparatively insensitive to the logarithmic term and to an adequate approximation the rate of change of energy of the particle is inversely proportional to the velocity of the particle relative to the other particles with which it is in continuous "remote" collision. For this reason, any particle in a stream approaches thermal equilibrium with the other particles in its own subdistribution and so each subdistribution approaches a Maxwellian distribution with its own temperature. Next in rate of progress is the approach of adjacent subdistributions (that is, subdistributions with adjacent values of velocity component parallel with the axis of the stream) to thermal equilibrium, or more accurately, adjacent subdistributions tend to acquire adjacent values of temperature at the same time that each subdistribution is acquiring a Maxwellian distribution. Least rapid in rate of progress is the conversion of momenta parallel with the axis into momenta transverse to the axis due to collisions between particles having large differences in velocity parallel with the axis.

As each subdistribution approaches a Maxwellian distribution, the temperature T_κ for that distribution (see Appendix C) is related to the mean kinetic energy due to components of velocity for each degree of freedom by

$$\tfrac{1}{2}kT_\kappa=\theta_\kappa=\phi_\kappa.$$

Substituting into Eq. (4) and transposing gives

$$kT_\kappa r\frac{d}{dr}\log\rho_\kappa=2e_\kappa\sum_\alpha e_\alpha\left(1-\frac{u_\kappa u_\alpha}{c^2}\right)\int_0^r \rho_\alpha 2\pi r dr. \quad (6)$$

Taking the derivative and dividing by r gives

$$kT_\kappa\nabla^2\log\rho_\kappa=4\pi e_\kappa\sum_\alpha e_\alpha\left(1-\frac{u_\kappa u_\alpha}{c^2}\right)\rho_\alpha, \quad (7)$$

where ∇^2 is the Laplacian in cylindrical coordinates.

The variables in these equations can be transformed to the frame of reference of an observer moving parallel with the axis at a velocity v as explained in Appendix C, and the Eqs. (7) become

$$kT_\kappa'\nabla^2\log\rho_\kappa'=4\pi e_\kappa\sum e_\alpha\left(1-\frac{u_\kappa' u_\alpha'}{c^2}\right)\rho_\alpha',$$

which are identical in form with Eqs. (7); that is, the Eqs. (7) are relativistically invariant in form, and any solution will be transformable to any other frame of reference.

[11] L. H. Thomas, Proc. Roy. Soc. (London) **121**, 464 (1928).

A solution of these equations is

$$\rho_\kappa=\rho_{\kappa 0}(1+ar^2)^{-2},\quad T_\kappa=ie_\kappa u_\kappa/2c^2k \tag{8}$$

where

$$i=\sum_\alpha e_\alpha u_\alpha\int_0^\infty \rho_\alpha 2\pi r dr$$

$$=\text{total electric current in the stream.}$$

In this solution, the total charge per unit length of stream,

$$q=\sum_\alpha e_\alpha\int_0^\infty \rho_\alpha 2\pi r dr,$$

is zero, which can be true only for an observer with a particular velocity parallel with the axis. This observer will be referred to as the "central observer." The solution as seen by any other observer whose velocity parallel with the axis of the stream is v relative to the central observer has the form

$$\rho_\kappa'=\rho_{\kappa 0}'(1+ar^2)^{-2},\quad T_\kappa'=\frac{i'e_\kappa' u_\kappa'}{2c^2k}-\frac{q'}{2k}e_\kappa, \tag{9}$$

where i' is the total current in the stream as seen by that observer, and q' is the total charge per unit length of stream as seen by that observer.

In the second phase of the stream described by this solution, space charge everywhere is neutralized as seen by the central observer but the same stream, as seen by any other observer may have either a positive or negative net space charge, depending upon the velocity of the observer.[12]

Substituting the solution (9) into Eq. (2) for the force on any particle in the stream gives

$$F_\kappa'=-\frac{ar}{1+ar^2}\left[\frac{i'e_\kappa u_\kappa'}{c^2}-q'e_\kappa\right]=-\frac{2ar}{1+ar^2}kT_\kappa'.$$

This shows that all the particles in any subdistribution whose axial velocity is such that a negative temperature would be required, are repelled from the axis and permanently lost from the stream. From the view-point of the central observer, all positive charges must move one way along the stream and all negative charges must move the opposite way. This early first-phase departure of those subdistributions moving the wrong way from the view-point of the central observer, has the effect of increasing the current in the stream and hence of increasing the temperatures which the remaining subdistributions may have and still be retained in the stream.

As each subdistribution is approaching a Maxwellian distribution, it is also approaching the well-known density distribution given by

$$\rho_\kappa=\rho_{\kappa R}\exp(-\chi_\kappa/kT_\kappa), \tag{10}$$

where $\rho_{\kappa R}$ is the density at some radial distance R, and χ_κ is the work done on a κ particle by the fields while it moves from a radius R to r. For large values of R and r, the force on the particle is approximately

$$F_\kappa=\frac{2e_\kappa}{r}\left[q-\frac{iu_\kappa}{c^2}\right],$$

and the energy χ_κ is

$$\chi_\kappa=2e_\kappa\left(q-\frac{iu_\kappa}{c^2}\right)\log\left(\frac{r}{R}\right).$$

The density for large radial distances obtained by substituting this into Eq. (10) is given by

$$\log\rho_\kappa=\left(\frac{2e_\kappa q-2ie_\kappa u_\kappa/c^2}{kT_\kappa}\right)\log r.$$

The number of these particles per unit length of stream lying beyond some large radius R_0,

$$N_{\kappa R0}=\int_{R0}^\infty \rho_\kappa 2\pi r dr,$$

is infinite if

$$ie_\kappa u_\kappa/c^2-e_\kappa q<kT_\kappa. \tag{11}$$

From this it follows that any subdistribution whose temperature is greater than twice that given by solution (9) loses particles permanently from the stream, and the redistribution of velocities of the remaining particles in that subdistribution results in a reduction in temperature of the remainder of that subdistribution until the temperature is not more than twice that given by solution (9).

The behavior of any subdistribution in a stream having densities like those of solution (9) but not necessarily temperatures given by solution (9) can be found by substituting for the density in the hydrodynamical equation of mass motion derived in Appendix B, Eq. (19):

$$\frac{d\dot{r}_{\kappa 0}}{dt}+\dot{r}_{\kappa 0}\frac{\partial\dot{r}_{\kappa 0}}{\partial r}=\frac{4\pi ar}{m_\kappa(1+ar^2)}\left[T_\kappa-\left\{\frac{ie_\kappa u_\kappa}{2c^2k}-\frac{q}{2k}e_\kappa\right\}\right]. \tag{12}$$

From this it is seen that those subdistributions with temperatures higher than those given by solution (9) have a mass motion away from the axis and are adiabatically cooled, while those with temperatures too low for solution (9) have a mass motion towards the axis and are adiabatically heated. Such expansions and contractions are not entirely free to proceed however. For example, if the subdistributions of one polarity of charge on the whole are too hot and those of the other

[12] This is not a violation of the relativistic invariance of the charge on any one particle, but it is due to the different ways in which the numerical densities of the different kinds of particles vary depending on their different velocities as discussed in reference 22.

are too cold, the motion of charge produces a space charge near the axis opposing the separation. If more of the subdistributions are too hot than too cold, the effect of the space charge separation is to draw both distributions along and still further heat them, possibly driving some of the temperatures above the criterion of (11) and so driving some of those particles out of the stream.

TWO-COMPONENT STREAM

The system discussed in the original paper[1] consisted of only two distributions. The solution obtained could be written

$$\rho_1=\left[1-\frac{u_2}{c}\frac{T_1u_2+T_2u_1}{(T_1+T_2)c}\right]\rho_0(1+ar^2)^{-2},$$
$$\rho_2=\left[1-\frac{u_1}{c}\frac{T_1u_2+T_2u_1}{(T_1+T_2)c}\right]\rho_0(1+ar^2)^{-2}, \tag{13}$$

where

$$\rho_0=\frac{2ac^2k(T_1+T_2)}{e^2(u_1-u_2)^2}.$$

The velocity of the central observer for this system is such that u_1 has a sign opposite to that of u_2 and the temperatures are related to the two velocities by

$$T_1/u_1=T_2/(-u_2)=K, \tag{14}$$

where K is the proportionality constant. The total current in this stream is

$$i=(2c^2k/e)K, \tag{15}$$

which is independent of the velocities u_1 and u_2 and of the constant a which determines the radial spread of the stream. The expression for the temperatures in Eqs. (8) of course can be written in the same form as Eq. (14); *viz*:

$$i=(2c^2k/e_\kappa)(T_\kappa/u_\kappa)=(2c^2k/e)K,$$

and this is also consistent with Eq. (3).

The total potential energy per unit length of a stream is derived in Appendix D and is

$$V=-2\sum_\alpha\sum_\beta e_\alpha e_\beta\left(1-\frac{u_\alpha u_\beta}{c^2}\right)\int_0^\infty\int_0^r \rho_\beta(\xi)2\pi\xi d\xi \times\log(r/R)\rho_\alpha(r)2\pi r dr,$$

where R is the radius at which the kinetic energy of a particle is zero. Because this is a matter of definition, R may be taken to equal $\sqrt{e}$.

In a two-component stream in its second phase as seen by the central observer, the potential energy per unit length of stream is

$$V=-(i^2/2c^2)\log a.$$

Consider now a stream which initially had radial distributions like those of Eqs. (13)

$$\rho_1=\rho_2=\rho_{00}(1+a_0r^2)^{-2},$$

and Maxwellian velocity distributions with temperatures like Eq. (14),

$$T_1/u_1=T_2/(-u_2)=K_0,$$

but which contained a current different from that given by Eq. (15),

$$i\neq(2c^2k/e)K_0.$$

The total energy per unit length of stream, which is constant, equals

$$h=h_a+NkT_1+NkT_2-(i^2/2c^2)\log a_0,$$

where h_a is the kinetic energy per unit length of stream due to axial components of momenta (which is decreasing only very slowly due to collisions between the two different distributions whose relative velocity is large); and N is the number of each kind of particle per unit length of stream so that NkT_1 and NkT_2 are the kinetic energies of the two distributions due to transverse momenta. The total energy per unit length of stream in its initial form may be written as

$$h=h_a+(ki/e)K_0-(i^2/2c^2)\log a_0,$$

and is to be compared with the equation for the stream after it has reached the quasi-steady state of the second phase:

$$h=h_a+(ki/e)K-(i^2/2c^2)\log a.$$

Subtracting, transposing, and substituting for K from (15),

$$\frac{1}{i}\left\{\frac{2c^2k}{e}K_0-i\right\}=\log\frac{a_0}{a}.$$

The quantities a_0 and a are related to the initial and final mean radial distances of particles $\bar{r}_0$ and $\bar{r}$ respectively by

$$\sqrt{a_0}=\pi/2\bar{r}_0 \quad\text{and}\quad \sqrt{a}=\pi/2\bar{r},$$

and

$$\bar{r}=\bar{r}_0\exp[(i_c-i)/2i], \tag{16}$$

showing that in this case the mean radial distance of particles $\bar{r}$ decreases exponentially with the excess of the stream current i over the value i_c given by Eq. (15).

HIGH-DENSITY STREAMS

When the densities are such that collisions cannot be taken to be infrequent during the travel of a charged particle between positions of maximum and minimum radial distance from the axis, the situation is much different and the methods used in the preceding are inadequate. Firstly, a current cannot be sustained for any appreciable time without applying an emf in the direction of the stream either by applying an electric

field in that direction or by electromagnetic induction. The application of such an emf in combination with the self-magnetic field of the stream produces orbits of the charged particles—principally the electrons, because they are the more readily accelerated—which tend to move the particles towards the axis but not in a simple manner. In addition to this, the application of an emf drives the electrons away from a Maxwellian velocity distribution and towards an Allis-Brown distribution[13] in which the mean thermal energy of the electrons is much greater than the mean thermal energy of the ions. The kinetic energy of random motion of the electrons continues to rise until the rate at which energy is fed into the stream by the applied emf equals the rate at which energy is dissipated, principally as bremsstrahlung or characteristic spectra of the gas or in producing ionizations. Even if these large electron thermal energies are related to a corresponding electron "temperature," equations like Eq. (3) or Eq. (12) cannot be invoked to calculate the minimum current for self-focusing because the cooperative action of the emf and the self-magnetic field of the stream in driving electrons towards the axis can in part overcome the tendency of the high electron temperature to disperse the stream as long as the emf is maintained.

In addition to the above, there is another reason that that any discussion of magnetic self-focusing in electric arcs[14] is somewhat academic. It is that arcs are essentially unstable for a quite different reason as has been demonstrated by Kruskal and Schwarzschild.[15] If the stream is initially not perfectly straight, but a short section in it is slightly displaced, the self-magnetic field of the stream current is greater on the concave side of the bend in the middle of the displaced section than on its convex side. The stream is pushed towards the convex side, exaggerating the middle bend while the reverse bends at each end of the middle bend begin to grow towards the other side. Thus, each bend grows and creates new bends which in turn also grow. This kind of instability in an arc is familiar to anyone who has seen the serpentine writhing of very high voltage arcs in air.

This kind of instability cannot exist in a low-density stream because the very rapid mixing in azimuth about the axis produced by the spreads in rates of precession about the axis quickly eliminates any kinks in the stream.

APPLICATIONS

The theory of low-density streams given here may be applied to the proton streams travelling from the sun towards the earth invoked in previous publications[9] to account for the aurorae. In these articles, it was supposed that the protons energe from the sun in a diverging jet at speeds of about 10^{10} cm/sec. Later studies have made it seem likely that the more usual speeds are of the order of 2×10^9 cm/sec so that $u^2\cong c^2/225$, as will be explained in a later publication. The divergence of the jet makes the mean "transverse" kinetic energy of the solar protons very much greater than the mean thermal energy of either the ions or the electrons in the residual ionized interplanetary matter, and consequently, the central observer is very nearly at rest with respect to the interplanetary matter. The greatest density of fast ions in a 10 000-ampere stream of 2×10^9-cm/sec protons in a stream whose mean radius is 1000 kilometers is one ion per 200 cm^3, while the density of interplanetary matter is generally conceded to be at least one ion and one electron per cm^3.

The interplanetary ions and electrons can be supposed to have Maxwellian velocity distributions both at the same temperature, but the high-velocity protons in the stream probably do not have a Maxwellian velocity distribution. Equation (6) can be applied to the interplanetary ions and electrons, respectively, as seen by an observer at rest relative to the interplanetary matter:

$$kTr\frac{d}{dr}\log\rho_2=4\pi e^2\int_0^r(\rho_1+\rho_2-\rho_3)rdr,$$

$$kTr\frac{d}{dr}\log\rho_3=-4\pi e^2\int_0^r(\rho_1+\rho_2-\rho_3)rdr,$$

where T is the temperature of the interplanetary matter; ρ_1, ρ_2, and ρ_3 are the numerical densities of the fast protons, the interplanetary ions and the interplanetary electrons respectively. Adding and integrating: $\rho_2\cdot\rho_3=$ a constant which equals the square of the numerical density, n, of each kind of particle remote from the stream and so is n^2 everywhere. If $\rho_1\ll n$ as it is in this case, $|n-\rho_2|$ and $|n-\rho_3|$ are each small, and the net charge density everywhere is small. Substituting for ρ_2 and ρ_3 in turn from $\rho_2\cdot\rho_3=n^2$ in $\rho_1+\rho_2-\rho_3=0$ gives

$$n-\rho_2=\tfrac{1}{2}\rho_1=\rho_3-n.$$

The proton stream in the plasma will be self-focusing if the current in the stream exceeds the critical current given by Eq. (4) with $q=0$:

$$i=c(2N\psi)^{\frac{1}{2}}, \tag{17}$$

where N is twice the number of fast protons per unit length of stream which is equal to the number of protons plus the excess of electrons over slow ions per unit length of stream; and ψ is the mean energy of those N fast protons and N excess slow electrons due to transverse components of velocity.

If, as assumed in the previous articles,[9] the fast protons come from a jet diverging with a half-angle α, and the temperature of the interplanetary ions and electrons is too low to affect materially the value of ψ, the values of critical current for 2×10^9-cm/sec protons in a cone of half-angle α are given by substituting

[13] W. P. Allis and S. C. Brown, Phys. Rev. **87**, 419 (1952).
[14] Called the "pinch effect" by Tonks. See reference 5.
[15] M. Kruskal and M. Schwarzschild, Proc. Roy. Soc. (London) **223**, 348 (1954).

TABLE I. Critical current in amperes for various cone half-angles.

α	1°	2°	5°	10°	20°
i_c	300	1200	7600	31 000	132 000

$\frac{1}{2}Nev=i$ in Eq. (17) where $v=2\times10^9$:

$$i\gtrsim 4c^2\psi/ev. \tag{18}$$

ψ is one-half the mean energy of the fast protons due to transverse components of velocity. Some values for various half-angles are tabulated in Table I.

Substitution of numerical values for a typical fast-proton stream as suggested above, in Eq. (5) shows that very little progress toward a Maxwellian velocity distribution is made by the fast protons in their time of travel from the sun to the earth and the stream will still be in its first phase when it reaches the earth in such a case. Although the actual current in the stream may be much greater than the critical current, it does not follow that the exponential shrinkage towards the axis given by Eq. (16) will occur. Such a shrinkage can not in fact occur for these non-Maxwellian distributions because of its approximate conservation of angular momentum of each individual fast proton, about the axis of the stream. The shrinkage which can occur in this early part of the first phase of the stream is determined by the distribution in angular momentum of the fast protons and not alone by the kind of considerations which led to Eq. (16).

Although the surviving fast protons leaving the jet at the sun may, and probably do, leave in a stream with an oddly shaped cross section far from cylindrical symmetry, the rapid mixing due to the spread in rates of precession about the axis will very quickly bring such a stream to cylindrical symmetry, but of course, the distributions in transverse momenta remain far from Maxwellian.

This theory of low-density streams is not adequate to explain the experiments of Cousins and Ware, and of Bostick, Levine, and Coombes,[2,3] both because large electromotive forces were applied to the stream and also because the gas densities used were too large. Thoneman, Cowhig, and Davenport[4] used densities which were too large for this theory to apply in its entirety, but it is interesting to note that they produced a large direct current using only an alternating emf. This seems to illustrate the strong tendency of a stream magnetically to throw out all subdistributions moving the wrong way as seen by a central observer[16] and so to increase the direct current in the stream. Thus, large densities and small mean particle velocity in the direction of the stream results in rapid effects of collisions with a rapid increase in mean kinetic energy due to transverse momenta, with the attendant rapid driving of subdistributions beyond the criterion of Eq. (11) so that there is a rapid loss of particles at the walls.

[16] W. H. Bennett, Phys. Rev. **90**, 387(A) (1953).

In conclusion the writer wishes to express his great appreciation for the opportunity to discuss with L. H. Thomas some of the mathematical methods used in this development.

MATHEMATICAL APPENDIX

A. Virial of Clausius in Cylindrical Coordinates

The probability that a charged particle of the κth kind is within a velocity range $d\dot{r}$ at $\dot{r}$, $d\dot{\phi}$ at $\dot{\phi}$ and $d\dot{z}$ at $\dot{z}$ at a position r, ϕ and z will be written

$$f_\kappa(r,\phi,z;\dot{r},\dot{\phi},\dot{z})d\dot{r}rd\phi d\dot{z},$$

where $\dot{r}$ is the velocity in the radial direction (direction of r); $\dot{\phi}$ is the angular velocity about the axis (direction of ϕ); and $\dot{z}$ is the velocity component parallel with the axis (direction of z). When this function is non-Maxwellian, it may be a function of the position coordinates. The function is normalized so that

$$\int_{-\infty}^{\infty}\int_{-\infty}^{\infty}\int_{-\infty}^{\infty} f_\kappa d\dot{r}r\dot{\phi}d\dot{z}=1.$$

The density ρ_κ of the κth kind of particle is a function of the position coordinates, only,—r, ϕ, and z. The velocity of mass motion of the κth kind of particle has components given by

$$\dot{r}_{\kappa 0}=\int\int\int \dot{r}f_\kappa d\dot{r}rd\phi d\dot{z},$$

$$r\dot{\phi}_{\kappa 0}=\int\int\int r\dot{\phi}f_\kappa d\dot{r}rd\phi d\dot{z},$$

$$\dot{z}_{\kappa 0}=\int\int\int \dot{z}f_\kappa d\dot{r}rd\phi d\dot{z}.$$

The velocity of any of the κth kind of particle may be considered to consist of the velocity of mass motion at the position of that particle plus the velocity of that particle relative to the velocity of mass motion, and the latter has components ξ, $r\eta$, and ζ where

$$\dot{r}=\dot{r}_0+\xi,\quad r\dot{\phi}=r\dot{\phi}_0+r\eta,\quad \dot{z}=\dot{z}_0+\zeta.$$

In the streams considered here, radial symmetry has been assumed so $\dot{\phi}_0=0$; and longitudinal uniformity has been assumed so $\partial\dot{z}_0/\partial z=0$. The mean square velocity of a particle of the κth kind relative to the velocity of mass motion has parts in the r and ϕ directions

$$\langle\xi_\kappa^2\rangle_{Av}=\int\int\int \dot{r}^2 f_\kappa d\dot{r}rd\phi d\dot{z}-\dot{r}_{\kappa 0}^2,$$

$$\langle\eta_\kappa^2\rangle_{Av}=\int\int\int \dot{\phi}^2 f_\kappa d\dot{r}rd\phi d\dot{z},$$

$$\langle\zeta_\kappa^2\rangle_{Av}=\int\int\int \dot{z}f_\kappa d\dot{r}rd\phi d\dot{z}-\dot{z}_{\kappa 0}^2.$$

If we write the mass of a particle of the κth kind as m_κ, the moment of inertia of that particle about the axis is $m_\kappa r^2$, and

$$\frac{1}{2}\frac{d^2}{dt^2}(m_\kappa r^2)=\frac{1}{2}m_\kappa\dot{r}^2+\frac{r}{2}m_\kappa\ddot{r},$$

where $m_\kappa\ddot{r}$ is related to the force F_κ exerted on that particle (in the radial direction in the streams assumed here) by $m_\kappa\ddot{r}=F_\kappa+m_\kappa r\dot{\phi}^2$. Substituting for F_κ from Eq. (2), integrating and summing over all particles in unit length of stream, and writing the moment of inertia of all particles in unit length of stream as I:

$$\frac{1}{4}\frac{d^2I}{dt^2}=\sum_\alpha\{\tfrac{1}{2}m_\alpha\dot{r}_{\alpha 0}^2+\tfrac{1}{2}m_\alpha\langle\xi_\alpha^2\rangle_{Av}+\tfrac{1}{2}m_\alpha r^2\langle\eta_\alpha^2\rangle_{Av}\}$$
$$+\sum_\alpha\sum_\beta e_\alpha e_\beta\left(1-\frac{u_\alpha u_\beta}{c^2}\right)\int_0^\infty\int_0^r\rho_\beta(s)2\pi s\,ds\rho_\alpha 2\pi r\,dr.$$

Reversing the order of integration in the last term and summing twice

$$\sum_\alpha\sum_\beta\int_0^\infty\int_0^r\rho_\beta(s)2\pi s\,ds\rho_\alpha 2\pi r\,dr$$
$$=\sum_\beta\sum_\alpha\int_0^\infty\int_r^\infty\rho_\alpha(s)2\pi s\,ds\rho_\beta 2\pi r\,dr$$
$$=\sum_\alpha\sum_\beta\int_0^\infty\int_r^\infty\rho_\beta 2\pi s\,ds\rho_\alpha 2\pi r\,dr.$$

Adding the first and last integral gives

$$\sum_\alpha\sum_\beta\int_0^\infty\int_0^\infty\rho_\beta 2\pi s\,ds\rho_\alpha 2\pi r\,dr=\sum_\alpha\sum_\beta N_\alpha N_\beta=N^2,$$

where N_α is the total number of particles of the αth kind per unit length of stream, and N is the total number of all particles per unit length of stream; so

$$\sum_\alpha\sum_\beta\int_0^\infty\int_0^r\rho_\beta 2\pi s\,ds\rho_\alpha 2\pi r\,dr=\tfrac{1}{2}\sum\sum N_\alpha N_\beta.$$

Writing ψ for the mean kinetic energy of particles due to transverse components of velocity,

$$\tfrac{1}{4}d^2I/dt^2=N\psi+\tfrac{1}{2}\{q^2-i^2/c^2\},$$

where $q=\sum_\alpha e_\alpha N_\alpha$ is the charge per unit length of stream and $i=\sum_\alpha e_\alpha u_\alpha N_\alpha$ is the electric current in the stream. From this, the stream will concentrate towards the axis, that is, it is self-focusing if $d^2I/dt^2<0$; that is,

$$i>c(2N\psi+q^2)^{\frac{1}{2}}.$$

B. Boltzmann's Equation in Cylindrical Coordinates

Using arguments analogous to those used by Jeans[17] but in cylindrical coordinates, Boltzmann's equation can be written for the particles of the κth subdistribution as

$$\frac{d(\rho_\kappa f_\kappa)}{dt}+\left(\frac{F_\kappa}{m_\kappa}+r\dot{\phi}^2\right)\frac{\partial(\rho_\kappa f_\kappa)}{\partial\dot{r}}$$
$$+\frac{1}{r}\left(\frac{\Phi_\kappa}{m_\kappa}-2\dot{r}\dot{\phi}\right)\frac{\partial(\rho_\kappa f_\kappa)}{\partial\dot{\phi}}+\frac{Z_\kappa}{m_\kappa}\frac{\partial(\rho_\kappa f_\kappa)}{\partial\dot{z}}$$
$$+\dot{r}\frac{\partial(\rho_\kappa f_\kappa)}{\partial r}+\dot{\phi}\frac{\partial(\rho_\kappa f_\kappa)}{\partial\phi}+\dot{z}\frac{\delta(\rho_\kappa f_\kappa)}{\partial z}=0,$$

where Φ_κ and Z_κ are the components of force on a κth kind of particle in the tangential and axial direction respectively and the radially symmetric and longitudinally uniform streams assumed here, are each equal to zero. Multiplying through by $\dot{r}/\rho_\kappa$ and integrating over the velocity ranges:

$$\frac{1}{\rho_\kappa}\frac{d(\rho_\kappa\dot{r}_{\kappa 0})}{dt}-\frac{F_\kappa}{m_\kappa}-r\langle\eta_\kappa^2\rangle_{Av}+\frac{2\dot{r}_{\kappa 0}^2}{r}+\frac{2\langle\xi_\kappa^2\rangle_{Av}}{r}$$
$$+\frac{r}{\rho_\kappa}\frac{\partial}{\partial r}\left(\frac{\rho_\kappa\dot{r}_{\kappa 0}^2}{r}\right)+\frac{r}{\rho_\kappa}\frac{\partial}{\partial r}\left(\frac{\rho_\kappa\langle\xi_\kappa^2\rangle_{Av}}{r}\right)+\frac{r}{\rho_\kappa}\frac{\partial}{\partial\phi}\left(\frac{\rho_\kappa\langle\xi_\kappa\eta_\kappa\rangle_{Av}}{r}\right)$$
$$+\frac{r}{\rho_\kappa}\frac{\partial}{\partial z}\left(\frac{\rho_\kappa\dot{r}_{\kappa 0}\dot{z}_{\kappa 0}}{r}\right)+\frac{r}{\rho_\kappa}\frac{\partial}{\partial z}\left(\frac{\rho_\kappa\langle\xi_\kappa\zeta_\kappa\rangle_{Av}}{r}\right)=0,$$

where

$$\langle\xi_\kappa\eta_\kappa\rangle_{Av}=\int\int\int(\dot{r}-\dot{r}_0)\phi f_\kappa d\dot{r}\,r\,d\phi\,d\dot{z}=0,$$

$$\langle\xi_\kappa\zeta_\kappa\rangle_{Av}=\int\int\int(\dot{r}-\dot{r}_{\kappa 0})(\dot{z}-\dot{z}_{\kappa 0})f_\kappa d\dot{r}\,r\,d\phi\,d\dot{z}=\dot{r}_{\kappa 0}\dot{z}_{\kappa 0},$$

and $\dot{z}_{\kappa 0}$ does not vary with r. In the above equation,

$$\frac{1}{\rho_\kappa}\frac{d(\rho_\kappa\dot{r}_{\kappa 0})}{dt}=\frac{d\dot{r}_{\kappa 0}}{dt}+\frac{\dot{r}_{\kappa 0}}{\rho_\kappa}\frac{d\rho_\kappa}{dt}.$$

$d\rho_\kappa/dt$ can be eliminated by using the equation of continuity:

$$\frac{d\rho_\kappa}{dt}+\frac{1}{r}\left\{\frac{\partial(r\rho_\kappa\dot{r}_{\kappa 0})}{\partial r}+\frac{\partial(r\rho_\kappa\dot{\phi}_{\kappa 0})}{\partial\phi}+\frac{\partial(r\rho_\kappa\dot{z}_{\kappa 0})}{\partial z}\right\}=0,$$

and in a radially symmetric and longitudinally uniform stream:

$$\frac{d\dot{r}_{\kappa 0}}{dt}+\dot{r}_{\kappa 0}\frac{\partial\dot{r}_{\kappa 0}}{\partial r}-\frac{F_\kappa}{m_\kappa}-r\langle\eta_\kappa^2\rangle_{Av}+\frac{1}{r\rho_\kappa}\frac{\partial}{\partial r}(r\rho_\kappa\langle\xi_\kappa^2\rangle_{Av})=0. \quad (19)$$

[17] J. H. Jeans, *Dynamical Theory of Gases* (Cambridge University Press, Cambridge, 1925), fourth edition, Chap. VIII.

In the steady state obtained by mixing, $\dot{r}_{\kappa 0}=0$. Multiplying through by $m_\kappa r/2$, writing the mean kinetic energy of the κth kind of particle due to radial motion as $\frac{1}{2}m_\kappa\langle\xi_\kappa^2\rangle_{Av}=\phi_\kappa$ and the mean kinetic energy due to tangential motion as $\frac{1}{2}m_\kappa r^2\langle\eta_\kappa^2\rangle_{Av}=\theta_\kappa$, and substituting for F_κ from Eq. (2):

$$e_\kappa\sum_\alpha e_\alpha\left(1-\frac{u_\kappa u_\alpha}{c^2}\right)\int_0^r \rho_\alpha 2\pi s\,ds + \theta_\kappa-\phi_\kappa-\frac{r}{\rho_\kappa}\frac{d(\rho_\kappa\phi_\kappa)}{dr}=0. \quad (20)$$

C. Relativistic Transformation of Variables

The transformation of velocities and of electric charge densities is explained in a book by McCrea.[18] Velocities are transformed by the well-known expression

$$u=\frac{u'+v}{1+u'v/c^2},$$

and the numerical densities are transformed by the seemingly less well known expression

$$\rho=\left(\frac{1+u'v/c^2}{(1-v^2/c^2)^{\frac{1}{2}}}\right)\rho'.$$

The charge on each charged particle is relativistically invariant but the numerical densities are not. It is for this reason that the charge density must be transformed.

The term "temperature" with all its usual implications cannot strictly speaking be applied to a subdistribution except as that subdistribution is viewed by an observer travelling with the velocity of that subdistribution. In the longitudinally uniform streams considered here, the effects of the thermal distribution in velocity component parallel with the axis cancel and only the distributions in velocity components transverse to the axis need be considered. The term temperature has been invoked here as a quantity proportional to θ_κ and to ϕ_κ which are each respectively proportional to the mass and to the square of the corresponding component of velocity. Thus, the temperature T' in a system of coordinates moving at a velocity v and used in this restricted sense is related to the T in the rest system of coordinates by

$$T'=T(m'/m)(u^2/u'^2) \quad \text{and} \quad T=T'(m/m')(u'^2/u^2).$$

Substituting for the ratios of mass and velocities squared[18]

$$T=\left(\frac{1-u'^2/c^2}{1-u^2/c^2}\right)^{\frac{1}{2}}\left(\frac{1-v^2/c^2}{(1+u'v/c^2)^2}\right)T'=\left(\frac{(1-v^2/c^2)^{\frac{1}{2}}}{1+u'v/c^2}\right)T'.$$

[18] W. H. McCrea, *Relativity Physics* (John Wiley and Sons, Inc., New York, 1954), fourth edition, Chaps 3 and 4 for velocities and Chap. 6 for electric charge. Note 8 on p. 61 is of particular interest in this connection.

D. Potential Energy per Unit Length of Stream

The force exerted on a charge e_κ with velocity u_κ parallel to the z-axis and at a distance r from a linear charge density λ_α parallel to the z-axis consisting of charges moving at a velocity u_α parallel to the z-axis is

$$\frac{2e_\kappa\lambda_\alpha}{r}\left(1-\frac{u_\kappa u_\alpha}{c^2}\right),$$

and the potential energy of that charge e_κ is

$$-\int_R^r 2e_\kappa\lambda_\alpha\left(1-\frac{u_\kappa u_\alpha}{c^2}\right)\frac{dr}{r} = -2e_\kappa\lambda_\alpha\left(1-\frac{u_\kappa u_\alpha}{c^2}\right)\log\left(\frac{r}{R}\right),$$

where the integration is performed from a finite radial distance R in order to avoid logarithmic infinities, where R is by definition the radial distance a charge must be from a linear charge for the potential energy to equal zero. The potential energy of a linear charge density λ_κ parallel to the z-axis (and to λ_α) at a distance r from λ_α is

$$-2\lambda_\kappa\lambda_\alpha\left(1-\frac{u_\kappa u_\alpha}{c^2}\right)\log\left(\frac{r}{R}\right).$$

Considering now an infinitely long thin shell of radius r, azimuthally uniform and longitudinally uniform, containing various kinds of charges of various axial velocities but mixed in uniform proportions everywhere in the shell. Among the charges in the shell, the αth kind of charge has N_α particles per unit length of shell, each with charge e_α and axial velocity u_α. The force exerted on a narrow ribbon of the κth kind of particle within an azimuthal angle of the shell $d\theta_\kappa$, by a narrow ribbon of the αth kind of particle within an angle $d\theta$ and located in the shell at an angle θ from $d\theta_\kappa$, is

$$\frac{2(N_\kappa/2\pi)d\theta_\kappa(N_\alpha/2\pi)d\theta}{2r\sin(\theta/2)}\left(1-\frac{u_\kappa u_\alpha}{c^2}\right),$$

and the potential energy equals

$$-\frac{e_\kappa e_\alpha N_\kappa N_\alpha}{2\pi^2}d\theta_\kappa d\theta\left(1-\frac{u_\kappa u_\alpha}{c^2}\right)\log\left(\frac{2r\sin(\theta/2)}{R}\right).$$

The potential energy of the κth ribbon due to all of the αth kind of charges is

$$-\frac{e_\kappa e_\alpha N_\kappa N_\alpha}{2\pi^2}d\theta_\kappa\left(1-\frac{u_\kappa u_\alpha}{c^2}\right)2\int_0^\pi \log\left(\frac{2r\sin(\theta/2)}{R}\right)d\theta = -\frac{e_\kappa e_\alpha N_\kappa N_\alpha}{\pi}\left(1-\frac{u_\kappa u_\alpha}{c^2}\right)\log\left(\frac{r}{R}\right)d\theta_\kappa,$$

and that due to all kinds of charge in the shell is

$$-\sum_\alpha \frac{e_\kappa e_\alpha N_\kappa N_\alpha}{\pi}\left(1-\frac{u_\kappa u_\alpha}{c^2}\right)\log\left(\frac{r}{R}\right)d\theta_\kappa.$$

The potential energy of all the κth kind of particle in the shell is

$$-\sum_\alpha \frac{e_\kappa e_\alpha N_\kappa N_\alpha}{\pi}\left(1-\frac{u_\kappa u_\alpha}{c^2}\right)\log\left(\frac{r}{R}\right)\int_0^{2\pi} d\theta_\kappa,$$

and potential energy of all kinds of charges in the stream, remembering that in summing twice, each charge is counted twice, is

$$-\sum_\alpha\sum_\beta e_\alpha e_\beta N_\alpha N_\beta\left(1-\frac{u_\alpha u_\beta}{c^2}\right)\log\left(\frac{r}{R}\right).$$

Suppose that the shell has an initial radius R so that the initial potential energy is zero, and that the shell is then shrunken to a small radius S so that the potential energy becomes

$$-\sum_\alpha\sum_\beta e_\alpha e_\beta N_\alpha N_\beta\left(1-\frac{u_\alpha u_\beta}{c^2}\right)\log\left(\frac{S}{R}\right),$$

after which the charges will be redeployed radially to density distributions $\rho(r)$ at radial distance r from the axis. The numbers of charges per unit length of shell are related to the density distributions after redeployment by

$$N_\alpha=\int_0^\infty \rho_\alpha(r)2\pi r dr.$$

The potential energy of the shrunken shell can be written

$$-\sum_\alpha\sum_\beta e_\alpha e_\beta\left(1-\frac{u_\alpha u_\beta}{c^2}\right)\log\left(\frac{S}{R}\right)\int_0^\infty\int_0^\infty \rho_\beta(\xi)2\pi\xi d\xi$$

$$\times\rho_\alpha(r)2\pi r dr=-2\sum_\alpha\sum_\beta e_\alpha e_\beta\left(1-\frac{u_\alpha u_\beta}{c^2}\right)\log\left(\frac{S}{R}\right)$$

$$\times\int_0^\infty\int_0^r \rho_\beta(\xi)2\pi\xi d\xi\rho_\alpha(r)2\pi r dr.$$

If in redeploying the charges, the charges are moved out to successive elementary shells beginning with the outermost, then in moving an element of the κth kind of charge $\rho_\kappa(r)2\pi r dr$ to radius r, the charges previously moved out to greater radial distances do not exert a force on these charges because of their symmetry as may be shown using Gauss' theorem, and only the charges left behind in the shrunken shell,

$$e_\alpha N_\alpha-\int_r^\infty e_\alpha\rho_\alpha 2\pi\xi d\xi=e_\alpha\int_0^r \rho_\alpha 2\pi\xi d\xi,$$

exert forces. The energy derived from moving all kinds of charges out to dr at r is

$$2\sum_\alpha\sum_\beta e_\alpha e_\beta\left(1-\frac{u_\alpha u_\beta}{c^2}\right)\log\left(\frac{r}{S}\right)\int_0^r \rho_\beta(\xi)$$

$$\times 2\pi\xi d\xi\rho_\alpha(r)2\pi r dr,$$

and the energy derived from moving all kinds of charges to all radii greater than S is

$$2\sum_\alpha\sum_\beta e_\alpha e_\beta\left(1-\frac{u_\alpha u_\beta}{c^2}\right)\int_S^\infty\log\left(\frac{r}{S}\right)\int_0^r \rho_\beta(\xi)$$

$$\times 2\pi\xi d\xi\rho_\alpha(r)2\pi r dr.$$

The total potential energy gained in shrinking the zero-energy shell to radius S and then expanding to density distributions $\rho_\alpha(r)$ is

$$-2\sum_\alpha\sum_\beta e_\alpha e_\beta\left(1-\frac{u_\alpha u_\beta}{c^2}\right)\int_0^\infty\log\left(\frac{S}{R}\right)$$

$$\times\int_0^r \rho_\beta 2\pi\xi d\xi\rho_\alpha 2\pi r dr,$$

$$-2\sum_\alpha\sum_\beta e_\alpha e_\beta\left(1-\frac{u_\alpha u_\beta}{c^2}\right)\int_0^\infty\log\left(\frac{r}{S}\right)$$

$$\times\int_0^r \rho_\beta 2\pi\xi d\xi\rho_\alpha 2\pi r dr,$$

$$+2\sum_\alpha\sum_\beta e_\alpha e_\beta\left(1-\frac{u_\alpha u_\beta}{c^2}\right)\int_0^S\log\left(\frac{r}{S}\right)$$

$$\times\int_0^r \rho_\beta 2\pi\xi d\xi\rho_\alpha 2\pi r dr.$$

As S is allowed to approach zero, the last term vanishes if the densities $\rho(r)$ are finite everywhere, which they would have to be in streams of the kind considered here, in order to avoid the infinitely rapid effects of collisions which would otherwise result from infinite densities. The potential energy per unit length of stream is obtained by adding the first two terms and is

$$-2\sum_\alpha\sum_\beta e_\alpha e_\beta\left(1-\frac{u_\alpha u_\beta}{c^2}\right)\int_0^\infty\int_0^r \rho_\beta(\xi)2\pi\xi d\xi$$

$$\times\log(r/R)\rho_\alpha(r)2\pi r dr.$$

Dissociation of Oxygen in the Upper Atmosphere

E. T. Byram, T. A. Chubb, and H. Friedman
U. S. Naval Research Laboratory, Washington, D. C.
(Received February 7, 1955)

The molecular oxygen content of the upper atmosphere between 110 and 130 km was determined by measuring the transmission of solar radiation in a narrow wavelength band from 1425 to 1500 A. The radiation was detected by means of an ultraviolet photon counter flown in an Aerobee rocket. At 130 km the concentration of O_2 was 10^{10} per cc. On the basis of the Rocket Panel density scale, 12 percent of the atmospheric oxygen was still undissociated.

MOLECULAR oxygen in the earth's upper atmosphere is dissociated by the action of solar ultraviolet light in the Schumann-Runge continuum below 1750 A. The degree of dissociation varies sharply with altitude and depends primarily on the solar intensity. For a 6000°K solar spectrum, theory[1] predicts a transition region about 10 kilometers thick, centered at a height of about 95 km, and essentially complete dissociation in *E*-layer. If the photospheric temperature is lower the rate of dissociation decreases and atmospheric mixing and diffusion begin to play an important role. Nicolet and Mange[2] have shown that the O_2 distribution may depart completely from photochemical equilibrium above 110 km if the solar temperature is as low as 4500°K.

It is possible to determine the partial pressure of O_2 independently of O and N_2 from a measurement of transmission of ultraviolet radiation in the spectral region near 1450 A at the maximum of the O_2 continuum. In this portion of the spectrum O_2 absorbs strongly and all other major atmospheric constituents are almost completely transparent. To perform the measurement in the upper atmosphere, a photon counter sensitive only to wavelengths near 1450 A was exposed from a rocket to the direct rays of the sun. The response of the detector at any particular altitude compared to the response at peak altitude was interpretable in terms of the intervening amount of atmospheric O_2.

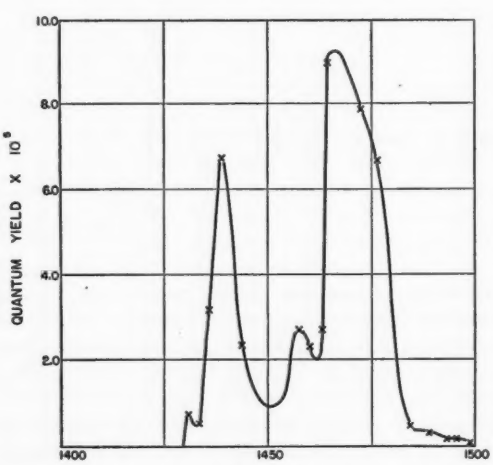

FIG. 1. Spectral sensitivity of photon counter filled with mixture of nitric oxide, helium, and xylene. Short-wavelength limit is characteristic of sapphire window. Long-wavelength limit is photoionization threshold of xylene.

INSTRUMENTATION

The first attempt at this type of measurement was made in a V-2 rocket experiment[3] in 1949. Although the data gave an indication of the rapid disappearance of O_2 above 100 km, the quantitative evaluation of O_2 concentration *versus* altitude was complicated by the fact that the detector exhibited a weak response to wavelengths longer than 1600 A. For the present experiments this difficulty was eliminated by the development of a photon counter which had high sensitivity between 1425 and 1500 A, but was essentially dead to light outside this band. The importance of the restriction on long wavelength sensitivity is apparent when the source of radiation resembles a blackbody with its maximum in the visible. If the effective sun temperature is 4500°K, the number of quanta between 1400 and 1500 A which enter the earth's atmosphere is about 2.9×10^{10} quanta cm^{-2} sec^{-1} as compared to 4.6×10^{12} quanta cm^{-2} sec^{-1} between 1500 and 2000 A. A satisfactory detector was made by filling a photon counter tube with a mixture of 43 mm NO, 640 mm He and 0.5 mm xylene. The window, which was mounted in the side of the tube, was a synthetic sapphire disk, 6 mm in diameter and 0.5 mm thick. The response of the tube is illustrated by the spectral sensitivity curve of Fig. 1 and may be attributed entirely to the photoionization of xylene. Longer wavelength response is suppressed by the capture of photoelectrons near the cathode by NO to form negative ions. The principle of operation of this type of tube is described in detail in a paper to be published.[4]

Calibration of the detector was carried out in the following manner. The response of the photon counter

[1] R. Penndorf, J. Geophys. Research **54**, 7 (1949).
[2] M. Nicolet and P. Mange, J. Geophys. Research **59**, 1 (1954).
[3] Friedman, Lichtman, and Byram, Phys. Rev. **83**, 1025 (1951).
[4] T. A. Chubb and H. Friedman, Rev. Sci. Instr. (to be published).

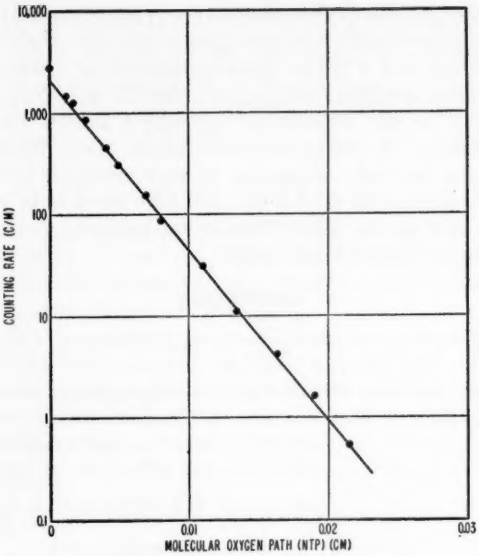

FIG. 2. Counting rate *versus* path length of light in molecular oxygen. Because of the broad maximum in the molecular oxygen continuum and the comparatively narrow band response of the photon counter, the semilog plot is almost a straight line with a slope of 386 cm^{-1} (base e).

to the light of a hydrogen discharge was obtained by means of a vacuum ultraviolet monochromator. The output of the monochromator was in turn measured by means of a photomultiplier, the front surface of which was coated with a fluorescent film of sodium salicylate. Finally, the multiplier and fluorescent film combination was calibrated by means of a standard Hg lamp at 2537 A. The fluorescent quantum efficiency of the salicylate was assumed to be independent of wavelength in accord with the measurements of Johnson *et al.*[5] and of Watanabe *et al.*[6]

To test the narrow band characteristic of the tube, it was exposed to the light of a corona discharge in hydrogen through an absorption column of air. By taking advantage of the fact that the intensity of the corona lamp could be varied over three decades without altering its spectral distribution, it was possible to measure the effective absorption coefficient of air over almost 4 decades. The results of this calibration are shown in Fig. 2 and support the conclusion that the entire response was confined to a narrow spectral region near the maximum of the O_2 absorption band. Each photon counter prepared for flight was checked similarly shortly before installation in the missile. The effective O_2 absorption coefficient determined in this way was used in calculating the amount of O_2 at high altitude from the rocket measurements.

The experiment was repeated in three Aerobee rockets which reached altitudes of 125, 106, and 130 km. The data of the two lower altitude flights are less complete, but appear to confirm the results of the last missile, on which the computations reported here are primarily based. The oxygen-measuring photon counter was one of a group of six counters of diverse types flown in the missile. Counting rates were continuously recorded throughout flight in the following manner. The pulse output of each counter drove its own thyratron ratemeter which delivered a signal to one channel of a 15-channel telemetering transmitter. As the rocket spun about its axis, each detector was in turn exposed to the direct rays of the sun. The angle between the sun and the normal to the counter window was measured by means of aspect calibrated photocells. The timed responses of the photon counters and aspect photocells together with radar tracking data (aided by a radar beacon transmitter in the rocket) furnished the raw data from which the oxygen distribution was derived.

EXPERIMENTAL RESULTS

The corrected counting rate *vs* altitude curve for the 1425–1500 A photon counter is shown in Fig. 3. These data were obtained by recording the peak counting rate on each rocket roll. The counting rate was corrected for losses due to counter dead-time. Next, an aspect correction was made to adjust for the angle between the sun and the normal to the counter window. The correction was determined from laboratory measurements of count rate *versus* aspect angle made by exposing similar counters to an ultraviolet lamp. At the peak, the dead-time correction amounted to 30 percent of the corrected count. During ascent to within one kilometer of peak, the rocket was very stable and the maximum aspect correction was 20 percent of the cor-

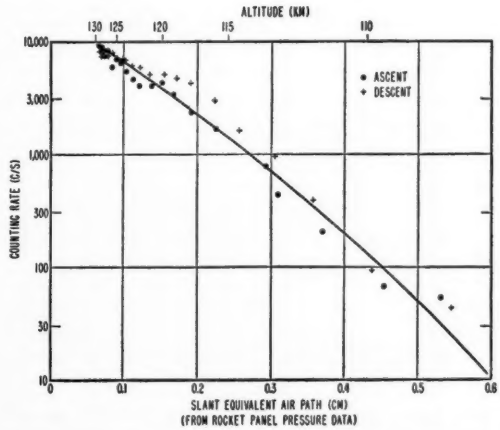

FIG. 3. Observed counting rate during flight of N.R.L. Aerobee 16 *versus* slant equivalent air path. In drawing the smooth curve greater weight was given to the ascent data since the required aspect corrections were smaller than for the descending portion of the flight.

[5] Johnson, Watanabe, and Tousey, J. Opt. Soc. Am. **41**, 702 (1951).
[6] Watanabe, Inn, and Zelikoff, J. Chem. Phys. **20**, 1969 (1952).

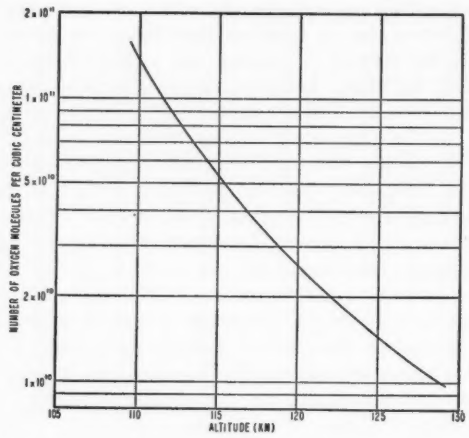

FIG. 4. Concentration of oxygen molecules *versus* altitude, computed from experimental data of Fig. 3.

rected count. On descent, the maximum aspect correction reached a value of 38 percent.

From the smooth curve drawn in Fig. 3, the number of O_2 molecules per cc was computed as a function of altitude and the result is shown in Fig. 4. An O_2 absorption coefficient of 386 cm^{-1} was used in calculating these results in accordance with the absorption measurements of Fig. 2. Figure 5 shows the total overhead vertical path of molecular oxygen reduced to NTP assuming that 0.43×10^{-3} cm-atmos of O_2 still remained above the missile at 130 km. This residual O_2 corresponded to an extrapolation of the count rate curve of Fig. 3 to a zero air path value of 16 500 counts/sec. Figure 6 shows the "percent dissociation of oxygen" as a function of altitude as computed from the amount of molecular oxygen shown in Fig. 4. Percent dissociation is expressed as,

$$\text{percent dissociation}=1-\frac{\rho(O_2)}{0.23\rho(\text{air})}, \qquad (1)$$

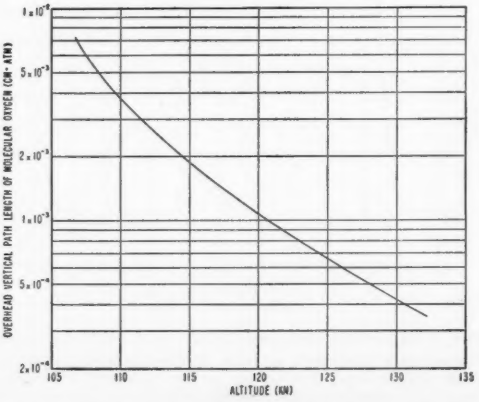

FIG. 5. Residual overhead O_2 path length *versus* altitude.

where $\rho(O_2)$ is the measured density of molecular oxygen and ρ(Air) is the assumed ambient density of air. In Fig. 6 Curve *A* is the "percent dissociation" based on ambient densities given by the Rocket Panel[7]; Curve *B* is the percent dissociation assuming $\frac{1}{3}$ Rocket Panel densities. The actual ambient densities above 100 km during the flight of Aerobee 16 were measured by air absorption of 44–60 A x-rays and were found to be less than 0.4 Rocket Panel densities and probably no more than 0.3 Rocket Panel values.

DISCUSSION

The rocket measurements show the existence of much larger quantities of molecular oxygen above 125 km than would be expected from a simple photochemical equilibrium. Since the time of diffusion becomes short compared to the time of dissociation above 125 km, an appreciable amount of O_2 will diffuse to the height

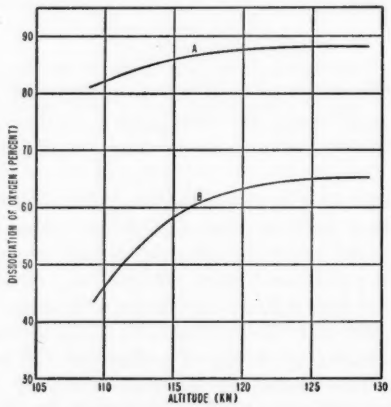

FIG. 6. Percent dissociation of atmospheric oxygen *versus* altitude. Curve *A* is based on air density published in Rocket Panel Report (see reference 7). Curve *B* is based on densities only one-third of the Rocket Panel values.

of F_2 region. Preliminary results of the present rocket measurements were used to support the theory[2] that the distribution of O_2 above 110 km is controlled by diffusive separation and turbulent mixing. At 170 km, Nicolet[8] computed an expected O_2 content at least 10^4 times as great as the photochemical values. The diffuseness of the transition region from O_2 to O is consistent with the comparatively weak solar intensity deduced from the photon counter measurements. In Aerobee 16, detectors which were sensitive in the spectral ranges 1230–1350 A and 1425–1500 A indicated photospheric radiation equivalent to blackbody emission at 3900°K and 4000°K respectively. This is in contrast to apparent solar temperatures of 5000°K at 2000 A[9] and 6000°K in the visible spectrum.

[7] Rocket Panel, Phys. Rev. **88**, 1027 (1952).
[8] M. Nicolet, J. Atm. and Terrest. Phys. **5**, 132 (1954).
[9] Johnson, Purcell, Tousey, and Wilson, Astrophys. J. **117**, 238 (1953).

The presence of O_2 at F-layer altitudes should have a profound effect on the rate of electron recombination as suggested by Bates and Massey.[10] Since atomic oxygen ions can be converted to molecular ions in collisions with neutral oxygen molecules, the molecular ions can then recombine with electrons by dissociative recombination,

$$e+O_2^+ \rightarrow O'+O''. \quad (2)$$

The recombination coefficient for this process may be as large as 10^{-7} cm^3 sec^{-1}. By contrast, in the absence of molecular oxygen, electron recombination proceeds by radiative recombination,

$$e+O^+ \rightarrow O+h\nu, \quad (3)$$

for which the recombination coefficient is of the order of 10^{-12} cm^3 sec^{-1}. Since the conversion of atomic to molecular ions,

$$O^+ + O_2 \rightarrow O_2^+ + O, \quad (4)$$

can take place by either charge exchange or by ion-atom interchange, a large reaction cross section is expected. According to Bates,[11] the rate coefficient for ion-atom interchange may be as high as 10^{-10} cm^3 sec^{-1}. The high-altitude O_2 concentrations indicated by the rocket experiment and the theoretical cross section for exchange ionization are sufficient to explain the recombination coefficients of 10^{-10} to 10^{-9} observed in F_2 region.[12] The manner in which the recombination coefficient decreases from E region to F_2 region depends on the partial pressure of O_2. The expected rate of decrease is sufficient to account for the production of a major portion of F_2 region by the same source of ionization that is responsible for F_1.[12,13]

[10] D. R. Bates and H. S. W. Massey, Proc. Roy. Soc. (London) **A192**, 1 (1947).

[11] D. R. Bates, Proc. Phys. Soc. (London) (to be published).

[12] Havens, Friedman, and Hulburt, Report of the Conference on the Physics of the Ionosphere, The Physical Society, London (1954).

[13] N. Bradbury, Terrestrial Magnetism and Atm. Elec. **43**, 55 (1938).

PHYSICAL REVIEW VOLUME 98, NUMBER 6 JUNE 15, 1955

Theory of Electron Penetration*

L. V. SPENCER
National Bureau of Standards, Washington, D. C.

(Received January 20, 1955)

The theory of electron penetration in an infinite medium under the combined influence of scattering and slowing down is developed to the point of numerical application. Sample calculations of energy dissipation *versus* distance from the source are compared with experiments by Frantz, by Clark, Brar, and Marinelli, and by Loevinger. The agreement is good provided that relativistic scattering cross sections are used. The energy loss is treated in the continuous slowing down approximation; the resulting error is appreciable only at extreme penetrations.

1. INTRODUCTION

THIS paper considers the following problem: A source of electrons with kinetic energy T_0 is embedded in a material. As the electrons move away from the source they lose energy and change direction. We want to determine the energy dissipated by the electrons at various locations in the material. A knowledge of the distribution of energy dissipation implies a knowledge of the spectral and directional distributions also, but this additional information need not be described explicitly.

Phenomenological work on this problem has been accomplished mainly by people interested in the biological effects of radiation. The most extensive effort of this type, and also the most recent, is that of Loevinger, whose paper contains a fairly complete summary of experimental work with beta-ray sources.[1] From a more basic standpoint the problem is essentially new, since few attempts—and those in unrealistic schematization—have been made to calculate electron spatial distributions taking into account both energy loss and direction changes, although both effects have a strong influence.[2,3] Many contributions have been made to-

* Work supported by the U. S. Atomic Energy Commission and the Office of Naval Research.

[1] R. Loevinger (private communication).

[2] For efforts to apply age diffusion theory to electron penetration problems see Bethe, Rose, and Smith, Proc. Am. Phil. Soc. **78**, 573 (1938) and W. C. Roesch, Hanford Report No. HW-32121, May 24, 1954 (unpublished). There can be hardly any doubt that this simple model gives better than an order-of-magnitude estimate of the distance electrons travel "on the average." However, two important features of the penetration are given wrongly: (a) The initial transient stage of the penetration when electrons move directly away from the source, which is particularly important for high-energy sources or for low-Z scattering materials; and (b) the deep-penetration trend. The results of this paper indicate that there is hardly any region of penetration in which age diffusion theory can be expected to provide a reasonable description.

[3] For calculations of electron backscattering see J. W. Weymouth, Phys. Rev. **84**, 766 (1951). Weymouth took into account energy losses as well as deflections, but only in the approximation of an energy-independent scattering cross section. He did not attempt to calculate electron spatial distributions.

wards understanding simpler situations, in which one or another effect is neglected. For example, many authors have neglected angular deflections in calculating spatial distributions as a function of energy loss.[4] This is the so-called straggling problem. Other authors have neglected energy loss effects in calculating angular distributions produced by penetration.[5] In addition, there has been work relating the deflections to energy losses neglecting the spatial dependence[6] and some work on energy losses neglecting *both* direction and spatial location.[7] A discussion of these partial problems together with their inter-relationships is given in the first part of Fano's paper on straggling and energy loss of charged particles.[8]

H. W. Lewis took the first step towards a more realistic theoretical treatment of the electron penetration when he wrote down formal expressions for the spatial moments of the electron distribution.[9] These were based on a continuous energy loss approximation. Both elastic and inelastic deflections were included in his derivation, the latter being considered as statistically independent of the energy losses. Lewis made no attempt to evaluate the moments numerically in a systematic way or to use them to obtain spatial distributions.

Following the publication of Lewis' paper, evaluation of a limited number of moments was accomplished in nonrelativistic approximation by Blanchard.[10] Blanchard also found very useful approximate expressions for the harmonic coefficients of the zeroth spatial moment, which have special interest.[6] Attempts were then made by Blanchard and others to construct spatial distributions from a knowledge of the first few moments.[10] The results were generally unsatisfactory, because the information contained in the first few moments did not seem sufficient for such a construction.

The essential information which was lacking in this earlier work was a knowledge of the asymptotic (deep-penetration) trend. Although complete knowledge of the spatial moments theoretically should yield the distribution, in practice it is not possible to calculate more than a finite, comparatively small number of spatial moments and these with imperfect accuracy. Construction of a spatial distribution is equivalent to extrapolating this finite set of imperfectly known moments to infinite order. Unless the trend of the high-order spatial moments is known from a determination of the deep-penetration spatial trend, such an extrapolation cannot be made with confidence.

Several developments have now made it possible to calculate realistic electron spatial distributions at least for situations in which bremsstrahlung energy losses may be neglected. First, methods were developed for rapid desk-computer calculation of large numbers of spatial moments. When numerical values for the moments were graphed, they showed very clearly the trend predicted by a Wick-type asymptotic calculation,[11] so much so that the high moments seemed to contribute little additional information. This "break" made spatial distribution constructions feasible. Next, methods had to be found for combining into an analytic form (a) the known values of a number of spatial moments, (b) the asymptotic trend, and (c) additional odds and ends of information about the distribution. This was not easy, because traditional methods did not seem to work. Eventually "function-fitting" techniques were developed similar to those which have proved useful in x-ray penetration problems,[12] and satisfactory constructions were made. Finally, a much better theoretical derivation of the all-important deep-penetration trend was discovered which removed remaining questions about its reliability and range of application.

The methods for calculating spatial moments are described in Secs. 2, 3, and 4. The deep-penetration trend is then considered (Sec. 5), but only in connection with a Wick-type argument (Appendix D) since the newer derivation will be presented in a later paper. Additional information which must be used in constructing distributions is given in Sec. 6. All the presentation up to this point deals explicitly with plane monodirectional and monoenergetic electron sources because they are easily visualized, although the principles apply to other types as well. The remaining sections contain material about several source types. The actual construction of distributions is discussed in Secs. 7 and 8. In Sec. 9 there are several examples of calculations in plane monodirectional geometry. These are compared with experiments by Frantz [see Sec. 9(B)]. In Sec. 10

[4] See L. Landau, J. Phys. (U.S.S.R.) **8**, 201 (1944); O. Blunck and S. Leisegang, Z. Physik **128**, 500 (1950); also, for heavy particles, K. R. Symon, Harvard thesis, 1948 (unpublished) whose results are extensively quoted by B. Rossi, *High Energy Particles* (Prentice-Hall Inc., New York, 1952), pp. 29 ff.

[5] E. J. Williams, Proc. Roy. Soc. (London) **169**, 531 (1939); S. Goudsmit and J. L. Saunderson, Phys. Rev. **57**, 24 (1940); G. Molière, Z. Naturforsch. **32**, 78 (1948); H. S. Snyder and W. T. Scott, Phys. Rev. **76**, 220 (1949); H. A. Bethe, Phys. Rev. **89**, 1256 (1953); and L. V. Spencer, Phys. Rev. **90**, 146 (1953). Also of this type but emphasizing mainly the backscattering are papers by W. Bothe, Z. Physik **54**, 161 (1929); Bethe, Rose, and Smith, Proc. Am. Phil. Soc. **78**, 573 (1938); M. C. Wang and E. Guth, Phys. Rev. **84**, 1092 (1951); T. Teichman, Atomic Energy Commission Document NYO-785, 1951 (unpublished); and E. J. Saletan, Atomic Energy Commission Document NYO-3990, 1952 (unpublished).

[6] C. H. Blanchard, National Bureau of Standards Circular 527, 1954, p. 9. Note that with the continuous energy loss approximation, which relates path length to energy loss, most of the papers of the preceding footnote can be considered in this category also.

[7] L. V. Spencer and U. Fano, Phys. Rev. **93**, 1172 (1954).

[8] U. Fano, Phys. Rev. **92**, 328 (1953).

[9] H. W. Lewis, Phys. Rev. **78**, 526 (1950).

[10] C. H. Blanchard (private communication).

[11] G. C. Wick, Phys. Rev. **75**, 738 (1949). This type of analysis was first applied to an electron penetration problem by Yang [C. N. Yang, Phys. Rev. **84**, 599 (1951)]. He derived the path length distribution for a fixed and small penetration. We seek the related penetration distribution for a fixed path length. Yang's limitation to small energy loss makes the Wick-type analysis much more straightforward than in the general case.

[12] L. V. Spencer, Phys. Rev. **88**, 793 (1952).

there are sample calculations for point and plane isotropic P^{32} sources which are compared with experiments by Clark, Brar, and Marinelli and by Loevinger.[1] In all comparisons, theory and experiment agree to perhaps three percent or better except where extraneous effects are to be expected. These extraneous effects are range straggling, which has not been included in the calculations and which becomes important at the very deepest penetrations, and a boundary at the source plane which is present in Frantz's experiment.

The remarks at the end are mainly concerned with methods for extending the theory to more general situations and including effects neglected in this treatment.

2. THE TRANSPORT EQUATION

Our presentation relates chiefly to monoenergetic and monodirectional sources which are distributed uniformly over an infinite plane and to scattering media which are homogeneous and without boundaries.[13] The use of monoenergetic sources is not a limitation since problems involving polychromatic sources can be solved by simple integration over monoenergetic source results. The consideration of only plane monodirectional geometry is likewise not particularly a limitation. Other simple geometries can be treated in the same way.[14] In particular, it is easily possible to convert a solution for a *plane isotropic* source into a solution for a *point isotropic* source. This conversion is discussed in Sec. 8.

If an electron source located at the plane $z=0$ emits monoenergetic electrons in the direction $\theta=0$ perpendicular to the source plane, Lewis' equation[9] describing the penetration may be written as follows:

$$-\frac{\partial I}{\partial r}+\cos\theta\frac{\partial I}{\partial z}=\int d\Omega' N\sigma(r,\Theta)\{I(r,\theta',z)-I(r,\theta,z)\}+(2\pi)^{-1}\delta(z)\delta(r-r_0)\delta(\cos\theta-1). \quad (1)$$

Here, $2\pi I(r,\theta,z)\sin\theta d\theta dr$ is the *flux* of electrons, with obliquities between θ and $\theta+d\theta$ and with residual ranges between r and $r+dr$, crossing the surface of a unit spherical probe located a distance z from the source plane. Likewise, $2\pi\sigma(r,\Theta)\sin\Theta d\Theta$ is the cross section per atom for deflecting an electron with residual range r through an angle of a size between Θ and $\Theta+d\Theta$, while N is the number of atoms per gram of material. The term on the right containing the Dirac delta functions specifies the electron source.[15]

By assuming that the electrons lose their energy continuously, a relation is established between the residual true range r and the kinetic energy of the electrons. The average rate of energy loss is the stopping power (dT/dr), for which theoretical expressions exist.[16] The connection between r and T is given by the following integral over the stopping power:

$$r(T)=\int_0^T dT(dT/dr)^{-1}. \quad (2)$$

Table I gives electron ranges which have been calculated numerically by integrating over stopping powers determined from the Bethe formula. Note that throughout this paper T expresses kinetic energy in mc^2 units while r is measured in g/cm^2.

At this point it is convenient to rescale the distance parameters, taking $r_0=r(T_0)$ as a unit. Defining $t=(r/r_0)$, $x=(z/r_0)$, $S(t,\Theta)=r_0N\sigma(r,\Theta)$, and $I(r,\theta,z)dr=I(t,\theta,x)dt$, the transport equation takes the form

$$-\frac{\partial I}{\partial t}+\cos\theta\frac{\partial I}{\partial x}=\int d\Omega' S(t,\Theta)\{I(t,\theta',x)-I(t,\theta,x)\}+(2\pi)^{-1}\delta(x)\delta(t-1)\delta(\cos\theta-1), \quad (3)$$

where the dimensionless energy parameter t varies from 0 to 1, while the space parameter x varies from -1 to $+1$.

The first step in treating this complicated equation is an expansion in spherical harmonics, which is easily performed with the aid of the well-known addition theorem. Defining

$$I_l(t,x)=2\pi\int_{-1}^{1}d(\cos\theta)P_l(\cos\theta)I(t,\theta,x),$$
$$S_l(t)=2\pi\int_{-1}^{1}d(\cos\Theta)\{1-P_l(\cos\Theta)\}S(t,\Theta), \quad (4)$$

Eq. (3) may be transformed to a linked system of differential equations:

$$-\frac{\partial I_l}{\partial t}+(2l+1)^{-1}\left\{(l+1)\frac{\partial I_{l+1}}{\partial x}+l\frac{\partial I_{l-1}}{\partial x}\right\}+S_l(t)I_l(t,x)=\delta(x)\delta(t-1). \quad (5)$$

The second step is a transformation in terms of spatial moments. The Eqs. (5) are multiplied by different powers of x and integrated over the whole range $-1<x<+1$. The resulting system of equations is the

[13] The calculation of boundary effects, even for the simplest geometries, is an unsolved problem. As mentioned in references 2 and 3, some attempts have been made assuming that the electrons do not lose energy or that scattering cross sections are energy independent; however, no method applicable to more general situations has yet been developed.

[14] L. V. Spencer and U. Fano, J. Research, Natl. Bur. Standards 46, 446 (1951), where a point-collimated source is also considered. The relation between point and plane isotropic sources is well known from neutron penetration literature.

[15] A word about dimensions: If $I(r,\theta,z)$ has dimensions number per cm^2 per steradian per (g/cm^2) residual range, $N\sigma(r,\Theta)$ being cm^2/g per steradian and r, z being measured in g/cm^2, the first three terms are obviously consistent and the source has the strength (integrated over r, z, Ω) of one electron per cm^2.

[16] H. A. Bethe, *Handbuch der Physik* (Verlag Julius Springer, Berlin, 1933), 24, Part 1, pp. 491 ff.; Ann. Physik 5, 325 (1930).

TABLE I. Stopping powers and corresponding residual ranges for electrons calculated from the Bethe formula. The mean ionization potential used is in each case given at the bottom of the column.

Mev	Beryllium Stopping power $mc^2/(g/cm^2)$	Beryllium Residual range g/cm^2	Polystyrene Stopping power $mc^2/(g/cm^2)$	Polystyrene Residual range g/cm^2	Air Stopping power $mc^2/(g/cm^2)$	Air Residual range g/cm^2	Aluminum Stopping power $mc^2/(g/cm^2)$	Aluminum Residual range g/cm^2
0.01	36.83	0.000298	44.55	0.000247	38.80	0.000285	33.25	0.000339
0.03	15.64	0.00211	18.92	0.00175	16.67	0.00199	14.625	0.00230
0.05	10.67	0.00521	12.91	0.00431	11.42	0.00490	10.101	0.00559
0.07	8.402	0.00939	10.17	0.00776	9.011	0.00880	8.008	0.00999
0.10	6.631	0.01734	8.026	0.01514	7.127	0.01619	6.362	0.01830
0.20	4.489	0.05457	5.435	0.04590	4.843	0.05074	4.356	0.05684
0.30	3.780	0.1026	4.576	0.08556	4.087	0.09521	3.690	0.1062
0.40	3.444	0.1571	4.171	0.1306	3.729	0.1456	3.377	0.1619
0.50	3.260	0.2156	3.947	0.1789	3.533	0.1996	3.206	0.2215
0.60	3.150	0.2768	3.814	0.2294	3.417	0.2560	3.105	0.2836
0.70	3.081	0.3397	3.731	0.2813	3.345	0.3139	3.044	0.3473
0.80	3.038	0.4037	3.679	0.3342	3.300	0.3729	3.007	0.4120
0.90	3.011	0.4684	3.646	0.3876	3.272	0.4324	2.985	0.4774
1.00	2.994	0.5336	3.626	0.4415	3.256	0.4924	2.973	0.5431
1.20	2.981	0.6646	3.611	0.5497	3.245	0.6129	2.967	0.6750
1.40	2.984	0.7959	3.614	0.6581	3.250	0.7335	2.975	0.8068
1.60	2.995	0.9269	3.627	0.7662	3.263	0.8537	2.991	0.9380
1.80	3.010	1.057	3.645	0.8738	3.281	0.9733	3.010	1.068
2.00	3.027	1.187	3.666	0.9809	3.301	1.092	3.031	1.198
2.20	3.046	1.316	3.689	1.087	3.323	1.210	3.053	1.327
2.40	3.065	1.444	3.712	1.193	3.345	1.328	3.076	1.454
2.60	3.084	1.571	3.736	1.298	3.367	1.444	3.098	1.581
2.80	3.103	1.698	3.759	1.403	3.389	1.560	3.119	1.707
3.00	3.122	1.824	3.781	1.506	3.410	1.675	3.141	1.832
4.00	3.208	2.442	3.886	2.017	3.508	2.241	3.237	2.446
5.00	3.281	3.045	3.975	2.515	3.591	2.792	3.318	3.043
6.00	3.346	3.635	4.054	3.002	3.664	3.332	3.390	3.626
8.00	3.451	4.786	4.181	3.952	3.783	4.382	3.506	4.760
10.00	3.536	5.906	4.283	4.876	3.878	5.403	3.598	5.862
	$I=60$ ev		$I_H=15.6$ ev $I_C=76.4$ ev		$I_N=80.5$ ev $I_O=92$ ev $I_A=207$ ev		$I=150$ ev	

Mev	Copper Stopping power $mc^2/(g/cm^2)$	Copper Residual range g/cm^2	Cadmium Stopping power $mc^2/(g/cm^2)$	Cadmium Residual range g/cm^2	Gold Stopping power $mc^2/(g/cm^2)$	Gold Residual range g/cm^2
0.01						
0.03	11.91	0.00288				
0.05	8.335	0.00690				
0.07	6.656	0.01220	5.735	0.01433		
0.10	5.323	0.02217	4.610	0.02586	3.926	0.03083
0.20	3.687	0.06791	3.219	0.07842	2.772	0.09214
0.30	3.142	0.1260	2.754	0.1448	2.386	0.1690
0.40	2.886	0.1913	2.538	0.2191	2.206	0.2546
0.50	2.749	0.2609	2.422	0.2982	2.111	0.3455
0.60	2.669	0.3332	2.356	0.3802	2.058	0.4395
0.70	2.622	0.4073	2.318	0.4640	2.028	0.5353
0.80	2.594	0.4823	2.296	0.5489	2.013	0.6322
0.90	2.579	0.5580	2.285	0.6344	2.006	0.7297
1.00	2.572	0.6340	2.281	0.7201	2.004	0.8273
1.20	2.573	0.7862	2.285	0.8916	2.012	1.022
1.40	2.585	0.9381	2.299	1.062	2.027	1.216
1.60	2.602	1.089	2.317	1.232	2.046	1.408
1.80	2.623	1.239	2.337	1.400	2.066	1.599
2.00	2.644	1.387	2.358	1.567	2.087	1.787
2.20	2.666	1.535	2.380	1.732	2.108	1.974
2.40	2.688	1.681	2.401	1.896	2.128	2.158
2.60	2.710	1.826	2.421	2.058	2.148	2.341
2.80	2.731	1.970	2.441	2.219	2.168	2.523
3.00	2.751	2.113	2.461	2.379	2.186	2.703
4.00	2.844	2.812	2.549	3.160		
5.00	2.921	3.491	2.621	3.917		
6.00	2.989	4.153	2.685	4.654		
8.00	3.099	5.437				
10.00	3.186	6.683				
	$I=310$ ev		$I=480$ ev		$I=790$ ev	

following:

$$-\frac{\partial I_{ln}}{\partial t}+S_l(t)I_{ln}(t)=n(2l+1)^{-1}\{(l+1)I_{l+1,n-1}(t)+lI_{l-1,n-1}(t)\}+\delta_{n0}\delta(t-1), \quad (6)$$

where

$$I_{ln}(t)=\int_{-1}^{1}dx x^n I_l(t,x). \quad (7)$$

As discussed in reference 9, formal solutions to Eqs. (6) may be written down. Using these formal solutions, or using Eqs. (6) in much the same manner as in x-ray penetration calculations,[14] the moment coefficients $I_{ln}(t)$ may be determined by numerical integration. However, the selection of numerical methods depends on the behavior of the functions $S_l(t)$. We therefore discuss these functions in the next section and in Appendix A. It turns out from a study of the $S_l(t)$ that other, simpler procedures than straightforward numerical integration may be used to obtain numerically the $I_{ln}(t)$.

3. CROSS SECTIONS

A. Screened Rutherford

The simplest approximate form for the nuclear scattering cross section is the Rutherford formula. For our purposes this cross section should be modified to take into account (a) the screening of the nuclear field by the atomic electrons, (b) deflections caused by inelastic collisions between electrons, and (c) relativistic effects.

As discussed by Bethe,[17] the screening effect may be accounted for by introducing a single parameter. We have chosen to introduce this screening constant η in the Rutherford expression by writing $\frac{1}{4}(1+2\eta-\cos\theta)^{-2}$ in place of the familiar factor $\sec^4(\theta/2)$. In our initial calculations, inelastic deflections were accounted for by means of a multiplicative factor $(Z+1)/Z$. The expression resulting from these modifications is the following:

$$2\pi N\sigma[r(T),\theta]=(3/4)(Z+1)(N_A\phi_0 Z/A)(T+1)^2\times T^{-2}(T+2)^{-2}(1+2\eta-\cos\theta)^{-2}, \quad (8)$$

where the functional relationship between T and r is that of expression (2). In (8), N_A is Avogadro's number, A is the atomic weight, and $\phi_0=(8\pi e^4/3m^2c^4)$. Note that this expression includes relativistic effects insofar as they modify the cross section for very small angles θ. The screening constant η can be determined from the formula of Molière[18]:

$$\eta=\frac{1}{4}\left[\frac{Z^{\frac{1}{3}}}{0.885(137)}\right]^2 T^{-1}(T+2)^{-1}\times[1.13+3.76(Z/137)^2(T+1)^2T^{-1}(T+2)^{-1}]. \quad (9)$$

[17] H. A. Bethe, Phys. Rev. **89**, 1256 (1953).
[18] G. Molière, Z. Naturforsch. **2A**, 133 (1947).

As is discussed in Appendix B, the cross section (8) leads to the following expression for the S_l's:

$$S_l[t(T)]=(Z+1)[3N_A\phi_0 Z/4A]\times(T+1)^2T^{-2}(T+2)^{-2}\tau_0 C_l,$$
$$C_0=0,$$
$$C_1=\ln(1+\eta^{-1})-(1+\eta)^{-1},$$
$$C_{l+1}=(2+l^{-1})(1+2\eta)C_l-(1+l^{-1})C_{l-1}-(2+l^{-1})(1+\eta)^{-1}. \quad (10)$$

B. Relativistic Forms

Nearly all of our initial calculations were performed by using the expressions (8) and (9). However, a later investigation indicated that if the simple angular dependence of (8) were replaced by the correct relativistic distribution given by the Mott formulas,[19] the S_l's would be modified by as much as 20 percent for large-Z scattering materials at energies as low as $T=1$. Such a modification would markedly affect the electron spatial distributions. It therefore seemed wise to base all further calculations on correct relativistic angular distributions. An investigation of the literature indicated that for some regions of Z and T these have been calculated while for others they apparently have not. Feshbach has made tabulations for a variety of Z's which can be used for $T>8$.[20] For $Z=80$ and a variety of T values, tabulations have been made by Bartlett and Watson[21] and by Massey.[22] For small Z it is possible to use the McKinley-Feshbach expressions.[23] There seem to be no tabulations or formulas approximating the Mott expression for intermediate Z and small T.[24]

A much less important improvement which has nevertheless seemed desirable is that of correcting more accurately for inelastic deflections. This can be done by introducing an additional factor which can be calculated from a formula due to Fano.[25] Although this modification tends to be small, it may be appreciable if Z is low enough.

For calculations in low-Z materials, we use the following expression for the cross section, which relies on the McKinley-Feshbach angular distribution:

$$2\pi N\sigma[r(T),\theta]=(Z+1)(3N_A\phi_0 Z/4A)(1+\epsilon)T^{-1}\times(T+2)^{-1}\beta^{-2}\{(1+2\eta-\cos\theta)^{-2}+2^{-1}\pi\alpha\beta(1-\cos\theta)^{-\frac{1}{2}}-\tfrac{1}{2}(\beta^2+\pi\alpha\beta)(1-\cos\theta)^{-1}\}, \quad (11)$$
$$\alpha=(Z/137), \quad \beta^2=T(T+2)(T+1)^{-2},$$

[19] N. F. Mott and H. S. W. Massey, *Theory of Atomic Collisions* (Oxford University Press, London, 1949), second edition, Chap. IV.
[20] H. Feshbach, Phys. Rev. **88**, 295 (1952).
[21] J. H. Bartlett and R. E. Watson, Proc. Am. Acad. Arts Sci. **74**, 53 (1940).
[22] H. S. W. Massey, Proc. Roy. Soc. (London) **A181**, 14 (1942).
[23] W. A. McKinley, Jr., and H. Feshbach, Phys. Rev. **74**, 1759 (1948).
[24] Note that this region is so big that angular distributions change too much to make interpolation feasible.
[25] U. Fano, Phys. Rev. **93**, 117 (1954).

TABLE II. Scattering parameters σ_l as a function of energy. Compare the exact values of columns 2 and 6 with the analytic approximation values in columns 3 and 7. Observe also the constancy of σ_l/σ_1 ratios.

	Aluminum				Gold			
		$\frac{3.193}{r(r+1.492)}$				$\frac{33.93}{r(r+2.086)}$		
Mev	(cm^2/g) $N\sigma_1$		σ_2/σ_1	σ_3/σ_1	(cm^2/g) $N\sigma_1$		σ_2/σ_1	σ_3/σ_1
2.0	0.9905	0.9907	2.838	5.381	4.902	4.902	2.613	4.631
1.6	1.406	1.401	2.830	5.353	6.948	6.895	2.598	4.581
1.2	2.193	2.183	2.818	5.311	10.80	10.68	2.576	4.512
0.9	3.404	3.396	2.804	5.264	16.64	16.52	2.552	4.436
0.7	4.997	4.998	2.789	5.216	24.18	24.18	2.527	4.363
0.5	8.385	8.413	2.766	5.142	39.77	40.39	2.489	4.254
0.3	18.78	18.82	2.724	5.013	84.78	89.04	2.417	4.056
0.1	127.9	115.5	2.621	4.692	462.3	519.9	2.195	3.440

where, according to Fano,

$$\epsilon=(Z+1)^{-1}(\ln 4\eta)^{-1} \times\{u_{in}-\ln[0.16Z^{\frac{1}{3}}(1+3.33\alpha/\beta)]\}, \quad (12)$$

$-u_{in}$ being a number which differs from one material to the next but which has a value in the neighborhood of 5. The expression for the S_l's which derives from (11) is

$$S_l[t(T)]=(Z+1)(3N_A\phi_0Z/4A)(1+\epsilon)T^{-1}(T+2)^{-1}\beta^{-2} \times\left\{C_l+2\pi\alpha\beta l-(\beta^2+\pi\alpha\beta)\sum_{i=1}^{l}i^{-1}\right\}r_0. \quad (13)$$

For calculations of electron penetration in gold, it proved convenient to represent the cross section by the following expression:

$$2\pi N\sigma[r(T),\theta]=(Z+1)(3N_A\phi_0Z/4A)(1+\epsilon)T^{-1} \times(T+2)^{-1}\beta^{-2}\{(1+2\eta-\cos\theta)^{-2} +B(1-\cos\theta)^{-1}+C+D(1-\cos\theta)\}, \quad (14)$$

where B, C, and D are determined so that (14) agrees with the Bartlett-Watson tabulations at appropriate angles. Such a form was found capable of representing the tabulations to 2 percent or better for all angles and all energies. The corresponding formula for the S_l's is

$$S_l[t(T)]=(Z+1)(3N_A\phi_0Z/4A)(1+\epsilon)T^{-1} \times(T+2)^{-1}\beta^{-2}\left\{C_l+2B\sum_{i=1}^{l}i^{-1} +2C(1-\delta_{l0})+2D(1-\delta_{l0}+\tfrac{1}{3}\delta_{l1})\right\}r_0. \quad (15)$$

Both (15) and (13) result from integrals evaluated in Appendix B.

C. Analytic Representations

The expressions (10), (13), and (15) are not simple. However, the S_l's may always be represented with considerable accuracy by the approximate form

$$S_l(t)\approx\alpha d_l/[t(t+\alpha)], \quad (16)$$

where α and d_l are numbers independent of t. The argument which suggested this formula, which was first made by Blanchard[26] and is contained in Appendix A, is not particularly conclusive. However, the accuracy of this representation can be easily demonstrated. For example, it is apparent that (16) holds if the scattering parameters $\sigma_l(r)=\int d\Omega\{1-P_l(\cos\theta)\}\sigma(r,\theta)$ are proportional to $r^{-1}(r+b)^{-1}$, where b is a constant. This, in turn, is the case if $\sigma_1(r)\propto r^{-1}(r+b)^{-1}$ and if the ratios $\sigma_l(r)/\sigma_1(r)$ are independent of r. Table II contains comparisons which demonstrate these proportionalities.

If the source energy is less than about 1 mc^2, an even simpler approximate expression agrees fairly well with the S_l's:

$$S_l(t)\approx d_l/t. \quad (17)$$

This is because the constant α becomes large for low source energies (see Appendix A).

We have used the approximate expressions (16) and (17) in all of our calculations of electron penetration. The discussion contained in the next two sections is based on these representations, which make possible far less laborious methods for the solution of the system (6) than direct numerical or analytical integration.

It should be noted that, as evidenced by Table II, the approximate expressions (16) and (17) are not particularly accurate for $t\ll 1$. This departure becomes somewhat more serious as l becomes larger. This should not particularly affect the accuracy of calculations based on (16) and (17) for several reasons: (a) These discrepancies occur when the electrons have very little of their range and energy left and may be expected to be nearly isotropic in direction. (b) In addition, the scattering cross section for small t becomes large. Thus, the small portion of the electron range where the discrepancy occurs is chiefly spent by the electrons in going around and around rather than in penetrating deeper into the medium. Finally, (c) the fact that the directional distribution of the electrons tends to be isotropic for small t simply means that the higher harmonics, where the discrepancy is larger, are of little importance.

[26] C. H. Blanchard (private communication).

4. CALCULATION OF MOMENTS

We can now discuss methods for calculating the spatial moments $I_{ln}(t)$. The use of the moments once they have been obtained is described in the sections following. For clarity, we relate our discussion mainly to expression (17) for the S_l's. The additional effort involved in using the more general expression (16) is mentioned only at the end of the section, the details being presented in Appendix C.

The formal solution of the differential Eqs. (6) has already been written down by Lewis[7]:

$$I_{ln}(t)=\int_t^1 dt' \exp\left\{-\int_t^{t'} dt'' S_l(t'')\right\} \times\{n(2l+1)^{-1}[(l+1)I_{l+1,n-1}(t') +lI_{l-1,n-1}(t')]+\delta_{n0}\delta(1-t')\}. \quad (18)$$

In general, the evaluation of the integrals in (18) must be done numerically. We may estimate the difficulty of such integrations by inserting into (18) the simple form (17) for $S_l(t)$. Use of (17) also makes possible analytic evaluation of at least some of the integrals, this being feasible only for $n\lesssim 4$ because of a rapid increase, with increasing n, in the complexity of the expressions for $I_{ln}(t)$.

With the use of (17), the exponential factor in the integrand of (18) becomes simply $(t'/t)^{d_l}$. As may be seen from Table II, the d_l become large as l increases. Thus the integrand of (18) has a factor which varies rapidly with t. It turns out that the $I_{ln}(t)$ also vary rapidly with t, especially near $t=1$, but in a more complicated manner. The whole integrand therefore varies rapidly with t while not being easily specified analytically. This makes numerical integration a far from trivial problem, especially if values for $I_{ln}(t)$, $n>4$, are desired.

In order to circumvent this difficulty, we investigated the possibility of writing the transport equation in terms of *integrals* of the $I_{ln}(t)$ which would be more tractable for numerical analysis. By dealing directly with the integrals we might also hope to reach more directly the energy dissipation distribution, since this involves integrals rather than the functions $I_{ln}(t)$ directly. The formulation in terms of residual range *moments* may be accomplished very easily, if (17) is used, by simply multiplying Eqs. (6) by a factor t^{p+1} and integrating each term over the whole range $0\leqslant t\leqslant 1$. The result of this operation is the following system of equations:

$$I_{ln}{}^p=\frac{n}{(d_l+p+1)}\left\{\frac{(l+1)}{(2l+1)}I_{l+1,n-1}{}^{p+1} +\frac{l}{(2l+1)}I_{l-1,n-1}{}^{p+1}\right\}+\delta_{n0}(d_l+p+1)^{-1}, \quad (19)$$

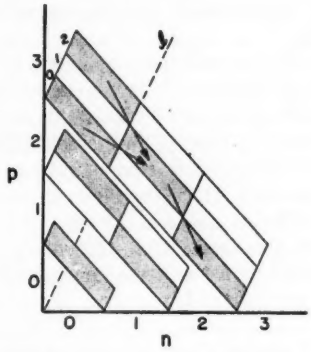

FIG. 1. Diagonal planes and linkages in the lattice of parameters relating to the recursive system (19). The shaded elements can be calculated chainwise as indicated by the arrows.

where

$$I_{ln}{}^p=\int_0^1 dt t^p I_{ln}(t). \quad (20)$$

The linkage between the *numbers* $I_{ln}{}^p$ has a very interesting structure. It obviously can be unraveled, for with $n=0$ the linkage term vanishes and $I_{l0}{}^p=(d_l+p+1)^{-1}$. From these numbers the $I_{l1}{}^p$ may be obtained, which in turn yield the $I_{l2}{}^p$, and so on. If we consider the three dimensional array with sides l, n, and p, all terms in (19) lie in the diagonal plane $(n+p)$ = constant. Further, within this plane the linkage has exactly the triangular structure noted in Fig. 2 of reference 14. Thus, if the elements $I_{ln}{}^p$ are known for fixed n, p and for $l\leqslant l_{\max}$, the elements $I_{l,n+1}{}^{p-1}$ in the next line of the plane may be calculated for $l\leqslant l_{\max}-1$. Since the first line in each diagonal plane, i.e., the line with $n=0$, may be calculated directly, triangular sections of the diagonal planes may be evaluated *independently of all* $I_{ln}{}^p$ *not in the section*. A few such triangular sections are indicated in Fig. 1.

Now the energy dissipation distribution $J(x)$ is given by the integral

$$J(x)=\int_0^1 dt(dT/dt)I_0(t,x). \quad (21)$$

This implies the following expression for the space moments of the energy dissipation distribution:

$$J_n=\int_0^1 dt(dT/dt)I_{0n}(t). \quad (22)$$

If, then, we approximate (dT/dt) by an analytic expression,

$$(dT/dt)\approx A_0t^{-\frac{1}{2}}+A_1t^{\frac{1}{2}}+A_2t^{\frac{3}{2}}, \quad (23)$$

we obtain an expression for the J_n in terms of the $I_{0n}{}^p$:

$$J_n=A_0I_{0n}{}^{-\frac{1}{2}}+A_1I_{0n}{}^{\frac{1}{2}}+A_2I_{0n}{}^{\frac{3}{2}}. \quad (24)$$

The half-integer exponents appear because at low energies $(dT/dt)\propto T^{-1}\propto t^{-\frac{1}{2}}$. We have found (23) to be

capable of representing stopping-power data quite satisfactorily.

Thus, to compute the space moments of the energy dissipation distribution it is necessary to compute elements with half-integer p values within a pyramidal volume in the l, n, p array. Such a calculation is easily accomplished with a desk computer by means of the recursive relations (19), the first ten moments J_n requiring hardly an afternoon's work.

For many problems, and particularly for source energies greater than 1 mc^2, the simple form (17) is not sufficiently accurate and it is necessary to make use of (16). A more involved argument, which is contained in Appendix C, can then be made which yields the following more complicated set of recursive relations:

$$\Phi_{ln}{}^{p}=\frac{\alpha n}{(2l+1)}\sum_{i=0}^{\infty}\frac{(i+1)}{(d_l+p+i+1)}\{(l+1)\Phi_{l+1,\,n-1}{}^{p+i+1}$$

$$+l\Phi_{l-1,\,n-1}{}^{p+i+1}\}+\delta_{n0}\alpha\sum_{i=0}^{\infty}\frac{(i+1)}{(d_l+p+i+1)}(1+\alpha)^{-p-i-1}, \tag{25}$$

where

$$\Phi_{ln}{}^{p}=\int_0^1 dt[t/(t+\alpha)]^{p}I_{ln}(t). \tag{26}$$

The terms in the sums indicated in (25) decrease in size approximately as $(1+\alpha)^{-i}$, while the basic type of linkage remains the same as in the simpler expression (19). In order to calculate moments with the recursive system (25) it is necessary to include enough terms in the calculation to obtain adequate convergence for the more important (smaller) values of p. In a calculation described in Sec. 10 with source energy 1.71 Mev, as many as 25 terms were included to calculate four spatial moments accurately to six significant figures.

A useful device which facilitates the evaluation of the sums in (25) is that of writing, e.g.,

$$\sum_{i=0}^{\infty}\frac{(i+1)}{(d_l+p+i+1)}\Phi_{l+1,\,n-1}{}^{p+i+1}$$

$$=\sum_{i=0}^{\infty}\left\{\sum_{i'=i}^{\infty}(d_l+p+i'+1)^{-1}\Phi_{l+1,\,n-1}{}^{p+i'+1}\right\}. \tag{27}$$

This makes it possible to evaluate simultaneously sums for all values of p for a given l, n combination. Using this device, the illustration just mentioned involving sums with 25 terms required little more than a day's work on a desk computer.

Both (25) and (19) are of a form ideally suited for automatic digital computers. As is mentioned in the next section, some results have been obtained by coding (19) for the SEAC. It is our intention to code (25) as well, in order to perform a wider variety of calculations for energies below 10 Mev. Note that (25) becomes ineffective for source energies above a few Mev because of slow convergence of the sums. For higher energies it may be feasible to use devices for speeding convergence or it may be necessary to derive a different expansion.

Note that in using (25) to obtain the energy dissipation distribution, we write (dT/dt) as a power series similar to (23) but with $[t/(t+\alpha)]$ as independent variable.

5. ASYMPTOTIC CONSIDERATIONS

The process of constructing a distribution from a limited number of moments implies an extrapolation of the moment sequence from the finite number actually calculated to an infinite number of moments. Such an extrapolation can only be done with confidence if the trend of the higher order moments has been established from a knowledge of the distribution near its limits, the so-called asymptotic behavior of the distribution. The determination of this asymptotic behavior requires an independent investigation which is quite different from that leading to the calculation of the spatial moments. Such an investigation has been performed and is to be reported in detail in a manuscript which will be submitted for publication at a later date. In order to make this paper self-contained, a simplified discussion using the method of Wick[11] is contained in Appendix D. Both the simplified and the more detailed arguments indicate that near the $x=1$ limit an analytic behavior similar to the function

$$f(x)=(1-x)^{-\frac{1}{2}}\exp\{-A/(1-x)\} \tag{28}$$

should be anticipated, where A is a constant which depends upon the source energy and the scattering material.

It is conceivable that the spatial distribution attains its asymptotic behavior only very near the limit. In this case knowledge of it could hardly be very useful. Indeed, if a form such as (28) is to prove helpful in constructing a distribution, it should provide a description of the distribution over such a large region of x that those spatial moments which we may be able to calculate reflect this asymptotic behavior. Otherwise our attempts at extrapolating the moment system must contain a large amount of guesswork. It follows that a method for determining the usefulness of a functional form such as (28) is simply to compare the moment trend of (28) with the moment trend of the unknown distribution.

An easily visualized way of making such a comparison is to consider another function with the same asymptotic behavior as (28), namely

$$g(x)=(-\ln x)^{-\frac{1}{2}}\exp\{A/\ln x\}. \tag{29}$$

The equivalence of (29) and (28) for our purpose is easily demonstrated by writing $x=1-(1-x)$ in (29) and expanding around $x=1$. The moments $g_n=$

$\int_0^1 dx x^n g(x)$ are as follows:

$$g_n = (\pi/A)^{\frac{1}{2}} \exp\{-[4A(n+1)]^{\frac{1}{2}}\}. \quad (30)$$

The form of (30) suggests that we plot logarithms of the electron spatial moments *versus* $(n+1)^{\frac{1}{2}}$. A moment trend similar to (30) would be demonstrated by a tendency for the points to lie on a straight line for large n.

A series of such plots is shown in Fig. 2, which utilizes the even spatial moments up to the 20th.[27] The solid lines in this figure were drawn with a straightedge. The circles represent the quantities $-\ln I_{0n}{}^p$ with $p=-\frac{1}{2}$. The fact that the straight line trend holds for moments as low as $n=4$ strongly supports the use of (28) or (29) in representing the unknown distribution.[28]

Having considered the behavior of the electron spatial distribution for $x\rightarrow+1$, a reasonable next step is a discussion of the asymptotic behavior in the other direction, namely for $x\rightarrow-1$. Unfortunately, it is not so easy to establish an analytic law for this backscattered part of the electron distribution. By taking linear combinations of the spatial moments and constructing thereby the sequence $\langle[(1-x)/2]^n\rangle$, which emphasizes the region $x\rightarrow-1$, it is possible to estimate that the behavior resembles the function $\exp\{-A'/(1+x)\}$. This is about the best that can be done at the present time. Fortunately, there is much less interest in the negative x portion of the electron distribution, and moment fitting methods can be used which do not require detailed information about this reverse asymptotic behavior.

6. FURTHER DISCUSSION OF THE DISTRIBUTION

In addition to moments and asymptotic trends, there are a number of other known characteristics which must be taken into account in constructing spatial distributions. The simplest of these are the observations that the distributions should be unimodal and everywhere positive, and that the mode should be located at some positive value of x.

Less obvious characteristics relate to questions of smoothness. It is clear that the distributions should vary smoothly from point to point, without oscillatory or discontinuous behavior, except at the electron source, whose distribution is δ-shaped at $x=0$. The type of discontinuous behavior to be expected at the source can perhaps best be understood by considering the limiting situation of no elastic scattering. In this case, which is closely approximated by heavy particles, electrons generated at $x=0$ would move together through the material to the end of their range. At each point x, all the electrons would have the residual range $t=(1-x)$ and would be dissipating energy at the rate $(dT/dt)_{t=(1-x)}$.

[27] The moment calculations on which Fig. 2 is based were performed with the aid of the SEAC using the screened Rutherford cross section (8) and the simple recursive system (19).

[28] A comparison of moment trends involving (28) rather than (29) can be made, but it is more complicated and less visual.

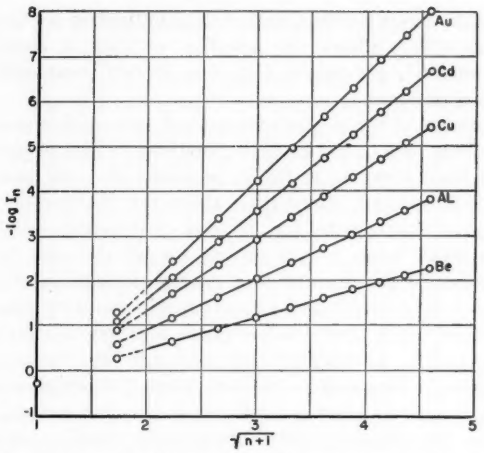

FIG. 2. A graph to demonstrate the asymptotic trend of the moments of electron spatial distributions. The circles represent moments calculated from the recursive system (19). The straight lines represent the trend of Eq. (30).

The energy dissipation distribution starts at $x=0$ with the value $(dT/dt)_{t=1}$; since it vanishes for $x<0$, the source induces a discontinuity of value and slope.[29]

Elastic scattering does not alter the existence or the size of these discontinuities. The distribution of energy dissipation reflects this discontinuous behavior of source energy electrons superposed on the continuous distribution of lower energy electrons, which may be scattered back to the source plane and behind it.

7. CONSTRUCTION OF THE DISTRIBUTION

A. General Discussion

All things considered, the spatial distributions are sufficiently complicated so as to require a fairly large number of constants in their description, i.e., five to ten rather than two or three. For the description must include the backscattering, the discontinuous behavior at $x=0$, the peak, and the asymptotic trend.

By far the best known moment fitting technique which can utilize an arbitrary number of moments is the polynomial method, and in our first attempts to construct spatial distributions we explored its possibilities. After trying it in various forms, e.g., Legendre expansions, expansions based on a weight function specifying the known asymptotic trend, and expansions in non-self-adjoint systems involving only even or odd moments, we finally turned to other methods because the convergence of these expansions was usually poor. The basic reason for this failure seems to be the following: The polynomial method requires the choice of a comparatively simple weight function which so closely estimates the distribution that only minor corrections of a slowly varying nature need to be made in the original estimate. The available quantitative infor-

[29] Note that there are discontinuities in the higher derivatives also, but they need not be considered.

mation about electron spatial distributions is not in a form which allows the selection of such a closely determined, yet simple (i.e., one or two parameter), initial estimate.

Instead of the polynomial method, our chief reliance has been on a "function fitting method."[12] This method has been very successful in problems of x-ray penetration in which information about the distribution is likewise inadequate for a good polynomial weight function.[30] Since it has proven useful, the next few paragraphs are devoted to a general description of it. For *point isotropic* and *plane isotropic* geometry problems, of which there has been little mention thus far in the paper, a different and probably less accurate moment fitting scheme has been used. A description of this latter procedure is contained in the next section.

In the function fitting method the distribution is represented by a sum of terms as follows:

$$J(x)\approx\sum_i a_i F(\beta_i,x). \tag{31}$$

Each term in the sum involves two parameters instead of one as in the polynomial method, and all terms have exactly the same form. The parameters α_i, β_i are determined so that a number of moments of the function on the right agree with moments of the unknown function on the left. This requires the solution of moment equations:

$$J_n=\sum_i a_i F_n(\beta_i). \tag{32}$$

The choice of $F(\beta,x)$ is made according to the following criteria: (a) $F(\beta,x)$ must be capable of describing the asymptotic trend, (b) $F(\beta,x)$ must be simple enough and flexible enough so that a superposition of several terms with different β is capable of describing other known characteristics of the distribution, and (c) $F(\beta,x)$ must have such a form that the Eqs. (32) are easily soluble. This last requirement can always be met if $F_n(\beta_i)$ has the form $(\beta_i)^n\omega_n$, where ω_n is a number independent of β.

The particular selection of $F(\beta,x)$ which has turned out to be most useful is the following:

$$\begin{aligned} F^{(\gamma)}(\beta,x)&=\beta^{-1}(1-x/\beta)^\gamma\exp\{-Ax/(\beta-x)\}, \quad 0\leqslant x\leqslant\beta \\ &=0, \quad x>\beta, \end{aligned} \tag{33}$$

where γ is a parameter which may be given different values in different problems. Note that with this selection, $\omega_n=\omega_n{}^{(\gamma)}=\int_0^1 dx x^n(1-x)^\gamma\exp\{-Ax/(1-x)\}$. There is some physical basis for this choice of approximating function beyond the selection criteria mentioned in the preceding paragraph. The energy dissipation distribution is obtained by summing the contributions of electrons with different residual ranges. Electrons with residual range t have an asymptotic behavior like that of (33) with $\beta=(1-t)$, as is evidenced, e.g., by expression (67) in Appendix D. Thus the energy dissipation distribution can be written in a form very suggestive of (31), (33).

It may appear surprising that a constant γ is inserted in (33) rather than $-\frac{3}{2}$, which yields precisely the expected asymptotic trend. The reason for this is that the factor $(1-x)^{-\frac{3}{2}}$ has the effect of creating a peak in the approximating function for A not too large. A superposition of several such functions with appreciably different β's must inevitably yield a "bumpy" distribution, which is not acceptable. For the aluminum and gold calculations discussed in Sec. 9, γ was chosen to be zero; while in the beryllium calculation γ was chosen to be $+1$. In each case the selection was made to obtain an approximating function capable of yielding smooth superpositions.

This raises the question as to whether the sum of several such smooth and monotonic functions is capable of producing a distribution which may indeed have a pronounced peak. This is possible, for if two terms in the sum have β's nearly equal and a's which are large and opposite in sign, the behavior of the two combined is similar to that of the function

$$\beta^{-1}(1-x/\beta)^{\gamma-2}\exp\{-Ax/(\beta-x)\}.$$

The choice (33) for $F(\beta,x)$ makes it possible to use the convenient device of fitting separately the even and odd moments. These two sets of moments can be considered as describing two different component distributions which are defined over the range $0\leqslant x\leqslant 1$ and which become asymptotically equal to each other. Each of the two component distributions can be represented by a sum of the form (31). This separate fitting of the even and odd component distributions has several advantages: It considerably simplifies the moment fitting problem, for the component distributions are ordinarily simpler and easier to fit. Further, instead of, say, eight simultaneous equations in the system (32), two systems of four equations each must be solved. The discontinuities at the source plane appear in a harmless and natural form in the component distributions. For example, a discontinuity in the distribution implies that the odd component distribution has a value at $x=0$ equal to the discontinuity size. Likewise, the even component distribution has a finite slope at $x=0$ equal to the (known) slope discontinuity.

Fitting even and odd component distributions separately has one additional advantage, namely it automatically yields an estimate of the accuracy of the approximation. Since the two component distributions become asymptotically the same, differences which appear in the separate constructions must reflect the error. This is important because function fitting techniques have no accompanying test of accuracy comparable with convergence criteria for polynomial approximations. In some cases the use of more and more moments in function fitting construction serves the same purpose, but more frequently the accuracy of

[30] M. Berger (to be published).

construction must be gauged by constructing distributions otherwise known or by comparing constructions based on different functions $F(\beta,x)$.[30]

B. Sample Outline

To illustrate the preceding discussion and to give further details we present here the outline of a typical construction which follows closely the method used for the gold and aluminum calculations of Sec. 9, and which relies on the simple expression (17) for S_l.

(a) First the moments J_n are determined numerically. This requires tabulating stopping powers, evaluating the integral (2) to determine electron residual ranges, calculating the numbers $d_l=S_l(t=1)$ using the appropriate formula for the cross section, computing the quantities $I_{0n}{}^{-\frac{1}{2}}$, $I_{0n}{}^{+\frac{1}{2}}$, and $I_{0n}{}^{\frac{1}{2}}$ from the system (19), and finally combining these quantities as indicated in (24).

(b) Next, the asymptotic constant A in the approximating function (33) must be determined. If moments up to, say $n=10$ have been calculated this is accomplished by solving the equation

$$\ln(J_8/J_{10})=(4A)^{\frac{1}{2}}\{(10.25+A/12)^{\frac{1}{2}}-(8.25+A/12)^{\frac{1}{2}}\}, \quad (34)$$

which corresponds to (70) in Appendix E. A simple iteration is used for this purpose.

(c) We choose $\gamma=0$, noting that the $F^{(0)}(\beta,x)$ superpose smoothly, and calculate the corresponding numbers $\omega_n{}^{(0)}$ with the aid of the formulas developed in Appendix E.

(d) The equations to be solved simultaneously can now be written down. Even and odd component distributions are to be determined separately, requiring the solution of the two systems:

$$\begin{aligned}&\textstyle\sum_i a_i\beta_i{}^n=J_n/\omega_n{}^{(0)}, \quad n=0, 2, 4, \cdots,\\ &\textstyle\sum_i a_i\beta_i{}^n=J_n/\omega_n{}^{(0)}, \quad n=1, 3, 5, \cdots.\end{aligned} \quad (35)$$

To the first of these systems we add one more equation which guarantees the known slope change at $x=0$, while to the second (odd) system we add an equation which guarantees the known discontinuity. These two equations are the following:

$$\begin{aligned}&\textstyle\sum_i a_i\beta_i{}^{-2}=A^{-1}(d/dt)(dT/dt)\,|_{t=1},\\ &\textstyle\sum_i a_i\beta_i{}^{-1}=(dT/dt)\,|_{t=1}.\end{aligned} \quad (36)$$

(e) To insure the appropriate asymptotic trend, we specify $\beta_0=1$ in both systems.

(f) To solve each of the two systems, a_0 is first eliminated by subtracting each equation from the succeeding one, i.e., the nth from the $n+2$nd. The resulting system can obviously be put in the form described in Appendix B of reference 12 and the solution proceeds as outlined there.

(g) The resulting even and odd component distributions are combined in the usual manner to obtain $J(x)$.

There is, of course, nothing unique about such a construction. Obvious variations from it are, e.g., use of a different approximating function $F(\beta,x)$, fitting moment combinations instead of the moments directly, solving a single system of equations instead of even and odd components separately, and modifying the moments to make the fitting easier. Such modifications may be desirable at any time and become a necessity in many problems such as, e.g., those in which it is difficult to calculate more than a small number of moments. The unifying feature about such a variety of construction methods is simply that they can all be expected to give similar answers if they express the same quantitative *and* qualitative information about the unknown distribution.[30]

8. PLANE AND POINT ISOTROPIC SOURCES

A. General Discussion

Most of this paper centers around the plane monodirectional source, the geometry of which is easily visualized. Of equal interest and perhaps greater practical importance are the plane and point isotropic sources concerning which an extensive literature exists.[1] The interest in these source types arises because the elementary radioactive source is isotropic.

The distribution resulting from a plane isotropic source may arise in two equivalent situations: (a) Point isotropic sources may be distributed uniformly on a plane. Measurements of the energy dissipated at various distances from the plane may then be made with a point detector. (b) Alternately, the source may actually be point isotropic while the measurement includes all the energy dissipated in a plane layer. If, then, $J^{pl}(|x|)dx$ is the energy dissipated in a plane layer located a perpendicular distance $|x|$ from a point isotropic source, and if $J^{po}(\rho)d\rho$ is the energy dissipated in a spherical shell of radius ρ concentric with the same source, the following relation must hold between the two distributions:

$$J^{pl}(|x|)=\frac{1}{2}\int_{|x|}^{1}\frac{d\rho}{\rho}J^{po}(\rho). \quad (37)$$

Note that x and ρ both measure distance in r_0 units. Multiplying (37) by $|x|^n$ and integrating over the whole range of x yields a corresponding relation between spatial moments

$$J_n{}^{pl}=(n+1)^{-1}J_n{}^{po}, \quad n=0, 2, 4, \cdots. \quad (38)$$

Because of symmetry all odd moments of the plane distribution vanish. Although odd moments of the point distribution do not vanish they cannot be easily calculated.[14] Thus, it is necessary to rely on even moments in the construction of spatial distributions for both geometries.

The simple relations (37) and (38) make it possible to change from one to the other situation readily. This is very useful, for the plane geometry is much the simpler for the purpose of calculating spatial moments. On the other hand, the point geometry yields spatial distributions which are both easier to discuss and easier to construct. We have therefore always calculated plane moments and then with the aid of (38) constructed distributions for the point geometry which could be transformed to plane distributions by means of (37). This last step has the additional advantage of providing the extra accuracy which accrues to numbers determined by integration.

The recursive systems for obtaining plane isotropic moments can be obtained from (19) and (25) by multiplying the source term by a Kronecker delta factor δ_{l0}, which selects only the isotropic angular component.

The characteristic features of a distribution $J^{po}(\rho)$ resulting from a point source are very similar to those already discussed for the distribution produced by a plane monodirectional source. The asymptotic trend is the same. The discontinuities discussed in Sec. 6 relate to the ordinate and slope of $J^{po}(\rho)$ at $\rho=0$. There is, of course, no backscattered distribution.

The construction of $J^{po}(\rho)$ from its moments and known characteristics can be accomplished by one or another form of the method described in the preceding section. However, we used a simpler (and probably less accurate) method which is described in Part B of this section. Our reasons for choosing this simpler scheme relate to our intention to compare with experiments performed using P^{32} beta rays. The P^{32} spectrum is continuous with an end point at about 1.71 Mev. We therefore decided to construct distributions for a series of monoenergetic sources within the energy region below 1.71 Mev and to integrate over the interpolated results to obtain a distribution relative to the P^{32} source spectrum. Because of the energies involved, most of these monoenergetic source calculations required the more complicated recursive system (25). Since (25) involves more desk computer work than (19), we did not want to calculate so many spatial moments—no more than four, to be precise. On the other hand, the final integration over monoenergetic source results "washes out" the detailed features of each component distribution and is therefore less demanding regarding their accuracy. It therefore seemed appropriate to rely on constructions involving few moments and only fair accuracy.

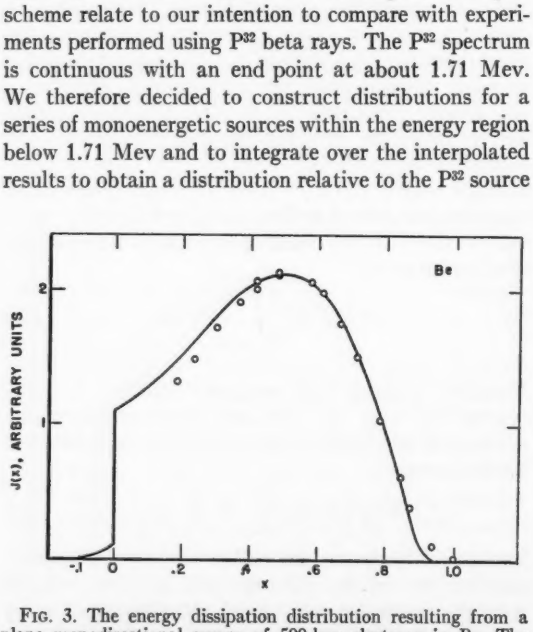

FIG. 3. The energy dissipation distribution resulting from a plane monodirectional source of 500-kev electrons in Be. The circles represent measurements by Frantz which correspond to source electrons with kinetic energy 570 kev. The abscissa is in units of the true range of the source electrons.

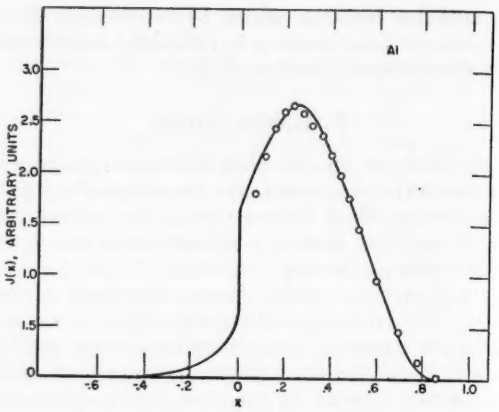

FIG. 4. The energy dissipation distribution resulting from a plane monodirectional source of 500-kev electrons in Al. The circles represent measurements by Frantz corresponding to 515-kev source electrons. The abscissa is in units of the source electron true range.

B. Construction of Distributions

To construct $J^{po}(\rho)$ we decided to use the following function, because of the simple expression for its moments [compare with (29)]:

$$\bar{K}(\rho)=c\rho^{\xi}(-\ln\rho)^{-\frac{1}{2}}\exp\{A/\ln\rho\}, \tag{39}$$

where c, ξ, A are constants. For $\xi>1$ this function not only vanishes at $\rho=0$ but also has zero slope. We therefore introduce these same characteristics into the distribution to be described by (39) by subtracting from $J^{po}(\rho)$ a function which has the same value and slope at $\rho=0$. This function, which we label $\bar{J}(\rho)$, is so chosen that the combination $J^{po}-\bar{J}$ has the same asymptotic behavior as J^{po} alone. In particular, we used

$$\bar{J}(\rho)=(a+b\rho)\exp\{-B/(1-\rho)\}, \tag{40}$$

where B is chosen slightly larger than the anticipated value for A, and a, b are adjusted to bring about agreement in slope and value with $J^{po}(\rho)$ at $\rho=0$. The final step in the construction is the determination of the constants c, ξ, A from the solution of equations which guarantee that three moments of $\bar{K}(\rho)$ have values identical with the corresponding moments of

$J^{p0}-\bar{J}$. We used for this purpose the zeroth, second, and sixth moments. The fourth moment served as a check on the accuracy of the representation, which has, of course, the form

$$J^{p0}(\rho)\approx\bar{K}(\rho)+\bar{J}(\rho). \tag{41}$$

9. EXAMPLES: PLANE MONODIRECTIONAL 500-kev SOURCES IN BE, AL, AND AU

A. Theoretical

These three calculations were performed with the intention of comparing with experiments by Frantz in which the ionization in an air gap is taken as a measure of the energy dissipated.[31] The space-residual range moments $I_{0n}{}^{p}$, which were in each case calculated using the recursive system (19), were therefore combined as in (24) to obtain the J_n, but with the constants A_0, A_1, A_2 relative to the stopping power in air in accordance with the Bragg-Gray principle.[32]

The construction of Al and Au spatial distributions followed closely the outline given in Sec. 7, the aluminum moments having been calculated using the $S_l(t)$ given by (13) while the gold moments were obtained using (15) Both constructions involved fitting the moments J_0 through J_7.

The calculation of spatial moments for the distribution in Be made use of (13) and proceeded without difficulty. The construction of the distribution, however, offered special problems. Beryllium has such a low Z that electrons are very little deflected until they have expended an appreciable fraction of their total range. As a result, (a) the asymptotic portion of the distribution is confined to a relatively narrow region of x; (b) the backscattered distribution is very small and tends to fall off rapidly because it is composed largely of very low energy electrons; and (c) the region between source and maximum is large enough to exhibit some structure such as, for example, an inflection. This situation, in which the electron distribution tends to become similar to the Bragg curve for heavy particles, is a fairly general one since it occurs in any scattering material if T_0 is large enough. (Of course, in situations where bremsstrahlung is important, our whole schematization breaks down anyway.)

To construct such a distribution it was not possible to use the same approximating function as for Al and Au, i.e., (33) with $\gamma=0$, because this family of functions does not yield a smooth superposition for small A. Instead, γ was set equal to $+1$ in (33). A corresponding change was made in the unknown distribution, namely $J(x)$ was replaced by $(1-x)J(x)$, so that our approximating function became, in effect, $\{\exp[-Ax/(\beta-x)]\}\times(\beta-x)/(1-x)$, instead of the exponential alone. This change is equivalent to replacing J_n with (J_n-J_{n+1}) in (35).

In treating separately even and odd components as in the sample outline of Sec. 7, it was implicitly assumed that the backscattered part of the distribution blended smoothly with the forward penetrating part. For Be this is not so because the backscattered distribution decreases very rapidly to the left of the source plane. This brings about an additional structure in the component distributions near $x=0$. We made allowance for this by introducing one more term in the sums (35). The contribution of this term is restricted to the region close to $x=0$ by assigning β a small value. To make certain that this additional term described the backscattering, the precise value for β was selected by trial and error so that the corresponding a's determined by the solution of the systems (35) were equal in magnitude and opposite in sign, the even system yielding a positive value.

With these modifications, construction of the Be distribution proceeded satisfactorily. The spatial moments J_0 through J_{10} were used, more being required than for Al and Au because of the use of moment differences and the need to account for additional structure. Had fewer moments been available, our construction would not have depended on the separate construction of even and odd component distributions.

The results of these three calculations are represented in Figs. 3, 4, and 5 by the solid lines. Note the discontinuities, the tremendous increase in the backscattering and the shift of the peak as Z increases, and the similarities between the Be distribution and a Bragg curve for heavy particles.

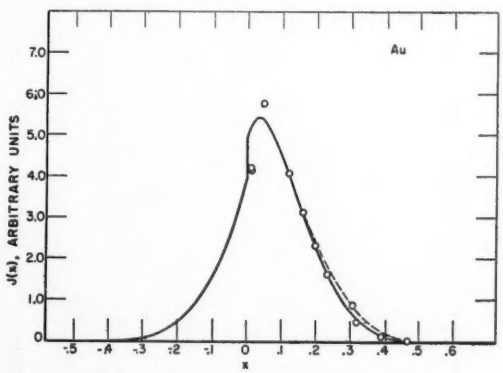

FIG. 5. The energy dissipation distribution resulting from a plane monodirectional source of 500-kev electrons in Au. The circles represent measurements by Frantz corresponding to 495-kev source electrons. The abscissa is in units of the source electron true range. The dashed curve relates to a calculation using the screened Rutherford differential cross section (8) instead of that given by the Mott formula, namely (14).

[31] F. Frantz (private communication).

[32] See L. H. Gray, Proc. Roy. Soc. (London) **A122**, 647 (1929). A more recent theory of cavity ionization takes into account effects neglected in Bragg-Gray theory, namely, those due to the travel of secondary electrons [L. V. Spencer and F. H. Attix (to be submitted for publication)]. We use Bragg-Gray here partly for consistency, since we have nowhere in this paper included secondary electron effects, and partly because changing to a more exact theory of cavity ionization would modify the normalization rather than the distribution shape.

B. Comparison with Experiment

As mentioned at the beginning of this section, F. Frantz has performed experiments which can be compared with the calculated distributions just discussed.[31] Unfortunately, the experimental geometry contained a boundary at $x=0$, so that some features of the comparison are not very meaningful. Still, the influence of the boundary has qualitative significance even at penetrations where it destroys the meaning of a quantitative comparison.

In the Frantz experiments, an accelerator beam of electrons impinged normally on plane foils of the scattering material. Immediately behind these foils was an aluminum-walled ionization chamber. Backing the ionization chamber was a thick slab of the scattering material. The lateral extension of all pieces of the apparatus was effectively infinite, so that the ionization chamber collected all ionization produced in the lateral plane of the air gap. Extrapolation-type measurements were made to verify this point.

Before the electron beam entered the initial foils and the ionization chamber, it passed through an aluminum exit foil on the accelerator tube and several centimeters of air at room pressure. This material, combined with half the ionization chamber thickness, amounted to a total of 15.5 milligrams per cm². An allowance for this initial penetration has to be made before comparing measurements with the theory. For measurements of electron penetration in aluminum this could be easily done by considering this initial material to be equivalent to an additional aluminum foil of thickness 15.5 milligrams per cm². For measurements in, say, gold a similar but slightly more complicated renormalization was carried out: First the mean cosine of the obliquity distribution resulting from the initial 15.5 mg/cm² was calculated. Next we determined the thickness of an equivalent gold foil which would produce the same mean cosine and added this equivalent foil thickness to all penetrations. Finally, the source energy was renormalized so that the mean energy of electrons penetrating the equivalent gold foil corresponded with the mean energy of electrons penetrating the actual initial aluminum-equivalent material.

Unfortunately, the initial penetration made it difficult to perform absolute measurements because of uncertainties in the strength of the initial electron beam. In comparing measurements with theory, the two were matched at a penetration sufficiently great that boundary effects should be negligible but not so great that statistical fluctuations or range straggling effects should be appreciable.

TABLE III. Energy dissipation distributions $[J^{po}(T_0,\rho)/J^{po}(T_0,0)]$ resulting from point isotropic sources in air emitting electrons of energy T_0. The symbol ρ represents the distance from the source in units of the initial true range.

ρ	$T_0=0.1$ Mev	0.3 Mev	0.5 Mev	0.7 Mev	1.0 Mev	1.4 Mev	1.71 Mev
0.00	1.000	1.000	1.000	1.000	1.000	1.000	1.000
0.05	1.037	1.025	1.019	1.012	1.010	1.005	1.003
0.10	1.102	1.071	1.055	1.039	1.032	1.021	1.018
0.15	1.196	1.140	1.109	1.083	1.069	1.048	1.037
0.20	1.322	1.235	1.186	1.147	1.122	1.089	1.072
0.25	1.483	1.357	1.287	1.233	1.195	1.147	1.121
0.30	1.670	1.509	1.415	1.343	1.288	1.222	1.186
0.35	1.910	1.690	1.565	1.474	1.400	1.314	1.266
0.40	2.172	1.898	1.739	1.627	1.532	1.424	1.362
0.45	2.454	2.125	1.930	1.798	1.679	1.549	1.473
0.50	2.738	2.357	2.118	1.968	1.827	1.677	1.586
0.55	2.993	2.571	2.288	2.124	1.963	1.798	1.695
0.60	3.174	2.727	2.395	2.227	2.054	1.881	1.771
0.65	3.204	2.764	2.403	2.243	2.077	1.905	1.795
0.70	2.999	2.607	2.230	2.096	1.940	1.802	1.703
0.75	2.362	2.149	1.801	1.714	1.599	1.509	1.438
0.80	1.609	1.447	1.169	1.133	1.070	1.036	1.000
0.85	0.635	0.592	0.452	0.458	0.438	0.443	0.438
0.90	0.066	0.066	0.045	0.056	0.049	0.054	0.057
0.92	0.009	0.013	0.007	0.008	0.009	0.011	0.011

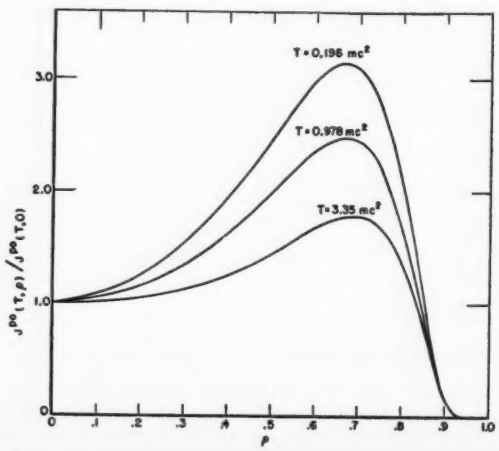

FIG. 6. Energy dissipation distributions resulting from point isotropic sources of monoenergetic electrons in polystyrene. The abscissa gives the penetration in fractions of the source electron true range.

The experimental values, as normalized and corrected for initial penetration, are represented by circles in Figs. 3, 4, and 5. In reducing the experimental penetrations to a scale of $x=z/r_0$, theoretical range-energy curves were used based on data from Table I. The source energies mentioned in the captions are the effective source energies obtained as already described, and the first experimental value gives a measure of the equivalent foil thickness. The question may be raised as to whether it makes sense to compare experimental values with a theoretical curve for a slightly different source energy; however, distribution *shapes* are known experimentally and expected theoretically to be rather independent of source energy particularly for nonrelativistic source energies.[33]

There is good agreement between calculated and

[33] See reference 6 and Fig. 6. Experimental verification of this is due to F. Frantz (private communication).

experimental values in Figs. 3, 4, and 5 except near the source plane $x=0$ and in the extreme tail to the right. Near the source plane, however, boundary effects should produce just such a decrease in experiment relative to theory as is observed, since the absence of the material behind the source plane allows the back-scattered electrons to escape behind the source instead of remaining in its proximity. Likewise, in the tail to the right, range straggling effects not included in the present theory should increase the experimental ionization over that predicted by theory. It is gratifying to note that the range straggling effect seems most serious for beryllium, while the boundary effect is biggest for gold, in agreement with qualitative expectation.

10. FURTHER APPLICATIONS: ISOTROPIC P^{32} SOURCES IN AIR AND POLYSTYRENE

Using methods described in Sec. 8, calculations were performed for isotropic monoenergetic sources in air and in polystyrene, the source energies T_0 being 0.1, 0.3, 0.5, 0.7, 1.0, 1.4, and 1.71 Mev. The 0.1 and 0.3 Mev calculations were accomplished using (19) while all the others used (25). Resulting spatial distributions for point isotropic sources in air are reproduced in Table III. Figure 6 compares similar distributions for several source energies in polystyrene, to illustrate shape changes with changing source energy.

To obtain spatial distributions for the continuous beta ray spectrum of P^{32}, we evaluated the integrals

$$J(s)=\int_0^1 d\tau P(\tau)J^{p0}(\tau,s/\tau), \tag{42}$$

where $P(\tau)d\tau$ is the P^{32} source spectrum, i.e., the number of electrons generated with ranges between τ and $\tau+d\tau$, τ being the range relative to that for the 1.71-Mev component, i.e., the spectrum end-point. The parameter s is the radial penetration distance measured in the same units. Our arrangement for evaluating (42) may be of some interest: We changed to the variable $\rho=s/\tau$, i.e., we wrote (42) in the form

$$J(s)=s^{-1}\int_0^1 d\rho\{(s/\rho)^2P(s/\rho)J^{p0}(s/\rho,0)\}\times\{J^{p0}(s/\rho,\rho)/J^{p0}(s/\rho,0)\}. \tag{43}$$

Graphs were then prepared of the slowly varying (with τ) function $\{J^{p0}(\tau,\rho)/J^{p0}(\tau,0)\}$, which was plotted *vs* τ for fixed values of ρ. Likewise, a graph was prepared of the function $\{\tau^2P(\tau)J^{p0}(\tau,0)\}$ plotted against τ. Numbers were read from these graphs for fixed s and evenly spaced ρ values (usually with 0.05 spacing).

To obtain $P(\tau)$, we took a theoretical allowed beta-ray spectrum $P(\eta)$,[34] where η is the electron momentum in mc units, and made the transformation

$$P(\tau)=P(\eta)\frac{d\eta}{d\tau}=P(\eta)\frac{(T+1)}{\eta}(dT/d\tau). \tag{44}$$

Note that $J^{p0}(\tau,0)$ is simply the stopping power, so that the first bracketed quantity in (43) contains the square of the stopping power in the factor multiplying $P(\eta)$.

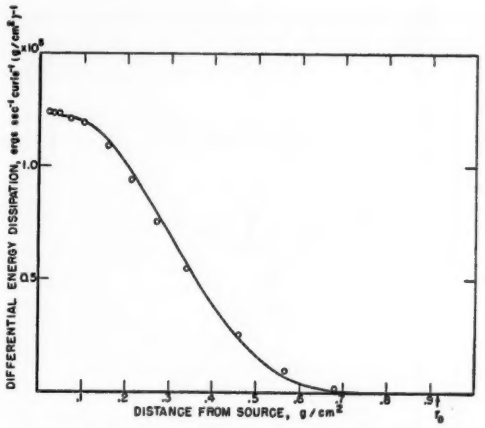

FIG. 7. The energy dissipated in spherical shells around a point isotropic P^{32} beta-ray source in air. The circles represent measurements by Clark, Brar, and Marinelli. Both theory and experiment are given in absolute units.

The P^{32} energy dissipation distributions for point geometry in air and plane geometry in polystyrene are the solid curves in Figs. 7 and 8. The circles in Fig. 7 represent measurements by Clark, Brar, and Marinelli,[35] while the circles in Fig. 8 represent measurements by Loevinger.[1] The theoretical distribution in both cases is given in absolute units. The results of Clark, Brar, and Marinelli given in Fig. 7 are also absolute; however the Loevinger results of Fig. 8 are only relative and were matched with the curve at 0.106 g/cm².

The general agreement is seen to be fairly good except in the tail of the distributions. The plane geometry comparison was put on semilog paper to illustrate the discrepancy which exists for large penetrations. The behavior of this discrepancy is just what would be expected if it were caused by range straggling, which introduces a smear that should increase measurements over theory more and more as the distribution falls more and more rapidly. Correspondingly, since the space integral is not affected by range straggling, the experimental values should fall slightly below theory for small penetrations.

11. REMARKS

The generally good agreement between experiments and the calculations herein described indicates that

[34] The allowed spectrum agrees well with the measurements of beta-ray spectroscopists for this isotope. See, e.g., H. Agnew, Phys. Rev. **77**, 655 (1950), and Sheline, Holtzman, and Fan, Phys. Rev. **83**, 919 (1951).

[35] Clark, Brar, and Marinelli, Radiology **64**, 94 (1955).

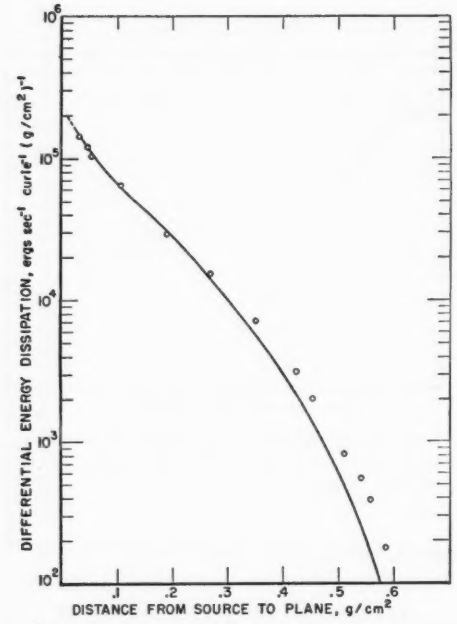

FIG. 8. The energy dissipated in plane layers near a point isotropic P^{32} source in polystyrene. The circles represent measurements by Loevinger. The theoretical curve is given in absolute units; however the experimental values were not absolute and were normalized to agree with theory at 0.106 g/cm^2.

dependable calculations are possible for all materials and for energies up to a few Mev.

One outstanding defect in the theory is the complete neglect of range straggling. A systematic development of the program outlined in reference 8 would include this effect. The simple degradation problem has already been so treated in reference 7. We intend to complete the theory in this respect.

A desirable extension of this theory would be towards higher energies than a few Mev including, if possible, energy losses due to bremsstrahlung with their inherent magnification of straggling effects.

Finally, it must be emphasized that the whole program undertaken so far is limited to infinite, homogeneous media. The extension of the theory to the treatment of boundary effects, for electrons as well as for x-rays, still represents a major obstacle.

I should like to thank Dr. U. Fano, Dr. C. H. Blanchard, and Dr. M. Berger for many discussions of this material, Dr. Fano again for editorial suggestions, and Miss Ida Hornstein for most of the numerical work involved in preparing tables and graphs.

APPENDIX A

As a first step in constructing an analytic form which may represent with reasonable accuracy the $S_l(t)$ regardless of the source energy, the stopping power must be written in as simple a form as possible. The most obvious simplification to make is that of considering the stopping number B, which is essentially a logarithmic function of the energy, to be a constant. Since the stopping power may be written

$$(dT/d\tau)=\tfrac{3}{4}(N_A\phi_0 Z/A)B\{1-(T+1)^{-2}\}^{-1}, \quad (45)$$

expression (2) may in the constant stopping number approximation be integrated to yield

$$\tau(T)=\{3N_A\phi_0 ZB/4A\}^{-1}T^2(T+1)^{-1}. \quad (46)$$

On the other hand, the simplest form to consider for the S_l's is expression (10), which may be written in the form

$$S_l=\tfrac{3}{4}(Z+1)(N_A\phi_0 Z/A)\tau_0 C_l \times\left\{\frac{(T+1)}{T^2}\right\}\left\{\frac{1}{[T^2/(T+1)]+4}\right\}. \quad (47)$$

If, therefore, we define $\alpha=\{3N_A\phi_0 ZB/4A\}^{-1}4/\tau_0$, we may rewrite (46) in the form $T^2/(T+1)=4t/\alpha$. Defining $d_l=\frac{1}{4}(Z+1)C_l/B$, it is easily seen that (47) takes the form (16). Further, α increases roughly as T_0^{-2} as the source energy T_0 decreases. Below about 0.5 Mev α is so large that (16) and (17) become equivalent.

This argument hinges on the constancy of α and d_l as the electron energy changes. The energy variation of α is obviously logarithmic. On the other hand C_l and B are both logarithmic functions of the energy, as can be seen from Eq. (10). Thus the energy variation of d_l, which derives from the ratio of these quantities, is slower than logarithmic.

The relativistic modification of the angular distribution of the elastic scattering cross section, which is not included in (47), would seem to disturb the approximate constancy of α and d_l. Fortunately, most of this additional energy dependence is accounted for by simply shifting the values of these constants slightly. Actually, the striking comparisons of Table II were achieved not by the use of theoretical values for these constants but rather by selecting the constants to achieve a good empirical fit to the cross-section tabulation.

APPENDIX B

In order to obtain the S_l expressions (10), (13), and (15) it is necessary to evaluate the integrals

$$\int_{-1}^{1} dy\{1-P_l(y)\}(1+2\eta-y)^{-2},$$

$$\int_{-1}^{1} dy\{1-P_l(y)\}(1-y)^{-q},$$

where $q=\frac{3}{2}$, 1, 0, and -1. The integrals involving the last two values of q are obvious from the orthogonality properties of the P_l and will not be mentioned further.

The integrals $G_l=\int_{-1}^{1}dy\{(1-P_l(y)\}(1-y)^{-1}$ may be evaluated by writing

$$G_{l+1}-G_l=\int_{-1}^{1}\{P_l(y)-P_{l+1}(y)\}(1-y)^{-1}dy.$$

Inserting the familiar Legendre recurrence formula,

$$P_l(y)-P_{l+1}(y)=\frac{1-y}{(l+1)}\{P_{l+1}'(y)+P_l'(y)\},$$

the integration gives the result

$$G_{l+1}-G_l=2(l+1)^{-1}.$$

By induction from the known values $G_0=1$ and $G_1=2$, the final result may be constructed:

$$G_l=2\sum_{i=1}^{l}i^{-1}. \tag{48}$$

In order to evaluate the integral $\int_{-1}^{1}dy\{1-P_l(y)\}\times(1-y)^{-\frac{1}{2}}$, we may start from a generating function for spherical harmonics:

$$\frac{(1-\epsilon^2)}{(1-2y\epsilon+\epsilon^2)^{\frac{1}{2}}}=\sum_{l=0}^{\infty}(2l+1)\epsilon^lP_l(y).$$

By integration, we obtain the equation

$$\int_{-1}^{1}dy\{1-P_l(y)\}(1-2y\epsilon+\epsilon^2)^{-\frac{1}{2}}=\frac{2(1-\epsilon^l)}{1-\epsilon^2}.$$

The limit of this as $\epsilon\to1$ yields the final result:

$$\int_{-1}^{1}dy\{1-P_l(y)\}(1-y)^{-\frac{1}{2}}=2\sqrt{2}l. \tag{49}$$

Finally, the integral

$$C_l=\int_{-1}^{1}dy\{1-P_l(y)\}(1+2\eta-y)^{-2}$$

may be immediately evaluated in terms of Legendre functions of the second kind:

$$C_l=\frac{\partial}{-2\partial(2\eta)}\{Q_0(1+2\eta)-Q_l(1+2\eta)\}. \tag{50}$$

For computation purposes a recursion system may be preferable. This can be easily obtained from the recursion relations between the associated functions Q_l^1. The result is given in (10).

APPENDIX C

In this appendix, the derivation of (25) from (18) and (16) will be sketched. As a first step in this derivation, the terms in (18) are each multiplied by $[t/(t+\alpha)]^p$ and integrated over the range $0<t<1$. Referring to the definition (26), we may write

$$\Phi_{ln}{}^p=\int_0^1 dt[t/(t+\alpha)]^p\exp\left\{-\int_t^1 dt''S_l(t'')\right\}\times\int_t^1 dt'\exp\left\{\int_{t'}^1 dt''S_l(t'')\right\}\times\left\{\frac{n}{(2l+1)}[(l+1)I_{l+1,\,n-1}(t')+lI_{l-1,\,n-1}(t')]+\delta_{n0}\delta(1-t')\right\}. \tag{51}$$

Next, this expression is integrated by parts. Defining

$$L_{lp}(t)=\exp\left\{\int_t^1 dt''S_l(t'')\right\}\int_0^t dt'[t'/(t'+\alpha)]^p\times\exp\left\{-\int_{t'}^1 dt''S_l(t'')\right\}, \tag{52}$$

the expression (51) takes the form

$$\Phi_{ln}{}^p=\int_0^1 dtL_{lp}(t)\frac{n}{(2l+1)}[(l+1)I_{l+1,\,n-1}(t)+lI_{l-1,\,n-1}(t)]+\delta_{n0}L_{lp}(1). \tag{53}$$

The evaluation of the integrals in the exponents of (52) may be accomplished by inserting the analytic form (16):

$$L_{lp}(t)=[t/(t+\alpha)]^p\int_0^t dt'[t'(t+\alpha)/t(t'+\alpha)]^{d_l+p}. \tag{54}$$

The transformation $y=[t'(t+\alpha)/t(t'+\alpha)]$ then leads to the forms

$$L_{lp}=\alpha[t/(t+\alpha)]^{p+1}\int_0^1 dyy^{d_l+p}\left[1-\frac{yt}{t+\alpha}\right]^{-2}=\alpha\sum_{i=0}^{\infty}\frac{(i+1)}{(d_l+p+i+1)}[t/(t+\alpha)]^{p+i+1}. \tag{55}$$

Inserting (55) into (53), we arrive at the recursion system (25).

APPENDIX D

The starting point for an investigation of the asymptotic trend of the electron spatial distribution is a Laplace transformation of Eq. (5). If the terms in Eq. (5) are multiplied by $\exp\{p[x-(1-t)]\}$ and integrated over the range $-\infty<x<(1-t)$, the resulting equation is

$$-\partial F_l/\partial t-\tfrac{1}{2}p\Delta_lF_l+S_l(t)F_l(p,t)=\delta(1-t), \tag{56}$$

where

$$F_l=\int_{-\infty}^{1-t} dx\,\exp\{p[x-(1-t)]\}I_l(x,t) \tag{57}$$

$$\Delta_l F_l=(l+\tfrac{1}{2})^{-1}\{(l+1)(F_{l+1}-F_l)-l(F_l-F_{l-1})\}.$$

The system of Eqs. (56) would be easy to solve were it not for the interlinkage term (57), which requires that all equations be solved simultaneously. Indeed, the different approaches to the problem of obtaining solutions *all* correspond to methods for "breaking through" this interlinkage term. For example, the calculation of moments involves a Taylor series expansion of the F around the point $p=0$. The interlinkage term is then of higher degree in p than the other terms and the equation is solved by iteration starting from zero order in p. Likewise, the familiar diffusion approximation breaks the interlinkage by setting F_2 equal to zero. Unfortunately, as mentioned in reference 2, this predetermines an incorrect asymptotic trend. It also makes no allowance for the tendency of electrons to maintain their original direction during the initial stage of the penetration. As can be seen from Figs. 2–4 there hardly exists a region where distribution of energy dissipation is not dominated either by the asymptotic trend or the initial straight-forward penetration, and thus the diffusion approximation is not applicable to this type of problem.

In the Wick method, the $F_l(p,t)$ are expanded in eigenfunctions of the difference equation

$$-(p/2)\Delta_l\psi(l,p,t)+S_l(t)\psi(l,p,t)=\lambda(p,t)\psi(l,p,t), \tag{58}$$

i.e., we write

$$F_l(p,t)=\sum_m a_m(p,t)\psi_m(l,p,t). \tag{59}$$

With this ansatz, (56) becomes

$$-\frac{\partial}{\partial t}\sum_m a_m(p,t)\psi_m(l,p,t)+\sum_m a_m(p,t)\lambda_m(p,t)\psi_m(l,p,t)=\delta(1-t), \tag{60}$$

in which the interlinkage term has disappeared.

Equations for the $a_m(p,t)$ may be obtained by multiplying (60) by $(l+\frac{1}{2})\psi_n(l,p,t)$ and summing over l. Because of the orthogonality of the ψ_m's, the result is

$$-\frac{\partial a_n}{\partial t}-\sum_m{}' M_{nm}(p,t)a_m(p,t)+\lambda_n(p,t)a_n(p,t)=\gamma_n(p)\delta(1-t), \tag{61}$$

where

$$M_{nm}=\sum_{l=0}^{\infty}(l+\tfrac{1}{2})\psi_n\frac{\partial\psi_m}{\partial t} \quad\text{and}\quad \gamma_n=\sum_{l=0}^{\infty}(l+\tfrac{1}{2})\psi_n(l,p,1).$$

The sum in (61) provides a linkage between the a_n's. Due to special scaling properties, this new linkage term in some cases either does not appear or can be shown to vanish in the asymptotic limit of large p. For our purpose the most obvious procedure is an iteration in terms of this linkage. In other words this term is neglected altogether in zeroth approximation. Its effect is then estimated by means of a new calculation in which the linkage term is calculated with the zeroth approximation solutions. Such a calculation has actually been carried out, but its results have been superseded by calculations of a somewhat different type which will be given in a separate paper. We shall carry the calculation here only as far as the zeroth approximation which neglects the interlinkage term altogether. The solutions to (61) are then

$$a_n{}^{(0)}(p,t)=\gamma_n(p)\exp\left\{-\int_t^1 dt'\lambda_n(p,t')\right\}, \tag{62}$$

where the superscript indicates zeroth approximation

This formal expression doesn't mean much until the eigenvalues λ_n have been estimated. Such an estimation is easily performed in the asymptotic limit of large p. (Note that according to (57), if t is fixed and p is large the important values of the quantity $[x-(1-t)]$ tend to be those near zero.) In this case the eigenvalues of the difference equation (58) approach those of the differential equation

$$-\frac{p}{2}\frac{1}{l}\frac{\partial}{\partial l}\frac{\partial}{\partial l}\psi(l,p,t)+\frac{\alpha d}{t(t+\alpha)}l^2\psi(l,p,t)=\lambda(p,t)\psi(l,p,t), \tag{63}$$

where l is now considered a continuous variable. Physically, this means that electrons which have penetrated nearly as far from the source plane as their path length allows must have a directional distribution peaked at $\theta=0$. It is then possible to describe them with an approximation which is accurate for small angles only and which leads to the differential equation (63).[11] Further, form (16) has been used for the $S_l(t)$, with the d_l approximated by dl^2. This approximation describes the directional distribution as a result of a diffusion process, and has been used already by Yang.[11]

Equation (63) is the Schroedinger equation pertaining to a plane oscillator, and its eigenvalues are easily calculated. The following expression for λ_n results:

$$\lambda_n=(n+1)(2\alpha pd)^{\frac{1}{2}}[t(t+\alpha)]^{-\frac{1}{4}}. \tag{64}$$

From this the $a_n{}^{(0)}$ can be obtained:

$$a_n{}^{(0)}=\gamma_n(p)\exp\left\{-p^{\frac{1}{2}}2(n+1)(2\alpha d)^{\frac{1}{2}}\times\ln\left[\frac{1+(1+\alpha)^{\frac{1}{2}}}{\sqrt{t}+(t+\alpha)^{\frac{1}{2}}}\right]\right\}. \tag{65}$$

For large p, the $a_0^{(0)}$ is much larger than the other terms, and the $F_0(p,t)$ is consequently represented by the single term

$$F_0 \sim \gamma_0(p)\psi_0(p,t) \exp\left\{-p^{\frac{1}{2}}(8\alpha d)^{\frac{1}{2}} \ln\left[\frac{1+(1+\alpha)^{\frac{1}{2}}}{t^{\frac{1}{2}}+(t+\alpha)^{\frac{1}{2}}}\right]\right\}. \quad (66)$$

In (66) the p variation of $\gamma_0(p)\psi_0(p,t)$ is so slow that this factor can be considered constant with p. By Laplace inversion of the $F_0(p,t)$, the following form for the electron spectrum is then obtained:

$$I_0(t,x) \sim \gamma_0\psi_0(t)\frac{u(t)}{2\sqrt{\pi}}[(1-t)-x]^{-\frac{1}{2}} \times \exp\left\{-\frac{u^2(t)}{4}[(1-t)-x]^{-1}\right\}, \quad (67)$$

where

$$u(t) = (8\alpha d)^{\frac{1}{2}} \ln\left[\frac{1+(1+\alpha)^{\frac{1}{2}}}{t^{\frac{1}{2}}+(t+\alpha)^{\frac{1}{2}}}\right].$$

The energy dissipation distribution requires an integration over t. For $x \approx 1$, the only contributions to the integral are from the region $t \approx 0$, and the expected asymptotic trend is therefore

$$J(x) \propto (1-x)^{-\frac{1}{2}} \exp\left\{\frac{-u^2(0)}{4(1-x)}\right\}, \quad (68)$$

which has the form (28).

It should be re-emphasized that this derivation is neither complete nor airtight and merely serves here to indicate that the analytic form (28) seems natural to the problem.

APPENDIX E

A useful recursion relation for the moments

$$F_n^{(-\frac{1}{2})} = \int_0^1 dx x^n (1-x)^{-\frac{1}{2}} \exp\{-Ax/(1-x)\}$$

can be obtained from a simple integration by parts:

$$\begin{aligned} F_n^{(-\frac{1}{2})} &= -A\int d\{\exp[-Ax/(1-x)]\}\{x^n(1-x)^{\frac{1}{2}}\} \\ &= A^{-1}\{nF_{n-1}^{(-\frac{1}{2})} - (2n+\tfrac{1}{2})F_n^{(-\frac{1}{2})} \\ &\qquad + (n+\tfrac{1}{2})F_{n+1}^{(-\frac{1}{2})}\}, \quad n>0 \\ &= (\pi/A)^{\frac{1}{2}}e^A \operatorname{Erfc}((2A)^{\frac{1}{2}}), \quad n=0. \end{aligned} \quad (69)$$

Unfortunately, higher moments can be calculated in this way only at the expense of accuracy. It is therefore necessary to develop an expression which is asymptotically accurate for the high order moments. This can be done by means of the transformation $x=\exp(-y)$:

$$F_n^{(-\frac{1}{2})} = \int_0^\infty dy e^{-(n+1)y} \exp\{-A(e^y-1)^{-1} - \tfrac{3}{2}\ln(1-e^{-y})\}.$$

Since large n implies that the important contributions to the integral come from small y, the bracketed term is now expanded in powers of y. The result of retaining powers up to the first is as follows:

$$\begin{aligned} F_n^{(-\frac{1}{2})} &\approx e^{A/2}\int_0^\infty dy y^{-\frac{1}{2}} \exp\{-(n+\tfrac{1}{4}+A/12)y - A/y\} \\ &\approx (\pi/A)^{\frac{1}{2}}e^{A/2} \exp\{-[4A(n+\tfrac{1}{4}+A/12)]^{\frac{1}{2}}\}. \end{aligned} \quad (70)$$

This is the desired asymptotic expression.

In the same way, a similar recursion expression can be written for the moments $F_n^{(0)}$:

$$\begin{aligned} F_n^{(0)} &= A^{-1}\{nF_{n-1}^{(0)} - 2(n+1)F_n^{(0)} + (n+2)F_{n+1}^{(0)}\} \\ &= 1 - Ae^A\{-\operatorname{Ei}(-A)\}, \end{aligned} \quad (71)$$

and also an asymptotically correct expression for large n:

$$\begin{aligned} F_n^{(0)} &\approx (n+1+A/12)^{-1}e^{A/2}L_1[4A(n+1+A/12)]^{\frac{1}{2}}, \\ L_1(y) &= yK_1(y). \end{aligned} \quad (72)$$

In calculating moments, particularly for large A, we have found it convenient to use the asymptotic expression to obtain two successive large moments, say $n=20, 21$. Lower moments are obtained by working the recursion expression (69) or (71) backwards. All moments are then slightly readjusted so that $F_0^{(0)}$ agrees with the value calculated from expression (69) or (71).

Superfluidity and Heat Transport in the Unsaturated Helium-II Film*

EARL LONG AND LOTHAR MEYER
Institute for the Study of Metals, University of Chicago, Chicago, Illinois
(Received February 24, 1955)

The mobility of unsaturated He-II films has been investigated by heat transport measurements as a function of thickness and temperature. The results confirm data from previous flow measurements that at a given temperature a certain number of layers are immobile, changing smoothly from ~2 at 1.3°K to ~10.5 at 2.0°K. All additional layers flow in a temperature gradient with about the same drift velocity, this velocity being of the same order of magnitude as that derived from the transfer rate of the saturated film. Films of thickness between 20–80 layers show superfluidity at and even slightly above the λ temperature of the bulk liquid.

INTRODUCTION

SOME experiments on heat transport by superfluid flow in thin films of adsorbed helium in the He-II region (below 2.19°K) have previously been reported by Bowers, Brewer, and Mendelssohn (BBM),[1] and a preliminary report of the experiments to be discussed in this paper has been given by the present authors.[2]

The experiments deal with thin films of adsorbed helium in an open wide tube with a chamber at each end, one provided with a heater and the other in good thermal contact with a heat reservoir, with sensitive thermometers attached to the tube so that temperature gradients along the conduction path may be determined. The tube and heater chamber are insulated by high vacuum. If helium gas is then admitted to the system, a film of adsorbed He is formed, the thickness being determined by the temperature and pressure. If heat is now applied to the heater chamber, and *if* superflow is possible under the prevailing conditions, the film (or part of it) will flow toward the source of heat, evaporate there, and the vapor will return via the open tube to the cool end, where it condenses to film, thus completing the heat transport cycle.

The film coverage in the cell is determined at each temperature by the saturation P/P_0, where P is the pressure of the vapor in equilibrium with the adsorbed phase and P_0 is the vapor pressure of the bulk liquid. The preliminary work of reference 2 showed that for a given film thickness the superfluid contribution to the heat transport appears abruptly at a certain temperature (the "onset" temperature). A film of a given thickness will not therefore exhibit superflow above this temperature. A plot of P/P_0 *vs* the "onset" temperatures is in agreement with the results of method I of earlier flow measurements of the present authors,[3] and is consistent with extrapolations to zero of the heat transport data reported by BBM (reference 1).

Since an apparatus can easily be constructed to have a very small thermal conductance in the absence of superflow, and since the heat transport by superflow in this system involves the heat of vaporization of the film in addition to the thermomechanical heat, the method provides a sensitive means of investigating the superfluid behavior of these thin films.

APPARATUS

The heat transport cell is shown schematically in Fig. 1; it resembles qualitatively the arrangement of reference 1. A copper-nickel alloy tube of 4.7 mm o.d. and 0.127 mm wall thickness was provided at the top with a copper chamber E, on which a manganin heater was wound, and at the bottom with another copper chamber D, immersed in the liquid He-II bath which surrounded the vacuum can A. Sensitive carbon thermometers[4] Th-1, Th-2, and Th-3 were sealed by glyptal or Corex varnish into heavy copper holders soldered at the top, middle, and bottom of the tube; the distance between the top and bottom thermometers was 10 cm, with the middle thermometer mounted halfway between.

The insulating vacuum in the can A was pumped through the tube P, which was provided with a radiation trap (not shown). The electrical connections are not shown; the thermometers were connected in series, with a common current lead, and with potential leads arranged so that the resistance of each thermometer could be measured independently. The thermometer leads were of No. 36 manganin wire, to provide connections of very low thermal conductance; the heater leads were of No. 40 copper wire, to minimize heating effects. All electrical leads were connected to kovar-glass terminals soldered to the bottom plate B of the vacuum

* Supported in part by a grant from the National Science Foundation.

[1] Bowers, Brewer, and Mendelssohn, Phil. Mag. **42**, 1445 (1951).

[2] E. Long and L. Meyer, Phys. Rev. **87**, 153 (1952). In the discussion of this note in the review by E. Long and L. Meyer, Phil. Mag. **44**, Supplement 2, 18–22 (1953), the values of the heat current shown in Fig. 13 are too high by a factor of ten, due to an error in reproduction.

[3] E. Long and L. Meyer, Phys. Rev. **79**, 1031 (1950); Phys. Rev. **85**, 860 (1952).

[4] These thermometers were nominal 100-ohm, ½-watt radio resistors made by the Speer Resistor Corporation, St. Mary's, Pennsylvania. Their resistance increased from 100 ohms at 300°K to 500–1000 ohms at 1.2°K. The sensitivity ranged from 100 to 300 ohms per degree in the liquid helium region. Their use offers a number of advantages for work such as this, although it was felt that calibration was required each time the apparatus was cooled to helium temperatures.

can, thus providing electrical connections of minimal thermal leakage from temperatures higher than that of the surrounding bath.

The helium gas was admitted to the conductance cell through the stainless steel capillary C, which was connected to a large buffer volume at room temperature, to ensure that heating of the chamber H did not increase the gas pressure in the cell.

The gas pressure P in the cell and the bath vapor pressure P_0 were measured using Octoil-S manometers and a Wild cathetometer of precision 0.02 mm.

A rather rigorous experimental procedure was required to ensure proper performance of the apparatus. The cell had such a low thermal conductance (in the absence of exchange gas in chamber A, or of a superfluid He film inside the cell) that the apparatus could not readily be cooled to working temperature without introducing exchange gas into chamber A. This then entailed a prolonged pumping period to ensure a vacuum in the insulating space sufficiently low that heat conduction by the gas across chamber A did not contribute to the heat transport in any appreciable way. Since it was considered necessary to calibrate the carbon thermometers, using exchange gas, each time the apparatus was cooled to helium temperatures, it was thus standard practice to calibrate[5] the thermometers during one working day, and then to pump the system overnight before proceeding with the heat transport experiments. In this manner insulating vacua below 10^{-6} mm Hg, usually $1-2\times10^{-7}$, were obtained, as measured on a liquid nitrogen-trapped RCA 1949 ion gauge mounted in the external vacuum system.

The resulting thermal conductance of the cell, without the contribution of the superfluid film, was 10–15 microwatts per degree, although no attempts were made to accurately measure this quantity, since it was sufficiently small to be ignored, even at the lowest heat transport levels observed with the superfluid film.

Because of the precision desired, it was necessary to maintain the temperature of the cryostat to a drift of 1 millidegree per hour or less during the measurements.

EXPERIMENTS

A series of experiments was carried out in which the heat transport was measured at a number of temperatures from 1.3°K to 2.0°K, with a number of film coverges being investigated at each temperature, all showing superfluid behavior.

The data for the temperatures and film coverages measured are summarized in Table I. P is the pressure measured in the system, P_0 the saturation vapor pressure of bulk liquid at the temperature of the bath; P/P_0 represents therefore the saturation at the bottom

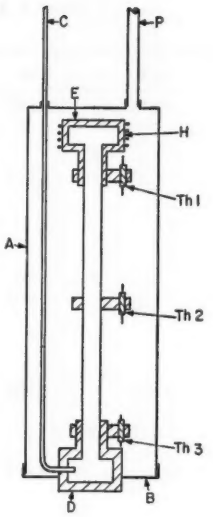

FIG. 1. Schematic drawing of the heat transport apparatus.

of the tube. $\dot{Q}$ is the heat input in microwatts, and ΔT is the measured temperature difference in millidegrees between the top and bottom thermometers, Th-1 and Th-3, separated by a 10-cm distance along the tube.

It should be remembered that the experiments are made at constant P and constant T of the reservoir and therefore that the values quoted for P/P_0 are for the bottom reservoir only. P/P_0 decreases towards the warm end with increasing ΔT and is thus somewhat in error. The error is small, except at the higher ΔT's, with which this work is not mainly concerned.

The heat current $\dot{Q}$ is a function of T, ΔT, and P/P_0. Figure 2 is qualitatively representative of the data at all temperatures and unsaturated film coverages in these measurements and gives $\dot{Q}$ in microwatts plotted against ΔT in millidegrees at constant temperature (1.700°K) of the thermal reservoir for different values of P/P_0.

Figure 2 shows that the heat current is not linearly dependent on the temperature gradient, but resembles qualitatively the cube root dependence which occurs in the heat conduction of liquid He-II.[6] Indeed, an analysis of the film data shows a fairly good agreement with a cube root law at low values of ΔT.

However, the resemblance can be only superficial: The heat current in liquid He-II can be described by

$$\dot{Q}=\text{const}(dT/dx)^{\frac{1}{3}},$$

where the constant comprises the geometry of the current and a factor representing the "conductivity." ΔT then remains a linear function of x, whatever the exponent of dT/dx may be.

In order to investigate this distribution of the temperature gradient, Th-2, mounted half-way along the tube, was used. A typical result is shown in Fig. 3, in

[5] All calibrations were based on the vapor pressure of liquid helium, as tabulated in the 1949 temperature scale—see H. van Dijk and D. Shoenberg, Nature **164**, 151 (1949). Although later evidence indicates that this scale is somewhat in error—see R. A. Erickson and L. D. Roberts, Phys. Rev. **93**, 957 (1954)—the deviations are not relevant to this experiment.

[6] Keesom, Saris, and Meyer, Physica **7**, 817 (1940).

TABLE I. Amount of heat in microwatts carried by superfluid films as a function of temperature T, saturation P/P_0 and temperature difference ΔT.

T, °K	P/P_0	$\dot{Q}$, watts	ΔT, °K×10³
1.313	0.598	3.97	0.9
		4.30	2.7
		5.72	17.1
	0.813	15.9	0.7
		22.9	1.3
		26.8	3.0
		31.1	5.2
		35.7	22.9
	0.905	15.9	0.5
		40.6	3.3
		51.4	12.7
		57.3	
1.503	0.704	0.64	1.2
		0.99	3.3
		1.43	
	0.774	1.43	0.2
		3.97	1.1
		4.30	2.9
		5.72	10.4
	0.846	10.2	0.1
		12.9	1.7
		15.9	11.7
	0.912	10.2	0.5
		15.9	0.8
		31.1	2.1
		35.7	4.6
		40.6	22.4
	0.955	31.1	0.3
		40.6	0.3
		63.5	1.6
		70.1	4.3
		76.8	10.0
1.700	0.892	4.3	1.1
		5.0	2.8
		5.7	9.2
0.932	5.0	5.0	0.4
		5.7	0.6
		7.8	0.6
		15.9	2.2
		17.2	3.6
		19.2	14.6
1.700	0.955	10.2	0.1
		15.9	0.2
		22.9	0.7
		31.1	2.7
		32.9	4.3
		35.7	12.3
	0.978	31.1	0.2
		40.6	0.6
		53.5	2.8
		70.0	5.7
		73.7	10.6
1.900	0.963	1.42	0.2
		2.55	3.3
		2.80	9.7
		3.35	29.3
	0.979	2.55	0.2
		5.7	0.5
		10.2	1.2
		12.9	5.0
		15.9	~25
	0.988	10.2	0.4
		15.9	0.5
		22.8	1.2
		26.8	2.9
		31.1	5.4
		35.7	11.7
	0.991	22.8	0.4
		31.1	0.5
		40.6	2.9
		45.9	5.7
		51.4	12.1
2.000	0.981	0.64	0.0
		1.43	3.3
		1.94	12.2
		2.54	0.0
	0.995	10.2	0.0
		19.2	0.1
		35.7	1.6
		45.9	3.5
		57.3	14.5

which the solid curve represents the ΔT between top and bottom of the tube (Th-3—Th-1), while the dashed curve is that between center and bottom (Th-2—Th-1). The temperature was 1.785°; the saturation P/P_0 was 0.927.

This temperature gradient along the lower half of the tube also obeys roughly a cube root law, within the accuracy of the measurements; however, the agreement may be fortuitous. It was suggested earlier (see reference 2) that if this finite but very small ΔT is real, then perhaps the film transport cannot be regarded as a true superfluid process. Unfortunately, the effect is so small, and the establishment of equilibrium between the thermometers and the flowing film so correspondingly uncertain to the required accuracy, that no definite conclusions can be drawn.

It is clear from these results that the observed temperature distribution must be a consequence of a change of the constant along the tube, i.e., the geometry and/or the "conductivity." As ΔT is increased at constant P, the value of P/P_0 at the warm end decreases; consequently the film becomes thinner in this region and its capacity to carry heat decreases correspondingly. Real superfluidity could even under these circumstances not produce a temperature gradient, only instability. We have therefore to assume that as soon as the thermal load exceeds a certain critical value heat resistance sets in rather sharply in the film. The continuity of the heat current then requires a considerable temperature gradient in this region of lower conductivity.[7] The re-

[7] If the film thickness can be represented by the isotherm $\ln(P/P_0)=k/d^3$ as shown by R. Bowers, Phil. Mag. 44, 487 (1953)

duction in film thickness can finally go so far that the moving part of the film evaporates completely before reaching the chamber H itself, and a small region of the tube below chamber H takes over the heat transport. Thus a short but finite length of the tube practically determines the resistance to the heat transport, with a very considerable local temperature gradient. This is the "runaway" phenomenon observed by BBM (reference 1); it may be seen clearly in Fig. 2 as the end of the curve which becomes almost parallel to the T axis.[8,9]

An analysis of these data and of the earlier flow data of reference 3 requires that values of the film thickness be derived from the saturations P/P_0 of the experiments, using the adsorption isotherms of He. The adsorption of He on this particular Cu–Ni tube surface is not known; however, the fact that the "onset" temperatures for superflow are the *same* in this arrangement[2] as in the flow measurements previously quoted lead to some confidence in the coverages derived below.

The adsorption measurements of Strauss,[10] on iron oxide, in fairly good agreement with those of Bowers[11] on metallic aluminum, are used here for this purpose.

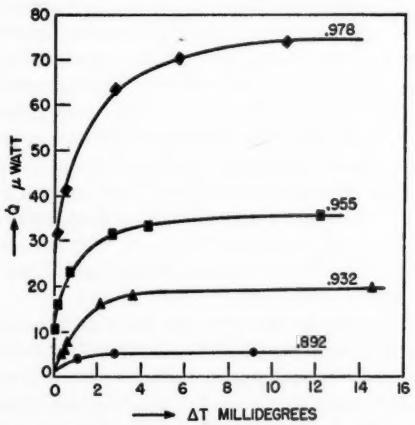

FIG. 2. Amount of heat in microwatts carried by films as a function of the temperature difference in millidegrees for different saturations P/P_0 at 1.700°K.

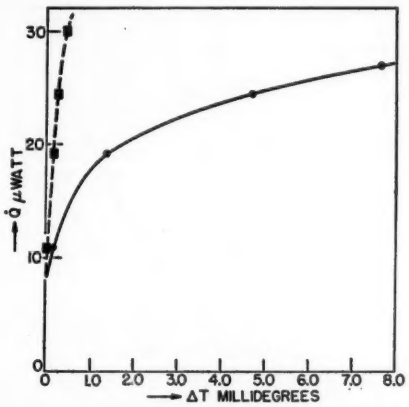

FIG. 3. Temperature difference between top and bottom thermometer (solid curve) and temperature difference between center and bottom thermometer (dashed curve) as functions of the heat input in microwatts.

In order to compute the average number of statistical layers adsorbed on a surface from the total quantity of adsorbate, it is inevitable that some assumptions be made concerning the layers nearest the wall. In the calculation made here, the quantity v_m (the amount adsorbed in the first completed monolayer) was that derived by Strauss from his isotherms, using the Brunauer-Emmett-Teller theory.[12] The quantity $\frac{1}{2}v_m$ was taken for the adsorption in the second monolayer, and then 0.28 cm^3/m^2 surface area was used for all subsequent layers. The number of layers derived in this way from the data of Strauss is consistently about two layers less than the values given by Bowers for the same saturation P/P_0. However, this is within the error, since Bowers, using a microbalance, was unable to measure the absolute values of the adsorption on his surfaces below $P/P_0 \sim 0.15$, and had to assume the amount adsorbed below this value, whereas Strauss measured these quantities in direct determination. Moreover, the consistency of the treatment is more important than the absolute magnitude.

In Fig. 4, $\dot{Q}$, again in microwatts, is plotted at constant ΔT (3 millidegrees) against the film thickness derived from P/P_0 and the adsorption isotherms in the manner described above, for each temperature of measurement. The 3 millidegree choice for ΔT is clearly arbitrary, but is one for which even at the warm end the film thickness should not deviate much from that derived for the lower end.

The intercepts with the abscissa in Fig. 3, i.e., the points for $\dot{Q}=0$, are not extrapolated from the points for finite $\dot{Q}$, but were calculated from the dependence of the "onset" temperatures for superflow upon the film

the apparent dependency of $\dot{Q}$ on $(\Delta T)^{\frac{1}{3}}$ can be a consequence of the isotherm, since a change of $\ln P$ is proportional to ΔT, in first approximation; ν therefore decreases proportional to $(\Delta T)^{\frac{1}{3}}$.

[8] It appears, however, difficult to explain all observed temperature gradients by assuming complete superfluidity with no ΔT at all along the greater part of the tube, and the whole resistance concentrated in a short length of the tube at the warm end. In many cases the heat resistance is so small that already less than a millimeter of tube length would produce it. It seems doubtful that such a short length would not eventually be swamped by film flow, and would be able to show the extraordinary stability of resistance observed in these experiments.

[9] In order to rule out the possibility that the evaporation of the film might produce the observed resistance, the chamber H was replaced by a copper bloc which reduced the area available for evaporation by a factor of about 8. No influence on the results could be observed, which indicates that the evaporation is probably not the rate determining step. Likewise, the resistance of the gas flow down the tube can be neglected, since less than 10^{-6} mm Hg ΔP is required.

[10] See E. Long and L. Meyer, Advances in Phys. 2, 18–22 (1953).

[11] R. Bowers, Phil. Mag. 44, 487 (1953).

[12] Brunauer, Emmett, and Teller, J. Am. Chem. Soc. 60, 309 (1938).

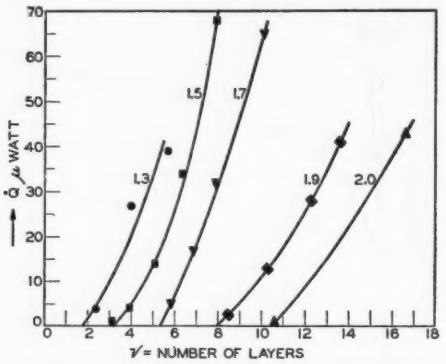

FIG. 4. Amount of heat in microwatts carried by superfluid films as a function of film thickness at constant temperature for different temperatures.

coverage as given in references 2 and 5. The consistency of the two methods in measuring the "onset" coverages for superflow is clearly shown in this treatment.

The slope of the curve for each temperature in Fig. 3, $\Delta\dot{Q}/\Delta\nu$ represents the differential amount of heat carried per added layer. A characteristic of the curves is that the slope does not change appreciably from the intercept $\dot{Q}=0$ to the highest values of $\dot{Q}$ measured for superfluid flow. Evidently the film behaves as though each further layer added to the film contributes about the same amount to the heat transport.

The amount of heat $\dot{Q}$ carried by a single layer in the film may be estimated by using an admittedly oversimplified picture: If it is assumed that the spacing of the He atoms in these adsorbed layers is equal to that in the bulk liquid, 3.6 A, then the number of atoms per cm circumference of the tube is $10^8/3.6$. If these atoms flow with a velocity v cm/sec, the number of atoms reaching the heat source per second and per cm circumference is $v\times10^{16}/(3.6)^2$. One mole of He carries $\sim$100 joules (heat of adsorption plus thermomechanical heat) in the heat transport process. One atom then carries $100/(6.06\times10^{23})$ joules, and one statistical layer carries per cm circumference per second:

$$v\times10^{-5}/[(3.6)^2\times6.06] \text{ joules.}$$

The circumference of the tube used in these experiments is 1.5 cm, if surface roughness is neglected. By using this value, and taking the slopes near the intercepts of Fig. 3, the values of v, the flow velocity, are obtained as shown in Table II. The values for v derived from the slopes at the highest heat currents shown in Fig. 3 are about 30 percent higher than those of Table II.

The results presented here are completely consistent with those obtained in direct flow experiments by method *I* of reference 3, whereas the different ranges of superfluidity observed by method *II* of reference 3 did not appear in the heat conduction experiments. We intend to investigate the question whether these differences are due to the fact that in method *II* a combination of temperature and pressure gradients was acting on the film or that eventually metastable films were responsible. The discrepancy between the "onset" temperatures of superfluidity and the maxima in the specific heat found by Frederikse[13] and discussed already in detail in reference 10 also still remains.

The data of these experiments suggest that at a given temperature a certain number of layers are immobile, that above this number superflow sets in, and that the flow in all additional layers caused by temperature gradients shows about the same drift velocity, this velocity being of the same order or magnitude as that derived from the film transfer or the heat conductivity of bulk liquid.

Very approximately the following picture can be given: The first layer near the wall (v_m) is solid-like, followed by a region of immobile layers, and only the layers additional to these behave like He II. This picture has qualitatively some similarity to that given by Mastrangelo and Aston[14] and by Atkins,[15] who relate the properties of the film in the field of force of the wall to that of bulk liquid under pressure. Such a treatment overlooks the fact that bulk liquid under hydrostatic pressure is in a uniform field of force, whereas the forces of the wall act only in one direction: that perpendicular to the wall. The forces in the other two directions, parallel to the wall, are completely different and have to be considered as stresses (surface tension). As a consequence, for example, the Gibbs free energy G of a liquid under pressure is greater than that under saturation pressure, since $(\partial G/\partial p)_T=v$, whereas the free energy of the film is smaller than that of the bulk liquid, since $P<P_0$.

Furthermore, if the transition from immobile layers to superfluid layers in the field of force of the wall would be related in a simple way to the λ line of the bulk liquid, the curve of the number of immobile layers n *vs* temperature T, shown in Fig. 5, should show a break at 1.75°K, where the melting curve intersects the λ line, and below this temperature all but the solid first layer v_m should be superfluid. The smooth curve found for n as a function of T is inconsistent with such a relationship.

TABLE II. Drift velocity of unsaturated films derived from the heat transport as a function of temperature.

T, °K	v, cm/sec
1.3	48
1.5	44
1.7	38
1.9	25
2.0	21

[13] H. P. R. Frederikse, Physica **15**, 860 (1949).
[14] S. V. R. Mastrangelo and J. G. Aston, J. Chem. Phys. **19**, 1370 (1951).
[15] K. R. Atkins, Can. J. Phys. **32**, 347 (1954).

In reality the number of immobile layers n is roughly proportional to the fraction of normal fluid ρ_n/ρ of the bulk liquid. This proportionality is improved if one deducts from n the first "solid" layer, as shown in Table III.

The physical meaning of Table III is probably that the forces of the wall tend to increase the fraction of normal fluid; this effect becomes more and more pronounced the thinner the film. If ρ_n is very small at great distances from the wall, i.e., in the bulk liquid, then in a region close to the wall there is a borderline in which ρ_n/ρ reaches 1 and the film becomes immobile. If ρ_n/ρ is already approaching 1 in the bulk liquid, then perhaps the forces of the wall are able to raise ρ_n/ρ to 1 at a greater distance, and a greater number of layers becomes immobile.

Table III and Fig. 5 show furthermore that for $\rho_n/\rho=1$ in the bulk liquid, i.e., at the λ point, only about 20 layers should be immobile. Since it is known that the film can be more than 100 layers thick, the question arises whether or not films of more than 20 layers would exhibit superfluidity at or eventually even above T_λ. Heat conduction experiments were therefore performed at a temperature of the helium bath $1\frac{1}{2}\pm0.2$ millidegrees below the λ point, taking $P_\lambda=38.1$ mm Hg[16,17] corresponding to 2.183°K of the conventional scale and $dP/dT=0.094$ mm/Hg/10^{-2} degree. Without a contribution of superfluidity, a heating by 0.3 microwatt produces a steady warming rate of about 2 millidegree/minute, as confirmed by a run at $P/P_0=0.8$, corresponding to about 7 layers. Using then (*a*) $P/P_0=0.9996$ ($P_{\text{bath}}-P_{\text{system}}=0.3$ mm oil, $P_{\text{bath}}=560$ mm oil) yielding an estimated film thickness of about 30 layers, and (*b*) 5 percent and 15 percent more gas in the apparatus than necessary to make $P_{\text{system}}=P_{\text{bath}}$, estimated film thickness 40–50 and 50–60 layers respectively, lead to the following results.

Heat inputs up to 2μw did not produce any measurable temperature difference between the bottom and top thermometers up to a temperature of 2.185°K of the conventional scale, i.e., 2 millidegrees above the bulk liquid λ point. Higher heating rates up to 7.3μw did produce increasing temperature differences in a slow runaway phenomenon. However, the warming rate with these heat inputs was up to at least 2.195°K of the conventional scale only a fraction of that found without contribution of superfluidity. These results indicate that films more than 20 layers thick show superfluid behavior at and above the λ point of the bulk liquid, as already suggested by earlier thermodynamic considerations.[18]

TABLE III. Comparison of the number of immobile layers n with the fraction of normal fluid ρ_n/ρ in the bulk liquid for different temperatures.

T	$(n-1)$	ρ_n/ρ	$(n-1)\rho/\rho_n$
1.3	1.0	0.042	23.8
1.5	1.9	0.106	17.9
1.7	4.1	0.222	18.4
1.9	7.0	0.420	16.6
2.0	9.5	0.552	17.2

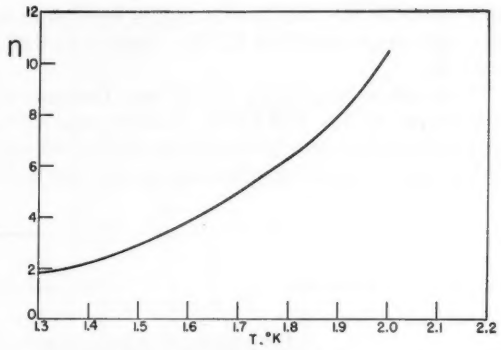

FIG. 5. Number of immobile layers n as a function of temperature.

In several cases the warm end of the apparatus cooled down from temperatures up to 2.192° (after switching off the heating current) much faster than a conductance of 10 microwatts/degree would allow, as would be expected for the case that the heat-carrying film is stable and in equilibrium. In several other cases, however, the cooling rate following a heating period dropped to the order of 10 microwatts/degree after a few minutes, showing that the stability range of the mobile film had been exceeded during the runaway phenomenon. However, the possibility cannot be completely excluded that the films showing superfluidity above T_λ are metastable.

Heat Transport in the Saturated Film ($P/P_0=1$)

It is hardly fruitful to make measurements for the condition $P/P_0=1$ as measured at the thermal reservoir, since the film thickness is reduced at the top by the gravitational field and as ΔT increases. The asymptotic infinity of the isotherm at $P/P_0=1$ produces extreme changes in thickness for minute changes in P/P_0 in this region,[19] so that the real thickness is indeterminable.

Therefore only a few measurements were made, between 1.7° and 2.1°K, with *excess liquid* in the cell. The resulting heat transport data were completely different from those of Table I and Fig. 2. After an initial heating rate at which no ΔT was detected within the accuracy of the experiment (0.0002°), a linear dependence of ΔT on $\dot{Q}$ occurred, until at a given critical heat input the ΔT rose exceedingly rapidly, and a "runaway" phenomenon occurred, as previously described. The

[16] E. Long and L. Meyer, Phys. Rev. **83**, 860 (1951).
[17] R. A. Erickson and L. D. Roberts, Phys. Rev. **93**, 957 (1954).
[18] L. Meyer and E. Long, Phys. Rev. **85**, 1035 (1952).
[19] See L. Meyer, Phys. Rev. **93**, 655–656 (1954).

ΔT's at which the critical heat inputs were observed were quite large (0.018° at 1.7°K), dropping to 0.005° at 2.1°K.

These critical heat inputs for the heat transport are proportional to the well-known transfer rate of the saturated film, as already reported by BBM (reference 1); however, the limiting initial heating rate (for which no ΔT was observed) was dependent on the amount of excess liquid in the cell. Further, the critical heat input observed was very high; at 1.7°K it was twenty-five times greater than that observed for the thickest film of Fig. 2. The experiments were not continued, since adequate interpretation seems difficult in view of the absence of a reliable estimate of the film thickness.

PHYSICAL REVIEW VOLUME 98, NUMBER 6 JUNE 15, 1955

Resonance Absorption of Sunlight in Twilight Layers

T. M. DONAHUE AND ROBERT RESNICK
The University of Pittsburgh, Pittsburgh, Pennsylvania
(Received February 9, 1955)

Solar radiation must pass at least once through the absorbing layer to reach the twilight zone of a layer of atoms scattering resonance radiation. The attenuation of the solar beam is calculated for resonance absorption and the resulting scattered intensity compared with the transparent layer model intensity for the same thickness of material. It is shown that in the case of sodium, the reduction in intensity for layers thicker than 10^9 atoms/cm² is too serious to permit the deduction of layer thickness from a simple theory which neglects imprisonment of resonance radiation.

INTRODUCTION

FROM measurements of the time variation in intensity of the sodium D lines at twilight and at dawn the location, distribution, and vertical thickness of the scattering layer of sodium atoms has been deduced.[1–4] The basic assumption that the light observed is scattered sunlight is supported by strong evidence.[5–7] Careful account has been taken of such important factors in the interpretation of the observations as refraction and attenuation by the gases of the lower atmosphere which the incident sunlight must traverse.[3,4] Unfortunately, an uncertainty in the intensity incident at the bottom of the Fraunhofer lines makes for an uncertainty as large as an order of magnitude in the deduced sodium thickness. Values given range from 2×10^9 atoms/cm² to 2×10^{10} atoms/cm². The layer appears to be located somewhere between 70 and 115 km above the earth's surface.

With the correction mentioned for general atmospheric extinction—which is of course independent of the sodium layer thickness—the flux incident in the twilight scattering layer is taken in these calculations to be uniform throughout the region. This assumption, however, neglects the fact that the sunlight incident on the sodium layer after sunset must pass once completely through the layer and, in general, partly through it again. It is the purpose of this note to give the results of a calculation of the consequent attenuation of the incident light by resonance absorption for layer thicknesses in the range from 2×10^9 atoms/cm² to 2×10^{10} atoms/cm². Appreciable attenuation under these conditions would not only force a revision upward of the layer thickness, but, because this in turn would imply further attenuation, would seem to suggest an altogether different treatment of the problem of twilight excitation. This is particularly true since this treatment neglects reradiated resonance photons. Under such conditions these should contribute a non-negligible component to the density of excited atoms in twilight.[8]

The importance of an accurate knowledge of the sodium layer thickness for the determination of the altitude of the nightglow D line emission has been pointed out in connection with a calculation of the effect of resonance absorption on the variation with zenith distance of the radiation from an airglow layer.[9]

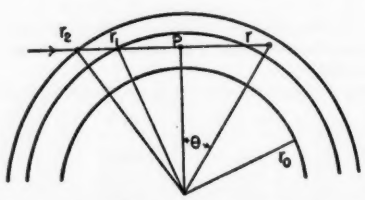

FIG. 1. Path of a photon through the absorbing layer to reach the point (r,θ). r_0 is the radius of the earth.

[1] D. R. Bates and H. S. W. Massey, Proc. Roy. Soc. (London) **A187**, 261 (1946).
[2] D. Barbier, Ann. Geophys. **4**, 193 (1948).
[3] D. M. Hunten, J. Atmos. Terrest. Phys. **5**, 44 (1954).
[4] D. M. Hunten and G. G. Shepherd, J. Atmos. Terrest. Phys. **5**, 57 (1954).
[5] A. Kastler, Compt. rend. **210**, 530 (1940).
[6] J. Bricard and A. Kastler, Ann. Geophys. **1**, 53 (1944); **6**, 286 (1950).
[7] Bricard, Kastler, and Robley, Compt. rend. **228**, 1601 (1949).
[8] A. Foderaro and T. M. Donahue, Phys. Rev. **91**, 1561 (1953).
[9] T. M. Donahue and A. Foderaro, J. Geophys. Research **60**, 75 (1955).

ABSORPTION OF INCIDENT SUNLIGHT IN SODIUM LAYER

Consider sodium atoms distributed in a layer between r_1 and r_2 as in Fig. 1, where r is the distance from the center of the earth. Let the density of atoms be

$$N(r)=N_0\exp[-\alpha(r-r_0)]. \tag{1}$$

The thickness of sodium traversed by a photon which reaches a point (r,θ) in the sodium layer is

$$L(r,\theta)=\int_{x(r_2)}^{x(r_1)}N(r')dx'+\int_{x(r_1)}^{x(r)}N(r')dx', \tag{2}$$

where

$$\begin{aligned}x'&=(r_2^2-p^2)^{\frac{1}{2}}-(r'^2-p^2)^{\frac{1}{2}},\\ p&=r\cos\theta,\end{aligned} \tag{3}$$

and θ is measured from "sunset." For $r_0<p<r_1$, this becomes

$$\begin{aligned}L(r,\theta)\cong&N_0(\pi p/2\alpha)^{\frac{1}{2}}\\ &\times(\mathrm{erf}w_2+\mathrm{erf}w-2\,\mathrm{erf}w_1)\exp[\alpha(r_0-p)],\end{aligned} \tag{4}$$

subject to the condition

$$(r'^2-p^2)^{\frac{1}{2}}\ll p \tag{6}$$

for all r' along the path of the photon, and where

$$w=[\alpha(r^2-p^2)/2p]^{\frac{1}{2}}, \tag{7}$$

w_2 being the value of w at $r=r_2$ and w_1 its value at $r=r_1$. For $r_2>p>r_1$, similarly,

$$L(r,\theta)\cong N_0(\pi p/2\alpha)^{\frac{1}{2}}(\mathrm{erf}w_2+\mathrm{erf}w)\exp[\alpha(r_0-p)]. \tag{8}$$

And for all values of θ in the fourth quadrant (before sunset),

$$L(r,\theta)\cong N_0(\pi p/2\alpha)^{\frac{1}{2}}(\mathrm{erf}w_2-\mathrm{erf}w)\exp[\alpha(r_0-p)]. \tag{9}$$

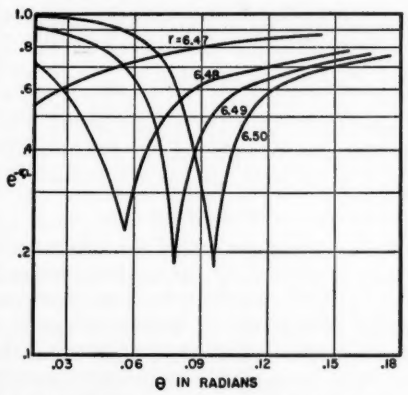

FIG. 2. Attenuation at the center of the sodium D_2 line ($^2S_{\frac{1}{2}}-^2P_{\frac{1}{2}}$) for solar radiation reaching points in the twilight layer defined by (r,θ), where r is the distance from the center of the earth and $r_0\theta$ is the distance on the surface from sunset. Vertical thickness of the sodium layer here is assumed to be 1.84×10^9 atoms/cm² column.

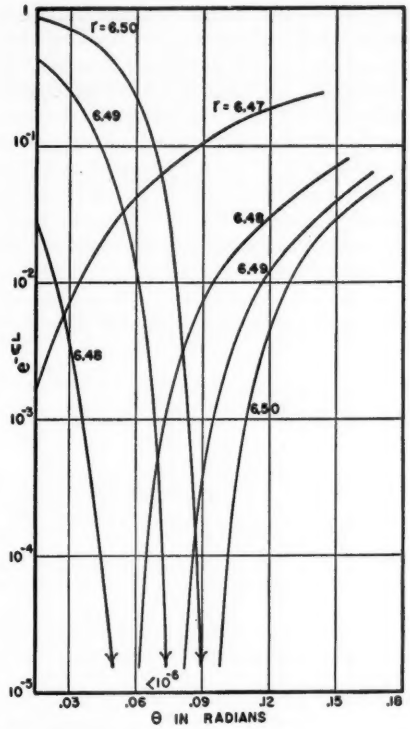

FIG. 3. Attenuation at the center of the sodium D_2 line ($^2S_{\frac{1}{2}}-^2P_{\frac{1}{2}}$) for solar radiation reaching points in the twilight layer defined by (r,θ), where r is the distance from the center of the earth and $r_0\theta$ is the distance on the surface from sunset. Vertical thickness of the sodium layer here is assumed to be 1.84×10^{10} atoms/cm² column.

THE SCATTERED INTENSITY

If the intensity per unit frequency of the light incident on the earth in the neighborhood of the Fraunhofer D lines is taken to be J_0, independent of frequency, then

$$J_0\exp[-\sigma(\nu)L]d\nu \tag{10}$$

will be the intensity incident between ν and $\nu+d\nu$ at the point (r,θ). $\sigma(\nu)$ is the cross section for absorption at frequency ν. The scattered intensity then, apart from small geometrical factors, would be

$$I(\theta)\propto\int_{r_1}^{r_2}\int\sigma(\nu)J_0N(r)\exp[-\sigma(\nu)L(r,\theta)]d\nu dr. \tag{11}$$

COMPUTATION FOR MODEL SODIUM LAYERS

$L(r,\theta)$ has been computed under the assumption that sodium is distributed between 70 and 100 km according to

$$N(r)=\begin{cases}0, & r<6.47,\\ N_0\exp[-127(r-6.40)], & 6.47<r<6.50,\\ 0, & r>6.50,\end{cases} \tag{12}$$

where distances are measured in thousands of km. Two values of N_0 have been assumed, 2.17×10^8 cm^{-3} and

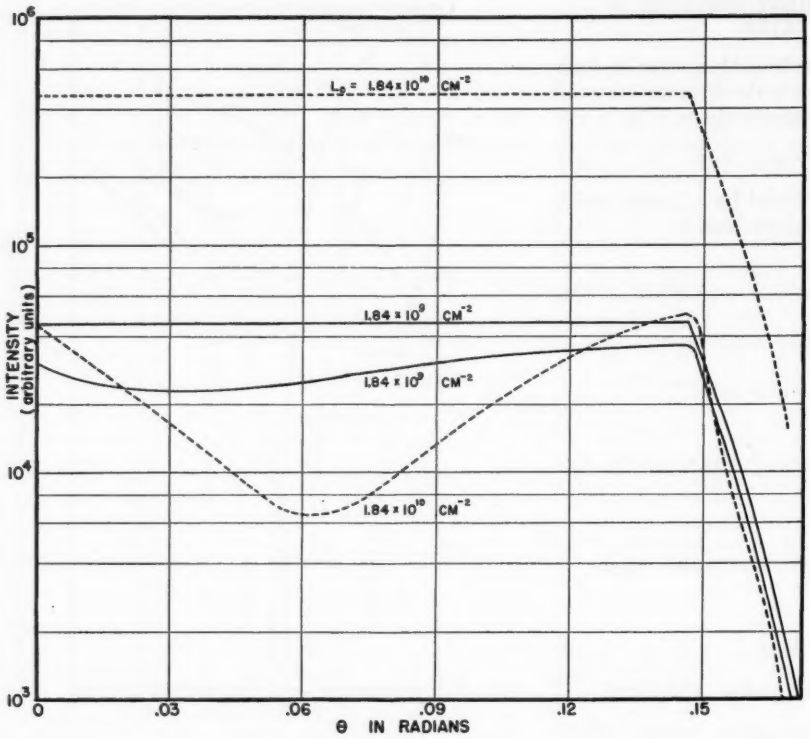

FIG. 4. Predicted intensity of radiation scattered from the zenith as a function of angle measured from sunset for the nonabsorbing sodium layers and the absorbing sodium layers of the same thicknesses. L_0 is the vertical thickness assumed. Curves are for the center of the D_2 component. The lower of each pair of curves is for an absorbing layer.

2.17×10^7 cm^{-3}. The first corresponds to a vertical thickness of 1.84×10^{10} sodium atoms/cm^2, the second to 1.84×10^9 per cm^2. Curves are drawn in Fig. 2 and Fig. 3 showing $\exp(-\sigma_0 L)$, where σ_0 is the absorption cross section at the center of the D_1 component and is here taken, for a Doppler line at 240°, to be 10^{-11} cm^2.

Traversal of even the less thick layer results in great attenuation, particularly in the time just after sunset. Furthermore, the incident flux of radiation in the region where twilight observations are usually made can be seen to vary appreciably with time (θ) and with altitude for fixed θ as well as to have suffered an over-all attenuation.

Integration at selected fixed values of θ of the product function of r,

$$N_0 \exp[-\alpha(r-r_0)] \exp[-\sigma_0 L(r,\theta)], \qquad (13)$$

gives a measure of the intensity scattered radially (zenith observation). This may be compared with

$$N_0 \int_{r(\theta)}^{r_2} \exp[-\alpha(r'-r_0)]dr', \qquad (14)$$

which would be the measure of the scattered intensity for the case of no resonance attenuation (see Fig. 4). The lower limit of integration $r(\theta)$ is the lowest illuminated point in the sodium layer at the angle θ. The logarithmic scale of intensity used in the figure obscures the very large effects calculated even for the thinner layer. The reduction in intensity is by a factor larger than 10 for the thicker layer and larger than 4/3 for the thinner layer throughout the twilight region. The relative intensities at two values of $r(\theta)$ the lower limit of illumination in the layer, are given in Table I.

TABLE I. Relative intensities for the two sodium layers of Fig. 4 at $\theta=0.1464$ and $\theta=0.1570$ radian. Here the intensities are all compared to that of the 1.84×10^{10} cm^{-2} layer normalized to 10 in arbitrary units.

	$r(\theta)=70$ km	$r(\theta)=80$ km
Thick layer—no attenuation	10.00	10.00
Thick layer—attenuated	1.07	0.60
Thin layer—no attenuation	1.00	1.00
Thin layer—attenuated	0.73	0.74

DISCUSSION

No other model sodium atmospheres have been considered here. It seems clear that no simple alteration in layer height or in the distribution would affect seriously the sizeable attenuation or lead to a qualitatively different shape of intensity curve. Neither has the full contribution of the doublet been computed as it would be given from (11). While it is true that the attenuation is most severe for the case selected, the other frequencies have a correspondingly lower probability of being scattered and observed. In fact, when absorption but not imprisonment is taken into account, as in this paper,

the scattered radiation should be strongly self reversed whenever the important part of the incident sunlight must travel through a thickness of sodium so great that $\sigma_0 L \gg 1$. For both of the examples treated here, this is the case. The fact that the actual twilight radiation is not self-reversed may perhaps be explained on the basis of replenishment of photons near the center of the line by imprisonment. It seems scarcely profitable to pursue all such refinements as these separately. Calculations are being made of the intensity of radiation which would be received near twilight in various zenith directions for several model sodium atmospheres in which the transport of imprisoned resonance radiation is accounted for. It would appear from these results that unless the observed zenith intensity in twilight is consistent with a vertical thickness of less than 10^9 atoms/cm^2, it is unsafe to conclude much about the distribution of sodium atoms without a careful account of the history of the resonance photons before they reach the scattering region. The inclusion of sodium layer absorption in the present simple theory of the twilight effect leads in fact to a very large "predicted" variation during early twilight for which there is no observational evidence. Such effects are expected to vanish when the contribution of the imprisoned resonance radiation to the density of excited atoms is properly accounted for.

PHYSICAL REVIEW VOLUME 98, NUMBER 6 JUNE 15, 1955

Statistical Analog of the Second Law

JOHN S. THOMSEN
Radiation Laboratory, Johns Hopkins University, Baltimore, Maryland
(Received February 24, 1955)

In recent papers Landsberg and the writer have used two different propositions to represent the statistical analog of the second law of thermodynamics. The difference is discussed and the writer's viewpoint presented. There is also included a necessary addition to a proof given in the author's previous analysis.

LANDSBERG[1] has recently given an extension and generalization of an analysis[2] by the writer. This analysis involved the logical relations among the second law of thermodynamics and certain propositions in statistical mechanics when the transition probabilities are assumed independent of time. Landsberg obtains analogous results except that the statistical implications of the second law appear to be different in the two analyses. These exceptions arise from the fact, clearly pointed out by Landsberg, that his proposition (H) is not completely analogous to the proposition (S) used by the writer. It seems desirable to clarify this difference.

The second law asserts that, aside from statistical fluctuations, the entropy of an isolated system will *never decrease, whatever initial values may be assigned to the macroscopic variable.* The statistical form of this law would seem to require that the statistical analog of entropy must never decrease, whatever initial values may be assigned to the probabilities. (The objection may be raised that certain initial distributions could be set up only by a Maxwell demon. In any event there are a very large variety of permissible distributions.) (S) is intended to meet precisely the above requirement. However, a system is said to obey Landsberg's (H) at a time T if the entropy is constant or increasing at the instant T—even though at a different time, or with different initial probabilities, the entropy may decrease. [For instance, in Landsberg's example (iii) the entropy will decrease if one takes $P_1=\frac{1}{6}+\epsilon$, $P_2=\frac{1}{3}$, and $P_3=\frac{1}{2}-\epsilon$. This decrease may be verified by a simple calculation; qualitatively it means that the system tends to the equilibrium distribution and that this distribution is less random than the initial one.] Thus (S) implies (H) but is a far stronger restrictive condition. Consequently it is possible to deduce certain statistical propositions from the second law alone if it is taken in the form (S), but not if it is taken as (H).

Dr. Landsberg[3] takes the view that (H) is too weak to represent the H-theorem, but that (S) is too strong. He feels that the connection of these propositions with the second law may require further investigation.

It should be noted that Lemma 4 in Landsberg's paper is really needed to complete the writer's[2] proof of Theorem 2 by showing that S is a minimum. As a counterexample, consider $f(x,y)=(x-y)^2-x^4$, which has a saddle-point at the origin but appears to have a minimum if only second-order terms are considered. This flaw in the proof was pointed out by Fröman.[4]

[1] P. T. Landsberg, Phys. Rev. **96**, 1420 (1954).
[2] J. S. Thomsen, Phys. Rev. **91**, 1263 (1953).
[3] P. T. Landsberg (private communication).
[4] P. O. Fröman, University Institute for Theoretical Physics, Copenhagen (private communication).

Symmetry Effects in Gas Kinetics. I. The Helium Isotopes

O. HALPERN, *% American Express Company, Zurich, Switzerland*

AND

R. A. BUCKINGHAM, *University College, London, England*

(Received January 26, 1955)

Continuing earlier investigations, we discuss in this paper the influence of the process of symmetrization of the wave functions of the colliding atoms upon various gas-kinetic cross sections. Through the choice of a suitable interaction potential it thus becomes possible to derive the temperature dependence of the viscosities of the two He isotopes near absolute zero; it is also possible to show that the differences between these two quantities is largely caused by the fact that the nuclei of He^3 and He^4 follow different statistics. The agreement between theory and experiment is not quite as satisfactory in the case of the viscosity of mixtures of the two isotopes. Finally, curves are presented showing the effect of symmetrization on various possible scattering experiments.

I. THEORETICAL DEVELOPMENT

IT was first established through observations on the collisions of charged particles that one needs to symmetrize the wave function when the interacting particles are identical. This principle of symmetrization was applied by Massey and Mohr[1] to the collision processes of neutral atoms and molecules in a gas. They considered in particular the collision cross sections determining viscosity, heat conductivity, and diffusion, showing the characteristic differences to be expected for similar and dissimilar particles. The results were applied to the interpretation of the observed temperature dependence of the transport properties of helium and hydrogen.

To apply these calculations to actual gases it was of course necessary to assume a law of force governing the collision processes. Since the effects due to symmetrization were rather small, and since furthermore these laws of force were not known precisely, a comparison of the theoretical results with observations did not give wholly convincing evidence for the need to symmetrize the wave function.

A subsequent investigation by Halpern and Gwathmey[2] modified the theoretical results just mentioned in several respects, and suggested an experimental approach which should make the observer more independent of the actual law of force. It was first pointed out that for H_2—as in general for all molecules and almost all atoms, excepting those with no electronic angular momentum and no nuclear spin—symmetrization must be carried out with care. In fact, apart from exceptional conditions, a better approach to reality would be to omit all symmetrization. This is so because all states with unequal internal quantum numbers must be considered as different. Alternatively one may say that since in a large number of states the wave function is to be symmetrized, while in a slightly smaller number of states it has to be antisymmetrized, the total result is almost equivalent to the use of Boltzmann statistics. For hydrogen in particular, except for a case mentioned below, this reduces the symmetrization effect very much.

It was further shown that the cross section for diffusion must not be calculated with a symmetrized wave function for any type of gas.

Now the fact that symmetrization should be carried out so much more carefully and rarely, led to a different approach which, it was hoped, would be less sensitive to assumptions concerning the law of force. Thus, consider the viscosity of H_2 at temperatures so low that almost all molecules occupy only the zeroth (para) or first (ortho) rotational levels. In para-H_2 no internal degrees of freedom need to be considered, so here the full principle of symmetrization holds true. In ordinary H_2 the ortho states have weight nine, so that in collisions between ortho molecules, as well as between ortho and para molecules, the symmetrization effect is practically negligible. We should therefore expect a noticeable difference in the viscosity of ordinary H_2 and para-H_2 at low temperatures.

In the paper quoted attention was also called to an isotope effect which according to the present theory could be expected to appear in the gas kinetic quantities. Different isotopes have in general different nuclear spins; the statistics of the electronic shell being the same, one should therefore expect (apart from any mass effect) characteristic differences in the expressions for viscosities, etc., caused by changes in symmetrization of the wave functions. As an illustration the case of neon was considered, neon being at that time the only element of which the isotopes were available and which had no electronic spin. However, the large mass and high boiling point of neon made the effect very small, and accordingly attention was later[3] called to the much more favorable example of He^4 and He^3. Since He^4 has no spin and follows Bose statistics, the orbital part of the wave function must be symmetrized in all collisions; He^3 has spin $\frac{1}{2}$ and follows Fermi statistics, and hence the orbital function must be anti-

[1] H. S. W. Massey and C. B. O. Mohr, Proc. Roy. Soc. (London) A141, 434 (1933); A144, 188 (1934).

[2] O. Halpern and E. Gwathmey, Phys. Rev. 52, 944 (1937).

[3] O. Halpern, Phys. Rev. 82, 561 (1951).

symmetrized in $\frac{3}{4}$ of all collisions of He^3 atoms, and symmetrized in the remaining $\frac{1}{4}$. Assuming for illustration that so low a temperature of observation could be used that most collisions are S-collisions, then the scattering cross section of He^4 (apart from the mass factor) must be expected to be four times that of He^3. This very unrealistic case is mentioned only to make evident that quite large differences can be expected in the two He isotopes.

Following the original contribution by Halpern and Gwathmey, several theoretical papers by other authors have given quantitative results for the temperature dependence of various properties of these isotopes, using more or less realistic forms for the law of force. Thus an early investigation by Buckingham and Massey[4] showed that symmetry effects in the second virial coefficient of He^4 might be significant below 1–2°K. This was substantiated later for He^3 by van Kranendonk, Compaan, and de Boer,[5] and in greater detail in the recent extensive calculations of Kilpatrick *et al.*[6] In connection with the gaseous viscosity of the He isotopes, measurable effects below 3°K were shown to occur by Buckingham and Temperley,[7] de Boer and Cohen,[8] and Buckingham and Scriven.[9] These are discussed in detail in later sections.

II. EXPERIMENTAL WORK

The theoretical views here summarized have only recently attracted the attention of experimentalists. Becker[10] and his collaborators have published several investigations of the differential effects in the viscosities of normal and para-H_2, (up to 90°K) normal and para-D_2 (at 15° and 20°K), and also of the two He isotopes at much lower temperatures. The observations showed that the collision cross sections in para-H_2 are very slightly *smaller* than those in ortho-H_2, when both are observed in their lowest rotational state. Now the assumption of a rigid sphere model, with the same collision radius for all molecules, leads to the result that the para-H_2 cross section should always be *larger* than that for the ortho-H_2 molecules. For interaction potentials with an attractive part it is true that this difference is appreciably modified in magnitude, and at some low temperatures may even be reversed in sign. Nevertheless, it seems unlikely that this behavior is reached at the temperatures at which Becker *et al.*, made their observations, and hence there is a clear indication that even for differential observations the law of force should not be assumed the same for all collisions. A slight admixture of noncentral forces, which can be expected to be present for ortho-H_2 molecules, would possibly lead to the observed effect and hide the small effect due to symmetrization. It is doubtful, however, whether theoretical calculations of the effect of such noncentral forces can be very useful; the parameters in the intermolecular potential are not well defined at present, so that any agreement between the few observations and the theory would likely be of more algebraic than physical significance.

The difficulties caused by noncentral forces do not occur in the case of the He isotopes; here the experiments have led to large differences between the viscosities of the kind expected from the theory. It is also probable that symmetrization effects in the collision of hydrogen molecules can be made evident by a differential experiment which can hardly be influenced by the presence of noncentral forces. We are referring to the scattering of para-H_2 molecules by para-H_2 and normal H_2, respectively. Since the symmetrization effect may be quite considerable for scattering through small angles, its detection becomes a question of intensity only. We have learned that Dr. Becker has started an experiment for the purpose of observing such an effect.

In the remainder of this paper we consider some properties of the He isotopes which can be derived from the usual quantal phases connected with collisions between He atoms. The viscosity results are presented in a form such that the quantum effects of symmetrization are most clearly distinguishable from the other quantum effects arising from the fact that the de Broglie wavelength associated with the collision is comparable with the atomic dimensions. In deriving the viscosity of He^3, appropriate use is made of the Enskog-Chapman theory for mixtures, the components of the mixture in this case being the atoms in various spin states. This procedure is further applied to find the viscosity of mixtures of the He isotopes. Finally, the effect of symmetry on the cross section for scattering of He atoms is considered in more detail than hitherto.

In a subsequent paper we shall return to the problem of hydrogen and deuterium, and shall present data which may be useful in relation to scattering and viscosity experiments with these gases.

III. VISCOSITY OF PURE He^3 AND He^4

We must first summarize the essential formulas used in deriving the viscosity η. In what follows it is assumed that the interatomic potential energy has the usual form corresponding to a steep repulsion at small distances combined with the usual van der Waals attraction at larger distances. It can be generally represented by

$$V(r) = -\epsilon f(\sigma),$$

where $\sigma = r/r_m$, ϵ and r_m being physical parameters repre-

[4] R. A. Buckingham and H. S. W. Massey, Proc. Roy. Soc. (London) **A168**, 378 (1938).
[5] van Kranendonk, Compaan, and de Boer, Phys. Rev. **76**, 998 and 1728 (1949).
[6] Kilpatrick, Keller, Hammel, and Metropolis, Phys. Rev. **94**, 1103 (1954).
[7] R. A. Buckingham and H. N. V. Temperley, Phys. Rev. **78**, 482 (1950).
[8] J. de Boer and E. G. D. Cohen, Physica **17**, 993 (1951).
[9] R. A. Buckingham and R. A. Scriven, Proc. Phys. Soc. (London) **65**, 376 (1952).
[10] E. W. Becker and O. Stehl, Z. Physik **133**, 615 (1952). Becker, Misenta, and Stehl, Z. Physik **136**, 457 (1953); Becker, Misenta, and Schmeissner, Z. Physik **137**, 126 (1954).

senting the depth and position of the minimum in $V(r)$, and $f(\sigma)$ a suitable shape function such that $f(1)=1, f'(1)=0$.

Using this interaction the viscosity cross section can be expressed in terms of the familiar phase shifts δ_L, obtained by solving the Schrodinger equation for different values of the collision parameter $k(=\pi Mv/h)$ and for integral values of the azimuthal quantum number L. Thus

$$Q_\eta=\frac{4\pi}{k^2}\sum_L \omega_L \frac{(L+1)(L+2)}{(2L+3)}\sin^2(\delta_{L+2}-\delta_L), \quad (1)$$

where ω_L takes different values according to the type of statistics used:

Statistics	Bose	Fermi	Classical
L even	$\omega_L=2$	0	1
L odd	$\omega_L=0$	2	1

For a given shape of interaction $f(\sigma)$, it is convenient to regard Q_η as a function of two variables K and Λ_m, where K $(=Mv^2/4\epsilon)$ is the relative kinetic energy of collision in units of ϵ, and $\Lambda_m[=h/(M\epsilon r_m^2)^{\frac{1}{2}}]$ is the ratio of the de Broglie wavelength for collision energy ϵ to the atomic diameter r_m. In place of Λ_m we sometimes use $\lambda=2\pi/\Lambda_m$.

We now define the following reduced quantities:

Reduced temperature $$T^*=\kappa T/\epsilon, \quad (2)$$

Reduced viscosity $$\eta^*=[r_m^2/(M\epsilon)^{\frac{1}{2}}]\eta, \quad (3)$$

Reduced viscosity cross section

$$S_\eta(K,\Lambda_m)=Q_\eta/(\tfrac{2}{3}\pi r_m^2), \quad (4)$$

Reduced integrated cross section

$$\bar{S}_\eta(T^*,\Lambda_m)=\frac{1}{3!}\int_0^\infty x^3 e^{-x} S_\eta dx, \quad (5)$$

where $x=K/T^*$. Both S_η and $\bar{S}_\eta$ would be unity in the classical theory of a gas of rigid spheres of diameter r_m. The integrated cross section $\bar{S}_\eta$ (sometimes written in the general theory of transport phenomena as $\Omega^{*(2,2)}$) is effectively the reciprocal of the reduced viscosity, since

$$\eta^*(T^*)^{-\frac{1}{2}}=\frac{5(1+q)}{16\pi^{\frac{1}{2}}\bar{S}_\eta}, \quad (6)$$

q here being a small higher-order correction which at low temperatures does not exceed 0.005.

The foregoing formulas, which involve the substitution of an appropriate quantal cross section in the Chapman-Enskog expression for η, are quite unambiguous when the gas consists of identical particles of mass M. Thus, if these are He^4 atoms, which have no net nuclear or electronic spin and should therefore follow Bose statistics, the viscosity can be obtained by calculating phases for even L only. The position is less simple for a pure He^3 gas, consisting of atoms with nuclear spin $\pm\frac{1}{2}$ in equal proportions. In several papers[7,8] it has been tacitly assumed that the correct quantal cross section to insert in (5) is

$$S_\eta(He^3)=\tfrac{1}{2}\{S_\eta(\text{Fermi})+S_\eta(\text{class.})\}$$
$$=\tfrac{1}{4}\{S_\eta(\text{Bose})+3S_\eta(\text{Fermi})\}, \quad (7)$$

since one-half of all collisions are between unlike atoms (with opposing spins) and for these no symmetrization is necessary.

To substantiate this procedure it is advisable to examine the extended form of the Chapman-Cowling and Enskog theory, developed by Curtiss and Hirschfelder[11] for gaseous mixtures. It is unnecessary to quote their general result here, as this is lengthy, but we consider first the simple case in which the gas contains two types of atom, of equal mass, in proportions x_1 and $x_2(=1-x_1)$. The viscosity of the mixture is then expressed in terms of the viscosities η_1 and η_2 of pure gases of the two types, and also of the viscosity η_{12} of a fictitious gas in which all collisions are assumed to occur between unlike atoms. In calculating η_1 and η_2, therefore, the proper symmetry must be applied; for η_{12} no symmetrization is necessary. In He^3 gas, in which atoms are distinguished by the orientation of their spin, we have the further simplification that $\eta_1=\eta_2$ and $x_1=x_2=\frac{1}{2}$. Leaving x_1 unspecified for the moment, we find from the Curtiss-Hirschfelder formula that

$$\frac{1}{\eta_{\text{mix}}}=\gamma+(\alpha-\gamma)\frac{x_1^2+x_2^2+cx_1x_2}{1+2cx_1x_2}, \quad (8)$$

where $\alpha=1/\eta_1, \gamma=1/\eta_{12}, \beta=(5/6A_{12}^*)\gamma$, and $c=(\alpha-\gamma)/(\beta+\frac{1}{2}\gamma)$. The quantity A_{12}^* is here the ratio of two collision integrals closely connected with diffusion of the two types of atom; in magnitude it is not far from unity.

Let η_{cl}, η_F, and η_B refer to the viscosities calculated using classical, Fermi, and Bose statistics, respectively, satisfying the relation $1/\eta_{cl}=\frac{1}{2}(1/\eta_F+1/\eta_B)$. Now for He^3, we must take $\eta_1=\eta_F$ and $\eta_{12}=\eta_{cl}$, whence it follows that $\alpha-\gamma=\frac{1}{2}(1/\eta_F-1/\eta_B)$. It is then clear that the term in $(\alpha-\gamma)$ is essentially a low temperature correction, since $\alpha-\gamma$ tends to zero at high temperatures, leaving $\eta_{\text{mix}}=\eta_{12}$ in this limit. However, when we insert $x_1=x_2=\frac{1}{2}$ as in the actual gas, we obtain at all temperatures,

$$1/\eta_{\text{mix}}=\gamma+\tfrac{1}{2}(\alpha-\gamma)=\tfrac{1}{4}(3/\eta_F+1/\eta_B).$$

This is exactly what is assumed in (7), but it should be noticed that the result depends on the two spins being equally abundant in the mixture. For any other distribution the value of η_{mix} depends on c, and therefore on A_{12}^*.

[11] C. F. Curtiss and J. O. Hirschfelder, J. Chem. Phys. **17**, 550 (1949).

Figure 1 shows the behavior of the viscosity cross sections defined previously for He^4 and He^3. These results have been calculated by using an interatomic potential of the form

$$f(\sigma)=f_1\sigma^{-6}(1+b\sigma^{-2})-f_2e^{-(\sigma-1)}, \qquad (9)$$

where

$$f_1=a/\{a(1+b)-6-8b\{, \quad f_2=-1+(1+b)f_1,$$

and the parameters a, b have been assigned the values 13.5, 0.2, respectively. For He^4, even-order phases using this type of potential have been given by Buckingham, Hamilton, and Massey,[12] and for He^3 they have been calculated by Scriven and Buckingham,[13] in each case for values of K sufficient to give the viscosity up to 5°K. For the present purpose, it was necessary to estimate odd order phases for He^4, and it was found possible to do this adequately without resorting to numerical integration of the wave equation. The values of λ^2 for He^4 and He^3 were taken to be 7.27 and 5.48 ($\Lambda_m=2.33$, 2.68, respectively). These correspond to a value of 122×10^{-32} erg cm^2 for ϵr_m^2, known from earlier work[12] to give reasonable agreement with the observed second virial coefficient of He^4 gas below 5°K.

In both Figs. 1(a) and 1(b) two pairs of curves have been given. The full-line curves correspond to the quantal statistics expected to hold [Bose for He^4, the mixture (7) for He^3]; the broken curves to the classical Boltzmann statistics. Since the classical mass factor ($M^{\frac{1}{2}}$) does not enter at this stage, the difference between the broken curves is a measure of the quantal mass effect, corresponding to the two values of λ^2 in the aforementioned. The departure of each full-line curve from its accompanying broken curve then shows how the cross section is affected by using the correct statistics, i.e., the symmetrization effect.

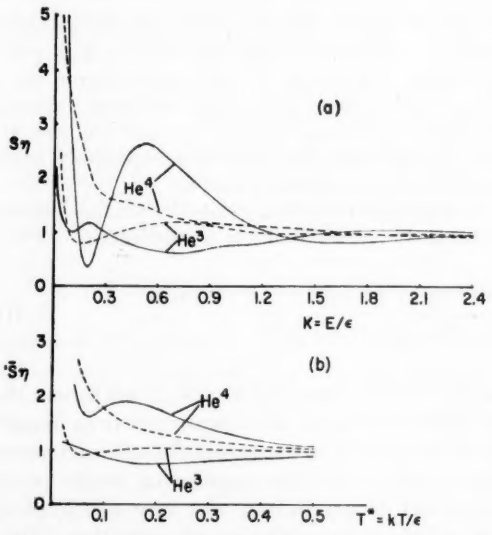

FIG. 1. Quantal viscosity cross sections of pure He^3 and He^4. (a) S_η, before averaging, as function of reduced collision energy K; (b) $\bar{S}_\eta$, after averaging, as function of reduced temperature T^*. Full-line curves correspond to actual statistics, dashed curves to classical Boltzmann statistics.

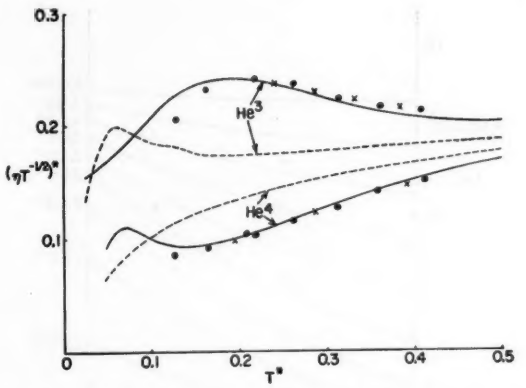

FIG. 2. Comparison of theoretical and observed viscosities of pure He^3 and He^4. Theoretical full-line curves correspond to actual statistics, dashed curves to classical statistics. Experimental points, due to Becker *et al.*, have been reduced by assuming $\epsilon/\kappa=10.2°$, $r_m=2.94$ A.

The chief features of the S_η curves are the rapid rise at small energies, and the considerable oscillations of the quantal statistical curves about those for classical statistics. These oscillations soon become very small for larger values of K, and as one would expect they are also much less marked in the variation of $\bar{S}_\eta$, which represents the result of averaging S_η with respect to the Maxwell velocity distribution. It should be noticed that the K and T^* scales are chosen so that for equal lengths, $K=3T^*$; this corresponds to the fact that the weighting function x^3e^{-x} has its maximum when $x=K/T^*=3$.

In Fig. 1(b), it is seen that when $T^*=0.5$ the curves are all fairly close to unity, which is the classical value for rigid spheres. However, for large T^* the value of $\bar{S}_\eta<1$ because the effective collision radius $<r_m$. For He^4 and $T^*>0.1$, the Bose curve is above the Boltzmann curve; this again is similar to the result for rigid spheres, but it should be noticed that when $T^*\simeq0.1$, a reversal occurs which is directly connected with the attractive part of the potential. For He^3, the behavior is complicated by the mixture of Bose and Fermi statistics. The other important point is that when $T^*>0.1$ the symmetrization effects, being in opposition for the two isotopes, enhance the mass effect, and indeed over much of the temperature range the difference in viscosity of the isotopes is due more to the different statistics than to the different masses.

In plotting S_η against K, and $\bar{S}_\eta$ against T^*, it has not been necessary to specify the energy parameter ϵ. This can in fact be chosen to give the best over-all agreement with observed viscosity values. Such a

[12] Buckingham, Hamilton, and Massey, Proc. Roy. Soc. (London) A179, 103 (1941).
[13] R. A. Scriven and R. A. Buckingham (to be published).

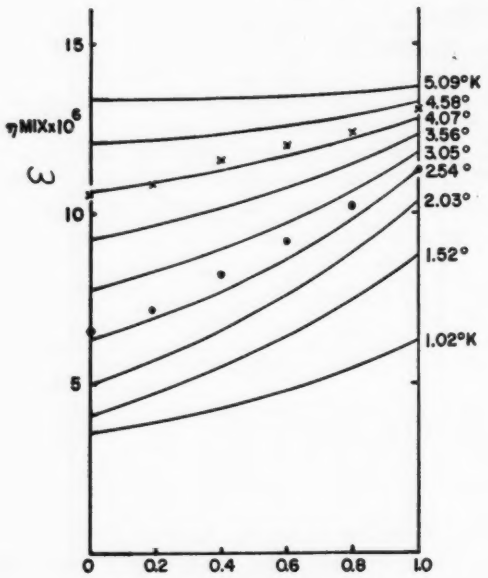

FIG. 3. Viscosity of mixtures of He^3 and He^4. Theoretical curves, calculated from formula (11) using potential with $\epsilon/\kappa=10.2°K$, $r_m=2.94$ A. Experimental points are due to Becker *et al.*; × at 4.15°K, ● at 2.64°K.

comparison is made in Fig. 2, where the theoretical values of $\eta^*(T^*)^{-\frac{1}{2}}$ for He^4 and He^3 are shown against the experimental values of Becker *et al.*, the temperatures being reduced by assuming $\epsilon/\kappa=10.2°K$. The excellent agreement for both isotopes is a clear vindication of the theory in general, of the method of symmetrization, and to some extent, of the choice of interaction.

IV. VISCOSITY OF HE^3–He^4 MIXTURES

Having considered the pure isotopes, it is natural to ask how the viscosity of a mixture of them depends on their relative concentration. In terms of the Curtiss-Hirschfelder mixture formula we can examine this by considering a mixture which contains a molar fraction x_1 of He^4 atoms, and fractions x_2 of each spin-type of He^3 atom, so that $x_1+2x_2=1$.

The first approximation to η_{mix} is given[11] by the ratio of two determinants,

$$\frac{1}{\eta_{mix}}=-\begin{vmatrix} h_1 & k_1 & k_1 \\ k_1 & h_2 & k_2 \\ k_1 & k_2 & h_2 \end{vmatrix} \div \begin{vmatrix} h_1 & k_1 & k_1 & x_1 \\ k_1 & h_2 & k_2 & x_2 \\ k_1 & k_2 & h_2 & x_2 \\ x_1 & x_2 & x_2 & 0 \end{vmatrix} = \frac{h_1(h_2+k_2)-2k_1^2}{(h_2+k_2)x_1^2-4k_1x_1x_2+2h_1x_2^2}, \quad (10)$$

where

$$h_1=\alpha_1x_1^2+(2\beta_1+\gamma_1/s)x_1x_2,$$
$$h_2=\alpha_2x_2^2+(\beta_1+\tfrac{1}{2}s\gamma_1)x_1x_2+(\beta_2+\tfrac{1}{2}\gamma_2)x_2^2,$$
$$k_1=-(\beta_1-\tfrac{1}{2}\gamma_1)x_1x_2,$$
$$k_2=-(\beta_2-\tfrac{1}{2}\gamma_2)x_2^2,$$

and

$$\alpha_1=1/\eta_1 \qquad \alpha_2=1/\eta_2,$$
$$\beta_1=5p^2/(6A_{12}^*\eta_{12}) \qquad \beta_2=5/(6A_{23}^*\eta_{23}),$$
$$\gamma_1=p^2/\eta_{12} \qquad \gamma_2=1/\eta_{23},$$
$$p^2=4M_1M_2/(M_1+M_2)^2 \qquad s=M_1/M_2.$$

M_1 and M_2 are the masses of He^4 and He^3 atoms respectively; η_1 is the viscosity of a (real) Bose gas of He^4 atoms, and η_2 that of a (fictitious) Fermi gas of He^3 atoms; η_{12} and η_{23} are also fictitious viscosities referring to collisions between one He^4 and one He^3 atom, and between two He^3 atoms respectively, calculated without any symmetrization.

By algebraic reduction, using the relation between x_1 and x_2, the formula for $1/\eta_{mix}$ becomes

$$\frac{1}{\eta_{mix}}=\frac{(s+\mu)\alpha_1x_1^2+4\gamma_1x_1x_2\{1/s-(1-\alpha_1\alpha_2'/\gamma_1^2)+\frac{1}{4}\mu(s+2+1/s)\}+(1/s+\mu)4\alpha_2'x_2^2}{(s+\mu)x_1^2+4x_1x_2\{(\alpha_1+\alpha_2')/\gamma_1-1+\mu\}+(1/s+\mu)4x_2^2}, \quad (11)$$

where $\mu=2\beta_1/\gamma_1$ and $\alpha_2'=\frac{1}{2}(\alpha_2+\gamma_2)$. It will be observed that β_2, which involves interdiffusion of the two spin components of He^3, has vanished from these expressions as it did for pure He^3.

All the quantities required to calculate η_{mix} are available, including A_{12}^* which is related to the diffusion coefficient of He^3 and He^4, and which has been evaluated for the above potential by Buckingham and Scriven.[9]

Figure 3 shows how the viscosity of the mixture depends on the molar fraction of He^3 present, for temperatures up to 5°K. The same values of the potential parameters, Λ_m and ϵ/κ, have been used as before. Also shown in the figure are the experimental values of Becker *et al.*[10] for 2.64° and 4.15°K. It will be seen that the theoretical curves show departures from linearity which, up to 3.5°K at least, are of the order of 5 percent when $x_1=2x_2=0.5$. The experimental results on the other hand do not indicate any very significant departure from linearity. One would expect that a deviation of 5 percent should be observable, since in general the experimental results of pure He^3 and pure He^4 appear to be consistent to within 2–3 percent and moreover Becker *et al.* claim to measure the fraction of He^3 present in mixtures to 2 percent. The point seems to deserve further investigation.

V. SCATTERING OF He^4 ATOMS

A further test of symmetrization effects would appear to be possible in the direct scattering of He atoms. The most sensitive comparison, and one not likely to depend critically on the chosen law of force, would be that of the differential cross section for scattering through 90° in the center-of-mass system, at fairly low thermal energies. Thus, since collisions involving antisymmetrization make no contribution to scattering through 90°, the cross sections corresponding to Bose statistics, classical statistics, and a 3:1 mixture of Fermi and Bose statistics, would be in the ratios 4:1:1, regardless of the collision energy. Differential cross sections which have been calculated for He^4-He^4, He^3-He^4 and He^3-He^3 collisions, assuming the appropriate statistics, although modified to some extent by mass effects, do show ratios which are substantially the same as the above and are not very sensitive to collision energy, at least when the energy parameter K exceeds about 0.2 (corresponding to 2°K).

For an observational test of the symmetrization effect therefore, the scattering near 90° is valuable because the effect is not obscured if the collision energies cover a fairly wide range. This is not necessarily so for scattering through small angles; although the effects of symmetry are still substantial, they are much more sensitive to the collision energy, and tend to average out over a range of energies. That this is likely can easily be seen by considering the variation with energy of the total scattering cross section, and its dependence on the statistics assumed, for say He^4-He^4 collisions. The analysis is essentially the same as for the viscosity cross section, though in place of (1) we have

$$Q_{sc}(K,\Lambda_m)=\frac{4\pi}{k^2}\sum_L \omega_L(2L+1)\sin^2\delta_L, \qquad (12)$$

and as a suitable reduced cross section, $S_{sc}=Q_{sc}/\pi r_m^2$. In addition to S_{sc} we have evaluated an average cross section $\bar{S}_{sc}$, by integrating S_{sc} with respect to energy and assuming a Maxwell distribution. Thus

$$\bar{S}_{sc}(T^*,\Lambda_m)=\int_0^\infty xe^{-x}S_{sc}dx, \qquad (13)$$

where $x=K/T^*$ as before.

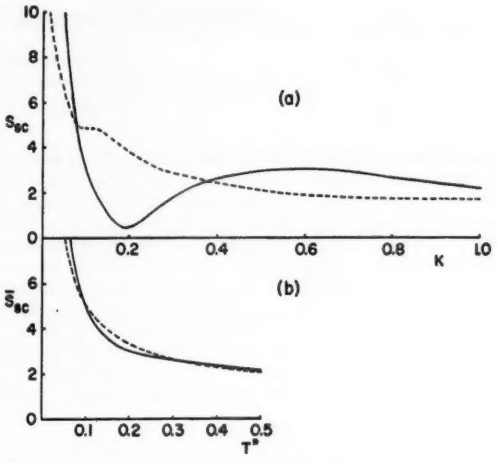

FIG. 4. Total scattering cross sections for He^4-He^4 collisions, (a) S_{sc}, before averaging, as a function of the reduced collision energy K; (b) $\bar{S}_{sc}$, after averaging, as a function of the reduced temperature T^*. Full-line curve corresponds to Bose statistics, dashed curve to classical statistics.

The presentation of these cross sections in Figs. 4(a) and 4(b) is exactly similar to that of the viscosity cross sections, except that the scales of K and T^* are now taken to be the same, since the weighting function xe^{-x} has its peak when $x=1$. The significant points are first, the oscillatory behavior of the S_{sc} curves for Bose and classical statistics with respect to each other, and secondly, the very marked diminution of these oscillations after the averaging carried out in $\bar{S}_{sc}$. This makes the detection of any symmetry effect from the total scattering cross section very difficult if the distribution of relative velocities is anything like Maxwellian; hence it is desirable that the collisions should be as nearly monoenergetic as possible. The same applies to measurements of the differential cross section at small angles, as indicated above. On the other hand it must be remembered, in connection with angular scattering near 90°, that, although the energy dependence is much less critical, the differential cross section at 90° is relatively small, about 5–10 percent of that near 0°.

Passage of Charged Particles through Plasma

JACOB NEUFELD AND R. H. RITCHIE*
Oak Ridge National Laboratory, Oak Ridge, Tennessee
(Received February 10, 1955)

The plasma has been treated phenomenologically as a homogeneous dispersive medium characterized by a "dielectric constant" which is a function not only of the frequency of the applied field (as in conventional dispersive media) but also on its wave number. The representation of plasma as a dispersive medium is subject to certain validity criteria which are satisfied for such typical cases as the ionosphere and electrical discharge through gases but is not satisfied for electrons in the conduction band of a metal. The passage of charged particles through plasma is investigated by means of straightforward application of Maxwell's equations for a dispersive medium. The Debye screening, which is applicable to the potential of an incident particle having velocity $V \ll \langle v^2 \rangle^{\frac{1}{2}}$ (where $\langle v^2 \rangle^{\frac{1}{2}}$ is the root mean square velocity of plasma electrons), loses its significance when $V \gg \langle v^2 \rangle^{\frac{1}{2}}$; and in the latter case, the potential decreases with the distance in accordance with an inverse cube law. The stopping power has been calculated for slow incident charged particles having $V \ll \langle v^2 \rangle^{\frac{1}{2}}$ and for fast particles having $V \gg \langle v^2 \rangle^{\frac{1}{2}}$ in a plasma comprising electrons distributed in accordance with Maxwell-Bolzmann and Fermi-Dirac statistics. For slow particles the results represent an extension of the formula of Fermi and Teller. An expression has been derived for the distribution of the polarization density in the space surrounding a moving particle.

I. INTRODUCTION

WITHIN the last several years, considerable interest has been shown in the study of an organized assembly of charged particles designated as "plasma," some of the important properties of which had been described earlier by Rayleigh,[1] Langmuir,[2] and Langmuir and Tonks.[3] A large portion of the recent literature devoted to this subject appeared in the U.S.S.R., initiated by A. Vlasov and his associates.[4–7] In the United States, the properties of plasma were studied by Bohm, Pines, Gross, and others.[8–12]

Plasma in its normal equilibrium state is characterized by a substantially equal density distribution of positive and negative charge. Consequently, the volume distribution of charge is practically zero, and the potential within the medium is determined by Poisson's equation $\nabla^2\varphi=0$. The positive charges are heavy and their motion may be neglected. Any disturbance in the plasma will tend primarily to disturb the distribution of electrons and produce polarization in the medium. To facilitate our problem, we assume that the positive nuclei have their charges spread our uniformly through the medium.

Our purpose is to study the classical interaction between an incident charged particle and a surrounding plasma. This subject has been treated extensively in the literature and several methods have been applied to determine specific aspects of the problem. Kronig and Korringa[13–15] and Vlasov[7] treated the problem by means of a hydrodynamical model of an electron gas. Vlasov[7] and Akhiezer and Sitenko,[16] applying a method originated by Vlasov, treated the electron collisions by means of a generalization of the Boltzmann transport equation which has been modified to take into account the long-range Coulomb forces. Fermi and Teller,[17] and Kwal[18,19] applied the method of binary collisions and took into account the plasma aspects of the problem by including in their treatment either the Debye length or the natural frequency of the plasma. Kramers[20] used the conventional form of the dielectric constant of an assembly of free stationary electrons in a classical electrodynamic calculation of the stopping power.

Our purpose is to re-examine the stopping power problem and to use a phenomenological approach in which the microscopic behavior of individual electrons in the plasma is ignored, adopting instead a macroscopic point of view and describing the electron assembly as a homogeneous, isotropic, dispersive medium. In conventional dispersive media, the dielectric constant depends on the frequency of the applied field. The dielectric constant of a plasma is characterized, however, by essentially different properties since it depends not only on the frequency but also on the wave number of the applied field. The dielectric properties of plasma have been considered by Gertenshtein[21,22] in the study of longitudinal waves passing through ionized media

* This paper is part of the thesis of one of the authors (R.H.R.) in partial fulfillment of the requirements for the Ph.D. degree at the University of Tennessee.

[1] Lord Rayleigh, Phil. Mag. (6), **11**, 117 (1906).
[2] I. Langmuir, Proc. Nat. Acad. Sci. **14**, 627 (1928).
[3] L. Tonks and I. Langmuir, Phys. Rev. **33**, 195 (1929).
[4] A. Vlasov, Zhur. Eksptl. i. Teort. Fiz. **8**, 291 (1938).
[5] A Vlasov, J. Phys. (U.S.S.R.) **9**, 25 (1945).
[6] L. Landau, J. Phys. (U.S.S.R) **10**, 25 (1946).
[7] A. Vlasov, *Teoria Mnogikh Chastits* (Gitl., Moscow-Leningrad, 1950).
[8] D. Bohm and D. Pines, Phys. Rev. **82**, 625 (1951).
[9] D. Bohm and E. D. Gross, Phys. Rev. **75**, 1851 and 1864 (1949).
[10] D. Pines and D. Bohm, Phys. Rev. **85**, 338 (1952).
[11] D. Pines, Phys. Rev. **92**, 626 (1953).
[12] D. Bohm and D. Pines, Phys. Rev. **92**, 609 (1953).
[13] R. Kronig and J. Korringa, Physica **10**, 406 (1943).
[14] R. Kronig and J. Korringa, Physica **10**, 800 (1943).
[15] R. Kronig, Physica **15**, 667 (1949).
[16] A. T. Akhiezer and A. G. Sitenko, Zhur. Ekspth. i. Teort. Fiz. **23**, 161 (1952).
[17] E. Fermi and E. Teller, Phys. Rev. **72**, 399 (1947).
[18] B. Kwal, Compt. rend. **230**, 1669 (1950).
[19] B. Kwal, J. phys. radium **12**, 805 (1951).
[20] H. A. Kramers, Physica **13**, 401 (1947).
[21] M. E. Gertsenshtein, Zhur. Eksptl. i Teoret. Fiz. **22**, 303 (1952).
[22] M. E. Gertsenshtein, Zhur. Eksptl. i Teoret. Fiz. **23**, 678 (1952).

and in an investigation on the scattering of radio-waves by inhomogeneities in the ionosphere. Gertsenshtein used Vlasov's approach and treated electron collisions by means of a generalized form of the Boltzmann transport equation. However, the phenomenological treatment, which is based on the straightforward application of Maxwell's equations properly modified to take into account the motion of the medium, clarifies the physical aspects of plasma behavior and facilitates the treatment of problems involving the interaction of charged particles with plasma.

In part II, using the phenomenological approach, we examine the behavior of the plasma and determine its response to an external disturbance. In part III we consider a specific case of a disturbance created by a moving point charge, and in part IV we derive the potential for a slowly moving point charge. The validity of the phenomenological approach is discussed in part V. In parts VI and VII we consider the field and the polarization charge density in the surrounding medium produced by an incident particle and the effectiveness of the plasma in stopping the particle.

II. ELECTRODYNAMICS OF THE PLASMA

We now consider the effect on the plasma of an impressed electric field $\mathbf{E}(\mathbf{r},t)$. We assume that the field perturbs the equilibrium motion of the electron assembly only slightly and that during the period of time in which the electrons may be considered as responding collectively to the applied field they execute approximately straight-line motion. This condition will be discussed in greater detail in a later section.

Let $nf(\mathbf{v})d\mathbf{v}$ be the number of electrons per unit volume possessing velocities in $d\mathbf{v}$ at $\mathbf{v}$, and $\int f(\mathbf{v})d\mathbf{v}=1$. As a result of the impressed electric field, the medium becomes polarized, and we designate by $\mathbf{P}_\mathbf{v}(\mathbf{r},t)d\mathbf{v}$ the polarization vector associated with the electrons having velocities in a region $d\mathbf{v}$ about $\mathbf{v}$. We shall place ourselves in the reference frame of the moving electrons and determine the equation of motion of the polarization vector. Neglecting the small Lorentz force due to the magnetic field, the equation of motion for the nonrelativistic case can be written as follows[23]:

$$\left(\frac{d^2}{dt^2}+g\frac{d}{dt}\right)\mathbf{P}_\mathbf{v}(\mathbf{r}_0+\mathbf{v}t,t)=\frac{ne^2f(\mathbf{v})\mathbf{E}(\mathbf{r}_0+\mathbf{v}t,t)}{m}, \quad (1)$$

where $\mathbf{r}_0$ is the position vector in the reference frame of the observer and m and e are the mass and charge of the electron, respectively. Damping of the motion of the polarization vector due to electron-ion and electron-electron collisions is represented by the damping constant g. Since the exact nature of this damping is not important to our discussion, it will be neglected at a later point.

[23] J. C. Slater and N. H. Frank, *Electromagnetism* (McGraw-Hill Book Company, Inc., New York, 1947), Chap. 9.

$\mathbf{P}_\mathbf{v}$ and $\mathbf{E}$ are now expressed as Fourier integrals,

$$\begin{Bmatrix}\mathbf{P}_\mathbf{v}(\mathbf{r},t)\\ \mathbf{E}(\mathbf{r},t)\end{Bmatrix}=\int d\mathbf{k}d\omega e^{i(\mathbf{k}\cdot\mathbf{r}-\omega t)}\begin{Bmatrix}\mathbf{P}_\mathbf{v}(\mathbf{k},\omega)\\ \mathbf{E}(\mathbf{k},\omega)\end{Bmatrix}, \quad (2)$$

and we find from Eq. (1) the following relation between $\mathbf{P}_\mathbf{v}(\mathbf{k},\omega)$, and $\mathbf{E}(\mathbf{k},\omega)$,

$$\mathbf{P}_\mathbf{v}(\mathbf{k},\omega)=-\frac{ne^2f(\mathbf{v})}{m}\frac{\mathbf{E}(\mathbf{k},\omega)}{(\omega-\mathbf{k}\cdot\mathbf{v})^2+ig(\omega-\mathbf{k}\cdot\mathbf{v})}. \quad (3)$$

Maxwell's equations in a medium moving with velocity $\mathbf{v}$ are well known[24] and may be written, for a nonmagnetic medium

$$\text{curl}\,\mathbf{E}=-(1/c)\dot{\mathbf{H}}, \quad (4a)$$

$$\text{div}\mathbf{H}=0, \quad (4b)$$

$$\text{curl}\mathbf{H}=\frac{1}{c}\dot{\mathbf{E}}+\frac{4\pi}{c}\int[\dot{\mathbf{P}}_\mathbf{v}+\text{curl}(\mathbf{P}_\mathbf{v}\times\mathbf{v})]f(\mathbf{v})d\mathbf{v}+\frac{4\pi\mathbf{j}}{c}, \quad (4c)$$

$$\text{div}\mathbf{E}=4\pi\left(\rho_1-\text{div}\int\mathbf{P}_\mathbf{v}f(\mathbf{v})d\mathbf{v}\right), \quad (4d)$$

where $\mathbf{j}$ and ρ_1 are applied current and charge densities, respectively, relative to the fixed reference system.

In the following we shall refer to various magnitudes such as $\mathbf{E}$, $\mathbf{H}$, etc., which are functions of $\mathbf{r}$, t and to their Fourier transforms which vary with $\mathbf{k}$, ω. In the first case, they will be identified as $\mathbf{E}(\mathbf{r},t)$, $\mathbf{H}(\mathbf{r},t)$, etc., and in the second case as $\mathbf{E}$, $\mathbf{H}$, etc. Expanding $\mathbf{H}(\mathbf{r},t)$, $\mathbf{j}(\mathbf{r},t)$, and $\rho_1(\mathbf{r},t)$ as was done in Eq. (2), using the relation (3) to eliminate $\mathbf{P}_\mathbf{v}$ from these equations and summing over all velocities of the plasma electrons, and dividing $\mathbf{E}$ into components $E_\parallel$ and $E_\perp$ parallel and perpendicular, respectively, to the wave vector $\mathbf{k}$, we find

$$i\mathbf{k}\times\mathbf{E}=i\omega/c\mathbf{H}, \quad (5a)$$

$$\mathbf{k}\cdot\mathbf{H}=0, \quad (5b)$$

$$i\mathbf{k}\times\mathbf{H}=-\frac{i\omega}{c}[\epsilon_\perp(\mathbf{k},\omega)\mathbf{E}_\perp+\epsilon_\parallel(\mathbf{k},\omega)\mathbf{E}_\parallel]+\frac{4\pi\mathbf{j}}{c}, \quad (5c)$$

$$i\mathbf{k}\cdot\mathbf{E}\epsilon_\parallel(\mathbf{k},\omega)=4\pi\rho_1, \quad (5d)$$

where

$$\epsilon_\perp=1-\frac{\omega_0^2}{\omega}\int\frac{f(\mathbf{v})d\mathbf{v}}{(\omega-\mathbf{k}\cdot\mathbf{v}+ig)}, \quad (6)$$

$$\epsilon_\parallel=1-\omega_0^2\int\frac{f(\mathbf{v})d\mathbf{v}}{(\omega-\mathbf{k}\cdot\mathbf{v})^2+ig(\omega-\mathbf{k}\cdot\mathbf{v})} \quad (7)$$

are the dielectric constants of the transverse and longitudinal electric fields, respectively. The expressions (6) and (7) agree with those obtained by Gertsenshtein[21] who, as stated previously, used a rather cumbersome

[24] M. Abraham and R. Becker, *Theorie d. Electrizitat* (B. G. Teubner, Leipzig, 1933), sixth edition, Vol. 2, p. 242.

method based on Boltzman transport equations modified by Vlasov.

In the expressions (6) and (7) the term

$$\omega_0=(4\pi ne^2/m)^{\frac{1}{2}}$$

is the "plasma frequency."

It is clear that the foregoing dielectric constants may be easily generalized to include both the effect of bound electrons which may be present in the medium as well as the effect of the motion of ions in the case of an ionized gas.

III. RESPONSE OF THE PLASMA TO A MOVING PART CHARGE

Assume that a particle having charge Ze and velocity V moves in a plasma. The corresponding charge and current densities are, therefore, as follows:

$$q(\mathbf{r},t)=Ze\delta(\mathbf{r}-\mathbf{V}t), \tag{8a}$$

$$\mathbf{j}(\mathbf{r},t)=Ze\mathbf{V}\delta(\mathbf{r}-\mathbf{V}t). \tag{8b}$$

We are working in a gauge in which the vector potential is pure transverse, so that the longitudinal field is derivable solely from the scalar potential φ. Therefore

$$-i\mathbf{k}\varphi=E_{\mathrm{II}}, \tag{9}$$

and we obtain from (5d) and (9)

$$\varphi=\frac{Ze}{2\pi^2}\frac{\delta(\omega-\mathbf{k}\cdot\mathbf{V})}{k^2\epsilon_{\mathrm{II}}}, \tag{10}$$

where

$$\epsilon_{\mathrm{II}}=\left[1-\omega_0^2\int\frac{f(v)d\mathbf{v}}{(\omega-\mathbf{k}\cdot\mathbf{v})^2+ig(\omega-\mathbf{k}\cdot\mathbf{v})}\right], \tag{11}$$

and $v\equiv|\mathbf{v}|$.

The expression (11) can be represented as

$$\epsilon_{\mathrm{II}}=1-\frac{4\pi\omega_0^2}{k^2}\int_0^\infty\frac{\zeta d\zeta}{(\omega/k-\zeta)}f(\zeta), \tag{12}$$

where we have set the damping constant $g=0$.

Substituting (10) in

$$\varphi(\mathbf{r},t)=\int d\mathbf{k}d\omega e^{i(\mathbf{k}\cdot\mathbf{r}-\omega t)}\varphi, \tag{13}$$

we obtain

$$\varphi(\rho,z,t)=\frac{Ze}{\pi V}\int_0^\infty\kappa d\kappa J_0(\kappa\rho)\int_{-\infty}^\infty\frac{e^{i\omega(z/V-t)}d\omega}{k^2\epsilon_{\mathrm{II}}}, \tag{14}$$

where z and ρ are the cylindrical coordinates of the field point, and ϵ_{II} is expressed by (12) in which

$$k^2=\kappa^2+\omega^2/V^2. \tag{15}$$

IV. DEBYE LENGTH

One of the most striking features of plasma behavior is the screening of an electric charge in the plasma. When $V\ll\langle v^2\rangle^{\frac{1}{2}}$, where $\langle v^2\rangle^{\frac{1}{2}}$ designates the root mean square of the plasma velocity, we obtain an exponentially screened Coulomb potential, characterized by the Debye length.[25] However, when $V\gg\langle v^2\rangle^{\frac{1}{2}}$, we obtain an essentially different behavior as will be discussed later.

For $V\ll\langle v^2\rangle^{\frac{1}{2}}$, and since $\omega=\mathbf{k}\cdot\mathbf{V}$ we approximate the expression (12) as follows:

$$\epsilon_{\mathrm{II}}=1+\omega_0^2/s^2k^2, \tag{16}$$

where

$$s^2=\left[2\pi\int_{-\infty}^\infty f(\zeta)d\zeta\right]^{-1}. \tag{17}$$

Substituting (16) and (17) in (14), we obtain

$$\varphi(\mathbf{r},t)=Ze\exp(-r/D)/r, \tag{18}$$

where $r=[\rho^2+(z-Vt)^2]^{\frac{1}{2}}$ is the distance from the moving particle to the point at which the potential is measured and

$$D=s/\omega_0 \tag{19}$$

is the Debye length representing the screening of the potential.

We shall now examine in more detail the electron velocity distributions $f(v)d\mathbf{v}$ and consider the "Maxwell-Boltzmann plasma" and the "Fermi-Dirac plasma" separately. Various concepts applicable to the Maxwell-Boltzmann plasma shall be designated by subscripts "MB" (i.e., s_{MB}, D_{MB}) and the corresponding concepts applicable to the Fermi-Dirac plasma shall be designated by subscripts "FD" (i.e., s_{FD}, D_{FD}).

In the MB plasma, the temperature T and the electron density n are such that the electrons are distributed in accordance with Maxwell-Boltzmann statistics. Thus

$$f(v)=\left(\frac{m}{2\pi k_BT}\right)^{\frac{3}{2}}\exp(-mv^2/2k_BT), \tag{20}$$

where k_B is the Boltzmann constant.

As examples of the MB plasma, we may cite an ionosphere for which $n\sim10^6$ cm^{-3}, $T\sim300$°K and a gaseous discharge for which $n\sim10^{11}$ cm^{-3}, $T=10\,000$°K. Substituting (20) in (17), we obtain

$$s_{MB}^2=\tfrac{1}{3}\langle v^2\rangle. \tag{21}$$

Taking into account (20), we can express the Debye length in its usual form,[25] i.e.,

$$D_{MB}=(k_BT/4\pi ne^2)^{\frac{1}{2}}, \tag{22}$$

The FD plasma represents an electron gas obeying Fermi-Dirac statistics. Thus

$$f(v)=\frac{2m^3}{nh^3}\left\{\exp\left[\frac{1}{k_BT}\left(\frac{mv^2}{k}-E_F\right)\right]+1\right\}^{-1}, \tag{23}$$

[25] P. Debye and E. Hueckel, Physik. Z. 24, 185 (1923).

where E_F designates the "Fermi energy," i.e.,

$$E_F=\frac{\hbar^2}{2m}\left(\frac{3n}{8\pi}\right)^{\frac{2}{3}}=\frac{mv_F^2}{2}, \tag{24}$$

where v_F is the maximum velocity for $T=0$.

Substituting (23) in (17), we obtain

$$s_{FD}^2=\tfrac{1}{3}v_F^2, \tag{25}$$

and taking into account (19), we can express the Debye length as follows:

$$D_{FD}=(\tfrac{1}{4}\pi a_0\lambda_F)^{\frac{1}{2}}, \tag{26}$$

where

$$a_0=\hbar^2/me^2; \quad \lambda_F=\hbar/mv_F. \tag{27}$$

V. VALIDITY OF THE METHOD

We shall now examine in more detail the restrictions that have to be imposed to justify the present treatment, and we shall consider the following: (*A*) the relative importance of close binary collisions and long-range interactions, (*B*) the applicability of a macroscopical picture to a microscopical electron assembly, and (*C*) the applicability of the classical (orbital) representation.

A. Close Collisions and Long-Range Interactions

The expressions (6) and (7) are based on an assumption that during the period of time in which the electrons respond collectively to the applied fields, they execute approximately straight-line motions. In reality, however, each electron undergoes continual collisions with positive charges and other electrons, and, as a result of such collisions, it deviates progressively from its path and continually loses energy. Any electron in a plasma will follow its rectilinear path at a constant velocity as long as the accidental encounters with other electrons have no appreciable influence. However, as time passes, the collisions with other electrons will have a cumulative effect as a result of which the direction of the electron motion changes and its velocity becomes appreciably different from its initial velocity. We shall define as the relaxation time τ_D the time interval, during which as a result of the cumulative effect of binary collisions the trajectory of the electron has deviated by an angle of $\pi/2$ from its original direction. Similarly the relaxation time τ_R will designate the time interval during which the energy exchanged in electronic collisions becomes of the same order of magnitude as the initial energy of the electron. The values τ_D and τ_R do not differ appreciably from each other and can be expressed as[26,27]

$$\tau_D\sim\tau_R\sim\frac{m\langle v^2\rangle^{\frac{3}{2}}}{9ne^4\ln(D_{MB}m\langle v^2\rangle/2e^2)}. \tag{28}$$

[26] L. D. Landau, Zhur. Eksptl. i Teoret. Fiz. **7**, 203 (1936).

[27] S. Chandrasekhar, *Principles of Stellar Dynamics* (University of Chicago Press, Chicago, 1942), pp. 48–79.

The values τ_R and τ_D can be determined approximately by means of the following rough arguments which we are giving since they provide a better physical insight into the problem than more rigorous calculations.

The energy loss of an incident electron can be expressed as[28]

$$-\frac{dW}{dz}=\frac{4\pi ne^4}{mv^2}\ln\frac{\rho_{\max}}{\rho_{\min}}\sim-\frac{\Delta W}{\Delta z}, \tag{29}$$

where ΔW represents the energy loss over a path Δz. Taking as the maximum impact parameter $\rho_{\max}=D_{MB}$ and as the minimum impact parameter the collision diameter $\rho_{\min}=2e^2/m\langle v^2\rangle$, we obtain

$$\Delta x\sim-\frac{\Delta W m\langle v^2\rangle}{4\pi ne^4\ln(D_{MB}m\langle v^2\rangle/2e^2)}. \tag{30}$$

Taking $\Delta W=-m\langle v^2\rangle/2$, we obtain

$$\tau_R=\frac{\Delta x}{\langle v\rangle}\sim\frac{m^2\langle v^2\rangle^{\frac{3}{2}}}{8\pi ne^4\ln(D_{MB}m\langle v^2\rangle/2e^2)}. \tag{31}$$

The relaxation time for a deviation through an angle of $\pi/2$ from the initial direction may be estimated from the multiple scattering theory of Williams[29] which gives for the mean square angle of deviation after traversing a path length X through a medium containing n scattering centers of charge Ze per cm^3,

$$\langle\theta^2\rangle\sim\frac{8\pi Z^2e^4nX}{m^2\langle v^2\rangle^2}\ln\left(\frac{181}{Z^{\frac{1}{3}}}\right)^2. \tag{32}$$

Setting $\langle\theta^2\rangle\sim\pi^2/4$, $\tau_D=X/\langle v^2\rangle^{\frac{1}{2}}$, and $Z=1$, We obtain

$$\tau_D=\frac{\pi m^2\langle v^2\rangle^{\frac{3}{2}}}{32Z^2e^4n\ln(181/Z^{\frac{1}{3}})^2}. \tag{33}$$

The expressions (31) and (33) for τ_R and τ_D give values of the same order of magnitude as the expression (28) derived by more rigorous considerations.

We shall now consider a term appearing in the denominator of (28) which for the specific examples of the MB plasma previously cited is

$$A=\ln(D_{MB}m\langle v^2\rangle/2e^2)\sim10. \tag{34}$$

The individual electron collisions can be neglected if

$$\omega_0^{-1}\ll\tau_R. \tag{35}$$

Taking into account (29) and (34), the above expression (31) leads to the following inequality:

$$n\ll0.05(k_BT/e^2)^3\sim10^7T^3. \tag{36}$$

[28] See for instance: E. Fermi, *Nuclear Physics* (University of Chicago Press, Chicago, 1950), p. 28.

[29] E. J. Williams, Proc. Roy. Soc. (London) **169**, 531 (1939).

The close interactions are, therefore, negligible for an electron gas of a relatively low density. For a high-density gas such that the close interaction becomes dominant, the assembly loses its "plasma" character and becomes similar to a gaseous assembly of uncharged particles.

B. Macroscopic Treatment

In our description of plasma, we were concerned with the macrosopic behavior of an electron assembly and the Debye length was derived as a macroscopic concept. In order to have an agreement with a microscopic picture in which there are n discrete particles per cm^3, we must require that

$$D>n^{-\frac{1}{3}}, \tag{37}$$

(1) *MB Plasma*

Substituting (29) in (37), we obtain

$$n<(k_BT/4\pi e^2)^3\sim 10^5T^3. \tag{38}$$

(2) *FD Plasma*

Substituting (26) in (37), we obtain

$$v_F>12.18v_0, \tag{39}$$

where $v_0=e^2/\hbar$.

C. Orbital Representation

(1) *Validity Criterion*

We have found in a preceding paragraph that any electron having velocity $V\ll\langle v^2\rangle^{\frac{1}{2}}$ produces in a plasma a potential $\varphi=-e\exp(-r/D)/r$. We may generalize our argument by stating that each individual electron in the plasma creates the potential φ. This argument is strictly applicable to all electrons having $v\ll\langle v^2\rangle^{\frac{1}{2}}$. For other electrons, the distribution of the potential does not change essentially and qualitatively the potential is still screened at a distance of the order of magnitude of D. It will be shown later that a fundamental change in the screening potential occurs only for electrons having $v\gg\langle v^2\rangle^{\frac{1}{2}}$, and the number of these electrons is negligible in a plasma in equilibrium.

We shall now determine whether or not the motion of an electron in a potential φ can be described by means of the classical (orbital) representation on which our treatment is based. According to Williams,[30] the orbital representation is valid if the following two requirements are fulfilled: (a) The uncertainty in the momentum of a perturbed electron is much smaller than the classical value of the momentum transfer caused by the perturbing field φ, and (b) the wavelength of the perturbed electron is much smaller than the radius of the perturbing field, which is assumed to be equal to D.

The criterion (a) leads to the following inequality:

$$\frac{|\varphi|er}{\hbar v}=\frac{e^2\exp(-r/D)}{\hbar v}\gg 1. \tag{40}$$

[30] E. J. Williams, Revs. Modern Phys. **17**, 217 (1945).

The condition (40) can never be satisfied for the whole region of space and consequently the orbital picture cannot be generally applied. We may associate with each value of v a radius

$$R=D\ln(e^2/\hbar v), \tag{41}$$

such that only for $r\ll R$ the orbital picture is valid. If, however, the region defined by the radius R is sufficiently large so as to include most of the space occupied by the scattering potential, i.e.,

$$R\gg D, \quad \text{or} \quad \ln(e^2/\hbar v)\gg 1, \tag{42}$$

then we may assume that the orbital picture applies to the whole space. The inequality (42) represents the Williams requirement (a).

The requirement (b) leads to the following inequality:

$$(\hbar/mv)/D\ll 1. \tag{43}$$

(2) *MB Plasma*

We shall apply now the inequalities (42) and (43). The first of these inequalities corresponds to $v\ll v_0$ or to

$$T\ll 13.5\times 1.16\times 10^4=15.7\times 10^4\ ^\circ\text{K}. \tag{44}$$

Substituting (22) in the inequality (43), we obtain

$$v^2\gg 4\pi\hbar^2ne^2/m^2kT. \tag{45}$$

We have from (36) and (38) that $n\ll n_{\max}$ where $n_{\max}=(k_BT/4\pi e^2)^3$. Substituting in (45) $n_{\max}$ in place of n, we obtain

$$v\gg v_{\max}=\hbar k_BT/4\pi me^2. \tag{46}$$

Since v has a range from zero to infinity, not all the electrons satisfy the inequality (46). However, if

$$\tfrac{1}{2}mv_{\max}{}^2\ll k_BT, \tag{47}$$

the number of electrons that do not satisfy the inequality (46) may be neglected, and it can be assumed that the inequality (43) holds true.

Substituting (46) in (47), we obtain

$$T\ll 10^7\ ^\circ\text{K}. \tag{48}$$

(3) *FD Plasma*

The inequality (42) requires that

$$v_F\ll v_0, \tag{49}$$

and substituting (26) in (43), we obtain

$$v^2\gg(4/\pi)v_0v_F. \tag{50}$$

Since v has a range of values from zero to v_F, the inequality (50) is not satisfied for all the electrons and the necessary requirement is

$$v_F\gg(4/\pi)v_0. \tag{51}$$

D. Conclusion

Our treatment of the MB plasma is justified if the following inequalities are satisfied: (36), (38), (44),

and (48). The inequality (38) is more stringent than (36), and (44) is more stringent than (48). Consequently, the criterion for the applicability of our method is expressed by (38) and (44). This criterion is satisfied for the two representative cases of MB plasma cited above.

The validity of the treatment of the FD plasma is contingent on the inequalities (39), (49), and (51). The inequality (49) is not compatible with (39) and (51) and, therefore, our validity criterion is not satisfied.

The phenomenological treatment of plasma as a dispersive medium can, therefore, be applied rigorously to such cases as electrical gaseous discharges, or the ionosphere. The criterion for our treatment is, however, rigorously not applicable to such cases as electrons in the conduction band of a metal.

VI. HIGH-VELOCITY INCIDENT PARTICLE

A. General

We shall now determine the response of the medium for an incident particle having charge Ze and velocity $V \gg \langle v^2 \rangle^{\frac{1}{2}}$. We are again confronted with the problem whether the space surrounding the particle track can be represented as a homogeneous dispersive medium characterized by the dielectric constant expressed by (6) and (7). Whether or not such a representation is acceptable depends upon the relative importance of close binary collisions and long-range interactions.

It is apparent that in the immediate neighborhood of the incident particle the electrons undergo very violent collisions. Consequently, the phenomenological representation cannot be used since it applies only to a plasma under the effect of a small perturbation. We shall designate the portion of the space close to the particle track as the region of "binary collisions" since in this region we take into account only the direct interactions of the incident particle with individual electrons. On the other hand, at large distances from the track, we deal with the "plasma region" since the perturbation exerted by the incident particle is small and the collective effect of the electrons is the dominant factor.

The binary collisions will produce a dominant effect if the momentum gain $p_\perp$ of each electron by the passage of the incident particle is large compared to the average momentum $m\langle v^2 \rangle^{\frac{1}{2}}$ of the electron in the undisturbed state, i.e.,

$$p_\perp = 2Ze^2/\rho V \gg m\langle v^2 \rangle^{\frac{1}{2}}, \tag{52}$$

from which

$$\rho \ll \frac{2Ze^2}{mV\langle v^2 \rangle^{\frac{1}{2}}} \sim \frac{Z}{D^2 n} \frac{\langle v^2 \rangle^{\frac{1}{2}}}{V}. \tag{53}$$

In the plasma region, the following criteria should be satisfied: (1) the momentum gain of each electron by the passage of the incident particle is small compared to the average momentum of the electron in the undisturbed state, and (2) the momentum gains of two neighboring electrons should not differ substantially one from the other.

According to the criterion (1) we should have

$$\rho \gg \frac{2Ze^2}{mV\langle v^2 \rangle^{\frac{1}{2}}} \sim \frac{5}{18\pi} \frac{Z}{D^2 n} \frac{\langle v^2 \rangle^{\frac{1}{2}}}{V}. \tag{54}$$

The criterion (2) requires that

$$(dp_\perp/d\rho)\Delta\rho \ll p_\perp, \tag{55}$$

where $\Delta\rho = n^{-\frac{1}{3}}$ is the average distance between two electrons in the plasma. Equation (55) yields

$$\rho \gg n^{-\frac{1}{3}}. \tag{56}$$

Consequently, the plasma region corresponds to impact parameters that satisfy both inequalities (54) and (56).

Our problem is complicated by the fact that the inequalities (54) and (56) do not limit precisely the extent of the plasma region. Even if we assume that the limit defining the plasma region is known, the question of how to treat the problem would arise. A similar situation arose in the study of fast charged particles passing through conventional dispersive media, and in this connection we shall mention the treatment by Fermi[31,32] and Huybrechts and Schönberg.[33] Fermi, assuming that the homogeneous dispersive medium occupies the whole space, calculated the energy loss in the region $\rho > \rho_1$ from the flux of the Poynting vector through a cylindrical surface of radius ρ_1 having its axis on the path of the particle. The energy loss for $\rho < \rho_1$ was calculated on the basis of conventional collision theory. Huybrechts and Schönberg modified the Fermi treatment by assuming that there are no electrons up to the distance ρ_1 and, therefore, the dielectric constant within the cylinder of radius ρ_1 has been taken to be equal to 1 and has a determined value $\epsilon(\omega)$ outside of this cylinder. They have dealt, therefore, with an inhomogeneous dielectric medium having a discontinuity at the surface of the cylinder.

Our treatment will be similar to the one by Fermi since it is simpler and seems to be more applicable to our problem as we do not know the value ρ_1 defininng the discontinuity of the medium.

B. Potential Distribution in Plasma

We shall now return to the expression (14) and determine the potential produced by the incident particle. As stated above, we assume that the homogeneous dispersive medium surrounds the particle track for all impact parameters and we attribute a physical meaning only to the solution for φ for values $\rho > \rho_1$. We shall

[31] E. Fermi, Phys. Rev. **56**, 1242 (1939).
[32] E. Fermi, Phys. Rev. **57**, 485 (1940).
[33] M. Huybrechts and M. Schönberg, Nuovo cimento **9**, 764 (1952).

determine φ also for small values of ρ since it is of some interest.

Since $V \gg \langle v^2 \rangle^{\frac{1}{2}}$, the expression (11) for ϵ_{II} can be expanded as follows

$$\epsilon_{\text{II}} = 1 - \frac{\omega_0^2}{\omega^2}\left[1 + \langle v^2 \rangle \frac{k^2}{\omega^2} + \langle v^4 \rangle \frac{k^4}{\omega^4} + \cdots\right], \tag{57}$$

where

$$\langle v^{2n} \rangle = \int v^{2n} f(v) d\mathbf{v}.$$

Substituting (57) in (14), we obtain

$$\varphi(\rho,z,t) = \frac{ZeV}{\pi} \int_0^\infty \kappa d\kappa J_0(\kappa\rho) \times \int_{-\infty}^{\infty} \frac{e^{i\omega(z/V-t)}\omega^2 d\omega}{(V^2\kappa^2+\omega^2)(\omega^2-\omega_0^2[1+\langle v^2\rangle k^2/\omega^2+\cdots])}.$$

When $\langle v^2 \rangle^{\frac{1}{2}} \ll V^2$ the term multiplying ω_0^2 in the denominator will be nearly unity. We observe that the roots of the denominator in addition to the pair $\omega = \pm i\kappa V$ are given by $\omega^2 = \omega_0^2[1+\langle v^2\rangle k^2/\omega^2+\cdots]$, and correspond to the existence of plasma oscillations. The ω contour should be chosen so as to pass above these singularities. Then for positions ahead of the incident particle, $z > Vt$, the ω contour may be closed in the upper half plane and the oscillations will exist only behind the particle. Since there is only the singularity $\omega = i\kappa V$ in the upper half plane, the potential ahead of the particle is represented as

$$\varphi(\rho,z,t) = Ze \int_0^\infty J_0(\kappa\rho) e^{-\kappa(z-Vt)} \frac{\kappa^2 d\kappa}{(\kappa^2+\omega_0^2/V^2)}. \tag{58}$$

To examine the behavior of this function, we note that if $(z-Vt) \ll V/\omega_0$, we may consider the integrand only for large κ. In this case,

$$\varphi(r) = Ze \int_0^\infty d\kappa J_0(\kappa\rho) e^{-\kappa(z-Vt)} = Ze/r, \tag{59}$$

where r is the distance from the charged particle in a coordinate system moving with the charged particle. When $r \gg V/\omega_0$, we look at the integrand when κ is small. We find, approximately,

$$\varphi(r) = Ze \frac{V^2}{\omega_0^2} \frac{d^2}{dz^2}\left(\frac{1}{r}\right), \tag{60}$$

which is identical with the potential due to an axial quadrupole. We see that the collective effect of the plasma is to cause the potential to fall off approximately as the inverse cube of the distance for large values of r. This result raises some question concerning the procedure of Kwal[18,19] and Van der Ziel[34] of employing an exponentially screened Coulomb potential which is valid for a slowly moving ($V \ll \langle v^2 \rangle^{\frac{1}{2}}$) particle when calculating individual energy transfer to electrons in plasma by fast charged particles. The screening parameter for a low velocity incident particle is of the order of the Debye length which in metals may be less than 1 A. The screening parameter V/ω_0 for a relativistic incident particle may be much larger, e.g., $\sim 10^2$ A.

For positions behind the incident particle, $Z < Vt$, the contour of integration must be closed in the lower half of the ω plane. There will then be the contributions from the pair of poles on the real axis and the pole at $\omega = -i\kappa V$. We assume that to a sufficient approximation the integral may be written

$$\varphi(z,\rho,t) = \frac{ZeV}{\pi} \int_0^\infty \kappa J_0(\kappa\rho) d\kappa \times \int_{-\infty}^{\infty} e^{i(\omega/V)(z-Vt)} \frac{\omega^2 d\omega}{(V^2\kappa^2+\omega^2)(\omega^2-\omega_0^2)}, \tag{61}$$

and

$$\varphi(z,\rho,t) = \varphi_{\text{I}}(z,\rho,t) + \varphi_{\text{II}}(z,\rho,t). \tag{62}$$

Corrections to the position of the poles on the real ω axis will be considered in the next section. Evaluation of the residue at the pole at $\omega = -i\kappa V$ gives an expression φ_{I} which is the analytical continuation of Eq. (58) into the region $z < Vt$, i.e., φ_{I} is again Coulombian for points close to the incident charge and falls off roughly as the inverse cube of the distance for large distances. That part of φ arising from the residue at the poles at $\omega = \pm\omega_0$ is purely oscillatory in $(z/V-t)$, i.e.,

$$\varphi_{\text{II}}(z,\rho,t) = 2(Ze\omega_0/V) \sin\omega_0(z/V-t) K_0(\rho\omega_0/V). \tag{63}$$

This represents the potential due to the polarization charge which is set into oscillation by the passage of the charged particle. In our neglect of damping, the polarization charge continues to oscillate with the plasma eigen-frequency ω_0. The logarithmic singularity of φ_{II} at the track of the particle is due to the erroneous use of an infinite upper limit in the integration. This will be examined in the next section.

C. Polarization Charge Density

The polarization charge density p may be expressed as

$$p = -i\mathbf{k}\cdot\mathbf{P}, \tag{64}$$

where $\mathbf{P}$ is the polarization vector. Further, since

$$i\mathbf{k}\cdot(\mathbf{E}+4\pi\mathbf{P}) = (Ze/2\pi^2)\delta(\omega-\mathbf{k}\cdot\mathbf{V}), \tag{65}$$

and $-i\mathbf{k}\cdot\mathbf{E} = k^2\varphi$,

$$p = -\frac{Ze}{(2\pi)^3}\delta(\omega-\mathbf{k}\cdot\mathbf{V}) + \frac{k^2\varphi}{4\pi}, \tag{66}$$

[34] A. Van der Ziel, Phys. Rev. 92, 35 (1953).

or, in configuration space

$$p(\rho,z,t)=\frac{Ze\omega_0^2}{(2\pi)^2V}\int_0^\infty \kappa d\kappa J_0(\kappa\rho)$$

$$\times\int_{-\infty}^{\infty} e^{i\omega(z/V-t)}\frac{d\omega(1+\langle v^2\rangle k^2/\omega^2+\cdots)}{\{\omega^2-\omega_0^2(1+\langle v^2\rangle k^2/\omega^2+\cdots)\}}. \quad (67)$$

We have postulated $\langle v^2\rangle^{\frac{1}{2}}\ll V$ so we find the roots of the denominator by successive approximation. The ω contour is chosen to pass above the poles on the real axis, to correspond to zero polarization charge ahead of the particle. Then, the roots of the denominator are approximately

$$\omega=\pm[\omega_0^2+\langle v^2\rangle(\omega_0^2/V^2+\kappa^2)]^{\frac{1}{2}}. \quad (68)$$

Evaluating the residues, we find for $(z/V-t)<0$

$$p(\rho,z,t)=\frac{Ze\omega_0}{2\pi V}\int_0^\infty \kappa d\kappa J_0(\kappa\rho)\left[\omega_0^2\left(1+\frac{\langle v^2\rangle}{V^2}\right)+\langle v^2\rangle\kappa^2\right]$$

$$\times\sin\left\{\left(\frac{z}{V}-t\right)\left[\omega_0^2\left(1+\frac{\langle v^2\rangle}{V^2}\right)+\langle v^2\rangle\kappa^2\right]^{\frac{1}{2}}\right\}. \quad (69)$$

The integral as written does not exist. However, we note that the upper limit may not be infinite since the dielectric is not capable of supporting oscillations whose wavelength is shorter than the average spacing between electrons in the medium.

To obtain an approximate solution we assume that the integral may be cut off at some finite upper limit designated by κ_m. Then

$$p(\rho,z,t)=-\frac{Ze}{2\pi V}\frac{d^2}{d\tau^2}\int_0^{\kappa_m}\kappa d\kappa J_0(\kappa\rho)$$

$$\times\frac{\sin\tau[\omega_0^2(1+\langle v^2\rangle/V^2)+\langle v^2\rangle\kappa^2]^{\frac{1}{2}}}{\omega_0^2(1+\langle v^2\rangle/V^2)+\langle v^2\rangle\kappa^2}, \quad (70)$$

where $\tau=(z/V)-t$. Now if ρ and τ are both large, the bulk of the integral will originate from reion of small κ, and we tentatively let $\kappa_m\to\infty$ and using an identity proven by Lamb,[35] write

$$p(\rho,z,t)=-\frac{Ze}{2\pi}\frac{d^2}{d\tau^2}\begin{cases}\dfrac{\cos\omega_0[\tau^2-\rho^2/\langle v^2\rangle]^{\frac{1}{2}}}{[\tau^2-\rho^2\langle v^2\rangle]^{\frac{1}{2}}} & \tau\langle v^2\rangle^{\frac{1}{2}}>\rho\\ 0 & \tau\langle v^2\rangle^{\frac{1}{2}}<\rho.\end{cases} \quad (71)$$

The singularity on the surface of the cone

$$z-Vt=(V/\langle v^2\rangle^{\frac{1}{2}})\rho$$

is fictitious; the polarization charge density actually has a finite maximum on this surface.

[35] H. Lamb, Proc. London Math. Soc. Sec. 2, 7, 122 (1909).

D. Stopping Power

(1) *General*

The space surrounding the particle track is subdivided into three regions: (a) The region of binary collisions within a cylinder having as axis the track of the particle and a radius ρ_1 satisfying the inequality (53), (b) the plasma outside of a similar cylinder having radius ρ_2, and satisfying the inequality (54), and (c) the intermediate region between cylinders having radii ρ_1 and ρ_2. The intermediate region includes the portion of space for which no adequate theory exists at present.

(2) *Plasma Region*

We wish to determine the energy lost by the incident particle to the portion of the plasma in the region $\rho>\rho_2$ to which the dielectric concept rigorously applies. To accomplish this, we will consider the force with which the polarization in the "far" region ($\rho>\rho_2$) reacts upon the incident particle. We imagine that the cylinder $\rho<\rho_2$ is removed from the infinite medium leaving the polarization in the far region unchanged. The stopping power is then given by the force exerted on the incident particle by the surface charge density (which is equal to the normal component of the polarization vector) on the inside of this cylinder and by that portion of the wake of volume polarization charge which lies in the far region.

Now

$$\mathbf{P}=\frac{iZe}{(2\pi)^3}\delta(\omega-\mathbf{k}\cdot\mathbf{v})\cdot\frac{1-\epsilon_{11}}{\epsilon_{11}}\frac{\mathbf{k}}{k^2}. \quad (72)$$

The surface charge density is

$$\sigma=-\hat{n}\cdot\mathbf{P}(\rho,z,t), \quad (73)$$

where $\hat{n}$ is a unit vector in the direction of the outward normal to the cylinder. The expression for the polarization charge is given in Eq. (64). Then

$$-\frac{dW}{dz}=2\pi Ze\left\{\rho_2\int_{-\infty}^{\infty}\frac{zdz}{(z^2+\rho_2^2)^{\frac{1}{2}}}\sigma(\rho_2,z)\right.$$

$$\left.+\int_{\rho_2}^{\infty}\rho d\rho\int_{-\infty}^{\infty}\frac{zdz}{(z^2+\rho^2)^{\frac{1}{2}}}p(\rho,z)\right\}, \quad (74)$$

where the variable z is understood to have its origin at the position of the incident particle. Inserting the Fourier integral representations for σ and p, and using the approximate form for the dielectric constant for $\langle v^2\rangle^{\frac{1}{2}}\ll V$ one finds after carrying out the integrations

$$-\frac{dW}{dz}=\frac{Z^2e^2\rho_2}{V(1+\beta_1^2)}\int_0^\infty\frac{\kappa d\kappa J_0(\kappa\rho)}{(\omega_0^2+\kappa^2V^2)}\omega'^3K_1(\rho_2\omega'/V), \quad (75)$$

where $\beta_1=\langle v^2\rangle^{\frac{1}{2}}/V$ and $\omega'=[\omega_0^2(1+\beta_1^2)+\beta_1^2V^2\kappa^2]^{\frac{1}{2}}$.

This may be shown to reduce to

$$-\frac{dW}{dz}=\frac{Z^2e^2}{(1+\beta_1^2)}\frac{\omega_0^2}{V^2}a\left\{K_0(a)K_1(a)+\frac{2\beta_1}{a}K_1\left(\frac{a}{\beta}\right)-\frac{a}{2}\int_{a/\beta_1}^{\infty}K_1(x)dx/x^3\right\}, \quad (76)$$

where $K_0(a)$ and $K_1(a)$ are modified Bessel functions of the second kind of the order 0 and 1, respectively,[36] and $a=\omega_0\rho_2/V$. Now if $a/\beta_1\gg1$,

$$-\frac{dW}{dz}=\frac{Z^2e^2a}{1+\beta_1^2}\frac{\omega_0^2}{V^2}\{K_0(a)K_1(a)+(2\pi)^{\frac{1}{2}}(\beta_1/a)^{7/2}e^{-a/\beta_1}\}. \quad (77)$$

Taking into account that

$$(2\pi)^{\frac{1}{2}}(\beta_1/a)^{7/2}e^{-a/\beta_1}\ll K_0(a)K_1(a), \quad (78)$$

we obtain

$$-\frac{dW}{dz}=\frac{Z^2e^2\rho_2\omega_0^2}{V^3(1+\beta_1^2)}K_0(\rho_2\omega_0/V)K_1(\rho_2\omega_0/V). \quad (79)$$

If $\rho_2\omega_0/V\ll1$, one may replace K_0 and K_1 by the first terms in their series expansions, obtaining:

$$-\frac{dW}{dz}=\frac{Z^2e^2\omega_0^2}{V^2(1+\beta_1^2)}\ln\frac{1.123V}{\omega_0\rho_2}, \quad (80)$$

which in the limit $\beta_1\to0$ reduces to

$$-\frac{dW}{dz}=\frac{Z^2e^2\omega_0^2}{V^2}\ln\frac{1.123V}{\omega_0\rho_2}. \quad (81)$$

It may be of interest to compare the above formula with the corresponding expression derived by Pines.[11] Using the present notation, the stopping power obtained by Pines can be expressed as follows:

$$-\frac{dW}{dz}=\frac{Z^2e^2\omega_0^2}{V^2}\left\{\ln\frac{k_0V(1-\beta_1^2)^{\frac{1}{2}}}{\omega_0}+\frac{\langle v^2\rangle^{\frac{1}{2}}\beta_1^2(1-\beta_1^2)k_0^2}{4\omega_0^2}\right\}, \quad (82)$$

where k_0 is a cut-off wave number.

Assuming $(1-\beta_1^2)^{\frac{1}{2}}\sim1$, we obtain from (82)

$$-\frac{dW}{dz}=\frac{Z^2e^2\omega_0^2}{V^2}\left\{\ln\frac{V}{\omega_0\rho_2}+\frac{\beta_1^2\langle v^2\rangle^{\frac{1}{2}}k_0^2}{4\omega_0^2}\right\}. \quad (83)$$

For the limiting case of $\beta_1=0$ the expression (83) is identical to (81) except for the factor 1.123 in the logarithm. However, for $\beta_1\neq0$ the expression (80) gives a decreased value for the stopping power, whereas according to the Pines formula (83) the stopping power increases by a much smaller amount.

[36] For tables of K_0 and K_1 functions, see for instance: *British Association for the Advancement of Science, Mathematical Tables* (Cambridge University Press, Cambridge, 1937), Vol. 6, pp. 264–271.

(3) *Binary Collisions*

The contribution of binary collisions to the stopping power is

$$-\frac{dW}{dz}=\frac{Z^2e^2\omega_0^2}{V^2}\ln\left(\frac{\rho_1}{b_{\min}}\right), \quad (84)$$

where

$$b_{\min}=Ze^2/mV^2 \quad \text{if} \quad Ze^2/\hbar V\gg1, \quad (85)$$

and

$$b_{\min}=h/2mV \quad \text{if} \quad Ze^2/\hbar V\ll1. \quad (86)$$

(4) *Total Stopping Power*

The contribution to the stopping power in the intermediate region for $\rho_1<\rho<\rho_2$ remains undetermined. In this intermediate region, both individual and collective interactions take place. By interpolating, it is seen that the contribution to the stopping power of any portion of the intermediate region comprising distances $d\rho$ about ρ is the same if calculated on the basis of collective interaction or individual interaction. We shall assume, therefore, that $\rho_1=\rho_2$ and is located somewhere in the intermediate region. By adding the contributions (81) and (84), we obtain for the total stopping power

$$-\frac{dW}{dz}=\frac{4\pi Z^2e^4}{mV^2}\ln\left(\frac{1.123V}{\omega_0b_{\min}}\right), \quad (87)$$

where $b_{\min}$ is given by (86).

VII. LOW-VELOCITY INCIDENT PARTICLE

A. Polarization Charge Density

In Sec. IV we found that to a first approximation a slowly moving incident particle in plasma gives rise to an exponentially screened Coulomb potential. We shall now determine the form of the polarization charge density to second order, taking into account in this treatment the damping of a disturbance in plasma due to the random motion of the medium.

To determine ϕ we shall need an approximate expression for the dielectric constant for the case $\langle v^2\rangle^{\frac{1}{2}}\gg V$. It may be written

$$\epsilon_{\rm II}=1+\frac{2\pi\omega_0^2}{k^2}\left[\int_{-\infty}^{\infty}f(u)du+\frac{\omega}{k}\int_{-\infty}^{\infty}\frac{f(u)du}{(u-\omega/k)}\right] \quad (88)$$

$$\simeq1+\frac{\omega_0^2}{k^2s^2}\left[1+i\frac{B}{s}\frac{\omega}{k}+O\left(\frac{\omega^2}{k^2}\right)\right], \quad (89)$$

where the constant B depends upon the kind of statistics assumed for the plasma, i.e., $B_{MB}=(\pi/2)^{\frac{1}{2}}$, $B_{FD}=\sqrt{3}\pi/6$. The imaginary term arises because the path of integration in the u-plane must be deformed so as to pass below the singular point $u=\omega/k$ as the damping constant g approaches zero. As in Sec. VI we write the Fourier integral expression for ϕ, using the approximation given above for $\epsilon_{\rm II}$. We then express the result as a power series in $\beta=V/s$, retaining only the first two

terms. We find then

$$p=\frac{Ze\omega_0^2}{4\pi s^2}\frac{e^{-r/D}}{r}+\frac{Ze\beta B\omega_0}{4\pi^2 s}\frac{Z}{r^3}$$
$$\times\{(1-a^2)[e^{-a}\,\mathrm{Ei}(a)-e^{a}\,\mathrm{Ei}(-a)]$$
$$+a[e^{a}\,\mathrm{Ei}(-a)+e^{-a}\,\mathrm{Ei}(a)+1]\},\quad(90)$$

where

$$\mathrm{Ei}(a)=\int_{-\infty}^{a}e^{x}dx/x$$

and $a=r/D=\omega_0 r/s$. The origin of coordinates ($r=0$) is taken at the position of the incident particle and moves with the particle. The z coordinate is measured along the path of the particle and is taken positive in the direction of motion of the particle.

B. Stopping Power

(1) *General Considerations*

We shall now determine the stopping power of an incident particle gaving charge Ze and velocity $V\ll\langle v^2\rangle^{\frac{1}{2}}$.

The energy loss per unit path length may be expressed in a way similar to that used for the high-velocity particle. We shall calculate the energy delivered to the plasma in the "far" region, i.e., to the region outside of a sphere of radius R whose center coincides with the position of the incident particle. Thus

$$-\frac{dW}{dz}=Ze\left\{2\pi\int_0^{\pi}\sin\theta\cos\theta\sigma(\theta,R)d\theta\right.$$
$$\left.+2\pi\int_0^{\pi}\sin\theta\cos\theta d\theta\int_R^{\infty}dr\,p(\theta,r)\right\},\quad(91)$$

where the coordinate system is chosen to move with the incident particle and to have its origin at the particle position. In this expression $\cos\theta=z/r$, $\sigma=-\hat{n}\cdot\mathbf{P}$ where $\hat{n}$ is a unit vector normal to the sphere of radius R in the outward direction, and p is the polarization charge density.

Using the above approximation for ϵ_{11} in the Fourier integral expressions for $\mathbf{P}$ and p and expanding the resulting formulas in a power series in β we find eventually, to the first power in β,

$$-\frac{dW}{dz}=\frac{Z^2e^2\omega_0^2\beta B}{3\pi V^2 a}\left\{\left(1+\frac{1}{a}+\frac{1}{a^2}\right)e^{-a}\,\mathrm{Ei}(a)\right.$$
$$\left.-\left(1-\frac{1}{a}+\frac{1}{a^2}\right)e^{a}\,\mathrm{Ei}(-a)-\frac{2}{a}\right\},\quad(92)$$

where $a=r/D$. If $a\ll1$,

$$-\frac{dW}{dz}=\frac{Z^2e^2\beta B\omega_0^2}{3\pi s^2}\ln\left(\frac{s^2}{3.17R^2\omega_0^2}\right).\quad(93)$$

In this phenomenological treatment we have excluded the region inside a sphere of radius R centered at the particle. This is the region of close collisions and the value of R depends upon whether we deal with MB or FD plasma.

(2) *MB Plasma*

In this case we choose R to be the average spacing between electrons in the medium,

$$R\simeq n^{-\frac{1}{3}},$$

or

$$a^2=4\pi e^2 n^{\frac{1}{3}}/k_B T.\quad(94)$$

Thus the nonuniformity of the medium is taken into account in an approximate way. The stopping power is found by substituting (94) in either (92) or (93).

(3) *FD Plasma*

We have previously found that the classical phenomenological representation is not strictly applicable to an FD plasma. However, we shall apply the expression (92) to an FD plasma, keeping in mind that in the past a classical treatment has been not infrequently used with satisfactory results in quantum-mechanical problems. We may cite the Thomas-Fermi statistical model of electron gas in an atom as well as various hydrodynamical models of perturbed electron gas, for instance, the one used by Bloch.[37] It is of interest to mention the calculation made by Bloch[38] of the stopping power of a particle having charge Ze and velocity V, such that $Ze^2/\hbar V\ll1$. Although the interaction of the particle with the surrounding electrons is not subject to an orbital representation, the stopping power has been calculated by using an impact parameter method and the quantum mechanical aspects of the problem have been taken into account by assuming that the minimum impact parameter is equal to $\hbar/mV$. We shall follow the general procedure used by Bloch.

Returning now to our problem we consider the close collision of a particle having velocity V with an electron gas having isotropically distributed velocities in the range from zero to v_F. The wavelength of most of the electrons as seen from the moving particle will be somewhat smaller, but of the same order of magnitude as $2\pi\lambda$. We shall subdivide the space surrounding the incident particle into two regions: region I within a sphere having its center at the position of the particle and radius $\pi\lambda_F$; and region II comprising the space

[37] F. Bloch, Z. Physik. **81**, 363 (1933).

[38] F. Bloch, "Lecture Series in Nuclear Physics," U. S. Atomic Energy Commission Report MDDC-1175 (U. S. Government Printing Office, Washington, D. C., 1947), p. 26.

outside of the sphere. The contribution to the stopping power from the region I is negligible, since in this region the incident particle traverses a wave packet that exerts on it electrical forces from various directions, thus giving partial cancellation. Therefore, we shall assume that the total contribution to the stopping power is due to the presence of plasma in the region II.

The expression for the stopping power can, therefore, be obtained by substituting $R=\pi\lambda_F$ in (94). Of particular interest is the case of $a_{FD}\ll 1$ which has been treated by Fermi and Teller[39] in a different manner. To determine the stopping power for this case, we substitute $R=\pi\lambda_F$ in (93), obtaining

$$-\frac{dW}{dz}=\frac{2}{3\pi}\frac{Z^2e^4m^2V}{\hbar^3}\ln\frac{v_F}{3.17\times 4\pi v_0}. \tag{95}$$

[39] E. Fermi and E. Teller, Phys. Rev. **72**, 399 (1947); see also N. Mott, Proc. Phys. Soc. (London) **137**, 1462 (1949).

Assuming that $v_F/v_0\gg 3.17\times 4\pi$, the formula (95) can be expressed as

$$-\frac{dW}{dz}=\frac{2}{3\pi}\frac{Z^2e^4m^2V}{\hbar^3}\ln\left(\frac{v_F}{v_0}\right). \tag{96}$$

This formula is identical to the corresponding formula by Fermi and Teller.

The Fermi-Teller formula does not apply to the conduction band of metals since it is derived under the assumption that $v_F\gg v_0$. In order to determine the stopping power for the conduction band of metals, the formula (92) would seem to be applicable.

ACKNOWLEDGMENTS

The authors would like to thank Dr. R. D. Present of the University of Tennessee for his suggestions and criticisms and Mr. A. Y. Sakakura of the U. S. Geological Survey for a helpful conversation concerning some of the analysis in this paper.

PHYSICAL REVIEW VOLUME 98, NUMBER 6 JUNE 15, 1955

Microwave Study of Positive Ion Collection by Probes*

GEORGE J. SCHULZ† AND SANBORN C. BROWN
Department of Physics and Research Laboratory of Electronics, Massachusetts Institute of Technology, Cambridge, Massachusetts

(Received February 14, 1955)

The theory of the positive ion saturation region of probes at low pressure is modified to take into account the directed current at the sheath edge. This drift current explains the discrepancy between the theoretical and experimental ratio of the electron saturation probe current to the positive ion saturation probe current. The theory is checked by using microwave methods to obtain an independent measurement of the ion density. Probe and microwave measurements are compared in the pressure region of 0.05–6 mm Hg in hydrogen, argon, and helium.

I. INTRODUCTION

SINCE the original work of Langmuir and Mott-Smith,[1] probes have been used extensively for the study of plasma properties in low-pressure gas discharges. The electron and positive ion densities, the electron temperature, and the plasma potential are determined from the volt-ampere characteristics of the probe, called the "probe curve." It is customary to divide the probe curve into three parts: the positive ion saturation, the region of partial collection of electrons, and the electron saturation.

When the probe potential is sufficiently negative with respect to the plasma in which the probe is inserted, the probe will attract positive ions and repel all electrons and thus the probe current consists only of positive ions. This is called the positive ion saturation. In the vicinity of the probe, only positive ions contribute to the space charge and the potential is a steep function of position; this region is called the sheath. At larger distances from the probe, both electrons and positive ions contribute to the space charge and the electric fields are small. The plasma in this region is disturbed by the withdrawal of positive ions to the probe.

As the magnitude of the voltage on the probe with respect to plasma potential is decreased, the probe starts collecting electrons. When the probe is near plasma potential, the probe curve exhibits a bend. At plasma potential, the probe is not covered by a sheath and electrons and ions reach the probe by diffusion. Electron densities may be determined from Langmuir's theory[1] when the bend in the probe curve is sharp.

When the gas pressure is high or when the probes draw a large current, the probe curve does not exhibit a sharp bend at plasma potential and no electron

* This work was supported in part by the Signal Corps, the Office of Scientific Research, Air Research and Development Command; and the Office of Naval Research.

† Now at Westinghouse Research Laboratories, East Pittsburgh, Pennsylvania.

[1] I. Langmuir and H. M. Mott-Smith, Gen. Elec. Rev. **27**, 449, 538, 762, 810 (1924).

saturation occurs.[2] At high pressure the diffusion coefficient is low and the electrons taken by the probe cannot be replenished by the diffusive flow from the plasma. In these cases it is advantageous to determine densities from the positive ion saturation of the probe curve. In a plasma, the net charge density $n_+ - n_-$ (where n_+ is the positive ion density and n_- is the electron density) is small and we can set $n_+ = n_- = n$. The positive ion density is equal to the electron density and we need not distinguish between the two.

This paper deals with the theory of positive ion collection by probes and the experimental verification of this theory. The experimental verification comes from the dependence of the probe current on probe voltage, pressure, and ion density. Microwave methods are used to measure the ion density.

II. CURRENT REACHING THE SHEATH EDGE

Before proceeding with the discussion of the ion current collected by a negative probe we shall discuss the ion current reaching the sheath edge. It is usually assumed that no electric field penetrates from the probe beyond a certain boundary called the sheath edge and that both electrons and ions have a Maxwellian velocity distribution at the sheath edge. Under these assumptions the random ion current density, J_r, reaches the sheath edge. The random current density is given by

$$J_r = en_0(kT_+/2\pi M)^{\frac{1}{2}}, \tag{1}$$

where T_+ is the positive ion temperature, M is the mass of the ion, k is Boltzmann's constant, e is the electronic charge, and n_0 is the plasma density of ions. The assumption of a Maxwellian velocity distribution for positive ions at the sheath edge is unsatisfactory because equilibrium is disturbed near the sheath by the drain of ions to the probe. Small electric fields and density gradients may penetrate beyond the sheath and cause a drift current of positive ions at the sheath edge. It will be shown that it is necessary to take this drift current into account.

Let us simplify the problem by treating a plane probe. The current density of positive ions at any point in the sheath, including the drift current at the sheath edge but neglecting collisions in the sheath, is given by

$$J_d = en[(2e/M)(V+w)]^{\frac{1}{2}}, \tag{2}$$

where J_d is the current density, V is the potential at any point in the sheath, w is the directed energy of ions reaching the sheath edge, and n is the ion density at any point.

Substituting the quantity (en) from Eq. (2) into Poisson's equation and using a Boltzmann distribution for the electrons, we obtain

$$\epsilon_0(d^2V/dx^2) = \{J_d[(2e/M)(V+w)]^{-\frac{1}{2}} - en_s \exp(-eV/kT_-)\}, \tag{3}$$

where ϵ_0 is the permittivity of free space and n_s is the density at the sheath edge. A Boltzmann distribution for the electrons is justified because electrons are reflected from the sheath and equilibrium prevails.

Introducing the variables

$$\phi = (e/kT_-)(V+w), \qquad A = [en_s/(\sqrt{2}J_d)](kT_-/M)^{\frac{1}{2}} \exp(\phi_0),$$
$$\phi_0 = (ew/kT_-), \quad B = (J_d/\epsilon_0)(kT_-/e)^{-\frac{1}{2}}(2e/M)^{-\frac{1}{2}},$$

The normalized space charge becomes, using Eq. (3)

$$(d^2\phi/dx^2) = -B[\phi^{-\frac{1}{2}} - 2A \exp(-\phi)]. \tag{4}$$

The quantities ϕ and ϕ_0 are potentials normalized with respect to the electron temperature. When A is large, a negative space charge will occur somewhere in the sheath.

There is no reason to believe that negative space charge exists in the sheath or in the plasma and it is necessary to exclude this possibility from the above equations. Thus A must be equal to or smaller than a certain critical value, A_0. A smooth joining of the space charge, ρ, at the sheath edge requires that $\rho \geq 0$ and $(d\rho/dx) \geq 0$ at the sheath edge, where $\phi = \phi_0$. The critical value A_0 is computed from Eq. (4) and its derivative by applying the conditions $\rho = 0$ and $(d\rho/dx = 0)$ at $\phi = \phi_0$.

The derivative of Eq. (4) is

$$(d^2\phi/dx^2) = -B[-0.5\phi^{-\frac{1}{2}} + 2A \exp(-\phi)]d\phi/dx, \tag{5}$$

and A_0 becomes

$$A_0 = \tfrac{1}{4}\phi_0^{-\frac{1}{2}} \exp(\phi_0) = \tfrac{1}{2}\phi_0^{-\frac{1}{2}} \exp(\phi_0).$$

This yields $\phi_0 = \frac{1}{2}$, and $A_0 = 1.165$. From Eq. (2) the drift current density at the sheath edge, $V = 0$, becomes, in terms of the ion density, n_s at the sheath edge,

$$J_d = n_s e(kT_-/M)^{\frac{1}{2}}, \tag{6}$$

and is thus proportional to the electron temperature. Wenzl[3] reached a similar conclusion from different considerations. The current density J_d given by Eq. (6) is caused primarily by small electric fields penetrating beyond the sheath edge and originates in the random current of the plasma at some distance from the sheath edge. The contribution of density gradients to the current density J_d can be neglected. Thus the penetrating electric field imparts to the ions a drift velocity $(kT_-/M)^{\frac{1}{2}}$. The corresponding potential difference between the undisturbed plasma and the sheath edge, V_s, is $V_s \approx \frac{1}{2}kT_-/e$. In the region between the sheath edge and the undisturbed plasma, electrons and positive ions are present in comparable quantities and therefore the density distribution can be approximated by a Boltzmann distribution. The density in the plasma, n_0, can be written in terms of the density at the sheath edge, n_s,

$$n_0 = n_s e^{eV_s/kT_-} = n_s\sqrt{\epsilon},$$

[2] R. L. F. Boyd, Proc. Roy. Soc. (London) **A201**, 329 (1950).

[3] F. Wenzl, Z. angew. Phys. **2**, 59 (1950).

where ϵ is the base of the natural logarithm. We can rewrite Eq. (6) in terms of the plasma density, n_0, as follows:

$$J_d = n_0 e (kT_-/M\epsilon)^{\frac{1}{2}}.$$

If the random current density J_r had been used instead of J_d in Eq. (3), A_0 would have been larger than 1.165, and negative space charge would have appeared near the edge of the sheath. So far we have discussed the current reaching the sheath edge at low pressure. At high pressures, it is better to assume that the random current density given by Eq. (1) reaches the sheath edge. Because ions make many collisions at high pressure their motion will remain approximately random up to the sheath edge.

III. CURRENT REACHING A CYLINDRICAL PROBE

(a) No Collisions in the Sheath

When the mean free path is larger than the sheath radius, ions will describe orbital motions in the sheath region of the probe negative with respect to the plasma. Assuming that the random current density J_r reaches the sheath edge, Mott-Smith and Langmuir[4] arrived at the following expression for the probe current, i, to a cylindrical probe:

$$i = 2\pi r_p L J_r \left\{ \frac{a}{r_p} P\left[\frac{r_p^2 \phi_p}{a^2 - r_p^2}\right]^{\frac{1}{2}} + \left[1 - P\left(\frac{a^2 \phi_p}{a^2 - r_p^2}\right)^{\frac{1}{2}}\right] \exp(\phi_p) \right\}. \quad (7)$$

Here r_p is the probe radius, L is the probe length, a is the sheath radius, V_p is the probe-to-plasma voltage, $\phi_p = eV_p/kT_+$ is the probe voltage normalized with respect to the positive ion temperature, and $P(x)$ is the error function defined by

$$P(x) = (2/\pi^{\frac{1}{2}}) \int_0^x \exp(-y^2) dy.$$

We shall follow the usual procedure and use J_r and correct the final equation for the drift current J_d.

In most practical applications involving small probes, $a \gg r_p$ and when the probe is saturated we also have $|eV_p/kT_+| \gg 1$. In fact, for positive ion saturation we must have, following Eq. (6), $|eV_p/kT_-| > 1$. With these approximations, the last term in Eq. (7) can be neglected and

$$i = 2\pi r_p L J_r (a/r_p) P[\phi_p^{\frac{1}{2}} r_p/a]. \quad (8)$$

The sheath size is determined by the Child-Langmuir equation, which in cylindrical coordinates is

$$i = (8\pi\epsilon_0/9)(2e/M)^{\frac{1}{2}}(L/r_p)(V_p^{\frac{1}{2}}/\beta^2), \quad (9)$$

where β^2 is a function of a/r_p.[5] Both Eq. (8) and Eq. (9) give the current arriving at the probe and we may equate the two expressions:

$$a/r_p P[\phi_p^{\frac{1}{2}} r_p/a]\beta^2 = (4/9)\sqrt{2}\phi_p^{\frac{1}{2}}/N_r, \quad (10)$$

where N is a dimensionless variable involving the density

$$N_r = (e/\epsilon_0) M^{\frac{1}{2}} J_r r_p^2 (kT_+)^{-\frac{1}{2}},$$

The subscript r or d will be used on N to indicate that J_r or J_d is to be used in the right-hand side of this equation.

Equation (10) was solved numerically, and a good approximation to the plotted curves was found to be

$$(a/r_p) P[\phi_p^{\frac{1}{2}} r_p/a] = 0.7\phi_p^{0.55}/N^{0.2}.$$

With this approximation, the positive ion saturation current reaching the probe at low pressure when the mean free path is larger than the sheath is given by

$$i = (2\pi r_p L J_r) 0.7 \phi_p^{0.55}/N_r^{0.2}. \quad (11)$$

The part of the equation in parentheses gives the current that would be collected if no sheath were present and the random current were collected by the probe. The second part is a correction factor resulting from the sheath size and orbital motion. The drift current at the sheath previously postulated can be taken into account by replacing J_r by J_d and, correspondingly, N_r by N_d. The coefficient 0.7 in Eq. (11) is approximate because the integration leading to Eq. (11) was performed over a Maxwellian distribution instead of a distribution which is displaced on the velocity axis. The displacement is caused by electric fields penetrating the sheath.

With a fixed probe and discharge conditions we obtain the proportionality

$$i \sim V_p^{0.55} n_0^{0.8}. \quad (12)$$

(b) One Collision in the Sheath

When an average ion makes one collision with an atom in the sheath, such an ion will lose energy and be trapped in the region of high negative potential in the sheath. The ion cannot escape and will eventually reach the probe. We can assume in this case that all the ions reaching the sheath will be collected by the probe.

This condition can be incorporated into the theory of Sec. III(a) by letting $P(\phi_p^{\frac{1}{2}} r_p/a)$ be unity. The function $\beta^2 a/r_p$ now appearing in Eq. (10) can be approximated by

$$\beta^2 a/r_p = 2.1(a/r_p)^{2.37}.$$

Although β is not applicable when collisions occur in the sheath,[5] the sheath size does not change appreciably as the pressure is increased. The assumption is therefore made that β can be used for calculating the sheath

[4] H. M. Mott-Smith and I. Langmuir, Phys. Rev. **28**, 727 (1926).

[5] I. Langmuir and K. B. Blodgett, Phys. Rev. **22**, 353 (1923).

thickness even when a few collisions occur in the sheath. Proceeding as in the orbital case, the ratio of the sheath to the probe radius becomes

$$a/r_p=0.6\phi_p{}^{0.63}/N_d{}^{0.422}. \tag{13}$$

The current reaching the probe becomes

$$i=2\pi r_p L J_d 0.6\phi_p{}^{0.63}/N_d{}^{0.422}, \tag{14}$$

or, in mks units,

$$i=2.2\times10^{-25}r_p{}^{0.156}M^{-\frac{1}{2}}Ln^{0.578}(kT_-/e)^{0.289}V_p{}^{0.63}.$$

(c) Few Collisions in the Sheath

When conditions are such that ions make several collisions in the sheath (between 2 and 10) the ions do not acquire mobility-controlled motions and we have to consider the elastic scattering of the ions in the sheath. This problem has been treated in connection with a study of hydrogen thyratrons.[6] The current density reaching the probe is reduced by the scattering of the ions; the ratio of the current density arriving at the probe to that arriving at the sheath is given by

$$(J/J_d)=\tfrac{1}{2}[3-\exp(-\nu_c t)]/(1+\nu_c t). \tag{15}$$

Here ν_c is the frequency of collision for positive ions, and t is the time spent by an unscattered ion in the sheath. Experimentally, we can measure J/J_d as a function of pressure, and since ν_c is proportional to the pressure, we can set $\nu_c t=\alpha p$. This equation becomes:

$$(J/J_d)=\tfrac{1}{2}[3-\exp(-\alpha p)]/(1+\alpha p). \tag{16}$$

Evaluating the derivative of the logarithm of J with respect to pressure as p approaches 0, we obtain

$$(d\ln J/dp)\,|_{p\to0}=-\alpha/2. \tag{17}$$

This relation will be used for the experimental evaluation of α. In the pressure region under discussion, the current reaching the probe is reduced from that given in Eq. (14) by the scattering factor given in Eq. (16).

(d) Many Collisions in the Sheath

When the gas pressure is so high that ions make many collisions with gas atoms in the sheath, their velocity will be controlled by mobility. Cobine[7] has treated the case of a plane probe at high pressure. Here, the equation for cylindrical geometry will be given.

The ion current at a distance r is given by $i=-2\pi r L n e\mu_+ E$, where μ_+ is the positive ion mobility and E is the electric field of the probe. Substituting this into Poisson's equation yields

$$d^2V/dr^2+(1/r)dV/dr=-i[2\pi r L\mu_+\epsilon_0(dV/dr)]^{-1}.$$

Integrating, rearranging, and applying the boundary conditions ($E=V=0$ at $r=a$; and $V=V_p$ at $r=r_p$), we obtain

$$i=2\pi\mu_+\epsilon_0 L V_p{}^2 r_p{}^{-2}\gamma^{-2}, \tag{18}$$

where

$$\gamma=[(a/r_p)^2-1]^{\frac{1}{2}}-(a/r_p)\ln\{a/r_p+[(a^2/r_p{}^2)-1]^{\frac{1}{2}}\}.$$

Equation (18) is the high-pressure equivalent of Eq. (9). Again, we need to equate the current given by Eq. (18) to the current arriving at the probe expressed in terms of the current reaching the sheath. The current density reaching the sheath edge at high pressure is assumed to be J_r. This current density is reduced by scattering in the sheath to a value $J=3J_r/(2\alpha p)$ obtained from the high-pressure limit of Eq. (16). The second equation for the current reaching the probe thus becomes

$$i=2\pi r_p L J_r(a/r_p)[3/(2\alpha p)]. \tag{19}$$

The function $\gamma(a/r_p)^{\frac{1}{2}}$ appears when Eq. (18) is equated

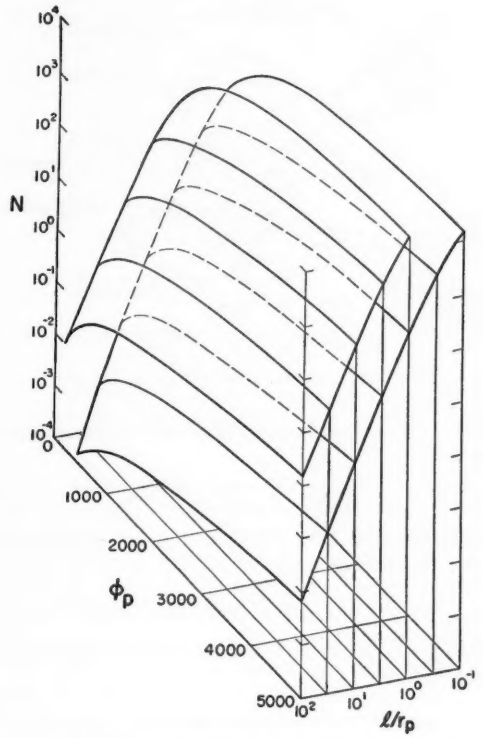

FIG. 1. Surfaces of constant number of collisions in the sheath. Above the top surface, ions make no collisions in the sheath; on the top surface, they make one collision; between the two surfaces, they make a few collisions; and below the bottom surface, they make many collisions.

[6] First Quarterly Progress Report, "Research Study on Hydrogen Thyratrons," Edgerton, Germeshausen, and Grier, Boston, 1951 (unpublished), p. 22. Although this reference treats the problem of electron scattering, the final expression can be applied to positive ions. On the first collision with an atom, ions will be scattered only in the forward direction at various angles. Those ions that have a sideways component may get scattered in the backward direction on the second collision, and soon the scattering will be spherically symmetrical, just as electron scattering.

[7] J. D. Cobine, *Gaseous Conductors* (McGraw-Hill Book Company, Inc., New York, 1941), p. 128.

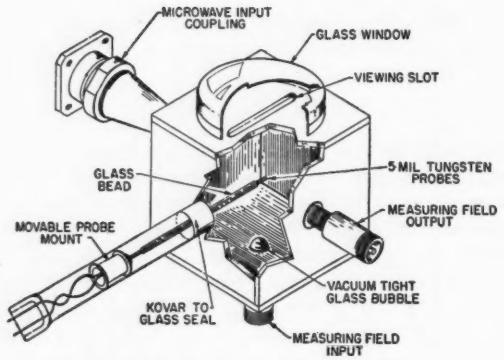

FIG. 2. Rectangular cavity with probe assembly.

to Eq. (19). A good approximation to this function is given by

$$\gamma(a/r_p)^{\frac{1}{2}}=1.37(a/r_p)^{1.75}. \quad (20)$$

Combining Eqs. (18), (19), and (20) in order to eliminate a/r_p, we obtain

$$i=5.2r_pLJ_r[(\tfrac{3}{2})^{0.714}/(\alpha P)][\phi_p{}^2/(N_r\rho)]^{0.286}, \quad (21)$$

where P is a dimensionless variable involving the pressure given by

$$P=[er_p/(\mu_+p\alpha)](kT_+M)^{-\frac{1}{2}}.$$

(e) Summary.

The previous discussion was divided into a consideration of four regions, based on the number of collisions an ion makes in the sheath. The number of collisions in the sheath depends on pressure and sheath size, which in turn is a function of ion density and probe voltage. Figure 1 relates the number of collisions in the sheath to the experimental parameters. The variables used are the normalized density N, the normalized probe voltage ϕ_p, and the normalized mean free path l/r_p, where l is the mean free path. The two sheets shown in Fig. 1 are surfaces of one and ten collisions, respectively. The surfaces thus divide space into three regions. Above the top surface we use the theory of Sec. III(a). The top surface is the region of applicability of the theory discussed under III(b). In the region between the two surfaces, ions make few collisions in the sheath, and the discussion of Sec. III(c) is applicable. Below the lower surface, ions make many collisions in the sheath and we use mobility controlled theory [Sec. III(d)]. Thus Fig. 1 indicates which equation should be used for evaluating probe data once the experimental conditions are known.

In constructing the two surfaces, use was made of Eq. (13). The condition of one collision in the sheath is $(a/r_p)-1=(l/r_p)$; substituting for a/r_p from Eq. (13) and rearranging, we have

$$\phi_p{}^{\frac{1}{2}}=3.3N[(l/r_p)+1]^{2.37}.$$

Similarly, the condition for ten collisions in the sheath is

$$\phi_p{}^{\frac{1}{2}}=3.3N[(10l/r_p)+1]^{2.37}.$$

IV. APPARATUS

Microwave techniques provide a tool for measuring electron densities in plasmas.[8] The electron density is proportional to the shift in resonant frequency of a cavity in which a discharge is maintained. In order to compare density measurements by the positive ion saturation of probes with those by microwave methods, the rectangular cavity shown in Fig. 2 was constructed. This is a vacuum-tight cavity, made of oxygen-free copper. It can be excited by microwaves in two modes with the electric fields perpendicular to each other. The resonant wavelength of the two TE_{110} modes are 9.88 centimeters and 10.57 centimeters, respectively.

Two tungsten probes, 0.005 inch in diameter, beaded with glass except for the tips, which are 4 mm long, were inserted in the center of the cavity, perpendicular to the electric fields of the two modes. The probes did not disturb the microwave behavior of the cavity.

Figure 3 shows a block diagram of the microwave circuits. A continuous-wave magnetron used for maintaining a steady gas discharge supplies about 10 watts to the cavity. The measuring section is used for rapid determinations of the shift in resonant frequency of the cavity when a discharge is maintained. A low-level, frequency-modulated signal from a klystron is coupled into the cavity and transmitted through it. It is picked up by a small coupling probe and connected to one input of the oscilloscope. The oscilloscope has two independent inputs to a differential amplifier. A portion of the signal from the klystron is transmitted through a calibrated wavemeter and a crystal and connected to the other input of the oscilloscope. Since the Q of the wave meter is much higher than that of the cavity, the signal transmitted through the wave meter will appear as a sharp spike on the oscilloscope; the signal transmitted through the cavity appears as a broad Q-curve. When the spike is superimposed on the maximum of the Q-curve by tuning the calibrated wave meter, the resonant frequency of the cavity can be read on the wave meter. Probe curves were taken with a Leeds and

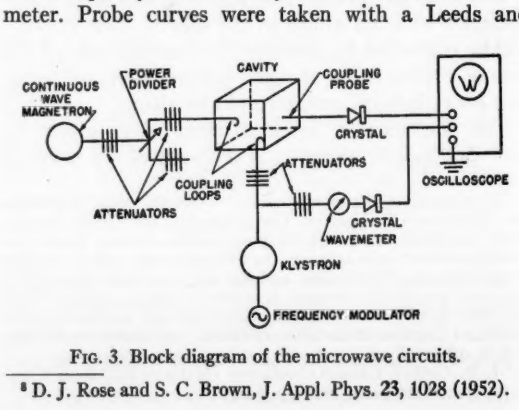

FIG. 3. Block diagram of the microwave circuits.

[8] D. J. Rose and S. C. Brown, J. Appl. Phys. 23, 1028 (1952).

Northrup X-Y recorder which automatically plots the probe current against probe voltage.

The cavity with the probe structure could be evacuated and baked at 400°C and the ultimate vacuum was 1×10^{-9} mm Hg. Bottled Airco gases were used. Experiments were performed in hydrogen, argon, and helium in the pressure range from 0.05 mm Hg to 6 mm Hg.

V. RESULTS

Since two probes are inserted into the plasma, the probe voltage could be applied either between cavity wall and one of the probes (single-probe operation) or between the two probes (double-probe operation). When a single probe is operated in the positive ion saturation region the probe curve is identical with the double-probe curve except that the voltage scale is shifted because of the different voltage reference point. Thus

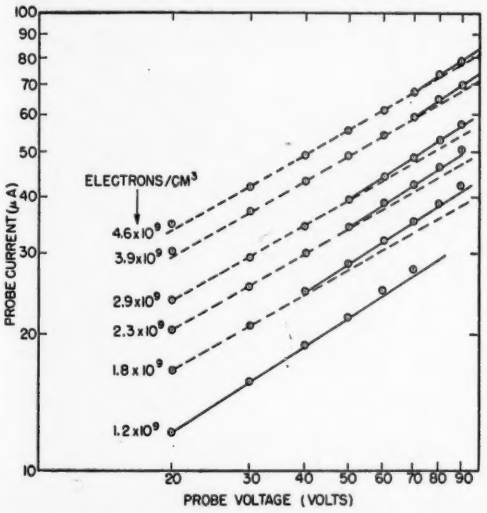

FIG. 4. Positive ion saturated probe current *vs* probe voltage in hydrogen, for several values of density, at a pressure of 0.055 mm Hg. Solid lines have a slope of 0.63; dashed lines have a slope of 0.55. The points are experimental.

it is unnecessary to differentiate between these two cases in the subsequent discussion. When the plasma-to-probe potential is needed for evaluating the probe curves, it is advantageous to use double probes. When one of the probes is operated well in the positive ion saturation region, the potential of the other probe will be close to plasma potential.[9]

In general, probe curves in hydrogen, argon, and helium were found to be reproducible. As an example of the results, the data for hydrogen will be presented.

Zero-to-One Collision in the Sheath.—We have shown that the current reaching the probe is proportional to $n^{0.8}V_p^{0.55}$ when no collisions occur in the sheath, and to $n^{0.58}V_p^{0.63}$ when one collision occurs in the sheath. These relationships were experimentally demonstrated

[9] E. O. Johnson and L. Malter, Phys. Rev. **80**, 58 (1950).

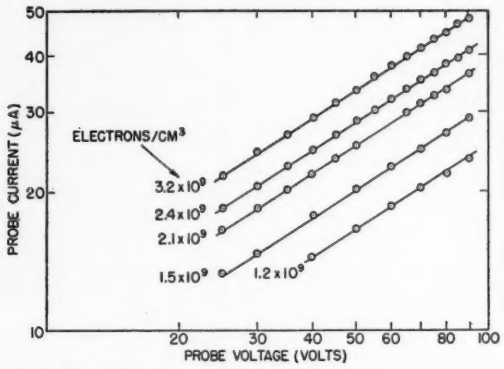

FIG. 5. Positive ion saturated probe current as a function of probe voltage in hydrogen at a pressure of 0.45 mm Hg. The lines have a slope of 0.63. The points are experimental.

by taking probe curves at specified pressures and densities as measured by the microwave measuring signal. The exponents on V_p are shown by the slope of the plot of i *vs* V_p in Figs. 4 and 5; the exponents on n are shown in Fig. 6.

Figure 4 shows a plot of the saturated positive ion probe current *vs* probe voltage at a pressure of 0.055 mm Hg. The top curve of this figure, for the highest density, has a slope of 0.55 over most of the region indicated, which is in good agreement with the theory of orbital motion. As the magnitude of the probe voltage is increased, the sheath expands and there is a greater probability for collision in the sheath. On the average, as soon as one collision occurs in the sheath, ions will stop describing orbital motion; this is evidenced by the change in slope in Fig. 4. The slope changes to 0.63 at higher voltages. The arrows mark the region where the slope changes. With decreasing

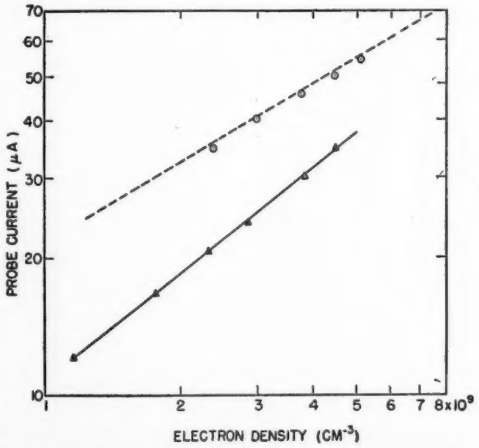

FIG. 6. Positive ion saturated probe current *vs* electron density in hydrogen. The solid line has a slope of 0.76; the dashed line is theoretical for one collision in the sheath. Experimental points: ⊙—one collision in the sheath (pressure=0.1 mm Hg, probe voltage=50 volts); △—no collisions in the sheath.

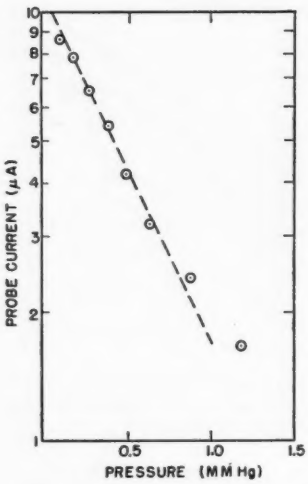

FIG. 7. Positive ion saturation current as a function of pressure at constant electron density and probe voltage in hydrogen. The slope of the dotted line is $\frac{1}{2}\alpha=2.2$.

density, and thus increasing sheath size, the arrows move to the left of the i against V_p plot, because less additional expansion of the sheath is required by the voltage.

As the pressure is increased, no orbital motion will take place at any density or voltage because collisions will always occur in the sheath. This is shown in Fig. 5. The slope of the i *vs* V_p curves is 0.63, as predicted by the theory for nonorbital motion.

Inserting the experimental parameters into Eq. (14) [$T_-\approx 25\,000°\text{K}$], the equation for nonorbital motion of molecular hydrogen ions becomes, in mks units,

$$i=3.6\times10^{-15}n_0^{0.58}V_p^{0.63}. \tag{22}$$

Figure 6 is a plot of i *vs* n. The encircled points show that both the exponent on n and the absolute value of Eq. (22) are in good agreement with experiment. The bottom curve on the same figure shows that the slope

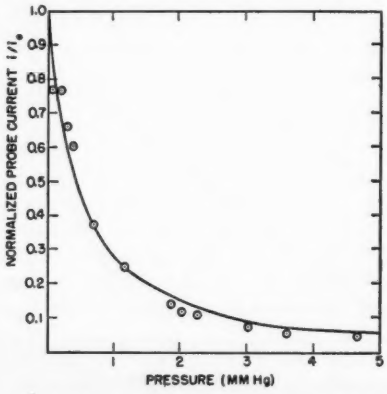

FIG. 8. Normalized positive ion probe current as a function of pressure at constant electron density and probe voltage in hydrogen. The probe current, i, is normalized to the extrapolated current, i_0, at zero pressure. The solid line is theoretical, with $\alpha=4.4$; the points are experimental.

of the i *vs* n curve in the region where no collisions occur in the sheath is 0.76, which should be compared with the theoretical value of 0.8. No significance is attached to this discrepancy.

Few Collisions in the Sheath.—In order to compare the theory of the transition range with experiment it is necessary to know the coefficient α. Equation (17) suggests that it can be evaluated from a semilogarithmic plot of i *vs* p at constant density and probe voltage. The slope of the ln$i$ *vs* p plot at low pressures is equal to $\frac{1}{2}\alpha$. This experiment is easily performed. The electron density in the cavity is kept constant by changing the microwave power incident on the cavity while the pressure is changed. As before, the electron density is monitored by the microwave measuring mode. Figure 7 shows a plot of i *vs* p, from which $\alpha=4.4$. The points at pressures below those shown in Fig. 7 must be dis-

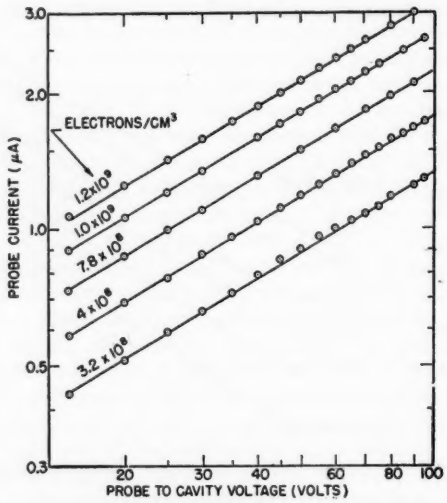

FIG. 9. Positive ion probe current *vs* probe voltage at a pressure of 3.0 mm Hg in hydrogen. The solid lines have a slope of 0.57.

carded, since orbital motion decreases the current collected by probes at these pressures. Therefore, the slope cannot be evaluated at zero pressure and the value of α may be in error by as much as 20 percent. Figure 8 is a comparison of the theory given in Eq. (16), using the value for α just determined, with experiment. The agreement between theory and experiment is better than would be expected.

Many Collisions in the Sheath.—When the experimental parameters are substituted into Eq. (21), we obtain

$$ip=1.3\times10^{-17}n_0^{0.71}V_p^{0.57}3/2\alpha. \tag{23}$$

As before, we shall verify the exponents of this equation. Figure 9 is a plot of i *vs* V_p on a log-log scale for various electron densities at constant pressure. The theoretical and experimental slopes agree. Figure 10 is a plot of (ip) *vs* n on a log-log scale. The slope of the experimental

points is 0.71 as predicted by theory and (ip) seems to be the proper parameter. The dotted line is a plot of Eq. (23). The absolute value of Eq. (23) is too low by a factor of 2. It may be that even at these high pressures the ions reaching the sheath edge have a small directed energy and thus cause the large current observed experimentally.

Experiments in argon show the same behavior as in hydrogen. In helium, the positive ion current collected by the probe is higher than predicted by the theories presented: at low pressure, by a factor of 2; at high pressures, by a factor of 4. This discrepancy is attributed to the liberation of electrons at the probe surface by metastable atoms. (The departure of an electron from the probe cannot be distinguished from the arrival of a positive ion at the probe.) The slope of the curves on

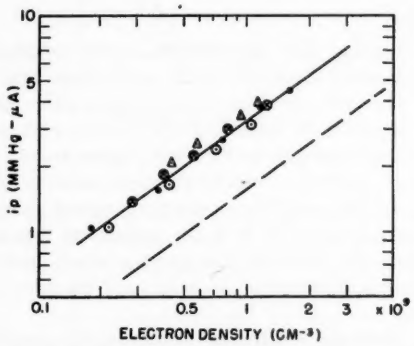

FIG. 10. Positive ion saturated probe current multiplied by pressure, as a function of electron density at constant probe voltage in hydrogen. The solid line has a slope of 0.71, the dashed line is the high-pressure theory. The experimental points were taken at the following pressures:

△—p=2.77 mm Hg; ⊗—p=3.58 mm Hg;
●—p=4.65 mm Hg; ⊙—p=5.95 mm Hg.

the i against V plot in helium checks the theoretical values both at low and high pressures.

VI. RATIO OF ELECTRON SATURATION CURRENT TO POSITIVE ION SATURATION CURRENT FOR SINGLE PROBES

Another test of the correctness of the expression for the current density arriving at the sheath edge derived in Sec. II, namely, that $J_d=n_0e(kT_-/\epsilon M)^{\frac{1}{2}}$ at the sheath edge, comes from the consideration of the ratio J_-/J_+ for single probes. J_- is the electron saturation current density and J_+ is the positive ion saturation current density. The simple Langmuir theory gives the following expression for J_-/J_+:

$$J_-/J_+=(T_-M/T_+m)^{\frac{1}{2}}, \tag{24}$$

where m is the mass of an electron. Many experimenters have reported that the ratio J_-/J_+ is much smaller than predicted by Eq. (24).[2,9] The theory derived here gives the ratio

$$J_-/J_+=J_-/J_d=[\epsilon M/(2\pi m)]^{\frac{1}{2}}, \tag{25}$$

where ϵ is the base of the natural logarithm. The ratio of electron to positive ion saturation currents expressed by Eqs. (24) and (25) is compared with two recent experimental[2,10] observations (using single probes) in Table I.

TABLE I. Ratio of electron to positive ion saturation currents.

Gas	Langmuir ratio	Experimental ratio	New ratio	Electron temperature
Hg	5000	200–400 (Howe)	390	23 000°K
A	3100	110–250 (Boyd)	180	45 000°K

VII. CONCLUSIONS

The current collected by a negatively biased probe or a double probe derived from theory checks with microwave determinations in the pressure range from 0.05 mm Hg to 6 mm Hg. Good agreement is obtained at low pressures; at high pressures the probe collected about twice the current predicted by the theory. The positive ion saturation of single and double probes can be used for evaluating plasma densities within a factor of 2 up to pressures of 6 mm Hg. The upper pressure limit for the usefulness of probes was not found.

ACKNOWLEDGMENTS

The authors wish to thank Professor W. P. Allis for many helpful suggestions.

[10] R. M. Howe, J. Appl. Phys. **24**, 881 (1953).

Field Measurements in Glow Discharges with a Refined Electron Beam Probe and Automatic Recording*

ROGER WARREN†
Department of Physics, University of California, Berkeley, California
(Received January 21, 1955)

By using a very sensitive and fully automatic magnetically compensated electron beam probe, the design of which is described elsewhere, studies were made of the fields in glow discharges some 40 cm long in a tube 10 cm in diameter with aluminum and copper cathodes at from 0.03 to 1.0 mm Hg pressure with currents ranging from 0.1 to 10 ma in flowing air, nitrogen, hydrogen, helium, and argon which were pure to 99.5 percent, but contaminated by vapors from various stopcock greases, waxes, and clean, but not outgassed, metals. Simultaneously, wall potentials and luminosities of the glows were measured and spectra of the cogent parts of the discharges were observed. Emphasis centered on the fields in the Crooke's dark space for discharge currents ranging upwards from the normal cathode fall region. Some stationary striations were also studied. The high resolving power obtained resulted in details of the dark space fields hitherto unrecognized which are amenable to theoretical interpretations to be given in a subsequent paper. Only the observed results are reported here.

INTRODUCTION AND DESCRIPTION OF THE GLOW DISCHARGES INVESTIGATED

THE development of an automatic field measuring device, described elsewhere,[1] enabled clear-cut and detailed determinations of the fields in glow discharges to be made in such small time intervals that discharge conditions did not change. The consistent and reproducible field strength *versus* position curves over ranges of current and pressure, show characteristic and uniform trends differing radically from the roughly linear variation with position previously reported by Aston,[2] Harris,[3] Geddes,[4] Stein,[5] and Little and von Engel.[6] The field curves for different gases differ mainly in the approximate values of the pressures at which evolutionary changes in the field curves occur. This uniformity enables a considerable consolidation of the data by certain reductions presenting curves amenable to theoretical analysis. It is the purpose of this paper to present the data for the gases studied, reserving theoretical interpretation, in so far as it has gone, for a later paper.

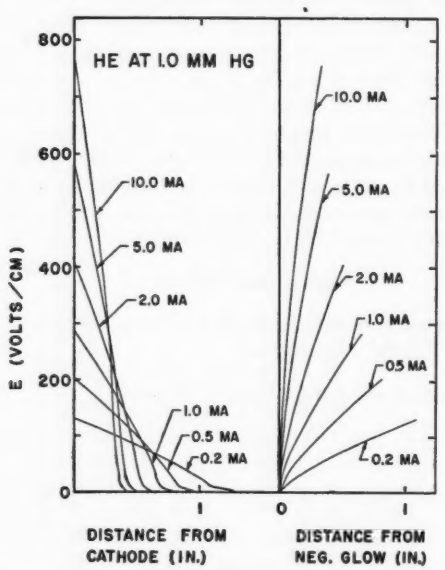

FIG. 1. Cathode fields in helium at a pressure of 1.0 mm Hg.

The discharge electrodes, normally of aluminum, were 40 cm apart, and had a diameter of 10 cm. The probing electron beam could measure fields ranging from 1000 or more volts per cm down to some 0.2 volt per cm. The beam could traverse the total length of the discharge in 40 minutes and the high-field cathode region in a small fraction of this time, the measured axial fields being automatically recorded on a chart together with the wall potentials determined at the same point.

All of the gases used, except air, namely, He, H_2, N_2, and A, were taken from metal cylinders. The indicated impurity content of these gases was less than one-half of one percent. The air was room air, dried and filtered. The gases were passed through a needle valve and then a liquid nitrogen trap before entering the discharge tube. A mercury diffusion pump continually exhausted the discharge tube through another liquid nitrogen trap, so that relatively clean dry gas was continually flowing through the tube. No attempt was made to use purer gases because of the unavoidable presence in the discharge tube of small amounts of vapor from rubber gaskets, sealing waxes, and greases. In the present tube

* This work was supported in part by the National Science Foundation, but in a far greater measure by the Office of Naval Research.
† Currently at the Westinghouse Research Laboratory, East Pittsburgh, Pennsylvania.
[1] R. W. Warren, Rev. Sci. Instr. (to be published).
[2] F. W. Aston, Proc. Roy. Soc. (London) A84, 526 (1911).
[3] T. Harris, Phil. Mag. 29, 192 (1915).
[4] A. E. M. Geddes, Proc. Roy. Soc. Edinburgh 46, 136 (1926).
[5] R. P. Stein, Phys. Rev. 89, 134 (1953).
[6] P. F. Little and A. von Engel, Proc. Roy. Soc. (London) A224, 209 (1954).

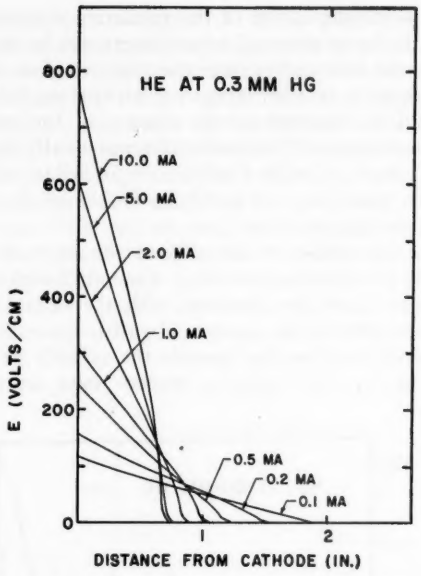

FIG. 2. Cathode fields in helium at a pressure of 0.3 mm Hg.

design, such sealing agents were essential to permit the movement of the electrodes. It is possible that, with great complexity and difficulty, a tube could be constructed using cleaner techniques involving sylphon bellows. Such an improvement, however, would come at a sacrifice of tube length and range of discharge variables effectively nullifying the objectives of this study.

The pressures investigated ranged from 0.03 to 1.0 mm Hg, the exact range depending upon the gas. The discharge power supply was limited to a maximum potential of 2000 volts and/or a maximum current of 10 ma. When decreasing the current from a high value the potential fell, since the discharge was then in the abnormal glow discharge region. Eventually the current reached the threshold value for the normal discharge after which the potential remained constant while the current decreased through a decrease in the diameter of the glow on the cathode, the current density remaining constant. Since field measurements made when the diameter of the discharge is materially less than that of the electrodes, lose their significance, measurements with this technique were carried out only from well into the abnormal region down to the threshold of the normal region, or else at the very lowest, to currents of 0.1 ma. Below currents of 0.1 ma, various difficulties were encountered including among others the gradual accumulation of carbon deposits on the cathode from decomposition of traces of stopcock grease.

It was impossible to measure fields in discharges run at pressures greater than 1.0 mm Hg or so since the spreading of the electron beam became too great. Smaller tube diameters and higher beam energies would permit measurements at higher pressures, but were not of interest in this study. The lower pressure limit corresponded to that pressure for which the tube would barely breakdown under the highest potentials available. The upper and lower pressure limits always differed by a factor of approximately ten. In consequence, when fields near the cathode were measured in this work, each gas was studied at three different pressures. The high pressure value chosen was close to the upper limit; the low pressure value chosen was one tenth of the high pressure, and close to the lower limit, while the intermediate pressure was about half way between. At each pressure, measurements were taken for currents of 10, 5, 2, 1, 0.5, 0.2, and 0.1 ma to the extent allowed by the other conditions of the measurements. In the data presented, all of the curves of field values at different positions taken at a given pressure and various currents were plotted on the same graph.

Results of Field Measurements Near the Cathode

The results of the measurements near the cathode in helium are shown in Figs. 1, 2, and 3. Owing to the newly discovered and revealing sharp downward bend observed in the field curves at the edge of the negative glow, it was found desirable, both in comparing the various curves and in relating the curves to theories to be presented in a later paper, to replot the measured field curves as a function of the distance from the cathode edge of the negative glow instead of the distance from the cathode, as is usually done. The measured fields under the better operating conditions usually dropped fairly sharply to zero near the cathode edge of the negative glow, thus establishing a basic

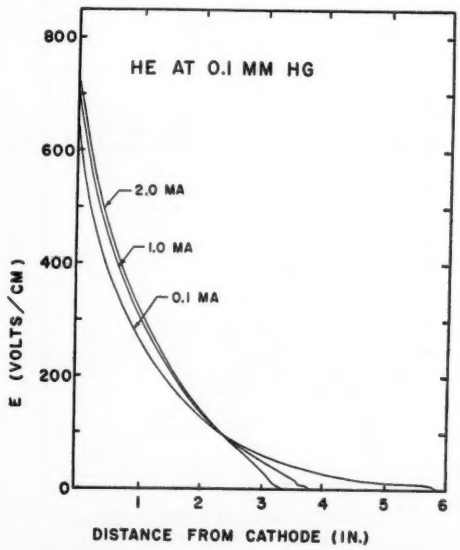

FIG. 3. Cathode fields in helium at a pressure of 0.1 mm Hg.

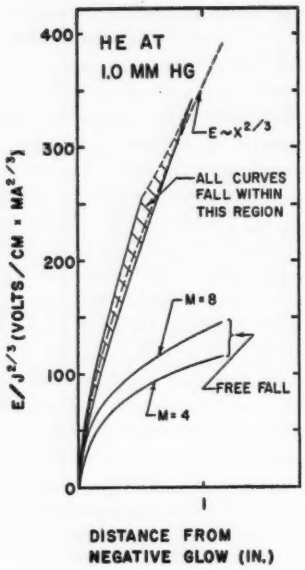

FIG. 4. Replotted cathode fields in helium at a pressure of 1.0 mm Hg.

trend. Since the edge of the glow was not always visually sharp and since the glow curved across the tube diameter, the fields observed did not always fall sharply all the way to zero. In these cases, the curves underwent an inflection near the axis, finally reaching zero more nearly asymptotically. It was assumed that the asymptotic approach of the fields to zero was caused by the averaging action of the measuring equipment and/or discharge effects of minor importance. In consequence, the field curves near the negative glow were extrapolated to zero following their initial sharp decline as would be expected in the absence of the minor disturbances noted. The modification was usually slight. Figure 1 shows a family of field curves for helium before and after replotting and modifying for the worst case, that at the high pressure.

Once the decline of the field at the edge of the negative glow was discovered, it was anticipated that the curves could be correlated with the form to be expected owing to the creation of an ion space charge by positive ions moving towards the cathode with a drift velocity. By applying modern data on drift velocities appropriate to the fields observed, a relationship between the field and ion current could be inferred. Thus, in addition to replotting as a function of the distance from the negative glow, each field curve was reduced in amplitude by the factor $J^{\frac{1}{3}}$, where J is the total discharge current in ma. Figures 4, 5, and 6, thus, contain curves of $E/J^{\frac{1}{3}}$ plotted against the distance from the negative glow and derived from the direct measurements obtained for helium, while Figs. 7 through 15 contain similar curves derived from the direct measurements obtained for all of the other gases except air. The field measurements in air are not given since in all cases the results are almost identical with those in nitrogen. The replotted and reduced field curves in a gas at a given pressure are often so similar that difficulty is found in reproducing them all clearly.

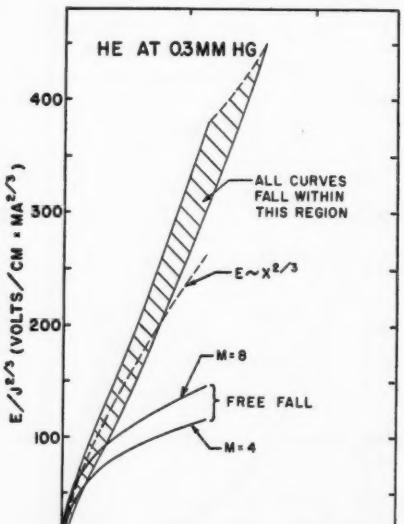

FIG. 5. Replotted cathode fields in helium at a pressure of 0.3 mm Hg.

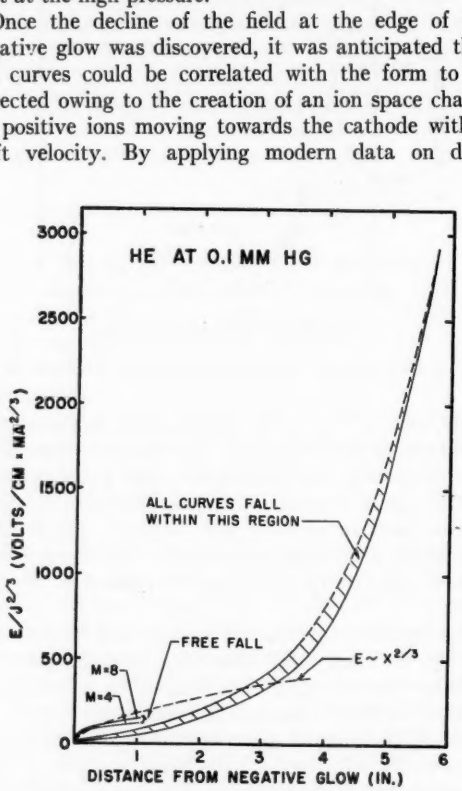

FIG. 6. Replotted cathode fields in helium at a pressure of 0.1 mm Hg.

In these cases, a restricted region is outlined on the graphs within which every curve falls.

To reverse the aforementioned procedure and derive the original field measurements from the data of Figs. 4 through 15, each curve need be only multiplied by $J^{\frac{1}{3}}$ where J is the total tube current for which the field is desired. The lengths of the reconstructed field curves are unknown, but since the length is such a strong function of the cathode condition and since the cathode condition changed for different currents and pressures, the lengths originally measured had little significance, therefore no valuable information has been lost. Additional curves on Figs. 1 through 15 labeled "free fall" and "$E \sim X^{\frac{1}{3}}$" refer to theoretical treatments presented in a later paper.

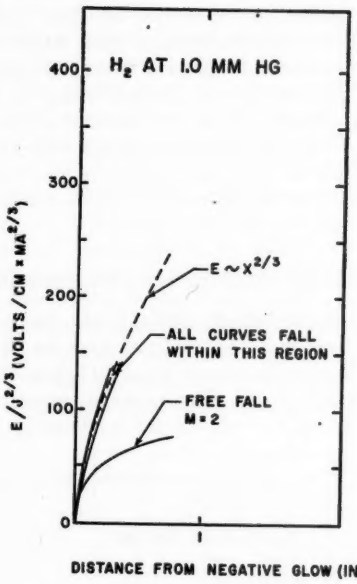

FIG. 7. Replotted cathode fields in hydrogen at a pressure of 1.0 mm Hg.

Accuracy and Significance of the Data

(1) Integration of the fields over the length of the discharge furnishes a very sensitive test of the accuracy of measurement since small errors in the extensive low-field regions could cause serious deviations from the applied potentials. Enough measurements were made to show that these errors were of the order of 2 percent. From this observation, from the fact that the magnetic field had little or not visible effect upon the cathode region of the discharge, and from a discussion given in the paper concerned with the measuring technique, it is concluded that the disturbing effect of the magnetic field upon the discharge was negligible. This is, of course, very important, for in spite of the great advantages of the compensating technique, it would be worthless if the compensating magnetic field

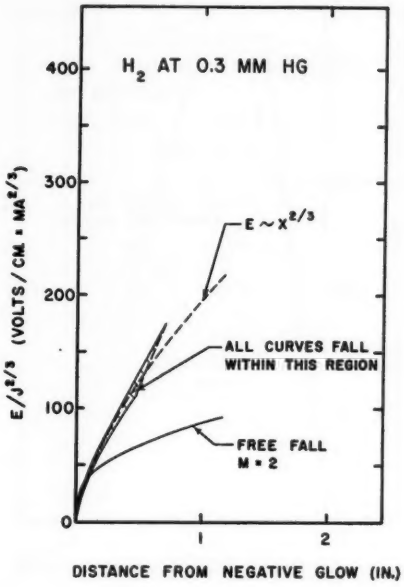

FIG. 8. Replotted cathode fields in hydrogen at a pressure of 0.3 mm Hg.

radically changed the electric field that it was being used to measure.

(2) It must always be remembered that the fields measured by the electron-beam probe are axial fields averaged across the diameter of the discharge tube. To investigate the variation of the axial field along a tube diameter, measurements were simultaneously made of

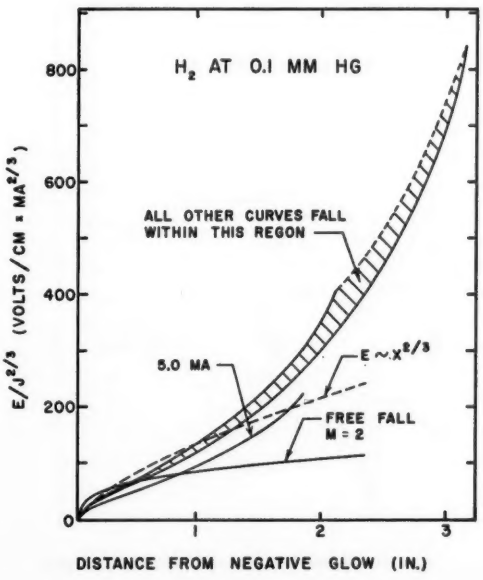

FIG. 9. Replotted cathode fields in hydrogen at a pressure of 0.1 mm Hg.

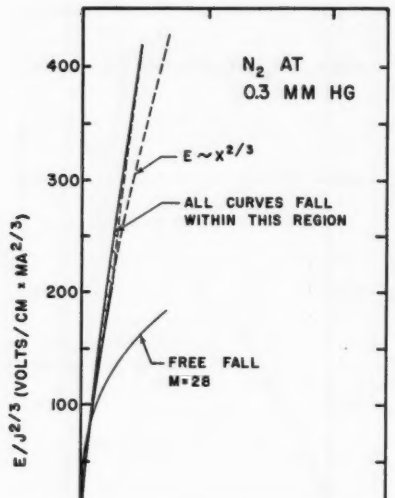

FIG. 10. Replotted cathode fields in nitrogen at a pressure of 0.3 mm Hg.

the potential of the walls of the discharge tube and the average electric field across a diameter. The field curve was then integrated, yielding an average potential curve. These curves are shown in Fig. 16. It can be seen that the wall field and wall potential are 20 percent or so less than the average field and average potential except near the cathode. Such is the case at most pressures and currents for all of the gases investigated. Because of this, the average field measured by the electron beam is not truly representative of the discharge alone, but also of the presence of the walls, unless the effect of the walls is confined to a small region of the discharge in the immediate vicinity of the walls. From observations of the variation of the light intensity in the tube across a diameter and through arguments involving the mechanics of the motion of the positive ions and electrons in the tube, it is believed that at high pressures, the wall field penetrates only a short distance into the discharge so that the measured average field is very nearly equal to the actual field at most points along a diameter of the tube. At low pressures, however, it appears that the wall field penetrates well into the tube so that near the negative glow, the field along the axis of the tube is about 10 percent higher than the average field, while near the cathode, it is about 10 percent lower. In most cases, therefore, the variation of the field along the path of the electron beam (due to the presence of the walls), is much greater than any errors introduced in measuring the field, and is, thus, more likely to affect the field measurements in such a way as to defeat attempts at interpretation.

Light Intensity Measurements Near the Cathode

In order to supplement the field data, measurements have also been made of the light intensity at various positions in the discharges. Figure 17 is an example, where enough of the simultaneously-measured field curves is shown to indicate the relationship between

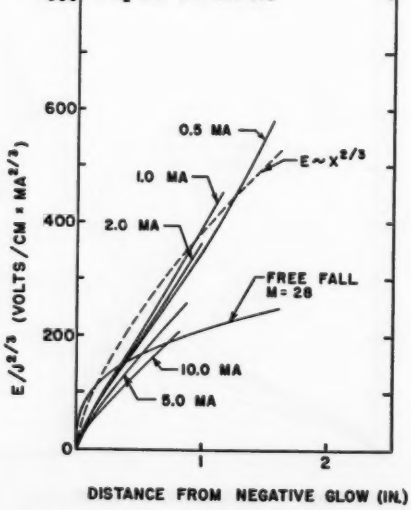

FIG. 11. Replotted cathode fields in nitrogen at a pressure of 0.1 mm Hg.

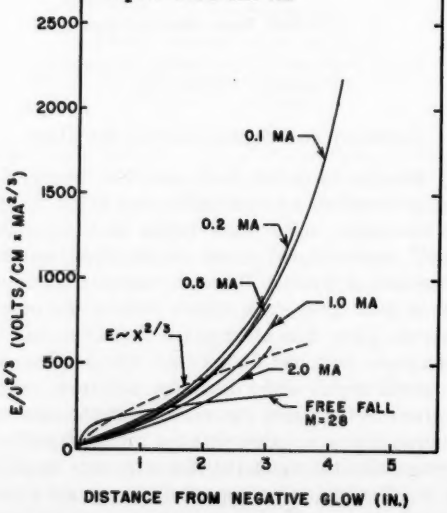

FIG. 12. Replotted cathode fields in nitrogen at a pressure of 0.03 mm Hg.

the position of the light maxima and the field minima. The exact shape of the intensity curves very near the cathode is determined by instrumental considerations. The numbers, 1 to 5, on the curves indicate discharge currents of 5 to 0.2 ma in that order. The light intensity peaks near the field minima are caused by excitation by electron impact, while the peaks near the cathode are probably to be ascribed to excitation by high-energy positive ions and neutral particles. This last conclusion is reached through a study of the light intensity curves, a study of spectra of the light emitted from the cathode region, and investigations of the light emitted from the canal rays using a pierced cathode. It should be noticed that the intensity peak at the cathode rises very rapidly as the tube current and, thus, the tube potential is increased.

It will be noticed that the segments of the field curves shown in Fig. 17 do not coincide with the field curves in nitrogen shown in Fig. 12. This results from the very marked changes in the characteristics of the cathode surface which occurred from time to time. For under operating conditions the cathodes inevitably had surfaces that were soiled to varying and changing degrees. Thus, undoubtedly, they were initially oxidized, but as time progressed they were somewhat cleaned by ion bombardment. In addition, especially at high discharge potentials, some of the hydrocarbon vapors, unavoidably present in the tube, were decomposed and visible deposits of carbon sometimes appeared on the cathode. During the short time for the measurement of a single field curve, however, the cathode characteristics were constant. However, as soon as the pressure or current was varied a considerable time had to elapse before the cathode characteristics settled down to new values so that more field measurements could be made.

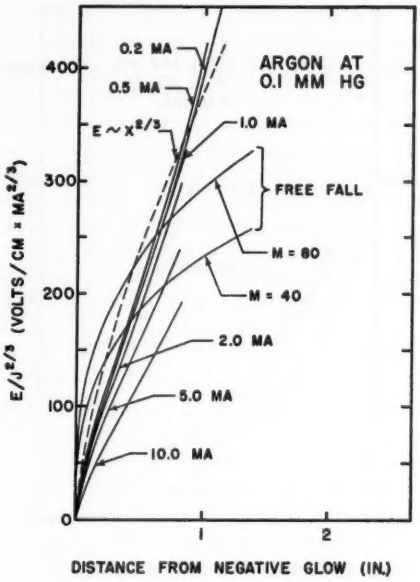

FIG. 14. Replotted cathode fields in argon at a pressure of 0.1 mm Hg.

The only reason that the families of curves in Figs. 1 to 15 appear as regular as they do, is that all of the curves in a family were taken on the same day in a

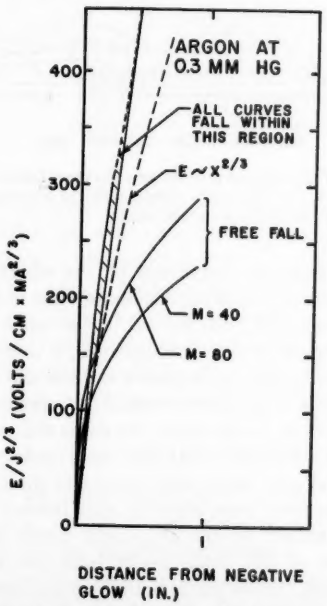

FIG. 13. Replotted cathode fields in argon at a pressure of 0.3 mm Hg.

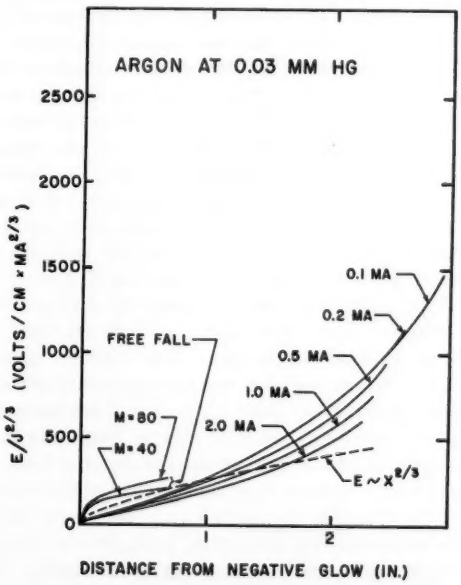

FIG. 15. Replotted cathode fields in argon at a pressure of 0.03 mm Hg.

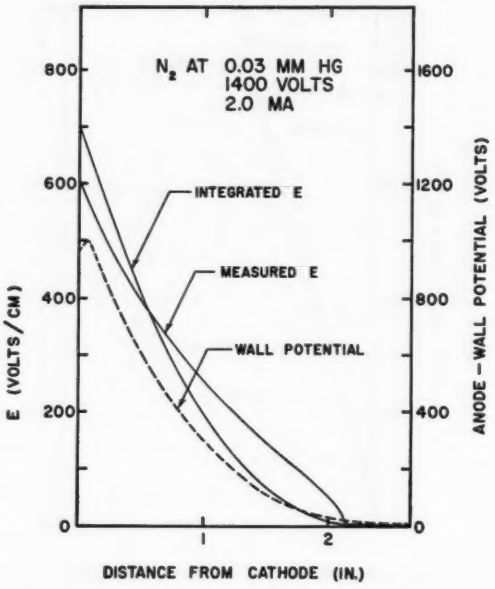

FIG. 16. The wall potential and average field in nitrogen.

systematic order (in order of decreasing current), so that the characteristics of the cathode surface also varied in some systematic way. If, after the last field measurement (lowest current) in a certain family of curves was taken, the first one (highest current) was repeated, a fair approximation to the original parameters could be achieved. However, if the discharges were then returned directly to the lowest current, it was impossible to repeat the same parameters. Apparently the high current discharges partly cleaned the cathode surface while the low current discharges did not, so that the past history of the cathode surface was very important in determining its characteristics for low currents, but not so much for high currents.

A further investigation of the effect of the cathode surface upon field measurements was made by operating discharges in a given gas at fixed pressures and current densities, but with different cathode materials and, necessarily, different discharge potentials and cathode-negative glow separations. It was found that if the measured fields were plotted against the distance from the negative glow, and not the distance from the cathode, all field curves taken with different cathode surfaces but identical pressures and currents were superimposed, even though some curves would extend further from the negative glow than others. Thus, the shape of the curves of the field *versus* the distance from the negative glow appears to be independent of the cathode characteristics. On the other hand, the length of this curve is determined, in part at least, by the cathode condition as is well known from other studies. This interesting observation will be discussed and interpreted in the following paper.

Field Measurements in Striations

Figure 18 is a reproduction of an actual field measurement of striations in nitrogen at a pressure of 0.3 mm Hg, a potential of 525 volts, and a current of 5.0 ma. The graph looks complicated because it actually consists of four separate curves. The recorder was at this time connected to measure alternately the average field and the wall potential. The vertical lines on the graph represent the recorder's transition from measuring one variable as a function of position to measuring the other.

Thus, starting on the left side of the tracing, fields and wall potentials were alternately measured near the aluminum anode with the measuring beam steadily moving closer to the aluminum cathode. At the center

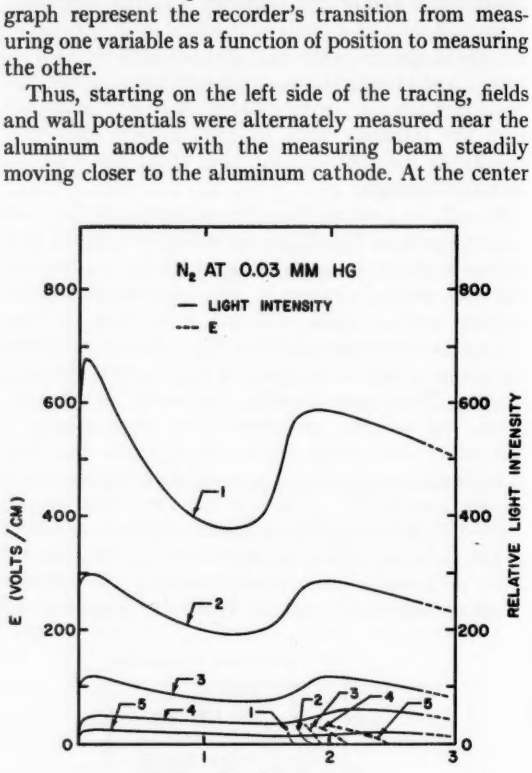

FIG. 17. The light intensities and average fields in nitrogen. The numbers, 1 to 5, on the curves indicate discharge currents of 5, 2, 1, 0.5, and 0.2 ma in that order.

of the tracing the potentials of the electrodes were reversed so that the old anode became the new cathode, but the electrodes still moved in the same direction. Because the electrodes were identical, it was possible to reverse their polarities in such a fashion and still retain the same discharge parameters. Thus, from the center of the graph on to the right, the fields that were measured were negative, and the wall potentials were returning to low values with respect to the anode.

Measurements were made in this fashion to permit a determination of the zero field condition, for an integration of the fields under both the direct and reversed field curves yields both a correct zero field and a correct potential drop per striation. In the case shown, the potential drop per striation was found by integration

to be 33.6 volts, while the potential drop per striation determined from the wall potential curves was 33.5 volts. This excellent agreement is fortuitous. However, within the precision of these measurements, the potential drop per striation appeared constant for each gas over the range of currents and pressures for which stable striations could be obtained. Generally also it seems that in inert gases the potential difference between striations was about the ionization potential while in molecular gases it was twice the ionization potential. Measurements were made of field curves under other conditions. In general, it was found that in the negative glow, the fields were from $\frac{1}{8}$ to $\frac{1}{2}$ volt per cm, and in the Faraday dark space, of about the same magnitude, occasionally dropping well below $\frac{1}{4}$ volt per cm. In unstriated positive columns, the fields were from 1 to 2 volts per cm. Since the field curves at the anode could take so many forms, no special study was made of them. These approximate values of the fields may depend greatly upon the gases, pressures, voltages, and, especially, the tube diameter used (since ambipolar diffusion to the walls largely determines the discharge economy there).

Again it must be mentioned that all field measurements are averages taken across a tube diameter. This is especially important in measuring striations, for the wall charges cause them to curve seriously. For example, striations six cm apart in the discharge tube, which is ten cm in diameter, are so curved that the striations at the axis of the tube are 1 to 3 cm closer to the cathode than they are at the walls. This causes no error in the determination of the potential drop per striation, but does give measured maxima and minima fields which are not as extreme as the actual ones. Thomson[7] has reported negative fields in striations and other observers have measured negative fields in the negative glow. None were observed in these measurements, either in the fields of the striations or in fields elsewhere in the discharge.

Field measurements were not taken in the positive column when light, voltage, or current oscillations or moving striations were observed. These phenomena were occasionally present when field measurements were taken in the cathode region of the tube. Visual observation of the fluorescent screen, however, showed no broadening of the spot which would have been expected if oscillating electric fields of any magnitude had penetrated into the cathode region of the discharge.

Spectrographic Observations

Spectrographic investigations of various regions of the discharges in all of the gases have been made. These lead to three general conclusions.

(a) Much of the light emitted from the negative glow and striations in the various gases is emitted from nitrogen impurity molecules. This is especially true for helium where all of the light emitted from the striations comes from the nitrogen impurity. One might have expected this, since the ionization and excitation potentials of nitrogen are so much less than those of helium, and since the positive column in any mixture of gases is characterized by electrons which have energies only high enough to occasionally ionize the constituent with the lowest ionization potential (unless some more involved ionization process occurs). Because of these observations, the characteristic potential per striation observed for each gas is probably not truly characteristic of the gas alone, but of the impurity content also.

(b) Relatively little of the light observed from the cathode glow is emitted by impurity molecules. This is probably because the excitation and ionization here are caused by high-energy positive ions and neutral particles, for high speed particles are likely to ionize and excite mixed gases more nearly in proportion to the concentration of the various constituents.

(c) It is believed that the majority of the ionization by electrons occurring in the negative glow is by fairly high energy electrons that also ionize and excite all gases with approximately equal probabilities. Field measurements taken both with impure helium (99.5 percent pure) and with a much purer helium sample were identical, while spectrographic investigations showed much weaker nitrogen bands and lines for the purer sample. Therefore, it is concluded that the current between the negative glow and the cathode, carried by positive ions formed mainly in the negative glow, is carried largely by ions of the main constituent

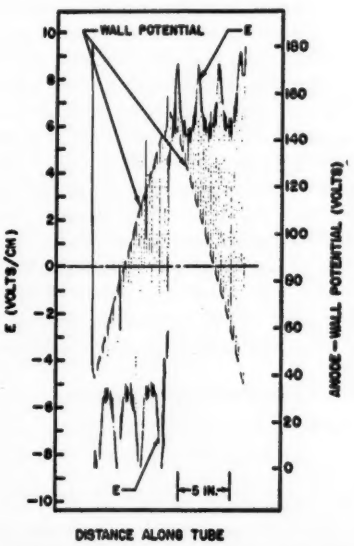

FIG. 18. Typical fields in striations in nitrogen. N_2 at 0.3 mm Hg, 525 volts, and 5.0 ma; 34 volts/striation.

[7] J. J. Thomson, Proc. Cambridge Phil. Soc. 15, 70 (1909).

gas and not by impurity ions. A great deal more work, however, would be necessary to establish this point definitely.

ACKNOWLEDGMENTS

The writer wishes to express his thanks to Professor Leonard B. Loeb, under whose direction this problem was undertaken, for his encouragement and valuable suggestions throughout its prosecution, and especially for his assistance in the presentation of the results. Thanks are also due to C. D. Maunsell and R. G. Westberg for assistance in taking the spectral and light intensity measurements.

PHYSICAL REVIEW VOLUME 98, NUMBER 6 JUNE 15, 1955

Interpretation of Field Measurements in the Cathode Region of Glow Discharges*

ROGER WARREN†
Physics Department, University of California, Berkeley, California
(Received January 24, 1955)

A theory for the cathode region of glow discharges is developed in which the major assumptions are: (a) electron emission from the cathode due to positive ion impact is the dominant secondary mechanism; (b) the probability of ionization by electrons occurring in the high-field cathode region is small, so that electrons carry a negligible portion of the total tube current there; and (c) in this region the positive ions drift towards the cathode with a velocity governed by a mobility law. This theory is found to agree well with measurements in abnormal discharges in various gases at pressures above about 0.1 mm Hg. For lower pressures, measurements indicate that a great number of electrons are present in the cathode-negative glow space, probably due to ionization by high-energy positive ions and molecules; and, that at high enough values of E/p, the application of a mobility theory becomes completely invalid.

GENERAL THEORY

General Mechanism of a Glow Discharge

IT is usually assumed that the dominant mechanisms operating in a glow discharge are the primary one of ionization of gas molecules by high-speed electrons and a secondary one of electron emission from the cathode due to the impact of positive ions. γ_i, the ratio of the electron current emitted from the cathode to the positive ion current striking it, ranges between 0.01 and 0.1. Other secondary mechanisms additional to γ_i but akin to it in action are known to occur in gaseous discharges. Some of these are: (a) photoemission from the cathode due to light coming mainly from the negative glow (Little and von Engel[1] have recently proposed a theory based upon this as the dominant cathode mechanism), (b) emission from the cathode due to the impact of metastable atoms or molecules (especially important in the rare gases), (c) ionization of the gas molecules by photons, excited molecules, and/or positive ions. However, because of the relatively high cathode fields and low pressures which favor large values of γ_i compared to other processes, the γ_i mechanism appears to dominate other secondary actions in glow discharges.

The Economy Condition

It will be assumed that all secondary mechanisms other than γ_i can be ignored. Since a glow discharge is self-sustaining and constant in all of its characteristics assuming that no oscillations exist, a certain economy relationship must hold. Namely, each electron emitted from the cathode must on the average cause just enough ionization so that those positive ions formed which return to the cathode cause just one new electron to be emitted. The economy condition may be written $\gamma_i GF=1$, where F is the total number of new electrons and positive ions formed per original electron and G is that fraction of the positive ions formed which arrive at the cathode. G includes losses of electrons and ions to wall and volume recombination. It may have a wide range of possible values.

The Current Continuity Condition

The sum of the electron and positive ion currents at any point in the tube must be a constant equal to the total tube current. Now, $1/(1+\gamma_i)$ of the tube current *at the cathode* must be carried by positive ions. Since positive ions move much more slowly than electrons of the same energy, the space charge of these positive current carriers will be much greater than that of the electrons and thus the net positive charge will be quite large near the cathode. The electric field necessary to achieve high electron velocities, however, is quite low. Therefore, the field in the discharge tube will fall almost to zero as soon as each emitted electron has formed more than $1/\gamma_i$ new ones by ionization. For when this relationship is satisfied, the electron density is high enough so that the tube current of electrons alone will be too high to satisfy the current continuity condition if some minimum field is exceeded. Therefore, the field

* Supported in part by the Office of Naval Research and the National Science Foundation.
† Now at Westinghouse Research Laboratories, East Pittsburgh, Pennsylvania.
[1] P. F. Little and A. von Engel, Proc. Roy. Soc. (London) A224, 209 (1954).

must be quite low with the consequence that some of the electrons are lost to the walls. This condition of high electron and positive-ion densities and low field occurs throughout the major part of the negative glow and to a lesser extent in the Faraday dark space.[2] At the end of the Faraday dark space and the beginning of the positive column, or first striation, the electron density has, mainly through wall losses, become sufficiently low so that the field needed to support the necessary tube current has risen. Ultimately the field rises sufficiently to give to the electrons an energy suitable for excitation and further ionization. In this way, the dwindling electron density is replenished, either constantly, as in a uniform positive column, or periodically as in striations.[2] The new electrons are themselves ultimately lost to the walls.[2] This outline of the variation with position to be expected in electron and positive ion densities and field values is in essential agreement with the explanations of other authors and most measurements. A few of the more striking agreements between observations and this outline will be given.

The current of positive ions and electrons lost to the walls of a tube for every centimeter of its length is proportional to the density of the positive ions and electrons and to the circumference of the tube. The tube current, however, is proportional to the positive ion and electron density and to the area of the tube. Therefore, for the lowest wall losses per cm of tube length, a large diameter tube is desirable. Now, it is observed that glow discharges in spherical vessels, i.e., very distant walls, are characterized by the absence of a positive column. The Faraday dark space appears to fill almost the whole tube. This is, thus, a rather concrete example of low wall losses in the Faraday dark space making unnecessary a positive column with its action of regeneration of positive ions and electrons.

Other observations show that the field in uniform positive columns, or the number of striations per cm of tube length in striated columns, increases as the tube diameter decreases other things remaining fixed. This can be explained by the higher rate of positive ion and electron production needed to offset the higher wall losses resulting from the decreased tube diameter. This higher production can only occur when the field or the striation density are higher, as observed.

A third example deals with the length of the Faraday dark space in a discharge run with a constant gas pressure but varying tube potentials and currents. Under any conditions, the electron current leaving the cathode is $\gamma_i/(1+\gamma_i)$ of the total tube current I. As will appear later in this report, for high and medium pressures and for abnormal discharges, no appreciable ionization occurs in the cathode region. Thus the electron current of $\gamma_i I/(1+\gamma_i)$ ma flows into the negative glow creating new positive ions and electrons. According to Lehmann[3] and Brewer and Westhaver,[4] the number of new ions and electrons produced in the negative glow is directly proportional to $\gamma_i I/(1+\gamma_i)$ and to the cathode-negative glow potential difference. Only a fraction of these new electrons are needed, however, to carry the tube current. The ratio of the available current to the actual tube current will be roughly proportional to the cathode-negative glow potential difference, assuming that γ_i is approximately constant. Thus, the excess of ions and electrons in the negative glow and Faraday dark space is greater the higher the tube potential and current. Therefore, the higher the potential and current are, the greater is the tube length needed to reduce the ion and electron density to the point where a positive column occurs. In agreement with this argument, the length of the Faraday dark space increases as the tube current and potential are increased.[2]

Thus, the picture of the cathode region is the following. In the negative glow where intense ionization and excitation occur, the tube current is dominantly electron current and the field and net space charge are very low. Near the cathode, the tube current is dominantly positive ion current, and this current contributes a large positive space charge. Between the negative glow and the cathode, the current is partly positive ion and partly electron but the net space charge is positive. Therefore, from Maxwell's law, the field increases steadily from nearly zero at the negative glow to a large value at the cathode.[2] The exact dependence of the field upon position is determined by the location of the ionization and the motion of the positive ions in the cathode region.

The Probable Location of the Ionization in the Cathode Region

From visual and photomultiplier observation of the intensity of the negative glow as a function of position, it is noticed that the part of the negative glow nearest the cathode seems to have a sharp edge, i.e., the intensity rises quite rapidly as the negative glow is approached from the cathode.[2] For most gases the probability for excitation by electron collision as a function of electron energy, especially for optically allowed transitions, is of approximately the same form as the probability for ionization. Therefore, since the amount of excitation appears to increase rapidly at the cathode edge of the negative glow, the amount of ionization should do likewise.

This rather abrupt increase in excitation and ionization can be understood, for most of the electron collisions in the Crooke's dark space and some of them in the negative glow involve electrons which have come directly from the cathode with generally few collisions

[2] R. W. Warren, preceding paper, Phys. Rev. **98**, 1650 (1955).

[3] J. F. Lehmann, Proc. Roy. Soc. (London) **A115**, 624 (1927).

[4] A. K. Brewer and J. W. Westhaver, J. Appl. Phys. **8**, 779 (1937).

and few if any collisions involving large energy loss. Therefore, if an ionizing collision does occur, the kinetic energy of the impacting electron may easily be several hundred electron volts, and thus the new electron will have an energy of about 40 ev and an isotropic velocity distribution. If these new electrons are formed in the high-field cathode region, they will be accelerated by the field and thus gain energy. As a result of this high energy, further collisions are not likely to result in ionization or excitation, and elastic collisions are likely to result in extremely small angular deflections. If, however, the new electrons are formed in the negative glow where the field is low, because of their isotropic velocity distribution, many will move *towards the cathode* and *against the weak field* until the field begins to rise at the cathode edge of the negative glow, where the electrons will be repelled. Since these low energy electrons are experiencing collisions, and since the angular deflections of low energy electrons upon collisions are distributed nearly isotropically, each electron will bounce back and forth in the gas, instead of speeding directly down the axis of the tube as in the Crooke's dark space. It will eventually cause further ionization and excitation at some point in the negative glow up to its cathode edge where the field rises. Since electrons formed by ionization have a distribution of energies, the sharpness of the cathode edge of the negative glow is only approximate. The recent work of Pringle and Farvis[5] on electron energy distributions in the negative glow of glow discharges in helium, as measured with a refined probe, agrees remarkably well with these ideas.

This discussion has demonstrated that a self-consistent explanation can be found for the visual appearance of many glow discharges on the assumption that the ionization in the cathode region is low until it increases abruptly on the cathode side of the negative glow, very near the position in the discharge where the field first approaches zero. This does not rule out the possibility that discharges can occur in which much of the ionization takes place in the central part of the high-field region. One would expect to achieve the greatest possible amount of ionization in this region for discharges operating at the lowest possible voltages and the longest possible cathode-negative glow spacings for a given pressure. Such conditions appear in what is called a normal glow discharge. Observations[2] there show that the cathode edge of the negative glow is visibly much less abrupt for normal discharges than for abnormal ones, indicating the presence of more ionization and excitation well into the Crooke's dark space.

Some rather inconclusive and indirect investigations[3,4,6–8] have been devised to evaluate the amount of ionization by electrons occurring in the cathode fall region. In most cases, it is believed that for discharges at low potentials, from 1 to 10 ionizing events take place between the cathode and the negative glow, while at high potentials, only 0.1 to 1 such event takes place.

An interesting calculation can be made using values of the normal glow discharge potential and data given by Lehmann for the average energy expended by electrons in forming a new electron-positive ion pair. By dividing the first of these by the second, a number F results which equals the maximum value for the average production of positive ions and electrons in the negative glow per incident electron if the electron is assumed to pass from the cathode through the high-field region without ionization. F is about five for most gases and cathode surfaces. Therefore, γ_i must be at least 0.2, and probably considerably more, in order that $\gamma_i GF = 1$. This is a high value for γ_i. Accordingly, in the case of the normal discharge, the assumption that no ionization occurs in the high-field region is probably incorrect. Instead, some electrons are produced there which then gain energy from the field, producing much more total ionization once they reach the negative glow than the same number of electrons all produced in the negative glow.

In developing a theory for the cathode region of an abnormal discharge then, it will be assumed that no appreciable ionization occurs in the cathode region but that instead, all of the production of new electrons and positive ions needed to satisfy the current continuity condition occurs in the negative glow up to a rather abrupt edge on the cathode side of the glow.[2] This edge occurs near the position in the cathode region at which the field has just approached zero.[2] Positive ions formed in the negative glow drift across the edge with low energy. From the edge on to the cathode the tube current must be carried almost entirely by positive ions. The exact form of the field in the cathode-negative glow spacing then depends only upon the law governing the motion of the positive ions. Positive-ion diffusion to the walls in this space can be ignored, for positive ions and electrons must be lost to the walls in equal numbers at all points. Since the electron current is so small, even if it were all lost to the walls with an equal positive-ion current, the fraction of the positive-ion current lost would be negligible.

A complete theoretical solution to the cathode region, giving the cathode-negative glow separation and potential, would involve an exact knowledge of both γ_i and the behavior of the negative glow. Because of ignorance concerning each, a complete solution is not achieved, but instead, a partial solution which predicts the form of the variation of the field with position, pressure and current is possible. This partial solution depends upon the law governing the motion of the positive ions. However, this motion is so complicated that different laws hold in different parts of discharges and for different

[5] D. H. Pringle and W. E. J. Farvis, Phys. Rev. **96**, 536 (1954).
[6] M. J. Druyvesteyn and F. O. Penning, Revs. Modern Phys. **12**, 87 (1940).
[7] P. L. Morton, Phys. Rev. **70**, 358 (1946).
[8] G. W. Johnson, Phys. Rev. **73**, 284 (1948).

operating parameters. It appears, however, that for large portions of many discharges a single law will hold. A theory, therefore, is developed for this case, and for comparison purposes, another theory is developed for the limiting case where the positive ions suffer no collisions in drifting from the negative glow to the cathode.

Various Theories for the Field in the Cathode Region

In an early theory of Ryde,[9] an attempt was made to describe accurately the dependence of the electric field upon position in the cathode region by using the aforementioned general theory with the special assumption that the positive ions move from the negative glow to the cathode without collisions of any kind. Under these conditions, the field in the cathode region can be calculated from a solution of the two equations $\nabla\cdot\mathbf{E}=d^2V/dx^2=4\pi\rho$ and $eV=Mv_+^2/2$. V and x, the potential and the position in the cathode region, are measured from the cathode edge of the negative glow. v_+, the speed of the positive ions of mass M moving towards the cathode is assumed to be zero at the cathode edge of the negative glow. v_-, the speed of the electrons, is always much greater than v_+ even at the cathode. ρ_+ and ρ_- are the positive-ion and electron-charge densities; J_+ and J_- are the positive-ion and electron-current densities; and ρ and J are the total charge and current densities. Now,

$$\rho=\rho_+-\rho_-=\frac{J_+}{v_+}-\frac{J_-}{v_-}=J_+\left(\frac{1}{v_+}-\frac{\gamma_i}{v_-}\right)=\frac{J}{1+\gamma_i}\left[\frac{1}{v_+}-\frac{\gamma_i}{v_-}\right],$$

and since $1/v_+\gg\gamma_i/v_-$,

$$\rho\simeq\frac{J}{(1+\gamma_i)}\frac{1}{v_+}.$$

However, $v_+=(2eV/M)^{\frac{1}{2}}$ so that

$$\frac{d^2V}{dx^2}\simeq\frac{4\pi J}{(1+\gamma_i)}\left(\frac{M}{2eV}\right)^{\frac{1}{2}}.$$

The solution of this last equation is

$$V=\left[\frac{9\pi J}{(1+\gamma_i)}\left(\frac{M}{2e}\right)^{\frac{1}{2}}x^2\right]^{\frac{2}{3}},$$

and

$$E=\left[\frac{8\pi J}{1+\gamma_i}\left(\frac{3Mx}{2e}\right)^{\frac{1}{2}}\right]^{\frac{2}{3}},$$

where the boundary conditions are $E=V=0$ at $x=0$. This will be called the "free fall" solution.

The resulting fields and potentials do not appear to agree with past measurements. It also seems probable that many positive-ion collisions occur in the cathode region since the cathode-negative glow separation corresponds to about thirty ionic mean free paths. Therefore, a more appropriate treatment in which collisions play a dominant role must be used. However, the "free fall" solution yields a useful limit since *under no circumstances can a legitimate solution to Maxwell's equation be found which involves a field versus position curve which falls beneath the "free fall" field curve* as long as $J=(1+\gamma_i)J_+$. This fact is not as obvious as it may at first appear, but may be proven to hold by some rather subtle reasoning involving the relations that the slope of any field curve is inversely proportional to the positive ion velocity at that point (from Maxwell's equation), and $e\int_0^{x'}Edx$ of any field curve must be greater than, or equal to, the energy of the positive ions at $x=x'$.

The recent work of Hornbeck and Wannier,[10] Hornbeck,[11] Hornbeck and Molnar,[12] and Varney[13] shows conclusively that the average velocity of positive ions in gases is determined by collisions with gas molecules, and for field to pressure ratios greater than about one hundred volts per cm-mm Hg, the velocity varies as $(E/p)^{\frac{1}{2}}$, i.e., $v_+=k'(E/p)^{\frac{1}{2}}$, where k' is a constant for each gas called the mobility. The upper limit to the E/p values permitted in these measurements was about 1000 volts cm-mm Hg. By assuming the above dependence to hold for all values of E/p, and using the general theory outlined above, it is possible to show that

$$\frac{dE}{dx}=\frac{4\pi J}{(1+\gamma_i)v_+}=\frac{4\pi Jp^{\frac{1}{2}}}{k'E^{\frac{1}{2}}(1+\gamma_i)}.$$

This has the solution

$$E=\left[\frac{6\pi Jp^{\frac{1}{2}}x}{k'(1+\gamma_i)}\right]^{\frac{2}{3}},$$

where the boundary conditions are $E=V=0$ at $x=0$. According to Wannier,[14] the constant k' is given in most cases by $k'=1.147(ep\lambda_i/M)^{\frac{1}{2}}$, where λ_i is the ionic mean free path which is in general about one third of a molecular mean free path. Thus

$$E=\left[\frac{6\pi Jx}{1.147(1+\gamma_i)}\left(\frac{M}{e\lambda_i}\right)^{\frac{1}{2}}\right]^{\frac{2}{3}}.$$

This is approximately the relationship originally formulated by Weizel, Rompe, and Schoen.[15] It will be called the "mobility" solution.

The "mobility" solution is valid only if enough collisions occur so that the positive ions are in equilibrium or near equilibrium with the impressed field. If the field were instantaneously to increase from a low value to a high one, the positive ions could not have an

[9] J. W. Ryde, Phil. Mag. **45**, 1149 (1923).

[10] J. A. Hornbeck and G. H. Wannier, Phys. Rev. **82**, 458 (1951).

[11] J. A. Hornbeck, Phys. Rev. **80**, 297 (1950); **83**, 374 (1951); **84**, 615 (1951).

[12] J. A. Hornbeck and J. P. Molnar, Phys. Rev. **84**, 621 (1951).

[13] R. N. Varney, Phys. Rev. **88**, 362 (1952); **89**, 708 (1953).

[14] G. H. Wannier, Bell System Tech. J. **32**, 170 (1953).

[15] Weizel, Rompe, and Schoen, Z. Physik **112**, 339 (1939).

average velocity given by $v_+=k'(E/p)^{\frac{1}{2}}$ until they had gained sufficient energy by traveling a distance in the field direction corresponding to a few mean free paths. Thus, if the field changes at a rate of less than about thirty percent per ionic mean free path, the relationship $v_+=k'(E/p)^{\frac{1}{2}}$ is approximately true. Obviously the field gradient far exceeds this rate near the origin, and thus, the solution depending upon the mobility law must be in error there. This failure near the origin is also evident from the behavior of the "mobility" curve of *E versus* position which violates the previous rule by falling beneath the "free fall" curve.

Further investigation shows that the failure of the simple "mobility" theory occurs for only a small fraction of the total cathode-negative glow spacing—that same fraction for which several other approximations of these simple theories also become invalid. Rough calculations indicate that the effects of the different approximations tend to cancel and that, in any case, the error introduced in the simple "mobility" theory is minor, to be of importance only very near the negative glow.

Various further modifications of the simple "mobility" theory have been attempted, mainly by assuming ionization by electrons to occur in the cathode region. A fairly complete account of these investigations, their assumptions, and their resulting theories is given in an excellent article by Druyvesteyn and Penning.[6] The main effect upon the field curves of ionization in the cathode region is an over-all decrease in the field values, being especially noticeable near the negative glow. If the ionization is intense enough, it can lead to anomalous field curves that are concave upwards rather than downwards near the cathode. Under all conditions of ionization, however, the positive ion current density *at the cathode* is related to the total current density by $J=J_+(1+\gamma_i)$. Therefore, if $v_+=k'(E/p)^{\frac{1}{2}}$,

$$\frac{dE}{dx}=\frac{4\pi J}{v_+(1+\gamma_i)}=\frac{4\pi J p^{\frac{1}{2}}}{k'E^{\frac{1}{2}}(1+\gamma_i)},$$

and therefore

$$E^{\frac{1}{2}}\frac{dE}{dx}=\frac{4\pi J p^{\frac{1}{2}}}{k'(1+\gamma_i)}$$

at the cathode, no matter how much ionization occurs at various places in the tube. Thus, at the cathode in any case, k' can be calculated if γ_i is known. Use will be made of this relationship later.

COMPARISON OF THEORY AND EXPERIMENT

The foregoing "mobility" solution will be tested against field measurements made by the author for abnormal glow discharges in a ten cm diameter tube filled with helium, hydrogen, nitrogen, or argon at pressures between 0.03 and 1.0 mm Hg, and for currents between 0.1 and 10 ma.[2,16]

The field measurements used were accurate to within a few percent, but only for pressures greater than about 0.1 mm Hg was the effect of the walls negligible, so that the theoretical treatments given here could be tested directly. For lower pressures, the equipotential surfaces in the discharge tube departed considerably from planes because of positive charges which accumulated on the walls. Therefore, a direct comparison of the measurements and such one-dimensional theories as those aforementioned might result in discrepancies of the order of 10 percent.

The previous paper contains three graphs for each gas presenting field measurements at three different pressures—1.0, 0.3, and 0.1 mm Hg for helium and hydrogen, and 0.3, 0.1, and 0.03 mm Hg for nitrogen and argon. Each graph contains curves of $E/I^{\frac{1}{2}}$ *versus* the distance from the negative glow, plotted for a number of different tube currents, I. Each graph also contains a curve of $[(8\pi/A)(3Mx/2e)^{\frac{1}{2}}]^{\frac{1}{2}}$ (where A equals the cathode area), which should equal $E/I^{\frac{1}{2}}$ according to the "free fall" theory, and a curve of $[6\pi p^{\frac{1}{2}}x/k'A]^{\frac{1}{2}}$ which should equal $E/I^{\frac{1}{2}}$ according to the "mobility" theory. This is done so that if either the "free fall" or "mobility" theory is exactly correct, all curves taken for a given gas at a given pressure but for different currents will fall together and coincide with either the "free fall" or "mobility" curve. By reducing all of the field measurements in this way, most of the important characteristics of the measurements can be made obvious.

For instance, especially for the light gases, the curves of $E/I^{\frac{1}{2}}$ at a given pressure but different currents are so similar that they all fall within a very small region on the graphs. Again, especially for the light gases and at high pressures, the $E/I^{\frac{1}{2}}$ curves fall well above the "free fall" curves indicating that collisions are playing an important part in the motion of the positive ions. At low enough pressure, however, the experimental curves fall well beneath the "free fall" curve, which can only occur if ionization is taking place in the cathode-negative glow space or if the cathode emission has increased enormously. From the extent to which the experimental curves fall beneath the "free fall" curves, it can be estimated that, in some cases, about 9/10 of the tube current in the cathode region is carried by electrons. From the parameters of such discharges, it seems highly unlikely that the new electrons can be formed through ionization by electrons, although the anomalous shape of the field curves leads one to expect a volume production of new electrons. From the work of Parker,[17] Varney,[18] Hagstrum,[19] and Berry and

[16] R. W. Warren, Rev. Sci. Instr. (to be published).
[17] J. H. Parker, Phys. Rev. **93**, 1148 (1954).
[18] R. N. Varney, Phys. Rev. **93**, 1156 (1954).
[19] H. D. Hagstrum, Phys. Rev. **89**, 244 (1953).

Abbott,[20] it is concluded that $(1+\gamma_i)\simeq 1$ and that energetic neutral particles cannot be contributing a very large additional γ. Other cathode mechanisms can, similarly, be ruled out. It thus seems most probable that the phenomenon accounting for the high electron production is none of these but instead, the ionization of gas molecules upon the impact of high-energy positive ions and neutral molecules.

According to the work of Rostagni[21] and Varney,[18] the probability of ionization of gas molecules is of about the same order for collisions with high-energy positive ions or neutral molecules, with values actually favoring collisions with molecules. Thus, in crossing the cathode-negative glow distance of about thirty ionic mean free paths, a positive ion will have collisions with molecules and the recoil neutral molecules will have collisions with other molecules. At high and medium pressures, very few of these collisions will involve energies greater than 100 volts. At low pressures, however, there will occur a total of perhaps 100 or so ion-molecule and molecule-molecule collisions involving energies greater than 100 electron volts for each positive ion leaving the negative glow. With ion and molecule energies of about 100 ev, the probability for the ionization of a gas molecule upon a collision is about 1 percent. Therefore, on the average, each positive ion will form of the order of one new positive ion and electron in its passage from the negative glow to the cathode. These new particles may themselves cause further ionization. In consequence, it is believed that this ionization can account for both the high electron production and an upcurving of the field curves near the cathode.

Additional studies, including those of the nature of canal rays,[2] indicate that the glow on the cathode of glow discharges is largely due to excitation by energetic ions and molecules. Therefore, the importance of energetic ions and molecules in the functioning of low-pressure discharges is further indicated.

In attempting to correlate the experimental field curves with the "mobility" theory, k' was allowed to assume various values so that the resulting "mobility" curves for each gas fitted the experimental curves as well as possible at the highest pressure. Once k' was fixed, new "mobility" curves were constructed for each gas at the lower pressures. If the "mobility" theory were exactly correct, all the experimental curves at all pressures should fall on these "mobility" curves. It was found that a good fit resulted for all gases at the high pressure and in addition for helium and hydrogen at the intermediate pressure and low E/p values. For lower pressures, as discussed above, ionization in the cathode-negative glow space precludes any comparison.

Since a fairly good agreement was found between the measurements and the "mobility" theory, especially for helium and hydrogen, it was felt that a comparison of the fitted k' values and the directly measured k' values of Hornbeck and Varney would be valid. Such a comparison depends upon the identification of the pertinent ion in each gas. However, little or nothing is known for the cathode region of glow discharges other than that many different ions can be present with k' values differing by a factor of perhaps two. In all cases where a comparison was possible, the experimental k' values differed from published values by a factor of about two or less. For instance, experimentally, $k'(\mathrm{He})=8.2\times10^4$ cm/sec (cm-mm Hg/volt)$^{\frac{1}{2}}$, while Hornbeck gives $k'(\mathrm{He}^+)=4.0\times10^4$ and $k'(\mathrm{He}_2^+)=8\times10^4$. $k'(\mathrm{He}_2^+)$ has been extrapolated from the low E/p values for which it was measured and may, therefore, be slightly in error. Probably the basic theory and the field measurements as affected by wall charges[2] are not accurate enough to permit much better agreement. Obviously, mass spectrographic analysis of the pertinent ion would be a great help in any other studies of this kind.

While what has gone before applies largely to the simple conditions at high pressures and fairly near the negative glow, the conditions near the cathode appear to be more complicated as originally indicated by Stein.[22] It was indicated above that k' could always be calculated at the cathode from $k'=4\pi Jp^{\frac{1}{2}}/(E^{\frac{1}{2}}dE/dx)$, no matter how much ionization was occurring. Such calculations give normal k' values at high pressures, values about three times too low at medium pressures, and values about ten times too low at low pressures. Several possible explanations may be suggested.

Since the gases used were only 99.5 percent pure, the pertinent ion might have changed from an ion of the main gas to one of the impurity, giving the observed low k' value near the cathode. However, in most cases, the probability for the reverse reaction is large enough to severely limit the impurity ion concentration. Impurity ions in nitrogen and argon would be likely to increase k' near the cathode which was not observed. Further tests with a purer gas showed no change in the field measurements, indicating the validity of the hypothesis that the pertinent ions were largely of the main gas, not of the impurity.

In mobility measurements in nitrogen, Varney found that near a critical E/p value, the nature of the positive ion changed back and forth between N_2^+ and N_4^+. Over a certain range of E/p near this critical value, the ion velocity and k' actually decreased with increasing E/p. It is not impossible that analogous changes occur in other gases giving a decreasing velocity and k' with increasing E/p, for E/p around 500.

Another possible explanation for the observed decrease in k' is more fundamental and more serious. The measurements of Hornbeck *et al.* were carried out in most cases for E/p values as high as 1000. It has been assumed that for higher values, k' remains constant,

[20] H. W. Berry and R. C. Abbott, Technical Report, Office of Naval Research from Syracuse University, June, 1954 (unpublished).

[21] A. Rostagni, Nuovo cimento **13**, 389 (1936).

[22] R. P. Stein, Phys. Rev. **89**, 134 (1953).

but this need not necessarily be so. As E/p increases, excitation and ionization by positive ions become more likely, and collision processes in general become more complicated. Most new complications tend to increase collision cross sections and decrease k'. Suggestions have even been made that in analogy to assumptions in solid state theory, for high enough E/p values, the ion velocity becomes independent of E/p, and thus k' decreases rapidly with increasing E/p. In any case, since two of the fundamental assumptions upon which the mobility law is based, i.e., elastic collisions and isotropic scattering upon collisions, fail at high E/p values, it is not surprising to find a theory based upon these assumptions also failing at high E/p. Some such drastic change in the mobility law must occur to explain the observed behavior of k' at the high E/p values (near 30 000) which occur in the measurements discussed here.

ACKNOWLEDGMENTS

The writer wishes to thank Professor Leonard B. Loeb who gave his active support and encouragement throughout the prosecution of this problem, for his suggestions in the interpretation of the measurements, and his help in the preparation of the publication.

PHYSICAL REVIEW VOLUME 98, NUMBER 6 JUNE 15, 1955

Motion and Spectrum of Arc Cathode Spot in a Magnetic Field

ROBERT M. ST. JOHN* AND J. G. WINANS
University of Wisconsin, Madison, Wisconsin
(Received December 23, 1954)

The velocity of the cathode spot of a mercury arc at the junction between liquid and metal in a transverse magnetic field has been measured for magnetic field strengths between 0 and 20 700 oersteds. The approximate doubling of retrograde velocity at about 11 000 to 15 000 oersteds was followed by an additional rapid rise of velocity at about 15 000 oersteds. Spectra of the arc showed Hg II and Hg III lines at the stronger magnetic fields. Radiation from the cathode spot showed mercury lines and a continuous spectrum which is especially intense at the lines. Some Hg lines are broadened symmetrically and others asymmetrically. If the broadening is due to a Stark effect, the electric field strength in the cathode spot region is greater than 6×10^6 volts/cm.

The arc mechanism previously proposed is extended to explain the rapid velocity rises with increasing magnetic field strength by associating them with the effect of Hg^{++} and Hg^{+++} ions.

INTRODUCTION

THE results of investigations on the motion of the cathode spot of an electric arc in transverse magnetic fields up to 12 000 oersteds were reported in an earlier article.[1] Both the direction and the magnitude of the velocity of the cathode spot are dependent upon the magnetic field strength, arc current, and pressure of an admixed inert gas.

With no inert gas in the arc tube and with a constant arc current, the velocity was retrograde or opposite to the force on the charged particles due to their motion through the magnetic field. The velocity changed as follows when the magnetic field strength was increased from 0 to 12 000 oersteds. First, the velocity increased rather linearly with field strength and then approached a saturation value. Finally, it rose rapidly to a value nearly double that at saturation. High-current arcs had greater velocities and exhibited the rapid velocity increases at lower magnetic field strengths than low-current arcs.

With an inert gas in the arc tube the spot velocity changed from forward (i.e., in the direction of the force due to motion through the magnetic field) to retrograde as the magnetic field strength was increased and an increase in arc current caused the velocity to increase in the forward direction.

With constant magnetic field strength and constant arc current and with a small amount of inert gas in the arc tube, the spot moved in the retrograde direction. Increasing the gas pressure caused the spot to slow down, stop, and finally move in the forward direction.

When an appreciable amount of inert gas was in the arc tube and conditions were such that the cathode spot was stationary, an increase in magnetic field strength caused the spot to move in the retrograde direction. This retrograde motion, however, could be overcome and the spot brought to rest again by either an increase in arc current or by an increase in gas pressure.

The spectrum of the radiation from the negative glow of the mercury arc in a very weak magnetic field showed Hg I lines and in a strong magnetic field showed both Hg I and Hg II lines. The spectrum of the radiation from the cathode spot was continuous with maxima of intensity at the Hg lines for all magnetic field strengths.

Smith[2] observed the arc motion and also the spectrum

* Now at the University of Oklahoma, Norman, Oklahoma.
[1] R. M. St. John and J. G. Winans, Phys. Rev. 94, 1097 (1954).
[2] C. G. Smith, Phys. Rev. 83, 194 (1951); 84, 1075 (1951).

of the arc spot for magnetic field strengths up to 16 500 oersteds. At the high magnetic fields he found some Hg III lines in the spectrum. Smith was the first to observe that at field strengths of about 9000 oersteds the spot velocity increased rapidly to nearly double the former value.

The present report describes observations of the motion of the cathode spot for magnetic field strengths up to 20 700 oersteds. In addition, the continuous spectrum from the cathode spot has been photographed with higher dispersion.

A possible explanation for the effects observed is presented. The mechanism proposed[1] to account for retrograde motion at the lower field strengths serves also with a slight modification to describe effects observed at higher field strengths.

APPARATUS

Figure 1 shows a cross section of an arc tube mounted between the poles of the magnet. The anode was a circular metal disk and the cathode consisted of a pool of mercury surrounding a circular metal stump. The wetting action caused the mercury to climb the stump when the stump was clean. The cathode spot attached itself to the cathode at the junction of the mercury and the stump. Thus the electric field and the path of the charged particles near the cathode were both horizontal. Since the magnetic field was vertical the charged particles near the cathode were subjected to horizontal forces because of their motion through the magnetic field. The cathode spot moved about the stump at the junction of the metal and the liquid. The metal used was molybdenum of high purity.

The high magnetic field strengths were obtained by using a large magnet with a small pole piece separation. The magnet, weighing three quarters of a ton, had a winding consisting of 48 pancake coils of copper tubing which permitted internal cooling. A closed system employing distilled water as the coolant was used in order to avoid clogging the coils. Heat was transferred from the coolant to a flowing stream of tap water by means of a heat exchanger.

The magnet current was supplied by a direct current generator whose voltage could be controlled by an operator near the magnet. An input of 200 amperes at about 200 volts was sufficient to saturate the magnetic circuit.

The magnet was equipped with pole pieces consisting of Armco iron rods $4\frac{11}{16}$ inches in diameter with conical ends fitted with carefully machined Permendur tips. The ends of the tips had a diameter of $1\frac{1}{16}$ inches. Holes were bored in the pole pieces to house the narrow arms of the arc tube as shown in Fig. 1.

The magnetic field in the region between the pole pieces was measured for various pole piece separations and magnet currents. Field strengths as high as 27 500 oersteds were obtained for a separation of $\frac{1}{2}$ inch. The magnetic field was quite uniform except near the pole axis where the holes were located. Magnetic field measurements were made using a coil rotating in the field with a constant angular velocity. The voltage output of the coil was proportional to the magnetic field strength. The rotating coil was calibrated by observing the voltage output when it rotated in a magnetic field which had been precisely measured with proton resonance equipment.

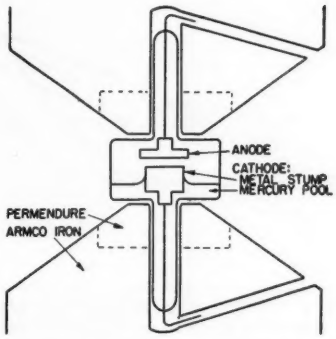

FIG. 1. Arc tube mounted between poles of the magnet (Vycor tube, large magnet).

The arc tubes used in earlier experiments were constructed of Pyrex. They had to be rather large and bulky to reduce the effect of stresses produced by the uneven heating caused by the hot electrodes. The Pyrex arc tubes were about 4 inches in diameter and $1\frac{1}{4}$ inches in height.

Attempts to produce smaller Pyrex tubes in order to utilize smaller pole piece separations were unsuccessful. The tubes cracked at the positions of largest curvature. The final arc tubes were therefore made of vycor and fused quartz. These tubes were able to withstand any thermal shocks caused by the operation of the arc. They were about $1\frac{3}{4}$ inches in diameter and $\frac{7}{8}$ inch in height. Their small volume tended to cause them to operate at a temperature higher than that for the larger tubes. An air stream was used to cool the tube when necessary.

The metal stump cathode had to be at least $\frac{3}{8}$ inch high to allow the mercury sufficient space to climb the sides without going over the top. The sides of the metal stumps were well polished to produce a very smooth race track for the arc spot. At times when mercury had been deposited on the top of the stump by condensation, the spot anchored on the top and raced about there. This tendency was greatly reduced by roughening the top.

In some arc tubes the metal stump had a shallow groove in the wall near the upper edge. If the junction of the mercury and the stump was below the groove, the groove acted as a special race track for the arc spot. When this prevented the spot from moving about the junction of the mercury and the stump, the mercury level was raised to place the junction at the deepest

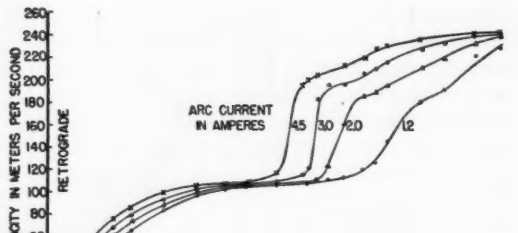

FIG. 2. Spot velocity as a function of magnetic field strength for constant arc currents. No inert gas.

part of the groove. This caused the arc spot motion to be very stable at the junction.

The motion of the cathode spot was observed by means of photoelectric cells. The output of a single cell and the output of an audio oscillator were fed into a cathode-ray oscilloscope to produce Lissajou figures. When closed loops were obtained, the spot motion frequency equalled the oscillator frequency. Frequencies ranged from 0 to about 5000 per second.

The direction of the spot motion was determined by using two photoelectric cells receiving light from two close segments of the spot path thus producing two close peaks on the cathode ray oscilloscope. By identifying each peak with the cell that produced it, the direction of motion of the spot was easily determined.

Spectra were obtained with small glass and quartz Hilger spectrographs, and with a Bausch and Lomb medium quartz spectrograph. An image of the arc tube was focused on the slit. To compare spectra of the cathode spot at various positions in its motion around the stump, the horizontal line of light from the moving cathode spot was focused on the spectrograph slit as a vertical line by using a 90° quartz prism properly oriented.

Microphotometer traces of the plates (Fig. 6) were made with a type *A* moll microphotometer equipped with a photo multiplier detector. Spectra of the cathode spot and of the negative glow were traced with the same base line for comparison.

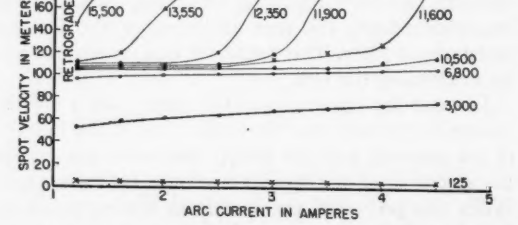

FIG. 3. Spot velocity as a function of arc current for constant magnetic field strengths. No inert gas.

RESULTS

A. Motion of Arc Cathode Spot

The cathode spot velocity depends upon magnetic field strength, arc current, and pressure of an inert gas. The temperature of the arc tube also affects the spot velocity. The velocity decreases with increase in temperature probably as a result of an increase in the mercury vapor pressure. Changes in the tube temperature arise from variations in the arc power dissipation which increases with an increase in magnetic field strength or increase in arc current. To minimize temperature variations the arc was first operated at an average power for about 10 minutes and then data was taken as rapidly as possible.

Figure 2 shows the spot velocity as a function of magnetic field strength for constant arc currents and no inert gas in the tube. The experimental points were obtained from a series of runs in which the magnetic field strength was held constant and the arc current varied. Data obtained by holding the arc current fixed and varying the magnetic field strength yielded curves identical to these, within experimental error, if the temperature was the same in both cases. At lower temperatures of the arc tube, the sharp rises in velocity occurred at lower magnetic field strengths.

For no inert gas present, the velocity is retrograde for all magnetic field strengths. With increasing field strength, and constant arc current, the velocity first increases rather linearly and then approaches a saturation value. Next it rises rapidly to a value nearly double that at saturation and then begins a second leveling off at a value of 1.8 times the velocity for the first plateau. Finally the velocity increases rapidly again, but less rapidly than in the previous rapid rise. The highest velocity attained by the spot was at a field strength of 20 700 oersteds and it was 2.3 times the value at the first plateau. As the velocity was still rising at the highest field strength, stronger magnetic fields would be necessary to obtain data concerning the maximum possible velocity.

The data were plotted in another manner in Fig. 3. This shows the spot velocity as a function of arc current for constant magnetic field strengths. The arc spot velocity increases in the retrograde direction as the arc current is increased when no inert gas is present. Over a limited range of magnetic field strength from about 11 600 to about 15 400 oersteds, a small change in arc current with constant field strength causes the retrograde velocity to nearly double.

The conditions required for the velocity to reach a value of 155 meters/sec (the midpoint of the very rapid velocity increase) are shown in Fig. 4. The magnetic field strength is plotted as a function of arc

current. An increase in arc current decreases the magnetic field strength needed to produce the very rapid change in velocity.

B. Spectra

Spectra of the mercury arc with the spot racing about the beveled edge of the top of the stump were obtained for magnetic field strengths from 150 to 22 000 oersteds with no inert gas in the arc tube. As the magnetic field strength is increased some lines are enhanced and many new lines appear. These new lines were found to be Hg I lines from highly excited or upper levels, Hg II lines (from singly charged ions), and Hg III lines (from doubly charged ions). The Hg III lines appear at about 4000 or more oersteds. The total potential drop across the arc was less than 15 volts for any magnetic field strength.

The spectrum of the radiation from the cathode spot gives Hg lines and a continuous spectrum while that from the negative glow shows only Hg lines. The intensity of the continuous spectrum from the cathode spot is greatest at and near the Hg lines as shown in Fig. 5. Some of the high-intensity continuous regions are symmetrically centered about Hg lines while others are asymmetrically attached to the lines. Asymmetrical continuous regions are found at the Hg lines 2983 A, 3341 A, 4046 A, 4358 A, and 5460 A.

Microphotometer traces of the spectrum are shown in Fig. 6. These show the position and width of the continuous spectrum maxima more clearly than the original plates. Two traces, each with the same base line, are given for each part of the spectrum. The trace which shows sharp lines is that for radiation from the negative glow. The trace exhibiting broad peaks is that for radiation from the cathode spot. The traces in parts (c) and (d) of Fig. 6 show the spectrum for two different exposure times.

Figure 7 shows a part of the arc spectrum taken by having a narrow horizontal section of the arc including the line of light from the moving cathode spot focused

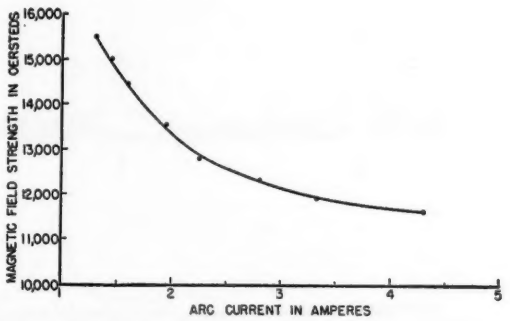

FIG. 4. Magnetic field strength as a function of arc current for spot velocity doubling effect.

as a vertical line on the spectrograph slit. The continuous spectrum shows a much greater intensity for the radiation from the spot as it comes into view around the edge of the stump (below the center of Fig. 7) than for the radiation from the spot as it travels normal to the direction of observation (upper part of Fig. 7).

DISCUSSION OF RESULTS

A. Motion of Arc Cathode Spot

A possible mechanism that is capable of providing a qualitative explanation of the observations of the spot motion has been proposed by St. John and Winans[1] and is shown in Fig. 8. The magnetic field is normal to the drawing. The potential difference across the cathode dark space must be 20 to 30 or more volts as evidenced by the appearance of Hg II and Hg III lines in the spectrum, but the total potential difference across the arc is only from 8 to 15 volts. This potential distribution requires a positive ion sheath very near the cathode and an electron cloud between this sheath and the anode. The cathode spot assembly, composed of the electrons in the cathode, the positive ion sheath, and the electron cloud, can be expected to be stable because of the electrostatic forces within it.

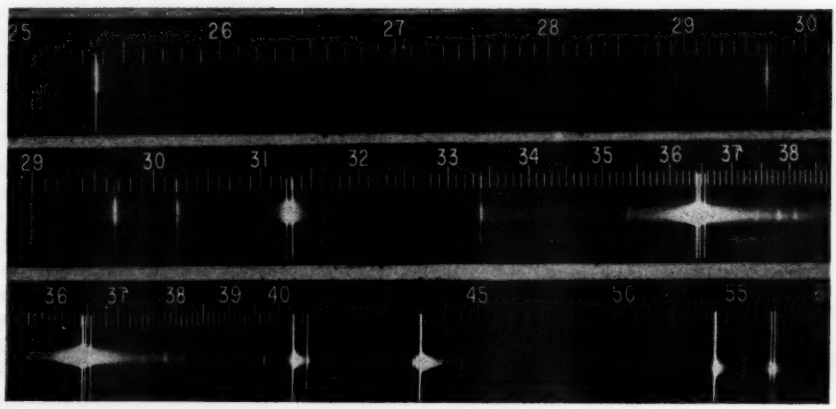

FIG. 5. Spectrum from a vertical section of a mercury arc. Continuous spectrum comes from cathode spot.

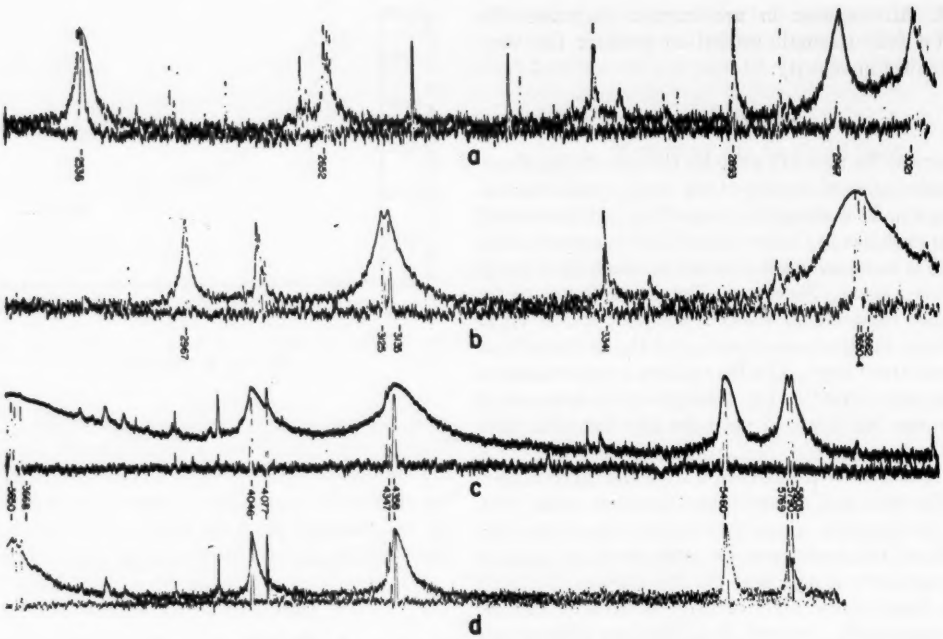

FIG. 6. Microphotometer traces of mercury arc spectrum.

Electrons, after acceleration through the cathode dark space, would travel a curved path because of the force exerted on them because of their motion through the magnetic field. Collisions between electrons and mercury atoms would produce new positive ions on the forward side of the cathode spot. The radius of curvature of an electron having 30-ev energy and traveling in a magnetic field of 18 000 oersteds is 10^{-3} cm. The mean free path for ionization for an electron of this energy travelling through mercury vapor at 5-cm pressure is about 5×10^{-3} cm. The cathode dark space is considered to be about 10^{-4} cm or less in thickness. The pressure is not known but is estimated to be not more than 5 cm since the bands of Hg_2 do not appear in the spectrum.

The cathode spot assembly and the electrons streaming toward the region of production of the new positive ions would exert electrostatic forces on the positive ions produced (forces F_1, F_2, F_3, and F_4 in Fig. 8).

The resultant force of attraction between the new positive ions and the cathode spot assembly produces a retrograde motion of the positive ions and a forward motion of the assembly. Since the assembly is much more massive than the relatively small group of new positive ions, it will move slowly forward while the new positive ions move rapidly in the retrograde direction.

With no inert gas present, the positive ions would approach the cathode spot assembly with an appreciable velocity tangent to the cathode. The mean free path of Hg^+ ions in 5 cm of mercury vapor is about 5×10^{-3} cm. Therefore the positive ions could overshoot the positive ion sheath before being driven to the cathode to start a new spot on the retrograde side. The positive ions would be driven to the cathode by the force due to their motion through the magnetic field and also by the electrostatic force due to their image charge.

Increasing the magnetic field strength with no gas present would have two effects. The first is the formation of the positive ions closer to the cathode surface; the second is an increase in the positive ion sheath potential and charge as shown by the appearance of Hg II and Hg III lines in the spectrum. These effects cause an increase in the tangential component of the resultant force exerted on the new positive ions.

The approximate doubling in the retrograde velocity for magnetic field strengths greater than about 11 000 oersteds with no inert gas present can be attributed to the production of Hg^{++} ions. The forces on doubly charged ions being twice that on singly charged ions, the retrograde velocity should be nearly doubled when Hg^{++} ions are dominant in the production of new cathode spots. The observed velocity after the first rapid rise was about 1.8 times that at the first plateau.

The additional fast increase in spot velocity, which occurs for magnetic fields stronger than those required for the doubling, probably can be associated with the effect of Hg^{+++} ions. The spectrum shows that excited Hg^{++} ions are produced rather abundantly at high magnetic field strengths. It is to be expected that Hg^{+++} ions are also produced. Their presence in numbers sufficiently great to allow them to dominate the production of new cathode spots should cause the spot

FIG. 7. Spectrum from a horizontal section of the arc spot path.

velocity to approach a value about three times that occurring at the first plateau. The maximum velocity attained by the spot was 2.3 times the value for the first plateau and this occurred at the highest magnetic field strengths obtainable. As the velocity was still increasing at this point, stronger magnetic fields would be necessary to obtain data concerning the plateau for this part of the curve.

With no inert gas present, increasing the arc current results in an increase in spot velocity in the retrograde direction. This can be associated with the increase in the charges of the cathode spot assembly. The result would be an increase in resultant force on each new positive ion and a consequent increase in overshooting by the positive ions.

The experimental observations given in Fig. 4 show that an increase in arc current decreases the magnetic field strength needed to give the approximate doubling of the velocity. A high current arc should supply the critical number of doubly charged ions required for velocity doubling at a lower magnetic field strength than a low current arc.

To describe the effect of adding an inert gas it can be recognized that the addition would reduce the overshooting because of collisions between Hg ions, and inert gas atoms. With enough inert gas, the forward motion of the cathode spot assembly should exceed the overshooting of new positive ions and a forward motion of the cathode spot should result.

The observation that with an added gas an increase in arc current changes the spot velocity toward the forward direction while with no added gas an increase in arc current changes the spot velocity toward the retrograde direction is also in agreement with the proposed mechanism. Referring to Fig. 8, an increase in arc current should increase the number of new positive ions and these in turn can be expected to cause a small percent increase in all of the charges in the cathode spot assembly. A doubling of the current should double the number of new positive ions but not double the charges in the cathode spot assembly. This would double the force on the cathode spot assembly with only a small increase in the force on each new positive ion. Since the new positive ions are impeded in their motion by the inert gas atoms, the increased force acts on the cathode spot assembly for a longer time than when no inert gas is present. The motion of the arc spot should therefore change toward the

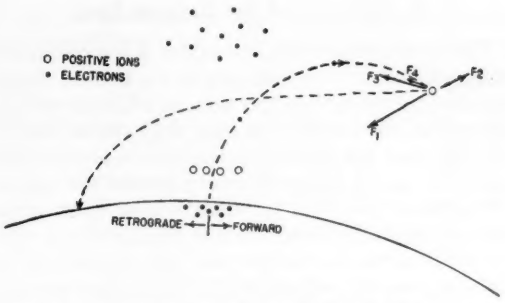

FIG. 8. The mechanism for a qualitative description of the cathode spot motion.

forward direction when an inert gas is present, and the current is increased.

When no inert gas is present, the result of an increase in force between new positive ions and cathode spot assembly is primarily an increase in the acceleration and final retrograde velocity of the new positive ions. An increase in current should therefore increase the velocity of the arc spot in the retrograde direction.

Cobine and Gallagher[3,4] observed that for arcs with various gases and electrodes, the pressure of gas needed to change the motion of the arc spot from retrograde to forward was approximately proportional to the ionization potential of the gas. This observation can also be qualitatively described by the mechanism illustrated in Fig. 8. A gas with a high ionization potential should require a high potential drop across the cathode dark space to maintain the arc. This means greater charge in all parts of the cathode spot assembly and this in turn means greater force on new positive ions. An increase in force on new positive ions means a more rapid retrograde motion at low pressure. The pressure necessary to stop the retrograde motion should therefore increase with the ionization potential of the gas.

It has been suggested by Ware[5] that the retrograde motion of an arc spot in a transverse magnetic field might be associated with the Ettingshausen effect which would cause a transfer of heat toward the retrograde direction to produce a higher temperature on the retrograde side of the cathode spot. If the arc spot tends to move to positions of higher temperature, a retrograde motion of the arc spot would result. Ware pointed out that, under these conditions, the spot should move in the forward direction either for high pressure of gas or for a higher magnetic field strength. The experimental observation that the retrograde velocity continues to increase to field strengths of more than 20 700 oersteds is therefore in disagreement with Wares' proposed mechanism.

[3] J. D. Cobine and C. J. Gallagher, Elec. Eng. **68**, 469 (1949).
[4] C. J. Gallagher, J. Appl. Phys. **21**, 768 (1950), and special publication of General Electric Company.
[5] A. A. Ware, Proc. Phys. Soc. (London) **A67**, 869 (1954).

B. Spectrum of Arc Cathode Spot

The mechanism for the production of the continuous radiation from the cathode spot is not known. Smith[6] observed the continuous spectrum to originate within a distance of 10^{-3} or 10^{-4} cm from the cathode surface. The fact that the continuous radiation is more intense when the spot is observed coming around the edge of the cathode than when travelling normal to the direction of observation indicates that the continuous spectrum is emitted by the gas near the cathode surface and not from the surface itself. For a surface emitting radiation, the brightness is independent of the section observed because of compensation of the area and obliquity factors. For radiation from the gas the number of emitters seen by an observer would be greater when he views a small projection of a thin region from the edge rather than from the side.

A continuous radiation with high intensity at the Hg lines, the intensity distribution being symmetric at some lines and asymmetric at others, indicates either a pressure effect or a Stark effect. Since the spectrum does not resemble the radiation from Hg_2 molecules[1] it was considered that the effects were not due to high mercury vapor pressure at the spot.

A thorough investigation of the Stark effect on Hg lines in electric fields up to 560 000 volts/cm was carried out by Ishida and Hiyama.[7] Their observations were made using a glow discharge tube of the Lo-Surdo type. In these experiments an image of the cathode dark space of the glow discharge was focused on the slit of a spectrograph. The electric field strength decreased from a very high value at the cathode surface to a very low value beyond the cathode dark space in the negative glow. Thus each point along the length of the spectrum line corresponded to light from a point in the discharge at which there was a constant and well defined electric field strength.

The presence of a strong electric field caused a splitting of lines into one or two components and a shift of the components. In addition, it caused the appearance of many lines that were forbidden in field free space by the selection rule $\Delta L=\pm 1$. Thus $S-S$, $P-P$, $S-D$, $S-F$, etc., lines appeared. As the electric field strength decreased, the wavelength of a forbidden line usually approached a value very near that for the wavelength of an allowed transition. Also all the components of any one line were shifted only to either longer or shorter wavelengths, never toward both.

An explanation of why some of the continuous spectrum peaks are symmetrically centered about atomic lines while others are asymmetrically attached to the lines can be made. An asymmetrical broadening can be the broadening of a single permitted line in one direction, the broadening being continuous because of the variation of the electric field strength within the dark space. A symmetrically centered broadening can be due to the broadening in one direction of an allowed line and a broadening in the other direction of a nearby forbidden or allowed line. An example of this is the broadening at the 2967 A line. The allowed line 2967 A ($6^3P_0-6^3D_1$) would produce the violet wing while a forbidden line 2970 A ($6^3P_0-7^1P_1$) which appears at high electric field strengths would cause the red wing of the broadening.

The observed asymmetrical broadenings in the cathode spot spectrum (2893 A, 3341 A, 4046 A, 4358 A, 5460 A) were those which would be expected from consideration of the work of Ishida and Hiyama.[7] In addition, consideration of their data leads one to expect symmetrical peaks with centers at 2967 A, 3131 A, 3650 A, and 5790 A as observed.

Ishida and Hiyama observed that the magnitudes of nearly all the line shifts, allowed and forbidden, were nearly proportional to the second power of the electric field strength (second-order Stark effect). The shifts obtained by Ishida and Hiyama were used in the present investigation to determine the electric field strengths present in the cathode dark space of the arc on the assumption that the observed broadening of the Hg lines is due to a second-order Stark effect. Table I shows data and calculated results for several Hg I transitions. This includes for each transition the width of the wing in wave numbers as obtained from microphotometer traces, and the shift at the line for an electric field strength of 0.5×10^6 volts/cm as given by Ishida and Hiyama. Also included in the table is the maximum electric field strength calculated on the assumption that the width of the wing is proportional to the square of the electric field strength. Hg lines included in the table were those not excessively overlapped by neighboring lines.

It is to be noted that the electric field strengths calculated from the broadening of the 2536 A, 4046 A, 4358 A, and 5460 A lines are two or three times larger than the field strengths obtained from the broadening of other Hg lines. Lines 2536 A, 4046 A, 4358 A, and 5460 A involve transitions that can be expected to follow the second-order effect to higher electric field strengths than any other transitions listed in the table before changing to a first-order effect.

In nonhydrogen-like atoms at the lower electric field strengths, the second-order Stark effect predominates over the first order effect. As the electric field strength is increased the first-order effect becomes dominant. The value of the electric field strength at which this change takes place depends upon the energy levels of the transition. When an atomic energy level has other levels of the same n nearby, the first-order shift sets in at lower electric field strengths than when the level is isolated.[8] The mercury 6^1S_0 and $6^3P_{0,1,2}$ levels are very

[6] C. G. Smith, Phys. Rev. **69**, 96 (1946).
[7] Y. Ishida and S. Hiyama, Inst. Phys. Chem. Research (Tokyo) **36**, 390 (1939).
[8] H. E. White, *Introduction to Atomic Spectra* (McGraw-Hill Book Company, Inc., New York, 1934), Chap. 20.

far removed from the other energy levels and the 7^3S_1 level is 1600 cm^{-1} from the nearest perturbing level. Other energy states involved in the transitions listed in Table I are all less than 450 cm^{-1} from possible perturbing levels. It is therefore possible that transitions involving only the 6^1S_0, $6^3P_{0,1,2}$, and 7^3S_1 levels will most nearly maintain a second-order Stark effect as the electric field strength is increased. These levels produce the 2536 A, 4046 A, 4358 A, and 5460 A lines.

It is probable that the other lines listed in Table I have the first-order Stark effect become dominant at an electric field strength of about 10^6 volts/cm and therefore do not yield the correct field strength when a second order calculation is made.

Assuming that the calculations of the electric field strength based on broadening of the 2536 A, 4046 A, 4358 A, and 5460 A lines to yield the most nearly correct value, the field strength is as high as 6×10^6 volts/cm in the cathode spot region.

Efforts were made to correct the microphotometer traces for the nonlinearity existing between plate opacity and the intensity of the spectrum radiation. These showed that a plot of intensity as a function of wavelength would have maxima with flatter peaks than those exhibited by the microphotometer traces. Thus the broadening of lines as determined from the microphotometer traces is a conservative estimate of the actual intensity broadening and therefore, the electric field strength calculated from the microphotometer traces represents a lower limit for the electric field strengths in the cathode spot.

According to the interpretation of line broadening described above the electric field strength at the cathode of an arc is probably great enough to cause field emission of electrons from the cathode. Dyke and Trolan[9] working with very clean metal surfaces in a very good vacuum observed field emission of electrons from electric field strengths of 2×10^7 volts/cm or more.

The photographs and microphotometer traces of the cathode spot spectrum show an additional broadening of lines which is small in comparison to the apparent Stark broadening. The asymmetrically broadened lines show a small broadening toward the side opposite the Stark broadening. This broadening can be due to either a pressure or Doppler broadening. Other observers of Stark broadening[10] have noted the same effect.

In addition to the very strong Hg lines discussed above there are many other Hg lines, allowed and forbidden, which arise from higher energy levels which should be present in the cathode spot spectrum. Hansen, Takamine, and Werner[11] found that the Stark effect shift of mercury levels increased with the energy of the level. A large Stark broadening for lines from high-energy levels could by overlapping, produce a continuous background such as that observed in the cathode spot spectrum.

Another possible source for the faint continuous background is free-free transitions as proposed by Finkelnburg.[12] This might arise from electrons moving through the positive ion sheath and radiating energy through transitions between hyperbolic orbits.

TABLE I. Line widths and electric field strengths in cathode spot.

Wavelength	Transition	Arc $\Delta\nu$ in cm^{-1}	$\Delta\nu$ in cm^{-1} for $E=0.5\times10^6$ v/cm	Calculated arc electric field strength (v/cm)
2536A	$6^1S_0-6^3P_1$	−94	−0.5	6.8×10^6
2893	$6^3P_1-8^3S_1$	−140	−7.5	2.2×10^6
2967	$6^3P_0-6^3D_1$	680	25	2.6×10^6
3125	$6^3P_1-6^3D_2$	715	46	2.0×10^6
3135	$6^3P_1-7^1P_1$	−1220	−70	2.1×10^6
3341	$6^3P_2-8^3S_1$	−240	−10	2.5×10^6
3650	$6^3P_2-6^3D_3$	980	25	3.1×10^6
3668	$6^3P_2-7^1P_1$	−2000	−70	2.7×10^6
4046	$6^3P_0-7^3S_1$	−182	−2	4.8×10^6
4347	$6^1P_1-7^1D_2$	−3700	−80	3.4×10^6
4358	$6^3P_1-7^3S_1$	−273	−1.3	7.2×10^6
5460	$6^3P_2-7^3S_1$	−150	−2	4.3×10^6
5802	$6^1P_1-7^1P_1$	−1800	−300	2.4×10^6

CONCLUSIONS

The retrograde motion of the cathode spot of a mercury arc in a transverse magnetic field with no inert gas present and the cathode spot at the junction between mercury and metal can be described in terms of Hg^+, Hg^{++}, Hg^{+++} ions overshooting the cathode spot assembly and starting new cathode spots in the retrograde direction.

A substantial amount of inert gas retards the overshooting of the positive ions to the extent necessary for the forward motion of the cathode spot assembly to produce an observable effect. This can account for the forward motion of the cathode spot with an inert gas present.

The continuous spectrum from the cathode spot can be associated with a Stark broadening of allowed and forbidden lines. Calculations of the electric field strength, based on the assumption that certain transitions follow a second-order Stark effect, yield a value of about 6×10^6 volts/cm.

This work was supported in part by a grant from the Research Corporation.

[9] W. P. Dyke and J. K. Trolan, Phys. Rev. 89, 799 (1953).
[10] J. D. Craggs and W. Hopwood, Proc. Phys. Soc. (London) 59, 755 (1947).
[11] Hansen, Takamine, and Werner, Kgl. Danske Videnskab. Selskab, Mat.-fys. Medd. 5, No. 3 (1923).
[12] W. Finkelnburg, Phys. Rev. 45, 341 (1934).

Thermodynamic Properties of Liquid Helium Three. I. The Specific Heat and Entropy*

THOMAS R. ROBERTS AND STEPHEN G. SYDORIAK
University of California, Los Alamos Scientific Laboratory, Los Alamos, New Mexico
(Received March 7, 1955)

Specific heats of saturated liquid He^3 have been measured between 0.37° and 2.36°K. The data fit the empirical equation, $C=0.577+0.388T+0.0613T^3$ (cal/mole deg), to about ±1.0 percent between 0.5° and 1.7°K. The standard deviations of most of the individual points are between 1 and 2 percent.

Entropy differences are calculated from the above equation and combined with a value of entropy of 1.44 cal $mole^{-1}$ deg^{-1} at 0.5°K to give the total entropies.

The difference between the total entropy and the entropy of nuclear spin disorder is remarkably linear with and nearly proportional to T.

The present and earlier warmup experiments give no indication of existence of a specific heat anomaly in liquid He^3 between 3.21°K and 0.37°K. The present work also shows that a λ transition comparable to that occurring in liquid He^4 will not be found in liquid He^3 at any temperature below 0.37°K.

INTRODUCTION

THIS is the first of a series of papers whose ultimate objective is the establishment of a thermodynamically consistent vapor pressure equation for liquid He^3. Subsequent papers will describe vapor pressure and thermomolecular pressure ratio measurements and the combination of these results into a thermodynamic equation.

Measurements of specific heats and vapor pressures are of interest in themselves because of their usefulness in designing cryogenic apparatus and planning experiments. In the case of He^3 these measurements take on added interest because they provide answers to the questions: (a) Is there a specific heat anomaly corresponding to a lambda type transition in the readily accessible temperature range? and (b) Is there any reason to expect that such a transition will occur at temperatures below the range of the experiments? Because of recent interest and activity in measuring specific heats,[1,2] this first paper will describe and analyze the specific heat measurements reported briefly earlier.[3]

EARLY WARMUP EXPERIMENT

The earliest experimental evidence on the specific heat of liquid He^3 was of a qualitative nature intended only to answer question (a). In 1949, Hammel and one of us[4] showed that no λ-type transition exists for He^3 in the temperature range from 0.86° to 3.21°K by observing the warmup of 20 mm^3 of liquid He^3 in a miniature glass Dewar. Since the slides shown at the 1949 M.I.T. conference were not reproduced in the published proceedings, they are repeated here as Fig. 1. Figure 1(c) gives the results of a check run on liquid He^4 which clearly demonstrates the existence of its λ transition by a strong inflection at 37.6 mm Hg. Absence of any such inflection in the He^3 warmup experiments shows that He^3 does not undergo a second order transition of the same type as He^4 in the temperature range covered.

APPARATUS

The specific heat measurements which are described in this paper were performed in a Dewar also used for vapor pressure measurements and shown in Fig. 2. At the bottom of the all-metal Dewar, shown immersed in a bath of He^4, is a seamless 1-cm diameter sphere spun from a 10-mil copper sheet. The sphere usually is filled at 50 percent packing with paramagnetic salt particles of about 1-mm size. Twin coils wound directly on the He^3 vacuum jacket and immersed in the He^4 bath are used to measure the salt susceptibility temperature, T^*. Further details will be given in the vapor pressure paper.

The sphere is connected by 70 Cu 30 Ni tubing to a brass block, S, which thermally shorts the inner wall of the Dewar to the He^4 bath. An axial hole through this block connects the upper and lower vacuum spaces. Various inserts, shown in Fig. 2, can be screwed into the threads in this block.

Mercury and oil manometers are used to observe pressure warmups and to calibrate the alum. The liquid temperature is controlled by a sensitive needle valve and a mechanical fore pump of special design.[5]

A sensitive 0 to 250 mm Hg bellows-type gauge on the exhaust side of this pump is used to measure N, the total number of moles of He^3 in the Dewar and manometer. The gauge can be calibrated against the Hg and oil manometers mentioned above and is found

* Work performed under the auspices of the U. S. Atomic Energy Commission.

[1] G. de Vries and J. G. Daunt, Phys. Rev. **92**, 1572 (1953); Phys. Rev. **93**, 631 (1954).

[2] Osborne, Abraham, and Weinstock, Phys. Rev. **94**, 202 (1954).

[3] T. R. Roberts and S. G. Sydoriak, Phys. Rev. **93**, 1418 (1954).

[4] S. G. Sydoriak and E. F. Hammel, Proceedings of the International Conference on the Physics of Very Low Temperatures (Massachusetts Institute of Technology, Cambridge, 1949), p. 42.

[5] We are indebted to R. L. Mills for design of this pump. It is uniquely adapted for work with He^3 because of its low displacement (50 cc), its requirement of only 10 drops of oil, and its reversible operation.

to be reproducible to 0.2 mm Hg at full scale and 0.05 mm Hg at low pressures. The calibrated volume of gauge and pump exhaust (when running) ranges from 72.1 cc to 75.2 cc in the range 0–250 mm Hg. To facilitate the measurement of N, a fixed 542 cc volume can be added.

The He³ used in these experiments contained 0.12 percent He⁴.

METHODS OF MEASUREMENT

The measurements were made by three methods which differ in the temperature range covered and in the means used to evaluate the heat input, $\dot{Q}$. In Method I, best suited to measurements above 1°K, $\dot{Q}$ is primarily the measured power input to an electrical heater but includes also a small correction for normal heat leak to the liquid. In Method II, employed at selected temperatures between 0.5° and 1.25°K, the heater is dispensed with and $\dot{Q}$ derived from the carefully measured evaporation rate of the liquid and the calculated latent heat.

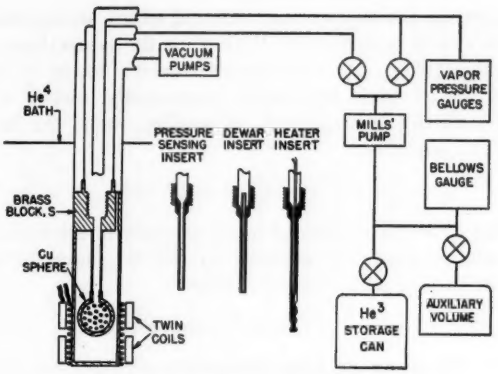

FIG. 2. He³ Dewar and manifold.

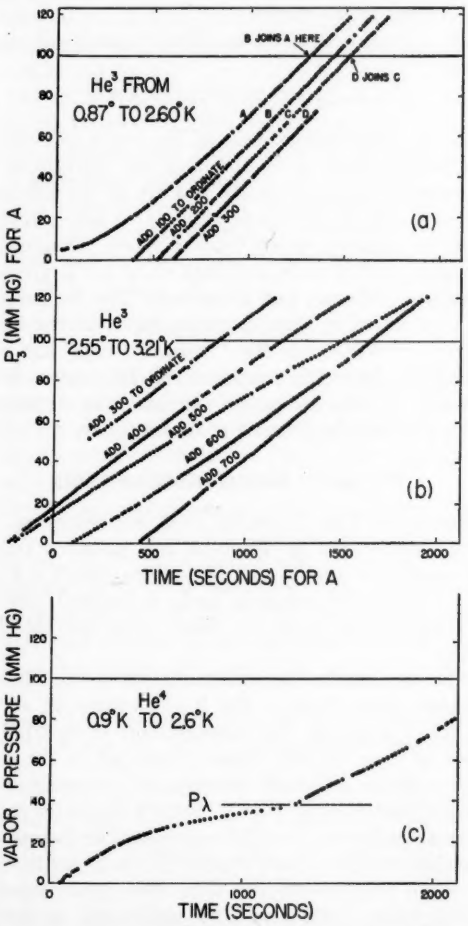

FIG. 1. Previously unpublished figures showing results of early liquid He warmup experiments of Hammel and Sydoriak performed in the Dewar in which He³ was first liquefied. Figure 1(c) shows a He⁴ warmup with a strong inflection at the lambda point. Note the absence of any such inflection in the He³ warmups of Figs. 1(a) and 1(b).

Method III is used at temperatures below 0.5°K attainable to us only by adiabatic demagnetization, $\dot{Q}$ being inferred by fitting the warmup rate when above 0.5°K to the specific heat from Method II.

The liquid He³ was contained in the copper sphere which served as the calorimeter. The noxious volume, i.e., the volume outside the calorimeter, was quite large in order to prevent excessive thermomolecular pressure ratios during vapor pressure measurements. Although this noxious volume was reduced considerably for the higher-pressure specific heat measurements, its effect was large on a single warmup. Therefore an experimental technique was used which canceled out the corrections for the noxious volume as well as for the calorimeter heat capacity. Warmup measurements were repeated with several different amounts of liquid. From the variation in warmup rate *versus* amount of liquid an apparent specific heat, C_a, is obtained. The calculated conversion to the actual specific heat, C, takes account of vapor warming and evaporation into that part of the dead space which changes with liquid level. To the extent that this region is isothermal, which is experimentally borne out, we show below that $C-C_a$ is dependent only on properties of He³. The conversion factor $C-C_a$ can then be in error only to the extent that calculable quantities such as latent heat, vapor density, etc., are in error.

DERIVATION OF WARMUP EQUATIONS

Since no expressions were found in the literature which applied to Methods I and II, the equations will be derived in some detail.

$\dot{Q}$, the heat flux reaching the calorimeter, is spent in warming (1) N_L moles of liquid, (2) the calorimeter of heat capacity C_{cal} and (3) n moles of vapor within the calorimeter, whose entire volume, v, is assumed to be at the liquid temperature, T. The heat flux is also

spent in the evaporation of liquid which accompanies its rise in temperature. With L as the latent heat of vaporization, C and c as the specific heats of the saturated liquid and vapor, respectively, and $\dot{T}$ and $\dot{N}_L$ as the warmup and evaporation rates, the heat flux is equal to:

$$\dot{Q}=(CN_L+C_{\text{cal}}+cn)\dot{T}-L\dot{N}_L. \quad (1)$$

Let n' be the number of moles of vapor in the noxious volume. During a warmup no He^3 is removed from the system, so $\dot{N}_L+\dot{n}+\dot{n}'=0$ and

$$\dot{N}_L=-[(dn/dT)+(dn'/dT)]\dot{T}. \quad (2)$$

In this paper all total derivatives with respect to T are taken along the saturation curve.

With V_v and V_L as the molal volumes of the vapor and liquid and β defined as V_L/V_v, the calorimeter volume is equal to $N_LV_L+V_v$ and

$$n=(v/V_v)-\beta N_L. \quad (3)$$

By appropriate substituting in Eq. (1) and dividing by $\dot{T}$, we find that

$$\dot{Q}/\dot{T}=CN_L+C_{\text{cal}}+c[(v/V_v)-\beta N_L] -L(1-\beta)^{-1}[(v/V_v^2)(dV_v/dT) +N_L(d\beta/dT)-(dn'/dT)]. \quad (4)$$

Up to this point the derivation has been essentially the same as that given by Osborne and Van Dusen[6] with the addition of the term n_v' for the vapor in the external dead space. Direct application of their experimental technique would involve the determination of C from Eq. (4) by a single determination of the average value of $\dot{Q}/\dot{T}$ over a small temperature interval. The calculation would involve detailed corrections for C_{cal}, n', and (dn'/dT).

Instead, we have canceled out these latter corrections experimentally by measuring $\dot{Q}/\dot{T}$ for several different values of N_L. Since n', and hence (dn'/dT), may be assumed independent of N_L, at any given temperature $\dot{Q}/\dot{T}$ should be a linear function of N_L with slope

$$C_a=[\partial(\dot{Q}/\dot{T})/\partial N_L]_T=C-\beta c-L(1-\beta)^{-1}(d\beta/dT), \quad (5)$$

as the apparent specific heat.

Actually N_L is not measured directly in our experiment, but N, the total number of moles of He^3 in the system, is. Since

$$N=N_L+n+n'=N_L(1-\beta)+(v/V_v)+n', \quad (6)$$

and n' is independent of N_L, it follows that $C_a=(1-\beta)[\partial(\dot{Q}/\dot{T})/\partial N]_T$. Thus the resulting expression for the specific heat of the saturated liquid,

$$C=(1-\beta)[\partial(\dot{Q}/\dot{T})/\partial N]_T+\beta c+L(1-\beta)^{-1}(d\beta/dT), \quad (7)$$

does not require any knowledge of the geometry or mass of the calorimeter, of the amount of liquid, or of the noxious volume.

The second and third terms of Eq. (7) are referred to as the vapor warming and evaporative terms, respectively. Their net sum is shown in Fig. 4.

Latent heats have been derived from the thermodynamic vapor pressure equation by a method equivalent to the use of the Clausius-Clapeyron equation. These results will be discussed in a later paper.

β and $d\beta/dT$ have been calculated from the data of Kerr[7] and the second virial coefficients, B, calculated by Kilpatrick, Keller, Hammel, and Metropolis.[8] Kerr's experimental vapor volumes are fitted best below 2.6°K by the virial equation in the inverse volume expansion:

$$V_v=(RT/p)(1+B/V_v). \quad (8)$$

This equation has been used for all vapor volume calculations in this paper.

The specific heat of the saturated vapor is calculated from:

$$c=c_{\text{vol}}+T(\partial p/\partial T)_V(dV_v/dT), \quad (9)$$

where c_{vol}, the specific heat of the vapor at constant volume, is taken as $(3/2)R$, and the derivatives are expressed in terms of dp/dT and dB/dT by differentiating Eq. (8). The values of p and dp/dT are calculated from an equation which fits our vapor pressure data between 0.4 and 1.0°K and data up to 1.5°K given by Abraham, Osborne, and Weinstock.[9] The temperature scale advanced by these authors, based on the Kistemaker corrections to the "Agreed" scale, has been used throughout the present work. Discussion of the pressure equation and possible variations in the temperature scale will be deferred to future papers.

Method I: Heater Measurements

For a Method I specific heat measurement, the paramagnetic salt is dissolved and siphoned out to make room for more liquid. The heater, shown in Fig. 2 with current and potential leads, is inserted, and the attached needle valve is closed to reduce the dead space.

The specific heat measurement consists in following pressure *versus* time as the liquid warms up several tenths of a degree. The measurement is repeated for three or four different liquid levels, all at the same heater power and bath temperature, to measure the proportionality of $\dot{Q}/\dot{T}$ to N. Table I shows the results of three such runs. Run I-B results will be discussed in sufficient detail to show that $\dot{Q}/\dot{T}$ is a linear function of N. In this run the N's were respectively equal to 18.51, 12.92, 7.89, and 3.57 millimoles, a fivefold variation in N. The variation in N_L, the moles of

[6] N. S. Osborne and M. S. Van Dusen, Bull. Natl. Bur. Standards 14, 397 (1917).

[7] E. C. Kerr, Phys. Rev. 96, 551 (1954).

[8] Kilpatrick, Keller, Hammel, and Metropolis, Phys. Rev. 94, 1103 (1954).

[9] Abraham, Osborne, and Weinstock, Phys. Rev. 80, 366 (1950).

liquid, is even greater than this since N includes the He³ vapor. Specific heats calculated from the two highest levels show no consistent difference from C's calculated from the two lowest levels. Thus for a more than fivefold variation in amount of liquid, $\dot{Q}/\dot{T}$ at a given temperature varies linearly with N as expected if Eq. (7) is valid.

$\dot{Q}$ includes a correction for conduction heat leaks and therefore gradually falls as T rises. Just prior to Run I-B, a measurement was made of normal heat leak at a low sphere temperature where high accuracy is possible. The result agreed to within 5 percent with a calculation based on the geometry of the Dewar and heater leads and on recently compiled thermal conductivity data for copper and Cu Ni.[10] Since the observed heat leak in Run I-B amounts at most to only 4.6 percent of the heater power input, it was felt that calculation of this small correction would be preferable to more extensive measurements at each value of T. In Run I-A the heater power was three times as great, so the calculated correction ranges only between 1.5 percent and 0.8 percent of the total $\dot{Q}$. The fact that there are no consistent differences in the results of these two runs is further evidence that the conduction calculations are not a serious source of error.

The values from Run I-C are based on only two warmups and hence have been weighted $\frac{1}{3}$ in calculating a specific heat equation. The relative weights are shown in the table.

Errors in Method I

All errors given in the tables or in the text are the calculated standard deviations or their estimated equivalent. Where data were not available for calculation of a standard deviation, the deviation was taken as one-half the estimated limit of error.

The errors in Table I are the total standard deviations for each value of C and include estimated deviations of ± 0.2 percent in both $\dot{Q}$ and N and ± 1 percent in the evaporative and vapor warming terms. The average total deviation for all the values below 2°K is about ± 2.0 percent with no systematic increase with pressure. This number represents mainly statistical errors calculated from the spread in observed C_a values due to dead space variations and timing errors. No estimate has been made of absolute errors in the temperature differences taken from the He³ scale.

TABLE I. Specific heats from Method I in cal/mole deg.

	Run I-A		Run I-B		Run I-C			Std	Relative
T°K	C_{ab}	C_{bc}	C_{ab}	C_{bc}	C_{cd}	C_{ab}	C	dev	weight
1.070	1.039	1.095	1.066	1.026	1.086		1.062	±0.017	1
1.157	1.069	1.132	1.144	1.135	1.190		1.114	0.019	1
1.256	1.170	1.161	1.181	1.190			1.176	0.012	1
1.364	1.198	1.259	1.255	1.273			1.246	0.022	1
1.452	1.403	1.283	1.273	1.356			1.329	0.032	1
1.527	1.404	1.349	1.371	1.405			1.382	0.020	1
1.608	1.470	1.369	1.485	1.422			1.436	0.030	1
1.695			1.553	1.526			1.540	0.028	½
2.231						2.047	2.047	0.047	⅓
2.358						2.391	2.391	0.049	⅓

[10] R. L. Powell and W. A. Blanpied, National Bureau of Standards Circular 556, 1954 (unpublished).

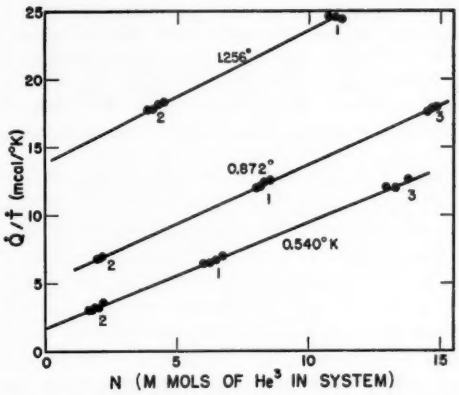

FIG. 3. The ratio of heat leak to warm-up rate plotted as a function of the total millimoles of He³ in the Dewar and manometer. The least squares fitted slope of the straight line through the points at a given temperature is the apparent specific heat, C_a. The data shown are from Method II.

Method II: C/L Measurements

For Method II measurements iron alum is used to measure $\dot{T}$, and the Dewar tube insert replaces the heater. To measure $\dot{Q}$ it is necessary to remove vapor without significantly altering the conduction heat leak to the liquid. By removing vapor only via the capillary which forms the inner wall of this Dewar tube insert, we eliminate heat exchange between the effluent vapor and the Cu Ni tube which joins the copper sphere to the brass block, S. We estimate that even if the bottom of this insert made perfect thermal contact to the liquid, which is certainly does not do, the effect on the $\dot{Q}$ measurement would be only about 0.7 percent in the worst case.

In Method II measurements the warmup interval is much smaller, usually about 0.04°K, which requires up to 30 minutes for a full capsule. It is not practical to tabulate the data in detail, since ten to twenty warmups were observed in each temperature region. Figure 3 shows some typical $\dot{Q}/\dot{T}$-*vs*-N data. Each plotted point corresponds to one warmup, the sequence of warmups within a cluster being in the order of decreasing N. As a means of detecting any possible monotonic variation in dead space the data were usually taken in the order half-full, nearly empty, and full. No persistent variation is dead space is evident. However it was found necessary to allow about half an hour for equilibration of the dead space after having condensed or removed a large fraction of the liquid.

In measuring the heat flux to the refrigerant in a Dewar by means of its evaporation rate one can either (a) attempt to hold the temperature constant while

TABLE II. Specific heats from Method II.

T°K	0.540	0.566	0.598	0.629	0.748	0.804	0.872	1.256
C cal/mole deg	0.811	0.790	0.815	0.854	0.895	0.930	0.956	1.223
Std dev	±0.013	0.012	0.010	0.011	0.013	0.014	0.017	0.035
L cal/mole	7.36	7.47	7.60	7.72	8.19	8.41	8.66	9.90

measuring $\dot{N}$ or (b) allow repeated warmup and cooldown over a narrow temperature interval, recording N for each warmup and time, t, at the moments the mean temperature is crossed during successive warmups. The latter technique was much better for our purposes. The amounts of gas withdrawn between successive warmups when divided by the time interval between arrivals at the average temperature, $\bar{T}$, and multiplied by the apparent latent heat[11] provided data for a continuous record of average heat leak including that during warmup. In fact, once a series of warmups was begun, very little time was spent in cooldowns, since these could be done quite rapidly. Thus the $\dot{Q}$ and $\dot{T}$ measurements were essentially concurrent.

This technique has several advantages besides a saving in time. Since the apparent latent heat is equal to $L/(1-\beta)$, the factor $(1-\beta)$ is canceled in Eq. (7), and no error is introduced due to errors in vapor density calculations except in the relatively small vapor warming and evaporative terms. The small changes in N between successive warmups used to calculate $\dot{Q}$ and the relatively large changes in N between series of measurements at the different liquid levels are both measured by the same metering system. Thus absolute errors in pressure calibration and volume measurements tend to be canceled.

Table II shows the results of Method II measurements. Latent heats have been calculated to an estimated accuracy of about ±0.5 percent. The latent heats used are shown in the table.

The standard error of temperature differences measured by the susceptibilities was ±0.2 percent. The error analysis shows that the net standard deviation for Method II measurements below 1°K is 1.5 percent of C.

Method III: Demagnetizations

For a Method III measurement, the Dewar tube insert is removed and replaced by a radiation shield, since one is interested only in obtaining the highest possible pumping speed, and therefore the lowest temperature, prior to a demagnetization. As noted above, $\dot{Q}$ was inferred from the slope of the warmup curve in the Method II region (above 0.5°K).

The results of runs III-A and III-B, with N's of 10.54 and 3.90 millimoles, respectively, are shown in Table III. The results were calculated for each warmup according to Eq. (1). The evaporative term varied from 6 percent to 19 percent of the C value while the paramagnetic salt heat capacity term varied between 4 percent and 10 percent. The vapor warming term was negligible. The standard deviations and relative weightings are shown in the table.

[11] See, for example, R. Berman and J. Poulter, Phil. Mag. 43, 1047 (1952).

INCIDENTAL TECHNICAL REMARKS

(a) Hand operation of the current reversing switch in the susceptibility apparatus primary circuit was not satisfactory. At each current reversal there is an interval when the magnetic field, due to the primary current, is low, the salt therefore is cooled, and some condensation takes place, resulting in a momentary surge of warm gas into the capsule. With manual operation the "off" interval and hence the magnitude of the surge are not reproducible, resulting in an erratic contribution to the average heat leak. The difficulty was solved by employing an electrical relay switch having a rapid and reproducible action, actuated every 30 seconds even during cooldown. With this arrangement the added heat leak came to several percent of the total at the highest primary current used but did not vary during a series of measurements and was therefore not a source of error.

(b) Use of exchange gas in the vacuum space was found to be highly undesirable. For an hour or so after beginning re-evacuation, temperature spurts of ~0.002° occurred on occasional warmups. The solution was to avoid breaking vacuum altogether.

(c) Removal of a large fraction of the liquid in the absence of heat exchange to the bath was accomplished by cycling a 10 kilogauss field several dozen times. The net irreversible heating was due to the effect noted in (a) above but on a grand scale. It reduced the removal time from several hours to several minutes.

(d) To protect the salt from dehydration the Dewar was kept cold for months at a time. A gradual rise in $\dot{Q}$ then occurred, amounting eventually to several times the calculated conduction heat leak. A small portion of the capsule was visible to room temperature radiation by way of the pumping port in block S. The rise in $\dot{Q}$ might have been due to an increase in emissivity of the capsule caused by gradual formation of ice on it. This explanation is consistent with the observation that the excess in $\dot{Q}$ was independent of bath or capsule temperature. For our purposes the added heat leak was actually an advantage since it helped mask out any remaining variation in conduction heat leak not taken care of by the Dewar tube insert. In the Method I measurements (without salt), this added heat leak was not present since the Dewar was allowed to warm up

TABLE III. Specific heats from Method III.

T(°K)	Run III-A	Run III-B	C	Std dev	Relative weight
0.369		0.742	0.742	±0.030	¼
0.417	0.740	0.733	0.737	0.020	½
0.463	0.749	0.744	0.747	0.021	¼

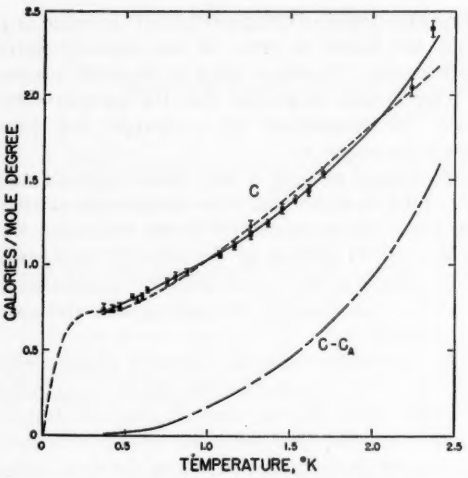

FIG. 4. The specific heat of saturated liquid He³. The points plotted are the experimental results of all three methods with the vertical bars indicating the standard deviations. The solid curve is the fitted empirical relation, Eq. (10). The dashed curve is calculated from $C=C_{spin}+0.88T$ and shows qualitatively how C can be extrapolated to 0°K without postulating a phase change. The lowest curve shows the calculated difference between true and apparent specific heat.

between runs and the vacuum pump trap then removed any water vapor which had leaked in.

DISCUSSION OF RESULTS

The specific heat data are plotted in Fig. 4. Methods I and II seem to join smoothly at 1°K. The data between 0.5° and 1.7°K fit the empirical equation

$$C=0.577+0.388T+0.0613T^3 \text{ (cal/mole deg)}, \quad (10)$$

with a mean deviation of 1.0 percent. The discussion of total errors in the various methods has shown that these errors are probably not much greater in magnitude than the scatter in the data and vary from 1.5 percent at 0.5°K to 2.0 percent at 1.7°K.

The two points above 2°K are less consistent with the equation. These points, as well as the data from Method III were only weighted between $\frac{1}{4}$ and $\frac{1}{2}$ as much as the other points in fitting the equation because they were obtained from fewer warmups. The weightings are shown in Tables I–III.

Our data are quite consistent with the equation published by Osborne, Abraham, and Weinstock[2] over the range of their measurements. The data of de Vries and Daunt[1] were obtained with much less liquid and show considerable scatter. Within their stated limits of accuracy of ±10 percent, their results are in agreement with the present work up to about 1.5°K but are 30 percent higher at 2.2°K.

Equation (10) is obviously unsatisfactory for extrapolation to zero degrees, since integration of C/T would yield a negatively infinite entropy at absolute zero. The terms of the equation have no theoretical significance. The equation may be integrated, however, to give entropy differences over the range of specific heat measurements. The resulting differences are combined with a value of the entropy at 0.5°K of 1.44 cal mole^{-1} deg^{-1} obtained from the thermodynamic vapor pressure equation and yield the entropies of the saturated liquid tabulated in Table IV and plotted in Fig. 5. A discussion of the derivation of the entropy at 0.5°K and comparisons with entropies derived solely from the vapor pressures will be deferred to a later paper. Entropy values reported by Weinstock, Abraham, and Osborne[2,12] are also plotted and are in good agreement.

NONSPIN ENTROPY AND SPECIFIC HEAT

The contribution to the entropy due to the disordering of the spins of the He³ nuclei has a limiting value of $R\ln 2$ or 1.377 cal/mole degree. As T approaches 0°K the nuclear spins become more and more ordered in anti-parallel pairs, and this entropy of spin disorder, S_{spin}, also decreases to zero. Pomeranchuk[13] has predicted that the spin ordering will begin to occur appreciably at temperatures of the order of 1°K due to the exchange effects in the liquid. The detailed variation of S_{spin} with T has been considered by Goldstein,[14] who establishes the relation

$$S_{spin}=[\chi(T)/\chi_0(T)]R\ln 2, \quad (11)$$

where $\chi(T)$ is the actual nuclear magnetic susceptibility and $\chi_0(T)$ is given by the limiting Curie-Langevin susceptibility law. Thus the measurements of χ by Fairbank, Ard, and Walters[15] can be used to calculate the spin entropy. Their Fig. 1 can be read as a plot of $S_{spin}/R\ln 2$. These spin entropies are given in Table IV and have been subtracted from calculated total entropy values to give the nonspin entropy, S_n.

TABLE IV. Total entropy, spin entropy, and nonspin entropy of saturated liquid He³ in cal/mole deg.

T(°K)	S	S_{spin}[a]	S_n
0.4	1.27	1.04	0.23
0.5	1.44	1.14	0.30
0.6	1.58	1.20	0.38
0.8	1.83	1.28	0.55
1.0	2.04	1.29	0.75
1.2	2.24	1.31	0.93
1.4	2.43	1.32	1.11
1.5	2.52	1.33	1.19
1.6	2.61	1.33	1.28
1.8	2.79	1.33	1.46
2.0	2.97	1.34	1.63
2.2	3.16	1.34	1.82
2.4	3.35	1.35	2.00
2.5	3.45		

[a] Spin entropies read from an enlarged copy of the figure of Fairbank, Ard, and Walters (see reference 15).

[12] Weinstock, Abraham, and Osborne, Phys. Rev. 89, 787 (1953).
[13] I. Pomeranchuk, J. Exptl. Theoret. Phys. (U.S.S.R.) 20, 919 (1950).
[14] L. Goldstein, Phys. Rev. 96, 1455 (1954).
[15] Fairbank, Ard, and Walters, Phys. Rev. 95, 566 (1954).

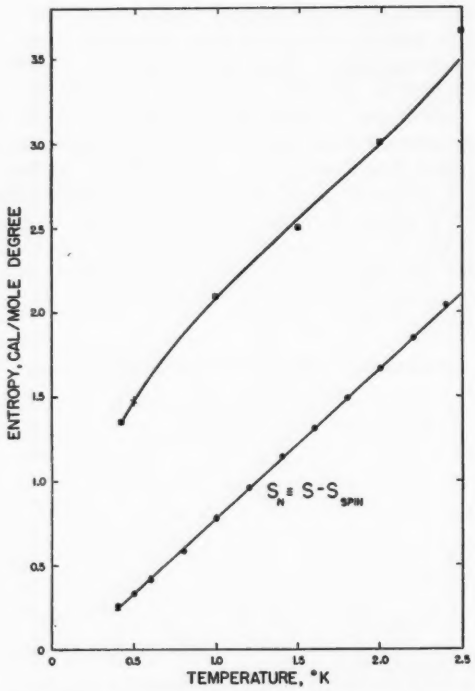

FIG. 5. Total entropy, S, and nonspin entropy, S_n, of saturated liquid He^3. Entropies given by Weinstock, Abraham, and Osborne are plotted as squares and are in reasonable agreement. The nonspin entropy is seen to be remarkably linear over its entire range and at 0.4°K is only 0.23 cal/mole deg. This value is an approximate upper limit to an entropy change which could be associated with a phase change in the liquid below 0.4°K.

The nonspin entropy points are plotted in Fig. 5. They are very nearly a straight line and fit the equation,

$$S_n = -0.12 + 0.88T \text{ (cal/mole deg)}, \qquad (12)$$

within ± 0.01 entropy unit. The negative constant either indicates the order of magnitude of error in the calculated absolute value of the entropy at 0.5°K or the deviation of S_n from a straight line below 0.4°. An error in the entropy scale may be introduced in any of several ways: by errors in the Kistemaker temperature scale or in the virial coefficients used, as well as by errors in the specific heat and vapor pressure measurements. These factors will be discussed in detail with respect to the thermodynamic vapor pressure relation. For example, recent measurements by Keller[16] indicate that the second virial coefficient is calculated[17] more closely by use of the Exp-6 potential instead of the Lennard-Jones potential. Use of these Exp-6 potential virial coefficients changes all the entropy values by about +0.07 unit, thus reducing the constant in Eq. (12) from −0.12 to −0.05. This value is just within the limits of error of the absolute entropy determination. Therefore there is no valid reason at the present time to assume that the nonspin entropy is not well represented by a straight line passing through the origin.

The nonspin entropy is only about 0.23 cal $mole^{-1}$ deg^{-1} at 0.4°K. Even if all this entropy were attributed to a phase change below 0.4°K, the transition would involve only 11 percent of the entropy change which Burton, Grayson Smith, and Wilhelm[18] associated with the He^4 λ transition by integrating over the specific heat anomaly.

Since the present work plus the early warmup experiments show that no second order phase occurs in liquid He^3 down to 0.4°K, we conclude that no transition comparable to the He^4 λ transition occurs in He^3 at any temperature. In fact, the analysis of the data indicates no reason whatsoever to postulate the existence of any phase change or specific heat anomaly below 0.4°K because all the entropy at this temperature is accounted for by S_{spin} and the simple linear S_n expression given above.

A reasonable extrapolation of the specific heat to temperatures below 0.4°K can be made by assuming that the proportionality of S_n to T persists in this range. The total specific heat is calculated as the sum of the specific heat of spin disorder, C_{spin}, and the nonspin specific heat, C_n. The latter, obtained by differentiating Eq. (12), is $C_n = 0.88T$. C_{spin} could be obtained by differentiating the experimental curve of χ/χ_0. Such differentiation is not warranted until the susceptibility data are better fitted by an empirical curve. Therefore we have used the values for C_{spin} calculated by Goldstein by differentiating the expression for χ/χ_0 for an ideal Fermi-Dirac gas of degeneracy temperature 0.45°K, which Fairbank has selected as the best fit to his data. The total specific heat, calculated according to the relation

$$C = C_{spin} + 0.88T, \qquad (13)$$

is shown as a dashed curve in Fig. 4. The extrapolation should be qualitatively correct, depending in detail on the analytical expressions for χ/χ_0 and C_n.

The remarkably high and apparently linear nonspin specific heat remains to be explained.

The authors gratefully acknowledge helpful discussions during the course of the present work with Dr. Louis Goldstein, Dr. J. E. Kilpatrick, and the entire staff of the Cryogenics Group, especially Dr. E. F. Hammel, Dr. W. E. Keller, Dr. E. C. Kerr, and Dr. H. S. Sommers.

[16] W. E. Keller (private communication).
[17] Kilpatrick, Keller, and Hammel, Phys. Rev. **97**, 9 (1955).
[18] Burton, Grayson Smith, and Wilhelm, *Phenomena at the Temperature of Liquid Helium* (Reinhold Publishing Corporation New York, 1940), p. 330.

Directional Breakdown in Alkali Halide Crystals*

M. E. Caspari†
Laboratory for Insulation Research, Massachusetts Institute of Technology, Cambridge, Massachusetts
(Received February 23, 1955)

The dc breakdown strength of sodium chloride, shown by von Hippel and Davisson to be independent of orientation at room temperature, also proves to be direction-independent at liquid nitrogen temperature. Experiments at room temperature reveal the existence of three types of breakdown paths: anodic, cathodic, and homogeneous field paths. Anodic paths are initiated by pre-breakdown discharges at the anode and are precisely orientated with respect to the crystallographic axes. Cathodic breakdown paths are initiated at point cathodes; their direction dependence differs from that of anodic paths. Finally, in strictly homogeneous fields the paths follow the direction of the field.

Measurements on various alkali halides between −160° and 325°C under strictly controlled field conditions confirm the findings of Davisson that the anodic path directions follow the sequence: random → [100] → [111] → [110] with increasing temperature. [111] paths, observed only in sodium salts, are usually accompanied by [110] or [100] paths. While the random → [100] transition takes place gradually over a temperature range of more than 100°C, the [100] → [110] transition in potassium and rubidium salts is sharp. With overvoltage this acuteness of the transition disappears, the path directions are shifted towards lower temperature forms and the temperature range of [111] paths in sodium salts is greatly extended. Mechanical deformation has little effect on the path directions. A phonon-Brillouin zone picture, as used by Offenbacher and Callen, but modified for inhomogeneous fields, is in good qualitative agreement with our observations. The electronic-Brillouin zone boundary and the crystalline potential may also influence the path directions.

INTRODUCTION

THE crystallographic orientation of breakdown paths was discovered independently and almost simultaneously by Inge and Walther,[1] von Hippel,[2] and Lass.[3] More recently, measurements at various temperatures were performed by Davisson[4] at this laboratory. Most of the experiments were carried out with point-plane electrode systems and pulsed voltages; von Hippel applied symmetrically arranged electrodes and homogeneous dc starting fields, and used semiconductor electrodes in order to prevent excessive destruction during breakdown.

The path directions in experiments with point-plane electrode systems proved to be dependent on the polarity of the needle, those from negative points being broader and less well defined than those from positive points. In the dc experiments of von Hippel[2] the paths progressed from the anode to the cathode, in NaCl at room temperature they were orientated in the [110] direction, but frequently changed into one of the four equivalent [111] directions close to the cathode, especially in thicker crystals and with overvoltage.

Davisson,[4] in tests at four different temperatures, found the breakdown paths confined to the three directions [100], [111], and [110] and traversing the sequence: random → [100] → [111] → [110] with increasing temperature for all alkali halide crystals, except lithium salts, where the picture is complicated by the appearance of "star patterns" (i.e., [*xxy*] paths).[5] The transition between path directions took place over a wide temperature range, and the transition temperatures were higher for crystals of lower lattice energies.

The orientation of the paths proved to be more rigorous at higher temperatures[4] and in crystals in which the radii of the constituent ions and their electronic polarizabilities were small.[2] Addition agents[6] influenced the path sequence as did an increase of temperature, while the application of overvoltages tended to shift the path sequence in the opposite direction.

Crystals of various bond structures and symmetry properties were studied by Inge and Walther,[1] von Hippel[2,7] and Lass[3] and the investigations extended by Kreft and Steinmetz,[8] and by Davisson,[4] who concluded that the possible path directions are dependent mainly on the macroscopic crystal symmetry and not on the bond type.

The existence of orientated surface paths was discovered by von Hippel[2,6] as well as the growth of dendrites orientated in definite crystallographic directions.[9]

A qualitative description of the formation of breakdown paths and the laws governing their directions was given by von Hippel[2,7,10] in his impact ionization theory. The nonexistence of a dependence of the breakdown strength on crystal orientation[11] was explained by the assumption that the breakdown strength is determined by the behavior of low-energy electrons too slow to discern lattice directions, while the breakdown paths

* Sponsored by the Office of Naval Research, the Army Signal Corps, and the Air Force.

† Present address: Department of Physics, University of Pennsylvania, Philadelphia, Pennsylvania.

[1] L. Inge and A. Walther, Z. Physik **64**, 830 (1930); **71**, 627 (1931).

[2] A. von Hippel, Z. Physik **67**, 707 (1931); **68**, 309 (1931); **75**, 145 (1932); Z. Elektrochem. **39**, 506 (1933).

[3] J. Lass, Z. Physik **69**, 313 (1931).

[4] J. W. Davisson, Phys. Rev. **70**, 685 (1946); **73**, 1194 (1948).

[5] According to a recent note, J. W. Davisson [Phys. Rev. **91**, 228 (1953)] found also unstable star patterns of the type [*xxy*] in several other alkali halide crystals at certain temperatures.

[6] A. von Hippel, Z. Physik **88**, 358 (1934).

[7] A. von Hippel, Ergeb. exakt. Naturwiss. **14**, 79 (1935); J. Appl. Phys. **8**, 815 (1937).

[8] F. Kreft and H. Steinmetz, Z. angew. Mineral. **1**, 144 (1938).

[9] A. von Hippel, Z. Physik **98**, 580 (1936).

[10] A. von Hippel, Trans. Faraday Soc. **42A**, 78 (1946).

[11] A. von Hippel, Z. Physik **75**, 161 (1932); A. von Hippel and J. W. Davisson, Phys. Rev. **57**, 156 (1940).

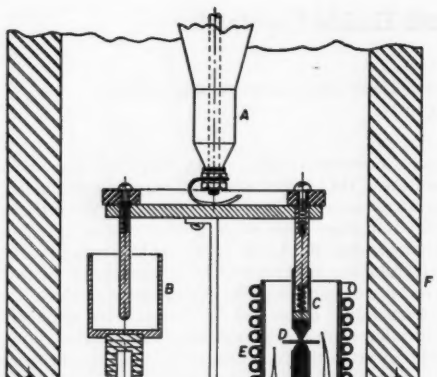

FIG. 1. Sample holder for breakdown tests under nitrogen pressure. (*A*) High voltage bushing, (*B*) variable balancing capacitor, (*C*) high-voltage electrode, (*D*) crystal, (*E*) cooling coil or heating element, (*F*) pressure vessel, (*G*) low-voltage lead, (*H*) thermocouple, and (*I*) pressure inlet and outlet.

are caused by electrons already accelerated to high velocities. The breakdown strength is reached when excess electrons can be accelerated by the applied field after overcoming the friction barrier of the lattice vibrations; impact ionization, avalanche formation and breakdown result. The directions laws were deduced from the assumption that breakdown takes place in those directions in which the electrons experience least friction. The friction losses are determined by the potential structure of the lattice and the scattering probability due to the excitation of lattice vibrations. In alkali halide crystals acceleration in the [110] direction is favored by the former mechanism and acceleration in the [111] direction by the latter. Von Hippel concluded, therefore, that [110] paths will be favored until the field is strong enough to allow the electrons to overcome the potential barriers of the lattice. In the latter case, [111] paths should be observed. A transition to [111] paths, therefore, is likely to occur near the cathode during the development of the breakdown because very high field gradients build up at the tip of the positive space charge channel as it approaches the cathode.

Based on von Hippel's qualitative concepts, Offenbacher and Callen[12] carried out a semiquantitative calculation of the laws governing direction breakdown in alkali halide crystals. The directional effects are accounted for by the anisotropic scattering, which an electron of high energy experiences in a polar lattice because of the anisotropic structure of the phonon-Brillouin zone, under the assumption that Umklapp processes are prohibited in the interactions of electrons with the polar lattice vibrations. The theory was able to explain semiquantitatively the path sequence with increasing temperature and the effect of addition agents or overvoltages on the path directions in the alkali halide crystals (with the exception of the lithium salts).

The present paper deals with a series of new experiments designed to establish the breakdown-path directions in some alkali halide crystals over a wide temperature range under controlled and, if possible, known field conditions, in order to draw more precise conclusions about the mechanism of breakdown-path formation. The independence of the breakdown field strength on the direction of the applied field, as established by von Hippel and Davisson[11] and confirmed by Vorobiev[13] on NaCl at room temperature, is of considerable importance for the theoretical explanation. The present study, therefore, starts by checking this fact once more and extending measurements to liquid nitrogen temperature.

I. DEPENDENCE OF BREAKDOWN STRENGTH ON FIELD ORIENTATION

Experimental Procedures

Breakdown strength measurements were performed on NaCl crystals under homogeneous field conditions at room and at liquid nitrogen temperatures; the field was applied in the [100] or the [110] direction. The crystal

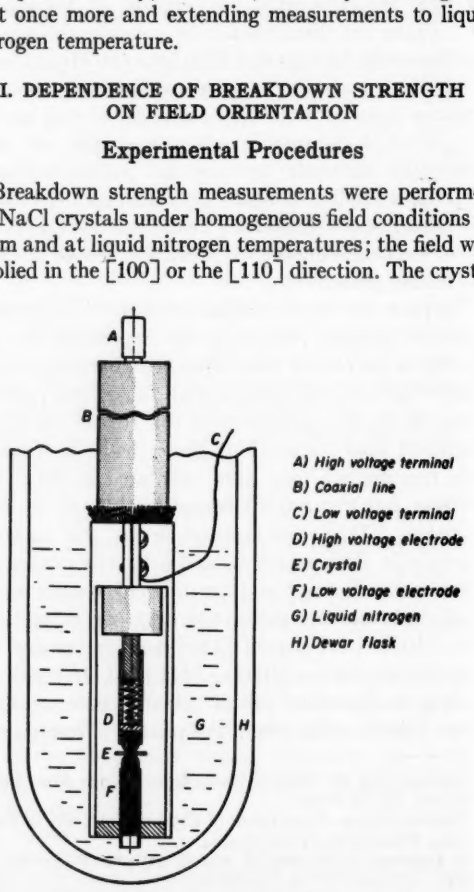

FIG. 2. Sample holder for breakdown tests at liquid nitrogen temperature.

[12] E. Offenbacher and H. B. Callen, Phys. Rev. **90**, 401 (1953).

[13] A. A. Vorobiev, Doklady Akad. Nauk S.S.S.R. **86**, 681 (1952).

plates (<0.25 mm thick and *ca* 1 cm² in area) were cut from the same NaCl single crystal (Harshaw Chemical Company) perpendicular to the [100] or [110] direction, ground to the correct thickness, and polished on soft silk moistened with NaCl solution.

Evaporated electrodes with diffuse boundaries were prepared in order to prevent prebreakdown discharges from the edges of the electrodes.[14] With this technique satisfactory dc breakdown tests can be performed under homogeneous field conditions on flat samples without resorting to recessed cavities.[15] For this purpose, a circular gold spot (*ca* 5 mm diam) was evaporated onto the center of the crystal sample in such a manner that the thickness of the gold layer was uniform at the center (*ca* 1 mm diam), but decreased rapidly towards the edge. In order to eliminate surface discharges from the edge of this diffuse gold layer, a thin semiconducting layer, produced by decomposition of $SnCl_4$, was applied to the crystal surface. The thickness of this layer was so adjusted that the conductivity was large compared to that of the crystal, but small enough to prevent destruction. An overall surface resistance of 10^{10} to 10^{11} ohms proved satisfactory for this purpose. The electrode conductivity thus varied from full metallic conduction at the center to a very low value near the edges of the sample. Breakdown occurred near the center of the gold spot and, as far as could be ascertained, without surface discharges.

The crystal with the evaporated electrodes was clamped between two aligned electrodes by light spring pressure. The experiments at room temperature were carried out in a bomb at 50 atmos of dry nitrogen in order to prevent discharges in the sample holder (Fig. 1). The high-voltage lead was introduced into the bomb through a Pyrex glass bushing. This sample holder served also over a wider temperature range; the sample could be heated by an electric heater or cooled by passing liquid nitrogen through a coil of copper tubing surrounding the crystal. At liquid nitrogen temperature the holder of Fig. 2 was used in a Dewar flask filled with liquid nitrogen.

The dc high-voltage source was a variable power supply consisting of a 50-kv transformer, half-wave rectifier, filter and protective resistor of 10 megohms. A small neon lamp, shunting a 1-megohm resistor and placed between the low-voltage electrode and ground served as indicator of breakdown.

TABLE I. Effect of direction of the applied field on the breakdown field strength of NaCl.

Temperature °C	Direction of applied field	Number of specimens	Breakdown strength Mv/cm Average	Maximum	Minimum	Standard deviation
23	[100]	5	1.46	1.54	1.35	0.064
23	[110]	5	1.42	1.51	1.38	0.048
−195	[100]	5	0.75	0.78	0.72	0.020
−195	[110]	5	0.74	0.83	0.68	0.055

[14] Y. Saito, J. Inst. Elec. Engrs. Japan **56**, 1036 (1936).
[15] A. von Hippel and R. S. Alger, Phys. Rev. **76**, 127 (1949).

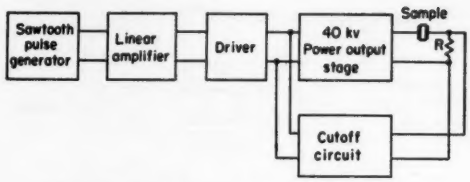

FIG. 3. Block diagram of electrical system.

Results

The results are summarized in Table I. No significant direction difference in the magnitude of the breakdown strength of NaCl is observed, either at room or at liquid nitrogen temperatures. The values of the breakdown strength are in good agreement with those obtained by von Hippel and Alger.[15] The maximum deviation, *ca* ±7.5 percent, is not large for this type of experiment; *ca* 2.5 percent of this may be due to random errors in the voltage and thickness determination.

II. MEASUREMENT OF BREAKDOWN-PATH DIRECTIONS UNDER CONTROLLED FIELD CONDITIONS

Crystal Preparation and Sample Holder

NaCl, LiF, and KBr single crystals were obtained from the Harshaw Chemical Company; RbI, RbCl, and NaBr were grown from the melt in this laboratory by A. Smakula and V. Sils. Most of the experiments were carried out on (100) crystal samples. Crystal sections thinner than 0.15 mm, as well as (110) sections not obtainable by cleavage, were prepared by grinding and polishing.

The sample holder was the pressure bomb of Fig. 1. The temperature in this bomb could be varied between −160° and 500°C at atmospheric pressure; at 50 atmos, only 325°C could be reached.

Electrical Equipment

The breakdown paths were produced by controlled-voltage pulses, which greatly facilitate breakdown-path formation and reduce the effect of field distortoin by migrating ions. A 40-kv peak voltage saw-tooth pulse generator (Fig. 3), designed by D. A. Powers of this laboratory, incorporates a voltage cut-off device triggered by the breakdown, so that overvoltages can be avoided. This pulse generator produces single pulses of approximately 50-μsec rise time and ½-μsec decay time by amplifying a positive low-voltage pulse. The resulting high-voltage negative pulse is applied to the high-voltage electrode of the sample and the low-voltage electrode connected to ground through a resistor R. The value of R must be so low that the voltage developed by the charging current is insufficient to fire

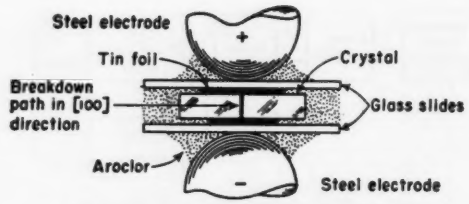

FIG. 4. Electrode arrangement for production of breakdown paths in homogeneous fields.

the thyratron; 12 000 ohms was found suitable. To make sure that the conduction current at breakdown exceeds the charging current by a considerable amount, a variable air capacitor in the sample holder could balance out the charging current; in general, this proved unnecessary.

The breakdown strength could be estimated by gradually increasing the plate voltage on the power amplifier until breakdown occurred and the thyratron fired. The errors in this type of measurement were not larger than 10 percent; for more accurate measurements the pulse shape could be photographed on a calibrated oscillograph screen.

Measurement of Breakdown-Path Directions

The breakdown paths were viewed under a stereomicroscope (12× magnification) in a dark field under uniform oblique illumination provided by a circular convex mirror surrounding the sample. The path direction was measured by determining the inclination and azimuthal angles (see Davisson[16]); the cleaved [100] edges of the crystal served as datum lines.

Room Temperature Experiments on Direction Breakdown in NaCl and KBr

In homogeneous field experiments the current at breakdown has to be limited to prevent excessive destruction.[2] This precludes the use of evaporated metal electrodes; the current was limited in our experiments by placing the crystal between two glass slides or by semiconducting electrodes.

For the first of these techniques, very thin crystal sections of KBr or NaCl were sandwiched between cover glasses (*ca* 0.1 mm thick) (Fig. 4); the breakdown strength of the two glass slides was larger than that of the crystal. The sandwich was placed between two ball-bearing electrodes and tin foil was placed on the crystal surfaces between sample and slides to insure that the boundaries remained equipotential surfaces. This was found necessary in order to prevent breakdown through the glass in the highly inhomogeneous field caused by breakdown through the crystal. The tinfoil electrode at the anodic side was made considerably larger than its opposite in order to reduce the danger of edge breakdown. Prebreakdown discharges along the surfaces of the crystal and the slides were prevented by a thin layer of Aroclor 1254 (Monsanto Chemical Company) between crystal and glass surfaces. The steel electrodes were also surrounded by Aroclor and the tests carried out in an atmosphere of dry nitrogen (50 atmos).

The presence or absence of prebreakdown discharges could be ascertained in two ways. The breakdown voltage is always much lower when such discharges occur, and the discharge could be photographed directly by placing a piece of film is contact with the crystal surface (Fig. 5).

The breakdown voltage could be obtained by carrying out the experiments without the tin foil. In this case, breakdown through the sample caused breakdown through the glass slides, and currents high enough for detection. The breakdown field strength of the crystal was calculated from the thicknesses and dielectric constants of crystal and glass slides under the assumption that conductivities could be neglected for pulses of such short duration. The onset of breakdown could not be detected with the tin foil; hence overvoltages were, in this case, unavoidable; furthermore, very thin crystal sections were required (<0.1 mm for NaCl).

The technique of using semiconducting electrodes[5] eliminates this difficulty and has the further advantage that inhomogeneous, as well as homogeneous fields, can be investigated. For room temperature experiments we used Ferramic I (General Ceramics Company), cut in the shape of planes, hemispheres (*ca* $\frac{1}{4}$-in. diam), or needles so that both homogeneous and inhomogeneous fields could be investigated. The tip of the needles was rather blunt (approximately a hemisphere of 0.1-mm radius), because sharper points were liable to damage the crystal surface and cause prebreakdown discharges around the point. The resistance of the electrodes varied between 5×10^6 and 5×10^7 ohms, depending on the electrode geometry employed. To initiate breakdown by prebreakdown discharges at the anode, the experiments could be made under nitrogen pressure in the absence of Aroclor or with Aroclor in the absence of pressure.

Successive saw-tooth pulses of *ca* 50-μsec duration and increasing peak voltage were applied until breakdown was indicated by the firing of the hydrogen thyratron. Alternatively, breakdown was achieved by a single pulse, overvoltage being avoided by the thyratron cut-off

TABLE II. The breakdown strength of KBr and NaCl at room temperature for various electrode arrangements.

Crystal	Breakdown strength Mv/cm: Evaporated gold electrodes[a]	Liquid electrodes (KBr solution)[a]	Crystal between glass slides (approximate values)
KBr	0.55	0.84	1.35
NaCl	1.46	1.65	1.75

[a] See reference 15.

[16] J. W. Davisson, Ph.D. Thesis, Massachusetts Institute of Technology, 1943 (unpublished).

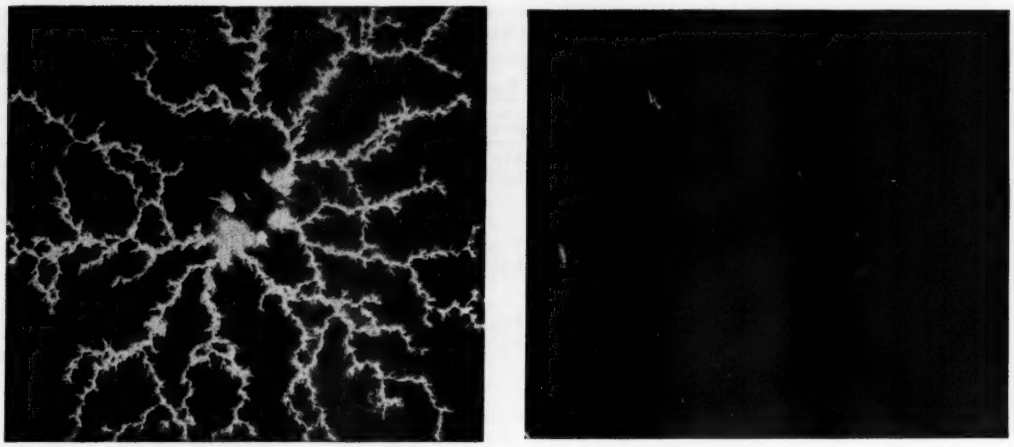

(a) (b)

FIG. 5. Suppression of surface discharges by Aroclor: (a) without Aroclor; (b) with Aroclor.

device. Breakdown voltage and path directions proved not significantly different for the two types of experiment. Samples were checked for the presence of partial, very fine breakdown paths that might not fire the thyratron; the crystals were so thin that no such partial breakdown paths occurred.

III. RESULTS

Experiments Between Glass Slides

The breakdown paths in both KBr and NaCl proved to be always orientated in the direction of the applied field (i.e., in the [100] direction in our experiment). This is the principal direction for KBr at room temperature, while in NaCl at room temperature [110] and [111] paths were observed in all previous experiments. The appearance of these [100] paths in KBr and NaCl was identical. Breakdown took place straight through the crystal, accompanied by slight cleavage on the surfaces.

The breakdown strengths of KBr and NaCl between glass slides are compared in Table II with those of von Hippel and Alger[15] obtained with various electrode systems. It seems clear that the breakdown strength obtained with the glass-slide technique is higher than with other electrode systems. This is especially striking in KBr for which the breakdown voltage was more than 100 percent higher than with metal electrodes. Since the insertion of the crystal between glass slides greatly reduces the field emission from the cathode, the results seem to confirm that the breakdown strength as usually measured is lowered by electron emission and space charge, as pointed out by von Hippel and Alger.[15]

Experiments with Ferrite Electrodes

The results for NaCl are shown in Table III; for KBr no particularly interesting results were obtained because the [100] direction is here dominant for both anodic and cathodic paths.

For (100) sections and homogeneous starting fields the breakdown proceeded straight through the thickness of the crystal, giving the appearance of paths orientated in the [100] direction, in agreement with the tests between glass slides. The orientation of the paths, however, was often not very definite. In (110) sections there was definite indication of some breakdown paths progressing through the crystal in [110] directions, but there were also [100] paths, especially in thicker crystals. These [100] paths were accompanied by relatively heavy destruction and appeared to originate from the cathode. It must, therefore, be concluded that the breakdown paths under homogeneous field conditions are at least in part governed by the direction of the applied field, but that [100] cathodic paths are also present under these conditions.

The point-plane electrode system with the needle as anode, but without prebreakdown discharges, gave essentially the same results as homogeneous starting fields. With cathodic points, however, the paths were definitely orientated in the [100] direction and accompanied by much destruction and cleavage, especially in (110) crystal sections.

When prebreakdown discharges were not suppressed, the characteristic breakdown paths obtained by von Hippel[2] appeared. The paths progressed from the anode to the cathode and were orientated in the [110] or [111] directions. This was true for all electrode geometries tried except for the point-plane system with the needle as cathode. In this case [100] directions were observed, even with prebreakdown discharges. The destruction caused by these cathodic discharges was always heavier than that caused by the anodic paths.

The [111] paths were favored by high breakdown voltages. Thus, in experiments carried out with dry

TABLE III. Dependence of the breakdown path directions on electrode shapes and immersion media for NaCl at room temperature (thickness of sections between 0.15 and 1 mm).

Insulating medium	Shape of ferrite electrodes: Anode	Cathode	Type of breakdown field		Breakdown field strength	Direction of breakdown paths: (100) crystal sections	(110) crystal sections	Comments
Aroclor + 50 atmos of dry nitrogen	Sphere	Sphere	Homogeneous starting field	No prebreakdown discharges	Very high	[100] at times somewhat random	Both [110] and [100]	Breakdown in part governed by applied field, but [100] paths also present especially in thicker crystals. (Cathodic paths)
	Sphere	Plane						
	Point	Plane	Inhomogeneous starting field. Anodic point		Very high	[100] at times somewhat random	[110] but also some [100]	
	Plane	Point	Inhomogeneous starting field. Cathodic point		Fairly high	[100]	[100]	Cathodic paths in [100] direction. Wavy paths; heavy destruction.
Aroclor alone	Sphere	Sphere	Inhomogeneous starting field. Breakdown initiated by discharges at anode		Rather low	Mostly [111] but also some [110]	Mostly [111] but also some [110]	Somewhat wavy, but narrow breakdown paths. Breakdown voltage higher than with nitrogen pressure only.
	Sphere	Plane						
	Point	Plane						
	Plane	Point	Inhomogeneous starting field. Breakdown initiated from cathode point		Fairly high	[100]	[100]	Cathodic paths
Nitrogen pressure alone (~50 atmos)	Sphere	Sphere	Inhomogeneous starting field. Breakdown initiated by discharge at anode		Very low	[110]	[110]	Very sharp and straight paths
	Sphere	Plane						
	Point	Plane						
	Plane	Point	Inhomogeneous starting field. Breakdown initiated from cathode point		Fairly high	[100]	[100]	Cathodic paths

nitrogen alone (50 atmos) as embedding medium, the breakdown voltage was very low and only [110] paths were observed. With Aroclor as ambient medium, but without nitrogen pressure, the breakdown voltage was considerably higher and [111] paths appeared, especially in thicker crystal sections. When the thyratron cut-off mechanism was not used and overvoltages therefore not avoided, the appearance of [111] paths was favored, especially near the cathode. The breakdown paths produced by a very fine needle as anode also favored the [111] direction, when prebreakdown discharges were reasonably well suppressed. In this case, however, destruction of the crystal surface was unavoidable.

Each breakdown test would normally result only in the formation of a single breakdown path; sometimes, however, as many as three or four paths appeared. When these paths were initiated by prebreakdown discharges at the anode by the use of dry nitrogen at 50 atmos without another embedding medium, their origins were found to lie on the circumference of a circle on the surface of the crystal, the center of which coincided with that of the electrode (Fig. 6). The radius of this circle was larger for spherical electrodes than for point electrodes and decreased with increasing nitrogen pressure. A path would progress in one of the four equivalent [110] directions favored by the field of the main electrode, and changed frequently towards the cathode into another of these [110] directions and rarely into a [111] direction. For Aroclor without pressure, the anodic breakdown paths proceeded mostly in the [111] direction from points very close to the anode. The prebreakdown discharges were caused mainly by faulty contact or the presence of bubbles. With a very fine needle as anode, the breakdown originated from the border of the destruction caused by the needle, but never from the needle itself, even when prebreakdown discharges were suppressed. Cathodic discharges and discharges in homogeneous fields originated directly from the electrodes.

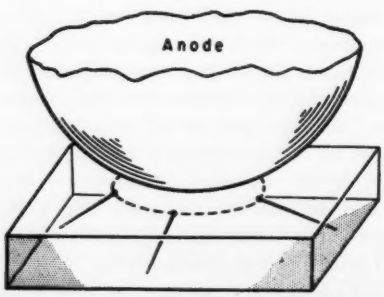

FIG. 6. Origin of breakdown paths.

These results apply to sample thicknesses >0.1 mm. In thin sections (<0.1 mm) breakdown was found to take place in the direction of the applied field irre-

spective of the electrode system or immersion medium, except for the point-plane electrode system with the needle as cathode. Here definite [100] paths were observed, originating from the cathode. No signs of prebreakdown discharges were detected in experiments with such thin sections of NaCl at room temperature.

The breakdown field strength under these various conditions varied strikingly. With homogeneous starting fields (and also with the point-plane system with the needle as anode, when prebreakdown discharges were avoided) the breakdown strength was high (somewhat larger than that observed with homogeneous fields and metal electrodes). The cathodic point-plane system, irrespective of the employment of adequate spark suppressants, also gave relatively high breakdown strengths, but lower than those with homogeneous fields. For breakdown initiated by anodic prebreakdown discharges, the breakdown voltage became low.

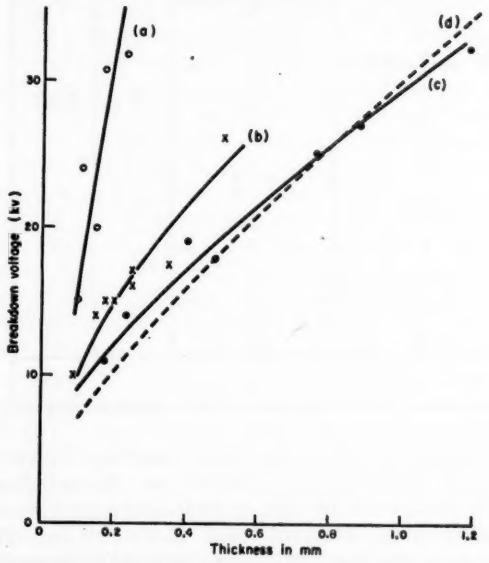

FIG. 7. Breakdown voltage of NaCl at room temperature as a function of the sample thickness: (*a*) Homogeneous electrode system (no prebreakdown discharges), (*b*) cathodic point-plane electrode system, (*c*) anodic breakdown with prebreakdown discharges, (*d*) theoretical calculation of Curve *c* based on the assumption that the breakdown voltage of the crystal is determined by the breakdown voltage of the insulating medium.

Further information is gained by plotting the breakdown voltage of NaCl as a function of sample thickness for these various types of starting fields (Fig. 7). A linear relationship exists for homogeneous fields (Curve *a*): deviations from linearity are observed for the cathodic point-plane electrode system (Curve *b*), accounted for by the inhomogeneity of the applied field. With a sphere-plane electrode system (sphere as anode) and dry nitrogen at 50 atmos as insulating medium, the characteristic is about linear at greater thicknesses (Curve *c*), but the gradient is much lower than for homogeneous fields. This curve suggests that the observed breakdown voltage in this case is the voltage needed to produce breakdown through the nitrogen.

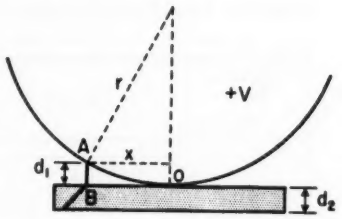

FIG. 8. Geometry of the sphere-plane electrode system.

The situation may be roughly analyzed as follows (Fig. 8): if V is the applied voltage and V_1 the voltage drop across the nitrogen at a distance x from the center of the spherical anode, this voltage drop across AB (neglecting curvature of the field lines) becomes

$$V_1=\frac{Vd_1}{d_1+(\epsilon_1'/\epsilon_2')d_2}, \tag{1}$$

where ϵ_1' and ϵ_2' are the dielectric constants of nitrogen and NaCl, respectively. Furthermore,

$$d_1=r-(r^2-x^2)^{\frac{1}{2}} \tag{2}$$

($r=\frac{1}{8}$ in. in our experiments).

If we approximate the breakdown voltage *vs* d_1 curve for nitrogen by a straight line as

$$V_{1b}=ad_1+V_0, \tag{3}$$

(with a and V_0 constants determined below), breakdown through the nitrogen at a given sample thickness d_2 will occur when the applied voltage V is so large that V_1 of Eq. (1) becomes tangent to this straight line (Fig. 9). The value V_b thus established represents the apparent breakdown voltage of the crystal, while d_{1b} determines the distance x from the center of the electrode at which breakdown will take place.

Hence breakdown occurs when the two real roots of the equation

$$Vd_1/(d_1+b)=ad_1+V_0, \tag{4}$$

coincide, that is, for

$$V^2-2(ab+V_0)V+(ab-V_0)^2=0, \tag{5}$$

where $b=(\epsilon_1'/\epsilon_2')d_2=\frac{1}{6}d_2$.

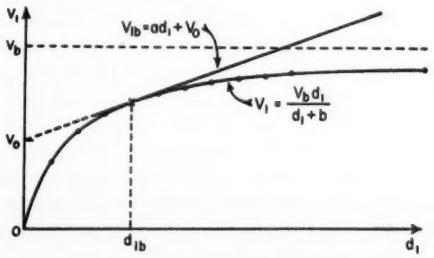

FIG. 9. Calculation of breakdown voltage.

TABLE IV. Temperature dependence of the breakdown path directions in some alkali halide crystals. $R \equiv$ random path, i.e., without orientation.

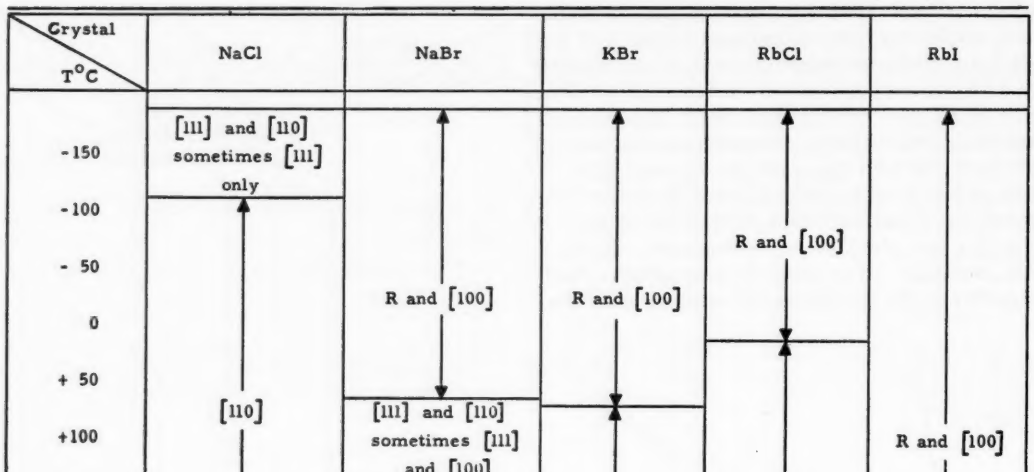

From Eq. (5)

$$V_b = (ab+V_0)+(4abV_0)^{\frac{1}{2}} = \tfrac{1}{6}ad_2+(\tfrac{2}{3}aV_0)^{\frac{1}{2}}(d_2)^{\frac{1}{2}}+V_0; \quad (6)$$

the thickness of the nitrogen layer at the place of breakdown is

$$d_{1b} = [V-(ab+V_0)]/2a = (V_0/6a)^{\frac{1}{2}}d_2^{\frac{1}{2}}. \quad (7)$$

The curve given by Eq. (6) can be fitted quite well to the experimental curve by choosing $a = 1\times10^6$ v/cm and $V_0 = 2$ kv (Fig. 7, Curve *d*). The value for V_0 was obtained by extrapolation of Posin's[17] data. Unfortunately, no experimental data are presently available for the slope factor a of Eq. (3), since the measurements of Posin refer to low pressures while those of Trump[18] apply to large gap widths. From Trump's data at gap widths down to $\frac{1}{8}$ in. and 600 psi, $a \simeq 8\times10^5$ v/cm; while from Posin's measurements at values of pd_1 from 100 to 300 [mm Hg×cm], a varies between 2×10^6 and 1.5×10^6 v/cm. Paschen's Law does not hold for the large pressures used in our experiments,[18] but a value of $a \simeq 10^6$ v/cm does not seem to be unreasonable. As a check, the distance x of the origin of the breakdown paths from the center of the anode can be calculated from Eqs. (7) and (2) and compared with the experimentally determined value (see Fig. 6). For a crystal of thickness $d_2 = 2\times10^{-2}$ cm, the calculated distance is 4.18×10^{-2} cm, in good agreement with the experimentally observed value of 4×10^{-2} cm. The interpretation that breakdown is initiated by prebreakdown discharges through the nitrogen under the above conditions, seems therefore substantiated.

[17] D. Q. Posin, Phys. Rev. **50**, 650 (1936).
[18] Trump, Cloud, Mann, and Hanson, Elec. Eng. **69**, 961 (1950).

Temperature Dependence of the Anodic Breakdown Paths

It was shown in the experiments on NaCl at room temperature that the anodic breakdown paths exhibiting the characteristic [110] or [111] directions could be produced only in the highly inhomogeneous field arising from prebreakdown discharges. The experiments on the temperature dependence of the anodic breakdown paths were, therefore, carried out in dry nitrogen as the embedding medium (600 psi at room temperature). Although the actual breakdown field remained unknown, the field conditions were more reproducible than when using different immersion media at various temperatures. Above 325°C the nitrogen density had to be reduced and the data are not strictly comparable with those of lower temperatures. The experiments were performed on (100) plates (thickness *ca* 0.25 mm) of NaCl, NaBr, KBr, RbCl, and RbI, and sometimes

checked on (110) crystal cuts. The composition of the ferrite electrodes (polished spherical anode and plane cathode) was changed for the different temperature ranges to provide adequate current limitation.

The results (Table IV) agree in the path sequence with those of Davisson's.[4] Only paths in the three basic directions occurred; [111] paths were confined to sodium salts. With increasing temperature the directions were found to change from random → [100] → [110] in potassium and rubidium salts, and from random → [100] → [111] → [110] in sodium salts.

Our results differ from Davisson's as follows: The path direction in KBr was definitely [110] at temperatures above 80°C, while Davisson[4] did not observe [110] paths in these crystals below 450°C. In addition, the [100] → [110] transition in KBr and RbCl was sharp; the transition temperature could be fixed to within ±5°C, whereas in Davisson's experiments[4] it extended sometimes over several hundred degrees.

In sodium salts the transition is complicated by the appearance of [111] paths. These were usually accompanied by [110] and, in some cases, [100] paths, so that a definite temperature for the [111] → [110] or the [100] → [110] transition could not be determined. In rare cases, only [111] paths were observed in NaCl between −150° and −160°C. In NaBr the temperature range of the [111] paths was approximately 50°C; above 120°, only [110] paths and below 65° only [100] paths were evident. In NaCl, above −140° only [110] paths appeared; [111] paths were observed below −140° and no [100] paths appeared down to −160°, the limit of our experiment. In KBr the [100] → [110] transition temperature was located at *ca* 70°, in RbCl at *ca* 20°C. Both path directions could be observed in a narrow range of about 10° around the transition temperature. The absolute value of the transition temperature changed by as much as 15° to 20° for crystal sections from different crystals or sometimes even different parts of the same crystal. No [110] paths were detected in RbI below 325°C.

It was difficult to distinguish between random and [100] paths, even when the measurements were performed on (110) crystal sections. Close to the transition temperatures, the paths were rigorously orientated in the [100] direction. As the temperature was lowered, the orientation became gradually less definite. It was therefore impossible to determine a temperature for a random → [100] transition. As the randomness of the paths became more apparent at lower temperatures, the origin of the paths moved closer to the point of contact between anode and crystal, the breakdown-voltage-thickness characteristic became more linear and the breakdown field strength approached the value measured with homogeneous fields.

Effect of Overvoltages on the Path Directions

Overvoltages could be produced by carrying out the experiments with Aroclor or silicone oil as embedding media, but without pressure. In this way breakdown was still initiated by prebreakdown discharges, but at higher voltages. In addition, the discharge through the medium was confined to narrower channels, producing high concentrations of space charge at the anode surface of the crystal and, hence, large field gradients in its immediate neighborhood. The effect of such overvoltages was to move the onset of the [110] paths to higher temperatures and the sharp [100] → [110] transition temperature in KBr and RbCl disappeared. Both paths coexisted over a temperature range of more than 150°C. This is probably due to the fact that the breakdown field strength varied from test to test, since the initiation of the predischarge depended on air bubbles in the medium or insufficient contact between medium and electrode. Also the transition temperature for [111] paths in NaCl and NaBr was shifted upwards, and the temperature range in which [111] paths could be produced greatly increased. [111] and [110] paths in NaCl were observed at temperatures as high as 150° to 200°C and [110] paths frequently changed into the [111] direction towards the cathode. At −192°C, with liquid nitrogen as insulating medium, [100] paths were found in NaCl.

Smaller overvoltages could be produced by operating the high-voltage equipment without cut-off device, but otherwise carrying out the test under nitrogen pressure. In this case, the sharp [100] → [110] transition in KBr and RbCl persisted, but the transition temperatures increased by about +25°C. Also [111] paths in conjunction with [110] paths appeared up to +30°C in NaCl.

The results of these tests indicate that overvoltages of varying magnitude may be responsible for the absence of sharp transition temperatures in Davisson's measurements[4] and for the discrepancies between his and our observations.

Effect of Mechanical Deformation on the Direction of the Breakdown Paths

Experiments were performed on deformed crystals to test the influence of strains, dislocations and glides on the direction and appearance of the breakdown paths. The crystals were deformed by bending or prismatic punching. In the former method a thin crystal section was heated to about 300°C (above the brittle point) and then bent. In the latter method a blunt ferrite needle was pressed into the crystal at about 300°C. At low needle pressures, the presence of strains could be detected under polarized light; at higher pressures the characteristic glide patterns, as observed by Smakula and Klein,[19] appeared. The blunt needle used for producing the deformation served as the anode in the breakdown experiment.

The breakdown paths in deformed crystals were almost identical with those in undeformed crystals. The

[19] A. Smakula and M. W. Klein, Phys. Rev. 84, 1043 (1951).

paths were, in general, not quite as sharp in deformed crystals, but the directions were still very well defined. Only under very strong deformation (accompanied by much destruction in the form of glides) would the paths lose their precise direction. The temperature dependence of the breakdown paths was also not appreciably influenced by deformation through bending. The [100] → [110] transition temperature of bent KBr crystals appeared to be slightly lower than that of undeformed crystals.

It can be concluded that the influence of mechanical deformation on the breakdown paths is not marked and that mechanical processes are not primarily responsible for the formation of breakdown paths.[20] Also, the speed of the breakdown process, which exceeds the velocity of sound, makes a mechanical explanation most unlikely.

Cathodic Breakdown Paths

The breakdown paths which originated from a cathodic needle in a point-plane electrode system were orientated predominantly in the [100] direction in all crystals tested (NaCl, NaBr, KBr, RbCl, RbI) irrespective of temperature. The destruction caused by these breakdown paths was always heavier than that of anodic paths, and the exact orientation often difficult to determine, especially at lower temperatures. In thin samples the appearance of the cathodic paths often strongly resembled that of paths produced with homogeneous fields.

Star Patterns in LiF

Preliminary experiments on LiF verified the existence of star patterns as observed by Davisson.[4] Star patterns could also be produced with the cathodic point-plane electrode system. Star patterns consisting of certain [*xxy*] paths were produced with a negative needle at a somewhat lower temperature than that with the positive needle. Since these results agreed closely with the detailed measurements of Davisson, the investigation of LiF was not pursued further. Contrary to the recent observations of Davisson,[5] however, no star patterns were observed at any temperature in NaCl, NaBr, KBr, RbCl, and RbI.

IV. DISCUSSION

Formation of Breakdown Paths

The results on NaCl at room temperature indicate the existence of three types of breakdown paths: anodic, cathodic, and homogeneous field paths.

The formation of anodic breakdown paths appears to be preceded by prebreakdown discharges, either through the medium surrounding the electrodes or along the surface of the crystal. The apparent breakdown voltage of the crystal, as measured for NaCl (Fig. 7), is governed by the breakdown voltage of the nitrogen insulation. The breakdown field strength is, therefore, low compared with that obtained with homogeneous fields and the anodic breakdown paths are, in consequence, initiated by highly inhomogeneous fields. The paths produced in this way are rigorously orientated with respect to the crystallographic structure and show the characteristic temperature dependence of the path directions.

The effect of these prebreakdown discharges is a twofold one: the establishment of very inhomogeneous starting fields (the tip of the prebreakdown spark forms essentially a point electrode in parallel with the anode) and the creation of photoelectrons inside the crystal. Impact ionization, avalanche formation and breakdown can occur only if sufficient electrons are available in the small volume around this space-charge anode where the field is strong enough to accelerate electrons across the friction barrier of the lattice vibrations.[2]

The importance of free electrons in the crystal for the formation of anodic breakdown paths is clearly seen in the old experiments of Inge and Walther.[1] Here the crystal sections were so thick that a single voltage pulse would produce only partial breakdown: the length of the anodic path from a single pulse could be greatly increased by irradiation of the crystal with x-rays. Hence, we conclude that the anodic breakdown paths are initiated by the combination of the effects of very inhomogeneous starting fields and of free electrons in the crystal, both originating from prebreakdown discharges.

Following von Hippel[2] the formation of anodic breakdown paths can now be described as closely analogous to the streamer mechanism of breakdown in gases and the formation of positive Lichtenberg figures. The starting field is determined by the breakdown voltage of the embedding medium surrounding the electrodes and by the concentration of the space charge left on the crystal surface by the predischarge, which acts as a "space-charge anode." The inhomogeneous field at the tip of the surface spark attracts electrons freed by photo-ionization from all directions within the crystal. In order to produce breakdown the starting field must be large enough to accelerate the free electrons near the tip to produce impact ionization in the crystal. In this way, a column of positive space charge, formed by impact ionization, will grow into the crystal and extend the space-charge anode.

The direction in which the positive space-charge channel will form is that in which free electrons accelerated towards the space-charge anode experience the least friction. Electrons which travel in such a direction will, on the average, arrive first at the space-charge anode in sufficient numbers to extend the positive space-charge channel in this direction. Hence, electrons attracted to the original anode at the surface of the crystal in less favorable directions, find them-

[20] The breakdown field strength, however, may be appreciably influenced by mechanical deformation. Calderwood, Cooper, and Wallace, Proc. Phys. Soc. (London) **B65**, 301 (1952).

selves soon in much weaker fields because the space-charge channel pushes ahead in the favorable direction. They are thus much less likely to produce heavy ionization (Fig. 10). In this way, it can be understood how a small difference in scattering probability in various directions can lead to the formation of complete breakdown paths in a definite direction.

If there is more than one direction of least friction, the breakdown path will proceed in that direction in which the composite field from the main anode and space-charge anode is largest (see Fig. 6). Once the space-charge channel has begun to form, the field from the tip of the new space-charge anode will tend to drive the space-charge column forward in the same direction. However, changes in direction are still possible when the field strength at the tip of the channel has increased sufficiently by its approach towards the cathode to change the direction of favorable acceleration of the free electrons. Thus changes from the [110] to [111] direction occur, for example, in NaCl towards the cathode. At places of impurities or faults the field at the tip can become more spherically symmetrical and changes between equivalent directions are much more likely, as we have actually observed in deformed crystals.

The supply of initial electrons in anodic paths created by photoionization, is relatively small. The fate of each starting electron and the secondary electrons it produces is therefore of great importance in the development of the breakdown path. The situation is very similar to the formation of positive Lichtenberg figures, where a new branch is formed by one starting electron and the secondary electrons it creates by impact ionization.[21]

In cathodic and homogeneous field paths, the starting electrons are obtained by field emission from the cathode and their number is very much larger that than produced by photoionization in the case of anodic paths. In homogeneous fields, this emission sets in before the breakdown field strength is reached, and a negative space-charge cloud develops in front of the cathode which steepens the field close to the anode.[15] When the voltage has been raised sufficiently, breakdown will be initiated at the anode and will progress towards the cathode. In this case, the homogeneous field acts over such a wide area and the number of free electrons is so large that any directed breakdown paths are smeared out by the many ionization processes occurring simultaneously. The apparent path direction, therefore, is that of the applied field.

On the other hand, breakdown paths produced by a cathodic point-plane electrode system are direction-dependent. They are initiated by electrons stemming from field emission which find themselves in extremely high fields in the immediate vicinity of the cathode (Fig. 10). Ionization, therefore, takes place very close

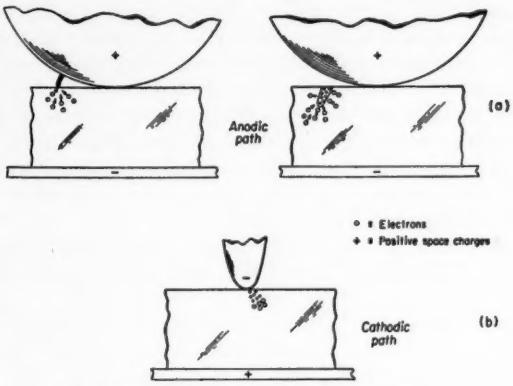

FIG. 10. Formation of anodic and cathodic breakdown paths.

to the cathode and first in such a direction in which the electrons experience the least friction. The positive space charge increases the field gradient at the cathode just as in the negative Lichtenberg figure[21] and more electrons are emitted into the crystal in the direction in which the ionization has taken place. Thus, the field responsible for the development of cathodic paths is very large. Since our experiments show that the path directions are very markedly influenced by the magnitude of the field strength, it is not surprising that the direction of cathodic paths differs from that of anodic paths at any particular temperature. Because a very large number of electrons are involved in this process, the paths are much broader than the anodic paths. In addition, the distance each electron travels in the crystal before it produces ionization is small and the influence of the lattice on the establishment of the favorable directions is therefore smaller than in anodic paths. The fact that a very large number of starting electrons are available for the formation of cathodic paths is clearly demonstrated in the experiments of Inge and Walther,[1] who found that in thick crystals the lengths of partial cathodic breakdown paths obtained from a single pulse of not too high peak voltage are not affected by x-ray irradiation. The cathodic paths, which often accompany the homogeneous field paths, are probably due to high field gradients at surface irregularities on the cathode.

When the breakdown strength of the crystal in homogeneous fields is smaller than that needed to break down the surrounding insulating medium, the breakdown paths change from the directional anodic paths to the nondirectional homogeneous field paths. Thus, homogeneous field paths are often observed in very thin crystals.

Directional Dependence of the Breakdown Paths

One mechanism leading to direction dependence is the difference in the scattering probabilities of electrons of high energy in various directions due to the structure

[21] F. H. Merril and A. von Hippel, J. Appl. Phys. **10**, 873 (1939).

of the Brillouin zone of the lattice vibrations. The direction of easiest acceleration is then a function of the electron energy. A calculation of this effect was carried out by Offenbacher and Callen,[12] who developed a semi-quantitative correlation between the energy of the electrons responsible for the formation of the breakdown paths and the temperature of the crystal, and thus obtained a temperature dependence of the breakdown path directions.

It would be useless to compare the quantitative results of Offenbacher and Callen with our experimental data, because the path directions are very dependent on the field strength and the magnitude of the fields responsible for the breakdown paths is not known in our experiments. We will, therefore, confine our discussion to the qualitative features of the Offenbacher-Callen theory.

As we have shown, the electric fields responsible for the formation of the breakdown paths are very inhomogeneous. The field attracts electrons from all directions in a large solid angle near the space-charge anode. Relatively small differences in the scattering probabilities between one direction and another may be sufficient for the development of breakdown paths in definite crystallographic orientations. The small differences in scattering probability in various directions predicted by the Offenbacher-Callen theory may therefore suffice for the formation of the orientated breakdown paths.

A theory based on the phonon-Brillouin zones in face-centered cubic crystals must lead to the sequence of path directions with increasing electron energy:

$$\text{random} \rightarrow [100] \rightarrow [111] \rightarrow [110] \rightarrow \{[110] \text{ and } [100]\} \xrightarrow{\text{competing}} [100].$$

The Offenbacher-Callen energy criterion is based on the argument that the collision frequencies must be large enough (and, therefore, the electron energies low enough) so that the lattice vibrations can impose the characteristic directions on the electrons in opposition to the applied field. This criterion does not apply to the actual case of strongly inhomogeneous fields.

A simple qualitative argument, however, can be made in the case of such inhomogeneous fields to establish which electron energies are of importance in determining the direction of the breakdown paths. Electrons are attracted to the space-charge anode from all directions and the path will progress in that direction in which, on the average, a sufficient number of electrons will arrive at the earliest time to produce impact ionization. At very low energies the probability of scattering in all directions is the same.[12] Hence, electrons of low energy are not decisive in determining the breakdown path directions. For electrons of very high energy the total collision probability is very low and they will be scattered hardly at all. Only electrons with energies between these extremes will cause the direction dependence of the breakdown paths. When the temperature is increased or impurities are added to the crystal, the total collision probability and also the total number of collisions between ionizations increases and the energy range contributing to directional effects will be shifted towards the high-energy side. One can, therefore, expect that, with increasing temperature, path directions corresponding to higher electron energies will appear, in agreement with the experimental results (see Table IV). Addition agents have the same effect, as observed.

According to Bardeen and Shockley,[22] the total collision probability is independent of the electric field, at least for homogeneous fields up to 10^5 v/cm. However the existence of overvoltages will shorten the ionizing distances and the time required to accelerate the electrons to the ionization energy, and, therefore, reduce the total number of collisions between ionizations, even if the collision probability remains unchanged. The effect of the decrease of the number of collisions between ionizations would be to shift the upper limit of the energy range in which differential scattering occurs towards lower energies and, hence, would change the path directions to those corresponding to lower energies, as observed.

The difference between cathodic and anodic paths can be explained easily by assuming that the cathodic paths are produced by much higher fields. It also follows from the detailed calculation of Offenbacher and Callen and from the considerations given above that at any particular temperature, crystals of small ionization energies and large lattice constants will exhibit paths corresponding to lower energy regions than crystals possessing large ionization energies and small lattice constants. This is in good agreement with the measurements of the path directions of various crystals at different temperatures[4] (see Table IV).

The Offenbacher-Callen approach of invoking the phonon-Brillouin zone is, at least, in qualitative agreement with our experimental results. Before any definite conclusions can be drawn, however, it would be necessary to evaluate the energy criterion for inhomogeneous fields more quantitatively. In particular, the fact that the [100] paths predicted for high electron energies and, therefore, high temperatures, are never observed requires careful consideration. It is possible that the dominant energy is always so low that even at very high temperatures, energies corresponding to the high energy [100] region are not decisive in determining the path directions.

The absence of [111] paths in potassium and rubidium salts and the large increase with overvoltages of the temperature region in which [111] paths are observed, is not easily explained by the phonon-Brillouin zone mechanism. The latter may be due to the effect of the electronic Brillouin zones since it is likely that the electrons in the conduction band will have to cross

[22] J. Bardeen and W. Shockley, Phys. Rev. 80, 69 (1950).

a zone boundary before producing ionization.[23] Although the conduction bands in alkali halide crystals almost certainly overlap, additional scattering of the electrons may become necessary at the zone boundaries, the amount of which might depend on the direction of motion of the electrons. However, since the energy gap between the two conduction bands in any direction is probably not large, there is a possibility that, in the presence of large overvoltages, the electrons might overcome the gap under the influence of the electric field, without much additional scattering.

In addition, the potential structure will also lead to direction-sensitive electronic motion. This influence of the crystal potential is, however, probably not very important, at least in alkali halide crystals, since it is unlikely to lead to the marked temperature-dependence of the directions of the breakdown paths, which is observed in these crystals. Furthermore, the absence of any dependence of the breakdown strength on the direction of the applied field is not so easily explained if this mechanism were decisive in the determination of the breakdown path directions.

The mechanism of differential scattering on account of the phonon-Brillouin zones presupposes the absence of Umklapp processes, which is strictly true only for the interactions of perfectly free electrons with the polar lattice vibrations. However, the probability of Umklapp processes in nonpolar crystals, such as diamond, may not be large.[24] If they are appreciable, however, the potential structure may be the principal factor governing the breakdown path directions in such crystals and temperature-insensitive breakdown paths can be expected.[25]

It is, at present, impossible to decide which of the several mechanisms is responsible for the formation of the breakdown paths in definite crystallographic orientations in a specific crystal under any particular conditions. Such an analysis is made especially difficult because of the fact that very small differences in the ease with which electrons are accelerated in various directions may lead to the formation of orientated breakdown paths. Only more rigorous quantitative calculations may finally lead to an answer to this problem.

ACKNOWLEDGMENTS

The author is greatly indebted to Professor A. R. von Hippel for suggesting the problem, for helpful advice, encouragement, and the loan of personal equipment. It is also a great pleasure to acknowledge the kind aid and advice of D. A. Powers, group leader of the High-Voltage Section, throughout this investigation and of W. B. Green during the early experimental stages. Mr. Powers designed the high-voltage equipment; J. Kalnajs gave help on chemical problems; Dr. A. Smakula and V. Sils provided alkali halide single crystals and many helpful discussions; and Dr. G. Economos prepared the ferrite ceramics which served as electrodes in most of our experiments.

[23] F. Seitz, Phys. Rev. **76**, 1376 (1949).
[24] W. R. Heller, Phys. Rev. **84**, 1130 (1951).

[25] Preliminary experiments by J. W. Davisson [Phys. Rev. **94**, 1437 (1954)] on rhombic sulfur seem to indicate that the path direction in this crystal does not change with temperature.

Time-Dependent Displacement Correlations and Inelastic Scattering by Crystals*

R. J. GLAUBER
Lyman Laboratory of Physics, Harvard University, Cambridge, Massachusetts
(Received January 18, 1955)

A function is defined which expresses quantum mechanically the correlation of the displacements of pairs of lattice points at different times due to the wave-like nature of crystal excitations. Methods are developed for summing implicitly the effects of multiple emission and absorption of lattice quanta occurring during a scattering process. The inelastic scattering cross sections found thereby are expressed entirely in terms of the time-dependent correlation function defined earlier. The resulting treatment thus emerges as a natural generalization of the static theory of x-ray scattering. The results are discussed in relation to a number of approximation methods.

I. INTRODUCTION

OF the particles whose scattering by crystal lattices is of experimental interest, electrons and photons show the simplest behavior energetically. The energies of these quanta are in general high enough that their exchanges of energy with the lattice system may be ignored and the collisions treated as approximately elastic. For particles as heavy as neutrons, however, the inelasticity is no longer negligible. The energies of neutrons with wavelengths suitable for interference experiments are quite comparable with those of the thermally excited vibrational quanta of the crystal. The absorption or emission of vibrational quanta therefore causes relatively appreciable changes of the neutron's kinetic energy. It is with the generalization of the theory to the treatment of such inelastic processes that the present work is chiefly concerned.

The deviations of a crystal lattice from perfect regularity due to thermal vibrations were first shown by Debye[1] to bring about a reduction in the intensities of the Laue spots formed in x-ray scattering. Later and more explicitly, quantum-theoretical investigations[2] have explained quantitatively the background of diffuse scattering which also results from thermal agitation. In particular, it has been shown that it is the correlation in the displacements of pairs of nearby scattering centers existing at any instant, which brings about the observed distributions of diffuse scattering. These displacement correlations are due to the wave-like nature of the lattice excitations, and may be expected to persist over finite intervals of time as well as distance. The latter fact is especially significant in the treatment of heavy-particle scattering since at the low energies of interest the particle's passage through a crystal cannot be approximated as instantaneous. It is natural then to introduce a function expressing the correlation of displacements of pairs of points in its dependence on intervals of time, as well as position in the lattice. This function is a direct generalization of the instantaneous correlation function associated with the treatment of x-ray scattering. We shall show that it furnishes, in fact, all of the information necessary for expressing the solution of the inelastic scattering problem. Recently, Van Hove has demonstrated the usefulness of defining analogous time-dependent correlation functions for more general types of scattering systems.[3]

The emission and absorption of vibrational quanta by a scattered particle is an intrinsically multiple process. Arbitrary numbers of quanta may be created, and arbitrary numbers absorbed in a single collision with the lattice. Problems of multiple quantum emission bearing considerable analogy to this have long been of interest in field theoretical contexts, and certain of the methods developed to handle them are well suited to the crystal problem. Use will be made of these without appealing to an explicit knowledge of field theory. Using the neutron case as an illustration we shall thereby derive a closed expression for the inelastic scattering cross section which is valid for all relevant initial energies and takes into account all possible quantum transitions. Previous treatments have mainly been confined either to one-quantum processes,[4] and therefore to low energies, or to the asymptotic limit of high energies.[5,6]

Before undertaking the calculation of the scattering it will be useful to discuss the relevant properties of the lattice.

II. THE DISPLACEMENT FIELD

The normal modes of crystal lattices bound by Hooke's-law forces are plane vibrational waves. The elastic energy of the crystal is quadratic in the amplitudes of these waves, which are therefore quantized in the way familiar for harmonic oscillators. The particle coordinates then become operators defined at each point of the lattice. We shall designate these collectively as the displacement field $\mathbf{u}(\mathbf{r}_j,t)$, that is the set of vector displacements at time t of the mass points whose

* A brief account of this work was presented at the Washington meeting of the American Physical Society, May 1, 1952 [Phys. Rev. 87, 189 (1952)]. See also Phys. Rev. 94, 751 (1954).

[1] P. Debye, Ann. Physik 43, 49 (1914).

[2] I. Waller, Uppsala Dissertation, 1925 (unpublished). For a review of this work and later contributions see M. Born, Repts. Progr. Phys. 9, 294 (1942–3).

[3] L. Van Hove, Phys. Rev. 95, 249 (1954); 95, 1374 (1954).

[4] This work is reviewed by J. M. Cassels, Progr. Nuc. Phys. 1, 185 (1950); see also reference 5.

[5] A. Akhiezer and I. Pomeranchuk, J. Exptl. Theoret. Phys. U.S.S.R. 17, 770 (1947).

[6] G. L. Squires, Proc. Roy. Soc. (London) A212, 192 (1952).

equilibrium positions are $\mathbf{r}_j$. In discussing this field more explicitly it will greatly simplify notation to specialize to the cases of lattices of identical atoms occupying equivalent positions. The extension to more general lattices is straightforward. Assuming then that there are N atoms in all, each of mass M, the expansion in plane waves of the α component ($\alpha=1, 2, 3$) of the displacement field will be[7]

$$u_\alpha(\mathbf{r},t)=\sum_{\mathbf{k},p} e_\alpha^{(p)}\left(\frac{\hbar}{2NM\omega}\right)^{\frac{1}{2}} \times(a_{\mathbf{k},p}e^{i(\mathbf{k}\cdot\mathbf{r}-\omega t)}+a_{\mathbf{k},p}^{\dagger}e^{-i(\mathbf{k}\cdot\mathbf{r}-\omega t)}). \quad (1)$$

Here $\mathbf{e}^{(p)}$ ($p=1, 2, 3$) are the three unit polarization vectors for waves of propagation vector $\mathbf{k}$ and angular frequency $\omega=\omega^{(p)}(\mathbf{k})$.

The amplitudes $a_{\mathbf{k},p}$ and $a_{\mathbf{k},p}^{\dagger}$ are the familiar operators of harmonic oscillator quantization. They destroy and create single quanta, respectively, in virtue of their commutation rules:

$$a_{\mathbf{k},p}a_{\mathbf{k}',p'}^{\dagger}-a_{\mathbf{k}',p'}^{\dagger}a_{\mathbf{k},p}=[a_{\mathbf{k},p},a_{\mathbf{k}',p'}^{\dagger}]=\delta_{\mathbf{k}\mathbf{k}'}\delta_{pp'}, \quad [a_{\mathbf{k},p},a_{\mathbf{k}',p'}]=0, \quad [a_{\mathbf{k},p}^{\dagger},a_{\mathbf{k}',p'}^{\dagger}]=0. \quad (2)$$

We shall later need the expectation values of certain rather general expressions involving these operators. It will be shown, however, that the results may be expressed in terms of those for the two bilinear combinations with nonvanishing expectation values,

$$\langle a_{\mathbf{k},p}^{\dagger}a_{\mathbf{k},p}\rangle=n_{\mathbf{k},p}, \quad \langle a_{\mathbf{k},p}a_{\mathbf{k},p}^{\dagger}\rangle=n_{\mathbf{k},p}+1, \quad (3)$$

where $n_{\mathbf{k},p}$ is the average number of quanta in the mode specified by $\mathbf{k}$ and p.

As we have already noted, the wave-like nature of crystal excitation causes correlations in the displacements of lattice points many unit cells apart which may also persist over long intervals of time. A measure of the correlations of position is furnished by the expectation values of the products of the displacement components at different points $\mathbf{r}$ and $\mathbf{r}'$, and times t and t'. In the absence of correlation the expectation values vanish. Their evaluation proceeds immediately by use of (3):

$$\langle u_\alpha(\mathbf{r},t)u_\beta(\mathbf{r}',t')\rangle=\sum_{\mathbf{k},p}\frac{\hbar}{2NM\omega}e_\alpha^{(p)}e_\beta^{(p)} \times\{(n_{\mathbf{k},p}+1)\exp[i(\mathbf{k}\cdot(\mathbf{r}-\mathbf{r}')-\omega(t-t'))] +n_{\mathbf{k},p}\exp[-i(\mathbf{k}\cdot(\mathbf{r}-\mathbf{r}')-\omega(t-t'))]\}. \quad (4)$$

Similarly constructed expectation values, usually called propagation functions, also play a central role in elementary particle theories. There their evaluation is simplified, however, by the vacuum's emptiness, for all practical purposes, of stray quanta. By contrast the background of thermally excited quanta of a lattice forms a Bose-Einstein gas of considerable concentration. The average quantum populations are given by the Planck distribution

$$n_{\mathbf{k},p}=[\exp(\hbar\omega^{(p)}(\mathbf{k})/\kappa T)-1]^{-1}, \quad (5)$$

in which κ is the Boltzmann constant and T the temperature. Expectation values such as (4), averaged over a thermal distribution of quantum states at temperature T, will be denoted by $\langle\ \rangle_T$. Thus the brackets $\langle\ \rangle_0$ which customarily denote the average in a space devoid of quanta, will retain their usual meaning.

The scattering calculations to be undertaken presently will be seen to require only the information about the crystal contained in the expression (4). The summation over propagation vectors may be replaced by an integration of the vector $\mathbf{k}/2\pi$ over a unit cell of the reciprocal lattice. For a given lattice temperature T, we are thus led to define a tensor correlation function

$$C_{\alpha\beta,T}(\mathbf{r}-\mathbf{r}',t-t')=\langle u_\alpha(\mathbf{r},t)u_\beta(\mathbf{r}',t')\rangle_T, \quad (6)$$

for which we find

$$C_{\alpha\beta,T}(\mathbf{r},t)=\frac{V_0\hbar}{16\pi^3M}\sum_p\int e_\alpha^{(p)}e_\beta^{(p)} \times\left\{e^{i(\mathbf{k}\cdot\mathbf{r}-\omega t)}+\frac{2\cos(\mathbf{k}\cdot\mathbf{r}-\omega t)}{\exp(\hbar\omega/\kappa T)-1}\right\}\frac{d\mathbf{k}}{\omega^{(p)}(\mathbf{k})}, \quad (7)$$

where V_0 is the volume of the unit cell. The first term of the integrand, which is temperature independent, gives the correlation of the zero-point vibrations $C_{\alpha\beta,0}(\mathbf{r},t)$, while the second adds the effect of thermal excitation.

For vanishing time arguments the correlation function is real-valued, which is to be expected since displacement operators evaluated at the same time commute, and their product is hermitian. Evaluated at different times, however, these operators do not in general commute, an expression of the fact that the corresponding position measurements cannot be carried out independently.[8] For finite time differences the correlation function is therefore complex-valued. It obeys the relation

$$C_{\alpha\beta,T}(\mathbf{r},t)=C_{\alpha\beta,T}^{*}(-\mathbf{r},-t), \quad (8)$$

the latter expression reducing, for the simple lattices under consideration to $C_{\alpha\beta,T}^{*}(\mathbf{r},-t)$.

For the rougher purposes of orientation, the Debye model may be used to evaluate the correlation function.

[7] Although the plane wave expansion defines a displacement field for all $\mathbf{r}$, only the values at the lattice points are needed, provided the individual scattering centers are translated rigidly.

[8] A sound cone may of course be defined similar to the light cone of electrodynamics, but the analogy is a crude one, since the exact commutation of the displacement operators holds only at equal times. It does not extend to other intervals outside the sound cone because of the impossibility of forming sharp wave packets within the crystal.

The integrations in **k**-space are then carried out over the volume of a sphere of radius $k_D=(6\pi^2/V_0)^{\frac{1}{3}}$. We may further assume the existence of a unique sound velocity $s=\omega/k$ for all quanta, thereby neglecting certain effects of anisotropy, polarization, etc. The constants s and k_D define the characteristic Debye temperature Θ through the relation $\kappa\Theta=\hbar s k_D$. With these simplications the polarization summation of (6) reduces to a factor of $\delta_{\alpha\beta}$, the unit tensor; orthogonal displacements are uncorrelated. The correlation function then assumes the form

$$C_{\alpha\beta,T}(\mathbf{r},t)=\delta_{\alpha\beta}C_T^{(D)}(\mathbf{r},t), \tag{9}$$

with

$$C_T^{(D)}(\mathbf{r},t)=\frac{3\hbar^2}{8\pi M\kappa\Theta k_D{}^2}\int\left\{e^{i(\mathbf{k}\cdot\mathbf{r}-skt)}+\frac{2\cos(\mathbf{k}\cdot\mathbf{r}-skt)}{\exp(\Theta k/k_DT)-1}\right\}\frac{d\mathbf{k}}{k}. \tag{10}$$

Evaluated for vanishing intervals of both space and time, the correlation function reduces to the mean-squared value of a displacement component ($\alpha=1$, 2, or 3).

$$C_T^{(D)}(0,0)=\langle u_\alpha{}^2(\mathbf{r},t)\rangle_T=\frac{3\hbar^2}{M\kappa\Theta}\{\tfrac{1}{4}+(T/\Theta)\Phi(\Theta/T)\}. \tag{11}$$

Here Φ is the function introduced by Debye

$$\Phi(x)=\frac{1}{x}\int_0^x\frac{ydy}{\exp(y)-1}, \tag{12}$$

which is discussed and tabulated in many references.[9]

At temperature zero the Debye correlation function reduces to elementary form

$$C_0^{(D)}(\mathbf{r},t)=\frac{3\hbar^2}{4M\kappa\Theta k_D{}^2r}\left\{\frac{1-\exp[ik_D(r-st)]}{r-st}+\frac{1-\exp[-ik_D(r+st)]}{r+st}\right\}. \tag{13}$$

More generally, for $T\ll\Theta$ the temperature-dependent term of the integrand of (8) may be expanded in powers of $\exp[-\Theta k/k_DT]$ and integrated in elementary terms. For high temperatures, $T\gg\Theta$, direct expansion in powers of $\Theta k/k_DT$ is possible, which leads to results expressible in terms of sine integrals.

III. THE POTENTIAL AND ITS TREATMENT

A particle scattered by an ideally rigid crystal would be subject to an exactly periodic potential.[10] We shall represent this function as a summation over the lattice points $\mathbf{r}_j$ of equivalent potentials centered about each of them.

$$V(\mathbf{r})=\sum_j\mathcal{V}(\mathbf{r}-\mathbf{r}_j). \tag{14}$$

In an elastically bound lattice the scattering centers are at any instant shifted from their equilibrium positions $\mathbf{r}_j$ by an amount given by the displacement field $\mathbf{u}(\mathbf{r}_j,t)$. In the present work we shall assume that the individual potentials are shifted rigidly along with their lattice-points, so that the total potential is represented by

$$V'(\mathbf{r},t)=\sum_j\mathcal{V}(\mathbf{r}-\mathbf{r}_j-\mathbf{u}(\mathbf{r}_j,t)). \tag{15}$$

In the Born approximation the scattering problem reduces to finding the matrix elements of this operator, and summing their squares over the various possible transitions.

Particular mention must be given the case of neutron scattering where the treatment proceeds by means of the Fermi pseudopotential approximation.[11] The short-range potentials between neutrons and nuclei are replaced by point interactions (delta functions) whose magnitudes are adjusted so that the scattering by isolated fixed nuclei is correctly represented by the Born approximation. That is, the interaction between a neutron (mass m) and a nucleus at $\mathbf{r}_j$ is taken to be $(2\pi\hbar^2/m)a_j\delta(\mathbf{r}-\mathbf{r}_j)$, where a_j is the bound scattering length.[12] The use of the Born approximation formalism is then extended to the case in which the nuclei are no longer fixed, so that the effective potential becomes

$$V'_{\text{neut}}(\mathbf{r},t)=(2\pi\hbar^2/m)\sum_j a_j\delta(\mathbf{r}-\mathbf{r}_j-\mathbf{u}(\mathbf{r}_j,t)). \tag{16}$$

Although the problem of finding the matrix elements of operator functions such as (15) has rather a general appearance, it may always be reduced by means of the fourier integral representations of the potentials to the problem of treating exponential functions of the quantized field $\mathbf{u}(\mathbf{r},t)$. The analysis required for these is particularly simple, as has been shown in other field-theoretical contexts.[13] By evaluating the matrix elements of these functions without expanding them in power series, we avoid the need to consider in detail the enormous variety of vibrational transitions the potential operator may induce. In effect the great number of degrees of freedom, which is responsible for this multiplicity, makes possible the use of field-theoretical methods which perform the summations automatically.

We shall require the matrix elements of operators of the form $\exp U$, where U is some linear combination of the components of the displacement field u_α. The only property of U needed for this purpose is that it is a sum of creation and destruction operators for all the

[9] See for example R. W. James, *Optical Principles of the Diffraction of X-Rays* (G. Bell and Sons, London, 1948).

[10] In the scattering of x-rays the periodic function of interest is, of course, the electronic charge density, rather than a potential. The mathematical analysis is so similar, however, that the methods of the present work carry over with a few simple substitutions.

[11] E. Fermi, Ricerca sci. **7**, 13 (1936).

[12] A review of the necessary information on neutron scattering is given in reference 4.

[13] R. J. Glauber, Phys. Rev. **84**, 395 (1951).

modes of the system. As the simplest example we write the reduced form of $\exp U$ for the emission or absorption of a single quantum in any mode, assuming that all the modes of the crystal are initially in specified quantum states. This is

$$\langle \exp U\rangle^{(1)} = U\left\langle \frac{d}{dU}\exp U\right\rangle = U\langle \exp U\rangle, \tag{17}$$

in which the expectation values on the right are to be taken in the initial state of the system. In effect (17) corresponds to a separation of a single factor of U, the one which is to perform the real creation or absorption in all possible ways from the terms of the series expansion of $\exp U$, together with the requirement that the remaining operators leave the state unchanged. It is easy to show that the neglect of the commutation rules in thus separating a creation or destruction operator leads to errors which are only of order $1/N$. Since N, the number of lattice points is usually enormous we shall consider (17) as exact. To find the reduced forms for n-quantum transitions an analogous procedure may be used to separate a factor of U^n, which must then be divided by $n!$ since each of the U's may be responsible for any of the transitions

$$\langle \exp U\rangle^{(n)} = \frac{U^n}{n!}\left\langle \frac{d^n}{dU^n}\exp U\right\rangle = (U^n/n!)\langle \exp U\rangle. \tag{18}$$

The occupation numbers of the crystal modes are of course never known precisely and transition probabilities calculated from (18) must be averaged over an ensemble of initial states at some temperature T. This procedure may be simplified by first performing the averaging directly on the expectation value occurring in (18). The eventual error incurred thereby once again vanishes with $1/N$. We therefore define an average reduced form of $\exp U$ for an n-quantum process at temperature T.

$$\langle \exp U\rangle_T^{(n)} = (U^n/n!)\langle \exp U\rangle_T. \tag{19}$$

To compute the averaged expectation value $\langle \exp U\rangle_T$ we consider the expression $\langle \exp\lambda U\rangle_T$ as a function of the variable λ. Differentiating, we have

$$\frac{d}{d\lambda}\langle \exp\lambda U\rangle_T = \langle U\exp\lambda U\rangle_T. \tag{20}$$

Since the expression on the right is a sum of diagonal matrix elements, only the one-quantum matrix element of the exponential can contribute to it. Then, replacing the exponential by $\langle \exp\lambda U\rangle_T^{(1)} = \lambda U\langle \exp\lambda U\rangle_T$, we obtain the differential equation

$$\frac{d}{d\lambda}\langle \exp\lambda U\rangle_T = \lambda\langle U^2\rangle_T\langle \exp\lambda U\rangle_T, \tag{21}$$

for which the solution sought is[14]

$$\langle \exp\lambda U\rangle_T = \exp(\tfrac{1}{2}\lambda^2\langle U^2\rangle_T). \tag{22}$$

This completes the evaluation of the averaged reduced form (19):

$$\langle \exp U\rangle_T^{(n)} = (U^n/n!)\exp(\tfrac{1}{2}\langle U^2\rangle_T). \tag{23}$$

IV. SCATTERING CALCULATIONS

The individual potentials $\mathcal{U}(\mathbf{r})$ of (14), we assume, have the Fourier integral representation

$$\mathcal{U}(\mathbf{r}) = \int F(\mathbf{k})\exp[i\mathbf{k}\cdot\mathbf{r}]d\mathbf{k}, \tag{24}$$

where, in particular for neutron scattering, $F(\mathbf{k}) = \hbar^2 a/(2\pi)^2 m$. The potential acting on the scattered particle is then

$$V'(\mathbf{r},t) = \int F(\mathbf{k})\sum_j \exp[i\mathbf{k}\cdot(\mathbf{r}-\mathbf{r}_j-\mathbf{u}(\mathbf{r}_j,t))]d\mathbf{k}. \tag{25}$$

The particle's initial state is represented by a plane wave, $\exp[i(\mathbf{p}\cdot\mathbf{r}-Et)]$, where $\mathbf{p}$ and E are the initial momentum and energy, divided by $\hbar$. Its final state $\exp[i(\mathbf{p}'\cdot\mathbf{r}-E't)]$ has, in general, a momentum differing in magnitude as well as direction. Introducing the differences

$$\Delta\mathbf{p} = \mathbf{p}'-\mathbf{p}, \quad \Delta E = E'-E, \tag{26}$$

the time-dependent matrix element for the transition, insofar as the particle variables are concerned, is

$$\begin{aligned} M(t) &= \int V'(\mathbf{r},t)\exp[-i(\Delta\mathbf{p}\cdot\mathbf{r}-\Delta Et)]d\mathbf{r} \\ &= (2\pi)^3 F(\Delta\mathbf{p})\sum_j \exp\{-i[\Delta\mathbf{p}\cdot(\mathbf{r}_j+\mathbf{u}(\mathbf{r}_j,t)) \\ &\qquad -\Delta Et]\}. \end{aligned} \tag{27}$$

This expression, however, is still an operator capable of inducing all possible vibrational transitions.

The rules formulated in the preceding section may be applied directly to find the reduced form of (27) for an n-quantum process. We identify the quantity $-i\Delta\mathbf{p}\cdot\mathbf{u}(\mathbf{r}_j,t)$ with U, and note that

$$\begin{aligned} \langle U^2\rangle_T &= -\langle(\Delta\mathbf{p}\cdot\mathbf{u})^2\rangle_T \\ &= -\sum_{\alpha\beta}\Delta p_\alpha\Delta p_\beta\langle u_\alpha(\mathbf{r}_j,t)u_\beta(\mathbf{r}_j,t)\rangle_T \qquad (28) \\ &= -\sum\Delta p_\alpha\Delta p_\beta C_{\alpha\beta,T}(0,0) \qquad (29) \\ &= -\Delta\mathbf{p}\Delta\mathbf{p}:\mathbf{C}_T(0,0), \qquad (30) \end{aligned}$$

[14] It may be noted that the present result holds true, whatever are the thermal weightings attached to the various degrees of excitation, i.e., even in nonequilibrium states. A similar theorem, due to F. Bloch [Z. Physik 74, 295 (1932)] which holds for oscillator systems with any number of modes requires explicitly the weightings of thermal equilibrium.

where the second line follows from the definition (6) of the correlation function, and in the third line dyadic notation is used to abbreviate the tensor product.

With the above identification of U, the relation (23) applied to (27) yields the effective transition operator for an n-quantum process:

$$\langle M(t)\rangle_T^{(n)} = (2\pi)^3 F(\Delta\mathbf{p}) \times\left\{\sum_j \frac{1}{n!}(-i\Delta\mathbf{p}\cdot\mathbf{u}(\mathbf{r}_j,t))^n e^{-i\Delta\mathbf{p}\cdot\mathbf{r}_j}\right\} \times\exp[-\tfrac{1}{2}\langle(\Delta\mathbf{p}\cdot\mathbf{u})^2\rangle_T] e^{i\Delta E t}. \quad (31)$$

The features of the elastic scattering which occurs when no quanta are emitted or absorbed are already apparent. For $n=0$ the absolute value, squared, of (31) exhibits Debye's classic result for the Laue-Bragg scattering. The pattern is the same as for a rigid lattice, but modulated in intensity[15] by a factor $\exp[-\langle(\Delta\mathbf{p}\cdot\mathbf{u})^2\rangle_T]$.

To compute the cross sections when quantum transitions do occur, it is convenient once more to develop a procedure which carries out implicitly the summations over the many processes possible. The expression for transition probabilities in the Born approximation may be written in the form

$$w = (2\pi/\hbar^2)\sum_f M_{if}^\dagger M_{fi}\delta(\mathcal{E}_f-\mathcal{E}_i), \quad (32)$$

where the matrix elements, if time-dependent, may be evaluated at any time, and the summation over final states is restricted, as shown, by the conservation of energy. Without this explicit restriction of the summation, (32) could be expressed as the diagonal element of a matrix product. This may be effected by noting that for any conservative system, the time integral of a matrix element contains the conservation condition. Thus, for example, we have

$$\int_{-\infty}^{\infty} M_{if}^\dagger(t)dt = M_{if}^\dagger(0)2\pi\delta(\mathcal{E}_f-\mathcal{E}_i),$$

which permits us to write (32) as the expectation value[16]

$$w = \frac{1}{\hbar^2}\left\{\int_{-\infty}^{\infty} M^\dagger(t)M(0)dt\right\}_{ii}. \quad (33)$$

The total probability of an n-quantum process, summed over all the forms it may take is found by substituting the matrix element (31). Because the initial state of the system remains unknown the probability must finally be averaged thermally to represent the effects of the real processes. We have then

$$w_n = \frac{1}{\hbar^2}\int_{-\infty}^{\infty}\langle\langle M^\dagger(t)\rangle_T^{(n)}\langle M(0)\rangle_T^{(n)}\rangle_T dt. \quad (34)$$

To find the cross section for scattering accompanied by n-quantum processes w_n must be multiplied by the usual state-density factor for the outgoing particle and divided by its incoming flux. We are led thus to define the n-quantum differential cross section:

$$\sigma_n(\mathbf{p}') = [m^2 p'/(2\pi\hbar)^3 p]w_n, \quad (35)$$

where the inelasticity leaves the magnitude p' of the final momentum unrestricted. The total cross section for the n-quantum process is obtained by integrating over energy $d(\hbar E')$ and solid angle $d\Omega'$.

$$\sigma_{n,\,\mathrm{tot}} = \int \sigma_n(\mathbf{p}')d(\hbar E')d\Omega'. \quad (36)$$

The only expectation value in (34) which remains to be found is that of the product of the quantized operators in the two factors of $\langle M\rangle_T^{(n)}$. It has the form

$$(n!)^{-2}\langle[i\Delta\mathbf{p}\cdot\mathbf{u}(\mathbf{r}_l,t)]^n;[-i\Delta\mathbf{p}\cdot\mathbf{u}(\mathbf{r}_m,0)]^n\rangle_T, \quad (37)$$

in which a semicolon has been placed between the factors as a reminder that the n real transitions induced by the operators to the right of it must be reversed by those to the left.[17] The pairing of the operators on the two sides which effects this takes place in $n!$ ways. Furthermore in the limit of large N the expectation value (37) for each pairing scheme reduces to the product of the expectation values for the corresponding pairs. Thus (37) reduces to the nth power of the correlation function

$$(n!)^{-1}\{\langle[\Delta\mathbf{p}\cdot\mathbf{u}(\mathbf{r}_l,t)][\Delta\mathbf{p}\cdot\mathbf{u}(\mathbf{r}_m,0)]\rangle_T\}^n = (n!)^{-1}\{\sum_{\alpha\beta}\Delta p_\alpha\Delta p_\beta\langle u_\alpha(\mathbf{r}_l,t)u_\beta(\mathbf{r}_m,0)\rangle_T\}^n = (n!)^{-1}\{\Delta\mathbf{p}\Delta\mathbf{p}:\mathbf{C}_T(\mathbf{r}_l-\mathbf{r}_m,t)\}^n. \quad (38)$$

The evaluation of the n-quantum differential cross section now proceeds directly by combining (31), (34), and (38) in (35). In particular we find that all of the knowledge required about lattice vibrations is contained in the time-dependent correlation function $\mathbf{C}_T(\mathbf{r}_l-\mathbf{r}_m, t)$. The summations to be performed over the lattice points $\mathbf{r}_l$ and $\mathbf{r}_m$ may be simplified by noting that only the difference $\mathbf{r}_l-\mathbf{r}_m$ appears in the summand. In the limit of large N the double summation therefore becomes N times the single summation over positions relative to a particular lattice point, chosen as origin. The expression for the n-quantum cross section, thus

[15] A simple way of viewing this is that $\langle M\rangle_T^{(0)}$ is just the matrix element of the thermally averaged potential. The latter, according to (31), may be expressed as $\int K_T(\mathbf{r}-\mathbf{r}')V'(\mathbf{r}')d\mathbf{r}'$, where $K(\mathbf{r}) = \langle\delta(\mathbf{r}-\mathbf{u})\rangle_T$ which, in a Debye crystal, is

$$(2\pi\langle u_\alpha^2\rangle_T)^{-\frac{3}{2}}\exp[-r^2/2\langle u_\alpha^2\rangle_T].$$

[16] This device was first used in a similar context by W. Lamb, Phys. Rev. 55, 190 (1939).

[17] If, in a single one of the factors of $(\Delta\mathbf{p}\cdot\mathbf{u})^n$ a pair of $\mathbf{u}$'s were used to both emit and reabsorb a quantum in a single mode, the number of real processes carried out would be $n-2$. Virtual processes of this type are already correctly accounted for in (31).

reduced, is

$$\sigma_n(\mathbf{p}')=\frac{(2\pi)^3Nm^2p'}{n!\hbar^5p}|F(\Delta\mathbf{p})|^2\exp[-\langle(\Delta\mathbf{p}\cdot\mathbf{u})^2\rangle_T]$$
$$\times\sum_j e^{i\Delta\mathbf{p}\cdot\mathbf{r}_j}\int_{-\infty}^{\infty}e^{-i\Delta Et}\{\Delta\mathbf{p}\Delta\mathbf{p}:\mathbf{C}_T(\mathbf{r}_j,t)\}^n dt. \quad (39)$$

The summation over n from zero to infinity to include all possible quantum processes is now immediate, and results in the introduction of the function $\exp[\Delta\mathbf{p}\Delta\mathbf{p}:\mathbf{C}_T(\mathbf{r}_j,t)]$ within the time integration. For purposes of illustration we specialize to the case of neutron scattering, for which we have noted $F(\Delta\mathbf{p})=\hbar^2a/(2\pi)^2m$. Then, defining the differential cross section for all quantum processes $\sigma(\mathbf{p}')=\sum_{(n)}\sigma_n(\mathbf{p}')$, we have

$$\sigma(\mathbf{p}')=\frac{Na^2p'}{2\pi\hbar p}\exp[-\langle(\Delta\mathbf{p}\cdot\mathbf{u})^2\rangle_T]\sum_j e^{i\Delta\mathbf{p}\cdot\mathbf{r}_j}$$
$$\times\int_{-\infty}^{\infty}\exp[-i\Delta Et+\Delta\mathbf{p}\Delta\mathbf{p}:\mathbf{C}_T(\mathbf{r}_j,t)]dt. \quad (40)$$

Although we have thus far assumed the lattice to consist of identical scatterers, the presence of spin- or isotope-dependent interactions will cause a fluctuation of the scattering length from one nucleus to another. In such cases, with the replacement of a^2 by $(a)_{Av}^2$, (40) represents the coherent scattering by the lattice. To this must be added the scattering, proportional to $(a^2)_{Av}-(a)_{Av}^2$, which results from the disorder of the system. The treatment of this incoherent scattering is the same, in relation to the lattice quanta, as the coherent scattering. The result is similar to (40) but, of course, lacks the interference effects represented by the sum over lattice points $\mathbf{r}_j$.

$$\sigma_{\text{inc}}(\mathbf{p}')=\frac{Np'}{2\pi\hbar p}[(a^2)_{Av}-(a)_{Av}^2]\exp[-\langle(\Delta\mathbf{p}\cdot\mathbf{u})^2\rangle_T]$$
$$\times\int_{-\infty}^{\infty}\exp[-i\Delta Et+\Delta\mathbf{p}\Delta\mathbf{p}:\mathbf{C}_T(0,t)]dt. \quad (41)$$

The incoherent cross section, which is in general also inelastic, is seen to depend only on the difference $\mathbf{C}_T(0,t)-\langle\mathbf{uu}\rangle_T=\mathbf{C}_T(0,t)-\mathbf{C}_T(00)$.

V. COMPARISON WITH APPROXIMATE METHODS

We have derived expressions for the inelastic scattering cross sections which are essentially exact in their treatment of lattice vibrations. In particular, the information required about the lattice is seen to be entirely contained in its characteristic tensor correlation function $C_{\alpha\beta,T}(\mathbf{r},t)$. Unfortunately our knowledge of the vibrational frequency distributions $\omega^{(p)}(\mathbf{k})$ in crystals is still too fragmentary in nearly all cases to permit explicit construction of these functions. It seems reasonable to hope, however, that some of the required data on frequency distributions can be found directly from measurements of the inelastic scattering of slow neutrons.[18] For the present we shall limit ourselves to the discussion of various approximation methods, which correspond to the use of incomplete knowledge of the correct correlation function. Equations (40) and (41) furnish a unified starting point for all such procedures.

One means of evaluating the expressions (40) and (41) proceeds by re-expressing them as the sums of n-quantum partial cross sections. The expansion will converge quite rapidly for small momentum transfers and low temperatures, that is for $(\Delta p)^2\langle u_\alpha^2\rangle_T<1$. In this case not many terms need be retained and the integrals required are only those of the corresponding powers of the correlation function. The one-quantum terms have been extensively investigated in this way,[4,5] and certain estimates made of higher-order effects,[5,6] all on the basis of the Debye model. As an illustration of this method applied to inelastic scattering, without restriction on the number of quanta, we write the cross section for incoherent neutron scattering by a Debye lattice at zero temperature, with energy loss $-\Delta E\leqq\kappa\Theta/\hbar$. Direct computation with (41), expanded, yields

$$\sigma_{\text{inc}}(\mathbf{p}')=(Np'/\hbar p)[(a^2)_{Av}-(a)_{Av}^2]$$
$$\times\exp[-(\Delta p)^2\langle u_\alpha^2\rangle_T]H(\Delta\mathbf{p},\Delta E), \quad (42)$$

where

$$H(\Delta p,\Delta E)=\delta(\Delta E)+\frac{1}{|\Delta E|}\sum_{n=1}^{\infty}\frac{1}{n!(2n-1)!}$$
$$\times\left(\frac{3\hbar^4(\Delta p)^2(\Delta E)^2}{2M(\kappa\Theta)^3}\right)^n. \quad (43)$$

The delta function $\delta(\Delta E)$ evidently represents elastic scattering in the zero-quantum case, and the terms following add the inelastic effects of all other quantum processes.

The scattering of x-rays and electrons by crystals, as we have noted earlier, is usually studied at energies high enough that the gain or loss of lattice quantum energies is relatively insignificant. In cases such as these, the final energies will be in a band so narrow that for any given direction of scattering they may be integrated over without appreciably disturbing the value of $\Delta\mathbf{p}$. Such integrations may be carried out on the cross sections (40) and (41). Letting $p'=p$, and holding $\Delta\mathbf{p}$ fixed, we may extend the limits of the ΔE integration to ∞ and $-\infty$, since it is assumed that only the central region contributes. The integrations over ΔE performed in this way place the delta function $\delta(t)$ within the time integrations which may then be performed directly. The results are seen to contain

[18] G. Placzek and L. Van Hove, Phys. Rev. **93**, 1207 (1954).

only the correlation function evaluated at time $t=0$.

$$\int \sigma_{\rm coh}(\mathbf{p}')d(\hbar E')$$

$$=N(a)_{Av}^2 \exp[-\langle(\Delta\mathbf{p}\cdot\mathbf{u})^2\rangle_T]$$

$$\times\sum_j \exp[i\Delta\mathbf{p}\cdot\mathbf{r}_j+\Delta\mathbf{p}\Delta\mathbf{p}:\mathbf{C}_T(\mathbf{r}_j,0)], \quad (44)$$

$$\int \sigma_{\rm inc}(\mathbf{p}')d(\hbar E')=N[(a^2)_{Av}-(a)_{Av}^2]. \quad (45)$$

These, of course, are just the results of the static treatment usually employed in the study of x-ray diffraction. They may be arrived at somewhat more directly by assuming the lattice vibration frequencies relatively so low that the passage of the particle through the system is effectively instantaneous. This makes it possible to replace the correlation function by its value for vanishing time intervals $C_{\alpha\beta,T}(\mathbf{r},0)$, the scattering being thereby represented as elastic $[\sigma(\mathbf{p}')\sim\delta(\Delta E)]$. A procedure for correcting the angular distributions resulting from the static approximation has been introduced by Placzek.[19] In the present context it corresponds directly to expanding the function $\exp[\Delta\mathbf{p}\Delta\mathbf{p}:\mathbf{C}_T(\mathbf{r},t)]$ in successive powers of t.

Another limit whose discussion is instructive is that of large momentum transfer and/or high crystal temperature, i.e., large values of $\langle(\Delta\mathbf{p}\cdot\mathbf{u})^2\rangle_T$. In such cases a detailed discussion of the coherent cross section shows that the interference effects represented by the lattice points $\mathbf{r}_j\neq 0$ become relatively small. For these points the correlation function is too small to compensate the negative exponent of the Debye-Waller factor. The coherent scattering in this limit comes entirely from the point $\mathbf{r}_j=0$, and is proportional to the incoherent scattering.[20]

The energy dependence of the incoherent scattering may also be found in the same limit, $\langle(\Delta\mathbf{p}\cdot\mathbf{u})^2\rangle_T\gg 1$, and we include it as a further illustration of the time-dependent method. The definition (7) of the correlation function shows that the real part of $C_{\alpha\beta,T}(0,t)$ is stationary at $t=0$, and as we shall see this corresponds to a maximum. Since asymptotically the principal contribution to the time integration will come from near $t=0$, we expand the correlation function:

$$C_{\alpha\beta,T}(0,t)=C_{\alpha\beta,T}(0,0)+tC_{\alpha\beta}^{(1)}+t^2C_{\alpha\beta,T}^{(2)}. \quad (46)$$

The coefficient $C_{\alpha\beta}^{(1)}$ may be obtained from (7):

$$C_{\alpha\beta}^{(1)}=-i(V_0\hbar/16\pi^3M)\sum_p \int e_\alpha^{(p)}e_\beta^{(p)}d\mathbf{k}.$$

Since the vibrational modes for each propagation vector are mutually orthogonal, this reduces to

$$C_{\alpha\beta}^{(1)}=-i(\hbar/2M)\delta_{\alpha\beta}, \quad (47)$$

an expression independent of the lattice structure. If the t^2 term were negligible, substitution of (46) in (41) at this point would yield $\sigma_{\rm inc}(\mathbf{p}')\sim\delta(\Delta E+(\hbar(\Delta p)^2/M))$. The scattering would in effect be by free particles of mass M.

The Debye approximation may be used to estimate the quadratic term of (46). This is

$$C_{\alpha\beta,T}^{(2)}=-(V_0\hbar/16\pi^3M)\delta_{\alpha\beta}$$

$$\times\int\{\tfrac{1}{2}+[\exp(\hbar\omega/\kappa T)-1]^{-1}\}\omega d\mathbf{k}$$

$$=-[\hbar\mathcal{E}(T)/2M]\delta_{\alpha\beta}, \quad (48)$$

where $\mathcal{E}(T)$ is defined as $\hbar^{-1}$ times the average thermal energy per lattice particle (including zero-point energy). The time integral required, of the exponential of a form quadratic in t may be performed immediately to yield a Gaussian distribution[5] of final energies centered about $\Delta E=-\mathcal{E}_r=-\hbar(\Delta p)^2/2M$, with a dispersion proportional to $[\mathcal{E}_r\mathcal{E}(T)]^{\frac{1}{2}}$. In the limit we have been discussing, the residual effects of interference in the coherent cross section may be estimated by similarly using the maxima of the real part of $C_T^{(D)}(\mathbf{r}_j,t)$ which occur near $t=\pm r_j/s$, where s is the sound velocity. For this purpose, however, it would be desirable to employ a correlation function representing dispersive effects more realistically.

Applications of the time-dependent method to neutron scattering by molecular systems will be discussed in a forthcoming paper.

[19] G. Placzek, Phys. Rev. 86, 377 (1952).

[20] A. Akhiezer and I. Pomeranchuk, reference 5, have discussed many quantum processes in the high energy limit, and have stated a form of (40), for the Debye model, retaining, in effect, only the central lattice point $\mathbf{r}_0=0$. The derivation given appears to omit certain terms leading to the Debye-Waller factors when the number of quanta is greater than zero, although these appear in the result stated. The same argument is repeated in their text, A. Akhiezer and I. Pomeranchuk, *Certain Topics in Nuclear Theory* (Moscow, 1950), revised second edition.

Atomic Heats of Copper, Silver, and Gold from 1°K to 5°K*

WILLIAM S. CORAK, *Westinghouse Research Laboratories, East Pittsburgh, Pennsylvania and Department of Chemistry, University of Pittsburgh, Pittsburgh, Pennsylvania*

AND

M. P. GARFUNKEL, C. B. SATTERTHWAITE, AND AARON WEXLER, *Westinghouse Research Laboratories, East Pittsburgh, Pennsylvania*

(Received December 20, 1954)

The atomic heats of copper, silver and gold have been determined in the temperature interval 1.0° to 5.0° K. The measured values can be described adequately by a linear plus a cubic term in temperature. Any deviations from this relationship are explainable in terms of inaccuracies in the presently accepted helium vapor pressure—temperature scale. In fact, it is shown that the temperature scale corrections, necessary to correct the data to the simple law given above, essentially agree with temperature scale corrections suggested by other work. Values of the coefficient of the linear term (electron heat capacity) and the Debye characteristic temperature have been derived and compared with several indirect determinations, as well as with other calorimetric data, where possible. The values of the electronic heat capacity determined in the work are consistently lower than those from previous work on copper and silver.

INTRODUCTION

MEASUREMENTS[1] of the atomic heat of the noble metals in the temperature region 1°K to 5°K have been undertaken in order (a) to extend the region in which the atomic heat of gold has been measured; (b) to investigate the anomaly reported in the atomic heat of silver by Keesom and Pearlman[2]; and (c) to repeat with greater accuracy the earlier measurements made on copper and silver by Keesom and Kok[3,4] so as to make possible a comparison of the experimental atomic heats with the theoretical predictions. Our preliminary experiments on these metals have already been reported.[5]

In the temperature region under consideration the atomic heat of these metals can be considered to be composed of two terms, one linear and one cubic in temperature:

$$c=\gamma T+\beta T^3. \tag{1}$$

The term linear in temperature is due to the conduction electrons and is related to the density of one-electron energy levels[6] by

$$\gamma=\tfrac{1}{3}\pi^2k^2\eta(\zeta), \tag{2}$$

where k is the Boltzman constant, $\eta(\epsilon)$ is the number of one electron states per unit energy at the energy ϵ, and ζ is the energy at the top of the Fermi distribution. Buckingham and Shafroth[7] have pointed out that the interaction between electrons and lattice may cause a modification of the density of electron states at low temperatures. This would change the temperature dependence and magnitude of the electronic heat capacity. The term in Eq. (1) that is cubic in temperature is the low-temperature approximation to the lattice heat capacity of a solid.[8] The coefficient, β, is related to the Debye characteristic temperature, Θ, by

$$\beta=(12/5)\pi^4R/\Theta^3, \tag{3}$$

where R is the molar gas constant. At *sufficiently* low temperatures it is expected that the Debye approximation will hold; but it is not known that the interval 1°K to 5°K is sufficiently low for these metals.[9] In the temperature region where the Debye approximation is valid, Θ should be simply related to the elastic constants of the material. Thus, at $T=0$°K it is expected that the Θ calculated from elastic constants will agree with that determined from heat capacity.

In order to be able to make the separation of the two terms in Eq. (1), and to compare these terms with the theory, it is necessary to obtain an accuracy of measurement which is not characteristic of the earlier work in this field. In the present work, the aim has been to maintain fractional errors in the determinations of atomic heat at less than 1 percent.

EXPERIMENTAL

In Fig. 1 is shown schematically the low-temperature portion of the apparatus, most of the details of which are given in the legend. The thermometer, a carbon resistor,[10] whose plastic insulation has been ground off,

* A portion of the research reported in this paper was submitted by William S. Corak to the Graduate School of the University of Pittsburgh in partial fulfillment of the requirements for the degree of Doctor of Philosophy.

[1] Westinghouse Research Report No. 60-94466-5-R1 gives, in addition to the material presented in this paper, schematic drawings of the electrical circuits and tables of calibration and heat capacity data. This report is available on request.

[2] P. H. Keesom and N. Pearlman, Phys. Rev. **88**, 140 (1952).

[3] J. A. Kok and W. H. Keesom, Leiden Comm. No. 245a.

[4] W. H. Keesom and J. A. Kok, Leiden Comm. Nos. 219d and 232d.

[5] Corak, Garfunkel, and Wexler, *Third International Conference on Low Temperature Physics* (Rice Institute, Houston, 1953).

[6] A. H. Wilson, *The Theory of Metals* (Cambridge University Press, Cambridge, 1953), p. 144.

[7] M. J. Buckingham and M. R. Shafroth, Proc. Phys. Soc. (London) **A67**, 828 (1954).

[8] A. H. Wilson, *The Theory of Metals* (Cambridge University Press, Cambridge, 1953), pp. 133–141.

[9] See reference 8, pp. 141–142.

[10] The properties of carbon resistors used as thermometers at low temperatures have been discussed by J. R. Clement and E. H. Quinnell, Rev. Sci. Instr. **23**, 213 (1952).

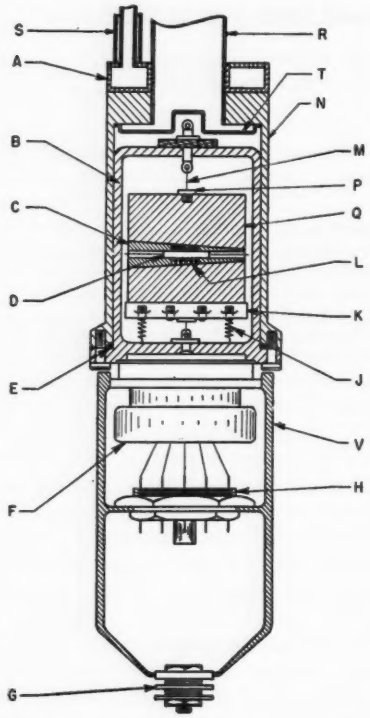

FIG. 1. Calorimeter. *A*, bulb of vapor pressure thermometer; *S*, vacuum jacketed tube to the vapor pressure thermometer; *N*, vacuum tight outer brass container; *R*, pumping tube; *T*, radiation shield; *B*, brass yoke; *Q*, sample; *M*, nylon thread; *P*, brass screws; *K*, beryllium-copper support ring; *J*, thermometer and heater leads; *C*, beryllium-copper tapered plug; *D*, carbon resistance thermometer; *L*, manganin resistance heater; *E*, gold "O" ring; *F*, wire-glass vacuum seal; *H*, coupling plug; *G*, bath heater; *V*, plastic holder.

is lacquered into the plug. Wound on the plug and lacquered in place is the heater, about 2000 ohms of 0.001-in. manganin wire. The ring, the plug with heater and thermometer, and the brass screws make up the addenda whose heat capacity must be subtracted from a measured heat capacity in order to obtain the heat capacity of the sample. The lead-in wires are 0.003-in. manganin wire. There are two current and two potential leads for the heater and for the resistance thermometer. The resistance of the current leads to the heater is approximately 5 ohms each; that of each of the other lead-in wires is about 35 ohms. The gold "O" ring[11] makes the vacuum seal between the brass yoke and the outer container.

In addition to the radiation shield shown in Fig. 1, a trap containing several baffles is located in the high vacuum pumping line just above the sample container. This has been inserted because crude estimates indicate that large amounts of energy (compared with energies involved in a measurement of heat capacity) can be given to the sample from room temperature radiation or from hot gas molecules.

The calorimeter portion of the apparatus is maintained at low temperatures by immersing it in liquid helium in a metal dewar. The dewar holds enough liquid to last for more than 24 hours, making it convenient to extend a heat capacity determination over an interval of several days without warming the apparatus above the temperature of liquid helium. The bath temperature is controlled by a pumping system which makes attainable temperatures down to $\sim$1.1°K.

A high-vacuum system is used to isolate the sample after it has been cooled to the bath temperature with helium gas as the exchange medium. The characteristics of this vacuum system have been discussed elsewhere.[12]

To measure both the current through and the potential difference across the carbon resistance a double potentiometer is used. The detector for the potentiometer is a dc amplifier whose output is fed into a Speedomax recorder, so that off-balance potential drops can be recorded as a function of time.

The power to the heater is determined by measurements of both current and potential drop made on a potentiometer. The time of heating is measured by a clock which is started by a relay which also closes the heater current circuit.

The samples are cylinders, 2-in. long by 1-in. diameter. The properties of the samples are given in Table I.

To obtain the heat capacity of a sample, measurements of heater voltage and current, time of heating, and thermometer resistance as a function of time are made. The initial and final temperatures, T_i and T_f, are computed from the resistance measurements, and heat capacity, C, is evaluated by the relationship,

$$C=EIt/(T_f-T_i), \tag{4}$$

where E = heater potential drop, I = heater current, and

TABLE I. Properties of samples.

Sample	Mass (grams)	Purity (%)	Vacuum anneal	Supplier
Cu	221.268	99.999+[a]	1000°C—3 hr	Amer. Smelt. and Ref. Co.
Cu holder	24.446	99.999+[a]	1000°C—3 hr	Amer. Smelt. and Ref. Co.
Ag	260.620	99.98[b]	700°C—4 hr	Handy and Harmon Co.
Ag holder	17.065	99.98[b]	700°C—4 hr	Handy and Harmon Co.
Au	486.38	99.99+[b]	950°C—4 hr	J. Bishop Co.

[a] Purity given by Smith, Smart, and Phillips, Am. Inst. Mining Met. Engrs. **143**, 272 (1941).
[b] Purity given by supplier.

[11] Wexler, Corak, and Cunningham, Rev. Sci. Instr. **21**, 259 (1950).
[12] M. P. Garfunkel and A. Wexler, Rev. Sci. Instr. **25**, 170 (1954).

t = time of heating. This is, then, the heat capacity at the average temperature $(T_f+T_i)/2$.

Figure 2 shows two typical recordings of thermometer potential drop as a function of time. The lower part of each curve corresponds to the drift of the temperature of the thermometer before heating; the rapid rise occurs during the heating. The height of the overshoot shows the lead that the temperature of the thermometer has over the temperature of the sample. When the heater power is turned off, the temperature of the thermometer falls back to the sample temperature which then continues to drift as before. As can be seen it is then a simple matter to extrapolate both the drift before and the drift after heating to the center point of the heating period. These extrapolated values of the thermometer potential drop are used to calculate the initial and final resistances. Finally, temperatures are obtained from the resistance-temperature relationship determined from a calibration of the carbon resistance against the vapor pressure of liquid helium.

The results of the measurements give the heat capacity of the particular sample plus the heat capacity of the addenda. Two measurements on silver (silver sample and silver holder) were combined to determine the heat capacity of the addenda. The addenda correction was then available for subtraction from measurements on the copper and gold samples.

A simple calculation of the thermal conductivity of helium gas at liquid helium temperatures shows that (for reasonable assumptions for the accommodation coefficient, i.e., of the order of unity) the pressures necessary for good isolation of the sample are 5×10^{-8} mm of Hg or better. These pressures are easily obtained, and in this experiment have been accurately measured.[12] However, it is only possible to measure the equilibrium pressure in the region of the sample. If, during the heating period helium gas were to be driven from the sample, reducing the insulating vacuum during the time of heating, it would not be detected if it were readsorbed by the walls. This gas would contribute to errors in the measured heat capacity in two ways: it would change the thermal coupling between sample and bath during heating, making extrapolation of drifts incorrect; and it would carry off its heat of adsorption, increasing the apparent value of the heat capacity. In order to investigate the effect of adsorbed gas, an experiment was performed with a copper holder which had approximately the same area as the copper sample but about 1/10 of the mass. The measured heat capacity of this holder was thus very sensitive to the effect of adsorbed gas. The copper holder was coupled to the helium bath with a fine wire, so that it could be cooled to the lowest temperatures without using helium exchange gas. The resulting increased drift rate was tolerated for this experiment. The experiment consisted of making measurements of the heat capacity of this holder, first without using helium gas to cool to the lowest temperature, and then with helium gas. The measurements could only be made down to 1.4°K because the thermal conductivity of the wire coupled with the extraneous heating in the sample maintained a difference of 0.2°K–0.3°K between the sample and the bath.

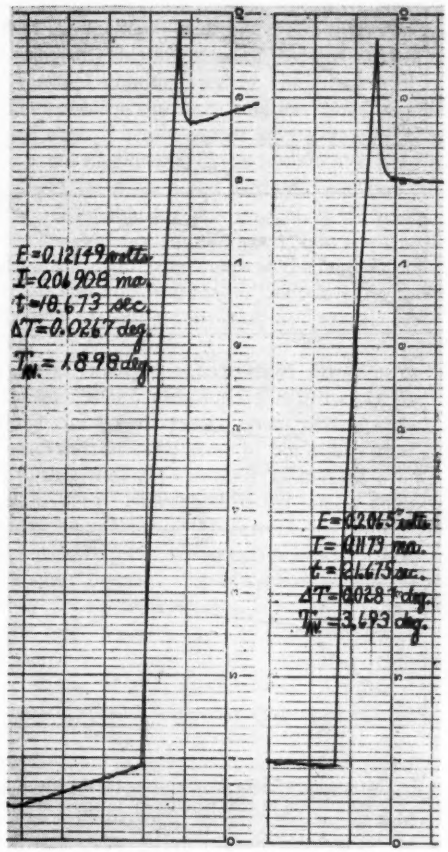

FIG. 2. Typical heating curves.

It was observed that when the sample was at the bath temperature, but thermally isolated from it, the temperature of the sample increased at rates corresponding to heat inputs anywhere from 30 ergs/min to several thousand ergs/min. Some of the sources of this energy may be (a) the dissipation of vibrational energy in either the sample or its suspension and leads, (b) hot gas molecules or room temperature radiation impinging on the sample, (c) electrical pickup being dissipated in the heater or thermometer, and (d) the dissipation of eddy currents induced in the sample by local magnetic fields. It was possible to select for the experimental work, periods of time during which the stray power input from these sources was consistently maintained in the range below 100 ergs/minute. This has been found adequate for the present measurements and, therefore, it was not considered worth the required effort to reduce further this stray energy input.

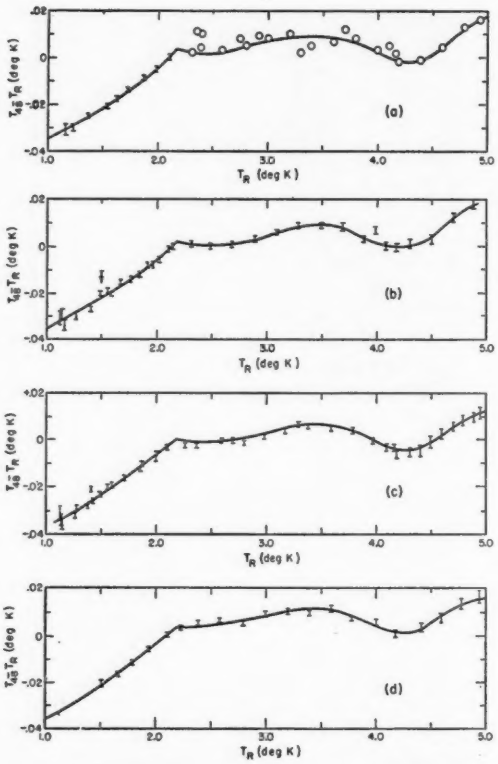

FIG. 3. Thermometer calibration curves (a) in silver holder, (b) in copper sample, (c) in gold sample, (d) in silver sample. The vertical lines in curves (b), (c), (d), and below ~2.2°K in curve (a) indicate the probable error of a measurement.

THERMOMETRY

The resistance thermometer used for all measurements was a ½-watt, 56-ohm, Allen-Bradley carbon composition resistor. The current used in measuring the resistance varied from 0.1 to 5.0 microampere, selected large enough to give adequate accuracy in determining resistance and small enough to give a negligible energy dissipation in the resistor. Calibrations were made as a function of current at several temperatures to find whether there was any current dependence of the resistance. In the range of currents used in this experiment, no current dependence was found.

The resistance thermometer was calibrated against the vapor pressure of liquid helium on the basis of the "agreed" helium vapor pressure-temperature scale of 1948.[13] (Temperatures and quantities which are derived from the temperature scale have a subscript, 48, if the above vapor pressure-temperature scale has been used.) Calibration points were taken at intervals of 0.2°K or less between 2.2°K and 5.0°K, and 0.15°K or less below 2.2°K. A complete calibration was made before each heat capacity experiment, and a few points were repeated after the experiment to check whether the thermometer had changed during the experiment. For calibration, the sample and thermometer were thermally coupled to the bath and vapor pressure thermometer by admitting helium at about 0.030 mm of Hg pressure to the calorimeter at 4.2°K. An experiment showed that this provided adequate coupling: under these helium pressure conditions, a heat input from the heater of several thousand ergs/minute caused a temperature rise of the thermometer of about 0.001°K, while the actual heat flow to the sample from stray sources during calibration was less than 100 ergs/minute.

The temperature of the bath was maintained constant for each calibration point by the regulation of the pressure of helium above the bath by control of the pumping speed. For temperatures above the lambda point of liquid helium, temperatures were always approached from above to avoid the possibility of supercooling the liquid below the surface. Temperature drifts were kept less than 0.0003°K/minute throughout the temperature range, with the exception of the region just above the lambda point where maximum drifts were sometimes as high as 0.001°K/minute.

The helium vapor pressure was measured with manometers of 16-mm precision bore tubing fitted with verniers capable of being read to 0.02 mm. Mercury was used in one manometer for measurements above the helium lambda point, and butyl sebacate in the other manometer for measurements below the lambda point. The butyl sebacate manometer was calibrated by periodic comparisons with the mercury manometer.

In order to calibrate the thermometer, an approximate equation was used which defines a resistance temperature, T_R, and a correction curve was plotted. A convenient two-parameter equation[14] between temperature and resistance, R, which fits remarkably well, is

$$\frac{1}{T_R}=\frac{a^2}{\log R}+b^2\log R+2ab.$$

Two experimental points were used to evaluate the constants a and b, and temperatures, T_R, calculated from the resistance, R, are given throughout the rest of this paper by the equation,

$$\frac{1}{T_R}=\frac{0.73914}{\log R}+0.28552\log R-0.91878, \qquad (5)$$

where R is expressed in ohms and T_R in degrees Kelvin. The calibration then consists of obtaining $T_{48}-T_R$ as a function of T_R. These data[1] are plotted in Fig. 3.

Two methods are commonly employed for obtaining the temperature at some point beneath the surface of a liquid helium bath by vapor pressure measurements: measuring the vapor pressure at the surface of the bath

[13] H. Van Dijk and D. Schoenberg, Nature **164**, 151 (1949).

[14] This equation was suggested to us by J. R. Clement.

and correcting this pressure with the hydrostatic pressure of the column of liquid to the point in question below the surface; or measuring the vapor pressure of helium condensed into a vapor pressure thermometer bulb at the point in question. Both of these methods have been used in these experiments and, therefore, a comparison of the relative reliability of the two methods can be made. The vapor pressure of the cryostat bath was used for the calibration of the thermometer when it was mounted in the silver holder; the vapor pressure thermometer was used for all other calibrations (above the lambda point). In using the bath vapor pressure, corrected for hydrostatic head, for determining temperature, it is assumed that the temperature at any point in the bath is given by the pressure at the surface plus the hydrostatic pressure to that point. This is an unstable temperature distribution in the liquid since the coldest, and therefore most dense, liquid is at the top, and thus, convection currents are set up which try to equalize the temperature throughout the bath to the temperature of the surface. In order to avoid equalization of temperature (since the time constant to reach this condition is unknown), heat was supplied to the bottom of the bath at the rate of 0.040 watt, maintaining vapor-liquid equilibrium throughout the bath, by generating a steady stream of bubbles which rise through the liquid.

As can be seen from the calibration curves of Fig. 3, the scatter of the points, determined from the vapor pressure of the bath [Fig. 3(a)], is many times that determined from the vapor pressure thermometer, [Figs. 3(b), (c), (d)], above the lambda point. In order to locate it exactly, the curve in Fig. 3(a) was assumed to be parallel to the other calibration curves of Fig. 3.

Below the lambda point, the objections to using the vapor pressure of the bath vanish, since the high thermal conductivity of helium II assures equality of temperature throughout the bath. Furthermore, at the lowest temperatures the effect of thermomolecular pressure differences, might be serious if the vapor pressure thermometer were used. Below about 1.4°K this effect was found to cause a difference in pressure reading between the vapor pressure thermometer and the bath. (Because of the superfluidity of helium II, no actual difference in temperature is expected.) For this reason, the vapor pressure of the bath was measured below the lambda point. In the case of the curve in Fig. 3(b) it was necessary to extrapolate the correction curve from 1.4°K down because the original calibration measurements were made with the vapor pressure thermometer, and therefore could not be used.

Uncertainties in temperatures due to the uncertainties in the various measurements comprising a temperature determination are shown by vertical lines on the calibration curves in Figs. 3(b), 3(c), and 3(d). The scatter of the points indicates about the same uncertainty. The correction to the temperature of the thermometer due to the hydrostatic head *difference* between the vapor pressure thermometer and the carbon thermometer has been omitted. This might seem justified in view of the high thermal conductivity of the brass wall of the calorimeter, but a simple calculation shows that even if the wall were of heavy copper a temperature difference of the same magnitude as the hydrostatic head difference could be maintained with a heat flow that is entirely reasonable for this geometry. However, since there is no evidence for this correction from a discontinuity of the calibration curve at the lambda point, the correction has not been made. Undoubtedly, there is a small error introduced by this hydrostatic head difference.

In a heat capacity measurement, errors in the slope of a thermometer calibration curve introduce fractional errors in the heat capacity equal to the slope error. Estimates of the slope error of our calibration curves indicate that they are less than 0.5 percent everywhere except in the neighborhood of the lamba point where they may be as large as 0.5 percent.

Approximately 125 calibration points have been taken on the same thermometer in such a way as to give a measure of the reproducibility. It was found that cycling between room temperature and liquid helium temperatures made no change in the resistance-temperature characteristic of the thermometer. Transferring the thermometer-heater assembly from one sample to another, which may have introduced slight mechanical strains, in some cases caused slight shifts in the *T vs R* curve. The total spread for the entire series of calibrations was less than 0.01°K over the whole range from 1° to 5°K.

The cusp in the calibration curves of Fig. 3 at about 2.2°K is, of course, not expected to be characteristic of the resistance-temperature relationship, but is thought to be due to an inaccurate relationship between temperature and the 1948 agreed temperature scale.

RESULTS

The heat capacity of a sample is obtained from a determination of the quantities on the right-hand side of Eq. (4). Heater current and potential drop and heating time are determined directly, as described in the experimental section. The mean temperature and the change in temperature during and due to heating, however, must be derived from resistance measurements of the thermometer. The resistance of the thermometer is, in general, known accurately enough to determine temperature to 0.0003°K. *Differences* in resistance, however, are known so that differences in temperature can be calculated to 0.0001°K.

From the combination of the data[1] for the silver holder and the silver sample, the heat capacity of the addenda and the atomic heat of silver have been determined. Since the measurements on the holder and the silver sample were not made at the same temperatures, it was necessary to smooth the holder data to combine with the data on the silver sample. The addenda cor-

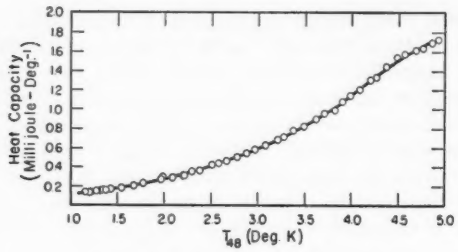

FIG. 4. Heat capacity of addenda.

rection has been plotted in Fig. 4, and it is from this curve that the addenda correction has been taken to obtain atomic heats for copper and gold from the measured heat capacities.

If c/T is written as a function of T^2, Eq. (1) yields a straight line with intercept γ, and slope β. The copper, silver, and gold data are plotted in this way in Figs. 5, 6, and 7, respectively. Only temperatures up to 4.2°K are included since it is not believed that the helium vapor pressure-temperature scale is sufficiently well known to make this plot meaningful above 4.2°K. On this scale, it is seen that a straight line is a good approximation to the data for all three of the metals. A determination of the constants of the lines by the method of least squares (for temperatures up to 4.2°K) gives the values listed in Table II for γ_{48} and Θ_{48}. The probable errors are determined from the scatter of the data from the straight line on the assumption that the errors are random. [In fact, the errors are not random but show a systematic deviation from Eq. (1) as shown in Fig. 8.]

In the experimental section an experiment to determine the effect of residual gas was described. The results of this experiment are plotted in Fig. 9. There are no observable differences between the measured heat capacities with gas and those without down to 1.4°K. Since the resolution corresponds to less than 1 percent of the heat capacity of the samples, it is concluded that there is no effect of gas down to 1.4°K.

The sample of copper reported on previously[5] was different from the sample being reported here, having a different analysis and history. It is reassuring to find that the present sample yields essentially the same values for the constants, γ_{48} and Θ_{48}, to within the accuracy of the former experiment.[15] The silver and gold results are also in agreement with our previous results.[15]

Recently, improvements to the 1948 helium vapor pressure-temperature scale have been proposed which include the whole temperature region from 1.0° to 5.2°K. Erickson and Roberts[16] have found inaccuracies in the 1948 scale in the region from 1.0° to 4.2°K from their measurements on magnetic susceptibilities of paramagnetic salts. Berman and Swenson[17] have proposed a new relationship between helium vapor pressure and temperature from 4.2°K to 5.2°K from a comparison of the vapor pressure of helium with a gas thermometer. The results of our experiments also suggest that the 1948 temperature scale is inaccurate. Figure 8 shows that all three noble metals have systematic deviations from Eq. (1). Since all three, although they have different lattice and electron heat capacities, show the same fractional deviations, it is probable that the deviations are attributable to the temperature scale. For this reason we have set up a

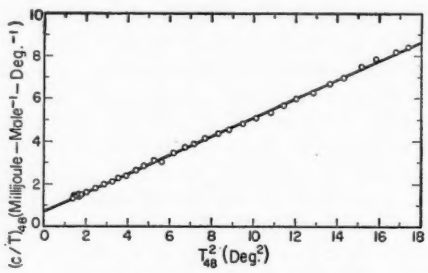

FIG. 7. Atomic heat of gold.

TABLE II. Atomic heat constants calculated from 1948 "agreed" temperature scale.

	Cu	Ag	Au
γ_{48} (millijoules-mole^{-1}-deg^{-2})	0.688±0.004	0.609±0.009	0.70±0.02
Θ_{48}(deg K)	343.2±1.3	225.0±0.5	164.1±0.3

FIG. 5. Atomic heat of copper.

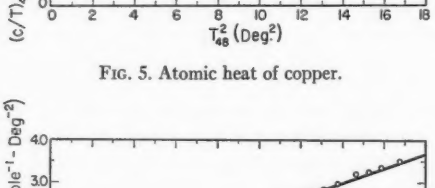

FIG. 6. Atomic heat of silver.

[15] Although the values reported at the conference were correct, the abstract for the conference gave values of γ_{48} that were a factor of 10^3 too large for all three metals. Also the comment about the temperature variation of Θ for the metals, which appears incorrectly in the abstract, was not given in the actual report.

[16] R. A. Erickson and L. D. Roberts, Phys. Rev. **93**, 957 (1954).

[17] R. Berman and C. A. Swenson, Phys. Rev. **95**, 311 (1954).

temperature scale, T_w, for each of the metals, designed so that Eq. (1) represents our results with the corrected values of atomic heat, c_w, and corrected constants γ_w and β_w. This condition leads to the following equation relating the uncorrected and corrected quantities:

$$T_{48}-T_w=\frac{1}{c_{48}}\left\{\frac{\gamma_{48}-\gamma_w}{2}(T_{48}'^2-T_{48}^2)+\frac{\beta_{48}-\beta_w}{4}(T_{48}'^4-T_{48}^4)+\int_{T_{48}}^{T_{48}'}[\delta c_{48}]_s dT\right\}, \quad (6)$$

where $\delta c_{48}=c_{48}-\gamma_{48}T_{48}-\beta_{48}T_{48}^3$, and $[\delta c_{48}]_s$ is the smoothed deviation curve, and T_{48}' is a constant of integration, selected so that the corrected scale, T_w,

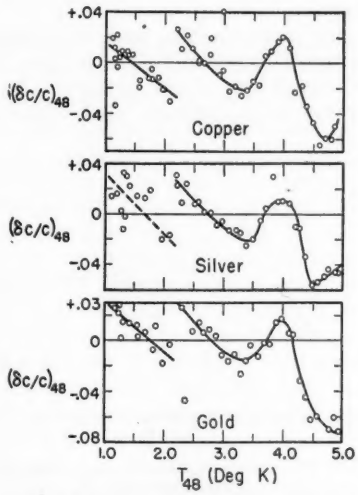

FIG. 8. Fractional deviation in atomic heats calculated on the 1948 temperature scale ($\delta c_{48}=c_{48}-\gamma_{48}T_{48}-\beta_{48}T_{48}^3$).

and the 1948 scale, T_{48}, agree at T_{48}'. The normal boiling point of helium was selected as T_{48}' since, Berman and Swenson[17] found no correction at that temperature. For a complete specification of the corrected temperature scale, T_w, it remained to evaluate the two constants γ_w and β_w in Eq. (6). Arbitrarily, the temperatures 1.6°K and 2.9°K were chosen as convenient and well separated temperatures for evaluating the constants. The corrections at these two points are approximately those of a smooth curve through the magnetic data of Erickson and Roberts,[16] namely at $T_{48}=1.600$°K, $T_{48}-T_w=+0.005$°K and at $T_{48}=2.900$°K, $T_{48}-T_w=+0.001$°K. The constants γ_w and β_w were then evaluated for each of the metals from Eq. (6). Temperature corrections, $T_{48}-T_w$, were calculated from Eq. (6) and plotted in Fig. 10. The points shown are from the magnetic data of Erickson and Roberts[16] below 4.2°K, and from the gas thermometry of Berman and Swenson[17] above 4.2°K. The agreement is within the scatter everywhere except below about 1.4°K where

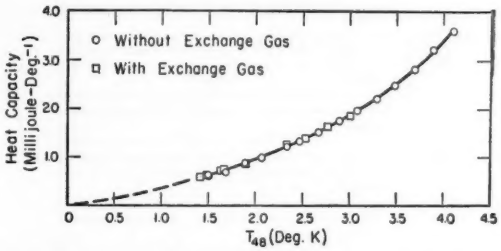

FIG. 9. Heat capacity of copper holder as determined with and without exchange gas.

our data are suspect (A 1 percent to 2 percent error in the heat capacities would explain the low temperature disagreement.) The differences between the curves for copper, silver, and gold are within the experimental error. The curves of Fig. 10 are not meant to be a proposal of a new helium vapor pressure-temperature relationship, but are rather to be considered as confirming evidence of the temperature scale errors pointed out by Berman and Swenson[17] and by Erickson and Roberts.[16] Furthermore, these results are considered to demonstrate that the present measurements show that the atomic heats of the noble metals can be described by Eq. (1) to the accuracy with which the temperature scale is known.

Since it appears that any of the three curves of Fig. 10 gives temperatures, T_w, which are closer to the thermodynamic temperature than the temperatures from the 1948 "agreed" scale, the values of γ_w and Θ_w as calculated from Eq. (6) are given in Table III. These are believed to be better approximations than the values calculated on the 1948 scale. If the atomic heat is now calculated from these constants, and the difference between the calculated and measured values is plotted, it is seen that the errors are random (Fig. 11); indeed, the procedure employed here has forced randomization. The probable errors in γ_w and Θ_w calculated from this scatter is considerably smaller than those calculated for γ_{48} and Θ_{48}. (Two or three points for each

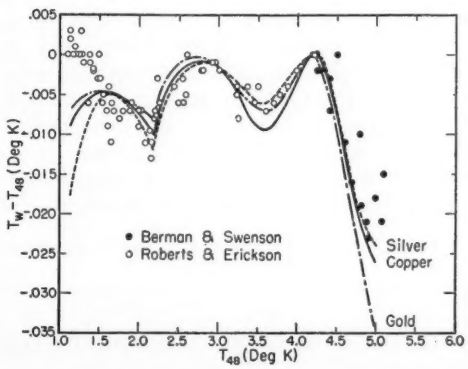

FIG. 10. Correction to the 1948 temperature scale calculated from the atomic heats of the noble metals.

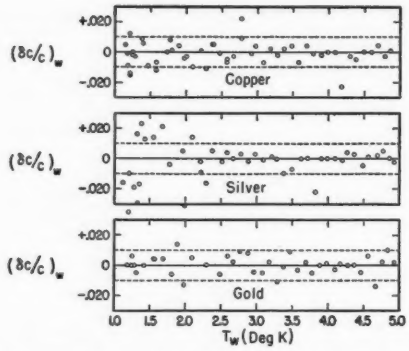

FIG. 11. Fractional deviations in the atomic heat calculated on the corrected temperature scale ($\delta c_w = c_w - \gamma_w T_w - \beta_w T_w^3$).

sample have been omitted from the plots of Fig. 11 since they were off the scale; however, they have been included in the estimate of the probable error.)

If the carbon resistance is recalibrated against one of the corrected temperature scales, then instead of the irregular curve of Fig. 3(c), the calibration becomes the smooth curve of Fig. 12. This is a much more reasonable dependence of resistance on temperature.

In order to estimate the probable error in a heat capacity determination at a temperature, T, errors in the following quantities are considered: (a) energy supplied to the sample; (b) the temperature rise of the sample; and (c) the mean value of the temperature.

The energy which is dissipated in the heater is determined from measurements of current, potential drop, and time of heating. These quantities all have uncertainties of less than 0.1 percent and therefore are not significant sources of error. However, it may be that not all of the energy dissipated in the resistance enters the sample and the addenda, but that a fraction may be drained off through the leads or may be carried off by the gas. The result of the experiment without gas shows that even at the lowest temperatures checked (about 1.4°K), the contribution of gas to the error in heat capacity of a sample is well under 1 percent and is negligible at higher temperatures. However, it is possible, since no experiment has been done to show otherwise, that an error of a few percent may occur from this source below 1.4°K. The heat that may be carried off through the leads has been estimated from the temperature rise of heater and thermometer, and appears to contribute less than 0.1 percent.

Errors introduced by uncertainty in the temperature rise due to heating are probably the largest sources of error of the experiment. The change in resistance is known accurately enough to determine temperature changes to about 0.6 percent. This results from limitations in reading and extrapolating the resistor potential drop *vs* time record and from limitations in the graphical interpolation of the temperature calibration curves. At the lowest temperatures, the drift rates are large, introducing a large uncertainty in extrapolation. This may contribute a percent or more error to the heat capacity measurements. There has been also introduced about a 0.1 percent rounding error from the calculations. These are all random errors and should show up in the results as scatter. The errors in heat capacity introduced by the uncertainty of the calibration of the thermometer, however, are systematic. They have been estimated to be less than 0.5 percent in the section on thermometry.

Finally, the errors, resulting from the uncertainty in the thermometer current and potential drop measurements, in the mean temperature are less than 0.1 percent over the range of temperatures used. There are also uncertainties in temperature due to the inaccuracies of the calibration. These are systematic errors which are less than 0.1 percent except at the lowest temperatures.

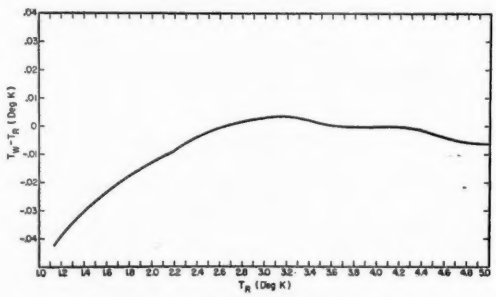

FIG. 12. Thermometer calibration curve using corrected temperature scale, T_w.

The errors which are expected to be statistical are about 0.8 percent to 0.9 percent. This is in agreement with the actual scatter (Fig. 11). The systematic errors that have been estimated above yield an uncertainty of 0.5 percent or less in a heat capacity determination.

There are still errors in heat capacity that are introduced by the uncertainty of the temperature scale. From the agreement between T_w and the temperature scale data of the authors quoted above,[16,17] these errors are expected to be everywhere less than 0.5 percent.

Table IV gives a comparison of our results with several calorimetric and indirect determinations of γ and Θ, for copper, silver, and gold. De Launay[18] and

TABLE III. Atomic heat constants calculated from corrected temperature scale.

	Cu	Ag	Au
γ_w(millijoules-mole^{-1}-deg^{-2})	0.688±0.002	0.610±0.005	0.743±0.014
Θ_w(deg K)	343.8±0.5	225.3±0.2	164.57±0.14

[18] J. De Launay, J. Chem. Phys. **22**, 1676 (1954). Case 2 of this paper has been used for comparison with this work, since it is evident that as 0°K is approached the elastic constants determined by low-frequency velocity-of-sound measurements are appropriate and *not* the constants corrected by subtraction of the contribution of the conduction electrons.

TABLE IV. Comparison of atomic heat constants from this work with previous calorimetric and indirect determinations.

		Cu		Ag		Au	
		γ (millijoules-mole^{-1} deg^{-2})	Θ (°K)	γ (millijoules-mole^{-1} deg^{-2})	Θ (°K)	γ (millijoules-mole^{-1} deg^{-2})	Θ (°K)
Calorimetric	This work	0.688	343.8	0.610	225.3	0.743	164.57
	Keesom and Kok[a,b]	0.74	335	0.67	230	...	...
	Keesom and Pearlman[d]	...	...	0.645[c] 0.782[c]	229.0[c] 229.5[c]	...	...
	Esterman, Friedberg, and Goldman[e]	0.75	335	...	...	...	...
	Rayne[f]	0.72	...	0.67	...	...	...
Indirect	De Launay[g]	...	345.3	...	...	...	...
	Leighton[h]	...	345	...	229	...	...
	Schulz[i]	0.72	...	0.61	...	0.62	...
	Jones[j]	0.69	...	...	...	...	...

[a] See reference 3.
[b] See reference 4.
[c] The authors give two pairs of values for γ and Θ, one pair below ~2.0°K and one above.
[d] See reference 2.
[e] See reference 24.
[f] See reference 25.
[g] See reference 18.
[h] See reference 19.
[i] See reference 20.
[j] See reference 22.

Leighton[19] have calculated the values of Θ from the elastic constants. Schulz[20] reported values for the effective mass, m^*, of the electrons from the room temperature absorptivity of the metals. These have been converted to electronic heat capacities as in Wilson,[21] on the assumption that there is one conduction electron per atom. Jones'[22] value of γ for copper was obtained from a density-of-states calculation.

The agreement between the derived values of γ and our calorimetric determinations is as close as can be expected (with the possible exception of gold) on the basis of the accuracies of the various measurements and the approximations of the theory. This agreement with quantities, determined from high-temperature measurements, and the linearity of the electronic terms in the region 1°K to 5°K lend no support to a low-temperature variation of the electron density of states resulting from electron-lattice interactions.[7] Of course, these are metals which show a very weak electron-lattice interaction, as is known from the high-temperature resistance, and would thus give a relatively small effect.

The values of Θ derived from elastic constants are in excellent agreement with our calorimetric data. Except for copper, where the elastic constants have been recently measured,[23] small disagreements may be due to the errors in the elastic constants rather than to limitations of the model.

Finally, the comparison of our results with various other calorimetric data show that our values for γ, although often within the probable error of the other authors,[2–4,24,25] are generally low, for both silver and copper. Our Θ values, however, are in somewhat better agreement. In the case of silver, no evidence is found for an anomaly of the type reported by Keesom and Pearlman.[2]

ACKNOWLEDGMENTS

We are pleased to acknowledge the contribution of Mr. George T. Cunningham, who constructed most of the apparatus and helped in its design. One of us (W.S.C.) wishes to express his gratitude to Dr. W. E. Wallace of the Department of Chemistry of the University of Pittsburgh for acting as his faculty adviser during the period of his graduate studies at that institution.

[19] R. B. Leighton, Revs. Modern Phys. **20**, 165 (1948). The elastic constants reported by De Launay (reference 18) are used here for copper in Leighton's equations to find Θ for copper.
[20] L. G. Schulz, Phys. Rev. **94**, 1422(A) (1954). The numerical values, which were given in the paper, do not appear in this abstract.
[21] A. H. Wilson, *The Theory of Metals* (Cambridge University Press, Cambridge, 1953), pp. 44, 146.
[22] H. Jones, Proc. Phys. Soc. (London) **49**, 250 (1937).
[23] The measurements have been made by Overton, as reported in reference 18.
[24] Estermann, Friedberg, and Goldman, Phys. Rev. **87**, 582 (1952).
[25] J. Rayne, Phys. Rev. **95**, 1428 (1954).

Photoelastic Observations of the Expansion of Alkali Halides on Irradiation*

W. PRIMAK, C. J. DELBECQ, AND P. H. YUSTER
Chemistry Division, Argonne National Laboratory, Lemont, Illinois
(Received February 24, 1955)

Alkali halide crystals subjected to a nonuniform irradiation by x-rays or high-energy deuterons are found to become anomalously birefringent. The effect has been studied in detail in lithium fluoride. It is shown that the birefringence is due to the photoelastic effect accompanying a nonuniform dilatation which is calculated from the measured birefringence with the aid of elasticity theory. The crystals are colored as a result of the irradiation; and from the absorption coefficients, the number of color centers per unit volume is calculated. It is found that the volume of vacancies per unit volume is approximately equal to the dilatation. A possible explanation for this result is that the vacancies associated with the color centers are generated at the jogs of edge dislocations during irradiation.

ANOMALOUS birefringence was first reported by Brewster (1815–1818); and by the end of the century, a large number of examples had been collected by Brauns.[1] A new example appeared when crystals of lithium fluoride[2] which had been bombarded by 21-Mev deuterons from the 60-inch Argonne National Laboratory cyclotron[3] for about one microampere sec/cm^2 (about 10^{13} deuterons/cm^2) were examined with polarized light. A number of other crystals were bombarded, but the effect was found only in alkali halides. Of those tried, lithium fluoride proved the most amenable to investigation because it did not become strongly colored in the visible region, because it was easy to handle, and because it possessed an effect which was stable. It was therefore chosen for a detailed investigation.

EXPERIMENTAL

Observation and Cause of the Birefringence

The first observations of the birefringence in deuteron-bombarded lithium fluoride were made with a petrographic microscope using the usual techniques of the full-wave plate and the quartz wedge. This method was supplanted with the technique suggested by Goranson and Adams.[4] The condenser of the microscope was removed, and for most of the observations the polarizer was illuminated with parallel white light. The polarizer was set parallel to a quarter-wave plate inserted in the slot. A long-focal-length objective was used, and the ellipticity produced by a specimen on the stage was determined from the analyzer setting. This arrangement of the microscope as a Goranson-Adams polarimeter will be designated in this paper as G.A. With the G.A. the retardation of a uniaxial specimen whose principle axis is set at 45 deg to the polarizer is $\lambda\theta/180$, where λ is the wavelength of the light and θ is the angular displacement required to restore extinction after inserting the specimen. A sharper zone of extinction is obtained in a specimen of variable birefringence when white light is used. It is assumed that extinction is obtained for the wavelength for which the $\lambda/4$ plate has been constructed. Because of a small amount of strain in the glass of the optical system, extinction without a specimen on the stage did not occur with the analyzer set exactly at 0° and varied slightly over the field. The accuracy of the retardation measurements was about 10 percent. The orientation of the crystals is given in terms of rectangular axes perpendicular to the cleavage planes of the crystal. In all cases the irradiating beam was nearly parallel to the y axis, and observations were made in the z direction (the microscope axis).

The appearance of a typical deuteron-bombarded lithium fluoride crystal examined with the G.A. is shown in Fig. 1 in a series of photographs taken at various analyzer settings. This crystal was 0.7 cm thick in the z direction. Except for two prominent scratches and the region beyond the field of the microscope, the dark areas are the result of extinction and are not due to absorption. It can be seen that the deuteron beam was at a small angle to y (almost parallel to the shorter edge of the crystal) forming two highly birefringent zones, a wider zone of 1.3 mm width represented by the strip at the top of each photograph and a narrower strip at the left side. These zones were colored as described by Delbecq *et al.*[3] The birefringence was not uniform, and as well as could be ascertained, the maximum birefringence corresponded to the maximum coloration and occurred at about the end of the deuteron range. A small birefringence is also seen in the unirradiated (and uncolored) region beyond the end of the range. The small, more strongly birefringent region in the lower left corner was caused by strains introduced by the cleaving chisel.

The magnitude of the observed retardations is seen to be small and could easily have been caused by the photoelastic effect of a small strain. Retardations of

* Based on work performed under the auspices of the U. S. Atomic Energy Commission.

[1] R. A. Brauns, *Die Optische Anomalien der Kristalle* (Preisschrift, Leipzig, 1891).

[2] The specimens used in this work were parallelopipeds cleaved from samples of commercial optical grade single crystals of lithium fluoride. These specimens are referred to as *crystals* in this paper.

[3] Delbecq, Ramler, Rocklin, and Yuster, Rev. Sci. Instr. **26**, 543 (1955).

[4] R. W. Goranson and L. H. Adams, J. Franklin Inst. **216**, 475 (1933).

this magnitude were produced by holding a cleaved face of a crystal for 20 to 40 seconds against a metal surface heated to several hundred degrees centigrade. However, there was no indication that the irradiated crystal had been heated so severely. The crystals were observed to be colored a light green in the irradiated zones when they were removed from the cyclotron beam, and the color was observed to change to a light yellow during the course of a day, in the same manner as had been previously observed by Pringsheim and Yuster for x-irradiated crystals.[5] Had any appreciable heating occurred, the color would have been a brownish-straw, the color observed when the crystals were heated subsequent to bombardment. The conclusion was checked by taking a crystal which had previously been uniformly colored lightly with hard x-rays, bombarding it with deuterons, and exploring the absorption of the region beyond the end of the range with the aid of a slit. Only the slightest alteration in the absorption spectrum was observed, proving the temperature could not have risen sufficiently to have produced enough strain to account for the observed retardations.

The birefringence of the deuteron-bombarded crystal may be explained by the strains accompanying a dilatation[6] due to irradiation, the expanded part being held in compression by the portion of the crystal beyond the end of the range. The sign of the birefringence is in conformity with this view. Further, there is apparent a birefringence of opposite sign in the part of the crystal beyond the end of the range of the deuterons, which part, according to this hypothesis, would be in tension.

Another crystal 0.84 cm thick along z, similar in appearance to the crystal shown in Fig. 1, was taken, and a small section containing the narrow irradiated zone (shown at the left of the photographs of Fig. 1) and about an equal thickness of the adjacent unirradiated zone cleaved off (cleavage perpendicular to x). After this was done, the diagonal birefringence pattern evident in Fig. 1 and also originally present in this crystal disappeared, and the birefringence pattern now present was parallel to the wide irradiated zone. The birefringence was measured in a direction perpendicular to the wide irradiation zone (as a function of y) down the center of the remaining crystal and is shown in Fig. 2(a). (This data will be referred to as the data for Crystal I.) This crystal was cleaved again, this time parallel to the wide irradiated zone (perpendicular to y) so that one piece contained the irradiated zone and about an equal thickness of unirradiated crystal. The birefringence as a function of y for this cleavage parallelopiped is also shown in Fig. 2(b) (Crystal II). The remaining unirradiated portion which had been cleaved off did not show any detectable birefringence, as was to be expected if the birefringence was caused by a dilatation in the irradiated portion. To increase the effect in the unirradiated portion, a crystal of thickness about $2\frac{1}{2}$ times the deuteron range was selected and bombarded first from one side and then from the other. The beam did not cover the whole of the faces of the crystal perpendicular to the deuteron beam and was about 0.8 cm wide along z. The appearance of this crystal with the G.A. is shown in Fig. 3. It is seen that a large birefringence is now found in the unirradiated portion of the crystal between the irradiated portions and is of a sign in conformance with the irradiated portions having expanded. The retardation (in angular settings of the analyzer required to produce extinction with white light) measured in the direction z is plotted for various values of y in Fig. 4 (Crystal III).

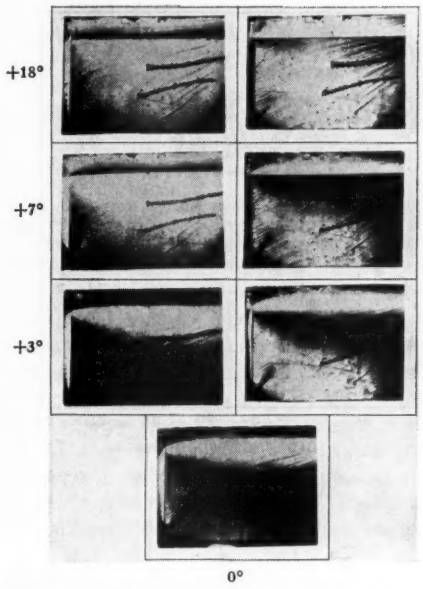

FIG. 1. Deuteron-bombarded lithium fluoride viewed with the Goranson-Adams polarimeter at various settings of the analyzer. Crystal about 5.5×7.9 mm bombarded by about 10^{13} deuterons/cm^2.

The birefringence is undoubtedly a somewhat steeper function near the end of the range than indicated in Figs. 2 and 4 because (a) with the optical arrangement employed, it was not possible to have the whole depth (along z) of the crystal in focus simultaneously; and (b) the plane of the end of the range may not have been exactly parallel to the microscope axis. From the behavior of the birefringence beyond the range, and from the evidence that the birefringence is not due to strains resulting from the heating of the crystal during the irradiation, it is concluded that the birefringence is due to the strains attending a dilatation in the irradiated region.

The birefringence was observed to diminish notice-

[5] P. Pringsheim and P. H. Yuster, Phys. Rev. 78, 293 (1950).

[6] The dilatation is defined as the ratio of the change in volume to the original volume. The dilatation due to irradiation is the dilatation which would be observed on irradiation in the absence of constraint.

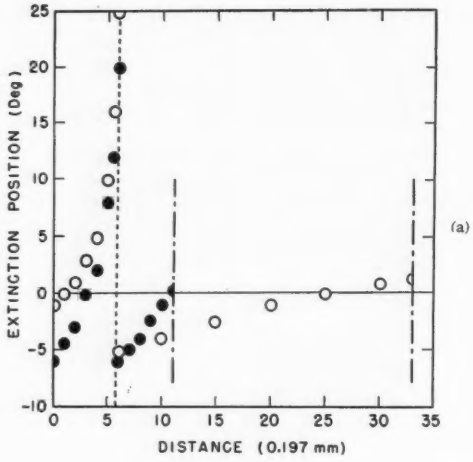

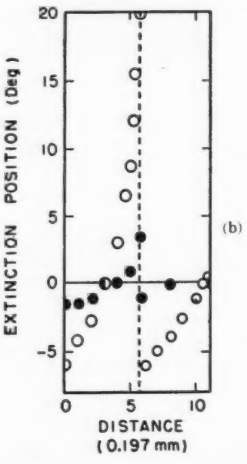

FIG. 2. Extinction position of the analyzer as a function of distance from the irradiated face of a crystal examined with the Goranson-Adams polarimeter. The dotted line is the edge of the colored region; the dot-dash lines, the edges of the respective crystals. (a) Open circles, Crystal I; darkened circles, Crystal II. (b) Open circles, Crystal II before bleaching; darkened circles, Crystal II after bleaching.

ably when the bombarded crystals were exposed under a Mineralight (a low-pressure mercury lamp) for several hours. The behavior of the color of x-irradiated crystals under a Mineralight has been described by Delbecq and Pringsheim,[7] and the behavior of these deuteron-bombarded crystals was found to be the same. The irradiated portion of the crystal, originally pale yellow, first became a light straw-brown. Then, after many hours of exposure under the Mineralight (1 to 2 days), the color bleached almost completely. The manner in which the birefringence of one crystal exposed under the Mineralight for 20 hours was affected, is shown in Fig. 2(b). It can be seen that the birefringence has been reduced to about 10 percent of its former value. Since the birefringence (and hence, the dilatation) diminishes with the bleaching of the color centers, it is concluded that they are associated with each other. Other evidence supporting this conclusion is that the birefringence curves (Figs. 2 and 4) are similar to the curves given by Delbecq *et al.*[3] for the color center concentration along the deuteron path; and, as well as can be determined, the sharp maxima in the color center concentration curves and the birefringence curves occur at the same point. (See Fig. 7.)

If the dilatation is associated with the color centers, it should be in evidence when other methods are used to produce color centers and should be observed through a birefringence if the experimental arrangement is suitable. In the arrangement shown in Fig. 5, a lithium fluoride crystal partially shielded with copper plates 3 mm thick was mounted 2 cm below the beryllium window of a Machlett x-ray tube operated at 50 kev and 50 ma. Two crystals were irradiated, one for three hours, and the other for four hours. Photographs of the first with the G.A. are shown in Fig. 6(A). The crystals were not uniformly colored in depth (along y) because of their large absorption coefficient for soft x-rays. The divergence of the x-ray beam is evident. The birefringence is seen to be greatest in the region at the side of the irradiated portion and has the sign expected if the irradiated portion had expanded. The second crystal showed a larger birefringence than the first. Its appearance after exposure under the Mineralight for about 20 hours is shown in the photographs of Fig. 6(B). There is some modification of the extinction pattern in the irradiated region (which had not been completely bleached by the Mineralight and possessed a straw color) by absorption. However, it is readily apparent that the birefringence in the second crystal after bleaching is much less than in the unbleached first crystal. It is thus seen that irradiation with x-rays

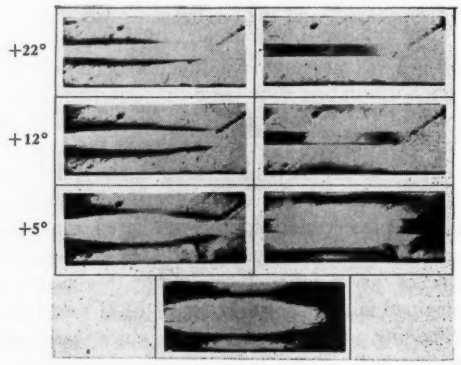

FIG. 3. Part of a crystal of lithium fluoride bombarded by deuterons, about 10^{13} deuterons/cm^2, from opposite faces as viewed with the Goranson-Adams polarimeter.

[7] C. J. Delbecq and P. Pringsheim, J. Chem. Phys. **21**, 794 (1953).

also produces the birefringence effect, and therefore it must be associated with the color centers rather than the irradiation agent.

Other crystals were examined after a deuteron bombardment of about 1 μa sec/cm^2. Similar birefringence effects were found in potassium chloride and potassium iodide, but for these substances the birefringence bore the opposite sign in accordance with their known photoelastic behavior.[8] No effects were observed for corundum or quartz bombarded by the deuteron beam perpendicular to the optic axis and viewed along the optic axis. No effect was found for spinel. No effect was found for calcium fluoride irradiated perpendicular to a cleavage face and examined parallel to the cleavage face.

Magnitude of the Photoelastic Effect

No values of the photoelastic constants of lithium fluoride could be found in the literature, and therefore the constant required for computing the dilatation was determined. A clamp in which a crystal could be compressed against a spring balance was constructed. With a force of 10 lb (along y) using a crystal of width 0.324 cm (along x), the rotation with the Goranson-Adams arrangement was found to be 11 degrees for white light, sodium light, and green mercury light (along z); and with a force of 19½ lb was found to be 22 degrees for white and mercury light, and 21 degrees for sodium light. The white light observations are therefore taken to represent the effect observed with light of wavelength 5500 A, and the photoelastic stress constant giving the retardation per cm for a unit stress along y and observation along z is taken to be

$$\frac{22}{180}5500\times10^{-8}\text{ cm}\frac{0.324}{8.7\times10^{6}}\frac{\text{cm}}{\text{dyne}}=2.5\times10^{-13}\text{ cm}^2/\text{dyne}.$$

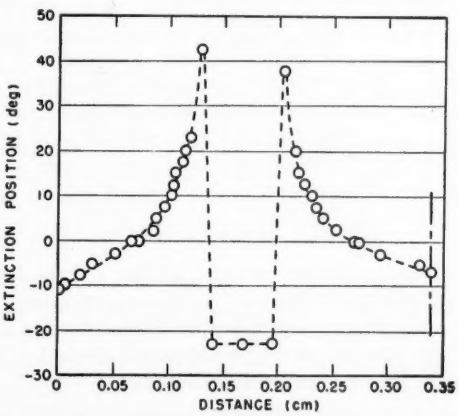

FIG. 4. Extinction position of the analyzer when examining a lithium fluoride crystal bombarded on opposite faces with deuterons. The edge of the crystal is shown by the dash-dot line.

[8] H. Mueller, Phys. Rev. 47, 953 (1935).

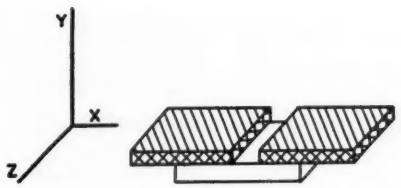

FIG. 5. Masking arrangement used for irradiating lithium fluoride crystals with x-rays from a Machlett tube. The x-rays came from above. The shaded sections represent copper plates against which the lithium fluoride crystal was held.

The reciprocal Young's modulus determined by Bergman is quoted by Hearmon[9] as 1.06×10^{-12} cm^2/dyne. Accordingly, the photoelastic strain constant which gives the retardation per cm along z for a unit strain along y ($\Delta y/y=1$) is about 0.23. Another crystal of width 0.271 cm with force 19½ lb gave a rotation of 20–25 degrees corresponding to a photoelastic strain constant between 0.17 and 0.22. The photoelastic strain constant is taken as 0.22 for the present purpose.

Determination of the Color Center Concentration

In a manner similar to that described elsewhere,[3] the absorption coefficient of the peak of the 450-mμ band was determined as a function of distance from the surface of a crystal exposed to the deuteron beam. The absorption coefficient of the F-band could not be measured as a function of distance in this manner owing to limitations in the apparatus. However, by cleaving the colored part of the crystal into four sections cut parallel to the irradiated face of the crystal, the average peak absorption coefficients of the F- and 450-bands could be calculated for each section. It was found that the ratio of the F-band peak to the 450-band peak was approximately constant and equal to 10 in each of the sections; therefore the ratio was assumed to have the value 10 at each point in the colored section of the crystal. Consequently not only the absorption coefficient of the 450-band, but also the absorption coefficient of the F-band was known as a function of distance from the irradiated surface of the crystal. The absorption coefficients for the F- and 450-bands in the region of highest color center concentration for Crystals I and II and Crystal III are listed in Table I. It is estimated that because of the approximations involved, the absorption coefficient of the F-band may be in error by as much as twenty percent.

The concentrations of F- and 450-centers were calculated by using Smakula's formula[10] relating the concentration to the half-width and peak absorption coefficient of the absorption band and the oscillator strength of the transition. Taking 0.22 and 0.82 ev as the half-widths of the 450- and F-bands, respectively, and assuming the oscillator strengths for these bands to be

[9] R. F. S. Hearmon, Revs. Modern Phys. 18, 428 (1946).
[10] A. Smakula, Z. Physik 59, 603 (1930).

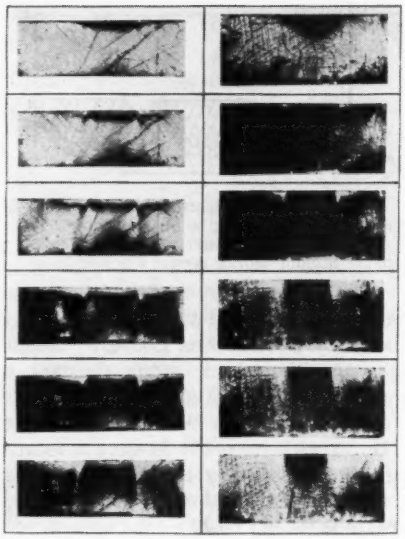

FIG. 6. Lithium fluoride irradiated with x-rays as viewed with the Goranson-Adams polarimeter at various settings of the analyzer. (A): A crystal irradiated for 3 hours. (B): Another crystal irradiated for 4 hours and then placed under a Mineralight for 20 hours.

unity, the concentrations of F- and 450-centers were determined as functions of distance from the irradiated surface of the crystal. The concentrations in the region of maximum color center concentration for Crystals I, II, and III are listed in Table I.

DISCUSSION

The birefringence observed in the case of the deuteron-irradiated specimens (Figs. 2 and 4) was, for a given value of y, constant for a considerable distance along x, and this may be taken as evidence that the data plotted in Figs. 2 and 4 may be taken as approximating the behavior of a body infinite along z and x and the same thickness as the crystal along y, and irradiated uniformly on the face perpendicular to y (an extension of Saint-Venant's principle). The problem is similar to the thermal expansion problem treated by Lord Kelvin and given by Love[11] and Timoshenko.[12] The notation used here is that of Love. The strains $e_{xx}\cdots e_{xy}$ are taken as the derivatives of the displacements, u, v, w, which are composed of two parts, those due to the permanent dilatation (in Kelvin's case due to thermal expansion, but here due to the dilatation caused by irradiation) and those due to elastic deformation. Love's treatment of the isotropic case can be extended to the cubic case most briefly by considering the appropriate strain energy function:

$$W=\tfrac{1}{2}c_{11}[(e_{xx}-\tfrac{1}{3}\delta)^2+(e_{yy}-\tfrac{1}{3}\delta)^2+(e_{zz}-\tfrac{1}{3}\delta)^2]+c_{12}[(e_{yy}-\tfrac{1}{3}\delta)(e_{zz}-\tfrac{1}{3}\delta)+(e_{zz}-\tfrac{1}{3}\delta)(e_{xx}-\tfrac{1}{3}\delta)+(e_{xx}-\tfrac{1}{3}\delta)(e_{yy}-\tfrac{1}{3}\delta)]+\tfrac{1}{2}c_{44}[e_{yz}^2+e_{zx}^2+e_{xy}^2],$$

where the dilatation due to irradiation is δ. The stresses, which are the partial derivatives of W with respect to the strains, are given by

$$X_x=(c_{11}-c_{12})e_{xx}+c_{12}\Delta-\beta\delta,$$
$$Y_y=(c_{11}-c_{12})e_{yy}+c_{12}\Delta-\beta\delta,$$
$$Z_z=(c_{11}-c_{12})e_{zz}+c_{12}\Delta-\beta\delta,$$
$$Y_z=c_{44}e_{yz};\quad Z_x=c_{44}e_{zx};\quad X_y=c_{44}e_{xy},$$

where the total dilatation is designated

$$\Delta\equiv e_{xx}+e_{yy}+e_{zz},$$

and

$$\beta\equiv\tfrac{1}{3}(c_{11}+2c_{12}).$$

The usual equations of equilibrium (no body force) apply:

$$\frac{\partial X_x}{\partial x}+\frac{\partial X_y}{\partial y}+\frac{\partial Z_x}{\partial z}=0\quad\text{etc.},$$

which in terms of the strains are:

$$(c_{11}-c_{12})\frac{\partial e_{xx}}{\partial x}+c_{12}\frac{\partial\Delta}{\partial x}+c_{44}\left(\frac{\partial e_{zx}}{\partial z}+\frac{\partial e_{xy}}{\partial y}\right)-\beta\frac{\partial\delta}{\partial x}=0,$$

$$(c_{11}-c_{12})\frac{\partial e_{yy}}{\partial y}+c_{12}\frac{\partial\Delta}{\partial y}+c_{44}\left(\frac{\partial e_{yz}}{\partial z}+\frac{\partial e_{xy}}{\partial x}\right)-\beta\frac{\partial\delta}{\partial y}=0,$$

$$(c_{11}-c_{12})\frac{\partial e_{zz}}{\partial z}+c_{12}\frac{\partial\Delta}{\partial z}+c_{44}\left(\frac{\partial e_{yz}}{\partial y}+\frac{\partial e_{zx}}{\partial x}\right)-\beta\frac{\partial\delta}{\partial z}=0.$$

The usual compatibility conditions and the usual surface tractions furnish the additional equations for solving the elasticity problem. It is now necessary to relate the optical effects to the elastic effects. It was hypothesized by Pockel and emphasized by Mueller[8] that the photoelastic birefringence is related to the strains. According to Mueller,[8] the retardation observed along z, R_z, due to a stress Y_y (in the absence of a permanent dilatation) is

$$R_z=n_z-n_y=\tfrac{1}{2}n^3(p_{11}-p_{12})e_{yy},$$

where the n's are the refractive indices, and the p's are the photoelastic constants. The retardation along z due to a stress X_z can be distinguished from that due to Y_y only by sign. Hence in the absence of stress the total retardation per cm observed along z is

$$R=r(e_{yy}-e_{xx}),$$

where r is $\frac{1}{2}n^3(p_{11}-p_{12})$ and was found to be 0.22 for lithium fluoride. It has been shown by Pockel that the change in index of refraction produced by a thermal

[11] A. E. H. Love, *A Treatise on the Mathematical Theory of Elasticity* (Dover Publications, New York, 1944), fourth edition, p. 131.

[12] S. Timoshenko, *Theory of Elasticity* (McGraw-Hill Book Company, Inc., New York, 1934), first edition, p. 203.

dilatation is practically the same as that produced by an elastic dilatation, and it therefore seems reasonable to assume that the same is true for an irradiation dilatation. Accordingly, it may be assumed that the above equation for R holds if the strains include both elastic strains and strains attending a permanent dilatation.

For the doubly infinite body being considered, δ is a function of y only; and from geometrical considerations, this must be true of the stresses and strains. The equations of equilibrium then become

$$\partial X_y/\partial y=0, \quad \partial Y_y/\partial y=0.$$

The stresses are given by

$$X_x=(c_{11}-c_{12})e_{xx}+c_{12}e_{yy}-\beta\delta,$$
$$Y_y=c_{11}e_{yy}+2c_{12}e_{xx}-\beta\delta,$$
$$X_y=c_{44}e_{xy}.$$

The equations of equilibrium in terms of the strains are therefore

$$c_{44}\partial e_{xy}/\partial y=0,$$
$$c_{11}\partial e_{yy}/\partial y+2c_{12}\partial e_{xx}/\partial y-\beta\partial\delta/\partial y=0,$$

and from the compatibility relations,

$$\partial^2 e_{xx}/\partial y^2=0.$$

Since the strains and δ are functions of y only, the equations can be integrated directly to give

$$e_{xy}=k_1,$$
$$c_{11}e_{yy}+2c_{12}e_{xx}-\beta\delta=k_2,$$
$$e_{xx}=k_3y+k_4.$$

It is convenient to place the unirradiated face of the crystal irradiated on one side at $y=0$ and the irradiated face at $y=a$; and to place the irradiated faces of a crystal irradiated equally from both sides at $y=\pm a$. From the surface tractions on the irradiated face,

$$X_2=X_y(a)=0; \quad Y_2=Y_y(a)=0; \quad Z_2=X_2;$$

it is seen by examination of the equations giving the stress in terms of the strain, that k_1 and k_2 are zero. Then

$$R=r(e_{yy}-e_{xx})=(3\beta r/c_{11})(\tfrac{1}{3}\delta-k_3y-k_4),$$

and writing R_0 for $-3\beta r(k_3y+k_4)/c_{11}$,

$$\delta=(R-R_0)c_{11}/\beta r.$$

The value of (k_3y+k_4) can be obtained from the birefringence in the unirradiated zone, for there $\delta=0$ and $R=R_0$. It is thus seen that the height of the birefringence curve above the line obtained by extending the birefringence curve for the unirradiated region into the irradiated region is proportional to the dilatation. For a crystal irradiated on opposite faces, e_{xx} must be an even function of y, and $k_3=0$; this fact is shown experimentally in Fig. 4. This condition does not apply to a crystal irradiated on one face as is confirmed by the data in Fig. 2. The birefringence at y can be calculated from the experimental data as before; hence,

$$R-R_0=\lambda(\phi-\phi_0)/180T,$$

where $\lambda=5500\times10^{-8}$, T is the thickness along z, ϕ is the analyzer setting causing extinction at y, and ϕ_0 is the value at y of the analyzer settings in the unirradiated region extrapolated into the irradiated region. From data collected by Hearmon[9] for s_{11} and s_{12}, it can be calculated that $c_{11}=1.178\times10^{12}$ dynes/cm^2 and $c_{12}=0.434\times10^{12}$ dynes/cm^2. Thus, δ can be computed at any value of y. The theory assumes no buckling has taken place. This would be true for a large crystal irradiated uniformly and equally on opposite faces. It would not in general be true for an unconstrained crystal irradiated on one face. The curvature of the birefringence along y in the unirradiated part of Crystal I as shown in Fig. 2(a) is probably due to buckling which would also produce a small change in other parts of the curve. From the form of the birefringence curve, it is apparent that the buckling effect in Crystal II would be small. The approximate dilatations computed for Crystals I and II using the foregoing theory are plotted in Fig. 7 as a function of the distance from the irradiated face. Because of the nonuniform irradiation, the results for Crystal III are not considered reliable to better than a factor of 2 and hence are not plotted.

TABLE I. Data for the regions of highest color center concentration.

Crystal	Absorption coefficient F-band	Absorption coefficient 450-band	Concentration of color centers F-centers	Concentration of color centers 450-centers
I and II	590 cm^{-1}	59 cm^{-1}	0.56×10^{19}/cm^3	1.5×10^{17}/cm^3
III	1900 cm^{-1}	190 cm^{-1}	2×10^{19}/cm^3	5×10^{17}/cm^3

Crystal	Concentration of vacancy pairs	Volume of vacancies per unit volume of crystal
I and II	0.59×10^{19}/cm^3	1×10^{-4}
III	2.1×10^{19}/cm^3	3×10^{-4}

The results presented in this paper permit one to speculate regarding some of the processes occurring during irradiation and bleaching. From the bleaching experiment, in which the birefringence decreased as the color centers were bleached, one can conclude that the vacancies which are left upon bleaching of the color centers are thermally unstable at room temperature and diffuse back to the original source of vacancies thus relieving the strain and diminishing the birefringence. It seems quite unlikely that this diffusion of vacancies is caused by point thermal spikes associated with the formation or decay of excitons[13,14] since the fundamental band of lithium fluoride is near 1200 A whereas the light from the bleaching lamp is extremely weak below 1850 A.

[13] F. Seitz, Phys. Rev. 89, 1299 (1953).
[14] C. J. Delbecq and P. H. Yuster, J. Chem. Phys. 22, 921 (1954).

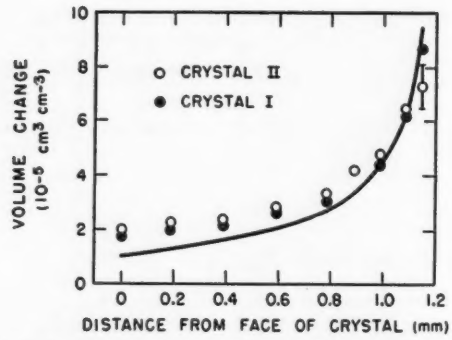

FIG. 7. A comparison of the dilatation (circles) computed from the birefringence with the volume of vacancies associated with the color centers per unit volume of crystal (solid curve) in a lithium fluoride crystal which had been irradiated with deuterons.

During the irradiation of alkali halides, vacancies are formed in excess of the number involved in the various electron excess and deficiency bands.[15] It is assumed that these excess vacancies diffuse back to the sources of vacancies and thus do not contribute to the strain. This assumption is based on an extrapolation of the conclusion drawn from the bleaching experiment referred to above; namely, that the vacancies which remain upon bleaching of the color centers are thermally unstable at room temperature and diffuse back to the original source of vacancies. Consequently, in attempting to relate the dilatation to the concentration of vacancies, only those vacancies associated with the color centers will be considered.

An *F*-center is generally considered to be a negative ion vacancy which has captured an electron[16] so that, associated with the *F*-centers of Crystals I and II, there are 0.56×10^{19} negative-ion vacancies per cm^3 in the region of maximum dilatation. The 450-center is thought by some[7] to be an *M*-center which is supposed to be an aggregate of one positive and two negative ion vacancies which has trapped an electron[17,18]; so for Crystals I and II there are 3×10^{17} negative ion vacancies per cm^3 and 1.5×10^{17} positive ion vacancies per cm^3 associated with the 450-centers in the region of maximum dilatation. Since the concentration of color centers is so high, it is reasonable to assume that for each negative ion vacancy formed during the irradiation a positive ion vacancy is also formed; and that the positive ion vacancies not accounted for in the preceding discussion are traps for the positive holes. Therefore in the region of maximum dilatation of Crystals I and II there is a concentration of 0.59×10^{19} vacancy pairs per cm^3, and the fraction of lattice sites which are vacant (which equals the volume of vacancies per unit volume assuming the volume of a vacancy equals the volume of the corresponding ion[19]) is 1×10^{-4}. In this manner the volume of vacancies per unit volume of crystal was determined as a function of distance from the irradiated surface of the crystal, knowing the concentrations of *F*- and 450-centers as functions of this distance. The solid curve in Fig. 7 is a plot of volume of vacancies per unit volume of crystal as a function of the distance from the irradiated face of crystal I or II; the circles (crystal II) and the filled circles (crystal I) show the dilatation as a function of distance from the irradiated face.

It is seen that the dilatation which occurs in lithium fluoride on irradiation is approximately equal to the volume of vacancies per unit volume associated with the color centers. This result is in accord with conclusions drawn by other investigators[20–22] who found that in the case of KCl the density change after production of color centers could be accounted for by an increase in the volume of the crystal approximately equal to the volume of the vacancies associated with the color centers. The techniques previously employed determined the average volume, or distance between the bounding faces. Accordingly, only the average effect could be determined (since the color center concentration in the crystals was not uniform), and the results were subject to the criticism that a surface alteration might have been measured. The present method is not subject to this criticism for the results depend upon a measurement of an effect taking place in the body of the crystal. The present method also has the advantage of determining the dilatation from point to point within the solid.

The fact that the local dilatation and the local volume of vacancies (associated with the color centers) per unit volume of crystal are approximately equal gives information concerning the principle source of the vacancies. According to the discussion given by Seitz,[19] it seems reasonable to assume that the volume of an ion vacancy associated with a color center is approximately equal to the volume of the corresponding ion and that the volume of a vacancy in an aggregate is approximately equal to the volume of the corresponding isolated vacancy. Therefore, if the vacancies associated with the color centers are formed by the dissolution of vacancy aggregates in the crystal or by the diffusion of vacancies from the surface, one would not expect the dilatation to be approximately equal to the volume of vacancies per unit volume of crystal. However, if the vacancies are generated predominantly at jogs in edge-type dislocations, as suggested by Seitz,[23] then one might expect an approximate equality between

[15] Delbecq, Pringsheim, and Yuster, J. Chem. Phys. **19**, 574 (1951); in Fig. 3 note the presence of the α band after the x-irradiation.

[16] For a review of the subject of color centers in alkali halides see F. Seitz, Revs. Modern Phys. **18**, 384 (1946); and F. Seitz, Revs. Modern Phys. **26**, 7 (1954).

[17] F. Seitz, Revs. Modern Phys. **18**, 405 (1946).

[18] M. Ueta, J. Phys. Soc. (Japan) **7**, 107 (1952).

[19] F. Seitz, Revs. Modern Phys. **18**, 397 (1946).

[20] Estermann, Leivo, and Stern, Phys. Rev. **75**, 627 (1949).

[21] H. Witt, Nachr. Akad. Wiss. Gottingen, Math.-physik. Kl. II-2, No. 4, 17 (1952).

[22] K. Sakaguchi and T. Suita, Technol. Repts. Osaka Univ. **2**, 177 (1952).

[23] F. Seitz, Phys. Rev. **80**, 239 (1950).

the dilatation and the volume of vacancies per unit volume. Therefore, these experiments would indicate that, of the three vacancy sources considered, jogs in edge-type dislocations are the main source of vacancies in lithium fluoride, and probably the other alkali halides, when subjected to ionizing radiation.

ACKNOWLEDGMENTS

The encouragement and stimulation provided by Dr. O. C. Simpson in the course of this work is appreciated. We are indebted to L. H. Fuchs for making some of the original observations of the birefringence of the deuteron-bombarded lithium fluoride crystals.

PHYSICAL REVIEW VOLUME 98, NUMBER 6 JUNE 15, 1955

Vibration Spectra and Specific Heats of Cubic Metals. II. Application to Silver

A. B. BHATIA,* *Division of Physics, National Research Council, Ottawa, Canada*

AND

G. K. HORTON, *Department of Mathematics, University of Alberta, Edmonton, Alberta, Canada*

(Received March 8, 1955)

The frequency spectrum of silver, and hence its specific heat C_v at constant volume as a function of temperature, are calculated by solving the secular equation derived in Part I of this work for the determination of the frequencies of the normal modes of vibration of a monovalent face-centered cubic metal. The calculations are made with two sets of elastic constants, namely with their values at absolute zero of temperature and at room temperature. The calculated C_v are compared with the experimental data and with the earlier calculations based on a two force-constant model (in contrast to the three appearing in our secular equation) by plotting the corresponding effective Debye temperatures Θ against temperature. It is found that, except for temperatures below about 7°K, the agreement between theory and experiment is satisfactory. It is shown that the discrepancy between the two sets of values below 7°K can be partly removed by making a choice for the elastic constants slightly different from that actually used in the calculation. However, it appears that the explanation of the entire discrepancy at low temperatures for silver and of a similar one found by Bhatia for sodium lies elsewhere.

I. INTRODUCTION

IN Part I of this work,[1] a model for monovalent cubic metals was proposed on the basis of which a secular equation determining the frequencies ω of the normal modes of vibration was derived. In contrast to the two force-constants occurring in the secular equation on which the earlier calculations of the frequency spectrum of metals are based, this equation contained three force-constants which were identified with the three independent elastic constants of a cubic metal. The frequency spectrum and specific heat C_v at constant volume of Na which has body-centered cubic structure were then calculated by solving the secular equation along the three principal directions of a cubic crystal, namely (100), (110), and (111) directions. In this paper, similar calculations for a typical face-centered cubic metal, namely silver, will be given. These calculations are made (i) with the room temperature values of the elastic constants and (ii) with the values of the elastic constants extrapolated to absolute zero of temperature. The results of these calculations are compared with the experimental data and with the earlier calculations of Leighton[2] by plotting the corresponding effective Debye temperatures Θ against the absolute temperature T. For temperatures above 7°K, the agreement between the present calculations and experiment is more satisfactory than obtained by Leighton. As the temperature is decreased below 7°K, the experimental $\Theta-T$ curve has first a maximum at about 5°K and then a minimum at a still lower temperature (see Fig. 2), while the theoretical $\Theta-T$ curve (both ours and Leighton's) slightly rises reaching a maximum at $T=0$°K. Possible causes of this discrepancy, and of a similar one found in I for sodium,[3] are discussed in Sec. III.

II. CALCULATION OF FREQUENCY SPECTRUM AND SPECIFIC HEAT OF SILVER

Basic Formulas

By making use of Eqs. (15) and (16b) of I in Eqs. (14) of I, the secular equation determining the angular frequencies ω of the elastic waves in a *face-centered cubic* metal may be written as

$$\lambda\rho\omega^2=\sum_{l,m,n}\{4a^{-2}[\sin^2\tfrac{1}{2}ka(Ll+Mm+Nn)]\times[\tfrac{1}{4}(c_{44}+\epsilon)\lambda-\epsilon l(l\lambda+m\mu+n\nu)]\}+\frac{(c_{11}-c_{44}+\epsilon)L(\lambda L+\mu M+\nu N)k^2}{1+(c_{11}-c_{44}+\epsilon)(k^2/4\pi e^2n_0^2)},\quad(1a)$$

and two similar equations obtained from (1a) by inter-

* National Research Laboratories Postdoctorate Fellow (on leave from I.C.I. Fellowship, Edinburgh University).

[1] A. B. Bhatia, Phys. Rev. **97**, 363 (1955); this paper is referred to as I and its notation employed here.

[2] R. B. Leighton, Revs. Modern Phys. **20**, 165 (1948).

[3] See reference 1, Fig. 3.

changing (l,m,n), (λ,μ,ν) and (L,M,N) as follows:

$$l\rightleftarrows m, \quad \lambda\rightleftarrows\mu \quad \text{and} \quad L\rightleftarrows M, \tag{1b}$$

and

$$l\rightleftarrows n, \quad \lambda\rightleftarrows\nu \quad \text{and} \quad L\rightleftarrows N. \tag{1c}$$

Here c_{11}, c_{44}, and c_{12} are the elastic constants, $\epsilon=c_{11}-c_{12}-2c_{44}$, k the wave number (2π times the reciprocal of the wavelength) of the elastic wave, and (L,M,N) and (λ,μ,ν) are the direction cosines of the propagation vector $\mathbf{k}(|\mathbf{k}|=k)$ and of the displacement vector respectively. Further, ρ is the density of the metal, n_0 the number of electrons (assumed to be 1 per atom) per cm^3, a the nearest-neighbor distance, (l,m,n) the direction cosines of the lines joining the ion at the origin and the nearest-neighbor ions and the summation in (1) is over all the nearest neighbors. In a face-centered cubic lattice, each ion has twelve nearest neighbors and (l,m,n) are to be taken as

$$|\sqrt{2}|^{-1}(\pm1,\pm1,0), \quad |\sqrt{2}|^{-1}(\pm1,0,\pm1),$$

and

$$|\sqrt{2}|^{-1}(0,\pm1,\pm1).$$

In the following, we shall need the solutions of (1) for $\mathbf{k}$-vectors lying along the three principal directions of a cubic crystal, namely (100), (110), and (111); the quantities referring to these three directions will be distinguished by the subscripts A, B, and C, respectively. Equations (1) are readily solved along these three directions in k-space and we find:

Direction A

$$(\lambda,\mu,\nu)=(100):\ \omega^2=\left(\frac{1}{a^2\rho}\right)\left[8(c_{44}-\epsilon)\sin^2\left(\frac{ka}{2\sqrt{2}}\right)+\frac{(c_{11}-c_{44}+\epsilon)k^2a^2}{1+\varphi k^2a^2}\right], \tag{2a}$$

$$(\lambda,\mu,\nu)=(010)\text{ or }(001):\ \omega^2=\left(\frac{1}{a^2\rho}\right)8c_{44}\sin^2\left(\frac{ka}{2\sqrt{2}}\right); \tag{2b}$$

Direction B

$$(\lambda,\mu,\nu)=(110):\ \omega^2=\left(\frac{1}{a^2\rho}\right)\left[2(c_{44}-3\epsilon)\sin^2\left(\frac{ka}{2}\right)+8c_{44}\sin^2\left(\frac{ka}{4}\right)+\frac{(c_{11}-c_{44}+\epsilon)k^2a^2}{1+\varphi k^2a^2}\right], \tag{2c}$$

$$(\lambda,\mu,\nu)=(1-,1,0):\ \omega^2=\left(\frac{1}{a^2\rho}\right)\left[2(c_{44}+\epsilon)\sin^2\left(\frac{ka}{2}\right)+8c_{44}\sin^2\left(\frac{ka}{4}\right)\right], \tag{2d}$$

$$(\lambda,\mu,\nu)=(001):\ \omega^2=\left(\frac{1}{a^2\rho}\right)\left[2(c_{44}+\epsilon)\sin^2\left(\frac{ka}{2}\right)+8(c_{44}-\epsilon)\sin^2\left(\frac{ka}{4}\right)\right]; \tag{2e}$$

Direction C

$$(\lambda,\mu,\nu)=(111):\ \omega^2=\left(\frac{1}{a^2\rho}\right)\left[2(3c_{44}-5\epsilon)\sin^2\left(\frac{ka}{\sqrt{6}}\right)+\frac{(c_{11}-c_{44}+\epsilon)k^2a^2}{1+\rho\varphi k^2a^2}\right], \tag{2f}$$

$$(\lambda,\mu,\nu)=(1,-1,0)\text{ or }(1,1,-2):\ \omega^2=\left(\frac{1}{a^2\rho}\right)\left[6(c_{44}+\tfrac{1}{3}\epsilon)\sin^2\left(\frac{ka}{\sqrt{6}}\right)\right]. \tag{2g}$$

In Eqs. (2), we have written for convenience

$$\varphi a^2=(c_{11}-c_{44}+\epsilon)/(4\pi e^2n_0^2). \tag{3}$$

The frequency spectrum will be calculated from the solutions (2) of (1) by Houston's[4] method. In this approximation, the frequency distribution function $G(\omega)$, defined such that $G(\omega)d\omega$ gives the number of frequencies lying between ω and $\omega+d\omega$, is given by

$$G(\omega)=\frac{FV}{(2\pi)^3}\cdot\frac{4\pi}{35}\sum_i\left[10k^2\left(\frac{dk}{d\omega}\right)_{i,A}+16k^2\left(\frac{dk}{d\omega}\right)_{i,B}+9k^2\left(\frac{dk}{d\omega}\right)_{i,C}\right], \tag{4}$$

where the $\sum_i$ $(i=1,2,3)$ denotes summation over the three solutions (frequencies) which (1) has for each $\mathbf{k}$, V the volume of the crystal under consideration and F is a normalization factor to be chosen such that

$$\int G(\omega)d\omega=3N_0V, \tag{5}$$

N_0 being the number of atoms per unit volume in the metal. If we denote the maximum value of k along the three directions A, B and C by $k_A(m)$, $k_B(m)$, and $k_C(m)$, respectively, the normalization factor F is determined by the equation [see I (26)]

$$\frac{FV}{(2\pi)^3}\cdot\frac{4\pi}{35}\cdot\frac{1}{3}[10k_A^3(m)+16k_B^3(m)+9k_C^3(m)]=N_0V. \tag{6}$$

As mentioned in I, the $\mathbf{k}$ vectors are to be restricted to the first Brillouin zone in k-space. For a face-centered cubic lattice, the first zone is marked by (111) and (200) planes and we may determine $k_A(m)$, $k_B(m)$, and $k_C(m)$ by finding the point of intersection of the $\mathbf{k}_A$ vector with the (200) plane and those of $\mathbf{k}_B$ and $\mathbf{k}_C$ vectors with the (111) plane. One finds[5]

$$k_A(m)=\sqrt{2}(\pi/a); \quad k_B(m)=\tfrac{3}{2}(\pi/a)$$

[4] W. V. Houston, Revs. Modern Phys. **20**, 161 (1948); a brief discussion of the merits and demerits of this method is given in I.

[5] The perpendicular distances from the origin to the various planes marking the zone are given in N. F. Mott and H. Jones, *The Theory of the Properties of Metals and Alloys* (Oxford University Press, London, 1936), p. 156. See, however, footnote 20 of I regarding notation.

and

$$k_C(m)=(\sqrt{\tfrac{3}{2}})(\pi/a). \quad (7)$$

Equations (6) and (7) give for F:

$$F=0.9554. \quad (8)$$

The frequency distribution function $G(\omega)$ is now easily obtained with the help of (4), (8), and (2). $G(\omega)$, thus obtained, contains in general a number of singularities which are characteristic of Houston's approximation. The area under them, however, is finite. For the purposes of numerical integrations (see below) these singularities will be replaced by finite peaks of equal area. Once $G(\omega)$ is known, the specific heat C_v *per atom* at constant volume is calculated by the formula

$$N_0VC_v=K\left(\frac{\hbar}{KT}\right)^2\int\frac{G(\omega)\omega^2\exp(\hbar\omega/KT)}{[\exp(\hbar\omega/KT)-1]^2}d\omega, \quad (9)$$

where $\hbar$ is Planck's constant divided by 2π and K is the Boltzmann constant.

Choice of Elastic Constants

Since the elastic constants vary with temperature, the frequency distribution function $G(\omega)$ will also depend on the temperature. Therefore, in calculating C_v from (9) at a given temperature T, one should use $G(\omega)$ appropriate to that temperature. However, such a procedure would entail a considerable amount of work since the integration in (9) can be, in general, carried out only numerically. Moreover, the effect of the deviations of the frequency spectrum from the Debye spectrum $[G(\omega)\propto\omega^2]$ on the specific heat is more pronounced at temperatures $T\lesssim\frac{1}{4}\Theta$ or $\frac{1}{2}\Theta$ ($\Theta\sim220$ for Ag) than at higher temperatures. Hence we shall calculate C_v as a function of temperature from the frequency distribution function $G(\omega)$ obtained by using the values of the elastic constants at 0°K. As we shall see in Sec. III, these calculated values of C_v, or rather the equivalent Debye temperatures Θ, do not agree well with the corresponding experimental values above about 50°K. In order to ascertain as to how much of this discrepancy is due to the neglect of the variation of the elastic constants with temperature, it was thought desirable to make also a calculation of C_v as a function of T with the distribution function $G^{(r)}(\omega)$ obtained by using the values of the elastic constants at room temperature. The experimental results should then lie in between these two sets of calculated values, approaching closely to the former set at low temperatures and to the latter at high temperatures.

The elastic constants of silver have been measured at room temperature by Roehl.[6] His values are:

$$\left.\begin{aligned}c_{11}&=12.0\\c_{12}&=8.97\\c_{44}&=4.37\end{aligned}\right\}\times10^{11}\text{ dynes/cm}^2\ (T=291°\text{K}). \quad (10)$$

As far as we know, measurements of c_{11}, c_{12}, and c_{44} at other temperatures have not been made. We have, therefore, to extrapolate Roehl's values to absolute zero. Eucken,[7] on the basis of a formula due to Grüneisen,[8] extrapolated the value of shear modulus η for a polycrystal of silver and found that $\eta(0°\text{K})/\eta(300°\text{K})=1.183$. Measurements by Schäfer[9] of η and of the Young's modulus E of polycrystalline silver in the temperature range 77–293°K, when linearly extrapolated to absolute zero, give $E_0/E_{300}=1.22$ and $\eta_0/\eta_{300}=1.24$; on the other hand, Grüneisen's[8] measurements of the bulk modulus in the temperature range 82–290°K yield for the corresponding ratio the value 1.11. From these somewhat scanty data, reliable extrapolation of the elastic constants to absolute zero is not feasible and we shall, following Leighton, take for the elastic constants at absolute zero the values obtained by multiplying the corresponding room temperature values by the value 1.183 evaluated by Eucken for η_0/η_{300}. This gives for the elastic constants at 0°K:

$$\left.\begin{aligned}c_{11}&=14.19\\c_{12}&=10.62\\c_{44}&=5.17\end{aligned}\right\}\times10^{11}\text{ dynes/cm}^2; \quad (11)$$

here c_{11} and c_{12} have been probably overestimated by a few percent.

It may be mentioned here that at low temperature the calculated values of Θ for the alkali and noble metals are more sensitive to the changes in c_{44} and the combination $c_{11}-c_{12}$ than in c_{11} or c_{12}. This may be easily seen by noting that both c_{44} and $c_{11}-c_{12}$ are much smaller than c_{11} or c_{12} and using an approximate formula for Θ, given by Bhatia and Tauber,[10] for the case for which there is no dispersion.

Results

In calculating the frequency distribution functions $G(\omega)$ and $G^{(r)}(\omega)$, we also need the values of N_0, the number of atoms per unit volume, and ρ, the density of the substance. These will be taken as

$$N_0=n_0=\sqrt{2}/(a^3)=5.9\times10^{22}/\text{cc}, \quad \rho=10.5\text{ g/cc}. \quad (12)$$

N_0 and ρ also, of course, vary with temperature, but the influence of this on present calculations is small and will be neglected here.

The frequency distribution function $G(\omega)$ is plotted against ω in Fig. 1 where the singularities of $G(\omega)$, characteristic of Houston's approximation, have been replaced by finite peaks of equal area. The distribution function $G^{(r)}(\omega)$, calculated with the room temperature

[6] H. Roehl, Ann. Physik **16**, 887 (1933).

[7] A. Eucken, Verhandl. deut. physik. Ges. **15**, 571 (1913).

[8] E. Grüneisen, Ann. Physik **33**, 1239 (1910).

[9] See *Landolt Börnstein Tables* (Verlag Julius Springer, Berlin, 1927), Erg. I, p. 19.

[10] A. B. Bhatia and G. E. Tauber, Phil. Mag. **45**, 1211 (1954). There is a misprint in this article in that the right-hand side of (5) should be multiplied by $\rho^{3/2}$, where ρ is the density of the substance.

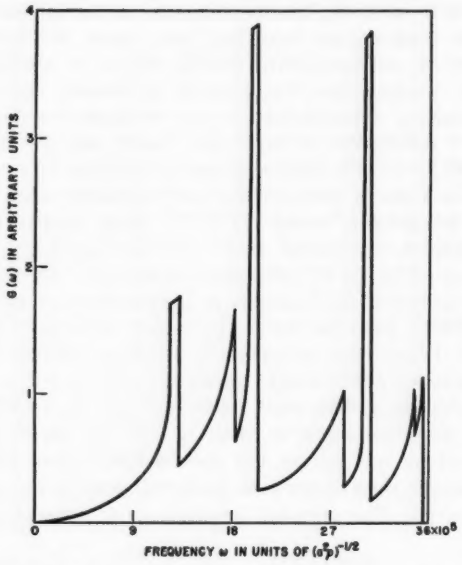

FIG. 1. The frequency spectrum $G(\omega)$ of silver calculated with the values of the elastic constants at 0°K. For convenience, the singularities have been replaced by finite peaks of equal area.

values of the elastic constants,[11] looks very much like $G(\omega)$ and will not be given here.

The specific heat C_v per atom at constant volume was then calculated at several temperatures from (9) by numerical integration. As is customary, instead of comparing the experimental and calculated values of C_v, we compare the corresponding effective Debye temperatures (Θ values) which may be obtained from C_v in the usual manner. We denote the Θ values obtained by using $G(\omega)$ and $G^{(r)}(\omega)$ in (9) by Θ and $\Theta^{(r)}$ respectively. Θ and $\Theta^{(r)}$ are plotted against the absolute temperature T in Fig. 2 [curves (a) and (b) respectively]. The Θ values deduced from the experimental data on specific heats are given by curve (c). The data above 15°K are due to Eucken *et al.* and Meads *et al.*,[12] while those below 15°K are due to Keesom and Kok.[13] In obtaining experimental Θ values at low temperatures, the specific heat C_v^e of the electrons was first subtracted from the observed C_v, the formula used for C_v^e being the usual one based on the free electron approximation. The experimental points show a rather wide scatter below about 5°K and only the smoothed-out curve is given in Fig. 2

As already mentioned, Leighton[2] has calculated Θ values for silver using a two force-constant model. The elastic constants used by him were the same as those given in (11). The Θ values obtained by him are shown in curve (d) of Fig. 2.

III. DISCUSSION

The discussion of the results may be conveniently divided into two parts: (i) above 7°K and (ii) below 7°K.

Above about 7°K

It will be seen from Fig. 2 that as the temperature is increased above 7°K, the curve (a), calculated with the values of the elastic constants at 0°K, follows closely the experimental curve (c) up to about 40°K and gives the magnitude and the position (about 20°K) of the minimum in the $\Theta-T$ curve correctly. In this temperature range, curve (a) agrees slightly better with the experiment than Leighton's curve. Above 40°K, the curve (a) rises above the experimental curve, the maximum discrepancy being about 10 percent. In this region, curve (d) agrees better with experiment than curve (a). On the other hand, curve (b) obtained in this paper by using the room temperature values of the elastic constants, though disagreeing at low temperatures, agrees fairly well with the experimental curve at high temperatures. If one calculated $\Theta(T)$ by inserting in (1) the elastic constants appropriate to each temperature T, the corresponding $\Theta-T$ curve will naturally lie between the curves (a) and (b) and will closely approach curve (a) at low temperatures and curve (b) at high temperatures. It will be noticed that the experimental $\Theta-T$ curve does possess these features and, therefore, the agreement between theory and experiment may be regarded as satisfactory above 7°K.

It may be recalled that the $\Theta-T$ curve for Na obtained in I using the elastic constants at 0°K lay higher than the experimental $\Theta-T$ curve above about 30°K. In view of the results obtained here, one can ascribe a good part of this discrepancy also to the neglect of the variation of the elastic constants with temperature in the calculations. We should mention, however, that these discrepancies may be partly also due to the inadequacy of the assumptions on which the secular equation was derived in I and of the approximate method of calculating the frequency spectrum.

Below about 7°K

In the temperature range 0–7°K, the theoretical and experimental $\Theta-T$ curves [(a) and (c)] are even qualitatively different from each other although the discrepancy is nowhere greater than about 6 percent in the Θ-values or 18 percent in the specific heats. As the temperature is decreased below 7°K, the experimental curve has first a maximum at about 5°K and then a minimum at about 2°K, while the theoretical curve (a) rises only slightly and has a rather flat maximum at 0°K. The following points may be mentioned in connection with this discrepancy:

[11] The actual elastic constants used in this calculation were: $c_{11}=12.2$, $c_{12}=9.1$, and $c_{44}=4.4$ in units of 10^{11} dynes/cm².

[12] Eucken, Clusius, and Woitinek, Z. anorg. u. allgem. Chem. **203**, 47 (1931); Meads, Forsythe, and Gauque, J. Am. Chem. Soc. **63**, 1902 (1941).

[13] W. H. Keesom and J. A. Kok, Proc. Acad. Sci. Amsterdam **35**, 301 (1932).

(i) The experimental values of C_v show a rather wide scatter and may have some systematic errors also.[14]

(ii) To obtain the lattice specific heat, we subtracted from the observed C_v, the specific heat C_v^e of the electrons as given by the formula for perfectly free electrons. Since for any actual metal deviations from this formula for C_v^e are to be expected and since at these low temperatures C_v^e is of the same order of magnitude as the lattice specific heat, the values for the latter deduced here from the observed C_v may be *considerably* in error from the actual values.

(iii) The calculated Θ values may be slightly in error due to the use of Houston's approximate method of calculating the frequency spectrum; however, a better method of approximating the frequency spectrum is unlikely to alter the general shape of the $\Theta-T$ curve.

(iv) There is some uncertainty in the values of the elastic constants at 0°K which have been obtained here by multiplying the room temperature values of all the three elastic constants by 1.183.

The points (i) to (iii) will not be discussed any further. In view of (iv), however, it will be interesting to study the effect of varying the elastic constants on the shape of the $\Theta-T$ curve in the neighborhood of $T=0$°K. For this purpose we expand the frequency distribution function in powers of ω^2; thus let

$$G(\omega)=V[\alpha_1\omega^2+\alpha_2\omega^4+\alpha_3\omega^6+\cdots], \tag{13}$$

where α_1, α_2, α_3, etc., are constants. Substituting (13) into (9), and introducing a new variable

$$x=\hbar\omega/KT, \tag{14}$$

we may write (9) in the form

$$N_0C_v=K\left(\frac{KT}{\hbar}\right)^3\sum_{n=1}\alpha_nI_n\left(\frac{KT}{\hbar}\right)^{2n-2}, \tag{15}$$

where

$$I_n=\int\frac{e^xx^{2n+2}}{(e^x-1)^2}dx. \tag{16}$$

In the integrals (16), the lower limit is zero, while, since we are now interested only in the low-temperature region, the upper limit may be taken to be infinity. Then[15]

$$I_1=4\pi^4/15,\quad I_2=16\pi^6/21,\quad I_3=64\pi^8/15. \tag{17}$$

Remembering that the Debye temperature Θ_0 at $T=0$°K is given by

$$\Theta_0=\left(\frac{9N_0}{\alpha_1}\right)^{\frac{1}{3}}\frac{\hbar}{K}, \tag{18}$$

[14] See, J. R. Clement, Phys. Rev. 93, 1420 (1954).
[15] See, for example, reference 2, p. 173.

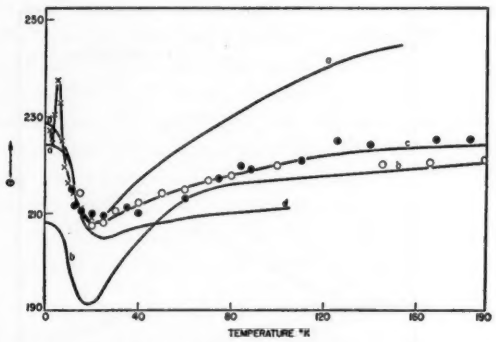

FIG. 2. The effective Debye temperature Θ for silver, as a function of temperature: Curve (a): present calculations with values of the elastic constants at absolute zero. Curve (b): present calculations with room temperature values of the elastic constants. Curve (d): Leighton's calculations. Curve (c): experimental; individual points marked by ×, ●, and ○ are due to Keesom and Kok, Eucken *et al.* and Meads *et al.*, respectively.

we may write (15) in the form

$$N_0C_v=\frac{12}{5}\pi^4KN_0\left(\frac{T}{\Theta_0}\right)^3\left[1+\frac{20\pi^2}{7}\left(\frac{\alpha_2}{\alpha_1}\right)\left(\frac{KT}{\hbar}\right)^2+16\pi^4\left(\frac{\alpha_3}{\alpha_1}\right)\left(\frac{KT}{\hbar}\right)^4+\cdots\right]. \tag{19}$$

Hence the equivalent Debye temperature Θ_T at a temperature T is given by $(T\ll\Theta)$:

$$\Theta_T=\Theta_0[1-(20\pi^2/21)(\alpha_2/\alpha_1)(KT/\hbar)^2+\cdots]. \tag{20}$$

From (2) it is clear that if α_2 is positive (α_1 is always positive), Θ_T will decrease if T is increased above zero; this is the behavior exhibited by the theoretical curves (a) and (b) of Fig. 2. On the other hand, if α_2 is negative, Θ_T will first increase as the temperature increases; eventually, of course, it will start to fall due to the presence of other terms in (20). We shall now examine the question as to whether one can make α_2 negative by choosing the elastic constants suitably. Since the elastic constants must be necessarily such that the crystal is elastically stable, we must have

$$c_{11}>0,\quad c_{11}-c_{12}>0,\quad c_{44}>0,\quad c_{11}+2c_{12}>0. \tag{21a}$$

Further, we restrict the present discussion to the cases for which the elastic anisotrophy $\epsilon=c_{11}-c_{12}-2c_{44}$ is negative or zero. (For all the cubic metals, the experimental value of $\epsilon\leqslant 0$.) Then, since from (21a) $c_{11}-c_{12}>0$, we have $-2c_{44}<\epsilon\leqslant 0$, or

$$-2<\sigma\leqslant 0, \tag{21b}$$

where $\sigma=\epsilon/c_{44}$.

Now let

$$\omega^2=\beta_1k^2+\beta_2k^4+\beta_3k^6+\cdots \tag{22}$$

be a solution of the secular equation along some particular direction in k-space. Then it may be easily

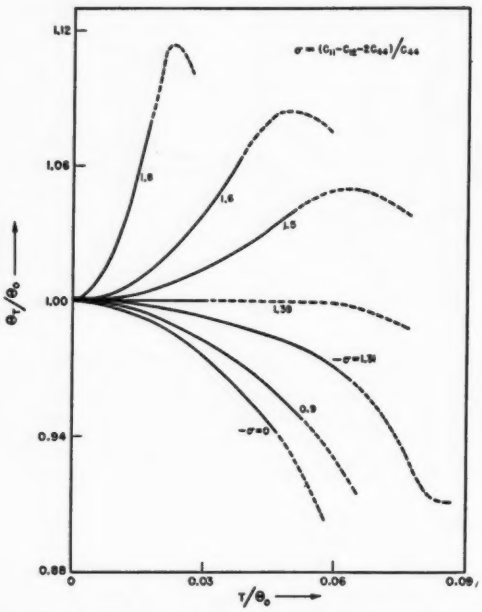

FIG. 3. Θ_T/Θ_0 as a function of T/Θ_0 at low temperatures for several values of $\sigma=(c_{11}-c_{12}-2c_{44})/c_{44}$; Θ_T and Θ_0 denote the effective Debye temperatures at temperatures T and 0°K respectively. The dotted parts of the curves represent only qualitatively the variation of Θ with T.

shown that

$$k^2\frac{dk}{d\omega}=\beta_1^{-3/2}\omega^2-\frac{5}{2}\beta_1^{-7/2}\beta_2\omega^4+\frac{7}{8}\beta_1^{-11/2}(9\beta_2^2-4\beta_1\beta_3)\omega^6+\cdots. \quad (23)$$

Since the coefficients β_1, β_2, β_3, etc., may be obtained from the solutions (2) of the secular equation, the coefficients α_1, α_2, etc., in (13) may be determined in Houston's approximation by making use of (23) and (4).

From the solutions (2) of (1), it may be readily verified that when the elastic constants satisfy the conditions (21), β_2 is always negative for the solutions (2a), (2b), (2c), (2f), and (2g) and hence their contributions to α_2 of (13) is always positive (β_1 is, of course, positive for every solution of (1), if (21a) is satisfied, as it must). However, β_2 for the solutions (2d) and (2e) is negative if $\sigma\equiv\epsilon/c_{44}>-5/4$ and $-5/3$, respectively, and positive otherwise. Hence, it is possible to make the contributions of these waves to α_2 negative without violating the conditions (21). A rough calculation, taking into account the contributions to α_2 from the transverse waves only,[16] shows that α_2 will be negative if

$$\epsilon/c_{44}\equiv\sigma<-1.39. \quad (24)$$

In Fig. 3, Θ_T/Θ_0 is plotted against T/Θ_0 for several values of σ. The dotted parts of these curves are not based on any detailed calculation and represent only qualitatively the variation of Θ_T with T. The qualitative nature of the curves may be understood from the fact that α_3 of (13) is positive for all σ and is in general the larger the smaller is σ. It should be mentioned that as σ tends to -2, Θ_0 itself tends to zero.

We give here values of σ for several face-centered cubic metals deduced from the room temperature values of the elastic constants.[17]

Metal	Cu	Ag	Au	Fe	Al	Pb
$-\sigma=-\epsilon/c_{44}$	1.375	1.310	1.315	0.59	1.16	1.5

It will be seen from this table that for all the three noble metals σ is only slightly greater than the critical value -1.39. It will be of interest to have experimental determinations of c_{44} and $c_{11}-c_{12}$ and hence of σ at very low temperatures for f.c.c. metals.[18]

It should be noted that when σ satisfies the condition (24), the theoretical $\Theta-T$ curve will have a maximum at some low nonzero temperature but will not have a minimum at a still lower temperature except at 0°K. The experimental $\Theta-T$ curve for Ag, however, shows a maximum at 5°K and also a minimum at about 2°K.

When the crystal is elastically isotropic, i.e., $\epsilon=0$, the condition (24) excludes the possibility of a maximum in the $\Theta-T$ curve at a low nonzero temperature. Another special case of interest is the one for which the interactions are entirely central and effective between the nearest neighbors only. The secular equation for the *face-centered cubic lattice* for this case may be obtained by putting $\frac{1}{2}c_{11}=c_{12}=c_{44}$ in (1). Then $\sigma=-1$ and again there is no possibility of a maximum in the $\Theta-T$ curve at low temperatures. This result remains unaffected even when the next nearest neighbor interaction is taken into account[19] and has been discussed by Leighton.[2] We should also mention here the work of Blackman[17] who discussed the anomalous behavior to be expected at the low-frequency end of the spectrum when the elastic constants satisfy certain equalities like

$$c_{44}/c_{11}=0, \quad (c_{11}-c_{12})/c_{11}=0,$$

or

$$c_{11}+2c_{12}+4c_{44}=0, \quad (c_{11}>0).$$

[16] The longitudinal waves contribute only little to α_2 since the β_1 for these waves are much larger than those for the transverse waves. The condition (24) is only slightly modified if the contribution of the longitudinal waves is also taken into account. It should also be remembered that we are throughout working in Houston's approximation; a more accurate method of calculating α_2 will presumably yield a slightly lower critical value of σ than -1.39 obtained here.

[17] Values of the elastic constants are taken from M. Blackman, Proc. Roy. Soc. (London) **A164**, 62 (1938).

[18] The elastic constants of Cu have been measured at room temperature and 4.2°K by J. Gaffney and W. C. Overton, Phys. Rev. **95**, 602 (1954). The value of σ at 4.2°K comes out to be -1.365.

[19] If we denote the Hooke's constants for nearest and next nearest neighbor interactions by γ_n and γ_{nn} respectively, $\gamma_{nn}/\gamma_n\sim-0.08$ for all the noble metals and $\gamma_{nn}/\gamma_n\sim0.25$ for sodium.

These equalities correspond to the velocities of some of the long elastic waves being zero. At low frequencies, $G(\omega)$ then becomes similar to the frequency spectrum of a one- or two-dimensional lattice. In practice, the elastic constants of any real crystal do not satisfy any of these equalities, though in some cases they are nearly satisfied.

Finally, we write down the expression for Θ_T for Ag obtained by using in (20) the values of the elastic constants given in (11):

$$\Theta_T=\Theta_0\left[1-\frac{22}{3}\left(\frac{T}{\Theta_0}\right)^2\right],$$

$$T\ll\Theta_0 \quad \text{and} \quad \Theta_0\sim 225°\text{K}. \quad (25)$$

From (25) one sees that the theoretical $\Theta-T$ curve for Ag is very flat near 0°K; for example, $\Theta_0-\Theta_5\sim 0.8°\text{K}$.

Low-Temperature Behavior of the Θ-T Curve for Body-Centered Cubic Metals

We have made an analysis similar to that given above from the solutions of the secular equation given in I for body-centered cubic metals. In this case α_2/α_1 of (20) is always positive, provided the elastic constants satisfy the conditions (21a) and (21b). Thus, for b.c.c. metals, the $\Theta-T$ curve calculated on the basis of the secular equation given in I will not have a maximum at a low nonzero temperature.[20] It should be mentioned that the experimental $\Theta-T$ curve for sodium does exhibit a maximum at about 2 or 3°K.

The formula governing the fall of Θ for sodium as the temperature is increased above zero is

$$\Theta_T=\Theta_0\left[-\frac{210}{3}\left(\frac{T}{\Theta_0}\right)^2\right],$$

$$T\ll\Theta_0 \quad \text{and} \quad \Theta_0\sim 139°\text{K}. \quad (26)$$

The theoretical rate of fall of Θ with increasing T is much greater here than for Ag.

[20] It may be mentioned that if $\epsilon>0$, the $\Theta-T$ curve for both b.c.c. and f.c.c. metals can have a maximum at a low nonzero temperature for suitable values of the elastic constants.

PHYSICAL REVIEW VOLUME 98, NUMBER 6 JUNE 15, 1955

Multiple Scattering of Slow Neutrons by Flat Specimens and Magnetic Scattering by Zinc Ferrite*

B. N. BROCKHOUSE,† *Physics Division, Atomic Energy of Canada Limited, Chalk River, Ontario, Canada*

AND

L. M. CORLISS AND J. M. HASTINGS, *Chemistry Department, Brookhaven National Laboratory, Upton, New York*

(Received March 7, 1955)

Measurements of scattering from Be, Pb, Bi, and Th under conditions where multiple scattering predominated were compared with predictions based on the work of Chandrasekhar and of Vineyard. Good agreement was obtained. A table of values of the expected multiple scattering by flat specimens is given. These results were used to correct measurements of diffuse scattering by zinc ferrite at room temperature and higher to obtain the differential magnetic cross section of the magnetic ions. The cross section shows interesting features which are discussed. At liquid nitrogen temperatures a small-angle scattering effect was found. This is interpreted as arising from short-range ferromagnetic ordering of the iron ions.

INTRODUCTION

MEASUREMENTS of the angular distribution of neutrons which are diffusely scattered by a paramagnetic substance can, in principle, lead to a determination of the spatial distribution of the magnetic electrons[1,2] and to information on the interactions between the magnetic ions.[3,4] It is necessary to obtain the angular distribution rather accurately, if more than the most qualitative information is to be gained. In particular it is necessary to have accurate information at small scattering angles if a questionable appeal to theory in extrapolating the scattering curve to zero scattering angle is to be avoided.[3] The apparatus used in these experiments was designed to permit working as close to the main beam as the angular acceptance of the counters would permit, under conditions of low and flat background. The diffusely scattered neutrons have a number of sources in addition to magnetic scattering, the most important being nuclear incoherent scattering, nuclear thermal diffuse coherent scattering and multiple scattering. In this paper a method of subtracting multiple scattering is described and experimentally verified.

* Research carried out at Brookhaven National Laboratory under the auspices of the U. S. Atomic Energy Commission. This paper was presented at the Chicago Meeting of the American Physical Society, November 27–28, 1953.

† Guest scientist in the Reactor Department, Brookhaven National Laboratory from April, 1953, to February, 1954.

[1] O. Halpern and M. H. Johnson, Phys. Rev. 55, 898 (1939).
[2] Shull, Strauser, and Wollan, Phys. Rev. 83, 333 (1951).
[3] J. H. Van Vleck, Phys. Rev. 55, 924 (1939).
[4] P. J. Bendt, Phys. Rev. 89, 561 (1953).

According to Halpern and Johnson[1] the differential scattering cross section of a free paramagnetic ion in an S state is

$$\sigma_{\text{mag}}=\frac{8\pi}{3}S(S+1)\left(\frac{e^2}{mc^2}\gamma\right)^2 f^2, \text{ cm}^2/(4\pi \text{ steradians}), \quad (1)$$

where S is the spin of the ion and γ is the magnetic moment of the neutron in nuclear magnetons. The form factor, f, is defined by

$$f=\int\int\int \psi^2 \exp(i\mathbf{q}\cdot\mathbf{r})dV, \quad (2)$$

where $\mathbf{q}$ is the vector change in momentum of the neutron. For a spherically symmetrical distribution (S-state),

$$f=\int_0^\infty r^2|\psi(r)|^2\frac{\sin\mu r}{\mu r}dr\equiv\int_0^\infty N(r)\frac{\sin\mu r}{\mu r}dr, \quad (3)$$

where $\mu=4\pi\sin\theta/\lambda$, ψ is the wave function of the appropriate spin shell normalized to make $f=1$ for $\mu=0$ and $N(r)$ is the spin distribution.

If the ions are coupled together so that the neutron can be scattered inelastically, the form factor in the forward direction is reduced from the value unity which applies to elastic scattering.[3] If in addition short-range ordering of the spins occurs the measured differential cross section per ion can be strongly altered from that given by Eq. (1), the form of the cross section being dependent on the details of the ordering. These effects have been observed by Bendt[4] and by Shull, Strauser, and Wollan.[2]

The dependence of the cross section on the spin distribution $N(r)$ is contained in the form factor, which can, in principle, be inverted to obtain the distribution. For such an inversion to give details of the distribution the measurements must extend over the entire range of μ in which f is appreciably different from zero. Because f is proportional to the square root of the cross section and therefore the intensity, this is a difficult condition to fulfill. The difficulty is aggravated by the fact that at large angles where the magnetic scattering is small, the thermal diffuse scattering is large and no satisfactorily accurate method of calculating it is known. In the present work the authors have tried to obtain accurate values of f, but the results do not justify inversion and a simpler method of analysis is used.

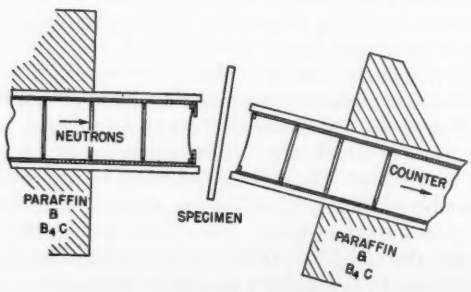

FIG. 1. Experimental arrangement.

EXPERIMENTAL ARRANGEMENTS AND METHODS

Two evacuated cadmium-lined collimators (Fig. 1) were added to the crystal spectrometer previously described[5] which was set for a wavelength of 1.062 A. The specimen in the form of a flat slab was mounted on the spectrometer table which was rotated at one half the speed of the counter. When temperatures other than room temperature were required the specimen was supported inside an evacuated scattering chamber which formed part of a liquid-nitrogen cryostat and which could also be used as a furnace.

To minimize air scattering, the air spaces between the evacuated collimators were kept as small as possible. Cadmium apertures intercepted neutrons scattered by the cadmium lining of the collimators, hence only those neutrons which were scattered twice by cadmium contributed to the background. Since the probability of a single scattering is about[6] 0.002 at our wavelength, the contribution from the double process is negligible.

A typical scattering pattern is shown in Fig. 2. The background with no specimen is also shown. To obtain the background with specimen, cadmium differences were measured. The net counting rate, N, is taken as

$$N=(N-N_{cd})_s-T(N-N_{cd})_b, \quad (4)$$

where T is the transmission of the specimen. The subscript cd refers to measurements made with 0.025 inch of cadmium in the beam, the subscripts s and b refer to measurements with and without specimen respectively.

Cross sections were computed as follows. The counting rate from diffuse elastic scattering may be expressed as

$$N=\left\{P_0\epsilon\frac{A}{4\pi r^2}\right\}S(2\theta)\equiv\left\{P_0\epsilon\frac{A}{4\pi r^2}\right\}S_0\sec\theta(T)^{\sec\theta-1}, \quad (5)$$

where $S(2\theta)d\Omega/4\pi$ is the fraction of the incident beam scattered into a solid angle $d\Omega$ and where P_0 is the number of neutrons in the beam per unit time, ϵ is the counter efficiency, A is the area of the collimator end, and r is its distance from the specimen.

The diffuse scattering cross section/(4π steradians)/molecule is

$$\sigma=\frac{1}{nT}(S_0-S_{M0})=\frac{1}{n(T)^{\sec\theta}\sec\theta}[S(2\theta)-S_M(2\theta)], \quad (6)$$

[5] Corliss, Hastings, and Brockman, Phys. Rev. **90**, 1013 (1953).
[6] B. N. Brockhouse, Can. J. Phys. **31**, 432 (1953).

where n is the number of molecules/cm² in the specimen and S_M represents the fraction multiply scattered computed as described in the following section. This diffuse scattering cross section is the sum of the nuclear incoherent, the magnetic diffuse and the coherent thermal diffuse cross sections, plus any diffuse scattering from defects. The cross sections were put on an absolute basis by comparison with the coherent scattering peaks of a nickel powder specimen. A value, $\sigma_{\text{coh}}=13.2\pm0.2$ barns for the coherent cross section of nickel as given by the U.S.A.E.C. Cross-Section Committee[7] and a value $2B=0.766\times10^{-16}$ for the constant in the Debye-Waller factor for nickel at room temperature were assumed. The integrated intensity of a peak is given by the usual formula

$$I_{hkl}=\left\{P_0\epsilon\frac{A}{4\pi r^2}\right\}\frac{\lambda^3}{\omega}\left[\frac{wN_A}{zMv}\right](T)^{\sec\theta}\times\exp\left[-2B\left(\frac{\sin\theta}{\lambda}\right)^2\right]\frac{(jF^2)_{hkl}}{\sin^2 2\theta}, \quad (7)$$

where ω is the angular velocity of the counter, w is the weight per unit area of the specimen, z is the number of molecules per unit cell, M is the molecular weight, v is the volume of a unit cell, N_A is Avogadro's number, θ is the Bragg angle, j is the multiplicity of the plane hkl, and F^2 is the structure factor for the plane.

To check the calibration the cross section of vanadium metal was measured near the forward direction, with the result that $\sigma_{\text{incoh}}=5.14$ barns/4π steradians as compared with the value 5.1 ± 0.1 barns accepted by the cross-section committee.[7]

Powdered specimens were contained in cassettes having $\frac{1}{32}$-inch aluminum windows. As the incoherent cross sectio of aluminum was measured and found to be less than 0.08 barn, no correction for incoherent scattering by the cassettes was necessary.

To correct for thermal diffuse scattering, the well-known "independent vibrations" approximation was used, purely for want of a better practical method. Thus we have taken

$$\sigma_{\text{T.D.}}=\sigma_{\text{coh}}[1-\exp[-2B(\sin\theta/\lambda)^2]]. \quad (8)$$

Where necessary, small corrections were applied for contamination of the beam by second-order neutrons, for effects of thermal expansion, and for thermal diffuse scattering by the aluminum windows of the cassettes.

MULTIPLE SCATTERING

The problem of multiple scattering in flat specimens was studied in some detail with a view to finding a satisfactory prescription for correction of magnetic and other diffuse scattering measurements. Following a suggestion by Vineyard,[8] multiple scattering calculations of Chandrasekhar[9] were reduced to a form suitable for easy application. Since the calculations apply to ideal experimental conditions not often met in practice, approximate corrections for deviation from the ideal geometry were computed. Measurements on a series of specimens in which multiple scattering is the major source of diffuse scattering showed that the method of treatment is satisfactory.

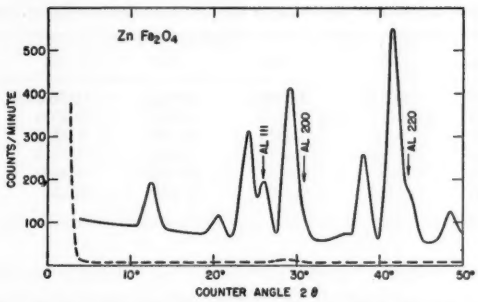

FIG. 2. Scattering pattern of $ZnFe_2O_4$ (solid line) and background with no specimen (dashed line). The transmission of the zinc ferrite specimen was 0.85.

In Chandrasekhar's treatment two parameters occur: the macroscopic total cross section of the specimen $\tau=\log_e T$, and the quantity $\omega=1-n\sigma_a/\tau$, where σ_a is the capture cross section per molecule and n is the number of molecules/cm². For isotropic primary scattering, the multiple scattering is a function of these two variables alone. The total scattering (at various angles) of neutrons incident normally on the flat specimen, was computed from Eq. (16), page 211 of reference 9, modified for use with neutrons. The multiple scattering was found by subtracting the primary scattering

$$\omega(e^{-\tau}-e^{-\tau\sec\theta})/(\sec\theta-1),$$

and then extrapolated graphically to the forward direction. This procedure was necessary because the expression for the multiple scattering is indeterminate when the angle of scattering equals the angle of incidence. The results are shown in columns 2 to 6 of Table I for values of ω from 0.5 to 1.0 (The tables of the functions[9] used in the computations only extend over this range of values.) The multiple scattering for smaller values of ω was calculated using the values for $\omega=1$, Vineyard's second order calculations[8] for $\omega=1$, the theorem that the multiple scattering can be expanded as a power series in ω corresponding to the different orders of scattering,[8,10] and the plausible assumption that the ratio of successive orders higher than the first

[7] *Neutron Cross Sections*, Atomic Energy Commission Report AECU-2040 and supplements (Technical Information Division, Department of Commerce, Washington, D. C., 1952).

[8] G. H. Vineyard, Phys. Rev. **96**, 93 (1954), and private communication. We are indebted to Dr. Vineyard for an advance copy of his calculations of second-order scattering.

[9] S. Chandrasekhar, *Radiative Transfer* (Clarendon Press, Oxford, 1950); Chandrasekhar, Elbert, and Franklin, Astrophys. J. **115**, 244 (1952).

[10] J. Tittman and C. Sheer, Phys. Rev. **83**, 746 (1951).

TABLE I. Multiple scattering in the forward direction (S_{M0}), computed following Chandrasekhar and Vineyard as discussed in the text.

$\tau \backslash \omega$	1.0	0.95	0.9	0.8	0.5	0.3	0.2	0.1	0.05
0.05	0.00515	0.00467	0.00421	0.00325	0.00127	0.000432	0.000190	0.000047	0.0000117
0.10	0.0177	0.0157	0.0139	0.0108	0.00402	0.00139	0.000605	0.000148	0.0000368
0.15	0.0356	0.0313	0.0289	0.0214	0.00780	0.00269	0.00117	0.000286	0.0000707
0.20	0.0578	0.0513	0.0452	0.0343	0.01215	0.00416	0.00180	0.00044	0.000108
0.25	0.0828	0.0731	0.0640	0.0490	0.0171	0.00570	0.00245	0.000594	0.000146
0.50	0.2435	0.210	0.1795	0.134	0.0432	0.0142	0.00597	0.00142	0.000348

is a constant. Good agreement was obtained between the two methods of calculation in their range of overlap.

Spot calculations showed that the angular dependence of the multiple scattering was closely the same as the primary scattering, *viz.*,

$$S_M(2\theta) = S_{M0} \sec\theta \exp[-\tau(\sec\theta - 1)],$$

at least up to $\tau = 0.25$ and scattering angle of 90°. The calculations are based on the assumption that primary scattering is isotropic. For all except the lightest elements this is a good approximation for incoherent scattering. Coherent scattering is concentrated in Debye-Scherrer cones, and hence is far from isotropic unless angular regions much larger than line separations are considered.

In order to determine whether this method of treating multiple scattering can justly be applied to coherent scattering by polycrystalline materials, measurements were made on a series of specimens of lead, bismuth, beryllium, and thorium. Near the forward direction, multiple scattering is the major source of diffuse scattering in these materials.[11] For thorium $\omega = 0.75$, for the others $\omega = 1.0$.[7] Some of the scatterers were sheet material with considerable preferred orientation. Figure 3 shows the measured diffuse scattering by these specimens in an angular range of about 10° near the forward direction, and the computed multiple scattering for $\omega = 1.0$ and $\omega = 0.75$. The experimental points must be corrected for thermal diffuse scattering according to Eq. (8). Also, because the theoretical curves were calculated for an extended source, scatterer, and counter, they do not apply precisely to the geometry of this experiment. Rather than modify the theoretical curves, we have chosen to apply a correction to the experimental points. Referring to the insert in Fig. 3, it can be seen that the source of multiply-scattered neutrons is more extended than the source of singly-scattered neutrons. In the experimental arrangement (Fig. 1) some of the neutrons multiply-scattered in the desired direction would not have been counted because they were excluded by the collimation. Calibration is carried out, however, by comparison with singly-scattered neutrons. Hence the measured multiple scattering is lower than the multiple scattering calculated for an extended scatterer and detector.

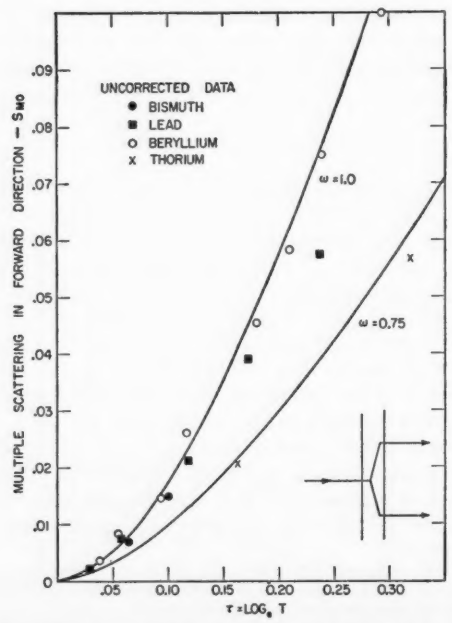

FIG. 3. The measured diffuse scattering near the forward direction plotted as a function of the parameter τ for various scatterers. The solid curves are calculated multiple scattering curves.

The fraction of *doubly*-scattered neutrons (η) which miss the counter because of this effect has been computed, using the isotropic approximation for the primary scattering, by calculating the fraction of doubly scattered neutrons which underwent their second scattering at a position in the specimen outside the area "seen" by the counter collimator. The integrals were evaluated numerically. In general η is a function of two parameters in addition to τ, *viz.*,

t = specimen thickness/counter collimator diameter,

ξ_0 = beam diameter/counter collimator diameter.

A sufficient condition that the correction be negligible is that $\tau(1-\xi_0)/t \gg 1$. The correction is fairly small if $\tau/t > 1$ and $\xi_0 < 1$. Keeping $\xi_0 < 1$ has the additional advantage that accidental variations in the angular sensitivity for single scattering are minimized. A further approximation was made in the computations. All

[11] Thorium is monoisotopic and has zero spin and therefore gives no incoherent scattering. The others have been shown to have very small incoherent cross sections by experiment (see reference 7).

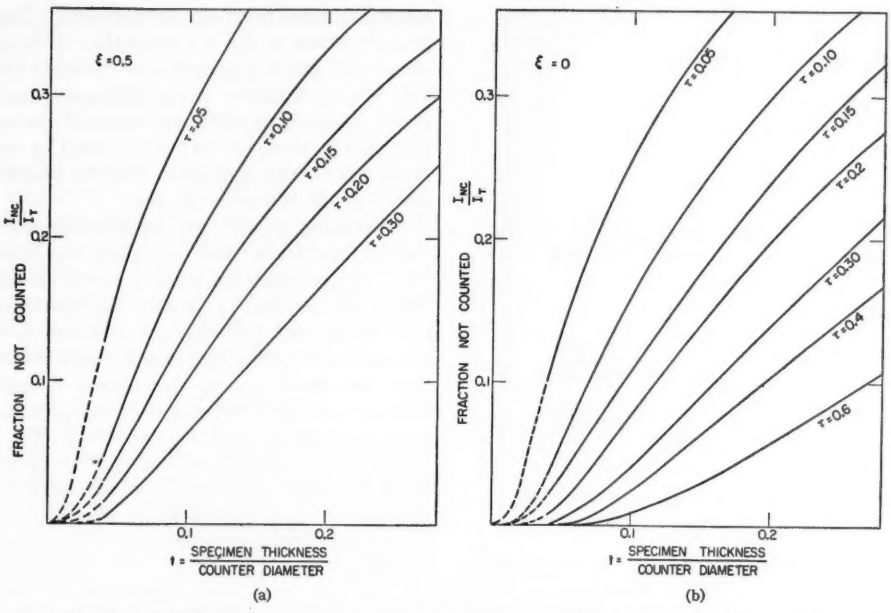

FIG. 4. Fraction of doubly scattered neutrons not counted for various thicknesses of scatterer. (a) Parameter $\xi=0.5$ based on $\xi_0=0.7$ as in this experiment. (b) $\xi=\xi_0=0$, pencil beam.

neutrons were assumed incident at a radial distance ξ from the center of the beam (in units of the counter diameter). For the apparatus $\xi_0=0.7$ and the computations were made for the case $\xi=(0.707\xi_0)=0.5$, corresponding to the mean radius of the beam. Computations were also made for the case of a pencil beam, $\xi=\xi_0=0$. The results are shown in Figs. 4(a) and 4(b).

The computed corrections ranged from a few percent for the beryllium specimens up to 35 percent for the thickest bismuth specimens and were applied to the experimental points of Fig. 3. The results, together with the computed multiple scattering curves for $\omega=0.75$ and 1.0 are shown in Fig. 5. The good agreement is evidence that the isotropic approximation is satisfactory, and gives confidence that this method of treatment of multiple scattering can be generally applied.

MAGNETIC SCATTERING BY ZINC FERRITE

Zinc ferrite[12] was selected as a material for study because the magnetic Fe^{3+} ions are supposedly in S states and therefore the theory of Halpern and Johnson[1] should apply except for possible effects of coupling. These coupling effects would themselves be interesting as an aid to understanding the magnetic properties of the important ferrite group.

The scattering curve at room temperature (Fig. 2) was analyzed near the forward direction and between the Bragg peaks. The results are shown in Fig. 6 as a differential cross section per molecule. In computing the multiple scattering correction, ω was taken to be 0.925.

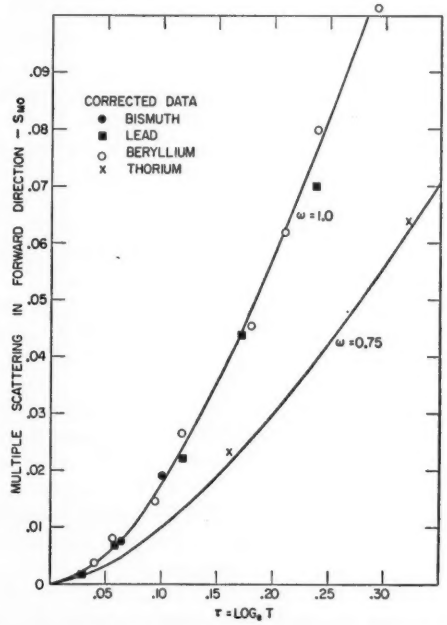

FIG. 5. Diffuse scattering near forward direction as given in Fig. 3 but corrected for thermal diffuse scattering and for neutrons which miss the counter. The solid curves are the same calculated multiple scattering curves as shown in Fig. 3.

[12] The specimen was kindly supplied by Dr. V. C. Wilson of the General Electric Research Laboratories. An analysis by Dr. R. W. Stoenner of Brookhaven National Laboratory showed 45.98 percent iron and 28.33 percent zinc compared with the stoichiometric composition 46.33 percent iron and 27.12 percent zinc.

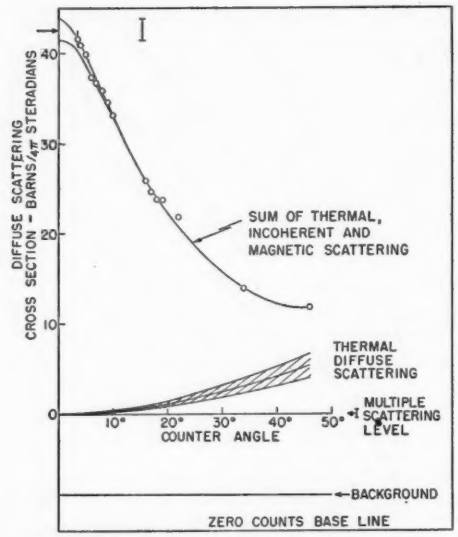

FIG. 6. Measured diffuse scattering cross section of zinc ferrite. The background shown is schematic.

The values of τ for the various specimens were about 0.15 and $t=0.12$, resulting in a value $\eta=0.16$ for the fraction of the multiple scattering that was not counted because of the finite size of counter aperture.

The Debye-Waller constant was found to be $2B=0.99\times10^{-16}$ from a powder pattern taken over an extended angular range, in agreement with an estimate of 0.96×10^{-16} made using the specific heat of Fe_3O_4.[13] The thermal diffuse scattering was calculated from Eq. (8) using the value $2B=0.99\times10^{-16}$. The temperature dependence of the diffuse scattering from 90°K to 450°K was studied, and within the uncertainties, was consistent with the calculated values for the total thermal diffuse scattering, though favoring somewhat smaller values. The incoherent scattering cross section of iron was taken as 0.4 barns/atom,[7] and that of zinc as 0.2 barn.[7] The resulting curve for the magnetic scattering cross section/iron atom is shown in Fig. 7.

The extrapolation to zero scattering angle takes account of the probable persistence to room temperature of a small amount of excess scattering at small angles. This will be discussed in the next paragraph. The extrapolation was made easier by the knowledge that, for small enough angles, the curve must be parabolic and concave downwards (if no short-range ordering occurs).

Estimated limits (broken lines) on the extrapolation are shown. For calculation of the form factor this is the major pertinent uncertainty (in addition to the normal errors of each point). For comparison of the cross section in the forward direction with the theoretical value of 21.2 barns (indicated by an arrow in Fig. 7), errors associated with the normalization of the scattering curve must also be considered. These include possible errors in the determination of the number of atoms/cm² in the specimen, the coherent cross section and other parameters of the nickel standard, and the multiple-scattering level. Estimates of the uncertainty produced by these causes are indicated by vertical bars in the figure. The agreement with the theoretical value is well within the uncertainties.

Small-angle scattering at liquid nitrogen temperature was larger than at room temperature as shown in Fig. 8(a). The temperature dependence of the excess scattering was studied by setting the spectrometer at a fixed angle and allowing the cryostat to warm up, meanwhile recording the counting rate. Measurements were also made at and above room temperature, including a careful comparison of the counting rates at room temperature (295°K) and 500°K. The results are shown in Fig. 8(b). From the figure it appears that a small amount (~2 percent) of the excess scattering persists to room temperature but the strong temperature-dependence suggests that it is probably almost completely absent at 500°K.

DISCUSSION

The presence of the small-angle scattering suggests that there may be short-range coupling between spins at the lower temperatures. A theoretical treatment of scattering of neutrons by such a system has not yet been given, but it seems reasonable to assume that the

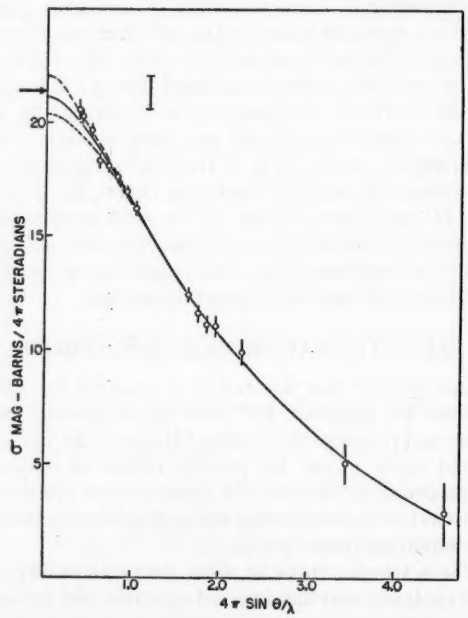

FIG. 7. Magnetic scattering cross section per Fe^{3+} ion in $ZnFe_2O_4$. To the left of the axis of ordinates the arrow indicates the theoretical value 21.2 barns. The short vertical bar opposite the arrow indicates the uncertainty arising from determinate errors as discussed in the text.

[13] R. W. Millar, J. Am. Chem. Soc. 51, 215 (1929).

result would not be very different from the familiar x-ray result[14]

$$I_M=\sum_{mn} f_m f_n \frac{\sin\mu r_{mn}}{\mu r_{mn}}, \tag{9}$$

where I_M is the measured scattering, f_m and f_n are the scattering factors for atoms m and n, and r_{mn} is the distance between them. For antiferromagnetically coupled atoms, f_m and f_n have opposite signs and, if they are of the same kind, equal magnitudes. For ferromagnetically coupled atoms, f_m and f_n have the same signs. In fact, as shown by the broken line in Fig. 8(a), the experimental results can be fitted by

$$\Delta\sigma=\sigma_{\text{mag}}\,0.31(\sin\mu r/\mu r), \tag{10}$$

with $r=2.98$ A, the shortest distance between iron atoms. This suggests that the effect is caused by ferromagnetic short-range coupling between nearest neighbors, and hence that the interaction between ions on the B (octahedral) sites is ferromagnetic. There is evidence against this interpretation in the properties of mixed ferrites[15] and in the fact, recently established,[16] that zinc ferrite is antiferromagnetic at helium temperatures. This latter fact could be explained by the existence of antiferromagnetic interactions between distant neighbors which are weaker than the ferromagnetic interactions between near neighbors. Such a picture seems reasonable because some distant iron neighbors are coupled by Fe−O−Fe links of large angle, while the nearest neighbors are coupled by 90° links. The importance of large-angle oxygen links in producing antiferromagnetism is now well known.[2,17,18] It should also be pointed out that a small amount of inversion [placing of iron ions on A (tetrahedral) sites] could produce marked effects because of the strong coupling between A and B sites and the large number of B neighbors coupled to any one A site. The degree of inversion of zinc ferrite, established as less than 5 percent,[19] could still be sufficient to produce effects as large as those observed but probably not of the right kind.

Calculations of the magnetic cross section using hydrogenic screened Coulomb wave functions[20] in Eq. (1) were compared with Fig. 7. It was not possible to get a fit within the supposed accuracy of the results. To obtain a fit it was necessary to add a long tail to the spin distribution, the tail comprising about 10 percent of the spins. Such a tail, representing spins not on the iron ions at all but on neighboring ions, might arise simply from persistence to room temperature of the small angle scattering in larger amount than assumed, or it might correspond to the charge transfer or promotion expected to take place in superexchange. The main part of the spin distribution had a maximum at about 0.45 A, in fair agreement with the results for ferromagnetic ferrites,[21] and consistent with the accepted value of 0.67 A for the crystallographic radius of the Fe^{3+} ion.[22]

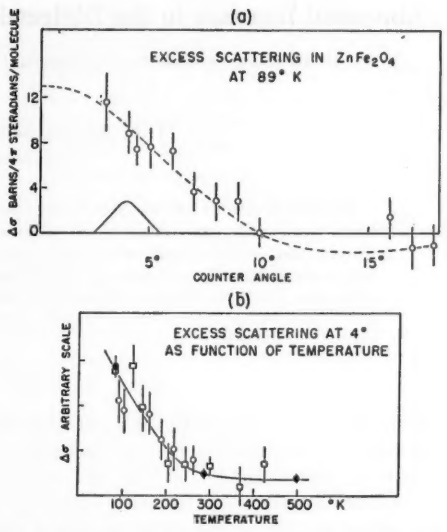

FIG. 8. (a) Difference between the differential scattering cross sections of zinc ferrite at 295°K and 89°K (with a small correction for thermal diffuse scattering applied). The dashed line represents a plot of Eq. (10). (b) Temperature dependence of the scattering at a mean angle of 4 degrees. Different symbols represent the results of different runs.

The authors wish to thank Dr. G. H. Vineyard, Dr. V. C. Wilson, and Dr. R. W. Stoenner for their contributions to the work. One of us (B.N.B.) wishes to express here his deep appreciation of the hospitality he enjoyed at Brookhaven National Laboratory during the time the Chalk River NRX reactor was closed down.

[14] A. H. Compton and S. K. Allison, *X-Rays in Theory and Experiment* (D. Van Nostrand Company, Inc., New York, 1935), second edition, p. 159.
[15] L. R. Maxwell and S. J. Pickart, Phys. Rev. **92**, 1120 (1953).
[16] L. M. Corliss and J. M. Hastings (to be published).
[17] P. W. Anderson, Phys. Rev. **79**, 350; **79**, 705 (1950).
[18] B. N. Brockhouse, Phys. Rev. **94**, 781 (1953).
[19] J. M. Hastings and L. M. Corliss, Revs. Modern Phys. **25**, 114 (1953).
[20] See reference 1, Eq. (7.3).
[21] Corliss, Hastings, and Brockman, Phys. Rev. **90**, 1013 (1953).
[22] R. W. G. Wyckoff, *Crystal Structures* (Interscience Publishers, Inc., New York, 1948), Vol. 1, Chap. III, Table on p. 15.

Abnormal Increase in the Dielectric Constant of an Electret-Forming Material

S. D. CHATTERJEE, *Department of Physics, University College of Science and Technology, Calcutta, India*

AND

T. C. BHADRA, *Bose Research Institute, Calcutta, India*

(Received February 3, 1955)

An electret with its two surfaces covered by plates which are connected together presents a situation in which the average (zero) field between the plates is composed to two equal and opposite parts, one due to the polarization and the other due to the charges on or adjacent to the plates. These opposing fields can be very large ($\sim 10^6$ volts/cm) and as a result, large fluctuations may be expected in the vicinities of individual molecules. For these reasons it is surmised that the dielectric constant of the material of an electret may show an abnormal value, depending upon "strength" of the electret. The experiments described verify the existence of such an abnormality.

SWANN[1] has shown that an electret with zero potential difference between its surfaces presents a very remarkable situation. Indeed, it can be regarded as having an enormous electrostatic field ($\sim 10^6$ volts/cm) due to surface charges in one direction and a similar field due to polarization in the other direction. The two fields practically balance in the average sense. Nevertheless, there will be fluctuations of the polarization field, which has a very large magnitude ($\sim 10^8$ volts/cm) in the immediate vicinity of an ion or a dipole. Such fluctuations, resulting in a lack of compensation by the surface charge field, will tend to leave the individual molecules in a state of high field perturbation. In such a case, one may expect the polarizability of molecules to change with the magnitude of field strength,[2] resulting in a variation of the dielectric constant of the medium.

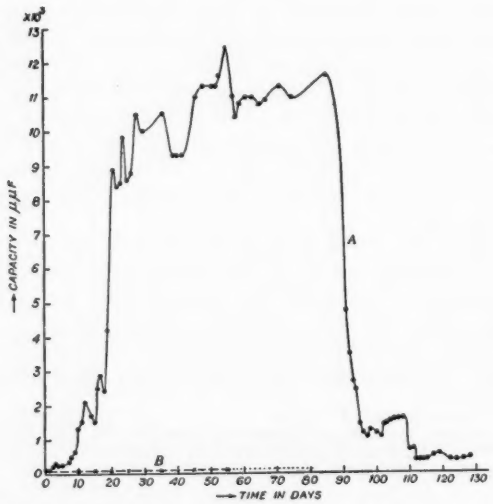

FIG. 1. Change in capacity as a function of time (A) for a polarized dielectric condenser, and (B) for an unpolarized dielectric condenser.

In a typical experiment, a fixed trimmer air condenser (capacity 23 $\mu\mu$f) was immersed in molten Carnauba wax in a small glass vessel. An electric field of 11.5 kv/cm was maintained between the plates of the condenser while the liquid wax was slowly allowed to cool and solidify. Finally, the field was removed. The capacity of the condenser was measured from day to day by means of a Marconi universal bridge. The bridge is operated by a 1-kc/sec oscillator and incidentally gives also the values of $Q(=1/\omega CR)$ or $\tan\delta(=1/Q)$.

The curve A in Fig. 1 shows the changes in the value of the capacity of the polarized dielectric condenser as a function of time, whereas the dotted curve B represents the case of a similar but unpolarized dielectric condenser, which serves as a control. It may be seen that after the initial couple of days, the capacity of the polarized condenser climbs steeply to more than a hundred times its original value and after hovering in the neighborhood of this elevated value for some length of time, rapidly tends to approach the original value.

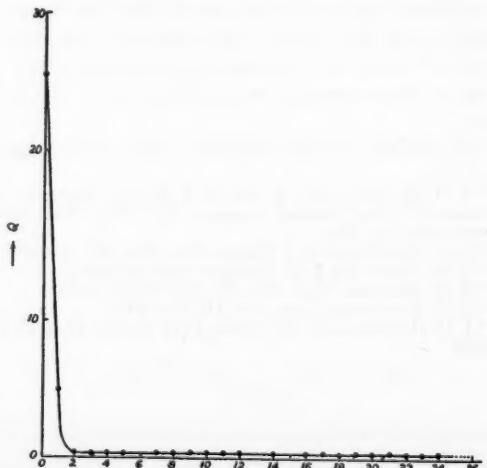

FIG. 2. Variation of Q as a function of time.

[1] W. F. G. Swann, J. Franklin Inst. 255, 513 (1953).
[2] Coulson, Maccoll, and Sutton, Trans. Faraday Soc. 48, 106 (1952).

This period of enhanced dielectric constant seems to depend upon the original conditioning field which created the electret and therefore determined its intrinsic polarization.

Figure 2 characterizes the variation of Q as a function of time. It may be seen that Q rapidly climbs down during the initial couple of days, and maintains a steady value at 0.42 during the period of high value of the capacity. It means that during the latter period, the capacity of the condenser varies inversely as its ac resistance. However, the rapid rise of $\tan\delta$ or "loss angle" during the initial couple of days indicates that the conduction current through the condenser increases rapidly in comparison with the charging current. Subsequently, they appear to maintain a constant phase angle, as if they increase in the same proportion.

An attempt to measure the dc conductivity of the polarized medium during its active period resulted in a slow but gradual diminution of a fairly large conduction current. As the current continues to flow, the polarized medium becomes "electrically purified," causing a simultaneous diminution in the value of the capacity of the condenser.

The original value of the capacity is restored after some time when the small dc field is withdrawn. Furthermore, a second condenser, located in the same polarized dielectric medium in a direction at right angles to the original condenser, also exhibited a rise in capacity, but to a somewhat lesser degree.

All these facts seem to suggest that free electrons are being liberated from the polarized molecules during the state of high field perturbation. Indeed, the possibility of such an effect had been envisaged by Oppenheimer[3] and Lanczos[4] in the case of the hydrogen atom. In the present case, the molecules become ionized by the removal of valence electrons in the fields of neighboring dipoles. These semifree electrons are recaptured when the polarization decays to some extent.

Further experiments are in progress.

We are indebted to Dr. W. F. G. Swann for his kind interest in this work.

[3] J. R. Oppenheimer, Phys. Rev. **13**, 66 (1928).
[4] C. Lanczos, Z. Physik **68**, 204 (1931).

PHYSICAL REVIEW VOLUME 98, NUMBER 6 JUNE 15, 1955

Overhauser Effect in Nonmetals

A. ABRAGAM
Centre d'Etudes Nucléaires de Saclay, Gif sur Yvette, Seine et Oise, France
(Received January 27, 1955)

A survey is made of different ways in which nuclear spins can relax through their interaction with electronic spins. It is shown that the maximum amount of nuclear polarization which can be obtained by saturating the electronic resonance depends: (a) on the type of interaction between electronic and nuclear spins, namely dipole-dipole type, scalar product type, or any combination of the two; (b) on the mechanism whereby the "lattice" provides the energy for the relaxation.

The case of a nucleus belonging to a paramagnetic ion is examined in some detail with reference to the recent experiment of Honig on arsenic-doped silicon. It is shown that while an Overhauser effect may be expected, this offers no support for an interpretation of Honig's results as a hundred percent nuclear polarization.

INTRODUCTION

OVERHAUSER'S proof[1] that saturation of the electronic resonance in metals would lead to a considerable enhancement of the nuclear polarization was based explicitly on the assumption of Fermi statistics for the conduction electrons. It was soon recognized, however,[2] that the assumption of Fermi statistics was by no means necessary and that consequently an Overhauser effect could be expected in paramagnetic substances as well.

However, the conditions under which exchange of energy can take place between the electronic and nuclear spins and the lattice are manifold, and a review of the different possibilities will give some information about the maximum amount of nuclear polarization to be expected in each case.

For simplicity, we assume the nuclear spin I to be one half. A larger value of I introduces mainly complications of notation but no fundamental changes.

We also assume that the experiment is done in a "large" external field H_0 applied along the z axis, the z components of the electronic and the nuclear spin being good or approximately good quantum numbers.

Finally, it is assumed that the nuclear spins have no direct coupling with the lattice and that their relaxation takes place through their coupling with the electronic spins. The magnetic interaction between an electronic spin $\mathbf{s}$ and a nuclear spin $\mathbf{I}$ can be written most generally as

$$\mathcal{H}_1 = \mathbf{I} \cdot \mathfrak{A} \cdot \mathbf{s},$$

[1] A. Overhauser, Phys. Rev. **89**, 689 (1953); **92**, 411 (1953).
[2] F. Bloch, Phys. Rev. **93**, 944 (1954); A. Overhauser, Phys. Rev. **94**, 768 (1954); J. Korringa, Phys. Rev. **94**, 1388 (1954).

where $\mathfrak{A}$ is a symmetrical tensor. $\mathcal{H}_1$ is sometimes written as

$$\mathcal{H}_1 = -(\mu_n/I)\mathbf{I}\cdot\mathbf{H}_e = -\hbar\gamma_n\mathbf{I}\cdot\mathbf{H}_e,$$

where $\mathbf{H}_e = -(I/\mu_n)\mathfrak{A}\cdot\mathbf{s}$ is called the magnetic field produced by electron at the nucleus. ($\mu_n = \hbar\gamma_n I$ is the magnetic moment of the nucleus.)

To make the relaxation of the nuclear spins possible, two conditions must be realized: (a) $\mathcal{H}_1$ must have matrix elements between states of the electron-nucleus system with different values of I_z, which it actually has unless the symmetrical tensor $\mathfrak{A}$ has only one nonvanishing component $\mathfrak{A}_{zz}$; (b) the energy required for these transitions must be available.

This second condition is often formulated as follows.[3] The electronic field $\mathbf{H}_e$ fluctuates in time and can be described as a random function of time. A nuclear flip requiring an energy $\hbar\omega_0$ will take place if the spectrum of the random function $H_e(t)$ contains the frequency ω_0. To be more specific, the Fourier transform of the correlation function $\varphi(\tau) = \langle H_e(t)\cdot H_e(t-\tau)\rangle$ must have a non vanishing value $J(\omega_0)$ for $\omega = \omega_0$. (For a vector random function like $\mathbf{H}_e$, the correlation function is in fact a tensor but this is immaterial here.)

The variation in time of the electron field $\mathbf{H}_e$ can be ascribed either to a variation of the tensor $\mathfrak{A}$ due to lattice vibrations in solids, Brownian motion in liquids etc., or to a time variation of the electron-spin $\mathbf{s}$ itself.

The physical meaning of this last statement is that the electron spins apart from their interaction with the nuclei have other, generally much more powerful, mechanisms of relaxation which will lead to electronic flips randomly distributed in time with a time constant corresponding to the electronic relaxation time T_{el}.

The two effects may of course exist simultaneously. The first or relaxation through motion will be predominant in the liquid solutions of paramagnetic ions of low viscosity,[3] the second or relaxation by random flips of the electronic spins will be predominant in diamagnetic crystals with paramagnetic impurities.[4] For brevity we shall from now on refer to these effects as nuclear relaxation of the first type or the second type. The nuclear relaxation in metals treated by Korringa[5] and Overhauser[1] can be considered as belonging to the first type, the time dependence in the electron nucleus interaction being caused by the relative motion of the conduction electrons and of the nuclei.

As long as one's interest is focused on nuclear spins only, it may be permissible to lump the electronic spins with the "lattice" and speak of a fluctuating electronic field $\mathbf{H}_e(t)$, inducing nuclear transitions, without making a distinction between the two causes of variation of $\mathbf{H}_e$. On the other hand, in the Overhauser effect where the fact that the electronic spins are not in thermal equilibrium is essential, they should be separated from the lattice and treated quantum mechanically.

[3] Bloembergen, Purcell, and Pound, Phys. Rev. **73**, 679 (1948).
[4] N. Bloembergen, Physica **15**, 386 (1949).
[5] J. Korringa, Physica **16**, 601 (1950).

We introduce explicitly into the Hamiltonian the operator $2\beta(\mathbf{H}'\cdot\mathbf{s})$ (β is a Bohr magneton) responsible for the relaxation of the electronic spins. $\mathbf{H}'$ can be thought of as a fluctuating magnetic field produced by the lattice. This expression does not imply any specific assumptions about the mechanism of the electronic relaxation and could for instance refer to the relaxation mechanism through spin-orbit coupling proposed by Kronig[6] and Van Vleck.[7]

We separate the tensor $\mathfrak{A}$ into a static part $\mathfrak{A}_0$ and a fluctuating part $\mathfrak{A}_1$. $\mathcal{H}'$ and $\mathfrak{A}_1$ can be described either as random time-dependent functions or in a more rigorous manner as operators having matrix elements between different lattice states, according to the general theory of relaxation of Bloch.[8]

The Hamiltonian for a nucleus interacting with an electron can thus be written:

$$\mathcal{H} = 2\beta H_0 s_z - (\mu_n/I)H_0 I_z + \mathbf{I}\cdot\mathfrak{A}_0\cdot\mathbf{s} + 2\beta\mathbf{H}'\cdot\mathbf{s} + \mathbf{I}\cdot\mathfrak{A}_1\cdot\mathbf{s}. \quad (1)$$

The first three terms constitute a static Hamiltonian $\mathcal{H}_0$. The last two terms induce transitions between different eigenstates of $\mathcal{H}_0$.

We shall now examine as an illustration a few special cases and calculate each time the maximum amount of nuclear polarization to be expected when the electron resonance is completely saturated.

Case 1. Nuclear Resonance in a Liquid Containing Paramagnetic Impurities

We make the following assumptions: (a) The interaction between the electronic and nuclear spins is of the dipole-dipole type. (b) The static part $\mathfrak{A}_0$ of the tensor $\mathfrak{A}$, equal to its time average, is washed out by the Brownian motion and vanishes. $\mathfrak{A} = \mathfrak{A}_1$. (c) The nuclear relaxation produced by the flip of the electronic spins can be neglected in comparison with the effect of the relative motion of the paramagnetic ion and the nucleus.[9] The relaxation process is of what we call the first type.

The interaction between the two spins can be written[10]:

$$\mathbf{I}\cdot\mathfrak{A}\cdot\mathbf{s} = -2\beta\gamma_n\hbar r^{-3}(A+B+C+D+E+F). \quad (2)$$

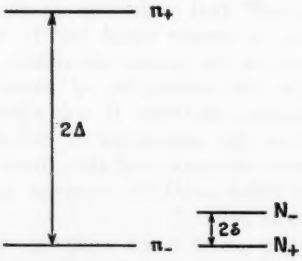

FIG. 1. Energy states and levels of the system electron plus nucleus in a liquid.

[6] R. Kronig, Physica **6**, 33 (1939).
[7] J. H. Van Vleck, Phys. Rev. **57**, 426 (1940).
[8] R. K. Wangsness and F. Bloch, Phys. Rev. **89**, 728 (1953); F. Bloch (to be published).
[9] N. Bloembergen, thesis, Leiden University, 1948 (unpublished), p. 98.
[10] Reference 9, p. 34.

The various terms correspond to the following changes of the components $I_z=M$ and $s_z=m$.

$$\begin{array}{llll}
\Delta M=0, & \Delta m=0, & A=I_zs_z(1-3\cos^2\theta), \\
\Delta M=\pm1, & \Delta m=\mp1, & B=-\tfrac{1}{4}\{I_+s_-+I_-s_+\}(1-3\cos^2\theta), \\
\Delta M=1, & \Delta m=0, \\
\Delta M=0, & \Delta m=1, & C=-\tfrac{3}{2}\{I_+s_z+I_zs_+\}\sin\theta\cos\theta\exp(-i\varphi), \\
\Delta M=-1, & \Delta m=0, \\
\Delta M=0, & \Delta m=-1, & D=-\tfrac{3}{2}\{I_-s_z+I_zs_-\}\sin\theta\cos\theta\exp(i\varphi), \\
\Delta M=1, & \Delta m=1, & E=\tfrac{3}{4}I_+s_+\sin^2\theta\exp(-2i\varphi), \\
\Delta M=-1, & \Delta m=-1, & F=\tfrac{3}{4}I_-s_-\sin^2\theta\exp(2i\varphi).
\end{array} \tag{3}$$

θ and φ are the polar angles of the vector $-\mathbf{r}/|r|$ with respect to the field H_0.

Figure 1 represents the energy states and the levels of the electron and the nucleus in the external field H_0.

The nuclear splitting 2δ is taken as positive if the gyromagnetic ratio of the nucleus is positive. The electronic splitting 2Δ is positive. The quantities 2Δ and 2δ are dimensionless and represent the energy splitting divided by kT. The rate of change of the population N_- of the nuclear state $M=-\frac{1}{2}$ is given by the equation

$$\begin{aligned}
dN_-/dt=&-bN_-n_+\exp(\Delta+\delta)+bN_+n_-\exp(-\Delta-\delta)\\
&-cN_-(n_++n_-)\exp(\delta)+dN_+(n_++n_-)\exp(-\delta)\\
&-eN_-n_-\exp(-\Delta+\delta)+fN_+n_+\exp(\Delta-\delta).
\end{aligned} \tag{4}$$

n_+ and n_- are the probabilities of finding an electron, interacting with the nucleus, in the state $+$ or $-$. The quantities b, c, d, e, f are the probabilities per unit time of transitions induced respectively by the operators B, C, D, E, F. Since these transitions are produced through interaction with a lattice in thermal equilibrium, appropriate Boltzmann factors are introduced in a symmetrical manner.

We now make the further assumptions customary in the theory of relaxation in nonviscous liquids: (a) The spectral intensities of A, B, C, D, E, F, are frequency independent or "white" for all the transitions involved. (b) The problem is isotropic in the sense that one may average the squares of the matrix elements over the angles.

With these assumptions, it is easily found that the ratios of the quantities b, c, d, e, f are 2:3:3:12:12. (c) The temperature is high so that Δ and δ are small numbers.

Expanding the exponentials in (4) and keeping the linear terms only, we find that for complete saturation of the electronic resonance ($n_+=n_-$) the equilibrium distribution of the nuclear populations is given by

$$\begin{aligned}
&N_-\{b(1+\Delta+\delta)+2c(1+\delta)+e(1-\Delta+\delta)\}\\
&\quad=N_+\{b(1-\Delta-\delta)+2d(1-\delta)+f(1+\Delta-\delta)\},
\end{aligned} \tag{5}$$

or to the same degree of approximation

$$N_+/N_-=1-\Delta-2\delta. \tag{6}$$

This should be compared with Overhauser's result where an interaction of the form $(\mathbf{I}\cdot\mathbf{s})$ is assumed, equivalent to making

$$c=d=e=f=0 \text{ in (5).}$$

There one finds

$$N_+/N_-=1+2\Delta+2\delta. \tag{7}$$

If we neglect the small quantity 2δ in (6) and (7), we see that the nuclear polarization due to dipole-dipole interaction is half of the one produced by the $(\mathbf{I}\cdot\mathbf{s})$ interaction and of opposite sign.

An observation of nuclear induction with a phase-sensitive detector should permit a discrimination between the two types of interaction.

Case 2. Nuclear Resonance in a Diamagnetic Crystal Containing Paramagnetic Impurities

Here the situation is exactly opposite insofar as relaxation of the nuclear spins is produced through the flips of the electronic spins rather than through their relative motion, and the last term of (1) $\mathbf{I}\cdot\alpha_1\cdot\mathbf{s}$ is absent from the Hamiltonian. Without the dipole-dipole coupling the eigenstates of the system: electron plus nucleus, are simply: (+,+), (+,−), (−,+), (−,−), the first sign in the parenthesis referring to s_z and the second to I_z. One can see from (3) that the dipole-dipole interaction couples each state with the three others. However because of their much smaller energy differences, states corresponding to the same electronic spin are much more strongly coupled together than those with opposite electronic spin and, to a very good approximation, only terms C and D with $\Delta m=0$, $\Delta M=\pm1$ should be retained in the Hamiltonian.

In order for the nuclear resonance to be observable at all we have to assume that the dipole-dipole interaction is much smaller than the nuclear splitting. We can then use perturbation theory and the level scheme is shown in Fig. 2.

The different eigenstates are given by the following formulas:

$$\begin{aligned}
&|b'\rangle=p|+,-\rangle-q|+,+\rangle, \quad |b\rangle=p|-,-\rangle+q|-,+\rangle,\\
&|a'\rangle=p|+,+\rangle+q|+,-\rangle, \quad |a\rangle=p|-,+\rangle-q|-,-\rangle,\\
&q=\tfrac{3}{4}r^{-6}\gamma_e\gamma_n\hbar\sin\theta\cos\theta\exp(i\varphi)(2\pi\nu_0)^{-1},\\
&h\nu_0=2kT\delta, \quad p^2+q^2=1, \quad p\cong1.
\end{aligned} \tag{8}$$

The perturbing Hamiltonian $2\beta(\mathbf{H}'\mathbf{s})$ responsible for the electronic relaxation will induce weak electronic

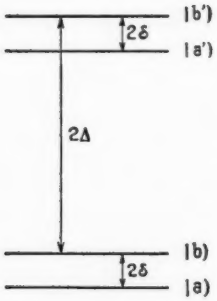

FIG. 2. Energy states and levels of the system electron plus nucleus in a solid.

transitions, of intensity proportional to q^2 between the states $|a')$ and $|b)$ and also between $|a)$ and $|b')$. These are the transitions responsibles for nuclear relaxation, going from states where the nuclear spin I_z is up to states where it is down. The strong transitions, $|a)\leftrightarrow|a')$ and $|b)\leftrightarrow|b')$ induced by $(\mathbf{H}'\cdot\mathbf{s})$ are the transitions of the electronic relaxation. If we assume that the electronic relaxation time T_{el} is long compared to the Larmor period of the nucleus (which is really equivalent to saying that the width of the different levels in Fig. 2 is smaller than the nuclear spacing), the nuclear relaxation time T_n is given by

$$(T_n)^{-1}\cong 4q^2(T_{el})^{-1}$$
$$\equiv (T_{el})^{-1}\gamma_e^2\gamma_n^2\hbar^2\sin^2\theta\cos^2\theta(2\pi\nu_0)^{-2}r^{-6}\cdot 9/4. \quad (9)$$

This is equivalent to Bloembergen's[4] formula (10) if one takes in this formula $s=\frac{1}{2}$, $\rho=4\pi T_{el}$ and neglects unity in comparison with $\rho^2\nu_0^2$ [the complete formula (10) of Bloembergen with the denominator $(1+\rho^2\nu^2)$, applicable if $\rho\nu$ is not large, obtains easily by our method, if the finite width of the electronic levels is taken into account by the Wigner-Weisskopf method].

The equations for the rate of change of the populations a and a' of the states $|a)$ and $|a')$ in the presence of an rf field are

$$da'/dt=(2T_{el})^{-1}[a\exp(-\Delta)-a'\exp(+\Delta)$$
$$-\lambda a'\exp(\Delta-\delta)+\lambda b\exp(-\Delta+\delta)]$$
$$+V(a-a'), \quad (10)$$
$$da/dt=(2T_{el})^{-1}[-a\exp(-\Delta)+a'\exp(+\Delta)$$
$$-\lambda a\exp(-\Delta-\delta)+\lambda b'\exp(\Delta+\delta)]+V(a'-a),$$

where V is the transition probability induced by the rf field, and λ is a small quantity equal to $4q^2\rho^2\nu_0^2(1+\rho^2\nu_0^2)^{-1}$. Similar equations can be written for the rates of change of b and b'.

At saturation, when $V\gg(2T_{el})^{-1}$, then $a=a'$, $b=b'$, and (10) gives for the ratio $(a+a')/(b+b')=a/b$ of nuclei with spin up, to those with spin down, under steady-state conditions:

$$b[\exp(\Delta+\delta)+\exp(-\Delta+\delta)]$$
$$=a[\exp(\Delta-\delta)+\exp(-\Delta-\delta)].$$

A linear expansion gives

$$a/b=1+2\delta, \quad (11)$$

which is simply the Boltzmann equilibrium distribution. No Overhauser effect is observed.

This can be easily understood on the basis of Kittel's argument[11]: In the sequence of transitions $(a'\rightarrow b\rightarrow b')$, the first one $|a')\rightarrow|b)$ due to relaxation, gives the energy $2\Delta-2\delta$ to the lattice, while the second $(b\rightarrow b')$, because of saturation, takes place through the rf field, and leaves the lattice unchanged. In the resultant transition $a'\rightarrow b'$, which corresponds to a net flip of a nuclear spin from $+$ to $-$, the lattice has received the energy $2\Delta-2\delta$. However, in the sequence $a\rightarrow b'\rightarrow b$, which also corresponds to a nuclear flip from $+$ to $-$, the lattice surrenders $2\Delta+2\delta$. Thus on the average it surrenders 2δ, leading to a nuclear Boltzmann factor $\exp(2\delta)\sim 1+2\delta$ in agreement with (11).

If the electron-nucleus interaction, instead of being dipole-dipole, were *purely* scalar the situation would have been different and an Overhauser effect would be possible in principle, as will appear more clearly from the next example. However, in that case only states with different values of the electronic spin, namely $(+,-|$ and $(-,+|$ could be coupled together. The admixture coefficients would become smaller by a factor $\nu_n/\nu_e=\mu_n/\mu_e$ and the nuclear relaxation times longer by a factor $(\mu_e/\mu_n)^2\sim 10^6$. This would make the assumption that nuclear relaxation operates mainly through an $(\mathbf{I}\cdot\mathbf{s})$ coupling with the paramagnetic impurity, unrealistic.

On the other hand, a reduced Overhauser effect may still be observed if the nuclear relaxation is not entirely of the second type and receives a contribution from the relative motion of the impurity and the nuclear spin.

One should add that, as Bloembergen[4] has shown, in order to be effective the process of nuclear relaxation by paramagnetic impurities should include nuclear spin diffusion which brings the nuclear spin to be relaxed, into the vicinity of the paramagnetic impurity.

Spin diffusion is not, however, a thermal process and if its rate is slow compared to electronic relaxation, it should have no influence on the previous conclusions.

Case 3. The Overhauser Effect inside a Paramagnetic Ion

We now assume that the nucleus under consideration belongs to a paramagnetic ion and that the experimental conditions are such that the hyperfine structure is resolved. This implies that (unless one is dealing with a single crystal) the tensor $\mathcal{A}_0$ is diagonal and reduces to a single constant A_0, for otherwise the anisotropy broadening would prevent the resolution of the hyperfine structure.

We shall make this assumption. The conclusions will, however, be essentially the same in a slightly more general case when the hyperfine structure has tetragonal symmetry and the magnetic field is applied along the tetragonal axis of a single crystal. We rewrite the

[11] C. Kittel, Phys. Rev. **95**, 589 (1954).

Hamiltonian of the electron-nucleus system as follows:

$$\mathcal{H}=2\beta H_0 s_z+A_0 s_z I_z+\tfrac{1}{2}A_0(s_+I_-+s_-I_+) -\hbar\gamma_n H_0 I_z+\mathbf{I}\cdot\mathfrak{A}_1\cdot\mathbf{s}+2\beta\mathbf{H}'\cdot\mathbf{s}. \quad (12)$$

There is an important change with the previous cases, namely that the direct coupling of the nuclear spin with the applied field $-\hbar\gamma_n H_0 I_z$ will normally be much smaller than the electron nucleus interaction $\mathbf{I}\cdot\mathfrak{A}\cdot\mathbf{s}$ and can be neglected. We assume $\beta H_0 \gg A_0$ (strong-field or Paschen-Back case).

The eigenfunctions of the static part of $\mathcal{H}$ corresponding to the three first terms of (12) will then be

$$|a'\rangle=|+,+\rangle,\quad |b'\rangle=p|+,-\rangle+q|-,+\rangle,$$
$$|a\rangle=p|-,+\rangle-q|+,-\rangle,\quad |b\rangle=|-,-\rangle, \quad (13)$$
$$p^2+q^2=1.$$

The coefficient q is small, of the order $A_0/\beta H_0$. p is thus nearly one.

$|a\rangle$ and $|a'\rangle$ are therefore essentially states with nuclear spin up and $|b\rangle$ and $|b'\rangle$ d states with nuclear spin down.

The energy levels are represented in Fig. 3.

We neglect the second-order differences between $E_{a'}-E_{b'}$ and E_b-E_a.

$$\Delta=\beta H_0/kT,\quad 2\delta=A_0/2kT.$$

Figure 3 corresponds to the assumption $A_0>0$. The two other terms of the Hamiltonian,

$$+2\beta\mathbf{H}'\cdot\mathbf{s}+\mathbf{I}\cdot\mathfrak{A}_1\mathbf{s}, \quad (14)$$

induce transitions between these four states.

In principle, even if the tensor $\mathfrak{A}_0$ is a multiple of the unity matrix, the fluctuating part $\mathfrak{A}_1$ produced by lattice vibrations need not be so. For simplicity we shall make the same assumption for $\mathfrak{A}_1$. The second term of (14) can then be written $A_1(\mathbf{I}\cdot\mathbf{s})$. [More general assumptions about $\mathfrak{A}_1$ do not lead to important changes as will be shown later]. The term $2\beta\mathbf{H}'\cdot\mathbf{s}$ induces strong transitions $|a\rangle\leftrightarrow|a'\rangle$ and $|b\rangle\leftrightarrow|b'\rangle$ through the $x-y$ components of $\mathbf{H}'$.

These are the transitions of the electronic relaxation. H_x' and H_y' also induce the weak transitions (of order q^2) $|a'\rangle\leftrightarrow|b'\rangle$ and $|a\rangle\leftrightarrow|b\rangle$. Finally H_z' induces weak transitions between $|b'\rangle$ and $|a\rangle$.

The term $A_1(\mathbf{s}\cdot\mathbf{I})$ also induces transitions between $|b'\rangle$ and $|a\rangle$. Table I gives the matrix elements between the different states.

We assume that the fluctuations of H_x', H_y', H_z',

TABLE I. Matrix elements of the perturbing Hamiltonian between the different eigenstates of the system.

	$\|a\rangle$	$\|a'\rangle$	$\|b\rangle$	$\|b'\rangle$
$\langle a\|$		$p(H_x'+iH_y')/2$	$q(H_x'-iH_y')/2$	$-pqH_z'+A_1/2$
$\langle a'\|$	$p(H_x'-iH_y')/2$			$q(H_x'-iH_y')/2$
$\langle b\|$	$q(H_x'+iH_y')/2$			$p(H_x'+iH_y')/2$
$\langle b'\|$	$-pqH_z'+A_1/2$	$q(H_x'+iH_y')/2$	$p(H_x'-iH_y')/2$	

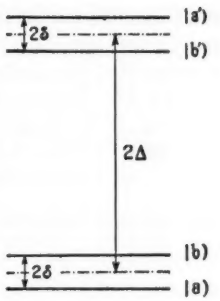

FIG. 3. Energy states and levels of the system electron plus nucleus belonging to the same atom.

and A_1 are incoherent so that in the squares of the matrix elements all cross products may be neglected. Let J_x, J_y, J_z, J_1 be the spectral densities of $H_x'^2$, $H_y'^2$, $H_z'^2$, A_1. The probabilities of the strong electronic transitions $|a\rangle\leftrightarrow|a'\rangle$ and $|b\rangle\leftrightarrow|b'\rangle$ are respectively proportional to $J_x(2\Delta+2\delta)+J_y(2\Delta+2\delta)$ and $J_x(2\Delta-2\delta)+J_y(2\Delta-2\delta)$. Since $\Delta\gg\delta$, it is reasonable (although not essential) to assume these two probabilities equal and call them W.

The weak transitions $|a\rangle\leftrightarrow|b\rangle$ and $|a'\rangle\leftrightarrow|b'\rangle$ will have transition probabilities which we will call $\lambda_1 W$. λ_1 is a small number of the order:

$$\lambda_1\sim q^2[J_x(2\delta)+J_y(2\delta)]/[J_x(2\Delta)+J_y(2\Delta)].$$

The partial probability of the transition $|a\rangle\leftrightarrow|b'\rangle$ due to H_z' can be written as $\lambda_2 W$, where

$$\lambda_2'\cong 4q^2 J_z(2\Delta)/[J_x(2\delta)+J_y(2\delta)].$$

If we assume that the spectrum of H' is "white" and isotropic, $\lambda_2'=2\lambda_1$. Finally the probability of the transition $|a\rangle\leftrightarrow|b'\rangle$ induced by A_1 will be represented by $\lambda_2'' W$. We assume $\lambda_2''\ll 1$ which is a consequence of the hypothesis that electronic relaxation times are much shorter than the nuclear times.

We introduce the ratio $\xi=(\lambda_2'+\lambda_2'')/\lambda_1$. If the nuclear relaxation is of the second type $\lambda_2''=0$, $\xi=\lambda_2'/\lambda_1$ and for a "white" isotropic spectrum $\xi\cong 2$. If on the other hand the nuclear relaxation is of the first type $\xi\sim\infty$. We can now write in the usual way the rates of change of the populations of the different levels:

$$\begin{aligned}
db'/dt=&-W\exp(\Delta-\delta)b'+Wb\exp(-\Delta+\delta)\\
&-\lambda_1 W\exp(-\delta)b'+\lambda_1 W\exp(\delta)a'\\
&-(\lambda_2'+\lambda_2'')W\exp(\Delta)b'\\
&+(\lambda_2'+\lambda_2'')\exp(-\Delta)a-V_b(b'-b);\\
db/dt=&W\exp(\Delta-\delta)b'-Wb\exp(-\Delta+\delta)\\
&-\lambda_1 W\exp(\delta)b+\lambda_1 W\exp(-\delta)a\\
&-V_b(b-b'); \quad (15)\\
da/dt=&-W\exp(-\Delta-\delta)a+W\exp(\Delta+\delta)a'\\
&-\lambda_1 W\exp(-\delta)a+\lambda_1 W\exp(\delta)b\\
&-(\lambda_2'+\lambda_2'')W\exp(-\Delta)a\\
&+(\lambda_2'+\lambda_2'')W\exp(\Delta)b'-V_a(a-a');\\
da'/dt=&W\exp(-\Delta-\delta)a-W\exp(\Delta+\delta)a'\\
&-\lambda_1 W\exp(\delta)a'+\lambda_1 W\exp(-\delta)b'-V_a(a'-a),
\end{aligned}$$

where V_b and V_a are the probabilities for the transitions $|b\rangle\leftrightarrow|b'\rangle$ and $|a\rangle\leftrightarrow|a'\rangle$ induced by the rf field. *Let us first assume* that we saturate both resonances simultaneously: $V_a\to\infty$, $V_b\to\infty$. We must in the system (15) make $a=a'$, $b=b'$. We get for steady state the following relation between a and b which are now the populations P_+ and P_- with nuclear spin up or down:

$$\begin{aligned}&-2\lambda_1 a\cosh(\delta)+2\lambda_1 b\cosh(\delta)-(\lambda_2'+\lambda_2'')\exp(-\Delta)a\\&\qquad+(\lambda_2'+\lambda_2'')\exp(\Delta)b=0,\\&P_+/P_-=a/b=[2\cosh(\delta)+\xi\exp(\Delta)]/\\&\qquad[2\cosh(\delta)+\xi\exp(-\Delta)].\end{aligned}\tag{16}$$

At high temperatures, a linear expansion of the exponentials gives

$$P_+/P_-\simeq 1+2\xi\Delta/(2+\xi).\tag{17}$$

If the relaxation is of the second type and the spectrum of H' isotropic and "white,"

$$P_+/P_-\cong 1+\Delta.$$

If the relaxation is mainly of the first type, ξ is very large and $P_+/P_-\sim 1+2\Delta$ which is the same as the Overhauser effect in metals. Equations (16) and (17) describe the intermediate situations.

If we saturate only one resonance, say $|a\rangle\leftrightarrow|a'\rangle$, we must make in (15) $V_a=\infty$, $V_b=0$, $a=a'$. Solving (15) for the ratios b/a and b'/a, one finds:

$$\begin{aligned}&b/a=\exp(\Delta-\delta)[2\cosh(\delta)+\xi\exp(-\Delta)]/\\&\qquad[2\cosh(\Delta)+\xi\exp(\delta)],\\&b'/a'=\exp(-\Delta+\delta)[2\cosh(\delta)+\xi\exp(-\Delta)]/\\&\qquad[2\cosh(\Delta)+\xi\exp(\delta)].\end{aligned}\tag{18}$$

The ratio $b/b'=\exp(2\Delta-2\delta)$ is the same as in the absence of saturation.

$$\begin{aligned}&P_+/P_-\cong 2a/(b+b')=[2\cosh\Delta+\xi\exp(\delta)]\\&\quad\times\{[2\cosh\Delta+\xi\exp(-\Delta)]\cosh(\Delta-\delta)\}^{-1},\end{aligned}\tag{19}$$

which by linear expansion gives

$$P_+/P_-\cong 1+\xi(\Delta+\delta)/(\xi+2)\cong 1+\xi\Delta/(\xi+2).\tag{20}$$

The polarization is half of what obtains by saturating both resonances.

The saturation of the $|b\rangle\leftrightarrow|b'\rangle$ resonance gives similar results:

$$\begin{aligned}&a/a'=\exp(2\Delta+2\delta),\\&P_+/P_-=\cosh(\Delta+\delta)[2\cosh(\delta)+\xi\exp(\Delta)]/\\&\qquad[2\cosh(\Delta)+\xi\exp(\delta)],\end{aligned}\tag{21}$$

giving by linear expansion:

$$P_+/P_-\simeq 1+\xi(\Delta-\delta)/(\xi+2)\cong 1+\xi\Delta/(\xi+2).\tag{22}$$

It should be mentioned that in solving Eq. (15) to obtain (18) or (21), terms of order λ^2 have been neglected.

The results (17), (20), and (22) can be interpreted by using Kittel's[11] considerations on energy balance between the lattice and the spin system.

It appears from these results that the Overhauser effect offers no explanation for Honig's[12] experiment on arsenic-doped silicon where a 100 percent nuclear polarization was claimed.

His experiment was performed in a field of 3000 gauss at 4°K. At this temperature, $2\Delta\sim 1/10$ and a linear expansion of the exponentials is permissible. The fact that As has spin $\frac{3}{2}$ rather than $\frac{1}{2}$ does not appear to be of help in removing the discrepancy.

GENERALIZATION

The three cases, which have been discussed separately in some detail, can be given an unified treatment.

We consider the system of an electron and a nucleus of spin $\frac{1}{2}$, interacting with each other, placed in a "strong" magnetic field H_0 and embedded in a "lattice" in thermal equilibrium.

The meaning of a "strong" field is that the electronic Zeeman Hamiltonian $2\beta Hs_z$ is much larger than the interaction between the electronic and nuclear spin so that s_z is an approximately good quantum number.

It does not necessarily imply that I_z is also a good quantum number. The latter will occur if the interaction between the electronic and the nuclear spin is much smaller than the *nuclear* Zeeman Hamiltonian $\gamma_n\hbar H_0 I_z$, a reasonable assumption when the electron and the nucleus do not belong to the same atom as in cases (1) and (2).

When the nucleus and the electron do belong to the same atom, I_z will only be a good quantum number if the tensor $\mathfrak{A}_0$ defined in Eq. (3) is isotropic or if, $\mathfrak{A}_0$ being anisotropic, the field H_0 is applied along one of its principal axes.

No restriction need be placed upon the fluctuating tensor $\mathfrak{A}_1$.

We shall restrict ourselves to the case where I_z is approximately a good quantum number.

Thus our system has four eigenstates $|a'\rangle$, $|a\rangle$, $|b'\rangle$, $|b\rangle$ described with a good approximation as

$$|+,+\rangle,\ |-,+\rangle,\ |+,-\rangle,\ |-,-\rangle.$$

The energy separations E_a-E_b and $E_{a'}-E_{b'}$ are much smaller than the electronic splittings $E_{a'}-E_a\simeq E_{b'}-E_b\simeq 2\Delta=2\beta H_0$, and may be neglected in a study of the Overhauser effect.

The coupling with the lattice induces relaxation transitions between these states.

The transitions $|a\rangle\leftrightarrow|a'\rangle$ and $|b\rangle\leftrightarrow|b'\rangle$ are strong electronic transitions and their probabilities can be written

$$\begin{aligned}&W_{aa'}\cong W_{bb'}=W\exp(-\Delta)\cong W(1-\Delta),\\&W_{a'a}\cong W_{b'b}\cong W(1+\Delta).\end{aligned}\tag{23}$$

As for the other transitions, it is easy to see that

[12] A. Honig, Phys. Rev. 96, 234 (1954).

without loss of generality their probabilities can be described by the following formulas, where λ_1, λ_2, λ_3 are small dimensionless quantities:

$$\begin{aligned} &W_{a'b'}\cong W_{b'a'}\cong W_{ab}\cong W_{ba}=\lambda_1 W,\\ &W_{b'a}\simeq\lambda_2 W(1+\Delta),\quad W_{ab'}\cong\lambda_2 W(1-\Delta),\\ &W_{a'b}\simeq\lambda_3 W(1+\Delta),\quad W_{ba'}\cong\lambda_3 W(1-\Delta). \end{aligned} \tag{24}$$

The equations for the rates of change of the populations a' and a are

$$\begin{aligned} (1/W)(da'/dt)=&-a'(1+\Delta)+a(1-\Delta)-\lambda_1(a'-b')\\ &-\lambda_3 a'(1+\Delta)+\lambda_3 b(1-\Delta)\\ &-(V/W)(a'-a),\\ (1/W)(da/dt)=&-a(1-\Delta)+a'(1+\Delta)-\lambda_1(a-b)\\ &-\lambda_2 a(1-\Delta)+\lambda_2 b'(1+\Delta)\\ &-(V/W)(a-a'). \end{aligned} \tag{25}$$

There are two analogous equations for b and b'. V is the transition probability due to the rf field. We assume now that the electronic transitions $|a\rangle\leftrightarrow|a'\rangle$ and $|b\rangle\leftrightarrow|b'\rangle$ are saturated by an applied rf field. Whether this requires a single frequency as in cases (1) and (2) or 2 different frequencies as in case (3) is immaterial.

To describe saturation under steady-state conditions we make $a=a'$, $b=b'$, and $da/dt=da'/dt=0$ in Eq. (25) and obtain for the nuclear polarization:

$$P_+/P_-\cong 1-2\Delta(\lambda_3-\lambda_2)/[2\lambda_1+\lambda_2+\lambda_3]. \tag{26}$$

The results of the three former cases are recapitulated in this formula:

Case (1): λ_1, λ_2, and λ_3 are proportional respectively to the quantities c, b, e of formula (5), i.e., to 3, 2, 12. We find

$$P_+/P_-=1-2\Delta(12-2)/(6+2+12)=1-\Delta, \tag{27}$$

in agreement with (6).

Case (2): $\lambda_3=\lambda_2$. There is here no Overhauser effect.

Case (3): $\lambda_3=0$, $\lambda_2/\lambda_1=\xi$. We obtain

$$P_+/P_-=1+2\Delta\xi/(2+\xi),$$

in agreement with (17).

OVERHAUSER EFFECT IN ZERO MAGNETIC FIELD

Kittel[11] remarks that a zero-field splitting, such as a Stark splitting in a paramagnetic ion with total electronic spin $S=1$ or a large quadrupole splitting for a nucleus of spin $I'=1$ (different from the nucleus whose nuclear resonance is observed), could play the role of the electronic Zeeman splitting in the Overhauser effect. This is true only if the two degenerate levels $S_z=\pm1$ or $I_z'=\pm1$ are separated by a small magnetic field so that it becomes possible to saturate one of the transitions, say $0\leftrightarrow+1$, without saturating the other.

Otherwise, no polarization effect can possibly occur, since there is no privileged direction for the electronic spins, along which the nuclei could be polarized. (This does not preclude nuclear alignment, as opposed to polarization, for nuclear spins larger than $\frac{1}{2}$.)

On the other hand, if the levels $S_z=\pm1$ are separated and only one of the two transitions is saturated, an Overhauser effect may occur, its magnitude depending as in the previous case on the kind of tensor coupling between the spins and on the details of the mechanism of relaxation.

CONCLUSION

This review of the Overhauser effect in paramagnetic substances is by no means complete since many more situations could arise. The purpose of this study was to show, by considering some simple but physically significant cases, that even when the relaxation of the nuclear spins is entirely determined by their coupling to the electronic spins, the maximum polarization to be expected from a complete saturation of the electron resonance depends very much on the detailed features of this coupling and sometimes on the details of the mechanism of relaxation of the electrons themselves. Useful information could thus be obtained from the study of the Overhauser effect in different media.

This work was performed during a stay in Geneva with the CERN theoretical group. It is great pleasure to acknowledge my indebtness to Professor F. Bloch, Director of CERN, for many illuminating discussions and suggestions.

Overhauser Nuclear Polarization Effect and Minimum Entropy Production

MARTIN J. KLEIN*
Department of Physics, Case Institute of Technology, Cleveland, Ohio
(Received February 16, 1955)

This paper gives a simple set of kinetic equations which describe the Overhauser method of producing nuclear polarization by saturating the electronic spin resonance. It is shown that thermodynamically the process consists of absorption of microwave energy and its conversion into heat. In the steady state this process satisfies the principle of minimum entropy production.

I. INTRODUCTION

OVERHAUSER has recently suggested a new method for polarizing nuclei in metals.[1] Overhauser's method requires that the principal mechanism for loss of energy by the nuclear spins be through their coupling to the electronic spins. When this condition is met and when the electronic spin resonance for the conduction electrons is saturated, the population distribution of the nuclear spins among their magnetic levels depends on the magnitude of the electronic magnetic moment rather than on the nuclear magnetic moment. It should therefore be possible to obtain substantial degrees of nuclear polarization under experimentally feasible conditions of temperature and magnetic field strength.[2]

Korringa has shown that Overhauser's method will also work in paramagnetic salts under appropriate circumstances.[3] Kittel has given a simple and general discussion of the Overhauser effect in terms of the general principles of statistical mechanics.[4]

It is the purpose of the present paper to look at the Overhauser effect from still another point of view. When conditions are arranged for producing nuclear polarization, the crystal absorbs microwave energy from an external source and converts this into thermal energy (of conduction electrons or lattice vibrations) in such a way that the population distribution is constant in time. In other words, an irreversible process is occurring and the magnetic system in which it occurs is in a steady state. Under these conditions the behavior of the system should be that required by the principle of minimum entropy production. The discussion which follows is therefore aimed at an added understanding of the Overhauser process from the viewpoint provided by the principle of minimum entropy production.

Before beginning the discussion it seems appropriate to restate the principle. It states that the steady state of a system in which an irreversible process is taking place is that state in which the rate of entropy production has the minimum value consistent with the external constraints which prevent the system from reaching equilibrium. When no such constraints exist the steady state is the equilibrium state in which the rate of entropy production has its absolute minimum, zero. For fuller treatment, the reader is referred to the thermodynamic discussions of the principle by Prigogine[5] and de Groot.[6] A discussion from the viewpoint of statistical mechanics has been given by the author and Meijer, and the present paper is closely related to that discussion.[7]

We must mention that the principle of minimum entropy production is not universally valid. Thermodynamically one can say that it is valid only when the Onsager relations are valid. This essentially requires small deviations from equilibrium. In Sec. III below we shall show the explicit conditions under which the Overhauser process satisfies the principle of minimum entropy production.

II. EQUATIONS FOR THE OVERHAUSER EFFECT

This section is devoted to the formulation of the basic equations for the Overhauser effect. We consider as simple an example as possible in order to emphasize the essential features of the situation.

We consider a nonmetallic crystal containing N nuclear spins, each of magnetic moment $\boldsymbol{\mu}_n$, and N electronic spins, each of magnetic moment $\boldsymbol{\mu}_e$. In an external magnetic field H, the nuclear Zeeman levels are $\pm\mu_n H$ (assuming spin $\hbar/2$). These levels will be denoted by ϵ_1, ϵ_2. The corresponding electronic Zeeman levels $\pm\mu_e H$ will be denoted by ϵ_a, ϵ_b. Let p_1 and p_2 be the probabilities of finding a nucleus in levels ϵ_1 and ϵ_2, and let p_a and p_b be the corresponding probabilities for the electronic levels. The p's are restricted by the two conditions:

$$p_1+p_2=1, \tag{1}$$

$$p_a+p_b=1. \tag{2}$$

We are interested in transitions between these states. It is essential to assume that the nuclei make transitions due only to the interaction with the electron spins, an interaction proportional to $\boldsymbol{\mu}_n\cdot\boldsymbol{\mu}_e$. This interaction will connect only the pairs of states $(1,b)$ and $(2,a)$ since

* This research was supported by a grant from the National Science Foundation.
[1] A. W. Overhauser, Phys. Rev. **92**, 411 (1953).
[2] T. R. Carver and C. P. Slichter, Phys. Rev. **92**, 212 (1953).
[3] J. Korringa, Phys. Rev. **94**, 1388 (1954).
[4] C. Kittel, Phys. Rev. **95**, 589 (1954).
[5] I. Prigogine, *Etude Thermodynamique des Phénomènes irréversibles* (Editions Desoer, Liège, 1947), Chap. V.
[6] S. R. de Groot, *Thermodynamics of Irreversible Processes* (Interscience Publishers, Inc., New York, 1951), Chap. X.
[7] M. J. Klein and P. H. E. Meijer, Phys. Rev. **96**, 250 (1954).

there are no other nonzero matrix elements. The electron spins can make transitions because of this interaction, but we assume that electronic transitions occur primarily because of electron spin-lattice interactions.[8] In the Overhauser effect the system is irradiated by a microwave field tuned to the electron spin resonance ($\hbar\omega=\epsilon_b-\epsilon_a=2\mu_e H$), and this field is therefore another cause of transitions of the electron spins.

Summing up the preceding discussion, we can write the following equations:

$$dp_1/dt=a_{2a,1b}p_2p_a-a_{1b,2a}p_1p_b, \tag{3}$$

$$dp_a/dt=(a_{ba}+c)p_b-(a_{ab}+c)p_a +a_{1b,2a}p_1p_b-a_{2a,1b}p_2p_a. \tag{4}$$

We need not write equations for dp_2/dt and dp_b/dt since they are the negatives of dp_1/dt and dp_a/dt respectively as required by Eqs. (1) and (2). The terms in Eqs. (3) and (4) can be identified as follows. The coefficient $a_{2a,1b}$ is the probability per unit time of a nuclear transition $2\rightarrow1$ coupled with an electronic transition $a\rightarrow b$, due to the $\mathbf{y}_n\cdot\mathbf{y}_e$ interaction. The coefficient a_{ba} is the probability per unit time of an electronic transition $b\rightarrow a$ due to the interaction of the electron with the heat bath of lattice vibrations. Finally, c is the electronic transition probability per unit time for transitions induced by the external microwaves. In each term the change per unit time is proportional to the transition probability and to the probability of occupation of the initial state.

The transition probabilities for the inverse transitions are determined by the following relations:

$$a_{ba}e^{-\epsilon_b/kT}=a_{ab}e^{-\epsilon_a/kT}, \tag{5}$$

$$a_{2a,1b}e^{-(\epsilon_2+\epsilon_a)/kT}=a_{1b,2a}e^{-(\epsilon_1+\epsilon_b)/kT}. \tag{6}$$

These relations follow from the fact that energy differences between initial and final states are made up in each case by energy exchanged with the heat bath at temperature T.[9]

The steady-state solutions of Eqs. (3) and (4), i.e., the solutions with $dp_1/dt=dp_a/dt=0$, can be written down. We obtain

$$p_b/p_a=(a_{ba}e^{-(\epsilon_b-\epsilon_a)/kT}+c)/(a_{ba}+c), \tag{7}$$

$$p_2/p_1=(p_b/p_a)e^{-(\epsilon_2-\epsilon_1)/kT}e^{-(\epsilon_b-\epsilon_a)/kT}. \tag{8}$$

The Overhauser effect follows immediately from these solutions. In the absence of the external microwave radiation, $c=0$, the system comes to equilibrium and $p_b/p_a=e^{-(\epsilon_b-\epsilon_a)/kT}$, $p_2/p_1=e^{-(\epsilon_2-\epsilon_1)/kT}$. The nuclear distribution is determined by the nuclear Boltzmann factor, i.e., the exponential of the ratio of the nuclear energy difference ($2\mu_n H$) to kT. In the case of complete saturation, $c\gg a_{ba}$, the occupations of the electronic Zeeman states approach equality ($p_b/p_a\rightarrow1$), and the nuclear population ratio is given by

$$p_2/p_1=e^{(\epsilon_b-\epsilon_a)/kT}e^{-(\epsilon_2-\epsilon_1)/kT}.$$

We see that the nuclear distribution is now determined primarily by the *electronic* Boltzmann factor which involves μ_e rather than μ_n (a factor of about 10^3). This is the essence of the Overhauser nuclear polarization method.

III. MINIMUM ENTROPY PRODUCTION

This section is devoted to the calculation of the rate of entropy production in our system and to the proof that the principle of minimum entropy production applies to this process. We may point out at the beginning that the "constraint," which prevents the system of nuclear and electronic spins from reaching thermal equilibrium at the temperature T of the heat bath, consists of the coupling to the "reservoir" of microwave power which continuously feeds energy into the system. When this microwave power is removed, $c=0$, the steady state is the equilibrium state.

The total rate of entropy production, dS/dt, is the sum of the rates of charge of the nuclear spin entropy, dS_n/dt, the electronic spin entropy, dS_e/dt, and the entropy of the heat bath dS_B/dt. Since the radiation is essentially monochromatic it does not contribute to the entropy. Consequently we can write the equation

$$dS/dt=dS_n/dt+dS_e/dt+dS_B/dt. \tag{9}$$

The first two terms in Eq. (9) can be evaluated in a simple way from the following equations for the nuclear and electronic spin entropies,

$$S_n=-Nk(p_1\ln p_1+p_2\ln p_2), \tag{10}$$

$$S_e=-Nk(p_a\ln p_a+p_b\ln p_b). \tag{11}$$

The time derivatives are obtained by using Eqs. (3) and (4).

The time rate of change of the entropy of the heat bath can be obtained by the following argument. Since all energy which enters or leaves the bath does so at temperature T, the rate of change of the bath's entropy is $(1/T)$ times the rate of change of the energy of the nuclear and electronic systems, omitting the energy exchanged by the electrons with the microwave radiation. Consequently we can write the equation

$$dS_B/dt=-(1/T)(dU_n/dt+d'U_e/dt), \tag{12}$$

where the prime on the derivative $d'U_e/dt$ means that the terms just mentioned must be omitted. The internal energies U_n and U_e are given by the equations

$$U_n=N(p_1\epsilon_1+p_2\epsilon_2), \tag{13}$$

$$U_e=N(p_a\epsilon_a+p_b\epsilon_b), \tag{14}$$

and their time derivatives are calculated with the help of Eqs. (3) and (4) omitting the terms proportional to c in Eq. (4).

[8] A. W. Overhauser, Phys. Rev. 89, 689 (1953).
[9] See the appendix of reference 7 for a detailed discussion.

Carrying out all of the operations previously indicated, we obtain the following expression for the total rate of entropy production:

$$\frac{dS}{dt}=-Nk\left[\alpha\left(p_2p_a-\frac{\rho}{\sigma}p_1p_b\right)\ln\left(\frac{p_1e^{\epsilon_1/kT}p_be^{\epsilon_b/kT}}{p_2e^{\epsilon_2/kT}p_ae^{\epsilon_a/kT}}\right)+\gamma(p_b-\sigma p_a)\ln\frac{p_ae^{\epsilon_a/kT}}{p_be^{\epsilon_b/kT}}+c(p_b-p_a)\ln\frac{p_a}{p_b}\right]. \quad (15)$$

The following abbreviations have been used: $\alpha=a_{2a,1b}$, $\gamma=a_{ba}$, $\rho=e^{-(\epsilon_2-\epsilon_1)/kT}$, $\sigma=e^{-(\epsilon_b-\epsilon_a)/kT}$.

In order to verify that the principle of minimum entropy production applies to our problem, we must write down the conditions for a minimum value of dS/dt. The derivatives of dS/dt with respect to p_1, p_2, p_a, and p_b are calculated from Eq. (15). Since the four variables are not all independent, we must introduce two Lagrange multipliers, μ and μ', to allow for the constraints expressed in Eqs. (1) and (2). Carrying out the indicated operations, we obtain the following four equations for dS/dt to be stationary.

$$\mu=Nk\left[\alpha(p_2p_a/p_1-\rho p_b/\sigma)+\alpha(\rho p_b/\sigma)\ln\frac{p_2e^{\epsilon_2/kT}p_ae^{\epsilon_a/kT}}{p_1e^{\epsilon_1/kT}p_be^{\epsilon_b/kT}}\right], \quad (16)$$

$$\mu=Nk\left[\alpha(\rho p_1p_b/\sigma p_2-p_a)+\alpha p_a\ln\frac{p_1e^{\epsilon_1/kT}p_be^{\epsilon_b/kT}}{p_2e^{\epsilon_2/kT}p_ae^{\epsilon_a/kT}}\right], \quad (17)$$

$$\mu'=Nk\left[\alpha p_2\ln\frac{p_1e^{\epsilon_1/kT}p_be^{\epsilon_b/kT}}{p_2e^{\epsilon_2/kT}p_ae^{\epsilon_a/kT}}+\alpha\left(\frac{\rho}{\sigma}\frac{p_1p_b}{p_a}-p_2\right)+\gamma\sigma\ln\frac{p_be^{\epsilon_b/kT}}{p_ae^{\epsilon_a/kT}}+\gamma\left(\frac{p_b}{p_a}-\sigma\right)+c\left(\frac{p_b}{p_a}-1+\ln\frac{p_b}{p_a}\right)\right], \quad (18)$$

$$\mu'=Nk\left[\frac{\alpha\rho}{\sigma}p_1\ln\frac{p_2e^{\epsilon_2/kT}p_ae^{\epsilon_a/kT}}{p_1e^{\epsilon_1/kT}p_be^{\epsilon_b/kT}}+\alpha\left(\frac{p_2p_a}{p_b}-\frac{\rho}{\sigma}p_1\right)+\gamma\ln\frac{p_ae^{\epsilon_a/kT}}{p_be^{\epsilon_b/kT}}+\gamma\left(\sigma\frac{p_a}{p_b}-1\right)+c\left(\frac{p_a}{p_b}-1+\ln(p_a/p_b)\right)\right]. \quad (19)$$

In order to complete the proof it is necessary to introduce the assumption that both p_b/p_a and $p_b/\sigma p_a$ differ from unity by small quantities, quantities whose square may be neglected. This assumption means that the electronic spin system must be close to being equally distributed between states a and b ($p_b\cong p_a$), and also that the Boltzmann factor $\sigma(=e^{-2\mu_eH/kT})$ must be close to unity. This last remark implies that at low temperatures and in strong fields, where the Overhauser effect is experimentally most likely to be important, the principle of minimum entropy production will not be satisfied. The Overhauser effect will of course exist under those conditions, but the steady state will not be the state of minimum entropy production.

When the assumption discussed in the preceding paragraph is valid it can be shown in a straightforward way that the steady state is the state of minimum entropy production. More precisely, it can be shown that (a) if there is a steady state, then Eqs. (16)–(19) for stationary dS/dt are satisfied with $\mu=\mu'=0$, and (b) if Eqs. (16)–(19) for stationary dS/dt are satisfied, then $\mu=\mu'=0$ and p_1, p_2, p_a, and p_b are constant in time.[10]

The final point to be established is that the stationary value of dS/dt in the steady state is actually a minimum. This results from a calculation of the deviation $\delta(dS/dt)$ from its value in the steady state. If p_i^0 are the steady-state values and δp_i their deviations, then direct algebraic manipulation leads to the result

$$\delta\left(\frac{dS}{dt}\right)=Nk\left\{\frac{\gamma+c}{p_a^0}\left[\left(\frac{p_b^0}{p_a^0}\right)^{\frac{1}{2}}\delta p_a-\left(\frac{p_a^0}{p_b^0}\right)^{\frac{1}{2}}\delta p_b\right]^2+\alpha\left[\frac{(p_2^0p_a^0)^{\frac{1}{2}}}{p_1^0}\delta p_1-\left(\frac{p_a^0}{p_2^0}\right)^{\frac{1}{2}}\delta p_2-\left(\frac{p_2^0}{p_a^0}\right)^{\frac{1}{2}}\delta p_a+\frac{(p_2^0p_a^0)^{\frac{1}{2}}}{p_b^0}\delta p_b\right]^2\right\}, \quad (20)$$

and this sum of squares is positive, implying that dS/dt is indeed a minimum in the steady state.

IV. DISCUSSION

The form of the entropy production in the steady state is of some interest as it lends itself to a direct physical interpretation. In the steady state the first two terms of Eq. (9) vanish and so does the first term in Eq. (12) because all these terms involve derivatives of the p_i. The only remaining contribution to the entropy production in the steady state is $-(1/T)(d'U_e/dt)$. We can therefore write

$$(dS/dt)_{\min}=-(N/T)\{(\gamma p_b-\gamma\sigma p_a)(\epsilon_a-\epsilon_b)\}, \quad (21)$$

and using the fact that $(dp_a/dt)=(dp_b/dt)=0$ this can be reduced with the help of Eq. (4). Our final expression is

$$(dS/dt)_{\min}=\{(\epsilon_b-\epsilon_a)/T\}Nc(p_a-p_b). \quad (22)$$

In other words entropy is produced in the steady state by transforming the quanta absorbed from the microwave radiation into thermal energy at tempera-

[10] The details of the proof are similar to those in reference 7, Sec. IV. See also J. S. Thomsen, Phys. Rev. 91, 1263 (1953), Sec. III; M. J. Klein, Phys. Rev. 97, 1446 (1955).

ture T. The first factor $(\epsilon_b-\epsilon_a)/T$ is the entropy increase for each quantum so transformed, and the second factor $Nc(p_a-p_b)$ is the net number of quanta absorbed per unit time.

In conclusion we may say that the viewpoint of irreversible thermodynamics and the principle of minimum entropy production provide additional insight into the nature of the Overhauser nuclear polarization effect.

ACKNOWLEDGMENTS

The author would like to express his thanks to Professor Jan Korringa of the Ohio State University for two helpful discussions.

PHYSICAL REVIEW VOLUME 98, NUMBER 6 JUNE 15, 1955

Work Function of Cadmium*

PAUL A. ANDERSON
State College of Washington, Pullman, Washington
(Received March 1, 1955)

The contact difference of potential Cd-Ba is measured by the electron beam and Kelvin methods. These measurements agree within the limits of reproducibility of either method alone and yield a work function value of 4.08±0.02 ev for the work function of cadmium films deposited on tantalum. The barium surfaces, formed by redistillation following fractional distillation, show their characteristic constancy and reproducibility to ±0.01 ev. Cadmium retains some gas after exhaustive multiple distillation. Measurements taken immediately after deposition of a Cd film and during its aging show (1) that freshly deposited Cd films are generally contaminated with gas which distills with the metal; (2) that the adsorbed gas is removed progressively by getter clean-up with an attendant rise in work function totalling 0.10 ev in extreme cases, and (3) that the work function thus established is constant and reproducible to 0.03 ev or better. Comparison of these measurements with our earlier work on zinc leads to the conclusion that a cadmium surface in equilibrium with the residual gas of a well-gettered tube contains so little adsorbed gas that its final work function can probably be accepted as characteristic of the clean metal.

THIS report describes further results in a program in which the external work functions of the pure metals are determined by measurement of their contact differences of potential with respect to a reference metal of known work function, barium. Earlier work in this laboratory[1] has shown that the work functions of zinc surfaces prepared by distillation of the outgassed metal in sealed-off, barium gettered tubes are highly reproducible and constant over long periods of time. Objective evidence for the absence of gaseous contamination was obtained by making the time interval between deposition and measurement of the surfaces short with respect to the time required for deposition of a monolayer of adsorbed gas. A series of similar measurements was carried out on cadmium in 1941 but was not reported at that time. A second series of measurements by a Kelvin technique[2] was completed recently. The results of the two series agree well and taken together constitute a reasonably thorough study of this metal. Since the experimental procedures follow closely those previously described,[1,2] only the variations in technique made necessary by the peculiarities of cadmium are emphasized here. The cadmium employed in these measurements was kindly supplied to me by the New Jersey Zinc Company with an analysis showing a total impurity content of less than 0.001 percent.

ELECTRON BEAM MEASUREMENTS

The high vapor pressure of cadmium at and below its melting point precludes satisfactory outgassing by the method of repetitive fusion commonly used in our work. A second troublesome property of cadmium is its extraordinarily low critical condensation temperature on glass; at room temperature surface migration is so pronounced that agglomeration of the condensate into isolated islands generally occurs. To meet these conditions, tubes of the type used in the measurements on zinc were modified as follows. (1) The multiple distilling arrangement shown in Fig. 1 was substituted for the "first and second vaporizers" of the zinc tubes, and (2) the targets on which the films were formed and measured were 10-mil tantalum foil disks; a 60-mil tungsten post and 60-mil tantalum crossbar replaced the glass target mount of the zinc tubes.

Before charging with cadmium and zinc, the tube was subjected to our standardized outgassing schedule.[1] After charging, the baking temperature was limited to 120°C to avoid vaporization of cadmium. While the tube was on the pumps, fusions of the barium and complete distillations of the cadmium were carried out alternately through ten complete cycles. After seal-off the fusions and distillations were continued until the

* This research was supported in whole or in part by the U. S. Air Force under a contract monitored by the Office of Scientific Research, Air Research and Development Command.
[1] P. A. Anderson, Phys. Rev. **57**, 122 (1940).
[2] P. A. Anderson, Phys. Rev. **88**, 655 (1952).

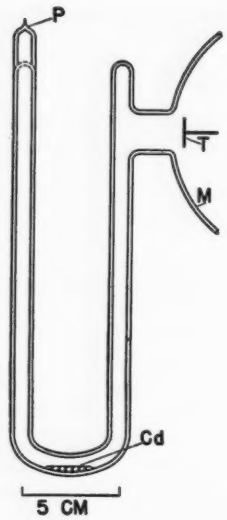

FIG. 1. Outgassing-dispensing tube for cadmium. The metal is distilled repetitively between the outer and inner walls by tubular heaters (not shown) while the condensing surface is cooled by CO_2-acetone. Both inner and outer walls are heated to dispense vapor to target T of measuring tube M. P=loading port for Cd.

electron emission test[3] showed that the evolution of gas during the heating of the metals had been reduced to a low level. A cadmium film was then laid down on one of the targets and its current-potential characteristic determined in the usual manner.[1] A succession of fresh films was then formed and measured to establish the reproducibility of the potential setting for cadmium. This procedure was then repeated for a series of barium films laid down over the cadmium. The entire schedule was then repeated for the second target.

Initial readings on the newly deposited cadmium films were reproducible to ± 0.06 volt, a reproducibility markedly inferior to that obtained for zinc.[1] On aging, the films showed a small and limited, but definite, drift toward higher work function. This drift totalled 0.10 volt in extreme cases and was largest for the films which showed the lowest initial work functions. The potential readings obtained after drifting ceased were reproducible to ± 0.03 v or better and gave a value of 1.55 ± 0.03 for the contact difference of potential Cd-Ba. The work function assigned to cadmium by these measurements is therefore $1.55+2.52=4.07$ ev. The behavior of cadmium on aging is probably due to the fact that when cadmium is distilled the gases contained in it vaporize with it; outgassing is attained only through differentiation between the condensation efficiencies of metal and gas and is never complete. On aging however, the gas which remains on the cadmium surface is removed progressively by the barium getter and the work function finally attained is that of the clean surface. This interpretation is consistent with our findings for zinc[1] which, like cadmium, has a low affinity for the residual gases present in a barium-gettered tube.

[3] P. A. Anderson, Phys. Rev. **75**, 1207 (1949).

KELVIN MEASUREMENTS

The tube employed in the Kelvin measurements on Cd-Ba was similar to those used for Ag-Ba,[2] but had no provision for electron beam measurements. The outgassing procedures followed the plan outlined in the aforementioned, but the preliminary distillations of cadmium were omitted with a view to testing the conclusion, reached in the earlier measurements, that exhaustive outgassing of the cadmium should be unnecessary if gas adsorbed on a cadmium surface during its deposition is subsequently removed by the barium getter. The barium and cadmium films were formed as in the Ag-Ba studies.[2] Eight sets of measurements on different pairs of Cd-Ba surfaces, in which each set included measurements taken immediately after deposition of the films and during their aging, were carried out during a 14-day period. The first set showed the effects of pronounced gas evolution from the first cadmium distillations, and abnormally low contact potentials. All measurements thereafter fell within the limits 1.55 ± 0.03 volts. As the measurements progressed, reproducibility improved and drift decreased. In the last two sets of measurements, which covered deposition-measurement intervals ranging from a few minutes to 24 hours, all readings fell within the limits 1.55–1.57 volts. The value 1.56 ± 0.01 volts is taken as representing the Kelvin measurements. Since sealed-off, barium gettered tubes always show a progressive lowering of residual gas pressure under the conditions obtaining in these experiments, the Kelvin results lend further support to the desorption mechanism discussed above. It now seems clear that zinc, cadmium, and silver belong to a class of metals which, when in equilibrium with the residual gas of a well-gettered tube, contain so little adsorbed gas that the measured work functions can be accepted as characteristic of the clean metals. Excellent reproducibility and constancy in the work function of cadmium can be expected under conditions which are easily obtained in sealed-off tubes.

Our value of 4.08 ± 0.02 ev for the work function of cadmium is very close to Bomke's[4] photoelectrically determined value (4.07 ev) and is in good agreement with the photoelectric measurements of Suhrmann and Pietrzyk[5] (4.10 ev). Other values have been reported by Klein and Lange[6] (4.00 ev), Schulze[7] (3.68 ev) and Lukirsky and Prilezaev[8] (3.75 ev).

[4] H. Bomke, Ann. Physik **10**, 579 (1931).
[5] R. Suhrmann and J. Pietrzyk, Z. Physik **122**, 600 (1944).
[6] O. Klein and E. Lange, Z. Elektrochem. **44**, 542 (1938).
[7] R. Schulze, Z. Physik **92**, 212 (1934).
[8] P. Lukirsky and S. Prilezaev, Z. Physik **49**, 236 (1928).

Solution of the Hartree-Fock-Slater Equations for Silicon Crystal by the Method of Orthogonalized Plane Waves

TRUMAN O. WOODRUFF*
California Institute of Technology, Pasadena, California, and Semiconductor Laboratory, Hughes Aircraft Company, Culver City, California
(Received March 4, 1955)

The orthogonalized plane wave (OPW) method is used to compute estimates of the energy eigenvalues associated with states for which $\mathbf{k}=0$ in the valence and conduction bands of a perfect silicon crystal; these estimates are given in Table I. A simple method for determining an approximate crystal potential is described. The importance of the requirement that exactly the same crystal potential be used to determine the crystal core states as is used in the OPW determination of the higher states is emphasized.

SLATER'S modified Hartree-Fock equations[1] in which the exchange terms have been simplified through the use of the free electron approximation (to be referred to as the Hartree-Fock-Slater equations) have been used to describe the electronic states in a perfect single crystal of silicon. For the core states (those which go into $1s$, $2s$, and $2p$ states of free silicon atoms as the lattice constant is allowed to approach infinity) the wave functions and energy eigenvalues were determined by means of the simplest form of the tight binding approximation. The energy eigenvalues associated with the valence and conduction states of zero wave vector were calculated by the use of Herring's orthogonalized plane wave method.[2]

In atomic units (the unit of energy is 13.6050 ev) the Hartree-Fock-Slater equations for a balanced-spin crystal are

$$[-\nabla^2+V(\mathbf{r})]\psi_i(\mathbf{r})=E_i\psi_i(\mathbf{r}), \tag{1}$$

where

$$V(\mathbf{r})=-2Z\sum_\nu\frac{1}{|\mathbf{r}-\mathbf{R}_\nu|}+2\sum_j\int\frac{\psi_j^*(\mathbf{r}')\psi_j(\mathbf{r}')}{|\mathbf{r}-\mathbf{r}'|}d\mathbf{r}'-6\left\{\frac{3}{8\pi}\sum_j\psi_j^*(\mathbf{r})\psi_j(\mathbf{r})\right\}^{\frac{1}{3}}, \tag{2}$$

$\psi_i(\mathbf{r})$ is the space dependent part of the wave function of the ith electron, the j-summation is over all occupied electron states, and the ν summation is over all lattice points in the crystal, each occupied by a nucleus of charge Z. In the computations for both core and valence and conduction states, $V(\mathbf{r})$ as given in (2) was replaced by

$$V^{(0)}(\mathbf{r})=\sum_\nu V^{(0)}{}_{\text{atomic}}(\mathbf{r}-\mathbf{R}_\nu), \tag{3}$$

with

$$V^{(0)}{}_{\text{atomic}}(\mathbf{r})=-\frac{2Z}{|\mathbf{r}|}+2\sum_{j=1}^{Z}\int\frac{\varphi_j^*(\mathbf{r}')\varphi_j(\mathbf{r}')}{|\mathbf{r}-\mathbf{r}'|}d\mathbf{r}'-6\left\{\frac{3}{8\pi}\sum_{j=1}^{Z}\varphi_j^*(\mathbf{r})\varphi_j(\mathbf{r})\right\}^{\frac{1}{3}}, \tag{4}$$

where $\varphi_j(\mathbf{r})$ is the space dependent part of the wave function of the jth electron in the valence state of the isolated atom. The radial parts of the isolated atom wave functions used in forming $V^{(0)}$ for silicon were obtained from Slater's empirical rules.[3] The approximate crystal core eigenfunctions and eigenvalues of this simple and very rough approximation to the crystal potential were determined; these crystal core eigenfunctions were then used in computing the orthogonality coefficients needed in the OPW calculation of valence and conduction states. The essential point is that exactly the same crystal potential was used in computing both the core and the valence and conduction states; the convergence difficulties encountered by Herman in his very extensive investigation of the germanium energy band structure[4] are probably to be attributed to the fact that his crystal core wave functions are not eigenfunctions of the same potential used in computing the higher states.[5]

For the four lowest-lying valence and conduction states in silicon with zero wave vector the sequences of estimates which have thus far been obtained from the OPW calculations are given in Table I. In this table, E_n was obtained as a root of the appropriate nth order secular equation. The unit of energy is 13.6050 ev. These calculations are being continued to permit a better evaluation of the convergence of the $\Gamma_{25'}$, Γ_{15},

TABLE I. Sequences of estimates of the energies of valence and conduction states in silicon crystal with $\mathbf{k}=0$.

	Γ_1	$\Gamma_{25'}$	Γ_{15}	$\Gamma_{2'}$
E_1[a]	−1.3498	−0.3996	−0.3996	0.0338
E_2	−1.4624	−0.7312	−0.5443	−0.0310
E_3	−1.4629	−0.7663		

[a] The subscript attached to E refers to the order of the secular determinant used in solving for E.

* Present address: Physics Department, University of Illinois, Urbana, Illinois.

[1] J. C. Slater, Phys. Rev. **81**, 385 (1951).
[2] C. Herring, Phys. Rev. **57**, 1169 (1940).
[3] J. C. Slater, Phys. Rev. **36**, 57 (1930); **42**, 33 (1932).
[4] F. Herman, Phys. Rev. **93**, 1214 (1954); Physica **20**, 801 (1954).
[5] This point is also discussed by J. Callaway, Phys. Rev. **97**, 933 (1955). The writer is indebted to Dr. Callaway for a prepublication copy of his paper.

and $\Gamma_{2'}$ solutions. A more detailed description of the work summarized here will be submitted to this journal.

The writer wishes to thank Dr. Harvey Winston of the Hughes Semiconductor Laboratory for helpful discussions of the symmetry properties of crystal wave functions and Dr. Frank Herman of the RCA Laboratories for information about his diamond and germanium calculations prior to their publication. This work was carried out while the writer was a member of the technical staff of the Semiconductor Laboratory of Hughes Aircraft Company and a holder of a Howard Hughes Fellowship.

PHYSICAL REVIEW VOLUME 98, NUMBER 6 JUNE 15, 1955

Fast-Neutron Bombardment of *n*-Type Ge

J. W. CLELAND, J. H. CRAWFORD, JR., AND J. C. PIGG
Oak Ridge National Laboratory, Oak Ridge, Tennessee

(Received January 20, 1955)

The effect of fast-neutron bombardment on the electrical properties of *n*-type Ge has been extensively studied by a variety of experiments. The initial rate of carrier removal, the shape of the bombardment curve, and the temperature dependence of electron concentration in bombarded specimens all indicate the production of two vacant states, one located below the middle of the forbidden energy band and the other located ~0.2 ev below the conduction band. These two vacant states are consistent with predictions of the model of James and Lark-Horovitz. Studies of mobility reveal that the additional scattering associated with bombardment-induced lattice disorder is more complex than charged impurity scattering in that it exhibits a much greater temperature dependence and is markedly dependent on electron concentration. Low-temperature exposure and subsequent warming experiments indicate that appreciable photoconductivity associated with minority-carrier trapping results from fast-neutron bombardment. The important minority-carrier traps appear to anneal during warming below room temperature.

I. INTRODUCTION

THE electrical properties of diamond-lattice semiconductors are extremely sensitive to lattice-disordering effects which result from bombardment with high-energy particles. Lattice defects produced by fast-neutron bombardment introduce localized energy states into the forbidden energy band of Si,[1] Ge,[1–3] and InSb.[4] The predominant effect of bombardment of Ge is the introduction of vacant states which may either trap electrons in *n*-type or behave as acceptors in *p*-type material. In addition, convincing evidence has been obtained for the production of occupied states, which lie too low in the forbidden energy band to act as donors in *n*-type material but may act as shallow hole traps.[3] The results obtained on Ge by other investigators using a variety of fast particles (deuterons,[1,5] α particles,[1,6,7] and fast electrons[8,9]) are in qualitative accord with those obtained with fast neutrons.

James and Lark-Horovitz[10] have proposed a model for the energy levels associated with Frenkel defects, defects which are generally expected to result from bombardment. This model has been used successfully in explaining qualitatively not only the more important features of the behavior of bombarded Ge but in addition the behavior of bombarded Si, which is quite different from that of Ge.[1] With suitable modification, this model has also been applied with reasonable success to bombarded InSb.[4] Although the results of Ge bombarded in the room temperature range are in qualitative agreement with the model, such is not the case for irradiations carried out at temperatures below 200°K. Quite complex annealing behavior has been observed on warming the specimens after irradiation at low temperatures with both fast neutrons[11] and deuterons.[12]

In order to investigate the nature of fast-neutron bombardment effects in more detail, a wide variety of experiments have been carried out and the range of consideration of important parameters has been extended. Specimens of both *n*- and *p*-type material with a wide range of carrier concentration have been irradiated in the ORNL graphite reactor for varying

[1] For a review of the early work on Si and Ge see K. Lark-Horovitz, in *Semi-Conducting Materials*, edited by H. K. Henisch (Academic Press, Inc., New York, 1951), p. 47 ff.
[2] Cleland, Crawford, Lark-Horovitz, Pigg, and Young, Phys. Rev. **83**, 312 (1951).
[3] Cleland, Crawford, Lark-Horovitz, Pigg, and Young, Phys. Rev. **84**, 861 (1951).
[4] J. W. Cleland and J. H. Crawford, Jr., Phys. Rev. **93**, 894 (1954); **95**, 1177 (1954).
[5] J. H. Forster, thesis, Purdue University, 1953 (unpublished).
[6] W. H. Brattain and G. L. Pearson, Phys. Rev. **80**, 846 (1950).
[7] K. Lark-Horovitz, *The Present State of Physics* (American Association for the Advancement of Science, Washington, D. C., 1954), p. 57 ff.
[8] E. E. Klontz and K. Lark-Horovitz, Phys. Rev. **86**, 643 (1952); see also E. E. Klontz, thesis, Purdue University, 1952 (unpublished).
[9] Brown, Fletcher, and Wright, Phys. Rev. **92**, 591 (1953).
[10] H. M. James and K. Lark-Horovitz, Z. physik. Chem. **198**, 107 (1951).
[11] Crawford, Cleland, Holmes, and Pigg, Phys. Rev. **91**, 243 (1953).
[12] Forster, Fan, and Lark-Horovitz, Phys. Rev. **91**, 229 (1953).

periods of time at both pile ambient and low temperature (~35°C to as low as −160°C). Hall coefficient and conductivity have been measured as a function of temperature after successive periods of exposure for a number of specimens irradiated in the room-temperature range, and conductivity measurements during various heating cycles have been obtained during and after low-temperature irraidation. These data permit an extensive test of the James, Lark-Horovitz model of bombardment-produced energy levels and, in addition, they yield much other information of interest.

Because of the extensiveness and complexity of the data taken as a whole, it has been decided to present here only the results obtained on n-type Ge, reserving all information pertaining to p-type Ge for a subsequent publication. The purpose of both papers will be to correlate, insofar as possible, experimental results with existing ideas concerning the nature of bombardment lattice defects and to point out additional problems which as yet do not fit into the existing theoretical framework. The results of ambient bombardment will be analyzed quantitatively on the basis of the theory of James and Lark-Horovitz. In the present paper, since n-type Ge alone is considered, only the positions of those defect-states which lie above the middle of the forbidden energy band can be determined. The effect of bombardment on mobility is next considered and, finally, the results of low-temperature irradiation of n-type Ge will be discussed.

II. THE MODEL OF JAMES AND LARK-HOROVITZ

Earlier ideas concerning energy levels associated with lattice defects[1] were based on single ionization of lattice vacancies and interstitial atoms. Hence a vacancy was expected to behave as an acceptor or an electron trap whereas an interstitial atom was expected to behave as a donor or a hole trap. However, examination of the conductivity σ *vs* bombardment time curves for n-type Ge revealed that extrapolation of the initial linear slope to zero conductivity gave a value of exposure which is only about one-half of that required to produce the conductivity minimum or intrinsic behavior. This behavior would seem to indicate the presence of two electron trapping centers, of which one is rather shallow. It was on the basis of this observation that James and Lark-Horovitz considered the possibility of multiple ionization. They find that, in a lattice with as high a dielectric constant as that of Ge, one might indeed expect states corresponding to the first and second ionization energies of the interstitial atom to lie in the forbidden energy band. Similarly, the energy required to put as many as two electrons into a vacant site is expected to lie in the forbidden gap. When both the interstitial and vacancy are present simultaneously, the electrons arising from the interstitial atoms are redistributed among all of the localized states to positions of lowest energy. Hence, for Ge they find the following levels of localized states: (1) a shallow vacant level corresponding to the first ionization of the interstitial atom which is estimated to lie ~0.05 ev below the bottom of the conduction band; (2) a deep vacant level below the middle of the conduction band which arises from either the second ionization of the interstitial or the second ionization of the vacancy; and (3) the two remaining levels, which are occupied and which lie near the top of the valence band. Because of the complex nature of the wave functions in the diamond lattice and because of the large perturbing effect of the defects, it is impossible to locate the levels any more precisely in the band scheme from theoretical considerations alone. It is evident, however, that, since their relative positions are sensitive to both dielectric constant and gap width, the situation might be expected to change markedly from one diamond lattice semiconductor to another.

Since in the present paper we are concerned with bombarded n-type Ge, only the vacant levels are of interest: One shallow level of electron traps which is only partly effective in removing electrons and a deep level which is completely effective. We assume that all chemical impurities are completely ionized (a good assumption for temperatures above 77°K for the usual doping agents) and that the intrinsic process is negligible over the whole range of consideration. The electron concentration is given by

$$n=n^0-N_s^--N, \tag{1}$$

where n^0 is the initial electron concentration, N_s^- is the concentration of occupied shallow traps, and N is the concentration of deep traps (which is identically equal to the Frenkel defect concentration). From the law of mass action it can be shown that N_s^- is given by

$$N_s^-=nNK_s/(1+nK_s), \tag{2}$$

where the equilibrium constant for the shallow trapping process (trap+electron$\rightleftharpoons$occupied trap) is given by

$$K_s=\frac{h^2e^{\epsilon_s/kT}}{\gamma(2\pi m_e kT)^{\frac{3}{2}}}, \tag{3}$$

in which ϵ_s is the depth of the shallow traps, m_e is the appropriate effective mass, and γ is the ratio of the statistical weights of the reactants to that of the product.[13] For the case in question the shallow trap is identified with a singly ionized interstitial atom. Hence $\gamma=4$. Substitution of Eq. (2) in Eq. (1) yields a quadratic in n, the solution of which is

$$n=\frac{(n^0-2N)K_s-1+\{[(n^0-2N)K_s-1]^2+4K_s(n^0-N)\}^{\frac{1}{2}}}{2K_s}. \tag{4}$$

Equation (4) may be used to test the two-level model.

[13] J. H. Crawford, Jr., and D. K. Holmes, Proc. Phys. Soc. London, **A67**, 294 (1954).

TABLE I. Values of K_s and ϵ_s obtained from initial rates of change of n during bombardment calculated from the simple two-acceptor-level model.

Sample	$(dn/dN)_{N=0}$	n^0 cm^{-3}	Temperature °K	K_s cm$^3\times10^{16}$	ϵ_s ev
1	1.42	8.9×10^{14}	304	6.95	0.213
2	1.63	2.03×10^{15}	300	8.40	0.205
3	1.67	7.4×10^{15}	313	2.74	0.194
4	1.85	1.12×10^{16}	313	5.05	0.211
5	1.74	1.18×10^{16}	309	2.41	0.187
6	1.76	1.21×10^{16}	313	2.54	0.193
7	1.75	1.24×10^{16}	313	2.42	0.191
8	1.86	2.02×10^{16}	309	3.04	0.194
9	2.07	1.58×10^{16}	313	...	...
10	2.50	2.43×10^{17}	300	...	...
11	1.87	2.92×10^{14}	195	229.0	0.184
				Average	0.197

III. DEFECT STATES IN n-TYPE Ge

It is possible to determine K_s and hence ϵ_s by three independent approaches. These are: (1) the variation of the initial slope as a function of n^0 of the n *vs* bombardment curve, (2) the application of Eq. (4) to the bombardment curve over the entire n-type range, and (3) the temperature dependence of electron concentration in bombarded Ge. If the model is valid, each approach should yield the same value for ϵ_s. We shall consider each of these in turn.

A. Initial Slopes of Bombardment Curves

It is evident from Eq. (4) that the initial rate of change of n with Frenkel defect concentration is

$$[dn/dN]_{N=0}=-(1+2K_sn^0)/(1+K_sn^0). \quad (5)$$

This rate is directly proportional to the initial change of conductivity σ per incident fast neutron, provided that the initial decrease in mobility is small compared to the initial rate of electron removal. If it is assumed that the defect concentration at the minimum of the σ *vs* $(nvt)_f$[14] curve is equal to the initial electron concentration,[15] $[dn/dN]_{N=0}$ is directly available from experiment and K_s may be determined from Eq. (5). ϵ_s may then be readily determined if m_e is known. For m_e we have used the indications of cyclotron resonance measurements of Lax and co-workers[16] which include the effect of spatial degeneracy of energy surfaces in K-space[17]:

$$m_e=[\omega_s^2m_xm_ym_z]^{\frac{1}{3}}=0.51m_0; \quad \omega_s=4.$$

Using these values in Eq. (3) leads to

$$\epsilon_s=8.63\times10^{-5}T[34.42+(\ln K_s)T^{\frac{1}{2}}]. \quad (6)$$

The results of analysis of initial slopes of σ *vs* $(nvt)_f$ curves for a number of n-type samples exposed under a variety of conditions are listed in Table I. It is evident from the values of ϵ_s that reasonably consistent results are obtained using this model. Samples 9 and 10, which do not yield agreement, exhibit a very broad minimum in the σ *vs* $(nvt)_f$ curve and apparently have an inhomogeneous impurity distribution. If such is the case, the minimum would be displaced toward longer exposures and would no longer correspond to $N=n^0$. The data for sample 11 were obtained at −78°C and reasonable agreement is indicated even at this temperature.

B. Fitting the Bombardment Curve

Equation (4) has also been used to calculate a bombardment curve using K_s as the adjustable parameter. The calculated points are compared with the experimental curve in Fig. 1. For purposes of convenience the concentration of electrons during the bombardment is expressed relative to the initial concentration (n/n^0) and the exposure is given in terms of N/n^0 under the assumption that $N=n^0$ at the point of conversion to p-type (the conductivity

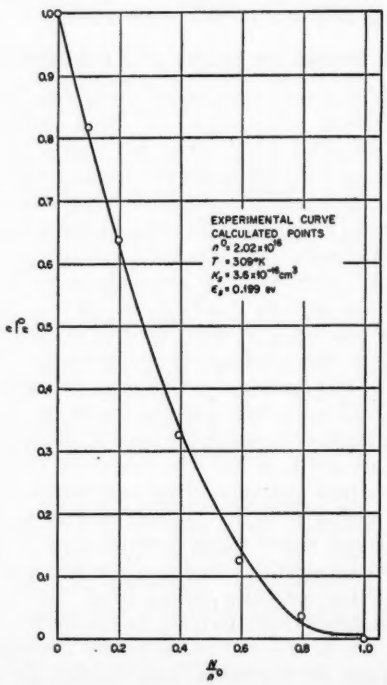

FIG. 1. Electron concentration *vs* defect concentration produced by bombardment of n-type germanium. For convenience the concentrations are expressed in units relative to the initial electron concentration. The points are calculated from Eq. (4) using the values of parameters shown on the figure.

[14] $(nvt)_f$ is defined as the weighted average integrated flux of those neutrons capable of displacing atoms. The absolute values may be in error by as much as a factor of two. Relatively, however, the scale used here is consistent with that used in references 1–4.

[15] This is not exactly true as was pointed out in reference 2, since the conductivity minimum does not correspond to the intrinsic condition $(p=n)$ but rather to $p=bn$ where b is the ratio of electron mobility to hole mobility. For the present application, however, the assumption is a good approximation.

[16] Lax, Zeiger, Dexter, and Rosenblum, Phys. Rev. **93**, 1418(L) (1954).

[17] We are indebted to H. C. Schweinler for pointing out this relationship.

minimum).[15] Since the electron concentration is inferred from the conductivity during irradiation using the initial value of mobility, it is inherently assumed that the mobility is unaffected by bombardment. As will be shown later this is not necessarily a good assumption since even at room temperature a considerable decrease in mobility may be expected for an exposure of this magnitude $[(nvt)_f = 1\times10^{16}\ \text{cm}^{-2}]$. However, for the initial half of the curve and at the end, this assumption is expected to be reasonably good. A rather good fit to the curve was obtained using $K_s = 3.6\times10^{-6}\ \text{cm}^3$ which corresponds to $\epsilon_s = 0.199$ ev. This value is in good agreement with those listed in Table I.

C. Temperature Dependence of n

It is possible to test the model more stringently by using Eq. (4) to calculate the temperature dependence of electron concentration in a bombarded n-type sample. For $n > 2N$, Eq. (4) predicts a transition with increasing temperature from a condition in which all the shallow traps are occupied to one in which these are completely empty. Since in the derivation of Eq. (4) the intrinsic process has been neglected and it is assumed that all chemical donors are completely ionized, n is temperature independent both above and below this transition region. When all shallow traps are filled, $n = n^0 - 2N$, a condition which readily permits fixing the value of N from experimental data.

Curves of log n *vs* $1/T$ for an n-type sample after various periods of irradiation at ~45°C and heat treatment are shown in Fig. 2. The values of n were obtained from Hall coefficient measurements and corrected for impurity scattering by the method of Johnson and Lark-Horovitz[18] as modified by Fan.[5] Although there is evidence that the additional scattering resulting from bombardment may not be of a charge center type (see below), it is evident from Curve I and the low-temperature portions of the curves after bombardment that this method of correction yields the expected temperature dependence for n arising from chemical impurities. Curve I is that of the sample before bombardment; Curves II, III, and IV were taken after exposures of $(nvt)_f = 2.9\times10^{15}$, 5.8×10^{15}, and 7.8×10^{15} cm^{-2}, respectively. The encircled point (point A) was measured after the specimen had stood at room temperature for one month subsequent to the final exposure and Curve V was taken during cooling after heating the specimen to 152°C for a short period of time (~10 min). In Fig. 3 the curves calculated from Eq. (4) by using $\epsilon_s = 0.199$ ev are compared with the experimental points of Curves IV and V of Fig. 2. Curve IV yields excellent agreement with the model using $n^0 = 2.80\times10^{16}\ \text{cm}^{-3}$ and $N = 1.27\times10^{16}\ \text{cm}^{-3}$.

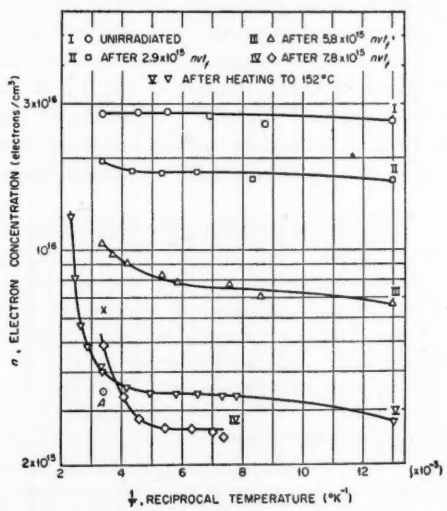

FIG. 2. Electron concentration in n-type Ge *vs* reciprocal temperature after various periods of exposure and subsequent treatment. The curves were obtained as follows: I on the original, II after $(nvt)_f = 2.9\times10^{15}$ cm^{-2}, III after 5.8×10^{15} cm^{-2}, and IV after 7.8×10^{15} cm^{-2}. All exposures were carried out at ~45°C. Point A was obtained after standing at room temperature for one month subsequent to the final exposure and curve V was taken after heating to 152°C for ~10 min.

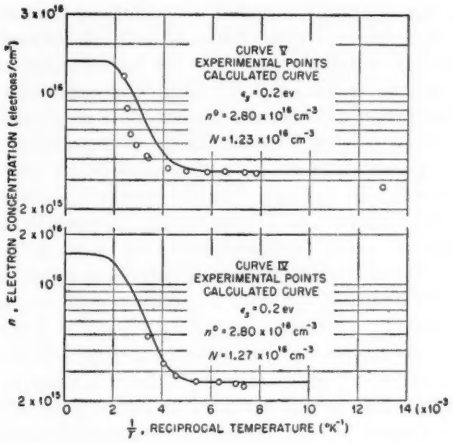

FIG. 3. Comparison of experiment with the two-level model. Equation (4) has been used to calculate Curves IV and V of Fig. 2 using 0.20 ev for the shallow trap depth. Values of N and n^0 inferred from experiment are indicated on the figure for the two curves.

In the case of Curve V, however, with $N = 1.23\times10^{16}$ cm^{-3} agreement is not so good since the model predicts a much more rapid initial rise of n with temperature in the transition range. At first glance it might appear that the heating has not only caused some annealing, increasing the low temperature value of n from 2.6×10^{15} to 3.4×10^{15} cm^{-3}, but has in addition increased the shallow trap depth. Closer examination, however, reveals that after standing for one month the electron concentration at room temperature decreased from 4.9×10^{15} to 3.5×10^{15} cm^{-3}. This change is in the opposite direction

[18] V. A. Johnson and K. Lark-Horovitz, Phys. Rev. **82**, 977 (1951).

from that normally expected to accompany the annealing of lattice defects. Such a decrease cannot be explained as being caused by the introduction of Ga by nuclear transmutation[19] since the maximum Ga concentration expected for the exposure in question is only $\sim 2\times10^{14}$ cm^{-3}. Consequently, it is probable that the apparent increase in shallow trap depth observed subsequent to heating actually resulted from some process which occurred during the one-month aging period at room temperature. One process which suggests itself is a clustering of defects, possibly interstitials. If such is the case, the shallow-trap concentration would no longer be equal to but rather less than the deep-trap concentration making Eq. (4) invalid. This hypothesis receives support from studies of the annealing kinetics of quenched-in lattice defects[20] and from current studies of room temperature aging of fast neutron bombarded Ge.[21]

In summary, it appears that the model suggested by James and Lark-Horovitz is justified experimentally when applied to n-type Ge irradiated at or near room temperature. Tests of the model using three different approaches all give consistent results and the shallow state appears to lie $\sim$0.2 ev below the bottom of the conduction band. This value is greater by a factor of four than the theoretically predicted value ($\sim$0.05 ev). The Purdue group finds similar indications in deuteron bombarded n-type Ge.[7]

IV. MOBILITY IN BOMBARDED n-TYPE Ge

The Hall coefficient and resistivity measurements taken after successive exposures for several specimens permit an examination of the additional charge carrier scattering introduced by bombardment. In Fig. 4, the Hall mobility[22] μ_H of the sample of Figs. 2 and 3 is plotted as a function of temperature after each exposure. Curve I was obtained before bombardment, Curves II, III, IV, and V were taken after cumulative exposures of $(nvt)_f = 2.9\times10^{15}$, 5.8×10^{15}, 7.2×10^{15} and 7.8×10^{15} cm^{-2}, respectively, and Curve VI was obtained after heating the specimen to 152°C for $\sim$10 min subsequent to the total exposure and aging at room temperature for one month. The mobility is decreased by bombardment over the whole temperature range. After a total exposure of 7.8×10^{15} cm^{-2} μ_H is decreased by a factor of two at room temperature and by more than an order of magnitude at 77°K. The negative temperature coefficient, evident in Curve I, which is characteristic of charge carrier scattering by thermal vibrations of the lattice ($\mu_H \propto T^{-\frac{3}{2}}$) is rapidly removed by exposure and Curve V possesses approximately a T^2 dependence. This behavior indicates that irradiation introduces additional scattering centers which scatter carriers more effectively at low temperature. It is interesting to note that the combination of room-temperature aging and the short anneal subsequent to exposure markedly improved the mobility over the entire range and restored, to an appreciable extent, the lattice-scattering temperature dependence. This behavior, coupled with indications of the previous section that the same combination of conditions subsequent to exposure apparently increased the depth of the shallow electron traps, seems to indicate that low-temperature annealing produces more extensive healing or rearrangement of lattice disorder than was previously expected.

Figure 5 is a plot of μ_H *vs* T for a specimen with a large initial electron concentration ($n^0\sim7\times10^{17}$ cm^{-3}) subjected to much heavier exposures. Curve I refers to the original specimen and Curves II, III, IV, V, and VI were obtained after fast neutron exposures of 7.2×10^{16}, 1.27×10^{17}, 1.61×10^{17}, 1.84×10^{17} and 2.01×10^{17} cm^{-2}, respectively. These curves exhibit the same qualitative behavior as those of Fig. 4, however, a considerably greater exposure was necessary for this specimen to remove lattice scattering behavior in the high-temperature range. In fact Curve II, which was obtained after an exposure about ten times as long as that of Curve V of Fig. 4, still shows a definite maximum, whereas Curve V shows almost no trace of the lattice-scattering process. This behavior seems to indicate that the charge carrier concentration is an important variable in the scattering process introduced by irradiation. Another important feature not apparent from Fig. 4 is that the temperature dependence of μ_H is enhanced by exposure. Whereas in curve V of Fig. 4 μ_H is apparently dependent on T^2 in the low-temperature region, Curves V and VI of Fig. 5 yield approximate $T^{3.2}$ and $T^{6.3}$ dependences, respectively. Hence a much more complex functional dependence of μ_H on T is indicated than a simple power law

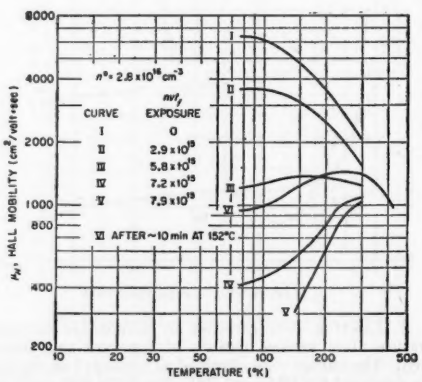

FIG. 4. Hall mobility *vs* temperature for the specimen of Fig. 2 after the indicated periods of exposure. Curve VI was obtained after standing for one month at room temperature and a short anneal at 152°C subsequent to the total exposure.

[19] Cleland, Lark-Horovitz, and Pigg, Phys. Rev. **78**, 814 (1950).
[20] S. Mayburg, Phys. Rev. **95**, 38 (1954).
[21] Cleland, Crawford, and Pigg (unpublished data).
[22] μ_H is defined as $\mu_H = R\sigma$ and is related to the true drift mobility μ by $\mu_H/\mu = r$, where r is the Hall parameter ($r = n_e eR$). In the case of spherical energy surfaces, for lattice scattering only, $r = 1.18$, whereas, for purely charge center scattering $r = 1.93$. [W. Shockley, *Electrons and Holes in Semiconductors* (D. Van Nostrand Company, Inc., New York, 1950), pp. 278, 279].

($T^{\frac{3}{2}}$) which would be expected for charge-center scattering according to either the Conwell-Weisskopf theory[23] or the theory of Brooks[24] and Herring.[25]

Since as a general rule the extraneous scattering becomes predominant compared to lattice scattering at sufficiently low temperatures, $1/\mu_H$ at 77°K is expected to be approximately proportional to the scattering probability per unit time arising from charged impurities originally present and the additional scattering processes introduced by bombardment. Figure 6 shows the variation of $1/\mu_H$ at 77°K with exposure for three n-type specimens. Curve I refers to the specimen of Figs. 2, 3, and 4 in which $n^0=2.7\times10^{16}$ cm^{-3}, Curve II refers to a sample with $n^0=3.8\times10^{16}$ cm^{-3}, and Curve III was obtained on the sample of Fig. 5 ($n^0=7\times10^{17}$ cm^{-3}). In every case the scattering probability increases with exposure at much more than a linear rate. Furthermore, the rate of increase is greater the smaller the initial electron concentration.

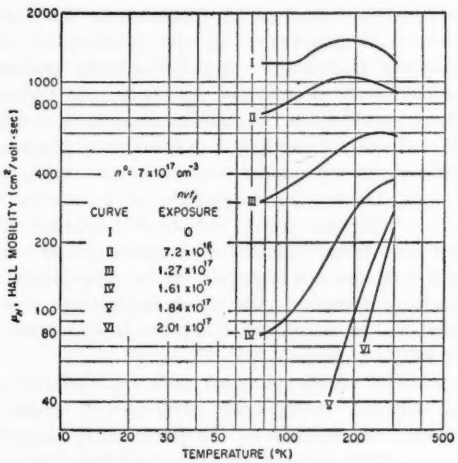

FIG. 5. Hall mobility *vs* temperature for n-type Ge after the indicated exposures, for a specimen with $n^0=7\times10^{17}$ cm^{-3}.

In order to make any definite statement concerning the nature of the scattering process or processes associated with the radiation-disarranged lattice, it is necessary to separate the effects of such from other known scattering mechanisms, i.e., scattering from lattice vibrations, charge centers, etc.[25] The information presently available is too scanty to warrant such a treatment. Consequently we shall only point out certain features for which any proposed scattering mechanism must account.

(1) There appears to be a large and apparently complex temperature dependence of μ_H which increases with bombardment (see Figs. 4 and 5). This behavior cannot be explained by the usual types of localized

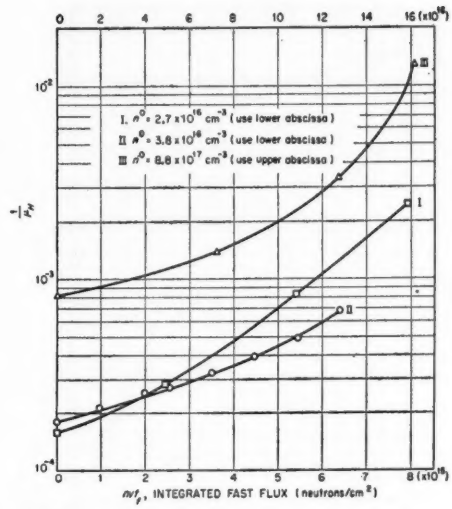
0 2 4 6 8 10 12 14 16 (x10^{16})
I. $n^0 = 2.7\times10^{16}$ cm^{-3} (use lower abscissa)
II $n^0 = 3.8\times10^{16}$ cm^{-3} (use lower abscissa)
III $n^0 = 6.8\times10^{17}$ cm^{-3} (use upper abscissa)
10^{-2}
10^{-3}
10^{-4}
$-|R|$
0 1 2 3 4 5 6 7 8 (x10^{16})
nvt_f, INTEGRATED FAST FLUX (neutrons/cm^2)

FIG. 6. Reciprocal of Hall mobility *vs* integrated fast-neutron flux for three n-type Ge specimens at 77°K. Note that the scale of the abscissa for Curve III is compressed by a factor of 20 relative to that of Curves I and II.

energy-dependent scattering mechanisms. Since the defects produced by bombardment are not expected to be completely randomly distributed, but to some extent localized in the region of the primary collision, it is reasonable to expect localized fluctuations in the defect concentration. These may give rise to small fluctuations in the electrostatic potential in the crystal and hence in the bottom of the conduction band. If such is the case, a complex dependence of scattering probability on the energy of the carrier would not be surprising.

(2) The rate of change of scattering probability with bombardment is sensitive to the electron concentration. Consequently, screening of localized charge fluctuations by charge carriers appears to be important.

(3) The scattering probability increases at a greater than linear rate (even greater than an exponential rate, see Fig. 6) with exposure. This behavior may also be related to the postulated fluctuations in defect concentration and to the extent of screening.

Studies of mobility in deuteron bombarded n-type Ge[5] seem to indicate that the decrease resulting from bombardment can be explained on the basis of charged scattering centers alone. This difference between deuteron and fast-neutron irradiated Ge may be due to a difference in the distribution of defects in the vicinity of the primary collision.

V. RESULTS OF LOW-TEMPERATURE BOMBARDMENT

Several n-type Ge samples have been irradiated in the low-temperature facility of the ORNL graphite reactor at temperatures below −100°C. The conductivity decreases with bombardment, indicating that electron removal by bombardment-produced acceptors is the predominant effect. The initial rates of electron removal,

[23] E. M. Conwell and V. F. Weisskopf, Phys. Rev. **77**, 388 (1950).
[24] H. Brooks, Phys. Rev. **83**, 879 (1951).
[25] P. P. Debye and E. M. Conwell, Phys. Rev. **93**, 693 (1954).

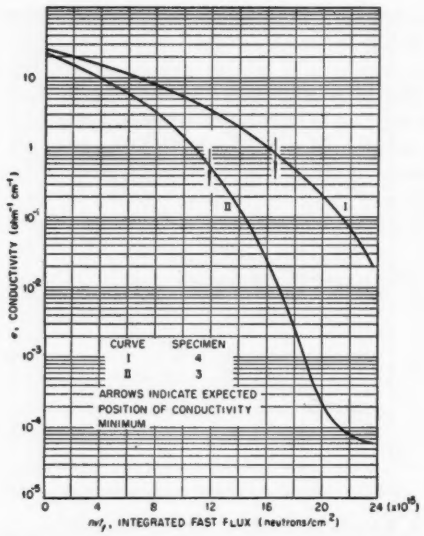

FIG. 7. Log conductivity *vs* integrated fast neutron flux for two specimens of *n*-type Ge (3 and 4 of Table II) exposed at 120°K. Curves I and II refer to specimens with $n^0=3.25\times10^{16}$ and 2.36×10^{16} cm^{-3} respectively. The arrows indicate the expected positions of the minima for a linear rate of introduction of Frenkel defects assuming the mobility to be unaffected by bombardment.

calculated under the assumption that the initial rate of decrease of μ_e is negligible,[26] are listed in Table II together with the initial electron concentrations n^0 and the temperatures of exposure T_e. The rate of removal is higher at these temperatures than at room temperature[2] by a factor of about 1.5. A portion of the enhanced rate of removal may be caused by the complete effectiveness of the shallow vacant states (see Sec. III). Inspection of Table I and Eq. (4), however, reveals that for the values of n^0 in question such a process can account for only 20 percent or less of the enhancement. It is uncertain whether the remaining 30 percent of the enhancement is because of an appreciable initial rate of decrease of μ_e with bombardment,[26] rendering the values of $[dn/d(nvt)_f]_{t=0}$ in Table II too large, or whether a portion of the acceptors introduced at low temperatures are unstable in the room temperature range.

Plots of log σ *vs* $(nvt)_f$ for Samples 3 and 4 of Table II are shown in Fig. 7. Sample 3 was bombarded to virtually the conductivity minimum, whereas Sample 4 was still definitely *n*-type after the exposure. Positions of the conductivity minima expected for a linear rate of defect introduction consistent with the values of $[dn/d(nvt)_f]$ of Table II are indicated by arrows. Since these do not correspond to the experimental positions of the minima, it appears that either the rate of defect introduction decreases with increasing exposure or the initial rate of change of mobility is comparable to the rate of electron removal.[26] Whatever the reason for this difference, the shape of the σ *vs* $(nvt)_f$ curve does not conform to expectation according to Eq. (4) in that it deviates from the expected linear behavior toward a less rapid decrease early in the bombardment. Consequently, it appears that the two-level vacant-state model is not adequate at these temperatures.

Even though the period of exposure covered by Fig. 7 is expected to produce a marked decrease in μ_e at these temperatures, the conductivity minimum approached by Sample 3 is several orders of magnitude higher than the intrinsic value calculated using the pre-bombardment value of μ_e. This seems to indicate that the intense ionizing radiation in the reactor excites an appreciable concentration of electron-hole pairs. This explanation is supported by the observation that immediately after reactor shut-down both specimens showed a further decrease of σ with time at constant temperature (114°K). The initial decrease was quite rapid, and was followed by a slower decay which was approximately exponential with a time constant of ~10 min. Hence the magnitude of σ reflects the expected variation of γ radiation intensity after reactor shut-down.[27] Since the concentration of excess electron-hole pairs is expected to be proportional to the exciting intensity, it is concluded that at least a portion of the excess conductivity is produced by photoelectric excitation.

In addition to the photoexcitation of electron-hole pairs, trapping of minority carriers will make an additional contribution to the photoconductivity.[28,29] Brown *et al.*[30] report that high energy electron bombardment at 78°K introduces minority carrier traps in appreciable concentrations into both *n*- and *p*-type Ge. There is convincing evidence that low-temperature fast neutron bombardment also introduces hole traps

TABLE II. Rates of removal of conduction electrons at low temperatures.

Sample	n^0(cm^{-3})	T_e(°C)	$[dn/d(nvt)_f]_{t=0}$
1	1.10×10^{18}	−157	−6.4
2	1.36×10^{17}	−157	−4.8
3	2.36×10^{16}	−153	−4.8
4	3.25×10^{16}	−153	−4.0
		Average =	−5.0

[26] This assumption may not be a good one at low temperatures. If μ_e before exposure is limited entirely by charged impurity scattering and if the additional scattering introduced during the early stages of bombardment is of this type, the initial decrease of σ caused by a decrease in μ_e is expected to be approximately one-half that produced by electron removal according to the Conwell-Weisskopf theory (reference 23) and the two-level model used in Sec. III. For the samples of Table I the impurity scattering contribution to μ_e is appreciable at these temperatures.

[27] Immediately after shut-down, that portion of the γ-ray flux which arises from (n,γ) and fission reactions disappears. An additional rapid decrease results from the decay of short-lived activities. After this initial rapid decrease, the γ-ray intensity is expected to decay at a rather slow, uniform rate.

[28] J. R. Haynes and J. A. Hornbeck, Phys. Rev. **90**, 152 (1953).

[29] H. Y. Fan, Phys. Rev. **92**, 1424 (1953).

[30] Brown, Fletcher, and Wright, Phys. Rev. **96**, 834 (1954).

into n-type Ge. After irradiation [$(nvt)_f = 2.4\times10^{16}$ cm^{-2}] and standing at 114°K for 40 min, Sample 4 was warmed in the reactor at a relatively uniform rate ($\sim$1°C min^{-1}) to 260°K and then recooled. The σ *vs* T curves are shown in Fig. 8, the solid and dashed curves referring to the warming and cooling operations, respectively. Two well-defined maxima falling at 134°K and 165°K are observed during warming. After the second maximum σ falls to a minimum value at $\sim$195°K and increases rapidly with further heating. The oscillatory behavior is interpreted as the successive escape of trapped holes (and their subsequent recombination with excess electrons) from two discrete trapping levels of different depth. It is assumed that at 114°K the γ-ray intensity is sufficient to saturate these traps and that the rate of heating is sufficiently low to preserve steady-state conditions. As the temperature is raised, a point is reached at which the rate of release of holes from traps becomes comparable to the rate of trapping and saturation is no longer possible. With further heating the traps empty rapidly, the transition from a filled to an empty condition occurring over a relatively narrow temperature range. Although it is possible in principle to calculate the trap depth ϵ_t from the position of the inflection point,[29] the situation is complicated in the present case by the strong and unknown temperature dependences of μ_e and n in the range of interest. Consequently, it is impossible to make a reliable estimate of the trap depths in question.

On cooling at about the same rate, one would expect the reappearance of the same maxima under steady-state conditions of excitation provided the traps are still present and the γ-ray intensity is unchanged. The cooling curve in Fig. 8 shows no such behavior and it is concluded that those traps which are responsible for the oscillatory behavior of the warming curve have annealed. This result is consistent with the findings on electron bombarded Ge.[30] That some sort of annealing has occurred during the temperature excursion is evident from the position of the cooling curve relative to the heating curve. The cooling curve lies appreciably above the warming curve at temperatures above 173°K. It crosses the warming curve at that point and attains a value at 113°K of only about one-half the value before heating. The increase in σ in the range above 173°K can be caused either by an improvement in μ_e which had been decreased by bombardment or by the annealing of a portion of the defects responsible for removing electrons, or more probably both. A decrease in σ after heating at the low temperature end of the curve is expected if the hole traps have annealed, since an important source of photo conductivity is thereby removed. It was possible to retrace the cooling curve at least as high as 200°K by subsequent warming.

The behavior attributed to trapping described in the aforementioned, was confirmed by the warming of an n-type sample in which σ was reduced from 52 to 2.3 ohm^{-1} cm^{-1} by bombardment at 116°K. Again two

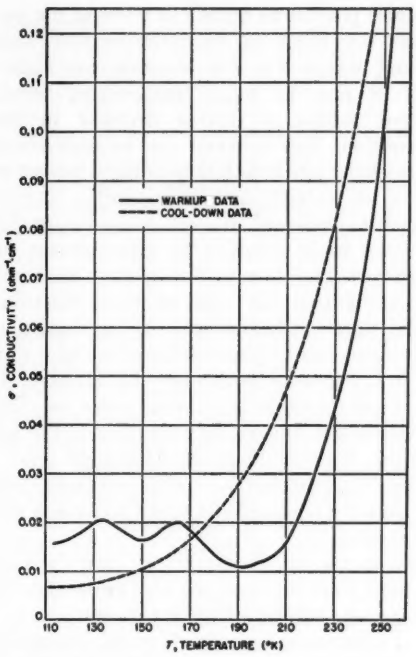

FIG. 8. Conductivity *vs* temperature for an n-type specimen of Ge obtained on warming and cooling after an exposure of $\sim3\times10^{16}$ neutrons cm^{-2} at 116($\pm$2)°K.

maxima in the σ *vs* T curve were observed during warming in the same temperature range. It is interesting to note in this connection that Sample 3, which was bombarded almost to the conductivity minimum and hence was essentially intrinsic, showed only a small indication of the first maximum and one at all of the second. Such behavior would be expected when the Fermi level lies deep in the forbidden band or near one of the trapping levels.[29]

VI. DISCUSSION

In the foregoing treatment the Frenkel-defect energy-level model of James and Lark-Horovitz[10] was extensively used as a basis for analyzing experimental data. This choice was considered reasonable because of the successful use of the model in explaining qualitatively the results obtained on bombarded Ge and Si. These studies indeed indicate that the predominant effect of fast neutron bombardment in the room temperature range is the introduction of two groups of vacant states, one shallow and one deep, which are consistent with the predictions of the model. Consequently, it is reasonable to conclude that disorder produced by bombardment at or near room temperature may be described as interstitial-vacancy pairs. The difference between the observed shallow-trap depth of $\sim$0.20 ev and the theoretically predicted depth (0.05 ev) is not considered serious in view of the approximations involved in the calculation of the latter.

It is also possible to explain in terms of the model in question the effect of room-temperature aging of irradiated *n*-type Ge. On standing for appreciable periods of time at room temperature, bombarded specimens exhibit a further decrease in electron concentration. This behavior can be understood if it is postulated that, in addition to the expected recombination of interstitials and vacancies there is an appreciable tendency at this temperature for the interstitials to be removed by some process such as clustering or migration to dislocations. Since removal of an interstitial also removes those electrons and localized states associated with it, the shallow trap is effectively replaced by one near the top of the valence band which is associated with the vacancy. It was pointed out that this hypothesis, which requires that the interstitial be the mobile component of the defect, is consistent with findings of Mayburg[20] and much additional support has been obtained from studies of the behavior of bombarded *p*-type Ge on room-temperature annealing.[31]

The results of exposure at low temperature (<-100°C) are not in accord with the model. The σ *vs* $(nvt)_f$ curves obtained at these temperatures exhibit a marked upward concavity in the range wherein a linear decrease is predicted by Eq. (4). This lack of agreement apparently indicates that the description of lattice disorder introduced at low temperature completely in terms of Frenkel defects is no longer valid. It seems reasonable to conclude that restriction of atomic motion by the lower thermal energy of the lattice leads to a more complex configuration of disorder. On warming this disorder of low thermal stability would be expected to rearrange to configurations of higher stability, e.g., isolated interstitials and vacancies. That some type of rearrangement takes place is indicated by the disappearance of minority-carrier traps during warming at temperatures below 260°K.

Although the work presented here and other information[31] on *p*-type Ge support strongly the Frenkel-defect model of energy levels, it is felt that this picture of fast-neutron-produced disorder should not be accepted without some reservation. In order for the model to be completely applicable, the interstitials and vacancies must be more or less randomly distributed throughout the lattice. As was pointed out earlier, one does not expect bombardment produced defects to be randomly distributed but rather to be localized to some extent in the region of the primary collision, with a resulting localized variation in carrier concentration. Because of the continuous neutron energy spectrum, any such fluctuation in defect density would itself be expected to vary widely both as to radial extent and absolute magnitude. Consequently, the nature of the effect on the over-all carrier concentration to be expected from the introduction of such a distribution of disorder is uncertain. The only manifestation which might be specifically attributed to such a situation is possibly the effect of bombardment on the electron mobility. As was postulated above, the large negative temperature dependence of the scattering probability and its marked dependence on electron concentration may result from localized fluctuations in the bottom of the conduction band. Additional experiments are necessary before the questions raised here can be answered unambiguously.

The nature of the annealable hole traps which produce photoconductivity during and subsequent to low-temperature (<-100°C) exposure is not at all clear. Since they disappear on warming, it is reasonable to conclude that they cannot be identified with those hole traps, stable at room temperature, which have been observed in *p*-type Ge.[3] The two groups of traps in question empty over a narrow temperature range. Therefore, they appear to have a discrete depth. We can only say that they are apparently associated with two definite types of composite defects. It should be pointed out that in addition to these there may be shallower traps which do not anneal and which become apparent at lower temperatures. Indications of these have been obtained at liquid nitrogen temperature on *n*-type specimens exposed at room temperature.[32] A more detailed study of minority-carrier trapping and associated photoconductivity in bombarded Ge is currently being carried out.

The authors are indebted to Miss Louise Roth of Purdue University who furnished the single crystal specimens of Ge used in these investigations. They also wish to thank D. K. Holmes and H. C. Schweinler of this laboratory for their discussions and critical comment. The assistance of E. S. Schwartz in some of the measurements is gratefully acknowledged.

[31] Cleland, Crawford, and Pigg (to be published).

[32] Cleland, Crawford, and Pigg (unpublished data).

Lattice Thermal Conductivity

J. S. DUGDALE AND D. K. C. MACDONALD
Division of Physics, National Research Council, Ottawa, Canada
(Received February 8, 1955)

Consideration of the anharmonic properties of a linear chain suggests that the dimensionless quantity $\alpha\gamma T$ is in general a measure of the anharmonicity of a lattice (α is the thermal expansion coefficient and γ the Grüneisen parameter). It is therefore proposed that the mean free path for lattice vibrations in an insulator should, in the classical temperature region, be approximately $A_0/\alpha\gamma T$, where A_0 is the lattice spacing. Reasonably good agreement with experiment is found.

DESPITE the pioneer work of Debye[1] and Peierls[2,3] in the theory of the thermal conductivity of insulating solids, we have still no quantitative expressions for the thermal conductivity in terms of the equilibrium properties of the solid. It is now generally agreed that a finite thermal conductivity depends essentially on the anharmonicity of the interatomic potential and consequently one should expect that there would be a close relationship between thermal conductivity and the thermal expansion which also depends intrinsically on the anharmonicity.

A particular problem of considerable interest is the interchange of momentum between the thermal flow and the lattice structure. Although Peierls has emphasized that the so-called "Umklappprozess" involving a Bragg reflection of the "phonons" with the quasi-periodic lattice will provide momentum transfer, we would like to point out that the essential differential expansion of the lattice under a thermal gradient itself already calls for such a momentum transfer. If, as is normal, the expansion coefficient is positive, the momentum will be absorbed by the differentially displaced atoms from the thermal flow in going from the hot to the cold end. On the other hand, were the thermal expansion to be negative (which in itself involves no contradiction with thermodynamics), this would imply a progressive absorption of momentum from the lattice by the thermal flow. The magnitude of the force per unit volume, say F, corresponding to this momentum transfer may be inferred from Brillouin's[4] expression for the radiation pressure due to diffuse thermal radiation in a solid, yielding $F\simeq\gamma CdT/dx$ (where γ is the Grüneisen parameter and C is the specific heat per unit volume).

Although we have not succeeded in deriving on a sound theoretical basis quantitative expressions for the thermal conductivity, it appears that in the analysis of lattice properties the dimensionless parameter $\alpha\gamma T$ (where α is the thermal expansion coefficient) always appears as a measure of the departure of the lattice from harmonic behavior (cf. Dugdale and MacDonald[5] and MacDonald and Roy[6]). If it is permissible, as Debye first did, to introduce a mean free path l for the lattice vibrations (or "phonons"), then in the classical temperature region it should vary inversely with temperature (as first predicted by Debye) and would be expected from Peierls' analysis (cf. Blackman[7]) to vary inversely with the square of the anharmonic coefficient. It, therefore, seems reasonable to assume that it has the form

$$l\simeq A_0/\alpha\gamma T, \tag{1}$$

where A_0 is the lattice constant. There may of course be some further dimensionless factor involving the frequency spectrum of the lattice, but we shall just assume the above simple form for the mean free path and estimate the thermal conductivity of some insulators on this basis. The thermal conductivity, K, is related to the mean free path by

$$K\simeq\tfrac{1}{3}C_v lv, \tag{2}$$

where C_v is the specific heat per unit volume and v is the velocity of sound in the solid, and Table I shows the results for those alkali halides for which experimental data are available. This table suggests that Eq. (1) offers a reasonable estimate of the mean free path.

TABLE I. Calculated and observed thermal conductivities for some alkali halides.[a]

Substance	$10^4\alpha$ (°C^{-1})	γ	C_v (cal/cc °C)	$10^{-5}v$ (cm/sec)	10^8A_0 (cm)	$100K_{calc}$ at 0°C (cal/cm °C sec)	$100K_{obs}$ at 0°C (cal/cm °C sec)
NaF	0.98	1.55	0.72	4.1_6	2.31	5.5	2.5
NaCl	1.10	1.63	0.43_2	3.3_2	2.81	2.8	2.4
NaBr	1.19	(1.56)	0.38	2.4_8	2.98	1.8	0.6
KF	1.00	1.45	0.29	3.2_8	2.67	2.1	1.7
KCl	1.01	1.60	0.32	3.0_0	3.14	2.3	2.5
KBr	1.10	1.68	0.28	2.4_8	3.29	1.5	0.9
KI	1.25	1.63	0.22_8	1.9_4	3.53	0.9	0.7
RbBr	1.04	(1.37)	0.24_1	1.9_5	3.43	1.4	0.9
RbI	1.19	(1.41)	0.20_2	1.7_2	3.66	0.9	0.8

[a] Experimental data on thermal conductivity from A. Eucken and G. Kuhn, Z. physik. Chem. **134**, 193 (1928). Remaining data from Landolt-Börnstein Tables (Verlag Julius Springer, Berlin, 1923); J. C. Slater, *Introduction to Chemical Physics* (McGraw-Hill Book Company, Inc., New York, 1939); and P. W. Bridgman, *The Physics of High Pressure* (G. Bell and Sons, Ltd., London, 1949).

[1] P. Debye, *Vorträge über die kinetische Theorie* (B. G. Teubner, etc., Leipzig, 1914).
[2] R. Peierls, Ann. Physik **3**, 1055 (1929).
[3] R. Peierls, Ann. inst. Henri Poincaré **5**, 177 (1935).
[4] L. Brillouin, *Wave Propagation in Periodic Structures* (McGraw-Hill Book Company, Inc., New York, 1946).
[5] J. S. Dugdale and D. K. C. MacDonald, Phys. Rev. **96**, 57 (1954).
[6] D. K. C. MacDonald and S. K. Roy, Phys. Rev. **97**, 673 (1955).
[7] M. Blackman, Phil. Mag. **19**, 989 (1935).

If, further, we apply Eq. (2) to an electrical conductor such as sodium, at room temperature we find $K_{latt} \simeq 8 \times 10^{-3}$ cals/cm °C sec, which is about 2 percent of the observed thermal conductivity of the metal. This is consistent with the usual assumption that the lattice conductivity in such metals is practically negligible in comparison with that due to the free electrons.

In the case of beryllium, the effective number of conduction electrons is sufficiently low that the intrinsic lattice conductivity can be observed experimentally. Powell[8] finds that the data may be expressed by

$$K_{latt} = [(64/T) - 0.036] \text{ cal/cm °C sec}, \quad (3)$$

valid between 320°K and 700°K. Because of the high characteristic temperature of beryllium (estimates vary between ~650°K and ~1040°K), this temperature-region cannot be considered as fully classical and this may account for the particular form of Eq. (3). However, if we take a value for α appropriate to classical behavior, Eq. (2) gives

$$K_{latt} \simeq (68/T) \text{ cal/cm °C sec}. \quad (4)$$

The close agreement with the dominant term of Eq. (3) must be regarded as fortuitous.

The ideal subjects for experimental investigation would seem to be the heavier inert gas solids. It is hoped to carry out experiments before long on such solids in our laboratories.

Note added in proof.—Two other recent articles of interest are: G. Leibfried and E. Schlömann, Gött. Nachr. IIa, 71 (1954); A. W. Lawson, "On the relation between thermal expansion and thermal conductivity in one-dimensional lattices" (unpublished).

[8] R. Powell, Phil. Mag. 44, 645 (1953).

PHYSICAL REVIEW VOLUME 98, NUMBER 6 JUNE 15, 1955

Magnetization Reversal in Thin Films*

R. L. Conger
U. S. Naval Ordnance Laboratory, Corona, California
(Received February 9, 1955)

An experiment has been performed which indicates that magnetization reversal in evaporated films of 80 percent Ni, 20 percent Fe, 2×10^{-5} cm thick takes place by domain rotation rather than by the motion of 180° domain walls.

THE magnetization reversal in single crystals with dimensions of the order of a centimeter has been investigated by Williams[1] and others. They have shown that the reversal takes place by the motion of 180° domain walls and that the wall velocity is controlled by eddy current effects. Magnetization reversal in most polycrystalline materials probably takes place by this process. However, if a ferromagnetic film is too thin to support domain walls, the magnetization reversal would be expected to take place by a different mechanism.

The thickness at which a thin ferromagnetic film ceases to support domain walls has been calculated by Kittel.[2] For a material with an anisotropy energy of 5×10^5 ergs/cm^3 and a wall energy of 3 ergs/cm, this thickness is 3×10^{-5} cm. Films thinner than this will tend to be single domain structures. Materials with anisotropy energy less than 5×10^5 ergs/cm^3 will have a poly-domain to single-domain transition thickness greater than 3×10^{-5} cm.

We have prepared ferromagnetic films 2×10^{-5} cm thick which should be single domain structures and have observed the magnetization reversal of these films. During the reversal process there is a large component of the magnetization perpendicular to the direction of the applied field in the plane of the film. This perpendicular component was not observed with thicker sheets of ferromagnetic material.

FIG. 1. Hysteresis loops of evaporated film.

* This work was supported by the Office of Naval Research.
[1] Williams, Shockley, and Kittel, Phys. Rev. 80, 1090 (1950).
[2] C. Kittel, Phys. Rev. 70, 965 (1946).

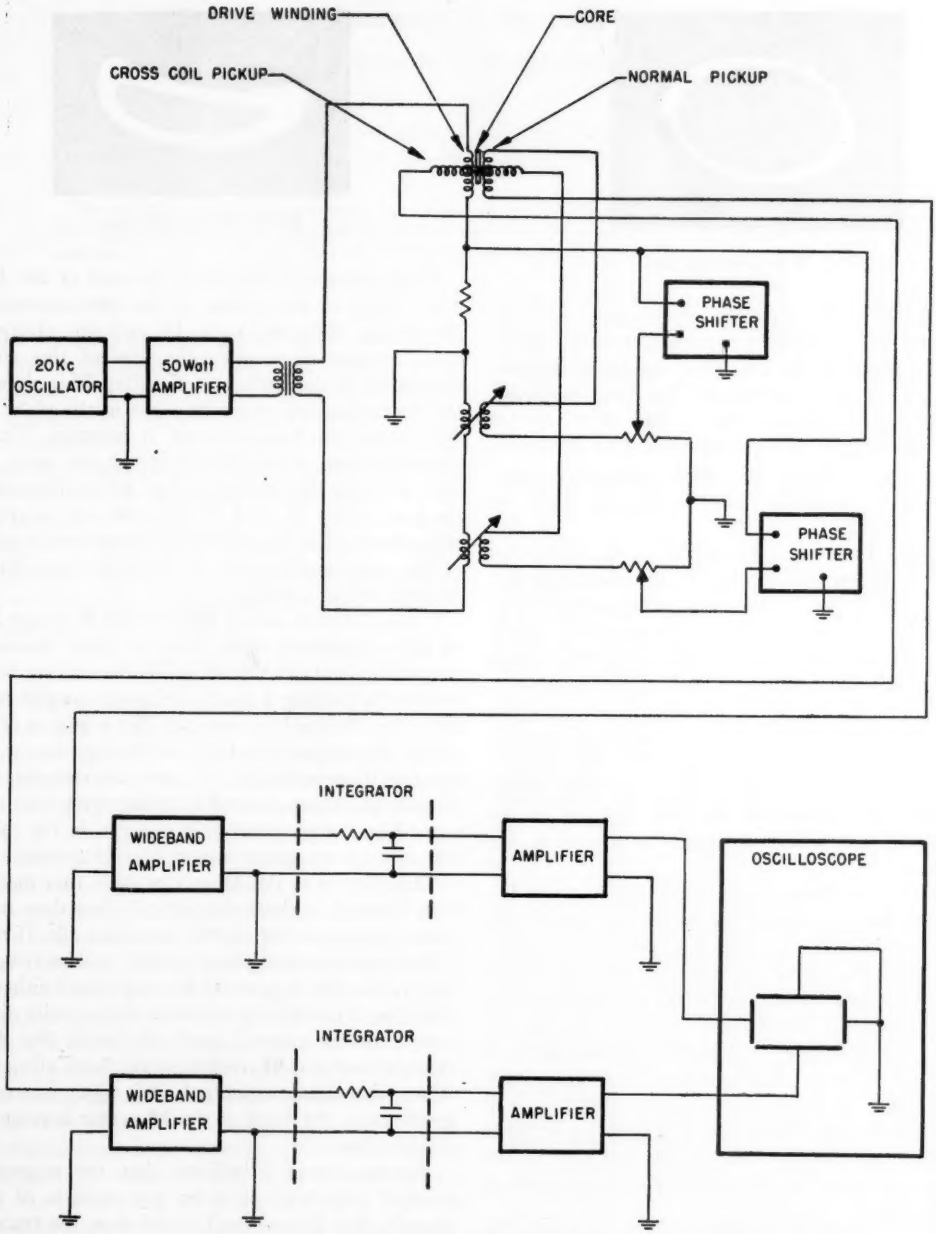

FIG. 2. *M* loop core tester.

The thin films used in this experiment were prepared by evaporating in a vacuum an iron-nickel alloy onto a heated glazed ceramic substrate. The films were in the form of circular disks about 1.5 cm in diameter and 2×10^{-5} cm thick. They had a mirror-like surface. Electrical conductivity measurements showed that the films were continuous layers.

The films had a composition of 80 percent Ni and 20 percent Fe. This alloy was chosen because its low anisotropy energy (about 10^4 erg/cm^3) would increase the tendency of the films to be single domain structures. Chemical composition and thickness of the films were determined by colorimetric chemical analysis using a spectrophotometer.

In order to align the crystals in the film, a magnetic field of several hundred oersteds was applied to the films during their deposition. Figure 1 shows two 60-cycle hysteresis loops for one of the films. The top loop

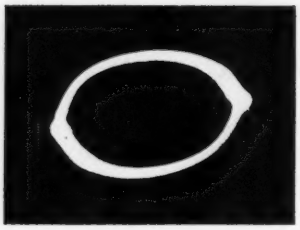

FIG. 3. M loop without bias.

FIG. 4. M loop with bias.

was measured in the direction of this field and the bottom loop was measured perpendicular to this direction in the plane of the film. The two loops indicate that a high degree of orientation has been obtained. Later experiments showed that a field of 0.5 to 1.0 oersteds was enough to produce films with hysteresis loops like thos of Fig. 1. Hysteresis loops were determined with an apparatus similar to that used by Crittenden.[3]

These thin films were examined in an apparatus which made it possible to observe the magnetization change as a pattern on a cathode-ray oscilloscope screen. The film was placed inside a coil assembly which consisted of 3 coils of 20 turns each. Two of the coils, the driving coil and the M_z pickup coil, had a common axis. The axis of the third coil, the M_r pickup coil, intersected the axis of the other two coils at right angles. The center of the three coils coincided. The axes of the driving coil and the M_z pickup coil were always tangential to the surface of the film. The axis of the third coil could be either tangential or normal to the film surface.

A 20-kc/sec oscillator supplied enough power to the driving winding to produce an oscillating field inside the coil of about 20 oersteds peak to peak. The voltage induced in the M_r pickup coil was amplified, integrated, and displayed as a vertical deflection on a cathode-ray oscilloscope screen. The voltage induced in the M_z pickup coil was amplified, integrated, and displayed as a horizontal deflection on the scope. Decoupling techniques similar to those used in the hysteresis loop equipment were used to eliminate all coupling between the driving and pickup coils except that due to the ferromagnetic material. Figure 2 is a block diagram of the apparatus.

As a result of this decoupling, the voltage induced in the pickup coils was proportional to $d\mathbf{M}/dt$ in the direction of the pickup coil axis. After this voltage was amplified and integrated with respect to time, its magnitude was proportional to the component of $\mathbf{M}$ in the direction of the coil axis.

[3] Crittenden, Hudimac, and Strough, Rev. Sci. Instr. 22, 872 (1951).

It was observed that when the axis of the M_r coil was normal to the surface of the ferromagnetic film, the voltage induced in the M_r coil was always very much smaller than when the axis of this coil was tangential to the surface of the film. This shows that the magnetization vector $\mathbf{M}$ stays in the plane of the film when the magnetization is reversed. Since the magnetization vector $\mathbf{M}$ remains in the plane of the film, the trace that is observed on the oscilloscope when the axes of the M_z and the M_r coils are tangential to the surface of the film represents the successive positions of the magnetization vector M as the direction of the magnetization is reversed.

Figure 3 shows such a trace of the $\mathbf{M}$ vector for one of the evaporated films. Then a small biasing field perpendicular to the direction of the driving field was applied by holding a small permanent magnet near the film. This changed the curve of Fig. 3 to that of Fig. 4. When the magnet was held near enough to the film to saturate it magnetically, the curve was reduced to a dot. These experiments showed that the curves were actually caused by the ferromagnetic material in the thin film, the only ferromagnetic material in the system.

These traces of the $\mathbf{M}$ vectors show that magnetization reversal in these evaporated films does not take place by the motion of 180° domain walls. If magnetization reversal took place by 180° wall motion, all the material in the film would be magnetized either in the direction of the driving field or in the opposite direction, except for the material inside the walls. For this case the trace of the $\mathbf{M}$ vector would be a straight line. When the thin evaporated film was replaced by a ferrite core, the trace of the $\mathbf{M}$ vector became such a straight line.

Figures 3 and 4 indicate that the magnetization reversal may take place by the rotation of a single domain. For this reversal mechanism, the trace of the $\mathbf{M}$ vector would be a circle or a semicircle. A steady magnetic biasing field could cause the $\mathbf{M}$ vector to move along a semicircular path, while with no biasing field present the vector could move on a circular path. Since Figs. 3 and 4 are approximately a circle and a semicircle, respectively, the single-domain rotation hypothesis will partly explain the shape of these curves.

Pressure Dependence of the Resistivity of Silicon

WILLIAM PAUL, *Division of Applied Science, Harvard University, Cambridge, Massachusetts*

AND

G. L. PEARSON, *Bell Telephone Laboratories, Murray Hill, New Jersey*

(Received February 28, 1955)

The variation of resistivity of high-purity single crystals of silicon has been measured as a function of hydrostatic pressure in the intrinsic range. The results are interpreted to give a decrease in energy gap between conduction and valence bands with applied pressure.

THE variation of resistivity of silicon crystals with hydrostatic pressure has been previously reported by Bridgman.[1] His measurements were made on relatively impure n- and p-type crystals up to 30 000 kg/cm² at room temperature. The resistivity showed marked hysteresis in a pressure cycle, which made it difficult to deduce the intrinsic behavior of the silicon. It was clearly necessary to measure the resistivity as a function of pressure in the intrinsic range of conductivity of purer samples, as they became available. The purpose of this note is to describe such experiments at pressures up to 7000 kg/cm².

APPARATUS

The pressure apparatus used is that developed by Bridgman[2] and yields pressures up to 7000 kg/cm² at temperatures up to 350°C, if one uses nitrogen, argon, or helium as transmitting gas. The pressure is measured with a manganin gauge. The pressure bomb was immersed in a bath of silicone oil whose temperature could be controlled to 0.03°C by a thyratron controller. The resistance variation due to temperature fluctuation was small compared to the effect of the pressure application. There is, however, a temporary change in temperature when the pressure is altered, and this change will be important if long time-constant trapping can take place in the sample (see Paul and Brooks[3] for this and further experimental details). No pressure run was started until the controller had been at its regulating temperature, and the resistance of the sample had remained constant, for an hour or more.

The n-type single crystals used had room temperature resistivity of 400 ohm-cm and became intrinsic around 130°C. The contacts to the silicon were of 0.25-mm gold wire bonded to the silicon in a 0.5-mm diameter bond. The crystals were some 2 cm long by 0.1 cm square. The current through the samples was between 5 and 20 microamperes. Readings of the resistivity, by a potentiometric method, were taken for both increasing and decreasing pressure, care being taken that temperature equilibrium had been re-established after each alteration of pressure.

[1] P. W. Bridgman, Proc. Am. Acad. Arts Sci. **79**, 142 (1951).
[2] P. W. Bridgman, Proc. Am. Acad. Arts Sci. **72**, 157 (1932), and Proc. Am. Acad. Arts Sci. **82**, 71 (1953).
[3] W. Paul and H. Brooks, Phys. Rev. **94**, 1128 (1954).

RESULTS

The resistivity ρ of an intrinsic semiconductor is given by

$$\rho=(1/e)[1/(\mu_e+\mu_p)](1/2A)\exp(E_g/2kT),$$

where μ_e and μ_p are the electron and hole mobilities, E_g the energy gap, and A is given by $A=(2\pi kT/h^2)^{\frac{3}{2}}\times(m_e m_p)^{\frac{3}{4}}$, where m_e and m_p are the effective masses for electrons and holes respectively. If we assume that the effective masses are independent of pressure (which is not necessarily accurate), then any change in intrinsic resistivity at fixed temperature is probably the net effect of a change in the energy gap E_g and the carrier mobilities μ_e and μ_p. The latter are usually determined from the resistivity *vs* pressure curves at low temperatures on fairly impure n- and p-type samples, where the (single-type) carrier density remains constant with pressure if the carriers are derived from shallow impurity levels.[4]

The experimental results for sample Si VI-270 are summarized in Fig. 1. The quoted resistivities were derived from the measured resistances at high pressure and high temperature and the dimensions at atmospheric pressure and room temperature. The error involved in disregarding any changes in dimensions of the crystals with pressure and temperature is small. The circles denote the zero-pressure resistivities, the crosses the resistivities at 6000 kg/cm². In the intrinsic range of conduction the resistivity has decreased with the increase in pressure, in the opposite direction to the behavior in germanium.[3]

The detailed pressure variation of resistivity for Si VI-270 at various temperatures is shown in Fig. 2; similar behavior is found for other n-type samples of the same resistivity. At the highest temperatures, in the intrinsic range, the resistivity variation is essentially linear and reversible. The slope of the resistivity *vs* pressure curve at the high-pressure end decreases slightly as the temperature is lowered and the onset of the "intrinsic" slope moves to higher pressures. At still lower temperatures, there is little over-all change of resistivity with pressure. We consider that the high-

[4] An argument for the germanium case, showing that the ionization of shallow levels is unlikely to be affected by pressure, is given by W. Paul and H. Brooks, reference 3.

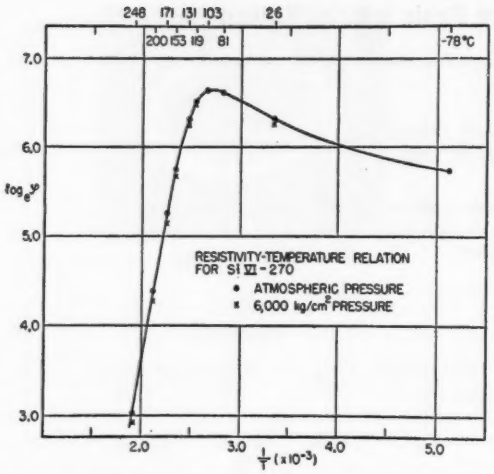

FIG. 1. Resistivity in ohm-cm *versus* reciprocal of temperature curve for Si sample VI-270 at two pressures.

temperature resistivity decrease with the pressure is an intrinsic property of the silicon, corresponding to decrease in the energy gap between conduction and valence bands. The existence of a break—although not sharp—in the resistivity *vs* pressure curves at intermediate temperatures and the shift in its position with temperature agrees with this supposition. The smaller rate of resistivity decrease at lower temperatures is consistent with the view that there is a higher proportion of impurity-derived electrons and that the concentration of these is less affected by the applied pressure. The uniform decrease of resistivity with pressure in the intrinsic range would give $(\partial E_g/\partial p)_T = -1.5\times10^{-12}$ ev per dyne/cm² at 250°C, *in the absence of any mobility changes*.

DISCUSSION

There are, however, some anomalous effects at the lower temperatures, and especially at low pressures. The points plotted in Fig. 2 represent the value of the resistance when it is estimated that the temperature has re-settled to its equilibrium value after a change in pressure. The change in the manganin gauge reading with time is one criterion for this re-establishment of temperature equilibrium, and past experience with the identical apparatus and trap-free germanium crystals provides additional good evidence for the equilibrating time. The resistivity determined in this way drops sharply on the initial application of pressure then flattens before finally going over into the intrinsic decrease. There is, also, hysteresis in this low-pressure region on relieving the pressure. Further, at fixed temperature and pressure there can occur slow changes of resistance with time, both on the outgoing and incoming pressure curves. The trend of the resistance away from the "initial" value is indicated by an arrow for some of the graph points. When the pressure is

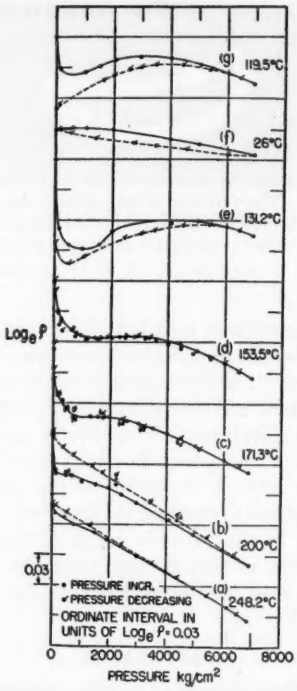

FIG. 2. Resistivity in ohm-cm *versus* pressure curve for Si sample VI-270 at various temperatures. The zero-pressure points (•) on the curves have the following values of $\log_e \rho$: (a) 3.03, (b) 4.39, (c) 5.27, (d) 5.75, (e) 6.29, (f) 6.325, (g) 6.51.

finally reduced to zero the resistivity is normally lower than it was before the run. If the temperature be maintained over an hour or two, the resistivity steadily increases to a value near its pre-run value.

It is likely that these hysteresis and time dependent effects are caused by an alteration with pressure of the density, or the electron occupation density, of deep lying traps[5] in the crystal, and with the temporary temperature change accompanying a change in pressure. The resistivity *vs* pressure curve obtained at low temperature, if one waited for trap equilibrium to be re-established after each temperature-pressure change, would probably be reversible but would not give the variation in electron mobility which is what is wanted from low-temperature experiments. *P*-type crystals that have been examined[6] thus far also show trapping effects which prevent the determination of the change in hole mobility with pressure. The mobility changes, and the correction to $(\partial E_g/\partial p)_T$ resulting, really require trap-free crystals although it might be possible to keep the traps filled at all pressures by suitable infrared irradiation. It is probable that the crystals examined by Bridgman, which gave wide resistance-pressure loops, contained traps, and perhaps even pressure-created traps.

[5] J. R. Haynes and J. A. Hornbeck, Phys. Rev. **90**, 152 (1953).
[6] In conjunction with G. B. Benedek.

The experiments described have been carried out in argon, nitrogen, and helium gases, with no significant difference in the results obtained. Additional work in isopentane to 30 000 kg per cm² at room temperature seems to suggest a small increase in the electron mobility with pressure, but the trapping effects make this less certain. However, no violent change in the electron mobility such as has been found for germanium[3] was observed. It must be emphasized that the trap effects which mask the mobility changes are not important at the highest temperatures, so that the decrease in resistivity with pressure there is genuine, and the deduction of an energy gap decrease with pressure could be invalidated only by improbably large increases in one or both of the carrier mobilities. The results reported here have been checked by examining the change in the optical absorption edge with pressure, up to 8000 kg/cm². The shift in the edge is towards longer wavelengths, or smaller energies, and is of about the same magnitude as in the above experiments.[7] It is intended to further check the results by examining the change in Hall mobility of electrons and holes with pressure.

ACKNOWLEDGMENTS

It is a pleasure to acknowledge the helpful advice given by Professor H. Brooks on all aspects of this investigation, and the assistance of Professor P. W. Bridgman in making available his apparatus and experience in high-pressure measurements.

[7] Warschauer, Paul, and Brooks, Bull. Am. Phys. Soc. **30**, No. 1, 54 (1955).

PHYSICAL REVIEW VOLUME 98, NUMBER 6 JUNE 15, 1955

Optical and Impact Recombination in Impurity Photoconductivity in Germanium and Silicon

N. Sclar and E. Burstein
United States Naval Research Laboratory, Washington, D. C.

(Received February 7, 1955)

The impact (three-body) recombination and optical recombination coefficients are calculated for hydrogen-like impurity centers in extrinsic germanium and silicon in thermal equilibrium. These have been compared with the phonon recombination coefficient calculated by Gummel and Lax for a similar model. It is found that the optical coefficient is always less than the phonon coefficient in the temperature range of interest. The impact ionization coefficient which is proportional to the free carrier concentration may be comparable with or greater than the phonon recombination coefficient at 4.2°K in the presence of background radiation and definitely exceeds it at higher temperatures. Comparison with experimental data indicates that none of the mechanisms considered can yet explain the observed time constants.

In phenomena involving deviations from the free charge carrier equilibrium concentration in semiconductors, there are generally several different mechanisms that tend to bring the system back to equilibrium. The time constant for the phenomenon will depend on which mechanism is dominant in effecting the return to equilibrium. The purpose of this note is to analyze the mechanisms contributing to the time constant for impurity photoconductivity in extrinsic semiconductors. This is accomplished by comparing the various recombination coefficients calculated on the basis of a simplified model. The recombination coefficients considered to be of importance are B_p, B_0 and $B_I n$. B_p is the phonon (nonradiative) recombination coefficient which consists of recombination with the emission of phonons; B_0 is the optical (radiative) recombination coefficient which consists of recombination with the emission of photons, and $B_I n$ is the impact (three-body) recombination coefficient which consists of recombination with the excitation of a second free carrier, i.e., the inverse of impact ionization. The simplified model used consists in representing the impurity centers as hydrogen-like. The bound charge carrier of effective mass m^* is considered to exist in a stationary state about the impurity ion under the influence of a net unit charge reduced by the dielectric constant of the medium. By using this model, the optical (radiative) and impact (three-body) recombination coefficients are calculated and compared with the phonon (nonradiative) coefficient calculated by Gummel and Lax for a similar model. Unfortunately, none of the mechanisms considered can yet explain the short time constants found experimentally.

Impurity photoconductivity due to the photoionization of bound charge carriers at neutral impurity centers is observed at low temperatures in germanium and silicon doped with elements from the III and V columns of the periodic table.[1,2] Under conditions of small signals, where deviations from the equilibrium concentration of charge carriers are small and where thermal equilibrium between the charge carriers and the lattice

[1] Burstein, Oberly, and Davisson, Phys. Rev. **89**, 331 (1953).
[2] V. B. Rollin and E. L. Simmons, Proc. Phys. Soc. (London) **B65**, 995 (1952); Burstein, Davisson, Bell, Turner, and Lipson, Phys. Rev. **93**, 65 (1954).

may be considered to be preserved, the equation governing the photoresponse is

$$\Delta\sigma/\sigma=\Delta n/n=S\tau/n, \tag{1}$$

where $\Delta\sigma/\sigma$ is the fractional change in conductivity produced by the incident radiation and $\Delta n/n$ is the corresponding fractional change in free charge carrier concentration. S is the rate of optical generation of carriers per unit volume by the incident radiation and τ is the time constant for photoconductivity which may be written as

$$\tau=1/(B_T N_c) \text{ sec}. \tag{2}$$

Here N_c is the concentration of compensated centers (equal to concentration of acceptors in n-type material and concentration of donors in p-type material) and B_T is the total recombination coefficient.

$$B_T=B_p+B_0+B_I n \text{ cm}^3 \text{ sec}^{-1}. \tag{3}$$

From Eq. (3) we see that when one of the recombination coefficients becomes dominant, it controls the time constant for photoconductivity.

The rate equation, neglecting diffusion and surface effects, which describes the transient behavior of the free charge carriers is

$$dn/dt=(A_p+A_0+A_I n)(N-N_c-n) +S-(B_p+B_0+B_I n)n(N_c+n). \tag{4}$$

N is the concentration of photoconductive centers, A_p is the probability of "thermal" ionization of the centers by the absorption of phonons associated with the lattice vibrations; A_0 is the probability of "thermal" ionization by the absorption of photons associated with the black body radiation within the specimen; and $A_I n$ is the probability of "thermal impact ionization" of the centers by free carriers. The word "thermal" here denotes that the processes described occur at thermal equilibrium. The B_p, B_0, and $B_I n$ are the corresponding "thermal" recombination coefficients already defined.

The A's and B's are related by the principle of detailed balance:

$$A_p/B_p=A_0/B_0=A_I n/B_I n=K, \tag{5}$$

where K, the equilibrium constant, is

$$K=(2\pi m^* kT/h^2)^{\frac{3}{2}} \exp(-E_i/kT), \tag{6}$$

where m^* is the effective mass of the charge carrier, E_i is the ionization energy of the center, and T is the absolute temperature. The other symbols have their customary meanings.

The impurity levels of the group III and group V impurity centers in germanium and silicon can be interpreted in terms of a hydrogen model.[3,4] The applicability of the hydrogen model allows ready calculation of the pertinent recombination coefficients by suitable modification of the theoretical results already available for the hydrogen atom. Each of the coefficients involve recombinations to excited states as well as to the ground state. For the purpose of comparing the relative order of magnitude of the coefficients, however, recombinations involving transitions only to the ground state are considered.

We now calculate B_0, the optical recombination coefficient. The cross section, R_0,[5] for the optical recombination of a hydrogen-like center in the medium of the semiconductor for the range of velocities of interest here is

$$R_0=\frac{(n')^3}{D}\frac{2^3\pi^2 e^2\hbar}{3m^{*2}c^3}\frac{E_i}{W}(\exp-4) \text{ cm}^2. \tag{7}$$

(n') is the refractive index, D is the dielectric constant of the medium, c is the velocity of light, W is the kinetic energy of the free carrier, and the other symbols have their customary meanings. The optical coefficient B_0 is obtained by multiplying R_0 by the speed of the charge carrier, v, weighting with the Boltzmann distribution and integrating over the speeds of the carriers.

$$B_0=\int_0^\infty R_0(v)vf(v)dv \text{ cm}^3 \text{ sec}^{-1}, \tag{8}$$

where

$$f(v)=\frac{4\pi B^3}{\pi^{\frac{1}{2}}}v^2\exp(-B^2v^2),$$

with $B^2=m^*/2kT$. Upon carrying through the indicated integration we obtain

$$B_0=\frac{(n')^3}{D}\left(\frac{m_0}{m^*}\right)^{5/2}\times 1.21\times 10^{-12}\frac{E_i \text{ (ev)}}{T^{\frac{1}{2}}} \text{ cm}^3 \text{ sec}^{-1}, \tag{9}$$

where m^*/m_0 is the ratio of effective mass to free-electron mass.

To calculate $B_I n$, the impact recombination coefficient, we calculate the rate of ionization and then use the principle of detailed balance to obtain the desired result. The cross section, Q_0, for ionization of a hydrogen-like center calculated by the Born approximation[6] is

$$Q_0=0.285\frac{4\pi e^4}{DE_i W}\ln\left(\frac{4WD}{0.048E_i}\right) \text{ cm}^2. \tag{10}$$

The use of the Born approximation tends to overestimate the cross section but it is known to give the correct order of magnitude. The probability of ionization, A_I, due to this mechanism is

$$A_I=\int_{v_i}^\infty Q_0 vf(v)dv \text{ cm}^3 \text{ sec}^{-1}, \tag{11}$$

[3] G. L. Pearson and J. Bardeen, Phys. Rev. **75**, 865 (1949).
[4] Burstein, Bell, Davisson, and Lax, J. Phys. Chem. **57**, 849 (1953).
[5] H. Bethe, *Handbuch Der Physik* (Verlag Julius Springer, Berlin, 1933), second edition, Vol. 24.1, pp. 477, 488.
[6] N. F. Mott and H. S. W. Massey, *Theory of Atomic Collisions* (Clarendon Press, Oxford, 1952), second edition, p. 247.

TABLE I. Summary of recombination coefficients at 4.2°K for hydrogen-like impurities in silicon and germanium.

Quantity[a]	Germanium		Silicon	
	n-type	p-type	n-type	p-type
E_i ionization energy (ev)	0.01	0.01	0.04	0.046
m^*/m effective mass ratio[b]	0.2	0.2	0.4	0.5
B_0 optical coefficient cm³ sec⁻¹	1.3×10^{-12}	1.3×10^{-12}	7.9×10^{-13}	5.2×10^{-13}
B_p phonon coefficient cm³ sec⁻¹	3.5×10^{-9}	7.3×10^{-9}	1.0×10^{-8}	1.9×10^{-8}
B_p/B_0	2.7×10^{3}	5.6×10^{3}	1.3×10^{4}	3.7×10^{4}
$B_I n$ impact coefficient cm³ sec⁻¹	$3.5\times10^{-18}\,n$	$3.5\times10^{-18}\,n$	$2.9\times10^{-19}\,n$	$1.2\times10^{-19}\,n$
$B_p/B_I=n^*$ cm⁻³	1.0×10^{9}	2.1×10^{9}	3.5×10^{10}	1.6×10^{11}
T^* (°K)	7.0	7.5	27	38

[a] n^* is the calculated free carrier concentration when the coefficients for impact and phonon recombination are equal. T^* is the minimum temperature at which n^* is given by Eq. (15) with $(N-N_c)/N_c$ chosen equal to 10.
[b] m^*/m is adjusted to fit the hydrogen model and is used for free as well as bound carriers.

where the lower limit of the integral is v_i, the velocity of the charge carriers corresponding to the ionization energy. This gives

$$A_I=\frac{5.88\times10^{-4}}{E_i\,(\text{ev})\,T^{\frac{1}{2}}}\left(\frac{m_0}{m^*}\right)^{\frac{1}{2}}\times\frac{(1+0.522\log_{10}D)}{D}\exp(-E_i/kT). \quad (12)$$

The principle of detailed balance yields

$$B_I=A_I/K. \quad (13)$$

Combining Eqs. (12), (13), and (6), we get the result

$$B_I=\frac{2.44\times10^{-19}}{T^2E_i\,(\text{ev})}\left(\frac{m_0}{m^*}\right)^2\frac{(1+0.522\log_{10}D)}{D}\ \text{cm}^6\ \text{sec}^{-1},$$

and the impact recombination coefficient

$$B_I n=\frac{2.44\times10^{-19}}{T^2E_i\,(\text{ev})}n\left(\frac{m_0}{m^*}\right)^2\times\frac{(1+0.522\log_{10}D)}{D}\ \text{cm}^3\ \text{sec}^{-1}. \quad (14)$$

For the range of temperatures where impurity photoconductivity is measured, the thermal equilibrium concentration of free carriers may be expressed as

$$n=[(N-N_c)/N_c]K. \quad (15)$$

The impact ionization recombination constant then becomes

$$B_I n=\frac{5.88\times10^{-4}}{E_i\,(\text{ev})}\frac{N-N_c}{N_c}\left(\frac{m_0}{m^*}\right)^{\frac{1}{2}}\frac{1}{T^{\frac{1}{2}}}\times\frac{(1+0.522\log_{10}D)}{D}\times\exp(-E_i/kT). \quad (16)$$

In practice, photoconductivity is usually measured in the presence of background radiation, in which case n will be orders of magnitude higher than that given by Eq. (15).

The phonon coefficient for recombination has been calculated by Gummel and Lax.[7] Their result is

$$B_p=\frac{256\pi^{\frac{1}{2}}\Omega\epsilon_1^2}{ME_iab}\frac{1}{(\tau_0 a)^4}\left(\frac{\hbar^2}{2m^*a^2kT}\right)^{\frac{1}{2}}\ \text{cm}^3\ \text{sec}^{-1}, \quad (17)$$

where Ω is the volume of unit cell, ϵ_1 is the Bardeen-Shockley deformation potential constant, M is the mass of one atom, b is the velocity of sound, a is the Bohr radius in the crystal, and τ_0 is the propagation constant of a phonon whose energy is equal to the ionization energy E_i. The constant ϵ_1 may be evaluated[8] in terms of the lattice mobility, the elastic constants of the material, and the effective masses of the charge carriers. Depending on the values of effective mass used, this coefficient may vary by a factor of two or three. If we take the mass of the free carrier equal to mass of the bound carrier, the effective masses cancel and we obtain

$$B_p=\frac{6.2\times10^{-38}b^5}{T^{\frac{1}{2}}[E_i\,(\text{ev})]^2\mu_L(300°\text{K})}. \quad (18)$$

E_i, the ionization energy, is expressed in electron volts, and μ_L (300°K) is the lattice mobility at 300°K. The above discussion is based on the applicability of the hydrogen model to impurities in silicon and germanium. For those impurities such as gold and copper which cannot be described in this way, the discussion does not apply although qualitatively similar discussions may be possible. Deviations from the simple hydrogen model also occur even for doping elements from the III and V columns of the periodic table, which may be attributed to the fact that the model does not take into account the structure of the conduction and valence band and the nature of the central atom of the impurity center.[9] Further, it should be emphasized that the recombination coefficients that have been calculated apply only when the temperature of the charge carrier and that of the lattice are the same. When this is not true, as for

[7] H. Gummel and M. Lax, Phys. Rev. **97**, 1469 (1955).
[8] W. Shockley and J. Bardeen, Phys. Rev. **77**, 407 (1950).
[9] Burstein, Picus, Henvis, Schulman, and Lax (to be published).

TABLE II. Comparison of theoretical and experimental time constants.

Specimen No.	Concentration of photoconductive centers $N-N_c$ (cm^{-3})	Concentration of compensated centers N_c (cm^{-3})	Conc. of free charge carriers in the presence of background radiation[a] n (cm^{-3})	τ (theoretical) (sec)	τ (experimental) (sec)
Ge 132	4×10^{15} (p)	$10^{13}-10^{15}$	2×10^{10}	$10^{-6}-10^{-8}$	5×10^{-11}
Si I-123[b]	2×10^{17} (p)	$10^{15}-10^{17}$	6×10^{7}	$10^{-7}-10^{-9}$	2×10^{-12}
Si I-103[b]	4×10^{15} (n)	$10^{14}-10^{15}$	1×10^{8}	$10^{-6}-10^{-7}$	5×10^{-9}
Si (R and S)[c]	2×10^{16} (p)	10^{16}	5×10^{8}	4×10^{-8}	5×10^{-11}

[a] Estimated by assuming mobility of 10^4 cm^2/volt sec for the germanium at 4.2°K and 10^3 cm^2/volt sec for the silicon.
[b] Burstein, Oberly, and Davisson, Naval Research Laboratory Report No. 3880, 1952 (unpublished).
[c] Data of Rollin and Simmons (reference 2) carried out at 20°K.

impact ionization induced by an electric field,[10] a somewhat different treatment must be used.[11]

We compare the recombination coefficients for the different processes at a given temperature, 4.2°K. This comparison is summarized in Table I for typical n- and p-type germanium and silicon specimens. The values given for the competing recombination coefficients have been calculated by assigning the effective masses indicated in the table. These were determined by requiring the hydrogen model to give the correct ionization energy. No allowance has been made for the structure of the valence and conduction band and for the differences in the effective masses for free and bound electrons, in view of the approximate nature of the calculation. From the table, we see that B_0 is always smaller than B_p, the ratio of these constants being about 10^3 and 10^4 in germanium and silicon, respectively. Further, from the identical temperature dependence of these coefficients, this will be the same for all temperatures in the range of interest. Thus, the optical process may always be neglected in favor of the phonon process in determining the time constant. It may be noted, however, that the impact recombination coefficient $B_I n$ is not necessarily small compared to B_p. Included in Table I is the concentration of free charge carriers n_I^* needed to make $B_I n$ equal to B_p. Such concentrations may actually occur in the presence of background radiation, so that, in the absence of explicit information about the free carrier concentration, it is not clear which mechanism is dominant at 4.2°K. Even in the absence of background radiation, however, the exponential temperature dependence of n_I^* causes the impact recombination to become dominant at higher temperatures. The minimum temperature T^* for which this occurs is seen to be about 7°K for germanium and about 30°K for silicon.

It is of interest to compare the time constants obtained by using Eq. (2) with experimentally measured values. To calculate the theoretical value, it is necessary to know the concentration of compensated centers and in the case of impact recombination, the concentration of free charge carriers. The concentration of compensated centers depends on the purification of the specimens and in this respect, earlier materials are likely to have higher concentrations of compensated carriers. Depending on the concentration of the dominant impurity, the concentration may vary from 10^{13}–10^{17} cm^{-3}. The concentration of free charge carriers can be obtained from an actual measurement of the Hall constant or from a measurement of the conductivity, and an estimate of the mobility. Using the latter method, we find that concentrations of free carriers in the presence of background radiation may attain the order of 10^{10} cm^{-3} in germanium and somewhat less than this in silicon. Of the three processes considered, this would make "impact" recombination dominant in germanium and phonon recombination dominant in silicon. In Table II[12] are listed the calculated time constants for p- and n-type silicon and for a p-type germanium sample together with experimental values of the time constant. Experimentally it is difficult to measure directly time constants shorter than about 10^{-4} second because of the combination of high specimen resistances, small signals and unavoidable capacitance associated with the mounting of the specimens in low-temperature dewars. From Eq. (1), however, it is possible to obtain an estimate of the time constant by determining experimentally $\Delta\sigma/\sigma$, S, and n and this is how the experimental time constants in Table II were obtained.

The theoretical results appear to give time constants that are larger than the experimental results by a factor of about a thousand. Recombination to higher bound states as well as to the ground state considered, may be expected to yield contributions to the recombination coefficients which will be of the same order of magnitude. This will not greatly affect the theoretical estimate of the time constant and does not resolve the discrepancy. It is felt that the use of the hydrogen model to describe impurities in germanium and silicon is not the cause of the large discrepancy but rather that it is due to another unknown mechanism for recombination which is dominant and which has not yet been considered.

[10] Sclar, Burstein, Turner, and Davisson, Phys. Rev. **91**, 215 (1953). Sclar, Burstein, and Davisson, Phys. Rev. **92**, 858 (1953).

[11] N. Sclar and E. Burstein (to be published).

[12] Lerman, Sclar, and Burstein (unpublished).

Microwave Determination of the Average Masses of Electrons and Holes in Germanium*

JAMES M. GOLDEY† AND SANBORN C. BROWN
Department of Physics and Research Laboratory of Electronics, Massachusetts Institute of Technology, Cambridge, Massachusetts
(Received March 3, 1955)

Free current carriers in a medium make a contribution to its dielectric coefficient. The present experiment utilizes this effect to determine the effective masses of electrons and holes in germanium by measuring the microwave dielectric coefficient at several temperatures. The dielectric coefficient was determined by measuring the complex transmission coefficient at 24.15 kilomegacycles/sec through a thin slab of germanium. The effective mass for electron was $(0.09\pm0.05)m_0$; for holes it was $(0.30\pm0.05)m_0$.

BENEDICT and Shockley[1,2] have measured the effective mass of electrons and holes in germanium by measuring the carrier contribution to the microwave dielectric coefficient. As shown in their first paper, the dielectric coefficient of a medium containing n free electrons (holes) per unit volume of mass m^* which collide with the lattice at a frequency ν_c is given by

$$K=K_0+\frac{\sigma_i}{\omega\epsilon_0}=K_0-\frac{ne^2}{m^*\epsilon_0(\nu_c^2+\omega^2)}, \tag{1}$$

where K_0 is the dielectric coefficient of the medium without the carriers present, σ_i is the imaginary component of the conductivity, and ω is the radian frequency of the applied field. If the electron density, the collision frequency, and the lattice dielectric coefficient, K_0, are known for a given sample, a measurement of K will give the effective mass of the carriers. Since the second term in the expression for K is temperature-dependent through ν_c, and K_0 is temperature independent, K_0 may be eliminated by making measurements at two or more temperatures.

In a semiconductor the electrons are not free, and one must take a critical look into Eq. (1) before applying it to these substances. Wilson[3] has obtained an expression for the dc conductivity of a metal or semiconductor. By making a simple extension of his work to the ac case, we obtain for the conductivity:

$$\sigma=n\int\left(\frac{\nabla_k\epsilon}{\hbar}\right)^2\frac{e^2}{\nu_c+i\omega}\frac{df_0}{d\epsilon}d^3k, \tag{2}$$

where ϵ is the energy relative to the band edge. Wilson's expression is the same as this except that it does not include the term $i\omega$. This expression is quite similar to that which one obtains for a free electron gas. In both cases f_0 is the equilibrium distribution function. In this expression $(\nabla_k\epsilon/\hbar)$ appears; in the free gas case it is replaced by v, the electron velocity. In the crystal, however, the group velocity of a wave packet centered about wave number k is given by $(\nabla_k\epsilon/\hbar)$.

In order to carry out the integration of Eq. (2) two things must be known about the semiconductor: the form of the electron energy state *vs* crystal momentum curve, and the dependence of the collision frequency ν_c on k. We have investigated the effect of different types of dependence of ν_c on k on the numerical values obtained for the mass.

Assuming spherical energy surfaces and using typical experimental data, we have calculated the effective mass for the two cases of constant collision frequency and constant mean free path. The same value was used for the mobility in each case. The numerical values obtained for the mass were the same to within less than 5 percent for the frequency employed in the present experiment. We shall therefore assume that ν_c is constant over the distribution in further calculation.

It has recently been proposed by Lax, Zeiger, Dexter, and Rosenblum[4] that the bottom of the conduction band in germanium lies along the 111 axes and that the surfaces of constant energy near the minimum are ellipsoids of revolution about these axes. If one assumes a model of this type, the so-called nondegenerate many-valley model, integration of (2) leads to (1) with the effective mass given by

$$m^*=3m_1m_2/(2m_1+m_2), \tag{3}$$

where m_1 is the longitudinal and m_2 the transverse mass.

Herring[5] has also examined this problem and has expressed his result in a different form. In place of (1), he obtains

$$K=K_0-\frac{n\mu\mu_Hm^*}{\gamma}\left[1-\frac{\omega^2m^{*2}\mu\mu_H}{\gamma e^2}\eta+O(\omega^4)\right], \tag{4}$$

where μ is the drift, and μ_H is the Hall mobility, m^* is as given in (3), γ is given by

$$\gamma=\frac{3r(2+r)}{(1+2r)^2},\quad\text{with } r=m_1/m_2, \tag{5}$$

* This work was supported in part by the Signal Corps; the Office of Scientific Research, Air Research and Development Command; and the Office of Naval Research.
† Now at Bell Telephone Laboratories, Murray Hill, New Jersey.
[1] T. S. Benedict and W. Shockley, Phys. Rev. **89**, 1152 (1953).
[2] T. S. Benedict, Phys. Rev. **91**, 1565 (1953).
[3] A. H. Wilson, *The Theory of Metals* (Cambridge University Press, London, 1953), second edition.
[4] Lax, Zeiger, Dexter, and Rosenblum, Phys. Rev. **93**, 1418 (1954).
[5] C. Herring, Bell System Tech. J. **34**, 237 (1955).

and η is

$$\eta=\frac{\langle\epsilon/\nu_c^4\rangle\langle\epsilon\rangle}{\langle\epsilon/\nu_c^2\rangle^2}, \tag{6}$$

where the angular brackets denote Maxwellian averages.

Herring's result follows directly from (2) but is more general than ours in that his only assumption with regard to ν_c is that it is a function of energy only. His expression gives a slightly different numerical value of the mass from that given by Eq. (1). This is because the mean free path is not constant over the distribution but is energy-dependent because of the intervalley scattering of electrons and the optical as well as acoustical mode intravalley scattering. His result, Eq. (4), allows the calculation of effective masses without a knowledge of the details of the scattering process, so long as μ, μ_H, and γ are known.

It has been suggested[6,7] that the top of the valence band in germanium is twofold-degenerate and that the energy near the band edge is given by

$$\epsilon=\epsilon_0+\frac{\hbar^2}{2m_0}\{Ak^2\pm[B^2k^4+2C^2(k_x^2k_y^2+k_y^2k_z^2+k_z^2k_x^2)]^{\frac{1}{2}}\}. \tag{7}$$

In this case there is a two-carrier system, one set of holes being in the band corresponding to the plus sign, the other in the band corresponding to the minus sign. For energy surfaces of this type we are again led to (1), with m^* given by

$$m^*=n\left(\frac{n_1}{m_1}+\frac{n_2}{m_2}\right)^{-1}, \tag{8}$$

where n_1 and n_2 are the densities in the two bands, $n=n_1+n_2$, and m_1 and m_2 are suitable average masses for the two bands. m_1 and m_2 depend on A, B, and C of (7) through the usual relation

$$m^*=\frac{1}{\hbar^2}\frac{\partial^2\epsilon}{\partial k^2}. \tag{9}$$

We have repeated the experiments of Benedict and Shockley using similar techniques. The measurements were made on a 24 000-Mc/sec microwave bridge by measuring the complex transmission coefficient for electromagnetic radiation through a thin slab of germanium. This quantity yields both the dielectric coefficient and the conductivity of the material.[8] Data were obtained on several samples, four of which were n-type and three of which were p-type. The room temperature resistivities of the samples were in the 3.5-6 ohm-cm range. Measurements were made at 295°K and 201°K. The electron (hole) density is constant in this range, the mobility being the only temperature-dependent quantity.

Our results do not agree with those of Benedict and Shockley. For electrons, we obtain a value of $M^*=0.10\pm0.05\ m_0$ if the calculations are made according to (1). We obtain a value of $m^*=0.08\pm0.04\ m_0$ for the electron mass if we use (4), assuming a value of 17 for the ratio of the longitudinal to the transverse mass as determined by the resonance experiments.[4] The mobility was observed to vary as $T^{-1.7}$, which is in good agreement with other measurements.[9] From our measurements we obtain $K_0=16.4\pm0.2$, also in good agreement with other values.[10]

On the p-type samples we measured a hole mass of $m^*=0.32\pm0.05\ m_0$. Here the mobility varied as $T^{-2.2}$, whereas the standard value[9] is $T^{-2.3}$. If we make the calculations assuming a $T^{-2.3}$ variation our data indicate a mass of $m^*=0.29\pm0.05\ m_0$. On the p-type samples, we obtained a value of 16.6 ± 0.3 for K_0.

Benedict and Shockley obtained a value of $m^*=0.6\ m_0$ for electrons, making their calculations in the same way that led us to $0.10\ m_0$. The cyclotron resonance experiments[4] give a value of $1.3\ m_0$ for m_1, and $0.08\ m_0$ for m_2, which, according to (3), gives $m^*=0.12\ m_0$. Magnetic susceptibility measurements by Crawford and Stevens[11] yield a value of $0.15\pm0.02\ m_0$ for the electron mass.

D'Altroy and Fan[12] at Purdue have measured microwave properties of germanium at 3 cm. Over a temperature range from 20°K to 300°K they measure an average hole mass of 0.63 m_0. They do not quote an electron mass.

For holes, Benedict obtained a mass of about $0.3\ m_0$, where he made his calculations according to (4), assuming γ and $\eta=1$. In the light of resonance experiments on p-type germanium[7] the ellipsoidal model does not appear to be correct for the valence band, however. From his data, it would appear that Benedict would have obtained a mass of about $0.45\ m_0$ had he made his calculations according to (1). In their susceptibility measurements, Crawford and Stevens obtained a hole mass of $m^*=0.23\pm0.03\ m_0$. The resonance experiments of Dexter, Zeiger, and Lax[7] determined values of the coefficients A, B, and C appearing in Eq. (7). We have used their values in a numerical integration of Eq. (2). This gives an effective mass, calculated according to Eq. (8), of $m^*=0.27\ m_0$.

In Table I we list these results and the temperatures at which they were obtained. Even though the resonance experiments were carried out at 4°K, we feel that there is some justification in comparing the present results with them in view of the susceptibility measurements. There has also been some recent theoretical

[6] Dresselhaus, Kip, and Kittel, Phys. Rev. **95**, 568 (1954).
[7] Dexter, Zeiger, and Lax, Phys. Rev. **95**, 557 (1954).
[8] C. G. Montgomery, *Techniques of Microwave Measurement* (Radiation Laboratory Series, McGraw-Hill Book Company, Inc., New York, 1947), Vol. II, p. 565.
[9] F. J. Morin, Phys. Rev. **93**, 62 (1954).
[10] H. B. Briggs, Phys. Rev. **77**, 287 (1950). (See also reference 1.)
[11] L. H. Crawford and D. K. Stevens, Phys. Rev. **94**, 1415(A) (1954); **92**, 1065 (1953).
[12] F. A. D'Altroy and H. Y. Fan, Phys. Rev. **94**, 1415(A) (1954).

TABLE I. Comparison of measurements on germanium.

Experimenters	Benedict, Shockley	Lax, Zeiger, Dexter	Crawford, Stevens	Present
Temperature	160–300°K	4°K	65–300°K	200°–300°K
Electron mass	$0.6\,m_0$	$0.12\,m_0$	$0.15\,m_0\pm0.02\,m_0$	$0.10\,m_0\pm0.05\,m_0$ $0.08\,m_0\pm0.04\,m_0$
Hole mass	$\approx0.45\,m_0$	$0.27\,m_0$	$0.23\,m_0\pm0.03\,m_0$	$0.29\,m_0\pm0.05\,m_0$ $0.32\,m_0\pm0.05\,m_0$

work by Abeles and Meiboom[13] on magnetoresistance in germanium. They find agreement between their theory and the experimental results obtained by Pearson and Suhl[14] at 77°K and 300°K on *n*-type germanium if they assume the eight ellipsoidal model and a mass ratio of 20. The mass ratio obtained in the resonance experiments was 17.

[13] B. Abeles and S. Meiboom, Phys. Rev. **95**, 72 (1954).
[14] G. L. Pearson and H. Suhl, Phys. Rev. **83**, 768 (1951).

The authors are indebted to Dr. B. Lax and Dr. H. Zeiger, of the Lincoln Laboratory, for helpful discussion; to Professor W. P. Allis of this Laboratory for help with the theory; and to Dr. John A. Hornbeck, of the Bell Telephone Laboratories, and Professor J. Earl Thomas, of the Lincoln Laboratory, for supplying the germanium samples. They would also like to thank Dr. C. Herring, of the Bell Telephone Laboratories, for permission to use his results prior to publication.

PHYSICAL REVIEW VOLUME 98, NUMBER 6 JUNE 15, 1955

Direct Measurement of the Effect of Polarization on Energy Loss*

E. L. GOLDWASSER, F. E. MILLS, AND T. R. ROBILLARD
Physics Department, University of Illinois, Urbana, Illinois

(Received October 8, 1954; revised manuscript received March 2, 1955)

The energy losses suffered by 15.7-Mev electrons in traversing samples of about one gram per cm² of absorber in gas and solid form have been measured. Two pairs of absorbers have been used; perfluorocyclobutane gas and its polymer, tetrafluoroethylene resin, "Teflon," and chlorotrifluoroethylene gas and its polymer, "Kel-F" plastic. The losses measured were of the order of one Mev and the resolution of the apparatus made possible an accuracy of 20 kev. The measured losses compared with theoretical predictions are as follows: Teflon—gas 1.33 Mev by experiment and 1.33 Mev by theory, solid 1.27 Mev by experiment and 1.24 Mev by theory; Kel-F—gas 1.29 Mev by experiment and 1.33 Mev by theory, solid 1.09 Mev by experiment and 1.11 Mev by theory.

INTRODUCTION

THERE has been a long series of discussions and experiments presented and performed in the study of ionization losses of charged particles in passing through material media.[1–12] Many of these have pursued, in particular, the effect of the density of the medium upon the ionization loss suffered by a charged particle in traversing that medium. In most cases this change in ionization loss (density or polarization effect) has been observed indirectly. It was the purpose of the present work to observe the difference directly by passing 15.7-Mev electrons through equal numbers of grams/cm² of gases and solids of the same chemical composition.

EXPERIMENTAL ARRANGEMENT AND PROCEDURE

The experimental arrangement and procedure followed were almost identical with those employed in the measurement of ionization loss and straggling of fast electrons.[12] For future reference the paper describing that work will be referred to as G.M.H. The experimental arrangement is shown in Fig. 1. The absorbers, both solid and gaseous, were contained in a brass cylinder 16 in. long and 2 in. in diameter. The ends of the cylinder were sealed with 5-mil foils of "Mylar" film. The entrance end was stopped down to a 1-in. diameter circular hole. The exit end was at the center of the scattering chamber and contained a horizontal

* Supported by the joint program of the Office of Naval Research and the U. S. Atomic Energy Commission.
[1] M. S. Livingston and H. A. Bethe, Revs. Modern Phys. **9**, 285 (1937).
[2] L. Landau, J. Phys. (U.S.S.R.) **8**, 201 (1944).
[3] E. Fermi, Phys. Rev. **57**, 485 (1940).
[4] O. Halpern and H. Hall, Phys. Rev. **73**, 477 (1948).
[5] G. C. Wick, Nuovo cimento (9) **1**, 302 (1943).
[6] R. M. Sternheimer, Phys. Rev. **88**, 851 (1952).
[7] T. Bowen and F. X. Roser, Phys. Rev. **85**, 992 (1952).
[8] C. S. Carter and W. L. Whittemore, Phys. Rev. **87**, 494 (1952).
[9] A. Hudson and R. Hofstadter, Phys. Rev. **88**, 589 (1952).
[10] Charles Warner, III, and Fritz Rohrlich, Phys. Rev. **93**, 406 (1954).
[11] Palmatier, Meers, and Askey, Phys. Rev. **94**, 766 (1954).
[12] Goldwasser, Mills, and Hanson, Phys. Rev. **88**, 1137 (1952).

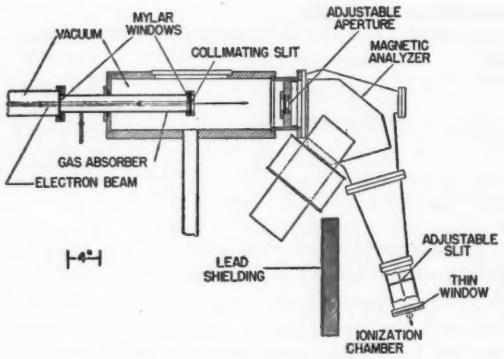

FIG. 1. Side view of absorber and analyzer.

gold slit $\frac{1}{16}$ in. high and $\frac{1}{2}$ in. long. The gaseous samples occupied the entire volume of this cylinder, while the solids were distributed evenly along its length in sections approximately $\frac{1}{32}$ in. thick. From the exit slit through the magnetic analyzer to the ionization chamber and vibrating reed detector, the experimental arrangement was identical with that described in G.M.H. The calibration and resolution of the equipment was also the same as in G.M.H.

ABSORBERS

In order to have an error of the order of 2 percent in the measured energy losses, it was necessary to use samples with a thickness of about 1 g/cm². Gases of high molecular weights had to be found to give thicknesses of this order in the available space at a convenient temperature and at a pressure which could be contained by relatively thin windows. Two different gas-solid pairs of absorbers were found which satisfy this criterion: perfluorocyclobutane gas (molecular weight =200) and its polymer, tetrafluoroethylene resin (Teflon); and chlorotrifluoroethylene gas (molecular weight=116.5) and its polymer, Kel-F plastic. These gases have a behavior which departs significantly from the ideal gas law in the region investigated. Thus in order to measure their thicknesses in g/cm², the length of the container and the density of the gas under the conditions of the experiment were accurately measured.

Perfluorocyclobutane is composed of fluorine and carbon in the ratio 2:1; chlorotrifluoroethylene is composed of fluorine, carbon, and chlorine in the ratio 3:2:1. A study made of the effect of chemical structure on stopping power[13] indicates that the effect of the chemical bonding involved in polymerization is negligible in the results of this experiment.

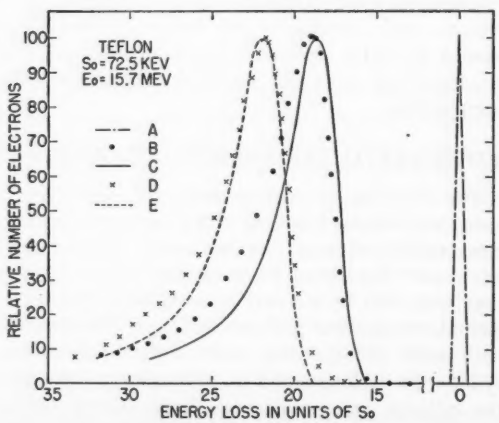

FIG. 2. Energy distributions of: (A) unobstructed electron beam; (B) experimental points for solid Teflon; (C) theoretical prediction for solid; (D) experimental points for Teflon's gaseous monomer; (E) theoretical prediction for gas.

THEORY

Theoretical work done by Landau[2] and others and described in G.M.H. gives for the most probable energy

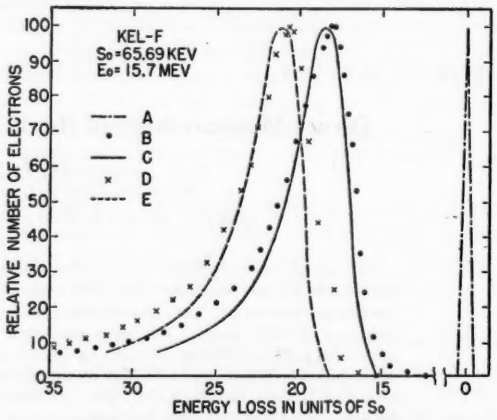

FIG. 3. Energy distributions of: (A) unobstructed electron beam; (B) experimental points for solid Kel-F; (C) theoretical prediction for solid; (D) experimental points for Kel-F's gaseous monomer; (E) theoretical prediction for gas.

loss:

$$\Delta_p = S_0\left[\ln\frac{2mc^2\beta^2 S_0}{(1-\beta^2)I^2} - \beta^2 + 0.37\right], \qquad (1)$$

where $S_0 = 2\pi e^4 nt/m\beta^2c^2$; m, e are the electron charge and mass, β is velocity of particle in units of the velocity of light, c; n=number of electrons/cc; and I is the mean ionization potential for the absorbing medium.

In this paper the I values used are calculated in accordance with the method described by Sternheimer.[6] This gives for Teflon $I_T=120$ ev and for Kel-F, $I_K=140$ ev. The energy loss in chemical compounds has been treated as if they were mixtures of the proper proportions of disassociated atoms. The mean ionization potential has been found to be, quite closely, directly

[13] T. J. Thompson, Phys. Rev. 92, 1083 (1953).

proportional to the atomic number, Z, and is commonly expressed in the form $I=KZ$. For the chemical compounds of this experiment, it may be written

$$I=KZ_{\text{eff}}, \tag{2}$$

where the effective Z of the compound is given by:

$$\ln\frac{1}{Z_{\text{eff}}^2}=\sum_i \frac{n_i}{n}\ln\frac{1}{Z_i^2}. \tag{3}$$

Here n_i and Z_i are the electron density and atomic number of the ith component of the compound. The values of I calculated above then correspond to $K=14.6$ for Teflon and $K=14.0$ for Kel-F. These numbers are somewhat higher than would be expected from the work of Bakker, Mather, and Segrè[14,15] as corrected by Sternheimer.[16]

Equation (1) does not take into account the shielding effects occurring in condensed media as a result of the polarization of the medium in the region of the path of the charged particle. This phenomenon has been treated theoretically by many authors.[3–6] All agree in one essential; that as the energy of the particle increases, its rate of energy loss asymptotically approaches a limiting value. As shown in G.M.H. this value is independent of the constant, I. The asymptotic value of the most probable energy loss is:

$$\Delta_{pc}=S_0[19.43+\ln(D/\rho)], \tag{4}$$

where ρ=volume density of the absorber in g/cm³ and D=surface density of the absorber in g/cm².

In between the region of no density effect and that of the asymptotic value of energy loss, the energy loss can be calculated by methods given by Sternheimer.[6] The solid and gas samples used in this work have density ratios of about 100. For the electron energy used, the gases both lay in the region of very small density effect, the solids in the region of asymptotic energy loss.

TABLE I. Theoretical and observed values of energy losses and straggling distribution widths in gaseous and solid samples.

		D g/cm²	ρ g/cm³	S_0 Mev	Expt. $\Delta_{\frac{1}{2}}$ Mev	Expt. Γ/S_0	Theory $\Delta_{\frac{1}{2}}$ Mev	Theory Γ/S_0
F_2C	Solid	0.9832	2.09	0.0725	1.27	4.7	1.24	3.98
	gas	0.9003	0.0218	0.0664	1.33	4.4	1.33	3.98
F_3C_2Cl	Solid	0.8889	2.13	0.0657	1.09	4.7	1.11	3.98
	gas	0.9135	0.0221	0.0675	1.29	4.6	1.33	3.98

[14] C. J. Bakker and E. Segrè, Phys. Rev. 81, 489 (1951).
[15] R. Mather and E. Segrè, Phys. Rev. 84, 191 (1951).
[16] R. M. Sternheimer, Phys. Rev. 93, 351 (1953).

DISCUSSION OF RESULTS

As described in G.M.H., the experimental data are more sensitive to the position of the "upper-half point" than to that of the peak of the straggling distribution. The "upper-half point" is the point having one-half of the peak intensity value and lying on the high-energy (steep) side of the peak. The shape of the Landau distribution is such that this point is related to the most probable value by the equation, $\Delta_{\frac{1}{2}}=\Delta_p-1.58S_0$. In Table I are given the unnormalized experimental results and corresponding theoretical values. The full width of the straggling distribution at $\frac{1}{2}$ intensity, Γ, is a parameter useful in considerations of the shape of the distribution and is also presented below. It was impossible to obtain identical gas and solid sample thicknesses. Therefore, for convenience, in plotting the results the parameter used is $\Delta_{\frac{1}{2}}/S_0$, since this has only a very small dependence on sample thickness. A small correction, $+\ln(D_{\text{solid}}/D_{\text{gas}})$, has been applied to normalize the thickness of each gas sample to that of its solid. The experimental results and corresponding theoretical curves, normalized in this way, are presented in Figs. 2 and 3.

TABLE II. Theoretical and observed values of the reduction in ionization loss by the density effect, for the two pairs of absorbers used.

	$\delta(\Delta_{\frac{1}{2}}/S_0)$ Observed	Theory
F_2C	2.8±0.4	3.0
F_3C_2Cl	2.6±0.4	2.6

The agreement of theoretical and experimental energy losses is well within the accuracy of the data. A systematic broadening of the experimental straggling distributions is observed. This was not true of the work described in G.M.H. and is thought to arise from electrons scattered from the walls of the brass sample container.

A comparison of the observed and calculated density effect, $\delta(\Delta_{\frac{1}{2}}/S_0)$, is made in Table II. The indicated errors are based on a 20-kev uncertainty in the absolute measurement of each energy.

ACKNOWLEDGMENTS

We should like to express our appreciation to the E. I. Dupont de Nemours and M. W. Kellog Companies for their cooperation in supplying the samples used in this experiment, also to Professor A. O. Hanson for his help at all stages of the work.

Water-Vapor-Induced *n*-Type Surface Conductivity on *p*-Type Germanium*

R. H. KINGSTON†
Lincoln Laboratory, Massachusetts Institute of Technology, Cambridge, Massachusetts
(Received November 3, 1954)

By utilizing a direct reading instrument it is possible to measure the *n*-type surface conductance of the *p*-type germanium in an *n-p-n* junction transistor as a function of relative humidity, ambient gas, and surface treatment. The results of these measurements indicate that the leakage conductance from the emitter to the collector may be predicted on the basis of a constant electron density at the surface which is independent of the applied bias but a critical function of the oxidation of the surface and the adsorbed gas. This conductance exhibits a transient character upon change in applied bias which may be correlated with similar transients in the conductance of a thin germanium crystal upon application of an external applied field. This comparison establishes that the inversion layer is caused by ionization of surface impurities rather than migration of ions along the surface. From the results of the experiments it is postulated that the density and type of carrier at the surface of an etched germanium crystal are a function of the surface treatment and gaseous ambient rather than the acceptor and donor density of the bulk germanium.

INTRODUCTION

EARLY in the study of the junction transistor[1] it was observed that the experimental behavior was not in complete agreement with the theory. In particular, variation of the ambient surrounding the semiconductor was found to cause anomalous changes in the electrical characteristics. These discrepancies, which were attributed to the surface of the semiconductor, were first studied by Brown[2] who explained one of the more troublesome phenomena, channeling. A channel consists of a thin layer of *n*-type material on the surface of the *p*-type base region of an *n-p-n* germanium junction transistor and produces an ohmic path from the emitter to the collector. Brown determined that this *n*-type inversion layer could be attributed to the presence of excess positive charge on the surface of the germanium as a result of the applied voltage between the *n*- and *p*-type regions of the transistor. He further showed that once the charge has been established by the applied bias, the unit can be immersed in a temperature bath (−78°C) and the charge stabilized. The conductance of the channel is then found to decrease with increasing bias until the excess positive charge on the surface is completely neutralized by ionized acceptors in the space-charge region beneath the surface. At this bias no conduction electrons are necessary to neutralize the surface charge and the channel "pinches off." In general this effect was found to be produced in the presence of water vapor although alcohol and other vapors produced similar results.

The work to be described in this paper is a quantitative study of the room temperature behavior of the channel in the presence of moist nitrogen and oxygen. Brown experienced difficulty in making bridge measurements of channel conductance at room temperature due to instability; therefore a direct reading instrument was used which made possible instantaneous measurements. In addition, the moisture content of the gas used as ambient was controlled precisely, in order to reduce these instabilities and obtain a quantitative relation between conductance and vapor pressure. The preliminary results already reported[3,4] have been modified and extended and, it is hoped, give a further insight into the structure of the surface as well as an explanation of some of the anomalies of junction diode and transistor behavior.

EXPERIMENTAL APPARATUS

1. Conductance Measurement

The circuit of Fig. 1 was used to obtain a direct reading of channel conductance as a function of the voltage, ambient, and surface treatment. Here the *n*-type emitter and collector are maintained at ground potential for dc. A low-impedance 1000-cps oscillator supplies a measuring signal across the series combination of the channel and an adjustable load resistor. The signal is then amplified and detected by a tuned amplifier and the output read directly as channel conductance after reference to a calibration chart. Since the maximum rms voltage across the channel is 0.1 volt, the power dissipated is at most 2 microwatts corresponding to a channel conductance of 2×10^{-4} mhos. The high selectivity of the amplifier allows measurements as low as 10^{-7} mhos without interference from

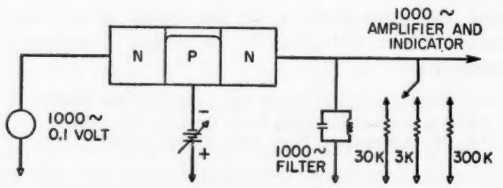

FIG. 1. Channel conductance measuring apparatus.

* The research in this document was supported jointly by the Army, Navy, and the Air Force under contract with the Massachusetts Institute of Technology.

† Staff Member, Lincoln Laboratory, Massachusetts Institute of Technology.

[1] Shockley, Sparks, and Teal, Phys. Rev. **83**, 151 (1951).

[2] W. L. Brown, Phys. Rev. **91**, 518 (1953).

[3] R. H. Kingston, Phys. Rev. **93**, 346 (1954).

[4] R. H. Kingston, Phys. Rev. **94**, 1416 (1954).

stray ac pickup or noise. Additional electrical measurements are described in the section on experimental results.

2. Humidity Control

In the preliminary experiments wet or dry nitrogen or oxygen were supplied by either bubbling the gas through water or passing it through a BaO drying tube. Later, when it was found that the amount of moisture was a critical quantity a system was devised for maintaining a selected set of relative humidities over the sample. This was accomplished by circulating the gas in a closed system over a saturated aqueous salt solution and through the chamber containing the specimen. The gas was circulated by a pump having a tight seal from the atmosphere and the apparatus was kept under a small partial pressure to prevent leakage of air into the system. The salt solution bottles and the sample chamber were kept in a water bath to maintain thermal equilibrium, since a slight difference in sample temperature and salt-bath temperature would produce a reasonable discrepancy in relative humidity over the sample. The salts used with their relative humidities are given in Table I. These were found in the International Critical Tables[5] and were chosen to have a negligible variation in relative humidity over the range of temperature, 20 to 30°C. The humidities were checked in the system with a standard dew-point indicator and found to be accurate within 2 to 3 percent.

TABLE I. Saturated aqueous salt solutions.

Salt	Relative humidity (percent)
LiCl	15
$MgCl_2$	32
K_2CO_3	43
NaBr	58
NaCl	75
$BaCl_2$	88

3. Sample Preparation

The data to be discussed were taken on bars from several n-p-n germanium grown-crystals. Specifically, those of Figs. 2 and 3 are from production type crystals kindly supplied by the Bell Telephone Laboratories and having dimensions and resistivities similar to those used by Brown. The remaining data were observed with a special crystal having a wide p-type base region thus facilitating accurate measurements of base width and resistivity. The constants for this crystal were determined by the methods of Goucher and Prince[6] and are given in Table II. The transistor structures were prepared by cutting the crystal into bars, wet-lapping with 600-mesh carborundum, and attaching nickel leads to the ends with antimony-tin solder. After etching in CP-4, the base contact was made by bonding a 0.002-in. gallium-doped gold wire to the base region. One advantage of the special wide-base crystal was the ease with which the bond could be located at the center of the base region. In the production-type crystals, having approximately 0.002-in. base width, the gold alloy region generally overlapped onto the collector material giving excess collector to base reverse current at high humidities, thus limiting the reverse biassing range. The samples, after bonding were rinsed in carbon tetrachloride, alcohol, and distilled water, mounted on a glass-taper lead assembly, and placed in the experimental chamber.

TABLE II. Constants of special n-p-n crystal

Base width	0.015 cm
Emitter resistivity	0.6 ohm-cm
Collector resistivity	10 ohm-cm
Base resistivity	3.3 ohm-cm
Acceptor density—N_A—(base)	1.1×10^{15} cm^{-3}
Fermi energy—ϕ_p—(base)	0.095 volt

EXPERIMENTAL RESULTS

Prior to the measurements on the samples discussed above, a plastic-encased transistor was measured with the conductance meter and found to give excellent agreement with Brown's low-temperature results. At room temperature, however, it was not possible to obtain a steady-state reading of channel conductance except at very low biases where the data were at the limit of sensitivity of the meter and also difficult to reproduce. Higher instantaneous readings of conductance could be obtained with a sudden reduction in applied bias after prolonged application, but the reading decayed in a few seconds to a negligible value.

The behavior of the bare n-p-n bars in a moist ambient was quite different from that of the plastic-encased transistors. At room temperature, in a sufficiently moist ambient, the channel conductance exhibited a reproducible steady-state value over a wide range of biases. The values of conductance were approximately inversely proportional to applied voltage and increased with humidity. Also a transient phenomenon was observed wherein the conductance decreased abruptly upon increase in bias and then increased to the new steady-state value with a time constant of the order of a second, with a small but measurable drift for the order of a minute. A similar transient was observed upon decrease in bias, the conductance increasing abruptly and decreasing to the new value. (The wide variation in time constant with humidity reported previously[3] is not observed when the conductance is measured directly. The early data was obtained by observation of the floating potential of the open-circuited emitter, after application of bias to the collector. The time constant measured was therefore that time in which the channel conductance

[5] *International Critical Tables* (McGraw-Hill Book Company, Inc., New York, 1926), Vol. 1, p. 67.
[6] F. S. Goucher and M. B. Prince, Phys. Rev. 89, 651 (1953).

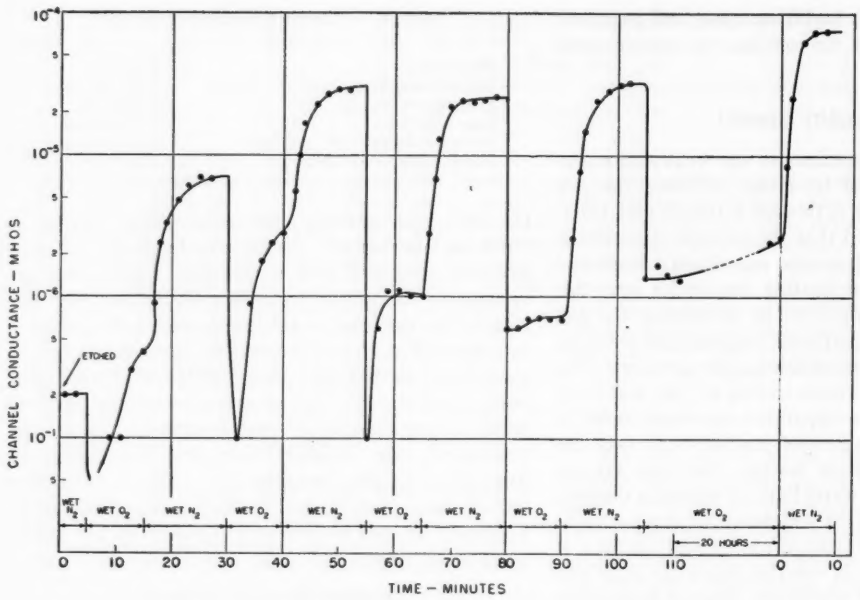

FIG. 2. Channel conductance *vs* time for wet oxygen and nitrogen exposure after etch with hydrofluoric acid.

increased by an amount comparable to the leakage conductance of the emitter circuit. Thus, for increasing channel conductance, corresponding to increasing humidity, the time for establishment of the floating potential decreased, since the emitter conductance is generally much smaller than that of the channel.) With the exception of some qualitative observations below, it was not possible to measure the channel conductance at low temperature on the bare units since freezing of the moisture on the surface of the bar produced erratic results.

Returning to the equilibrium behavior at room temperature, it was soon found that the early data had two serious shortcomings. First, the humidity, which was controlled by bubbling nitrogen through a variable-temperature water bath, was not sufficiently reproducible. Second, and most important, the data were found to be a critical function of the amount of oxidation of the germanium surface. That is, after the bonding and cleaning operation, exposure to oxygen produced an irreversible increase in channel conductance for a given relative humidity in nitrogen.

This effect was studied in more detail and a typical experimental curve is shown in Fig. 2. At the beginning of the run, the sample was etched in hydrofluoric acid which is assumed to remove all but the last few layers of oxide on the surface. The sample was then exposed to wet nitrogen, approximately 75 percent relative humidity, and the reverse bias set at approximately 1.0 volt. The ambient was then varied as shown along the time axis, the moisture content of the oxygen being the same as that of the nitrogen. There are two pertinent conclusions to be drawn from this graph. First, as noted above, the channel conductance increases monotonically with exposure to oxygen, when measured either in an oxygen or nitrogen ambient. This is further confirmed by the lack of any conductance increase if the sample is left in wet nitrogen for several hours after the hydrofluoric acid etch. Second, the channel conductance in wet oxygen is generally an order of magnitude lower than in wet nitrogen at the same time in the oxidation process. The gradual rise to equilibrium upon change from oxygen to nitrogen is probably caused by the speed at which the oxygen on the surface is removed, however the abrupt decrease in conductance upon re-exposure to oxygen in the initial cycles is as yet unexplained. After the last long oxygen exposure, the curves of Fig. 3 were obtained in the same ambients. The expected inverse voltage behavior is evidenced here along with the previously cited decrease of conductance in the oxygen ambient.

To obtain an accurate measurement of the channel conductance as a function of relative humidity, the circulating system was used with nitrogen, since, from Fig. 2, the surface was known to be stable in such an ambient. As mentioned in the previous section, it was desirable that the base layer of the transistor be wide enough to assure accurate measurements of the width and the resistivity of the *p*-type base material. Therefore the special crystal described in Table II was utilized and the sample had cross-sectional dimensions of 0.096 by 0.108 cm. The data of Fig. 4 were taken at a temperature of 24°C and were reproducible over all voltages and humidities. To avoid the effects of any slight oxidation throughout the experiment, the bar was initially exposed to oxygen for several hours to establish a stable layer. In addition to the data of Fig. 4, measurements taken in wet N_2 after different exposure

times to oxygen always gave the same shape curves with an overall shift in magnitude corresponding to the changes observed in Fig. 2. It was not possible to obtain these data immediately after the hydrofluoric acid etch, however, since, in this condition, the conductance meter was not sensitive enough to give a reading for biases greater than about one volt. Neither was it possible to measure the wet oxygen ambient conductance, except on a well-oxidized surface, since the changes in conductance due to oxidation obscured the changes due to applied bias. Similar data was obtained using helium in place of nitrogen, indicating that the nitrogen only acts as a carrier for the water.

The channel capacitance was measured at several humidities by means of a substitution type circuit operating at 700 kcps. The reverse capacitance of the emitter and collector in parallel were first measured in a dry nitrogen ambient and then in the desired humidity, the difference between the two readings giving the contribution of the channel. This capacitance was found to be a definite function of humidity in agreement with the theory discussed in the next section. The experimental points for 88 percent relative humidity are plotted in Fig. 9 in modified form in conjunction with the theoretical treatment.

Since the relaxation phenomena should give information about the mechanism of channel formation, it was studied in more detail with the circuit of Fig. 5(a). The two batteries and switch at the center of the figure allow a step of voltage to be applied to the base and the battery at the left supplies a small current through the channel so that the output voltage to the scope is directly proportional to the channel conductance. Using a step voltage of approximately 0.1 volt, the conductance transient, shown at the right was found to have the same time constant over the range of bias voltages used in the previous data. The time of decay to half of the peak value varied from about 1.0 second at 32 percent humidity and decreased to the order of 0.1 second at 100 percent humidity. By cooling the chamber containing the transistor while moist nitrogen was flowing, it was also possible to observe a 1.0-second transient at temperatures as low as −25°C. Since the chamber wall was at a much lower temperature than that measured on the transistor with a thermocouple, the effective humidity was probably quite low and the result is only significant insofar as it indicates presence of the transient at temperatures well below freezing.

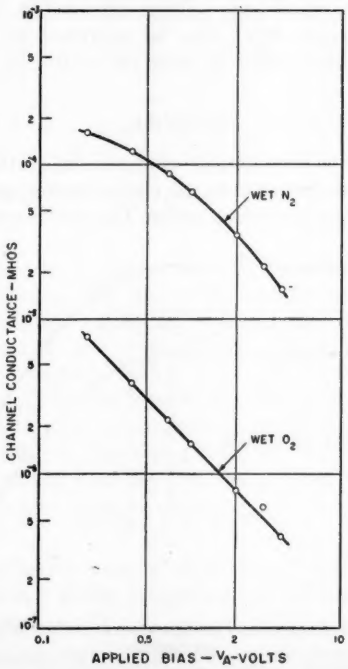

FIG. 3. Channel conductance *vs* applied voltage in wet oxygen and nitrogen after treatment shown in Fig. 2.

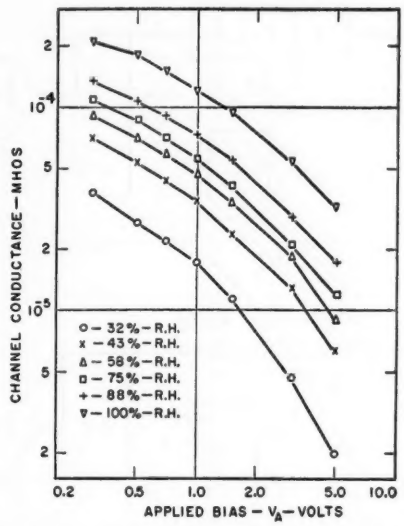

FIG. 4. Channel conductance *vs* applied bias on an oxidized surface for several values of humidity in a nitrogen ambient.

A similar experiment was performed using a configuration similar to that used by Pearson and Shockley[7] to investigate surface states on germanium. In Fig. 5(b), the conductance of a thin slab of high resistivity *p*-type germanium is measured as a function of the electric field applied perpendicular to the surface. The sample was etched in the same manner as the transistor, and by means of the plane parallel electrode an electric field of approximately 10 000 volts per cm could be applied by closing the switch in the diagram. The conductance change was displayed on an oscilloscope by observing the voltage across the load resistor. The behavior of the conductance upon application of the field was indistinguishable from the behavior of the

[7] G. L. Pearson and W. Shockley, Phys. Rev. **74**, 232 (1948).

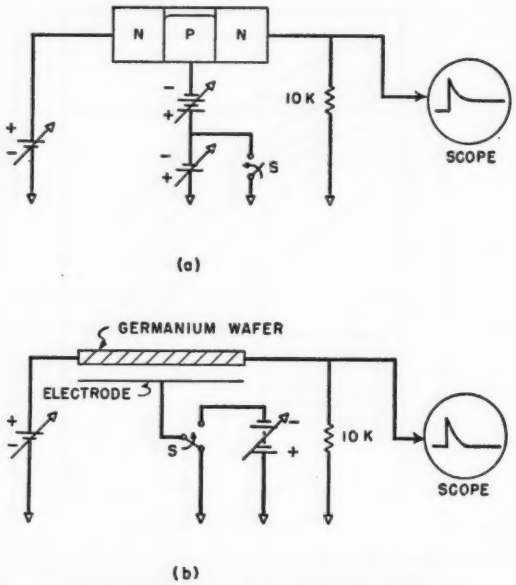

FIG. 5. Circuits for measuring relaxation time (a) for the channel and (b) for the field-effect.

channel except that after the occurrence of the transient sketched at the right of the figure, the conductance returned to its original value.[8] The decay times also behaved in the same manner with humidity and temperature, and in this case the value of 1.0 second was found to hold not only for low humidities but also for a completely dry ambient. The structure of this decay curve and that of the channel have not been studied in detail and there is evidence that neither is a simple exponential. At least in the case of the channel, there is an observable drift toward equilibrium for the order of a minute. The significance of these observations on the field effect will be discussed in connection with the physical model of the channel.

In addition to the above information several other observations are of interest. One is the occurrence of an extraneous channel conductance under conditions of surface contamination. If the sample was not carefully cleaned after the bonding operation the conductance was found to decrease with applied bias until a bias of several volts was reached, at which point the conductance became constant and independent of further increases in bias. Accompanying this effect was an abnormal increase in the reverse current supplied to the emitter and collector regions. Since this anomaly could always be eliminated by etching in hydrofluoric acid, carefully rinsing in distilled water, and reoxidizing the surface, it might well be caused by ionic surface conduction similar to that discussed by Law.[9] Finally it should be noted that under the above clean conditions, the dc reverse current from the n-type to the p-type material increased by at most 5 microamperes from its dry value at the highest measuring voltages and the highest humidity. This means that the load resistances in the conductance-measuring circuit were shunted by a minimum of one megohm, thus producing a negligible effect on the accuracy of the reading.

[8] This transient phenomenon has been observed independently by D. T. Stevenson of this laboratory and S. R. Morrison of the University of Illinois (private communication).

[9] J. T. Law, Proc. Inst. Radio Engrs. 42, 1367 (1954).

THEORETICAL MODEL

In an earlier publication[3] the inverse voltage behavior of the channel was explained by assuming constant electron mobility and a fixed impurity level having a time constant comparable to the relaxation times observed. Later, at the suggestion of H. Brooks of Harvard University, the mobility was taken proportional to the effective thickness of the channel[4] on the basis of calculations of mobilities in thin films.[10] Concurrent with this revision of the theory, Schrieffer[11] presented detailed calculations of mobility in a channel, and the following theory utilizes results which he kindly made available previous to publication.

By using the model of Fig. 6, similar to that used by Brown, the channel is represented by the electrons in the potential well just beneath the surface. $\mathcal{E}_i$ is the electrostatic potential corresponding to the Fermi energy for intrinsic material, and the potentials, ϕ_p and ϕ_s, are the deviations of the quasi Fermi levels from the intrinsic value for holes in the bulk and electrons at the surface, respectively. These last two quantities and V_A, the applied bias, will be expressed in volts. The channel conductance may be converted to a specific surface conductance in mhos per square by the relationship,

$$g=G/WC, \tag{1}$$

where G is the channel conductance, g, the specific surface conductance, C, the circumference, and W, the width of the p-type base region. The specific conductance

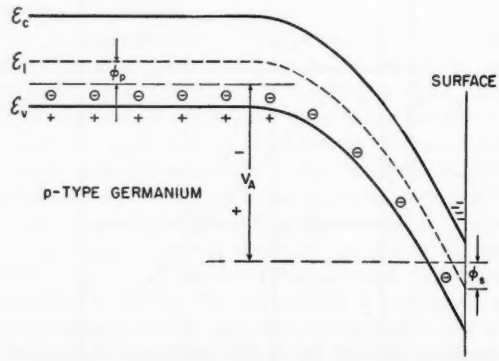

FIG. 6. Energy band configuration at surface of p-type germanium.

[10] E. H. Sondheimer, Advances in Phys. 1, 11 (1952).

[11] J. R. Schrieffer, Phys. Rev. 94, 1420 (1954).

may then be written:

$$g=qN\mu_{\text{eff}}, \tag{2}$$

where q is the electron charge, N, the number of electrons per unit surface area and μ_{eff} is the effective mobility of electrons in the channel. Assuming that the free electron charge at the surface is small compared with the charge produced by acceptor ions in the depletion layer, the electric field perpendicular to the surface may be calculated to be

$$E_s=[2qN_A(V_A+\phi_s+\phi_p)/\kappa\epsilon_0]^{\frac{1}{2}}, \tag{3}$$

from a solution of Poisson's equation. This expression is the same as that for the field at the center of an abrupt p-n junction. To determine N, the number of electrons per unit area, integration from the surface into the bulk gives

$$N=n_ie^{q\phi_s/kT}\int_0^\infty e^{-qE_sx/kT}dx=\frac{kT}{qE_s}n_ie^{q\phi_s/kT}=wn_ie^{q\phi_s/kT}, \tag{4}$$

where w is defined as the channel thickness and is the distance in which the electrostatic potential rises by kT/q or the electron density falls to $1/e$ of its value at the surface. Here, E_s is assumed constant over the important range of x or alternatively w is much less than the thickness of the space-charge layer. In terms of this thickness, Schrieffer's mobility calculation gives

$$\mu_{\text{eff}}=3w\mu_n/l_s, \quad w\ll l_s, \tag{5}$$

where l_s is the mean free path for lattice scattering. When the appropriate terms in electron concentration and mobility are combined, the specific surface conductance is found to be proportional to the square of the channel thickness and consequently inversely proportional to the electrostatic potential between the bulk and the surface, $\psi=V_A+\phi_s+\phi_p$. The result is

$$g=\tfrac{3}{2}[k\epsilon_0(kT/q)^2(n_i/N_A)(\mu_n/l_s)e^{q\phi_s/kT}]\times(V_A+\phi_s+\phi_p)^{-1}. \tag{6}$$

It may be seen by inspection that, for voltages large compared to ϕ_s plus ϕ_p, the conductance varies inversely with applied bias if ϕ_s is held constant. Since the experimental data show a similar inverse relationship, the value of ϕ_s for each humidity has been obtained from the curves of Fig. 4 at large bias and the data replotted in Fig. 7 as specific surface conductance *versus* effective bias, $V_A+\phi_s+\phi_p$. In this calculation the mean free path is obtained from the relationship[12]

$$\mu_n=4ql_s/3(2\pi m^*kT)^{\frac{1}{2}}, \tag{7}$$

with the effective mass, m^*, 0.12 times the mass of the free electron,[13] giving l_s equals 8.8×10^{-6} cm at room temperature.

[12] W. Shockley, *Electrons and Holes in Semiconductors* (D. Van Nostrand Company, Inc., New York, 1950), p. 277.

[13] B. Lax, International Conference on Semiconductors, Amsterdam, July, 1954 (to be published in Physica).

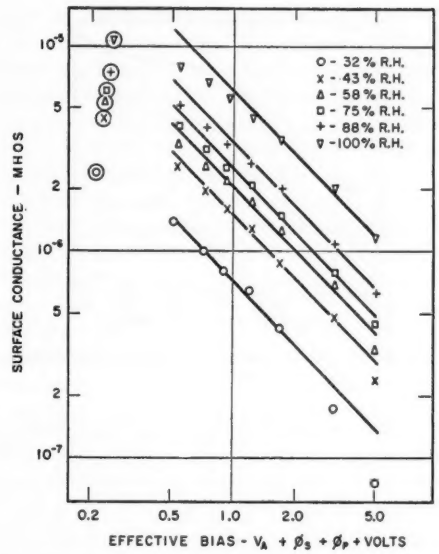

FIG. 7. Specific surface conductance *vs* effective bias. The solid lines are the theory for large bias and the circled points at the left, for zero bias.

Verifying the approximations, the calculated channel thickness, w, for an effective bias, $V_A+\phi_s+\phi_p$, of one volt, is

$$w=kT/qE_s=1.6\times10^{-6}\text{ cm}, \tag{8}$$

with E_s equal to 1.6×10^4 volt/cm from Eq. (3). Thus, except at effective biases less than one volt, taking the channel thickness much less than the mean free path for lattice scattering is a good approximation. As assumed for Eq. (4), this value for w is also much less than the space charge thickness. The free electron charge in the channel at the same bias may be calculated from Eqs. (2) and (5), giving

$$qN=gl_s/3\mu_nw=(5.1\times10^{-4})g\text{ coul/cm}^2, \tag{9}$$

where g is expressed in mhos. From the value of E_s, the charge of the ionized acceptors is found to be

$$Q_A=k\epsilon_0E_s=2.3\times10^{-8}\text{ coul/cm}^2, \tag{10}$$

again evaluated at one-volt effective bias. Referring to Fig. 7 and using Eq. (9), the free electron charge in the channel varies from 3.6×10^{-10} to 3.1×10^{-9} coulomb per cm^2, from the lowest to the highest humidity. This is seen to be much less than the charge due to the acceptor ions, thus agreeing with the assumption for the electric field at the surface.

In addition to this calculation at large applied bias, it is also possible to compute the channel conductance at zero applied bias for the values of ϕ_s previously obtained. This is accomplished by a numerical integration of Poisson's equation[14] and utilization of the effective mobility as calculated by Schrieffer.[11] These

[14] R. H. Kingston and S. F. Neustadter (to be published).

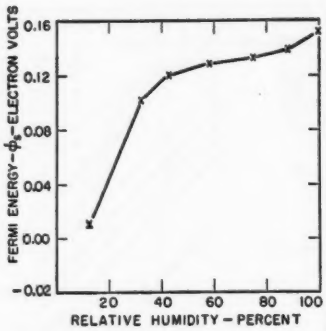

FIG. 8. Values of ϕ_s obtained from Fig. 7 for a well-oxidized surface in moist nitrogen.

calculated points are circled on Fig. 7 and show good agreement with the extrapolated conductance data at low biases. The zero bias value of conductance cannot be measured directly, of course, since under this condition there is no longer a high impedance isolating the p-type from the n-type regions of the semiconductor.

Thus, for a given ambient, as the bias is increased, the positive charge on the surface increases with E_s, such that ϕ_s is maintained constant. The value of ϕ_s, based on this model, has been plotted in Fig. 8. The lowest point, at 15 percent relative humidity, is only an estimate based on readings taken below one-volt bias, where there is no assurance that the conductance obeys the inverse voltage law.

In calculating the channel capacitance it is first necessary to consider that the data were measured at 700 kcps so that the period of the applied voltage is much shorter than the observed relaxation time of the channel. For this reason it will be assumed that the positive charge on the surface producing the channel is fixed and the only charge which changes with the applied signal is that produced by the acceptor ions, N_A, the electrons in the channel, N, and any charge residing in surface recombination states, similar to those proposed by Brattain and Bardeen.[15] This assumption is the same as that made by Brown[2] for the treatment of the channel at low temperatures. The capacitance per unit area may be written

$$C_1/A = dQ/dV_A, \tag{11}$$

where dQ is the change in charge per unit area at the surface or by neutrality the change in acceptor charge at the inside of the space charge region. Now ψ, the electrostatic potential between the bulk and surface is given by $V_A+\phi_s+\phi_p$; therefore,

$$d\psi = dV_A + d\phi_s, \tag{12}$$

since ϕ_p is a constant. By referring to Fig. 6, it may be seen that if V_A is increased, then the corresponding increase in ψ is diminished by a decrease in ϕ_s, since the reduction in the number of electrons at the surface must be accompanied by a shift in the Fermi energy toward the valence band. This shift in ϕ_s occurs instantaneously since the electrons in the channel are in equilibrium with the n-type material in the emitter and collector regions. Similarly it is assumed that any electrons in surface recombination centers will be released in a time short compared to the period of the applied frequency, as done by Brattain and Bardeen.[15] The change in charge with a change in ψ may be found by writing

$$dQ = qN_A dx, \tag{13}$$

where dx is the change in width of the space charge region. But if the space charge widens by this amount, then ψ at the surface must increase by

$$d\psi = E_s dx. \tag{14}$$

Combining Eqs. (13) and (14) gives

$$C_0/A = dQ/d\psi = qN_A/E_s,$$

where C_0/A is also the capacitance obtained for an abrupt p-n junction between p-type material of acceptor density, N_A, and n-type material of infinite conductivity. To find the true capacitance dQ/dV_A it is necessary to find the relationship between dQ and $d\phi_s$. The charge in the channel may be written

$$Q = -q[wn_i + n_{a0}]e^{q\phi_s/kT}, \tag{15}$$

where n_{a0} is the density of electrons in donor type surface states when ϕ_s is zero, as defined by Brattain and Bardeen.[15] It is assumed that the acceptor type states are completely filled and they are therefore neglected. The change in charge is then

$$dQ = -[wn_i + n_{a0}]q^2 e^{q\phi_s/kT} d\phi_s/kT, \tag{16}$$

and rewriting, using Eq. (8), gives

$$dQ = -[n_i + n_{a0}/w]qe^{q\phi_s/kT} d\phi_s/E_s. \tag{17}$$

The true channel capacitance, C_1/A, may then be found from

$$C_1/C_0 = dV_A/d\psi = [1+(wN_A e^{-q\phi_s/kT}/wn_i + n_{a0})]^{-1}. \tag{18}$$

Since the channel is, in reality, a distributed RC transmission line, it was necessary to correct the above expression by the factor

$$\frac{C_{\text{meas}}}{C_1} = \frac{1}{2x}[\tanh x(1-\tan x \tanh x) + \tan x(1+\tan x \tanh x)][1+(\tan x \tanh x)^2]^{-1},$$

where

$$x = (wC/8G)^{\frac{1}{2}}, \tag{19}$$

which is the effective capacitance as measured from both ends of an RC line having a total conductance, G, and total capacitance, C. The best fit with the data was

[15] W. H. Brattain and J. Bardeen, Bell System Tech. J. 32, 1 (1953).

found if the contribution of n_{a0} was neglected, and Fig. 9 shows the three theoretical curves and the experimental data corresponding to a relative humidity of 88 percent and $\phi_s=0.14$ volt. A similar agreement was found for the same humidity with a partially oxidized sample having a value of ϕ_s of 0.10 volt. Since the surface states were found to have no effect on the measured capacitance as expected from Eq. (18), then either they do not maintain equilibrium with the conduction band at 700 kcps or their density is too small to affect the result. In this latter case, from Eq. (18),

$$n_{a0} \ll w n_i = 5 \times 10^7 \text{ cm}^{-2}, \tag{20}$$

which is a factor of 10^4 smaller than the same quantity estimated by Brattain and Bardeen.[15]

DISCUSSION

The pertinent results of the experiment and theory may be summarized as follows: (1) The variation of channel conductance and capacitance may be explained on the basis of a constant ϕ_s at the surface determined by the ambient and the oxidation of the surface. (2) Whenever the applied bias is changed, the channel conductance shows an instantaneous change followed by a gradual relaxation to a new steady-state value. (3) The magnitude of ϕ_s, or consequently the free-electron density at the surface, increases with oxidation and also with water vapor pressure. (4) Moist nitrogen produces a value of ϕ_s approximately 0.1 volt higher than oxygen of the same moisture content on a surface having the same oxide layer thickness.

With the possible exception of the data taken at 32 percent relative humidity, the results indicate that for electric fields at the surface up to 3×10^4 volts per cm, the positive surface charge varies in such a way as to maintain ϕ_s constant. This observation is further verified by the field-effect experiment where it was found that even in a dry nitrogen ambient it was not possible to produce a steady-state change in ϕ_s with applied external fields of the same order of magnitude. Before considering this behavior in detail, it is first necessary to consider the mechanism of charge establishment on the surface. Brown[2] postulated two possibilities for this phenomenon. First, mobile positive ions on the surface might drift onto the p-type material as a result of the applied field between the n- and p-type material; or second, neutral impurities on the surface might become positively ionized as a result of the departure from equilibrium of the underlying semiconductor. Now it is apparent that the relaxation effect observed with the channel is a result of the time dependence of one or the other of these processes. In fact, it was as a means of differentiating the two, that the field-effect experiment was carried out. Since there is no field parallel to the surface of the semiconductor in this experiment, it follows that the aforementioned second mechanism, is that which maintains ϕ_s constant. Therefore, since the relaxation times behave in the same manner for the channel, it is concluded that the positive surface charge is produced by ionization of impurity levels at the surface of the semiconductor. A further qualitative argument in favor of this mechanism is the lack of a pronounced change in the relaxation time as the temperature is decreased below 0°C. If the transient were attributable to mobile charges one would certainly expect a marked increase in relaxation time as the water on the surface solidified. These experiments do not eliminate the possibility of ionic migration, of course, and it is quite probable that, in cases of surface contamination, both mechanisms might be operative.

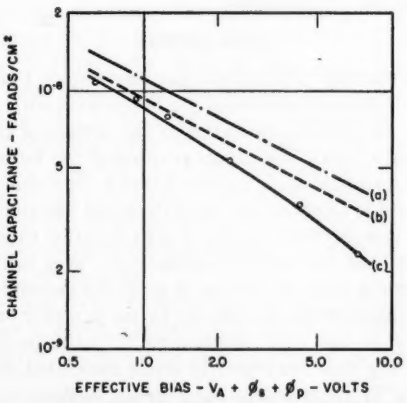

FIG. 9. Channel capacitance *vs* effective bias. (*a*) C_0/A, theory for a junction with infinite donor density, see text. (*b*) C_1/A, theory including effect of channel electrons, and (*c*), C_{meas}/A, theory and experiment including transmission loss.

Examining the relaxation phenomenon in detail, consider the behavior of the surface in Fig. 6, if the field is increased instantaneously by a sudden increase in V_A. As described in the capacitance treatment in the previous section, there must be an instantaneous decrease in the electron density in the channel, since the larger field must now be compensated by more positive charge. But this decrease, which corresponds to an abrupt decrease in channel conductance, is equivalent to a movement of the Fermi level toward the valence band. Consequently, any states at the surface will correspondingly lose electrons to the bulk and the experiments indicate that these states are dense enough to require a return to the original Fermi energy to maintain charge balance. Now, at first, one might suspect that the states which are producing this clamping of ϕ_s are the recombination centers proposed by Brattain and Bardeen.[15] That this is not the case is evident from the relaxation times observed, since it is inconceivable that such states would require the order of a second to reach equilibrium if they are to take part in the surface recombination process. An additional objection to clamping by recombination centers is the wide variation of ϕ_s with gaseous ambient. This would require that the state energy and density is a function of the ambient which is in complete dis-

agreement with the aforementioned authors' observations. A much more plausible explanation is based on the occurrence of additional states either in or on the surface oxide layer. If one assumes a distribution of neutral and charged ions in this region which is directly related to the gaseous ambient, then the relative ionization will be a function of the position of the Fermi level of the underlying material. If their density is large enough then any small shift in this Fermi level will cause a large readjustment of charge distribution, electrons being transferred between the bulk germanium and the energy states of the ions. Quantitatively, consider that a change in electric field of the order of 3×10^4 volts per cm is found to produce a negligible change in Fermi energy from the experimental data. Now this change in field requires a net change in positive surface charge of 4×10^{-8} coulomb per cm^2 or a change in electron density of 3×10^{11} per cm^2. Since a monolayer of adsorbed ions on germanium has a density of about 10^{15} per cm^2, it is seen that only a small change in the position of the Fermi level would result in the required charge. It follows that the relaxation time may be attributed to the rate at which electrons may transfer between these ions and the bulk germanium and that the dependence of ϕ_s upon gaseous ambient and oxide layer thickness is associated with the ionization energies and densities of the ions present in or on the oxide layer.

It follows from the preceding arguments that items (3) and (4) in the summary of results can be explained on the basis of the position of the various energy levels associated with thickness of the oxide layer and the adsorbed species. Qualitatively, for a given oxide thickness, ϕ_s is highest for water vapor in an inert ambient and decreases with decreasing vapor pressure or addition of oxygen. The opposite extreme, ϕ_s most negative, or the surface most p-type, would be expected for dry oxygen, ozone, or hydrogen peroxide ambients. Such an effect is observed both by Brattain and Bardeen[15] in their contact potential measurements and by Christensen[16] in studies of p-type channels on n-type material. This behavior may be seen to conform with the idea that the more oxidizing or electronegative the ambient the lower the ϕ_s of the germanium surface. The rise of ϕ_s with increased oxide thickness, also observed by Brattain and Bardeen,[15] is not as easily explained but is undoubtedly connected with such problems as the deviation of the germanium dioxide from stoichiometry and any electrostatic field in the layer. An investigation of the structure of the oxide on the surface should explain many of these details.

The capacitance data are in good agreement with the channel theory; however, the density of surface states required to fit the theory is in serious disagreement with the results of Brattain and Bardeen.[15] Upon further examination, this is not too surprising since their model neglects interaction of the ions on the surface with the Fermi level of the germanium. As for the estimated surface density obtained by Brown,[2] it is difficult to make a direct comparison since his model, utilizing a continuous distribution of states *versus* energy, does not lend itself to comparison with the aforementioned data which are based on a discrete level. It should be pointed out, incidentally, that Brown's theoretical calculation does not take into account the variation of mobility with applied bias and thus the numerical results are subject to some error.

These experiments lead to the postulate that ϕ_s at the surface of germanium is determined not by the donor or acceptor concentration in the bulk but by the oxide thickness and external ambient. This follows from a general extension of the process of the clamping of ϕ_s by the adsorbed ions, and is further verified by the field-effect experiment where it was found that no steady-state change in Fermi energy could be produced with either polarity of field in either a dry or moist ambient. In detail, consider the extreme case of a sample of p-type germanium of resistivity 1.0 ohm-cm, with an inversion layer at the surface corresponding to an n-type resistivity of 1.0 ohm-cm. This would require a value of ϕ_s at the surface of 0.11 volt and the internal field, E_s, at the surface may be calculated to be 1.5×10^4 volts per cm. But from the field-effect experiment, it is found that fields of this order of magnitude may be terminated by the charged ions in the surface layer with no measurable change in position of ϕ_s. Therefore, it follows that the ions present will determine the carrier density at the surface rather than the underlying donor or acceptor impurities. Just how generally this postulate may be applied is not certain; however, experiments of the type carried out by Morrison[17] should establish the range of validity.

As for the application of the experimental results to the behavior of germanium devices, it has been shown elsewhere[18] that the reverse leakage of a p-n junction diode in a moist ambient may be explained on the basis of the above model.

CONCLUSION

The channel conductance has been shown to depend upon a constant position of the Fermi level with respect to the electrostatic potential at the surface of the germanium crystal. The actual position of the Fermi level or the quantity, ϕ_s, is in turn found to be a function of the state of oxidation of the surface and the ambient to which it is exposed. Studies of the relaxation time of the channel and the surface conductance in a field-effect experiment indicate that ϕ_s is generally determined by the surface conditions and not by the acceptor or donor density of the bulk germanium.[19] Qualitatively, one might say that the impurity levels associated with the

[15] H. Christensen, Proc. Inst. Radio Engrs. **42**, 1371 (1954).

[17] S. R. Morrison, J. Phys. Chem. **57**, 860 (1953).

[18] A. L. McWhorter and R. H. Kingston, Proc. Inst. Radio Engrs. **42**, 1376 (1954).

[19] This same general behavior was predicted by J. Bardeen, Phys. Rev. **71**, 717 (1947).

surface and adsorbate are dense enough to overcome the effects of the bulk impurities. One major difference, of course, is that these impurity levels require the order of a second to come to equilibrium with the bulk whereas the normal doping impurities reach equilibrium instantaneously as far as present physical measurements are concerned. Thus, a complete description of the properties of a germanium crystal requires a knowledge of the bulk resistivity and the equivalent surface resistivity. Just how and why the surface resistivity varies with ambient and surface treatment is therefore of utmost importance in the study of the electronic properties of germanium.

ACKNOWLEDGMENTS

The author is indebted to C. R. Grant for preparation of the samples and most of the physical measurements and to G. I. Hitchcox for the instrumentation. M. Green, A. L. McWhorter, and J. E. Thomas, Jr., are also to be thanked for their criticisms and suggestions, and G. W. Pratt, Jr., for a critical reading of the manuscript.

PHYSICAL REVIEW VOLUME 98, NUMBER 6 JUNE 15, 1955

Lattice Resistance to Dislocation Motion at High Velocity

EDWARD W. HART
General Electric Research Laboratory, Schenectady, New York
(Received December 23, 1954)

Dissipative effects at high velocities, resulting from coherent collisions of dislocations with the lattice sites, have been estimated and found to be too small to limit the dislocation velocity.

I. INTRODUCTION

A LONG-STANDING question in the theory of dislocations and in the application of the theory to mechanisms of plastic deformation is that which concerns the permissible velocities for motion of a dislocation in a crystal lattice. More explicitly, one would like to know whether or not the lattice presents large resistance to dislocation motion when the velocity is large. The answer to this question is of particular importance in the consideration of dislocation processes that depend on the ability of the dislocation to conserve kinetic energy over any considerable portion of its trajectory.

Leibfried[1] first considered the effect of the scattering of lattice vibration waves by dislocations as a resistive effect. This work was later critically evaluated and corrected by Nabarro[2] who concluded that resistive contributions from this mechanism would be negligible. The purpose of the present report is to investigate the inelastic collisions between the dislocations and the lattice sites. This effect was first proposed as an energy loss mechanism by Orowan,[3] but no quantitative estimates have yet been made for this dissipation. It is proposed to make an estimate here in terms of coherent dislocation oscillations.

Peierls[4] and Nabarro[5] have shown that the presence of the lattice provides a reference frame for a variation of the energy of a dislocation as a function of its position relative to the lattice points. These authors made an approximate calculation for an edge dislocation lying along a ⟨100⟩ direction of a simple cubic crystal, and they deduced the energy per unit length, V, as a function of displacement x in the direction of the Burgers vector, to be of the form

$$V=E_0[1+\alpha\cos(4\pi x/b)], \tag{1}$$

where

$$E_0=Gb^2/4\pi(1-\nu),$$
$$\alpha=2\exp[-2\pi/(1-\nu)],$$

b is the Burgers vector, G is the shear modulus, and ν is Poisson's ratio. As the dislocation moves through the lattice it then experiences a sinusoidally varying force per unit length,

$$f=-dV/dx$$
$$=(4\pi/b)\alpha E_0\sin(4\pi x/b), \tag{2}$$

in addition to any applied uniform driving force. At sufficiently high velocities this lattice force will produce an oscillation of the dislocation position about its mean position of uniform translation. The oscillation results in radiation of elastic energy by the dislocation and a resultant rate of energy loss which will give rise to a resistive force in its motion through the lattice.

The oscillatory driving force is probably overestimated by the Peierls-Nabarro calculation, but, since the purpose of this investigation is to obtain an upper estimate of the resistive force, it will not be inappropriate. The same comment applies to the assumption that the dislocation is always aligned in the lattice so

[1] Günther Leibfried, Z. Physik **127**, 344 (1950).
[2] F. R. N. Nabarro, Proc. Roy. Soc. (London) **A209**, 278 (1951).
[3] E. Orowan, Proc. Phys. Soc. (London) **52**, 8 (1940).
[4] R. E. Peierls, Proc. Phys. Soc. (London) **52**, 34 (1940).
[5] F. R. N. Nabarro, Proc. Phys. Soc. (London) **59**, 256 (1947).

that all parts of its length experience the same force at the same time and so oscillate with the same phase.

II. CALCULATION

Eshelby[6] has shown that the mean rate $\bar{R}$ of energy radiation per unit length per unit time by a dislocation of Burgers' vector b, oscillating with angular frequency ω and amplitude of oscillation displacement l, is given by

$$\bar{R}=\tfrac{1}{32}Gb^2l^2k^2\omega, \tag{3}$$

where $k=\omega/c$ and c is the velocity of elastic shear waves. Equation (3) was derived for screw dislocations, but it will be used here in the same form for any type of dislocation. Now, if the dislocation is moving through the lattice with velocity v, and if its oscillations from its mean position are small compared to b, it will experience an oscillatory force per unit length of the form

$$f=(4\pi/b)\alpha E_0 \sin\omega t, \tag{4}$$

where

$$\omega=2\pi(2v/b). \tag{5}$$

These equations follow directly from Eq. (2).

In its oscillatory motion the dislocation experiences an additional force due to its radiation field. A portion of this radiation force, which is easily calculated, is resistive and operates to limit the amplitude of oscillation. The remainder of the radiative force produces a reactive effect which modifies the effective mass per unit length of the dislocation. The only importance of this latter effect is the possibility of resonance. Although the reactive term cannot be determined with any high precision, it seems unlikely that any resonance could occur for frequencies ω less than the characteristic Debye frequencies. In consonance with the degree of approximation which is characteristic of the other elements of the present calculation both radiation forces are neglected here in the determination of the oscillation amplitude.

The mass per unit length of the dislocation is given closely by E_0/c^2. The equation of motion for the oscillation of the dislocation can now be written as

$$(E_0/c^2)d^2\xi/dt^2=(4\pi/b)\alpha E_0 \sin\omega t, \tag{6}$$

where ξ is the displacement of the dislocation from its mean position in the frame of reference moving with velocity v parallel to the dislocation motion. The solution of Eq. (6) is

$$\xi=-l\sin\omega t, \tag{7}$$

where

$$l=4\pi\alpha b(c/b\omega)^2. \tag{8}$$

Substitution of Eq. (8) in Eq. (3) will now give $\bar{R}$ as a function of ω or v. It is most interesting, however, to convert $\bar{R}$ to a resistive force or stress. This dissipative stress τ_d is readily computed from the consideration that, if the dislocation is to be maintained in motion at the velocity v in spite of the energy loss rate $\bar{R}$, an additional stress must be applied to provide a power input equal to $\bar{R}$. The stress must then satisfy the relationship

$$\tau_d bv=\bar{R}. \tag{9}$$

Now from Eq. (4) the minimum stress τ_0 required to move the dislocation in the lattice from rest is $(4\pi/b^2)\alpha E_0$, and for simplicity the appearance of Poisson's ratio may be neglected in E_0. Then $\tau_0=\alpha G$, and

$$\tau_d/\tau_0=(4\pi/32)\alpha(v/c)^{-2}$$
$$\simeq\tfrac{1}{2}\alpha(v/c)^{-2}.$$

Now, since α is of the order of 10^{-4} when ν is $\frac{1}{3}$, it is apparent that the resistive stress is negligibly small for $v/c>0.1$. With the exception of possible uncertainty in the reactive radiation term as previously discussed, the result as expressed in Eq. (10) is an upper estimate of the resistive stress which a dislocation experiences in moving through the crystal as a result of "collisions" with the lattice sites.

The approximations which lead to an equation of motion like Eq. (6) render Eq. (10) inapplicable at low velocities and the indicated increase of τ_d with decreasing v/c is not really unlimited. Whatever the resistance is at very low velocity, however, it decreases as the velocity increases. Thus, if a sufficient stress is applied to produce any acceleration at low velocities, the dislocation can eventually attain the relatively high velocity considered here.

It is not to be inferred from the foregoing development that there may not be further dynamical dissipative effects at velocities still higher than those considered here, i.e., at velocities more than about one-half the velocity of sound. In fact, it has been reported[7] that recent unpublished work by J. D. Eshelby has shown the presence of dissipation at very high velocities caused by the dispersion of sound waves in a crystal lattice.

[6] J. D. Eshelby, Proc. Roy. Soc. (London) **A197**, 396 (1949).

[7] N. F. Mott, Nature **174**, 377 (1954).

Effect of Plastic Deformation on the Electrical Conductivity of Silver Bromide*†

WILLIAM G. JOHNSTON‡
Department of Physics, The University of Chicago, Chicago, Illinois
(Received March 2, 1955)

Plastic deformation of AgBr at and below room temperature produces a conductivity increase that varies linearly with strain. The conductivity increase has a low activation energy, exhibits dispersion at low frequencies, and recovers slowly at room temperature. A small anisotropy in the conductivity increase can be produced which indicates that the increase is greater parallel to the slip planes than perpendicular to them. The conductivity increase is attributed to regions of disorder that are introduced by the deformation, and these regions of disorder appear to be piled-up groups of dislocations in the slip planes of the work-hardened crystal.

I. INTRODUCTION

REGIONS of disorder in crystals, such as grain boundaries, are known to have high-diffusion coefficients compared to the normal lattice.[1–3] It is reasonable to expect that the regions of disorder that are introduced by plastic deformation will act as similar paths of fast diffusion,[4,5] and, in the case of ionic crystals, as paths of high electrical conductivity. The work of Hevesy and Obrutsheva[6] on self-diffusion in lead, and the work of Matano[7] on copper-zinc alloys is to be interpreted in this manner. In general it is difficult to measure directly the diffusion in cold-worked materials because at temperatures high enough to achieve measurable diffusion the effects of plastic deformation recover rapidly. However, in ionic crystals the effect of deformation on the conductivity can be studied, since the electrical conductivity and self-diffusion are both due to the motions of ions[8]; and the conductivity can be measured at low temperatures so that the effects of cold work recover slowly.

AgBr is an ionic crystal with the rock salt structure. The intrinsic conductivity is reasonably well understood as the result of the work of Teltow[9] and Kurnick.[10] The predominant lattice defect is the Frenkel defect, consisting of a silver interstitial ion and a silver ion vacancy. The interstitial ion has the higher mobility, its mobility being about 10^3 greater than that of the vacancy at room temperature. Above 100°C all specimens of pure AgBr exhibit the same conductivity, but at lower temperatures, in the "structure-sensitive" region, the individual specimens exhibit conductivities that may differ appreciably. It is seen in Fig. 1 that above about 60°C all of the specimens have the same conductivity which is the same as the intrinsic conductivity extrapolated from the high temperature measurements of Kurnick.[10] Below 60° the polycrystals have a higher conductivity than do the single crystals, and there is some variation among the individual single crystals. The specimens employed in this experiment were of almost constant purity so that the variation in the low-temperature conductivity is not due to impurities.[11] The most applicable explanation for this structure-sensitive conductivity is due to Smekal,[12] who suggested that it arises from the motions of ions along internal surfaces of abnormally low activation energy.

Plastic deformation produces two effects that might lead to an increase in the conductivity of an ionic crystal. First, large numbers of dislocations are formed which may well serve as the internal regions of low activation energy conceived by Smekal. Second, there will be vacancies and interstitial ions produced by the moving dislocations through mechanisms discussed by Seitz[13] and Mott.[14] These point defects are extra charge carriers which cause an increase in the conductivity. The work of Gyulai and Hartly[15] on NaCl is to be interpreted in terms of the latter effect.[16] In their work a 12 percent deformation of NaCl at 40°C produced a conductivity increase of a factor of 60. This increase decayed rapidly, falling to one-half maximum in 0.1 min and it had disappeared after 20 min. According to Seitz,[16] the rapid recovery was due to the association of the positive and negative vacancies that were formed during the deformation. The rate of formation of the

* Based on a thesis submitted to the Department of Physics, The University of Chicago in partial fulfillment of the requirements for the degree of Doctor of Philosophy.

† This work was supported in part by the Office of Naval Research.

‡ Present address: General Electric Research Laboratory, Metallurgy and Ceramics Research Department, Schenectady, New York.

[1] A. LeClaire, *Progress in Metal Physics* (Interscience Publishers, Inc., New York, 1953), Vol. 4, p. 205.
[2] R. Smoluchowski, *Imperfections in Nearly Perfect Crystals*, edited by W. Shockley (John Wiley and Sons, Inc., New York, 1952), p. 451.
[3] D. Turnbull, *Atom Movements* (American Society for Metals, Cleveland, 1951), p. 129.
[4] A. H. Cotrell, *Theoretical Structural Metallurgy* (Edward Arnold and Company, London, 1948), Chap. XII.
[5] C. Zener, *Imperfections in Nearly Perfect Crystals*, edited by W. Shockley (John Wiley and Sons, New York, 1952), p. 289.
[6] G. Hevesy and A. Obrutsheva, Nature **115**, 674 (1925).
[7] C. Matano, Japan. J. Phys. **9**, 41 (1934).
[8] N. F. Mott and R. W. Gurney, *Electrical Processes in Ionic Crystals* (Oxford University Press, London, 1950), Chapter II.
[9] J. Teltow, Ann. Physik **5**, 63, 88 (1950).
[10] S. W. Kurnick, J. Chem. Phys. **20**, 218 (1952).
[11] E. Koch and C. Wagner, Z. physik. Chem. **38B**, 295 (1937).
[12] A. Smekal, *Handbuch der Physik* (Verlag Julius Springer, Berlin, 1933), Vol. 24/2, p. 878.
[13] F. Seitz, Advances in Phys. **1**, 43 (1952).
[14] N. F. Mott, Phil. Mag. **43**, 1151 (1952).
[15] Z. Gyulai and D. Hartly, Z. Physik **51**, 378 (1928).
[16] F. Seitz, Phys. Rev. **80**, 239 (1950).

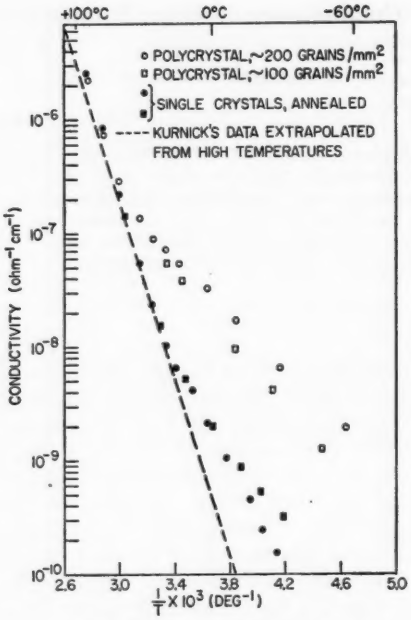

FIG. 1. Conductivity of annealed crystals of AgBr.

neutral vacancy pairs is controlled by the mobility of the sodium vacancy. It is to be expected that in AgBr there will be interstitial ions and vacancies formed during deformation; but the mobilities of the silver interstitial ions and vacancies near room temperature are so great that the point defects decay very rapidly. If the conductivity increase which is observed in the present experiment were due to silver interstitials or vacancies, it can be calculated from the mobilities[10] that the conductivity would decay to half-maximum in less than 10^{-2} sec at 30°C. Actually, it is observed that the conductivity increase decays to half-maximum in about 10^5 sec, so that the effect which is studied here is not due to point defects created during the deformation.

It has been pointed out that the dislocations produced during deformation may act as paths of high conductivity. The work of Turnbull and Hoffman[17] on grain boundary self-diffusion in silver indicates that the high diffusion rate along small-angle grain boundaries is due to diffusion along the individual dislocation "pipes" that form the grain boundary. It has been suggested by Hart[18] that the major enhancement of diffusion by cold-work is due to preferential diffusion along the dislocation pipes produced by the cold work.

An edge dislocation in an ionic crystal of the AgBr type is shown in Fig. 2 (after Seitz[19]). The plane shown is an (001) plane and the electrical charges alternate on successive (001) planes. The slip plane, *AC*, is a (110) plane and the slip direction is $[1\bar{1}0]$. The dislocation is formed by the insertion of two extra atomic half-planes which are enclosed by dotted lines. Beyond the edges of these half-planes there is an expansion of the lattice.[20] The stress in that region is relieved by the presence of interstitial ions or vacancies, both of which have a positive volume change associated with them.[10] This leads to a lower activation energy for the creation of such point defects in that region. The activation energy for mobility along the dislocation is also lowered due to the dilation of the lattice. Calculations are not available for the activation energy for conduction along a dislocation. The work of Turnbull and Hoffman[17] indicates that in silver the activation energy for self-diffusion along a dislocation is about 20 000 cal/mole, compared to 46 000 cal/mole in the normal lattice.

II. EXPERIMENTAL PROCEDURE

The AgBr was prepared by precipitation from Mallinkrodt HBr and $AgNO_3$. Spectrographic analysis indicated the presence of about 0.001 percent of Cu, Mg, and Fe, with less than measurable amounts of other metallic impurities. The sulfur content was not appreciably greater than 0.0002 percent.

Single crystals were grown by withdrawal from the melt (Czochralski method) at the rate of 0.5 in./hr. After machining to size, the surface of the crystal was removed with a KCN solution. The crystals were annealed for 24 hr at 400°C, and cooled to room temperature at 25 deg/hr. The growth and anneal were in air atmosphere. Most specimens were $\frac{1}{4}$ in. diam and $\frac{3}{8}$ in. long; shorter specimens were used for high-frequency measurements, and longer specimens were used when accurate strain measurements were desired.

Specimens were deformed by compression in the apparatus shown in Fig. 3, by loading the ram with weights or with a compressed air piston, while the strain was measured with a displacement indicator in units

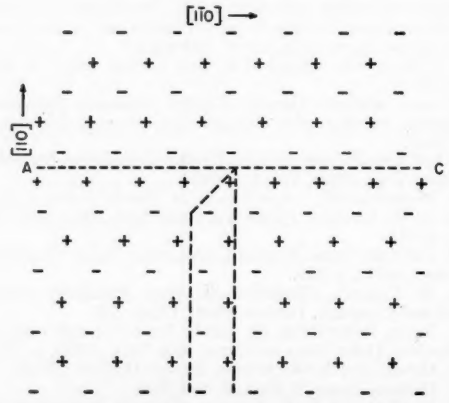

FIG. 2. Edge dislocation in AgBr-type crystal.

[17] D. Turnbull and R. E. Hoffman, Acta Metallurgica 2, 419 (1954).
[18] E. W. Hart, see reference 17.
[19] F. Seitz, *Plastic Deformation Symposium*, Carnegie Institute of Technology (Office of Naval Research, Washington, D. C., 1950).
[20] A. H. Cottrell, *Dislocations and Plastic Flow in Crystals* (Oxford University Press, London, 1953), p. 57.

of 0.0001 in. Silicone oil served as a temperature bath, and to prevent moisture from condensing on the specimen. A thermocouple was placed within $\frac{1}{4}$ in. of the specimen and the apparatus was enclosed in a lightproof can.

Electrodes were applied with silver paint. The parallel resistance of the specimen was measured by placing it in parallel with an air condenser and measuring the capacity and dissipation factor of the combination with a General Radio Company capacitance bridge, type 716-C. Unless otherwise stated, the measurements were made at 30 cps or 100 cps. For a study of dispersion the range of 20 cps to 20 000 cps was used. Approximately 1 v/cm was applied to the crystals.

The specimen was loaded with increments of from 3 kg/cm² to 30 kg/cm². Usually the conductivity was measured after each load increment so that the deformation may have been spread out over a period of six or eight minutes. When the absolute value of the conductivity was of interest the deformation was limited to 8 or 10 percent, so that an accurate correction for change of geometry could be made.

III. EXPERIMENTAL RESULTS

A. Conductivity-Strain Dependence

In Fig. 4 are shown the conductivity increases produced in two single crystals that were $\frac{1}{4}$ in. square and $\frac{7}{8}$ in. long, and oriented so that the axis was in the [100] direction. The conductivity increased linearly with strain up to about 2.5 percent strain. This linearity extends down to 0.1 percent strain and, in some crystals, as high as 6 percent strain.

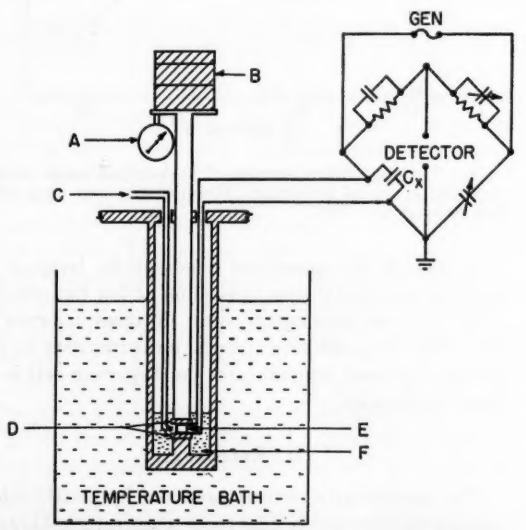

FIG. 3. Apparatus for deforming crystals and measuring ac conductivity. *A*—displacement gauge, *B*—deforming load, *C*—thermocouple, *D*—quartz insulating disks, *E*—specimen crystal, *F*—silicone oil bath.

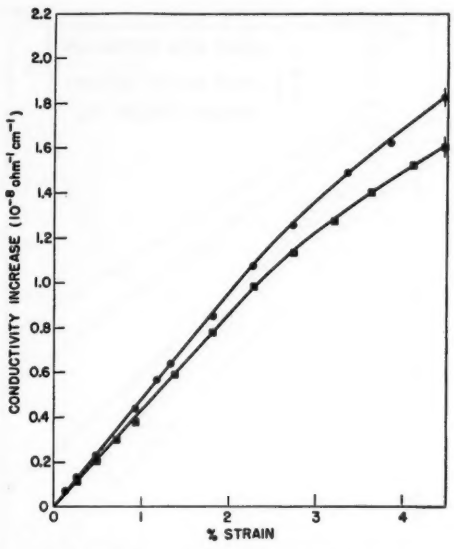

FIG. 4. Conductivity increase of two single crystals deformed at 30°C. The initial conductivity was 1.35×10^{-8} ohm^{-1} cm^{-1}. Measured at 100 cps.

The departure from linearity at high strains appears to be associated with the fact that at the higher stresses there is transient creep during the time it takes to make the measurements. If the conductivity increases linearly with instantaneous strain but not with transient creep strain, the negative curvature of the plot of total strain *versus* conductivity is to be expected.

The conductivity increase shown in Fig. 4 is about 1.6×10^{-8} ohm^{-1} cm^{-1} at 30°C for a 4 percent strain. With extreme deformation of 75 percent in compression it is possible to produce increases as great as 50×10^{-8} ohm^{-1} cm^{-1}.

B. Temperature Dependence of the Conductivity Increase

The temperature dependence of the conductivity increase of a deformed single crystal measured at 30 cps and 100 cps is shown in Fig. 5. The top curve indicates that the activation energy is 5800 cal/mole immediately after deformation. Low-frequency measurements soon after deformation characteristically give values of 5500 to 6500 cal/mole for the activation energy of the conductivity increase. The two lower solid curves show that the activation energy of the conductivity increase gets larger during recovery, approaching the behavior of the annealed crystal.

The activation energy of 5800 cal/mole can be compared with the 18 450 cal/mole that is characteristic of the intrinsic conductivity in AgBr.[10] The value of 5800 cal/mole lies between the 4700 cal/mole for the mobility of silver interstitial ions and the 11 200 cal/mole for the mobility of silver vacancies.

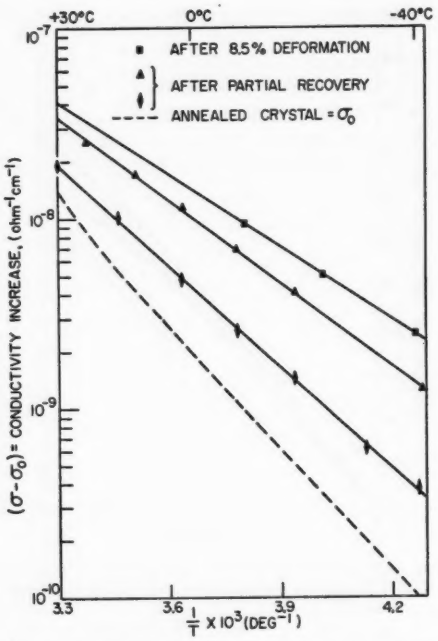

FIG. 5. Conductivity increase of a single-crystal specimen deformed in compression. Top curve was taken after deformation at −24°C. The second curve was taken after 2-hr recovery at 30°C, and the lowest solid curve was taken after 80-hr recovery at 30°C. Measured at 30 cps and 100 cps.

C. Frequency Dependence of the Conductivity Increase

At high temperatures, conductivity measurements of AgBr single crystals exhibit a dispersion that is characteristic of electrode polarization effects, and which has been studied by Friauf.[21] Below 200°C these electrode polarization effects are small, and at 100°C there is no dispersion in the intrinsic conductivity between 20 cps and 20 000 cps. At still lower temperatures, however, a dispersion again appears which seems to be characteristic of the structure-sensitive conductivity, and which increases greatly with plastic deformation. Figure 6 shows the conductivity of an annealed single crystal that has very little dispersion at 30°C. After a 10 percent deformation the frequency dependence is pronounced. The behavior of an annealed polycrystal is more like that of the deformed single crystal than like the annealed single crystal.

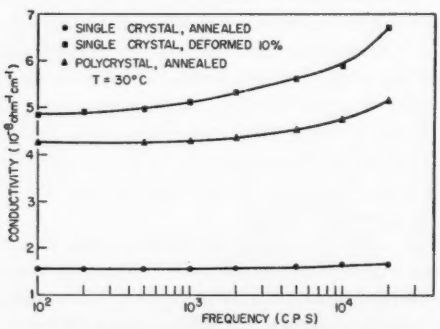

FIG. 6. Frequency dependence of conductivity.

[21] R. J. Friauf, J. Chem. Phys. 22, 1329 (1954).

As a result of this dispersion the activation energy of the conductivity increase produced by deformation appears to depend on the measuring frequency. This is seen in Fig. 7 where the conductivity increase of a single crystal after 10 percent deformation is shown as measured at several frequencies. For each frequency the points can be approximated by a straight line whose slope indicates an activation energy. The values obtained range from 4600 cal/mole at 20 000 cps to 6300 cal/mole at 100 cps.

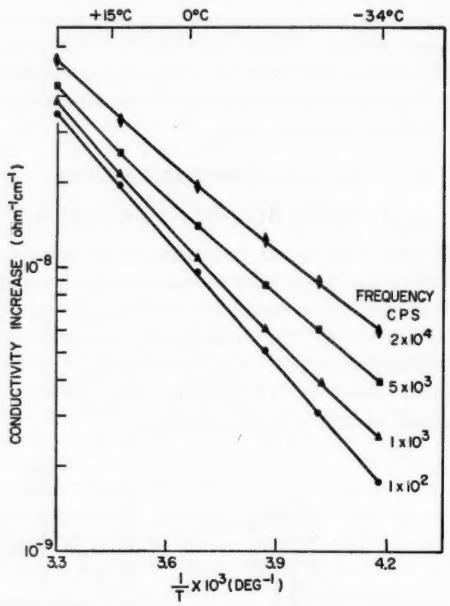

FIG. 7. Conductivity increase of a deformed single crystal measured at several frequencies. Measurements were made after 2-hr recovery at +30°C.

In Fig. 8 the normalized conductivity increase at each temperature is seen to level off at low frequencies. This is a true leveling-off since dc measurements at 0°C yield the same results as do measurements at 100 cps. At the lower temperatures the dispersion sets in at lower frequencies.

D. Recovery

The conductivity increase produced by plastic deformation recovers slowly near room temperature. Figure 9 shows the receovery of a single crystal that was deformed 8.5 percent at 29.6°C and allowed to recover with the load removed. The experimental points can

be fitted with the expression

$$\Delta\sigma=\Delta\sigma_0-a\log(t/t_0+1), \qquad (1)$$

where t is the recovery time, a and t_0 are constants. This is the equation for recovery that Kuhlmann, Masing, and Raffelsieper,[22] and Cottrell and Aytekin[23] have used to fit data for the recovery of yield stress in aluminum and zinc, respectively. The yield stress of AgBr recovers at a rate comparable with the recovery of conductivity as shown in Fig. 10.

The activation energy for the recovery of a single crystal deformed 8.5 percent with a load of 110 kg/cm² was determined. The recovery rate at 29.6°C was compared with the recovery rate when the temperature was changed to a new value in the range of 14°C to 60°C. The conductivity measurements were all made at 29.6°C. The relative recovery rates obtained in this manner are plotted in Fig. 11, and the slope corresponds to an activation energy of 18 500±1500 cal/mole. This value is the same as the activation energy for conductivity by silver interstitial ions in the intrinsic range.[10]

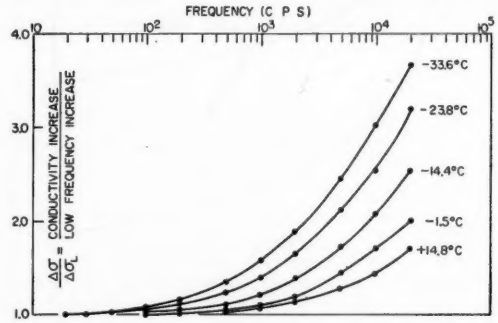

FIG. 8. $(\Delta\sigma/\Delta\sigma_L)$ = conductivity increase divded by the low-frequency increase to give a normalized curve at each temperature.

The plot is linear although the measurements for the various points were made at different stages of recovery. The uppermost point was measured while the conductivity recovered from 53 percent to 63 percent of total recovery, and the data for the bottom point was obtained while the conductivity recovered from 25 percent to 35 percent. This implies that the activation energy for recovery does not depend on the stage of recovery. In this connection, there is some question as to whether the activation energy for recovery of yield stress is a function of the yield stress.[24,25]

The conductivity recovers also when there is no recovery of yield stress, i.e., when the deforming stress is left on the specimen. Figure 12 shows the transient creep of a specimen that was deformed 4 percent in instantaneous deformation, and the applied stress kept constant thereafter. The creep initially followed the Andrade $t^{\frac{1}{3}}$ law. The conductivity of the specimen recovered during the transient creep, although not as rapidly as did a specimen from which the load was removed after a 4 percent instantaneous strain (dotted curve). Equation (1) fits the data for recovery with load on or with load off quite well, as is shown in Fig. 13. If anything, it fits the data for recovery with the load on

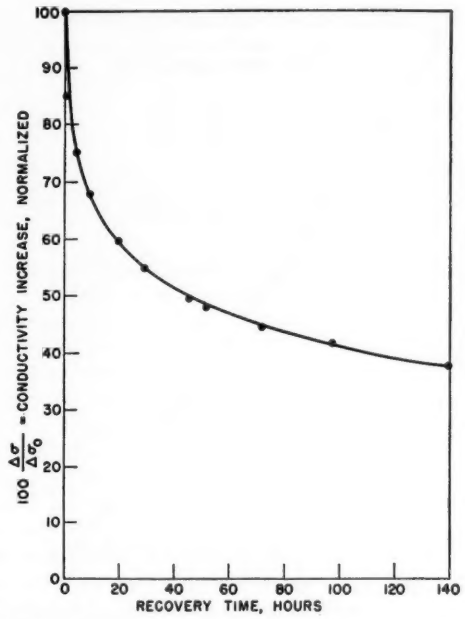

FIG. 9. Recovery of conductivity increase of a deformed single crystal. $\Delta\sigma_0$ is the conductivity increase after the instantaneous deformation, when $t=0$. The solid curve is $100(\Delta\sigma/\Delta\sigma)_0=100-11.4\log(t/0.57+1)$. Measured at 100 cps.

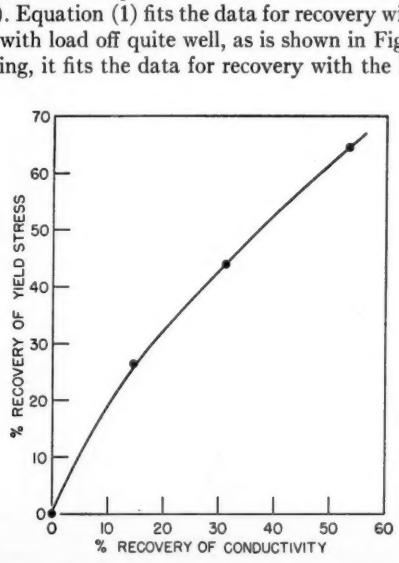

FIG. 10. Recovery of yield stress *vs* recovery of conductivity of a single crystal after 8.5 percent deformation at 29.6°C. Measured at 100 cps.

[22] Kuhlmann, Masing, and Raffelsieper, Z. Metallikunde **40**, 241 (1949).
[23] A. H. Cottrell and V. Aytekin, J. Inst. Metals **77**, 389 (1950).
[24] P. A. Beck, Advances in Phys **3**, 245 (1954).
[25] Drouard, Washburn, and Parker, Trans. Am. Inst. Mining Met. Engrs. **197**, 1226 (1953).

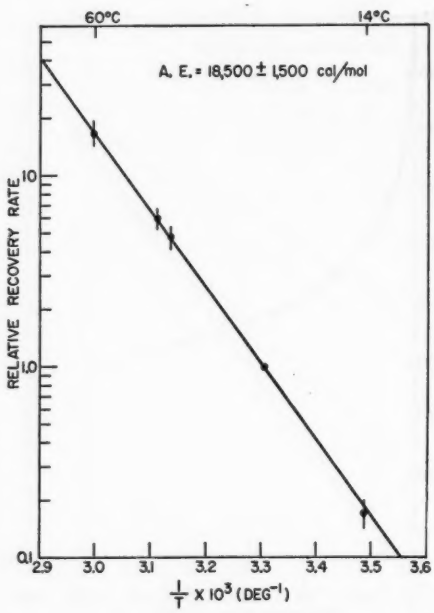

FIG. 11. Temperature dependence of recovery rate of conductivity of a deformed single crystal. Measurements made at 100 cps.

better, the difference being more obvious for small recovery times when a log plot is made of the data.

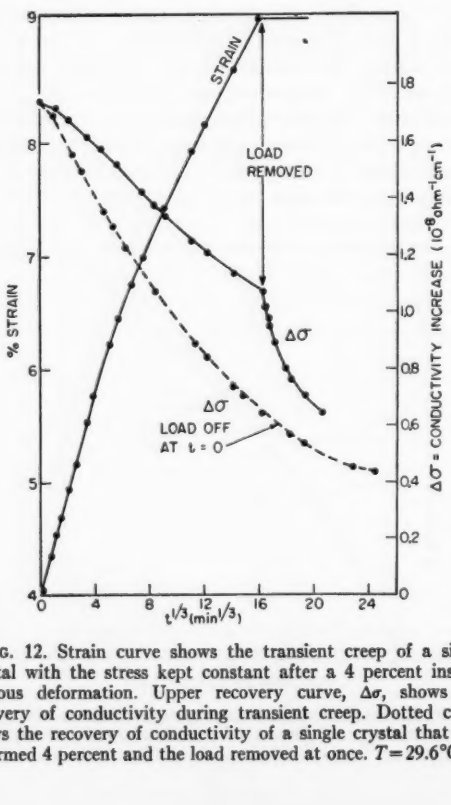

FIG. 12. Strain curve shows the transient creep of a single crystal with the stress kept constant after a 4 percent instantaneous deformation. Upper recovery curve, $\Delta\sigma$, shows the recovery of conductivity during transient creep. Dotted curve shows the recovery of conductivity of a single crystal that was deformed 4 percent and the load removed at once. $T = 29.6$°C.

E. Anisotropy of the Conductivity Increase

In order to compare the conductivity increase parallel to the slip plane with the increase perpendicular to the slip plane it is desirable to obtain slip on a single slip system. Single-crystal shear specimens were machined to 0.250 in. by 0.375 in. by 0.090 in., with the (011) plane parallel to the large faces. These (011) faces were fastened with Duco cement to the apparatus shown in Fig. 14, so that the shear would be along the (011) planes and in the $[0\bar{1}1]$ direction. Although the motion of the apparatus was constrained to a pure shear displacement, the crystals did not deform in pure shear on a single slip system. There was evidence of some slip on intersecting slip systems, but most of the slip was

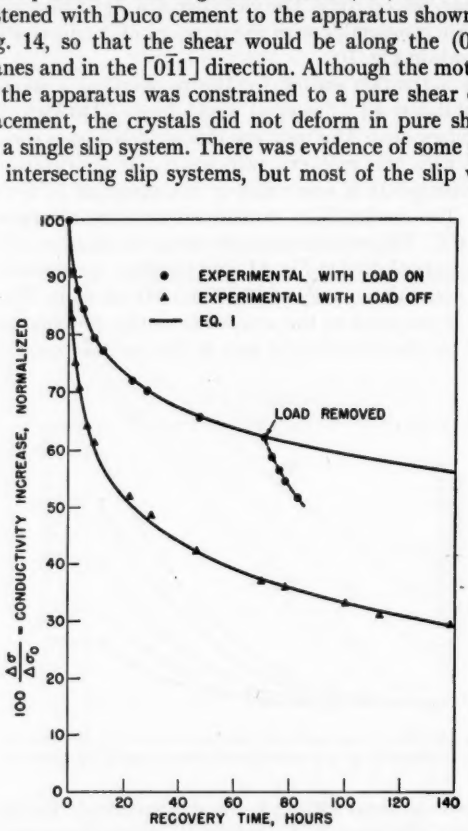

FIG. 13. Recovery of conductivity of single crystal with load on (upper curve), and recovery with load off (lower curve). The calculated curves are $100(\Delta\sigma/\Delta\sigma_0) = 100 - a\log(t/t_0+1)$, with $a = 9.13$ and $t_0 = 1.13$ hr for the upper curve, and $a = 11.8$ and $t_0 = 0.34$ hr for the lower curve.

on the desired system. Measurements made after a 10 percent shear strain indicated that the conductivity increase was about 40 percent greater parallel to the slip plane than perpendicular to it. There appeared to be no anisotropy in the slip plane. The results for three crystal deformed in this manner are shown in Table I. The large estimated errors resulted from the relatively small conductivity increase that could be produced, and from the contamination of the surfaces of the crystals in removing and reapplying electrodes.

F. Polycrystals

Small-grain polycrystals were prepared by casting, and annealed at 250°C for 24 hours. The temperature

dependence of the conductivity of a specimen with 200 grains/mm² is shown in Fig. 15. The annealed polycrystal has a higher conductivity with a lower activation energy than does the annealed single crystal. The effect of deformation on the polycrystal appears to be about the same as on the single crystal. The deformed single crystal behaves very much like the annealed polycrystal. In Fig. 6 the frequency dependence of the conductivity of a polycrystal was more like that of a deformed single crystal than an annealed single crystal. This similarity between grain boundary conduction and deformation conductivity is to be expected if both are characteristic of disordered regions of the crystal. The main difference in the two is that the grain boundary conductivity does not recover.

IV. DISCUSSION

An understanding of the mechanism whereby the conductivity of AgBr changes during plastic deformation should include the following main features of the experimental results: (a) Linear dependence of conductivity on strain; (b) low activation energy of the conductivity increase which changes as the crystal recovers; (c) frequency dependence of the conductivity increase; (d) time dependence of recovery; and (e) anisotropy of the conductivity increase.

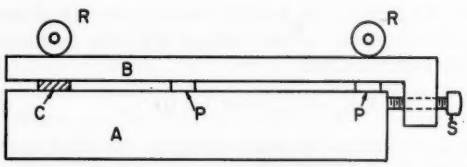

FIG. 14. Shear apparatus for thin crystal, C, which is glued to parts A and B of the apparatus. The rollers, R, and the spacers, P, constrain the motion of part B to a pure shear displacement. The screw, S, is used to provide the deforming force.

It was pointed out in the introduction that the conductivity increase due to deformation cannot be attributed to interstitial ions or vacancies formed during the deformation because these point defects would decay much faster than the observed recovery. Further arguments are that the conductivity due to point defects would not exhibit the observed dispersion, and the activation energy of the conductivity increase cannot be correlated with the activation energy for the mobility of interstitial ions or vacancies.

The indefinite and variable activation energy and the dispersion of the conductivity increase point to an inhomogeneous mechanism in line with Smekal's[12] idea of internal regions of high conductivity, rather than to a change in the bulk conductivity. On the assumption that plastic deformation causes the introduction of regions of high conductivity into the crystal, one can devise a simple model that exhibits qualitatively the observed behavior.

Consider the undeformed crystal as depicted in Fig. 16(a). Neglecting the parallel capacitance of the crystal, we can consider it as a simple resistance, R_0 in Fig. 16(b), when the electrodes are placed on the surfaces indicated by the arrows. The undeformed crystals behave as such simple resistances, showing little dispersion. In Fig. 16(c) the effect of the deformation has been to introduce a uniform region of high conductivity material, ab, that extends completely across the crystal. In Fig. 16(d) the increase in parallel conductance of the crystal is merely $1/R_d$, where R_d is the resistance of the high conductivity strip. The conductivity increase would exhibit the temperature dependence of R_d, and there would be no dispersion. However, such a model can be changed slightly to give a more realistic behavior.

Figure 16(e) depicts a deformed crystal in which the region of high conductivity does not extend completely through the crystal; but it has a gap, cd, the resistivity of the material in the gap being much higher than that in the regions ac and db. If the resistance of the high-conductivity material is R_d and that of the gap is R_g, the equivalent circuit can be depicted as in Fig. 16(f). The low-frequency or dc resistance of the lower branch

TABLE I. Anisotropy of conductivity increase in single crystals.[a]

Crystal	$\Delta\sigma_e/\Delta\sigma_0$	$\Delta\sigma_s/\Delta\sigma_s$
A	1.48±0.25	1.10±0.35
B	1.42±0.18	0.93±0.25
C	1.38±0.18	1.05±0.25

[a] $\Delta\sigma_0$ was measured perpendicular to the slip plane. $\Delta\sigma_e$ was parallel to the slip plane and perpendicular to the slip direction. $\Delta\sigma_s$ was parallel to the slip plane and in the slip direction.

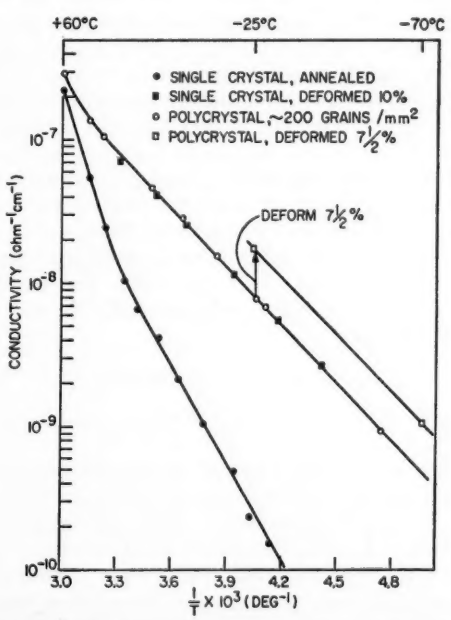

FIG. 15. Conductivity of a polycrystalline specimen before and after deformation. Single-crystal behavior is shown for comparison. Measurements were made at 30 cps and 100 cps.

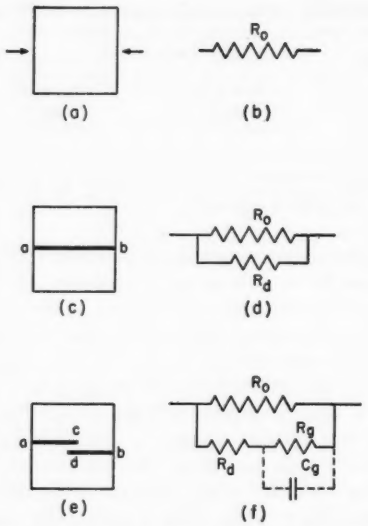

FIG. 16. (a)—Model of an annealed crystal. (b)—Equivalent circuit of (a), neglecting parallel capacitance. (c)—Deformed crystal with homogeneous region of high conductivity, *ab*, extending through the crystal. (d)—Equivalent circuit for (c). (e)—Deformed crystal with interrupted region of high conductivity material. (f)—Equivalent circuit for (e).

of the circuit is R_d+R_g, and the increase in conductance of the specimen is

$$\Delta G=1/(R_d+R_g)=(1/R_d)/(1+R_g/R_d). \qquad (2)$$

If the gap is very small then $R_g/R_d\ll 1$, and the increase in conductance is $1/R_d$, which would exhibit the low activation energy characteristic of the high-conductivity region. As the ratio R_g/R_d increases, the temperature dependence of the conductivity increase would change from the low activation energy of R_d to some higher value, eventually approaching the activation energy of R_g. The recovery process in such a model can be viewed as one in which the quantity R_g/R_d increases as the gap gets larger, or as the gap gets larger and the amount of high conductivity material decreases.

Across the gap, *cd*, there will be an associated capacitance, designated as C_g in Fig. 16(f). The parallel resistance of the circuit consisting of R_d, R_g, and C_g can be written as

$$R_p=R_g(ay^2+2y+1)/(ay+1), \qquad (3)$$

where $y=R_d/R_g$, and $a=1+(R_gC_g\omega)^2$. ω is $2\pi\times$frequency.

At low frequencies, $a=1$ and the parallel resistance is the same as the low-frequency resistance written above. At very high frequencies $a\gg 1$, and the parallel resistance is $R_p=yR_g=R_d$, which has a low activation energy. At low frequencies there is some contribution from the high-restivity material in the gap that results in a higher apparent activation energy. This accounts for the apparent change of activation energy with frequency as indicated in Fig. 7.

The model proposed, in which there are regions of high conductivity separated by regions of lower conductivity, will exhibit an activation energy that changes with recovery, and it will exhibit a dispersion such as is actually observed. The shortcomings of the model are clear. We have employed a single R_g and a single R_d, whereas a deformed crystal will have large numbers of such interrupted paths. If, indeed, we are to consider dislocations as regions of high conductivity, we may expect to find as many as 10^{11} or 10^{12} dislocations/cm^2 in a deformed crystal. Where we have employed a single gap in the high-conductivity material there will actually be many interruptions, ranging from very large gaps that have the conductivity of the normal material, to very small gaps which have a higher conductivity because the stress fields of nearby dislocations produce dilatation in those regions. Such a distribution of gap size means that the frequency dependence of a real crystal will be spread out over a much larger range of frequencies than would be the case for the model above.

With such a model one may calculate an approximate lower limit for the frequency at which dispersion should be observed. It is seen in Eq. (3) that when $R_gC_g\omega\ll 1$, the parallel resistance will be the same as the dc value. When $R_gC_g\omega\cong 1$, the parallel resistance will depart from the dc value. In the product R_gC_g the geometric factors cancel out and

$$R_gC_g=k_0/[\sigma(4\pi)(9\times 10^{11})], \qquad (4)$$

where k_0 is the low-frequency dielectric constant, and σ is the conductivity of the gap material in ohm^{-1} cm^{-1}. The lowest conductivity that can occur in the gap is that of the undeformed crystal, σ_0, so that the lowest value of the frequency for which $R_gC_g\omega=1$ is

$$\omega_{\min}=1/(R_gC_g)_{\max}=(4\pi)(9\times 10^{11})\sigma_0/k_0. \qquad (5)$$

There should be no dispersion at frequencies appreciably below this value. From the curves in Fig. 8 we can take the value of the observed frequency at which $\Delta\sigma/\Delta\sigma_L=1.10$ as the lowest frequency at which dispersion is observed. In Table II this experimental value is compared with $\omega_{\min}/2\pi$ calculated in the above manner. The calculated lower limit for dispersion is in agreement with the observed dispersion.

A simple physical description of the cause of dispersion can be given. At low frequencies there will be a pile-up of charge at the boundaries of the high-conductivity regions since the motion out of these regions

TABLE II. Calculated and observed low-frequency limit for dispersion.

Temperature (°C)	$f_{\min}$(calc) (cps)	f_{obs} for $\Delta\sigma/\Delta\sigma_L=1.10$ (cps)
+14.8	760	1200
−1.5	280	600
−14.4	140	280
−23.8	80	140
−33.6	46	100

restricted by the low conductivity of the gap material. The polarization due to such blocked charges will oppose the applied field and the conductivity of the disordered region will be lowered. At much higher frequencies the charges in the high-conductivity regions can move in phase with the applied voltage without causing appreciable pile-up of charge at the boundaries of these regions. The effect is similar to the high-temperature polarization of AgBr, where the blocking of charges occurs at the surface of the electrodes, rather than at internal boundaries.[21]

An upper limit of 4600 cal/mole can be placed on the activation energy for conduction in the disordered regions of the crystal. The value of 4600 cal/mole was observed at the highest frequency employed, and it should be more characteristic of the disordered regions than are the values obtained at lower measuring frequencies.

The foregoing discussion suggests that the conductivity in a deformed crystal is increased by the introduction of interrupted paths of high conductivity, or of low activation energy. The anisotropy of the conductivity increase indicates that these paths of high conductivity tend to lie parallel to the slip planes. Dislocations should behave as regions of low activation energy for conduction; and, after a deformation, the dislocations are distributed in the slip planes of the work-hardened crystal. It would appear that only those dislocations that are close enough together to form a well-connected path through the crystal can contribute to the low-frequency conductivity measurements on large crystals. Isolated dislocations are short segments of high-conductivity material imbedded in the normal crystal, so that their contribution to the low-frequency conductivity is small.

If the low-frequency conductivity increase is due to dislocations that are close enough together to form a fairly well connected path through the crystal, the model proposed by Mott[14,26] for a work-hardened crystal can be employed to give a more detailed picture of the conductivity increase and the recovery after deformation. In this model dislocations are produced dynamically at Frank-Read sources in groups of n, where n may be as high as 1000. After moving some average distance, L, the dislocations become piled up at obstacles in the slip planes. L is on the order of 10^{-2} cm in metals. If N Frank-Read sources per unit volume have each produced n dislocations that move an average distance, L, the strain is

$$\epsilon = NnL^2b, \tag{6}$$

where b is the Burgers vector. The obstacles that stop the dislocations may be sessile dislocations that are formed by slip on intersecting slip systems.

In the crystals deformed in this experiment the deformation has been on more than one slip system, so that there would be the necessary obstacles for such a model. The model predicts a parabolic law for work hardening, which is the type of work hardening that was observed in this experiment.

After the deformation there are groups of n dislocations piled up at obstacles throughout the crystal. These may form a network which provides high-conductivity paths throughout the specimen. Immediately after deformation all the dislocations are piled up so that they will all contribute to the conductivity. We may then write the conductivity increase as

$$\Delta\sigma \propto Nn. \tag{7}$$

From Eq. (6) and Eq. (7) it can be seen that is L is constant the conductivity will increase linearly with strain,

$$\Delta\sigma \propto \epsilon, \tag{8}$$

which is the relationship that is observed experimentally, for small strains, as is shown in Fig. 4.

As soon as the piled-up groups are formed, dislocations will begin to escape by climbing from the slip planes and moving to regions of the crystal where they are relatively isolated, eventually perhaps leading to a polygonization. Such escaping dislocations are lost to the low-frequency conductivity process. The rate of escape of piled-up dislocations from a group can be written as

$$dn/dt = -\nu \exp(-W/kT), \tag{9}$$

where ν is a frequency, and W is the activation energy for climb. Mott suggests that W is of the form

$$W = W_0 - \gamma s b^3 n, \tag{10}$$

where W_0 is the activation energy for climb of a free dislocation, b is the interatomic distance, s is the yield stress, and γ is a constant of the order unity. The reasoning here is essentially that the work expended in moving a jog one atomic distance is the force on the jog, snb^2, times the distance it moves, b.[27] If the load remains on the specimen, s is constant and

$$dn/dt = -\nu \exp\{-(W_0 - \gamma s b^3 n)/kT\}. \tag{11}$$

This can be integrated to give

$$n = n_0 - (1/\beta)\log(t/t_0+1), \tag{12}$$

where n_0 is the initial number of dislocations in a piled-up group, and

$$\beta = \gamma s b^3/kT, \tag{13}$$

$$t_0 = (1/\beta\nu)\exp(W_0/kT - n_0\beta). \tag{14}$$

The experimental quantity plotted in Fig. 13 is a normalized conductivity increase, $(\Delta\sigma/\Delta\sigma_0)\times 100$. Since $\Delta\sigma$ is proportional to n, Eq. (12) can be written as

$$(\Delta\sigma/\Delta\sigma_0)\times 100 = 100 - (100/n_0\beta)\log(t/t_0+1). \tag{15}$$

This expression is the same equation that was used to fit the data for recovery in Fig. 13, and it is seen that

[26] N. F. Mott, Phil. Mag. 44, 742 (1953).

[27] See reference 21, p. 188.

$100/n_0\beta=9.1$, when $s=4\times10^7$ dynes/cm^2, $T=303$°K, and $b=2.88\times10^{-8}$ cm. If one takes $\gamma=1$, the number of dislocations initially present in a piled-up group can be calculated to give $n_0=480$. This value is in agreement with estimates of up to 1000 for this number in metals.

The calculation of recovery rate when the deforming load is removed is not as straightforward as the above calculation for the recovery of conductivity during transient creep. The reason is that during recovery with the load off the yield stress, s, changes, and it may be a function of n; so Eq. (11) does not integrate to give the observed type of recovery equation. This is the same difficulty that arises in the calculation of recovery of yield stress with this model.[26]

The activation energy for climb of a free dislocation can be calculated, using $t_0=1.13$ hr (Fig. 13), and $n_0=480$. We follow Mott in taking $\nu=10^{12}$ sec^{-1}, and calculate from Eq. (14) that $W_0=26\,300$ cal/mole. This value of W_0 can be used to calculate the activation energy for recovery of the crystals for which data is presented in Fig. 11. The applied load was 110 kg/cm^2 and we may take s to be the maximum resolved shear stress of 55 kc/cm^2. Equation (10) indicates that

$$W=W_0-\gamma s b^3 n_0=17\,100 \text{ cal/mole}, \qquad (16)$$

which is in agreement with the observed activation energy for recovery of 18 500±1500 cal/mole. Equation (10) indicates that the activation energy for recovery is a function of s and n, so that it should change during recovery. The change of activation energy with recovery was not observed in the data presented in Fig. 11, but the experimental work has not been extensive enough to settle this point. It would appear that such a dependence of activation energy on recovery must be investigated quite carefully.[22–25]

The activation energy for climb of a free dislocation, W_0, should be the activation energy for self-diffusion.[28] In AgBr this would be the activation energy for self-diffusion of bromine, which is the slower of the two ions. At high temperatures the work of Christy[29] on creep in AgBr indicates that the activation energy for diffusion of bromine is on the order of 60 000 cal/mole. The calculations of Dienes[30] for alkali halides suggest that the bromine vacancies in AgBr may be transported as vacancy pairs formed with silver vacancies. The mobility of such a pair would be on the order of the mobility of a single silver vacancy. It is also probable that some of the transport of the bromine is along dislocations with a low activation energy. If the activation energy for diffusion of silver ions is as low as 4600 cal/mole in the disordered regions, as compared with 18 450 cal/mole in a normal crystal, it is not unreasonable to suppose that the energy for diffusion of bromine ions in such disordered regions can be 26 300 cal/mole as compared with 60 000 cal/mole in the normal crystal. The present interpretation of the experiment indicates that the activation energy for diffusion of bromine in a deformed single crystal of AgBr is on the order of 26 300 cal/mole.

[28] N. F. Mott, Proc. Phys. Soc. (London) **B64**, 729 (1951).
[29] R. W. Christy, Acta Metallurgica **2**, 284 (1954).
[30] G. J. Dienes, J. Chem. Phys. **16**, 620 (1948).

VI. CONCLUSIONS

Plastic deformation of AgBr produces a conductivity increase, at and below room temperature, that varies linearly with strain for small strains, has a low activation energy, exhibits dispersion, and recovers slowly. An anisotropy in the conductivity increase indicates that it is greater parallel to the slip planes than perpendicular to them. The conductivity increase is due to the creation of regions of disorder in the crystal. The activation energy for conduction in the disordered regions is less than 4600 cal/mole, compared with 18 450 cal/mole for the intrinsic conductivity. The regions of disorder appear to be groups of dislocations that are piled-up in the slip planes of the work-hardened crystal. The indefinite and variable activation energy, and the dispersion are consequences of the inhomogeneous nature of the disordered regions. If the conductivity increase is proportional to the number of piled-up dislocations, Mott's model of a work-hardened crystal leads to a linear strain-conductivity relation, and to the proper time-dependence for recovery of conductivity during transient creep. The interpretation of the recovery on the basis of this model indicates that the activation energy for diffusion of bromine in deformed crystals of AgBr at low temperatures is on the order of 26 000 cal/mole.

VII. ACKNOWLEDGMENTS

The author is grateful to his sponsor, Professor A. W. Lawson, for his advice and encouragement during the course of this investigation. It is a pleasure to acknowledge helpful discussions with members of the Institute for the Study of Metals, and in particular with Dr. M. H. Cohen. The author is indebted to the Shell Oil Company for the grant of a fellowship during part of this work.

Nuclear Magnetic Resonance Saturation and Rotary Saturation in Solids*

ALFRED G. REDFIELD†
Division of Applied Science, Harvard University, Cambridge, Massachusetts

(Received March 14, 1955)

Nuclear spin-lattice relaxation times of Al^{27} in pure Al and Cu^{63} in annealed pure Cu have been measured with a nuclear induction spectrometer, by the method of saturation. The experimental values of T_1 are 4.1 ± 0.8 milliseconds for Al^{27} and 3.0 ± 0.6 milliseconds for Cu^{63}, in reasonable agreement with theory.

The dispersion mode of the nuclear resonance was also observed, and it was found that χ' (the real part of the rf susceptibility) does not saturate at the same level as the absorption, χ'', but remains roughly constant out to a radio-frequency field intensity of about 2 gauss. Both χ' and χ'' become narrower and nearly Lorentzian in shape above saturation. When the dc magnetic field modulation is increased from 14 to 41 cps the phase of the dispersion signal lags behind the modulation, presumably because the modulation period is then comparable to T_1. Large dispersion signals above saturation have also been observed for the Na^{23} resonance in NaCl.

This behavior of the dispersion mode is in conflict with the predictions of Bloembergen, Purcell, and Pound and of the Bloch equations. The validity of these theories is re-examined, and it is concluded that although they are applicable to nuclear resonance in liquids and gases, and to solids at small rf intensities, they contain incorrect assumptions as applied to solids at high rf power levels. The theory of Bloembergen, Purcell, and Pound is based on an assumption equivalent to that of a spin temperature. It is shown that the spin state cannot be strictly described by a spin temperature because the phases of the spin quantum states are not incoherent, as required by the temperature concept. The transverse decay of the nuclear magnetization predicted by the Bloch equations is shown to be partially forbidden by energy and entropy considerations if a large rf field at the resonance frequency is continuously applied to the solid.

A theory is developed which is applicable only to solids at rf magnetic field intensities well above the saturation level and which is in reasonable agreement with the experimental observations. The Hamiltonian is transformed to a coordinate system rotating at the frequency of the rf field. The resulting time-dependent parts of the spin-spin interaction are nonsecular perturbations on the time-independent part, and can therefore be ignored. Statistical mechanics is applied to the remaining stationary spin Hamiltonian; specifically it is assumed that the spin system is in its most probable macrostate (a canonical distribution of quantum states) with respect to the transformed spin Hamiltonian. This assumption is justified because the transformed spin Hamiltonian is effectively time independent and the spin-lattice interaction is small, and it is analogous to assumptions basic to classical acoustics and fluid mechanics. The spin-lattice interaction merely determines the expectation value of the transformed spin Hamiltonian, which can be readily calculated under the assumption that the expectation value of the spin angular momentum of each spin is relaxed independently to its thermal equilibrium value by the lattice in time T_1. Both fast and slow modulation of the dc magnetic field can be treated.

"Rotary saturation" is observed by applying an audio-frequency magnetic field to the sample in the dc field direction while observing the dispersion derivative at resonance with a large rf field H_1. When the audio-frequency approaches γH_1 the dispersion signal decreases and goes through a minimum. The effect is easily treated theoretically in solids, liquids and gases by using a rotating coordinate system, and is a rotary analogue of ordinary saturation. It is a convenient method for calibrating rf magnetic fields and appears potentially capable of providing useful information on the solid state. Experimental data on rotary saturation are presented and discussed.

I. INTRODUCTION

THIS paper reports an experimental and theoretical study of nuclear magnetic resonance in solids at high rf magnetic field intensity. Metallic copper and aluminum were experimentally investigated, and the original objective of this work was to obtain nuclear spin-lattice relaxation times in these metals for comparison with the observed[1] Knight shifts[2] and the theory of Korringa,[3] which relates the relaxation times and Knight shifts to the electronic structure of the metals. The spin lattice relaxation times were measured by the method of saturation.

In the course of these measurements it was found that the dispersion mode of the nuclear resonance signal behaves in a way which is in conflict with the existing theories[4–6] of magnetic resonance saturation. As a result, the validity of these theories as applied to solids was re-examined, and a theory was developed along somewhat different lines which appears to agree with experiment for rf magnetic field intensities well above the saturation level. This theory also suggested the possibility of observing an effect which we call "rotary saturation," analogous to ordinary saturation but taking place in the effective field of a rotating coordinate system.

II. SATURATION DATA AND DISCUSSION

The experimental apparatus was a nuclear induction spectrometer[4] similar to those previously built by Weaver[7] and by Jeffries.[8] The details will be described elsewhere. The most important new feature of this equipment was a suitable calibrating circuit, permitting relative measurements of rf nuclear susceptibility to be made independent of receiver gain, rf level, and other variables. The output of this spectrometer yields the

* Partially supported by the Office of Naval Research.
† National Science Foundation Postdoctoral Fellow 1953–1954.
[1] H. S. Gutowski and B. R. McGarvey, J. Chem. Phys. **20**, 1472 (1952).
[2] W. D. Knight, Phys. Rev. **76**, 1259 (1949).
[3] J. Korringa, Physica **16**, 601 (1950).
[4] F. Bloch, Phys. Rev. **70**, 460 (1946).
[5] Bloembergen, Purcell, and Pound, Phys. Rev. **73**, 679 (1948) (henceforth referred to as BPP).
[6] A. M. Portis, Phys. Rev. **91**, 1071 (1953).
[7] H. E. Weaver, Phys. Rev. **89**, 923 (1953).
[8] C. D. Jeffries (private communication to Professor Bloembergen). We are indebted to Professor Jeffries for information on his spectrograph.

derivatives of the real and imaginary susceptibilities[9] χ' and χ''. The rf intensity was determined to an accuracy of better than 5 percent using the method of rotary saturation described below. All data were obtained at room temperature.

Powdered samples of pure aluminum and annealed pure copper were prepared as described by Bloembergen and Rowland.[10] In these samples, electric quadrupole effects are relatively small and can evidently be neglected.[10,11]

The relative absorption at resonance was measured by integrating the recorded absorption signal. The absorption data are plotted in Fig. 1, for an rf frequency of 7.6 Mc/sec and a magnetic field modulation frequency of 14 cps. In both aluminum and copper the absorption appears to follow the expected[4-6] dependence on rf field intensity for a system of dipolar coupled spins:

$$\chi''(\nu_0,H_1)=\chi''(\nu_0,0)[1+\tfrac{1}{2}\gamma^2H_1^2T_1g(\nu_0)]^{-1}, \quad (1)$$

where $\chi''(\nu_0,H_1)$ is the imaginary part of the nuclear magnetic susceptibility, $g(\nu)$ is the shape function of the unsaturated resonance, ν_0 is the resonance frequency, and H_1 is the magnitude of the rotating rf field.[12]

The shape function $g(\nu)$ is normalized with respect to integration over frequency:

$$\int_0^\infty g(\nu)d\nu=1. \quad (2)$$

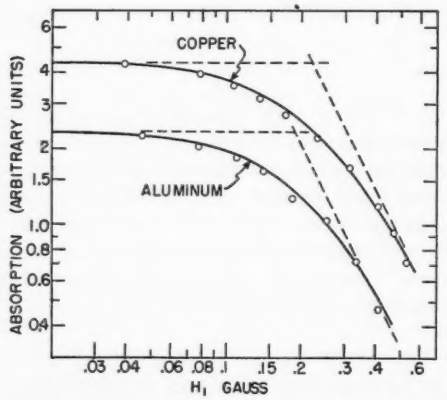

FIG. 1. Relative absorption at resonance $\chi''(\nu_0)$ as a function of rf field intensity. The units of $\chi''(\nu_0)$ are not the same for aluminum and copper in this figure.

[9] Throughout this paper we use χ to denote the $x-x$ component of the complex susceptibility tensor defined by $\mathbf{M}=\mathrm{Re}[(\chi'+i\chi'')\mathbf{H}\exp i\omega t]$, where M is the oscillatory magnetization produced by the rf field $\mathbf{H}\cos\omega t$. The experimentally observed quantity is the off-diagonal element χ_{yz} which is equal to $\pm i\chi_{zz}$ for a spin system in a large dc magnetic field.

[10] N. Bloembergen and T. J. Rowland, Acta Metallurgica **1**, 731 (1953).

[11] T. J. Rowland, Acta Metallurgica (to be published).

[12] Throughout this paper the rf field intensity, denoted by H_1, will be the amplitude of one of the circularly polarized modes which comprise the applied linearly polarized rf field of peak amplitude $2H_1$.

Values of $g(\nu_0)$ were obtained by integrating the integrated absorption signal, and T_1 was obtained from the data of Fig. 1 using Eq. (1). As will be discussed below, there is some question about the correctness of (1), but it is believed that values of T_1 obtained in this way are reasonably accurate.

Korringa[3] has developed the theory of nuclear magnetic relaxation and the Knight shift in metals. His theory has been discussed by Bloembergen and Rowland[10] and by Holcomb and Norberg.[13] Korringa obtains the result

$$T_1^{-1}=\frac{4\pi kT}{\hbar}\rho^+(\epsilon_0)\rho^-(\epsilon_0)\left[\frac{8\pi v_0g\beta^2P_F}{3}\right]^2, \quad (3)$$

where v_0 is the atomic volume, $\rho^\pm(\epsilon_0)$ are the densities of electronic states per unit volume per unit energy range for spins up and down respectively, evaluated at the Fermi level, P_F is the electronic probability density evaluated at the nucleus for an electron in the Fermi surface (assuming that the electronic wave function is normalized to unity over the atomic volume v_0), g is the nuclear g-factor $\mu_N/I\beta$, and β is the Bohr magneton. In deriving this equation the effect of electronic correlations and of possible P-character (asymmetry) in the electronic wave function has been neglected.[10] The latter assumption is approximately justified unless the P-character part of the electronic wave function is much greater than the S-character part.

Korringa also obtained a value for the Knight shift which can be written

$$(\Delta H/H_0)^2=\hbar/\pi kTg^2T_1, \quad (4)$$

where T_1 is given by (3), ΔH is the Knight shift in gauss, and H_0 is the applied magnetic field in gauss. The effect of electronic correlations is also neglected in this expression.

In Table I are listed experimental values of $g(\nu_0)$, T_1 and $\Delta H/H_0$, together with the theoretical values of T_1 obtained from Eq. (4) and the experimental values of $\Delta H/H_0$. Also included in Table I are the values of $v_0P_Fm^*/m$ obtained from Eq. (3) and the experimental T_1 values, assuming the electrons in the metal can be treated as a Fermi gas with $m^*=m$, and with one electron per atom. The quantity v_0P_F is the magnitude of the square of the wave function at the nucleus for an average electron at the Fermi level, relative to that predicted by the plane-wave approximation. Since relaxation effects due to possible P-character in the electronic wave function have been neglected in (3), the values of $v_0P_Fm^*/m$ given in Table I must be regarded as upper limits.

The discrepancy between the theoretical and experimental values of T_1 in copper is probably due to electronic correlation effects. According to Pines,[14] it is

[13] D. F. Holcomb and R. E. Norberg, Phys. Rev. **98**, 1074 (1955).

[14] D. Pines (private communication). We wish to thank Dr. Pines for permission to quote him.

reasonable to assume that correlations affect T_1 only by changing the density of electronic states from $\rho^{\pm}(\epsilon_0)$ to ρ_c, where ρ_c is the actual density of states of the correlated electron gas. The corresponding change in T_1 is $[\rho^{\pm}(\epsilon_0)/\rho_c]^2$, which Pines estimates to be approximately unity in both copper and aluminum. Correlations will also affect the Knight shift by increasing the paramagnetic susceptibility of the electron gas from χ_p, its uncorrelated value, to χ_{pc}. The corresponding increase in the Knight shift is χ_{pc}/χ_p, which Pines estimates to be 1.35 for copper and 1.3 for aluminum. If we apply these corrections to (4), we get theoretical T_1 values of 4 milliseconds for copper and 8.5 milliseconds for aluminum. The agreement with experiment is good for copper and poor for aluminum. The remaining discrepancy in aluminum may be due to the effect of possible P-character of the electronic wave function, the existence of which is likely because the valence electron of an aluminum atom is a P-electron. The data in both aluminum and copper are in poor agreement with extrapolation from measurements[15,16] of T_1 at low temperatures.

TABLE I. Experimental values of the inverse line width, relaxation time, and Knight shift, and related theoretical predictions of the relaxation time and mean electronic probability density at the nucleus.

	Aluminum	Copper
$g(\nu_0)$ milliseconds	0.212 ± 0.02[a]	0.228 ± 0.02[b]
T_1 milliseconds[b]	4.1 ± 0.8	3.0 ± 0.6
$\Delta H/H_0$[c]	0.237×10^{-2}	0.161×10^{-2}
T_1 milliseconds (theoretical)	5.06	2.26
$(m^*/m)v_0P_F$[b]	250	260

[a] T. J. Rowland (private communication).
[b] Present research.
[c] See reference 1.

The derivatives of the absorption and dispersion obtained in aluminum at various rf intensities are shown in Fig. 2. The resonance curves observed in copper are similar at high rf levels, but more nearly Gaussian at low rf levels.

The important feature of these curves is the fact that the dispersion does not saturate at the same level as the absorption, but remains roughly constant out to a level of several gauss rf. As will be discussed below, this behavior is in strong conflict with the existing theories of magnetic resonance saturation in solids, which predict that both the absorption and dispersion should decrease (near resonance) at the same level, according to (1). Portis[6] has observed similar nonsaturation of the dispersion in the case of paramagnetic resonance in F-centers, but the saturation behavior of the absorption was different. The theory developed by Portis for the case of F-centers is not applicable here, because the different nuclei are tightly coupled by the dipolar interaction.

[15] N. J. Poulis, Physica **16**, 373 (1950).
[16] N. Bloembergen, Physica **15**, 588 (1949).

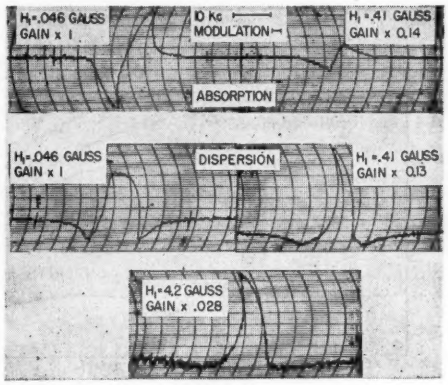

FIG. 2. Absorption and dispersion signals in pure aluminum at various rf power levels. The modulation was 14~ in phase with the lock-in detector and the resonance frequency was about 7.6 megacycles per second.

The absorption line becomes narrower above saturation, as previously reported by Abell and Knight,[17] and similar narrowing occurs in the derivative of the dispersion. This is also in conflict with theory, which predicts that the absorption and dispersion curves should both broaden upon saturation.

The audio phase of the signal at the output of the receiver was not the same as the phase of the modulation applied to the dc magnetic field H_0. In the limit of small modulation frequency, the nuclear resonance signal and the modulation appear to be in phase, and the output of the lock-in amplifier probably represents the true derivative of the absorption and dispersion. As the modulation frequency is increased, however, the nuclear resonance signal lags behind the modulation. The apparent derivative of the absorption or dispersion, as indicated by the lock-in detector, is then not the true derivative, and a resonance signal can also be observed by changing the lock-in detector phase to 90° with respect to its normal setting. This phenomenon is evidently not directly related to the nonsaturation of the dispersion mode noted in the paragraph immediately above. The phase lag of the resonance signal relative to the modulation is evidently a consequence of the fact that the modulation period is comparable to T_1. A similar phase lag can be observed in systems obeying the Bloch equations, as experimentally and theoretically investigated by Halbach.[18]

In Figs. 3 and 4 are shown the apparent dispersion derivatives at resonance in copper and aluminum, observed with two different modulation frequencies and with the lock-in detector adjusted to detect signals either in phase or in quadrature with the modulation. The in-phase data obtained at 14 cps are apparently very nearly what would be observed in the limit of low modulation frequency, ("slow passage") and therefore

[17] D. F. Abell and W. D. Knight, Phys. Rev. **93**, 940 (1954).
[18] K. Halbach, Helv. Phys. Acta **27**, 259 (1954).

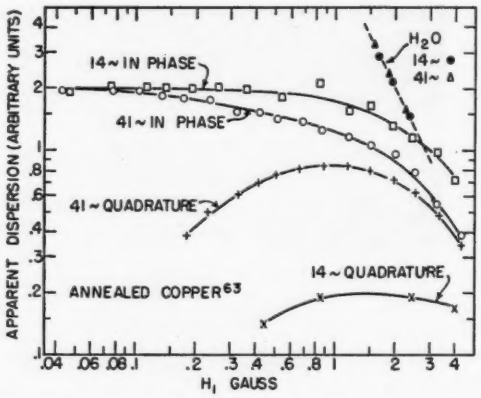

FIG. 3. Apparent relative dispersion derivatives at resonance per resonating nucleus as a function of rf power, for Cu^{63} in annealed copper and protons in impure water. The modulation frequency and phase relative to the lock-in detector are as marked.

nearly correctly represent the behavior of the true derivative of the steady-state dispersion.

For purposes of calibration and comparison, Figs. 3 and 4 also include the derivative of the dispersion at resonance of protons in water at the same frequency (thus at a smaller magnetic field) as that used to obtain the aluminum and copper data. The water was heavily doped with paramagnetic impurity (manganese sulfate) and the relaxation time of the protons was of the order of $\frac{1}{5}$ millisecond. The Bloch equations predict that well above saturation the derivative of the real part of the nuclear susceptibility of such a sample should be (at resonance)

$$\frac{\partial\chi'}{\partial H_0}=\frac{\chi_0 H_0 T_{2H}}{2H_1^2 T_{1H}}, \tag{6}$$

where χ_0 is the proton contribution to the static nuclear susceptibility and T_{2H} and T_{1H} are the transverse and longitudinal relaxation times[4] for the protons in the sample. The water and metal samples occupied nearly the same volume in the nuclear induction head, so that no geometrical correction is necessary for comparison.

The quantity plotted in Figs. 3 and 4 is the output of the lock-in detector divided by the product of the rf input level to the nuclear induction head, the modulation amplitude, the total number of resonated nuclei in the sample, the Q-factor of the receiver coil in the nuclear induction head, and the over-all gain of the receiver and lock-in detector. Of these corrections, the first and the last two were given automatically by the calibration circuit. In the limit of low modulation frequency the quantity plotted in Figs. 3 and 4 should be the relative contribution per nucleus to the rf susceptibility derivative at resonance. The accuracy of these data is thought to be better than ± 20 percent.

Apparently these effects are not limited to metals, but are characteristic of solids in general, well below their melting points. In insulating solids the observed dispersion signals are in most cases different from what they are in metals, because the relaxation time is likely to be longer than the period of the dc magnetic field modulation. In Fig. 5 are shown dispersion signals obtained from two NaCl samples of different purity. In the impure NaCl, the relaxation time is thought to be long compared to the modulation period and short compared to the several minutes required to pass through resonance. A similar dispersion curve can be obtained from distilled water at high rf levels, as discussed by Halbach.[18] In the Harshaw NaCl the relaxation time is clearly of the order of the time (about one minute) taken to sweep through the resonance, as indicated by the asymmetry and hysteresis in the observed dispersion signal.

We conclude this section by noting that the shape and magnitude of the observed dispersion signals in both metals and insulators can be accounted for by the assumption that in the limit of large H_1 the Bloch equations hold with $T_1 \simeq T_2$, rather than $T_2=\frac{1}{2}g(\nu_0)$ as is required to yield the correct line width below saturation. This assumption will be more or less justified in the next section, and the resulting predictions and comparison with experiment will be discussed there and in Sec. IV.

III. THEORY

A. Previous Saturation Theories

We now discuss the previous theories[4–6] of magnetic resonance saturation which lead to incorrect predictions of the magnitude of the dispersion at high rf field intensities in solids. Throughout this paper we are concerned with solids in which the nuclei can be regarded as fixed in their lattice positions, and we neglect diffusion and lattice vibrations. This is justified only well below the melting point.

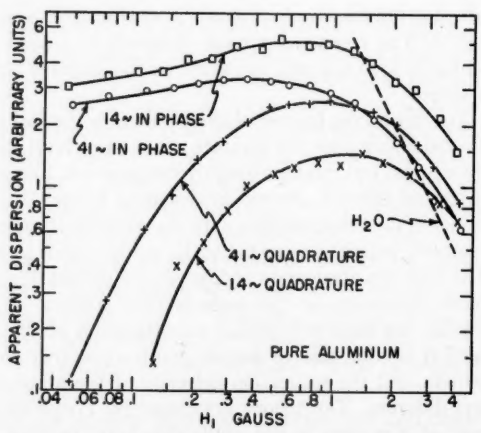

FIG. 4. Apparent relative dispersion derivatives at resonance per resonating nucleus as a function of rf power, for Al^{27} in pure aluminum and protons in impure water. The units of $N^{-1}\partial\chi'/\partial H_0$ are the same as in Fig. 2 and to avoid confusion the actual H_2O data are omitted and only the dotted line through the H_2O points of Fig. 2 is included.

The theory developed by BPP[5] is the simpler of the two approaches to saturation in magnetic resonance, and is based on three assumptions. The first of these is that the effect of the spin-lattice interaction is to relax the spins to their equilibrium state in a time T_1. This is evidently correct, at least to a good approximation, in most cases. The second assumption is that the spins interact strongly with one another, so that energy absorbed at one frequency of the dipolar broadened resonance line is quickly transferred to all the spins, whether or not they are in a local field exactly corresponding to the applied rf frequency. This assumption has been discussed by Bloembergen[19] and by Portis,[6] and appears to be justified in this case because of the possibility of mutual spin flips between neighboring nuclei brought about by the dipolar interaction. The third assumption of the BPP theory is that the complex rf susceptibility is proportional to the difference in population of the nuclear spin levels and is not affected by the presence of the rf field except in so far as the spin level populations are. When the spin system becomes saturated the populations of the spin levels become more nearly equal and it follows directly from this assumption that both the real and imaginary parts of the rf susceptibility saturate in the same way.

If the line shape is assumed to be Lorentzian[20] below saturation, the predictions of the BPP theory are in agreement with those of the Bloch equations (under steady-state conditions) and, apparently, with experiment in the case of most gases and liquids. As discussed below, the BPP theory also predicts the correct asymptotes for χ'' in solids for the limits $H_1 \to 0$ and $H_1 \to \infty$, and, therefore, the correct qualitative behavior of χ'' over the whole range of H_1 (except in the special case of inhomogeneity broadening).[6] The BPP prediction of the variation of M_z just at the onset of saturation is also correct. Evidently, these predictions are valid in solids because they are based only on the first two assumptions of the BPP theory. The predictions concerning the dispersion above saturation, which are in marked disagreement with the experimental data of Sec. II, are a consequence of the third assumption, and it appears certain that the trouble lies here.

Bloembergen[19] has pointed out that the BPP theory must be incorrect when a large rf field is applied to a solid in which $T_1 \neq T_2$ because in the limit as $H_1 \to \infty$ the line width is predicted to be $\gamma H_1 \sqrt{(T_1/T_2)}$ rather than γH_1 as expected from the uncertainty principle and the transition probability associated with the rf field.

The assumption that the complex susceptibility is proportional to the difference in population of the adjacent nuclear spin levels is equivalent to the assumption that the spin system behaves as if it were at equilibrium at a spin temperature higher than the lattice temperature, corresponding to the actual distribution of

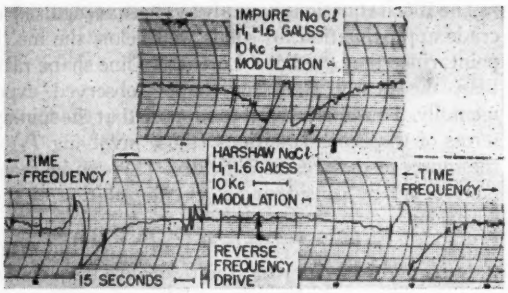

FIG. 5. Apparent dispersion derivatives in samples of NaCl of different purity. The Na^{23} nucleus was observed at a frequency of about 7.5 megacycles. The modulation frequency was 41 cps in phase with the lock-in detector.

nuclear spins among the $2I+1$ levels. Evidently, the assumption of an equilibrium distribution of spin states, i.e., a spin temperature, is not justified in the case of saturation, where the spins are subject to a large time-dependent secular perturbation. Although the amplitudes of the spin states may be described by a Boltzmann distribution, the phases of the quantum states are not random, as would be the case[21] at thermal equilibrium and as is required in most quantum-mechanical perturbation calculations. This can be seen from the fact that M_x and M_y, the transverse components of nuclear magnetization, are not zero and cannot in general be made arbitrarily small compared with M_z if the system is saturated. A random distribution of quantum phases would lead to zero transverse magnetization. For this reason it is surprising that the simple assumption of a spin temperature predicts the same behavior for a Lorentzian line as the more detailed assumptions of the Bloch equations.

The Bloch equations[4] are based on the assumptions that the interaction of the spins with the lattice and with each other can be considered independently of their interaction with the externally applied magnetic field, and that the effect of spin-lattice and spin-spin interactions can be described by simple relaxation terms. They predict a Lorentzian line shape and saturation behavior similar to that predicted by BPP, apparently in good agreement with experiment for most liquids and gases. Detailed theoretical justification of the Bloch equations has been given by Wangsness and Bloch[22] and by Kubo and Tomita,[23] but their work is applicable only to liquids and gases in which the correlation time of the motion of the nuclei is short compared to the Larmor period. These authors neglect the effect of the rf field on the relaxation process, and Bloch and Wangsness also consider the spins as independent of each other, which, as they recognize, is not justified in the case of solids.

[19] N. Bloembergen, thesis, Leiden (unpublished), p. 49.
[20] G. E. Pake and E. M. Purcell, Phys. Rev. **74**, 1184 (1948); **75**, 534 (1949).
[21] R. C. Tolman, *Principles of Statistical Mechanics* (Oxford University Press, New York, 1930), Chap. IX.
[22] R. K. Wangsness and F. Bloch, Phys. Rev. **89**, 728 (1953).
[23] R. Kubo and K. Tomita, J. Phys. Soc. (Japan) **9**, 888 (1954).

The Bloch equations have always been recognized as a crude approximation for solids well below the melting point, since they predict a Lorentzian line shape rather than the nearly Gaussian shape[20] observed experimentally. Thus it is natural to suppose that the spin-spin terms of the Bloch equations (those involving T_2) are the source of the present difficulty. This can be seen in more detail by considering a specific solution of these equations.

Suppose that a circularly polarized rf field of magnitude H_1 and frequency ω_0 (the resonance frequency) is continuously applied to the solid, and suppose that initially the nuclear magnetization $\mathbf{M}$ is in the direction of the rf field and of magnitude M_1. Assume that $T_1 \gg T_2$ as is the case in most solids at low temperatures. The terms in the Bloch equations involving T_1 can then be neglected during a time comparable to T_2, and the prediction of the Bloch equations is that $\mathbf{M}$ will remain parallel to $\mathbf{H}_1$ and will decay exponentially to zero in a time T_2.

In the course of this decay work M_1H_1 is done by the spin system on the external magnetic field; this energy can come only from the internal (spin-spin) energy of the spin system. The energy cannot come from the lattice, because we have implicitly neglected the spin-lattice interaction by neglecting the T_1 term in the Bloch equations. Speaking somewhat classically and loosely we can say that the initial state corresponds to n excess spins aligned in the rf field direction and the final state corresponds to no excess spins aligned in any specific direction and $\mathfrak{N}$ excess spins aligned preferentially in the direction of the magnetic fields of their neighbors. Conservation of energy requires that

$$nH_1 = \mathfrak{N}\delta H, \tag{6}$$

where δH is of the order of the rms magnetic field at a nucleus due to its neighbors, or approximately the half-width of the resonance line in gauss.

The decay predicted in time T_2 by the Bloch equations is an irreversible process in a thermally isolated spin system, and the entropy of the system must increase. The initial entropy of the spin system is the same as that for a spin system with n excess spins parallel to a fixed magnetic field:

$$S_i = S_0 - kn^2/N. \tag{7}$$

S_0 is the maximum entropy of the spin system corresponding to complete chaos, k is Boltzmann's constant, N is the total number of spins, and for simplicity we assume that the spin is $\frac{1}{2}$.

By analogy with (7), the entropy of the final state is expected to be approximately given by

$$S_F = S_0 - k\mathfrak{N}^2/N. \tag{8}$$

This assumption can be justified by a detailed calculation similar to that of Appendix A discussed below.

From (6), (7), and (8) it follows that the spin entropy increases during the decay only if $H_1 \lesssim \delta H$. Thus for sufficiently large H_1 the Bloch equations are evidently incorrect, because they predict an irreversible process in which the entropy decreases.

The actual final value of $\mathbf{M}$ after such a transverse decay can be estimated by maximizing the entropy, subject to the condition that energy must be conserved. We assume that the entropy is $S_0 - k(n^2+\mathfrak{N}^2)/N$ and require that $nH_1 + \mathfrak{N}\delta H$ be a constant. If $\mathfrak{N}$ is initially zero the entropy is a maximum if n, and therefore M, is finally $[1+(\delta H)^2/H_1^2]^{-1}$ times its initial value, and the external energy $-MH_1$ is $H_1^2/(\delta H)^2$ times the internal spin-spin energy.

To summarize, for $H_1 \lesssim \delta H$ the spin system is unable to take up the entire energy of the nuclear magnetization with respect to the rf magnetic field, and the transverse decay predicted by the Bloch equations is partially forbidden. As will be discussed in the next section such a process is further inhibited by the rapid decrease of the suitable transition probabilities as the rf field is increased.

These considerations suggest that in the limit of large H_1 the x,y components of the Bloch equations should be modified. The modification can most easily be presented in a coordinate system[24] rotating about the z-axis at the rf frequency ω (not necessarily the resonance frequency) with its x-axis in the direction of the circularly polarized rf field H_1. In such a coordinate system the modified Bloch equations are

$$\dot{M}_{xr} = \gamma[\mathbf{M}_r \times \mathbf{H}_{er}]_{xr} - M_{xr}/T_{2e}, \tag{9a}$$

$$\dot{M}_{yr} = \gamma[\mathbf{M}_r \times \mathbf{H}_{er}]_{yr} - M_{yr}/T_2, \tag{9b}$$

$$\dot{M}_{zr} = \gamma[\mathbf{M}_r \times \mathbf{H}_{er}]_{zr} - (M_{zr} - M_0)/T_1. \tag{9c}$$

The subscript r denotes a quantity measured with respect to the rotating coordinate system, and H_{er} is the effective magnetic field.[23] $\mathbf{H}_{er}$ is given by

$$\mathbf{H}_{er} = \left(H_0 - \frac{\omega}{\gamma}\right)\mathbf{k}_r + H_1\mathbf{i}_r, \tag{10}$$

where $\mathbf{i}_r$ and $\mathbf{k}_r$ are unit vectors in the x_r and z_r directions in the rotating system.

In (9) T_{2e} is of the order of T_1 and is a transverse spin-lattice relaxation time, since, as discussed at length above, the spin-spin collisions are unable to relax the magnetization in the direction of a large rf field. T_2 is still the correct relaxation time to use in the y-component of (9) because a decay in the y-direction (rotating frame of reference) involves no change in energy. Solution of (9) leads to the prediction

$$\chi' = \frac{\frac{1}{2}\chi_0 T_2 T_{2e}\omega_0(\omega_0 - \omega)}{(\omega-\omega_0)^2 T_2 T_{2e} + \gamma^2 H_1^2 T_1 T_2 + 1} \tag{11a}$$

$$\chi'' = \chi' T_{2e}^{-1}(\omega_0 - \omega)^{-1}. \tag{11b}$$

[24] Rabi, Ramsey, and Schwinger, Revs. Modern Phys. **26**, 167 (1954), to which the reader is referred for an excellent introduction to the use of rotating coordinates.

The Lorentzian dispersion predicted by (11a) is in reasonable agreement with both the shape and order of magnitude of the observed dispersion at high rf fields. Unfortunately (11) is quantitatively applicable only at the highest rf fields attainable. To obtain quantitative results at lower rf fields it is necessary to consider the problem in more detail.

To conclude our discussion of the existing saturation theories we may mention another defect in the Bloch equations. As usually written,[4] they predict that the effect of the spin-lattice interaction is to relax the nuclear magnetization toward its static equilibrium value $\chi_0 H_0 \mathbf{k}$ in time T_1, where $\mathbf{k}$ is a unit vector in the z direction. Actually it is more reasonable to assume that the magnetization relaxes toward the value $\chi_0 \mathbf{H}$ corresponding to the instantaneous applied field $\mathbf{H}$. The theory and experiment in the present paper will be restricted to the case $H_0 \gg H_1$ so that $H_0\mathbf{k}$ and $\mathbf{H}$ very nearly coincide in magnitude and direction, and this consideration is unimportant.

B. Rotating Coordinate Representation

If we neglect the interaction with the lattice, the complete Hamiltonian of the spin system is[25]

$$\mathcal{H}_s = g\beta H_0 \sum_j I_{jz} + g\beta 2H_1(\cos\omega t)\sum_j I_{jx} + g^2\beta^2 \sum_{k>j}(r_{jk}^{-3}\mathbf{I}_j\cdot\mathbf{I}_k - 3r_{jk}^{-5}\mathbf{r}_{jk}\cdot\mathbf{I}_j\,\mathbf{r}_{jk}\cdot\mathbf{I}_k) + \sum_{k>j}\tilde{A}_{jk}\mathbf{I}_j\cdot\mathbf{I}_k, \quad (12)$$

where H_0 is the dc field, $2H_1$ is the applied linearly polarized rf field[12] of frequency ω, and the spin operators I_j are expressed in units of $\hbar$. All nuclei are assumed to have the same g-factor and spin; the case of two magnetic ingredients will be considered later. The last term is included for generality; evidence for the existence of such a mutual nuclear interaction in solids has been discussed by Bloembergen and Rowland[26] and by Ruderman and Kittel.[27] The analogous interaction between nuclei in molecules was first suggested by Ramsey and Purcell.[28]

The spin wave function ψ obeys Schrödinger's equation:

$$-i\hbar\dot{\psi} = \mathcal{H}_S\psi. \quad (13)$$

We will use the transformations

$$\psi = R_{y\Theta}\psi_r = R_{y\Theta}R_{z\omega t}\psi_\rho, \quad (14)$$

where

$$R_{z\omega t} = \exp(-i\omega t\textstyle\sum_j I_{jz}), \quad (15)$$

$$R_{y\Theta} = \exp(-i\Theta\textstyle\sum_j I_{jy}), \quad (16)$$

$$\Theta = \tan^{-1}[\gamma H_1/(\omega-\omega_0)]. \quad (17)$$

Then it follows that

$$-i\hbar\partial\psi_r/\partial t = (-\hbar\omega\textstyle\sum_j I_{zj} + R_{z\omega t}\mathcal{H}_S R_{z\omega t}^{-1})\psi_r \equiv \mathcal{H}_{er}\psi_r, \quad (18)$$

and

$$-i\hbar\partial\psi_\rho/\partial t = R_{y\Theta}\mathcal{H}_{er}R_{y\Theta}^{-1}\psi_\rho \equiv \mathcal{H}_{e\rho}\psi_\rho. \quad (19)$$

The unitary transformation $R_{z\omega t}$ can be regarded as a transformation to a coordinate system rotating about the z-axis with frequency ω (note that this is the rf frequency, not necessarily the resonance frequency ω_0). As above, the subscript r is used to denote quantities in this coordinate system and $\mathcal{H}_{er}$ is the effective Hamiltonian in the r-system.

$R_{y\Theta}$ corresponds to a further transformation to a coordinate system fixed with respect to the r-system, whose z-axis coincides with the effective magnetic field direction, and whose y-axis coincides with the y-axis of the r-system. Θ is the angle between the effective magnetic field $\mathbf{H}_{er}$ in the rotating coordinate system[24] and the z-axis in the fixed system. Quantities in this system are denoted by the subscript ρ.

The Hamiltonians $\mathcal{H}_{er}$ and $\mathcal{H}_{e\rho}$ in (18) and (19) are readily obtained from the fact that the operators $\mathbf{I}_j$ transform like vectors under the rotations corresponding to $R_{z\omega t}$ and $R_{y\Theta}$. Since the $\mathbf{I}_j$ occur only in scalar products the same result can be achieved by applying the inverse rotation to the other vector of the scalar product. Thus $\mathbf{I}_j\cdot\mathbf{I}_k$ is invariant under these transformations while the $\mathbf{r}_{jk}$ are transformed under the inverse rotation. This procedure is simply an algebraic shortcut; actually the $\mathbf{r}_{jk}$ are invariant parameters and the $\mathbf{I}_j$ undergo transformation. In this way we get

$$\mathcal{H}_{er} = g\beta\mathbf{H}_{er}\cdot\textstyle\sum_j \mathbf{I}_j + \sum_{k>j}(A_{jk}\mathbf{I}_j\cdot\mathbf{I}_k + B_{jk}I_{jz}I_{kz}) + \text{time-dependent part}, \quad (20)$$

$$\mathcal{H}_{e\rho} = g\beta H_{er}\textstyle\sum_j I_{jz} + \sum_{k>j}\{A_{jk\rho}\mathbf{I}_j\cdot\mathbf{I}_k + B_{jk\rho}I_{jz}I_{kz} + D_{jk\rho}[I_{j+}I_{k+} + I_{j-}I_{k-}] + E_{jk\rho}[(I_{j+}+I_{j-})I_{kz} + I_{jz}(I_{k+}+I_{k-})]\} + \text{time-dependent part}, \quad (21)$$

where

$$A_{jk} = \tilde{A}_{jk} + g^2\beta^2 r_{jk}^{-3}(\tfrac{3}{2}\xi_{jk}^2 - \tfrac{1}{2}), \quad (22)$$

$$B_{jk} = -3g^2\beta^2 r_{jk}^{-3}(\tfrac{3}{2}\xi_{jk}^2 - \tfrac{1}{2}), \quad (23)$$

$$A_{jk\rho} = \tilde{A}_{jk} + (\tfrac{3}{2}\cos^2\Theta - \tfrac{1}{2})(A_{jk} - \tilde{A}_{jk}), \quad (24)$$

$$B_{jk\rho} = (\tfrac{3}{2}\cos^2\Theta - \tfrac{1}{2})B_{jk}, \quad (25)$$

$$D_{jk\rho} = \tfrac{1}{4}\sin^2\Theta B_{jk}, \quad (26)$$

$$E_{jk\rho} = \tfrac{1}{2}\sin\Theta\cos\Theta B_{jk}, \quad (27)$$

$$H_{er} = |\mathbf{H}_{er}| = [H_1^2 + (H_0 - \omega/\gamma)^2]^{\frac{1}{2}}. \quad (28)$$

Here $I_{j\pm}$ are the raising and lowering operators $I_{jx} \pm iI_{jy}$ having selection rules $\Delta M_{Ij} = \pm 1$ respectively, and ξ_{jk} is the z-direction cosine of $\mathbf{r}_{jk}$. The time dependent parts of these Hamiltonians contain terms like $I_{j\pm}I_{k\mp}$, $I_{j\pm}I_{kz}$, $I_{jz}I_{k\pm}$, etc., with time dependences $\exp(\pm i\omega t)$, $\exp(\pm 2i\omega t)$.

[25] J. H. Van Vleck, Phys. Rev. **74**, 1168 (1948).
[26] N. Bloembergen and T. J. Rowland, Phys. Rev. **97**, 1679 (1955).
[27] M. A. Ruderman and C. C. Kittel, Phys. Rev. **96**, 99 (1954).
[28] N. F. Ramsey and E. M. Purcell, Phys. Rev. **85**, 143 (1952).

We now assume $H_0 \gg H_{er} \cong \delta H$ and apply Dirac perturbation theory to Schrödinger's equation in the rotating coordinate systems [Eqs. (18) and (19)]. The time-dependent part of $\mathcal{H}_{er}$ (or $\mathcal{H}_{ep}$) is a nonsecular perturbation on the time-independent part. It connects states for which $\Delta M_I = \pm 1$ for one or two nuclei, and for it to be secular these states must differ in effective energy[29] by $\pm\hbar\omega \simeq \pm\gamma\hbar H_0$ or $\pm 2\hbar\omega \cong 2\gamma\hbar H_0$. Actually such states will differ in effective energy[29] by about $c\gamma\hbar(H_{er} \pm \delta H)$, with $c=0$, 1, or 2, so the condition for a secular perturbation is not satisfied and the time-dependent part of $\mathcal{H}_{er}$ can be ignored for most purposes.[30] It will be noted that these time-dependent terms are the same ones neglected by Van Vleck[25] in his calculation of the moments of the absorption line, plus a term corresponding to the component of applied rf field rotating in the opposite direction from that of the rotating coordinate system.

If H_{er} is very large (but still much less than H_0) the fourth and fifth terms of $\mathcal{H}_{ep}$ are nonsecular perturbations, since, being time-independent, to be secular they must connect eigenstates of the first three terms of $\mathcal{H}_{ep}$ having the same effective energy, whereas actually they connect states differing in effective energy by about one or two times $\gamma\hbar(H_{er} \pm \delta H)$. Under these circumstances we can ignore these terms and $\mathcal{H}_{ep}$ conserves M_{zp}, the nuclear magnetization in the effective field direction. It should be noted that to ignore these terms the transition probabilities associated with them must be much smaller than T_1^{-1}. Thus this procedure is valid only for H_{er} very much larger than the resonance line width.

Conservation of M_{zp} leads to a system of equations similar to (9), whose solution in the limit of large H_1 is identical with (11). We do not go into details because the theory is not applicable to any experimentally attainable situation. Experimentally we are limited to rf field intensities comparable to the resonance line width.

C. Canonical Distribution in the Rotating System

In the previous section we obtained a transformed spin Hamiltonian which was effectively independent of time. A time-independent Hamiltonian is convenient to work with because the concepts of statistical mechanics can be more easily applied to it and because the effective energy[29] of the spin system can change only through the spin-lattice interaction. The spin-lattice interaction terms of the Hamiltonian acquire an additional explicit time dependence as a result of the transformation to the rotating system, but if H_{er} is large enough, these terms can be considered as a small perturbation which transfers effective energy between the spin system and the lattice and eventually determines the value of the effective energy of the spin system.

As in the statistical mechanics of stationary systems we consider a Gibbsian ensemble of systems, each consisting of the solid with the rf field continously applied to it. Suppose that the (time-dependent) spin-lattice interaction is somehow turned off, and that the average expectation values of the lattice Hamiltonian and transformed spin Hamiltonian ($\mathcal{H}_{er}$) are known. In the absence of further information the distribution of states in the ensemble is still highly ambiguous, but the *most probable* distribution is a canonical distribution of states with respect to the lattice and the *transformed* Hamiltonian. Associated with this canonical distribution are two temperatures, determined by the canonical average expectation values of the lattice and transformed spin Hamiltonians. One of these is the lattice temperature, which is presumably positive in any physically attainable solid. The other will be called the effective spin temperature, which is positive or negative depending on whether the average expectation value of the effective spin Hamiltonian $\mathcal{H}_{er}$ is negative or positive. The situation is closely analogous to that in the fixed coordinate system if the spin-lattice interaction is turned off and if no rf field is applied. In that case the most probable state of the system is also represented by a canonical distribution of states, with lattice and spin temperatures which are not necessarily equal. Negative spin temperatures are easily attained (with pulse techniques) in insulating crystals in which the spin-lattice interaction is very small. In both the fixed and the rotating coordinate systems the lattice and (effective) spin temperatures can be different because the spin and lattice Hamiltonians commute, and it is sensible to talk about canonical distributions of states only because the lattice and (effective) spin Hamiltonians are time-independent (except for some nonsecular perturbations) in both cases.

We now consider what happens if we turn on the spin-lattice interaction and wait for a time long compared to the spin-lattice relaxation time, but short compared to the time required for the rf field to heat up the lattice appreciably. In the absence of the rf field and in the fixed coordinate system, the spin system will approach a canonical distribution of states with equal spin and lattice temperatures. In the presence of the rf field, in the rotating system, the spin-lattice interaction will change the average expectation value of the effective spin Hamiltonian to some quasi-equilibrium value. We have no rigorous assurance that the spin system will remain in a canonical distribution of states with respect to $\mathcal{H}_{er}$ but we *assume* that it will. This assumption can

[29] "Effective energy" will be used to denote effective energy with respect to the rotating coordinate system, i.e., with respect to the time independent part of $\mathcal{H}_{er}$ or $\mathcal{H}_{ep}$, *not* the total energy in the fixed system, which is no longer a constant of the motion. The word "effective" will denote any quantity defined or measured in the rotating system.

[30] If $H_{er} < \delta H$ it becomes questionable to ignore the time-dependent part of $\mathcal{H}_{er}$, since then this "perturbation" is larger than the "unperturbed" part of the Hamiltonian. For the same reason it may be incorrect to ignore the oppositely rotating component of circularly polarized rf field which is always present when a linearly polarized field is applied. These considerations are probably not as important as might be thought, because these perturbations are very far from secular; furthermore, experimental evidence discussed below indicates that transitions produced by these time dependent parts of $\mathcal{H}_{er}$ and $\mathcal{H}_{ep}$ are negligible.

be regarded as an admission of our ignorance concerning the system; lacking detailed information, we simply assume that the system is in its most probable state for the limit of zero spin-lattice interaction. The actual effective spin temperature in the steady state is determined by the lattice temperature and the spin-lattice interaction, and depends on H_0, H_1, and ω. Unlike the static case with no rf field, the effective spin temperature is different from the lattice temperature and can actually be negative. The reason for this difference is that the spin-lattice interaction in the rotating system contains an explicit time dependence which is not present in the fixed system.

An analogous problem is that of a gas in a fairly well-insulated bottle, connected to one or more temperature baths by heat leaks. To find, say, the pressure of the gas it is necessary to assume immediately that the gas molecules are in their most probable state (a Boltzmann distribution) subject to the constraint that they have some definite energy (corresponding to the gas temperature). The problem is then reduced to finding the gas temperature as determined by the various heat leaks (corresponding to the spin-lattice interaction) and temperature baths (corresponding to the lattice). If the bottle is constrained to move it is necessary to transform to the bottle's coordinate system before applying statistical mechanics to the gas, in analogy to the rotating coordinate transformation used here. All of classical acoustics and fluid mechanics are based on assumptions similar to those used in this paper since it is always assumed that matter possesses the same thermodynamic properties viewed from a suitably moving coordinated system and in suitably small pieces as it does at rest in a fixed coordinate system. When temperature, pressure, or velocity gradients in a gas become too large, this assumption breaks down (i.e., at low pressures and in shock waves) and the theory becomes difficult. Likewise, in the case of spins when the spin-lattice interaction becomes too large, the assumptions used here break down and the theory is difficult.

A rigorous justification of this procedure would be extremely difficult, if not impossible. It might be based on something analogous to the Boltzmann H-theorem. The least that can be said for this assumption is that above saturation it is the only simple one that is not obviously wrong.

The assumption that the spin system is in a canonical distribution of states with respect to $\mathcal{H}_{er}$ leads immediately to the conclusion that the magnetization $\mathbf{M}_r$ is in the direction of the effective field $\mathbf{H}_{er}$, just as in the static case the magnetization $\mathbf{M}$ is in the direction of $\mathbf{H}_0$. The effective external energy of the spin system is $-\mathbf{M}_r\cdot\mathbf{H}_{er}=-M_{z\rho}H_{er}$, where $M_{z\rho}$ is the z_ρ component of magnetization in the ρ coordinate system. We define a spin-spin energy in the rotating system which contains all the spin-spin terms of $\mathcal{H}_{er}$:

$$\mathcal{H}_{SS}=\sum_{j>k}(A_{jk}\mathbf{I}_j\cdot\mathbf{I}_k+B_{jk}I_{jz}I_{kz}). \tag{29}$$

The internal spin-spin energy is comparable to the external energy when the effective external field H_{er} becomes comparable to the local fields at the nuclei due to their neighbors (i.e., approximately the line width in gauss) just as in the static case.[31] In Appendix A it is shown that

$$\langle\langle\mathcal{H}_{SS}\rangle\rangle=-[(\delta H)^2/H_{er}{}^2]M_{z\rho}H_{er}, \tag{30}$$

where $\langle\langle O\rangle\rangle$ denotes the canonical average expectation value of the operator O, and

$$(\delta H)^2=\tfrac{1}{2}\langle(\Delta H)^2\rangle_{Av}+\frac{I(I+1)}{\hbar^2\gamma^2N}\sum_{k>j}\bar{A}_{jk}{}^2. \tag{31}$$

Here $\langle(\Delta H)^2\rangle_{Av}$ is the second moment of the unsaturated resonance line as calculated by Van Vleck.[25]

The reasoning which leads to (30) is essentially the same as that used in Sec. III(b) to find the state of maximum entropy of the spin system after a transverse Bloch decay, and the $(\delta H)^2$ used there is the quantity given by (31). The state of maximum entropy of a system for a given energy is, of course, described by the canonical distribution of states corresponding to that energy.

The problem is solved if the value of $\langle\langle\mathcal{H}_{er}\rangle\rangle$ can be determined, because we can write

$$\begin{aligned}\langle\langle\mathcal{H}_{er}\rangle\rangle&=-M_{z\rho}H_{er}+\langle\langle\mathcal{H}_{SS}\rangle\rangle\\&=-M_{z\rho}H_{er}[1+(\delta H)^2/H_{er}{}^2].\end{aligned} \tag{32}$$

Transforming back to the fixed system we have (since $\mathbf{M}_r$ is in the direction of $\mathbf{H}_{er}$)

$$M_z\simeq M_{z\rho}\sin\Theta\cos\omega t, \tag{33a}$$

$$M_y\simeq M_{z\rho}\sin\Theta\sin\omega t, \tag{33b}$$

$$M_z\simeq M_{z\rho}\cos\Theta. \tag{33c}$$

To determine the expectation value of $\mathcal{H}_{er}$ we use a simple relaxation assumption to account for the spin-lattice interaction. The physical reasoning which follows is justified in more detail and under more general conditions in Appendix B. We assume here that the effect of the spin-lattice interaction is to relax each nucleus independently into its equilibrium state in a time T_1:

$$[\partial/\partial t]_{SL}\langle\langle\mathbf{I}_j\rangle\rangle=-(\langle\langle\mathbf{I}_j\rangle\rangle-\mathbf{I}_0)/T_1, \tag{34}$$

where the left-hand side is the spin-lattice contribution to the time derivative of the expectation value of $\mathbf{I}_j$, and $\mathbf{I}_0$ is the static thermal equilibrium value of $\mathbf{I}_j$, given by

$$\mathbf{I}_0=\tfrac{1}{3}g\beta I(I+1)\mathbf{H}/kT. \tag{35}$$

Here the applied field $\mathbf{H}$ can be closely approximated by $H_0\mathbf{k}$ (since $H_1\ll H_0$).

It might seem more logical to assume that the nuclei are relaxed along the effective field instead of the actual applied field, so that we should use $\mathbf{H}_{er}$ in (35) instead of $\mathbf{H}$. That this would be incorrect follows from the fact

[31] J. H. Van Vleck, J. Chem. Phys. 5, 320 (1937).

that the electrons, which are responsible for the relaxation, are almost completely unaffected by the rf field and effectively see only the large field H_0 in the z-direction. Furthermore, if we were to use the effective field in (35) we would get obviously incorrect predictions for the dispersion.

Equation (34) implies that T_{2e}, the transverse electronic relaxation time defined previously, is equal to T_1. This assumption is in accord with theory[12,23,32] for metals, assuming the electrons are in a Fermi distribution of states.

We assume that the spin-lattice interaction does not perturb the spin system cononical distribution appreciably except to bring about a slow change in $\langle\langle \mathcal{H}_{er}\rangle\rangle = \langle\langle \mathcal{H}_{e\rho}\rangle\rangle$, the transformed spin Hamiltonian average expectation value. The spin lattice relaxation can be fictionally regarded as a two-step process. The first process is the scattering of the nuclear spin into a completely random orientation, in a time T_1. The second process is a scattering of the spin into an orientation with probability governed by the Boltzmann distribution of states with respect to the externally applied magnetic field, in an infinitesimal time after the first scattering. These two processes correspond respectively to the two terms on the right-hand side of (34). The change in $\langle\langle \mathcal{H}_{er}\rangle\rangle$ with time is the sum of the separate changes brought about by these two processes.

The rate of change of $\langle\langle \mathcal{H}_{er}\rangle\rangle$ due to the first (random) scattering is

$$[\partial/\partial t]_{SLR}\langle\langle \mathcal{H}_{er}\rangle\rangle = +M_{z\rho}H_{er}/T_1 - 2\langle\langle \mathcal{H}_{SS}\rangle\rangle/T_1. \quad (36)$$

The external effective spin energy $-M_{z\rho}H_{er}$ (expectation value of the first term of $\mathcal{H}_{er}$) is proportional to the sum of expectation values of components of the $\mathbf{I}_j$, and is thus expected to decay to zero in time T_1 for random scattering of the spins, corresponding to the first term in (36). The spin-spin energy $\langle\langle \mathcal{H}_{SS}\rangle\rangle$, on the other hand, is quadratic in the components of the $\mathbf{I}_j$, and is therefore expected to decay at twice the relative (logarithmic) rate of the external energy; thus the factor two in the last term of (36).

The effect of the second (Boltzmann) scattering is to change the nuclear magnetization at a rate $+\mathbf{M}_0/T_1$, where $\mathbf{M}_0=\chi_0\mathbf{H}\simeq\chi_0 H_0\mathbf{k}$ (in the fixed coordinate system). The corresponding rate of increase of the effective external energy $-\mathbf{M}\cdot\mathbf{H}_{er}$ is $-(\mathbf{M}_0/T_1)\cdot\mathbf{H}_{er}$. The change in the spin-spin energy is negligible, since the local fields at the nuclei are random in orientation, to a very good approximation. Thus the rate of change of $\langle\langle \mathcal{H}_{er}\rangle\rangle$ due to the Boltzmann scattering is the same as that of the effective external energy:

$$[\partial/\partial t]_{SLB}\langle\langle \mathcal{H}_{er}\rangle\rangle = -M_0 H_{er}\cos\Theta/T_1. \quad (37)$$

To obtain the steady-state value of $M_{z\rho}$ we use (30) and (32), and set the sum of (36) and (37) equal to zero. The result is

$$M_{0\rho}=\frac{M_0\cos\Theta}{1+2(\delta H)^2/H_{er}^2}, \quad (38)$$

where $M_{0\rho}$ is the quasi-equilibrium value of $M_{z\rho}$ for constant H_0, H_1, and ω.

The dispersion is given by

$$\chi'=\frac{M_{xr}}{2H_1}=\frac{M_{0\rho}\sin\Theta}{2H_1}, \quad (39)$$

or

$$\chi'=\frac{M_0\gamma(\omega_0-\omega)}{2\{(\omega_0-\omega)^2+\gamma^2[H_1^2+2(\delta H)^2]\}}, \quad (40)$$

so that above saturation the dispersion is Lorentzian and the dispersion derivative at resonance is

$$\frac{\partial\chi'}{\partial H_0}=\frac{\chi_0 H_0}{2[H_1^2+2(\delta H)^2]}. \quad (41)$$

Equation (33) implies that the nuclear magnetic absorption is zero above saturation. Actually, (33) is an approximation and $\mathbf{M}_r$ is not precisely in the direction of $\mathbf{H}_{er}$. At any rf level there is finite absorption which can be predicted by invoking conservation of energy in the fixed system. Energy is transferred from the spin system to the lattice at a rate $-H_0(M_z-M_0)/T_1$. Equating this to the energy absorbed by the spin system from the rf field, which is $2\omega H_1^2\chi''$, we get

$$\chi''\cong H_0(2H_1\chi'\cot\Theta-M_0)/2T_1H_1^2\omega, \quad (42)$$

or

$$\chi''=\frac{\gamma^2[H_1^2+2(\delta H)^2]H_0M_0}{2\{(\omega-\omega_0)^2+\gamma^2[H_1^2+2(\delta H)^2]\}T_1H_1^2\omega}. \quad (43)$$

This is a Lorentzian line, of the same width as would be predicted by the Bloch equations below saturation for $T_2=\gamma^2[H_1^2+2(\delta H)^2]^{-1}$. At resonance (43) agrees with the asymptotic values of χ'' given by the Bloch and BPP theories. The same is true of off resonance in the limit of very large H_1. This agreement corresponds to the fact that, for any theory, under these conditions $M_z\to 0$ and χ'' is uniquely determined by this simple conservation of energy argument. The fact that all theories yield the same asymptotic χ'' means that the saturation method of obtaining T_1 used in Sec. II is substantially correct. This is not necessarily true if the maximum absorption derivative, rather than the integrated absorption derivative, is used to obtain T_1. Error in the saturation determination of T_1 can also be introduced by the use of a magnetic field modulation period comparable with or less than T_1, as is usually the case experimentally. Fast modulation is treated in Sec. III(e).

The theory developed above is valid only for large H_{er}. If H_{er} becomes comparable to the value of H_1 at which the absorption begins to saturate, the spin-lattice

[32] N. Bloembergen (private communication).

interaction can no longer be regarded as a small perturbation and the magnetization **M** will tend toward the z-axis with a value M_0, rather than toward the direction of H_{er}. Treatment of the intermediate case would be extremely difficult.

The theory is also invalid in the case of large H_{er} but small H_1; i.e., in the case of $\Theta \simeq 0$ or $\Theta \simeq \pi$ (off resonance). In this case the spin-lattice interaction is still in a sense a small perturbation, but the last two terms of $3\mathcal{C}_{ep}$ approach zero. These terms help bring about the transfer between external and internal effective spin energy which is required by the assumption of a canonical distribution of spin states with respect to $3\mathcal{C}_{ep}$. If the transition probabilities due to these terms are smaller than T_1^{-1}, then M_{zp} is conserved and the treatment at the end of the previous section applies. The fact that M_{zp} is conserved in the limit of small H_1 and finite H_{er} means that $M_{zp} \simeq M_z \simeq M_0$ in this case; i.e., the nuclear magnetization approaches its thermal equilibrium value, as is expected on elementary grounds.

We may summarize these limitations with the statement that the theory is valid in the range of H_1 well above the level where the absorption begins to saturate.

Some of the predictions of the theory are summarized in Fig. 6, which shows χ'' and $\partial\chi'/\partial H_0$ at resonance as a function of H_1. At low fields χ'' is determined by the line shape and the Kronig-Kramers relation for zero frequency:

$$\chi_0 = \frac{2}{\pi}\int_0^\infty \frac{\chi''(\nu)d\nu}{\nu}, \tag{44}$$

so that

$$\chi''(\nu_0) = \tfrac{1}{2}\pi\nu_0\chi_0 g(\nu_0). \tag{45}$$

The low rf field dispersion derivative, $\partial\chi'/\partial H_0$, is also determined by the Kronig-Kramers relations[20] and the line shape. We assume that the line is Gaussian. Using Eq. (11) of reference 20 (with the factor $\frac{1}{2}$ mentioned in the erratum)[20] and comparing Eq. (10), reference 20, with Eq. (15), reference 25, we get for a Gaussian line of second moment $\langle(\Delta H)^2\rangle_{Av}$:

$$\partial\chi'/\partial H_0 = \chi_0 H_0/2\langle(\Delta H)^2\rangle_{Av}. \tag{46}$$

This is the low rf field limit assumed in Fig. 6 for the case (curve *a*) of pure dipolar broadening ($\tilde{A}_{jk}=0$). If there exists an exchange-type interaction ($\tilde{A}_{jk}\neq 0$) the resonance line will be exchange-narrowed and the dispersion derivative will be increased (curve *b*).

The region indicated by the dotted lines in Fig. 6 cannot be treated theoretically, but χ'' and $\partial\chi'/\partial H_0$ in this region are expected to undergo a smooth transition between their low and high rf field values, as indicated.

The solid lines in Fig. 6 for large H_1 represent the predictions of (41) and (43). In the limit of large H_1 the dispersion derivative is $M_0/2H_1^2$ (assuming $T_1=T_{2e}$) independent of the spin-spin interaction. At intermediate values of H_1, for pure dipolar interaction

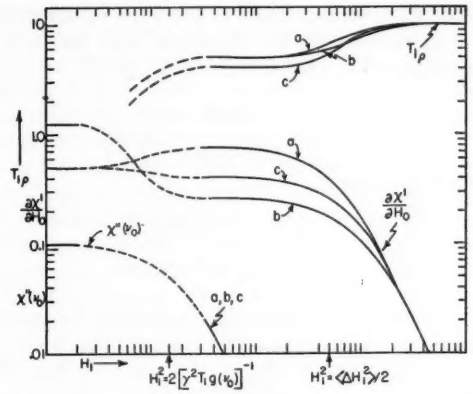

FIG. 6. Qualitative theoretical predictions of χ'', $\partial\chi'/\partial H_0$, and $T_{1\rho}$ at resonance for the cases of pure dipolar coupling (curve *a*), strong exchange-type coupling (curve *b*), and two magnetic ingredients (curve *c*). χ'' is in units of $5\pi\chi_0\nu_0 g(\nu_0)$, $\partial\chi'/\partial H_0$ is in units of $\chi_0 H_0/\langle(\Delta H)^2\rangle_{Av}$, and $T_{1\rho}$ is in units of $T_1/10$.

($\tilde{A}_{jk}=0$), (31), and (41) predict that $\partial\chi'/\partial H_0$ should approach a plateau of value $3\chi_0 H_0/4\langle(\Delta H)^2\rangle_{Av}$ (curve *a*). The presence of exchange-type interaction will increase δH^2 and thus lower the height of the plateau (curve *b*).

In the theory outlined above it is implicitly assumed that parts of the spin-lattice interaction can be included in the spin Hamiltonian as classical perturbations. These parts are the Knight shift in metals and the chemical shift in insulators, accounted for by replacing H_0 by $H_0+\Delta H$, and the possible mutual nuclear spin interactions due to the electrons in the solid, of which the last term of (12) is an example. We know of no rigorous justification for this splitting up of the spin-lattice interaction into stationary and relaxation parts, but it seems physically quite reasonable.

In insulating crystals, where spin diffusion[33] usually plays an important role in the relaxation process, the theory above may not be directly applicable, although the qualitative conclusions are apparently correct. Spin diffusion is expected to be affected by the presence of the large rf field. More specifically, (34) probably represents an oversimplification of the relaxation process.

In metals, (34) may also be an oversimplification of the actual relaxation process. Equation (34) would almost certainly hold if it were also time-averaged in a suitable way, but it probably does not represent the details of the nuclear relaxation correctly. In particular, the relaxation of neighboring nuclear spins by the conduction electrons may not be independent, but may instead be correlated in some way, owing to the finite extent of the electron wave functions. In this case the reasoning behind (37) would probably still be correct, but (36) would have to be replaced by the less specific equation

$$[\partial/\partial t]_{SLR}\langle 3\mathcal{C}_{er}\rangle = -\langle 3\mathcal{C}_{er}\rangle/T_{1\rho}, \tag{47}$$

[33] N. Bloembergen, Physica **15**, 426 (1949).

where $T_{1\rho}$ is greater than $\frac{1}{2}T_1$ (for $T_{2e}=T_1$) for small H_1 and approaches T_1 (or in general T_{2e}) for large H_1. Equations (30), (32), (37), and (47) yield

$$M_{0\rho}=\frac{T_{1\rho}M_0\cos\Theta}{T_1[1+(\delta H)^2/H_{er}^2]}, \tag{48}$$

and at resonance

$$\frac{\partial\chi'}{\partial H_0}=\frac{T_{1\rho}\chi_0 H_0}{2T_1[H_1^2+(\delta H)^2]}. \tag{49}$$

$T_{1\rho}$ can be experimentally determined by observing the phase of the dispersion signal relative to the magnetic field modulation, as discussed in Sec. III(e) below.

Equation (47) may appear at first sight to be inconsistent with (36), when the spin relaxation is incoherent. Actually, this is not the case, since $\langle\langle\mathcal{H}_{SS}\rangle\rangle$ and $M_{z\rho}H_{er}$ are related to $\langle\langle\mathcal{H}_{er}\rangle\rangle$ by (30) and (32). If we solve these four equations for $T_{1\rho}$ we get the same expression obtained in Sec. III(e) in connection with the theory of fast modulation with incoherent relaxation [Eq. (63)].

Bloembergen[32] has suggested a method of calculating $T_{1\rho}$ in those metals for which the nuclear spin-spin interaction $A_{jk}\mathbf{I}_j\cdot\mathbf{I}_k$ is the predominant term in $\mathcal{H}_{SS}$. This is the case[26,27] in most of the heavier metals, probably including copper and aluminum. Equation (47) can be written (assuming $T_1=T_{2e}$)

$$[\partial/\partial t]_{SLR}\langle\langle\mathcal{H}_{er}\rangle\rangle=M_{z\rho}H_{er}/T_1-\langle\langle\mathcal{H}_{SS}\rangle\rangle/T_{SS}. \tag{50}$$

The term $M_{z\rho}H_{er}/T_1$ in (50) is deduced in the same way as in (36). T_{SS}^{-1} is a suitable average of the probability that, of two neighboring nuclei, either one will be flipped by an electron without the other. If the electron wavelength is very short it is expected that the relaxation will be incoherent and that $T_{ss}=\frac{1}{2}T_1$ as in (36).

T_{ss} can be estimated by considering nearest neighbors separated by a distance $\mathbf{r}_{jk}$. The important nuclear-electronic interaction is $A[(\mathbf{I}_j\delta(\mathbf{r}-\mathbf{r}_j)+\mathbf{I}_k\delta(\mathbf{r}-\mathbf{r}_k)]\cdot\mathbf{S}$, where $\mathbf{S}$ is the electronic spin operator and A is an interaction constant. For a transition involving $\mathbf{k}$ and $\mathbf{k}'=\mathbf{k}+\Delta\mathbf{k}$ as initial and final electronic propagation vectors this interaction becomes

$$\begin{aligned}&AP_F(e^{i\Delta\mathbf{k}\cdot\mathbf{r}_j}\mathbf{I}_j+e^{i\Delta\mathbf{k}\cdot\mathbf{r}_k}\mathbf{I}_k)\cdot\mathbf{S}\\&=\tfrac{1}{2}e^{-\Delta\mathbf{k}\cdot\mathbf{r}_k}AP_F\{(\mathbf{I}_j+\mathbf{I}_k)[\cos(\Delta\mathbf{k}\cdot\mathbf{r}_{jk})\\&\quad+i\sin(\Delta\mathbf{k}\cdot\mathbf{r}_{jk})+1]\\&\quad+(\mathbf{I}_j-\mathbf{I}_k)[\cos(\Delta\mathbf{k}\cdot\mathbf{r}_{jk})+i\sin(\Delta\mathbf{k}\cdot\mathbf{r}_{jk})-1]\}.\end{aligned} \tag{51}$$

$\mathbf{I}_j+\mathbf{I}_k$ commutes with $A_{jk}\mathbf{I}_j\cdot\mathbf{I}_k$ and thus does not contribute much to the decay of $\langle\langle\mathcal{H}_{SS}\rangle\rangle$ unless the term $B_{jk}I_{jz}I_{kz}$ is relatively large. Assuming B_{jk} small, most of the relaxation of $\mathcal{H}_{SS}$ results from the term involving $\mathbf{I}_j-\mathbf{I}_k$, with transition probabilities proportional to $2-2\cos(\Delta\mathbf{k}\cdot\mathbf{r}_{jk})$. We assume that the energy contours in k-space are spherical, in which case $k\simeq k'\simeq k_m$, the Fermi level value of k, and that all directions in k-space are equally probable for the initial and final states. T_{SS} is then proportional to the average of $2-2\cos[(\mathbf{k}-\mathbf{k}')\cdot\mathbf{r}_{jk}]$ over all directions of k and k', keeping $k=k'=k_m$, and is normalized by the requirement $T_{SS}\to\frac{1}{2}T_1$ as $k_m\to\infty$. In this way we get

$$T_{SS}^{-1}\simeq 2T_1^{-1}\{1-[1-\cos(2k_m r_{ij})]/2k_m^2r_{ij}^2\}. \tag{52}$$

If it is assumed that there is one electron per atom in the Fermi gas, then $k_m r_{jk}=3.36$ for a face-centered cubic crystal and (52) indicates that $T_{SS}\simeq\frac{1}{2}T_1$, yielding almost the same predictions as (41) and (43). Only if $k_m r_{jk}\lesssim\pi/2$, or if the conduction band is almost filled and can be described as an almost empty band of positive holes with $k_m r_{jk}\lesssim\pi/2$, will there be an appreciable effect due to coherent relaxation of neighboring nuclei.

D. Two Magnetic Ingredients

There are two limiting cases to be considered when there are two or more types of spin in the lattice.

The first of these is typified by F-centers whose electron spin resonance is broadened by hyperfine interaction with the surrounding nuclear spins. Although the different F-centers in an alkali halide are magnetically coupled in theory via nuclear spin diffusion and direct interaction with each other, in fact such coupling is negligible over a length of time comparable to T_1 (electronic) because the spin-spin transitions involved are highly forbidden energetically by the relatively large local field differences experienced by the different spins. Then the F-centers must be regarded as decoupled and the assumption of a canonical distribution of states with respect to the transformed Hamiltonian abandoned. Portis[7] has developed an exact theory for this case.

The other limiting case is typified by two different nuclear species in the same crystal. In this case the local field differences between nuclei are relatively small and spin diffusion can take place.[33] Following Van Vleck we use primes to denote the spins whose resonance is not being observed; the rf frequency ω is supposed to be near the resonant frequency of the unprimed spins. The spin Hamiltonian is given by Van Vleck.[25] We transform to a rotating system as before, using the transformation $R_{z\omega t}$ in which the sum over the I_{jz} is carried out over all the nuclei, primed and unprimed. The transformed Hamiltonian is

$$\begin{aligned}\mathcal{H}_{er}=&g\beta\mathbf{H}_{er}\cdot\textstyle\sum_j\mathbf{I}_j+\sum_{k>j}(A_{jk}\mathbf{I}_j\cdot\mathbf{I}_k+B_{jk}I_{jz}I_{kz})\\&+\textstyle\sum_{j',k}C_{j'k}I_{j'z}I_{kz}\\&+\textstyle\sum_{k'>j'}A_{j'k'}\mathbf{I}_{j'}\cdot\mathbf{I}_{k'}+B_{j'k'}I_{j'z}I_{k'z}\\&+g'\beta[H_0\mathbf{k}_r-(\omega/\gamma')\mathbf{i}_r+H_1\mathbf{k}_r]\cdot\textstyle\sum_{j'}\mathbf{I}_{j'},\end{aligned} \tag{53}$$

Here g' and γ' are respectively the g factor and gyromagnetic ratio of the primed ingredient, $A_{j'k'}$ and $B_{j'k'}$ are given by (22) and (23) and

$$C_{jk'}=\tilde{A}_{jk'}+(1-3\xi_{jk'}^2)gg'\beta^2r_{jk'}^{-3}. \tag{54}$$

In (53) we have neglected time-dependent terms as before. We can also neglect the term $g'\beta H_1 \sum I_{j'x}$ which is nonsecular if $|\omega-\gamma' H_0|$ is much greater than the resonance line width of the unprimed nuclei. The term involving $\sum I_{j'z}$ then commutes with the rest of the Hamiltonian and can be ignored, since the unprimed spins are not affected directly by the rf field.

The remaining terms of the Hamiltonian are secular perturbations and do not commute with each other. This means that they are coupled together, with the rather surprising result that effective energy can be transferred from the unprimed system to the primed system. When rf energy is absorbed by the unprimed spins, part of this energy will be transferred to the primed system via the interaction $\sum C_{jk'} I_{jz} I_{k'z}$. This energy will be entirely in the form of spin-spin (internal) energy; the external energy of the primed spins (expectation value of the last term of $\mathcal{H}_{er}$) will be unchanged. The average populations of the primed spin levels will remain at their equilibrium values, but the primed spins will become more ordered in orientation with respect to their local fields.

The statements in the previous paragraph may appear to contradict the usual assumption that two different nuclear magnetic ingredients in a solid interact entirely independently with the rf field, from which it would follow that the primed system is unaffected by rf power at the resonant frequency of the unprimed system. Actually this assumption is not quite true, since the spin-spin energy of the primed system evidently increases in this case. For most purposes this energy is negligibly small compared to the external energy (in the fixed system) of the primed system, which is unaffected by the rf field. Only in the present case, where effective energy is the important quantity, will the spin-spin energy be important, and then only in determining the behavior of the unprimed nuclei.

As before we assume that at high rf levels the spin system is in a canonical distribution of states with respect to the retained parts (all but the last term) of the effectively time-independent transformed Hamiltonian $\mathcal{H}_{er}$. As a consequence of this assumption, the part of the nuclear magnetization due to the unprimed spins is in the effective field direction with magnitude M_{zp} while that due to the primed spins remains at its thermal equilibrium value in the z-direction.

The effect of the unlike neighbors can be expressed in terms of the ratio $(\delta H)^2/H_{er}^2$ of internal spin-spin energy to external (unprimed) spin energy. In Appendix C it is shown that

$$(\delta H)^2=\tfrac{1}{3}\langle(\Delta H)^2\rangle_u+I(I+1)(fN\hbar^2\gamma^2)^{-1} \times(\textstyle\sum_{j\neq k}\tilde{A}_{jk}+\sum_{j'\neq k'}\tilde{A}_{j'k'})+\langle(\Delta H)^2\rangle_{pu} +\tfrac{1}{3}(f'/f)\langle(\Delta H)^2\rangle_p, \quad (55)$$

where $\langle(\Delta H)^2\rangle_u$ is the contribution of the unprimed ingredient to the second moment[25] of its resonance, $\langle(\Delta H)^2\rangle_{pu}$ is the contribution of the primed magnetic ingredient to the second moment of the unprimed resonance, $\langle(\Delta H)^2\rangle_p$ is the contribution of the primed ingredient to the second moment of the primed resonance, N is the total number of both ingredients, and fN and $f'N$ are the numbers of unprimed and primed nuclei respectively.

If the relaxation times of the two types of nuclei are equal the quasistatic equilibrium value $M_{0\rho}$ of the unprimed magnetization $M_{z\rho}$ is given by (38) using the same reasoning as before, with χ_0 taken to be the unprimed contribution to the static susceptibility. If the relaxation times of the unprimed and primed nuclei are T_1 and T_1', then it can be shown (Appendix C) that

$$M_{0\rho}=M_0\cos\Theta\{1+H_{er}^{-2}[2(\delta H)^2{}_u+2(\delta H)^2{}_p T_1/T_1' +\langle(\Delta H)^2\rangle_{pu}(1+T_1/T_1')]\}^{-1}, \quad (56)$$

where $(\delta H)^2{}_u$ is equal to the first two terms of $(\delta H)^2$ [Eq. (55)], $(\delta H)^2{}_p$ equals the third and fifth terms of $(\delta H)^2$, and M_0 is the unprimed contribution to the static equilibrium magnetization.

As before, the theory is valid only for rf field levels above saturation, and if the spin-lattice interaction results in correlated scattering for neighboring spins the remarks at the end of Sec. III(c) apply.

The predicted behavior of χ'' and $\partial\chi'/\partial H_0$ at resonance for a crystal with two magnetic ingredients is shown in Fig. 6. The absorption is as before, except that $g(\nu_0)$ may be different and the parameters of the saturation curve refer only to the unprimed nuclei. The predicted dispersion shown is that for a crystal in which the observed (unprimed) nuclei are in the minority, the relaxation times T_1 and T_1' are comparable, and the absorption is gaussian below saturation. The plateau in $\partial\chi'/\partial H_0$ above saturation is reduced relative to that for the pure case (curve a) because of the additional spin-spin interaction of the unlike nuclei. The line shape above saturation is the same as for one magnetic ingredient, with a suitable increase in $(\delta H)^2$.

E. Fast and Intermediate Modulation

When the period of the magnetic field modulation becomes comparable to the spin-lattice relaxation time the observed absorption and dispersion signals above saturation will differ from those obtained if T_1 is very short. The same remark applies if the rf amplitude or frequency is modulated. In solids it is difficult to avoid modulation effects because, except for the heavier metals, the nuclear relaxation time at 300°K is greater than 10 milliseconds, requiring modulation frequencies ω_m of 10 cps or less. Such low modulation frequencies are seldom used in practice, because of noise and stability considerations. This is evidently why the nonsaturation of the dispersion reported here has not been previously observed.

Another reason for considering fast modulation is that by so doing it is possible to obtain the spin lattice relaxation time. This possibility has been exploited by

Halbach,[18] who has developed the theory of fast magnetic field modulation for systems obeying the Bloch equations.

Theories[5,6] of fast modulation based on the assumption of a spin temperature lead to incorrect results, even for systems obeying the Bloch equations. In these theories it is assumed that, for $\omega_m T_1 \gg 1$, the spin temperature is that corresponding to the average values of H_0, H_1, and ω. Actually, for $T_1^{-1} \ll \omega_m \ll \gamma H_1$ the nuclear magnetization will remain in the direction of the effective field, and thus its z-component and temperature will vary sinusoidally with the z-component of the effective field.

In this section we treat only modulation of the magnetic field H_0. Frequency modulation of the rf field is equivalent, and amplitude modulation of H_1 can be treated similarly. We assume that $\omega_m \ll \gamma H_1$ and that ω_m is much smaller than the unsaturated line width, so that modulation effects of the type considered by Karplus[34] are negligible.

The applied magnetic field is

$$\mathbf{H} = (\bar{H}_0 + H_m \cos\omega_m t)\mathbf{k} + (2H_1 \cos\omega t)\mathbf{i}. \quad (57)$$

In addition to the explicit time dependence of $\mathbf{H}$ in (57), ω also increases or decreases very slowly in time as the spectrometer sweeps through the resonance line.

In general the x-component of magnetization is (to first order)

$$M_x = (M_x' + M_{x1}' \cos\omega_m t + M_{x2}' \sin\omega_m t)\cos\omega t + (M_x'' + M_{x1}'' \cos\omega_m t + M_{x2}'' \sin\omega_m t)\sin\omega t, \quad (58)$$

where M_x', M_{x1}', etc. are constant in time (or vary only very slowly as ω is varied).

The apparent dispersion derivatives are defined as

$$\partial\chi_1'/\partial H_0 = M_{x1}'/2H_1H_m, \quad (59a)$$

$$\partial\chi_2'/\partial H_0 = M_{x2}'/2H_1H_m, \quad (59b)$$

$$\partial\chi_1''/\partial H_0 = M_{x1}''/2H_1H_m, \quad (59c)$$

$$\partial\chi_2''/\partial H_0 = M_{x2}''/2H_1H_m. \quad (59d)$$

$\partial\chi_1'/\partial H_0$ and $\partial\chi_1''/\partial H_0$ are the apparent dispersion and absorption derivatives observed when the lock-in detector is adjusted in phase with the modulation, and $\partial\chi_2'/\partial H_0$ and $\partial\chi_2''/\partial H_0$ are the apparent dispersion and absorption derivatives observed when the lock-in detector is adjusted 90° out of phase (in quadrature) with the modulation.

The Hamiltonian is transformed to a rotating system as before, but Θ and H_{er} depend on time sinusoidally with frequency ω_m. This frequency is so low that it induces no appreciable transitions between the eigenstates of $\mathcal{H}_{er}$, and it can be regarded as a reversible adiabatic (slow) perturbation of the spin system (not the whole system, as $\omega_m T_1 \gtrsim 1$). It is then reasonable to assume as before that the spin system remains in its highest entropy macrostate; i.e., in a canonical distribution of states.

In Appendix B it is shown that this assumption leads to the equation (for one magnetic ingredient)

$$\frac{d}{dt}\langle\langle \mathcal{H}_{er}\rangle\rangle = \frac{d}{dt}\langle\langle \mathcal{H}_{ep}\rangle\rangle = \frac{M_{zp}H_{er}}{T_1} - \frac{2\langle\langle \mathcal{H}_{SS}\rangle\rangle}{T_1} - \frac{M_0 \cos\Theta H_{er}}{T_1} - \mathbf{M}_r \cdot \frac{\partial \mathbf{H}_{er}}{\partial t}. \quad (60)$$

Using (32) gives

$$\frac{d}{dt}\langle\langle \mathcal{H}_{SS}\rangle\rangle = \frac{(+M_{zp}H_{er} - M_0 \cos\Theta H_{er} - 2\langle\langle \mathcal{H}_{SS}\rangle\rangle)}{T_1} + \frac{\partial \mathbf{M}_r}{\partial t} \cdot \mathbf{H}_{er}. \quad (61)$$

Equation (60) also follows directly from the first law of thermodynamics[35] for the transformed Hamiltonian $dU_{er}' = dQ_{er} + \mathbf{M}_r \cdot d\mathbf{H}_{er}$, where U_{er}' is the effective energy of the spin system $\langle\langle \mathcal{H}_{er}\rangle\rangle$, and Q_{er} is the effective heat transferred from the lattice to the spin system via the spin-lattice interaction. Application of thermodynamics to $\mathcal{H}_{er}$ is valid because the changes in $\mathcal{H}_{er}$ are reversible (slow) and the coupling to the lattice is assumed weak.

The assumption of a canonical distribution of states implies as before that the magnetization is in the direction of $\mathbf{H}_{er}$ with magnitude M_{zp}, and that $\langle\langle \mathcal{H}_{SS}\rangle\rangle = -M_z[(\delta H)^2/H_{er}]$. Substituting into (61) we get

$$\dot{M}_{zp} = -(M_{zp} - M_{0p})/T_{1p} + M_{zp}\dot{H}_{er}H_{er}^{-1}[1 + H_{er}^2/(\delta H)^2]^{-1}, \quad (62)$$

where

$$T_{1p} = T_1[1 + (\delta H)^2/H_{er}^2][1 + 2(\delta H)^2/H_{er}^2]^{-1}, \quad (63)$$

and M_{0p} is given by (38).

Similar reasoning shows that when two magnetic ingredients are present (62) still holds, and M_{0p} and T_{1p} are given by (48) and (56). If the spin-lattice relaxation is correlated between neighbors the considerations at the end of Sec. III(c) apply, and T_{1p} is the same quantity introduced there. M_{0p} is again given by (48) and T_{1p} can be empirically determined as described below.

If T_{1p} is large compared to the time taken to sweep through the entire resonance, we can neglect the term $(M_{zp} - M_{0p})/T_{1p}$ in (62). Assuming that initially ω is well off resonance ($|H_0 - \omega/\gamma| \gg \delta H, H_1$) and $\pm M_{zp} \simeq M_z = M_0$, we get

$$M_{zp} = \frac{\pm M_0}{[1 + (\delta H)^2/H_{er}^2]^{\frac{1}{2}}}, \quad (64)$$

[34] R. Karplus, Phys. Rev. **73**, 1020 (1948).

[35] W. P. Allis and M. A. Herlin, *Thermodynamics and Statistical Mechanics* (McGraw-Hill Book Company, Inc., New York, 1952), Eq. (48-5).

and

$$\partial\chi_1'/\partial H_0=\pm\partial/\partial H_0\frac{M_0\sin\Theta/2H_1}{[1+(\delta H)^2/H_{cr}^2]^{\frac{1}{2}}}, \quad (65)$$

$$\partial\chi_2'/\partial H_0\simeq\partial\chi_1''/\partial H_0\simeq\partial\chi_2''/\partial H_0\simeq 0. \quad (66)$$

The plus or minus sign in (64) and (65) depends on whether ω is initially less or greater than the resonance frequency. This is the case Bloch[4] calls adiabatic fast passage. The present analysis shows that to observe a fast passage signal it is not necessary to sweep through the resonance in a time short compared to T_2, as previously supposed,[4] but only in time short compared to T_1. In the case of solids, where $T_1\gg T_2$, this makes observation of fast passage signals much easier. It is, of course, still necessary to use rf levels well above the saturation level.

If $T_{1\rho}\cong T_1$ is short compared to the time taken to pass through resonance, we can regard ω as fixed, and the first-order solution of (62) is

$$M_{z\rho}=\bar{M}_{0\rho}+M_1\cos\omega_m t+M_2\sin\omega_m t, \quad (67)$$

where $\bar{M}_{0\rho}$ is the quasi-steady-state value of $M_{z\rho}=M_{0\rho}$ corresponding to $H_0=\bar{H}_0$. M_1 and M_2 are given by

$$M_1=-(1+1/\omega_m^2T_{1\rho}^2)^{-1}\times\left(\frac{\bar{M}_{0\rho}H_m\cos\Theta}{H_{cr}[1+H_{cr}^2/(\delta H)^2]}-\frac{H_m}{\omega_m^2T_{1\rho}^2}\frac{\partial M_{0\rho}}{\partial H_0}\right), \quad (68)$$

$$M_2=\frac{1}{\omega_mT_{1\rho}}\left(-M_1+H_m\frac{\partial M_{0\rho}}{\partial H_0}\right). \quad (69)$$

Here $\partial M_{0\rho}/\partial H_0$ is evaluated for $H_0=\bar{H}_0$. (68) and (69) are obtained by substituting (67) into (62) and setting $M_{0\rho}=(H_m\cos\omega_m t)\,\partial M_{0\rho}/\partial H_0+\bar{M}_{0\rho}$.

The apparent dispersion derivatives are [from Eqs. (33), (58), (59), and (67)]

$$\partial\chi_1'/\partial H_0=M_1'\sin\Theta/2H_1H_m-\bar{M}_{0\rho}\sin^2\Theta\cos\Theta/2H_1^2, \quad (70)$$

$$\partial\chi_2'/\partial H_0=M_2'\sin\Theta/2H_1H_m. \quad (71)$$

At resonance,

$$\partial\chi_1'/\partial H_0=(1+\omega_m^2T_{1\rho}^2)^{-1}\partial\chi'/\partial H_0, \quad (72)$$

$$\partial\chi_2'/\partial H_0=\omega_mT_{1\rho}\partial\chi_1'/\partial H_0. \quad (73)$$

Here $\partial\chi'/\partial H_0$ is the true dispersion derivative at resonance in the limit of slow modulation. Equation (73) shows that the relaxation time $T_{1\rho}$ can be experimentally determined from the ratio of the in-phase to the quadrature dispersion signals, and the true dispersion derivative can be calculated from (72). This method of measuring the relaxation time was previously suggested and applied to liquids by Halbach.[18] Similar effects have evidently also been observed by Portis and Shaltiel.[36] It will be noted that the relaxation times can also be measured by modulating the rf power level, as is sometimes more convenient for microwave studies of paramagnetic relaxation.

The apparent absorption derivatives are obtained from conservation of energy considerations in the fixed coordinate system. The rate of transfer of energy from the spins to the lattice is to a good approximation $H_0(M_0-M_z)/T_1$. Conservation of energy[35] for the spin system then requires that

$$\frac{d}{dt}\langle\langle\mathcal{H}_s\rangle\rangle=-H_0(M_0-M_z)/T_1-\mathbf{M}\cdot\frac{\partial\mathbf{B}}{\partial t}. \quad (74)$$

Using the fact that $\langle\langle\mathcal{H}_s\rangle\rangle\simeq H_0M_z$ and $\partial\mathbf{B}/\partial t\simeq\partial\mathbf{H}/\partial t$, and averaging over one rf period, we get

$$H_0(M_0-M_z)/T_1=-\omega H_1(M_x''+M_{x1}''\cos\omega_m t+M_{x2}''\sin\omega_m t)+H_0\dot{M}_z. \quad (75)$$

Equations (33), (58), (59), and (75) can be solved for the apparent absorption derivatives. The result is complicated and will be omitted. The absorption signal depends on both the modulation frequency and phase. Since it is not customary to adjust a lock-in detector with extreme care, the phase of the observed signal in previous measurements of T_1 by saturation must be regarded as uncertain, and the reported values of T_1 correspondingly uncertain. The resulting errors in T_1 are not likely to be greater than a factor of two or three because the onset of saturation will still occur at level $H_1\simeq 2[\gamma^2T_1g(\nu_0)]^{-\frac{1}{2}}$ corresponding to the point where the rf transition probability is comparable to the spin-lattice transition probability. Fast modulation will only change the details of the absorption saturation and apparent asymptotic absorption at resonance for large H_1.

The predicted dependence of $T_{1\rho}$ on rf field is shown in Fig. 6, assuming uncorrelated spin-lattice relaxation between neighbors. In the limit of large H_1, $T_{1\rho}$ equals T_1 (or more generally T_{2e}; here we assume as usual $T_1=T_{2e}$). At the value of H_1 corresponding to the knee of the dispersion curve $T_{1\rho}$ undergoes a transition to $T_1/2$ for a single magnetic ingredient, or to some other value for two magnetic ingredients as indicated by (48) and (56). Below saturation the observed dispersion signal is expected to be in phase with the modulation and to correspond to the true dispersion derivative. The observed $T_{1\rho}$ as defined by (73) is then expected to decrease in some unpredicted way corresponding to the dotted lines in Fig. 6.

IV. COMPARISON WITH EXPERIMENT

We have not made a detailed analysis of the observed line shapes, but it appears that they are in agreement with the predictions of the theory. In the metals the absorption and dispersion derivatives above saturation

[36] A. M. Portis and D. Shaltiel, Phys. Rev. 98, 264(A) (1955).

are very nearly Lorentzian[20] and have the expected width. The apparent dispersion derivatives in NaCl at large rf fields appear to be in agreement with the theory, assuming $\omega_m T_1 \gg 1$ and, for the impure NaCl, assuming T_1 short compared to the few minutes taken to sweep through the resonance, or, for the Harshaw NaCl, assuming T_1 comparable to the time taken to sweep through the resonance.

The observation of the adiabatic fast passage[4] signal in the Harshaw NaCl is evidence that we were justified in neglecting the time-dependent terms in $\mathcal{H}_{sr}$ and $\mathcal{H}_{sp}$ [Eqs. (20) and (21)]. If these terms could induce transitions among the different eigenstates of the time-independent part of the transformed Hamiltonian then the magnetization in the z_ρ-direction, $M_{z\rho}$, would be destroyed when ω passed through resonance. The observations on the Harshaw NaCl indicate that the relaxation time of $M_{z\rho}$ produced by these terms is greater than about one minute, so that they can be neglected for most purposes.

We now reconsider the absorption data of Fig. 1. In the limit of large H_1, (43) indicates that χ'' should approach $\chi_0 H_0/2T_1\gamma H_1^2$. In the limit of small H_1 the Kronig-Kramers relations indicate that χ'' should approach $\frac{1}{2}\pi\chi_0\nu_0 g(\nu)$, where $g(\nu)$ is the normalized unsaturated line shape. An attempt has been made to draw these asymptotes for the data of Fig. 1. The asymptotes should cross at the value of H_1 given by $\frac{1}{2}\gamma^2 H_1^2 T_1 g(\nu_0)=1$. In this way we get 5.5 milliseconds for T_1 in aluminum and 3.55 for copper. Since it is uncertain whether the asymptotes drawn in Fig. 1 are the true ones these values of T_1 must be regarded as upper limits. In addition, inaccuracies in the absorption data may introduce as much as 20 percent error in T_1. These values of T_1 are not necessarily more reliable than those obtained in Sec. II, and do not appreciably alter the conclusions reached there concerning the electronic structure. They lead to values of $v_0 P_F m^*/m$ of 220 for aluminum and 240 for copper.

The dispersion data of Figs. 2 and 3, together with (72) and (73), yield values of the true dispersion derivative contribution per nucleus shown in Fig. 7. Also shown in Fig. 7 is the relative dispersion derivative per proton for protons in water doped with paramagnetic impurity. This is the same H_2O line shown in Figs. 2 and 3. To get the absolute magnitude of $N^{-1}\partial\chi'/\partial H_0$ for comparison with experiment we can use either the H_2O data or the aluminum or copper dispersion derivative below saturation as a calibration.

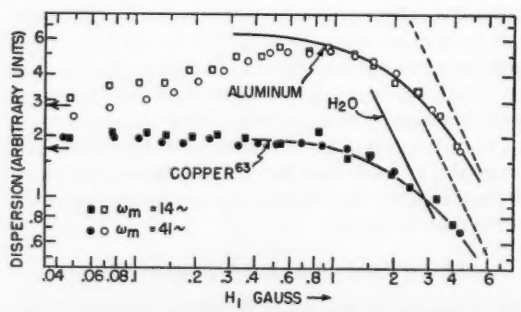

FIG. 7. Slow passage dispersion derivatives at resonance per resonated nucleus, as a function of rf power, inferred from the data of Figs. 2 and 3. The units of $N^{-1}\partial\chi'/\partial H_0$ are the same as in Figs. 2 and 3.

In order to use the proton dispersion as a calibration it is necessary to assume a value of T_{2H}/T_{1H} in (5). Wangsness and Bloch[22] predict that this ratio is unity for protons in water relaxed by paramagnetic impurities, as considered here. The same result follows[32,37] from a somewhat more general theory of Kubo and Tomita.[23] Solomon[37] has recently measured T_{1H} and T_{2H}, using spin echo techniques for protons in water containing Fe ions. For Fe concentrations up to that required to reduce T_1 to one millisecond he finds that $T_{1H}/T_{2H}=1.0\pm0.03$, in agreement with theory. Unfortunately the dispersion derivative observed in water in Fig. 7 is inconsistent with that observed below saturation in copper and aluminum (which is rigorously determined by the Kronig-Kramers relations and the unsaturated absorption line shape) unless we assume $T_{1H}/T_{2H}\simeq 2$. Thus it appears that either the errors in the data are greater than the conservative estimate of ± 20 percent, or that there is something wrong with the theory of nuclear resonance in liquids. The latter possibility should not be taken too seriously in view of the rather preliminary nature of the data, but it may be that the high concentration of paramagnetic impurities ($\simeq$1 percent) could cause a decrease in the intensity of the dispersion signal because the rms value of the rapidly fluctuating local fields seen by the nuclei is larger than the applied field H_0.

In view of this difficulty we adopt the less accurate (but theoretically more rigorous) alternative of using the dispersion signal in aluminum and copper below saturation as a calibration. We approximate the line shape with an inverted truncated parabola:

$$\begin{aligned} g(\nu)&=3a^{-3}(a^2-\nu^2)/2 \quad \text{for} \quad \nu^2<a^2, \\ g(\nu)&=0 \qquad\qquad\qquad\ \ \text{for} \quad \nu^2>a^2. \end{aligned} \tag{76}$$

This is an excellent approximation for aluminum and a fair one for copper, which has a more nearly Gaussian resonance line than aluminum. Inserting (76) into the Kronig-Kramers relations and evaluating the second moment leads to

$$\partial\chi'/\partial H_0=0.3\chi_0 H_0/\langle(\Delta H)^2\rangle_{Av}, \tag{77}$$

or

$$N^{-1}\partial\chi'/\partial H_0=0.6\pi I(I+1)\nu_0\gamma/3kT\langle(\Delta H)^2\rangle_{Av}, \tag{78}$$

where $\langle(\Delta H)^2\rangle_{Av}$ is the second moment of the line. If the line were assumed to be Gaussian the factor in (78) would be 1.0 instead of 0.6. In copper (78) predicts a

[37] I. Solomon (private communication). We are indebted to Dr. Solomon for permission to quote him prior to publication.

dispersion derivative which is expected to be slightly too small, because of the more nearly Gaussian shape of the copper resonance.

In aluminum the predicted second moment $\langle(\Delta H)^2\rangle_{Av}$ is 7.5 gauss,[2] neglecting possible anisotropic electronic coupling[26] between nuclei. Gutowski and McGarvey[1] report an experimental value of 10.5 gauss[2] and Rowland[38] a value of 8.7 gauss.[2] We assume a value of 9 gauss.[2] In copper Gutowski and McGarvey[1] report that experimentally $\langle(\Delta H)^2\rangle_{Av}$ is 6.3 gauss,[2] in reasonable agreement with their theoretical prediction of 5.6 gauss.[2] We use their experimental value. Corrections[1] to $\langle(\Delta H)^2\rangle_{Av}$ which depend on T_1 are negligible compared to the other approximations and uncertainties in the theory.

We use the aluminum dispersion derivative as a primary calibration, and assume that its experimental value (upper horizontal arrow in Fig. 7) is given correctly by (78). The copper dispersion derivative below saturation is then somewhat greater than the prediction of (78) (lower horizontal arrow), as expected. The discrepancies between the experimental points for aluminum at small H_1 are almost certainly due to experimental error.

The dotted lines in Fig. 7 are the predicted high rf field asymptotes for the dispersion derivatives, again using the low rf field aluminum dispersion as a calibration. The predicted asymptote is $N^{-1}\partial\chi'/\partial H_0 \rightarrow \chi_0 H_0/2NH_1^2$, as obtained from either (10) or (41), assuming $T_1=T_{2e}$. The solid curves in Fig. 7 for large H_1 correspond to the prediction of (41), taking $(\delta H)^2=3.4$ gauss^2 for aluminum and 5.0 gauss^2 for copper. In aluminum the plateau predicted for $\partial\chi'/\partial H_0$ at intermediate fields is not resolved, owing to the relatively small ratio of T_1 to $(\gamma\delta H)^{-1}$ compared to that assumed for the predictions of Fig. 6. In copper the plateau evidently nearly coincides with the value of $\partial\chi'/\partial H_0$ below saturation.

In Fig. 8 are plotted experimental values of $T_{1\rho}$ obtained from (73) and the data of Figs. 2 and 3. For large H_1 the observed $T_{1\rho}$ values agree fortuitously well with the values of T_1 obtained in the beginning of this section, and disagree with the values of T_1 in Table I.

The behavior of $T_{1\rho}$ is in conflict with (63), which is based on the assumption of incoherent relaxation of neighboring nuclei implicit in (35). If this assumption were correct $T_{1\rho}$ should reach a plateau of about $\frac{1}{2}T_{1\rho}$ at the value of $H_1(\simeq 1$ gauss) at which the intermediate plateau of the dispersion derivative occurs. Such a plateau apparently exists but the value of $T_{1\rho}$ is too large. Such a large discrepancy cannot be explained by coherent nuclear relaxation unless the electronic band structure is appreciably different from the free electron approximation with one electron per atom. We do not know the reason for this behavior.

Since the discrepancy in $T_{1\rho}$ is evidently real, at least in the case of copper, we are forced to use the more empirical approach described at the end of Sec. III. For $H_1 \lesssim 1$ gauss, $T_{1\rho}$ can be approximated by

$$T_{2e}[1+(\delta H)^2/H_1^2][1+\alpha(\delta H)^2/H_1^2]^{-1}, \qquad (79)$$

where T_{2e} is 5.5 milliseconds for aluminum and 3.55 milliseconds for copper, and α is 1.7 for aluminum and 1.3 for copper. T_{2e} is used in (79) because $T_{1\rho}$ is expected to approach T_{2e}, the transverse spin-lattice relaxation time, in the limit of large H_1 and at resonance.

If we assume that $T_1=T_{2e}$ as would be indicated by the values of T_1 obtained at the beginning of this section, (49) predicts the same dependence of $\partial\chi'/\partial H_0$ as before (solid lines in Fig. 7) if we take $(\delta H)^2=4$ gauss^2 for aluminum and 7.7 gauss^2 for copper.

A third interpretation of the data obtains if we assume that the values of T_1 in Table I are correct. This assumption is in conflict with the prediction[13,22] $T_1=T_{2e}$ for a nucleus in a Fermi gas of electrons. The predicted asymptote of $\partial\chi'/\partial H_0$ is increased by T_{2e}/T_1 and (41) is in reasonable agreement with the data if we take $(\delta H)^2=5.9$ gauss^2 for aluminum and 10 gauss^2 for copper.

We now estimate the theoretical value of $(\delta H)^2$. If we assume $\bar{A}_{jk}=0$, $(\delta H)^2$ is predicted by (31) and (55) to be 2.5 to 3 gauss^2 for aluminum and 2.85 to 3.1 gauss^2 for copper. The lower limits of these estimates correspond to the classical dipolar interaction between nuclei and the upper limits correspond to the fact that the observed[1,39] second moments of the resonance line are ten to twenty percent larger than their theoretical values, possibly because of additional psuedo-dipolar[26] coupling between nuclei via the conduction electrons.

It is clear that the observed values of $(\delta H)^2$ cannot be explained by classical dipolar coupling alone. Ruderman and Kittel have calculated the magnitude of the exchange-type coupling between nuclei due to the conduction electrons; the result of their calculation can be

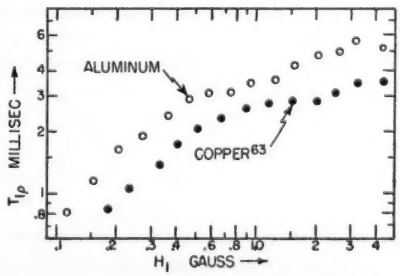

FIG. 8. The relaxation time $T_{1\rho}$ as obtained from the 41 cps data of Figs. 2 and 3.

[38] T. J. Rowland (private communication). This is the average value of two runs and is thought to be at least 10 percent accurate. The accuracy is difficult to estimate because of uncertainties in the wings of the line.

[39] K. Kambe, Phys. Rev. (to be published).

written [using Eq. (2)]:

$$\tilde{A}_{jk}=\frac{\hbar[2k_m r_{jk}\cos(2k_m r_{jk})-\sin(2k_m r_{jk})]}{8\pi^2 m^* r_{jk}^{-4}(T_{1j}T_{1k})^{\frac{1}{2}}kT}\left(\frac{\pi v_0}{3}\right)^{\frac{1}{2}}. \quad (80)$$

T_{1j} and T_{1k} are the relaxation times of nuclei j and k, and the relaxations represented by these times are assumed due only to the S-character of the electronic wave function near the Fermi surface; if the electronic P-character contributes to the relaxation (80) estimates too large a value for $\tilde{A}_{jk}$. To obtain (80) Ruderman and Kittel also assume that the electronic energy contours in k space are spherical, corresponding to an effective mass m^* and a wave number k_m at the Fermi level.

For $m^*=m$ and the values of T_1 in Table I, (80) predicts that $\hbar^{-1}\tilde{A}_{jk}=80\sim$ for nearest neighbors in aluminum and $\hbar^{-1}\tilde{A}_{jk}=140\sim$ for nearest Cu^{63} neighbors in copper. These values lead to additional contributions to $(\delta H)^2$ due to nearest neighbors only of about 0.3 gauss^2 for both aluminum and copper. To agree with experiment we have to assume that $\tilde{A}_{jk}$ is about 2 times its theoretical value in aluminum, and about 3 times in copper. These factors are rather large, but might result from a small effective mass or a complex band structure. An exchange-type interaction of this magnitude might still be small enough to cause relatively little exchange narrowing of the unsaturated resonance, as is observed. Unfortunately for this interpretation, Kambe[38] has predicted theoretically that in copper $m^*\cong m$ so that an anomalously large $\tilde{A}_{jk}$ is not expected.

We may summarize this section by saying that the theory agrees fairly well with experiment provided we assume that the exchange-type coupling constant $\tilde{A}_{jk}$ is two or three times greater than its theoretical value, and that the relaxation of neighboring nuclear spins is coherent to a degree considerably greater than would be expected from simple considerations. These observations are consistent with the assumption of an almost filled or almost empty band with a small effective mass. There appears to be no independent support for such an assumption. If we assume instead a simple electronic structure with one electron per atom and $m^*=m$, the agreement between theory and experiment is not so good, but is considerably improved over that of previous[4–6] theories of saturation as applied to solids. Finally, we should re-emphasize the fact that the interpretation of this section is based on a questionable calibration, owing to the disagreement of the proton calibration with the other data.

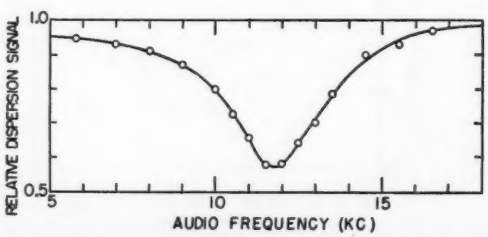

FIG. 9. Rotary saturation run on protons in water heavily doped with manganese ions. H_1 was thought to be 3.0 gauss, H_a was about 0.6 gauss, and the magnetic field modulation was 1 gauss peak-to-peak.

V. ROTARY SATURATION

The effect which we have called rotary saturation was suggested by the previous use of the rotating coordinate system representation. Much of the theory above will be useful in treating this effect in solids, but it is not necessary to understand Sec. III in order to understand rotary saturation, as it is also a consequence of the Bloch equations.

The effect is observed in a liquid obeying the Bloch equations as follows: the dispersion derivative signal is observed at resonance well above saturation, using a magnetic field modulation amplitude H_m which is a sizable fraction of the rf amplitude H_1, and a modulation period ω_m^{-1} much larger than T_1 and T_2 (or T_{2e} in the case of a solid). An audio-frequency magnetic field of frequency ω_a and amplitude[40] H_a, oriented in the z direction, is also applied to the sample. When the audio-frequency approaches the frequency

$$\omega_a=\gamma H_{er}\simeq\gamma H_1, \quad (81)$$

the dispersion signal is observed to decrease, and it goes through a minimum when the condition (81) is satisfied. The frequency γH_{er} is the classical nutation frequency of the nuclei in the rf magnetic field.

Figure 9 shows a rotary saturation run obtained with water heavily doped with paramagnetic (Mn^{++}) ions. The dispersion minimum frequency of 12.75 kc corresponds to the proton resonance frequency in a field of 3.0 gauss. Search coil measurements indicated that in the run of Fig. 9, H_1 was 3 gauss within the probable experimental error; these measurements of H_1 were rather inaccurate because of the uncertain geometric factors involved. Actually the run of Fig. 9 was used to calibrate the rf field for use in the other runs reported in this paper, and the rf field in this run was therefore *assumed* to be 3.0 gauss. The theoretical justification for this assumption will be given below.

Rotary saturation can be understood by transforming to the rotating coordinate system. In Fig. 10(a) is shown $\mathbf{H}_{er}$ during a positive peak of the 14 cps magnetic field modulation. The Bloch equations predict that in the absence of the applied audio field and in the limit of large H_1 the magnetization will be approximately in the direction of $\mathbf{H}_{er}$ with a magnitude $M_{zp}=M_0\cos\Theta T_{2H}/T_{1H}$. At the negative peak of the modulation the situation depicted by the dotted arrows in Fig. 10(a) applies. The observed rf dispersion signal is proportional to M_{zp}.

The action of the audio field H_a in the rotating

[40] Throughout this paper, peak values of the audio magnetic field will be used.

coordinate system can be seen by analogy to ordinary saturation in the fixed coordinate system, Fig. 10b. If $\Theta \simeq 90°$ the correspondences $H_{er} \rightarrow H_0$, $M_{0\rho} \rightarrow M_0$, and $H_a \rightarrow 2H_1$ apply, and the spin relaxation processes are almost the same in the two coordinate systems (identical if $T_1 = T_2$ as is frequently the case). In ordinary saturation the rf field $2H_1$ reduces the amplitude of M_z to some value less than its equilibrium value M_0. In rotary saturation the audio field H_a reduces the amplitude of $M_{z\rho}$ to some value less than its quasi-static equilibrium value $M_{0\rho}$. As a consequence the observed dispersion signal is correspondingly reduced, as in Fig. 9. Power is also absorbed from the audio field, but this absorption is normally too small to observe directly.

Rotary saturation can also occur off resonance, for $|H_0 - \omega/\gamma| \simeq H_1$, although it is most directly observed at resonance. As before, the audio field is most effective in reducing the magnetization $M_{z\rho}$ and the dispersion signal when the condition $\omega_a = \gamma H_{er}$ is obeyed. The effectiveness of the audio field is reduced by a factor $\sin^2\Theta$ since only the square of the component of $\mathbf{H}_a$ perpendicular to $\mathbf{H}_{er}$ acts in the double saturation. Some rather complicated dispersion derivative traces can be obtained by using various fixed values of ω_a

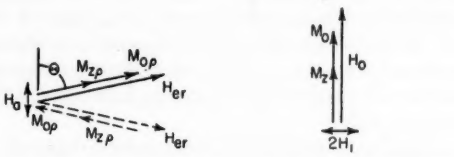

FIG. 10. Explanation of rotary saturation.

greater than γH_1. These signals all appear to be consistent with this simple picture.

Rotary saturation can be treated theoretically in liquids by transforming to a doubly rotating coordinate system,[24] the first rotation being about H_0 at frequency ω, the second about H_{er} at frequency ω_a. We ignore the circularly polarized component of H_a which rotates at frequency $2\omega_a$ in the doubly rotating system, and we also ignore the time dependent parts of the relaxation terms (involving T_1 and T_2), which vary sinusoidally with frequency ω_a. The resulting expression for $M_{z\rho}$ is similar to that for M_z as predicted by the Bloch equations for ordinary saturation, with the substitutions (for $\Theta \simeq 90°$) $M_0 \rightarrow M_{0\rho}$, $H_0 \rightarrow H_{er}$, $2H_1 \rightarrow H_a$, $M_z \rightarrow M_{z\rho}$, $\omega \rightarrow \omega_a$, $T_1 \rightarrow T_2$, and $T_2^{-1} \rightarrow \frac{1}{2}(T_1^{-1} + T_2^{-1})$. Thus the minimum of $M_{z\rho}$ and the dispersion signal should indeed occur when $\omega_a = \gamma H_{er}$, which near resonance corresponds to $\omega_a = \gamma H_1$.

The time dependent parts of the transformed Bloch equations will introduce some error in this solution and are probably responsible for the asymmetry in the run of Fig. 9. They will probably not introduce more than a few percent error in the determination of H_1 by this method.

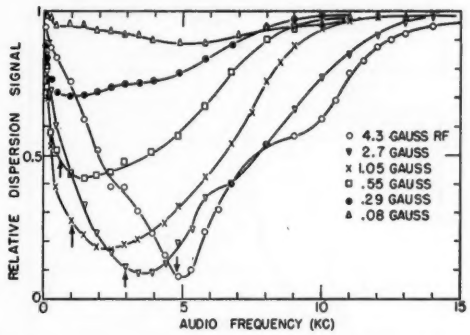

FIG. 11. Rotary saturation runs in pure aluminum. The audio amplitude H_a was about 2 gauss, the modulation amplitude was 2.5 gauss peak-to-peak, and the resonance frequency was about 7.6 megacycles. The arrows indicate the frequency $\gamma H_1/2\pi$ for the various runs.

In Fig. 11 are shown some rotary saturation runs in aluminum, for various values of H_1. In solids the line width is determined by the static dipolar interaction among different spins rather than by collision broadening as in the case of liquids. For low rf fields the dipolar interaction displaces the minimum to a frequency above γH_1 (indicated by arrows in Fig. 11), but for large H_1 the minimum very nearly coincides with the predicted nutation frequency.

Rotary saturation in solids can be treated theoretically in the rotating system in the same way that ordinary saturation was treated by BPP, because the analogy of Fig. 10 also applies to the case of solids. The effective[29] energy absorbed per second by the spins from the audio field is (for $\Theta \simeq 90°$)

$$\tfrac{1}{2}\omega\chi_a'' H_a^2, \tag{82}$$

where χ_a'' is the imaginary part of the audio susceptibility in the z, or x_ρ (approximately) direction. Since the system is assumed to be in a canonical distribution of states with respect to $\mathcal{H}_{er}$, for small H_a, we can write

$$\chi_a'' = \tfrac{1}{4}\omega(M_{0\rho}/H_{er}) f(\nu_a) \tag{83}$$

where $M_{0\rho}/H_{er}$ is the rotary analog of χ_0, and $f(\nu_a)$ is a normalized shape function similar to that defined by Broer.[41,42] (83) is consistent with a rotary version of the Kronig-Kramers relations and can be derived in the same way as the analogous equation for ordinary paramagnetic resonance.

The effective energy absorbed per unit time by the lattice from the spin system is [from Eqs. (37), (47), and (48)]

$$\left[\frac{\partial}{\partial t}\right]_{SL} \langle\langle \mathcal{H}_{er} \rangle\rangle = -(\langle\langle \mathcal{H}_{er} \rangle\rangle - \langle\langle \mathcal{H}_{er} \rangle\rangle_0)/T_{1\rho} = (M_{z\rho} - M_{0\rho}) H_{er}[1 + (\delta H)^2/H_{er}^2]/T_{1\rho}. \tag{84}$$

[41] L. J. F. Broer, thesis, Amsterdam, 1945 (unpublished); and Physica **10**, 801 (1943).
[42] A. Wright, Phys. Rev. **76**, 1826 (1949).

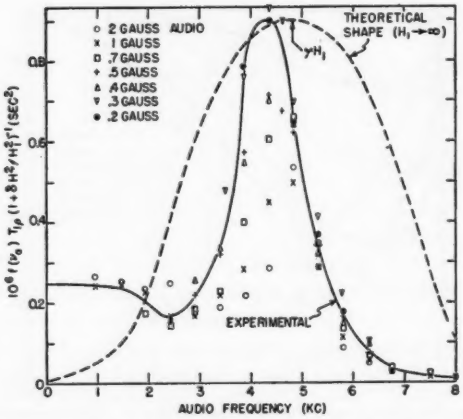

FIG. 12. Values of $f(\nu_a)T_{1\rho}[1+(\delta H)^2/H_1^2]^{-1}$ obtained from double saturation data for aluminum. H_1 was 4.3 gauss, the modulation was 2.5 gauss peak-to-peak, and ν_0 was about 7.6 megacycles. The arrow indicates the frequency $\gamma H_1/2\pi$.

Here $\langle\langle \mathcal{H}_{er}\rangle\rangle_0 = M_{0\rho}H_{er}[1+(\delta H)^2/H_{er}^2]$, the quasi-equilibrium value of $\langle\langle \mathcal{H}_{er}\rangle\rangle$.

In the quasi-steady state the thermal rate of decrease of $\langle\langle \mathcal{H}_{er}\rangle\rangle$ given by (84) must equal the rate at which (effective) energy is absorbed from the audio magnetic field, given by (82). If we assume, following BPP, that (83) holds under the substitution $M_{0\rho}\to M_{z\rho}$ in arbitrarily large H_a, we get

$$M_{z\rho}/M_{0\rho} = \{1+\tfrac{1}{2}H_a^2\omega_a^2 f(\nu_a)T_{1\rho}H_{er}^{-2} \times[1+(\delta H)^2/H_{er}^2]^{-1}\}^{-1}. \quad (85)$$

The observed rf susceptibility is thus reduced by a factor equal to the right-hand side of (85).

Actually, the assumption that $M_{z\rho}$ can be substituted for $M_{0\rho}$ in (83), for arbitrary H_a, is not justified. This is the same erroneous assumption made in the BPP theory[5] of ordinary saturation, as discussed in Sec. III(a). Equation (85) is expected to hold only for small H_a, where $M_{z\rho}/M_{0\rho}\simeq 1$.

The shape function $f(\nu_a)$ can be determined experimentally by making a series of runs at constant H_1 and different H_a and ω_a, and using (85) to determine $f(\nu_a)T_{1\rho}[1+(\delta H)^2/H_{er}^2]^{-1}$. Data obtained in this way for aluminum and copper are shown in Figs. 12 and 13. In drawing the experimental curve (solid line) through these data we have given the greatest weight to those points obtained at low audio power levels, since (85) is expected to be more accurate at these levels.

Integration of the solid curves in Figs. 12 and 13 yields values of $T_{1\rho}[1+(\delta H)^2/H_1^2]^{-1}$ of 5.6 milliseconds for copper and 2.2 milliseconds for aluminum. These times differ from values predicted from the previously estimated $T_{1\rho}$ and $(\delta H)^2$ by a factor of about two. The value for copper is too large and that for aluminum is too small. The reason for this discrepancy is not known.

We have not attempted to analyze the shape function $f(\nu_a)$ in detail, but we can make a few general remarks. A considerable number of theoretical predictions concerning $f(\nu_a)$ can be made using the methods of Van Vleck[25] and Wright,[42] but the Hamiltonian $\mathcal{H}_{er}$ has fewer secular terms than the spin Hamiltonian $\mathcal{H}_S$ in the fixed coordinate system, and therefore the theoretical work of Wright[42] is not directly applicable here. As expected, $f(\nu_a)$ has definite peaks at zero frequency and at γH_1. The significance, if any, of the small departures of the resonant peaks from the value γH_1 is not known. These departures may be due in part to experimental error.

In the limit of large H_{er}, $f(\nu_a)$ is expected to be a symmetrical curve centered about the resonance frequency γH_1, and the moments of $f(\nu_a)$ in this case have been calculated by Van Vleck. It is noteworthy that if $\tilde{A}_{jk}=0$ the secular part of $\mathcal{H}_{e\rho}$ [first three terms of Eq. (20)] contains a spin interaction identical in form and exactly half as large as the secular part of the Hamiltonian in the fixed coordinate system. This implies that $g(\nu)$, the rf line shape, should be exactly similar and twice as broad as $f(\nu_a)$. The expected shapes $f(\nu_a)\sim g(2\nu)$ are plotted in Figs. 12 and 13; here $g(\nu)$ was obtained experimentally. The observed $f(\nu_a)$ is considerably narrower than the predicted shape, which may be due in part to the fact that H_1 is not very large and is in fact comparable to the predicted line width. Another possible reason for the narrow observed $f(\nu_a)$ may be the terms $\tilde{A}_{jk}\mathbf{I}_j\cdot\mathbf{I}_k$, which are expected to produce exchange narrowing of $f(\nu_a)$. It is rather surprising that they do not also produce appreciable exchange narrowing of the rf resonance line.

It is amusing to note that if $1-3\cos^2\Theta=0$ and H_1 is large, the line width should be zero, except for a small spin-lattice relaxation broadening. In the case of the data of Figs. 12 and 13 the modulation was not large enough to induce such narrowing.

In conclusion we may say that besides providing an accurate calibration of the rf field, rotary saturation is a relatively simple way to study the properties of spin systems in small magnetic fields. This statement is based on the fact that the time dependent part of $\mathcal{H}_{er}$ really can be neglected to a very good approximation, so that rotary saturation is really closely analogous to ordinary saturation.

VI. CONCLUDING REMARKS

The theory and experiment in this paper demonstrate the usefulness of the rotating coordinate representation in resonance problems. The rotating coordinate representation should be useful in treating other types of relaxation and spin interaction than those considered here. For example, the rotary saturation experiment indicates that the perturbations responsible for transverse (T_2 or T_{2e}) relaxation of nuclei are those of frequency γH_1, rather than zero frequency.

All the theory in this paper can, of course, be applied to paramagnetic resonance under suitable conditions. In the case of ferromagnetic resonance the approximations

made above are presumably invalid, but some progress might be made along similar lines.

An as yet unexploited consequence of this work is the feasibility of measuring spin temperatures and relaxation times and obtaining negative temperatures in solids by the method of adiabatic fast passage. The experimental technique would be similar to that employed by Drain[43] and others[44] to measure relaxation times in liquids.

The implications of this research concerning the interpretation of previous work are rather unimportant, except for the probable errors in previous fast modulation saturation measurements of T_1, as discussed in Sec. III. The optimum signal to noise ratio predicted by Bloch and BPP is too small by a factor of about T_2/T_1, provided the dispersion mode is observed under conditions of slow passage. This gain is usually offset by the additional apparatus noise at high rf power levels, and by the fact that T_1 is frequently so long that slow passage is impractical.

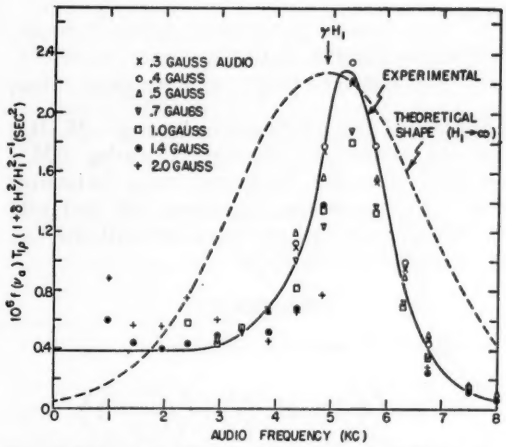

FIG. 13. Values of $f(\nu_a)T_{1\rho}[1+(\delta H)^2/H_1^2]^{-1}$ for Cu^{63} in annealed copper. The values of H_1, H_a, and modulation are the same as those in Fig. 12. The arrow indicates the frequency $\gamma H_1/2\pi$.

ACKNOWLEDGMENTS

I wish to thank Professor N. Bloembergen for suggesting this area of research and for many stimulating discussions and comments. I would also like to thank Dr. T. J. Rowland for experimental advice, Professor H. Brooks for several discussions, and Mr. R. H. Silsbee, Dr. K. Tomita, and Professor J. H. Van Vleck for commenting on the manuscript.

APPENDIX A

The method used to calculate the ratio of the effective external energy $M_{z\rho}H_{er}$ to internal spin-spin effective energy is similar to that used by Van Vleck[31] to calculate the specific heat of a spin system. However, the form of the Hamiltonian is slightly different and the calculation is simplified by the use of the density matrix[21] formalism.

The assumption of a canonical distribution of states with respect to the transformed spin Hamiltonian is equivalent to the assumption that the state of the solid is described by the density matrix (in the r-rotating system)

$$\rho \simeq C \exp(-\mathcal{H}_{er}/kT^* - \mathcal{H}_L/kT). \tag{86}$$

Here C is a normalizing factor making $\mathrm{Tr}\rho=1$, T^* is a constant analogous to an effective spin temperature in the rotating system, $\mathcal{H}_L$ is the lattice (nonspin) Hamiltonian, and T is the lattice temperature. TrO denotes the trace (diagonal sum) of the operator O. The spin-lattice interaction $\mathcal{H}_{SL}$ (or $\mathcal{H}_{SLR}$ transformed to the rotating coordinate system) is neglected since it is assumed to be small. The first term of the exponential (86) represents the assumption that the spin system is in a canonical distribution of states with respect to $\mathcal{H}_{er}$, corresponding to the spin effective temperature T^*. The second term represents the assumption that the lattice (electrons, lattice vibrations, etc.) is relatively unaffected by the rf field and can be described by the temperature T.

In practice we can assume that T^* is large enough for us to write

$$\rho \simeq (1-\mathcal{H}_{er}/kT^*)\rho_L, \tag{87}$$

where

$$\rho_L = C \exp(-\mathcal{H}_L/kT). \tag{88}$$

The expectation value of $\mathcal{H}_{er}$ averaged over the canonical ensemble is

$$\langle\langle \mathcal{H}_{er} \rangle\rangle = \mathrm{Tr}\mathcal{H}_{er}\rho \cong (\mathrm{Tr}\mathcal{H}_{er}\rho_L - \mathrm{Tr}\mathcal{H}_{er}^2\rho_L/kT^*). \tag{89}$$

This expression is easily evaluated by using a representation in which the operators I_{jz} and $\mathcal{H}_L$ are diagonal. In this case we can write $C^{-1}=(2I+1)^N \mathrm{Tr}_L \times \exp(-\mathcal{H}_L/kT)$ where N is the total number of spins and $\mathrm{Tr}_L O$ denotes the diagonal sum of the operator O over all the eigenvalues $\mathcal{E}_L$ of $\mathcal{H}_L$, keeping the quantum numbers m_{Ij} (eigenvalues of I_{jz}) fixed. In the same representation we can write

$$\mathrm{Tr}\mathcal{H}_{er}^2\rho_L = (\mathrm{Tr}_I\mathcal{H}_{er}^2)(\mathrm{Tr}_L\rho_L), \tag{90}$$

where $\mathrm{Tr}_I\mathcal{H}_{er}^2$ denotes the diagonal sum of $\mathcal{H}_{er}^2$ over the quantum numbers m_{Ij}, keeping the quantum number $\mathcal{E}_L$ fixed. This relation follows directly from the diagonality of $\mathcal{H}_{er}$ with respect to the $\mathcal{E}_L$ and of $\mathcal{H}_L$ with respect to the m_{Ij}.

Using the easily verified relations:

$$\mathrm{Tr}_I I_{j\nu}I_{k\mu} = \tfrac{1}{3}I(I+1)(2I+1)^N\delta_{j,k}\delta_{\nu,\mu}, \tag{91}$$

$$\mathrm{Tr}_I I_{j\nu}I_{k\mu}I_{m\xi}I_{n\eta} = (1/9)I^2(I+1)^2(2I+1)^N\delta_{i,k}\delta_{\mu,\nu}\delta_{m,n}\delta_{\xi,\eta}, \tag{92}$$

where $\nu, \mu, \xi, \eta = x, y, z$ and $j \neq m$, $k \neq n$, we can evaluate $\mathrm{Tr}\mathcal{H}_{er}^2\rho_L$ and similarly show that $\mathrm{Tr}\mathcal{H}_{er}\rho_L$ is zero. The

[43] L. E. Drain, Proc. Phys. Soc. (London) A26, 301 (1949).
[44] Ciaroti, Cristiani, Giulotto, and Lanzi, Nuovo cimento 12, 519 (1954).

result is

$$-kT^*\langle\langle\mathcal{H}_{er}\rangle\rangle=\tfrac{1}{3}Ng^2\beta^2H_{er}^2I(I+1)+(1/9)I^2(I+1)^2\sum_{k>j}(3\tilde{A}_{jk}^2+\tfrac{2}{3}B_{jk}^2). \quad (93)$$

The first term of $\langle\langle\mathcal{H}_{er}\rangle\rangle$ is the external energy $-\mathbf{M}_r\cdot\mathbf{H}_{er}$, as can be verified by directly calculating $\langle\langle\mathbf{M}_r\rangle\rangle=\langle\langle g\beta\sum\mathbf{I}_j\rangle\rangle$ using (87). The second term is the internal spin-spin effective energy. Equations (30) and (31) follow directly from (93) on comparison with the Van Vleck[25] expression for $\langle(\Delta H)^2\rangle_{Av}$.

APPENDIX B

The equation of motion of $\langle\langle\mathcal{H}_{er}\rangle\rangle$ is

$$\frac{d}{dt}\langle\langle\mathcal{H}_{er}\rangle\rangle=\left\langle\left\langle\frac{i}{\hbar}[\mathcal{H}_r,\mathcal{H}_{er}]\right\rangle\right\rangle+\left\langle\left\langle\frac{\partial\mathcal{H}_{er}}{\partial t}\right\rangle\right\rangle, \quad (94)$$

where $\mathcal{H}_r$ is the total Hamiltonian $\mathcal{H}=\mathcal{H}_L+\mathcal{H}_{SL}+\mathcal{H}_S$ transformed to the r-system:

$$\mathcal{H}_r=\mathcal{H}_L+\mathcal{H}_{SLR}(t)+\mathcal{H}_{er}. \quad (95)$$

Since $\mathcal{H}_{er}$ commutes with itself and $\mathcal{H}_L$, (94) becomes

$$\frac{d}{dt}\langle\langle\mathcal{H}_{er}\rangle\rangle=\langle\langle\partial\mathcal{H}_{er}\rangle\rangle-\mathbf{M}_r\cdot\frac{\partial\mathbf{H}_{er}}{\partial t}. \quad (96)$$

The abbreviation ∂O is used for $-i\hbar^{-1}[\mathcal{H}_{SLR},O]$, so that $\langle\langle\partial O\rangle\rangle$ is the time rate of change of the canonical average expectation value $\langle\langle O\rangle\rangle$ of O, due to the (time dependent) spin-lattice interaction $\mathcal{H}_{SLR}$. In the treatment of fast or intermediate passage the first and last terms of (96) are retained [Eq. (65), Sec. III(e)], while under steady-state conditions they are by definition zero, and the second term is therefore also zero. $\langle\langle\partial\mathcal{H}_{er}\rangle\rangle$ is also referred to in Sec. III as $[\partial/\partial t]_{SL}\langle\langle\mathcal{H}_{er}\rangle\rangle$. Assuming that the spin-lattice interaction $\mathcal{H}_{SL}$, and therefore the transformed interaction $\mathcal{H}_{SLr}$, is linear in the operators I_{jz}, I_{jy}, I_{jz}, we get

$$\langle\langle\partial\mathcal{H}_{er}\rangle\rangle=g\beta\sum_j\mathrm{Tr}(\partial\mathbf{I}_j)\cdot\mathbf{H}_{er}\rho+g^2\beta^2\sum_{j\neq k}[A_{jk}^2\,\mathrm{Tr}(\partial\mathbf{I}_j)\cdot\mathbf{I}_k\rho+B_{jk}^2\,\mathrm{Tr}(\partial I_{jz})I_{kz}\rho]. \quad (97)$$

In (97) ρ is understood to be given by (87).

To evaluate (97) we use the assumption (34), which in slightly more general form can be written

$$\mathrm{Tr}(\partial I_{jz})\rho'=-\mathrm{Tr}I_{jz}\rho'/T_{2e}, \quad (98a)$$

$$\mathrm{Tr}(\partial I_{jy})\rho'=-\mathrm{Tr}I_{jy}\rho'/T_{2e}, \quad (98b)$$

$$\mathrm{Tr}(\partial I_{jz})\rho'=-(\mathrm{Tr}I_{jz}\rho'-I_0)/T_1. \quad (98c)$$

Here we have temporarily abandoned the assumption $T_1=T_{2e}$, and ρ' is a density matrix describing an arbitrary state of the spin system. Thus $\rho'=\rho_I\rho_L$, where ρ_I is an arbitrary function of the spin operators for which $\mathrm{Tr}\rho_I=(2I+1)^N$. Use of the various operators 1, $1+I_{j\xi}$, $1+I_{j\xi}I_{k\eta}$, $1+I_{j\xi}I_{k\eta}I_{k\xi}$ (with $\xi,\eta,\zeta=x,y,z$, and j, k and ξ,η,ζ not necessarily identical or nonidentical) for ρ_I yields

$$\mathrm{Tr}(\partial I_{jz})\rho_L=I_0/T_1, \quad (99)$$

$$\mathrm{Tr}(\partial I_{j\nu})I_{j\nu}\rho_L=-\tfrac{1}{3}I(I+1)/T_{2e}, \quad (100)$$

$$\mathrm{Tr}(\partial I_{jz})I_{jz}\rho_L=-\tfrac{1}{3}I(I+1)/T_1, \quad (101)$$

$$\mathrm{Tr}(\partial I_{j\nu})I_{jz}I_{k\nu}^2\rho_L=-(1/9)I^2(I+1)^2/T_1, \quad (102)$$

$$\mathrm{Tr}(\partial I_{j\nu})I_{j\nu}I_{k\mu}^2\rho_L=-(1/9)I^2(I+1)^2/T_{2e}, \quad (103)$$

where $j\neq k$; $\mu=x,y,z$; $\nu=x,y$. All other traces occurring in (97) are zero. Using these expressions we get

$$\langle\langle\partial\mathcal{H}_{er}\rangle\rangle=Ng\beta\left(H_0-\frac{\omega}{\gamma}\right)\frac{I_0}{T_1}-\frac{Ng^2\beta^2I(I+1)}{3kT^*}\times\left[\left(H_0-\frac{\omega}{\gamma}\right)^2\frac{1}{T_1}+\frac{H_1^2}{T_{2e}}\right]+I^2(I+1)^2\sum_{j\neq k}\left\{-A_{jk}^2\left[\frac{1}{9T_1}+\frac{2}{9T_{2e}}\right]-\frac{B_{jk}^2}{9T_1}-\frac{2A_{jk}B_{jk}}{9T_1}\right\}. \quad (104)$$

$\langle\langle\mathbf{M}_r\rangle\rangle=\mathrm{Tr}g\beta\sum_j\mathbf{I}_j\rho$ is easily shown to be a vector in the direction of $\mathbf{H}_{er}$ or $\mathbf{k}_\rho$, of magnitude

$$M_{z\rho}=I(I+1)g^2\beta^2NH_{er}/3kT^*. \quad (105)$$

The static equilibrium magnetization M_0 is given by the same formula with $M_{z\rho}\to M_0$, $T^*\to T$, and $H_{er}\to H_0$. Therefore (104) can be written

$$\langle\langle\partial\mathcal{H}_{er}\rangle\rangle=-(M_{z\rho}-M_{0\rho})[1+(\delta H)^2/H_{er}^2]H_{er}/T_{1\rho}, \quad (106)$$

where

$$T_{1\rho}=\frac{M_{0\rho}[1+(\delta H)^2/H_{er}^2]T_1}{M_0\cos\Theta}, \quad (107)$$

and

$$M_{0\rho}=\frac{M_0\cos\Theta(T_1^{-1}\cos^2\Theta+T_{2e}^{-1}\sin^2\Theta)^{-1}}{T_1[1+\alpha(\delta H)^2/H_{er}^2]}. \quad (108)$$

If

$$\tilde{A}_{jk}=0,\quad \alpha=\left(\frac{16}{9T_1}+\frac{2}{9T_{2e}}\right)(T_1^{-1}\cos^2\Theta+T_{2e}^{-1}\sin^2\Theta)^{-1}.$$

If $T_{2e}=T_1$, and $\tilde{A}_{jk}$ is not necessarily zero, Eqs. (38) and (63) of Sec. III follow immediately.

In this calculation $\mathcal{H}_{SL}$ and $\mathcal{H}_{SLr}$ contain only the time dependent part of the spin-lattice interaction which is responsible for the relaxation, while $\mathcal{H}_S$ and $\mathcal{H}_{er}$ contain time independent parts which result from the spin-lattice interaction (i.e., chemical shift, Knight shift, and electron coupled spin-spin interactions).[26,27] As discussed in Sec. III(c), this procedure is hard to justify rigorously but seems reasonable physically.

APPENDIX C

We assume that the system is described by the density matrix

$$\rho = C \exp\{\mathcal{H}_{er1}/kT^* + [g\beta H_0 \sum_{j'} I_{j'z} + \mathcal{H}_L]/kT\}, \quad (109)$$

where $\mathcal{H}_{er1}$ contains all the time-independent terms of $\mathcal{H}_{er}$ [Eq. (53)] except the last. The reason for including all the spin-spin terms of $\mathcal{H}_{er}$ is discussed in Sec. III(d).

The ratio of external unprimed spin energy to internal spin-spin energy is obtained by evaluating $\langle\langle \mathcal{H}_{er1} \rangle\rangle$. Proceeding as in Appendix A, (55) easily follows.

The equation of motion of $\langle\langle \mathcal{H}_{er1} \rangle\rangle$ is given by (96) with the substitutions $\mathcal{H}_{er} \rightarrow \mathcal{H}_{er1}$ and the density matrix (109) for that of (86). Evaluation of the various terms is similar to the procedure of Appendix B. Equations (99) to (103) hold for the substitutions $j \rightarrow j'$ and/or $k \rightarrow k'$ under suitable additional substitution of $\mathbf{I}_0'$, T_1', and T_{2e}'. (48) and (56) then follow easily from the assumption $T_1 = T_{2e}$ and $T_1' = T_{2e}'$.

PHYSICAL REVIEW VOLUME 98, NUMBER 6 JUNE 15, 1955

Theory of Electroluminescence

W. W. PIPER AND F. E. WILLIAMS
General Electric Research Laboratory, Schenectady, New York

(Received February 11, 1955)

The theoretical basis for exciting luminescence by the application of an electric potential to a crystalline dielectric or semiconductor is considered. Three mechanisms of excitation are each shown to be theoretically feasible in appropriate solids and with suitable local field conditions: (1) the ionization of impurity systems directly by an electric field, (2) the acceleration of conduction electrons or positive holes in the valence band to kinetic energies sufficient to excite or ionize impurity systems or valence electrons by inelastic collisions, and (3) injection of charge carriers. Radiative de-excitation is feasible by two mechanisms: (a) direct recombination of conduction electrons and holes in the valence band, and (b) optical transitions characteristic of impurity systems known as activators. The characteristics of electroluminescence proceeding by these processes are examined theoretically.

INTRODUCTION

ELECTROLUMINESCENCE of various crystalline phosphors has been reported in the literature over a period of twenty-five years.[1–5] Various mechanisms have also been proposed.[2,3,5–7] In this paper the general mechanisms for converting an electrical potential applied to a crystal into luminescence will be examined theoretically. Previously considered mechanisms are, of course, included as well as others which may have more significance as the number of types of electroluminescent crystals increases.

Electroluminescence is the excitation of luminescence as a result of the existence of an applied potential difference in the phosphor material. The definition includes luminescence induced by any mechanism of injection of electrons or holes into the phosphor or any mechanism of creating free charge carriers in the phosphor if the energy of the emitted radiation originates in the electric potential difference applied to the phosphor. Cathodoluminescence is excluded since in this case the excitation energy is supplied initially to electrons by an external field.

It is well known that solid-state luminescence usually originates from excited impurity systems called activators which have dimensions of the order of an interatomic distance. To radiate in the visible portion of the spectrum, the activator system must have an excited state at least 2 ev higher than the ground state. An electroluminescent mechanism utilizing an activator system must in some way localize 2 or 3 ev of the energy available in the applied potential to the atomic dimensions of the activator system and transfer this energy to the activator. If the activator is left in an excited state, it is then able to radiate a photon in returning to the ground state. Ionization of the center is also a permissible mechanism, provided conduction electrons are available or are made available subsequently.

The most straightforward mechanism of electroluminescent excitation is direct field ionization of the activator system. Since the ionized state of the activator system is at least 2 ev above the ground state, the field strength necessary to ionize these centers at a reasonable rate would normally be in excess of the dielectric breakdown strength of the crystalline matrix. Breakdown in materials with suitable band gaps for luminescence normally occurs by an avalanche mechanism, rather than by field ionization of the valence electrons. Nevertheless, direct field ionization of the activator system

[1] O. Lossev, Phil. Mag. **6**, 1024 (1928).
[2] G. Destriau, Phil. Mag. **38**, 700 (1947).
[3] Lehovec, Accardo, and Jamgochian, Phys. Rev. **83**, 603 (1951).
[4] Payne, Mager, and Jerome, Illum. Eng. **45**, 688 (1950).
[5] W. W. Piper and F. E. Williams, Phys. Rev. **87**, 151 (1952); Brit. J. Appl. Phys., Supplement No. 4, **6**, 39 (1955).
[6] D. Curie, J. phys. radium **13**, 317 (1952).
[7] J. F. Waymouth and F. Bitter, Phys. Rev. **95**, 941 (1954).

essentially by quantum-mechanical tunneling is feasible if the high-field region in the neighborhood of the activator atom is sufficiently localized to prevent breakdown.

A second mechanism which does not require as large a field is the excitation of impurity systems by inelastic collisions. Electrons injected into the conduction band in the presence of a sufficiently strong electric field have an appreciable probability of attaining enough kinetic energy to excite or ionize an activator system by means of an inelastic collision. The excited activator could alternatively radiate a photon or become ionized either thermally or with the aid of the local electric field. Electrons may be injected into the conduction band in the presence of high fields either at the surface of the crystal or in the bulk of the crystal from donor levels or occupied traps too deep to be ionized thermally. In a completely analogous manner, positive holes can be injected into the valence band from the surface or from acceptor centers or hole traps and attain sufficient kinetic energy to excite an activator system by means of an inelastic collision.

A third method of exciting electroluminescence is the introduction of both types of free charge carriers into a particular region of a crystal. This may be accomplished by the injection of minority carriers into *p*-type or *n*-type material from the surface or at a *p-n* junction within the crystal. Alternatively both species may be injected into intrinsic material. A strong electric field is not required for the charge carrier injection mechanism.

Radiative de-excitation by means of an optical transition of an activator system is a well-known mechanism[8,9] of solid-state luminescence and will not be discussed further. In addition, the direct recombination of holes in the valence band and conduction electrons will be shown to be a possible source of radiation under conditions of large concentrations of charge carriers.

FIELD IONIZATION

If the activator center in the phosphor crystal is to be directly ionized by the applied field, the most serious problem is dielectric breakdown of the crystal before sufficient local field strength has been attained. The breakdown strengths of the alkali halides are approximately 10^6 volts/cm.[10] The breakdown field for most crystalline phosphors quite probably does not differ from this value by more than a factor of three.

It has been well established that the mechanism of breakdown of crystalline insulators is that of acceleration of conduction electrons to sufficient kinetic energy to ionize further valence electrons and thus multiply into a breakdown current. This mechanism dominates over Zener breakdown (field ionization of the valence electrons) except possibly for crystals with a forbidden band gap appreciably less than one electron volt. The field requirements for Zener breakdown increase as the square of the band gap and at larger band gaps exceed the field requirements for breakdown by avalanche.

Franz[11] has made calculations not only for field ionization of valence electrons but also for electrons trapped in a square well potential. His calculations for the field necessary to ionize this localized center reduces to good approximation to the expression

$$E_i=\frac{10^7\epsilon_g^{\frac{1}{2}}}{8+\log_{10}E_i\tau}\epsilon^{\frac{1}{2}}, \tag{1}$$

if E_i is measured in volts/cm, τ, the decay constant of the center in sec, and ϵ, the depth of the well in ev, and if the lattice constant is 5 A and the radius of the trap is 3 A. For example, with a band gap, ϵ_g, of 6 ev a field of 6×10^6 volts/cm is necessary to ionize with a decay constant of 10^{-3} sec a square well center 2 ev deep.

Both avalanche and Zener breakdown compete with the direct field ionization of a localized center. The breakdown strength of crystals ruptured by an avalanche of ionizing events is quite insensitive to crystal thickness except for very thin high-field configurations. If the assumption is made that a fixed number of multiplications must occur before breakdown, then the field strength increases as the high-field region becomes thinner. At the breakdown field strengths mentioned above, the mean multiplication distance has been shown to vary quite rapidly with the field[12] which means the field strength is not strongly dependent on thickness. However, in the region of very high fields, as pointed out by Wolff,[13] the mean multiplication distance, $\bar{\lambda}$, varies proportionally with the reciprocal of the field, and an ionizing event occurs for a potential difference equivalent to an energy not much larger than the band gap. Thus in this region the breakdown strength, E_B, may be written as

$$E_B=Na\epsilon_g/t, \tag{2}$$

where ϵ_g is the band gap energy; t, the thickness of the high-field region; $a\epsilon_g$, the mean energy for ionization; and N, the number of multiplications necessary to produce breakdown. An upper limit of thickness for direct field ionization can be calculated to the accuracy of the constants in (1) and estimates of the constants in (2).

$$t\leqslant\frac{Na\epsilon_g}{E_i}=\frac{Na\epsilon_g^{\frac{1}{2}}}{10^7\epsilon^{\frac{1}{2}}}(8+\log_{10}E_i\tau). \tag{3}$$

If one assumes a representative value of 4 for $a\epsilon_g^{\frac{1}{2}}$ and uses Seitz's estimate of 40 multiplications to cause rupture,[12] direct field ionization of a center 2 ev deep will have a time constant as small as 10^{-3} sec at fields

[8] F. Seitz, J. Chem. Phys. **6**, 150, 454 (1938).
[9] F. E. Williams, J. Chem. Phys. **19**, 457 (1951).
[10] A. von Hippel and R. S. Alger, Phys. Rev. **76**, 127 (1949).
[11] W. Franz, Ann. Physik (6) **11**, 17 (1953).
[12] F. Seitz, Phys. Rev. **76**, 1376 (1949).
[13] P. A. Wolff, Phys. Rev. **95**, 1415 (1954).

lower than the field for breakdown by avalanche if the thickness is less than 0.7 micron. Crystals with larger band gaps can tolerate a larger value of thickness.

A minimum thickness of the high-field region is determined by the energy requirement for direct field ionization, and for the 2-ev transition is 30 A. The efficiency of electroluminescence by field ionization will be a maximum near this minimum thickness since energy is absorbed from the point of ionization to the edge of the high-field region.

A second limitation of the direct field ionization mechanism is competition with Zener breakdown of the lattice. Again using Franz's calculations, the following expression, similar to (1) but for Zener emission from the valence band, may be written for the field E_v necessary to induce valence electron emission with a time constant, τ_v.

$$E_v=\frac{6\times10^6}{7+\log_{10}(E_v\tau_v)}\epsilon_g^2. \tag{4}$$

E_v is in volts/cm and ϵ_g in ev. The lattice constant is again taken as 5 A. For equal emission probability per unit volume of valence states and localized states which differ in concentration by 10^6, (ϵ/ϵ_g) is determined by (1) and (4) and is 0.6. This ratio changes to 0.7 for an impurity concentration of one percent. Hence the band gap requirements to prevent Zener breakdown are quite reasonable.

The possibility of direct field excitation without ionization exists for an activator system whose emitting state can be perturbed by the applied potential to an energy low enough to permit a reasonable occupation probability of this state from the ground state. If this perturbation, $\Delta\epsilon$, of the transition energy is due to a difference in polarizability, $\Delta\alpha$, of the two states, the difference in the induced dipole moments, Δp, will be

$$\Delta p=2(\Delta\epsilon)/E, \tag{5}$$

and

$$\Delta\alpha=\Delta p/E, \tag{6}$$

where E is the applied electric field. For an applied field as large as 10^8 volts/cm and $\Delta\epsilon=2$ ev, Δp and $\Delta\alpha$ are 20×10^{-18} esu cm and 30×10^{-24} cm^3 respectively. Both values are too high to be realized experimentally in the near future.

Activator systems having a minimum ionization energy in dielectric phosphors with large band gaps should be most suitable for electroluminescence by the direct field ionization mechanism. Observation of infrared electroluminescent emission by the direct field ionization mechanism is most probable because of the lower ionization energy and consequent lower field required. The emitting state of the activator system should be only a few tenths of an electron volt below the conduction band.

Unambiguous identification of the direct field ionization mechanism of electroluminescence has not yet been reported experimentally.

IONIZATION BY IMPACT

In order to produce electroluminescence by inelastic collisions of high-velocity electrons and activator systems, at least three conditions must exist. High-field regions capable of accelerating charge carriers to large kinetic energies must be produced, electrons or holes must be injected into this high-field region, and activator atoms must be suitably located to absorb by collision a significant fraction of the energy extracted from the field by the charge carriers.

The behavior of conduction electrons in high electric fields has been studied quite extensively by many investigators[10,13,14] in connection with the dielectric breakdown strength of solids. These investigators are in agreement on the main features of the mechanism. Electrons in an electric field are subjected to the force of acceleration of the field and a retarding force resulting from an interaction with the vibrational waves of the lattice. With sufficient field strength the electrons may overcome the frictional barrier and attain enough energy to ionize valence electrons. If occupied localized impurity states exist in the forbidden band of the crystal, the high-energy electrons will also have a certain probability of losing energy to these centers by inelastic collisions. The relative probabilities of this event and the ionization of valence electrons will depend on the energy and concentration of these impurity systems as well as the nature of the crystal lattice. The capture of holes by the localized systems following the ionization of valence electrons may also occur with appreciable probability.

Seitz[12] has emphasized the importance of nonpolar modes of lattice vibration at high energies even in an ionic crystal. These modes impose a frictional barrier at high kinetic energies of a conduction electron. Thus, with an electric field applied to the crystal, there may be a group of electrons which possess energies large compared with kT. If this barrier occurs at an energy close to the excitation or ionization energy of the impurity, there then will be an enhanced relative probability of excitation of the impurity.

Since this mechanism of electroluminescence is operating at field strengths not greatly inferior to the strength necessary for dielectric breakdown, field configurations contributing to stability against breakdown are important. For example, a thin high-field region in series with a thick low-field region would permit operation over a broader range of applied voltages without reaching an unstable breakdown condition. If the crystal possessed a high-impedance barrier region, this condition would be realized. A crystal with nonlinear characteristics such that the width of the high-field region, as well as the magnitude of the field, is

[14] H. Frohlich, Proc. Roy. Soc. (London) **188**, 521, 532 (1947).

dependent on the applied voltage, is particularly stable against dielectric breakdown.

Several types of barriers are physically possible, each having different electrical characteristics which might aid in the experimental identification of the mechanism for a specific phosphor system. A Mott-Schottky exhaustion-type barrier has already been proposed by Piper and Williams[5] to explain the characteristics of single crystals of ZnS:Cu. The barrier to be effective must be close to a conducting electrode. Charge from donor levels is swept from the volume in front of the electrode and further charge cannot flow into the crystal from the electrode due to a difference of work function or the presence of an insulating layer. As the potential difference across the crystal is increased, the exhaustion layer broadens and the barrier fields increase as the square root of applied potential.

An insulating intrinsic layer is another suitable type of barrier. This barrier would remain constant in thickness and the field which would be independent of position in the barrier would vary linearly with applied voltage.

A further possibility is a *p-n* junction biased in the reverse direction. An idealized example of a junction is a linear variation of the difference of donor and acceptor concentrations through the junction. The exhaustion region increases in width with increasing applied voltage, and for this example the field strength would vary as the two-thirds power of the voltage.

In order to produce electroluminescence, free charge carriers must be injected into the high-field region of the crystal after the field has been established. This can be accomplished in a variety of ways. The carriers may be injected from the surface of the crystal. Donors, acceptors, and filled traps are also a source of free carriers. The position of these sources may be in the high-field region itself if their binding energies are sufficient to permit the field to reach an appropriate value without the charge carrier being prematurely released. The sources may also occupy an adjacent volume if the carriers are swept into the high-field region after being released. The release of the carriers may occur thermally or the ionization may occur due to the presence of the high field. Photon absorption is also possible. If the absorption is in the fundamental band, a localized center is not needed and two free charges of opposite sign are released for each absorbed photon.

If the mean distance for the acceleration of a carrier up to an ionization event is less than the width of the barrier, then the effects of multiplication must be considered. The size of the avalanches will, of course, depend critically on the field strength. Postulating the creation of carriers by the absorption of photons in the fundamental band, or by thermal or field ionization of impurity systems excited by the absorption of photons, the interesting possibility of light amplification was predicted by Williams.[14a] The amplification depends on sufficient local field so that either the charge carriers created by the incident radiation attain sufficient kinetic energy for the excitation by impact of the activator systems several times in their mean lives or the charge carriers created by the incident radiation form avalanches of prebreakdown magnitudes and excitation by impact of a number of activators per incident photon is attained. The electroluminescence of ZnS:Cu phosphors has been identified with the impact mechanism of excitation.[5] Light amplification in ZnS:Mn phosphor films has recently been observed experimentally by Cusano.[15]

CHARGE CARRIER INJECTION

In semiconducting material, charge carrier injection provides a third mechanism for electroluminescence. The charge carrier can be injected either through the surface of the crystal or from a *p-n* junction biased in the forward direction.

In the case of *n*-type material, the Fermi level would be well above the ground state of the activator centers so that these centers would have their ground state occupied. The injection of a hole in the valence band if trapped by an activator would ionize this center. The center would then electrostatically attract and trap a conduction electron. The trapped electron would initially occupy an excited state and upon returning to the ground state emit a photon. Other localized centers would constitute competitive mechanisms for hole annihilation. These alternate mechanisms would not necessarily result in the radiation of visible light.

For *p*-type material, free holes are available to ionize the activator system for activators with ground states above the valence band. In this case, injected conduction electrons if captured by the activator center would result in luminescence. The supply of holes in the valence band would reionize the activator system in preparation for the next radiative event.

The absence of a local field and applied potential threshold leads to several characteristics of the charge carrier injection mechanism of electroluminescence. For the *p-n* junction, for example, with no applied potential thermal excitation leads to some injection and consequent light emission, limited in radiation density, however, by the characteristics of a black body at the lattice temperature. With small applied potentials the injection process will be markedly temperature-dependent. The electroluminescent efficiency will depend on the carrier lifetime of the injected charge carriers. Modulation by photon absorption should be possible for the carrier injection mechanism of electroluminescence. In addition, if the photons create charge carriers which are trapped, thereby yielding a space charge facilitating the transport of carriers of opposite sign which are

[14a] F. E. Williams, Phys. Rev. **98**, 547 (1955).
[15] D. A. Cusano, Bull. Am. Phys. Soc. **30**, No. 1, 30 (1955); Phys. Rev. **98**, 546 (1955).

subsequently captured by the activator systems, light amplification is feasible. The electroluminescence of SiC has been attributed to the charge carrier injection mechanism.[8]

DIRECT RADIATIVE RECOMBINATION

The activator centers would not be necessary in a crystal whose band gap lies in the appropriate range. Holes and electrons are capable of direct recombination by the mechanism of photon emission. This process can compete successfully with the nonradiative mechanism in material of sufficiently high purity and high carrier concentration. Emission of this sort has already been observed in the infrared in germanium.[16] Smith recently reported injected electroluminescence in CdS and attributes the emission to direct radiative recombination.[17] Van Roosbroeck and Shockley have developed a formula for the total rate of radiative recombination.[18] Applying this expression to an intrinsic material whose absorption coefficient abruptly rises to 10^5 cm^{-1} at 2 ev and which has a refractive index of $\sqrt{10}$ near the absorption edge, one obtains a rate of recombination, $\mathcal{R}$, under conditions of thermal equilibrium at room temperature of

$$\mathcal{R}=5.3\times10^{-7}\ \text{cm}^{-3}\ \text{sec}^{-1}. \tag{7}$$

For an arbitrary concentration of holes and electrons, the recombination rate is

$$\mathcal{R}_c=(np/n_i^2)\mathcal{R}, \tag{8}$$

where n_i is the equilibrium concentration of holes and electrons in intrinsic material, n, the free electron concentration, and p, the free hole concentration. This is clearly a bimolecular mechanism. The nonradiative recombination rate is essentially bimolecular as long as the probability of thermal dissociation following capture of a charge carrier by the center is large compared to the probability of capture of a charge carrier of opposite sign. However, at sufficiently high concentrations of free charge carriers, the mechanism becomes monomolecular and the ratio of radiative and nonradiative rates will favor the radiative process. This ratio reduces to

$$(\mathcal{R}_c/\mathcal{R}_{NR})=n_c\sigma_i/(\delta N\sigma_{NR}), \tag{9}$$

where the subscript NR refers to the nonradiative rate of recombination, n_c and N the concentrations of the majority injected carriers and nonradiative centers and σ the cross sections of the two mechanisms. Depending upon the ratio of holes and electrons, δ varies between 0.5 and 1.

The cross section for the radiative process for the case of the 2-ev band gap is

$$\sigma_i=\mathcal{R}/(n_i^2v), \tag{10}$$

where v is the thermal velocity of the free electrons and holes. At room temperature σ_i is approximately 10^{-16} cm^2. If the nonradiative cross section has a conventional atomic value of the order of 10^{-15} cm^2, then the injected carrier concentration must rise to ten times the nonradiative center concentration for the recombination rates to be equal.

SUMMARY

The threshold fields required for electroluminescence distinguish the three excitation mechanisms. Approximate local fields of 10^7 and 10^5 volts/cm are necessary for the direct field ionization and the impact excitation mechanisms respectively. The charge carrier injection mechanism does not have a field threshold. The sequence of events necessary for impact excitation and carrier injection indicates that modulation by incident radiation of electroluminescence occurring by these mechanisms is feasible. Only for the carrier injection mechanism operating with small applied potential is a pronounced temperature dependence of electroluminescence predicted. There is good reason to believe that additional electroluminescent materials will be devised and that the three general mechanisms analyzed theoretically are sufficiently comprehensive to include all experimentally realizable systems.

ACKNOWLEDGMENTS

The authors wish to acknowledge several helpful discussions on the injection mechanism with R. N. Hall and the helpful criticism of the manuscript by M. H. Hebb.

[16] J. R. Haynes and H. B. Briggs, Phys. Rev. **86**, 647 (1952); R. Newman, Phys. Rev. **91**, 1313 (1953).
[17] R. W. Smith, Bull. Am. Phys. Soc. **30**, No. 1, 30 (1955).
[18] W. van Roosbroeck and W. Shockley, Phys. Rev. **94**, 1558 (1954).

Charge Distributions of Oxygen and Neon Ions Passing through Gases*

EDWARD L. HUBBARD AND EUGENE J. LAUER
Radiation Laboratory, University of California, Berkeley, California
(Received January 10, 1955)

Electrons were stripped from accelerated oxygen and neon ions by passing them through a gas. Magnetic deflection was used to select the energy and charge of the incident ions and to determine the distribution of ionic charges in the stripped beam. As the amount of gas that the ions passed through was increased, the peak of the charge distributions first shifted toward higher charge states and then became constant as equilibrium was established between capture and loss of electrons. At equilibrium in argon the charge distributions were bell-shaped, with a width of 1.8 charge states at half maximum. The average ionic charges for 3.3-, 6.1-, and 8.7-Mev O ions were 3.5, 4.8, and 5.2, respectively, and for 3.1-, 7.1-, and 10.3-Mev Ne ions 3.3, 4.9, and 6.0, respectively.

INTRODUCTION

THE state of ionization of oxygen and neon ions passing through gases with a few Mev kinetic energy has been measured. The main incentive for this work was to test the feasibility of using gas stripping as a source of highly charged "heavy" ions for injection into the heavy-ion linear accelerators that are being constructed at the University of California Radiation Laboratory and at Yale University. It was hoped that this test program would reveal the ion velocity necessary to produce the desired charge states, the number of atoms/cm^2 of gas in the stripper necessary to reach an equilibrium distribution of charge states, and whether or not some gases produce appreciably higher charges than others.

Considerable information is available on the capture and loss of electrons by protons and helium ions passing through matter.[1] Lassen[2] has measured the average charge of fission fragments passing through solids and gases, and theories for the capture and loss of electrons by fission fragments have been worked out by Bohr,[3] Bell,[4] and Bohr and Lindhard.[5] Measurements of the state of ionization of accelerated nitrogen ions emerging from thin foils have been published during 1954 by Reynolds, Scott, and Zucker,[6] Reynolds and Zucker,[7] and Stephens and Walker.[8] Very little information is available, however, on the stripping in gases of ions in the mass region near oxygen and neon.

EXPERIMENTAL PROCEDURE

The 4-megavolt Van de Graaff, which is normally used to inject protons into the UCRL 40-foot linear accelerator, was used to accelerate oxygen and neon ions for this experiment. The ions were made in the regular proton source by supplying oxygen or neon instead of hydrogen. Figure 1 is a plan view of the accelerators and the auxiliary equipment used. The ions formed in the ion source were accelerated in the Van de Graaff column, coasted through the linear accelerator (with the rf turned off), passed through the gas stripper, were deflected through 12.6° by the analyzing magnet, and finally were detected in a stationary Faraday cup. The stripper, shown in Fig. 2, was similar to one used by Bittner[9] to strip He ions. It consisted of a stainless steel tube $\frac{1}{8}$ inch in inside diameter and 20 inches long. The tube was suspended in a vacuum chamber on Wilson seal rods with offset connections so that it could be aligned with the beam. Gas could be admitted from a flexible tygon hose connected at the center of the tube. A diffusion pump connected to the vacuum jacket maintained a pressure of a few hundredths μ Hg at the ends of the tube. A McLeod gauge was used to measure the pressure at the center of the tube and ion gauges read the pressure in

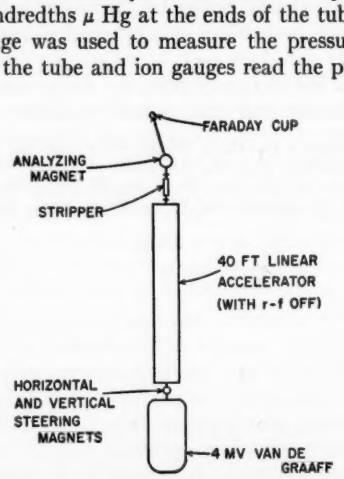

FIG. 1. Layout of accelerators and experimental apparatus.

* This work was done under the auspices of the U. S. Atomic Energy Commission.

[1] S. K. Allison and S. D. Warshaw, Revs. Modern Phys. **25**, 779 (1953).

[2] N. O. Lassen, Kgl. Danske Videnskab. Selskab, Mat.-fys. Medd. **23**, No. 2 (1945); Phys. Rev. **68**, 142 (1945); Kgl. Danske Videnskab. Selskab, Mat.-fys. Medd. **25**, No. 11 (1949); Phys. Rev. **79**, 1016 (1950); Kgl. Danske Videnskab. Selskab, Mat.-fys. Medd. **26**, No. 5 (1951); Kgl. Danske Videnskab. Selskab, Mat.-fys. Medd. **26**, No. 12 (1951).

[3] N. Bohr, Kgl. Danske Videnskab. Selskab, Mat.-fys. Medd. **18**, No. 8 (1948).

[4] G. I. Bell, Phys. Rev. **90**, 548 (1953).

[5] N. Bohr and J. Lindhard, Kgl. Danske Videnskab. Selskab, Mat.-fys. Medd. **28**, No. 7 (1954).

[6] Reynolds, Scott, and Zucker, Phys. Rev. **95**, 671 (1954).

[7] H. L. Reynolds and A. Zucker, Phys. Rev. **95**, 1353 (1954).

[8] K. G. Stephens and D. Walker, Phil. Mag. **45**, 543 (1954).

[9] J. W. Bittner, Rev. Sci. Instr. **25**, 1058 (1954).

the vacuum jacket of the stripper and in the linear accelerator tank.

When oxygen or neon was used in the ion source it was found that not only singly ionized ions came out of the Van de Graaff, but doubly and triply ionized ions as well. Ions that emerged from the accelerating column with a particular charge had a continuum of energies extending down from the energy which an ion of that charge would gain by falling through 4 megavolts. The origin of the energies that are not integral multiples of 4 Mev is thought to be change of charge of the ions due to collisions with gas atoms in the column. The column of this Van de Graaff is pumped from the exit end only and is estimated to contain 70 μ-cm of gas, which is sufficient to produce the distribution of charge states observed. The steering magnets between the Van de Graaff and the linear accelerator can be adjusted so that only ions of a single charge state and a narrow range of energies enter the stripper.

The procedure in making runs was as follows: the leak rate into the center of the tube was set to provide the desired pressure; then the current received by the Faraday cup was plotted as a function of the analyzing-magnet current while the beam energy and current were held constant. The magnet current was swept slowly and continuously by hand, and the output voltage of the electrometer connected to the Faraday cup was plotted *vs* magnet current on a Speedomax *x-y* recorder. Figure 3 gives an example of the spectra due to 6.9-Mev Ne^{+2} ions with various pressures in the stripper. The peaks represent ion currents of about 10^{-11} amp. The charges corresponding to the peaks in a monochromatic spectrum could be identified because the fields were inversely proportional to the charges. After identification of the e/m of a peak, its energy was determined from the magnet current, the magnetization curve of the magnet, and a calibration point obtained by observing the current required to deflect 31.5-Mev protons through the same angle.

In agreement with theory, no significant loss in kinetic energy by the ions due to passing through the gas was observed (i.e., the loss was less than 1 percent).

To obtain the distribution in charge states for a spectrum, the peak amplitude of the current in each charge state was divided by its charge number to obtain the relative number of ions per second, or the "ion current." Each ion current was then divided by the sum of the ion currents to give the fraction of the ions in that charge state.

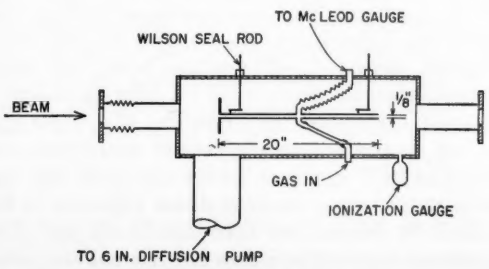

FIG. 2. Cross-sectional view of gas stripper.

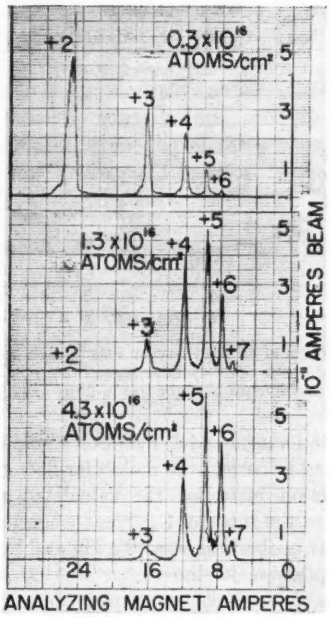

FIG. 3. Samples of spectra for 6.9-Mev Ne^{+2} ions stripped in argon for pressures of 1μ, 13μ, and 47μ at the center of the stripper tube. The numbers of atoms/cm² for these pressures are 0.3×10^{16}, 1.3×10^{16}, and 4.3×10^{16}, respectively.

To correct for fluctuations in the incident-beam current during the plotting of a spectrum, three spectra were taken under each set of conditions, and the fractional ion currents quoted are the averages of the three values. In some cases the ions under investigation could not be separated completely from the other components of the Van de Graaff beam with the steering magnets. In these cases the maximum possible systematic error in subtracting unwanted components from a spectrum has been added to the rms deviations from the average of the three runs to obtain the experimental uncertainties quoted. It was assumed that the relative heights of the peaks were not affected by multiple scattering in the gas. This is in agreement with theory and with the observed line widths, since theory indicates that multiple scattering in the gas is nearly independent of ionic charge and no dependence upon ionic charge was observed.

The readings of the pressure gauges were used to calculate the number of atoms/cm² of gas that the beam passed through before entering the analyzing magnet. For the lower pressures used the flow in the tube was molecular, and the pressure fell linearly from its value at the center to that at the ends of the tube. For higher pressures in the transition region between

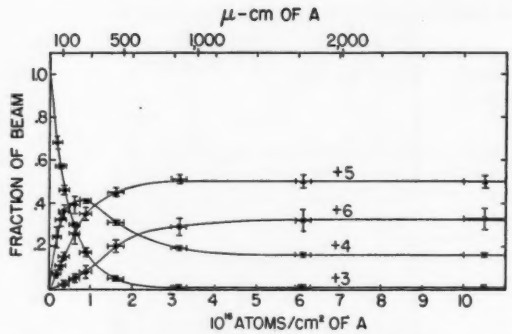

FIG. 4. Fraction of 8.7-Mev oxygen ions in each charge state *vs* the amount of argon gas they have passed through. The scale at the top gives the amount of argon gas in units of (μ Hg)-cm.

molecular and viscous flow, Knudsen's empirical equation was used to correct the molecular-flow calculation. This correction increased the calculated number of atoms/cm² in the tube by 1 percent when the pressure at the center of the tube was 40 μ Hg and by 4 percent when the pressure at the center was 80 μ Hg. The residual gas in the linear accelerator and the mercury vapor in the stripper tube from the untrapped McLeod gauge caused some stripping even when no gas was admitted to the tube. The errors indicated in the number of atoms/cm² include the uncertainty from the mercury vapor pressure and the linear accelerator pressure as well as the uncertainty in the McLeod gauge readings.

RESULTS

Figure 4 shows the distribution in charge states of 8.7-Mev oxygen ions *vs* the number of atoms/cm² of argon gas that the beam has penetrated. These ions entered the gas as O^{+3} ions. As the gas pressure was increased the distribution at first shifted toward higher charges and eventually approached an equilibrium distribution that did not change with further increase in pressure. 40 μ Hg pressure at the center of the 50 cm tube, or about 10^3 μ-cm, or about 3.5×10^{16} atoms/cm², brings each of the charge states to within 1 percent of its final equilibrium current. There is no evidence for charge exchange due to collisions with the metal tube wall, but we cannot rule out the possibility that as many as 10 percent of the original O^{+3} ions were changed to higher states by this process.

The equilibrium distributions in argon were found for oxygen ions of three different energies and for neon ions of three different energies. These data are summarized in Figs. 5 and 6, respectively, where the fraction of ions in each charge state is plotted *vs* the charge. In this energy range smooth curves drawn through the points indicate a roughly symmetrical bell-shaped distribution. Changing the energy shifts the whole curve without appreciably changing its shape or width. The 8.7-Mev oxygen distribution illustrates an exception to this rule. If this distribution were symmetrical there would be about 5 percent O^{+7} ions; actually none were observed. This is not surprising in view of the relatively large binding energies of the *K*-electrons.

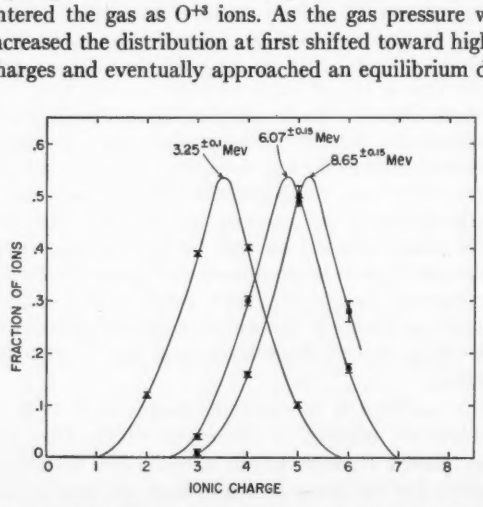

FIG. 5. The ordinate is the fraction of 3.3-, 6.1-, and 8.7-Mev oxygen ions in each charge state after passing through enough argon to produce equilibrium distributions. The abscissa is the charge of the ions in units of the charge of an electron.

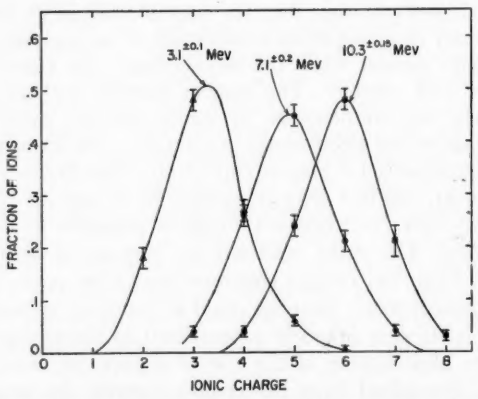

FIG. 6. Fraction of 3.1-, 7.1-, and 10.3-Mev neon ions in each charge state after passing through enough argon to produce equilibrium distributions.

Several different stripping gases were tried to see if some produced higher charges than others. H_2, He, N_2, and A gases were compared, using 7.1-Mev neon ions, and no significant difference was found between the equilibrium distributions. N_2, Kr, and Xe gases were compared, using a 7.2-Mev oxygen beam, and again the equilibrium distributions did not differ significantly. However, the number of atoms/cm² of stripper gas required to produce an equilibrium distribution decreased as its Z increased. Lassen has found that the steady-state average charge of fission fragments in He is about 10 percent less than that in H_2 gas.[2] The experiment reported here does not rule out the possibility of an effect of this magnitude.

Lassen also observes an increase of the average charge with increasing gas pressure, which he attributes to a contribution to electron loss of excited states with lifetimes comparable to the time between excitations. He finds an increase in average charge of about 7 percent per 10 mm increase in gas pressure. In our experiment the highest pressures used were about 0.1 mm, so that this effect was not detectable.

Gluckstern has calculated electron capture and loss cross sections using a modification of Bell's theory.[4] In the following paper[10] he compares his theoretical results with cross sections deduced from Fig. 4 and with the equilibrium distributions in charge states given in Figs. 5 and 6.

We wish to acknowledge valuable contributions to this experiment by many members of the linear accelerator operating crew and of the groups from Yale University and from the Radiation Laboratory that are designing the heavy-ion accelerators.

[10] R. L. Gluckstern, following paper [Phys. Rev. 98, 1817 (1955)].

PHYSICAL REVIEW VOLUME 98, NUMBER 6 JUNE 15, 1955

Electron Capture and Loss by Ions in Gases*

ROBERT L. GLUCKSTERN
Yale University, New Haven, Connecticut
(Received January 10, 1955)

Capture and loss cross sections for ions of intermediate atomic number ($Z_1=8$ to 18) passing through low-pressure gases have been calculated. A modified form of Bell's model was used, leading to lower capture cross sections than the original model. The resulting equilibrium charge distributions obtained compare favorably with the experimental results of Hubbard and Lauer. The individual cross sections were obtained from the observed dependence of the charge distribution on the stripper thickness; these results agree reasonably well with the predictions of the calculations. Capture and loss of two electrons in a single collision may be significant, but the effect on the charge distributions should not be too great.

I. INTRODUCTION

THE heavy-ion linear accelerators at the University of California Radiation Laboratory and at Yale University are being designed to include gas strippers to increase the efficiency of the ion acceleration. Experiments described in the preceding paper have been performed by Hubbard and Lauer[1] to determine the charge distributions for stripping oxygen and neon ions in various gases, using the University of California Radiation Laboratory 4-Mv Van de Graaff injector to the 40-foot proton accelerator. The purpose of this paper is to compare their results with predictions based primarily on the model that Bell[2] used for investigation of the charge distribution of fission fragments in gases.

The most recent theoretical investigations of electron capture and loss have been undertaken by Bohr,[3] Bell,[2] and Bohr and Lindhard.[4] Bohr[3] and Bohr and Lindhard[4] use a simplified Fermi-Thomas model for the electron shielding, and base their estimate of capture and loss cross sections on general features of a classical description of the ion-atom collision. Bell[2] uses a more detailed Fermi-Thomas model for the position, velocity, and "binding force" of the electrons involved in the collision. According to Bohr and Lindhard,[4] the agreement between the predictions of the two methods for fission fragments is good, considering the complicated nature of the actual collision. In this paper a slight modification of Bell's method is used to calculate the loss and capture cross sections and the charge distributions for stripping of oxygen through argon ions in a variety of stripping gases for a velocity range $3v_0$ to $7v_0$ ($v_0=c/137$).

II. CALCULATION OF CROSS SECTIONS AND EQUILIBRIUM CHARGE DISTRIBUTIONS

The stripping pressures used by Hubbard and Lauer[1] are sufficiently small that the time between successive loss or capture collisions is much greater than the average lifetime of excited electron states induced in the ion in these collisions.[5] For this reason the ion can be considered in its ground state before each collision, and Bell's model of a "rarefied" gas stripper applies.

For the capture cross section, Bell's model is applied with the stripper electrons assumed to be located at the "half-charge" radii determined from a Fermi-Thomas model, i.e., the total charge inside the sphere corresponding to the nth electron is $Z_2-n+\frac{1}{2}$. The capture cross section for each stripper electron by a point charge representing the ion is calculated by kinematic considerations regarding the liberation and

* This work was performed at the Radiation Laboratory, University of California, and was supported by the U. S. Atomic Energy Commission Contract AT (30-1) 1691.

[1] E. L. Hubbard and E. J. Lauer, preceding paper [Phys. Rev. 98, 1814 (1955)].

[2] G. I. Bell, Phys. Rev. 90, 548 (1953).

[3] N. Bohr, Kgl. Danske Videnskab. Selskab, Mat.-fys. Medd. 18, No. 8 (1948).

[4] N. Bohr and J. Lindhard, Kgl. Danske Videnskab. Selskab, Mat.-fys. Medd. 28, No. 7 (1954).

[5] As estimated by Bohr and Lindhard [reference 4, Eq. (6.4)].

probability of escape of that particular electron. The total capture cross section is then the sum of the individual capture cross sections for each electron.

For the loss cross section, positive-ion Fermi-Thomas functions are obtained by a perturbation technique from the neutral atom functions.[6] The loss cross section for each ion electron (located at the appropriate "half-charge" radius) is obtained by considering the electron to be scattered by a Coulomb-like stripper core according to the Rutherford cross section. The core charge is determined from a Fermi-Thomas charge distribution

TABLE I. Loss and capture cross sections for oxygen ions in various strippers calculated using Bell's model directly.

$\sigma_{pq}/\pi a_0^2$.

$p\rightarrow q$	v/v_0	$Z_2=1$[a]	$Z_2=7$	$Z_2=18$	$Z_2=80$
2→3	3	0.47	3.6	6.6	12.2
	5	0.20	2.4	4.9	9.7
	7	0.099	1.57	3.5	7.5
3→4	3	0.170	1.80	3.6	6.8
	5	0.089	1.42	3.2	6.8
	7	0.049	0.97	2.4	5.5
4→5	3	0.056	0.77	1.69	3.3
	5	0.042	0.80	1.85	4.2
	7	0.026	0.56	1.59	3.9
5→6	3	0.010	0.24	0.64	1.57
	5	0.016	0.35	0.88	2.2
	7	0.013	0.32	0.92	2.4
3→2	3	0.56	2.0	3.2	7.4
	5	0.063	0.37	0.72	1.66
	7	0.016	0.11	0.22	0.65
4→3	3	1.00	3.4	5.2	11.8
	5	0.111	0.62	1.21	2.7
	7	0.028	0.19	0.40	1.07
5→4	3	1.54	5.0	8.2	16.6
	5	0.173	0.95	1.77	4.0
	7	0.043	0.29	0.61	1.60
6→5	3	2.2	7.0	10.7	22.0
	5	0.25	1.3	2.4	5.4
	7	0.063	0.40	0.84	2.2

[a] See reference 7.

on the basis of a radius determined by classical considerations involving the impact parameter. Only those electrons deflected sufficiently to escape from the ion are considered lost, and the total loss cross section is then taken as the sum of the individual loss cross sections.

The results of calculations of loss and capture of electrons for oxygen ions stripped by hydrogen ($Z_2=1$),[7] nitrogen ($Z_2=7$), argon ($Z_2=18$), and mercury ($Z_2=80$), using Bell's model, are given in Table I, where σ_{pq} is the

[6] E. B. Baker, Phys. Rev. **36**, 630 (1930); P. Gombas, *Die statistische Theory des Atoms und ihre Andwendungern* (Springer-Verlag, Berlin, 1949).

[7] The stripper atom model for $Z_2=1$ was taken as the usual Bohr hydrogen atom rather than the Fermi-Thomas model used for the other strippers.

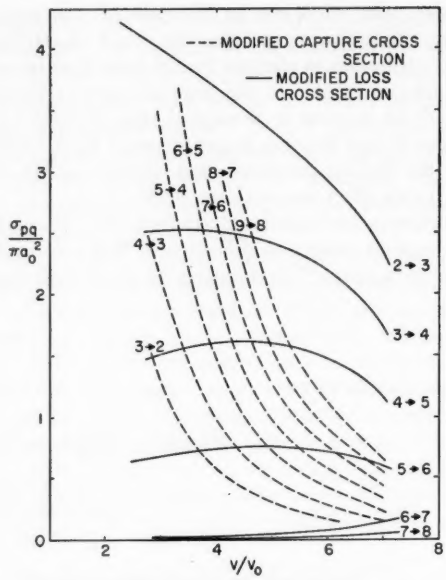

FIG. 1. Modified capture and loss cross sections for oxygen ions in argon.

cross section for going from an ionic charge p to an ionic charge q, $a_0=\hbar^2/me^2$ is the Bohr radius, and $v_0=c/137$.

If the ions pass through a sufficient thickness of gas, an equilibrium distribution of ion charge states is reached long before any significant energy degradation takes place. The fractions of the various ions in this equilibrium distribution are given by

$$N_p/N_q=\sigma_{qp}/\sigma_{pq};\quad \sum N_p=1.$$

The resulting average charge for oxygen ions, using the information in Table I, is given in Table II.

The average charge, as well as the entire charge distribution, seems to increase slightly with increased Z of the stripper, not inconsistent with the experimental determination of no significant variation with Z_2. The average charge measured, however, is about 1 unit greater than that predicted. As this would correspond to a fairly large discrepancy in the pertinent cross sections, Bell's model was re-examined.

In Bell's calculation of capture, the cross section is obtained as a sum of the individual capture cross sections for each stripper electron. The model for capture that Bell uses, however, does not take into account the fact that in collisions with small impact parameters,

TABLE II. Average charge for equilibrium distribution of oxygen ions in various strippers.

v/v_0	$Z_2=1$[a]	$Z_2=7$	$Z_2=18$	$Z_2=80$
4	3.0	3.8	3.8	3.8
5	3.4	4.3	4.5	4.5
6	3.8	4.7	4.9	5.0

[a] See reference 7.

for which the capture cross sections are greatest, one should *not* sum the individual capture cross sections. One should instead consider, at an impact parameter r_0, the probability $P(r_0)$ of capturing *any* electron. The total capture cross section, according to Bell's prescription, would then be

$$\sigma_c = 2\pi \int P(r_0) r_0 dr_0.$$

Application of this modification leads to the conclusion that the results given in Table I for capture are overestimates. A survey of different ions and different strippers indicated that a simple but adequate modification is to take 40 percent of the previously calculated capture cross sections in the range of ion Z_1, stripper Z_2,

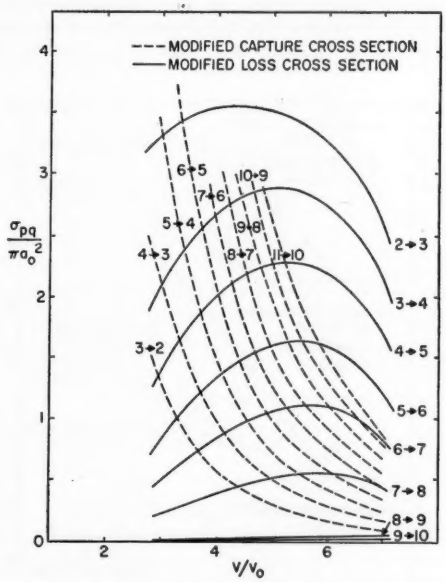

FIG. 2. Modified capture and loss cross sections for neon ions in argon.

and ion velocity of interest. Since this raises the average equilibrium charge, it can be expected to improve the agreement with experiment.

Another difficulty in applying Bell's model to capture and loss of electrons from relatively light ions is that the Fermi-Thomas description of the ion electrons cannot be expected to be accurate for high-charge states. For this reason, and also to simplify the calculation of the loss cross sections for different ions and different strippers, a modification was made in which the ion electrons were located in concentric shells with radii chosen to match the known ionization potentials. Although no account of the readjustment of the orbits is taken as electrons are added, the model should be more realistic for the K electrons and even possibly for the first few L electrons. For ions with many electrons

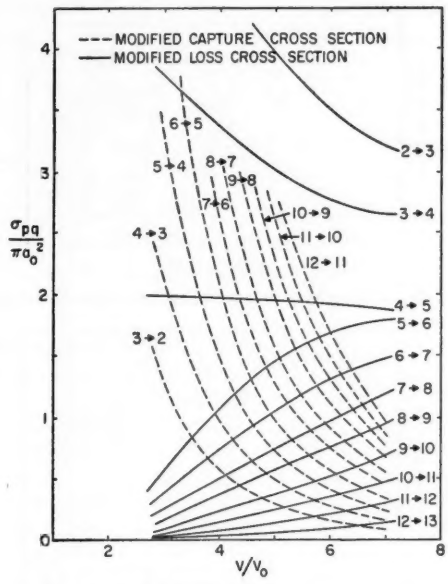

FIG. 3. Modified capture and loss cross sections for phosphorous ions in argon.

one should undoubtedly return to a Fermi-Thomas distribution.

Using the modifications described above (i.e., capture cross sections reduced to 40 percent of the original values and loss cross sections obtained from an ion whose electron orbits are determined directly from the ionization potentials) one obtains the loss and capture cross sections shown in Figs. 1 through 4 for oxygen

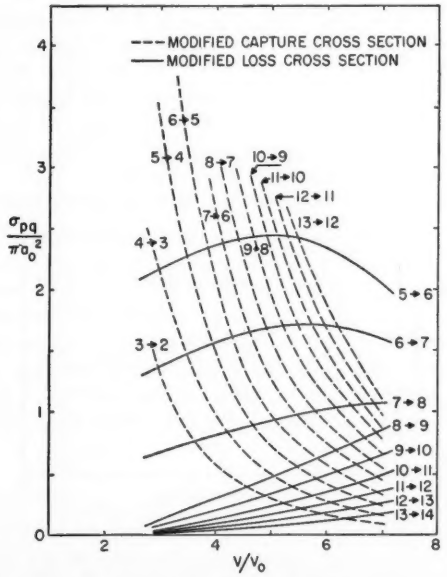

FIG. 4. Modified capture and loss cross sections for argon ions in argon.

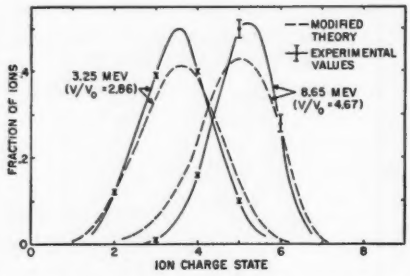

FIG. 5. Charge distribution at equilibrium for oxygen ions in argon.

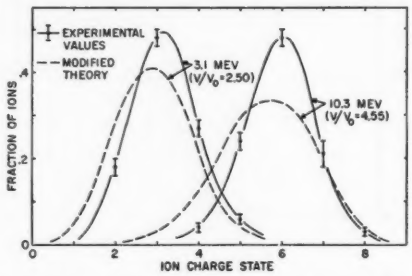

FIG. 6. Charge distribution at equilibrium for neon ions in argon.

($Z_1=8$), neon ($Z_1=10$), phosphorus ($Z_1=15$), and argon ($Z_1=18$) ions being stripped in argon. Figures 5 and 6 contain corresponding charge distributions calculated for subsequent comparison with experiment, and Fig. 7 contains the predictions for argon ions with $v/v_0=4$ and 6.

III. COMPARISON WITH EXPERIMENT

A. Charge Distributions

As can be seen from Figs. 5 and 6, the agreement between the measured and calculated charge distributions is quite good. The peaks coincide fairly well although the measured widths are somewhat smaller than those calculated. The predicted and measured average charges as a function of energy are shown in Fig. 8. Experimental results of Reynolds, Scott, Wyly, and Zucker[8] and Stephens and Walker[9] for nitrogen ions in foils are also included. The agreement with the results of Hubbard and Lauer[1] is good, the largest discrepancy being 0.3 of a charge state. The same is true of the data using foils,[8,9] where the experimental results are 0.2 to 0.4 of a charge state higher than the predicted values. Bohr and Lindhard[4] point out that foils are expected to give higher average charges than gases because the loss cross sections should be greater for ions that do not have sufficient time to return to their ground states after a collision. It would, however, be dangerous to consider this comparison between experiment and theory in Fig. 8(c) as a verification of the "density" effect, because of the crudeness of the basic model and inaccuracies in the experiment.

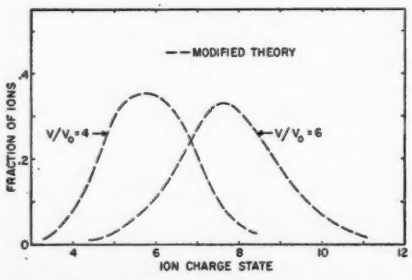

FIG. 7. Charge distribution at equilibrium for argon ions in argon.

[8] Reynolds, Scott, and Zucker, Phys. Rev. **95**, 671 (1954); H. L. Reynolds and A. Zucker, Phys. Rev. **95**, 1353 (1954); Reynolds, Wyly, and Zucker, Phys. Rev. **98**, 1825 (1955).
[9] K. G. Stephens and D. Walker, Phil. Mag. **45**, 543 (1954).

B. Cross Sections

The individual capture and loss cross sections can in principle be obtained from the dependence of the charge distribution on stripper thickness shown in Fig. 4 of

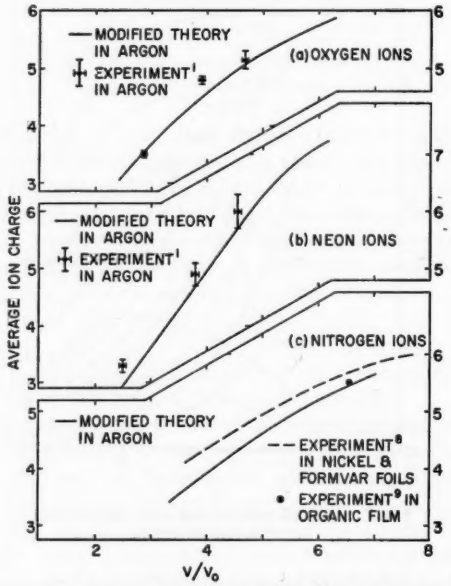

FIG. 8. Average ion charge *vs* ion velocity.

the preceding paper.[1] One has, for example,

$$dN_4/dx=-\sigma_{43}N_4-\sigma_{45}N_4+\sigma_{34}N_3+\sigma_{54}N_5,$$

where x is the stripper thickness measured in atoms/cm^2 and N_p is the fraction of ions with charge p. Knowledge of the x dependence of the N_p and dN_p/dx therefore overdetermine the σ_{pq}. The experimental uncertainties, however, particularly in the dN_p/dx, prevent obtaining a unique set of values for the cross sections. A least-squares fit was obtained leading to the values for 8.7-Mev oxygen ions in argon in Table III. The predicted cross sections, obtained from Fig. 1, are given for comparison.

The cross sections agree remarkably well with those predicted in Fig. 1. The only consistent discrepancy seems to be that the capture cross sections for low-charge states are smaller than expected, causing the experimental equilibrium charge distributions to be slightly narrower than those predicted. The variation of the charge distributions with stripper thickness corresponding to the cross sections in Table III for the least-squares fit are shown in Fig. 9, together with the experimental points. As can be seen, the curves in Fig. 9 fall primarily within the experimental error. Two possible weak points in the comparison, however, are

(1) The peak in the fraction of 4+ ions seems to occur somewhat earlier than indicated by the data;

(2) The fractions of 5+ and 6+ ions rise a little more slowly than indicated by the data.

TABLE III. Comparison of experimental and theoretical cross sections for 8.7-Mev oxygen ions ($v/v_0=4.7$) in argon. The values listed are $\sigma_{pq}/\pi a_0^2$.

$p\rightarrow q$	Experimental[a,b]	Theoretical[c]
3→4	2.27±0.1	2.65
4→5	1.77±0.15	1.75
5→6	0.81±0.2	0.80
4→3	0.14±0.1	0.65
5→4	0.57±0.15	0.95
6→5	1.22±0.2	1.30

[a] Determined from a least-squares fit to the data in Fig. 4 of the preceding paper.
[b] Errors listed are estimated from the uncertainty in the data.
[c] Obtained from Fig. 1.

IV. DISCUSSION OF RESULTS

The following general features of the results appear evident:

(1) The capture cross section is independent of the particular ion, and varies approximately as the square of the ionic charge and inversely as the 3.5 power of the velocity. The numerical values agree quite well with those obtained from Eq. (4.5) of Bohr and Lindhard.[4]

(2) The loss cross sections reach a maximum in the region of interest. The variation of these loss cross sections depends quite sensitively on the model used for the ion electrons. There appears to be some question whether Eq. (4.2) of Bohr and Lindhard is applicable in the region of ion Z_1 of interest here.

(3) The charge distributions do not vary much in width as the ion velocity is changed. The average charge is independent of the stripper material over a wide range of Z_2, and increases with velocity until one starts to ionize the K shell, at which time the average charge increases less rapidly.

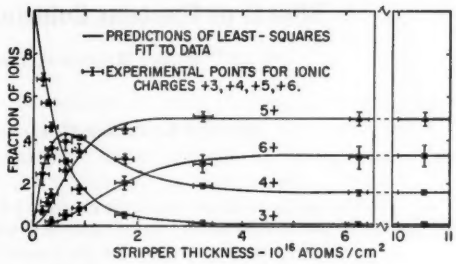

FIG. 9. Charge distribution *vs* stripper thickness for 8.7-Mev oxygen ions.

As can be seen from Fig. 9, the least-squares fit to the data does not go through the experimental points as closely as one might hope. One possible reason is that the assumption of transitions only between adjacent charge states may not be valid. The possible presence of double and triple jumps is suggested by the rapid rise of the 5+ and 6+ ions in Fig. 9. Attempts were made to fit the data using double and triple jumps; although the new parameters lead to a closer fit to the data, the experimental uncertainties do not permit one to show the definite existence of these two- and three-charge state transitions. On the other hand, an attempt was made to use Bell's model to calculate these multiple-jump cross sections. This proved difficult; however, crude estimates lead readily to the conclusion that the cross sections for both loss and capture transitions of two-charge states may be as high as 50 percent of the corresponding single-charge transition cross sections. Under these circumstances the single-jump cross sections in Figs. 1 through 4 would have to be modified. The resolution of the question whether or not multiple-charge transitions are important evidently requires either a more detailed model of the collision, or sufficiently accurate data as a function of stripper thickness, particularly near the zero thickness limit.

ACKNOWLEDGMENTS

The author would like to express his gratitude to the University of California Radiation Laboratory for its hospitality during the course of this work. Thanks are also due to Professor R. Beringer for many fruitful discussions. In addition the author would like to express his appreciation to members of the UCRL computing and differential analyzer staffs, who assisted with much of the computation and cross-section fitting.

Effects of Electron Collisions on the Width of Spectral Lines*

HENRY MARGENAU, *Yale University, New Haven, Connecticut*

AND

BENNETT KIVEL, *Los Alamos Scientific Laboratory, Los Alamos, New Mexico*

(Received March 4, 1955)

The conditions under which the charges of a plasma take on particle characteristics and can be treated by classical mechanics are stated in terms of the half-width of the thermodynamic wave packet.

A simple derivation is given for the quantity γ_U defined in a previous paper (the line width resulting in the absence of degeneracy), which shows the formula there developed to be correct for large γ_U; this removes the earlier restrictions.

IN a recent paper[1] the quantum theory of line-broadening by electrons was developed and applied to the Lyman alpha line of hydrogen. Two questions were left open in that investigation; the present note is put forth to answer them.

The first has to do with a fundamental aspect of the action by the charged constituents of a plasma upon atoms. There are theories in which the charges are regarded as classical particles; in our publication the electrons were treated as waves. The results can be vastly different, especially when the atomic line is susceptible of a linear Stark effect. It is well known, for example, that the Holtsmark theory[2] of broadening by positive ions (a classical approach based on the particle concept) is successful in explaining the widths of the Balmer lines from the sun and from electrical discharges of moderate excitation. If the electrons, which are equally numerous in both instances, were treated in similar fashion the result would be at odds with the data. This problem has been considered by Spitzer[3] and by Inglis and Teller.[4] Their answers leave room, however, for a simple and basic approach which will be given in part I.

In the application made in K.B.M., it was found that the "universal effect" was small when compared with the widths resulting from polarization. The universal effect was therefore left in a state of approximation that is invalid when $\gamma_U/\gamma > 1$; (γ_U = width caused by electron impacts, γ = natural line width). In many interesting instances this ratio is large. In part II, we offer a simple argument which tends to show that the result previously obtained is correct for large values of γ_U/γ also, subject of course to the restrictions of the Born approximation which is used in both cases.

I.

When do the charged constituents of a plasma take on particle characteristics? If all ions were known to have a single, sharp energy then clearly their correct representation is in terms of infinite waves, regardless of masses or velocities. In that case, many problems have classical answers provided the wave number k is large; scattering, for example, leads to classical results if the De Broglie wavelength:

$$\lambda \ll a, \tag{1}$$

a being the dimension of the obstacle.

In a plasma, however, each particle suffers energy changes as a result of collisions. The energy fluctuations can be described in two ways: (1) by forming wave packets which move in time and (2) by employing an ensemble with a constant statistical matrix, ρ. The coefficients of the wave packet and ρ are related, as we shall see.

The *finite size* of the wave packet may also occasion the validity of classical mechanics. Although the physical reason for this reduction is quite different from that involved in criterion (1), the correctness of the classical approximation is nonetheless expressible by the same inequality, somewhat modified in its meaning, for a *thermal ensemble*. This, as will be shown, is because in a thermal ensemble the variance of speeds equals the mean speed.

In a strict mathematical sense the wave packet and the ensemble pictures are not compatible, the former representing a nonstationary pure case and the latter a stationary mixture. Still there is a fairly obvious connection between them; it arises from the fact that observables must have the same values for both.

If an atom is placed amid the moving constituents of the plasma, its experiences are not well represented by reference to ensemble properties; rather, it sees the detailed turmoil of interacting wave packets. When an ion collides with the atom, the latter in a sense "measures" its position and the ion becomes a locally concentrated probability. At this instant, the ion's energy is least accurately defined because of its interaction with the atom. Then follows a process of diffusion in which, classically speaking, the ion recoils from the atom until, in the next collision, another particle effects again a concentration of probability. The speed of diffusion happens to be the "root mean square" thermal speed.

* Work supported by the Office of Naval Research and the U. S. Atomic Energy Commission.

[1] Kivel, Bloom, and Margenau, Phys. Rev. **98**, 495 (1955), here abbreviated K.B.M.

[2] J. Holtsmark, Physik. Z. **25**, 73 (1924); H. Margenau and R. Meyerott, Astrophys. J. **121**, 194 (1955).

[3] L. Spitzer, Phys. Rev. **55**, 699 (1939).

[4] D. R. Inglis and E. Teller, Astrophys. J. **90**, 439 (1939).

No interesting features will be lost if the simple algebra of our problem is written for particles moving in one dimension. Choosing a representation in which the wave number k is diagonal, we find that the statistical matrix is likewise diagonal and its elements have the form

$$\rho_{k'k''}=p_{k'}\delta_{k'k''}, \tag{2}$$

wherein $p_{k'}$ is the ordinary gas-kinetic probability distribution, e.g.,

$$p_{k'}=l^{-1}(2\pi m\kappa T)^{-\frac{1}{2}}\exp\left\{-\frac{\hbar^2k'^2}{2m\kappa T}\right\} \tag{3}$$

for a canonical ensemble. Among the symbols, κ is Boltzmann's constant and l the length confining the particles. We note that (2) is constant in time but not elementary ($\rho^2\neq\rho$). The probability that a particle shall have a wave number k is

$$\mathrm{Tr}(\rho\rho^k)=p_k, \tag{4}$$

and its mean energy is

$$\mathrm{Tr}(\rho H)=\textstyle\sum_k p_kE_k. \tag{5}$$

Here ρ^k is the matrix corresponding to the pure case k, $\rho_{k'k''}{}^k=\delta_{k'k}\delta_{k''k}$ and $E_k=\hbar^2k^2/2m$.

A wave packet, on the other hand, is represented by the wave function

$$\psi(x,t)=\textstyle\sum_k c(k,t)e^{ikx}. \tag{6}$$

It corresponds to the statistical matrix

$$r_{k'k''}=c(k',t)c(k''t)^*,$$

which is not diagonal but indempotent ($r^2=r$) and therefore representative of a pure case. Furthermore, it is a function of the time because the c's have to satisfy Schrödinger's time equation. We now correlate the two descriptions by requiring that r shall satisfy Eqs. (4) and (5), as does ρ. This means

$$p_k=|\,c(k,t)\,|^2.$$

The time-dependent phase factors of the coefficients c are not determined by this relation. If we take, quite arbitrarily, $c(k)=p_k{}^{\frac{1}{2}}$ at the time $t=0$, this will produce via (6) a wave packet of minimum size, and according to the preceding physical considerations, that instant corresponds to a collision. Subsequently the Schrödinger equation takes over, modifies the phases and spreads the packet.

At the time of a collision, then, we may write (6) in the form

$$\psi(x)=\int p_k{}^{\frac{1}{2}}e^{ikx}dk.$$

For a canonical distribution, Eq. (3), we thus obtain a Gaussian wave packet,

$$\psi(x)\propto\exp[-(m\kappa T/\hbar^2)x^2],$$

and the probability ψ^2 has a "width" equal to

$$s=\hbar/(2m\kappa T)^{\frac{1}{2}}. \tag{7}$$

It is the same as the *mean* De Broglie wavelength, $s=\bar{\lambda}$. Let it be noted, however, that the width arises from the existence of an *ensemble* of velocities and has in principle nothing to do with the mean velocity.

To demonstrate this point we might take for p_k a uniform distribution about the mean value k_0 and of width $2\Delta k$:

$$p_k=1/2\Delta p, \quad \text{if} \quad k_0-\Delta k\leqslant k\leqslant k_0+\Delta k;$$

otherwise it is zero. We then obtain

$$|\psi(x)|^2\propto[\sin(\Delta k\cdot x)/x]^2,$$

a probability packet which has a half-width $x_{\frac{1}{2}}\cong 1/\Delta k$, quite independent of k_0. The identity of s and $\bar{\lambda}$ is an accident occurring for a thermal distribution of velocities (and for all distributions in which $\bar{k}=0$). In general, the speed of diffusion of a Gaussian wave packet of half-width s is $\hbar/ms$, and in view of (7) this turns out to be the root-mean-square speed of the particles.

The use we wish to make of these considerations is fairly plain. If the radiating atom is to mistake the ion (or electron) with which it collides for a particle, the size of the wave packet at the moment of impact must be no greater than the atom itself. In that case, as the ion moves away, its packet will spread until its size is of the order of a mean free path when the ion makes its next collision with another atom. Hence the criterion for particle behavior:

$$s=\bar{\lambda}\leqslant a, \tag{8}$$

and we shall for present purposes take a to be the first Bohr radius (Lyman α line). The similarity of (8) and (1) has been explained.

With respect to the mass of the ions, relation (8) says

$$m\geqslant\hbar^2/2a^2\kappa T. \tag{9}$$

For $\kappa T=\frac{1}{2}$ ev (approximately the temperature of the sun's surface) this reads

$$m\geqslant 10^{-26}\text{ g},$$

and shows that the classical particle representation is valid for hydrogen ions, but not for electrons, as is known to be the case empirically. Perhaps it is interesting to add that Eq. (9) justifies in a measure the particle approximation for electron broadening of the Balmer lines, because of the larger a-values involved. Legitimacy of the particle approximation, expressed by (9), is not synonymous, however, with validity of the statistical theory of Holtsmark, which contains further approximations.

The present discussion also clarifies another point. A wave mechanical treatment like that of K.B.M., even if it operates with a matrix ρ corresponding to a thermal ensemble, will not automatically reduce to the classical

theories (impact or statistical); for in order to feature the granularity of the electron waves a transition from the constant mixture (2) to the nonstationary pure case (6) is required.

II.

We shall derive a formula for the half-width γ_U arising from the universal effect defined and treated previously in K.B.M., by considering *only* the states of a perturbing electron which moves in the field of an atom. This field changes in time because the atom is suddenly excited by a light wave, or, in the case of emission, it makes a downward transition. The result for these two cases is the same.

Let the electron's energy in the initial state be $\epsilon_i=(\hbar^2/2m)k_i^2$, its final energy being ϵ_f. The corresponding amplitudes are d_i and d_f; $d_i=1$ at time $t=0$. If, after a long time, the state of the electron is represented by d_f, it has lost energy $\epsilon_i-\epsilon_f$; the atom-radiation field has gained this amount and the frequency of the atomic line is shifted to the blue by $\Omega_{if}=\hbar^{-1}(\epsilon_i-\epsilon_f)$. Hence

$$\lim_{t\to\infty}|d_f(\Omega_{if})|^2\propto I(\Omega_{if}) \tag{10}$$

$I(\Omega_{if})$ being the intensity of the line at a frequency Ω_{if} beyond its normal frequency.

We treat the perturbation, P, as a change in the Hamiltonian of the free electron. In the excited state, $H=H_e+C_{22}$; before excitation it is H_e+C_{11}. Hence $P=C_{22}-C_{11}$ in the notation of K.B.M. Our interest is in large electron broadening, i.e., in a situation where the natural life time of the excited state is much greater than the time during which the perturbation causes the electron to pass from its initial to some final state. The natural life time therefore sets no effective limit in the following considerations, and the limit for t in Eq. (10) is proper.

The equations for the amplitudes are

$$i\hbar\dot{d}_i=\textstyle\sum_f d_fP_{fi}e^{-i\Omega_{fi}t}, \tag{11}$$

$$i\hbar\dot{d}_f=d_iP_{if}e^{-i\Omega_{if}t}. \tag{12}$$

If we put $d_i=e^{-\gamma t}$, integrate (12) and substitute in (11) we find

$$\gamma=\sum_f\left|\frac{P_{if}}{\hbar}\right|^2\frac{e^{i\Omega_{if}t+\gamma t}-1}{i\Omega_{if}+\gamma}. \tag{13}$$

As is usual, the sum over final states is now converted to an integral:

$$\sum_f\rightarrow\int\frac{V}{(2\pi)^3}2\pi k_f^2dk_f\sin\theta d\theta,$$

where θ is the angle between $\mathbf{k}_i$ and $\mathbf{k}_f$, the wave number vectors of the electron, and V is the volume per electron. If ω is written for $\hbar k_i^2/2m$, the integration over k_f in (8) can be carried out according to the formula

$$\int f(\omega_f)\frac{e^{i(\omega_i-\omega_f)t+\gamma t}-1}{i(\omega_i-\omega_f)+\gamma}d\omega_f\doteq\pi f(\omega_i),$$

and we are left with

$$\gamma=\frac{V}{(2\pi)^2}\frac{k_im\pi}{\hbar^2}\int|P_{if}|^2\sin\theta d\theta, \tag{14}$$

the understanding being that the integrand is to be taken at $k_f=k_i$ (our previous resonance approximation). But P_{if}, which is $C_{11}-C_{22}$, was evaluated in K.B.M. and shown to be $(4\pi e^2/VK^2)(F_{11}-F_{22})$, the F's being form factors and

$$K^2=k_i^2+k_f^2-2k_ik_f\cos\theta\equiv x/a^2.$$

From this last relation $\sin\theta d\theta$ is computed, and Eq. (14) gives

$$\gamma=\frac{2\pi e^4}{V}\frac{a^2m}{\hbar^3k_i}\int_0^{x_+}\left(\frac{F_{11}-F_{22}}{x}\right)^2dx \tag{15}$$

with $x_+=4k_i^2/a^2$. In K.B.M., the remaining integral was called S_U; it was calculated and plotted as a function of initial electron speeds. If, furthermore, we take a to be the first Bohr radius (Lyman alpha line), replace V by $1/n$ and $\hbar k_i$ by mv_i, Eq. (15) reduces to the previous expression for the line width resulting from the universal effect:

$$\gamma_U=2nv_i\pi(\hbar/mv_i)^2S_U.$$

This simple derivation might not be altogether convincing in the absence of our earlier more ponderous considerations. It does show, however, that the restriction to small γ_U is unnecessary, and it adds to the physical meaning of the effect in question.

That the line has the characteristic dispersion shape follows from Eq. (10) in conjunction with the integrated Eq. (12):

$$I(\Omega)\propto(\Omega^2+\gamma^2)^{-1}.$$

Cross Section for Electron Capture and Loss by 26-Mev Nitrogen Ions

H. L. REYNOLDS, L. D. WYLY,* AND A. ZUCKER
Oak Ridge National Laboratory, Oak Ridge, Tennessee
(Received February 17, 1955)

Electron capture and loss cross sections were measured for 26-Mev nitrogen ions in Zapon. Charge groups, separated by the fringing magnetic field of the cyclotron, were passed through Zapon foils sufficiently thin so that charge equilibrium was not achieved. The relative intensities of the nonequilibrium charge distributions were analyzed to determine the ratios of the cross sections. It was found that $\sigma_{56}/\sigma_{67}=2.6$, $\sigma_{56}/\sigma_{65}=3.8$, and $\sigma_{67}/\sigma_{76}=0.78$. If it is assumed that the average atom in Zapon has a mass of 14, the cross sections for electron capture and loss for 26-Mev nitrogen ions are, in cm²/atom: $\sigma_{56}=7.6\times10^{-18}$, $\sigma_{65}=2.0\times10^{-18}$, $\sigma_{67}=2.9\times10^{-18}$, $\sigma_{76}=3.8\times10^{-18}$. Nonequilibrium charge distributions as a function of foil thickness are given for initial beams consisting entirely of any one of the ion groups N^{7+}, N^{6+}, or N^{5+}.

INTRODUCTION

THE study of the capture and loss of electrons by moving ions has been in progress since this process was first observed for alpha particles by Henderson[1] in 1922. A survey of the work done in this field has been made by Allison and Warshaw.[2] Until recently the investigations have been limited to protons, alpha particles, and fission fragments, but the advent of heavy-ion accelerators has allowed the study to be extended to ions of intermediate mass. The range of nitrogen ions in nickel and emulsion together with the average charge as a function of velocity has been measured by Reynolds *et al.*[3] Stephens and Walker[4] have measured the equilibrium charge distributions for nitrogen ions at 15 Mev while Reynolds *et al.*[5] have measured the equilibrium charge distribution for nitrogen ions from 6 to 26 Mev.

The cross sections for capture and loss of electrons cannot be obtained from equilibrium charge distributions without complementary nonequilibrium measurements. In this paper, nonequilibrium measurements are described which allow a determination of the cross section for electron capture and loss by 26-Mev nitrogen ions in Zapon. The charge distributions as a function of Zapon surface density are also presented for incident beams of pure N^{5+}, N^{6+}, or N^{7+}.

EXPERIMENTAL METHOD

The experimental arrangement is similar to that described previously.[5] Triply charged 26-Mev nitrogen ions were allowed to pass through a slit 0.001 in. wide on which was placed a Zapon foil approximately 25 μg/cm² thick, see Fig. 1. In passing through the foil the nitrogen ions were stripped to their equilibrium charges of five, six, and seven electronic charges. While passing to the second slit, approximately 4 inches from the first slit, these three charge groups were separated spatially by the fringing magnetic field of the cyclotron, so that by moving the second slit to the appropriate positions any one of these individual charge groups could be selected to pass through the second slit. A very thin Zapon foil, 6 μg/cm² or less, was placed on the second slit. (Zapon foils could be made thinner than foils of any other material available.) If this second foil was thin enough, the distribution obtained was not an equilibrium distribution and the relative line intensities could be used to determine the electron capture and loss cross sections, as described later. After leaving the second foil the charge groups were separated by the fringing magnetic field over a path length of about 8 inches, and detected by Ilford C-2 emulsions. The relative line intensities in the emulsion were measured with a Leeds and Northrup photodensitometer which was calibrated by methods described previously.[5] In order to reduce the number of exposures required it was possible to pass two primary charge groups at one time through the second foil. This was accomplished by making the first foil thick enough (about 25 μg/cm²) to cause an appreciable amount of multiple scattering, so that upon reaching the second slit two of the charge groups overlapped. However, the direction of travel of each group was different when passing through the second slit which would have caused a separation in the groups by the time they reached the emulsion even if there were no magnetic field between the second slit and the emulsion. With the proper field between the second slit and the detector six charge lines due to the two initial charge groups were observed. If, for example, the six- and seven-charge groups were selected by the second slit, six lines appeared at the detector arranged in the order l_{77}, l_{67}, l_{76}, l_{66}, l_{75}, l_{65}, where the first subscript indicates the charge of the ions after passing through the first foil and the second subscript, the charge of the ions after passing through the second foil. The line l_{67}, for example, is produced by N^{7+} ions which were obtained from the N^{6+} ions incident on the second foil.

The second slit was movable from outside the vacuum,

* Permanent address: School of Physics, Georgia Institute of Technology, Atlanta, Georgia.

[1] B. H. Henderson, Proc. Roy. Soc. (London) **A102**, 496 (1922).
[2] S. K. Allison and S. D. Warshaw, Revs. Modern Phys. **25**, 779 (1953).
[3] Reynolds, Scott, and Zucker, Phys. Rev. **95**, 671 (1954); H. L. Reynolds and A. Zucker, Phys. Rev. **96**, 393 (1954).
[4] K. G. Stephens and D. Walker, Phil. Mag. **45**, 543 (1954).
[5] Reynolds, Wyly, and Zucker, Phys. Rev. **98**, 474 (1955).

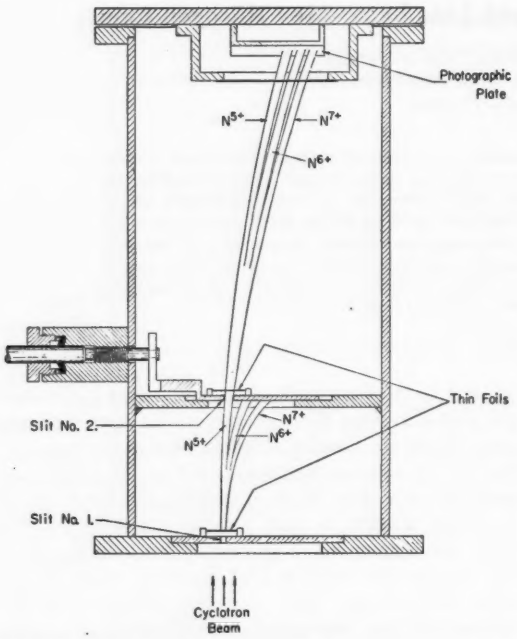

FIG. 1. Chamber used for nonequilibrium measurements. The cyclotron fringing field is perpendicular to the paper. A particular charge group can be selected by adjusting slit two. The nonequilibrium distribution is obtained in foil two and detected with the photographic plate.

and adjusted for each run to accept the proper lines by visual observation of a phosphor placed at the top of the chamber in the position normally occupied by the emulsion. Emulsion exposures were usually less than one second in duration.

The thin Zapon foils were made by spreading diluted Zapon on distilled water and picking up the thin films on $\frac{3}{4}$-in. diameter copper rings. The thinnest foils obtainable in this manner were about 2.5 $\mu g/cm^2$. After being used the foils were cut away from their holders and weighed on a precision torque balance. Although the balance used had a sensitivity of only ten micrograms per division, it was found that, with a system of telescopes and sufficient care, weighings could be repeated to within 2 μg. The balance was calibrated by dividing a one square centimeter piece of aluminum foil weighing 0.190 mg into eight pieces and weighing each piece individually. The total weight obtained by adding the individual weights agreed with the previously measured 0.190 mg within 10 μg, indicating that the balance was linear down to the lowest weight measured.

RESULTS

Nonequilibrium charge distributions were obtained for each of the three initial charge groups, N^{5+}, N^{6+}, and N^{7+}, with five different foils. Four of the five foils were successfully weighed. The results are shown in Table I. The first column gives the foil number while the second column gives the surface density of the foils in micrograms per square centimeter. N_{ij} is the fraction of the ion beam leaving the foil with charge j, resulting from the ion beam of charge i incident on the foil. It is estimated the probable error in N_{ij} is 0.02. The foil surface densities have a probable error of 15 percent due to the inaccuracies of the weighing.

The foils were of uniform surface density over their useful area. The slit length was approximately $\frac{1}{2}$ inch so that a large part of a foil was sampled with one exposure. The position of a foil was changed relative to the slit for repeated exposures. The relative intensities of the lines were found to be independent of the position along the slit or of the position of the foil, within the expected errors, except for one foil which was discarded.

The initial energy of the nitrogen beam was determined by observing the energy of recoil protons, as described previously.[5] The estimated width of the energy distribution at half maximum is about 600 kev.

DISCUSSION

If the possibility of transferring two electrons in a single encounter is neglected and the contribution due to ions of charge lower than five, which constitute less than 1 percent of the beam at 26 Mev, are ignored the equations describing the nonequilibrium state may be written as follows:

$$d\alpha/d\tau=\beta\sigma_{65}-\alpha\sigma_{56},$$
$$d\beta/d\tau=\gamma\sigma_{76}+\alpha\sigma_{56}-\beta(\sigma_{67}+\sigma_{65}),$$
$$\alpha+\beta+\gamma=1,$$

where α, β, and γ are the fraction of the ions in the five-, six-, and seven-charge states respectively, σ_{ij} is the cross section for change of charge from i to j, and τ is the foil thickness. These equations can be solved in the usual manner, giving the following results:

$$\alpha=ae^{z\tau}+be^{y\tau}+C/B, \quad \beta=\frac{d\alpha/d\tau+\alpha\sigma_{56}}{\sigma_{65}},$$

where $z=\frac{1}{2}[-A+(A^2-4B)^{\frac{1}{2}}]$, $y=\frac{1}{2}[-A-(A^2-4B)^{\frac{1}{2}}]$, $A=\sigma_{56}+\sigma_{65}+\sigma_{67}+\sigma_{76}$, $B=\sigma_{56}(\sigma_{67}+\sigma_{76})+\sigma_{65}\sigma_{76}$, and $C=\sigma_{65}\sigma_{76}$. The constants a and b are determined by the boundary conditions which, for the three initial lines

TABLE I. Data obtained for the five foils used in the experiment. N_{ij} indicates the fraction of particles with charge j resulting from particles of initial charge i.

Foil No.	Surface density $\mu g/cm^2$	N_{55}	N_{56}	N_{57}	N_{65}	N_{66}	N_{67}	N_{75}	N_{76}	N_{77}
1	5.4	0.273	0.512	0.215	0.139	0.567	0.294	0.086	0.392	0.522
2	3.2	0.392	0.492	0.116	0.133	0.664	0.203	0.064	0.325	0.611
3	3.8	0.370	0.485	0.145	0.126	0.639	0.235	0.072	0.333	0.595
4	...	0.511	0.409	0.080	0.132	0.712	0.156	0.056	0.294	0.650
5	5.9	0.231	0.521	0.248	0.146	0.558	0.296	0.129	0.388	0.483

at $\tau=0$, are

$$\alpha=1, \quad \gamma=\beta=0;$$
$$\beta=1, \quad \alpha=\gamma=0;$$
$$\gamma=1, \quad \alpha=\beta=0.$$

Thus, three sets of solutions for the data are obtained. The constants a and b are pure numbers and they contain only the ratios of the cross sections. Therefore, the product $\sigma_{ij}\tau$ can be computed without a knowledge of τ and the relative values of all four cross sections σ_{56}, σ_{65}, σ_{67}, and σ_{76}, can be obtained without knowing the thickness of the foil. Two of the three sets of equations are, of course, redundant. A graphical trial and error method was used to obtain a best fit for all of the data to the three sets of equations. In Fig. 2, the fraction of the beam in each charge state is plotted as a function of $\sigma_{56}\tau$ for initial conditions of $\alpha=1$, $\beta=1$, and $\gamma=1$, respectively. The ratio of $\sigma_{56}/\sigma_{67}=2.6$ was found to give the best fit to the data. The ratios σ_{56}/σ_{65} and σ_{67}/σ_{76} are determined by the equilibrium conditions. The values of these ratios used in Fig. 2 are 3.8 and 0.78 which differ slightly from previously published ratios[5] although they are within the quoted errors. It is estimated that these ratios have a probable error of approximately 15 percent.

Since the value of τ is known, the figures also have the abscissa labeled with τ, the surface density of the Zapon foils in $\mu g/cm^2$; the charge distribution is thus shown as a function of foil thickness from zero to near equilibrium thickness for initial charges of N^{5+}, N^{6+}, or N^{7+}. The best relation between $\sigma_{56}\tau$ and τ was determined by a least-squares method. The part of the figure for initial charge of five may be applied to any initial charge smaller than five since the stripping cross section for lower charged ions will be so large that the incident beam will have a charge of five when a thickness of foil much less than that considered here has been penetrated.

In the determination of the actual cross sections the inaccuracy of the weighings enters. The cross sections in units of $cm^2/\mu g$ of Zapon are as follows:

$$\sigma_{56}=0.34, \quad \sigma_{65}=0.090, \quad \sigma_{67}=0.13, \quad \sigma_{76}=0.17.$$

To obtain the values in the customary units of cm^2 per atom, assumptions must be made as to the contributions that the various atoms in zapon make to the cross section. Zapon is said by the manufacturer[6] to be a solution of nitrocellulose in various solvents. It probably has the same stoichiometric formula as nitrocellulose

[6] Atlas Powder Company, Stamford, Connecticut.

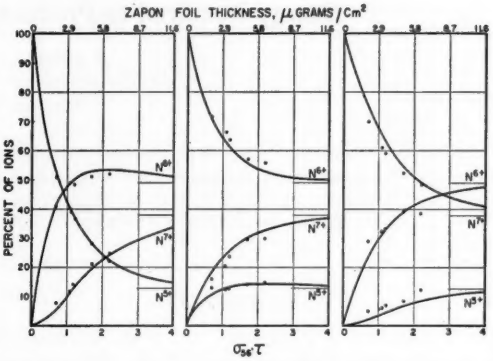

FIG. 2. The percentage of ions in a given charge state after passing through zapon foils of various thicknesses is plotted as a function of $\sigma_{56}\tau$ and the zapon thickness. The plots from left to right represent charge distributions for initial beams of N^{5+}, N^{6+}, and N^{7+} respectively. Experimental points are shown as dots. The calculated "best fits" are shown as solid lines.

made as nitrated cotton, which is $C_6H_8O_9N_2$. With the assumption that the cross section per electron is not appreciably greater for hydrogen than for carbon, nitrogen, or oxygen, zapon may be considered to consist of atoms having an average mass near that of nitrogen and, therefore, to contain about 4.5×10^{16} atoms/μg. With these assumptions, the cross sections for electron capture and loss in cm^2 per atom by 26-Mev nitrogen in a solid material with Z near 7 are

$$\sigma_{56}=7.6\times10^{-18}, \quad \sigma_{67}=2.9\times10^{-18},$$
$$\sigma_{65}=2.0\times10^{-18}, \quad \sigma_{76}=3.8\times10^{-18}.$$

It should be emphasized that the inaccuracies in these numbers are large, perhaps of the order of 20 percent.

These values can be compared with measurements made of the capture and loss cross sections for alpha particles. For example, the value of σ_{12} for helium ions in air[2] at 650 kev is 6.2×10^{-17} cm^2/atom. This energy corresponds to 28-Mev nitrogen ions if the ion velocities are taken in the same ratio as their bound electron velocities. The larger cross section for He^+ is at least partially due to the fact that the Bohr geometrical cross section is twelve times larger for He^+ than for N^{6+}. Of course, the influence of the medium traversed and the mechanism of the capture and loss process have to be considered in any detailed comparison of the cross sections.

The thin zapon foils were prepared by Mary Gilliam, and much of the experimental apparatus was constructed by J. G. Harris.

Energy Required to Produce One Ion Pair for Several Gases*

J. WEISS AND W. BERNSTEIN
Brookhaven National Laboratory, Upton, New York
(Received February 25, 1955)

The absolute values of W, the energy required to produce one ion pair, for electrons have been determined for several gases. A parallel plate extrapolation ionization chamber in conjunction with a ferrous sulfate dosimeter was used. The gases investigated were air, nitrogen, oxygen, carbon dioxide, argon, methane, and ethylene; and the absolute values of W were 33.9, 34.8, 30.9, 32.6, 25.5, 26.8, and 26.3 ev, respectively.

INTRODUCTION

IN a previous publication,[1] we have described an experimental determination of G, the oxidation yield of the ferrous sulfate reaction, in which the energy absorbed by the solution was measurd with an extrapolation ionization chamber for which the Bragg-Gray principle was valid. It was apparent, in the case of electrons, that discrepancies in the published values of W, the energy required to produce one ion pair, for various gases, introduced an uncertainty into all energy measurements performed with ionization chambers. It was also apparent that this technique could be used for accurate determinations of W for any gas, provided an accurate G value could be obtained by an independent measurement. Two such measurements are available at the present time: 15.45 ions/100 ev by cathode-ray bombardment techniques[2] and 15.8 ions/100 ev by calorimetry.[3] Perhaps the most significant advantage of this technique is that one may obtain W values using fast electrons without the use of an extremely large chamber, and neither a knowledge of the electron energy spectrum nor the absolute electron disintegration rate is required.

EXPERIMENTAL EQUIPMENT

Measurements were made with x-rays from a $\frac{1}{4}$-in. thick gold target in the Brookhaven Chemistry Department electron Van de Graaff generator operated at 2 Mv. It was assumed that the average x-ray energy was of the order of 1 Mev.[4] A copper absorption curve showed no detectable low-energy components (<100 kev), and therefore photoelectric processes could be ignored.

The parallel plate ionization chamber, based upon a design of G. Failla, is shown in Fig. 1. The plates were made of 1-cm thick polystyrene; their interior surfaces were coated with a thin layer of aquadag. A groove, approximately 0.004 cm wide, 0.005 cm deep, and 2.54 cm in diameter, was scribed on the rear plate to provide the collecting electrode and guard ring. The cable connectors were type BNC Teflon insulated, and were mounted so that all air spaces, seen by the collecting electrode, were eliminated. Since the observed ionization current/unit volume in a parallel plate chamber must be extrapolated to zero volume, the chamber spacing could be changed by rotating the rear plate. The ionization currents were measured across a $1.022\times10^{7}\pm0.5$ percent ohm calibrated resistor[5] with a calibrated vibrating reed electrometer.[6] At all spacings the chamber was operated with a fixed potential gradient which was sufficient to insure saturation.

The chamber spacings at which measurements were taken were determined by a measurement of the chamber capacitance. It was not possible to use an ac bridge capacitance measurement method because of the losses in the aquadag surfaces, and therefore a dc method employing a vibrating reed electrometer as a null detector was used. The vibrating reed air coupling capacitor was calibrated against a guard-ringed capacitor which had been calibrated against a standard air capacitor.[7] The ionization chamber capacity was then obtained in terms of the air coupling capacitor. The resistance between the guard ring and collector was sufficiently high so that drift was negligible. Figure 2 is a plot of $1/C$ as a function of the number of turns of the rear plate from an arbitrary starting point.

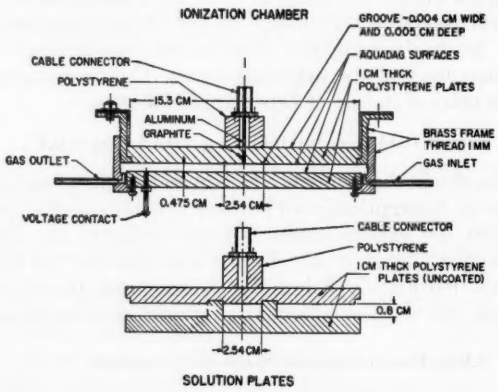

FIG. 1. Drawing of the ionization chamber and the solution plates.

* This work was performed under the auspices of the U. S. Atomic Energy Commission.

[1] Weiss, Bernstein, and Kuper, J. Chem. Phys. **22**, 1593 (1954).
[2] R. H. Schuler and A. O. Allen (to be published).
[3] Lazo, Dewhurst, and Burton, J. Chem. Phys. **22**, 1370 (1954).
[4] Miller, Motz, and Cialella, Phys. Rev. **96**, 1344 (1954).
[5] F. M. Glass and R. K. Abele, Rev. Sci. Instr. **21**, 493 (1950). The bridge was calibrated against a standard 10^{7} ohm resistor calibrated at the National Bureau of Standards.
[6] Vibrating Reed Electrometer, Model 30, Applied Physics Corporation, Pasadena, California.
[7] Precision Condenser, 722D, General Radio Company, Cambridge, Massachusetts.

For the solution measurements, the chamber plates were replaced with another set of plates (Fig. 1) arranged to provide a cell 2.54 cm in diameter and 0.8 cm high, surrounded with 1 cm thick polystyrene walls. With this arrangement it is possible to reproduce the position of the solution cell and ionization chamber sensitive volume accurately; also the scattered radiation pattern arising from the brass holder and the general environment would be identical for both ionization chamber and solution measurements. The chemical solutions were made using reagent grade ferrous ammonium sulfate, reagent grade sodium chloride, cp sulfuric acid, and distilled water. In all cases the solutions were $10^{-3}M$ ferrous ion, $10^{-3}M$ chloride ion, and $0.8N$ sulfuric acid. Analyses of the solutions were made with a Beckman quartz photoelectric spectrophotometer at a wavelength of 305 mμ, using 2174 for the molar extinction coefficient of ferric ion at 24°C.

The chamber was suspended 34 cm from the gold target for both solution and ionization chamber measurements by three thin steel cables. The chamber position was accurately reproduced each time it was removed by using a positioning device which was attached to the front of the Van de Graaff generator. The various gases were flowed through the chamber at an approximately constant rate; a 10-min flushing period at higher rates was allowed before measurements were begun. Cp tank gases were used, and no special precautions with respect to purity were taken.

Since the x-ray output of the accelerator is dependent upon the operating current and voltage, both of which may fluctuate, the experimental measurements were performed in the following manner. For the ionization current measurements, which were instantaneous measurements, the voltage was maintained constant and the ionization current was recorded as a function of target current. In the case of the solution measurements, it was thought advisable to use a current integrator to record the total radiation received by the solution rather than to try to maintain a constant current. Since the solution irradiation was of the order of 1000 seconds, it was necessary to maintain the voltage constant manually.

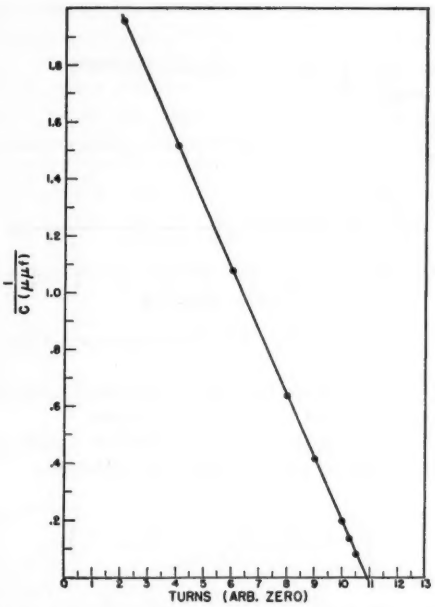

FIG. 2. Plot of reciprocal of the capacitance of the ionization chamber *versus* turns from an arbitrary starting position.

RESULTS

The ionization currents were determined using air, nitrogen, oxygen, carbon dioxide, methane, ethylene, and argon as the chamber fillings. These currents were derived from a least-squares fit to the ionization current-target current curves; in all cases, including the determination of the extrapolation correction, the ionization current corresponding to a target current of 100 μa was used. The ionization currents (normalized to STP and including the extrapolation correction) obtained for the different gases with a chamber volume of 3.39 ± 0.01 cm^3 are listed in column 2, Table I. Figure 3 shows the extrapolation curves obtained with air and argon fillings; curves were not obtained for the other gases since their Z was not significantly different from that of air. At the small spacings, measurements were taken with both plus and minus collecting voltage

TABLE I. Summary of experimental data and results.

Gas	Ionization current[a] (10^{-9} amp)	$(NZ)\times10^{30}$[a]	$I(V)$	K_{gas}^{poly}	K_{air}^{gas}	W(ev)	$\frac{W_{gas}}{W_{air}}$	Mean W(ev)$_{Jesse}$	$\left(\frac{W_{gas}}{W_{air}}\right)_{Failla}$
Air	3.76±0.07	3.89	83.2[b]	1.040	1.00	33.9±0.8	1.00	34.1	1.00
N_2	3.57±0.04	3.77	80.5[b]	1.036	1.005	24.8±0.5	1.026	34.7	1.034
O_2	4.51±0.05	4.31	92.0[b]	1.053	0.988	30.9±0.5	0.912	30.9	0.914
CO_2	5.92±0.05	5.95	87.4[c]	1.047	0.994	32.6±0.4	0.966	32.9	0.968
A	5.77±0.04	4.85	195.0[d]	1.167	0.891	25.5±0.3	0.751	26.4	...
CH_4	3.61±0.04	2.69	40.5[c]	0.952	1.093	26.8±0.4	0.788	27.3	0.820
C_2H_4	5.75±0.06	4.33	51.4[c]	0.980	1.062	26.3±0.4	0.773	26.3	0.778

[a] Normalized to STP.
[b] Calculated from $I=11.5Z$.
[c] E. Segrè, *Experimental Nuclear Physics* (John Wiley and Sons, Inc., New York, 1953), p. 203.
[d] W. Siri, *Isotopic Tracers and Nuclear Radiation* (McGraw-Hill Book Company, Inc., New York, 1949), p. 79.

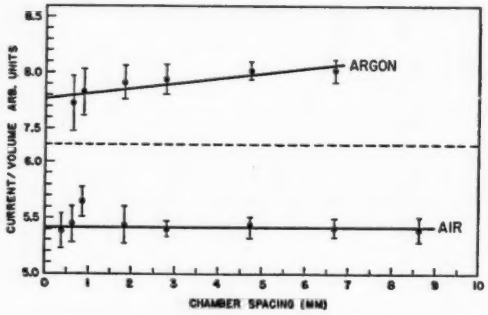

FIG. 3. Extrapolation curves for air and argon fillings.

polarities, and the average current was used to eliminate the contribution of the primary electrons.

It has been shown[1] that the absolute values of W can be calculated from the following equation:

$$W=E\Big/\left(J\times\frac{(NZ)_{\text{soln}}}{(NZ)_{\text{gas}}}K_{\text{gas}}{}^{\text{poly}}\right),$$

and that the ratio, $W_{\text{gas}}/W_{\text{air}}$, is given by the following equation:

$$\frac{W_{\text{gas}}}{W_{\text{air}}}=\frac{J_{\text{air}}}{J_{\text{gas}}}\frac{(NZ)_{\text{gas}}}{(NZ)_{\text{air}}}K_{\text{air}}{}^{\text{gas}},$$

where E=energy absorbed/cc/sec. by the solution, J=corrected number of ion pairs/cc/sec, STP, (NZ) =number of electrons/cc, STP, $K_{\text{gas}}{}^{\text{poly}}$=stopping power per electron$_{\text{poly}}$/stopping power per electron$_{\text{gas}}$, and $K_{\text{air}}{}^{\text{gas}}$=stopping power per electron$_{\text{gas}}$/stopping power per electron$_{\text{air}}$.

The values of $(NZ)_{\text{gas}}$, $K_{\text{gas}}{}^{\text{poly}}$, and $K_{\text{air}}{}^{\text{gas}}$ are tabulated in columns 3, 5, and 6, Table I; the number of electrons per cc of solution was 3.42×10^{23} at STP. The quantities, $K_{\text{gas}}{}^{\text{poly}}$ and $K_{\text{air}}{}^{\text{gas}}$, were derived from Bethe's equation[8] for the energy loss of electrons. This equation is valid provided the electron energy is greater than the binding energy of the electrons of the gas or wall, and is below 1 Mev so that polarization effect corrections may be ignored. $K_{\text{air}}{}^{\text{gas}}$ and $K_{\text{gas}}{}^{\text{poly}}$ were calculated for an electron energy of 128 kev, corresponding to $v/c=0.6$. These quantities vary by less than 2 percent over the energy range, 10 kev–700 kev. In these calculations it was necessary to use values for the average excitation potential; these are listed in column 4, Table I. In the case of compounds, the average excitation potential was calculated from those of the constituent atoms by the Bragg rule; 61 volts were used for the average excitation potential of polystyrene.

The energy absorbed in ev per cc per sec by the solution is given by the following equation:

$$E=\frac{100Y}{G}=OD\frac{N\times100}{\text{time}\times G\times\epsilon}=\text{ev/cc sec},$$

where Y=ferric ion yield (ions/cc sec), G=ferric ions/100 ev, OD=optical density/cm, N=Avogadro's number, and ϵ=extinction coefficient, 2.174×10^{6} μmoles^{-1} cc^{-1} cm^{-1}.

In order to correct for the change in solid angle and the absorption of x-rays because of the depth of the solution cell, the solution was extrapolated to zero volume as shown in Fig. 4. Since the energy calibration of the accelerator had changed at the time the solution extrapolation measurements were made, the data shown in Fig. 4 were used only to obtain the magnitude of the correction. The result of 8 determinations was a ferric ion yield of $(3.32\pm0.015)\times10^{13}$ ions/cc sec including the extrapolation correction. It should be pointed out that the 8 determinations included two in which the solution used was the same as that used in the cathode-ray bombardment determination by Schuler and Allen,[2] and in all cases their spectrophotometer and extinction coefficient were used.

The absolute values of W, calculated using the cathode-ray G value of 15.45 ± 0.15 are tabulated in column 7, Table I; the errors listed for W, which include the error in G, are standard deviations. If the calorimetric value of 15.8 ± 0.3 is used, the W values are decreased by the factor 0.975. The ratios $W_{\text{gas}}/W_{\text{air}}$ are tabulated in column 8, Table I. For comparison with other investigations, the W values for the gases based on 26.4 ev for argon as determined by Jesse and Sadauskis,[9] and the W's relative to air determined by Failla[10] are listed in columns 9 and 10, Table I.

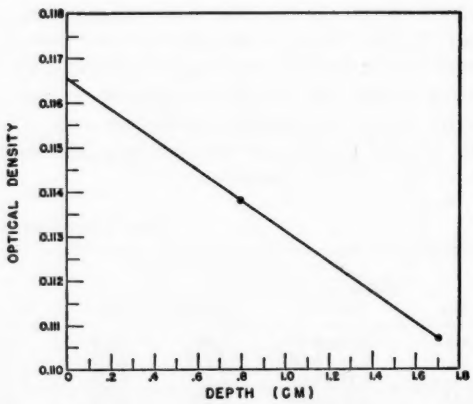

FIG. 4. Extrapolation curve for solution cell.

[8] E. Segrè, *Experimental Nuclear Physics* (John Wiley and Sons, Inc., New York, 1953), p. 254.

[9] W. P. Jesse and J. Sadauskis, Phys. Rev. **97**, 1668 (1955). We are indebted to W. P. Jesse for informing us of their results before publication.

[10] G. Failla and H. H. Rossi, U. S. Atomic Energy Commission Report, NYO 4582 (unpublished).

The ratios W_{gas}/W_{air} are in excellent agreement with the ratios determined by Jesse and by Failla; in both their determinations the stopping power ratio did not enter into the calculations since the total electron energy was absorbed in the gas. In our determination, however, it was necessary to use the stopping power ratios since only a fraction of the electron energy was expended in the gas. The excellent agreement between the two methods indicates that the error in the calculation of the stopping power ratio is small. The absolute values of W for the different gases are also in excellent agreement with Jesse's results; the value of 25.5 ± 0.3 ev obtained for argon is probably low because of the extreme sensitivity of argon to impurities. It should be pointed out that both Jesse and Failla used low-energy electrons in their investigations; these results include considerably higher electron energies. The accuracy of the absolute values of W is, of course, dependent upon the accuracy of the value of G and the calculated stopping power ratios which are used, and also upon the purity of the gases. Further experiments are planned in which the stopping power ratios will be experimentally determined and the purity of the gases will be carefully controlled.

ACKNOWLEDGMENTS

The authors wish to thank A. O. Allen, R. H. Schuler, G. Failla, R. L. Chase, and J. B. H. Kuper for their assistance and helpful suggestions. The ionization chamber was constructed and mounted by E. H Foster and C. Tomesch; D. Clareus assisted with many of the experimental measurements.

PHYSICAL REVIEW VOLUME 98, NUMBER 6 JUNE 15, 1955

Measurement of Absorption Coefficients for Photoionizing Radiations in Low-Pressure Gases with a Space Charge Detector*

C. D. MAUNSELL
Department of Physics, University of California, Berkeley, California†

(Received January 17, 1955)

A Kingdon cage space-charge detector has been used to measure the production of positive ions in a low-pressure gas due to absorption of photons produced by electron impact excitation in another region of the same gas. Absorption coefficients were measured by changing the source to detector separation. High-purity vacuum techniques were used to avoid contamination of the gas. No ionization was found in hydrogen. For nitrogen the molecular cross section was 4.1×10^{-16} cm² and for argon the atomic cross section was 3.1×10^{-16} cm². Tentative suggestions are made as to the processes responsible for these total absorption cross sections being much larger than the photoionization cross sections for monochromatic radiations in the ionization continuum region.

THE role of photoionization as an important secondary mechanism in gas discharges, particularly near the anode in asymmetric fields as in the burst pulses and streamers of positive point corona has been extensively discussed by Loeb.[1] A large number of measurements have been made of the absorption coefficients for the radiations producing such photoionization under discharge conditions.[2] Such measurements when carried out at high pressures do not allow accurate evaluation of the very high absorption cross sections required to explain the small distance scale of the burst pulses and streamers. In making measurements at lower pressures it is important to see that any currents measured are due to photoionization arising in the gas and not from photoelectrons emitted from electrodes or walls. The space-charge detector of Kingdon[3] and Hertz[4] seemed ideally suited for this purpose. This operates on the principle that introduction of a few positive ions into the electron space charge of a space charge limited diode gives a large increase in the electron current. The amplification so obtained makes it possible to detect positive ions in the presence of slow electrons.

The Kingdon cage was first applied to the detection of photoionization in gases and vapors by Mohler.[5] It was adapted for measuring relative cross sections for photoionization in alkali vapors by Lawrence and Edlefsen[6] who used two diodes with a balanced technique to eliminate fluctuations due to variations in

* This work was supported by the Office of Naval Research.
† Currently at the Pacific Naval Laboratory, Esquimault, British Columbia.

[1] L. B. Loeb, *Fundamental Processes of Electrical Discharge in Gases* (John Wiley and Sons, Inc., New York, 1939), Chap. X, Sec. 8, pp. 520 ff.; L. B. Loeb, Phys. Rev. **73**, 798 (1948); **94**, 224 (1954).

[2] E. Greiner, Z. Physik **81**, 543 (1933); A. M. Cravath, Phys. Rev. **47**, 254 (1935); G. Dechene, J. phys. radium **7**, 533 (1936); H. Raether, Z. Physik **110**, 611 (1938); W. Schwiecker, Naturwiss. **28**, 380 (1940); Z. Physik **116**, 562 (1940); S. H. Liebson, Phys. Rev. **74**, 694 (1948); Jaffe, Craggs, and Balakrishnan, Proc. Phys. Soc. (London) **B62**, 39 (1949).

[3] K. H. Kingdon, Phys. Rev. **21**, 408 (1923).

[4] G. Hertz, Z. Physik **18**, 307 (1923).

[5] F. L. Mohler, Phys. Rev. **28**, 46 (1926); Proc. Natl. Acad. Sci. U. S. **12**, 494 (1926).

[6] E. O. Lawrence and N. E. Edlefsen, Phys. Rev. **34**, 233 (1929).

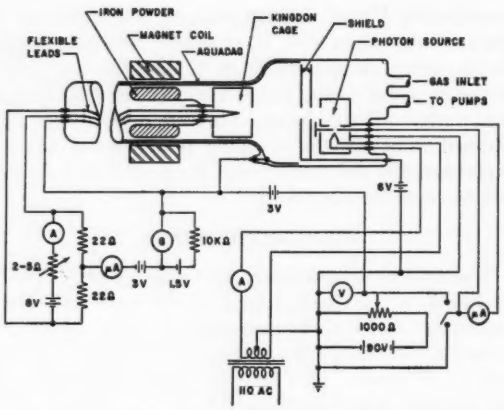

FIG. 1. Cross section of experimental tube with circuit diagram.

filament current or vacuum conditions. In this form it was used in gases by Varney and Loeb.[7] Berry and Varney[8] later showed that traces of oxygen caused much of the fluctuation and that under the purest conditions the use of a second balance diode was not needed.

APPARATUS

A cross section of the experimental tube is shown in Fig. 1 which includes a circuit diagram showing the electrical connections to the various elements. All electrodes except for tungsten filaments were made of nickel sheet. The Kingdon cage was mounted on a glass slider in which iron powder was sealed to enable the position of the detector to be adjusted by an external magnet. Electrical connections to the detector were made by flexible copper leads insulated by glass beads. Unfortunately these provided a variable leakage resistance between the anode and cathode leads which caused considerable noise in the detector circuit along with zero shift whenever the detector was moved. The noise prevented using the galvanometer at high sensitivity so most measurements were taken with a sensitivity of 0.2 μa/cm.

The photon source produced radiation by excitation of the gas contained in a field-free box through bombardment by an electron beam of variable energy. Photons from the source reached the detector through collinear holes in the source, isolating shield, and detector. The tube was made of borosilicate glass. The inside of the wall in the region between the isolating shield and the detector was coated with aquadag to prevent the formation of wall charges which might cause spurious currents in the detector. There was a narrow longitudinal stripe cleared through the aquadag so that the separation between source and detector could be found by measuring the distance between two fiducial marks, one on the glass slider on which the detector was mounted and the other on the tube wall.

Potentials on the various elements of the tube were arranged so that neither electrons nor positive ions from the source could reach the detector and that positive ions formed in the gas between the shield and detector would be driven away from the detector. When the voltage on the source was removed to check the detector zero, the Kingdon cage circuit was left at the same voltage with respect to ground to prevent leakage currents from changing.

The experimental tube formed part of a high-purity vacuum system arranged for taking measurements of photoionization under dynamic conditions of gas flow through the tube. The gas was admitted to the tube from glass flasks through a vacuum valve of the Alpert[9] type. The pressure in the experimental tube was adjusted by use of a second vacuum valve between the tube and a liquid nitrogen cooled trap preceding a mercury diffusion pump. Before admitting each gas the experimental tube was outgassed by baking at 400°C along with the valves, a Westinghouse WL-5966[10] ionization gauge and an RCA 1936 thermocouple gauge. After bakeout the metal elements of the tube were further outgassed by the use of a small induction heater. The outgassing procedure was continued until with all filaments in the tube hotter than for normal operation the background pressure was less than 10^{-8} mm. The gas supply flasks were equipped with break-offs which were opened after the outgassing was completed by the use of glass encased iron slugs moved by an external magnet. For each gas used the thermocouple gauge was calibrated against a McLeod gauge which was connected to the vacuum system on the pump side of the cold trap. This calibration was done essentially under static conditions and the results were then used to read the pressure under the dynamic flow conditions. The vacuum system was continuously pumped from the start of the outgassing procedure until measurements on the gas were completed.

Absorption measurements were taken by adjusting gas pressure, source voltage and current to the desired values, setting the Kingdon cage filament current so that the current through the galvanometer connected in the bucking circuit was small. The galvanometer then measured essentially all the change in plate current of the detector diode. For a number of separations between source and detector the galvanometer reading was taken with source voltage on and off. The difference between these readings was taken as proportional to the ionization produced in the detector as had been found by Lawrence and Edlefsen.[6]

Since the solid angle which the entrance hole for photons in the detector subtends at the source is a function of distance, the relationship between the galvanometer deflection Δ and the separation x between

[7] R. N. Varney and L. B. Loeb, Phys. Rev. **48**, 822 (1935).
[8] H. W. Berry and R. N. Varney, Phys. Rev. **57**, 1063(A) (1940).
[9] D. Alpert, J. Appl. Phys. **24**, 860 (1953).
[10] R. T. Bayard and D. Alpert, Rev. Sci. Instr. **21**, 571 (1950).

source and detector will be of the form

$$x^2\Delta \sim e^{-\mu x},$$

where μ is the effective total absorption coefficient in cm^{-1} for the radiation responsible for the photoionization. Thus a semilogarithmic plot of $x^2\Delta$ against x gives a value of μ from the slope of a straight line fitting these points. To compare the amounts of photoionization under different conditions, for each run the value of $x^2\Delta$ at $x=3$ cm taken from the straight line was recorded as I, the intensity of photoionization. Figure 2 shows examples of these logarithmic plots for two pressures of nitrogen. These are reasonably linear although the range of separations is hardly adequate for a definitive test. This occurred because the arrangement of the flexible leads to the detector did not allow greater motion.

RESULTS AND DISCUSSION

Nitrogen

Unlike the result of Varney and Loeb[7] who found only very weak ionization in nitrogen, a considerable ionization has been found in this study. Professor Loeb states that it is probable that their studies were carried out nearer threshold energy and at somewhat higher values of pressure times distance which would have militated against their having observed this phenomenon.

Figure 3 shows the absorption coefficients obtained as a function of pressure for Airco "reagent grade" nitrogen for a series of runs at a source voltage of 50 volts and a source electron current of 200 μa. Results appeared to be very similar at other voltages and currents and also for tank nitrogen which had been passed over hot copper and through a cold trap into a previously baked out flask which was sealed off when filled and later opened in the same manner as the commercial flask. No measurements of absorption coefficients could be obtained for source voltages near threshold because of the small signal to noise ratio.

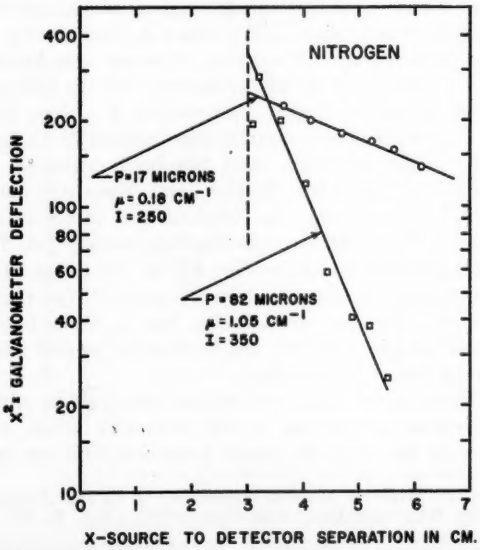

FIG. 2. Semilogarithmic plot showing evaluation of absorption coefficient and intensity of photoionization.

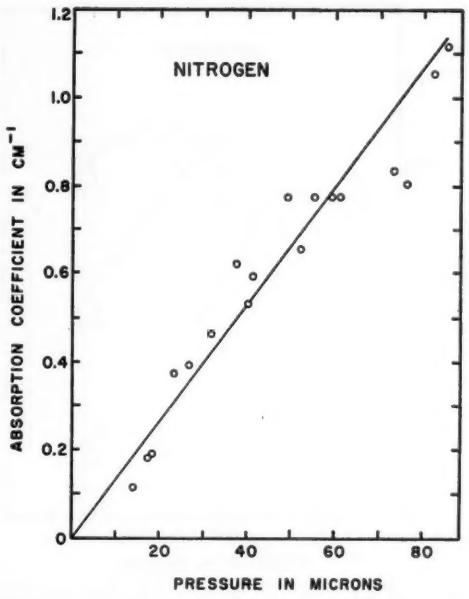

FIG. 3. Absorption coefficient as a function of pressure—nitrogen.

The absorption coefficients give a molecular cross section of 4.1×10^{-16} cm^2 independent of pressure as compared with the value of 2.5×10^{-17} cm^2 found by Weissler and his co-workers[11] for the photoionization continuum. They did find a total cross section of 1.0×10^{-16} cm^2 at a point about 0.5 A from the head of an unclassified absorption band found by Worley[12] at 765 A. There may also be other features in this wavelength region with even higher absorption cross sections. Thus it may be possible that the ionization measured here is due to photoionization directly by absorption of photons emitted from states of neutral nitrogen of greater energy than the lowest ionization potential. The ionization cross section in this region is only a part of the total absorption and the light output of the source at this wavelength seems likely to be small, although a knowledge of the distribution of light from a source like that used here would be of interest. *Note added in proof.*—In a private communication, Weissler states that Maunsell's data include Worley's band[12] which Weissler's data did not and that Maunsell's value may well be correct.

The experimental intensity of photoionization is shown as a function of pressure by the points in Fig. 5.

[11] Weissler, Lee, and Mohr, J. Opt. Soc. Am. 42, 84 (1952); Wainfan, Walker, and Weissler, J. Appl. Phys. 24, 1318 (1953).
[12] R. E. Worley, Phys. Rev. 64, 207 (1943).

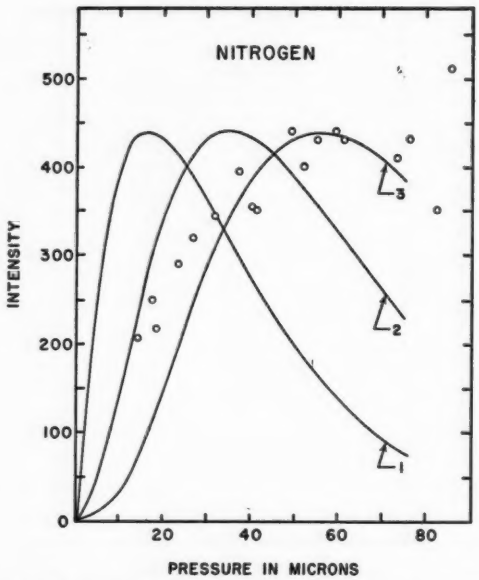

FIG. 4. Intensity of photoionization as a function of pressure—nitrogen. The points are experimental, the curves are theoretical for different degrees of pressure dependence.

These appear to show a flat maximum near $p=55$ microns with $I=440$. An attempt was made to see if some idea of the process of photoionization could be discovered by a study of this. With a photon source independent of gas pressure and a direct photoionization process, the number of positive ions produced in a detector of length l at a distance x from the source will be given by a relation of the form

$$I\sim e^{-\mu x}(1-e^{-\mu l}). \quad (1)$$

With a source of the type used here the light output would be expected to be proportional to pressure, p, so that one should have

$$I\sim pe^{-\mu x}(1-e^{-\mu l}). \quad (2)$$

If the ionization process requires a collision between an excited and a normal molecule then an extra factor proportional to pressure is required to give

$$I\sim p^2e^{-\mu x}(1-e^{-\mu l}). \quad (3)$$

With the use of the linear relation between μ and p of Fig. 3 and adjusting to the amplitude of the observed maximum the curves of Fig. 4 were calculated. The position of the maximum fits the higher-pressure dependence of curve 3 but the lower-pressure points lie above it. Probably the assumptions on which the calculations were based are oversimplified but the results do indicate that there may well be pressure dependent effects involved. Of course, since both source and detector are operated at the same pressure, it is impossible to state in which the pressure dependence is occurring.

When measurements on one flask of pure nitrogen were completed about 0.1 percent hydrogen was added by breaking open a small tube of hydrogen by an iron slug. 0.5 percent oxygen was added to another flask by the same technique. These experiments were tried to see if there was any change in the ionization of the resulting mixed gas by the well-known ionization of impurities by collision with excited states of the main gas. No such effect was noted probably because of the rapid clean up of both hydrogen and oxygen by the tungsten filaments as discussed by Dushman.[13] Also even if the hydrogen were not completely cleaned up, the fact that its ionization potential is very close to that of nitrogen would not be expected to lead to much extra ionization since there are not enough highly excited nitrogen states to ionize hydrogen.

Hydrogen

Tank hydrogen which had been purified by passing over hot copper and through a cold trap before being sealed into a previously baked and evacuated flask was used. Considerable cleanup occurred on turning on the filaments but by increasing the flow rate any desired pressure could be maintained. No photoionization could be observed at any pressure up to 60 microns, in agreement with the result of Mohler.[5] Adding 0.1 percent nitrogen did not produce any ionization which is not surprising, since the ionization potential of nitrogen is higher than that of hydrogen and thus photons which cannot ionize hydrogen should not be expected to be able to ionize nitrogen.

Argon

In conformity with the results of Mohler[5] and of Varney and Loeb,[7] ionization was observed in argon. For Airco "electronic grade" argon the absorption coefficient as a function of pressure is shown in Fig. 5. For pressures below 30 microns, an atomic cross section of 3.1×10^{-16} cm^2 seems satisfactory but the effective cross section at higher pressures is less than this. A theoretical photoionization cross section of 3×10^{-17} cm^2 at the ionization limit has been estimated by Dalgarno.[14] Wainfan, Walker, and Weissler[15] found 1.7×10^{-17} cm^2 near the threshold and values in the range 1.0–2.5×10^{-17} cm^2 at wavelengths to 473 A. The total absorption cross section will be higher than this photoionization cross section at lines in the region between the two series limits, but a direct photoionization process would not be expected to give much production of positive ions.

There are at least two complex processes by which absorption of photons of the resonance series with energies less than the atomic ionization limit can pro-

[13] Saul Dushman, *Scientific Foundations of Vacuum Technique* (John Wiley and Sons, New York, 1949), Chap. X, Sec. 5, pp. 673 ff.

[14] A. Dalgarno, Proc. Phys. Soc. (London) **A65**, 663 (1952).

[15] Wainfan, Walker, and Weissler, Gaseous Electronics Conference, 1954, Paper F2 (unpublished).

duce ionization. One of these is the pressure dependent mechanism of Hornbeck and Molnar,[16] by which an argon atom excited to within about 0.7 volt or less of the ionization limit can produce an ionized molecule by collision with an unexcited atom. This could lead to photoionization by the process

$$A+h\nu\rightarrow A^*,$$
$$A^*+A\rightarrow A_2^++e.$$

Another possible process which could involve the same states would involve ionization of a photoexcited atom by impact with one of the relatively low energy electrons of the detector. This reaction would be

$$A+h\nu\rightarrow A^*,$$
$$A^*+(e+\text{K.E.})\rightarrow A^++2e.$$

This process could act, not as a secondary mechanism, but only to increase the first Townsend coefficient. Mechanisms like these could explain the observed decrease in cross section at higher pressure by an increased contribution either from the wings of the lines involved or from more weakly absorbed lines.

A decision as to the type of ionization produced might be made by an accurate pressure-dependence study at low pressures where the noise level of the present apparatus did not allow accurate measurements to be made. A fitting to theoretical intensity curves of the type tried for nitrogen cannot be used for argon because the absorption coefficient is not linear with pressure. Another possible way of getting at the process responsible might be a mass spectrometric analysis of the ions produced.

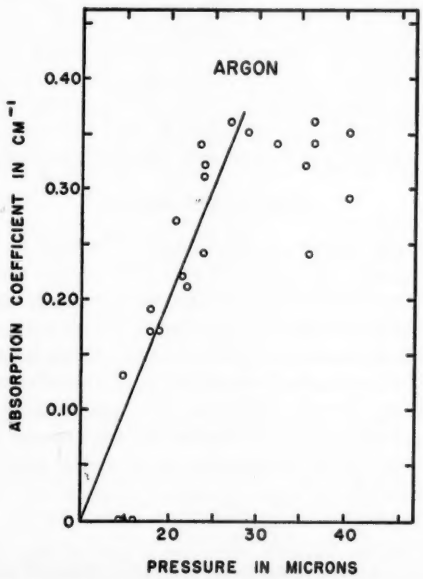

FIG. 5. Absorption coefficient as a function of pressure—argon.

[16] J. A. Hornbeck and J. P. Molnar, Phys. Rev. 84, 621 (1951).

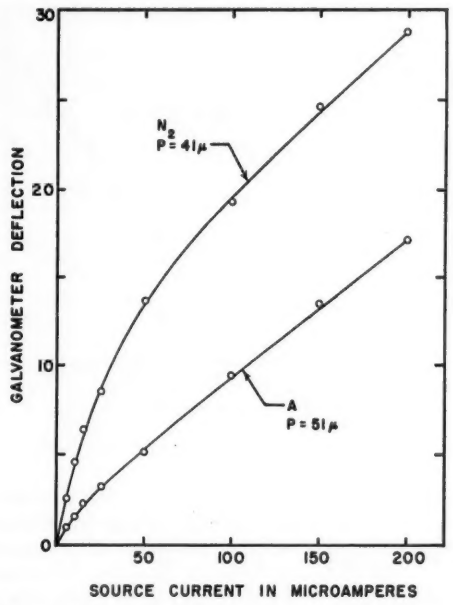

FIG. 6. Photoionization as a function of source current.

0.1 percent nitrogen added to the argon produced no noticeable changes, so that excited states of argon could not produce much ionization of nitrogen, probably because of the small difference in ionization potential.

Variation with Source Conditions

Figure 6 shows the variation of the galvanometer deflection as the current was changed in the exciting electron beam. For these curves the source voltage was fixed and the detector was not moved between readings. For neither nitrogen nor argon is the dependence linear as might be expected for a single-photon process nor steeper than linear as would be caused by a multiple-photon process. For both the curvature is like that for some sort of saturation process and is much more pronounced in nitrogen than in argon. It cannot be definitely stated whether the cause of this arises in the source or detector. If it is due to a nonlinearity in the detector, this would require a correction to be made to the points from which the absorption coefficients were calculated. This would have the effect of increasing the coefficients above those shown earlier so the cross sections shown should be considered as minimum values. At the same time, correcting the points would make the curves less linear, becoming steeper at greater separations. This is the opposite effect to that to be expected from a superposition of absorptions of different radiations where the effective absorption coefficient becomes less at greater distances. The assumption that the nonlinearity is in the source leads to less difficulty. Here it is possible that space-charge effects can cause a spreading of the electron beam and hence of the

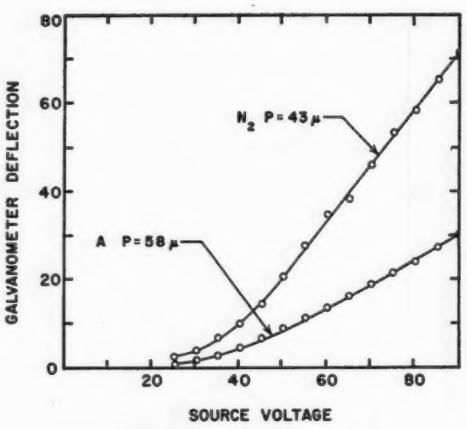

FIG. 7. Photoionization as a function of source voltage.

region of gas-emitting radiation. Since the photons are collimated at the source such spreading would cause a decrease in the efficiency of the source with increasing current. The lower curvature in argon could be due to the greater effective cross section in argon than in nitrogen for ionization by 50-volt electrons.[17] The greater number of positive ions formed would produce less spreading of the electron beam. Unfortunately the geometry of the source is not conducive to calculating the distribution of excitation in the source.

The variation of photoionization with the voltage accelerating the source electron beam is given in Fig. 7. The source current of 100 μa used for these curves could not be maintained at low source voltages, but tests in this region with lower currents indicated that the detector response approached zero slowly as the voltage neared the ionization potential with no sharp threshold. Some of the tests were made with a pulsed-filament supply so that the electron beam did not have a spread in energy due to the voltage drop along the source filament. The excitation curves do not resemble those for excitation or ionization of a single state, which show a well-defined threshold followed by a rapid rise to a maximum. Instead they look more like the total excitation cross-section curves of Maier-Leibnitz,[18] which however extended for only a few volts above the ionization energy.

CONCLUSIONS

The fact that the absorption coefficients measured in this study for radiations producing photoionization in gases are considerably larger than those determined for monochromatic radiations of energy greater than the ionization potential indicates that under gas discharge conditions the process of photoionization may be a complex one. Ionization produced through photoexcitation followed by molecular ion formation by a process like that of Hornbeck and Molnar[16] might produce secondary electrons in uniform fields and does act as a secondary mechanism leading to self-sustaining discharges in asymmetric fields. At the same time the other complex ionization process discussed earlier in which low-energy electrons ionize the photoexcited states can only act to augment the primary ionization process where there is already a supply of electrons. In any event, processes such as the Hornbeck and Molnar and the Penning effects increase the first Townsend coefficient as statically measured from two to twenty fold. It is not difficult to account for the large observed cross sections with the aid of such indirect processes in addition to the direct process.

The mere observation of ionization due to photon absorption in a study of this type does not prove that it will be important as a secondary process in gas discharges, since the low-energy electrons of the Kingdon cage may be involved. On the other hand, if ionization is not observed there is no guarantee that it may not be important in discharges at higher pressure. This can occur since materially lower absorption cross sections would reduce the amount of ionization below that observable here. In addition there might be other pressure-dependent effects involved.

One especially interesting field in which photoionization has been invoked as a mechanism is the positive point corona with burst pulses and streamers in oxygen, air, and other mixtures containing oxygen. This has been extensively discussed by Loeb.[1] It would thus be of great interest to study the photoionization in oxygen and other gases containing oxygen. This cannot be done by the Kingdon cage technique as used here because of the reaction of the oxygen with the tungsten filaments.

ACKNOWLEDGMENTS

I deeply wish to thank Professor Leonard B. Loeb who suggested and directed the work on this problem for his continued advice and encouragement during the course of this research. I also wish to thank the present and former members of his research group for many helpful discussions, especially Dr. J. H. Parker for advice on vacuum technique and gas-handling procedure. I am grateful to the Physics Department glassblower Mr. M. R. Corbett for much skillful work.

[17] K. T. Compton and C. C. Van Voorhis, Phys. Rev. **26**, 436 (1925); **27**, 724 (1926).
[18] H. Maier-Leibnitz, Z. Physik **95**, 499 (1935).

Microwave Spectrum of Carbon Monsulfide*

RICHARD C. MOCKLER† AND GEORGE R. BIRD‡
Columbia University, New York, New York

(Received March 7, 1955)

CS was produced by an electrical discharge through CS_2 and continuously flowed through a conventional Stark spectrometer. The $J=0\rightarrow1$ transitions of the isotopic species $C^{12}S^{32}$, $C^{12}S^{33}$, $C^{12}S^{34}$, and $C^{13}S^{32}$ were observed in their vibrational ground states. $C^{12}S^{32}$ was also observed in its first excited vibrational state. The spectra yield the following molecular constants: In Mc/sec,

$$B_e(C^{12}S^{32}) = 24\,584.352 \pm 0.015,$$
$$B_e(C^{12}S^{33}) = 24\,381.011 \pm 0.027,$$
$$B_e(C^{12}S^{34}) = 24\,190.198 \pm 0.014,$$
$$B_e(C^{13}S^{32}) = 23\,205.215 \pm 0.020,$$
$$\alpha(C^{12}S^{32}) = +177.544 \pm 0.026,$$
$$eqQ(C^{12}S^{33}) = +12.835 \pm 0.026,$$

Dipole moment = 1.97 ±0.02 Debye units,
Equilibrium bond distance = 1.5349±0.0002 A,

where B_e = equilibrium rotational constant, α = vibration-rotation interaction constant, and eqQ = electric quadrupole coupling constant.

The mass ratios calculated from the above B_e values are: $S^{32}/S^{34} = 0.941246\pm22$, $S^{32}/S^{33} = 0.9696909\pm32$, and $C^{12}/C^{13} = 0.9228447 \pm 20$.

Nuclear magnetic interactions of S^{33} were also detected. The coefficient C of the $C\mathbf{I}\cdot\mathbf{J}$ coupling term was found to have the value 0.019±0.015 Mc/sec.

INTRODUCTION

THE present investigation was undertaken primarily as a wedge to develop techniques that would facilitate microwave absorption studies of rather short-lived molecules and free radicals. CS was considered a suitable first choice since it exhibits rather long lifetimes[1] at least in glass and quartz apparatus. In the experiment described here, CS was produced by an electrical discharge in CS_2. The CS was flowed through a Stark spectrometer, and its pure rotation spectrum was observed in the 6-mm region.

The $J=0\rightarrow1$ transitions of a number of isotopic species were measured (Table I) in their ground vibrational state. The $J=0\rightarrow1$ transition in the first excited vibrational state was also observed for the most abundant species $C^{12}-S^{32}$. From these measured transitions the molecular constants B_e, r_e, and α were calculated and tabulated in Table II. From the values of B_e for the various isotopic species, certain mass ratios of sulfur and carbon isotopes were calculated (Table III). The dipole moment was determined (Table II) from the second-order Stark effect of the $J=0\rightarrow1$ transition of $C^{12}-S^{32}$ in its ground vibrational state.

The hfs resulting from the S^{33} nuclear quadrupole interaction was completely resolved. The quadrupole coupling constant determined from this hfs together with the coupling coefficients of other sulfur compounds permitted a reasonable structure for CS to be proposed. The measured spacings in the hfs required the introduction into the interaction Hamiltonian of a term involving the interaction of the magnetic moment of S^3 with the magnetic field produced by the rotation of the molecule as a whole (an $\mathbf{I}\cdot\mathbf{J}$ interaction term).

The OH free radical has been observed by Sanders, Schawlow, Dousmanis, and Townes[2] at microwave frequencies by use of a technique similar to that described here. However, in the case of OH, Zeeman modulation was used for detection purposes instead of Stark modulation (Zeeman modulation being suitable for free radicals). The electronic ground state of CS has been shown to be a $^1\Sigma^+$ state from its ultraviolet spectrum.[3] Consequently, it should probably be classified as a molecule and not as a free radical. Because CS was observed in the nonmagnetic ground state, Stark modulation was most suitable.

EXPERIMENTAL PROCEDURE

The small moment of inertia of CS requires that the lowest rotational transition, $J=0\rightarrow1$, fall in the 6-mm microwave region. Although klystrons are available in this region, it was found most convenient to use the second harmonic of a K-band klystron for all of the measurements. The frequency multiplication and de-

TABLE I. Frequencies of the observed transitions of CS.

Molecule	Transition	Frequency, Mc/sec
$C^{12}S^{32}$	$J=0\rightarrow1$, $v=0$	48 991.000±0.006
$C^{12}S^{32}$	$J=0\rightarrow1$, $v=1$	48 635.912±0.040
$C^{12}S^{34}$	$J=0\rightarrow1$, $v=0$	48 206.948±0.006
$C^{13}S^{32}$	$J=0\rightarrow1$, $v=0$	46 247.472±0.020
$C^{12}S^{33}$	$J=0\rightarrow1$, $v=0$	
	$F=3/2\rightarrow3/2$	48 589.068±0.010
	$F=3/2\rightarrow5/2$	48 585.906±0.010
	$F=3/2\rightarrow1/2$	48 583.264±0.010

* A preliminary report was given at the North Carolina Meeting of the American Physical Society, March, 1953 [Phys. Rev. **91**, 222 (1953)].

† The present research was done while this author was a Union Carbide and Carbon Postdoctoral Fellow at Columbia University. Present address: National Bureau of Standards, Boulder, Colorado.

‡ The present research was done while this author was a National Research Council Postdoctoral Fellow at Columbia University. Present address: Department of Chemistry, The Rice Institute, Houston, Texas.

[1] P. J. Dyne and D. A. Ramsay, J. Chem. Phys. **20**, 1055 (1952).

[2] Sanders, Schawlow, Dousmanis, and Townes, Phys. Rev. **89**, 1158 (1953). Also the OD spectrum has recently been reported by G. C. Dousmanis, Phys. Rev. **94**, 789(A) (1954).

[3] For references see G. Herzberg, *Spectra of Diatomic Molecules* (D. Van Nostrand Company, Inc., New York, 1950), p. 523.

TABLE II. Molecular constants.

$B_e(C^{12}S^{32})$	$= 24\,584.352 \pm 0.015$ Mc/sec
$\alpha_e(C^{12}S^{32})$	$= 177.544 \pm 0.026$ Mc/sec
$B_e(C^{12}S^{33})$	$= 24\,381.011 \pm 0.027$ Mc/sec
$B_e(C^{12}S^{34})$	$= 24\,190.198 \pm 0.014$ Mc/sec
$B_e(C^{13}S^{32})$	$= 23\,205.215 \pm 0.020$ Mc/sec
eqQ	$= +12.835 \pm 0.026$ Mc/sec
I·J coefficient, C	$= +0.019 \pm 0.015$ Mc/sec
Dipole moment	$= 1.97 \pm 0.02$ Debye units
Equilibrium bond distance,[a] r_e	$= 1.5349 \pm 0.0002$ A

[a] $h = (6.62363 \pm 0.0016) \times 10^{-27}$ erg sec.

tection techniques were according to usual procedures.[4] Stark modulation was used.

A 60-cycle discharge of about 1100 v and about 30 ma was used for the production of CS. The discharge was in CS_2 at a pressure of approximately 0.7 mm, the vapor pressure of CS_2 at the temperature of a dry ice-acetone mixture. The separation of the aluminum electrodes was about two feet and the diameter of the discharge tube one inch. A considerable amount of free sulfur is formed in the discharge and condenses on the walls of the tube. CS polymerizes on the walls of the apparatus including the absorption cell as a black solid. Thin films appear dark red. This polymer gives a convenient indication of the existence of CS.

CS_2 was prevented from entering the absorption cell by interposing a cold trap between the discharge tube and the cell. The trap was maintained at -122°C by an acetone-solid ether mixture. At this temperature CS_2 has no measurable vapor pressure and the CS itself is not condensed. The CS was pumped continuously through the six-foot X-band Stark cell throughout the final observations. The remaining CS that went completely through the cell without polymerizing was trapped in a liquid nitrogen trap. It was found that CS would be accumulated for several hours at liquid nitrogen temperatures. The CS polymerizes explosively when the temperature is raised above -195°C (and sometimes without a deliberate increase in temperature), a rather annoying feature of the substance. The glass trap was usually shattered by one of these explosions.

Although the accumulation of CS polymer in the absorption cell does effect microwave transmission and the behavior of the Stark modulation system, spectroscopy may be done for periods of about thirty hours or more. The polymer is a fairly good insulator and only after many hours of use was the resistance across the Stark voltage input observed to be low. The polymer formed on the mica cell windows had no noticeable effect on microwave transmission.

After long periods of use, a corona discharge occurs between the Stark septum and the walls of the cell at Stark voltages above about 200 v. It is believed that this corona discharge is initiated by flakes of CS polymer that scale off of the cell walls. If the temperature of the intermediate trap is then raised to about -100°C to permit CS_2 to enter the cell under these conditions of breakdown the CS spectrum may be observed even after turning off the discharge tube. Apparently CS is formed in the corona. Under the proper conditions, the CS spectrum is more intense than when using the discharge tube without breakdown. The ions and free electrons produced in the discharge provide a considerable noise source and a continuous absorption modulated at the frequency to which the phase sensitive detector is tuned. The breakdown is usually detected in the receiving system in addition to the superposed spectrum. For this reason the original technique using the discharge tube was used in making the quoted measurements.

The cell was kept at dry ice temperatures for all of the measurements in the ground vibrational state. Line breadths were about 300 kc/sec. Room temperatures were used for the excited vibrational state measurements, higher temperatures favoring a higher population in the excited state.

From observation of the persistence of the spectral lines after discharge was turned off, the lifetime of the CS in the brass absorption cell was about 2 or 3 seconds at the longest. The lifetime depended upon the conditions of the cell.

The technique employed here for the study of the CS spectrum could probably be used for a number of other molecules and free radicals with lifetimes of the order of one-half second. Variations of the technique, in particular methods by which the desired molecule or fragment could be produced inside the absorption cell, would probably permit investigation of molecules of even shorter lifetimes. Such a possibility was suggested by the observation of the CS spectrum during Stark break down in the current experiment.

RESULTS

The rotational transition frequencies of a diatomic molecule for the selection rule $J=+1$ are given to good approximation by

$$\nu = 2[B_e - \alpha_e(v+\tfrac{1}{2})](J+1) - 4D_e(J+1)^3 \qquad (1)$$

neglecting hyperfine structure. Here $B_e = h/8\pi^2 I_e$ is the equilibrium rotational constant, α_e is the vibrational-rotational interaction constant, $D_e = 4B_e^3/\omega_e^2$ is the

TABLE III. Mass ratio comparisons.[a]

Mass ratio	Result from present data	Result from mass spectrographic and nuclear data
S^{32}/S^{34}	0.9412462 ± 22	0.9412446 ± 6
S^{32}/S^{33}	0.9696909 ± 32	0.9696905 ± 10
C^{12}/C^{13}	0.9228447 ± 20	0.9228395 ± 11

[a] These and other comparisons are made in some detail in the article by Geschwind, Gunther-Mohr, and Townes, Revs. Modern Phys. 26, 444 (1954).

[4] Gordy, Smith, and Trambarulo, *Microwave Spectroscopy* (John Wiley and Sons, Inc., New York, 1953).

centrifugal distortion constant, and v is the vibrational quantum number. The measured frequencies of the $J=0\rightarrow1$ transitions of several isotopic combinations are recorded in Table I.

The values of D_e necessary for the calculation of the B_e and α_e values were determined from the vibrational frequency ω_e obtained from the ultraviolet data[3] for $C^{12}S^{32}$. The various molecular constants obtained from the spectra are included in Table II. The masses used in the calculations are from the mass spectrographic data of Ogata and Matsuda.[5] The B_e and α_e values for $C^{12}S^{32}$ compare nicely with the ultraviolet results.[3]

Comparison of the mass ratios calculated from the CS spectra with the best present values obtained from mass spectrographic and nuclear reaction data are made in Table III.

Comparison of the sulfur ratios is satisfactory but comparison of the C^{12}/C^{13} ratio is not within the supposed experimental errors. Additional data from the spectra of diatomic molecules would be useful. Perhaps the spectrum of CO would be suitable for another determination of the C^{12}/C^{13} ratio.

The nuclear spin of S^{33} is $\frac{3}{2}$. The $J=1$ state is split into a triplet. An analysis of the data for $C^{12}S^{33}$ indicates that the hyperfine structure of the $J=0\rightarrow1$ transition does not arise entirely from the interaction of the nuclear quadrupole moment with the rest of the molecule. There is a measurable $\mathbf{I}\cdot\mathbf{J}$ interaction between the spin of S^{33} and the rotational angular momentum. Equation (1) must then be modified by the addition of two interaction terms. The interaction energy then has the form

$$E=-eqQ(\text{Casimir function})+\tfrac{1}{2}C[F(F+1)-I(I+1)-J(J+1)]. \quad (2)$$

The quadrupole coupling constant eqQ and the $\mathbf{I}\cdot\mathbf{J}$ coupling coefficient C are given in Table II together with the other calculated molecular constants. The positive value for C is in keeping with the positive nuclear magnetic moment of S^{33}. The small separations of the hfs lines made intensity comparison and assignment particularly easy since all three lines could be observed together on the oscilloscope.

The dipole moment of $C^{12}S^{32}$ in its ground vibrational state was determined from its Stark effect. The Stark cell was calibrated with the known Stark effect of OCS in the usual way. The result is included in Table II.

DISCUSSION

A reasonable bond structure for CS may be deduced from the measured quadrupole coupling constant[6] of $C^{12}S^{33}$ and from consideration of other sulfur-containing molecules for which the quadrupole coupling has been measured. This has already been done by one of us (G.R.B.) and C. H. Townes.[7] For completeness we shall consider this problem again here.

First suppose that the nonhybridized structures,

$$C^+-S^-, \quad C=S, \quad \text{and} \quad C^-\equiv S^+,$$

are plausible structures. The measured bond distance favors a combination of the latter two structures. Furthermore the eqQ of C^+-S^- is negative, whereas the observed value is positive. Therefore we assume that C^+-S^- does not contribute significantly. A combination of the remaining two structures with appropriate hybridization can be shown to give a suitable set of structures.

The dipole moment and bond distance of CS indicate that the unhybridized $C^-\equiv S^+$ structure would contribute about 27 percent. But the unhybridized $C=S$ structure contributes a negative eqQ and $C^-\equiv S^+$ has a zero eqQ value. Then to attain the measured eqQ for the molecule hybridization is necessary. Fifty percent s-hybridization gives consistent results. With this hybridization $C=S$ gives a zero eqQ value and $C^-\equiv S^+$ the value 34.4 Mc/sec if one assumes that the coupling per unbalanced p electron is -55 Mc/sec.[7] Now with hybridization, instead of $C^-\equiv S^+$ contributing 27 percent it contributes 40 percent. This gives an eqQ for the molecule of $+13.8$ Mc/sec which compares satisfactorily with the measured value $+12.84$ Mc/sec.

Thus for the structure of CS we choose $C=S$ to have 60 percent importance and $C^-\equiv S^+$ to have 40 percent importance, each with 50 percent s-hybridization of the p_σ bonds.

ACKNOWLEDGMENTS

The authors wish to express their gratitude to Dr. William Shurcliff who first suggested the possibility of observing the microwave spectrum of CS. Thanks are especially due to Mr. Paul Fletcher who helped with many of the measurements and to Professor C. H. Townes for many helpful discussions and for his active interest throughout the progress of the research. We also thank Dr. Gene Silvey for his invaluable cooperation and his aid with the chemical problems. Thanks are also due Dr. Joseph Klein for his aid with the frequency multiplication and detection problems involved in the experimentation.

[5] K. Ogata and H. Matsuda, Phys. Rev. **89**, 27 (1953).
[6] C. H. Townes and B. P. Dailey, J. Chem. Phys. **17**, 782 (1949).
[7] G. R. Bird and C. H. Townes, Phys. Rev. **94**, 1203 (1954).

Static Magnetic Field Quenching of the Orthopositronium Decay: Angular Distribution Effect*

V. W. HUGHES,† S. MARDER,‡ AND C. S. WU
Columbia University, New York, New York

(Received February 28, 1955)

An effect of the angular dependence of the annihilation radiation from the magnetic substates of orthopositronium has been observed in an experiment similar to that of Deutsch and Dulit. Quanta due to positron annihilations were observed at a direction of 90° to a magnetic field. The fraction, f, of orthopositronium decaying by three-quantum annihilation can then be computed, and at high values of the field f was found to be less than $\frac{2}{3}$. The value $\frac{2}{3}$ is expected statistically since only annihilation radiation of the $M=0$ substate is affected by the field. Our observation is understandable if Drisko's formulas for the angular distribution of the annihilation radiation from the different magnetic substates are considered.

The ratio of the decay rates of parapositronium to orthopositronium can be computed from values of f *vs* the field, after corrections are made for the angular distribution of the quanta. Our data yield $\lambda_p/\lambda_o=1302$ with a probable error of ±15 percent, in agreement with the theoretical value of 1114.

1. INTRODUCTION

THE mode of annihilation of ground state ($n=1$) positronium is known to be affected by a static magnetic field. In the absence of a magnetic field positronium exists either in the para-state ($^1S_0$, $M=0$) or in the ortho-state ($^3S_1$, $M=0, \pm 1$). From the conservation laws of energy, linear momentum, angular momentum, and a component of angular momentum, it follows that a parapositronium atom at rest will decay by the emission of two quanta which have the same energy (mc^2), which propagate in opposite directions, and which are polarized in mutually perpendicular directions.[1,2] An orthopositronium atom at rest will decay by the emission of three quanta whose energies sum to $2mc^2$; the energy distribution of the annihilation quanta has been calculated from conventional quantum electrodynamics. The three quanta will propagate in a single plane, and the directions of propagation and polarization will be such as to conserve linear and angular momentum and a component of angular momentum. The decay rate of parapositronium (λ_p) is 8.03×10^9 sec^{-1} and of orthopositronium (λ_o) is 7.21×10^6 sec^{-1}.[3]

In the presence of a magnetic field the $M=\pm1$ magnetic substates of orthopositronium are still pure ortho-states, and will decay by the three quantum annihilation characteristic of orthopositronium decay. On the other hand, the $M=0$ state of orthopositronium has a small admixture of para-state due to the interaction with the magnetic field, and hence can decay either by three-quantum annihilation or by two-quantum annihilation. The relative probabilities of these two modes of decay depends, of course, on the amount of admixture of para-state and on the ratio of the decay rates of parapositronium to orthopositronium. The $M=0$ state of parapositronium will similarly have a small admixture of ortho-state, but since the orthopositronium decay rate is so small compared to the parapositronium decay rate, this $M=0$ state will still decay predominantly by two-quantum annihilation for practical values of the magnetic field. Thus the principal effect of a static magnetic field is to increase the amount of two-quantum annihilation relative to three-quantum annihilation. In a known magnetic field the amount of quenching of three-quantum annihilation will depend on two parameters: (1) the energy difference between parapositronium and orthopositronium, (2) the ratio of the decay rates of parapositronium to orthopositronium.

The original experiment of Deutsch and Dulit[4] on the static magnetic field quenching of orthopositronium decay was done by a study of the energy distribution of the γ-ray annihilation radiation as a function of the magnetic field. Ore and Powell's theoretical value of the ratio of the decay rates of parapositronium to orthopositronium was assumed, and the experimental data were then used to derive a value for the energy difference between parapositronium and orthopositronium to an accuracy of about 10 percent. Pond and Dicke[5] studied the magnetic quenching of orthopositronium decay by observing the number of two-quantum annihilations by coincidence counting. If one assumes the theoretical ratio of parapositronium to orthopositronium decay rates, their data yield the energy difference to an accuracy of about 25 percent. More recently Deutsch, Brown, and Weinstein[6] have measured the energy separation between parapositronium and orthopositronium by inducing a radio-frequency transition between the magnetic sublevels

* This work was partially supported by the U. S. Atomic Energy Commission.

† Present address: Physics Department, Yale University, New Haven, Connecticut.

‡ To be submitted in partial fulfillment of the Ph.D. thesis requirement at Columbia University.

[1] J. A. Wheeler, Ann. N. Y. Acad. Sci. **48**, 219 (1946).

[2] C. N. Yang, Phys. Rev. **77**, 242 (1950).

[3] A. Ore and J. L. Powell, Phys. Rev. **75**, 1696 (1949).

[4] M. Deutsch and E. Dulit, Phys. Rev. **84**, 601 (1951).

[5] T. A. Pond and R. H. Dicke, Phys. Rev. **85**, 489 (1952).

[6] M. Deutsch and S. C. Brown, Phys. Rev. **85**, 1047 (1952); Weinstein, Deutsch, and Brown, Phys. Rev. **94**, 758 (1954); **98**, 223 (1955).

of orthopositronium, and report a value $(2.03370 \pm 0.00050) \times 10^5$ Mc/sec. Wheatley and Halliday[7] measured the quenching of three-quantum annihilation by observing the change in the triple coincidence rate with magnetic field. Using the value obtained for the energy separation from the radio-frequency experiment, they give a value for the ratio of parapositronium to orthopositronium decay rates of 1050 ± 140, compared with Ore and Powell's theoretical result of 1114.

The present paper reports the effect of the angular dependence of the annihilation radiation of the magnetic substates of orthopositronium on the observed magnetic quenching of orthopositronium in an experiment similar to that of Deutsch and Dulit. Recently Drisko has redone the calculation of Ore and Powell on the annihilation radiation from orthopositronium, but without averaging over angles and has thus obtained angular distribution formulas.[8] Our experimental data are in good agreement with his calculation. An effect of the angular dependence of the annihilation radiation from the magnetic substates of orthopositronium in agreement with Drisko's calculation was also observed by Wheatley and Halliday.[7]

If the value of the energy separation is taken from the recent radio-frequency experiment, the present experiment gives the ratio of parapositronium to orthopositronium decay rates. The angular distribution effect must be considered if a value for this ratio is to be obtained which is correct even as to sign and order of magnitude. The value obtained is 1302 with a probable error of ± 15 percent, which is in adequate agreement with the theoretical value of 1114. A preliminary report on this work has been given.[9]

2. THEORY OF THE EXPERIMENT

The part of the Hamiltonian for positronium which includes the "hyperfine structure" interaction (which leads to the energy difference between parapositronium and orthopositronium) and the interaction with the magnetic field is

$$\mathcal{H}=\mathcal{H}_0+g^-\mu_0\mathbf{s}^-\cdot\mathbf{H}+g^+\mu_0\mathbf{s}^+\cdot\mathbf{H}, \tag{1}$$

in which $\mathcal{H}_0$ is the spin-dependent "hyperfine structure" operator,[10] s^- and s^+ are the spin angular momentum operators for the electron and positron respectively, $g^-(\simeq 2)$ and g^+ are their spin gyromagnetic ratios, μ_0 is the Bohr magneton, and $H=H_z$ is a constant magnetic field applied in the z direction. Note further that $g^+=-g^-$. To first-order perturbation theory in the magnetic interaction the state functions for a field H, which correspond adiabatically to the zero field states $J=1$, $M=0$ and $J=0$, $M=0$, are, respectively,

$$\begin{aligned}\psi_1&=u(1,0)+au(0,0),\\ \psi_0&=u(0,0)-au(1,0),\end{aligned} \tag{2}$$

in which J is the total angular momentum quantum number, M is the quantum number for component of total spin angular momentum in the z direction, $u(1,0)$ and $u(0,0)$ are the zero-field eigenstates for $J=1$, $M=0$ and for $J=0$, $M=0$, respectively. The quantity $a=\mu_0 g^- H/W$, in which W—a positive quantity—is the energy difference between orthopositronium and parapositronium.

Halpern[11] has given a discussion of the theory of the quenching of the orthopositronium decay in a constant magnetic field. Upon using his results the fraction, F, of $M=0$ orthopositronium atoms which will decay by three-quantum annihilation in a magnetic field is

$$F=\frac{(1-a^2)\lambda_o}{(1-a^2)\lambda_o+\lambda' a^2}, \tag{3}$$

in which $\lambda'=\lambda_p-\lambda_o\simeq\lambda_p$. The two-quantum decay of $M=0$ parapositronium is negligibly affected by the presence of the magnetic field, as was pointed out in the introduction. The experimental data can be analyzed to yield the fraction, f, of orthopositronium atoms which will decay by three-quantum annihilation. The quantity f is given by

$$f=\frac{2}{3}+\frac{F}{3}=\left(1+\frac{\lambda_p}{\lambda_o}\frac{2}{3}\frac{a^2}{(1-a^2)}\right)\Big/\left(1+\frac{\lambda_p}{\lambda_o}\frac{a^2}{(1-a^2)}\right). \tag{3'}$$

For high fields f approaches the value $\frac{2}{3}$, which is expected statistically since only the $M=0$ ortho-state is affected by the magnetic field.

The angular distributions of the annihilation quanta from the three-quantum decay of the different magnetic substates of orthopositronium are required for the interpretation of the experimental data. Drisko has repeated the calculation of the three-quantum annihilation of orthopositronium without integrating over angles or averaging over the three spin states, and has thus developed formulas which give the relative number of quanta per unit solid angle and per unit frequency interval for the single quanta emitted by the magnetic sublevels of orthopositronium. His formulas are[8]

$$\begin{aligned}&(M=0):\ \tfrac{1}{2}[\sin^2\theta\Psi(k)+\tfrac{1}{2}(3\cos^2\theta-1)\Phi(k)],\\ &(M=+1 \text{ or } M=-1):\\ &\qquad\tfrac{1}{4}[(1+\cos^2\theta)\Psi(k)-\tfrac{1}{2}(3\cos^2\theta-1)\Phi(k)],\end{aligned} \tag{4}$$

in which θ is the angle between the quantization axis (direction of $\mathbf{H}$) and the direction of observation of the quantum, and k is the energy of the quantum in

[7] J. Wheatley and D. Halliday, Phys. Rev. **88**, 424 (1952).
[8] We are grateful to Professor G. C. Wick and Dr. R. Drisko for prepublication information on this calculation. R. Drisko, Phys. Rev. **95**, 611(A) (1954), and article to be published in Phys. Rev.
[9] Marder, Hughes, and Wu, Phys. Rev. **95**, 611(A) (1954).
[10] J. Pirenne, Arch. sci. phys. et nat. **29**, 265 (1947).
[11] O. Halpern, Phys. Rev. **94**, 904 (1954).

units of mc^2. The functions $\Psi(k)$ and $\Phi(k)$ are

$$\Psi(k)=8\left[\frac{2-k}{k}+\frac{2(1-k)}{k^2}\ln(1-k)+\frac{(1-k)k}{(2-k)^2}-2\frac{(1-k)^2}{(2-k)^3}\ln(1-k)\right],$$
$$\Phi(k)=8\left[\frac{k}{2(2-k)^2}-\frac{(1-k)}{(2-k)^3}\ln(1-k)-\frac{4(1-k)}{k^3}-\frac{(2-k)^2}{2k^3}-\frac{3(2-k)(1-k)}{k^4}\ln(1-k)\right]. \quad (5)$$

$\Psi(k)$ is the energy spectrum given by Ore and Powell.[3] The angular distribution of the quanta is independent of ϕ, the azimuthal angle measured about the z-axis.

3. EXPERIMENTAL ARRANGEMENT

The principal features of the experiment are similar to those of Deutsch and Dulit.[4] In the present experiment the positron source was Cu^{64} produced by neutron bombardment of 99.9 percent pure copper in the Brookhaven pile. The source was never used sooner than 8 hours after its production because of the time for delivery and the time for setting up the experiment; this necessary delay, of course, eliminated any possible short-lived impurity radiations. The source strength at the beginning of a run was customarily about 50 mC. The form of the source was a disk $\frac{1}{2}$ in. in diameter and 0.001 in. in thickness.

The experimental arrangement is shown in Fig. 1. The electromagnet has a 9-in. pole face and a gap width of about 3 in.; it is powered from eight 3000-ampere-hour 2-volt submarine batteries, and is capable of producing fields up to about 7000 gauss. Rose shims were placed on the pole faces, and nuclear resonance absorption measurements indicated that the field was uniform to within about 1 percent throughout a cylindrical volume between the pole faces which had a radius of 3 in. measured from the axis of the magnet. A circular brass cylinder 6 in. in diameter and $2\frac{1}{2}$ in. in height is supported between the pole faces with its axis along the magnet axis. The positron source is glued with Duco cement to the center of one of the parallel ends. A substantial amount of lead shielding is included within the cavity so that there are no direct paths from the source to the portion of the side wall that is viewed by the scintillation spectrometer. In this way the amount of annihilation radiation, which reaches the detector because of positrons annihilating in the brass walls, is minimized. The cavity is connected to a pumping system consisting of a VMF 50 oil diffusion pump and a mechanical pump. Because of an unfortunate history, rather long thin tubing is involved so that the pumping speed for evacuating the cavity is only about 3 liters/sec. Customarily the cavity is evacuated to a pressure of about 10^{-3} mm before being filled with the desired gas. Gas pressures in the cavity of between 1 and 2 atmospheres are used.

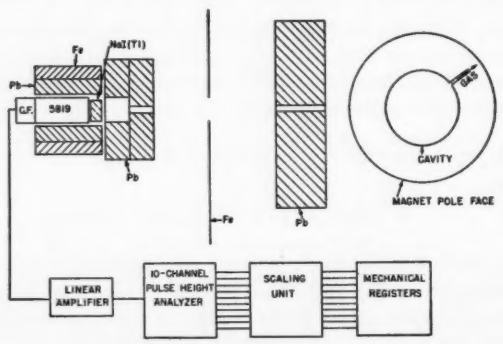

FIG. 1. Experimental arrangement.

Gamma rays due to positron annihilations are observed with a scintillation spectrometer in a direction at 90° to the direction of the magnetic field. Extensive lead shielding provided with a $\frac{1}{2}$ in. viewing hole is placed between the cavity and the crystal which is about 23 in. from the center of the magnetic field. Furthermore, an iron shield is connected so as to minimize stray flux from the magnet at the detector. The scintillation spectrometer uses a NaI(Tl) crystal and a 5819 photomultiplier tube, placed inside a lead and iron shield. The pulses from the photomultiplier are fed through a cathode follower and linear amplifier into a ten-channel differential pulse-height analyzer of conventional design using 1N38 Germanium diodes and thence into scalers and mechanical registers. Each channel of the analyzer can be expanded into 10 subchannels to obtain a detailed view of the energy spectrum. A subchannel spans an energy range of about 7.5 kev. Before each run the scintillation spectrometer is calibrated with a Na^{22} and a Cs^{137} source; during the course of an experiment (~12 hours) the calibration changes at most 2 subchannels.

4. GAMMA-RAY ENERGY SPECTRA

The observed energy spectra arise from several processes.

(1) Positron annihilation in the gas either as free positron-electron annihilation or as annihilation from the bound states of parapositronium or orthopositronium. The free positron-electron annihilation radiation will be a two-quantum process indistinguishable from the parapositronium decay.

(2) Positron annihilation from the walls of the container, which will be principally two-quantum annihilation.

(3) Degradation of the gamma rays arising from the above processes, due principally to Compton effect collisions in the gas or in the container walls.

The negative beta particles emitted by Cu^{64} will be completely absorbed in the container. There is a 1.34-

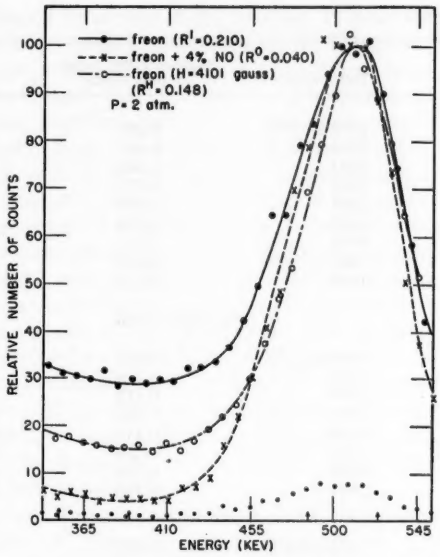

FIG. 2. Positron annihilation spectra: Number of counts *vs* γ-ray energy, normalized to 100 at the peak. Number of counts in vacuum with no magnetic field is indicated by small solid circles at bottom of graph. Peak region from 485 to 530 kev and valley region from 345 to 390 kev are indicated by arrows.

Mev gamma ray which occurs with the relative frequency (No. of γ)/(No. of β^+)=0.05 and will contribute to the background.

The magnetic quenching effect to be observed is a conversion of a certain amount of the three-quantum orthopositronium decay to two-quantum parapositronium decay, which will shift counts from the lower energy distribution characteristic of orthopositronium decay to the energy mc^2 characteristic of parapositronium decay. Compton degradation and the energy resolution of the apparatus tend to obscure this effect. Another complicating factor is a possible change in the background wall counts, and, in general, a change in the distribution of positron decays throughout the cavity when the magnetic field is changed. These factors will be discussed in detail later in the section on analysis of data.

The curves in Fig. 2 show some observed spectra. The solid curve drawn through the solid dots was observed with freon 12 (CCl_2F_2) in the cavity at a pressure of 2 atmospheres, and with no magnetic field present. The peak counting rate occurs for an energy of about 510 kev (mc^2). The counting rate in the valley region about 400 kev is contributed in part by degraded gamma rays from either two quantum or three quantum decays. The dashed curve drawn through the crosses was observed with the same conditions as for the previous curve with the exception that a small amount of NO gas was added. (The NO added contributed about 4 percent of the pressure of 2 atmospheres.) The large reduction in the valley to peak ratio, from about 0.210 to 0.040, caused by the introduction of the NO is interpreted as due to the conversion of all orthopositronium to parapositronium by collisions with NO molecules. Finally, the dot-dash curve through the open circles is observed with freon alone at a pressure of 2 atmospheres and with a magnetic field of 4101 gauss. The reduction in the valley to peak ratio compared to the ratio for curve 1 is interpreted as due to the conversion of $M=0$ orthopositronium annihilation from the three-quantum to the two-quantum decay, and is the static magnetic field quenching effect to be studied. All three curves were normalized to the same value at an energy of 510 kev.

5. ANALYSIS OF DATA

(5.1) Simplest Approach

To determine f, the fraction of orthopositronium atoms which decay by three-quantum annihilation, the following analysis is applied to spectra of the three types given in Fig. 2. The following formulas give the number of counts in the peak and valley regions in terms of the relevant parameters:

$$\begin{aligned} P^1&=N_pg_p+N_ag_p+N_og_o,\\ V^1&=N_ph_p+N_ah_p+N_oh_o,\\ P^0&=N_pg_p+N_ag_p+N_og_p,\\ V^0&=N_ph_p+N_ah_p+N_oh_p,\\ P^H&=N_p{}^Hg_p+N_a{}^Hg_p+N_o{}^Hfg_o+N_o{}^H(1-f)g_p,\\ V^H&=N_p{}^Hh_p+N_a{}^Hh_p+N_o{}^Hfh_o+N_o{}^H(1-f)h_p, \end{aligned} \tag{6}$$

in which the superscripts 1, 0, and H refer respectively to the conditions pure freon and no field, freon plus NO and no field, and freon and a field H. P is the number of counts in the peak of the energy spectrum which was arbitrarily taken to include counts in 6 subchannels which is an energy range of about 45 kev. V is the number of counts in the valley of the energy spectrum which was again taken to include counts in 6 subchannels. The quantities N_a, N_p, and N_o are, respectively, the number of free positron-electron annihilations, the number of parapositronium atom annihilations, and the number of orthopositronium atom annihilations in the region of the cavity viewed by the spectrometer. The quantity g_p is the average probability that an annihilation γ ray from a parapositronium decay will be counted in the peak region of the energy spectrum. This factor depends upon γ-ray degradation effects, the spatial distribution of annihilation events, the solid angle subtended by the detecting crystal, and the efficiency and resolution of the scintillation spectrometer. The average probability that an annihilation γ ray from a free positron-electron annihilation will be counted in the peak region is taken to be the same quantity, g_p. The quantity g_o is the average probability that a γ ray from an orthopositronium decay will be counted in the peak region. For the valley

TABLE I. γ-ray counts.

Condition		Peak counts	Valley counts	Ratio of valley counts to peak counts	$f(H)$
Case 1: Freon alone, no field					
	9:50 P.M.	13 594±0.9%	2798±1.9%	0.206	
	11:10 P.M.	12 856	2581	0.201	
	11:55 P.M.	12 316	2532	0.206	
	12:55 P.M.	11 476	2304	0.201	
	1:20 A.M.	11 269	2307	0.205	
	2:15 A.M.	10 815	2157	0.199	
	5:20 A.M.	9256	1953	0.211	
	6:20 A.M.	8595	1801	0.210	
	7:15 A.M.	8429	1818	0.216	
				Average=0.206	
Case H: Freon alone, field H					
H=1788 gauss	10:40 P.M.	19 784±0.7%	3296±1.7%	0.167	0.805
H=2572 gauss	11:30 P.M.	22 352	3546	0.159	0.734
H=3284 gauss	12:20 P.M.	24 927	3599	0.144	0.716
H=4101 gauss	1:40 A.M.	26 859	3912	0.146	0.675
H=5620 gauss	2:35 A.M.	30 524	4306	0.141	0.631
H=6590 gauss	3:50 A.M.	31 692	4261	0.134	0.588
H=6940 gauss	5:00 A.M.	29 681	4024	0.136	0.595
H=1140 gauss	6:00 A.M.	11 007	2091	0.190	0.933
Case 0: Freon plus NO, no field					
	8:05 A.M.	10 105±1%	474±4.6%	0.047	
	8:15 A.M.	10 052	437	0.043	
	8:25 A.M.		462	0.046	
				Average=0.0453	
No gas, no field[a]	1:55 A.M.	1084±3%	140±8.5%	0.129	
	7:40 A.M.	713	104	0.146	

[a] Note: Data on the condition no gas and magnetic field present were not taken on the run for which data are given in this table. However, data taken on other runs indicated that at a field of about 2500 gauss such a background reading has a number of counts in the valley about 3.5 percent of the gas plus field valley count and a number of counts in the peak about 0.7 percent of the gas plus field peak count.

region the corresponding probability factors are designated by h_p and h_o.

It is seen from the formulas that the same probability factors are used for the three different experimental conditions, which implies the assumption that the spatial distribution of the annihilations is the same in the three cases. Though it would be expected that this assumption is true for cases 1 and 0, it is not so apparently true for case H in which the motion of the positrons is greatly influenced by the presence of the magnetic field. Nevertheless, it is believed to be a good assumption, because the collimation of the γ-ray detection system is good enough so that only a small number of the counts arise from background wall counts in any of the cases, and spatial redistributions throughout the volume of the gas would not be expected to change the probability factors appreciably. It should be noticed that in case 0 the probability factors associated with orthopositronium atoms are taken to be g_p and h_p, which corresponds to the assumption that all orthopositronium atoms formed are quenched by collisions with NO molecules so that they decay by two-quantum annihilation. The assumptions have been implicitly made in the formulas (6) that the number of free positron-electron annihilations and the numbers of parapositronium and orthopositronium atoms formed are the same in the case of freon alone or of freon plus NO. However, it is not assumed that $N_p=N_p{}^H$, for example, since the presence of the magnetic field could change the number of positronium atoms formed in the active region of the gas. Finally, it is assumed for all three cases that $N_o=3N_p$ and $N_a=KN_p$, in which K is a constant; or that the relative number of orthopositronium to parapositronium atoms is the statistical weight factor in the three cases, and that the relative number of free positron-electron annihilations to parapositronium decays is the same in all three cases. Effectively, various of these assumptions imply that background counts arising from the annihilation of positrons in the cavity walls are neglected; this assumption will be discussed later in this section.

The experimental data give directly values for the P's and V's, and, with the assumptions mentioned above, Eqs. (6) can be solved for f to yield:

$$f=1/(1+y), \tag{7}$$

in which $y=\rho(R^1-R^H)/(R^H-R^0)$, where $\rho=P^1/P^0$, $R^1=V^1/P^1$, with analogous definitions for R^0 and R^H.[12]

Data from a typical run are shown in Table I. Each of the entries for number of counts corresponds to an observation time of 5 minutes and is the sum of the counts from 6 subchannels or from an energy range of about 45 kev. The percentage statistical accuracy is

[12] M. Deutsch, Massachusetts Institute of Technology Progress Report, August 31, 1951 (unpublished).

indicated for several of the readings. It is seen that for case 1 the statistical accuracy for the determination of the ratio of valley counts to peak counts is about 2 percent, and that the various determinations agree within expected statistical limits. For case H the counting rates are increased over those of case 1 by as much as a factor of 3 at high magnetic field values; this increase is due to the focusing of the positrons by the magnetic field in the center of the cavity which is the region viewed by the spectrometer. The statistical accuracy with which the ratios of valley counts to peak counts can be determined in case H is somewhat better than for case 1. The largest statistical uncertainty is encountered in case 0 because of the small number of valley counts; furthermore, these data were customarily taken at the end of a run when the source strength was weakest, because of the difficulty of cleaning out all the NO from the system in a reasonably short time once it had been admitted.

A few remarks must be made about the treatment of background wall counts which was employed to obtain the ratio of valley to peak counts given in the table. The method of analysis of the data assumed that all of the γ rays originate from annihilations in the gas and that none come from annihilations in the container walls. This assumption was essential because, otherwise, if wall annihilations occurred and if the number of wall annihilations relative to the number of gas annihilations varied with variation of the magnetic field, the shape of the energy spectrum would change with field for this reason alone. In actuality some counts are expected to arise from annihilations in the walls, so the problem is to subtract these counts from the peak and valley counts before beginning the analysis as presented. The data in Table I include peak and valley counts for the condition of no gas and no field. The majority of these counts arise from positron annihilations; only a small percentage of these counts would originate from the 1.34-Mev γ ray of Cu^{64} or external radiation sources (cosmic rays, laboratory contamination, etc.) as is clear from the energy spectrum for this case. The peak and valley counts in this case are about $\frac{1}{10}$ of the counts observed in case 1 when freon is present. The valley counts observed with no gas present are about $\frac{1}{3}$ of the valley counts observed in case 0 with freon plus NO, however, and the uncertainty as to the proper method of subtracting the wall background counts from the case 0 valley counts is an important source of error in this experiment. Peak and valley counts are also given in Table I for the condition of no gas but with a field present. At the higher fields these background counts amount only to about 3 percent of the case H counts.

The method of subtracting background wall counts consists in arbitrarily subtracting from the valley or peak counts observed in any case $\frac{1}{2}$ of the valley or peak counts observed with no gas and corresponding magnetic field. The motivation for this procedure is the remark that the background wall counts observed in the no gas case are certainly higher than would be expected when gas is present, because in the latter case the majority of the positrons will annihilate in the gas rather than in the walls. By subtracting $\frac{1}{2}$ of the no-gas counts an error of less than this subtracted number is expected. For cases 1 and H the corresponding error in valley-to-peak ratio is less than 1 percent; for case 0 it is less than 10 percent. The total uncertainty produced in f as a result of background counts is thus about 2 percent.

Values of $f(H)$ computed from these data by using Eq. (7) are shown in the last column. The quantity ρ is taken to be 0.82. The statistical counting accuracy to which the various values of $f(H)$ are determined is about $2\frac{1}{2}$ percent.

The magnetic field was measured either by the observation of the frequency of a nuclear resonance absorption for H or Li^7,[13] or by the use of a GE flip coil fluxmeter. Values of the field measured by nuclear resonances are quoted to four figures and those measured by the fluxmeter are quoted to three figures. In all cases the accuracy to which the field is measured at a particular region together with the homogeneity of the field (measured at times other than during a run) suffice to determine H over the region of interest to within at least 1 percent, which is quite adequate for this experiment.

A principal factor limiting the accuracy in the determination of $f(H)$ is the stability of the scintillation spectrometer. No temperature control of the NaI(Tl) crystal or of critical circuit components was provided. The circuit instabilities—due mainly to the characteristics of the 1N38 diodes which perform the pulse-height analysis function—were such that longer running times and hence higher counting rates would not have been too profitable. Furthermore the ambiguities in the treatment of background wall counts is of the order of the statistical accuracy.

Figure 3 includes a plot of all the experimentally determined values of f *vs* the magnetic field; in most

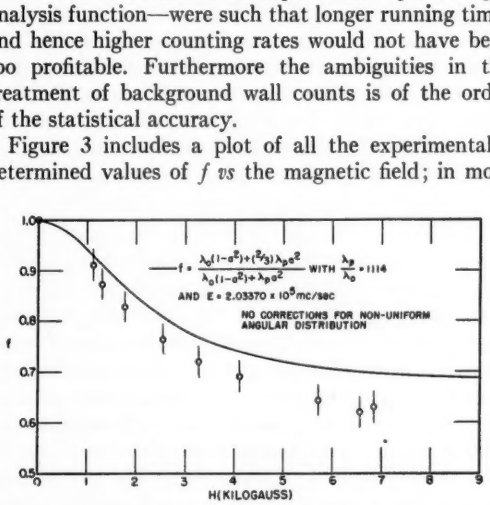

FIG. 3. Theoretical curve and experimental points for the fraction, f, of orthopositronium which decays by three-quantum annihilation as a function of the magnetic field. All experimental data were taken in freon at about two atmospheres pressure.

[13] R. V. Pound and W. D. Knight, Rev. Sci. Instr. **21**, 219 (1950).

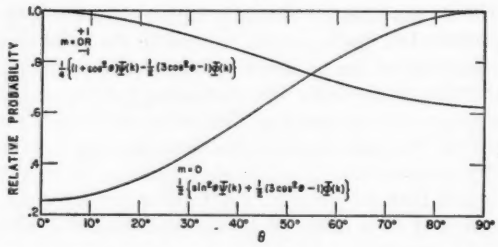

FIG. 4. Plot of Drisko's formulas for the relative probability of emission of annihilation quanta with energy kmc^2 by magnetic substates of orthopositronium. An average is taken over k between 0.71 and 0.79 as indicated by:

$$\int_{0.71}^{0.79}\Phi(k)dk\Big/\int_{0.71}^{0.79}\Psi(k)dk=0.229.$$

cases a point at a particular field is the average of several determinations of f made on independent runs. All data were taken in freon at about two atmospheres pressure. Errors which include counting statistics and background uncertainties are indicated for the points. The solid curve is a plot of the theoretical quenching formula (3′); the theoretical value of $\lambda_p/\lambda_o(=1114)$ is taken and the experimental value of the energy separation between parapositronium and orthopositronium is used. It is quite clear that the experimental points fall consistently below the theoretical curve. Additional data of somewhat less accuracy than the above were obtained with SF_6 and argon at two atmosphere pressure, and exhibited the same behavior as shown for the data of Fig. 3.

(5.2) Effect of Angular Distribution of Annihilation Radiation

The explanation for this discrepancy lies in the difference in the angular distribution of the annihilation quanta from the different magnetic substates of orthopositronium. Figure 4 is a plot of Drisko's formula for the relative probability of emission of annihilation quanta from the magnetic substates of orthopositronium as a function of angle for the energy range defined by $0.71\leq k\leq 0.79$ which corresponds to the valley region of our energy spectra. It is seen that there is a higher probability for the emission of an annihilation quantum in a direction at 90° to the field direction from the $M=0$ state of orthopositronium than from the $M=\pm 1$ substates. Such an angular distribution is of the right kind to explain the observed discrepancy, because by quenching the three-quantum decay of $M=0$ orthopositronium by a magnetic field (the decay of the $M=\pm 1$ substates are unaffected by the presence of the field), one removes more than $\frac{1}{3}$ of the triplet annihilation quanta observed by the scintillation crystal which is viewing at 90° to the direction of H.

Hence the formulas (6) used for the analysis of the experimental data must be modified to recognize this angular distribution effect, as indicated in the following equations:

$$\begin{aligned}P^1&=N_pg_p+N_ag_p+\tfrac{1}{3}N_oG_0g_o+\tfrac{2}{3}N_oG_1g_o,\\ P^0&=N_pg_p+N_ag_p+N_og_p,\\ P^H&=N_p{}^Hg_p+N_a{}^Hg_p+\tfrac{1}{3}N_o{}^HFG_0g_o\\ &\quad+\tfrac{1}{3}N_o{}^H(1-F)g_p+\tfrac{2}{3}N_o{}^HG_1g_o.\end{aligned}\tag{8}$$

There will be corresponding expressions for V^1, V^0, and V^H in which there will appear H_0 and H_1 instead of G_0 and G_1. In these formulas, for example, the product G_0g_o replaces g_o of Eqs. (6), and the product has the same meaning of average probability that an annihilation gamma ray from $M=0$ orthopositronium three-quantum decay shall be counted in the peak region. There is a corresponding interpretation for the product G_1g_o. The G's are introduced to take into account the difference in these probabilities for the different magnetic substates. It is permissible to set $G_0=1$, and then G_1 is the probability that a decay γ ray from a three-quantum decay of $M=+1$ or $M=-1$ orthopositronium will be emitted in a direction at 90° to the magnetic field (the observation direction) relative to the same probability for $M=0$ orthopositronium. This quantity can be evaluated from Eq. (4) as:

$$G_1=\frac{\Psi(k)+\frac{1}{2}\Phi(k)}{2[\Psi(k)-\frac{1}{2}\Phi(k)]}.\tag{9}$$

Its average value over the peak energy range from 470 to 510 kev is evaluated as $G_1(=0.62)$. In an analogous fashion take $H_0=1$ and evaluate $H_1(=0.80)$ over the valley energy range $k=0.71$ to 0.79 or from 360 to 400 kev. (The difference between these energy intervals and those shown in Fig. 2 is not significant in the evaluation of the G's and H's.)

$$\begin{aligned}&f=1/(1+Z),\\ &Z=\rho(R^1-R^H)/(R^H-R^0+C),\\ &C=\frac{2(1-H_1)}{1+2H_1}(R^1\rho-R^0K')+\frac{2(1-G_1)}{1+2G_1}R^H(K'-\rho),\\ &K'=(1+K)/(4+K).\end{aligned}\tag{10}$$

It will be noticed that if there were no difference in the angular distribution of the annihilation radiation from the different magnetic substates of orthopositronium, then $G_1=H_1=1$ and the formulas for f would be identical to Eq. (7).

In the above expression for f there appears the quantity K which is the relative number of free positron-electron annihilations to parapositronium decays. The quantity K can be determined in a manner similar to that used by Pond.[14] The increase in the number of peak counts between case 1 and case 0 (i.e., caused by the addition of a small amount of NO) is interpreted as due to the conversion of all orthopositronium atoms

[14] T. A. Pond, Phys. Rev. 85, 489 (1952).

to parapositronium atoms. Assuming equal probabilities for the formation of parapositronium and any magnetic substate of orthopositronium, one third of this observed increase will be the number of decays due to parapositronium atoms in case 1. The number of free positron-electron annihilations is then the number of peak counts in case 1 minus the number of parapositronium decays in case 1 as just determined and minus the fraction of orthopositronium decays which would appear among the peak counts in case 1 (this fraction is estimated from the γ-ray energy distribution curve of Ore and Powell[8]). An estimate of background wall counts can be made by observing the peak counts in the absence of gas in the cavity. As seen from Table I, the background counts amount to only about 10 percent of the gas counts; background counts can be subtracted from the peak counts of case 1 before the indicated calculation is performed. By such a calculation it is found that $K=16$ for freon; this value is the same magnitude as the values found by Pond for other gases.

By using this value for K, values of $f(H)$ can be computed for data like that given in Table I. It should be emphasized that, although K is not accurately known, it is sufficiently well known for the purpose at hand. The quantity K appears only in the part of formula (10) which represents the correction due to the angular distribution effect. Furthermore, K appears in the combination $K'=(1+K)/(4+K)$ which changes only slowly with change in K, when K is substantially greater than 1, as is the case here. Solutions were obtained for other values of K within a reasonable range and also for other reasonable values of G_1 and H_1; within statistical experimental errors these various solutions did not differ significantly.

Figure 5 shows the data of Fig. 4 recomputed to take into account the angular distribution effect. Statistical errors are indicated on the points. The experimental points are regarded as in adequate agreement with the theoretical quenching curve.

6. DETERMINATION OF RATIO OF DECAY RATES OF PARAPOSITRONIUM AND ORTHOPOSITRONIUM

For the determination of the ratio λ_p/λ_o from the experimental data, the following procedure is used. The correct form for the theoretical quenching curve is taken to be formula (3′). The energy separation between orthopositronium and parapositronium is taken as 2.0337×10^5 Mc/sec from the radio-frequency experiment, and the magnetic field was measured so that a is determined. Hence a value of f, calculated from the experimental data as described for Fig. 5, will yield a corresponding value of λ_p/λ_o, which will be designated Λ. Λ is given by $\Lambda=(1-F)/AF$, in which $A=a^2/(1-a^2)$. It will be appreciated that the greatest accuracy in the determination of Λ will come from experimental points which fall on the rapidly changing part of the magnetic quenching curve, and hence greatest weight must be given to these points. Formally, the uncertainty in the ratio Λ can be related to the uncertainty in the determination of $F(H)$ by the expression:

$$\Delta\Lambda=\Delta F/AF(F+\Delta F) \text{ in which } f=(2+F)/3.$$

For values of H above 5500 gauss, F is less than about 0.12, and, indeed, is of the order of ΔF so that $\Delta\Lambda$ can be large; and the weighting factor, which would be proportional to $1/(\Delta\Lambda)^2$, is considerably less than $\frac{1}{10}$ for all such points, relative to points taken at lower fields. Actually only experimental data for fields below about 4000 gauss are used for the determination of Λ. The value of Λ depends very critically upon the value of f so that a 2 percent error in f leads to an error in Λ of about 20 percent.

A determination of Λ, to provide a least squares fit to the theoretical formula (3′) for f, yields $\Lambda=1302$ with a standard deviation of ±100. An error of ±15 percent is assigned as a probable error to account principally for statistical counting errors and uncertainties in the treatment of the background. This value is in reasonable agreement with the theoretical value of 1114.

If the effect of collisions on the quenching of the decay of orthopositronium were appreciable under the experimental conditions, a correction would need to be made in the above procedure for computing λ_p/λ_o. Deutsch[15] has studied the rate of collision quenching of orthopositronium in freon and quotes a value of 0.3×10^6 sec^{-1} atmos^{-1}. Deutsch remarks, however, that this value is "rather uncertain," and it appears from the published data that the collision quenching may well be zero within the experimental error. If the value for collision quenching of 0.6×10^6 sec^{-1} at 2 atmos is used, our data would yield $\lambda_p/\lambda_o=1410$ under the assumption that collision quenching is the same for all magnetic substates of orthopositronium. In view of the uncertainty of the collision quenching rate, no correction is made for this effect in the value of $\lambda_p/\lambda_o(=1302)$ quoted above.

A more accurate measurement of λ_p/λ_o would require a considerable reduction in vacuum background counts, a greater statistical counting accuracy, improved sta-

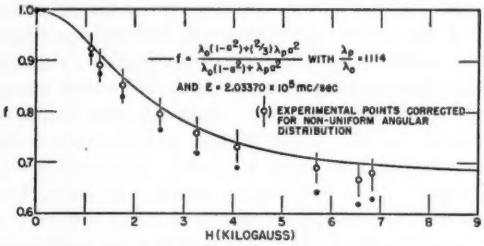

FIG. 5. Similar to Fig. 3 with the inclusion of corrections for the angular dependence of the annihilation radiation from the magnetic substates of orthopositronium. Solid dots are uncorrected points of Fig. 3.

[15] M. Deutsch, Phys. Rev. 83, 866 (1951).

bility of the scintillation spectrometer, a better knowledge of the collision quenching rate, and perhaps a more careful calculation of the angular distribution correction as regards averaging over the peak and valley energy regions. Furthermore, it was observed upon numerous occasions that the valley-to-peak ratio in freon would decrease with time over a period of several hours, suggesting some mechanism which was quenching positronium—perhaps a buildup of a gas impurity or of ionization due to the radioactivity. By sufficiently frequent changes of the gas this effect was believed to introduce no error in the determination of f to the order of 2 percent, but for any greater accuracy the effect would be troublesome.

It might be worth mentioning that one motivation for a more precise measurement is that the presence of $2S$ orthopositronium might be exhibited as an apparent high value of the ratio λ_p/λ_0. Indeed a 10^{90} increase in the apparent value of λ_p/λ_0 as calculated in this paper would result if the relative number of $2S$ positronium atoms to $1S$ positronium atoms is of the order of 1 to 30. A higher precision measurement of λ_p/λ_o is being planned, and a measurement of the magnetic quenching effect at $\theta=0°$ is under way.

PHYSICAL REVIEW VOLUME 98, NUMBER 6 JUNE 15, 1955

Rotational Excitation by Slow Electrons. II*

E. GERJUOY AND S. STEIN†
University of Pittsburgh, Pittsburgh, Pennsylvania, and Westinghouse Research Laboratories, East Pittsburgh, Pennsylvania
(Received March 14, 1955)

Theoretical cross sections for the rotational excitation of homonuclear molecules by slow electrons are applied to calculation of the fractional energy loss per collision (λ) in H_2. The theoretical losses are not more than $2.5(2m/M)$ and except at the lowest energies studied ($\sim$0.1 ev) are smaller than observed.

It would be desirable to have more direct experimental evidence of rotational excitation. For this reason we have calculated λ at 77°K in pure para-hydrogen and in normal hydrogen at that temperature. At electron energies $\sim$0.075 ev, the two λ's should differ by about 50 percent. Similarly, because of the altered rotational distribution, λ for deuterium differs from λ for H_2. Such differences, if observed, could hardly be accounted for on any other basis than rotational excitation.

I. INTRODUCTION

IN a previous paper[1] cross sections were calculated for the rotational excitation of homonuclear diatomic molecules by very slow electrons. These cross sections were used to compute λ, the average fractional energy loss per collision. In nitrogen it was found that, at energies below the vibrational threshold, excitation of rotational levels easily accounted for the observed excess of λ' (λ in units of $2m/M$) above the purely elastic value of unity. The calculations of I are here applied to hydrogen for which recent swarm measurements are also available.[2]

In Fig. 1 are compared the theoretical and observed values of λ' for H_2. The notation and procedure used to compute the curves are the same as in I. In hydrogen,[3,4] $B=7.5\times10^{-3}$ ev, $Q=0.393$ in units of ea_0^2, and we use a total cross section[5] $\sigma_t=13.5\pi a_0^2$, independent of energy. The calculations apply to H_2 at 290°K, with a Boltzmann distribution of rotational levels. The theoretical values of λ' are seen to be smaller than the experimental values even at average energies well below the vibrational threshold (0.54 ev). Our estimate of the energy loss due to rotational excitation accounts for only about half the observed excess of λ above $2m/M$. It is unlikely that these departures between the theory and observations are wholly due to vibrational excitation by higher energy electrons in the swarm.[6] The significance of the discrepancy between the curves of Fig. 1 is difficult to

* This research was supported in part by the U. S. Air Force under a contract monitored by the Office of Scientific Research, Air Research and Development Command. Part of a Thesis (by S.S.) submitted in partial fulfillment of the requirements for the degree of Doctor of Philosophy.

† Now at Westinghouse Atomic Power Division, Pittsburgh, Pennsylvania.

[1] E. Gerjuoy and S. Stein, Phys. Rev. **97**, 1671 (1955); referred to as I.

[2] R. W. Crompton and D. J. Sutton, Proc. Roy. Soc. (London) **A215**, 467 (1952).

[3] G. Herzberg, *Spectra of Diatomic Molecules* (D. Van Nostrand and Company, New York, 1950), second edition, p. 532.

[4] N. J. Harrick and N. F. Ramsey, Phys. Rev. **88**, 228 (1952).

[5] L. J. Varnerin, Jr., Phys. Rev. **84**, 563 (1951).

[6] For average electron energies of about 0.1 ev and assuming a Maxwellian distribution in the swarm, the magnitude of the vibrational excitation cross section required to account for the difference between the theoretical and experimental curves of Fig. 1 is $\sim0.3\pi a_0^2$. This probably is an underestimate of the required cross section since the tail of the electron energy distribution is expected to fall off more rapidly than Maxwellian. T. Holstein, Phys. Rev. **70**, 367 (1946); D. Barbiere, Phys. Rev. **84**, 653 (1951). Little is known about the value of the vibrational cross section near threshold, but the measured values at higher energies are much smaller than $0.3\pi a_0^2$. H. Ramien, Z. Physik **70**, 353 (1931); Chao, Wang, and Shen, Science Record (China) **2**, 358 (1949). Moreover, none of the somewhat disparate theoretical estimates are nearly this large. H. S. W. Massey, Trans. Faraday Soc. **31**, 556 (1935); T. Y. Wu, Phys. Rev. **71**, 111 (1947); P. M. Morse, Phys. Rev. **90**, 51 (1953); T. R. Carson, Proc. Phys. Soc. (London) **A67**, 909 (1954).

assess.‡ In H_2, the theoretical and experimental uncertainties in λ' are qualitatively similar to those in N_2 (Appendix of this paper), as are the complications involved in comparing the theoretical and experimental curves of Fig. 1. These results in H_2 reinforce the conclusion, voiced in I, that it would be desirable to have more direct experimental evidence that rotational excitation is a significant mechanism in the energy loss of slow electrons in homonuclear diatomic molecules. The differences between the low temperature rotational distributions of ortho- and para-H_2, and of D_2, suggest an experiment (Sec. II) which may be able to elucidate this question.

II. LOW-TEMPERATURE LOSSES

If rotational excitation is important in the energy loss of slow electrons, it may be expected that at low gas temperatures, with only the lowest rotational levels populated, λ' will change sharply at mean energies near an excitation threshold and will be sensitive to changes in the rotational distribution. In H_2, the lowest ($J=1$, and $J=2$) excited states lie at 0.015 and 0.045 ev above the ground ($J=0$) state. Thus at liquid air temperatures (77°K, $kT=0.0066$ ev) only the lowest rotational states are appreciably occupied. Also, the first excitation threshold in para-H_2 ($J=0\rightarrow J=2$) is 0.045 ev, while excitation of ortho-H_2 cannot occur below 0.075 ev ($J=1\rightarrow J=3$).

These remarks motivate the calculations summarized in Fig. 2, which exhibits λ' as a function of electron energy ϵ_a, in pure para-H_2 at[7] 77°K (curve A), and in normal[8] H_2 at that temperature (curve B), using $\sigma_t=13.5\pi a_0^2$. The losses at 77°K in normal D_2 (curve C) are also shown for comparison, again with $\sigma_t=13.5\pi a_0^2$. The assumption that σ_t is the same in ortho- and para-H_2, and in D_2, is discussed in Sec. III.

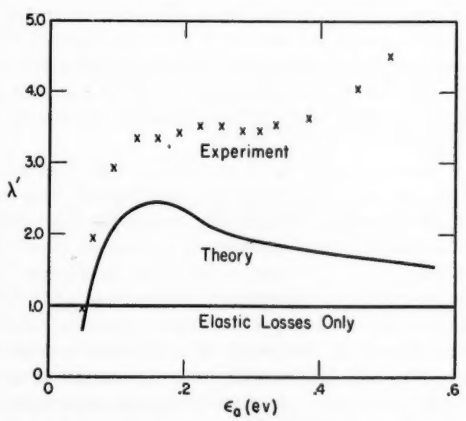

FIG. 1. Fractional energy loss per collision in H_2 (in units of $2m/M$), *vs* electron energy. ($T=290$°K.)

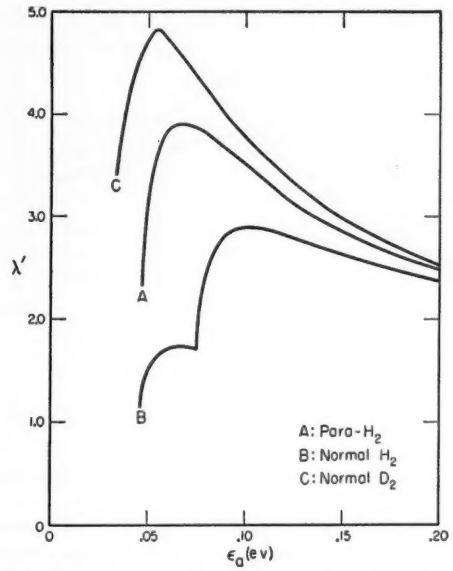

FIG. 2. Fractional energy loss per collision (in units of $2m/M$), *vs* electron energy. ($T=77$°K.)

At higher energies, all three curves of Fig. 2 rapidly approach each other. This result may be understood from Eq. (26) of I, which is increasingly valid as the electron energy is increased, and which shows that the rotational losses at high energies are independent of the rotational distribution and depend on the nature of the molecule only through the factor Q^2MB/σ_t. The quadrupole moment, Q, must be virtually the same for H_2 and D_2, while for these two gases the rotational constant, B, is inversely proportional[3,9] to the mass M. At lower energies, there is a distinct difference between curve C and the hydrogen curves, mainly due to the smaller threshold energies in D_2. The abrupt break in curve B occurs at the $J=1\rightarrow J=3$ threshold. At this energy, where only 25 percent of the normal H_2 mole-

‡*Note added in proof.*—We have adopted Varnerin's value of σ_t since his electrons are very nearly in thermal equilibrium, so that there is no uncertainty concerning the electron distribution function. However, Phelps (private communication) has made electron drift velocity measurements at very low E/p, i.e., with electron swarms which also must be very nearly in thermal equilibrium, and obtains $\sigma_t=10.5\pi a_0^2$, in good agreement with Crompton and Sutton (see reference 2). With this value of σ_t the agreement between the theoretical and experimental curves of Fig. 1 is considerably improved, especially at $\epsilon_a<.2$ ev.

[7] At electron energies above 0.045 ev, the calculated losses at 77°K are negligibly smaller than for a gas at absolute zero.

[8] At any temperature an ortho-para mixture in the ratio of the statistical weights is termed "normal;" i.e., the ortho-para ratio in normal H_2 is 3:1, and in normal D_2 is 2:1. In the absence of catalysts, the half-life for conversion of pure para-H_2 or of normal H_2 to the 77°K equilibrium mixture is very large, of the order of years at atmospheric pressure. The same is true for D_2, of course. In the swarm experiments, the electronic magnetic moment can catalyze the reaction. The electron densities are so low, however, that comparing with the known conversion by O_2 it is apparent that the half-life will not be seriously reduced in the presence of the swarm. See A. Farkas, *Ortho-hydrogen, Para-hydrogen, and Heavy Hydrogen* (Cambridge University Press, Cambridge, 1935), p. 79.

[9] G. Herzberg, see reference 3, pp. 141–143.

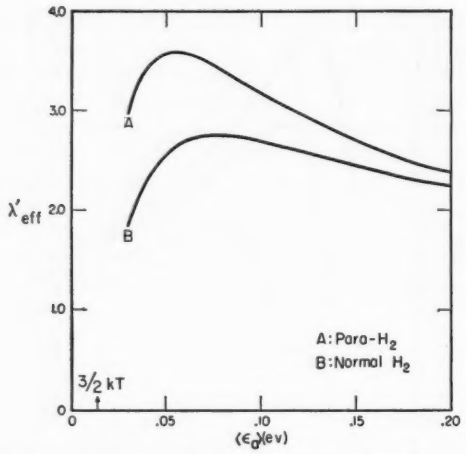

FIG. 3. Average low-temperature energy losses *vs* average energy.

cules can undergo inelastic collisions, the difference between curves *A* and *B* is most marked, the very large effect resulting in part from the somewhat fortuitous circumstance that the pure para-H_2 curve peaks at the same energy.

The curves in Fig. 2 are drawn for monoenergetic electrons and, as explained in Sec. III of I, must be averaged in some complicated fashion over the electron energy distribution in order to be directly comparable with the experimental fractional energy losses. That the averaging process is unlikely to wash out the differences between the curves of Fig. 2 is indicated by Fig. 3. Curves *A* and *B* of Fig. 3 are simple averages over a Maxwellian distribution of electron velocities of the corresponding curves of Fig. 2. Specifically, the quantity λ' plotted in Fig. 2 is given by Eq. (25) of I, namely

$$\lambda'=\frac{M}{2m}\frac{1}{N\sigma_t v_a\epsilon_a}\frac{dW}{dt},$$

whereas in Fig. 3 we plot as a function of $\langle\epsilon_a\rangle$ the quantity

$$\lambda_{eff}'=(M/2m)(\langle\epsilon_a\rangle\langle N\sigma_t v_a\rangle)^{-1}\langle dW/dt\rangle,$$

where the angular braces indicate an average over the electron distribution. The average energy loss per collision is $\langle dW/dt\rangle/\langle N\sigma_t v_a\rangle$ and λ_{eff}' has been taken to be this quantity divided by $(2m/M)\langle\epsilon_a\rangle$, the expected average elastic energy transfer per collision. For constant σ_t this definition makes λ_{eff}' identical with the fractional energy loss factor η (in units of $2m/M$) which is customarily reported.[10]

It appears therefore that comparison of low temperature swarm experiments in para-H_2, normal H_2, and in D_2, can yield significant information concerning the importance of rotational excitation in these homonuclear molecules. A further advantage of these proposed measurements is that the comparison is to be made at electron energies so low that vibrational excitation, if it is important at room temperature (Fig. 1), is here reduced by several orders of magnitude. We conclude that distinct differences in the measured values of λ' in these proposed experiments will be strong evidence in favor of the importance of rotational excitation in these and other gases, while failure to observe any differences, though perhaps open to other interpretations, will suggest strongly that the calculations of I overestimate the rotational excitation cross sections.

III. TOTAL CROSS SECTIONS

In Fig. 2, we have computed λ', the fractional energy loss per collision, on the presumption that the energy losses of slow electrons in H_2 are due largely to rotational excitation, i.e., to relatively infrequent inelastic collisions. It was also assumed that the total collision probability—inelastic plus elastic—is independent of the molecular rotational state. The observed differences between the values of λ' in para- and normal H_2 could prove very unlike the differences between curves *A* and *B* of Figs. 2 or 3, if the total cross sections σ_t actually were unequal in ortho- and para-H_2. Of course, if there are no inelastic losses, $\lambda'=1$, independent of σ_t. Thus, whether or not σ_t is the same for ortho- and para-H_2, it remains true that distinct differences in the measured values of λ' in low temperature swarm experiments in para- and normal H_2 will be strong evidence in favor of the importance of rotational excitation. However, we are concerned with the possibility that differences in σ_t may fortuitously cause the values of λ' to be very nearly identical in para- and normal H_2, so that the proposed experiments, when performed, might give the erroneous impression that rotational excitation is not a significant energy loss mechanism. Similar remarks pertain to the comparison of λ' for H_2 and D_2.

For these reasons it is gratifying that theoretical justification can be given for the assumption that σ_t is the same in ortho- and para-H_2, and in D_2. The difference between H_2 and D_2 stems solely from the dissimilar vibrational wave functions in these two molecules, both molecules having the same equilibrium separation,[3] but the D_2 oscillations being confined to a somewhat smaller region.[9] However, the range of oscillation is small in either case, and between H_2 and D_2 the deviation in $[s-s_e]_{Av}/s_e$, where s_e is the equilibrium separation, is only a few percent.[11] The cross sections for these molecules can hardly fail to be about equally close, as is evidenced by the success to within a few percent of calculations using a rigid rotator in the very analogous problem[12] of the scattering of slow neutrons by ortho- and para-H_2. Moreover, the inelastic cross sections, Eq. (20) of I, are very much smaller than the reported $\sigma_t=13.5\pi a_0^2$; consequently, equality of the elastic cross

[10] L. G. H. Huxley and A. A. Zaazou, Proc. Roy. Soc. (London) **A196**, 402 (1949), see p. 419.

[11] N. F. Ramsey, Phys. Rev. **87**, 1075 (1952).

[12] M. Hamermesh and J. Schwinger, Phys. Rev. **71**, 678 (1947).

sections σ_e implies equality of the total cross sections. Thus for the purposes of this paper it is sufficient that at low energies σ_e in H_2 be very nearly independent of the molecular rotational state. That this is indeed the case stems from the fact that, apart from the small contribution of long-range forces [comparable to the inelastic cross sections in Eq. (20) of I], the zero energy elastic cross section involves only incoming and outgoing s-waves, coupling through the spherical part of the interaction. At zero energy, consequently, the interaction, Eq. (12) of I, can be replaced by its spherical part, which part is readily seen to yield a scattering amplitude independent of J. A more detailed analysis[13] shows that σ_e remains very nearly independent of rotational state at energies less than a few tenths of an electron volt.

In conclusion, we stress: (1) We have not found any experimental comparisons of the total cross sections, and therefore are forced to rely on a theoretical argument. (2) Since our argument is wholly theoretical, and in many respects qualitative, we feel it would be worth while to measure these total cross sections using some suitable and identical procedure, e.g., Varnerin's.[5] (3) The swarm mobility and diffusion measurements[2] which yield λ' also yield a measurement of σ_t, so that the proposed swarm experiments can check, albeit somewhat equivocally[14] our assumption about σ_t.

[13] S. Stein, thesis, University of Pittsburgh, 1955 (unpublished).

[14] Since the swarm experiments determine an effective σ_t from complicated averages over the electron distribution, and since the electron energy distribution is affected by inelastic losses, it is possible for the swarm experiments to indicate unequal σ_t even though the total cross sections in these gases actually are the same. Thus, for definitive experiments detailed knowledge of the distribution functions is required, but we may expect that there should be at least qualitative significance to comparing the magnitudes of $\sigma_{t\,\mathrm{eff}}$ in different gases.

We are happy to thank Dr. Arthur V. Phelps for his very helpful comments.

APPENDIX

The examination of the validity of the theory in H_2 parallels I, Sec. IV. Because both Q and the molecular radius r_0 are smaller in H_2 than in N_2, and because we are here interested in even slower electrons than in the previous paper, the only question requiring detailed examination is the ratio A_1/A_2 of "near-" and "far-" field amplitudes. Using, much as in I, the Wang potential[15] with the nuclei at their equilibrium separation to compute for H_2 the quantity $f_a(\theta)$, we obtain for small k_a

$$A_1=1.8(k_a a_0)^2 A_2. \tag{1}$$

Estimating $f_a(\theta)$ from the measured elastic cross section gives nearly the same result, the factor being 2.3 instead of 1.8. At the vibrational threshold, Eq. (1) makes $A_1/A_2=0.07$; at 0.075 ev, $A_1/A_2=0.01$. These numbers indicate that the cross sections of I are valid for H_2 at electron energies below the vibrational threshold, and are surely valid at the very low energies of interest in the proposed low-temperature experiments.

[15] S. C. Wang, Phys. Rev. **31**, 579 (1928).

PHYSICAL REVIEW VOLUME 98, NUMBER 6 JUNE 15, 1955

Generation of Coulomb Wave Functions by Means of Recurrence Relations

IRENE A. STEGUN AND MILTON ABRAMOWITZ
Computation Laboratory, National Bureau of Standards, Washington D. C.

(Received March 9, 1955)

A discussion of the computation of Coulomb wave functions from their recurrence relations is given. Specifically, it is demonstrated that the regular solution F_L and the irregular solution G_L may be obtained recursively based on the knowledge of the functions for $L=0$.

THE present paper is concerned with the computation of the regular and irregular Coulomb wave functions F_L and G_L, for L a positive integer, with the aid of the recurrence relations satisfied by these functions. Thus if y_L stands for either $F_L(\eta,\rho)$ or $G_L(\eta,\rho)$ we have[1]

$$L\frac{dy_L}{d\rho}=(L^2+\eta^2)^{\frac{1}{2}}y_{L-1}-\left(\frac{L^2}{\rho}+\eta\right)y_L, \tag{1}$$

$$(L+1)\frac{dy_L}{d\rho}=\left[\frac{(L+1)^2}{\rho}+\eta\right]y_L-[(L+1)^2+\eta^2]^{\frac{1}{2}}y_{L+1}, \tag{2}$$

$$L[(L+1)^2+\eta^2]^{\frac{1}{2}}y_{L+1}=(2L+1)\left[\eta+\frac{L(L+1)}{\rho}\right]y_L-(L+1)[L^2+\eta^2]^{\frac{1}{2}}y_{L-1}. \tag{3}$$

[1] J. L. Powell, Phys. Rev. **72**, 626–627 (1947).

In addition, we have the Wronskian relations

$$F_L'G_L-F_LG_L'=1, \tag{4}$$

$$F_{L-1}G_L-F_LG_{L-1}=L(L^2+\eta^2)^{-\frac{1}{2}}. \tag{5}$$

The method is entirely similar to that employed for the generation of Bessel functions of integral order.[2] This is to be expected in view of the fact that the functions F_L and G_L bear the same relation to each other as the Bessel functions J_n and Y_n or the modified Bessel functions I_n and K_n; namely, for $L\to\infty$, that F_L is a decreasing function of L while G_L is an increasing function of L. The recurrence relation (3) will be stable when applied in decreasing order to F_L and in increasing

[2] Bessel Functions, Part II (British Association for the Advancement of Science, Cambridge, 1952). The method is credited to J. C. P. Miller.

order to G_L. By this we mean no error will be propagated if we generate $F_L(G_L)$ in decreasing (increasing) order. The technique described may be applied for other sets of functions such as the spherical Bessel functions.

To generate the functions G_L we need only be able to calculate G_0 and G_0'. The application of (2) will produce G_1 and then (3) may be used to obtain as many values of G_L as may be desired.

To determine the values of F_L recursively for given η and ρ it would appear that F_L and F_L' (say) would be required as starting values for some $L>0$. Actually, this is not the case as we shall show. We can start with arbitrary values $\bar{F}_L$ and $\bar{F}_{L+1}$ which we consider as the values of the solution of the respective differential equations at the given η and ρ. Then, given $\bar{F}_{L+1}$, there is a one-parameter family of α and β such that

$$\alpha F_{L+1}+\beta G_{L+1}=\bar{F}_{L+1}. \tag{6}$$

In order to fix α and β uniquely we require that

$$\alpha F_L+\beta G_L=\bar{F}_L. \tag{7}$$

Then, by virtue of (5) we can solve this system for α and β. For example, with $\bar{F}_L=1$, $\bar{F}_{L+1}=0$ we get

$$\alpha=G_{L+1}\frac{\{(L+1)^2+\eta^2\}^{\frac{1}{2}}}{(L+1)}, \quad \beta=-\alpha\frac{F_{L+1}}{G_{L+1}}. \tag{8}$$

If we now generate a sequence $\bar{F}_m\equiv\alpha F_m+\beta G_m$ for $m=L-1, L-2, \cdots 1, 0$ by the use of (3) we have

$$\bar{F}_m=\alpha\left\{F_m-\frac{F_{L+1}}{G_{L+1}}G_m\right\}. \tag{9}$$

Since $F_L\to 0$ and $G_L\to\infty$ as $L\to\infty$ we may choose L so large that the second factor in the brackets can be made as small as we please and thus

$$\bar{F}_m\sim\alpha F_m \tag{10}$$

where $\alpha=\alpha(L,\eta,\rho)$ and α is defined in (8).

It is now clear that if α is known we can determine F_m from $\bar{F}_m$. However, the knowledge of α implies the knowledge of G_{L+1}. On the other hand, if for some integer m where $0\leq m\leq L'\ll L$ we know F_m, then by virtue of (10) we can determine $\alpha\sim\bar{F}_m/F_m$ and use this value of α to calculate F_k for $0\leq k\leq L'\ll L$ from the corresponding $\bar{F}_k$. In particular we can therefore take $\alpha=\bar{F}_0/F_0$ provided $F_0\neq 0$. In practice, this means that if η and ρ are near a zero of F_0 we should choose some other value for m, say $m=1$.

In those situations where the G_L are also desired the procedure may be modified in the following manner. From G_0 and G_0' we generate the sequence G_m in increasing order, the sequence $\bar{F}_m$ being generated from $\bar{F}_L, \bar{F}_{L+1}$ in decreasing order as above. However, instead of computing α from $\bar{F}_0\sim\alpha F_0$ we can now use

$$F_0G_1-F_1G_0=\alpha^{-1}(\bar{F}_0G_1-\bar{F}_1G_0)=(1+\eta^2)^{-\frac{1}{2}},$$

which follows from (5) for $L=1$.

As an illustration of the method let us take $\eta=5$, $\rho=5$ starting with $\bar{F}_{31}=0$, $\bar{F}_{30}=0.1$. Generating the values of $\bar{F}_m$ carrying ten figures, we get

$$\begin{aligned}
&\bar{F}_{20}=13854\ 08764, && F_{20}=0.0^{13}1883\ 426_8,\\
&\bar{F}_{11}=35942\ 29977.\times 10^7, && F_{11}=0.0^6 4886\ 261_1,\\
&\bar{F}_{10}=17217\ 50614.\times 10^8, && F_{10}=0.0^5 23406\ 746_8,\\
&\quad\cdots && \quad\cdots\\
&\bar{F}_1=16379\ 10103.\times 10^{12}, && F_1=0.02226\ 695_7,\\
&\bar{F}_0=20355\ 68006.\times 10^{12}, && F_0=0.02767\ 301_2.
\end{aligned}$$

To eight significant figures the value of $F_0=0.02767\ 3012$, from which we find $\alpha^{-1}=1.3594737\times 10^{-23}$. An independent calculation shows that the values of F_L indicated above are correct to approximately eight significant figures. Starting now with $G_0=18.1933$ and $G_1=21.7261$ and generating the successive values of G_L, we get ultimately $G_{19}=79310\ 46945\times 10^2$, $G_{20}=62908\ 14544\times 10^3$. Checking the results with the Wronskian relation (5) shows the values of G_{19} and G_{20} to be correct to approximately six significant figures. Similar calculations were made for $\eta=10$, $\rho=1$ and $\eta=1$, $\rho=10$ with comparable success.

A suggested procedure for carrying out the aforementioned technique is as follows. Suppose the values of F_m and G_m are desired for $0\leq m\leq L'$. Then choose two values of L (say, L and $L+5$) with $L\gg\rho$ and $L\gg L'$. Generate the sequences F and G for both values of L and compare. If the results do not agree for $0\leq m\leq L'$ then start with $L+10$ and compare the results with those for $L+5$.

The derivatives F_L' and G_L' can be generated from (1) and (2) to provide a check once the desired F_L and G_L have been obtained. An additional check is obtained from (4).

The values of F_m may also be derived in the following manner. Once the values of $\bar{F}_m$ have been generated, it remains only to determine the normalizing factor α. This may be done with the aid of the relations[3]:

$$\rho\cos\rho=\left(\frac{e^{2\pi\eta}-1}{2\pi\eta}\right)^{\frac{1}{2}}\sum_{L=0}^{\infty}(2L+1)\cos\delta_L(\eta)\cdot F_L(\eta,\rho), \tag{11}$$

$$\rho\sin\rho=\left(\frac{e^{2\pi\eta}-1}{2\pi\eta}\right)^{\frac{1}{2}}\sum_{L=0}^{\infty}(2L+1)\sin\delta_L(\eta)\cdot F_L(\eta,\rho), \tag{12}$$

where

$$\delta_0=0,$$

$$\delta_L(\eta)=\frac{L\pi}{2}+\sum_{k=1}^{L}\arctan(\eta/L).$$

Since this procedure will yield the values of F_0 and F_1, only G_0 need be computed independently. G_1 will be found from (5) with $L=1$, and (3) may then be employed to generate as many additional values of G_L as may be desired.

[3] The authors are indebted to their colleague, Dr. P. Henrici, for having provided them with these relations.

Letters to the Editor

PUBLICATION of brief reports of important discoveries in physics may be secured by addressing them to this department. The closing date for this department is five weeks prior to the date of issue. No proof will be sent to the authors. The Board of Editors does not hold itself responsible for the opinions expressed by the correspondents. Communications should not exceed 600 words in length and should be submitted in duplicate.

Collision Alignment of Molecules, Atoms, and Nuclei

NORMAN F. RAMSEY*

Clarendon Laboratory, Oxford, England, and Harvard University, Cambridge, Massachusetts

(Received April 4, 1955)

RECENTLY, there have been a number of experiments on the polarization of scattered beams of particles. Such polarization is reasonable in scattering since the axial spin vector of the particle can be associated with the axial angular momentum vector that is related to the angle of scattering. However, in the transmitted beam no simple polarization is expected since there is no axial vector with which the particle spin can be associated. However, it is the purpose of this note to point out that if the particle spin is greater than $\frac{1}{2}$, the orientation properties frequently described as alignment[1,2] can be achieved in the transmitted beam, e.g., the spin orientation states corresponding to $M_I=\pm 1$ relative to the direction of motion may be more occupied than the state $M_I=0$. This alignment of the transmitted beam is related to the more complex orientations achievable in the scattered beam when the spin is greater than $\frac{1}{2}$.[3] However, from an experimental point of view alignment of the transmitted beam instead of a scattered beam has the advantage that the transmitted beam intensity is ordinarily much greater. For particles of spin I, the order k of the degree of orientation[2] of the transmitted beam may include any even number up to $2I$.

With beams of molecules attenuated by a scattering vapor, the geometrical shape of the molecule leads to a considerable dependence of the cross section upon M_J. For example, with beams of linear molecules attenuated by a monatomic scattering vapor whose kinetic velocities are considerably less than those of the molecular beam, factors of two or more in cross section may exist between the $M_J=0$ and $M_J=\pm J$ states. For such a case amounts of molecular alignment can be achieved for an attenuation of the beam by only a factor of two or so. For higher atomic velocities of the attenuating gas the amount of alignment is reduced but is still appreciable. In any specific case the amount of alignment produced depends on the molecular shape, the mean velocity of the incident molecule (no alignment can result from pure S scattering), the mean velocity of the scattering atom, and the mean rotational angular velocity of the molecules.

Atoms in electronic P or higher states similarly should be aligned in atomic beams that have been attenuated by scattering.

In experiments with either atoms or molecules, the existence of collision alignment should be observable in many ways. For example, in molecular beam magnetic resonance experiments with molecular hydrogen,[4] separate nuclear resonances occur for different values of M_J so the relative intensity of these resonances should be modified by attenuation with a scattering gas. Alternatively, observations of the apparent cross section in successive scattering attenuators should indicate the occurrence alignment by a diminution in the apparent cross section in the last attenuator in comparison with the first. In such an experiment, however, care must be taken to distinguish this effect from those corresponding to the changes in molecular velocity distribution by the attenuation.

In addition to its value as a tool for the study of collision phenomena and molecular shapes, collision alignment should be useful in some cases as a replacement for the inhomogeneous deflecting fields in molecular and atomic beam magnetic resonance experiments. For example, if an atomic beam passes through two successive attenuation regions, the total attenuation will be less if the atom retains its orientation than if it is reoriented between the two attenuation regions. Consequently, a diminution in transmitted beam intensity indicates the presence of a resonance reorientation of the atom. An atomic beam magnetic resonance experiment with collision alignment of the atoms possesses the advantage that much broader and more intense beams can be used than with the conventional molecular beam resonance method.

At least in principle, collision alignment of transmitted nuclear particles could be achieved for nuclei of spin greater than $\frac{1}{2}$. However, the significance of collision alignment in nuclear research is diminished by the fact that most high-energy nuclear particles have spins of 0 or $\frac{1}{2}$. Although the deuteron has a spin of 1, nuclear attenuation experiments are made more difficult by its electrical charge and consequent ionization energy losses. However, some alignment of the transmitted beam should occur in high-energy deuteron total cross-section experiments[5] and a slight departure from simple exponential attenuation should arise from alignment. Even with incident nucleons of spin 0 or $\frac{1}{2}$, alignment considerations affect nuclear reaction problems. For example, Bohr and Mottelson[6] find nuclear surface deformations as large as 30 percent for some nuclei while the transit time of an incident high-energy nucleon past a nucleus is small compared to the rotational period of the deformed surface. Consequently, even from purely

geometrical considerations nuclear reactions will take place dominantly with nuclei in preferred states of alignment.

* Partially supported by the John Simon Guggenheim Memorial Foundation.

[1] B. Bleaney, Phil. Mag. **42**, 441 (1951) and O. J. Poppema, thesis, Rijksuniversiteit te Groningen, 1954 (unpublished).

[2] S. R. De Groot, Physica **18**, 1201 (1952).

[3] L. Wolfenstein, Phys. Rev. **92**, 123 (1953); W. Lakin and L. Wolfenstein, Phys. Rev. **90**, 365(A) (1953); and A. Simon, Phys. Rev. **90**, 326 (1955).

[4] Kolsky, Phipps, Ramsey, and Silsbee, Phys. Rev. **87**, 395 (1952).

[5] Millburn, Birnbaum, Crandall, and Schecter, Phys. Rev. **95**, 1268 (1954).

[6] A. Bohr and B. R. Mottelson, Kgl. Danske Videnskab. Selskab, Mat.-fys. Medd. **27**, No. 16 (1953).

Saturation of Nuclear Electric Quadrupole Energy Levels by Ultrasonic Excitation*

W. G. Proctor and W. H. Tantila

Department of Physics, University of Washington, Seattle, Washington

(Received April 4, 1955)

We have observed the decrease in the population difference between the degenerate $m=\pm\frac{1}{2}$ and the $m=\pm\frac{3}{2}$ quadrupole energy levels of Cl^{35} in $NaClO_3$ following a long pulse of ultrasonic excitation at the transition frequency. The experiment was performed at the temperature of liquid nitrogen, for which the transition frequency is 30.63 Mc/sec and the thermal relaxation time 0.94 sec.

The population difference was measured by the amplitude of the transient nuclear induction signal following a short (50 μsec) pulse of radio-frequency magnetic flux at the transition frequency.[1] In our experiment, the signals were induced in a second coil, a receiver coil, perpendicular to the exciting or transmitter coil, as suggested by Dean.[2] The sodium chlorate crystal, about 1 cm^3 in volume, located between the above coils, received ultrasonic energy in the (1,0,0) direction across a polished face in contact with the polished face of a long, narrow halite crystal. The latter was joined similarly to a second halite crystal, joined in turn to an X-cut quartz crystal, used as an ultrasonic transducer. Rubber-vaseline vacuum grease was used as an interface medium. The halite crystals, about 1 cm^2 in cross section, were each about 4 cm long, separating the quartz transducer from the $NaClO_3$ sample by about 8 cm. The transducer was excited by a second transmitter of variable frequency; current reached the transducer through a coaxial cable, of which the outer, grounded conductor was flared out at the end to enclose the quartz transducer completely and make contact with the silver coating of its outside face, thus preventing magnetic fields from originating from the transducer to a great extent.

The ultrasonic pulse was 0.3 second in duration; the rf power supplied to the transducer was about 5 watts. After a delay of about 0.03 second, the population difference was examined. The cycle was repeated at 1-second intervals. Depending upon a number of variables, it was observed that the amplitude of the transient was diminished to 20 percent or less of its equilibrium amplitude only when the transducer was excited at the transition frequency. To separate the ultrasonically induced quadrupole transitions from a spurious effect which would be obtained by dipole transitions caused by magnetic flux leaking into the sample region, the resonant transmitter and receiver coils were short-circuited by relays during the ultrasonic excitation period. Further, after a small gap ($\sim\frac{1}{2}$ mm) was introduced between the sample crystal and its neighboring halite crystal, interrupting the path of ultrasonic energy while providing a geometry and transducer loading for which one would expect almost identical leakage fluxes, no attenuation was discernable. A further possible spurious effect, due to the generation of a temperature gradient in the sample crystal, is not likely since the transducer heating should not be frequency-dependent; the transducer, driven at the third harmonic, tuned broadly when loaded.

Quantitative measurements are now under way. The experiment was performed in order to be able to measure the direct and Raman process contributions to the thermal relaxation time.[3]

We would like to thank Professor E. A. Uehling and Dr. C. H. Chang for the stimulation of their continued interest.

* This research was supported by the United States Air Force, through the Office of Scientific Research of the Air Research and Development Command.

[1] M. Bloom and R. E. Norberg, Phys. Rev. **93**, 638 (1954).

[2] C. Dean, Phys. Rev. **96**, 1053 (1954).

[3] J. Van Kranendonk, Physica **20**, 781 (1954).

Experimental Evidence for Thermal Spikes in Radiation Damage*

W. Primak

Chemistry Division, Argonne National Laboratory, Lemont, Illinois

(Received April 18, 1955)

Theoretical work[1-3] and experimental measurements of stopping power indicate that toward the ends of their ranges in solids, energetic atoms lose $\sim 10^4$ ev to the lattice at a rate of about 10^9–10^{10} ev/cm. Brooks[4] discussed the resultant temperature fluctuations (termed thermal spikes). He showed that the thermal spikes in the electronic system are small, behave nearly independently, and cannot produce marked structural effects. For the lattice, the temperature distribution would be between cylindrical and spherical

$$T \sim 3(10^{-21})(q/c)(x^2t)^{-1}\exp(-r^2/4x^2t) \quad \text{or}$$
$$10^{-21}(Q/c)(x^2t)^{-\frac{1}{2}}\exp(-r^2/4x^2t),$$

where the symbols mean: T, temperature (°C); q, rate of energy loss (ev/cm); c, volume heat capacity (cal/cm³); x, thermal diffusivity (cm/sec¹); t, time (sec); r, radial distance (cm); Q, total significant energy loss (ev). Thus after $\sim 10^{-11}$ sec, the thermal spike encompasses $\sim 10^4$ atoms which are experiencing a temperature rise ~ 10°C in good conductors, e.g., metals, graphite, and diamond, and several hundred degrees in intermediate conductors, e.g., quartz. Effects have been attributed[5,6] to these thermal spikes in some cases where propagation or conservation mechanisms could be invoked to permit the energy of the thermal spike to be effective before it was dissipated. However, since the displacement rates, the energy loss rates, and the proper values of the physical properties are all uncertain, it has not been possible, in general, to evaluate the contribution of the thermal spikes to the irradiation effects which are observed. In a poor conductor, like vitreous silica, the corresponding temperature rises should be several thousand degrees and hence readily observable.

Primak, Fuchs, and Day[7,8] investigated the changes in properties observed in vitreous silica and quartz irradiated simultaneously in a nuclear reactor and found that the damage could be readily followed by measuring density changes. Initially (below 2 units),[9] the density of vitreous silica increased about 0.18 percent per unit, and the density of quartz decreased about 0.07 percent per unit; by 60 units, the change in vitreous silica had saturated at 2.1 to 2.7 percent while the density of quartz had decreased about 5 percent; and by 1000 units, the quartz had become completely vitreous and indistinguishable from the irradiated vitreous silica. The density changes in quartz were followed in greater detail over the range 50–200 units by Wittels and Sherrill[10,11] who found that in this range, the dilatation of quartz accelerated to a rate 0.2 percent/unit (about 3 times as great as that observed in the early stages of irradiation by Primak, Fuchs, and Day) before it began to saturate. Such a damage-dosage curve is quite unique since most substances show a simple saturation curve for their property changes on irradiation. Since the thermal conductivity (and hence the thermal diffusivity) is changing with the other properties,[12] it seems reasonable to attribute the effect to the increasing contribution of the thermal spikes to the damaging since the slowing down processes must necessarily remain much the same. This is more reasonable than Wittels' and Sherrill's[11] mechanism, which, since the density is decreasing and the structure "opening up" on irradiation, should lead to simple saturation. Further, free interstitials do not seem to be present for an differential thermal analysis there is little or no stored energy[13] found in irradiated quartz[8] and none in irradiated vitreous silica.[14] Supporting evidence for the importance of the thermal spike mechanism of damage in disordered silica structures is the character of the annealing of irradiated vitreous silica[15] and the marked decrease of coherent x-ray scattering resulting from the irradiation of quartz and absent for some other substances (e.g., diamond and silicon carbide) which show large property changes on irradiation.[7,13]

The thermal spike mechanism may be of similar importance in the metamictization of minerals, and it may be necessary to modify the views expressed in earlier articles[7,13] accordingly.

* Based on work performed under the auspices of the U. S. Atomic Energy Commission.

[1] H. M. James, Oak Ridge National Laboratory Report ORNL-307, March, 1949 (unpublished).
[2] F. Seitz, Discussions Faraday Soc. **5**, 271 (1949).
[3] F. W. Brown, North American Aviation Company Report NAA-SR-4, February, 1948 (unpublished).
[4] H. Brooks, Knolls Atomic Power Laboratory Report KAPL-360, August, 1950 (unpublished).
[5] W. Primak, Argonne National Laboratory Internal Memorandum ANL-OCS-412, January, 1955 (unpublished).
[6] F. Seitz, Phys. Rev. **98**, 1530(A) (1955).
[7] Primak, Fuchs, and Day, Phys. Rev. **92**, 1064 (1953).
[8] Primak, Fuchs, and Day, Bull. Am. Ceram. Soc. **33**, No. 4, Program page 25, following page 130 (April, 1954) (to be published).
[9] One unit is about 10^{18} n/cm^2 effective in producing damage; see reference 13.
[10] Units used by Wittels and Sherrill and by Primak have not been reconciled yet.
[11] M. Wittels and F. A. Sherrill, Phys. Rev. **93**, 1117 (1954).
[12] R. Berman, Proc. Roy. Soc. (London) **A208**, 90 (1951).
[13] W. Primak, Phys. Rev. **95**, 837 (1954).
[14] W. Primak (unpublished).
[15] W. Primak and H. Szymanski (to be submitted for publication).

Superfluidity in Liquid He³†

M. J. Buckingham

Department of Physics, Duke University, Durham, North Carolina

(Received March 7, 1955)

In a recent note, Rice[1] has suggested that, at sufficiently low temperatures, the liquid state of the helium isotope He³ may exhibit superfluidity. This conclusion is based on the results[2] of a pair-cell model for the liquid, which leads to a spectrum for excited states, corresponding to the hindered rotational states of a pair of atoms. In this spectrum, there is a finite energy gap between the ground and first-excited states and the presence of this gap led to the suggestion of superfluidity below some temperature lower than that corresponding to the energy gap.

It is the purpose of this note to point out that a simple extension of these considerations shows that a finite gap in the spectrum cannot be expected for a liquid of Fermi particles, so that, like the ideal gas model, the cell model actually leads one to expect the absence of superfluidity in liquid He³.

Let us consider a pair model for a quantum liquid. If the lifetime of the rotational states is not long com-

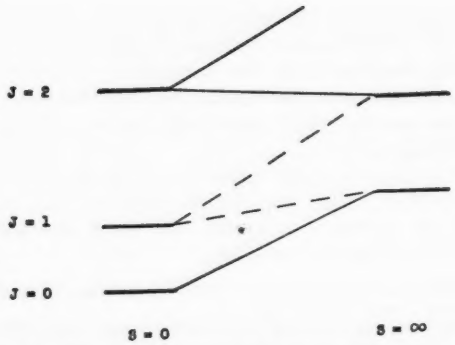

FIG. 1. Schematic dependence of rotational energy levels on the magnitude S of hindrance to rotation. Full lines represent symmetric states. Broken lines represent antisymmetric states.

pared with the period of rotation, the energy values of the states could not be sharply defined, and would be spread over a range of the same order as the energy itself. Thus, we could not assume, in this case, the existence of a finite gap between the ground and excited states.

Without committing ourselves as to its validity, let us then for the moment accept the alternative assumption; namely that the lifetime is long compared to the period. This means that the orientation of the rotation of a given pair is fixed and we must require that the hindrance to rotation (the magnitude of which we denote by a parameter S) provided by neighboring atoms is constant in time for that particular pair. For example, if we suppose, with Rice, that the average hindrance corresponds roughly to restricting a pair to motion in a plane, we could represent by S the maximum of potential as a function of angle in this plane; the potential being that of the van der Waals repulsive forces due to other atoms. We note that the effective diameter of the rotational orbits is of the same order as the mean distance between atoms, and that the whole system is to represent a *liquid* state. Even at the absolute zero of temperature the fluctuations in the relative positions of neighboring atoms should then result in some pairs having no other atoms within their orbit—these will be nearly free to rotate ($S \rightarrow 0$). Others must find neighboring atoms within their orbit so as completely to restrict their rotation ($S \rightarrow \infty$). We do not require an infinite local density to make S infinite; we merely require a few neighboring atoms (which must be considered fixed, if S is to be constant) sufficiently close to prevent our pair of atoms from exchanging position. We are thus forced to the conclusion that S will assume values ranging from zero to infinity for different pairs in the liquid.

Figure 1 indicates the well-known way in which the rotational energy levels vary with the magnitude of restriction. For large S, each level becomes degenerate, a component arising from what were both odd and even J values (angular momentum) when $S=0$.

Now for J even (or zero), the state is symmetric in the space variables; for odd J, antisymmetric. If the atoms we are considering are Fermi particles with spin $\frac{1}{2}$ (He^3 atoms), the even-J states must be antisymmetric in the spin variables—i.e., the atoms in the pair have opposite spin. For odd J the spins must be parallel. We must consider both odd and even rotational states and the preceding argument shows that the energy difference between the ground and first excited states for different pairs is not the same, but must include values ranging down to zero. If, however, our atoms are Bose particles (He^4) we must include only those rotational states which are symmetric—i.e., those with even J. In this case, the excited and lowest state do not degenerate, and we would expect a finite minimum energy for excitation.

If we can assume that there is no short-range crystalline order in a quantum liquid, our conclusion then is that the pair-rotator model leads to results qualitatively different for atoms of different statistics. Unlike He^4, He^3 does not possess a finite energy gap. Dr. Rice, in private discussions, has suggested that it may, after all, be a sufficient condition for superfluidity, if some (rather than all) atoms have a nonvanishing minimum excitation energy; thus in liquid He^4 near the λ point, only a small fraction is superfluid. Our argument above can say nothing, of course, about the criterion for superfluidity, but it may be pointed out that this suggested sufficient condition would be satisfied even by an ideal gas of Fermi particles at low enough temperatures.

It may be added that the agreement[3] with the observed entropy, susceptibility, etc., that can be achieved by assuming a sharp spectrum would not be greatly altered by the spreading of the levels discussed here, since present experimental results only extend down to temperatures where the effects of such spreading should be small.

† Work supported in part by the National Science Foundation.
[1] O. K. Rice, Phys. Rev. **97**, 558 (1955).
[2] P. J. Price, Phys. Rev. **97**, 259 (1955); O. K. Rice, Phys. Rev. **97**, 263 (1955).
[3] H. N. V. Temperley, Phys. Rev. **97**, 835 (1955).

Interpretation of Donor State Absorption Lines in Silicon*

WALTER KOHN
Department of Physics, Carnegie Institute of Technology, Pittsburgh, Pennsylvania
(Received April 4, 1955)

IN a recent note,[1] we have reported theoretical results for the positions of excited electronic donor levels in Si. Somewhat similar results were also obtained independently by Kleiner.[2] In the meantime Burstein,

Picus, and Henvis[3] have informed us of results of infrared absorption measurements on arsenic- and phosphorus-doped silicon. We should like to suggest an interpretation of their absorption lines leading to very good agreement with our theoretical results, which have since been supplemented by calculations of the $(3p, m=\pm1)$ level and of oscillator strengths, as well as by a more refined calculation of the $(2p, m=0)$ level, which in reference 1 had a slightly larger uncertainty.

Theoretical results for the lowest four excited states to which optical transitions take place at all appreciably are listed in Table I. The quoted intensities are for arsenic donors and have an uncertainty of perhaps ±30 percent (phosphorus donors give slightly different values.)

TABLE I. Optically excited donor states; theory.

States	Energy below continuum (in units of 0.01 ev)	Intensity of transition from 1s ground state (arbitrary scale)
$2p, m=0$	-1.09 ± 0.02	4.0
$2p, m=+1$ and -1	-0.59 ± 0.01	10.6
$3p, m=0$	-0.57 ± 0.06	0.4
$3p, m=+1$ and -1	-0.29 ± 0.005	3.1
$4p, f, m=+1$ and -1	No detailed results	No detailed results

It will be seen that the $(1s)-(3p, m=0)$ transition is quite likely to escape detection in view of its small intensity and the proximity of the latter level to the $(2p, m=\pm1)$ level (see Table I). The lowest three observed transitions I, II, III should then be associated with the $(2p, m=0)$, $(2p, m=\pm1)$ and $(3p, m=\pm1)$ levels. The fourth observed transition, IV, is very likely to be associated with the $(4p, f, m=\pm1)$ level but no detailed theoretical results are available.

Table II contains the experimental results with the suggested interpretation and Table III compares the spacings between the observed lines with the corresponding theoretical spacings. The agreement between theory and experiment is very satisfactory.[4]

TABLE II. Observed infrared absorption lines.[a]

Observed line	Energy above the ground state (in units of 0.01 ev) As-donors	P-donors
I: $(1s) \rightarrow (2p, m=0)$	4.23	3.44
II: $(1s) \rightarrow (2p, m=\pm1)$	4.72[b]	3.97
III: $(1s) \rightarrow (3p, m=\pm1)$	5.06	
IV: $(1s) \rightarrow (4p, f, m=\pm1)$	5.21	

[a] These were kindly communicated to us by Dr. Picus and are more accurate than those mentioned in reference 2.
[b] E. Burstein *et al.*, find consistently a small secondary peak on this line which may be associated with the $3p$, $m=0$ level (see Table I).

By combining the experimental energy differences between the excited states and the ground state with the theoretical positions of the excited states, relative to the continuum, we obtain the following ionization energies of the ground states. As: 0.0533±0.0003 ev; P: 0.0455±0.0003 ev.

TABLE III. Spacings of excited states.

States	Energy difference (in units of 0.01 ev) Theory	Observed
$(2p, m=\pm1) - (2p, m=0)$	0.50 ± 0.02	0.49 (As) 0.53 (P)
$(3p, m=\pm1) - (2p, m=\pm1)$	0.30 ± 0.01	0.34 (As)
$(4p, f, m=\pm1) - (3p, m=\pm1)$	No detailed results	0.15 (As)

The agreement between theory and experiment, which has been described, constitutes a verification of the consistency of the effective mass formalism: The same effective masses which govern cyclotron resonances also determine quite accurately the positions of the impurity states of "p"-symmetry, as had been theoretically anticipated.[5]

A detailed report is in preparation.

* Supported in part by the Office of Naval Research.

[1] W. Kohn and J. M. Luttinger, Phys. Rev. **97**, 1721 (1955); see also Phys. Rev. **98**, 1561(A) (1955).

[2] W. H. Kleiner, Phys. Rev. **97**, 1722 (1955). I am indebted to Dr. Kleiner for sending me a copy of his paper before publication.

[3] I am grateful to these authors for acquainting me with their results, obtained with Bell Telephone Laboratories specimens, which will shortly be published.

[4] W. H. Kleiner, reference 2, has associated the lowest four transitions with the $(2p, m=0)$, $(2p, m=\pm1)$, $(3p, m=0)$, and $(3p, m=\pm1)$ levels. By not omitting the $(3p, m=0)$ level he finds poor agreement between theory and experiment.

[5] W. Kohn and J. M. Luttinger, Phys. Rev. **98**, 915 (1955). The position of the ground state is not well described by the theory (which predicts −0.029 ev for all donors) because it penetrates into the imperfectly understood region near the donor nucleus.

New Method in X-Ray Crystal Structure Determination Involving the Use of Anomalous Dispersion

Y. OKAYA, Y. SAITO,* AND R. PEPINSKY

X-Ray and Crystal Structure Laboratory, Department of Physics, The Pennsylvania State University, University Park, Pennsylvania

(Received April 27, 1955)

WHEN incident x-rays strike a crystal, and the wavelength of the x-rays is just shorter than a resonance level of a particular atom in the crystal, the radiation is scattered with abnormal phase and amplitude. In such a case, Friedel's rule does not hold, and $|F_{hkl}| \neq |F_{\bar{h}\bar{k}\bar{l}}|$. Excellent use of this phenomenon has been made in determinations of absolute configurations of structures which may exist in enantiomorphous arrangements.[1] The technique employed heretofore has involved determination of the structure except for choice between enantiomorphous forms, without anoma-

lous scattering, and then utilization of the influence of anomalous dispersion upon a limited number of structure factors to decide on the absolute configuration.

The present analysis concerns a direct procedure for obtaining information concerning the structure and absolute configuration of a noncentrosymmetric crystal containing anomalously scattering atoms.

The structure factor F_{hkl} can be written as

$$F_{hkl}=\sum_j f_j \exp[2\pi i(hx_j+ky_j+lz_j)] = \sum_j f_j \exp[i\theta_j(hkl)], \quad (1)$$

where

$$\theta_j(hkl)=2\pi(hx_j+ky_j+lz_j). \quad (2)$$

For normal scattering, the atomic scattering factors f_j are real. In the case of anomalous scattering, however,

$$f_j=f_j'+if_j''. \quad (3)$$

It can be shown readily, then, that

$$F_{hkl}^2=\sum_{j,i}(f_j'f_i'+f_j''f_i'')\cos 2\pi[h(x_j-x_i)+k(y_j-y_i)+l(z_j-z_i)]+\sum_{j,i}(f_j'f_i''-f_j''f_i') \times \sin 2\pi[h(x_j-x_i)+k(y_j-y_i)+l(z_j-z_i)], \quad (4)$$

the summation being extended over all pairs of j and i.

We now construct two Patterson series, using F_{hkl}^2 as coefficients:

$$P_c(u,v,w)=\sum_{\substack{hkl\\-\infty}}^{\infty} F_{hkl}^2 \cos 2\pi(hu+kv+lw), \quad (5)$$

$$P_s(u,v,w)=\sum_{\substack{hkl\\-\infty}}^{\infty} |F_{hkl}|^2 \sin 2\pi(hu+kv+lw). \quad (6)$$

The even function $P_c(u,v,w)$ contains peaks of heights equal to $f_j'f_i'+f_j''f_i''$ at the points $\pm(u,v,w)=\pm[(x_j-x_i)(y_j-y_i)(z_j-z_i)]$; the odd function $P_s(u,v,w)$ shows peaks of height $f_j'f_i''-f_j''f_i'$ at the points (u,v,w), together with peaks of height $-(f_j'f_i''-f_j''f_i')$ at $(-u,-v,-w)$. $P_c(u,v,w)$ and $P_s(u,v,w)$ represent the real and the imaginary parts respectively of the convolution of the distribution of scattering power in the unit cell.

If the jth and the ith atoms are of the same kind, the peaks at $\pm[(x_j-x_i)(y_j-y_i)(z_j-z_i)]$ in $P_s(u,v,w)$ disappear. Thus P_s indicates only interactions between different kinds of atoms. If only one atom, say the mth, scatters x-rays with anomalous phase and amplitudes, we have

$$f_j'=f_j,\ f_j''=0 \quad (j\neq m),$$
$$f_j''\neq 0 \quad (j=m).$$

Then $P_s(u,v,w)$ has peaks of height f_jf_m'' at $[(x_j-x_m),(y_j-y_m),(z_j-z_m)]$ and $-f_jf_m''$ at $[(x_m-x_j),(y_m-y_j),(z_m-z_j)]$. Since the peaks at $[(x_j-x_m)(y_j-y_m)(z_j-z_m)]$ and $[(x_m-x_j)(y_m-y_j)(z_m-z_j)]$ are positive and negative respectively, we can distinguish between them; hence we can specify the *magnitude* and *direction* (including the *sense*) of the vector between the mth and jth atoms.

The only limitations to the determinations of these vectors will arise from accidental superposition of positive and negative peaks, due to pseudocentric symmetry in disposition of some atoms about an anomalous scatterer. This overlapping can be reduced by suitable sharpening of the scattering factors, through the use of standard techniques.

Both a Patterson function without anomalous scattering, and P_c in the case of anomalous scattering, contain $N(N-1)$ peaks for N atoms in the cells. P_s contains only $2n(N-n)$ peaks, where n is the number of anomalously scattering atoms per cell. Half of these latter peaks are positive, and half negative; and all result from interactions between anomalous scatterers and normally scattering atoms only. One immediate advantage of this is the possibility of selection of nonrotational vectors for use in image-seeking methods of Patterson map deconvolution.[2]

When the number of anomalously scattering atoms is small, the advantages of the use of P_s in a complete noncentrosymmetric structure determination, and not merely for the establishment of absolute configuration, are obvious. With but one anomalous scatterer per asymmetric unit of a cell, an absolute-configuration analysis is possible directly in three dimensions. Methods for the "engineering" of crystals of optically active organic molecules with desirable symmetries and suitable anomalous scatterers have been discussed recently by one of us (R.P.).[3] If crystals with amenable distributions of anomalous scatterers *can* be prepared, and sufficient care can be taken to obtain accurate scattered intensity information, the phase problem for moderately complex noncentric structures can be greatly alleviated if not fully solved.

The method has been successfully applied in a direct determination of the structure and absolute configuration of $[d-Co(en)_3]Cl_3\cdot NaCl\cdot 6H_2O$. The structure and absolute configuration of this crystal were previously determined, via the standard anomalous dispersion method, by Saito *et al.*[4] The above example of the new method will be published elsewhere.

The writers are indebted to Dr. V. Vand for helpful discussions. This development was supported by a contract with the Physiology Branch, Office of Naval Research, and a grant from the National Institute of Arthritis and Metabolic Diseases of the National Institutes of Health.

* On leave from Department of Chemistry, Osaka City University, Osaka, Japan.

[1] J. M. Bijvoet, Nature **173**, 888 (1954).

[2] M. J. Buerger, Acta Cryst. **3**, 87 (1950); **4**, 531 (1951).

[3] R. Pepinsky, *Methods in the X-Ray Analysis of Organic Compounds* (X-Ray and Crystal Analysis Laboratory, The Pennsylvania State University, University Park, 1955).

[4] Saito, Nakatsu, Shiro, and Kuroya (to be published).

X-Ray Measurements on Low-Temperature Neutron-Irradiated Graphite*

DAVID T. KEATING
Brookhaven National Laboratory, Upton, New York
(Received April 18, 1955)

NATURAL graphite compacted into highly oriented briquettes[1] has been irradiated in the liquid nitrogen facility of the Brookhaven reactor. Four samples were irradiated at −196°C for various exposures, the longest being 4.085×10^{19} *nvt* integrated flux. All x-ray measurements were made at −196°C.

The investigation of graphite irradiated at low temperature was initiated in the belief that appreciably more damage would be retained in the graphite at liquid nitrogen temperature than has been observed for graphite irradiated at 30°C.[2] Preliminary findings would seem to substantiate this hypothesis.

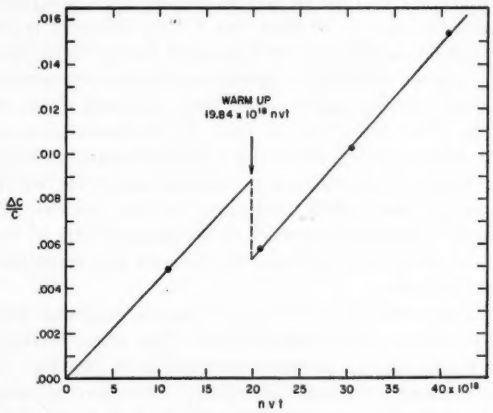

FIG. 1. Plot of $\Delta c/c$ as a function of integrated neutron flux. (Warmup is shown as discontinuity in growth curve.)

Preirradiation measurements were carefully made on line shapes and positions of the (002), (004), (006), and (008) reflections on all four samples. The samples were then placed in the liquid nitrogen facility in the reactor. The program called for extraction of one sample for examination approximately every 10^{19} *nvt*. After extracting the first sample, the irradiations were interrupted by failure of the commercial power to the laboratory. A lack of power prevented the control systems from functioning properly, and the three remaining samples suffered a warming-up period of 12 hours, but were not subjected to irradiation during the interval. The maximum temperature reached is estimated not to have exceeded 90°C. The program was continued as planned.

The fractional change in "*c*"-axis spacing computed from the change in $K_{\alpha1}$ peak position of each of the four orders was plotted against $\frac{1}{2}(\cos^2\theta/\sin\theta+\cos^2\theta/\theta)$ and extrapolation made to zero value of this function. Figure 1 is a plot of $\Delta c/c$ as a function of neutron exposure. The discontinuity indicated by the dashed vertical line has been drawn at the exposure for which the warm up occurred. The rate of "*c*"-axis growth before and after warmup is essentially the same and about 41 percent of the damage annealed out during the warm up. The rate of "*c*"-axis growth, 4.75 percent per 10^{20} *nvt*, is larger than any graphite "*c*"-axis growth ever observed resulting from irradiation in the Brookhaven reactor. The fastest growth for any graphite previously exposed in the Brookhaven reactor was for a sample exposed at approximately 50°C which showed a growth rate of 2.35 percent per 10^{20} *nvt*. The recovery upon warming up is in reasonable agreement with the increased rate of growth. While this evidence is not conclusive, it supports the hypothesis in the aforementioned. Precise evidence can only be given by complete annealing studies which are being made.

The x-ray reflections broaden appreciably. The broadening is characterized by very long tailing of the (00*l*) reflections with a sharp crystalline peak remaining. This peak is shifted corresponding to an increase in "*c*"-axis spacing and is greatly reduced in height after irradiation. Figure 2 shows the (006) reflection before and after an irradiation of 4.085×10^{19} *nvt*. Both reflections are from diffractometer traces re-

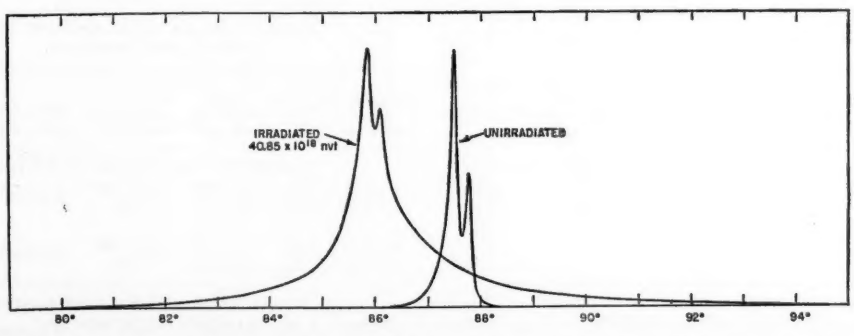

FIG. 2. The (006) reflection before and after an irradiation of 4.085×10^{19} *nvt*. (From diffractometer traces with background subtracted.) The intensities are not to the same scale.

corded at −196°C with background subtracted. The two traces are not shown to the same scale.

The preliminary evidence shown indicates that more damage is retained in graphite irradiated at low temperatures. The annealing studies which are being done and irradiations at 30°C in the liquid nitrogen facility itself should prove conclusively whether appreciably more damage is retained in graphite irradiated at liquid nitrogen temperature.

* Under the auspices of the U. S. Atomic Energy Commission.

[1] The briquettes were tediously prepared from natural graphite flakes oriented by hand and compacted with a small amount of Bakelite powder as a binder by D. L. Chipman at the Massachusetts Institute of Technology. The briquettes were eventually heated to 3000°C for 1½ hours by J. C. Bowman at the National Carbon Research Laboratories in Cleveland.

[2] For a brief historical review of still unpublished work on graphite, see F. Seitz, Phys. Today **5**, No. 6, 6 (1952).

Electrical Breakdown in Germanium at Low Temperatures*

F. J. Darnell† and S. A. Friedberg
Department of Physics, Carnegie Institute of Technology, Pittsburgh, Pennsylvania

(Received April 29, 1955)

THE application of electric fields exceeding a few volts per cm to rather pure germanium specimens at low temperatures is known[1,2] to produce a marked drop in electrical resistivity. This breakdown effect has been attributed[3] to an increase in the concentration of mobile electrons or holes resulting from impact ionization of impurities normally neutral at these temperatures by free carriers accelerated by the necessary velocities by the applied field. Ryder, Ross, and Kleinman[4] indirectly confirmed this hypothesis by showing that their pulse observations at 20°K are consistent with a carrier concentration rise of about 30 percent.

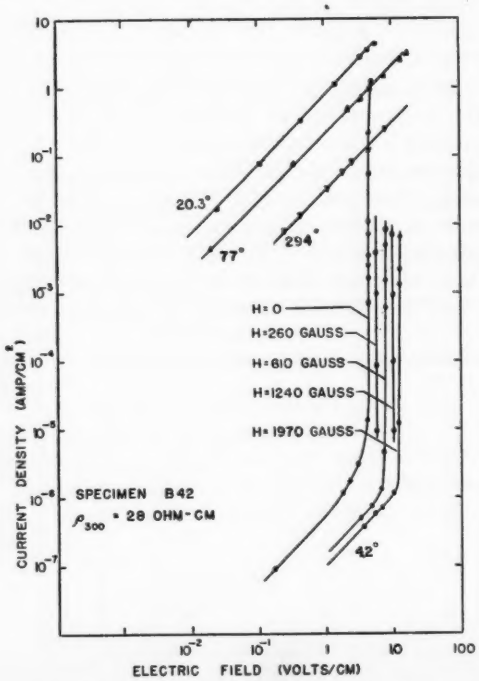

FIG. 1. Current density *vs* applied electric field for single-crystal specimen B42.

Using a constant-field technique, we have determined the current-electric field characteristics of several germanium specimens as functions of temperature and transverse magnetic field. Changes in carrier concentration associated with breakdown have been followed directly by means of the Hall effect.

A logarithmic plot of current density *vs* electric field is shown in Fig. 1 for an *n*-type, single-crystal specimen (resistivity $\rho_{300°K}=28$ ohm cm). Ohmic behavior is indicated on such a plot by a straight line of slope one. Only one set of helium temperature results is reproduced although similar curves have been obtained down to 0.1°K. The critical electric field, E_e, has been taken as that field for which the curve begins its nearly vertical rise rather than the poorly defined value for which deviation from ohmic behavior is first evident. E_e chosen in this way appears to be characteristic of the bulk material and not sensitive to such factors as surface treatment.

As indicated in Fig. 1, a transverse magnetic field increases the critical electric field. This effect becomes more pronounced the purer the specimen (see Fig. 2), i.e., the longer the mean free time, τ, between collisions of a carrier with impurity atoms (which do most of the scattering at the lowest temperatures). Clearly, such a field reduces the energy imparted to the carriers responsible for impact ionization by the electric field in a mean free path. Hall voltages were measured, therefore, as functions of magnetic field, H, and extrapolated to $H=0$ in order to eliminate the effect of H upon carrier concentration. Values of the Hall coefficient, R, determined in this way at points above and below E_e are given for two typical specimens in Table I, as well as the resistivities, ρ, at these points. Included also are

TABLE I. Changes in Hall coefficient and resistivity with breakdown.

Electric field volts/cm	T °K	Hall coefficient cm³/coul	Resistivity ohm-cm	$\frac{R(E<E_e)}{R(E>E_e)}$	$\frac{\rho(E<E_e)}{\rho(E>E_e)}$
Sample B42 ($\rho_{300}=28$ ohm cm *n*-type)					
$E<4.4$	4.18	1.6×10^{12}	1.3×10^{6}	6.3×10^{4}	3.5×10^{4}
$E>4.4$	4.18	2.6×10^{7}	37		
$E<4.8$	1.26	1.8×10^{13}	2.2×10^{6}	5.5×10^{5}	5.1×10^{4}
$E>4.8$	1.26	2.3×10^{7}	43		
Sample B22 ($\rho_{300}=1.6$ ohm cm *n*-type)					
$E<6.0$	4.18	6.9×10^{11}	3.2×10^{6}	2.1×10^{5}	3.6×10^{4}
$E>6.0$	4.18	3.3×10	90		

the ratios $R(E<E_c)/R(E>E_c)$ and $\rho(E<E_c)/\rho(E>E_c)$. These are seen to be of roughly the same magnitude, i.e., the resistivity decreases on breakdown in nearly the same ratio as the carrier concentration increases. This agrees with the impact ionization picture. The discrepancies in these ratios are due probably to a mobility reduction resulting from the increased number of ionized scattering centers produced at breakdown.

Values of E_c for several specimens increased slightly as the temperature was lowered from 4° to 1°K becoming essentially constant in the region from 1° to 0.1°K. These results together with those obtained in the range 10° to 20°K, which show E_c increasing with temperature, suggest that E_c passes through a minimum in the region 5° to 10°K. This could correspond to the mobility maximum occurring when ionized impurities begin to dominate lattice vibrations in the scattering of carriers. Comparison of E_c for different samples at the same temperature also indicates that E_c varies inversely with carrier mobility in accord with the assumed breakdown mechanism.

TABLE II. Calculated mean free times and paths at 4.2°K.

Sample	Resistivity (300°K) ohm-cm	Type	Assumed m^*/m_0	τ_0 sec	l_0 cm
B42	28	n	0.11	0.7×10^{-10}	1.1×10^{-4}
B22	1.6	n(Sb)	0.11	0.3×10^{-10}	0.2×10^{-4}
B12	1.2	p(Ga)	0.30	0.6×10^{-10}	0.6×10^{-4}

Having determined experimentally the dependence of E_c upon H, (see Fig. 2) we can estimate values of the mean free time, τ, between collisions of carriers. A typical carrier may be considered to be accelerated from rest by the field E_c and to acquire sufficient energy so that its mean free path, l, can end in an ionizing collision. If the energy acquired between collisions when $H=0$ is equated to that gained with $H=H$ and if l for the two cases is assumed the same, then one may show[5] that $E_{cH}/E_{c0}=2/[1+\cos\frac{1}{2}\omega_c\tau]$, where E_{cH} and E_{c0} are the values of E_c for the transverse magnetic fields H and zero respectively and $\omega_c=eH/m^*c$. Values of τ obtained by solving this equation may be extrapolated to $H=0$ giving times τ_0 as listed in Table II. These agree well with values of τ determined from the cyclotron resonance line widths for similar material.[6] With this crude picture values of l_0 may also be estimated. Some typical values obtained by extrapolation to $H=0$ are given in Table II.

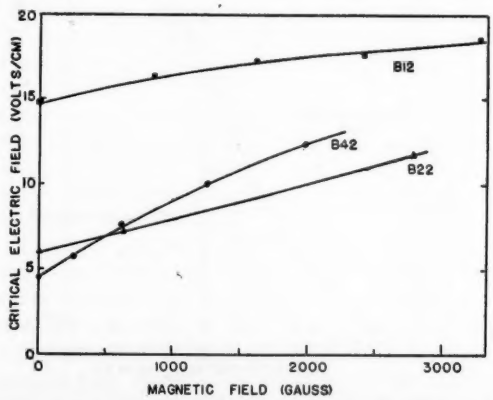

FIG. 2. Critical electric field for breakdown *vs* transverse magnetic field for three specimens at 4.2°K.

* Supported by the National Science Foundation and the Office of Naval Research.

† Based on part of a thesis to be submitted by F. J. Darnell to the Carnegie Institute of Technology in partial fulfillment of the requirements for the degree of Doctor of Philosophy.

[1] Estermann, Foner, and Zimmerman, Phys. Rev. **75**, 1631(A) (1949).

[2] A. N. Gerritsen, Physica **15**, 427 (1949).

[3] Sclar, Burstein, Turner, and Davisson, Phys. Rev. **91**, 215(A) (1953).

[4] Ryder, Ross, and Kleinman, Phys. Rev. **95**, 1342 (1954).

[5] A different result giving nearly the same values of τ_0 may be obtained by assuming the radial distance traversed between collisions in each case to be the same. The approximation in which thermal motion is regarded as predominant gives poorer values of τ_0.

[6] Dresselhaus, Kip, and Kittel, Phys. Rev. **92**, 827 (1953).

Electron Voltaic Study of Electron Bombardment Damage and its Thresholds in Ge and Si

J. J. LOFERSKI AND P. RAPPAPORT
Radio Corporation of America, RCA *Laboratories*, *Princeton, New Jersey*

(Received April 25, 1955)

HIGH-ENERGY electron bombardment of single-crystal germanium or silicon introduces defects which induce changes in minority carrier lifetime,[1] τ, and when the damage is thousands of times greater, changes in resistivity,[2] ρ. If the semiconductor is made into an electron voltaic cell,[3] it can be shown that the short-circuit current, I_s, which is induced to flow through the cell by electron bombardment, is proportional to $\tau^{\frac{1}{2}}$. Thus observations of I_s share the sensitivity but avoid the difficulties encountered in a direct measurement of τ. The purpose of this letter is to show how the changing short circuit current, I_s, can be related to the properties of the defects, and to present experimental results for bombardment damage thresholds determined by this method.

The method depends on the existence of a reciprocal relation between τ and the number of recombination centers[4] introduced by bombardment, N_r, i.e.,

$$1/I_s^2 \propto 1/\tau \propto N_r\sigma f(E_t-E_f), \qquad (1)$$

where σ is the cross section for capture of minority carriers at the defect and $f(E_t-E_f)$ is a function of the separation between the energy level of the defects, E_t, and the Fermi energy, E_f. This function has been

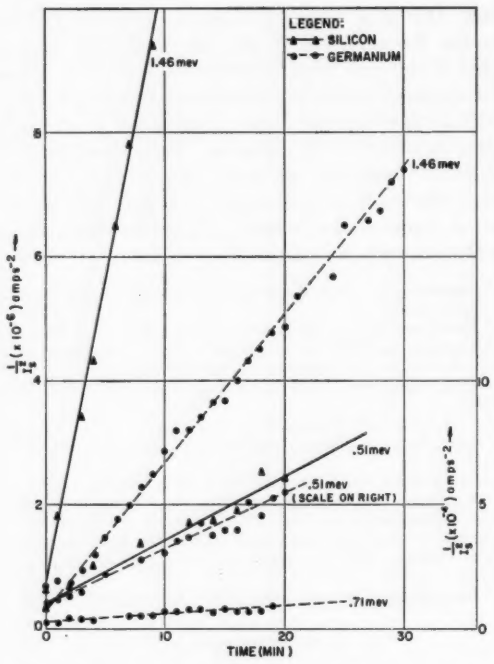

FIG. 1. Typical plots of $1/I_s^2$ *vs* bombardment time, t, for different energies of bombardment. The scale on the left should be used except where indicated.

formulated for such a recombination process by Hall[5] and Shockley and Read.[6] Furthermore, N_r is a linear function of bombardment time, t:

$$N_r \propto N_B t \Delta, \tag{2}$$

where N_B is the flux of high-energy electrons, and Δ is an average cross section for producing a defect. Note that Δ depends on V_B, the energy of the bombarding particles. Substitution of (2) into (1) results in

$$1/I_s^2 \propto N_B \sigma f(E_t - E_f) t \Delta.$$

Thus, if plots are made of $1/I_s^2$ against t, the slopes of such plots, $d(1/I_s^2)/dt \equiv \nu$, yield information about the damage such as the following:

(a) If N_B and $f(E_t - E_f)$ are constant for a group of samples bombarded by monokinetic electrons of different energies, V_B, it is possible to plot ν *vs* V_B, which is proportional to Δ *vs* V_B, and to locate $V_{B\,\min}$, the threshold for producing defects.

(b) If V_B, N_B, and Δ are constant and E_F is varied by using samples of different resistivity, it is possible to trace $f(E_t - E_F)$, and to compare it with theory.[5,6]

(c) If V_B, N_B, and Δ are constant and $E_t - E_f \gg kT$, then $f(E_t - E_f) = 1$, i.e., highly doped material, and the ratio of ν's for n- and p-type materials yields the ratio of σ_p/σ_n, i.e., of the cross section for capture of holes and of electrons by the recombination centers.

Preliminary results for (a) were obtained by using electrons produced by a Van de Graaff machine in which V_B was variable from 0.3 to 2 Mev.[7] The resistivity of the n-type germanium used in the diodes was between 0.2 and 0.4 ohm cm while that of the p-type silicon was 35 ohm cm. The samples were exposed at room temperature for about 30 minutes to bombarding currents (I_B) of 10^{-7} ampere at each energy. Typical plots of $1/I_s^2$ *vs* t for silicon and germanium are shown in Fig. 1, where V_B is the running parameter. Figure 2 shows a linear plot of ν (the slopes of lines such as those in Fig. 1) *vs* V_B for both Ge and Si. For Ge, the experiments have shown the damage is readily detectable for $V_B = 510$ kev, whereas the Si damage was still appreciable at the lowest energies available in the Van de Graaff. The threshold $V_{B\,\min}$ has been interpreted as the energy a primary particle must have in order to impart enough energy (E_L) to an atom in the crystal to displace it irreversibly from its normal position. Thus our experiments indicate that for Ge, $E_{L\,\min} \leq 23$ ev. This is lower than the 31 ev observed by Klontz who used changes in ρ at liquid air temperatures to detect the presence of the vacancies.[2]

Analysis of the results for silicon is more difficult because of the low-energy cutoff of the Van de Graaff. If, however, a linear extrapolation of the curve is made, $V_{B\,\min} \leq 280$ kev so that $E_{L\,\min} \leq 27.6$ ev. These values of $E_{L\,\min}$ should be compared to the theoretical

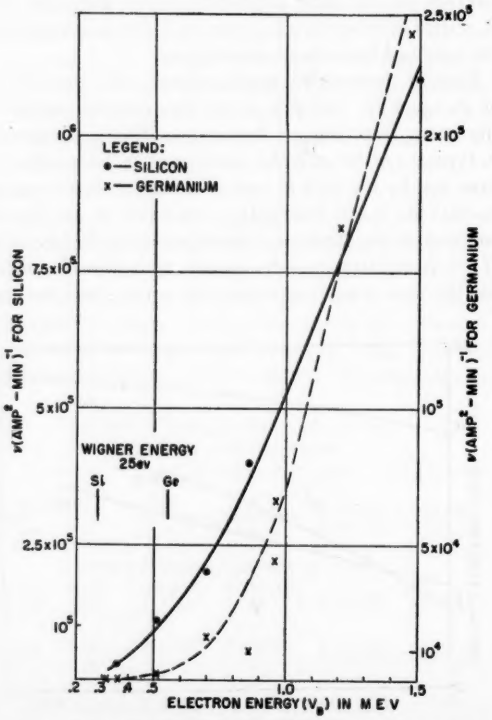

FIG. 2. The slopes, $\nu \equiv d(1/I_s^2)/dt$ of lines like those in Fig. 1, plotted *vs* the energy of the bombarding particles. The scale on the left applies to Si, that on the right to Ge.

value of this quantity, i.e., the Wigner energy of ~25 ev.[8]

A more complete report of this work is in preparation, and it will include results of experiments outlined in parts (b) and (c).

[1] P. Rappaport, Phys. Rev. **94**, 1409(A) (1954).
[2] E. Klontz, Purdue University dissertation, 1948 (unpublished).
[3] P. Rappaport, Phys. Rev. **93**, 246 (1954).
[4] A. Rose, RCA Rev. **12**, 362 (1951).
[5] R. N. Hall, Phys. Rev. **87**, 387 (1952).
[6] W. Shockley and W. R. Read, Phys. Rev. **87**, 835 (1952).
[7] The work was done on a Type AD2 machine at the High Voltage Engineering Corporation in Cambridge, Massachusetts. The authors wish to thank Mr. A. John Gale, who supervised the adaptation of the machine for these experiments.
[8] F. Seitz, Discussions Faraday Soc. **5**, 271 (1949).

Alternative Explanation of the Waymouth-Bitter Experiments

LAURENCE BURNS
Sylvania Electric Products Inc., Salem, Massachusetts
(Received April 5, 1955)

WAYMOUTH and Bitter[1] have reported some significant experiments on electroluminescence excited by field pulses of known time constant with certain cubical ZnS:Cu, Pb phosphors. They found that if the electroluminescent lamp was first irradiated with infrared to bring it to a consistently reproducible initial state, then there was practically no luminescence when the field was applied, but luminescence would occur when the field was removed. It was suggested[1,2] that this might be due to ionization of the activator centers, with the field holding the electrons at the positive side of the working portion of the crystal, with luminescence occurring by recombination when the field was released.

An alternative explanation is now proposed. The electrons are assumed to come from donor levels of low energy, say 0.2 ev, and hence either come from initially ionized donors or are released by low fields. These electrons will accordingly migrate to the positive side of the working portion of the crystal at low fields, too low to accelerate the electron to the 2 ev or so energies necessary for impact excitation of the activator. Thus when the field reaches its full value, there will be no electrons that it can accelerate across the working part of the crystal. The electrons will have all gone over slowly to the positive side.

When the applied field is removed, however, the maximum reverse field due to polarization of the crystal will occur at, or close to, the instant of removal of the field. The electrons will therefore begin to move back to their donors in a high field, becoming accelerated to energies high enough for excitation of any activator atoms encountered along the way. Luminescence will thus occur when the field is removed.

The foregoing is true if the applied field is removed shortly after it reaches its maximum value. The electrons will be largely untrapped and free to return to their donors. The longer the applied field is maintained, however, the more electrons will become trapped, and the traps in zinc sulfide, particularly with lead present, will be deeper than the donor levels, for example about 0.5 ev. The electrons held in these traps will not all be released with the collapse of the applied field, and hence the luminescence on removal of the applied field will be reduced.

On the reapplication of the field, however, the electrons will no longer all be free to move at low fields, but will not be released from their traps until the field reaches a higher value, high enough to then accelerate the electrons sufficiently for impact ionization. Thus, if the field is initially applied, maintained for a time, and then removed, luminescence will occur on reapplication of the field. This is in accord with the experimental results of Waymouth and Bitter.

As the time interval between removal and reapplication of the field is increased, more electrons will escape from traps before reapplication and hence the luminescence on reapplication of the field will be smaller.

Irradiation by infrared to empty the traps will also reduce the luminescence on reapplication of the field, all these results being in accord with the Waymouth-Bitter experimental findings.

The reason for the trapping of electrons when the applied field is maintained for a long enough period is presumably the fact that the dielectric material in which the phosphor particles are embedded has a definite, though extremely small, resistance, so that a small direct current will flow through the device, some electrons from the direct flow being trapped as they pass through the working portion of the crystal, and being compensated for by electrons leaving the positive side and passing into the dielectric.

[1] J. F. Waymouth and F. Bitter, Phys. Rev. **95**, 941 (1954).
[2] L. Burns, J. Electrochem. Soc. **100**, 572 (1953).

Average Crystal Potential

JOSEPH L. BIRMAN
Sylvania Electric Products Inc., Physics Laboratories, Bayside, New York
(Received April 8, 1955)

IN this note, we will discuss the calculation of the average potential in an infinite nonionic crystal, and show that the Frenkel-Bethe formula[1] can be obtained from the Fourier representation of the total crystal potential. In what follows, the Fourier transform $\Gamma(\mathbf{n})$ of a function $G(\mathbf{r})$ is given by

$$\Gamma(\mathbf{n})=\mathfrak{F}(G(\mathbf{r}))=\int G(\mathbf{r})\exp(-2\pi i\mathbf{n}\cdot\mathbf{r})d\mathbf{r}/v_a, \quad (1)$$

where $\mathbf{n}$ and $\mathbf{r}$ are running vectors in Fourier and crystal space respectively, magnitudes η and r, and v_a is the volume of the primitive cell.

We consider a crystal in which the total charge density at a typical lattice site, taken as origin, is $R(\mathbf{r})=Z[\delta(\mathbf{r})-R_S(r)]$, where Z is the atomic number, and $R_S(r)$ is a spherically symmetric electron density of content $+1$; there is no net charge at any site. Let $\mathrm{P}(\mathbf{n})=\mathfrak{F}(R(\mathbf{r}))$, $\mathrm{P}_S(\eta)=\mathfrak{F}(R_S(r))$, $\Phi(\mathbf{n})=\mathfrak{F}(V(\mathbf{r}))$, where $V(\mathbf{r})$ is the potential due to $R(\mathbf{r})$. Then from Poisson's equation,

$$\Phi(\mathbf{n})=\mathrm{P}(\mathbf{n})/4\pi^2\eta^2=Z[v_a^{-1}-\mathrm{P}_S(\eta)]/4\pi^2\eta^2, \qquad (2)$$

where[2]

$$\mathrm{P}_S(\eta)=\frac{2\pi}{v_a}\int_0^\infty \frac{J_{\frac{1}{2}}(2\pi\eta r)}{(\eta r)^{\frac{1}{2}}}R_S(r)r^2dr. \qquad (3)$$

The average crystal potential is $\lim_{\eta\to 0}\Phi(\eta)$. Using the Taylor expansion[3] of $J_{\frac{1}{2}}(2\pi\eta r)$ in (1)–(3), we have

$$\Phi(\eta)=Z(4\pi^2v_a\eta^2)^{-1}\left[1-4\pi\int_0^\infty R_s(r)r^2dr + \frac{8\pi^3}{3}\eta^2\int_0^\infty R_s(r)r^4dr-O(\eta^4)\right]. \qquad (4)$$

The first integral in (4) is $(4\pi)^{-1}$ by the normalization, so

$$\Phi(000)=\frac{2\pi Z}{3v_a}\int_0^\infty R_s(r)r^4dr=\frac{2\pi}{3v_a}Z\langle r^2\rangle_{\mathrm{Av}}, \qquad (5)$$

which is the Frenkel-Bethe result. If the crystal has a basis, (5) must be summed over each species present.

Thus the contribution of one type of particle to the average crystal potential can be directly determined from the appropriate atomic scattering factor, $f(\sin\vartheta/\lambda)=Z\mathrm{P}_S(\eta)$. Near $\eta=0$,

$$Z\mathrm{P}_S(\eta)=[Z/v_a-4\pi^2\Phi(000)\eta^2+O(\eta^4)]. \qquad (6)$$

Since the largest contribution to $\mathrm{P}_S(\eta)$ at small η comes from the outer or valence electrons,[4] the average crystal potential is primarily determined by the valence electron density. Crystal binding will of course greatly distort the valence electrons from their configuration in the free atom. Hence in general one cannot use the *free* atom scattering factors to determine the average crystal potential, unless accurate x-ray Fourier synthesis of the crystal electron density shows that the same scattering factors apply to the atom bound in the crystal.

For an ionic crystal the net charge at each site, P(000), is not zero so it is not clear that this analysis should apply. If, however, the excess or deficiency of charge is treated separately from the neutral complex of core plus compensating charge,[5] then (5) can apply to the neutral complex, while the excess density makes no contribution. We hope to discuss the average crystal potential again at a later date.

The author wishes to thank Professor P. P. Ewald with whom he has discussed many questions concerning crystal potentials. The comments of Dr. D. R. Frankl and A. Lempicki have been most helpful.

[1] J. Frenkel, Z. Physik **59**, 649 (1930); H. Bethe, Ann. Physik **87**, 55 (1928), see footnotes 1 and 2 on p. 106 and Eq. (85) on p. 109.

[2] S. Bochner and K. Chandrasekharan, *Fourier Transforms* (Princeton University Press, Princeton, 1949), p. 67 ff.

[3] G. N. Watson, *Bessel Functions* (The Macmillan Company, New York, 1945), second edition, p. 15.

[4] R. W. James, *The Optical Principles of the Diffraction of X-rays* (G. Bell and Sons, Ltd., London, 1950), pp. 125–129.

[5] J. L. Birman, Phys. Rev. **97**, 897 (1955); see also erratum, Phys. Rev. **98**, 1871 (1955). Note that in *both* (4.2) and (4.3) the average potential is made equal to zero, which is a consequence of the use of the sums $\psi^{(1)}(\mathbf{r};\alpha)$ and $\psi^{(2)}(\mathbf{r};\alpha)$.

Magnetic Susceptibility of α Manganese at Low Temperatures*

A. Arrott, B. R. Coles,† and J. E. Goldman

Laboratory for Magnetics Research, Carnegie Institute of Technology, Pittsburgh, Pennsylvania

(Received April 29, 1955)

RECENT measurements of the specific heat in α manganese[1] at liquid helium temperatures yield a value for the electronic term that is very large compared to other elements of the first transition series. This implies a very high density of states at the Fermi surface of the 3*d*-4*s* band which could on the band picture lead to strong magnetic effects. To investigate this, measurements of the magnetic susceptibility were undertaken in the range of temperature between 1.8°K and room temperature. Previous measurements of the susceptibility of α Mn by Serres[2] and Kriessman and McGuire[3] show a maximum in the susceptibility in the neighborhood of 150°K but these measurements were only taken down to liquid nitrogen temperatures. Shull[4] has studied this material by means of neutron diffraction and finds evidence for a feeble antiferromagnetism at low temperature which disappears at approximately 100°K. Since the completion of this work, more recent measurements by Kriessman and McGuire to lower temperatures[5] have come to our attention and in these a marked increase in susceptibility is reported.

The measurements were made by an induction technique[6] in which a disk-shaped sample is translated between two detecting coils connected in series opposition. The magnetic moment is obtained by measuring the dc current that must be supplied to a third coil, that is wound on the sample and which rides with the sample, in order to balance out the detected signal. The entire coil and sample assembly is suspended in a Dewar designed to eliminate the need for liquid nitrogen in the field-sensitive region[7] and sits between the pole pieces of an A. D. Little electromagnet. With this

method, susceptibilities of the magnitude measured in this experiment may be measured to an accuracy of 1 percent.

Two samples of α Mn were employed in this investigation. One was from a cast ingot[8] and was pickled prior to measurement; the other was a packed capsule of electrolytic flakes and was from the same sample used by Shull in his neutron diffraction investigation. The results are tabulated in Table I. The room temperature

TABLE I. Mass susceptibility of α Mn, $\chi\times10^6$.

T°K	Electrolytic	Cast ingot	Cast ingot degassed
300	10.6	8.8	8.9
120–170	10.9	9.6	···
90	10.7	9.4	···
77	10.5	9.9	···
4.2	11.5[a]	15.0[a]	9.0[a]

[a] Magnetization in a field of 10 kilogauss on a virgin magnetization curve ($\times10^3$).

susceptibility for both samples was of the order of 10^{-5} emu/g and in good agreement with previously measured values. Both samples also show the maximum below 200°K that is found by the earlier investigators.

The cast sample shows an increasing susceptibility below 100°K. At helium temperatures the sample is definitely ferromagnetic with a remanence of some 0.07 emu/g. The magnetization at each field is increased over the room temperature values by approximately the remanence. The magnetization at 10 kg is approximately 70 percent greater at 4.2°K than at 77°K. The remanence decreases rapidly between helium and hydrogen temperatures but persists to approximately 60°K. This behavior appears to be consistent with the susceptibility curve of Kriessman and McGuire. However, for the electrolytic sample, which is similar to that of Kriessman and McGuire, the increase in susceptibility at helium temperatures is nowhere near so marked, being less than 10 percent. A remanence is still observed but amounts to but 0.005 emu/g. It is well known[9] that many alloys and compounds of manganese, including the hydride and nitride, are ferromagnetic. Chemical analysis of the case sample did indeed show the sample to contain 0.4 percent (atomic) hydrogen, 0.11 percent oxygen, and 0.09 percent nitrogen. Analysis of the electrolytic sample from the diffuse background in the neutron diffraction pattern shows the hydrogen content to be no greater than 0.02 percent. On the supposition that the observed ferromagnetism may have been caused by the presence of interstitial impurities, the "ferromagnetic" sample was given a vacuum anneal treatment of 500°C which presumably removes most of the common interstitial impurities. Following the anneal this sample showed a 2 percent increase in susceptibility at room temperature. At helium temperatures, however, its susceptibility was within 2 percent of its room temperature value and the remanence was down to 0.003 emu/g. One may thus conclude that the onset of ferromagnetism in manganese is associated with the presence of interstitial impurities and the increase observed by Kriessman and McGuire at low temperatures is probably due to the presence of impurities in their sample and is not an intrinsic property of the manganese. Further investigation of the quantitative aspects of this effect and its interpretation is being undertaken in this Laboratory.

The authors are indebted to Dr. C. J. Kreissman and Dr. T. R. McGuire for making the results of their research available in advance of publication and to Dr. G. Derge for the vacuum fusion analyses.

* Supported by the Office of Naval Research and the U. S. Army Signal Corps.

† FOA Fellow on leave from Imperial College, London, England.

[1] Guthrie, Friedberg, and Goldman, Bull. Am. Phys. Soc. **30**, No. 1, 42 (1955).

[2] A. Serres, J. phys. radium **9**, 377 (1938).

[3] C. J. Kriessman and T. R. McGuire, Phys. Rev. **90**, 374 (1953). Their curve is reproduced in a paper by C. J. Kriessman and H. B. Callen [Phys. Rev. **94**, 837 (1954)] who also give an interpretation based on the band theory.

[4] C. G. Shull and M. K. Wilkinson, Revs. Modern Phys. **25**, 100 (1953).

[5] C. J. Kriessman and T. R. McGuire, Phys. Rev. **98**, 936 (1955).

[6] A. Arrott, thesis, Carnegie Institute of Technology, 1953 (to be published).

[7] W. E. Henry and R. L. Dolecek, Rev. Sci. Instr. **21**, 496 (1950).

[8] Supplied by National Research Corporation and obtained through the kind cooperation of Professor J. G. Daunt.

[9] R. Becker-Döring, *Ferromagnetismus* (Verlag Julius Springer, Berlin, 1939), p. 100.

Infrared Absorption of Silicon Near the Lattice Edge

G. G. MACFARLANE AND V. ROBERTS
Radar Research Establishment, Malvern, England

(Received March 24, 1955)

WE have measured the absorption of a polycrystalline specimen of 100 ohm-cm silicon in the neighborhood of the lattice edge at temperatures from 20°K to 3330°K. High resolution was obtained by the use of glass prisms, the method being to measure the transmitted radiation intensity with and without the specimen present, to deduce the reflection coefficient from the constant value of the transmission coefficient at wavelengths well beyond the absorption edge, and to calculate the absorption from these data.

The results, shown in Fig. 1, indicate that, as with germanium,[1] the absorption constant, K, is well represented at low levels by a law of the form

$$K=A\left[\frac{(h\nu-E_G-k\theta)^2}{1-e^{-\theta/T}}+\frac{(h\nu-E_G+k\theta)^2}{e^{\theta/T}-1}\right].$$

The best fit is obtained with $\theta=600$°K, for which value the full lines in Fig. 1 are drawn. E_G, which in the theory

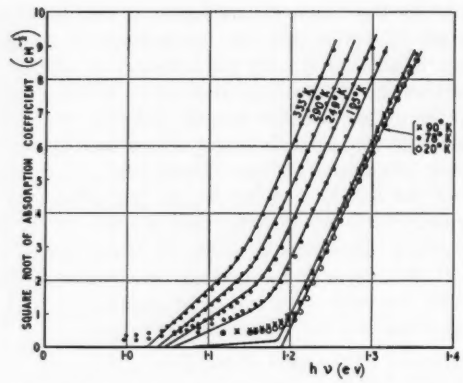

FIG. 1. Dependence of absorption constant on photon energy for silicon.

of indirect transitions[1,2] is the energy gap, varies with temperature as shown in Fig. 2. It behaves quadratically at low temperatures just as for germanium. We observe that our values for K agree substantially with those of Fan, Shepherd, and Spitzer[3] at room temperature.

From cyclotron resonance experiments[4,5] we know that the energy maximum of the valence band is at the origin and equal energy minima occur along the six [1,0,0] axes of momentum in the conduction band. According to the theory that the absorption tail

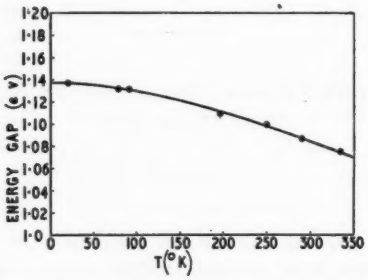

FIG. 2. Dependence of energy gap on temperature for silicon.

beyond the lattice edge is due to indirect transitions, $k\theta$ is then the energy of the longitudinal acoustic wave with momentum equal to the momentum of the electrons at the minimum of the conduction band. From the known values of the elastic constants of silicon[6] and the theory of vibrations of the diamond lattice,[7] we estimate that the conduction band minima occur at a momentum of 9.0×10^7 cm^{-1}, which is about 7/9 of the distance from the center to the edge of the Brillouin zone in the [1,0,0] direction.

We have attempted to correlate the intrinsic carrier concentration n_i of Morin and Maita[8] with our values of E_G. We find

$$n_i=4.82\times10^{15}T^{\frac{3}{2}}(\bar{m}/m_0)^{\frac{3}{2}}N_c^{\frac{1}{2}}\exp(-E_G/2kT),$$

where $\bar{m}=0.44m_0$ is calculated from the effective masses of holes and electrons[4,5] and $N_c=6$ is the number of energy minima in the conduction band. At $T=333$°K this gives $n_i=1.50\times10^{11}$ cm^{-3}. Morin and Maita give data for n_i only above 450°K but if these data are extrapolated to 333°K, using their empirical formula, one gets $n_i=1.65\times10^{11}$ cm^{-3}. The discrepancy is about 10 percent.

Acknowledgment is made to The Chief Scientist, British Ministry of Supply, for permission to publish this letter.

[1] G. G. Macfarlane and V. Roberts, Phys. Rev. **97**, 1714 (1955).
[2] Hall, Bardeen, and Blatt, Phys. Rev. **95**, 559 (1954).
[3] Fan, Shepherd, and Spitzer. Proceedings of Conference on Photoconductivity, Atlantic City, 1954 (unpublished).
[4] Dexter, Lax, Kip, and Dresselhaus, Phys. Rev. **96**, 222 (1954).
[5] R. N. Dexter and B. Lax, Phys. Rev. **96**, 223 (1954).
[6] H. J. McSkimin, J. Appl. Phys. **24**, 988 (1953).
[7] H. M. J. Smith, Trans. Roy. Soc. (London) **A241**, 105 (1948).
[8] F. J. Morin and F. P. Maita, Phys. Rev. **96**, 28 (1954).

New Radiation Resulting from Recombination of Holes and Electrons in Germanium

J. R. HAYNES
Bell Telephone Laboratories, Murray Hill, New Jersey
(Received April 12, 1955)

INTRINSIC radiation from germanium due to recombination of injected holes and electrons has been reported by Haynes and Briggs[1] and by Newman.[2] The results of these investigations show that the maximum of the energy radiated from the specimens used occurs at a wavelength of about 1.8μ. This result is in good agreement with that calculated by van Roosbroeck and Shockley[3] and by Newman[2] using the principle of detailed balancing and the optical absorption data of Briggs.[4] Recently, however, evidence has been found which shows that additional radiation is produced by a different recombination mechanism resulting in a second maximum at a wavelength of 1.5μ.

Evidence for this radiation was first found in the examination of radiation produced in germanium by a technique which is shown schematically in Fig. 1. The

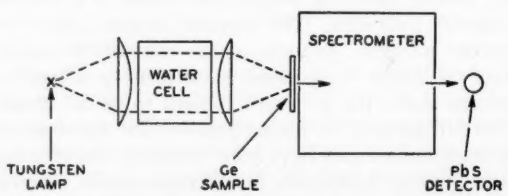

FIG. 1. Schematic arrangement used to measure recombination radiation as a function of wavelength.

light from a ribbon filament tungsten lamp was passed through a water absorption cell 10 cm long and focused on a thin slice of germanium (1.2×10^{-2} cm thick).

The radiation from the opposite side of the germanium was analyzed with a spectrometer and detected by a lead sulfide cell. Experiment shows that the water cel transmits less than 10^{-10} of the incident radiation at wavelengths longer than 1.4μ and the germanium transmits less than 10^{-10} of the radiation shorter than 1.4μ. It is therefore clear that no measurable light from the tungsten source will enter the spectrometer. Thus any detectable radiation must have its origin in recombination of electrons and holes produced by the light.

In this way, the intensity of the recombination radiation from the germanium sample was measured as a function of wavelength from 1.3 to 2.1μ. The results obtained were qualitatively in agreement with previous data obtained using p-n junctions biased in the forward direction. In this case, however, it is clear that the emergent radiation must be multiplied by a correction factor to take account of the rapidly varying absorption constant over the range of wavelengths considered. Since the diffusion lengths of the excess carriers were long compared to the sample thickness and the surface was treated to insure a low surface recombination velocity, it is reasonable to assume that both the minority carrier density and volume recombination take place uniformly throughout the sample thickness. Under these conditions the recombination radiation energy produced in the germanium, J_0, is given by

$$J_0 = J\alpha d/(1-e^{-\alpha d}), \quad \text{for} \quad \alpha d > 1,$$

where J is the measured emergent energy at a given wavelength, α is the optical absorption constant, and d is the sample thickness.

When this correction was applied to the measured radiation using the absorption data of Briggs, the resultant curve shows a large second peak at about 1.5μ.

We were at first unable to understand this result since the principle of detailed balancing when applied to Briggs' absorption data gives no suggestion of such radiation. Recent data of Dash, Newman, and Taft,[5] as well as those of Fan, Shepherd, and Spitzer[6] show, however, that although the data of Briggs taken with single-crystal germanium are correct, his data taken with evaporated films ($\lambda < 1.55\mu$) are not valid for single-crystal material.

Calculated values of the recombination radiation energy produced per unit volume as a function of wavelength, obtained by using this new absorption data and the analysis of van Roosbroeck and Shockley, are shown in Fig. 2. It is evident that in addition to the former maximum at 1.75μ a second peak at 1.52μ is obtained.[7]

It is difficult to show experimentally the existence of this second peak without resorting to the correction described, since the optical absorption for this radiation is high. Direct experimental evidence for its existence

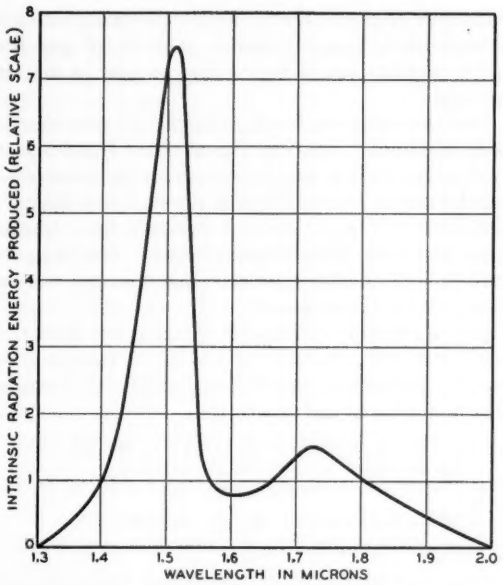

FIG. 2. Shape of radiant energy produced by the recombination of electrons and holes in germanium as a function of wavelength calculated using the optical absorption data of Dash, Newman, and Taft and the theory of van Roosbroeck and Shockley.

can only be obtained using specimens $\sim 1\times 10^{-3}$ cm thick or less.

Data obtained by using a germanium sample 1.5×10^{-3} cm thick are shown in Fig. 3, in which is plotted emergent energy as a function of wavelength. These data, corrected for absorption to give the photon energy produced per unit volume as a function of wavelength, are also shown in the figure by the dotted line. The

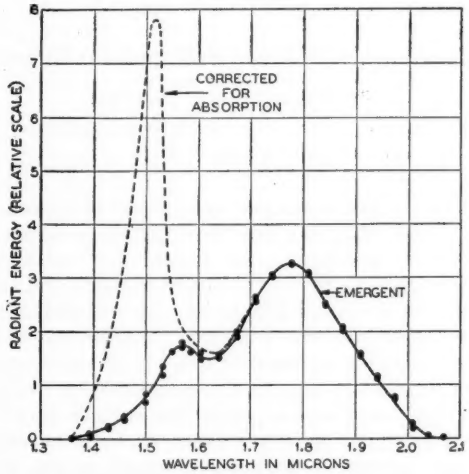

FIG. 3. Plot of experimental data obtained using a germanium sample 1.3×10^{-3} cm thick showing measured emergent radiation as a function of wavelength. The dotted curve was obtained from the solid line by correcting for absorption in the sample. (Data taken by using a p-n junction with forward bias.)

data leave no doubt that a double maximum exists in intrinsic recombination energy. The fit of the corrected curve to theory is probably as good as may be expected.[8]

This new radiation having a calculated maximum at 1.52μ (0.81 ev) is probably due to direct transitions at $k=0$, as has already been suggested for the corresponding absorption process,[5,6] while the radiation having a maximum at 1.75μ (0.70 ev) is due to indirect transitions involving phonon cooperation.[9] This suggests that the (000) minimum in germanium is only ~0.1 ev above the (111) minimum.[10]

It is a pleasure to thank C. Herring for theoretical interpretation, J. A. Burton and J. A. Hornbeck for valuable discussions, and W. Flood and W. C. Westphal for the specimens and data.

[1] J. R. Haynes and H. B. Briggs, Phys. Rev. **86**, 647 (1952).
[2] Roger Newman, Phys. Rev. **91**, 1313 (1953).
[3] W. van Roosbroeck and W. Shockley, Phys. Rev. **94**, 1558 (1954).
[4] H. B. Briggs, J. Opt. Soc. Am. **42**, 686 (1952).
[5] Dash, Newman, and Taft, Bull. Am. Phys. Soc. **30**, No. 1, 53 (1955).
[6] Fan, Shepherd, and Spitzer, Conference on Photoconductivity (to be published).
[7] A further result of this additional radiation is to reduce the value of the lifetime of excess carriers in intrinsic material as calculated by van Roosbroeck and Shockley from 0.75 sec to 0.25 sec.
[8] Increased emergent radiation at longer wavelengths due to multiple internal reflections make the longer wavelength maximum too large compared to that at shorter wavelength by a factor of ~1.7 or more, depending on whether the reflections are specular or partially diffuse.
[9] That the first absorption edge is indirect was pointed out by C. Herring [Phys. Rev. **93**, 943 (1954)] and is in accordance with the detailed theory of Bardeen, Blatt, and Hall [Atlantic City Photoconductivity Conference (to be published)].
[10] This agrees with theoretical estimates: see F. Herman, Phys. Rev. **95**, 847 (1954); R. H. Parmenter (unpublished).

Overhauser Nuclear Polarization Effect

W. A. Barker* and A. Mencher†
Swiss Federal Institute of Technology, Zürich, Switzerland
(Received April 18, 1955)

THE degree of nuclear polarization which can be attained by the Overhauser[1] effect in metals or nonmetals depends on the nuclear spin relaxation mechanisms. We consider a system of nuclei and electrons in which the nuclei may relax by any or all of the following independent processes: (1) nuclear spin flip accompanied by an electron spin flip in the opposite sense, (2) nuclear spin flip accompanied by an electron spin flip in the same sense, and (3) nuclear spin flip without an accompanying electron spin flip. In the hyperfine contact interaction originally discussed in this connection by Overhauser, only the first type of relaxation occurs. In the dipolar part of the hyperfine interaction all three types of relaxation are present.

An application of the thermodynamic arguments of Brovetto and Cini[2] leads to the following expression for the ratio of the populations of adjacent Zeeman levels:

$$\frac{M_m}{M_{m-1}}=\left[\frac{1-(1-s)\tanh|\gamma_e|\hbar H_0/2kT}{1+(1-s)\tanh|\gamma_e|\hbar H_0/2kT}\right]^{(f^{(1)}-f^{(2)})} \times\exp[\gamma_n+(f^{(1)}-f^{(2)})|\gamma_e|]\frac{\hbar H_0}{kT}. \quad (1)$$

The quantities $f^{(1)}$, $f^{(2)}$, and $f^{(3)}$, the sum of which is unity, denote, respectively, the fraction of nuclei relaxing by each of the three processes described in the foregoing, and s is the saturation parameter. When $s=1$, this expression reduces to that obtained by Kittel[3] on the basis of statistical arguments, and for other appropriate limiting values of s and the f's it reduces properly to known results.††

The perturbation method of Overhauser may be applied to relaxation processes (2) and (3) as well as to process (1) and leads to the following expression for the ratio of populations:

$$M_m/M_{m-1}=1+\alpha+\tfrac{1}{2}\alpha^2+\text{higher order terms}, \quad (2)$$

where

$$\alpha\equiv[\gamma_n+s(f^{(1)}-f^{(2)})|\gamma_e|]\hbar H_0/kT.$$

To this order, Eq. (2) agrees with the corresponding expansion of Eq. (1), and with the expansion of $\exp\alpha$. Although these different expressions no longer agree for terms of order α^2, for most purposes the use of the more convenient approximate form $\exp\alpha$ is permissible. In addition the perturbation approach permits the calculation of the relaxation times, a possibility not afforded by the thermodynamic method. It should also be pointed out that although Eq. (1) appears reasonable in every respect, its derivation involves the application of classical thermodynamics to a system in a steady state rather than in a state of thermal equilibrium. We intend to discuss at a later time the justification of Eq. (1) on the basis of the thermodynamics of irreversible processes.

The only observations published thus far of the Overhauser effect [in metallic lithium[4] and in the α,α-diphenyl-β-picrylhydrazyl (DPPH) free radical[5]] indicate that the enhancement of the nuclear population difference between adjacent Zeeman levels is about one order of magnitude smaller than the theoretically predicted value[1] of $s|\gamma_e|/\gamma_n$. In view of these results,[6] we were interested to see what effect the dipolar term in the hyperfine interaction had, and therefore calculated the value of $f^{(2)}/f^{(1)}$ for metallic lithium using the wave functions of Kohn.[7] Although the Li wave function has a 73 percent admixture of p-state and only a 20 percent admixture of s-state, we found that $f^{(2)}$ is less than 1 percent of $f^{(1)}$.

We would like to suggest the possibility in principle of a supplementary method of investigating exchange and correlation effects in metals. It is easily shown either from the free electron approximation or the Bloch

theory that the Overhauser effect quenches the Knight shift as $(1-s)$. That is, when $s=0$ the Knight shift has its maximum value, and when s approaches 1 the Knight shift disappears linearly. On the other hand, according to the Bohm-Pines collective electron theory[8] which takes into account the exchange and correlation effects that are neglected by the free electron and Bloch theories, one would not expect a simple linear quenching. Observed deviations from linearity would thus provide a measure of the exchange and correlation effects.

We expect to submit a more detailed account to this Journal in the near future.

We would like to express our appreciation to Professor W. Pauli and Professor G. Busch for comments and encouragement and to A. Thellung and C. Enz for helpful discussions. We are indebted to Professor W. Kohn for providing us with the wave functions for metallic lithium.

* On leave of absence from St. Louis University, St. Louis, Missouri.

† Fellow in Switzerland of the Institute of International Education.

†† It should be emphasized that the thermodynamic result [Eq. (1)] applies only when the electrons obey Boltzmann statistics. It is, however, interesting to note that the nuclear population ratio is independent of the electron statistics for complete saturation and is relatively insensitive to these statistics for other values of s [see C. Kittel, reference 3, and P. Brovetto and S. Ferroni, Nuovo cimento, **12**, 90 (1954)].

[1] A. W. Overhauser, Phys. Rev. **92**, 411 (1953).
[2] P. Brovetto and G. Cini, Nuovo cimento **11**, 618 (1954).
[3] C. Kittel, Phys. Rev. **95**, 589 (1953).
[4] T. P. Carver and C. P. Slichter, Phys. Rev. **92**, 212 (1953).
[5] Beljers, van der Kint, and van Wieringer, Phys. Rev. **95**, 1683 (1954).
[6] After this calculation was completed we were advised by Professor C. P. Slichter that the nuclear-nuclear dipolar interaction is very probably the mechanism responsible for the reduced enhancement in lithium.
[7] W. Kohn, Phys. Rev. **96**, 590 (1954).
[8] D. Bohm and D. Pines, Phys. Rev. **82**, 625 (1951); **85**, 338 (1952); **92**, 609 (1953); and D. Pines, Phys. Rev. **92**, 626 (1953); **95**, 1091 (1954).

Deformation of Viscoelastic Plates Derived from Thermodynamics

M. A. Biot

Shell Development Company, New York, New York

(Received April 13, 1955)

In a previous publication,[1] the problem of bending of a viscoelastic plate of uniform thickness h was used as an example of application of variational principles in irreversible thermodynamics. We considered a two-dimensional deformation parallel with the x, y plane and corresponding displacement components u, w, along the x and z directions. The coordinate z is directed along the thickness. We assumed that the displacement could be represented by

$$u=zu_1(x), \quad w=w_0(x). \tag{1}$$

It should be pointed out that this representation is a particular case of the more general one where the displacements are expanded in a Taylor series of the coordinate z, namely,

$$u=\sum_{n=0}^{\infty} u_n z^n, \quad v=\sum_{n=0}^{\infty} v_n z^n, \quad w=\sum_{n=0}^{\infty} w_n z^n. \tag{2}$$

The u_n, v_n, w_n are functions of x and y. Application of the variational method with such expressions leads to a very general theory of viscoelastic plates represented by partial differential equations in x and y with time operator coefficients. This, of course, applies to plates of constant or variable thickness. The question then arises as to the number of terms required in the expression (2) in order to represent the deformation with adequate accuracy. This can be answered, of course, only by considering each individual problem and will depend on the type of material and deformation as well as on the accuracy requirements.

The approximation (1) represents an expansion to the first order and was introduced only for the purpose of presenting a simplified example of the variational method. The approximation is only valid for materials which elongate with a small lateral contraction and therefore does not apply in the case of incompressibility. A better approximation is given by expanding u and w to the second order in z. Because of the particular nature of the problem, we may assume that u is an odd function and w an even function of z. Hence expressions (2), expanded to the second order, are

$$u=u_1z, \quad w=w_0+w_2z^2. \tag{3}$$

The invariant in this case is

$$I=\tfrac{1}{2}(2Q+R)(e_{xx}^2+e_{zz}^2)+Re_{xx}e_{zz}+2Qe_{zx}^2, \tag{4}$$

with the time operators P and Q. The terms e_{xx}^2, e_{zz}^2 and $e_{xx}e_{zz}$ are all of the second order z^2, while e_{zx}^2 contains a term independent of z and terms of the order z^2 and z^4. To be consistent, of course, we should retain at least all terms of the order z^2. However, we shall drop both z^2 and z^4 terms in e_{zx}^2. There is some justification for this from a physical standpoint in the present case. Furthermore, it leads to agreement with the classical theory of bending of plates in the elastic case. Applying, then, the variational method as indicated in reference 1, we find

$$-(2Q+R)\frac{h^3}{12}\frac{d^2u_1}{dx^2}-\frac{Rh^3}{6}\frac{dw_2}{dx}+Qh\left(\frac{dw_0}{dx}+u_1\right)=0,$$

$$Qh\frac{d}{dx}\left(\frac{dw_0}{dx}+u_1\right)=-f, \tag{5}$$

$$2(2Q+R)w_2+R\frac{du_1}{dx}=0.$$

In this derivation, we assume that the load f applied to the plate is distributed uniformly throughout the

thickness. The last equation is equivalent to the condition that the stress component σ_{zz} vanishes. Eliminating all variables except w_0 in (5), we find

$$\frac{d^4w_0}{dx^4}=\frac{f}{B_1}-\frac{1}{Qh}\frac{d^2f}{dx^2}. \tag{6}$$

This equation is of the same form as found previously[1] except for the operator B, which is

$$B_1=\tfrac{1}{3}h^3Q(Q+R)/(2Q+R). \tag{7}$$

This operator coincides with the coefficient in the theory of bending of plates for the elastic case.

[1] M. A. Biot, Phys. Rev. **97**, 1463 (1955).

Errata

Expansion of Copper Bombarded by 21-Mev Deuterons, WILLIAM R. MCDONELL AND HENRY A. KIERSTEAD [Phys. Rev. **93**, 247 (1954)]. A numerical error in the calculation of the volume change corresponding to the deflection of the copper tube has necessitated a downward revision of the reported expansion by a factor of 10. The ordinate of the graph shown should thus read $\Delta V/V\times10^4$ and the deflection sensitivity 0.24 mm per 0.01 percent volume change. This results in an expansion equal to about $\frac{1}{10}$ the atomic volume of displaced atoms predicted by the Seitz theory.

Further experiment has verified the magnitude of the bombardment-induced deflection, but has shown that only a small fraction anneals out at room temperature, contrary to the implication of the initial report. A summary of the annealing characteristics has been published [Henry A. Kierstead, Phys. Rev. **98**, 245(A) (1955)].

Self-Diffusion in Copper, A. KUPER, H. LETAW, JR., L. SLIFKIN, E. SONDER, AND C. T. TOMIZUKA [Phys. Rev. **96**, 1224 (1954)]. It has been pointed out to us by Dr. A. D. LeClaire that certain aspects of the statistical analysis of our data are in error. The corrected representation for the self-diffusion coefficient in copper over the temperature range 685–1062°C is $D=0.20\exp(-47\,120/RT)$ cm²/sec. The probable errors in the frequency factor aad activation energy are ±0.03 cm²/sec and ±0.33 kcal/mole, respectively. The frequency factor calculated by Zener's theory is 0.28 cm²/sec which is in excellent agreement with the experimental value.

Capture-Positron Branching Ratios, P. F. ZWEIFEL [Phys. Rev. **96**, 1572 (1954)]. The statement made that the conclusions of Sherr and Miller[1] concerning the amount of Fierz interference present in the decay of Na^{22} were "invalidated" was worded incorrectly. Actually, as Sherr has pointed out,[2] the inclusion of screening effects in the calculation of the branching ratio reduces the value of C_A/C_T from (-1 ± 2) percent to (0 ± 2) percent. Because of uncertainties in the experiment as well as other approximations in the calculated value of λ_k/λ_+, the conclusion of Sherr and Miller that the amount of Fierz interference is "less than several percent" is essentially unchanged.

Sherr has pointed out further[2] that it would be possible to repeat the experiment with a higher degree of accuracy. If this should be done, a more accurate calculation of λ_k/λ_+, including the effects of finite nuclear size,[3] various second-order corrections,[4] and the change in the end point of the positron spectrum due to screening,[5] might provide a better upper limit to the amount of Fierz interference present.

[1] R. Sherr and R. H. Miller, Phys. Rev. **93**, 1076 (1954).
[2] R. Sherr (private communication).
[3] M. E. Rose and D. K. Holms, Phys. Rev. **83**, 190 (1951); H. Brysk and M. E. Rose, unclassified Oak Ridge National Laboratory Report ORNL-1830 (unpublished).
[4] P. F. Zweifel, Phys. Rev. **95**, 112 (1954); M. E. Rose and R. K. Osborne, Phys. Rev. **93**, 1315 (1954).
[5] P. F. Zweifel, thesis, Duke University (unpublished).

Radioactivity of In^{117} and Sb^{117}, CARL L. MCGINNIS [Phys. Rev. **97**, 93 (1955)]. The percent modes of decay of the 1.9-hr in^{117m} are correctly given in Table I, page 95, but incorrectly given in the abstract, page 93, and on Fig. 5, page 96.

Possible Triple-Scattering Experiments, L. WOLFENSTEIN [Phys. Rev. **96**, 1654 (1954)]. In Eqs. (2.5) and (2.6) $\sin\beta$ should be replaced by $(-\sin\beta)$. In Table I, β should be replaced $(-\beta)$ and the columns e_{3s} and e_{3s}' should be interchanged. Also in Eq. (3.3) the term $PI_0\mathbf{n}$ should not be divided by $2(2s+1)$.

Radiative Corrections to Muon Decay, R. J. FINKELSTEIN AND R. E. BEHRENDS [Phys. Rev. **97**, 568 (1954)]. In Eq. (1), the third term "ln2" should read "4 ln2," and the last term "$-(\epsilon_m^2-4\epsilon_m\epsilon-17\epsilon^2)/3\epsilon^2$" should read "$-(\epsilon_m^2+4\epsilon_m\epsilon-17\epsilon^2)/3\epsilon^2$."

Decay of Co^{57}, L. MADANSKY AND F. RASETTI [Phys. Rev. **97**, 837 (1955)]. It was pointed out to us by Dr. M. A. Grace that our suggested decay scheme is incompatible with the results obtained by him and his collaborators at Oxford. We performed further experiments and established that our previous measurements with an NaI(Tl) crystal containing the active cobalt were erroneous, presumably owing to inefficiency of the scintillating crystal in the vicinity of the Co atoms, causing

failure to record x-rays and low-energy electrons. Using a new, more efficient crystal, we found that the numbers of 120-kev and 14-kev transitions are about equal, in agreement with the decay scheme shere the transitions occur in the above order. We also observe that the 14-kev transition follows the 120-kev transition with a delay of the order of 10^{-7} second in agreement with the results of the Oxford group. From the ratio of the total number of 14-kev transitions measured with the activity embedded in the crystal, to the number of emitted gamma rays measured with an external source, we conclude that the conversion coefficient for this line is about 6.5.

Effect of Overlap on Electrostatic Lattice Potentials in Ionic Crystals, JOSEPH L. BIRMAN [Phys. Rev. **97**, 897 (1955)]. Equation (4.1′) should be labelled (4.11). The value of $\varphi(\frac{1}{2},\frac{1}{2},\frac{1}{2};0)$ in zinc blende should be given as $-0.1440|e|/a$ and the upper curve in Fig. 4 should start at this value.

Polarization of Nucleons Elastically Scattered from Nuclei, R. M. STERNHEIMER [Phys. Rev. **97**, 1314 (1955)]. Professor Wolfenstein has informed me that the sign of β in his equation defining β [Phys. Rev. **96**, 1654 (1954)] should be changed. Therefore, in Eq. (49), the minus sign should be omitted. In Figs. 8 and 10, the ordinate should be changed from β to $-\beta$. The curves of R *vs* θ of Figs. 9 and 11 would be somewhat altered by the change of sign of β. However, this does not affect the main conclusions about the behavior of R *vs* θ.

Excitation Function of the $C^{12}(p,pn)C^{11}$ Reaction in the Bev Region, R. L. WOLFGANG AND G. FRIEDLANDER [Phys. Rev. **96**, 190 (1954)]. All cross-section ratios in Table I and all cross sections in Fig. 1 should be multiplied by 1.12 to correct for the difference in backscattering of positrons and electrons.

Author Index to Volume 98

References with (A) are to abstracts of papers presented at meetings of the American Physical Society; references with (T) designate title only. References with (L) are to Letters to the Editor. References with (E) are to Errata.

Aamodt, L. C. and P. C. Fletcher. Magnetic moment and mass of Cl^{36}—1317

—— **and P. C. Fletcher.** Spin, quadrupole moment, and mass of Se^{75}—1224

Abragam, A. Overhauser effect in nonmetals—1729

Abraham, Bernard M., Darrell W. Osborne, and Bernard Weinstock. Heat capacity and entropy of liquid He^3 from 0.23 to 2°K: nuclear alignment in liquid He^3—551(L)

Abrahams, Elihu. Interaction between spin waves and conduction electrons in ferromagnetic metals—387

Abramowitz, Milton (see Stegun, Irene A.)—1851

Acharya, Y. V. G. Momentum transfer and heat diffusion in mixing of coaxial turbulent jets—1142(A)

Adams, E. N. Auxiliary conditions in Bohm-Pines theory of electron gas—1130(L)

—— Plasma oscillations in metals—947

Adams, N. I., Jr. (see Kovarik, A. F.)—46

Adel, Arthur. Cyclical variations in effective radiation temperature of ozone region—282(A)

Adkins, R. H. and J. G. Brennan. Intermediate coupling model of Li^6—235(A)

Ajzenberg, F. (see Rubin, A.)—1185(A)

Albrecht, H. O. and C. E. Mandeville. Storage of energy in BeO—1546(A)

—— (see Mandeville, C. E.)—1569(A)

Albritton, B. R., Jr. (see Mobley, R. C.)—232(A)

Alburger, D. E. and A. W. Sunyar. Decay of Bi^{207}—276(A)

Aldrich, L. T. (see Wetherill, G. W.)—250(A)

Alers, P. B. Thermal magnetoresistance of Zn at liquid He temperatures—1180(A)

Alexander, L. E. X-ray diffraction studies of crystallization in elastomers—1547(T)

Alexeff, Igor. (see Bina, Melvin J.)—251(A)

—— (see Jennings, B.)—582

Alexis, Lucien V., Sr. Force—Its nature, structure, and generation (creation) (as disclosed by $f \times t = m$)—1176(A)

Alger, R. S. and R. D. Jordan. Energy requirement for F-center formation—1550(A)

Allen, G., R. Webeler, and S. Barile. Multiple scattering of low-energy α-particles in gas—1168(A)

Allen, J. S. (see Maxson, D. R.)—230(A)

Allen, Leland C. Interpolation scheme for energy bands in solids—993; 1193(A)

Allen, Lew, Jr. Photodisintegration of deuteron by 95-Mev bremsstrahlung—705

Allen, R. B. and H. E. Farnsworth. Effect of ion-bombardment cleaning of Ge on point contact rectification—1179(A)

Allen, William A., Joe M. Mapes, and Earle B. Mayfield. Shock waves in air produced by waves in plate—256(A)

Allin, Elizabeth J., W. F. J. Hare, and R. E. MacDonald. Infrared absorption of liquid and solid hydrogen—554(L)

Allison, B. A. (see Faust, W. R.)—224(A)

—— (see Scherrer, V. E.)—224(A)

Alperovitch, Edward A. and J. Malcolm Miller. Occurrence of Tc^{98} in nature—262(A)

Alpert, D. H. Experiments at very low pressures—278(T)

Alter, B. E. K. and C. W. Curtis. Propagation of plastic strain along Pb bars—1151(A)

Alvarez, Luis W., Frank S. Crawford, Jr., and M. Lynn Stevenson. Elastic scattering of 1.6-Mev γ rays from C—280(A)

—— (see Paramentier, D.)—284(A)

Ambler, E., R. P. Hudson, and G. M. Temmer. Anisotropic γ radiation from aligned Nd^{147}—230(A)

Ames, I., H. S. Sack, and R. M. Wood. Dielectric dispersion in ZnS phosphors—1545(A)

Ammiraju, P., M. Rinehart, K. C. Rogers, and L. M. Lederman. Absorption of pions in C and N—1188(A)

Ancker, Betsy, Thomas H. Hazlett, and Earl R. Parker. Relationship between small angle dislocation boundaries and creep—1151(A)

Anderson, A. B. C. Growth, coalescence, and decay of vortices in jet accompanying Pfeifentone—256(A)

Anderson, A. G., R. L. Garwin, E. L. Hahn, J. W. Horton, G. L. Tucker, and R. M. Walker. Spin echo serial storage memory—283(A)

Anderson, C. D. Unstable particles—255(T)

Anderson, H. L. (see Glicksman, M.)—239(A)

—— (see Kruse, U.)—1188(A)

Anderson, John D., Robert W. Kenney, and Charles A. McDonald, Jr. Angular distribution of bremsstrahlung photons—258(A)

Anderson, John H. (see Holzman, G. R.)—542(L)

Anderson, K. A. (see Winckler, J. R.)—1411

Anderson, Paul A. Work function of Cd—1739

Anderson, P. W. (see Weiss, M. T.)—925

Anderson, T. H. Scintillation studies on activated alkali halides—281(A)

Andrews, R. D. Retraction of oriented polystyrene monofilaments—1547(A)

—— (see Gurnee, E. F.)—1547(A)

Aniansson, Gunner. New method for measuring the α-particle range and straggling in liquids—300

Antal, J. J., R. J. Weiss, and G. J. Dienes. Long wavelength neutron transmission as absolute method for determining concentration of lattice defects in crystals—1541(A)

Anthony, R. L. (see Ivory, J. E.)—1558(A)

Apker, L. Photoelectric experiments on excitation-energy transfer in crystals—1558(T)

Arams, Frank R. and Hans K. Jenny. Wide range electronic tuning of microwave cavities in gas atmospheres—562(A)

Argo, H. V. (see Hemmendinger, A.)—70

Argyres, P. N. and A. H. Kahn. Calculation of g-factor of metallic Li—226(A)

Armenteros, R., B. Gregory, P. Hendel, A. Lagarrigue, L. Leprince-Ringuet, F. Muller, and C. Peyrou. Results on heavy charged mesons—275(A)

Armstrong, A. H. (see Frye, G. M., Jr.)—241(A)

Arnold, J. S. Ultrasonic technique for nondestructive evaluation of metal to metal adhesive bonds—283(A)

Arnold, W. H. and J. Ballam. Analysis of charged V events—1204(A)

——, **J. Ballam, A. L. Hobson, R. Ronald Rau, George T. Reynolds, S. B. Treiman, and V. A. Van Lint.** Analysis of charged V events—275(A)

——, **J. Ballam, G. K. Lindeberg, and V. A. J. Van Lint.** Example of the cascade decay of a negative hyperon—838(L)

Aron, J. and D. Kahn. Effect of plastic deformation on surface resistivity of Cu wires—246(A)

Arrott, A., B. R. Coles, and J. E. Goldman. Magnetic susceptibility of α-Mn at low temperatures—1864(L)

—— **and J. E. Goldman.** Magnetic susceptibility in Zn ferrite—1201(A)
Asaro, F., F. Stephens, and I. Perlman. γ rays in the α decay of 100^{254}—260(A)
——, **Frank S. Stephens, Jr., S. G. Thompson, and I. Perlman.** γ-rays of 100^{254}—19
—— (see Hummel, John P.)—22; 261(A)
—— (see Perlman, I.)—262(A)
—— (see Stephens, F.)—261(A)
Aschenbrenner, F. A. Low-energy protons from targets bombarded by 15-Mev deuterons—657
Ashkin, J. (see Feiner, F.)—239(A)
Atkins, K. R. Slope of λ curve of liquid He—319
—— Surface tension of liquid He^4 and liquid He^3—1181(T)
Attix, F. H. (see Spencer, L. V.)—233(A)
Auer, P. L. Phenomenological theory of Townsend breakdown in dielectrics—320
Auerbach, T. and J. B. French. Angular momentum coupling in deuteron reactions—1276
Augustyniak, W. (see McReynolds, A. W.)—418
Averbach, B. L. and P. S. Rudman. Effect of cold work on local order—1554(A)
—— (see Kulin, S. A.)—1566(A)
—— (see Kurtz, A. D.)—1543(A)
—— (see Rudman, P. S.)—1554(A)
Azaroff, L. V. (see Brophy, J. J.)—228(A)

Babcock, H. D. (see Simpson, J. A.)—1402
Babcock, H. W. (see Simpson, J. A.)—1402
Babiskin, J. (see Steele, M. C.)—359
Bach, D. R., C. R. Lubitz, and P. V. C. Hough. Tensor force interaction energies for configurations important in O^{18} and F^{18}—235(A)
Bacon, Roger and Charles S. Smith. Elastic constants of Ag and Ag alloys—1553(A)
Bailey, L. Evan. Angle and energy distributions of charged particles from the cyclotron bombardment of Ni and Ag by 200-Mev protons—275(A)
Bair, Joe K. (see Willard, Harvey B.)—669; 1184(A)
Baker, E., A. Caretto, J. Cumming, G. Friedlander, J. Hudis, and R. Wolfgang. Excitation functions of radioactive products from interaction of high-energy protons with Pb—242(A)
Baker, Winslow F., R. E. Williams, and J. Rainwater. Elastic scattering of π mesons from nuclei. II—1188(A)
—— (see Williams, Ross)—1188(A)
Bakker, C. J. Plans of CERN for its laboratories—1191(T)
Baldwin, F. B. (see Ivory, J. E.)—1558(A)
Baldwin, G. C. Betatron orbit stability studies—1152(A)
Ballam, J. (see Arnold, W. H.)—275(A); 838(L); 1204(A)
Ballard, Stanley S. (see McCarthy, Kathryn A.)—271(A)
Banas, E. M. and B. A. Mrowca. Nuclear spin-spin relaxation time in polymers—1548(A)
——, **B. A. Mrowca, and E. Guth.** Nuclear magnetic relaxation in natural and synthetic rubbers—265(A)
Bandel, H. W. Measurement of current during formative time lag of sparks in uniform fields in air—560(A)
Bandtel, Kenneth C., W. J. Frank, L. Higgins, and B. J. Moyer. Reaction $H^3(p,t)\pi^0$ at 340-Mev proton energy—269(A)
—— (see Dixon, Dwight R.)—259(A)
Banet, Leo. Simple, empirical mass spectrum of fundamental particles—1176(A)
Barber, W. C. Specific ionization of high-energy electrons—276(A)
——, **W. D. George, and D. D. Reagan.** Absolute cross section for reaction $C^{12}(\gamma,n)C^{11}$—73
—— (see George, W.)—276(A)
Barbour, J. P. (see Dyke, W. P.)—263(A)
—— (see Trolan, J. K.)—262(A)
Barile, S. (see Allen, G.)—1168(A)
Barkas, Walter H., Frances M. Smith, and Wallace Birnbaum. Range straggling in nuclear track emulsion—605
Barker, W. A. and A. Mencher. Overhauser nuclear polarization effect—1868(L)
Barnes, George. Field emission from Re: emission pattern corresponding to hexagonal crystal structure—262(A)
Barnes, R. G. and P. J. Bray. Pure quadrupole resonances in Sb and Bi compounds—1182(A)
—— (see Bray, P. J.)—1182(A)
Barnett, C. F. and P. M. Stier. Electron capture cross section for protons—1537(A)
—— (see Stier, P. M.)—1149(A)
Barredo, Joseph G. Physical model of semiconductors—229(A)
—— Statistics for electrical phenomena—1542(A)
Barrett, A. H. (see Mandel, M.)—1159(A)
Barshay, S. (see Colladay, G. S.)—269(A)
Bartlett, James H. Helium wave equation—1067
Barut, A. O. Formulation of probability theory as physical theory—274(A)
Bashkin, S. and R. R. Carlson. γ rays from proton bombardment of Li^6—230(A)
——, **R. R. Carlson, and E. B. Nelson.** Radiative capture of protons by N^{14}—1184(A)
Batten, Hugh W. Plasma fluctuations in crossed electric and magnetic fields—559(A)
Battey, J. F. (see Baum, R. M.)—923
Baum, R. M. and J. F. Battey. Electron capture probability of upper Cu acceptor level in Ge—923
Beams, J. W. Effect of centrifugal field upon rate of transfer through He II film—1138(L)
Bean, C. P. (see Roberts, B. W.)—225(A)
Bearden, J. A. Latest developments in atomic constants—1530(T)
Beck, F. Stability of phase boundary inside superconductor—852
Becker, J. H. Studies of crystal growth, and electrical and optical properties of gray Sn—1192(A)
Becker, R. L. (see Darden, S. E.)—1147(A)
Becker, W. M. and K. Lark-Horovitz. Single-crystal layers of Ge semiconductors—228(A)
Bedard, F. and H. Meissner. Contact resistance between superconductors and normal conductors—1539(A)
Bedo, D. E. and D. H. Tomboulian. Intensity distribution among spectral orders in grazing incidence spectrograph—242(A)
Beer, A. C. Transport effects in p-type Ge—1542(T)
—— (see Harman, T. C.)—1532(A)
—— (see Willardson, R. K.)—227(A)
Behrends, R. E. (see Finkelstein, R. J.)—1155(A); 1870(E)
Belinfante, Frederick J. Emission of negative-energy gravitons by matter—1175(A)
—— Use of flat-space metric in Einstein's curved universe, and "Swiss-cheese" model of space—793
—— **and J. C. Swihart.** Quantized linear theory of gravitation—222(A)
Bemski, G., W. A. Nierenberg, and H. B. Silsbee. Cosine interaction in CsF and RbF—470
Benczer, N. (see Farrelly, B.)—1172(A)
—— (see Lidofsky, L.)—1186(A)
Benedek, G. B., W. Paul, and H. Brooks. Pressure dependence of resistivity, Hall effect, and magnetoresistance in Ge—1193(A)
Benedict, W. S., G. E. Moore, and S. Silverman. Collision line widths and shapes in vibration-rotation bands of HCl—1551(A)

Bennett, Arthur L. and Henry W. Wedaa. Detonation in gas at low pressure—256(A)
Bennett, C. O. (see Spitzer, W.)—228(A)
Bennett, Robert B. (see Ch'en, Shang-Yi)—281(A)
Bennett, W. (see Marder, S.)—1173(A)
Bennett, Willard H. More general theory of magnetic self-focusing—1169(A)
—— Self-focusing streams—1584
Bent, R. D., T. W. Bonner, and J. H. McCrary. Nuclear pairs from 3.4-Mev state in Ca^{40}—1325
——, **T. W. Bonner, J. H. McCrary, and R. F. Sippel.** γ radiation from deuteron bombardment of N^{14}—1198(A)
——, **T. W. Bonner, and R. F. Sippel.** Pair spectrometer measurements of radiations from excited states of light nuclei—1237
—— (see Bonner, T. W.)—1198(A)
Benzer, Seymour. Genetic fine structure and its relation to deoxyribonucleic acid molecule—1534(T)
Beretta, L., E. Clementel, and C. Villi. Phase shift analysis of 240-Mev p-p scattering—1526(L)
Berger, A. G. (see Walsh, J. L.)—265(A)
Bergmann, Peter G. Existence of Dirac generating functions—544(L)
—— **and Irwin Goldberg.** Dirac bracket transformations in phase space—531
—— **and Irwin Goldberg.** Transformations in phase space and Dirac brackets—1175(A)
—— (see Lebowitz, Joel)—1165(A)
—— (see Newman, Ezra)—1176(A)
Berlincourt, Ted G. and M. C. Steele. Oscillatory Hall effect, magnetoresistance, and magnetic susceptibility of graphite single crystal—227(A); 956
—— (see Overton, William C., Jr.)—1180(A)
Berman, A. S. (see Weissberg, H. L.)—1540(A)
Bernstein, H. and R. H. Kingston. Photomultiplication at surface of Ge—1566(A)
Bernstein, J. and Abraham Klein. Exchange current effects in two-nucleon system—1155(A)
Bernstein, S. (see Dabbs, J. W. T.)—1512(L)
Bernstein, W. (see Weiss, J.)—1828
Berry, Chester R. Change in KCl lattice dimensions by soft x-rays—934; 1540(A)
Besdin, D. J. and Joseph H. Robinson III. Magnetic moment of free electrons—272(A)
Beshers, D. N. and J. S. Koehler. Temperature dependence of internal friction in Cu—1553(A)
Betchov, R. Production of vorticity in isotropic turbulence—1142(A)
Bethe, H. A. π mesons and nucleons—1177(T)
Betts, D. D. and J. D. Jackson. Double electron capture by α particles in He—1149(A)
Beyster, J. R., R. L. Henkel, R. A. Nobles, and J. M. Kister. Inelastic collision cross sections at 1.0-, 4.0-, and 4.5-Mev neutron energies—1216
—— (see Walt, M.)—677
Bhadra, T. C. (see Chatterjee, S. D.)—1728
Bhatia, A. B. Vibration spectra and specific heats of cubic metals. I. Theory and application to Na—245(A)
—— **and G. K. Horton.** Vibration spectra and specific heats of cubic metals. II. Application to Ag—1715; 1181(A)
Biedenharn, L. C. and C. M. Class. Soluble problem in theory of Coulomb excitation—691
—— **and A. Simon.** Analysis of angular distribution data by electronic computers—1153(A)
Bina, Melvin J., Igor Alexeff, and Richard M. Sanders. Evapor-ion pump developments—251(A)
Bingham, H. H., J. C. Keck, and A. V. Tollestrup. Photoproduction of neutral mesons in H and D—1187(A)
Binnie, W. P. Crystal structure of InBi—228(A)
Biot, M. A. Deformation of viscoelastic plates derived from thermodynamics—1869(L)
Bird, George R. Microwave spectrum of NO_2—1160(A)
—— (see Mockler, Richard C.)—1837
Birkhoff, R. D. (see Rohr, R. C.)—1266
Birman, Joseph L. Average crystal potential—1863(L)
—— Bond dipoles and piezoelectricity in zincblende semiconductors—1567(A)
—— Effect of overlap on electrostatic lattice potentials in ionic crystals—1871(E)
Birnbaum, Wallace (see Barkas, Walter H.)—605
Biscoe, J. (see Brackett, T. E.)—1210(A)
Bishop, G. R. and J. P. Perez Y Jorba. Spins and parities of excited states of Ce^{140} and Sr^{88}—89
Bitter, F. and J. F. Waymouth. Analysis of plasma of fluorescent lamps. I—1148(A)
—— (see Waymouth, J. F.)—1148(A)
Blair, J. M. (see Stratton, T. F.)—629
Blakewood, C. H. (see Lane, C. T.)—1196(A)
Blaser, J. P. (see Feiner, F.)—239(A)
Blatt, F. J. Effect of vacancies and interstitials on electrical properties of Cu—245(A)
——, **M. C. Huse, and R. A. Rubenstein.** Resistivity due to point imperfections in Cu—1553(A)
Bleakney, Walker (see Griffith, Wayland)—1143(A)
Blewitt, T. H., J. K. Redman, F. A. Sherrill, and R. R. Coltman. Mechanical twinning in Cu—1555(A)
Blizard, J. L. B. Fundamental research in United States—1211(A)
Block, Martin M. Production of K mesons by protons of Cosmotron energy—1156(A)
——, **E. M. Harth, W. B. Fowler, R. P. Shutt, A. M. Thorndike, and W. L. Whittemore.** Charged V particle production in p-p collision—248(A)
—— (see King, D. T.)—1203(A)
Block, R. C. and H. W. Newson. Total neutron cross-sections in kev region: separated isotopes of Ni and Ce—1162(A)
Bloembergen, N. Nuclear spin exchange in solids—1183(T)
Blois, M. S., Jr. Vacuum deposition of magnetic alloy films—281(A)
Bloom, Arnold L. Nuclear induction in inhomogeneous fields—1105
Bloom, S. (see Kivel, B.)—495
Bloom, Stewart D. New technique for observing cyclotron phase grouping—233(A)
Blosser, H. G., T. H. Handley, and M. K. Hullings. Survey of (p,n) reactions at 11.7 Mev—1198(A)
Bludman, S. A. and D. L. Judd. Aberrations and fringing effects in modified Siegbahn-type magnetic spectrometer—283(A)
Blumenfeld, H., E. T. Booth, L. M. Lederman, and W. Chinowsky. Production of unstable particles in C and Pb by 2-Bev pions—1203(A)
Blunt, R. F., H. P. R. Frederikse, and W. R. Hosler. Properties of Mg_2Sn—1533(A)
Bodansky, D. and A. M. Sachs. Interaction of 46-Mev π^+ mesons in deuterium—240(A)
Bodine, J. H. and F. B. Thiess. Optical absorption spectra of ThO—1532(A)
Boehm, F., P. Marmier, and J. W. M. DuMond. L-conversion in pure $E2$ transitions—280(A)
—— (see Marmier, P.)—280(A)
Bollinger, L. M., D. A. Dahlberg, R. E. Cote, H. E. Jackson, and G. E. Thomas. Neutron transmission measurements at the new Argonne reactor, CP-5—223(A)
—— (see Cote, R.)—1162(A)
Bond, John W., Jr. Recombination in argon shock front—285(A)
—— Shock front structure in argon—256(A)

Bondelid, R. O. (see Fagg, L. W.)—1538(A)
Bonner, T. W., R. D. Bent, and J. H. McCrary. Nuclear pairs from proton bombardment of Ca^{40}—1198(A)
—— (see Bent, R. D.)—1237; 1198(A); 1325
Boorse, Henry (see Smith, Bernard)—328
Booth, E. T. (see Blumenfeld, H.)—1203(A)
Boquet, F. L. (see Meyer, R. A.)—1531(A)
Borgnis, F. E. Specific directions of longitudinal wave propagation in anisotropic media—1000
Bowers, Raymond (see Melamed, Nathan T.)—1545(A)
Bowman, Harry R. and Lloyd G. Mann. γ rays accompanying spontaneous fission of Cf^{252}—277(A)
Boyle, W. S. and P. Kisliuk. Departure from Paschen's law of breakdown in gases—560(A)
—— (see Kisliuk, P.)—560(A)
Bracewell, Ronald N. Radio astronomy—278(T)
Brackett, T. E., R. D. Dunlap, and J. Biscoe. Small angle x-ray scattering by system iso-octane-*n*-heptforane—1210(A)
Brady, J. J., M. B. Larson, and T. A. O'Halloran. Internal friction as function of cold work of copper reeds at low frequencies—271(A)
—— (see Brick, R. O.)—282(A)
—— (see Perry, R. L.)—281(A)
Bragaw, Chester G., Jr. Biaxial creep fracture of high polymers—1559(A)
Bramley, Arthur. Properties of CdS films deposited in vacuo—246(A)
Bramson, H. J. Electron spectrum from muon decay—1187(A)
Brandt, Werner. Calculation of compressibility of polyethylene from energy of interaction between ($-CH_2-$) groups—243(A)
Braner, A. (see Halperin, A.)—1135(L)
Branscomb, Lewis M. and Stephen J. Smith. Electron affinity of atomic O—1127(L)
—— **and Stephen J. Smith.** Experimental cross section for photodetachment of electrons from H^- and D^-—1028
Braunstein, R. and J. W. Trischka. Molecular constants and nuclear-molecular interactions of Li^7F^{19} by molecular beam electric resonance method—1092
Bray, P. J. and R. G. Barnes. As^{75} pure quadrupole resonance—1182(A)
—— (see Barnes, R. G.)—1182(A)
Bray, Ralph. Minority carrier extraction in Ge—229(A)
Breen, R. J. and M. R. Hertz. γ radiation from Po neutron sources—599
Breitman, Leo. Glass transitions in polymer-plasticizer systems—1559(A)
Brennan, J. G. (see Adkins, R. H.)—235(A)
Brick, R. O., J. J. Brady, and M. D. Pearson. Penetration into rarer medium in total reflection of microwaves—282(A)
Brock, E. G. and J. E. Taylor. Field emission from Ti single crystals—1169(A)
Brockhouse, B. N. Slow neutron spectrometry—New tool for study of energy levels in condensed systems—1171(A)
—— Study of energy levels in solids, liquids, and magnetic materials by scattered slow neutrons—1171(T)
——, **L. M. Corliss, and J. M. Hastings.** Multiple scattering of slow neutrons by flat specimens and magnetic scattering by Zn ferrite—1721
Brode, Harold L. Blast from sphere of high-pressure gas—1158(A)
Brodnyan, J. (see Philippoff, W.)—1549(A)
Broersma, S. Nuclear magnetic relaxation of nonuniform systems—1182(A)
Broida, Herbert P. Afterglow of solid N_2—563(A)
Brolley, J. E., Jr., and F. L. Ribe. Energy loss by 8.86-Mev deuterons and 4.43-Mev protons—1112
Brooks, H. Properties of Ge and Si at high pressures—244(T)
—— (see Benedek, G. B.)—1193(A)
—— (see Warschauer, D. M.)—1193(A)
Brophy, J. J., N. Rostoker, and L. V. Azaroff. Semiconducting properties of FeO thermistor material—228(A)
Brown, Fielding and Charles L. Gravel. Direct observation of domain rotation in ferrites—442
Brown, Frederick C. Electron mobility in AgCl: Comparison of experiment with theory—263(A)
—— Properties of electrons and holes in AgCl—1549(T)
Brown, L. Carlton and Dudley Williams. Nuclear magnetic moment of K^{39}—1537(A)
Brown, Sanborn C. (see Champion, K. S. W.)—559(A)
—— (see Goldey, James M.)—1192(A); 1761
—— (see Rose, David J.)—310
—— (see Schulz, George J.)—1642; 559(A)
—— (see Weinstein, R.)—223(A)
Brown, W. L. Surface potential and surface charge distribution from semiconductor field effect measurements—1565(A)
—— (see Montgomery, H. C.)—1565(A)
Brown, W. W. Nuclear interactions of cosmic rays in Al—275(A)
Browne, C. I. (see Prestwood, R. J.)—1324
Broyles, Arthur. Stark fields from ions in plasma—1166(A)
Brubaker, W. M. Influence of space charge on potential distribution in mass spectrometer ion sources—563(A)
Brueckner, K. A. Energy levels of π-mesonic atoms—769
—— Nuclear saturation and independent-particle model of nucleus—244(T)
——, **R. J. Eden, and N. C. Francis.** High-energy reactions and evidence for correlations in nuclear ground state wave function—1445
Bube, Richard H. Temperature dependence of width of band gap in several photoconductors—431
Buckingham, M. J. Superfluidity in liquid He^3—1855(L)
Buckingham, R. A. (see Halpern, O.)—1626
Bugg, W. (see Stier, P. M.)—1149(A)
Burch, W. E. (see Newman, R.)—1536(A)
Burger, R. M., H. E. Farnsworth, and R. E. Schlier. Adsorption of H_2 and O_2 on Ge—1179(A)
—— (see Farnsworth, H. E.)—250(A)
Burgess, John C. Apparent limit of convergence of perturbation series solution for free undamped Duffing equation with hardening spring—257(A)
Burk, D. L. (see Friedberg, S. A.)—1200(A)
Burkhard, E. L. and J. H. Lewis. Ionization of air by γ rays—1154(A)
Burkhardt, Louis C. (see Sawyer, George A.)—1305
Burns, Laurence. Alternative explanation of Waymouth-Bitter experiments—1863(L)
Burson, S. B., W. C. Jordan, and J. M. LeBlanc. Decay of $_{22}Ti^{51}$ (5.8 min)—230(A)
—— (see LeBlanc, J. M.)—39
Burstein, Elias, G. Picus, B. Henvis, and M. Lax. Optical properties of group III elements in Si—1536(A)
—— (see Davisson, J. W.)—1544(A)
—— (see Lipson, H. G.)—1535(A)
—— (see Sclar, N.)—1178(A); 1757
—— (see Teitler, S.)—1561(A)
Burton, W. K. Canonical invariance in Lagrangian quantum mechanics—555(L)
Burwell, J. R., R. W. Huggett, and R. W. Thompson. Example of τ^+-decay in flight—101
——, **R. W. Huggett, and R. W. Thompson.** New evidence concerning specific identity of θ^0 decay fragments and statistics of θ^0 particle—247(A)
—— (see Huggett, R. W.)—248(A)
—— (see Kim, Y. B.)—248(A)

Buschert, R., I. G. Geib, and K. Lark-Horovitz. Structure of liquid Te—1157(A)
Butler, J. W. γ-ray thresholds in $F^{19}(d,n\gamma)Ne^{20}$ reaction—241(A)
Butler, S. T. and M. H. Friedman. Partition function for system of interacting Bose-Einstein particles—287
—— (see Friedman, M. H.)—294
Byram, E. T., T. A. Chubb, and H. Friedman. Dissociation of O_3 in upper atmosphere—1594

Cabrera, N. and M. M. Levine. Polytypism and dislocations—1543(A)
Caldwell, David O. and J. Reginald Richardson. Elastic scattering of 20.6-Mev protons by deuterons—28
Callaway, Joseph. Electron band structure of Fe—1150(A)
Callen, H. B. (see Kriessman, C. J.)—1562(A)
Campbell, E. C., R. W. Pelle, F. C. Maienschein, and P. H. Stelson. Decay and fast neutron excitation of Zr^{90m}—1172(A)
Cantwell, Murray. Molecular excitation in β decay—235(A)
Carbone, Robert J., Gerald Stone, and Edgar Everhart. Cross section measurements for large angle collisions of He, Ne, and A ions with argon gas atoms at energies from 25–100 kev—1150(A)
—— (see Everhart, Edgar)—1045
—— (see Stone, Gerald)—1150(A)
Caretto, A. (see Baker, E.)—242(A)
Carlson, R. R. and E. B. Nelson. γ rays from low-energy proton bombardment of Be—1310
—— (see Bashkin, S.)—230(A); 1184(A)
Carr, R. J. (see Glass, R. A.)—261(A)
Carter, R. S. Resonance parameters in U^{238}—1161(A)
Case, K. M. Decomposition of generalized Duffin-Kemmer algebra—1189(A)
—— (see Moldauer, P. A.)—1190(A)
Caspari, M. E. Direction breakdown in alkali halide crystals—1170(A); 1679
Cassel, Hans M. Thermal expansion and aerodynamic stability of open flames—1143(A)
Castle, J. G., Jr. Magnetic resonance properties of raw cokes—1564(A)
Castle, J. W. (see Hamilton, J. F.)—1557(A)
Chamberlain, Owen. High-energy proton polarization studies involving triple scattering—266(T)
—— **and John D. Garrison.** p-p scattering experiments at 170 and 260 Mev—1167(A)
—— (see Tripp, R.)—266(A)
—— (see Ypsilantis, T.)—267(A); 840(L)
Champion, K. S. W. and S. C. Brown. Plasma resonance—559(A)
Chandrasekhar, S. Theory of turbulence—1158(T)
—— **and G. Herzberg.** Energies of ground states of He, Li^+, and O^{6+}—1050
Chang, W. Y. (see del Castillo, G.)—1163(A)
Chatterjee, S. D. and T. C. Bhadra. Abnormal increase in dielectric constant of electret-forming material—1728
Ch'en, Shang-Yi, Robert B. Bennett, and Oleg Jefimenko. Absorption bands of Rb in presence of foreign gases—281(A)
Cheng, L. S., Virginia C. Ridolfo, M. L. Pool, and D. N. Kundu. Radioactive Tl^{204} and Bi^{207}—231(A)
Chetham-Strode, A., Jr. (see Hummel, J. P.)—22
Chikazumi, Sōshin and Kenzō Suzuki. Domain patterns on rolled single crystal of Ni_3Fe—1130(L)
Chinowsky, W. (see Blumenfeld, H.)—1203(A)
Choppin, G. R., B. G. Harvey, S. G. Thompson, and A. Ghiorso. Nuclear properties of 100^{250}—1519(L)
—— (see Ghiorso, A.)—1518(L)
Choquard, P. F. (see Willardson, R. K.)—227(A)
Chou, C. N. and Marcel Schein. Scintillation counter study of energy spectra of cosmic-ray photons and electrons at 11 200 feet—162
Chraplyvy, Z. V. Some considerations concerning relativistic two-particle wave-equations—244(T)
Chrétien, Max. Radiative corrections to electron scattering—1515(L)
Christensen, H. Ultraviolet light induced surface channel and carrier lifetime effects in Ge—1178(A)
Christy, R. F. α decay of spheroidal nuclei—1205(A)
—— Reactions and models of light nuclei—260(T)
Chubb, T. A. (see Byram, E. T.)—1594
Chupp, W. W. (see Goldhaber, Gerson)—267(A)
Church, E. L. and J. E. Monahan. Internal conversion in L and M subshells—718
—— **and A. W. Sunyar.** Rotational states of excitation in U^{234}—1186(A)
Clark, D. (see Piccioni, O.)—275(A)
Clark, J. (see Wolff, G.)—1179(A)
Clark, M. A. (see Graham, R. L.)—1173(A)
Clarke, Edward N. Ge surface conductivity and effects of water vapor—1178(A)
Class, C. M. (see Biedenharn, L. C.)—691
—— (see Risser, J. R.)—1183(A)
Cleland, J. W., J. H. Crawford, Jr., and J. C. Pigg. Fast-neutron bombardment of n-type Ge—1742
Clementel, E. (see Beretta, L.)—1526(L)
Cobble, J. W. (see Glass, R. A.)—261(A)
Cohen, Alvin J. Impurity induced color centers in fused silica—1550(A)
Cohen, Bernard L. Angular distributions and yields of neutrons from (p,n) reactions—49; 1206(A)
——, **B. L. Ferrell-Bryan, D. J. Coombe, and M. K. Hullings.** Angular distribution of fission fragments from 22-Mev proton-induced fission of U^{238}, U^{235}, U^{233}, Th^{232}, and Th^{230}—685
—— **and E. Newman.** Anomalous dependence of F_p/F_n on bombarding energy—1198(A)
Cohen, David (see Shaw, Harlan)—259(A)
Cohen, E. Richard and J. W. M. DuMond. Comments on Straumanis' concepts regarding Avogadro's number—1128(L)
Cohen, Stanley. Effect of anomalous nucleon magnetic moment on π^0 lifetime—749
Cohen, Victor W. Spins and moments of radioactive nuclei—1174(T)
—— (see Gilbert, D. A.)—1194(A)
Coleman, C. and R. Smoluchowski. Grain boundary diffusion in Al-Cu system—1555(A)
Coles, B. R. (see Arrott, A.)—1864(L)
Colladay, G. S. and S. Barshay. Second-neighbor interaction in two-dimensional graphite lattice—270(A)
Collins, F. M. Dimensional changes during heat treatment thermal expansion of polycrystalline carbons and graphites—1564(A)
Collins, George B. (see Ridgway, S. L.)—247(A)
Collins, R. J., F. W. Reynolds, and G. R. Stilwell. Electrical and optical properties of GaSb films—227(A)
—— (see Spitzer, W.)—1536(A)
Collins, T. L. (see White, F. A.)—1174(A)
Coltman, R. R. (see Blewitt, T. H.)—1555(A)
Compton, W. Dale. Self-diffusion of Ag in AgCl—1543(A)
Conger, R. L. Magnetization reversal in thin films—1752
Conn, Willi M. Metallic deposits and shock waves due to electrically "exploded" wires—1551(A)
Conwell, E. M. Impurity band conduction in Ge and Si—1178(A)
Cook, E. J. and G. F. Pieper. Forty-channel pulse height analyzer—1154(A)

Cool, R. (see Piccioni, O.)—275(A)
Cooley, William J. (see Van Horn, David D.)—245(A)
Coombe, D. J. (see Cohen, B. L.)—685
Cooper, C. B. (see Enck, F. D.)—237(A)
Cooper, John N. (see Green, D. Wayne)—466
Cooper, Raymond D. and Dan J. Zaffarano. Photodisintegration of C, O, and N in nuclear emulsions—1199(A)
Coor, T., D. A. Hill, W. F. Hornyak, L. W. Smith, and G. Snow. Nuclear cross sections for 1.4-Bev neutrons—1369
Copeland, Paul L. and B. Pearson de Lany. Statistics of exponential distribution of exponential populations applied to distribution of arc lives—251(A)
—— (see de Lany, B. Pearson)—251(A)
Corak, William S., M. P. Garfunkel, C. B. Satterthwaite, and Aaron Wexler. Atomic heats of Cu, Ag, and Au from 1°K to 5°K—1699
Corbett, J. W. and W. W. Watson. Thermal diffusion in multiple component isotopic mixtures—1165(A)
Cork, Bruce. University of California bevatron—266(T)
Cork, J. M. (see LeBlanc, J. M.)—39
Corliss, L. M. (see Brockhouse, B. N.)—1721
Cornelius, R. (see Sargent, C. P.)—1349
Corrsin, S., A. L. Kistler, and V. O'Brien. Measurements of velocity and temperature fluctuations behind hot grid—1142(A)
—— (see Ruetenik, J. R.)—1142(A)
Cote, R. E. and L. M. Bollinger. $\Gamma_n^0/\bar{D}$ for slow neutron resonances—1162(A)
—— (see Bollinger, L. M.)—223(A)
Cox, J. T. (see Mizushima, Masataka)—1034; 1159(A)
Crasemann, Bernd and D. L. Manley. Radioactivity of Co^{57}—66; 279(A)
Crawford, Frank S., Jr. (see Alvarez, Luis)—280(A)
—— (see Paramentier, D.)—284(A)
Crawford, J. H., Jr., and D. K. Stevens. Magnetic susceptibility in InSb—1532(A)
—— (see Cleland, J. W.)—1742
Crewe, A. V. Beam extraction of Liverpool synchrocyclotron—1191(T)
Crosbie, E. A. and M. Hamermesh. Coupling of betatron and phase oscillations in synchrotron—233(A)
Crowe, K. M., R. M. Friedman, and H. Motz. π^- counting by delayed coincidence—268(A)
—— (see Motz, H.)—268(A)
Crowe, R. W. and J. C. Devins. Sparking potential and molecular structure of hydrocarbon gases—560(A)
Crussard, J. (see Walker, W. D.)—240(A); 1416
Cuevas, J. (see Krasner, Sol)—1149(A)
Culler, G. (see Fernbach, S.)—273(A)
—— (see Sherman, N.)—273(A)
Culler, Vaughn and R. W. Waniek. Experimental evidence for optical model for neutrons between 60 and 110 Mev—1148(A)
Cumming, J. (see Baker, E.)—242(A)
Curtis, C. W. (see Alter, B. E. K.)—1151(A)
Cusano, D. A. Field enhanced solid-state luminescence—1169(A)
—— Radiation-controlled electroluminescence and light amplification in phosphor films—546(L)

Dabbs, J. W. T., L. D. Roberts, and S. Bernstein. "Brute force" polarization of In^{115} nuclei; angular momentum of 1.458-ev neutron resonance—1512(L)
Dahlberg, D. A. (see Bollinger, L. M.)—223(A)
Dallaporta, N. Investigations of Italian school—1166(T)
D'Altroy, F. and H. Y. Fan. Effective mass of carriers and relaxation time in Ge—1561(A)
Danforth, W. E. Short-time polarization in ThO—1177(A)
Daniels, W. B. (see Smith, Charles S.)—1553(A)
Darden, S. E., A. Okazaki, and R. L. Becker. Determination of nuclear level density—1147(A)
Darin, S. R. (see Taylor, G. R.)—1558(A)
Darnell, F. J. and S. A. Friedberg. Electrical breakdown in Ge at low temperatures—1178(A); 1860(L)
Das, T. P. and D. K. Roy. Spin echoes with four pulses—extension to n pulses—525
—— **and A. K. Saha.** Electric quadrupole interaction and spin echoes in crystals—516
Dash, W. C. Birefringence in Si—1536(A)
——, **R. Newman, and E. A. Taft.** Optical absorption in single crystals of Ge and Si—1192(A)
—— (see Newman, R.)—1536(A)
Daunt, J. G. and J. Korringa. Susceptibility and entropy of F-centers—1550(A)
Davidon, W. C. (see Kruse, U.)—1188(A)
Davis, G. L. (see Wetherill, G. W.)—250(A)
Davis, L., jr. (see deMars, G. A.)—539(L); 1565(A)
—— (see Statz, H.)—540(L); 1566(A)
Davis, R. E. (see Goldberg, Colman)—1192(A)
Davisson, J. W., Elias Burstein, and P. L. Smith. Prismatic slip in crystals—1544(A)
Day, R. B., R. L. Mills, J. E. Perry, Jr., and F. Scherb. n-p scattering at 20 Mev—279(A)
DeBretteville, A., Jr. Second-order transition in $BaTiO_3$—1563(A)
Dehmelt, H. G. Paramagnetic resonance of atomic phosphorus—1181(A)
Déjardin, Georges, Joseph Janin, and Ivan Eyraud. Spectroscopic study of discharge and afterglow produced in nitrogen by pulsed microwaves—1149(A)
de Lany, B. Pearson and Paul L. Copeland. Duration of Hg arcs in evacuated bulbs coated with rare earths—251(A)
—— (see Copeland, Paul L.)—251(A)
Delbecq, Charles J., P. Pringsheim, and P. H. Yuster. Optical and electrical properties of LiF x-rayed at liquid nitrogen temperature—237(A)
—— (see Primak, W.)—237(A); 1708
—— (see Yuster, Philip)—233(A)
del Castillo, G., A. Snyder, L. Grodzins, and W. Y. Chang. Nuclear interaction of sea-level, cosmic-ray particles with C and Pb—1163(A)
—— (see Snyder, A.)—1163(A)
deMars, G., H. Statz, and L. Davis, Jr. Conductance of p-type inversion layers on n-type Ge—1565(A)
——, **H. Statz, and L. Davis, Jr.** Measurement and interpretation of conductance of p-type inversion layers on Ge—539(L)
—— (see Statz, H.)—540(L); 1565(A)
Denman, Eugene D. (see Richards, Hans Kohn)—250(A)
DeSorbo, W. and D. Turnbull. Precipitation in small spheres of Pb-Sn alloy—1554(A)
DeStaebler, Herbert, Jr., and B. V. Sreekantan. Nature of neutral secondary particle produced in decay of $K_{\pi 3}$-meson—1520(L)
Deutsch, M. (see Weinstein, R.)—223(A)
Devins, J. C. (see Crowe, R. W.)—560(A)
DeWire, J. W. (see Swartz, C. E.)—1164(A)
Dexter, D. L. Resistivity of dilute alloys—543(L)
—— Smakula's equation in insulating solids—1533(A)
Dexter, R. N. Third harmonic cyclotron resonance of holes in Ge—1560(A)
Dicke, R. H. (see Romer, R. H.)—1160(A)
Dieckamp, H. Shear modulus recovery of electron irradiated Cu—1531(A)
Dieke, G. H. Spectroscopy of solids—1558(T)
Dienes, G. J. (see Antal, J. J.)—1541(A)
Dillinger, J. R. (see Fleming, P. J.)—1196(A)

Dillon, J. A., Jr., and M. L. Dillon. Origins of papers presented at regular meetings of American Physical, Acoustical, and Optical Societies in 1954—1211(A)
Dillon, M. L. (see Dillon, J. A., Jr.)—1211(A)
Dingle, R. B. Diamagnetic resonance in electronic conductors—550(L)
Dixon, Dwight R. and Kenneth C. Bandtel. Photodisintegration of deuterons by high-energy γ rays—259(A)
Doggett, W. O. (see Petroff, M. D.)—279(A)
Domm, Ulrich and Hermann Foettinger. Stability of vortex streets with consideration of diffusion of vorticity of individual vortices—1142(A)
Donahue, T. M. and Robert Resnick. Resonance absorption of sunlight in twilight layers—1622
Donnay, J. H. Crystallographic significance of some recent results in solid-state physics—1558(T)
Doty, Paul. Size and shape of nucleic acids as revealed by physical-chemical techniques—1531(T)
Douglas, R. A. (see Galonsky, A.)—586
—— (see Jones, K. W.)—241(A)
Dousmanis, G. C. Magnetic hyperfine effects and electronic structure of NO—1160(A)
Downs, B. W. Polarization of deuteron—258(A)
—— Variation calculation of polarizability of deuteron—194
——, **D. G. Ravenhall, and D. R. Yennie.** Electric quadrupole effects in scattering of high-energy electrons by heavy nuclei—277(A)
—— (see Yennie, D. R.)—277(A)
Doyama, M. (see Kuczynski, G. C.)—270(A)
Doyle, W. T. and A. B. Robbins. Energy levels in F^{17} and Al^{26}—1185(A)
Dresden, M. Collective description of electron gas—1165(A)
Dresselhaus, G., A. F. Kip, and C. Kittel. Cyclotron resonance of electrons and holes in Si and Ge crystals—368
——, **A. F. Kip, C. Kittel, and G. Wagoner.** Cyclotron and spin resonance in InSb—556(L)
Dreyfus, Russell W. and Paul W. Levy. Heat treatment of irradiated NaN_3—1541(A)
Drougard, M. E., R. Landauer, and D. R. Young. Dielectric behavior of $BaTiO_3$ in paraelectric state—1010; 1563(A)
—— (see Huibregtse, E. J.)—1562(A)
Drummond, J. E. and L. Wilcox. Oscillations of plasma with skew velocity distribution transverse to static magnetic field—558(A)
—— (see Wilcox, L.)—263(A)
Dryden, Hugh L. Fifty years of boundary layer theory and experiment—1143(T)
Duboc, Charles A. Theory of Ag-halide photolysis—1557(A)
Dudziak, Walter, Ryokichi Sagane, and James Vedder. Photomeson production from H, D, and C—269(A)
—— (see Sagane, Ryokichi)—269(A)
Dugdale, J. S. and D. K. C. MacDonald. Lattice thermal conductivity—1751
Dumke, William P. Generalized deformation potential theory for n-type Ge—230(A)
DuMond, J. W. M. (see Boehm, F.)—280(A)
—— (see Cohen, E. Richard)—1128(L)
—— (see Marmier, P.)—280(A)
Duncan, B. J. and L. Swern. Temperature effects in ferrites at microwave frequencies—1201(A)
Dunlap, R. D. (see Brackett, T. E.)—1210(A)
Dunlap, W. C., Jr. Au, an "amphoteric" impurity element in Ge—1535(A)
Dunnam, F. E. (see Ralph, D. C.)—249(A)
Dunning, K. L. (see Fagg, L. W.)—1538(A)
Dutton, David. Localized photoconductivity in PbS films—1549(A)
Dyke, W. P., J. P. Barbour, J. K. Trolan, and E. E. Martin. Electrical stability of T-F emitter—263(A)
—— (see Trolan, J. K.)—262(A)
Dyson, Freeman J. Electron spin resonance absorption in metals. II. Theory of electron diffusion and skin effect—349
Dzurus, M. (see Hennig, G.)—227(A)

Eatherly, W. P. Effect of radiation damage on electrical and thermal properties of graphite—1531(T)
Eaton, V. E. Physics is an art—1177(T)
Eden, R. J. and N. C. Francis. Nuclear models—1205(A)
—— (see Brueckner, K. A.)—1445
Ehler, A. W. and G. L. Weissler. Absorption of radiation in vacuum uv by N atoms produced in discharge plasma in N_2—561(A)
Ehrenreich, H. and A. W. Overhauser. Mobility of holes in Si and Ge—1533(A)
Eisberg, R. M. (see Palevsky, H.)—492
Eisinger, J. T. (see Gossett, C. R.)—724
Ekstein, Hans and Norman Rostoker. Quantum correction to shot effect—222(A)
—— (see Gilbert, T. L.)—1200(A)
—— (see Rostoker, Norman)—222(A)
Elliot, J. O. Differential elastic scattering of 14-Mev neutrons—1147(A)
—— (see Faust, W. R.)—1147(A)
Elliott, David (see Probstein, Ronald F.)—1143(A)
Emmerich, W. S. Neutron cross sections in 4-Mev range—1148(A)
Emrich, Raymond J. and Robert L. Peterson. Pressure variation in shock tube flow—1141(A)
—— (see Williams, Albert C.)—1158(A)
Enck, F. D. and C. B. Cooper. Elastic constants and specific heat of KCl at elevated temperatures—237(A)
Engel, Olive G. Mechanism of high-speed-waterdrop erosion of methyl methacrylate plastic—236(A)
Englefield, M. J. Direct evaluation of fractional parentage coefficients using Young operators: normalization of four-particle wave functions—1213
Enns, J. H., R. L. Martin, and E. Katz. Sequence experiment for study of reciprocity law failure at low intensities—1556(A)
—— (see Martin, R. L.)—1556(A)
Epstein, Saul T. Derivation of Feynman-Dyson rules from time-independent theory—196
Eriksen, Erik (see Foldy, Leslie L.)—775; 1190(A)
Ernst, H. (see Hayward, R. W.)—231(A)
Etzel, H. W. Detection of vacancies created in NaCl by x-rays—1531(A)
Evans, Marjorie W., Frank I. Given, and William E. Richeson, Jr. Effects of attenuating materials on detonation induction distances in gases—256(A)
Everhart, Edgar, R. J. Carbone, and Gerald Stone. Differential cross-section measurements for large-angle collisions of He, Ne and A ions with A atoms at energies to 100 kev—1045
—— (see Carbone, Robert J.)—1150(A)
—— (see Stone, Gerald)—1150(A)
Evett, A. A. Theoretical evaluation of binding energy of HEH—1191(A)
Eyraud, Ivan (see Déjardin, Georges)—1149(A)

Fagg, L. W., E. A. Wolicki, R. O. Bondelid, K. L. Dunning, and S. Snyder. Coulomb excitation of energy levels in Te and Ag—1538(A)
Fairbank, Henry A. and J. Wilks. Heat transport and boundary layer resistance in He II below 1°K—1196(A)
Fairhall, A. W. Fission of Bi by 22-Mev deuterons—276(A)
Famularo, K. F. (see Stratton, T. F.)—629

Fan, H. Y. (see D'Altroy, F.)—1561(A)
—— (see Kaiser, W.)—966
—— (see Schulz-DuBois, E.)—1561(A)
—— (see Spitzer, W.)—228(A); 1536(A)
—— (see Stoeckmann, F.)—1535(A)
Farney, G. K. (see Hahn, T. M., Jr.)—1183(A)
Farnsworth, H. E., R. E. Schlier, and R. M. Burger. Low-energy electron diffraction studies of Ge crystal surface—250(A)
—— (see Allen, R. B.)—1179(A)
—— (see Burger, R. M.)—1179(A)
—— (see George, T. H.)—1179(A)
—— (see Schlier, R. E.)—250(A)
—— (see Woodcock, R. F.)—1152(A)
Farrall, George A. and Charles R. Mingins. Open screen technique in electron microscopy—1211(A)
Farrelly, B., L. Koerts, R. van Lieshout, N. Benczer, and C. S. Wu. Radiations of Sb^{122}—1172(A)
—— (see Koerts, L.)—1172(A); 1230
Faust, W. R., R. C. O'Rourke, and J. O. Elliot. Cloudy crystal ball analysis of 14-Mev elastic neutron scattering data—1147(A)
——, **V. E. Scherrer, and B. A. Allison.** γ-γ coincidences produced by inelastic scattering of 2.5-Mev neutrons—224(A)
—— (see Scherrer, V. E.)—224(A)
Feder, R. and A. S. Nowick. Anomalous behavior of Cu_3Au quenched from above 600°C—1152(A)
Feher, George and A. F. Kip. Electron spin resonance absorption in metals. I. Experimental—337
—— **and R. A. Levy.** Electron spin resonance in frozen metal-ammonia solutions—264(A)
Feiner, F., J. Ashkin, J. P. Blaser, and M. O. Stern. Differential cross sections for pion-proton scattering at 150 and 170 Mev—239(A)
Feld, Bernard T. Deuteron model for π-meson and photon capture by complex nuclei—1155(A)
—— Photomeson production from H—238(A)
Feldman, David. Nonrelativistic interaction between two nucleons—1456
Feldmann, W. L. (see Pearson, G. L.)—1567(A)
Ferentz, M. and N. Rosenzweig. Tabulation of F coefficients—222(A)
Ferguson, K. R. Optical absorption bands induced in γ irradiated glass—1542(A)
Fernbach, S., G. Culler, and N. Sherman. Optical model analysis of scattering of 14-Mev neutrons. II. Polarization effects—273(A)
—— (see Sherman, N.)—273(A)
Ferrell-Bryan, B. L. (see Cohen, B. L.)—685
Ferry, John D. (see Plazek, D. J.)—1548(A)
—— (see Williams, Malcolm L.)—1549(A)
Feshbach, Herman. Relativistic wave equations—801
—— **and S. I. Rubinow.** Equivalent two-body method for triton—188
Feuer, Paula. Electronic states in perturbed periodic lattice—1193(A)
Fine, S. (see Rittner, E. S.)—545(L)
Fink, Richard W. and Berol L. Robinson. K and L x-ray intensities in Cs^{131} decay—1293
—— (see Robinson, Berol L.)—231(A)
Finkelnburg, Wolfgang. Very high temperature arcs—562(A)
Finkelstein, David. Spin models—1175(A)
Finkelstein, R. J. and R. E. Behrends. Radiative corrections to muon decay—1155(A); 1870(E)
Firle, T. E. and H. Winston. Noise measurements in semiconductors at very low frequencies—1567(A)
Fischbach, D. B. and A. S. Nowick. Creation of potential difference across NaCl crystals by deformation—1543(A)
Fiske, M. D. Effect of hydrostatic pressure on superconducting transition—244(T)
—— (see Schmitt, R. W.)—246(A)
Fleming, John R. and J. J. Lord. Ionization loss in nuclear emulsions—268(A)
Fleming, P. J., J. H. Werntz, Jr., and J. R. Dillinger. Dependence of transfer rates of He II film on film length—1196(A)
Fletcher, P. C. (see Aamodt, L. C.)—1224; 1317
Fletcher, R. C. Hyperfine splitting in electron-spin resonances of donors in Si—252(T)
——, **F. R. Merritt, and W. A. Yager.** Cyclotron resonances in Ge at 1.4°K—1560(A)
Flom, D. G. Frictional properties of teflon—1548(T)
Foettinger, Hermann (see Domm, Ulrich)—1142(A)
Foldy, Leslie L. and Erik Eriksen. Vacuum polarization and p-p scattering—775; 1190(A)
Foley, H. M. (see Sessler, A. M.)—6
Folger, R. L., P. C. Stevenson, and G. T. Seaborg. High-energy proton spallation-fission of U—107
Foote, H. L., Jr. Slow neutron resonant scattering—1161(A)
—— (see Sailor, V. L.)—224(A)
Forbush, Scott E. World-wide variations in cosmic-ray intensity 1937–1952—1163(A)
—— (see Graham, John W.)—1348
Ford, Kenneth W. Calculations of energy-levels for intermediate nuclei—244(T)
—— Predicted 0+ level in $_{40}Zr^{90}$—1516(L)
Forrester, A. Theodore, Richard A. Gudmundsen, and Philip O. Johnson. Photoelectric mixing of incoherent light—1169(A)
Forstat, H. and C. A. Reynolds. "Closed" fountain effect and compressibility of He II—1196(A)
Forster, H. H. and A. Rosen. Decay of Ru^{103}—1172(A)
Forster, Michael J. Unilateral compression of rubber—1559(A)
Fowler, Charles A., Jr. (see Fryer, Edward M.)—270(A)
Fowler, E. C. (see Morris, T. W.)—1167(A)
—— (see Walker, R. M.)—1203(A)
Fowler, J. L. and C. H. Johnson. Differential elastic scattering cross section for neutrons on N—728
Fowler, J. M., S. S. Hanna, and G. E. Owen. $Be^9(n,2n)Be^8$ reaction—249(A)
—— **and C. E. Roos.** Response of anthracene and stilbene to low-energy protons and x-rays—996
Fowler, W. B., R. P. Shutt, A. M. Thorndike, and W. L. Whittemore. Production of heavy unstable particles by 1.37-Bev pions—121
—— (see Block, M. M.)—248(A)
—— (see Morris, T. W.)—1167(A)
Fox, R. E. Precision measurements of ionization probabilities of monoenergetic electrons—1159(T)
—— (see Hickam, W. M.)—557(A)
Fox, Raymond and R. W. Waniek. Bilateral development of thick nuclear emulsions—1153(A)
—— (see Waniek, R. W.)—1148(A)
Fox, T. G. and S. Loshaek. Viscosity-molecular weight relationship for long chain polymers in bulk or in concentrated solution—1549(A)
Francis, N. C. (see Brueckner, K. A.)—1445
—— (see Eden, R. J.)—1205(A)
Frank, R. M. and J. L. Gammel. p-He^3 interaction—1204(A)
Frank, W. J. (see Bandtel, K. C.)—269(A)
Frankl, D. R. Electroluminescence in ZnS single crystals—238(A)
Fraser, J. S. and J. C. D. Milton. γ-γ directional correlation in Er^{166}—1173(A)
—— (see Milton, J. C. D.)—1173(A)

Fred, Mark, Frank S. Tomkins, and William F. Meggers. Nuclear moments of Ac^{227}—1514(L)
Freda, A. R. and G. C. Kuczynski. Effect of external stresses upon rate of ordering of AuCu—270(A)
Frederikse, H. P. R. and W. R. Hosler. Galvano-magnetic effects in InSb—1532(A)
—— (see Blunt, R. F.)—1533(A)
Freedman, M. S. (see Porter, F. T.)—214(L)
Fregeau, J. H. and R. Hofstadter. Inelastic electron scattering from C at 188 Mev—1184(A)
Freistadt, Hans. Connection between recent theories of Bohm, De Broglie, Dirac, and Schrödinger—1176(A)
French, J. B. and B. J. Raz. Deuteron reactions and j-j coupling shell model—1523(L)
—— (see Auerbach, T.)—1276
Fretter, W. B., E. W. Friesen, G. E. Kepler, and A. Lagarrigue. Results on K particles—1202(A)
Freund, H. (see Loebner, E. E.)—1545(A)
Freund, R. E. (see Schwertz, F. A.)—1134(L)
Friedberg, S. A. and D. L. Burk. Specific heats of Zn ferrite and Zn chromite at low temperatures—1200(A)
—— (see Darnell, F. J.)—1178(A); 1860(L)
—— (see Guthrie, G.)—1181(A)
Friedlander, G. (see Baker, E.)—242(A)
—— (see Miller, J. M.)—1197(A)
—— (see Miskel, J. A.)—1197(A)
—— (see Piccioni, O.)—275(A)
—— (see Wolfgang, R. L.)—1871(E)
Friedman, Abraham, S. and Irwin Oppenheim. Statistical thermodynamics of isotope effects. II. Equation of state of H_2 istopes at intermediate densities—258(A)
Friedman, H. (see Byram, E. T.)—1594
Friedman, M. B. (see Ludloff, H. F.)—1140(A)
Friedman, M. H. and S. T. Butler. Bose-Einstein condensation of an imperfect gas—294
—— (see Butler, S. T.)—287
Friedman, R. M. (see Crowe, K. M.)—268(A)
—— (see Motz, H.)—268(A)
Friesen, E. W. (see Fretter, W. B.)—1202(A)
Fritzsche, H. and K. Lark-Horovitz. Hall effect and resistivity of InSb at low temperatures—1532(A)
—— (see Lark-Horovitz, K.)—1532(A)
Frost, L. S. and A. V. Phelps. Cumulative ionization processes in He positive column—559(A)
Fry, W. F., J. Schneps, and M. S. Swami. Delayed disintegration of nuclear fragments—247(A)
Frye, G. M., Jr., A. H. Armstrong, and L. Rosen. $B^{11}(n,\alpha)Li^8(\beta)Be^{8*}(2\alpha)$ reaction from 12 to 20 Mev—241(A)
Fryer, Edward M. and Charles A. Fowler, Jr. Magnetic domains in single crystal of Co near 275°C by longitudinal Kerr effect—270(A)
Fuller, E. G. and Evans Hayward. Self-absorption or self-indication in nuclear elastic scattering experiment—1537(A)
Fuller, J. C. and D. C. Ralph. Angular distribution of neutrons from reaction $D(d,n)He^3$ at 100 kev—248(A)
Fuller, Melvin Otis. Disintegration of O by 300-Mev neutrons—274(A)
Furlong, L. R. and C. F. Ravilious. Low-temperature luminescence and absorption of CdS—954

Gaffney, John (see Overton, W. C., Jr.)—969
Gallagher, J. J., W. C. King, and C. M. Johnson. Microwave spectrum of $N^{15}O^{16}$—1551(A)
Galonsky, A., R. A. Douglas, W. Haeberli, M. T. McEllistrem, and H. T. Richards. d-He differential scattering cross sections—586
—— **and J. Judish.** n-p scattering at 17.9 Mev—1168(A)
—— **and M. T. McEllistrem.** Energy levels of Li^6 from d-He differential cross sections—590
Gammel, J. L. (see Frank, R. M.)—1204(A)
Gamow, G. Transfer of information from nucleic acids to proteins—1534(T)
Gardiner, V. (see Hoffman, Joseph G.)—1195(A)
Gardner, Andrew L. Measurements of electron density in long-lived nitrogen afterglows—263(A)
—— (see Kunkel, W. B.)—558(A)
Garfunkel, M. P. (see Corak, William S.)—1699
Garrett, C. G. B. Physical properties of Ge surfaces—278(T)
Garrido, L. (see Waniek, R. W.)—1148(A)
Garrison, John D. (see Chamberlain, Owen)—1167(A)
—— (see Morris, T. W.)—1167(A)
Garwin, R. L. (see Anderson, A. G.)—283(A)
Gasiorowicz, S. Modified Holtzmark distribution—257(A)
—— (see Riddell, R., Jr.)—257(A)
Geballe, T. H. and G. W. Hull. Seebeck effect in Si—940
Gebbie, H. A. Excess noise and trapping in Ge—1567(A)
Geer, E. H., E. B. Nelson, and E. J. Wolicki. α-α angular correlation in $B^{11}(p,\alpha\alpha)He^4$—241(A)
Geib, I. G. (see Buschert, R.)—1157(A)
Gell-Mann, M. Theoretical views on new particles—255(T)
George, T. H., H. E. Farnsworth, and R. E. Schlier. Adsorption of O_2 and N_2 by Ti—1179(A)
—— (see Schlier, R. E.)—250(A)
George, W. D., W. Barber, and D. Reagan. Absolute cross section for reaction $C^{12}(\gamma,n)C^{11}$—276(A)
—— (see Barber, W. C.)—73
Gerjuoy, E. and S. Stein. Rotational excitation by slow electrons—557(A)
—— **and S. Stein.** Rotational excitation by slow electrons. II—1848
Germer, L. H. (see Kisliuk, P.)—560(A)
Ghiorso, A., B. G. Harvey, G. R. Choppin, S. G. Thompson, and G. T. Seaborg. New element mendelevium, atomic number 101—1518(L)
—— (see Choppin, G. R.)—1519(L)
Gibson, John B. Thermal scattering of electrons between bands in metal—1151(A)
Gilbert, D. A. and Victor W. Cohen. Nuclear spin and hfs interaction in 3.1-hr Cs^{134m}—1194(A)
Gilbert, F. C. Analysis of disintegration products from reactions of 125-Mev deuterons with Li nuclei—275(A)
Gilbert, T. L. Determination of polydisperse aerosol size distributions from analysis of light scattering data—242(A)
——, **J. M. Kelly, and H. Ekstein.** Rapid remagnetization of thin Mo permalloy tapes—1200(A)
Given, Frank I. (see Evans, Marjorie W.)—256(A)
Givens, M. Parker (see Koester, Charles J.)—1543(A)
Glaser, D. A. Bubble chambers for experiments in high-energy nuclear physics—1191(T)
Glaser, Vladimir. New relativistic two-body equation—840(L)
Glaser, Walter. Foundation of wave-mechanical theory of the electron—1176(A)
Glass, Neel W. and J. Reginald Richardson. Radionuclides Al^{24}, P^{35}, Cl^{38}, and Sc^{40}—1251
Glass, R. A., R. J. Carr, J. W. Cobble, and G. T. Seaborg. Fission-spallation competition in heavy elements—261(A)
Glasser, R. G. Relation between multiple Coulomb scattering and residual range in nuclear emulsion—174
Glassgold, A. E. Scattering of high-energy electrons by nuclei—1360
Glauber, R. J. Time-dependent displacement correlations and inelastic scattering by crystals—1692
Glaubman, Michael J. Radioactive decay of 65-hour Sb^{122}—645; 1172(A)

Glick, H. (see Smith, W.)—1141(A)
Glicksman, M. and H. L. Anderson. Scattering of 165-Mev pions by protons—239(A)
—— (see Kruse, U.)—1188(A)
Gluckstern, Robert L. Analysis of electron stripping data—276(A)
—— Electron capture and loss by ions in gases—1817
Goddard, Pliny E. (see Nail, Nelson R.)—1557(A)
Goebel, Charles J. Pion-nucleon *s*-wave phase shift from *ps-ps* with cutoff—273(A)
Goldberg, Colman and R. E. Davis. Hall effect in *p*-type Ge—1192(A)
Goldberg, Irwin (see Bergmann, Peter G.)—531; 1175(A)
Goldberg, J. N. New approximation method for gravitational field equations—1175(A)
Goldberg, Seymour. Studies of anode pre-breakdown phenomena in thyratrons—558(A)
Goldey, James M. and Sanborn C. Brown. Carrier effective masses in Ge—1192(A)
—— **and Sanborn C. Brown.** Microwave determination of average masses of electrons and holes in Ge—1761
Goldhaber, Gerson, W. W. Chupp, S. J. Goldsack, J. Lannutti, and F. Webb. Heavy meson and hyperon production at the bevatron—267(A)
—— **and Stephen J. Goldsack.** Measurements on *K* particles and their decay products—1203(A)
—— (see Goldhaber, S.)—1203(A)
—— (see Goldsack, Stephen J.)—284(A)
—— (see Lannutti, Joseph)—258(A)
Goldhaber, M. (see Mihelich, John W.)—1185(A)
Goldhaber, S., Gerson Goldhaber, H. H. Heckman, and F. M. Smith. Heavy mesons and hyperons from targets bombarded by 4.8- and 5.7-Bev protons—1203(A)
—— (see Heckman, Harry H.)—1202(A)
Goldman, J. E. (see Arrott, A.)—1201(A); 1864(L)
—— (see Guthrie, G.)—1181(A)
Goldsack, Stephen J. and Gerson Goldhaber. Multiple scattering microscope for "constant sagitta" measurements—284(A)
—— (see Goldhaber, Gerson)—267(A); 1203(A)
—— (see Lannutti, Joseph)—258(A)
Goldsmith, G. J. and D. E. Hill. Photoconductivity in paraterphenyl single crystals—238(A)
—— (see Hill, D. E.)—238(A)
—— (see Kleitman, D.)—1544(A)
Goldstein, Louis and James Reekie. Spatial distribution of atoms in liquid He^4—857
Goldwasser, E. L., L. J. Koester, and F. E. Mills. Elastic photoproduction of π^0 mesons for He—239(A)
——, **F. E. Mills, T. R. Robillard.** Direct measurement of effect of polarization on energy loss—1763
Goodenough, J. B. and A. L. Loeb. Theory of ionic ordering, crystal distortion, and magnetic exchange due to covalent forces in spinels—391
Goodman, Clark (see Mark, Hans)—249(A); 279(A); 1245
—— (see McClelland, Clyde)—249(A)
Gordon, J. P. Molecular amplification and generation of microwaves with applications to spectroscopy and to time standards—1159(T)
Gordon, R. B. and A. S. Nowick. Elastic modulus of x-irradiated rock salt—1540(A)
Gordon, S. (see Grossweiner, L. L.)—243(A)
Gordy, Walter (see Mizushima, Masataka)—1034; 1159(A)
Gossett, C. R., G. C. Phillips, and J. T. Eisinger. Absolute magnetic analysis of $F^{19}(p,p')F^{19*}$ reaction—724
Graetzer, H. G. and E. C. Pollard. Upper limit to lifetime of compound nucleus—1184(A)
Graham, John W. and Scott E. Forbush. Solar flare and magnetic storm effects in cosmic-ray intensity near geomagnetic N pole—1348
Graham, R. L., J. L. Wolfson, and M. A. Clark. Disintegration of 27-hr Ho^{166}—1173(A)
Grannis, F. H. (see McGuire, T. R.)—1562(A)
Gravel, Charles L. (see Brown, Fielding)—442
Green, A. E. S. and Kiuck Lee. IPM mass surface—1205(A)
Green, D. Wayne, John N. Cooper, and James C. Harris. Stopping cross sections of metals for protons of energies from 400 to 100 kev—466
Green, G. K. Brookhaven 25-Bev synchrotron—266(T)
Green, Louis C. (see Lewis, Margaret N.)—1210(A); 1020
Green, Milton. Magnistor, solid-state electronic valve—1169(A)
Green, Mino and J. A. Kafalas. Oxidation of clean surfaces of Ge below 25°C—1566(A)
Green, R. E. and A. T. Stewart. Angular correlation of photons from positron annihilation in light metals—486
—— (see Stewart, A. T.)—232(A)
Greenberg, D. H. (see van Lieshout, R.)—1171(A)
Greenberg, J. Mayo. Variational principle for total scattering amplitude—1189(A)
Gregg, E. C. (see Robson, J. W.)—233(A)
—— (see Stearns, R. L.)—232(A)
Gregory, B. (see Armenteros, R.)—275(A)
Griffith, G. L. γ radiation from neutron inelastic scattering—579
Griffith, Wayland and Walker Bleakney. Diffusion analogy for shocks interacting with thermal boundary layers—1143(A)
Grimm, G., L. J. Rainwater, and W. W. Havens, Jr. Slow neutron velocity spectrometer using Nevis synchrocyclotron—1161(A)
Grimsal, E. G. Hall coefficient in anisotropic media—229(A)
Grodzins, L. Multiple scattering of 2.5-Mev positrons by 0.1 mil Au foil—279(A)
—— (see del Castillo, G.)—1163(A)
Gross, E. P. Inertial effects and dielectric relaxation—1191(A)
—— Temperature effect of paramagnetic line shape—1561(A)
Grossweiner, L. L. and S. Gordon. Mechanism of photochemical reactions catalyzed by red-mercuric sulfide—243(A)
Gruen, Dieter M. (see Henry, Warren E.)—1200(A)
Gudmundsen, Richard A. (see Forrester, A. Theodore)—1169(A)
Guernsey, Janet B. Neutron cross sections for Zr—1210(A)
—— **and A. Wattenberg.** Neutron inelastic scattering—1147(A)
Gunther-Mohr, G. R. (see Koenig, S. H.)—228(A)
Gupta, Suraj N. Multiple photon production in electron-positron annihilation—247(T)
—— Multiple photon production in quantum electrodynamics—1502
Gupta, U. C. (see Miller, D. W.)—1184(A)
Gurnee, E. F., L. T. Patterson, and R. D. Andrews. Apparatus for making simultaneous stress and birefringence measurements on polymers—1547(A)
Gursky, Martin L. Particle motion in anisotropic harmonic oscillator well—1205(A)
Guth, Eugene. Dirac's method using complex variables in quantum mechanics—273(A)
—— (see Banas, E. M.)—265(A)
—— (see Harris, C. W.)—272(A)
—— (see Lockary, T. E.)—274(A)
—— (see Mullin, C. J.)—277(A)

—— (see Sells, R. L.)—272(A)
—— (see Wang, Ming Chen)—274(A)
Guthrie, G., S. A. Friedberg, and J. E. Goldman. Electronic specific heat of α-Mn—1181(A)

Haake, Claus H. Temperature dependence of electroluminescence—1544(A)
Haar, Lester. Ideal gas thermodynamic properties of isotopic hydrides of group of diatomic free radicals—1551(A)
Haeberli, W. (see Galonsky, A.)—586
Haffner, James W. Limitations of stripping theory in inelastic deuteron scattering—1156(A)
Hagstrum, Homer D. Ejection of electrons from contaminated metals by positive ions—561(A)
Hahn, Beat and Robert Hofstadter. High-energy electron scattering in Rh, Ta, W, and U—278(A)
Hahn, E. L. and B. Herzog. Diffusion model for nuclear precession relaxation in solids—265(A)
—— (see Anderson, A. G.)—283(A)
—— (see Herzog, B.)—226(A)
Hahn, T. M., Jr., B. D. Kern, and G. K. Farney. Excitation curve of reaction $B^{10}(p,\gamma)C^{11}$—1183(A)
—— (see Rayburn, L. A.)—701
Halford, Ralph S. (see Zwerdling, Solomon)—243(A)
Hall, R. N. (see Newman, R.)—1536(A)
Halperin, A. and A. Braner. Thermal bleaching of color centers—1135(L)
Halpern, J. (see Triebwasser, S.)—1562(A)
Halpern, O. and R. A. Buckingham. Symmetry effects in gas kinetics. I. He isotopes—1626
Hama, Francis R. Relations between one- and three-dimensional functions in isotropic turbulence and direct measurement of energy transfer function—1142(A)
Hamermesh, M. (see Crosbie, E. A.)—233(A)
Hamilton, D. R. Focusing atomic-beam apparatus—1174(T)
Hamilton, J. F., F. A. Hamm, and J. W. Castle. Displacement of latent image in photographic emulsion grains—1557(A)
Hamm, F. A. (see Hamilton, J. F.)—1557(A)
Handler, Harry E. and J. Reginald Richardson. γ-γ directional correlation in $Cl^{34}\rightarrow S^{34}$ decay—281(A)
Handley, T. H., W. S. Lyon, and E. L. Olson. Ho^{167}—688
—— (see Blosser, H. G.)—1198(A)
Hanna, S. S. Energy levels of Be^{8}—1530(T)
—— (see Fowler, J. M.)—249(A)
—— (see Segel, R. E.)—1538(A)
Hans, H. S., Babulal Saraf, and C. E. Mandeville. Coincidence studies of disintegration of Pm^{151} and Nd^{147}—1173(A)
Hanscome, T. D. and D. K. Willett. Magnetic analyzer for nuclear reactions—232(A)
—— (see Holmgren, H. D.)—241(A)
Hanson, A. O. Photodisintegration of deuterium—234(T)
Hare, W. F. J. (see Allin, Elizabeth J.)—554(L)
Harman, T. C., R. K. Willardson, and A. C. Beer. Effect of impurities on mobility in *n*-type InSb—1532(A)
—— (see Willardson, R. K.)—227(A)
Harrick, N. J. Attempt to detect high mobility holes in Ge using drift mobility technique—1131(L)
Harris, C. W. and E. Guth. Role of coordination number in Lee-Yang lattice gas—272(A)
—— (see Sells, R. L.)—272(A)
Harris, E. G. Disordering of polyatomic solids by neutrons—1151(A)
Harris, G. G. *K* mesons produced by 2.2 and 3 Bev protons—1202(A)
Harris, James C. (see Green, D. Wayne)—466
Harrison, S. E. (see Kriessman, C. J.)—1562(A)
Harrison, W. A. and Frederick Seitz. Theory of radiation damage—1530(A)
Hart, Edward W. Lattice resistance to dislocation motion at high velocity—1775
Harth, E. M. (see Block, M. M.)—248(A)
Harvey, B. G. (see Choppin, G. R.)—1519(L)
—— (see Ghiorso, A.)—1518(L)
Harvey, John A. Level spacings of heavy nuclei—1162(A)
Hastings, J. M. (see Brockhouse, B. N.)—1721
Hauver, G. (see Zernow, L.)—1551(A)
Havens, W. W., Jr. (see Grimm, G.)—1161(A)
Havill, J. R. (see Tautfest, G. W.)—280(A)
Hawkins, William Bruce. Orientation and alignment of Na atoms by means of polarized resonance radiation—478
Hayden, R. J. (see Wasserburg, G. J.)—250(A)
Hayn, C. H. and Vincent P. Jacobsmeyer. Photoconductivity of pyrolytic layers of B—237(A)
Haynes, J. R. New radiation resulting from recombination of holes and electrons in Ge—1866(L)
Hayward, Evans (see Fuller, E. G.)—1537(A)
Hayward, R. W. and D. D. Hoppes. Disintegration of Se^{75}—1172(A)
——, **D. D. Hoppes, and H. Ernst.** Disintegration of Nb^{91} and Nb^{95}—231(A)
Hazlett, Thomas H. (see Ancker, Betsy)—1151(A)
Heberle, J., H. Reich, and P. Kusch. New method for investigating hfs of metastable state—1194(A)
—— (see Reich, H.)—1194(A)
Heckman, Harry H., S. Goldhaber, and F. M. Smith. Observations of K^{+} mesons—1202(A)
—— (see Goldhaber, S.)—1203(A)
Heckrotte, Warren. Production of high-energy neutrons and deuterons from stripping of He—259(A)
Heikes, R. R. Magnetic transformation in MnBi—1199(A)
—— Relation of magnetic structure to electrical conductivity in NiO and related compounds—225(A)
Heims, S. P., D. R. Yennie, and D. G. Ravenhall. W.K.B. approximation to phase shifts—278(A)
Heinberg, M. (see Page, L. A.)—206(L)
Hellens, R. L. (see Jennings, B.)—582
Hemmendinger, A. and H. V. Argo. Reaction $D(t,\alpha)n$ at 1.5 Mev—70
Hempstead, C. F. and L. G. Parratt. Localized energy states in crystalline alkali chlorides—1170(A)
Hendel, P. (see Armenteros, R.)—275(A)
Henkel, Richard L. (see Beyster, J. R.)—1216
—— (see Seagrave, John D.)—666
Hennig, G. and M. Dzurus. Donor impurities in graphite—227(A)
Henry, Warren E. Antiferromagnetism of Yb_2O_3 at liquid He temperatures—226(A)
—— Magneto-electric effects in Ge in strong magnetic fields—1534(A)
—— Quantized spin paramagnetism in free radical near magnetic saturation—252(A)
—— **and Dieter M. Gruen.** Saturation magnetization and remanence of β-UH_3—1200(A)
Henshaw, D. G. (see Hurst, D. G.)—224(A)
Henvis, B. (see Burstein, E.)—1536(A)
Herman, Robert, G. E. Moore, S. Silverman, and R. F. Wallis. Vibration-rotation line intensities in HCl and DCl—1550(A)
—— **and R. F. Wallis.** Model for room temperature bleaching of *F* centers by *F* light in x-rayed NaCl—1171(A)
Hernqvist, K. G. and E. O. Johnson. Retrograde motion in gas discharge plasmas—1576
Herring, D. F. (see Jones, K. W.)—241(A)
Hertz, M. R. (see Breen, R. J.)—599
Hertzberg, A. (see Smith, W.)—1141(A)
Herzberg, G. Lamb shift of 1*S* level of deuterium—223(A)
—— (see Chandrasekhar, S.)—1050

Herzfeld, C. M. Strong crystal field theory of magnetic resonance for d^8 configurations—226(A)
Herzog, B. and E. L. Hahn. Relaxation time modification by double nuclear resonance—226(A)
—— (see Hahn, E. L.)—265(A)
Heydenburg, N. P. and G. M. Temmer. Assignment of energy levels by Coulomb excitation with 5.7-Mev α particles—1198(A)
—— (see Temmer, G. M.)—1198(A); 1308
Hibdon, Carl T. and Alexander Langsdorf, Jr. Total neutron cross sections in kev region: Be, B, C, F, Ti, Ni, and Bi—223(A)
Hickam, W. M. and R. E. Fox. Negative ion formation using monoenergetic electrons—557(A)
Hicks, Donald A., John Ise, Jr., and Robert V. Pyle. Spontaneous-fission neutrons of Cf^{252} and Cm^{244}—1521(L)
—— (see Ise, John, Jr.)—1199(A)
Hiedemann, E. A. Ultrasonic light modulators for spectroscopy and measurement of very short time intervals—242(T)
Higgins, L. (see Bandtel, K. C.)—269(A)
Hildebrand, R. H. Use of Glaser bubble chambers in photographing nuclear events—227(T)
Hill, D. A. (see Coor, T.)—1369
Hill, D. E. and G. J. Goldsmith. Dark conduction in paraterphenyl single crystals—238(A)
—— (see Goldsmith, G. J.)—238(A)
Hill, R. D. Model for asymmetric fission—1272
——, **E. O. Salant, and M. Widgoff.** Chi meson produced by 3-Bev protons—247(A)
Hockney, R. W. and P. V. C. Hough. Coulomb effects in (d,p) reaction—234(A)
Hodson, A. L. (see Arnold, W. H.)—275(A)
Hoffman, D. C. (see Prestwood, R. J.)—1324
Hoffman, Joseph G., N. Metropolis, and V. Gardiner. Monte Carlo methods in study of cell growth—1195(A)
Hofstadter, Robert. Electron scattering and nuclear structure—277(T)
—— **and Robert W. McAllister.** Electron scattering from proton—217(L)
—— (see Fregeau, J. H.)—1184(A)
—— (see Hahn, Beat)—278(A)
—— (see McIntyre, John A.)—158
Holcomb, D. F. and R. E. Norberg. Nuclear spin relaxation in alkali metals—1074
—— (see Norberg, R. E.)—226(A)
Holden, A. N., B. T. Matthias, W. J. Merz, and J. P. Remeika. New class of ferroelectrics—546(L)
Holder, B. E. and M. P. Klein. Isotope abundance ratios by nuclear magnetic resonance—265(A)
—— (see Klein, M. P.)—265(A)
Holladay, W. G. and R. G. Sachs. Evidence for pion-pion interaction—1155(A)
Holland, D. H. Lattice space quantization of coupled meson and nucleon fields—788; 273(A)
Holland, R. E., D. R. Inglis, and F. P. Mooring. Search for excited states of Be^8—240(A)
Hollander, J. M. and M. I. Kalkstein. Radiations of Ba^{128}—Cs^{128}—260(A)
—— (see Smith, W. G.)—262(A); 1258
Holmgren, H. D., T. D. Hanscome, and D. K. Willett. Q values for $O^{17}(d,p)O^{18}$ and $O^{18}(d,p)O^{19}$ reactions—241(A)
Holt, N. Total neutron cross section of Eu in 0.001 to 0.01 ev region—1162(A)
Holtzberg, Frederic (see Triebwasser, Sol)—1201(A)
Holzman, G. R., John H. Anderson, and W. Koth. Spin-lattice relaxation time of Si^{29} nucleus in pure fused silica—542(L)
Hong, K. and S. Mrozowski. Studies of elastic modulus of carbons—1565(A)
Hooton, John A. and Walter J. Merz. Etch patterns and ferroelectric domains in $BaTiO_3$ single crystals—409
Hoover, C. W., Jr., and R. K. Smither. Secondary electron resonance discharge mechanism. II—1149(A)
—— (see Smither, R. K.)—1149(A)
Hopkins, R. L. Elastic strain energy stored in mechanically disturbed surfaces—1567(A)
Hoppes, D. D. (see Hayward, R. W.)—231(A); 1172(A)
Hornbostel, J. and E. O. Salant. Capture of negative K mesons—218(L)
—— **and E. O. Salant.** Heavy unstable particles from captured K^- mesons—1202(A)
Hornyak, W. F. (see Coor, T.)—1369
Horton, G. K. (see Bhatia, A. B.)—1181(A); 1715
Horton, J. W. (see Anderson, A. G.)—283(A)
Horwitz, Nahmin. Čerenkov counter flux measurement of cosmic-ray alphas at 41°—165
Hosler, W. R. (see Blunt, R. F.)—1533(A)
—— (see Frederikse, H. P. R.)—1533(A)
Hough, P. V. C. (see Bach, D. R.)—235(A)
—— (see Hockney, R. W.)—234(A)
Hove, John E. Two-medium theory of thermal conductivity of artificial graphite: Interpretation—1563(A)
Howard, Brian T. Theory of electroluminescence—1544(A)
Howard, Louis N. Vortices produced by shocks—1141(A)
Howard, R. A. (see Stier, P. M.)—1149(A)
Hubbard, Edward L. and Eugene J. Lauer. Charge distributions of O and Ne ions passing through gases—1814
—— **and Eugene J. Lauer.** Stripping electrons from accelerated O and Ne ions—276(A)
Huber, Elsa L. Breakdown processes in nitrogen, oxygen, and mixtures—560(A)
Hudis, J. (see Baker, E.)—242(A)
Hudson, Gilbert G. Streamers in positive point-to-plane breakdown in air—264(A)
Hudson, R. P. (see Ambler, E.)—230(A)
Huggett, R. W., J. R. Burwell, and R. W. Thompson. New examples of anomalous V^0 particles—248(A)
—— (see Burwell, J. R.)—101; 247(A)
—— (see Kim, Y. B.)—248(A)
Hughes, D. J. Neutron widths of nuclear energy levels—1161(A)
—— (see Levin, J. S.)—1161(A)
Hughes, V. W., S. Marder, and C. S. Wu. Static magnetic field quenching of orthopositronium decay: Angular distribution effect—1840
—— (see Marder, S.)—1173(A)
—— (see Teutsch, W. B.)—1174(A)
Huibregtse, E. J., M. E. Drougard, and D. R. Young. Electromechanical behavior of single crystals of $BaTiO_3$—1562(A)
Hull, G. W. (see Geballe, T. H.)—940
Hullings, M. K. (see Blosser, H. G.)—1198(A)
—— (see Cohen, B. L.)—685
Hulm, J. K. Superconducting Re alloys and compounds—1539(A)
Hummel, John P., F. Asaro, and I. Perlman. α decay of Pa^{231}—261(A)
——, **Frank S. Stephens, Jr., Frank Asaro, A. Chetham-Strode, Jr., and I. Perlman.** α and γ spectra of Cf^{246}—22
—— (see Stephens, F.)—261(A)
Hurley, J. P., S. W. Rudman, and P. S. Jastram. Angular correlation in decay of Co^{56}—1187(A)
Hurst, D. G. and D. G. Henshaw. Slow neutron scattering by liquid He—224(A)
Husain, A. and E. Pickup. Mass spectrum of shower particles from cosmic-ray interactions—136
—— (see Pickup, E.)—247(A)

Huse, M. C. (see Blatt, F. J.)—1553(A)
Hutchison, C. A., Jr. Paramagnetism of the transuranic elements—272(T)
Hutson, Andrew R. Velocity analysis of thermionic emission from single-crystal W—889
Hyde, Earl K. (see Mathur, Hirdaya B.)—79; 261(A)

Igo, G. (see Wertheim, M. S.)—1
Ihsan, M. A. Nuclear energy levels of Be^8 from $Li^7(d,n)Be^8$—689
Inchauspé, Nicolas. Photoconductivity in KI—1550(A)
—— Polarization in insulating crystals—1543(A)
Ingham, H. (see Pearlstein, E.)—1530(A)
—— (see Smoluchowski, R.)—1530(A)
Inghram, Mark G. Mass-spectrometric analysis of ions produced in field ion microscope—1159(T)
—— (see Porter, Richard F.)—242(A)
Inglis, D. R. (see Holland, R. E.)—240(A)
Ise, John, Jr., Donald A. Hicks, and Robert V. Pyle. Neutron multiplicity spectrum from spontaneous fission—1199(A)
—— (see Hicks, Donald A.)—1521(L)
Ishii, S. (see Sakamoto, M.)—552(L)
Itoh, Takashi (see Shimoda, Koichi)—1160(A)
Ivory, J. E., F. B. Baldwin, and R. L. Anthony. Experimental study of behavior of rubbers in simple shear—1558(A)
Iwersen, John E. and W. S. Koski. γ rays in decay of Na^{25}—1307

Jackson, H. E. (see Bollinger, L. M.)—223(A)
Jackson, J. David (see Betts, D. D.)—1149(A)
—— (see Sharp, R. T.)—1128(L)
Jacobsmeyer, Vincent P. (see Hayn, C. H.)—237(A)
Jahn, Robert G. Refraction of shock waves at gaseous interface—1141(A)
Jakobson, Mark J. (see Repp, Gordon W.)—268(A)
—— (see White, R. Stephen)—269(A)
Jamieson, C. P. Thermal conductivities of carbons and graphites—1564(A)
Janin, Joseph (see Déjardin, Georges)—1149(A)
Jankus, V. Z. Electrodisintegration of deuteron—278(A)
Jarmie, Nelson. Excitation function of $O^{16}(t,n)F^{18}$—41
Jastram, P. S. Angular correlation of aligned nuclei—1164(T)
—— (see Hurley, J. P.)—1187(A)
—— (see Wood, G. T.)—1187(A)
Jastrow, Robert. Many-body problem with strong forces—1479
Jauch, J. M. (see Rohrlich, F.)—222(A)
Jaumot, F. E., Jr., and R. L. Smith. Self-diffusion in Zn at low temperatures—1555(A)
—— (see Sawatzky, A.)—1555(A)
Jaynes, E. T. Matrix treatment of nuclear induction—1099
Jeffries, C. D. (see Sogo, P. B.)—265(A); 1316
Jefimenko, Oleg (see Ch'en, Shang-Yi)—281(A)
Jenkins, F. A. and D. R. Speck. Phase change on reflection from multilayer films—282(A)
—— (see Speck, D. R.)—282(A)
Jennings, B., J. Weddell, I. Alexeff, and R. L. Hellens. Scattering of 4.4-Mev neutrons by Fe and C—582
Jenny, Hans K. (see Arams, Frank R.)—562(A)
Jentschke, W. K. (see Maxson, D. R.)—230(A)
Jeppesen, Myron A. Raman and fluorescence spectra of allyl diglycol carbonate—1211(A)
Jesse, William P. and John Sadauskis. Comparison of energy to make an ion-pair in various gases for α and β particles—1150(A)
Jillson, D. C. and A. C. Sheckler. Segregation coefficient of As in Ge as function of crystal growth variables—229(A)
—— (see Sheckler, A. C.)—229(A)
Johnson, C. H. (see Fowler, J. L.)—728
—— (see Trail, C. C.)—249(A)
Johnson, C. M. (see Gallagher, J. J.)—1551(A)
Johnson, E. O. (see Hernqvist, K. G.)—1576
Johnson, M. H. and E. Teller. Classical field theory of nuclear forces—260(T); 783
Johnson, O. E., R. G. Johnson, and L. M. Langer. Evidence for 0+ first excited state in Zr^{90}—1517(L)
Johnson, Philip O. (see Forrester, A. Theodore)—1169(A)
Johnson, R. F. (see Webb, L. A.)—234(A)
Johnson, R. G. (see Johnson, O. E.)—1517(L)
Johnson, V. A. Electrical conductivity of liquid Te—1567(A)
—— (see Seidel, G. M.)—230(A)
Johnston, William G. Effect of plastic deformation on electrical conductivity of AgBr—1777
Jona, F., G. Shirane, and R. Pepinsky. Dielectric, x-ray, and optical study of ferroelectric $Cd_2Nb_2O_7$ and related compounds—903
——, **G. Shirane, and R. Pepinsky.** Optical properties and twinning of $PbZrO_3$ single crystals—1201(A)
Jones, K. W., M. T. McEllistrem, R. A. Douglas, D. F. Herring, and E. Silverstein. Angular distributions and excitation functions of $C^{13}(d,p)$ reaction—241(A)
Jones, L. W., K. R. Symon, K. M. Terwilliger, and D. W. Kerst. Synchrotron application of reverse field types of fixed field alternating gradient magnets—1153(A)
—— (see Kerst, D. W.)—1153(A)
—— (see Terwilliger, K. M.)—1153(A)
Jordan, R. D. (see Alger, R. S.)—1550(A)
Jordan, W. C. (see Burson, S. B.)—230(A)
Jossem, E. L. and L. G. Parratt. Energy levels in metallic K—1151(A)
Jost, Res. (see Newton, Roger G.)—1189(A)
Judd, D. L. (see Bludman, S. A.)—283(A)
Judish, J. (see Galonsky, A.)—1168(A)
Jurić, Mira K. Angular distribution of disintegration products from $O^{16}(d,p)O^{17}$, $Be^8(d,p)Be^{10}$, and $Be^9(d,t)Be^8$ reactions—85

Kac, Mark. Foundation of kinetic theory of gases—255(T)
Kafalas, J. A. (see Green, Mino)—1566(A)
Kahn, A. H. (see Argyres, P. N.)—226(A)
Kahn, B. and W. S. Lyon. Decay of Y^{91}—58
Kahn, D. (see Aron, J.)—246(A)
Kaiser, H. F. Synchro-microtron—233(A)
——, **W. T. Mayes, and W. J. Willis.** Electron beam extraction from X-band microtron—1538(A)
Kaiser, W. and H. Y. Fan. Infrared absorption of InSb—966
Kalkstein, M. I. (see Hollander, J. M.)—260(A)
Kane, R. P. Recurrence phenomenon in 24-hour variation of cosmic-ray intensity—130
Kanter, M. A. Self-diffusion in natural graphite crystals—1563(A)
Kantrowitz, Arthur and Harry Petscheck. Approach to equilibrium ionization following strong shock waves in A—1141(T)
Känzig, Werner. Space charge layer near surface of a ferroelectric—549(L)
—— **and Masayasu Ueta.** Generation of electron traps by plastic flow—236(A)
Kao, L. P. and E. Katz. Theory of anisotropy of magnetoresistance for single crystals—1534(A)

Kaplan, Joseph. Upper atmosphere—278(T)
—— Upper-atmospheric studies during international geophysical year—1159(T)
Kaplon, M. F. Abundance of Li, Be, and B in primary cosmic radiation—1164(T)
Karplus, Robert. Ferromagnetic Hall effect—1542(T)
—— **and Malvin A. Ruderman.** Applications of causality to scattering—771
—— **and M. A. Ruderman.** Some implications of causality for scattering—260(T)
Kassner, D. (see Piccioni, O.)—275(A)
Katz, E. Photographic "order principle"—1556(A)
—— (see Enns, J. H.)—1556(A)
—— (see Kao, L. P.)—1534(A)
—— (see Martin, R. L.)—1557(A)
Katz, Samuel. Velocity of explosively-induced shock in steel—256(A)
Kauffman, J. W. and J. S. Koehler. Formation energy of lattice vacancies in Au—245(A)
Kavanagh, R. W. (see Sherr, R.)—1185(A)
Kay, I. and H. E. Moses. Determination of scattering potential from spectral weight function—1190(A)
Keating, David T. X-ray measurements on low-temperature neutron-irradiated graphite—1859(L)
Keck, J. C. (see Bingham, H. H.)—1187(A)
Kedesdy, H. (see Matare, H. F.)—1179(A)
Keesom, P. H. and N. Pearlman. Anomaly in low-temperature atomic heat of Ag—548(L)
—— **and N. Pearlman.** Heat capacity measurements on pure and slightly reduced rutile (TiO_2) at very low temperatures—1539(A)
—— (see Pearlman, N.)—1539(A)
Keller, William E. Pressure-volume isotherms of He^3 between 1.5 and 3.8° K—1571
Kelly, J. M. (see Gilbert, T. L.)—1200(A)
Kenney, Robert W. (see Anderson, John D.)—258(A)
Kenty, Carl. Studies of active N in rare gases—563(A)
Kepler, G. E. (see Fretter, W. B.)—1202(A)
Kereiakes, J. G. X-ray analysis of compressed KCl powder crystals—553(L)
Kern, B. D. (see Hahn, T. M., Jr.)—1183(A)
Kerner, Edward H. and Joseph G. Logan. Invariant characteristics of one-dimensional binary lattices—1165(A)
Kerr, J. and C. Wert. Magnetic coercive force in alloys of Fe and N—225(A)
Kerst, D. W. Review of MURA high-energy accelerator programme—236(T)
——, **K. M. Terwilliger, K. R. Symon, and L. W. Jones.** Fixed field alternating gradient accelerator with spirally ridged poles—1153(A)
—— (see Jones, L. W.)—1153(A)
—— (see Terwilliger, K. M.)—1153(A)
Kerth, Leroy and Byron L. Youtz. Elastic and inelastic scattering of 90-Mev neutrons by deuterons—259(A)
Keywell, Frank. Measurements and collision theory of high vacuum sputtering—561(A)
Kierstead, Henry A. Expansion of Cu bombarded by 19-Mev deuterons—245(A)
—— (see McDonell, William R.)—1870(E)
Kiive, P. and H. T. Pinnick. Temperature dependence of magnetic susceptibility of carbons and polycrystalline graphites—1564(A)
Kim, Y. B., J. R. Burwell, R. W. Huggett, and R. W. Thompson. Evidence for charge asymmetry of $V^{\pm}$ particles—248(A)
King, D. T. and M. M. Block. Nuclear absorption of fast charged hyperon—1203(A)
King, R. W. Supermultiplet structure and spin dependent forces—235(A)
King, W. C. (see Gallagher, J. J.)—1551(A)
Kingston, R. H. Water vapor induced n-type surface conductivity on p-type Ge—1766
—— **and A. L. McWhorter.** Relaxation effects in field-induced surface conductance—1191(A)
—— (see Bernstein, H.)—1566(A)
Kington, Joe D. (see Willard, Harvey B.)—669; 1184(A)
Kip, A. F. Cyclotron resonance in solids—272(T)
—— (see Dresselhaus, G.)—368; 556(L)
—— (see Feher, George)—337
Kisliuk, P., W. S. Boyle, and L. H. Germer. Electrical breakdown in high vacuum—560(A)
—— (see Boyle, W. S.)—560(A)
Kisslinger, Leonard S. Scattering of mesons by light nuclei—761
—— Scattering of π mesons by nuclei—239(A)
Kister, J. M. (see Beyster, J. R.)—1216
Kistler, A. L. (see Corrsin, S.)—1142(A)
Kittel, C. Electron transfer mechanism for ultrasonic attenuation in metals—1181(A)
—— Theory of valence-band structure of Ge and Si—1542(T)
—— (see Dresselhaus, G.)—368; 556(L)
—— (see Mitchell, A. H.)—271(A)
Kivel, Bennett. Electron broadening and shift of spectral lines of He—1055
—— Electron impact broadening of spectral lines of He—1195(A)
——, **S. Bloom, and H. Margenau.** Electron impact broadening of spectral lines—495
—— (see Margenau, Henry)—1822
Klein, Abraham and Bruce H. McCormick. Meson pair theory—1428; 1155(A)
—— (see Bernstein, J.)—1155(A)
—— (see McCormick, Bruce H.)—1155(A)
Klein, M. P. and B. E. Holder. Magnetic susceptibility measurements by nuclear magnetic resonance—265(A)
—— (see Holder, B. E.)—265(A)
Klein, Martin J. Overhauser nuclear polarization effect and minimum entropy production—1736
Kleitman, D. and G. Goldsmith. Conduction in phthalocyanine crystals—1544(A)
Klema, E. D. (see Lazar, N. H.)—710; 1186(A)
Klick, Clifford C. (see Lambe, John)—1545(A); 909
—— (see Patterson, D. A.)—1546(A)
Klontz, E. E., R. R. Pepper, and K. Lark-Horovitz. Electrical properties of electron bombarded Ge—1535(A)
—— (see Stoeckmann, F.)—1535(A)
Kmetko, E. A. Properties of powdered Ge and effects of heat-treatment—1535(A)
Knapp, Myron W. and Wilson M. Powell. Negative pions from neutron bombardment of deuterons—1188(A)
Knight, W. D. (see Walsh, J. L.)—265(A)
Knowles, J. W. Anomalous absorption of neutrons in single crystals—224(A)
Kobayashi, S. (see Sakamoto, M.)—552(L)
Koehler, J. S. Quenching-in of vacancies in pure Ag—1562(T)
—— (see Beshers, D. N.)—1553(A)
—— (see Kauffman, J. W.)—245(A)
Koenig, S. H. and G. R. Gunther-Mohr. Low-temperature electrical conductivity of Ge—228(A)
Koerts, L., P. Macklin, B. Farrelly, R. van Lieshout, and C. S. Wu. Radiations of I^{126}—1172(A); 1230
—— (see Farrelly, B.)—1172(A)
Koester, Charles J. and M. Parker Givens. Extreme uv absorption spectrum of AgCl—1543(A)
Koester, Louis J., Jr. Low-energy photoproduction of π^0 mesons in H: Differential cross sections at 135°—211(L)
—— Photoproduction of π^0 mesons in H—239(A)
—— (see Goldwasser, E. L.)—239(A)

—— (see Mills, F. E.)—210(L)
Kofoed-Hansen, O. Coupling in nuclear β decay—1164(T)
Kohman, T. P. (see Simanton, J. R.)—260(A)
Kohn, Walter. Interpretation of donor state absorption lines in Si—1856(L)
—— Spin resonance widths of electrons in donor states in Si —1561(A)
—— Theory of hyperfine splitting of donor states in Si—252(T)
—— **and J. M. Luttinger.** Theory of donor states in Si—915
—— **and J. M. Luttinger.** Theory of energy levels of donor electrons in Si—1178(A)
Kolchin, Eleanor K. (see Lewis, Margaret N.)—1210(A); 1020
Kolin, Alexander. New method of microelectrophoresis—1195(A)
Kolsky, Harwood G. Method for numerical solution of transient hydrodynamic shock problems in two space dimensions—1158(A)
Korringa, J. Satellites in soft x-ray spectrum of Zr—1556(A)
—— (see Daunt, J. G.)—1550(A)
Koski, W. S. (see Iwersen, John E.)—1307
Koster, G. F. Density of states curve for Ni—901
—— Extension of Hund's rule—514
Koth, W. (see Holzman, G. R.)—542(L)
Kovarik, A. F. and N. I. Adams, Jr. Redetermination of disintegration constant of U^{238}—46
Kovasznay, Leslie S. G. Experimental study of shock wave turbulence interaction—1141(A)
Kraichnan, Robert H. Special-relativistic derivation of generally covariant gravitation theory—1118
Kramer, Mary J. Molecular orientation produced in polymethyl methacrylate by hot stretching—1170(A)
Krasner, Sol and J. Cuevas. Electron loss cross sections of moving He atoms—1149(A)
Kraybill, H. L. (see Walker, R. M.)—1203(A)
Kriessman, C. J., S. E. Harrison, and H. B. Callen. Ionic distribution in Mg ferrite—1562(A)
—— **and T. R. McGuire.** Magnetic susceptibility of Hf and Mn—936
Krimm, S. and C. Y. Liang. Infrared spectrum and structure of polyvinylidene chloride—1547(A)
—— (see Liang, C. Y.)—1548(A)
Krohn, Victor E., T. B. Novey, and S. Raboy. Gyromagnetic ratio of 6×10^{-8} sec Np^{237} by angular-correlation techniques—1187(A)
—— (see Raboy, Sol)—24; 231(A); 1187(A)
Kroll, Norman M. and Walter Wada. Internal pair production associated with emission of high-energy γ rays—1355
—— (see Mills, Robert L.)—1489
Krueger, G. C. Investigation of quantitative phase contrast method for examining nonhomogeneous media—1157(A)
Krumbein, A. D. (see Wiser, H. L.)—303
Kruse, U. E., H. L. Anderson, W. C. Davidon, and M. Glicksman. Positive pion scattering by H at 189 Mev—1188(A)
—— (see Teem, J. M.)—259(A)
v. Krzywoblocki, M. Z. New fundamentals of fluid dynamics—251(A)
Kuczynski, G. C. and M. Doyama. Second transition in $AuCu_3$—270(A)
—— (see Freda, A. R.)—270(A)
Kulin, S. A., A. D. Kurtz, and B. L. Averbach. Effect of dislocations on recombination of holes and electrons in Ge and Si—1566(A)
—— (see Kurtz, A. D.)—1543(A)
Kundu, D. N. (see Cheng, L. S.)—231(A)
Kunkel, W. B. and A. L. Gardner. Ionization accompanying long-lived nitrogen afterglow—558(A)
Kuper, Alan B., H. Letaw, Jr., L. Slifkin, E. Sonder, and C. T. Tomizuka. Self-diffusion in Cu—1870(E)
—— **and Carl T. Tomizuka.** Diffusion of Cu and Zn in ordered and disordered CuZn—244(A)
Kurbatov, J. D., B. B. Murray, and M. Sakai. Energy levels of Se^{76} appearing in disintegration of As^{76}—674
Kurşunoğlu, Behram. Proton bremsstrahlung—1156(A)
Kurtz, A. D., S. A. Kulin, and B. L. Averbach. Determination of dislocation densities with double crystal spectrometer—1543(A)
—— (see Kulin, S. A.)—1566(A)
Kusch, P. (see Heberle, J.)—1194(A)
—— (see Reich, H.)—1194(A)

Lafferty, D. L. (see Rayburn, L. A.)—701
Lagarrigue, A. *S*-particles and charged heavy particles—255(T)
—— (see Armenteros, R.)—275(A)
—— (see Fretter, W. B.)—1202(A)
Lagerstrom, P. Structure of solutions of Navier-Stokes equation for high and low Reynolds numbers—1141(T)
Lakin, W. Spin polarization of deuteron—139
Lamb, W. E., Jr. (see Maiman, T. H.)—1194(A)
Lambe, John. Recombination processes in CdS—985
—— **and Clifford C. Klick.** Model for luminescence and photoconductivity in sulfides—909; 1545(A)
Landauer, R. (see Drougard, M. E.)—1010; 1563(A)
Landel, Robert F. (see Williams, Malcolm L.)—1549(A)
Landon, H. H. and V. L. Sailor. Radiation width variations in slow neutron resonances of Eu and In—225(A); 1267
—— (see Sailor, V. L.)—224(A)
—— (see Wood, R. E.)—639
Lane, A. M., R. G. Thomas, and E. P. Wigner. Giant resonance interpretation of nucleon-nucleus interaction—693
—— **and C. F. Wandel.** Evaluation of imaginary part of nuclear complex potential—1524(L)
—— (see Wilkinson, D. H.)—235(A)
Lane, C. T., R. G. Wheeler, and C. H. Blakewood. Second sound attenuation in rotating He II—1196(A)
Langer, L. M. (see Johnson, O. E.)—1517(L)
Langsdorf, Alexander, Jr., J. E. Monahan, and F. Paul Mooring. Measurement of neutron transmission cross sections by self-indication technique—1148(A)
—— (see Hibdon, Carl T.)—223(A)
—— (see Monahan, J. E.)—1147(A)
Lannutti, Joseph, Gerson Goldhaber, and Stephen J. Goldsack. Stars formed by protons of 3.2 Bev from the Bevatron—258(A)
—— (see Goldhaber, Gerson)—267(A)
Larach, Simon and John Turkevich. Magnetic properties of ZnS and CdS phosphors—1015
Lark-Horovitz, K. and H. Fritzsche. Hall effect and resistivity of *p*-type Ge at low temperatures—1536(A)
—— (see Becker, W. M.)—228(A)
—— (see Buschert, R.)—1157(A)
—— (see Fritzsche, H.)—1532(A)
—— (see Klontz, E. E.)—1535(A)
—— (see Schulz-DuBois, E.)—1561(A)
—— (see Stoeckmann, F.)—1535(A)
Larson, M. B. (see Brady, J. J.)—271(A)
Lauer, Eugene J. (see Eugene, J.)—276(A)
—— (see Hubbard, Edward L.)—1814
Laurman, J. A. and S. A. Schaaf. Flow near leading edge of flat plate—1540(A)
Lawson, A. W. Recent experiments on high-pressure phenomena at Chicago—244(T)

Lax, Benjamin. Cyclotron resonance in semiconductors—1560(T)
—— **and Laura M. Roth.** Propagation and plasma oscillation in semiconductors with magnetic fields—548(L)
Lax, M. (see Burstein, E.)—1536(A)
—— (see Teitler, S.)—1561(A)
Lazar, N. H. and E. D. Klema. Decay of Bi^{207}—710; 1186(A)
LeBlanc, J. M., J. M. Cork, and S. B. Burson. Decay of 3.5-min metastable state of Sb^{122}—39
—— (see Burson, S. B.)—230(A)
Lebowitz, Joel and Peter G. Bergmann. Statistical ensemble representing stationary nonequilibrium states—1165(A)
Lederman, L. M. (see Ammiraju, P.)—1188(A)
—— (see Blumenfeld, H.)—1203(A)
—— (see Sargent, C. P.)—1349
Lee, Kiuck (see Green, A. E. S.)—1205(A)
Lee, T. D. and C. N. Yang. Conservation of heavy particles and generalized gauge transformations—1501
Lee, T. H. (see Winsor, L. P.)—562(A)
Lehman, G. W. Computation of electron density and density of states in narrow bands in crystals—1542(A)
Lehovec, Kurt, Alma Marcus, and Kurt Schoeni. Forward characteristic of point contact rectifier—1179(A)
——, **Alma Marcus, and Kurt Schoeni.** Theory of magnetic rectifier—229(A)
Leiss, J. E., C. S. Robinson, and S. Penner. Photoproduction of π^+ mesons from H near threshold—201(L); 1188(A)
Leivo, W. J. and R. Smoluchowski. Semiconducting diamond—1532(A)
Leonard, B. P., Jr. (see Little, R. N., Jr.)—634
Lepore, Joseph V. and Maurice Neuman. Statistical model for high-energy events—1484
Leprince-Ringuet, L. (see Armenteros, R.)—275(A)
Letaw, Harry, Jr. (see Kuper, A.)—1870(E)
—— (see Portnoy, William M.)—1536(A)
Levin, J. S. and D. J. Hughes. Radiation widths of nuclear energy levels—1161(A)
Levine, M. M. (see Cabrera, N.)—1543(A)
Levinger, J. S. Velocity-dependent nuclear potential—1205(A)
Levinson, Carl A. Nuclear configuration interaction with singlet two-body forces—1205(A)
Levy, A. (see Feher, G.)—264(A)
Lévy, Maurice M. Effect of renormalization on meson-nucleon S-scattering—1470
Levy, Paul W. Reactor and γ-ray induced coloring in Corning fused silica—1541(A)
—— (see Dreyfus, Russell W.)—1541(A)
—— (see Rosenwasser, Hyman)—1541(A)
Levy, R. A. Electron spin resonance in liquid alkali metals—264(A)
Lewis, J. H. (see Burkhard, E. L.)—1154(A)
Lewis, Margaret N., Louis C. Green, Marjorie M. Mulder, Paul C. Milner, and Eleanor K. Kolchin. Computed transition probabilities for x-ray continua of K—1020
——, **Louis C. Green, Marjorie M. Mulder, Paul C. Miller, and Eleanor K. Kolchin.** Computed transition probabilities for x-ray K-edge of K—1210(A)
Li, Chi Yao and A. S. Nowick. Critical temperature for self-induced ordering in Ag-Zn solid solutions—1152(A)
—— **and A. S. Nowick.** Effect of quenching and neutron irradiation on atomic mobility in Cu-Al alloy—1531(A)
—— (see Nowick, A. S.)—1556(A)
Liang, C. Y. and S. Krimm. Normal vibrations and infrared spectrum of polytetrafluoroethylene—1548(A)
—— (see Krimm, S.)—1547(A)
Lidofsky, L., N. Benczer, P. Macklin, and C. S. Wu. β decay of RaE—1186(A)
Lieshout, R. van (see Koerts, L.)—1230
Likely, J. G. $Li^6(p,d)Li^5$ reaction—1538(A)
Lin, C. C. Motion in boundary layer over flat plate with sudden change of speed—1143(A)
Lind, D. A. (see Van Loef, J. J.)—224(A)
Lindeberg, G. K. (see Arnold, W. H.)—838(L)
Lindqvist, Torsten and C. S. Wu. Inner bremsstrahlung from A^{37}—231(A)
Linhart, P. B. (see Price, P. J.)—243(A)
Lipson, H. G., E. Burstein, and P. L. Smith. Optical effects in plastically deformed Ge—1535(A)
Lipson, J. and J. H. Reynolds. Performance data for high-sensitivity mass spectrometer—283(A)
Little, Elizabeth A. Dynamic behavior of domain walls in $BaTiO_3$—978; 1201(A)
Little, R. N., Jr., B. P. Leonard, Jr., J. T. Prud'homme, and L. C. Vincent. Liquid scintillator measurements of angular elastic scattering of neutrons from C, Al, and S—634
Livingston, M. S. Design for a strong-focusing electron synchrotron—266(T)
Lockary, T. E. and E. Guth. Theory of successive orientational phase transitions in two- and three-dimensional systems—274(A)
Lockett, Andrew M. 3-body exchange magnetic moments of H^3 and He^3—1204(A)
Loeb, A. L. (see Goodenough, J. B.)—391
Loebner, E. E. and H. Freund. Stacked barriers in electroluminescent ZnS crystal—1545(A)
Loferski, J. J. and P. Rappaport. Electron voltaic study of electron bombardment damage and its thresholds in Ge and Si—1861(L)
Logan, Joseph G. (see Kerner, Edward H.)—1165(A)
Lokanathan, S. and J. Steinberger. Search for improbable meson decays—240(A)
Long, A. L. (see Simanton, J. R.)—260(A)
Long, Donald and Park H. Miller, Jr. Effect of pressure on electrical properties of InSb—1192(A)
Long, Earl and Lothar Meyer. Superfluidity and heat transport in unsaturated He-II film—1616
Long, Robert R. Internal finite gravity waves in stratified fluid—1144(A)
Longini, R. L. (see McKelvey, J. P.)—1566(A)
Lönsjö, O., O. Os, and R. Tangen. Yield of high-energy γ rays from proton capture in Be^9—727
Lord, J. J. (see Fleming, John R.)—268(A)
Loshaek, S. (see Fox, T. G.)—1549(A)
Love, William F. (see Passaglia, Elio)—1006
Lovejoy, D. R. Surface tension of He^3—1196(A)
Low, Francis E. and David Pines. Mobility of slow electrons in polar crystals—414
Low, W. Paramagnetic resonance spectrum of some doubly activated phosphors—426
—— Possibility of nuclear radiation detector by means of electroluminescent phosphors—556(L)
Lowry, Ralph A. and Glenn H. Miller. Measurement of ionization yield of low-energy ions in gas—243(A)
Lubitz, C. R. (see Bach, D. R.)—235(A)
Luckey, George W. Effect of Br on dark conductivity of AgBr and its relation to photoconductivity—1558(A)
—— Some recent studies of light absorption photoconductivity and photolysis of Ag halide crystals—1549(T)
Ludloff, H. F. and M. B. Friedman. Difference solution of shock diffraction problem—1140(A)
Lundberg, John Lauren. Molecular weight distributions of polymers: I. Speculations on polymerizations to equilibrium—1559(A)

Luttinger, J. M. Quantum theory of cyclotron resonance for degenerate bands—1560(A)
—— Recent developments in effective-mass theory for semiconductors—252(T)
—— (see Kohn, W.)—1178(A); 915
Lutz, B. C. (see Segel, S. L.)—1183(A)
Lyon, W. S. (see Handley, T. H.)—688
—— (see Kahn, B.)—58

MacDonald, A. (see Matare, H. F.)—1179(A)
MacDonald, A. D. and J. H. Matthews. High-frequency ionization coefficients in Ne-A mixtures—1070
—— (see MacLennan, I. A.)—559(A)
MacDonald, D. K. C. (see Dugdale, J. S.)—1751
MacDonald, R. E. (see Allin, Elizabeth J.)—554(L)
MacDonald, William M. Isotopic spin impurity in light nuclei—234(A)
—— Isotopic spin selection rule for electric dipole transitions—60
Macfarlane, G. G. and V. Roberts. Infrared absorption of Si near lattice edge—1865(L)
Machlup, Stefan. Relaxation of monatomic crystal lattice around vacancy—1556(A)
MacKenzie, K. R. (see Sonett, C. P.)—280(A)
Mackin, R. J., Jr., W. B. Mims, and W. R. Mills, Jr. γ-rays from deuteron bombardment of C^{13}—43
Mackinnon, L. Absorption of 10 Mc/sec sound in polycrystalline Mg rod between 1.5 and 4.2°K—1210(A)
—— Absorption of 10 Mc/sec sound pulses by superconducting polycrystalline Sn rod—1181(A)
Macklin, P. (see Koerts, L.)—1172(A); 1230
—— (see Lidofsky, L.)—1186(A)
MacLennan, I. A. and A. D. MacDonald. Effect of mean free path variation on high frequency breakdown—559(A)
Madansky, L. and F. Rasetti. Decay of Co^{57}—1870(E)
Maienschein, F. C. (see Campbell, E. C.)—1172(A)
Maiman, T. H. and W. E. Lamb, Jr. Triplet fine structure of He—1194(A)
Maitland, C. G. and A. O. McCoubrey. Effect of temperature on lifetime of metastable Hg molecules—558(A)
Major, J. K. Calibration of linear amplifiers with Hg relay pulse generator—1210(A)
Malenka, B. J. Asymmetry in deuteron pickup by high-energy polarized protons—1156(A)
—— Deuteron pickup by high-energy polarized protons—843(L)
Malmberg, Philip R. Elastic scattering of protons from Li^7—1167(A)
—— (see Sun, K. H.)—1154(A)
Mandel, M. and A. H. Barrett. Pure rotational spectra of Tl halides—1159(A)
Mandelkern, Leo (see Roberts, Donald E.)—1559(A)
Mandeville, C. E. and H. O. Albrecht. Storage of energy in BeO—1546(A)
——, **Jagdish Varma, and Babulal Saraf.** Ir^{194}—94; 1185(A)
—— (see Hans, H. S.)—1173(A)
—— (see Saraf, B.)—1206(A)
—— (see Swann, C. P.)—1183(A)
Manley, D. L. (see Crasemann, Bernd)—66; 279(A)
Mann, A. K. Elastic scattering of 0.41 and 0.66 Mev γ rays by Sn and Pb—234(A)
—— (see Stephens, W. E.)—241(A); 839(L)
Mann, Lloyd G. (see Bowman, Harry R.)—277(A)
Manning, Irwin and Laszlo Tisza. Variational principles in irreversible thermodynamics—1165(A)
Mapes, Joe M. (see Allen, William A.)—256(A)
Marcus, Alma (see Lehovec, Kurt)—229(A); 1179(A)
Marcus, Jules A. Oscillatory Hall effect and magnetoresistance of Bi—1540(A)
Marcus, Paul M. Anisotropic electronic stress and Mg alloys—1552(A)
Marder, S., W. Bennett, C. S. Wu, and V. W. Hughes. Effect of static electric field on positronium formation—1173(A)
—— (see Hughes, V. W.)—1840
Margenau, Henry. Electron effects in spectral line broadening—1195(A)
—— **and Bennett Kivel.** Effects of electron collisions on width of spectral lines—1822
—— (see Kivel, B.)—495
—— (see Meyerott, Roland E.)—1195(A)
Mark, Hans, Clyde McClelland, and Clark Goodman. Electric excitation of certain medium-weight nuclei by protons—1245
——, **Clyde McClelland, and Clark Goodman.** Electric excitation of nuclei near closed 50 proton and neutron shells—249(A)
——, **Clyde McClelland, and Clark Goodman.** Proton bremsstrahlung—279(A)
—— (see McClelland, Clyde)—249(A)
Markowitz, S. (see Miller, J. M.)—1197(A)
Marmier, P., F. Boehm, and J. W. M. DuMond. Energy levels of Hf^{177}—280(A)
—— (see Boehm, F.)—280(A)
Marshak, H. and H. W. Newson. Total neutron cross sections in kev region: Sc, V, Mn, and Co—1162(A)
Marshall, J., L. Marshall, and V. A. Nedzel. Differential p-p scattering cross sections at 419 Mev—1513(L)
—— (see Marshall, L.)—1398
Marshall, Leona. Experiments with high-energy proton beams—266(T)
—— **and J. Marshall.** Direction of proton spin polarization produced by elastic scattering—1398
—— (see Marshall, J.)—1513(L)
Martin, E. E. (see Dyke, W. P.)—263(A)
—— (see Trolan, J. K.)—262(A)
Martin, G. M., F. L. Roth, and R. D. Stiehler. Behavior of nonpigmented rubber vulcanizates in tension—1559(A)
Martin, R. L., J. E. Enns, and E. Katz. Low-intensity reciprocity law failure for pure AgBr emulsions of different grain size—1557(A)
—— (see Enns, J. H.)—1556(A)
Marton, L., J. Arol Simpson, and T. F. McCraw. Single scattering of 20-kev electrons in solids—1168(A)
—— (see Mendlowitz, H.)—1168(A)
Mason, W. P. Dislocation relaxations at low temperatures and determination of limiting shearing stress of metal—1136(L)
Matare, H. F., H. Kedesdy, A. MacDonald, and A. Petersen. Study of electrical characteristics of grain boundaries—1179(A)
Mathur, Hirdaya B. and E. K. Hyde. Isomeric states in the chain $Mo^{90} \rightarrow Nb^{90} \rightarrow Zr^{90}$—261(A)
—— **and Earl K. Hyde.** Radiations of Mo^{90} and isomeric states of Nb^{90}—79
Matossi, Frank. Polarization effects on brightness waves of electroluminescence—434; 1545(A)
—— **and S. Nudelman.** Electroluminescence excited with short field pulses—238(A)
—— (see Nudelman, S.)—238(A); 1545(A)
Matthews, David L. Vortex created by shock passing over vertical wall—1140(A)
Matthews, J. H. (see MacDonald, A. D.)—1070
Matthias, B. T. (see Holden, A. N.)—546(L)
Maunsell, C. D. Measurement of absorption coefficients for photoionizing radiations in low-pressure gases with space charge detector—1831
—— Photoionization by absorption in gas of radiations from discharge in same gas—263(A)

Maurer, R. D. Light scattering from optical glass—1544(A)
Maxson, D. R., J. S. Allen, and W. K. Jentschke. Electron-neutrino angular correlation in β decay of Ne^{19}—230(A)
Mayburg, Sumner. Lattice defects in Si—1177(A)
—— Ring diffusion as mechanism of self-diffusion in Ge—1134(L)
Mayes, W. T. (see Kaiser, H. F.)—1538(A)
Mayfield, Earle B. (see Allen, William A.)—256(A)
Mays, J. M., R. G. Shulman, and D. W. McCall. Nuclear magnetic resonance in semiconductors: GaSb and InSb—1182(A)
—— (see Shulman, R. G.)—1182(A)
—— (see Slichter, W. P.)—1559(A)
Mazenko, J. J. (see Schwertz, F. A.)—1133(L); 1169(A)
McAllister, Robert W. (see Hofstadter, Robert)—217(L)
McBride, John J. (see Westrum, Edgar F.)—270(A)
McCaffrey, F. (see Silver, M.)—270(A)
McCall, D. W. (see Mays, J. M.)—1182(A)
—— (see Shulman, R. G.)—1182(A)
McCarthy, Kathryn A. and Stanley S. Ballard. Thermal conductivity of Ge at ambient temperatures—271(A)
McClelland, Clyde, Hans Mark, and Clark Goodman. Electric excitation of heavy nuclei with protons—249(A)
—— (see Mark, Hans)—249(A); 279(A); 1245
McClure, J. W. Axial ratios in hexagonal crystals—449
McConnell, H. M. (see Reilly, C. A.)—264(A)
McCormick, Bruce H. and Abraham Klein. Meson pair theory—1155(A)
—— (see Klein, Abraham)—1428
McCoubrey, A. O. (see Maitland, C. G.)—558(A)
McCrary, J. H. (see Bent, R. D.)—1198(A); 1325
—— (see Bonner, T. W.)—1198(A)
McCraw, T. F. (see Marton, L.)—1168(A)
McDonald, A., Jr. (see Anderson, John D.)—258(A)
McDonell, William R. and Henry A. Kierstead. Expansion of Cu bombarded by 21-Mev deuterons—1870(E)
McEllistrem, M. T. (see Galonsky, A.)—586; 590
—— (see Jones, K. W.)—241(A)
McFarland, Robert H. (see Swanson, Robert E.)—1063
McGee, J. F. Long-wavelength x-ray reflection microscope—282(A)
McGinnis, Carl L. Disintegration of 5.8-day Sb^{120}—1172(A)
—— Radioactivity of In^{117} and Sb^{117}—1870(E)
McGowan, F. K. (see Stelson, P. H.)—249(A)
McGuire, T. R., E. J. Scott, and F. H. Grannis. Antiferromagnetism in Cr_2O_3 crystal—1562(A)
—— (see Kriessman, C. J.)—936
McHale, J. L. and R. M. Thaler. Variational expressions for N-channel collision parameters—1189(A)
—— **and R. M. Thaler.** Variational principle for tensor forces—273(A)
—— (see Thaler, R. M.)—1189(A)
McIntyre, John A. and Robert Hofstadter. Scattering of 192-Mev electrons from deuterium—158
McKelvey, J. P. and R. L. Longini. Recombination of injected carriers at dislocation edges in semiconductors—1566(A)
McKeown, Marilyn (see McReynolds, A. W.)—418
McReynolds, A. W. Diffuse magnetic neutron diffraction—1200(A)
——, **W. Augustyniak, Marilyn McKeown, and D. B. Rosenblatt.** Neutron irradiation effects in Cu and Al at 80°K—418
—— (see Smith, L. W.)—1167(A)
McWhorter, A. L. Surface traps and $1/f$ noise in Ge—1191(A)
—— (see Kingston, R. H.)—1191(A)
Mead, S. W. (see Petroff, M. D.)—279(A)
Meadows, J. W. (p,a) and (p,ab) reactions at 100 Mev—744
Medved, David B. Photoconductivity and photodesorption in ZnO—237(A)
Meggers, William F. (see Fred, Mark)—1514(L)
Meisenheimer, R. G. (see Reilly, C. A.)—264(A)
Meissner, Hans. Theory of paramagnetic effect in superconductors—1539(A)
—— (see Bedard, F.)—1539(A)
Melamed, Nathan T. and Raymond Bowers. Origin of luminescence in Cu activated ZnS phosphors—1545(A)
Melvin, M. A. Freundlich red-shift formula—884
Mencher, A. (see Barker, W. A.)—1868(L)
Mendlowitz, H. and L. Marton. Scattering of 20-kev electrons in thin films—1168(A)
Menes, M. Investigation of buildup processes in argon discharge—561(A)
Menon, M. G. K. Investigations of Bristol school—1166(T)
Mercure, R. (see Rense, William A.)—1195(A)
Merritt, F. R. (see Fletcher, R. C.)—1560(A)
Merz, Walter J. (see Holden, A. N.)—546(L)
—— (see Hooton, John A.)—409
Meshkov, S. and C. W. Ufford. Matrix elements of nuclear p^8 configuration—1204(A)
Metropolis, N. (see Hoffman, Joseph G.)—1195(A)
Metzger, Franz R. Angular distribution of resonance fluorescence radiation from 411-kev level in Hg^{198}—1186(A)
—— Spin and lifetime of 439-kev excited state of Hg^{202}—200(L)
Meyer, Lothar (see Long, Earl)—1616
Meyer, Peter and J. A. Simpson. Changes in amplitude of cosmic-ray 27-day intensity variation with solar activity—247(A)
Meyer, R. A. and F. L. Boquet. Conductivity of teflon and polyethylene during γ irradiation—1531(A)
Meyerott, Roland E. and Henry Margenau. Line broadening by electrons: Validity of simple theories—1195(A)
Michalik, E. R. (see Schwertz, F. A.)—1133(L)
Michel, L. Universal Fermi interaction—1164(T)
—— **and A. S. Wightman.** Covariant formalism describing polarization of spin one-half particles—1190(A)
Mihelich, John W. and M. Goldhaber. Evidence for mixed $M3+M4$ isomeric transition—1185(A)
Milford, F. J. Projection operator for Rarita-Schwinger equation—1488
Miller, D. W., U. C. Gupta, V. K. Rasmussen, and M. B. Sampson. Energy levels in N^{14} by inelastic α-scattering—1184(A)
Miller, E. E. Physical theory for capillary flow—251(A)
Miller, Glenn H. (see Lowry, Ralph A.)—243(A)
Miller, J. Malcolm. Radio chemical studies on nuclear reactions at the Cosmotron—260(T)
——, **G. Friedlander, and S. Markowitz.** Competition between (α,pn) and $(\alpha,2n)$ reactions on Cr^{50}—1197(A)
—— (see Alperovitch, Edward A.)—262(A)
—— (see Miskel, J. A.)—1197(A)
Miller, Park H., Jr. (see Long, Donald)—1192(A)
—— (see Rau, Richard)—1533(A)
Miller, Paul. Work function difference of Au and AuO from contact potentials with respect to Ge and Pt—1552(A)
Miller, Paul C. (see Lewis, Margaret N.)—1210(A)
Miller, W. C. (see Ruane, T. F.)—1166(A)
Mills, F. E. and L. J. Koester, Jr. Low-energy photoproduction of π^0 mesons from H: Total cross section—210(L)
—— (see Goldwasser, E. L.)—239(A); 1763
Mills, Robert L. Integral equations of meson-nucleon system—1156(A)
—— **and Norman M. Kroll.** Fourth-order radiative corrections to atomic energy levels. II—1489
—— (see Day, R. B.)—279(A)

Mills, W. R., Jr. (see Mackin, R. J., Jr.)—43
—— (see Sherr, R.)—1185(A)
Milner, Paul C. (see Lewis, Margaret N.)—1020
Milton, G. M. (see Milton, J. C. D.)—1173(A)
Milton, J. C. D., J. S. Fraser, and G. M. Milton. Long-lived isomer of Ho^{166}—1173(A)
—— (see Fraser, J. S.)—1173(A)
Mims, W. B. (see Mackin, R. J., Jr.)—43
Minden, Henry T. Molecular distortion caused by hindered rotation—1160(A)
Mingins, Charles R. (see Farrall, George A.)—1211(A)
Minshall, Stanley. Investigation of polymorphic transition in Fe at 130 kilobars—271(A)
Miskel, J. A., M. L. Perlman, G. Friedlander, and J. M. Miller. Excitation functions for reactions of Cu with high-energy protons—1197(A)
Mitchell, A. H. and C. Kittel. Donor and acceptor ionization energies in Si and Ge—271(A)
Mitchell, E. N. Velocity spectrum of cosmic-ray particles at twelve-grams atmospheric depth—1163(A)
—— (see Winckler, J. R.)—1411
Mitchell, J. W. Research on Ag halides—1549(T)
Mizushima, Masataka, J. T. Cox, and Walter Gordy. Zeeman effect in rotational spectrum of NO—1034; 1159(A)
Mobley, R. C. and B. R. Albritton, Jr. Amplitude and frequency stabilized adjustable high-frequency oscillator—232(A)
Mockler, Richard C. and George R. Bird. Microwave spectrum of CS—1837
Moldauer, P. A. and K. M. Case. Nonrelativistic limit of spin $k+\frac{1}{2}$ particle wave equations—1190(A)
Monahan, J. E. and A. Langsdorf, Jr. Analysis of neutron self-indication transmission cross sections—1147(A)
—— (see Church, E. L.)—718
—— (see Langsdorf, A.)—1148(A)
Montgomery, H. C. and W. L. Brown. Field effect in Ge—1565(A)
—— (see Pearson, G. L.)—1567(A)
Montroll, Elliott. Effect of dimensionality on long-range order in crystals—255(T)
Moore, G. E. (see Benedict, W. S.)—1551(A)
—— (see Herman, R.)—1550(A)
Moore, J. (see Foote, H. L.)—1161(A)
—— (see Sheer, C.)—565
Mooring, F. Paul (see Holland, R. E.)—240(A)
—— (see Langsdorf, A.)—1148(A)
Morgan, G. W. Wave propagation in elastic tubes filled with streaming, viscous liquid—1157(A)
Morris, T. W., J. D. Garrison, E. C. Fowler, W. B. Fowler, R. P. Shutt, A. M. Thorndike, and W. L. Whittemore. p-p scattering at 900 Mev—1167(A)
Morrison, P. Diffusion of cosmic rays in earth-sun region—1163(A)
Moser, Frank and Franz Urbach. Ag halide phosphors—1557(A)
—— (see Nail, Nelson R.)—1557(A)
Moses, H. E. (see Kay, I.)—1190(A)
Motz, H., K. M. Crowe, and R. M. Friedman. π^-/π^+ ratios in asymmetric nuclei—268(A)
—— (see Crowe, K. M.)—268(A)
Moyer, Burton J. (see Bandtel, K. C.)—269(A)
—— (see Shaw, Harlan)—259(A)
Mrowca, B. A. (see Banas, E. M.)—265(A); 1548(A)
Mrozowski, S. Physical properties of carbons and porosity—1564(A)
—— (see Hong, K.)—1565(A)
Mulder, Marjorie M. (see Lewis, Margaret N.)—1210(A); 1020
Muller, F. (see Armenteros, R.)—275(A)
Mullin, C. J. and E. Guth. Theory of nuclear excitation in inelastic electron scattering—277(A)
Munick, Raymond J. Electrical conduction in plastics—236(A)
Murakawa, Kiyoshi. Nuclear moments of Nb^{93}, La^{139}, Os^{187}, and Hg^{201}—1285
Murray, B. B. (see Kurbatov, J. D.)—674
Murray, R. B. and L. D. Roberts. Magnetic and thermal properties of $MnCl_2$ at liquid He temperatures—1180(A)
—— (see Roberts, L. D.)—1180(A)

Nail, Nelson R., Frank Moser, Pliny E. Goddard, and Franz Urbach. Optical absorption measurements on Ag halide crystals—1557(A)
Nakano, Yoshihiro. Scattering of high-energy neutrons and Johnson-Teller type nuclei—842(L)
Nambu, Yoichiro. Structure of scattering matrix—803
Nathans, Robert and Paul F. Yergin. (γ,n) cross sections in Zr^{90} and Zr^{91}—1197(A)
—— **and Paul F. Yergin.** Photoneutron cross sections in Mg^{24}, Mg^{25}, Zr^{90}, Zr^{91}—1296
—— (see Yergin, P. F.)—1198(A)
Nedzel, V. A. (see Marshall, J.)—1513(L)
Need, John Logan. Mechanism of reaction $C^{12}+p\rightarrow p+3\alpha$ at 32 Mev—1538(A)
Neher, H. Victor and Edward A. Stern. "Knee" of the cosmic-ray latitude curve—845(L)
Nelson, E. B. (see Bashkin, S.)—1184(A)
—— (see Carlson, R. R.)—1310
—— (see Geer, E. H.)—241(A)
Nervik, Walter E. and Glenn T. Seaborg. Ta spallation and fission induced by 340-Mev protons—261(A)
Neufeld, Jacob and R. H. Ritchie. Passage of charged particles through plasma—1632
Neuman, Maurice (see Lepore, Joseph V.)—1484
—— (see Gasiorowicz, S.)—257(A)
—— (see Riddell, R., Jr.)—257(A)
Neumark, Gertrude. Influence of electric field on thermoluminescence of ZnS crystals—1546(A)
Neuringer, L. J. Effect of pressure on absorption edges of Te—1193(A)
Newman, Ezra and Peter G. Bergmann. Lagrangians linear in "velocities"—1176(A)
—— (see Cohen, B. L.)—1198(A)
Newman, R., W. C. Dash, R. N. Hall, and W. E. Burch. Visible light from Si p-n junction—1536(A)
—— (see Dash, W. C.)—1192(A)
—— (see Tyler, W. W.)—461; 1192(A); 961
Newson, H. W. (see Block, R. C.)—1162(A)
—— (see Marshak, H.)—1162(A)
Newton, C. M. (see Panofsky, W. K. H.)—751
Newton, Roger G. Radiative corrections to electron scattering—1514(L)
—— **and Res Jost.** Construction of non-central potentials from S-matrix—1189(A)
Niday, James B. Half-Life of Rb^{86}—42
Nielsen, John P. Secondary recrystallization analogy in heterogeneous liquid system—1157(A)
Nierenberg, W. A. (see Bemski, G.)—470
Nilan, T. G. and W. S. Paxton. Domain configuration and crystallographic orientation in grain-oriented Fe-Si alloy—1200(A)
Nisenoff, M. (see Schulz-DuBois, E.)—1561(A)
Nishikawa, Tetsuji (see Shimoda, Koichi)—1160(A)
Nobles, R. A. (see Beyster, J. R.)—1216
Nolle, A. W. Nuclear magnetic resonance relaxation times for polyisobutylene in CCl_4 solution—1560(A)
Norberg, R. E. and D. F. Holcomb. Nuclear spin relaxation in alkali metals near their melting points—226(A)
—— (see Holcomb, D. F.)—1074

Novey, T. B. α-γ directional correlation in Th^{228}—232(A)
—— (see Krohn, V. E.)—1187(A)
—— (see Porter, F. T.)—214(L)
—— (see Raboy, S.)—1187(A)
Nowick, A. S. and Chi Yao Li. Mechanism of grain boundary relaxation in metals and alloys—1556(A)
—— (see Feder, R.)—1152(A)
—— (see Fischbach, D. B.)—1543(A)
—— (see Gordon, R. B.)—1540(A)
—— (see Li, Chi Yao)—1152(A); 1531(A)
Nudelman, Sol and Frank Matossi. Effects of electric fields on ultraviolet excited ZnS phosphors—1545(A)
—— **and F. Matossi.** Time-average light output from electroluminescent phosphors—238(A)
—— (see Matossi, F.)—238(A)

O'Brien, V. (see Corrsin, S.)—1142(A)
Odell, F. A. Strain propagation in nylon yarns loaded transversely at high speeds—1548(T)
Odian, A. C., W. Rankin, P. C. Stein, and A. Wattenberg. Neutrons in coincidence with photoprotons—248(A)
Oehme, Reinhard. Possible experiments to determine transition matrix for p-p scattering—216(L)
—— Scattering of polarized nucleon beams—147
O'Halloran, T. A. (see Brady, J. J.)—271(A)
Okaya, Y., Y. Saito, and R. Pepinsky. New method in x-ray crystal structure determination involving use of anomalous dispersion—1857(L)
Okazaki, A. (see Darden, S. E.)—1147(A)
Oleson, N. L. Instantaneous probe measurements of travelling striations in argon glow discharge—559(A)
Olson, E. L. (see Handley, T. H.)—688
Oppenheim, Irwin. Statistical thermodynamics of isotope effects. I. Theory of equilibrium processes—258(A)
—— (see Friedman, Abraham)—258(A)
Ore, Aadne Entropy of radiation—887
Orear, Jay. D-wave solution to pion-proton scattering data—1155(A)
—— Scattering of 23-Mev positive pions on H—239(A)
O'Rourke, R. C. Problem in shower theory—"Approximation A"—1190(A)
—— (see Faust, W. R.)—1147(A)
—— (see Saenz, A. W.)—1166(A)
Os, O. (see Lönsjö, O.)—727
Osborne, Darrell W. (see Abraham, Bernard M.)—551(L)
Otter, F. A., Jr. Thermoelectric power and resistivity of dilute alloys of Mn, Pd, and Pt in Cu, Ag, and Au—1552(A)
Overhauser, A. W. (see Ehrenreich, H.)—1533(A)
Overton, William C., Jr., and Ted G. Berlincourt. Pressure dependence of de Haas-van Alphen parameters in Bi crystal at 4.2°K—1180(A)
—— **and John Gaffney.** Temperature variation of elastic constants of cubic elements. I. Cu—969
Owen, G. E. Neutron physics at Johns Hopkins University—1530(T)
—— (see Fowler, J. M.)—249(A)

Page, L. A., M. Heinberg, J. Wallace, and T. Trout. Angular correlation in two-photon annihilation in quartz—206(L)
Pagnia, H. and F. Stockman. Thermal formation of colloids from F centers in KCl crystals—236(A)
Pake, G. E. Paramagnetic resonance of free radicals—272(T)
—— **and R. H. Sands.** Hfs in paramagnetic resonance of V ions in solution—266(A)
Pal, Yash. Investigations of Indian school—1166(T)
Palevsky, H. and R. M. Eisberg. Magnetic scattering of slow neutrons by gaseous oxygen—492
—— (see Zimmerman, R. L.)—1162(A)
Panofsky, W. K. H. Progress with Stanford linear accelerator—266(T)
——, **C. M. Newton, and G. B. Yodh.** Pion production by electrons—751
Pao, Yoh-Han. Extension of Hertz theory of impact to viscoelastic case—1548(A)
Paramentier, D., A. J. Schwemin, L. W. Alvarez, F. S. Crawford, Jr., and M. L. Stevenson. Four-inch diameter liquid hydrogen bubble chamber—284(A)
Park, David. Magnetic rotation phenomena in polycrystalline ferrite. II—438
Parker, Earl R. (see Ancker, Betsy)—1151(A)
Parratt, L. G. (see Hempstead, C. F.)—1170(A)
—— (see Jossem, E. L.)—1151(A)
Parzen, Philip. Integral equation solution of space-charge wave propagation—257(A)
Passaglia, Elio and William F. Love. Electrical resistance of Cu-Au alloys at low temperatures—1006
Pasternak, J. (see Salkovitz, E. I.)—271(A)
Pattee, Howard, H., Jr. Metal vacuum joint suitable for field emitters—283(A)
Patterson, D. A. and C. C. Klick. Low-temperature luminescence in KCl:Tl—1546(A)
Patterson, L. T. (see Gurnee, E. F.)—1547(A)
Patton, B. J. (see Stephens, W. E.)—839(L)
Paul, H. and R. M. Steffen. Extranuclear effects on directional correlation of Ta^{181} γ rays—231(A)
Paul, William and G. L. Pearson. Pressure dependence of resistivity of Si—1755
—— (see Benedek, G. B.)—1193(A)
—— (see Warschauer, D. M.)—1193(A)
Paxton, W. S. (see Nilan, T. G.)—1200(A)
Pearlman, N. and P. H. Keesom. Atomic heat of graphite between 1° and 20°K—1539(A)
—— (see Keesom, P. H.)—548(L); 1539(A)
Pearlstein, E., H. Ingham, and R. Smoluchowski. Energy dependence of radiation effects in solids—1530(A)
—— (see Smoluchowski, R.)—1530(A)
Pearson, G. L., H. C. Montgomery, and W. L. Feldmann. Noise in Si p-n junction photocells—1567(A)
—— (see Paul, William)—1755
Pearson, M. D. (see Brick, R. O.)—282(A)
Peaslee, D. C. Pion photoproduction ratios—239(A)
Peed, W. F. (see Rogosa, G. L.)—1173(A)
Peelle, Robert. Differential cross sections for scattering of protons by C as function of incident proton energy—1184(A)
—— (see Campbell, E. C.)—1172(A)
Peierls, R. E. (Title to be announced)—1166(T)
Pell, E. M. Reverse current and carrier lifetime as function of temperature in Ge and Si junction diodes—1536(A)
Penner, S. (see Leiss, J. E.)—201(L); 1188(A)
Pepinsky, Ray (see Jona, F.)—1201(A); 903
—— (see Okaya, Y.)—1857(L)
—— (see Shirane, Gen)—1201(A)
Pepper, R. R. (see Klontz, E. E.)—1535(A)
Percus, Jerome K. and George J. Yevick. New extension of collective coordinates for many-body problem—1164(A)
—— (see Yevick, George J.)—1164(A)
Perez Y Jorba, J. P. (see Bishop, G. R.)—89
Perl, M. L., I. I. Rabi, and B. Senitzky. Nuclear electric quadrupole moment of Na^{23} by atomic beam resonance method—611
—— (see Senitzky, B.)—1537(A)
Perlman, I., F. Stephens, and F. Asaro. γ rays of Ra^{225} and Tl^{209}—262(A)
—— (see Asaro, Frank)—19; 260(A)
—— (see Hummel, J. P.)—22; 261(A)
—— (see Stephens, F.)—261(A)

Perlman, M. L. (see Miskel, J. A.)—1197(A)
Perlow, G. J. Neutron spectrometer for 100–500 kev region —223(A)
Perring, J. K. and J. S. Story. Thermodynamic theory of fission—1525(L)
Perry, J. E., Jr. (see Day, R. B.)—279(A)
Perry, R. L. and J. J. Brady. Changes in photoelectric probability factor resulting from surface contamination of Al—281(A)
Persh, Jerome. Study of behavior of boundary layer in region of transition from laminar to turbulent flows—1144 (A)
Peshkin, M., J. H. Roberts, and V. L. Telegdi. Polarized neutrons on Li^6—1204(A)
Petersen, A. (see Matare, H. F.)—1179(A)
Peterson, L. (see Winckler, J. R.)—1411
Peterson, Robert L. (see Emrich, Raymond J.)—1141(A)
Petroff, M. D., S. W. Mead, and W. O. Doggett. Radioactivity of Sn^{109}—279(A)
Petscheck, Harry (see Kantrowitz, Arthur)—1141(T)
Pevsner, Aihud (see Ritson, D. M.)—1168(A)
—— (see Williams, Ross)—1188(A)
Peyrou, C. (see Armenteros, R.)—275(A)
Phelps, A. V. Diffusion and volume loss coefficients of He metastable atoms and molecules—558(A)
—— (see Frost, L. S.)—559(A)
Philippoff, W. and J. Brodnyan. Dynamic properties of glucose glass—1549(A)
Phillips, G. C. (see Gossett, C. R.)—724
Piccioni, O., D. Clark, R. Cool, G. Friedlander, and D. Kassner. External proton beam at Cosmotron—275(A)
Pickup, E. and A. Husain. Identity of shower particles in stars in region 1–2× minimum ionization—247(A)
—— (see Husain, A.)—136
Picus, G. (see Burstein, E.)—1536(A)
Pieper, G. F., G. S. Stanford, and P. von Herrmann. (α,p) reaction studies—1185(A)
—— (see Cook, E. J.)—1154(A)
—— (see Stanford, G. S.)—1154(A)
Pigg, J. C. (see Cleland, J. W.)—1742
Pines, David (see Low, Francis E.)—414
Pinnick, H. T. (see Kiive, P.)—1564(A)
Piotrowski, Edward A. (see Ziomek, Joseph S.)—243(A)
Piper, W. W. and F. E. Williams. Theory of electroluminescence—1809
Plazek, D. J. and John D. Ferry. Dynamic mechanical properties of concentrated cellulose trinitrate solutions—1548(A)
Pleasonton, Frances (see Snell, Arthur H.)—1174(A)
Plendl, H. S. and F. E. Steigert. Levels in Sc^{41}—1538(A)
Pollard, E. C. (see Graetzer, H. G.)—1184(A)
Pomerantz, Martin A. Latitude effect of cosmic radiation at low altitudes—105
Pool, M. L. (see Cheng, L. S.)—231(A)
Porter, F. T., M. S. Freedman, T. B. Novey, and F. Wagner, Jr. First-forbidden nonunique β spectra in Re^{186} —214(L)
Porter, Richard F., Paul Schissel, and Mark G. Inghram. Mass spectrometric study of gaseous species in Si-SiO_2 system—242(A)
Porter, W. C. (see Swann, C. P.)—1183(A)
Portis, A. M. and D. Shaltiel. Electron spin resonance in irradiated alkali halides—264(A)
Portnoy, William M., Harry Letaw, Jr., and Lawrence Slifkin. Self-diffusion in Ge—1536(A)
Powell, Wilson M. (see Knapp, Myron W.)—1188(A)
Pratt, George W., Jr. Localized states at boundary of two crystals—1543(A)
Preston, R. S. (see Walker, R. M.)—1203(A)
Prestwood, R. J. $(n,2n)$ cross section of Na^{23} at 14.1 Mev —47
——, **H. L. Smith, C. I. Browne, and D. C. Hoffman.** Positron emission from Np^{234}—1324
Price, J. (see Risser, J. R.)—1183(A)
Price, P. J. Configuration interaction and holes—1533(A)
—— **and P. B. Linhart.** Specific heat of He^3-He^4 solutions —243(A)
Price, William E. (see Rabin, Herbert)—1154(A)
Primak, W. Experimental evidence for thermal spikes in radiation damage—1854(L)
——, **C. J. Delbecq, and P. H. Yuster.** Photoelastic observations of expansion of alkali halides on irradiation—1708
——, **P. H. Yuster, and C. J. Delbecq.** Photoelastic observation of expansion of alkali halides in irradiation—237(A)
Pringsheim, P. (see Delbecq, C. J.)—237(A)
Probstein, Ronald F. and David Elliott. Transverse curvature effect in compressible axially symmetric laminar boundary layer flow—1143(A)
Proctor, W. G. and W. H. Tanttila. Saturation of nuclear electric quadrupole energy levels by ultrasonic excitation —1854(L)
Prud'homme, J. T. (see Little, R. N., Jr.)—634
Pyle, Robert V. (see Hicks, Donald A.)—1521(L)
—— (see Ise, John, Jr.)—1199(A)

Rabi, I. I. (see Perl, M. L.)—611
—— (see Senitzky, B.)—1537(A)
Rabin, Herbert and William E. Price. Co^{60} field distributions using Ag activated phosphate glass—1154(A)
Raboy, Sol and Victor E. Krohn. γ-γ correlation of Pb^{204m} —231(A)
—— **and V. E. Krohn.** Theorem on angular correlation—24
——, **T. B. Novey, and V. E. Krohn.** Attenuation of α-γ angular correlation of Am^{241} in liquid-film sources—1187 (A)
—— (see Krohn, V. E.)—1187(A)
Rainwater, James (see Baker, W. F.)—1188(A)
—— (see Williams, Ross)—1188(A)
Rainwater, L. J. (see Grimm, G.)—1161(A)
Ralph, D. C. and F. E. Dunnam. Neutron yields as function of energy in reactions $Li^7(d,n)Be^8$ and $Be^9(d,n)B^{10}$— 249(A)
—— (see Fuller, J. C.)—248(A)
Ramler, Warren (see Yuster, Philip)—233(A)
Ramsey, Norman F. Collision alignment of molecules, atoms, and nuclei—1853(L)
Rankin, W. (see Odian, A. C.)—248(A)
Rappaport, P. (see Loferski, J. J.)—1861(L)
Rasetti, F. (see Madansky, L.)—1870(E)
Rasmussen, J. O. and H. Slätis. Decay scheme of Np^{239}— 261(A)
Rasmussen, Stanley W. (see Williams, John H.)—56; 1167(A)
Rasmussen, V. K. (see Miller, D. W.)—1184(A)
Rasor, Ned S. Annealing kinetics of lattice defects in evaporated Cu films—1555(A)
Rau, R. Ronald (see Arnold, W. H.)—275(A)
Rau, Richard and P. H. Miller, Jr. Faraday effect in semiconductors at microwave frequencies—1533(A)
Ravenhall, D. G. and D. R. Yennie. Phase shift analysis of high-energy electron scattering—277(A)
—— (see Downs, B. W.)—277(A)
—— (see Heims, S. P.)—278(A)
—— (see Yennie, D. R.)—277(A)
Ravilious, C. F. (see Furlong, L. R.)—954
Rawitscher, George. Effect of extended size of nucleus on μ-meson pair photoproduction—272(A)

Rayburn, L. A., D. L. Lafferty, and T. M. Hahn. γ rays from inelastic scattering of neutrons in Al, Mg, and Ag—701
Raychaudhuri, Amalkumar. Relativistic cosmology. I—1123
Raz, B. J. (see French, J. B.)—1523(L)
Reagan, D. D. Energy dependence of photoyields of N^{17}—258(A)
—— (see Barber, W. C.)—73
—— (see George, W.)—276(A)
Redfield, Alfred G. Nuclear magnetic resonance saturation in solids—1787
—— Nuclear resonance saturation in solids—1182(A)
Redlich, Martin G. Shell theory for nuclei with mass 19—199(L)
Redman, J. K. (see Blewitt, T. H.)—1555(A)
Reed, George W. U^{235} thermal neutron fission yields at masses 90 and 91—1327
Reekie, James (see Goldstein, Louis)—857
Reich, H., J. Heberle, and P. Kusch. hfs of metastable H—1194(A)
—— (see Heberle, J.)—1194(A)
Reif, F. Nuclear magnetic resonance studies of imperfect ionic crystals—1549(T)
Reilly, C. A., H. M. McConnell, and R. G. Meisenheimer. Nuclear magnetic resonance spectra of annular samples—264(A)
Remeika, J. P. (see Holden, A. N.)—546(L)
Rennemann, Conrad, Jr. Minimum drag bodies of revolution in nonuniform supersonic flow field—1140(A)
Rense, William A. and R. Mercure. Oxygen gas continuous absorption in extreme uv—1195(A)
Repp, Gordon W., Mark J. Jakobson, and R. Stephen White. π^+ photomeson production at 180°. Experimental arrangement—268(A)
—— (see White, R. Stephen)—269(A)
Resnick, Robert (see Donahue, T. M.)—1622
Reynolds, C. A. (see Forstat, H.)—1196(A)
Reynolds, F. W. (see Collins, R. J.)—227(A)
Reynolds, George T. (see Arnold, W. H.)—275(A)
—— (see Van Lint, V. A. J.)—1203(A)
Reynolds, H. L., L. D. Wyly, and A. Zucker. Cross section for electron capture and loss by 26-Mev N ions—1825
——, **L. D. Wyly, and A. Zucker.** Equilibrium charge distribution of energetic N ions—474; 242(A)
—— (see Zucker, A.)—1150(A)
Reynolds, J. B. Energy levels in B^9 and Be^7 from reactions $C^{12}(p,\alpha)B^9$ and $B^{10}(p,\alpha)Be^7$—1289
—— (see Rubin, A.)—1185(A)
Reynolds, J. H. High-sensitivity mass spectrometer—283(A)
—— (see Lipson, J.)—283(A)
Rhein, W. J. Angular distribution of fast neutrons scattered from Pb—1300
Ribe, F. L. (see Brolley, J. E., Jr.)—1112
Rice, O. Comparison of energy excitations in liquid He^3 and He^4—847
Richards, H. T. (see Galonsky, A.)—586
Richards, Hans Kohn and Eugene D. Denman. Measurement of ionizing radiation by frequency variation using ferroelectric material—250(A)
Richardson, J. Reginald. European accelerators—266(T)
—— (see Caldwell, David O.)—28
—— (see Glass, Neel W.)—1251
—— (see Handler, Harry E.)—281(A)
Richeson, William E., Jr. (see Evans, Marjorie W.)—256(A)
Riddell, R., Jr., M. Neuman, and S. Gasiorowicz. Dynamical friction—257(A)
—— (see Gasiorowicz, S.)—257(A)
Ridgway, S. L. and George B. Collins. Evidence for γ rays from hyperons or heavy mesons produced by cosmotron protons—247(A)
Ridolfo, Virginia C. (see Cheng, L. S.)—231(A)
Rightmire, R. A. (see Simanton, J. R.)—260(A)
Rinehart, M. (see Ammiraju, P.)—1188(A)
—— (see Sargent, C. P.)—1349
Risser, J. R., J. Price, and C. M. Class. Angular distributions of resolved neutron groups from $B^{11}(d,n)C^{12}$ reaction—1183(A)
Ritchie, R. H. (see Neufeld, Jacob)—1632
Ritow, Herman. Field effect of space charge in intermittent glow in hydrogen—251(A)
Ritson, D. M., A. Pevsner, and R. L. Zimmerman. Scattering of 100-Mev γ rays from C—1168(A)
Rittner, E. S. and S. Fine. Localized photoeffect in PbS photocells—545(L)
Robbins, A. B. (see Doyle, W. T.)—1185(A)
Roberts, B. W. and C. P. Bean. Magnetic domain patterns observed by Kerr effect in BiMn alloy—225(A)
Roberts, Donald E. and Leo Mandelkern. Nature of stark rubber—1559(A)
Roberts, J. H. (see Peshkin, M.)—1204(A)
Roberts, L. D. and R. B. Murray. Magnetic and thermal properties of UI_3 at liquid He temperatures—1180(A)
—— (see Dabbs, J. W. T.)—1512(L)
—— (see Murray, R. B.)—1180(A)
Roberts, S. Interpretation of optical properties of metal surfaces—1151(A)
Roberts, Thomas R. and Stephen G. Sydoriak. Thermodynamic properties of liquid He^3. I. Specific heat and entropy—1672
Roberts, V. (see Macfarlane, G. G.)—1865(L)
Robillard, T. R. (see Goldwasser, E. L.)—1763
Robinson, Berol L. and Richard W. Fink. Electromagnetic radiations of Cs^{189}—231(A)
—— (see Fink, Richard W.)—1293
Robinson, C. S. (see Leiss, J. E.)—201(L); 1188(A)
Robinson, G. W. Emission spectra of some polyatomic molecules—1550(A)
Robinson, John E. Electronic relaxation time in graphite—227(A)
Robinson, Joseph H., III (see Besdin, D. J.)—272(A)
Robinson, W. H. and R. Smoluchowski. Small-angle scattering of x-rays by surface irregularities—1555(A)
Robson, J. W., R. L. Stearns, and E. C. Gregg. Emergent electron distribution resulting from bremsstrahlung incident on thin scatterer—233(A)
—— (see Stearns, R. L.)—232(A)
Rocklin, Sol (see Yuster, Philip)—233(A)
Rogers, J. V. (see Walsh, J. L.)—265(A)
Rogers, K. (see Sargent, C. P.)—1349
Rogers, K. C. (see Ammiraju, P.)—1188(A)
Rogosa, G. L. and W. F. Peed. U L_I x-ray transition from separated isotopes—1173(A)
Rohr, R. C. and R. D. Birkhoff. K-shell internal conversion coefficients—1266
Rohrlich, F. Infrared divergence in bound state problems—181
—— **and J. M. Jauch.** Infrared divergence—222(A)
Romer, R. H. and R. H. Dicke. Reduction of Doppler width of microwave lines—1160(A)
Roos, C. E. (see Fowler, J. M.)—996
Rose, Basil. Recent work with polarized protons at Harwell—1191(T)
Rose, David J. Magnification and resolution of field emission electron microscope—1169(A)
—— Redetermination of ionization coefficient η for H—558(A)

—— **and Sanborn C. Brown.** High-frequency gas discharge plasma in hydrogen—310
Rosen, A. (see Forster, H. H.)—1172(A)
Rosen, L. (see Frye, G. M., Jr.)—241(A)
Rosenblatt, D. B. (see McReynolds A. W.)—418
Rosenbluth, A. W. and M. N. Rosenbluth. Application of the Monte Carlo method to the theory of liquids—260(T)
Rosenbluth, M. N. (see Rosenbluth, A. W.)—260(T)
Rosenwasser, Hyman, and Paul W. Levy. Radiation induced coloring of NaN_3—1541(A)
Rosenzweig, N. (see Ferentz, M.)—222(A)
Ross, M. Theory of pion photoproduction—1156(A)
Rostoker, Norman and Hans Ekstein. Quantum theory of noise—222(A)
—— (see Brophy, J. J.)—228(A)
—— (see Ekstein, Hans)—222(A)
Roth, F. L. (see Martin, G. M.)—1559(A)
Roth, Laura M. (see Lax, Benjamin)—548(L)
Rothman, M. A. (see Swann, C. P.)—1183(A)
Rothstein, Jerome. Correlation of expansion coefficient anomaly in quenched Cu_3Au with properties of ordered Cu_3Au—1554(A)
—— Dislocation model of liquids—1157(A)
—— Order-disorder and ionic conductivity in Ag_2HgI_4—271(A)
Rott, N. Unsteady viscous flow in vicinity of stagnation point—1144(A)
Rourke, F. M. (see White, F. A.)—1174(A)
Roy, S. K. (see MacDonald, D. K. C.)—525
Ruane, T. F., B. Waldman, and W. C. Miller. Absolute cross sections for Coulomb scattering of 1.75-Mev electrons —1166(A)
Rubenstein, R. A. (see Blatt, F. J.)—1553(A)
Rubin, A., F. Ajzenberg, and J. B. Reynolds. Neutrons from proton bombardment of P^{31}—1185(A)
Rubin, Sylvan and D. C. Sachs. High-resolution magnetic spectrometer—284(A)
—— (see Tautfest, G. W.)—280(A)
Rubinow, S. I. Variational principle for scattering with tensor forces—183
—— (see Feshbach, Herman)—188
Ruderman, Malvin A. Polarization and cross section for inelastic scattering—267(A)
—— Theory of indirect nuclear-exchange interaction in metals—1183(T)
—— (see Karplus, Robert)—260(T); 771
Rudman, P. S. and B. L. Averbach. Measurements of x-ray diffuse scattering from Co-Pt disordered solid solutions and of long-range order for alloy CoPt—1554(A)
—— (see Averbach, B. L.)—1554(A)
Rudman, S. W. (see Hurley, J. P.)—1187(A)
Ruetenik, J. R. and S. Corrsin. Equilibrium turbulent flow in slightly divergent channel—1142(A)

Sachs, A. M. (see Bodansky, D.)—240(A)
Sachs, D. C. (see Rubin, Sylvan)—284(A)
Sachs, R. G. n-p mass difference and structure of nucleon—244(T)
—— (see Holladay, W. G.)—1155(A)
Sack, H. S. (see Ames, I.)—1545(A)
Sack, W. S. Decay times of luminescence and photoconductivity in AgCl—1549(T)
Sadauskis, John (see Jesse, William P.)—1150(A)
Saenz, A. W. and R. C. O'Rourke. Magnetic moment of Fermi-Dirac gas—1166(A)
Sagane, Ryokichi, Walter Dudziak, and James Vedder. Positron spectrum from the decay of the μ meson—269(A)
—— (see Dudziak, Walter)—269(A)
Saha, A. K. (see Das, T. P.)—516
Sailor, V. L., H. H. Landon, H. L. Foote, Jr., and R. E. Wood. Problems in analysis of neutron resonance data—224(A)
—— (see Landon, H. H.)—225(A); 1267
—— (see Wood, R. E.)—639
Saito, Y. (see Okaya, Y.)—1857(L)
Sakai, M. (see Kurbatov, J. D.)—674
Sakamoto, M., S. Kobayashi, and S. Ishii. Effect of O_2 gas on photoconductivity of BaO—552(L)
Salant, E. O. Heavy mesons produced in interaction of 2-3-Bev particles—1166(T)
—— (see Hill, R. D.)—247(A)
—— (see Hornbostel, J.)—218(L); 1202(A)
Salkovitz, Edward I., J. Pasternak, and A. I. Schindler. Brillouin zone studies of alloys. III. Matthiessen's rule for dilute Mg alloys—271(A)
—— **and A. I. Schindler.** Resistivity of dilute Mg alloys—543(L); 1553(A)
—— (see Schindler, A. I.)—1552(A)
Salpeter, E. E. 7.68-Mev level in C^{12} and stellar energy production—1183(A)
Sampson, M. B. (see Miller, D. W.)—1184(A)
Sanders, Richard M. (see Bina, Melvin J.)—251(A)
Sandoz, G. (see Stauss, H. E.)—271(A)
Sands, R. H. Paramagnetic resonance absorption in glass—266(A)
—— (see Pake, G. E.)—266(A)
Saphir, G. Scattering and absorption of 50-Mev π^+ mesons in Pb—269(A)
Saraf, Babulal, J. Varma, and C. E. Mandeville. Radiations from Y^{90}, Zr^{97}, Pr^{142}, and Pr^{143}—1206(A)
—— (see Hans, H. S.)—1173(A)
—— (see Mandeville, C. E.)—94; 1185(A)
Sargent, C. P., R. Cornelius, M. Rinehart, L. M. Lederman, and K. Rogers. Diffusion cloud chamber study of very slow mesons. I. Internal pair formation—1349
Satterthwaite, C. B. (see Corak, William S.)—1690
Saunders, V. I. (see West, W.)—1557(A)
Savedoff, Malcolm. Gas-dynamics effects of star formation —1158(T)
Savitt, Jacob. Method for observation of ionization profile behind explosive produced shocks in air—1158(A)
Sawatzky, A. and F. E. Jaumot, Jr. Isothermal anneal study of quenched and cold-worked Cu-Pd alloys—1555(A)
Sawyer, George A. and Louis C. Burkhardt. Search for reaction $T(d,\gamma)He^5$—1305
Schaaf, S. A. (see Laurman, J. A.)—1540(A)
Scharff-Goldhaber, Gertrude and Joseph Weneser. Higher excited states of even-even nuclei—1186(A)
—— **and J. Weneser.** The system of even-even nuclei—212(L)
Schein, Marcel (see Chou, C. N.)—162
Scherb, F. (see Day, R. B.)—279(A)
Scherrer, V. E., W. R. Faust, and B. A. Allison. Cascade γ rays from 2.5-Mev neutron bombardment of Au, I, and Cr—224(A)
—— (see Faust, W. R.)—224(A)
Schiefer, H. F. Stress-strain relationships in yarns subjected to rapid impact loading—1548(T)
Schiff, L. I. Electric monopole transitions in C^{12} and O^{16}—1281
—— Excited states of C^{12} and O^{16}—235(A)
—— Nuclear dispersion contribution to high-energy electron scattering—278(A); 756
Schiller, Ralph. New interpretation of Dirac equation—1176(A)
Schindler, Albert I. Ferromagnetic Hall effect of Ni alloys —1199(A)

—— **and E. I. Salkovitz.** Brillouin zone studies of alloys. IV. Additional Hall data of Mg alloys—1552(A)
—— (see Salkovitz, E. I.)—271(A); 543(L); 1553(A)
Schissel, Paul (see Porter, Richard F.)—242(A)
Schlier, R. E. Structure of evaporated Cu films on Ti—1555(A)
——, **H. E. Farnsworth, and T. H. George.** Low-energy electron diffraction studies of Ti crystal surface—250(A)
—— (see Burger, R. M.)—1179(A)
—— (see Farnsworth, H. E.)—250(A)
—— (see George, T. H.)—1179(A)
Schmitt, R. W. and M. D. Fiske. Low temperature resistance minimum—246(A)
Schneps, J. (see Fry, W. F.)—247(A)
Schoeni, Kurt (see Lehovec, Kurt)—229(A); 1179(A)
Schulte, H. F. (see Sicinski, H. S.)—1140(A)
Schulz, George J. and Sanborn C. Brown. Microwave study of positive ion collection by probes—559(A); 1642
Schulz-DuBois, E., M. Nisenoff, H. Y. Fan, and K. Lark-Horovitz. Spin resonance in neutron irradiated Si—1561(A)
Schwarzschild, Martin. Turbulence in stellar atmospheres—1158(T)
Schweber, S. S. (see Wightman, A. S.)—812
Schwemin, A. J. (see Paramentier, D.)—284(A)
Schwertz, F. A. and R. E. Freund. Voltage-dependence of electroluminescent brightness. II. Chemically-deposited phosphor films—1134(L)
—— **and J. J. Mazenko.** Light output from dielectric-imbedded electroluminescent phosphors—1169(A)
——, **J. J. Mazenko, and E. R. Michalik.** Voltage-dependence of electroluminescent brightness. I. Dielectric-imbedded phosphors—1133(L)
Sciama, Dennis. Formation of galaxies—1158(T)
Sclar, N. and E. Burstein. Optical and impact recombination in impurity photoconductivity in Ge and Si—1178(A); 1757
Scott, E. J. (see McGuire, T. R.)—1562(A)
Seaborg, G. T. (see Folger, R. L.)—107
—— (see Ghiorso, A.)—1518(L)
—— (see Glass, R. A.)—261(A)
—— (see Nervik, Walter E.)—261(A)
Seagrave, John D. and Richard L. Henkel. Total cross section of deuterium for neutrons from 0.2 to 22 Mev—666
Seeman, N., M. M. Shapiro, and B. Stiller. Cosmic-ray observations of $K^{\pm}$ mesons—1202(A)
Segel, R. E. and S. S. Hanna. Polarization measurement in $D(d,p)H^3$ reaction—1538(A)
Segel, S. L. and B. C. Lutz. Impurity effects on nuclear quadrupole spectrum of Cl^{35}—1183(A)
Segelken, W. G. and H. C. Torrey. Quadrupolar splitting of nuclear resonance lines in alums—1537(A)
Segrè, Emilio. Experiments on high-energy polarized protons—1191(T)
—— (see Tripp, R.)—266(A)
—— (see Ypsilantis, T.)—267(A); 840(L)
Seidel, G. M. and V. A. Johnson. Verification of Bridgman relation for mixed semiconductor—230(A)
Seidl, F. G. P. Recent mechanical improvements in Brookhaven fast chopper—1161(A)
Seitz, Frederick. Source of disordering of alloys during irradiation—1530(A)
—— (see Harrison, W. A.)—1530(A)
Seldin, E. J. Density-resistivity relationships in baked carbons—1565(A)
Sells, R. L., C. W. Harris, and E. Guth. Random walk methods in statistical mechanics of one-dimensional systems—272(A)
Selove, W. Angular distribution of pickup deuterons for 95-Mev protons on C, and implications as to internal interactions in C—208(L)
—— (see Teem, J. M.)—259(A)
Senio, P. (see Tucker, C. W., Jr.)—1541(A)
Senitzky, B., I. I. Rabi, and M. L. Perl. Quadrupole moments of Rb^{85} and Rb^{87}—1537(A)
—— (see Perl, M. L.)—611
Senitzky, I. R. Quantum effects in interaction between electrons and high-frequency fields. II—875
Sessler, A. M. and H. M. Foley. Hfs of He^{3+} and He^3—6
Shaltiel, D. (see Portis, A. M.)—264(A)
Shapiro, M. M. (see Seeman, N.)—1202(A)
Sharp, R. T. and J. David Jackson. Orthogonality of Furry-Sommerfeld-Maue wave functions and their use in perturbation theory—1128(L)
Shaw, Harlan, David Cohen, Burton J. Moyer, and Charles Waddell. Analysis of high-energy photons from cyclotron target—259(A)
Shaw, T. M. (see Windle, J. J.)—281(A)
Sheckler, A. C. and D. C. Jillson. Minority carrier lifetime as function of crystal growth variables—229(A)
—— (see Jillson, D. C.)—229(A)
Sheer, C. and J. Moore. Measurement of scattering cross sections for low-energy neutron resonances—565
Sheline, Raymond K. (see Wilkinson, Joseph R.)—1538(A)
Shen, K. Y. and S. F. Singer. Experiment for determining anisotropy of primaries—1546(A)
Sherman, Dora F. Interactions of 380-Mev α particles in Ilford G.5 emulsion—259(A)
Sherman, N., G. Culler, and S. Fernbach. Optical model analysis of scattering of 14-Mev neutrons—273(A)
—— (see Fernbach, S.)—273(A)
Sherr, R., R. W. Kavanagh, and W. R. Mills. Energy levels of Al^{26}—1185(A)
Sherrill, F. A. (see Blewitt, T. H.)—1555(A)
Shibuya, Yoshio and Seichi Tanuma. Paramagnetism observed at superconducting transition—938
Shimoda, Koichi, Tetsuji Nishikawa, and Takashi Itoh. Microwave spectrum of methylamine—1160(A)
Shirane, Gen and Ray Pepinsky. Anomalous optical properties of ferroelectric $PbTiO_3$—1201(A)
—— (see Jona, F.)—1201(A); 903
Shull, C. G. Magnetic structure of Fe—1562(T)
Shulman, C. I. Measurement of shot noise in CdS crystals—384
Shulman, R. G., J. M. Mays, and D. W. McCall. Nuclear magnetic resonance in semiconductors: Exchange broadening and line shapes—1182(A)
—— (see Mays, J. M.)—1182(A)
Shutt, R. P. High-energy interaction at Cosmotron—255(T)
—— (see Block, M. M.)—248(A)
—— (see Fowler, W. B.)—121
—— (see Morris, T. W.)—1167(A)
Sicinski, H. S. and H. F. Schulte. Mach number and yaw angle determination for conical flow regimes using two surface-flow angle indicators—1140(A)
Siegel, Armand (see Wiener, Norbert)—1190(A)
Silsbee, H. B. (see Bemski, G.)—470
Silver, E. G. (see Waniek, R. W.)—1148(A)
Silver, M., R. S. Witte, and F. McCaffrey. Rectification in thin films of PbS—270(A)
Silverman, S. (see Benedict, W. S.)—1551(A)
—— (see Herman, R.)—1550(A)
Silverstein, E. (see Jones, K. W.)—241(A)
Simanton, J. R., R. A. Rightmire, A. L. Long, and T. P. Kohman. Long-lived radioactive Al^{26}—260(A)
Simon, Albert. Ambipolar diffusion in magnetic field—317
—— (see Biedenharn, L. C.)—1153(A)

Simpson, J. Arol, H. W. Babcock, and H. D. Babcock. Association of "unipolar" magnetic region on sun with changes of primary cosmic-ray intensity—1402
—— (see Marton, L.)—1168(A)
—— (see Meyer, Peter)—247(A)
Sinclair, Rolf M. γ radiation from interaction of 44-Mev neutrons with Fe^{54} and Fe^{56}—1147(A)
Singer, S. F. New method for measuring low-energy spectrum of primary cosmic rays—1547(A)
—— Origin of charge spectrum of primaries—1163(A)
—— (see Shen, K. Y.)—1546(A)
—— (see Wentworth, R. C.)—1546(A)
Sinsheimer, R. L. Chemistry of nucleic acids—1531(T)
Sippel, R. F. (see Bent, R. D.)—1198(A); 1237
Skolnik, W. Scattering of 195-Mev pions by deuterium—240(A)
Slater, J. C. One-electron energies of atoms, molecules, and solids—1039
Slätis, H. (see Rasmussen, J. O.)—261(A)
Slichter, C. P. Nuclear resonance and study of metals—272(T)
Slichter, W. P. and J. M. Mays. Proton magnetic resonance in polyamides—1559(A)
Slifkin, Lawrence (see Kuper, A.)—1870(E)
—— (see Portnoy, William M.)—1536(A)
Smith, Alan W. Two-medium theory of thermal conductivity of artificial graphite: Experimental—1563(A)
Smith, Bernard. Role of substrate, surface-finish, film-height, and temperature in He II film transport—1196(T)
—— **and Henry A. Boorse.** He II film transport. I. Role of substrate—328
Smith, Charles G. Anchored Hg arc cathode spot—562(A)(A)
Smith, Charles S. and W. B. Daniels. Elastic constants of Fe-Si alloys—1553(A)
—— (see Bacon, Roger)—1553(A)
Smith, Frances M. (see Barkas, Walter H.)—605
—— (see Goldhaber, S.)—1203(A)
—— (see Heckman, Harry H.)—1202(A)
Smith, H. L. (see Prestwood, R. J.)—1324
Smith, J. Y. Tabulations of cosmic abundances—250(A)
Smith, Lyle W. Measurement of scattering constant in nuclear emulsion—100
——, **A. W. McReynolds, and G. A. Snow.** Elastic p-p angular distributions from 440 to 1000 Mev—1167(A)
—— (see Coor, T.)—1369
Smith, P. L. (see Davisson, J. W.)—1544(A)
—— (see Lipson, H. G.)—1535(A); 1535
Smith, R. L. (see Jaumot, F. E., Jr.)—1555(A)
Smith, R. V. Photomultiplier transit time measurements—1170(A)
Smith, R. W. Edge electroluminescence from CdS crystals at low dc fields—1169(A)
Smith, Stephen J. (see Branscomb, Lewis M.)—1028; 1127(L)
Smith, W., H. Glick, A. Hertzberg, and W. Squire. Schlieren studies of flow behind strong shocks—1141(A)
Smith, W. G. and J. M. Hollander. Neutron deficient chains of mass 187 through 191—262(A)
—— **and J. M. Hollander.** Radiochemical study of neutron-deficient chains in noble metal region—1258
Smither, R. K. and C. W. Hoover, Jr. Secondary electron resonance discharge mechanism. I—1149(A)
—— (see Hoover, C. W., Jr.)—1149(A)
Smoluchowski, R., E. Pearlstein, and H. Ingham. Radiation effects in solids produced by nuclear disintegrations—1530(A)
—— (see Coleman, C.)—1555(A)
—— (see Leivo, W. J.)—1532(A)
—— (see Pearlstein, E.)—1530(A)
—— (see Robinson, W. H.)—1555(A)
Smythe, W. R. and R. M. Worlock. π^0 photoproduction from protons and deuterium nucleons, II—269(A)
—— (see Worlock, R. M.)—269(A)
Snell, Arthur H. and Frances Pleasonton. Magnetic and electric deflection spectrometry of neutrino recoils in A^{37}—1174(A)
Snow, G. A. (see Coor, T.)—1369
—— (see Smith, Lyle W.)—1167(A)
Snyder, A. and G. del Castillo. Momentum distribution of low-energy cosmic-ray particles—1163(A)
—— (see del Castillo, G.)—1163(A)
Snyder, S. (see Fagg, L. W.)—1538(A)
Softky, Sheldon D. Millisecond γ emitter from protons on Ta—280(A); 736
—— Photodisintegration of C^{12} by 330-Mev bremsstrahlung—173
Sogo, P. B. and C. D. Jeffries. Nuclear magnetic moments of Cl^{36}, Rh^{103}, and W^{183}—1316
—— **and C. D. Jeffries.** Nuclear magnetic moments of Rh^{103} and W^{183}—265(A)
Sonder, E. Effect of low concentrations of impurity on diffusion in Ag—245(A)
—— (see Kuper, A.)—1870(E)
Sonett, C. P. and K. R. MacKenzie. Relative stopping powers for 20-Mev protons—280(A)
Sparrow, E. M. Laminar free convection from vertical surfaces for prescribed variations of (1) wall heat transfer rate, or (2) of wall temperature—1140(A)
Speck, D. R. and F. A. Jenkins. Preliminary report on the quadrupole moment of Nb—282(A)
—— (see Jenkins, F. A.)—282(A)
Spencer, L. V. Theory of electron penetration—1597
—— **and F. H. Attix.** Theory of cavity ionization—233(A)
Spencer, T. W. Reflection of acoustical pressure pulse from liquid-solid plane boundary—1540(A)
Spicer, William E. X-ray-induced luminescence from air—1061
Spinrad, B. I. Threshold values of internal conversion coefficients for K-shell—1302
Spitzer, W., C. O. Bennett, and H. Y. Fan. Pressure dependence of absorption edge in Ge and Si—228(A)
——, **R. J. Collins, and H. Y. Fan.** Infrared absorption in n-type Ge—1536(A)
Squire, W. (see Smith, W.)—1141(A)
Sreekantan, B. V. (see DeStaebler, Herbert, Jr.)—1520(L)
Stanford, G. S. and G. F. Pieper. Fast coincidence system with amplitude discrimination—1154(A)
—— (see Pieper, G. F.)—1185(A)
Stapp, Henry P. Analysis of triple scattering and correlation experiments—267(A)
Statz, H., L. Davis, Jr., and G. deMars. Nonsteady state conductance of inversion layers and structure of surface states on Ge—1566(A)
——, **L. Davis, Jr., and G. A. deMars.** Structure of surface states at Ge-Ge oxide interface—540(L)
—— (see deMars, G. A.)—539(L); 1565(A)
Stauss, H. E. and G. Sandoz. Linear magnetostriction of some ternary Co-Fe-Ni alloys—271(A)
Stearns, R. L., J. W. Robson, and E. C. Gregg. Determination of bremsstrahlung spectrum produced by 18-Mev electrons—232(A)
—— (see Robson, J. W.)—233(A)
Steele, M. C. Hall effect and magnetoresistance oscillations of Sb single crystals in magnetic fields at liquid He temperatures—1180(A)
—— **and J. Babiskin.** Oscillatory thermomagnetic properties of Bi single crystal at liquid He temperatures—359
—— (see Berlincourt, Ted G.)—227(A); 956
Steffen, R. M. (see Paul, H.)—231(A)

—— (see Zobel, W.)—1186(A)
Stegun, Irene A. and Milton Abramowitz. Generation of Coulomb wave functions by means of recurrence relations—1851
Steigert, F. E. (see Plendl, H. S.)—1538(A)
—— (see Yamamoto, S.)—1210(A)
Stein, P. C. (see Odian, A. C.)—248(A)
Stein, S. (see Gerjuoy, E.)—557(A); 1848
Steinberger, J. (see Lokanathan, S.)—240(A)
Stelson, P. H. and F. K. McGowan. Angular distribution of γ rays from Coulomb excitation—249(A)
—— (see Campbell, E. C.)—1172(A)
Stephens, Frank S., Jr., J. Hummel, F. Asaro, and I. Perlman. α groups and angular correlation of Am^{243}—261(A)
—— (see Asaro, Frank)—19; 260(A)
—— (see Hummel, J. P.)—22
—— (see Perlman, I.)—262(A)
Stephens, William E. and A. K. Mann. Energy spectrum of photoprotons from C—241(A)
——, **A. K. Mann, B. J. Patton, and E. J. Winhold.** Fine structure in the (γ,p) reaction in O—839(L)
—— (see Toms, M. Elaine)—626
Stern, Edward A. (see Neher, H. Victor)—845(L)
Stern, Frank. Valence wave functions for $3d^74s$ and $3d^8$ configurations of atomic Fe—1552(A)
Stern, M. O. (see Feiner, F.)—239(A)
Sternheimer, R. M. Angular distribution of pions from θ^0 decay—205(L)
—— Polarization of nucleons elastically scattered from nuclei—1156(A); 1871(E)
Stevens, D. K. Magnetic susceptibility of fast neutron bombarded crystalline quartz—1541(A)
—— (see Crawford, J. H.)—1532(A)
Stevenson, Donald T. Surface-recombination velocity and surface conductance of thin Ge slabs—1566(A)
Stevenson, M. Lynn (see Alvarez, Luis)—280(A)
—— (see Paramentier, D.)—284(A)
Stevenson, P. C. (see Folger, R. L.)—107
Stewart, A. T. and R. E. Green. Angular correlation of photons from positron annihilation in light metals—232(A)
—— (see Green, R. E.)—486
Stewart, Leona. Neutron spectrum and absolute yield of Pu-Be source—740
Stiehler, R. D. (see Martin, G. M.)—1559(A)
Stier, P. M., C. F. Barnett, R. A. Howard, and W. Bugg. Charge states of H ions in gases—1149(A)
—— (see Barnett, C. F.)—1537(A)
Stiller, B. (see Seeman, N.)—1202(A)
Stilwell, G. R. (see Collins, R. J.)—227(A)
St. John, Robert and J. G. Winans. Motion and spectrum of arc cathode spot in magnetic field—562(A); 1664
Stockman, F. (see Pagnia, H.)—236(A)
Stoeckmann, F., E. Klontz, H. Y. Fan, and K. Lark-Horovitz. Photoconductivity of electron-bombarded Ge—1535(A)
Stone, Gerald, Robert Carbone, and Edgar Everhart. Validity criteria for calculating differential cross section for collisions of kev ions with atoms—1150(A)
—— (see Carbone, Robert J.)—1150(A)
—— (see Everhart, Edgar)—1045
Story, J. S. (see Perring, J. K.)—1525(L)
Stratton, T. F., J. M. Blair, K. F. Famularo, and R. V. Stuart. Experimental determination of the absolute differential cross sections for $O^{16}(d,p)O^{17}$, $O^{16}(d,p)O^{17*}$ and $O^{18}(d,p)O^{19*}$ reactions—629
Strauch, Karl. Double-scattering experiment with 96-Mev protons—234(A)
—— Elastic scattering of protons—1168(T)
Stuart, R. V. (see Stratton, T. F.)—629
Stubbins, Warren Fenton. Experimental ion source for 184-inch cyclotron—274(A)
Studier, W. H. Nuclear properties of elements 98, 99, 100—227(T)
Sun, K. H., P. R. Malmberg, and P. Szydlik. Photographic amplification in α-particle autoradiography—1154(A)
Sunyar, A. W. Fast $E2$ transitions—653
—— (see Alburger, D. E.)—276(A)
—— (see Church, E. L.)—1186(A)
Sutherland, G. B. B. M. Infrared analysis of structure of proteins and nucleic acids—1534(T)
Sutton, R. B. Polarization effects on high-energy p-p reactions—266(T)
Suura, H. Radiative correction to electron scattering—278(A)
Suzuki, Kenzō (see Chikazumi, Sōshin)—1130(L)
Swami, M. S. (see Fry, W. F.)—247(A)
Swann, C. P., M. A. Rothman, W. C. Porter, and C. E. Mandeville. γ rays from proton capture in Li^7—1183(A)
Swann, W. F. G. Results of limitations on space current densities in galactic and intergalactic space—871; 1546(A)
Swanson, John A. Saturation Hall constant and magneto-resistance in semiconductors—1534(A)
Swanson, Robert E. and Robert H. McFarland. Temperature sensitivities of sensitized fluorescence spectrum of Th—1063
Swartz, C. D. Methods of fast neutron spectroscopy—1530(T)
Swartz, C. E. and J. W. DeWire. Preliminary studies with high-energy photon spectrometer—1164(A)
Swenson, C. A. P-V isotherms of 10 000 atmospheres at 4.2°K for four alkali metals and some condensed gases—244(T)
Swern, L. (see Duncan, B. J.)—1201(A)
Swiatecki, W. J. Average nuclear potentials and densities—204(L)
—— Nuclear surface energy and diffuseness of nuclear surface—203(L)
Swihart, J. C. (see Belinfante, F. J.)—222(A)
Sydoriak, Stephen G. (see Roberts, Thomas R.)—1672
Symon, Keith R. Fixed field alternating gradient accelerators—1152(A)
—— (see Jones, L. W.)—1153(A)
—— (see Kerst, D. W.)—1153(A)
—— (see Terwilliger, K. M.)—1153(A)
Szydlik, P. (see Sun, K. H.)—1154(A)

Taft, E. A. (see Dash, W. C.)—1192(A)
Tangen, R. (see Lönsjö, O.)—727
Tannenwald, P. E. and H. J. Zeiger. Multiple resonances in cobalt ferrite—1562(A)
Tanttila, W. H. (see Proctor, W. G.)—1854(L)
Tanuma, Seichi (see Shibuya, Yoshio)—938
Taub, A. H. Determination of flows behind stationary and pseudo-stationary shocks—1140(T)
Tauber, G. E. Energy levels of Pb^{206}—1204(A)
—— (see Wu, Ta-You)—222(A)
Tautfest, G. W., J. R. Havill, and Sylvan Rubin. Proton scattering from N^{14}—280(A)
Taylor, G. R. Stress-optical studies on amorphous and polycrystalline elastomers—1547(T)
—— **and S. R. Darin.** Tensile strength of elastomers—1558(A)
Taylor, J. C. Self-energy effects on meson-nucleon scattering according to Tamm-Dancoff method—201(L)
Taylor, J. E. (see Brock, E. G.)—1169(A)
Tchen, C. M. Statistical theory of shear turbulence in parallel flow—1158(A)
Teem, J. M., W. Selove, and U. E. Kruse. Interaction of 95-Mev protons with He^4—259(A)

Teitler, S., M. Lax, and E. Burstein. Absorption by free and bound holes in *p*-type Ge—1561(A)
Telegdi, V. L. (see Peshkin, M.)—1204(A)
Teller, E. (see Johnson, M. H.)—260(T); 783
Temmer, G. M. and N. P. Heydenburg. Multipolarity of γ transitions in F^{19} and Na^{23} by Coulomb excitation—1198(A)
—— **and N. P. Heydenburg.** Properties of excited states of Pd and Cd nuclei by Coulomb excitation—1308
—— (see Ambler, E.)—230(A)
—— (see Heydenburg, N. P.)—1198(A)
Tenny, F. H. (see Van Lint, V. A. J.)—1203(A)
Terwilliger, K. M., L. W. Jones, D. W. Kerst, and K. R. Symon. Application of fixed field alternating gradient principle to betatrons and cyclotrons—1153(A)
—— (see Jones, L. W.)—1153(A)
—— (see Kerst, D. W.)—1153(A)
Teutsch, W. B. and V. W. Hughes. Theory of effect of static electric field on positronium formation—1174(A)
Tewes, Howard A. Excitation functions for some proton-induced reactions of Th—25
Thaler, R. M. and J. L. McHale. *S*-matrix in terms of phenomenological collision parameters—1189(A)
—— (see McHale, J. L.)—273(A); 1189(A)
Thiess, F. B. (see Bodine, J. H.)—1532(A)
Thomas, G. E. (see Bollinger, L. M.)—223(A)
Thomas, R. G. Correction to exponential dependence of neutron transmissions—77
—— (see Lane, A. M.)—693
Thompson, R. W. (see Burwell, J. R.)—101; 247(A)
—— (see Huggett, R. W.)—248(A)
—— (see Kim, Y. B.)—248(A)
Thompson, S. G. (see Asaro, Frank)—19
—— (see Choppin, G. R.)—1519(L)
—— (see Ghiorso, A.)—1518(L)
Thomsen, John S. Statistical analog of second law of thermodynamics—1625
Thomson, Robb. Dislocation line energy and slip in NaCl and AgCl crystals—1171(A)
Thorndike, A. M. (see Block, M. M.)—248(A)
—— (see Fowler, W. B.)—121
—— (see Morris, T. W.)—1167(A)
Tisza, Laszlo (see Manning, Irwin)—1165(A)
Tobocman, W. (see Utiyama, R.)—780
Tollestrup, A. V. (see Bingham, H. H.)—1187(A)
Toman, L. (see Wolff, G.)—1179(A)
Tomboulian, D. H. (see Bedo, D. E.)—242(A)
Tomita, K. Rotational transition in solid H—1197(A)
Tomizuka, Carl T. (see Kuper, Alan B.)—244(A); 1870(E)
Tomkins, Frank S. (see Fred, Mark)—1514(L)
Toms, M. Elaine and William E. Stephens. Photoprotons from Pb^{208} and Ta—626
Torrey, H. C. (see Segelken, W. G.)—1537(A)
Trail, C. C. and C. H. Johnson. $Li^7(d,n)Be^8$ neutron spectrum and differential cross section—249(A)
Treiman, S. B. (see Arnold, W. H.)—275(A)
—— (see Van Lint, V. A. J.)—1203(A)
Triebwasser, Sol and J. Halpern. Curie constant, spontaneous polarization, and latent heat in ferroelectric—1201(A)
—— **and Frederic Holtzberg.** Ferroelectric behavior of solid solutions of $KNbO_3$ and $KTaO_3$—1201(A)
Tripp, R. Proposed method for obtaining high-energy polarized proton beam—1167(A)
——, **C. Wiegand, T. Ypsilantis, O. Chamberlain, and E. Segrè.** Experimental determination of complete scattering matrix in proton carbon collision—266(A)
—— (see Ypsilantis, T.)—267(A); 840(L)
Trischka, J. W. (see Braunstein, R.)—1092
Trolan, J. K., J. P. Barbour, E. E. Martin, and W. P. Dyke. Emission from single lattice step of clean W—262(A)
—— (see Dyke, W. P.)—263(A)
Trout, T. (see Page, L. A.)—206(L)
Truitt, Robert Wesley. Determination of transonic pressure drag on wedges by throat station method—1139(A)
Tucker, C. W., Jr., and P. Senio. X-ray scattering effects in irradiated boron carbide—1541(A)
Tucker, G. L. (see Anderson, A. G.)—283(A)
Turkevich, John (see Larach, Simon)—1015
Turnbull, D. (see DeSorbo, W.)—1554(A)
Turner, C. M. Performance characteristics of BNL research electrostatic accelerator—233(A)
Twersky, V. Scattering of electromagnetic waves by bounded lattice of parallel cylinders—257(A)
Tyler, W. W. and R. Newman. Hall mobility of optically excited carriers in Ge—961; 1192(A)
——, **R. Newman, and H. H. Woodbury.** Properties of Ge doped with Ni—461
—— (see Woodbury, H. H.)—1534(A)

Ueta, Masayasu (see Känzig, Werner)—236(A)
Ufford, C. W. (see Meshkov, S.)—1204(A)
Urbach, Franz (see Moser, Frank)—1557(A)
—— (see Nail, Nelson R.)—1557(A)
Urey, H. C. Temperature of primitive earth—236(T)
Utiyama, R. and W. Tobocman. Conservation of parity and new particles—780

Van Horn, David D. and William J. Cooley. Interpretation of dimensional changes on dezincification of α brass—245(A)
van Lieshout, R., D. H. Greenberg, and C. S. Wu. Decay of Cr^{48}—1171(A)
—— (see Farrelly, B.)—1172(A)
—— (see Koerts, L.)—1172(A)
Van Lint, V. A. J., George T. Reynolds, S. B. Treiman, and F. H. Tenny. Correlation of planes in V particle decay events—1203(A)
—— (see Arnold, W. H.)—275(A); 838(L)
Van Loef, J. J. and D. A. Lind. Inelastic scattering of neutrons by Fe, F, Mn, and I—224(A)
Van Roosbroeck, W. Theory of photomagnetoelectric effect in semiconductors—1533(A)
Van Vleck, J. H. Paramagnetism of solids—1558(T)
Varma, Jagdish (see Mandeville, C. E.)—94; 1185(A)
—— (see Saraf, B.)—1206(A)
Varney, Robert N. Diffusion of ions and electrons in electric field—558(A)
Vasileff, H. D. Thermal ionization of interstitials in cubic ZnS—237
Vedder, James (see Dudziak, Walter)—269(A)
—— (see Sagane, Ryokichi)—269(A)
Villaire, A. E. and L. F. Wouters. Fission fast counter using gas scintillation principle—280(A)
Villi, C. (see Beretta, L.)—1526(L)
Vincent, L. D. (see Little, R. N., Jr.)—634
von Herrmann, P. (see Pieper, G. F.)—1185(A)

Wada, Walter (see Kroll, Norman M.)—1355
Waddell, Charles (see Shaw, Harlan)—259(A)
Wagner, F., Jr. (see Porter, F. T.)—214(L)
Wagner, P. E. Contact charging between monocrystalline nonconductors and metals—264(A)
Wagoner, G. (see Dresselhaus, G.)—556(L)
Wainfan, N., W. C. Walker, and G. L. Weissler. Photoionization cross sections of CO_2, A, H_2, and H_2O—561(A)
—— (see Walker, W. C.)—562(A)

Waldman, B. (see Ruane, T. F.)—1166(A)
Walker, R. M., R. S. Preston, E. C. Fowler, and H. L. Kraybill. Production of neutral V events in Pb by neutrons from cosmotron—1203(A)
—— (see Anderson, A. G.)—283(A)
Walker, W. C., N. Wainfan, and G. L. Weissler. Photoelectric yields of metals in vacuum ultraviolet—562(A)
—— (see Wainfan, N.)—561(A)
Walker, W. D. $\Lambda^0 - \theta^0$ production in $\pi^- - p$ collisions at 1 Bev—1407
—— **and J. Crussard.** Interactions of 1.5-Bev π^- mesons—240(A)
—— **and J. Crussard.** π^--nucleon collisions at 1.5 Bev—1416
Wall, F. T. Statistical calculation of dimensions of coiling type macromolecules—1547(T)
Wallace, J. (see Page, L. A.)—206(L)
Wallace, P. R. Modification of one-particle model for nuclear radiative transitions—1205(A)
Wallis, R. F. (see Herman, Robert)—1171(A); 1550(A)
Walsh, Edward N. (see Ziomek, Joseph S.)—243(A)
Walsh, J. L., A. G. Berger, J. V. Rogers, and W. D. Knight. Direct measurement of nuclear spin-lattice relaxation time—265(A)
Walt, M. and J. R. Beyster. Interaction of 4.1-Mev neutrons with nuclei—279(A); 677
Wandel, C. F. (see Lane, A. M.)—1524(L)
Wang, Ming Chen and Eugene Guth. Two-dimensional Coulomb scattering in quantum mechanics—274(A)
Wangsness, Roald K. Magnetic resonance for arbitrary field strengths—927
—— Magnetic resonance in ferrimagnetic containing an arbitrary number of sublattices—1200(A)
Waniek, R. W., R. Fox, L. Garrido, and E. G. Silver. Interaction of high-energy neutrons with Mo—1148(A)
—— (see Culler, Vaughn)—1148(A)
—— (see Fox, Raymond)—1153(A)
Warren, Roger. Electric field measurements in glow discharge using refined electron beam technique—263(A)
—— Field measurements in glow discharges with refined electron beam probe and automatic recording—1650
—— Interpretation of field measurements in cathode region of glow discharges—1658
Warschauer, D. M., W. Paul, and H. Brooks. Effect of pressure on optical absorption edge in Si and Ge—1193(A)
Wasserburg, G. J. and R. J. Hayden. Branching ratio of K^{40} and age of meteorites—250(A)
Watson, J. D. Nucleic acid structure as revealed by x-ray diffraction—1531(T)
Watson, K. M. Partial-wave analysis of experimental photomeson cross sections and its interpretation—234(T)
Watson, W. W. (see Corbett, J. W.)—1165(A)
Wattenberg, A. (see Guernsey, Janet B.)—1147(A)
—— (see Odian, A. C.)—248(A)
Wayland, Harold. Quantitative fluid flow visualization with streaming birefringence—255(A)
Waymouth, J. F. and F. Bitter. Analysis of plasma of fluorescent lamps. II—1148(A)
—— (see Bitter, F.)—1148(A)
Weatherly, T. L. (see Williams, Quitman)—1159(A)
Webb, F. (see Goldhaber, Gerson)—267(A)
Webb, J. H. Ultra-short light-and-voltage pulses applied to Ag-halide crystals by turbine-driven mirror and electrical contacts—1558(A)
Webb, L. A. and R. F. Johnson. Effect of temperature upon scintillation efficiency of NaI(Tl)—234(A)
Webeler, R. (see Allen, G.)—1168(A)
Weber, J. Remarks on fluctuation dissipation theorem—1165(A)
Wechsler, Monroe S. Effect of quench on structure of Au—245(A)
Wedaa, Henry W. (see Bennett, Arthur L.)—256(A)
Weddell, J. (see Jennings, B.)—582
Weertman, J. Theory of steady-state creep based on dislocation climb—246(A)
Weinstein, R., M. Deutsch, and S. Brown. Fine structure of positronium—223(A)
Weinstock, Bernard. Nuclear alignment in liquid He^3—227(T)
—— (see Abraham, Bernard M.)—551(L)
Weiss, J. and W. Bernstein. Energy required to produce one ion pair for several gases—1828
Weiss, M. T. and P. W. Anderson. Ferromagnetic resonance in Ferroxdure—925
Weiss, R. J. (see Antal, J. J.)—1541(A)
Weissberg, H. L. and A. S. Berman. Velocity and pressure distributions in turbulent pipe flow with uniform wall suction—1540(A)
Weissler, G. L. (see Ehler, A. W.)—561(A)
—— (see Wainfan, N.)—561(A)
—— (see Walker, W. C.)—562(A)
Welber, Benjamin. Effect of superconducting transition on internal friction of Sn—1196(A)
Welton, T. A. Possible convergence of mass renormalization—1175(A)
Weneser, Joseph (see Scharff-Goldhaber, Gertrude)—212(L); 1186(A)
Wentworth, R. C. and S. F. Singer. Albedo contribution in measurement of cosmic-ray primaries—1546(A)
Werntz, J. H., Jr. (see Fleming, P. J.)—1196(A)
Wert, C. Internal friction in some Fe-Al alloys—246(A)
—— (see Kerr, J.)—225(A)
Wertheim, M. S. and G. Igo. Isotope shift in x-ray spectra of heavy elements—1
West, W. and V. I. Saunders. Photographic effects in single crystals of AgBr—1557(A)
Westrum, Edgar F., Jr., and John J. McBride. Temperature dependence of heat capacity of molybdenite—270(A)
Wetherill, G. W., L. T. Aldrich, and G. L. Davis. Potassium-argon ages of lepidolites—250(A)
Wexler, Aaron (see Corak, William S.)—1690
Wheeler, R. G. (see Lane, C. T.)—1196(A)
White, F. A., T. L. Collins, and F. M. Rourke. Mass spectrometric search for naturally occurring isotopes of low abundance—1174(A)
White, Harrison C. Quantum-mechanical calculation of interatomic force constants in Cu—1552(A)
White, L. D. g factor of electron in $2S$ state of H—1194(A)
White, R. Stephen, Mark J. Jakobson, and Gordon W. Repp. π^+ photomeson production at 180°. Experimental results—269(A)
—— (see Repp, Gordon W.)—268(A)
Whittemore, W. L. (see Block, M. M.)—248(A)
—— (see Fowler, W. B.)—121
—— (see Morris, T. W.)—1167(A)
Widgoff, M. (see Hill, R. D.)—247(A)
Wiegand, C. (see Tripp, R.)—266(A)
—— (see Ypsilantis, T.)—267(A); 840(L)
Wiener, Norbert. Hopf-Wiener equation system and matrix factorization—255(T)
—— **and Armand Siegel.** Joint probabilities and transition probabilities in differential-space quantum theory—1190(A)
Wightman, A. S. and S. S. Schweber. Configuration space methods in relativistic quantum field theory. I—812
—— (see Michel, L.)—1190(A)
Wigner, Eugene P. Development of compound-nucleus model—1177(T)
—— Lower limit for energy derivative of scattering phase shift—145
—— (see Lane, A. M.)—693

Wilcox, L. and J. E. Drummond. Plasma oscillations in static magnetic field—263(A)
—— (see Drummond, J. E.)—558(A)
Wildhack, W. A. Instrumentation research at National Bureau of Standards—282(T)
Wilkinson, D. H. Giant resonances of nuclear photodisintegration—1164(T)
—— **and A. M. Lane.** Importance of parentage of nuclear states for nuclear reaction phenomena—235(A)
Wilkinson, Joseph R. and Raymond K. Sheline. Nuclear levels in V^{48} as determined by decay of Cr^{48}—1538(A)
Wilks, J. (see Fairbank, Henry A.)—1196(A)
Willard, Harvey B., Joe K. Bair, and Joe D. Kington. Elastic scattering angular distributions of fast neutrons on light nuclei—669
——, **J. D. Kington, and J. K. Bair.** $C^{13}(p,\gamma)N^{14}$ reaction —1184(A)
Willardson, R. K., T. C. Harman, P. F. Choquard, and A. C. Beer. Usually large magnetoresistive effects in InSb for specialized boundary conditions—227(A)
—— (see Harman, T. C.)—1532(A)
Willett, D. K. (see Hanscome, T. D.)—232(A)
—— (see Holmgren, H. D.)—241(A)
Williams, Albert C. and Raymond J. Emrich. Mass flow in shock tube—1158(A)
Williams, Dudley (see Brown, L. Carlton)—1537(A)
Williams, Ferd E. Theoretical basis for light-amplifying phosphors—547(L)
—— (see Piper, W. W.)—1809
Williams, John H. and Stanley W. Rasmussen. Elastic scattering of 9.76-Mev protons by He—56
—— **and Stanley W. Rasmussen.** Scattering of 9.76-Mev protons by He^4—1167(A)
Williams, Malcolm L., Robert F. Landel, and John D. Ferry. Temperature dependence of relaxation mechanisms in amorphous polymers and other glass-forming liquids—1549(A)
Williams, Quitman and T. L. Weatherly. Microwave spectrum of NOBr—1159(A)
Williams, Robert W. High-energy cross sections. I. Size of nucleus—1387
—— High-energy cross sections. II. Nucleon-nucleon cross section at cosmic-ray energies—1393
Williams, Ross, Winslow Baker, Aihud Pevsner, and James Rainwater. Elastic scattering of π mesons from nuclei. I—1188(A)
—— (see Baker, W. F.)—1188(A)
Willis, W. J. (see Kaiser, H. F.)—1538(A)
Wilson, Allan N. μ meson ionization in argon at energies 10 to 100 Bev—268(A)
Winans, J. G. (see St. John, Robert M.)—562(A); 1664
Winckler, J. R., E. N. Mitchell, K. A. Anderson, and L. Peterson. Measurement of Čerenkov radiation from positive and negative π-mesons—1411
Windle, J. J. and T. M. Shaw. Microwave dielectric measurements on single fibers—281(A)
Winhold, E. J. (see Stephens, W. E.)—839(L)
Winsor, L. P. and T. H. Lee. Properties of dc arc in magnetic field—562(A)
Winston, H. (see Firle, T. E.)—1567(A)
Wiser, H. L. and A. D. Krumbein. Mechanism of termination of Geiger plateau region—303
Witmer, Enos E. Apparent importance of $(7/2)^6$ in representation of nuclear masses as multiples of electron mass —1174(A)
Witte, R. S. (see Silver, M.)—270(A)
Wolfenstein, L. Polarization effects in reaction $p+p\rightarrow\pi^+ + d$—766
—— Possible triple-scattering experiments—1870(E)
Wolff, G., L. Toman, and J. Clark. Relationship among hardness, energy gap, and melting point of diamond-type and related structures—1179(A)
Wolfgang, R. L. and G. Friedlander. Excitation function of $C^{12}(p,pn)C^{11}$ reaction in Bev region—1871(E)
—— (see Baker, E.)—242(A)
Wolfson, J. L. (see Graham, R. L.)—1173(A)
Wolicki, E. A. (see Fagg, L. W.)—1538(A)
Wolicki, E. J. (see Geer, E. H.)—241(A)
Wolke, R. L. Angular distribution of fragments from 450-Mev proton fission of Bi—1199(A)
Wood, G. T. and P. S. Jastram. Polarization correlation in decay of Co^{60}—1187(A)
Wood, R. E., H. H. Landon, and V. L. Sailor. Parameters for neutron resonance in Au—639
—— (see Sailor, V. L.)—224(A)
Wood, R. M. (see Ames, I.)—1545(A)
Woodbury, H. H. and W. W. Tyler. Properties of Ge doped with Mn—1534(A)
—— (see Tyler, W. W.)—461
Woodcock, R. F. and H. E. Farnsworth. Effects of heat treatment and ion-bombardment cleaning on catalytic activity of pure Ni surface—1152(A)
Woodruff, Truman O. Solution of Hartree-Fock-Slater equations for Si crystal by method of orthogonalized plane waves—1741
Woodyard, J. R. Charge-exchange accelerator—284(A)
Worlock, R. M. and W. R. Smythe. π^0 photoproduction from protons and deuterium nucleons, I—269(A)
—— (see Smythe, W. R.)—269(A)
Wouters, L. F. (see Villaire, A. E.)—280(A)
Wright, Ray H. Physical concepts relating to transonic wind tunnels—1139(T)
Wu, C. S. (see Farrelly, B.)—1172(A)
—— (see Hughes, V. W.)—1840
—— (see Koerts, L.)—1172(A); 1230
—— (see Lidofsky, L.)—1186(A)
—— (see Lindqvist, Torsten)—231(A)
—— (see Marder, S.)—1173(A)
—— (see van Lieshout, R.)—1171(A)
Wu, Ta-you and G. E. Tauber. Relativistic energy of two-electron atoms—222(A)
Wyly, L. D. (see Reynolds, H. L.)—242(A); 474; 1825
—— (see Zucker, A.)—1150(A)

Yafet, Y. Spin-orbit effects in conduction electron-spin resonance—1542(T)
Yager, W. A. (see Fletcher, R. C.)—1560(A)
Yagoda, Herman. Mesonic decay of ejected nuclear fragment—153
—— Pion-pair production in nuclear emulsion—103; 1187(A)
Yamaguchi, Yoshio and Yoriko Yamaguchi. Photodisintegration of deuteron—69
Yamaguchi, Yoriko (see Yamaguchi, Yoshio)—69
Yamamoto, S. and F. E. Steigert. Background tracks in nuclear emulsions—1210(A)
Yang, C. N. (see Lee, T. D.)—1501
Yennie, D. R., D. G. Ravenhall, and B. W. Downs. Modified Born approximation for electron scattering calculations—277(A)
—— (see Downs, B. W.)—277(A)
—— (see Heims, S. P.)—278(A)
—— (see Ravenhall, D. G.)—277(A)
Yergin, Paul F. and Robert Nathans. (γ,n) cross sections in Mg^{24} and Mg^{25}—1198(A)
—— (see Nathans, Robert)—1197(A); 1296
Yevick, George J. and Jerome K. Percus. Comments on Feynman's atomic theory of liquid He—1164(A)
—— (see Percus, Jerome K.)—1164(A)

Yilmaz, Huseyin. Wave functions and transition probabilities for light atoms—1190(A)
Yntema, G. B. Superconducting winding for electromagnet —1197(A)
Yodh, Gaurang B. Charged pion production in *n-p* collisions —268(A)
—— Production of charged pions in *n-p* collisions—1330
—— (see Panofsky, W. K. H.)—751
Young, D. R. (see Drougard, M. E.)—1010; 1563(A)
—— (see Huibregtse, E. J.)—1562(A)
Youngblood, J. F. Low-temperature dielectric measurements —1201(A)
Youtz, L. (see Kerth, Leroy)—259(A)
Ypsilantis, T., C. Wiegand, R. Tripp, E. Segrè, and O. Chamberlain. Depolarization in scattering of polarized protons by H at 310 Mev—267(A)
——, **C. Wiegand, R. Tripp, E. Segrè, and O. Chamberlain.** Rotation of polarization vector and depolarization in *p-p* scattering—840(L)
—— (see Tripp, R.)—266(A)
Yuster, Philip H., Sol Rocklin, Warren Ramler, and Charles Delbecq. Crystal technique for measuring cyclotron beam energies—233(A)
—— (see Delbecq, C. J.)—237(A)
—— (see Primak, W.)—237(A); 1708

Zaffarano, Dan J. (see Cooper, Raymond D.)—1199(A)
Zeiger, H. J. Boltzmann theory of cyclotron resonance for warped spherical energy surfaces—1560(A)
—— (see Tannenwald, P. E.)—1562(A)
Zener, Clarence. Classical theory of temperature dependence of magnetic crystalline energy—225(A)
Zernike, F. Problems of diffraction of light with demonstrations by Video—272(T)
Zernow, L. and G. Hauver. Cine-microscopy of sparks exploding wires, and fracture at framing rates $> 10^6$/second —1551(A)
Zimmerman, E. J. Response of anthracene to low-energy protons and He ions—1153(A)
Zimmerman, R. L. and H. Palevsky. Inelastic scattering of cold neutrons by Al—1162(A)
—— (see Ritson, D. M.)—1168(A)
Ziomek, Joseph S., Edward A. Piotrowski, and Edward N. Walsh. Normal coordinate treatments and calculated thermodynamic properties of $POCl_3$, POF_3, $PSCl_3$, and PSF_3—243(A)
Zobel, W. and R. M. Steffen. Magnetic moment of 0.247-Mev excited state of Cd^{111}—1186(A)
Zucker, A., H. L. Reynolds, and L. D. Wyly. Cross sections for electron capture and loss by 26-Mev N ions—1150(A)
—— (see Reynolds, H. L.)—242(A); 474; 1825
Zweifel, P. F. Capture-positron branching ratios—1870(E)
—— Nuclear orbital assignments for Ta^{180}—1174(A)
Zwerdling, Solomon and Ralph S. Halford. Direct production of spectroscopic specimens from single crystals by controlled growth from vapor; infrared absorption anisotropy and induced molecular motion in single crystal of benzene—243(A)

PHYSICAL REVIEW VOLUME 98, NUMBER 6 JUNE 15, 1955

Analytic Subject Index to Volume 98

References with (A) are to abstracts of papers presented at meetings of the American Physical Society; references with (L) are to Letters to the Editor; references with (E) are to Errata. Items are listed under the following categories:

Acoustics
Astrophysics
Atomic and Molecular Beams
Atomic Mass and Abundance
Atomic Structure and Spectra
Biophysics
Chemical Effects and Properties
Constants, Standards, Units
Cosmic Radiation
Crystalline State
Dielectrics and Dielectric Properties
Diffraction
Diffusion
Elasticity and Plasticity
Electrical Conductivity and Resistance
Electrical Discharges
Electrical Properties
Electromagnetic Theory and Electrodynamics
Electrons and Positrons
Elementary Particle Interactions
Errata
Field Theory
Films, Properties
Fluid Dynamics
Gamma Rays
Gases
Geophysics
Helium, Liquid
Imperfections in Solids
Ionization
Ions
Ions and Electrons, Mobility
Liquids
Luminescence
Magnetic Properties
Magnetic Resonance
Mathematical Methods
Mechanics
Mesons and Hyperons
Methods and Instruments
Microwaves
Miscellaneous
Molecular Aggregates
Molecular Structure and Spectra
Neutrino
Noise
Nuclear Fission
Nuclear Moments and Spin
Nuclear Protoeffects
Nuclear Reactions, General
Nuclear Reactions Induced by α Particles and He^3
Nuclear Reactions Induced by Deuterons and Tritons
Nuclear Reactions Induced by Mesons
Nuclear Reactions Induced by Neutrons
Nuclear Reactions Induced by Protons
Nuclear Spectra
Nuclear Structure Theory
Optical Properties
Proceedings of the American Physical Society
Quantum Electrodynamics
Quantum Mechanics
Radiation
Radioactivity
Range and Energy Loss of Particles
Relativity and Gravitation
Scattering, General
Scattering of α Particles
Scattering of Deuterons
Scattering of Electrons and Positrons
Scattering of Mesons
Scattering of Neutrons
Scattering of Protons
Semiconductors
Spectra, General
Statistical Mechanics and Thermodynamics
Superconductivity
Thermal Properties
X-Rays

Absorption of Radiation (see **Radiation**)
Acoustics
Absorption of 10-Mc/sec sound in polycrystalline Mg rod between 1.5 and 4.2°K, L. Mackinnon—1210(A)
Absorption of 10-Mc/sec sound pulses by superconducting polycrystalline Sn rod, L. Mackinnon—1181(A)
Electron transfer mechanism for ultrasonic attenuation in metals, C. Kittel—1181(A)
Growth, coalescence, and decay of vortices in jet accompanying Pfeifentone, A. B. C. Anderson—256(A)
Reflection of acoustical pressure pulse from liquid-solid plane boundary, T. W. Spencer—1540(A)
Saturation of nuclear electric quadrupole energy levels by ultrasonic excitation, W. G. Proctor and W. H. Tanttila —1854(L)
Temperature variation of elastic constants of cubic elements. I. Cu, W. C. Overton, Jr., and John Gaffney—969
Adsorption (see **Gases**)
Aerodynamics (see **Fluid Dynamics**)
Afterflow (see **Electrical Discharges**)
Alloys (see **Crystalline State**)
Annihilation (see **Electrons and Positrons**)
Antiferroelectric Phenomena (see **Dielectrics and Dielectric Properties**)
Antiferromagnetism (see **Magnetic Properties**)
Arcs (see **Electrical Discharges**)
Astrophysics
Association of "unipolar" magnetic region on sun with changes of primary cosmic-ray intensity, J. A. Simpson, H. W. Babcock, and H. D. Babcock—1402
Branching ratio of K^{40} and age of meteorites, G. J. Wasserburg and R. J. Hayden—250(A)
Diffusion of cosmic rays in earth-sun region, P. Morrison —1163(A)
Freundlich red-shift formula, M. A. Melvin—884
Modified Holtzmark distribution, S. Gasiorowicz—257(A)
Results of limitations on space current densities in galactic and intergalactic space, W. F. G. Swann—871; 1546(A)
Self-focusing streams, Willard H. Bennett—1584
7.68-Mev level in C^{12} and stellar energy production, E. E. Salpeter—1183(A)
Tabulations of cosmic abundances, J. Y. Smith—250(A)
Atmosphere (see **Geophysics**)
Atomic and Molecular Beams
Collision alignment of molecules, atoms, and nuclei, Norman F. Ramsey—1853(L)
Electron loss cross sections of moving He atoms, Sol Krasner and J. Cuevas—1149(A)
g factor of electron in $2S$ state of H, L. D. White—1194(A)
Hfs of metastable H, H. Reich, J. Heberle, and P. Kusch —1194(A)
Molecular constants and nuclear-molecular interactions of Li^7F^{19} by molecular beam electric resonance method, R. Braunstein and J. W. Trischka—1092
New method for investigating hfs of metastable state, J. Heberle, H. Reich, and P. Kusch—1194(A)
Nuclear electric quadrupole moment of Na^{23} by atomic beam resonance method, M. L. Perl, I. I. Rabi, and B. Senitzky—611
Nuclear spin and hfs interaction in 3.1-hr Cs^{134m}, D. A. Gilbert and Victor W. Cohen—1194(A)
Rb^{85} and Rb^{87} quadrupole moments, B. Senitzky, I. I. Rabi, and M. L. Perl—1537(A)
Atomic Mass and Abundance
Apparent importance of $(7/2)^6$ in representation of nuclear masses as multiples of electron mass, Enos E. Witmer —1174(A)
Cl^{36} magnetic moment and mass, L. C. Aamodt and P. C. Fletcher—1317
High-sensitivity mass spectrometer, J. H. Reynolds—283(A)
Isotope abundance ratios by nuclear magnetic resonance, B. E. Holder and M. P. Klein—265(A)
Mass spectrometric search for naturally occurring isotopes of low abundance, F. A. White, T. L. Collins, and F. M. Rourke—1174(A)
Microwave spectrum of CS, Richard C. Mockler and George R. Bird—1837
Occurrence of Tc^{98} in nature, Edward A. Alperovitch and J. Malcolm Miller—262(A)
Performance data for high-sensitivity mass spectrometer, J. Lipson and J. H. Reynolds—283(A)
Pure rotational spectra of Tl halides, M. Mandel and A. H. Barrett—1159(A)
Spin, quadrupole moment, and mass of Se^{75}, L. C. Aamodt and P. C. Fletcher—1224
Tabulations of cosmic abundances, J. Y. Smith—250(A)
Atomic Structure and Spectra
Ac^{227} nuclear moments, Mark Fred, Frank S. Tomkins, and William F. Meggers—1514(L)
Computed transition probabilities for x-ray continua of K, Margaret N. Lewis, Louis C. Green, Marjorie M. Mulder, Paul C. Milner, and Eleanor K. Kolchin—1020; 1210(A)
Diffusion and volume loss coefficients of He metastable atoms and molecules, A. V. Phelps—558(A)
Effect of static electric field on positronium formation, S. Marder, W. Bennett, C. S. Wu, and V. W. Hughes —1173(A)
Effects of electron collisions on width of spectral lines, Henry Margenau and Bennett Kivel—1822
Electron affinity of atomic O, Lewis M. Branscomb and Stephen J. Smith—1127(L)
Electron broadening and shift of spectral lines of He, Bennett Kivel—1055
Electron effects in spectral line broadening, Henry Margenau—1195(A)
Electron impact broadening of spectral lines, B. Kivel, S. Bloom, and H. Margenau—495
Electron impact broadening of spectral lines of He, Bennett Kivel—1195(A)
Energies of ground states of He, Li^+, and O^{6+}, S. Chandrasekhar and G. Herzberg—1050
Energy levels of π-mesonic atoms, K. A. Brueckner—769
Fine structure of positronium, R. Weinstein, M. Deutsch, and S. Brown—223(A)
Fourth-order radiative corrections to atomic energy levels. II, Robert L. Mills and Norman M. Kroll—1489
g factor of electron in $2S$ state of H, L. D. White—1194(A)
Helium wave equation, James H. Bartlett—1067
Hfs of He^{3+} and He^3, A. M. Sessler and H. M. Foley—6
Hfs of metastable hydrogen, H. Reich, J. Heberle, and P. Kusch—1194(A)
Isotope shift in x-ray spectra of heavy elements, M. S. Wertheim and G. Igo—1
Lamb shift of $1S$ level of deuterium, G. Herzberg—223(A)
Line broadening by electrons: Validity of simple theories, Roland E. Meyerott and Henry Margenau—1195(A)
Nb quadrupole moment, D. R. Speck and F. A. Jenkins —282(A)
New method for investigating hfs of metastable state, J. Heberle, H. Reich, and P. Kusch—1194(A)
Nuclear moments of Nb^{93}, La^{139}, Os^{187}, and Hg^{201}, Kiyoshi Murakawa—1285
One-electron energies of atoms, molecules, and solids, J. C. Slater—1039
Relativistic energy of two-electron atoms, Ta-You Wu and G. E. Tauber—222(A)

Static magnetic field quenching of orthopositronium decay: Angular distribution effect, V. W. Hughes, S. Marder, and C. S. Wu—1840
Temperature sensitivities of sensitized fluorescence spectrum of Th, Robert E. Swanson and Robert H. McFarland—1063
Theory of effect of static electric field on positronium formation, W. B. Teutsch and V. W. Hughes—1174(A)
Triplet fine structure of He, T. H. Maiman and W. E. Lamb, Jr.—1194(A)
U L_1 x-ray transition from separated isotopes, G. L. Rogosa and W. F. Peed—1173(A)
Valence wave functions for $3d^7 4s$ and $3d^8$ configurations of atomic Fe, Frank Stern—1552(A)
Wave functions and transition probabilities for light atoms, Huseyin Yilmaz—1190(A)

Auger Effect (see **Atomic Structure and Spectra; X-Rays**)
Aurora (see **Astrophysics; Geophysics**)

Barkhausen Effect (see **Magnetic Properties**)
Biophysics
Monte Carlo methods in study of cell growth, Joseph G. Hoffman, N. Metropolis, and V. Gardiner—1195(A)
Boson Theory (see **Field Theory**)
Bremsstrahlung (see **Radiation**)
Broadening of Spectral Lines (see **Atomic Structure and Spectra; Molecular Structure and Spectra; Spectra, General**)

Capture Cross Sections (see **Electrons and Positrons; Nuclear Reactions; Radiation**)
Čerenkov Effect (see **Radiation**)
Chemical Effects and Properties
Effects of heat treatment and ion-bombardment cleaning on catalytic activity of pure Ni surface, R. F. Woodcock and H. E. Farnsworth—1152(A)
Mechanism of photochemical reactions catalyzed by red-mercuric sulfide, L. L. Grossweiner and S. Gordon—243(A)
New method of microelectrophoresis, Alexander Kolin—1195(A)
Oxidation of clean surfaces of Ge below 25°C, Mino Green and J. A. Kafalas—1566(A)
Theory of Ag-halide photolysis, Charles A. Duboc—1557(A)
Chemical Reactions (see **Chemical Effects and Properties**)
Chemiluminescence (see **Luminescence**)
Cold Emission (see **Electrical Properties**)
Colloids (see **Chemical Effects and Properties; Molecular Aggregates**)
Compton Effect (see **Radiation**)
Conductivity, Electrical (see **Electrical Conductivity and Resistance**)
Conductivity, Thermal (see **Thermal Properties**)
Constants, Standards, Units
Apparent importance of $(7/2)^6$ in representation of nuclear masses as multiples of electron mass, Enos E. Witmer—1174(A)
Simple, empirical mass spectrum of fundamental particles, Leo Banet—1176(A)
Straumanis' concepts regarding Avogadro's number, E. Richard Cohen and J. W. M. DuMond—1128(L)
Cosmic Radiation (see also **Mesons and Hyperons**)
Albedo contribution in measurement of cosmic-ray primaries, R. C. Wentworth and S. F. Singer—1546(A)
Association of "unipolar" magnetic region on sun with changes of primary cosmic-ray intensity, J. A. Simpson, H. W. Babcock, and H. D. Babcock—1402
Čerenkov counter flux measurement of cosmic-ray alphas at 41°, Nahmin Horwitz—165
Changes in amplitude of cosmic-ray 27-day intensity variation with solar activity, Peter Meyer and J. A. Simpson—247(A)
Cosmic-ray observations of K^* mesons, N. Seeman, M. M. Shapiro, and B. Stiller—1202(A)
Diffusion of cosmic rays in earth-sun region, P. Morrison—1163(A)
Experiment for determining anisotropy of primaries, K. Y. Shen and S. F. Singer—1546(A)
Identity of shower particles in stars in region $1\text{–}2\times$ minimum ionization, E. Pickup and A. Husain—247(A)
"Knee" of cosmic-ray latitude curve, Victor H. Neher and Edward A. Stern—845(L)
Latitude effect of cosmic radiation at low altitudes, Martin A. Pomerantz—105
Mass spectrum of shower particles from cosmic-ray interactions, A. Husain and E. Pickup—136
Momentum distribution of low-energy cosmic-ray particles, A. Snyder and G. del Castillo—1163(A)
New method for measuring low-energy spectrum of primary cosmic rays, S. F. Singer—1547(A)
Nuclear interaction of sea-level, cosmic-ray particles with C and Pb, G. del Castillo, A. Snyder, L. Grodzins, and W. Y. Chang—1163(A)
Nuclear interactions of cosmic rays in Al, W. W. Brown—275(A)
Origin of charge spectrum of primaries, S. F. Singer—1163(A)
Preliminary studies with high-energy photon spectrometer, C. E. Swartz and J. W. DeWire—1164(A)
Problem in shower theory—"Approximation A," R. C. O'Rourke—1190(A)
Recurrence phenomenon in 24-hour variation of cosmic-ray intensity, R. P. Kane—130
Results of limitations on space current densities in galactic and intergalactic space, W. F. G. Swann—871; 1546(A)
Scintillation counter study of energy spectra of cosmic-ray photons and electrons at 11 200 feet, C. N. Chou and Marcel Schein—162
Solar flare and magnetic storm effects in cosmic-ray intensity near geomagnetic N pole, John W. Graham and Scott E. Forbush—1348
Velocity spectrum of cosmic-ray particles at twelve-grams atmospheric depth, E. N. Mitchell—1163(A)
World-wide variations in cosmic-ray intensity 1937–1952, Scott E. Forbush—1163(A)
Cosmology (see **Astrophysics; Relativity and Gravitation**)
Critical Potentials (see **Atomic Structure and Spectra; Molecular Structure and Spectra**)
Cross Section (see **Electrons and Positrons; Nuclear Reactions; Radiation; Scattering**)
Crystal Counters (see **Methods and Instruments**)
Crystalline State (see also **Electrical Properties; Imperfections in Solids; Magnetic Properties; Semiconductors; etc.**)
Absorption of 10-Mc/sec sound in polycrystalline Mg rod between 1.5 and 4.2°K, L. Mackinnon—1210(A)
Absorption of 10-Mc/sec sound pulses by superconducting polycrystalline Sn rod, L. Mackinnon—1181(A)
Adsorption of O_2 and N_2 by Ti, T. H. George, H. E. Farnsworth, and R. E. Schlier—1179(A)
Anisotropic electronic stress and Mg alloys, Paul M. Marcus—1552(A)
Annealing kinetics of lattice defects in evaporated Cu films, Ned S. Rasor—1555(A)
Anomalous behavior of Cu_3Au quenched from above 600°C, R. Feder and A. S. Nowick—1152(A)
Atomic heat of graphite between 1° and 20°K, N. Pearlman and P. H. Keesom—1539(A)

Crystalline State (Continued)
Auxiliary conditions in Bohm-Pines theory of electron gas, E. N. Adams—1130(L)
Average crystal potential, Joseph L. Birman—1567(L)
Axial ratios in hexagonal crystals, J. W. McClure—449
Brillouin zone studies of alloys. III. Matthiessen's rule for dilute Mg alloys, E. I. Salkovitz, J. Pasternak, and A. I. Schindler—271(A); IV. Additional Hall data of Mg alloys, A. I. Schindler and E. I. Salkovitz—1552(A)
Calculation of compressibility of polyethylene from energy of interaction between ($-CH_2-$) groups, Werner Brandt —243(A)
Calculation of g-factor of metallic Li, P. N. Argyres and A. H. Kahn—226(A)
Changes in KCl lattice dimensions by soft x-rays, Chester R. Berry—1540(A); 934
Configuration interaction and holes, P. J. Price—1533(A)
Contact charging between monocrystalline nonconductors and metals, P. E. Wagner—264(A)
Correlation of expansion coefficient anomaly in quenched Cu_3Au with properties of ordered Cu_3Au, Jerome Rothstein—1554(A)
Critical temperature for self-induced ordering in Ag-Zn solid solutions, Chi Yao Li and A. S. Nowick—1152(A)
Crystal growth, and electrical and optical properties of gray Sn, J. H. Becker—1192(A)
Crystal structure of InBi, W. P. Binnie—228(A)
Density of states curve for Ni, G. F. Koster—901
Diamagnetic resonance in electronic conductors, R. B. Dingle—550(L)
Dielectric, x-ray, and optical study of ferroelectric $Cd_2Nb_2O_7$ and related compounds, F. Jona, G. Shirane, and R. Pepinsky—903
Diffusion of Cu and Zn in ordered and disordered CuZn, Alan B. Kuper and Carl T. Tomizuka—244(A)
Dimensional changes during heat treatment thermal expansion of polycrystalline carbons and graphites, F. M. Collins—1564(A)
Direct production of spectroscopic specimens from single crystals by controlled growth from vapor; infrared absorption anisotropy and induced molecular motion in single crystal of benzene, Solomon Zwerdling and Ralph S. Halford—243(A)
Dislocation relaxations at low temperatures and determination of limiting shearing stress of metal, W. P. Mason—1136(L)
Disordering of polyatomic solids by neutrons, E. G. Harris —1151(A)
Donor and acceptor ionization energies in Si and Ge, A. H. Mitchell and C. Kittel—271(A)
Donor impurities in graphite, G. Hennig and M. Dzurus—227(A)
Dynamic behavior of domain walls in $BaTiO_3$, Elizabeth A. Little—1201(A); 978
Effect of cold work on local order, B. L. Averbach and P. S. Rudman—1554(A)
Effect of external stresses upon rate of ordering of AuCu, A. R. Freda and G. C. Kuczynski—270(A)
Effect of low concentrations of impurity on diffusion in Ag, E. Sonder—245(A)
Effect of overlap on electrostatic lattice potentials in ionic crystals, Joseph L. Birman—1870(E)
Effect of pressure on absorption edges of Te, L. J. Neuringer—1193(A)
Effect of quench on structure of Au, Monroe S. Wechsler —245(A)
Effects of heat treatment and ion-bombardment cleaning on catalytic activity of pure Ni surface, R. F. Woodcock and H. E. Farnsworth—1152(A)
Elastic constants of Ag and Ag alloys, Roger Bacon and Charles S. Smith—1553(A)
Elastic constants of Fe-Si alloys, Charles S. Smith and W. B. Daniels—1553(A)
Electrical characteristics of grain boundaries, H. F. Matare, H. Kedesdy, A. MacDonald, and A. Petersen—1179(A)
Electron band structure of Fe, Joseph Callaway—1150(A)
Electron density and density of states in narrow bands in crystals, G. W. Lehman—1542(A)
Electron mobility in AgCl: Comparison of experiment with theory, Frederick C. Brown—263(A)
Electron transfer mechanism for ultrasonic attenuation in metals, C. Kittel—1181(A)
Electronic relaxation time in graphite, John E. Robinson —227(A)
Electronic specific heat of α-Mn, G. Guthrie, S. A. Friedberg, and J. E. Goldman—1181(A)
Electronic states in perturbed periodic lattice, Paula Feuer —1193(A)
Emission from single lattice step of clean tungsten, J. K. Trolan, J. P. Barbour, E. E. Martin, and W. P. Dyke—262(A)
Energy levels in metallic K, E. L. Jossem and L. G. Parratt—1151(A)
Etch patterns and ferroelectric domains in $BaTiO_3$ single crystals, John A. Hooton and Walter J. Merz—409
Expansion of Cu bombarded by 19-Mev deuterons, Henry A. Kierstead—245(A)
Expansion of Cu bombarded by 21-Mev deuterons, William R. McDonell and Henry A. Kierstead—1870(E)
Experimental evidence for thermal spikes in radiation damage, W. Primak—1854(L)
Extension of Hund's rule, G. F. Koster—514
Ferroelectric behavior of solid solutions of $KNbO_3$ and $KTaO_3$, Sol Triebwasser and Frederic Holtzberg—1201 (A)
Field emission from Re: Emission pattern corresponding to hexagonal crystal structure, George Barnes—262(A)
Formation energy of lattice vacancies in Au, J. W. Kauffman and J. S. Koehler—245(A)
Generation of electron traps by plastic flow, Werner Känzig and Masayasu Ueta—236(A)
Grain boundary diffusion in Al-Cu system, C. Coleman and R. Smoluchowski—1555(A)
Inelastic scattering of cold neutrons by Al, R. L. Zimmerman and H. Palevsky—1162(A)
Internal friction as function of cold work of Cu reeds at low frequencies, J. J. Brady, M. B. Larson, and T. A. O'Halloran—271(A)
Internal friction in some Fe-Al alloys, C. Wert—246(A)
Interpolation scheme for energy bands in solids, Leland C. Allen—993; 1193(A)
Interpretation of dimensional changes on dezincification of α brass, David D. Van Horn and William J. Cooley —245(A)
Interpretation of optical properties of metal surfaces, S. Roberts—1151(A)
Invariant characteristics of one-dimensional binary lattices, Edward H. Kerner and Joseph G. Logan—1165 (A)
Investigation of polymorphic transition in Fe at 130 kilobars, Stanley Minshall—271(A)
Isothermal anneal study of quenched and cold-worked Cu-Pd alloys, A. Sawatzky and F. E. Jaumot, Jr.—1555(A)
Lattice resistance to dislocation motion at high velocity, Edward W. Hart—1775
Lattice thermal conductivity, J. S. Dugdale and D. K. C. MacDonald—1751
Linear magnetostriction of some ternary Co-Fe-Ni alloys, H. E. Stauss and G. Sandoz—271(A)
Localized energy states in crystalline alkali chlorides, C. F. Hempstead and L. G. Parratt—1170(A)

Localized states at boundary of two crystals, George W. Pratt, Jr.—1543(A)
Long wavelength neutron transmission as absolute method for determining concentration of lattice defects in crystals, J. J. Antal, R. J. Weiss, and G. J. Dienes—1541(A)
Low-energy electron diffraction studies of Ge crystal surface, H. E. Farnsworth, R. E. Schlier, and R. M. Burger—250(A)
Low-energy electron diffraction studies of Ti crystal surface, R. E. Schlier, H. E. Farnsworth, and T. H. George —250(A)
Low-temperature resistance minimum, R. W. Schmitt and M. D. Fiske—246(A)
Magnetic domains in single crystal of Co near 275°C by longitudinal Kerr effect, Edward M. Fryer and Charles A. Fowler, Jr.—270(A)
Mass spectrometric study of gaseous species in Si-SiO_2 system, Richard F. Porter, Paul Schissel, and Mark G. Inghram—242(A)
Measurements of x-ray diffuse scattering from Co-Pt disordered solid solutions and of long-range order for alloy CoPt, P. S. Rudman and B. L. Averbach—1554(A)
Mechanical twinning in Cu, T. H. Blewitt, J. K. Redman, F. A. Sherrill, and R. R. Coltman—1555(A)
Mechanism of grain boundary relaxation in metals and alloys, A. S. Nowick and Chi Yao Li—1556(A)
Minority carrier lifetime as function of crystal growth variables, A. C. Sheckler and D. C. Jillson—229(A)
Mobility of slow electrons in polar crystals, Francis E. Low and David Pines—414
Neutron irradiation effects in Cu and Al at 80°K, A. W. McReyonlds, W. Augustyniak, Marilyn McKeown, and D. B. Rosenblatt—418
New method in x-ray crystal structure determination involving use of anomalous dispersion, Y. Okaya, Y. Saito, and R. Pepinsky—1857(L)
Nuclear spin relaxation in alkali metals, D. F. Holcomb and R. E. Norberg—1074
One-electron energies of atoms, molecules, and solids, J. C. Slater—1039
Optical properties and twinning of $PbZrO_3$ single crystals, F. Jona, G. Shirane, and R. Pepinsky—1201(A)
Order-disorder and ionic conductivity in Ag_2HgI_4, Jerome Rothstein—271(A)
Oscillatory Hall effect, magnetoresistance, and magnetic susceptibility of graphite single crystal, Ted G. Berlincourt and M. C. Steele—227(A); 956
Overhauser effect in nonmetals, A. Abragam—1729
Overhauser nuclear polarization effect, W. A. Barker and A. Mencher—1868(L)
Overhauser nuclear polarization effect and minimum entropy production, Martin J. Klein—1736
Photoconductivity of pyrolytic layers of B, C. H. Hayn and Vincent P. Jacobsmeyer—237(A)
Photographic effects in single crystals of AgBr, W. West and V. I. Saunders—1557(A)
Physical properties of carbons and porosity, S. Mrozowski —1564(A)
Plasma oscillations in metals, E. N. Adams—947
Polytypism and dislocations, N. Cabrera and M. M. Levine —1543(A)
Precipitation in small spheres of Pb-Sn alloy, W. DeSorbo and D. Turnbull—1554(A)
Prismatic slip in crystals, J. W. Davisson, Elias Burstein, and P. L. Smith—1544(A)
Quantum-mechanical calculation of interatomic force constants in Cu, Harrison C. White—1552(A)
Random walk methods in statistical mechanics of one-dimensional systems, R. L. Sells, C. W. Harris, and E. Guth—272(A)
Relationship among hardness, energy gap, and melting point of diamond-type and related structures, G. Wolff, L. Toman, and J. Clark—1179(A)
Relaxation of monatomic crystal lattice around vacancy, Stefan Machlup—1556(A)
Role of coordination number in Lee-Yang lattice gas, C. W. Harris and E. Guth—272(A)
Rotational transition in solid hydrogen, K. Tomita—1197 (A)
Satellites in soft x-ray spectrum of Zr, J. Korringa—1556 (A)
Second-neighbor interaction in two-dimensional graphite lattice, G. S. Colladay and S. Barshay—270(A)
Second transition in $AuCu_3$, G. C. Kuczynski and M. Doyama—270(A)
Secondary recrystallization analogy in heterogeneous liquid system, John P. Nielsen—1157(A)
Segregation coefficient of As in Ge as function of crystal growth variables, D. C. Jillson and A. C. Sheckler—229(A)
Self-diffusion in natural graphite crystals, M. A. Kanter—1563(A)
Self-diffusion in Zn at low temperatures, F. E. Jaumot, Jr., and R. L. Smith—1555(A)
Slow-neutron spectrometry—New tool for study of energy levels in condensed systems, B. N. Brockhouse—1171(A)
Smakula's equation in insulating solids, D. L. Dexter—1533(A)
Small-angle scattering of x-rays by surface irregularities, W. H. Robinson and R. Smoluchowski—1555(A)
Solution of Hartree-Fock-Slater equations for Si crystal by method of orthogonalized plane waves, Truman O. Woodruff—1741
Source of disordering of alloys during irradiation, F. Seitz—1530(A)
Specific directions of longitudinal wave propagation in anisotropic media, F. E. Borgnis—1000
Storage of energy in BeO, H. O. Albrecht and C. E. Mandeville—1546(A)
Straumanis' concepts regarding Avogadro's number, E. Richard Cohen and J. W. M. DuMond—1128(L)
Structure of evaporated Cu films on Ti, R. E. Schlier—1555(A)
Temperature dependence of heat capacity of molybdenite, Edgar F. Westrum, Jr., and John J. McBride—270(A)
Temperature dependence of internal friction in Cu, D. N. Beshers and J. S. Koehler—1553(A)
Temperature variation of elastic constants of cubic elements. I. Cu, W. C. Overton, Jr., and John Gaffney—969
Theory of anisotropy of magnetoresistance for single crystals, L. P. Kao and E. Katz—1534(A)
Theory of energy levels of donor electrons in Si, W. Kohn and J. M. Luttinger—1178(A)
Theory of ionic ordering, crystal distortion, and magnetic exchange due to covalent forces in spinels, J. B. Goodenough and A. L. Loeb—391
Thermal bleaching of color centers, A. Halperin and A. Braner—1135(L)
Thermal conductivities of carbons and graphites, C. P. Jamieson—1564(A)
Thermal formation of colloids from *F* centers in KCl crystals, H. Pagnia and F. Stockman—236(A)
Thermal ionization of interstitials in cubic ZnS, H. D. Vasileff—237
Thermal scattering of electrons between bands in metal, John B. Gibson—1151(A)
Time-dependent displacement correlations and inelastic scattering by crystals, R. J. Glauber—1692
Two-medium theory of thermal conductivity of artificial graphite: Experimental, Alan W. Smith—1563(A); Interpretation, John E. Hove—1563(A)

Crystalline State (Continued)
Vibration spectra and specific heats of cubic metals. I. Theory and application to Na, A. B. Bhatia—245(A); II. Application to Ag, A. B. Bhatia and G. K. Horton—1715; 1181(A)
X-ray analysis of compressed KCl powder crystals, J. G. Kereiakes—553(L)
X-ray measurements on low-temperature neutron-irradiated graphite, David T. Keating—1859(L)

Diamagnetism (see **Magnetic Properties**)
Dielectrics and Dielectric Properties
Abnormal increase in dielectric constant of electret-forming material, S. D. Chatterjee and T. C. Bhadra—1728
Anomalous optical properties of ferroelectric $PbTiO_3$, Gen Shirane and Ray Pepinsky—1201(A)
Bond dipoles and piezoelectricity in zincblende semiconductors, Joseph L. Birman—1567(A)
Curie constant, spontaneous polarization, and latent heat in ferroelectric, S. Triebwasser and J. Halpern—1201(A)
Dielectric behavior of $BaTiO_3$ in paraelectric state, M. E. Drougard, R. Landauer, and D. R. Young—1010; 1563(A)
Dielectric dispersion in ZnS phosphors, I. Ames, H. S. Sack, and R. M. Wood—1545(A)
Dielectric, x-ray, and optical study of ferroelectric $Cd_2Nb_2O_7$ and related compounds, F. Jona, G. Shirane, and R. Pepinsky—903
Dynamic behavior of domain walls in $BaTiO_3$, Elizabeth A. Little—978; 1201(A)
Electromechanical behavior of single crystals of $BaTiO_3$, E. J. Huibregtse, M. E. Drougard, and D. R. Young—1562(A)
Etch patterns and ferroelectric domains in $BaTiO_3$ single crystals, John A. Hooton and Walter J. Merz—409
Ferroelectric behavior of solid solutions of $KNbO_3$ and $KTaO_3$, Sol Triebwasser and Frederic Holtzberg—1201(A)
Inertial effects and dielectric relaxation, E. P. Gross—1191(A)
Low-temperature dielectric measurements, J. F. Youngblood—1201(A)
Microwave determination of average masses of electrons and holes in Ge, James M. Goldey and Sanborn C. Brown—1761
Microwave dielectric measurements on single fibers, J. J. Windle and T. M. Shaw—281(A)
New class of ferroelectrics, A. N. Holden, B. T. Matthias, W. J. Merz, and J. P. Remeika—546(L)
Optical properties and twinning of $PbZrO_3$ single crystals, F. Jona, G. Shirane, and R. Pepinsky—1201(A)
Phenomenological theory of Townsend breakdown in dielectrics, P. L. Auer—320
Second-order transition in $BaTiO_3$, A. DeBretteville, Jr.—1563(A)
Space charge layer near surface of ferroelectric, Werner Känzig—549(L)
Diffraction (see also **Scattering**)
Anomalous absorption of neutrons in single crystals, J. W. Knowles—224(A)
Diffuse magnetic neutron diffraction, A. W. McReynolds—1200(A)
Low-energy electron diffraction studies of Ge crystal surface, H. E. Farnsworth, R. E. Schlier, and R. M. Burger—250(A)
Low-energy electron diffraction studies of Ti crystal surface, R. E. Schlier, H. E. Farnsworth, and T. H. George—250(A)
Small-angle scattering of x-rays by surface irregularities, W. H. Robinson and R. Smoluchowski—1555(A)
Structure of evaporated Cu films on Ti, R. E. Schlier—1555(A)
X-ray analysis of compressed KCl powder crystals, J. G. Kereiakes—553(L)
Diffusion
Diffusion analogy for shocks interacting with thermal boundary layers, Wayland Griffith and Walker Bleakney—1143(A)
Diffusion model for nuclear precession relaxation in solids, E. L. Hahn and B. Herzog—265(A)
Diffusion of Cu and Zn in ordered and disordered CuZn, Alan B. Kuper and Carl T. Tomizuka—244(A)
Diffusion of ions and electrons in electric field, Robert N. Varney—558(A)
Effect of low concentrations of impurity on diffusion in Ag, E. Sonder—245(A)
Electron spin resonance absorption in metals. II. Theory of electron diffusion and skin effect, Freeman J. Dyson—349
Grain boundary diffusion in Al-Cu system, C. Coleman and R. Smoluchowski—1555(A)
Interpretation of dimensional changes on dezincification of α brass, David D. Van Horn and William J. Cooley—245(A)
Ring diffusion as mechanism of self-diffusion in Ge, Sumner Mayburg—1134(L)
Self-diffusion in Cu, A. Kuper, H. Letaw, Jr., L. Slifkin, E. Sonder, and C. T. Tomizuka—1870(E)
Self-diffusion in Ge, William M. Portnoy, Harry Letaw, Jr., and Lawrence Slifkin—1536(A)
Self-diffusion in natural graphite crystals, M. A. Kanter—1563(A)
Self-diffusion in Zn at low temperatures, F. E. Jaumot, Jr., and R. L. Smith—1555(A)
Self-diffusion of Ag in AgCl, W. Dale Compton—1543(A)
Thermal diffusion in multiple component isotopic mixtures, J. W. Corbett and W. W. Watson—1165(A)
Discharge of Electricity in Gases (see **Electrical Discharges**)
Disintegration and Excitation of Nucleus (see **Nuclear Reactions**)
Dynamics (see **Mechanics**)

Elasticity and Plasticity
Apparent limit of convergence of perturbation series solution for free undamped Duffing equation with hardening spring, John C. Burgess—257(A)
Behavior of nonpigmented rubber vulcanizates in tension, G. M. Martin, F. L. Roth, and R. D. Stiehler—1559(A)
Behavior of rubbers in simple shear, J. E. Ivory, F. B. Baldwin, and R. L. Anthony—1558(A)
Biaxial creep fracture of high polymers, Chester G. Bragaw, Jr.—1559(A)
Calculation of compressibility of polyethylene from energy of interaction between ($-CH_2-$) groups, Werner Brandt—243(A)
Creation of potential difference across NaCl crystals by deformation, D. B. Fischbach and A. S. Nowick—1543(A)
Deformation of viscoelastic plates derived from thermodynamics, M. A. Biot—1869(L)
Dislocation line energy and slip in NaCl and AgCl crystals, Robb Thomson—1171(A)
Dislocation relaxations at low temperatures and determination of limiting shearing stress of metal, W. P. Mason—1136(L)
Dynamic mechanical properties of concentrated cellulose trinitrate solutions, D. J. Plazek and John D. Ferry—1548(A)
Dynamic properties of glucose glass, W. Philippoff and J. Brodnyan—1549(A)

Effect of external stresses upon rate of ordering of AuCu, A. R. Freda and G. C. Kuczynski—270(A)
Effect of plastic deformation on surface resistivity of Cu wires, J. Aron and D. Kahn—246(A)
Effect of quenching and neutron irradiation on atomic mobility in Cu-Al alloy, Chi Yao Li and A. S. Nowick —1531(A)
Effect of superconducting transition on internal friction of Sn, Benjamin Welber—1196(A)
Elastic constants and specific heat of KCl at elevated temperatures, F. D. Enck and C. B. Cooper—237(A)
Elastic constants of Ag and Ag alloys, Roger Bacon and Charles S. Smith—1553(A)
Elastic constants of Fe-Si alloys, Charles S. Smith and W. B. Daniels—1553(A)
Elastic modulus of x-irradiated rock salt, R. B. Gordon and A. S. Nowick—1540(A)
Elastic strain energy stored in mechanically disturbed surfaces, R. L. Hopkins—1567(A)
Electromechanical behavior of single crystals of $BaTiO_3$, E. J. Huibregtse, M. E. Drougard, and D. R. Young— 1562(A)
Extension of Hertz theory of impact to viscoelastic case, Yoh-Han Pao—1548(A)
Generation of electron traps by plastic flow, Werner Känzig and Masayasu Ueta—236(A)
Internal friction as function of cold work of Cu reeds at low frequencies, J. J. Brady, M. B. Larson, and T. A. O'Halloran—271(A)
Internal friction in some Fe-Al alloys, C. Wert—246(A)
Investigation of polymorphic transition in Fe at 130 k.b., Stanley Minshall—271(A)
Mechanical twinning in Cu, T. H. Blewitt, J. K. Redman, F. A. Sherrill, and R. R. Coltman—1555(A)
Neutron irradiation effects in Cu and Al at 80°K, A. W. McReynolds, W. Augustyniak, Marilyn McKeown, and D. B. Rosenblatt—418
Photoelastic observation of expansion of alkali halides in irradiation, W. Primak, P. H. Yuster, and C. J. Delbecq —237(A); W. Primak, C. J. Delbecq, and P. H. Yuster —1708
Prismatic slip in crystals, J. W. Davisson, Elias Burstein, and P. L. Smith—1544(A)
Propagation of plastic strain along Pb bars, B. E. K. Alter and C. W. Curtis—1151(A)
Relationship between small-angle dislocation boundaries and creep, Betsy Ancker, Thomas H. Hazlett, and Earl R. Parker—1151(A)
Shear modulus recovery of electron-irradiated Cu, H. Dieckamp—1531(A)
Specific directions of longitudinal wave propagation in anisotropic media, F. E. Borgnis—1000
Studies of elastic modulus of carbons, K. Hong and S. Mrozowski—1565(A)
Temperature dependence of internal friction in Cu, D. N. Beshers and J. S. Koehler—1553(A)
Temperature dependence of relaxation mechanisms in amorphous polymers and other glass-forming liquids, Malcolm L. Williams, Robert F. Landel, and John D. Ferry—1549(A)
Temperature variation of elastic constants of cubic elements. I. Cu, W. C. Overton, Jr., and John Gaffney— 969
Tensile strength of elastomers, G. R. Taylor and S. R. Darin—1558(A)
Theory of steady-state creep based on dislocation climb, J. Weertman—246(A)
Ultrasonic technique for nondestructive evaluation of metal to metal adhesive bonds, J. S. Arnold—283(A)
Unilateral compression of rubber, Michael J. Forster— 1559(A)
Vibration spectra and specific heats of cubic metals. I. Theory and application to Na, A. B. Bhatia—245(A); II. Application to Ag, A. B. Bhatia and G. K. Horton— 1715; 1181(A)
Electrical Breakdown (see **Dielectrics and Dielectric Properties; Electrical Discharges**)
Electrical Conductivity and Resistance (see also **Semiconductors; Superconductors**)
Brillouin zone studies of alloys. III. Matthiessen's rule for dilute Mg alloys, E. I. Salkovitz, J. Pasternak, and A. I. Schindler—271(A); IV. Additional Hall data of Mg alloys, A. I. Schindler and E. I. Salkovitz—1552(A)
Conduction in phthalocyanine crystals, D. Kleitman and G. Goldsmith—1544(A)
Conductivity of Teflon and polyethylene during γ irradiation, R. A. Meyer and F. L. Boquet—1531(A)
Contact resistance between superconductors and normal conductors, F. Bedard and H. Meissner—1539(A)
Creation of potential difference across NaCl crystals by deformation, D. B. Fischbach and A. S. Nowick— 1543(A)
Dark conduction in *para*-terphenyl single crystals, D. E. Hill and G. J. Goldsmith—238(A)
Density-resistivity relationships in baked carbons, E. J. Seldin—1565(A)
Effect of Br on dark conductivity of AgBr and its relation to photoconductivity, George W. Luckey—1558(A)
Effect of impurities on mobility in *n*-type InSb, T. C. Harman, R. K. Willardson, and A. C. Beer—1532(A)
Effect of O_2 gas on photoconductivity of BaO, M. Sakamoto, S. Kobayashi, and S. Ishii—552(L)
Effect of plastic deformation on electrical conductivity of AgBr, William G. Johnston—1777
Effect of plastic deformation on surface resistivity of Cu wires, J. Aron and D. Kahn—246(A)
Effect of pressure on electrical properties of InSb, Donald Long and Park H. Miller, Jr.—1192(A)
Effect of quench on structure of Au, Monroe S. Wechsler —245(A)
Effect of vacancies and interstitials on electrical properties of Cu, F. J. Blatt—245(A)
Electrical conduction in plastics, Raymond J. Munick— 236(A)
Electrical conductivity of liquid Te, V. A. Johnson—1567 (A)
Electrical resistance of Cu-Au alloys at low temperatures, Elio Passaglia and William F. Love—1006
Electronic relaxation time in graphite, John E. Robinson —227(A)
Energy dependence of radiation effects in solids, E. Pearlstein, H. Ingham, and R. Smoluchowski—1530(A)
Ferromagnetic Hall effect of Ni alloys, Albert I. Schindler —1199(A)
Formation energy of lattice vacancies in Au, J. W. Kauffman and J. S. Koehler—245(A)
Galvanomagnetic effects in InSb, W. R. Hosler and H. P. R. Frederikse—1532(A)
Hall coefficient in anisotropic media, E. G. Grimsal—229 (A)
Hall effect and magnetoresistance oscillations of Sb single crystals in magnetic fields at liquid He temperatures, M. C. Steele—1180(A)
Hall effect and resistivity of InSb at low temperatures, H. Fritzsche and K. Lark-Horovitz—1532(A)
Localized photoconductivity in PbS films, David Dutton— 1549(A)
Low temperature resistance minimum, R. W. Schmitt and M. D. Fiske—246(A)
Magnistor, solid-state electronic valve, Milton Green— 1169(A)

Electrical Conductivity and Resistance (Continued)
Model for luminescence and photoconductivity in sulfides, John Lambe and Clifford C. Klick—909
Neutron irradiation effects in Cu and Al at 80°K, A. W. McReynolds, W. Augustyniak, Marilyn McKeown, and D. B. Rosenblatt—418
Optical and electrical properties of LiF x-rayed at liquid nitrogen temperature, C. J. Delbecq, P. Pringsheim, and P. H. Yuster—237(A)
Order-disorder and ionic conductivity in Ag_2HgI_4, Jerome Rothstein—271(A)
Oscillatory Hall effect and magnetoresistance of Bi, Jules A. Marcus—1540(A)
Oscillatory Hall effect, magnetoresistance, and magnetic susceptibility of a graphite single crystal, Ted G. Berlincourt and M. C. Steele—227(A); 956
Photoconductivity and photodesorption in ZnO, David B. Medved—237(A)
Photoconductivity in KI, Nicolas Inchauspé—1550(A)
Photoconductivity in *para*-terphenyl single crystals, G. J. Goldsmith and D. E. Hill—238(A)
Photoconductivity of pyrolytic layers of B, C. H. Hayn and Vincent P. Jacobsmeyer—237(A)
Physical properties of carbons and porosity, S. Mrozowski—1564(A)
Polarization in insulating crystals, Nicolas Inchauspé—1543(A)
Pressure dependence of de Haas-van Alphen parameters in Bi crystal at 4.2°K, William C. Overton, Jr., and Ted G. Berlincourt—1180(A)
Pressure dependence of resistivity of Si, William Paul and G. L. Pearson—1755
Properties of CdS films deposited *in vacuo*, Arthur Bramley—246(A)
Recombination processes in CdS, John Lambe—985
Rectification in thin films of PbS, M. Silver, R. S. Witte, and F. McCaffrey—270(A)
Relation of magnetic structure to electrical conductivity in NiO and related compounds, R. R. Heikes—225(A)
Resistivity due to point imperfections in Cu, F. J. Blatt, M. C. Huse, and R. A. Rubenstein—1553(A)
Resistivity of dilute alloys, D. L. Dexter—543(L)
Resistivity of dilute Mg alloys, Edward I. Salkovitz and A. I. Schindler—543(L); 1553(A)
Self-diffusion of Ag in AgCl, W. Dale Compton—1543(A)
Semiconducting diamond, W. J. Leivo and R. Smoluchowski—1532(A)
Statistics for electrical phenomena, Joseph G. Barredo—1542(A)
Temperature dependence of width of band gap in several photoconductors, Richard H. Bube—431
Theory of anisotropy of magnetoresistance for single crystals, L. P. Kao and E. Katz—1534(A)
Thermoelectric power and resistivity of dilute alloys of Mn, Pd, and Pt in Cu, Ag, and Au, F. A. Otter, Jr.—1552(A)

Electrical Discharges
Absorption of radiation in vacuum uv by N atoms produced in discharge plasma in N_2, A. W. Ehler and G. L. Weissler—561(A)
Active nitrogen in rare gases, Carl Kenty—563(A)
Afterglow of solid N_2, Herbert P. Broida—563(A)
Ambipolar diffusion of magnetic field, Albert Simon—317
Analysis of plasma of fluorescent lamps. I, F. Bitter and J. F. Waymouth—1148(A); II, J. F. Waymouth and F. Bitter—1148(A)
Anchored Hg arc cathode spot, Charles G. Smith—562(A)
Anode pre-breakdown phenomena in thyratrons, Seymour Goldberg—558(A)
Breakdown processes in nitrogen, oxygen, and mixtures, Elsa L. Huber—560(A)
Cumulative ionization processes in He positive column, L. S. Frost and A. V. Phelps—559(A)
Departure from Paschen's law of breakdown in gases, W. S. Boyle and P. Kisliuk—560(A)
Diffusion of ions and electrons in electric field, Robert N. Varney—558(A)
Directional breakdown in alkali halide crystals, M. E. Caspari—1679
Duration of Hg arcs in evacuated bulbs coated with rare earths, B. Pearson de Lany and Paul L. Copeland—251(A)
Effect of mean free path variation on high-frequency breakdown, I. A. MacLennan and A. D. MacDonald—559(A)
Electric field measurements in glow discharges using refined electron beam probe techniques, Roger Warren—263(A); 562(A)
Electrical breakdown in high vacuum, P. Kisliuk, W. S. Boyle, and L. H. Germer—560(A)
Electron density in long-lived nitrogen afterglows, Andrew L. Gardner—263(A)
Experimental cross section for photodetachment of electrons from H^- and D^-, Lewis M. Branscomb and Stephen J. Smith—1028
Field effect of space charge in intermittent glow in hydrogen, Herman Ritow—251(A)
Field measurements in glow discharges with refined electron beam probe and automatic recording, Roger Warren—1650
High-frequency gas discharge plasma in hydrogen, David J. Rose and Sanborn C. Brown—310
High-frequency ionization coefficients in Ne-A mixtures, A. D. MacDonald and J. H. Matthews—1070
Influence of space charge on potential distribution in mass spectrometer ion sources, W. M. Brubaker—563(A)
Instantaneous probe measurements of travelling striations in argon glow discharge, N. L. Oleson—559(A)
Integral equation solution of space-charge wave propagation, Philip Parzen—257(A)
Interpretation of field measurements in cathode region of glow discharges, Roger Warren—1658
Investigation of buildup processes in argon discharge, M. Menes—561(A)
Ionization accompanying long-lived nitrogen afterglow, W. B. Kunkel and A. L. Gardner—558(A)
Measurement of absorption coefficients for photoionizing radiations in low-pressure gases with space charge detector, C. D. Maunsell—1831
Measurement of current during formative time lag of sparks in uniform fields in air, H. W. Bandel—560(A)
Mechanism of termination of Geiger plateau region, H. L. Wiser and A. D. Krumbein—303
Microwave study of positive ion collection by probes, George J. Schulz and Sanborn C. Brown—559(A)
Motion and spectrum of arc cathode spot in magnetic field, Robert St. John and J. G. Winans—562(A)
Negative-ion formation using monoenergetic electrons, W. M. Hickam and R. E. Fox—557(A)
Oscillations of plasma with skew velocity distribution transverse to static magnetic field, J. E. Drummond and L. Wilcox—558(A)
Phenomenological theory of Townsend breakdown in dielectrics, P. L. Auer—320
Photoionization by absorption in gas of radiations from discharge in same gas, C. D. Maunsell—263(A)
Plasma fluctuations in crossed electric and magnetic fields, Hugh W. Batten—559(A)
Plasma oscillations in static magnetic field, L. Wilcox and J. E. Drummond—263(A)

Plasma resonance, K. S. W. Champion and S. C. Brown—559(A)
Properties of dc arc in magnetic field, L. P. Winsor and T. H. Lee—562(A)
Recombination in argon shock front, John W. Bond, Jr.—285(A)
Retrograde motion in gas discharge plasmas, K. G. Hernqvist and E. O. Johnson—1576
Secondary electron resonance discharge mechanism. I, R. K. Smither and C. W. Hoover, Jr.—1149(A); II, C. W. Hoover, Jr., and R. K. Smither—1149(A)
Sparking potential and molecular structure of hydrocarbon gases, R. W. Crowe and J. C. Devins—560(A)
Spectroscopic study of discharge and afterglow produced in N by pulsed microwaves, Georges Dejardin, Joseph Janin, and Ivan Eyraud—1149(A)
Statistics of exponential distribution of exponential populations applied to distribution of arc lives, Paul L. Copeland and B. Pearson de Lany—251(A)
Streamers in positive point-to-plane breakdown in air, Gilbert G. Hudson—264(A)
Very high temperature arcs, Wolfgang Finkelnburg—562(A)
Wide-range electronic tuning of microwave cavities in gas atmospheres, Frank R. Arams and Hans K. Jenny—562(A)
X-ray-induced luminescence from air, William E. Spicer—1061

Electrical Properties (see also **Dielectrics and Dielectric Properties; Electrical Conductivity and Resistance; Semiconductors; Superconductors**)
Changes in photoelectric probability factor resulting from surface contamination of Al, R. L. Perry and J. J. Brady—281(A)
Contact charging between monocrystalline nonconductors and metals, P. E. Wagner—264(A)
Directional breakdown in alkali halide crystals, M. E. Caspari—1170(A); 1679
Ejection of electrons from contaminated metals by positive ions, Homer D. Hagstrum—561(A)
Electrical characteristics of grain boundaries, H. F. Matare, H. Kedesdy, A. MacDonald, and A. Petersen—1179(A)
Electrical stability of *T-F* emitter, W. P. Dyke, J. P. Barbour, J. K. Trolan, and E. E. Martin—263(A)
Electron voltaic study of electron bombardment damage and its thresholds in Ge and Si, J. J. Loferski and P. Rappaport—1861(L)
Emission from single lattice step of clean tungsten, J. K. Trolan, J. P. Barbour, E. E. Martin, and W. P. Dyke—262(A)
Field emission from Re: Emission pattern corresponding to hexagonal crystal structure, George Barnes—262(A)
Field emission from Ti single crystals, E. G. Brock and J. E. Taylor—1169(A)
Localized photoeffect in PbS photocells, E. S. Rittner and S. Fine—545(L)
Magnification and resolution of field emission electron microscope, D. J. Rose—1169(A)
Measurements and collision theory of high vacuum sputtering, Frank Keywell—561(A)
Metal vacuum joint suitable for field emitters, Howard H. Pattee, Jr.—283(A)
Photoelectric mixing of incoherent light, A. Forrester, Richard A. Gudmundsen, and Philip O. Johnson—1169(A)
Photoelectric yields of metals in vacuum uv, W. C. Walker, N. Wainfan, and G. L. Weissler—562(A)
Seebeck effect in Si, T. H. Geballe and G. W. Hull—940
Short-time polarization in ThO, W. E. Danforth—1177(A)
Statistics for electrical phenomena, Joseph G. Barredo—1542(A)
Thermoelectric power and resistivity of dilute alloys of Mn, Pd, and Pt in Cu, Ag, and Au, F. A. Otter, Jr.—1552(A)
Velocity analysis of thermionic emission from single-crystal tungsten, Andrew R. Hutson—889
Work function difference of Au and AuO from contact potentials with respect to Ge and Pt, Paul Miller—1552(A)
Work function of Cd, Paul A. Anderson—1739

Electrodynamics (see **Electromagnetic Theory and Electrodynamics**)

Electrolysis (see **Chemical Effects and Properties**)

Electromagnetic Theory and Electrodynamics
Faraday effect in semiconductors at microwave frequencies, Richard Rau and P. H. Miller, Jr.—1533(A)
Galvanomagnetic effects in InSb, W. R. Hosler and H. P. R. Frederikse—1532(A)
Integral equation solution of space-charge wave propagation, Philip Parzen—257(A)
Quantum effects in interaction between electrons and high-frequency fields. II, I. R. Senitzky—875
Scattering of electromagnetic waves by bounded lattice of parallel cylinders, V. Twersky—257(A)
Self-focusing streams, Willard H. Bennett—1584
Theory of magnetic self-focusing, Willard H. Bennett—1169(A)

Electron Diffraction (see **Diffraction; Scattering of Electrons and Positrons**)

Electron Optics (see **Electromagnetic Theory and Electrodynamics**)

Electronic Tubes (see **Methods and Instruments**)

Electrons and Positrons (see also **Electromagnetic Theory and Electrodynamics; Elementary Particle Interactions; Scattering of Electrons and Positrons**)
Angular correlation in two-photon annihilation in quartz, L. A. Page, M. Heinberg, J. Wallace, and T. Trout—206(L)
Angular correlation of photons from positron annihilation in light metals, A. T. Stewart and R. E. Green—232(A); R. E. Green and A. T. Stewart—486
Effect of static electric field on positronium formation, S. Marder, W. Bennett, C. S. Wu, and V. W. Hughes—1173(A)
Fine structure of positronium, R. Weinstein, M. Deutsch, and S. Brown—223(A)
Static magnetic field quenching of orthopositronium decay: Angular distribution effect, V. W. Hughes, S. Marder, and C. S. Wu—1840
Theory of effect of static electric field on positronium formation, W. B. Teutsch and V. W. Hughes—1174(A)

Electrons, Mobility (see **Ions and Electrons, Mobility**)

Electrons, Scattering of (see **Scattering of Electrons and Positrons**)

Electrons, Secondary (see **Electrical Properties**)

Electrons, Thermionic (see **Electrical Properties**)

Electro-Optical Effects (see **Optical Properties**)

Electrostriction (see **Dielectrics and Dielectric Properties**)

Elementary Particle Interactions
Applications of causality to scattering, Robert Karplus and Malvin A. Ruderman—771
Charged pion production in n-p collisions, Gaurang B. Yodh—268(A)
Charged V-particle production in p-p collision, M. M. Block, E. M. Harth, W. B. Fowler, R. P. Shutt, A. M. Thorndike, and W. L. Whittemore—248(A)
Classical field theory of nuclear forces, M. H. Johnson and E. Teller—783

Elementary Particle Interactions (Continued)
Conservation of parity and new particles, R. Utiyama and W. Tobocman—780
Differential cross sections for pion-proton scattering at 150 and 170 Mev, F. Feiner, J. Ashkin, J. P. Blaser, and M. O. Stern—239(A)
Differential p-p scattering cross sections at 419 Mev, J. Marshall, L. Marshall, and V. A. Nedzel—1513(L)
Diffusion cloud-chamber study of very slow mesons. I. Internal pair formation, C. P. Sargent, R. Cornelius, M. Rinehart, L. M. Lederman, and K. Rogers—1349
D-wave solution to pion-proton scattering data, Jay Orear —1155(A)
Effect of renormalization on meson-nucleon S-scattering, Maurice M. Lévy—1470
Elastic photoproduction of π^0 mesons for He, E. L. Goldwasser, L. J. Koester, and F. E. Mills—239(A)
Elastic p-p angular distributions from 440 to 1000 Mev, L. W. Smith, A. W. McReynolds, and G. A. Snow—1167(A)
Electrodisintegration of deuteron, V. Z. Jankus—278(A)
Electron scattering from proton, Robert Hofstadter and Robert W. McAllister—217(L)
Evidence for pion-pion interaction, W. G. Holladay and R. G. Sachs—1155(A)
Exchange current effects in two-nucleon system, J. Bernstein and Abraham Klein—1155(A)
High-energy cross sections. II. Nucleon-nucleon cross section at cosmic-ray energies, Robert W. Williams—1393
Integral equations of meson-nucleon system, R. L. Mills—1156(A)
Interactions of 1.5-Bev π^- mesons, W. D. Walker and J. Crussard—240(A)
$\Lambda^0-\theta^0$ production in $\pi^- - p$ collisions at 1 Bev, W. D. Walker—1407
Low-energy photoproduction of π^0 mesons from H: Total cross section, F. E. Mills and L. J. Koester, Jr.—210(L)
Low-energy photoproduction of π^0 mesons in H: Differential cross sections at 135°, Louis J. Koester, Jr.—211(L)
Meson pair theory, Bruce H. McCormick and Abraham Klein—1155(A)
Negative pions from neutron bombardment of deuterons, Myron W. Knapp and Wilson M. Powell—1188(A)
Nonrelativistic interaction between two nucleons, David Feldman—1456
n-p scattering at 17.9 Mev, A. Galonsky and J. Judish—1168(A)
n-p scattering at 20 Mev, R. B. Day, R. L. Mills, J. E. Perry, Jr., and F. Scherb—279(A)
Nuclear absorption of fast charged hyperon, D. T. King and M. M. Block—1203(A)
Phase shift analysis of 240-Mev p-p scattering, L. Beretta, E. Clementel, and C. Villi—1526(L)
Photodisintegration of deuteron by 95-Mev bremsstrahlung, Lew Allen, Jr.—705
Photodisintegration of deuterons by high-energy γ rays, Dwight R. Dixon and Kenneth C. Bandtel—259(A)
Photomeson production from H, Bernard T. Feld—238(A)
Photomeson production from H, D, and C, Walter Dudziak, Ryokichi Sagane, and James Vedder—269(A)
Photoproduction of neutral mesons in H and D, H. H. Bingham, J. C. Keck, and A. V. Tollestrup—1187(A)
Photoproduction of π^+ mesons from H near threshold, J. E. Leiss, S. Penner, and C. S. Robinson—201(L); 1188(A)
Photoproduction of π^0 mesons in hydrogen, L. J. Koester —239(A)
π^--nucleon collisions at 1.5 Bev, W. D. Walker and J. Crussard—1416
π^+ photomeson production at 180°. Experimental arrangement, Gordon W. Repp, Mark J. Jakobson, and R. Stephen White—268(A); Experimental results, R. Stephen White, Mark J. Jakobson, and Gordon W. Repp —269(A)
π^0 photoproduction from protons and deuterium nucleons, I, R. M. Worlock and W. R. Smythe—269(A); II, W. R. Smythe and R. M. Worlock—269(A)
π^-/π^+ ratios in asymmetric nuclei, H. Motz, K. M. Crowe, and R. M. Friedman—268(A)
Pion-nucleon s-wave phase shift from ps-ps with cutoff, Charles J. Goebel—273(A)
Pion photoproduction ratios, D. C. Peaslee—239(A)
Polarization effects in reaction $p+p\rightarrow\pi^++d$, L. Wolfenstein—766
Positive pion scattering by H at 189 Mev, U. Kruse, H. L. Anderson, W. C. Davidon, and M. Glicksman—1188(A)
Possible experiments to determine transition matrix for p-p scattering, Reinhard Oehme—216(L)
p-p scattering at 900 Mev, T. W. Morris, J. D. Garrison, E. C. Fowler, W. B. Fowler, R. P. Shutt, A. M. Thorndike, and W. L. Whittemore—1167(A)
p-p scattering experiments at 170 and 260 Mev, Owen Chamberlain and John D. Garrison—1167(A)
Production of charged pions in n-p collisions, Gaurang B. Yodh—1330
Production of K mesons by protons of Cosmotron energy, Martin M. Block—1156(A)
Rotation of polarization vector and depolarization in p-p scattering, T. Ypsilantis, C. Wiegand, R. Tripp, E. Segrè, and O. Chamberlain—840(L)
Scattering of 23-Mev positive pions on hydrogen, Jay Orear—239(A)
Scattering of 165-Mev pions by protons, M. Glicksman and H. L. Anderson—239(A)
Scattering of 192-Mev electrons from deuterium, John A. McIntyre and Robert Hofstadter—158
Self-energy effects on meson-nucleon scattering according to Tamm-Dancoff method, J. C. Taylor—201(L)
Statistical model for high-energy events, Joseph V. Lepore and Maurice Neuman—1484
Theory of pion photoproduction, M. Ross—1169(A)
Vacuum polarization and p-p scattering, Leslie L. Foldy and Erik Eriksen—775; 1190(A)
Elements (see **Atomic Mass and Abundance**)
Energy Loss of Particles (see **Range and Energy Loss of Particles**)
Energy States of Atoms (see **Atomic Structure and Spectra**)
Energy States of Molecules (see **Molecular Structure and Spectra**)
Energy States of Nucleus (see **Nuclear Reactions; Nuclear Spectra; Nuclear Structure Theory**)
Equations of State (see **Chemical Effects and Properties**)
Errata
Capture-positron branching ratios, P. F. Zweifel—1871(E)
Co^{57} decay, L. Madansky and F. Rasetti—1870(E)
Effect of overlap on electrostatic lattice potentials in ionic crystals, Joseph L. Birman—1870(E)
Excitation function of $C^{12}(p,pn)C^{11}$ reaction in Bev region, R. L. Wolfgang and G. Friedlander—1870(E)
Expansion of Cu bombarded by 21-Mev deuterons, William R. McDonell and Henry A. Kierstead—1870(E)
In^{117} and Sb^{117} radioactivity, Carl L. McGinnis—1870(E)
Polarization of nucleons elastically scattered from nuclei, R. M. Sternheimer—1156(A); 1870(E)
Possible triple-scattering experiments, L. Wolfenstein—1870(E)

Radiative corrections to muon decay, R. J. Finkelstein and R. E. Behrends—1155(A); 1870(E)
Self-diffusion in Cu, A. Kuper, H. Letaw, Jr., L. Slifkin, E. Sonder, and C. T. Tomizuka—1870(E)
Errors of Measurement (see **Methods and Instruments**)
Evaporation (see **Liquids**)
Excitation of Atoms (see **Atomic Structure and Spectra**)
Excitation of Molecules (see **Molecular Structure and Spectra**)
Excitation of Nucleus (see **Nuclear Reactions; Nuclear Spectra; Nuclear Structure Theory**)
Explosion Phenomena (see **Fluid Dynamics**)

Faraday Effect (see **Optical Properties**)
Ferroelectric Phenomena (see **Dielectrics and Dielectric Properties**)
Ferromagnetism (see **Magnetic Properties**)
Field Emission (see **Electrical Properties**)
Field Theory (see also **Quantum Electrodynamics**)
Classical field theory of nuclear forces, M. H. Johnson and E. Teller—783
Configuration space methods in relativistic quantum field theory. I, A. S. Wightman and S. S. Schweber—812
Conservation of heavy particles and generalized gauge transformation, T. D. Lee and C. N. Yang—1501
Construction of noncentral potentials from *S*-matrix, Roger G. Newton and Res Jost—1189(A)
Covariant formalism describing polarization of spin one-half particles, L. Michel and A. S. Wightman—1190(A)
Decomposition of generalized Duffin-Kemmer algebra, K. M. Case—1189(A)
Effect of renormalization on meson-nucleon *S*-scattering, Maurice M. Lévy—1470
Emission of negative-energy gravitons by matter, F. J. Belinfante—1175(A)
Exchange current effects in two-nucleon system, J. Bernstein and Abraham Klein—1155(A)
Integral equations of meson-nucleon system, R. L. Mills—1156(A)
Lagrangians linear in "velocities," Ezra Newman and Peter G. Bergmann—1176(A)
Lattice space quantization of coupled meson and nucleon fields, D. H. Holland—788; 273(A)
Meson pair theory, Abraham Klein and Bruce H. McCormick—1428; 1155(A)
New approximation method for gravitational field equations, J. N. Goldberg—1175(A)
New relativistic two-body equation, Vladimir Glaser—840(L)
Nonrelativistic interaction between two nucleons, David Feldman—1456
Nonrelativistic limit of spin $(k+\frac{1}{2})$ particle wave equations, P. A. Moldauer and K. M. Case—1190(A)
Pion-nucleon *s*-wave phase shift from *ps-ps* with cutoff, Charles J. Goebel—273(A)
Possible convergence of mass renormalization, T. A. Welton—1175(A)
Projection operator for Rarita-Schwinger equation, F. J. Milford—1481
Quantized linear theory of gravitation, F. J. Belinfante and J. C. Swihart—222(A)
Radiative corrections to muon decay, R. J. Finkelstein and R. E. Behrends—1155(A); 1870(E)
Self-energy effects on meson-nucleon scattering according to Tamm-Dancoff method, J. C. Taylor—201(L)
Spin models, David Finkelstein—1175(A)
3-body exchange magnetic moments of H^3 and He^3, Andrew M. Lockett—1204(A)
Transformations in phase space and Dirac brackets, Peter G. Bergmann and Irwin Goldberg—1175(A)

Films, Properties
Annealing kinetics of lattice defects in evaporated Cu films, Ned S. Rasor—1555(A)
Crystal growth, and electrical and optical properties of gray Sn, J. H. Becker—1192(A)
Electrical and optical properties of GaSb films, R. J. Collins, F. W. Reynolds, and G. R. Stilwell—227(A)
Localized photoconductivity in PbS films, David Dutton—1549(A)
Magnetization reversal in thin films, R. L. Conger—1752
Phase change on reflection from multilayer films, F. A. Jenkins and D. R. Speck—282(A)
Properties of CdS films deposited *in vacuo*, Arthur Bramley—246(A)
Rectification in thin films of PbS, M. Silver, R. S. Witte, and F. McCaffrey—270(A)
Structure of evaporated Cu films on Ti, R. E. Schlier—1555(A)
Vacuum deposition of magnetic alloy films, M. S. Blois, Jr.—281(A)
Fine Structure (see **Atomic Structure and Spectra**)
Fission of Nucleus (see **Nuclear Fission**)
Fluctuation Phenomena (see **Noise**)
Fluid Dynamics
Behavior of boundary layer in region of transition from laminar to turbulent flows, Jerome Persh—1144(A)
Blast from sphere of high-pressure gas, Harold L. Brode—1158(A)
Determination of transonic pressure drag on wedges by throat station method, Robert Wesley Truitt—1139(A)
Detonation in gas at low pressure, Arthur L. Bennett and Henry W. Wedaa—256(A)
Difference solution of shock diffraction problem, H. F. Ludloff and M. B. Friedman—1140(A)
Diffusion analogy for shocks interacting with thermal boundary layers, Wayland Griffith and Walker Bleakney—1143(A)
Effects of attenuating materials on detonation induction distances in gases, Marjorie W. Evans, Frank I. Given, and William E. Richeson, Jr.—256(A)
Equilibrium turbulent flow in slightly divergent channel, J. R. Ruetenik and S. Corrsin—1142(A)
Experimental study of shock wave turbulence interaction, Leslie S. G. Kovasznay—1141(A)
Flow near leading edge of flat plate, J. A. Laurman and S. A. Schaaf—1540(A)
Growth, coalescence, and decay of vortices in jet accompanying Pfeifentone, A. B. C. Anderson—256(A)
Internal finite gravity waves in stratified fluid, Robert R. Long—1144(A)
Laminar free convection from vertical surfaces for prescribed variations of (1) wall heat transfer rate, or (2) of wall temperature, E. M. Sparrow—1140(A)
Mach number and yaw angle determination for conical flow regimes using two surface-flow angle indicators, H. S. Sicinski and H. F. Schulte—1140(A)
Mass flow in shock tube, Albert C. Williams and Raymond J. Emrich—1158(A)
Metallic deposits and shock waves due to electrically "exploded" wires, Willi M. Conn—1551(A)
Method for numerical solution of transient hydrodynamic shock problems in two space dimensions, Harwood G. Kolsky—1158(A)
Method for observation of ionization profile behind explosive-produced shocks in air, Jacob Savitt—1158(A)
Minimum drag bodies of revolution in nonuniform supersonic flow field, Conrad Rennemann, Jr.—1140(A)
Momentum transfer and heat diffusion in mixing of coaxial turbulent jets, Y. V. G. Acharya—1142(A)

Fluid Dynamics (Continued)
Motion in boundary layer over flat plate with sudden change of speed, C. C. Lin—1143(A)
New fundamentals of fluid dynamics, M. Z. v. Krzywoblocki—251(A)
Physical theory for capillary flow, E. E. Miller—251(A)
Pressure variation in shock tube flow, Raymond J. Emrich and Robert L. Peterson—1141(A)
Production of vorticity in isotropic turbulence, R. Betchov —1142(A)
Quantitative fluid flow visualization with streaming birefringence, Harold Wayland—255(A)
Recombination in argon shock front, John W. Bond, Jr.—285(A)
Reflection of acoustical pressure pulse from liquid-solid plane boundary, T. W. Spencer—1540(A)
Refraction of shock waves at gaseous interface, Robert G. Jahn—1141(A)
Relations between one- and three-dimensional functions in isotropic turbulence and direct measurement of energy transfer function, Francis R. Hama—1142(A)
Schlieren studies of flow behind strong shocks, W. Smith, H. Glick, A. Hertzberg, and W. Squire—1141(A)
Shock front structure in argon, John W. Bond, Jr.—256(A)
Shock waves in air produced by waves in plate, William A. Allen, Joe M. Mapes, and Earle B. Mayfield—256(A)
Stability of vortex streets with consideration of diffusion of vorticity of individual vortices, Ulrich Domm and Hermann Foettinger—1142(A)
Statistical theory of shear turbulence in parallel flow, C. M. Tchen—1158(A)
Thermal expansion and aerodynamic stability of open flames, Hans M. Cassel—1143(A)
Transverse curvature effect in compressible axially symmetric laminar boundary layer flow, Ronald F. Probstein and David Elliott—1143(A)
Unsteady viscous flow in vicinity of stagnation point, N. Rott—1144(A)
Velocity and pressure distributions in turbulent pipe flow with uniform wall suction, H. L. Weissberg and A. S. Berman—1540(A)
Velocity and temperature fluctuations behind hot grid, S. Corrsin, A. L. Kistler, and V. O'Brien—1142(A)
Velocity of explosively-induced shock in steel, Samuel Katz—256(A)
Vortex created by shock passing over vertical wall, David L. Matthews—1140(A)
Vortices produced by shocks, Louis N. Howard—1141(A)
Wave propagation in elastic tubes filled with streaming, viscous liquid, G. W. Morgan—1157(A)
Fluorescence (see **Luminescence**)
Friction (see **Mechanics**)

Galvanomagnetic Effect (see **Magnetic Properties**)
Gamma Rays (see also **Nuclear Reactions; Nuclear Spectra; Range and Energy Loss**)
Angular correlation of photons from positron annihilation in light metals, A. T. Stewart and R. E. Green—232(A); R. E. Green and A. T. Stewart—486
Elastic scattering of 0.41 and 0.66 Mev γ rays by Sn and Pb, A. K. Mann—234(A)
Elastic scattering of 1.6-Mev γ rays from C, Luis W. Alvarez, Frank S. Crawford, Jr., and M. Lynn Stevenson—280(A)
Ionization of air by γ rays, E. L. Burkhard and J. H. Lewis—1154(A)
Scattering of 100-Mev γ rays from C, D. M. Ritson, A. Pevsner, and R. L. Zimmerman—1168(A)

Gases
Adsorption of H_2 and O_2 on Ge, R. M. Burger, H. E. Farnsworth, and R. E. Schlier—1179(A)
Adsorption of O_2 and N_2 by Ti, T. H. George, H. E. Farnsworth, and R. E. Schlier—1179(A)
Departure from Paschen's law of breakdown in gases, W. S. Boyle and P. Kisliuk—560(A)
Effect of mean free path variation on high frequency breakdown, I. A. MacLennan and A. D. MacDonald—559(A)
Inertial effects and dielectric relaxation, E. P. Gross—1191(A)
Symmetry effects in gas kinetics. I. He isotopes, O. Halpern and R. A. Buckingham—1626
Geophysics
Branching ratio of K^{40} and age of meteorites, G. J. Wasserburg and R. J. Hayden—250(A)
Cyclical variations in effective radiation temperature of ozone region, Arthur Adel—282(A)
Dissociation of O_2 in upper atmosphere, E. T. Byram, T. A. Chubb, and H. Friedman—1594
Potassium-argon ages of lepidolites, G. W. Wetherill, L. T. Aldrich, and G. L. Davis—250(A)
Resonance absorption of sunlight in twilight layers, T. M. Donahue and Robert Resnick—1622
Glasses (see **Molecular Aggregates**)
Gravitation (see **Relativity and Gravitation**)
Gyromagnetization (see **Magnetic Properties**)

Hall Effect (see **Electrical Conductivity and Resistance**)
Heat Capacity (see **Thermal Properties**)
Heat Conduction (see **Thermal Properties**)
Heat of Dissociation and Formation (see **Molecular Structure and Spectra**)
Heat of Fusion (see **Thermal Properties**)
Heat of Vaporization (see **Thermal Properties**)
Helium, Liquid
"Closed" fountain effect and compressibility of He II, H. Forstat and C. A. Reynolds—1196(A)
Comparison of energy excitations in liquid He^3 and He^4, O. Rice—847
Dependence of transfer rates of He II film on film length, P. J. Fleming, J. H. Werntz, Jr., and J. R. Dillinger —1196(A)
Effect of centrifugal field upon rate of transfer through He II film, J. W. Beams—1138(L)
Feynman's atomic theory of liquid He, George J. Yevick and Jerome K. Percus—1164(A)
He II film transport. I. Role of substrate, Bernard Smith and Henry A. Boorse—328
Heat capacity and entropy of liquid He^3 from 0.23 to 2°K: Nuclear alignment in liquid He^3, Bernard M. Abraham, Darrell W. Osborne, and Bernard Weinstock—551(L)
Heat transport and boundary layer resistance in He II below 1°K, Henry A. Fairbank and J. Wilks—1196(A)
Pressure-volume isotherms of He^3 between 1.5 and 3.8°K, William E. Keller—1571
Second sound attenuation in rotating He II, C. T. Lane, R. G. Wheeler, and C. H. Blakewood—1196(A)
Slope of λ curve of liquid He, K. R. Atkins—319
Slow neutron scattering by liquid He, D. G. Hurst and D. G. Henshaw—224(A)
Spatial distribution of atoms in liquid He^4, Louis Goldstein and James Reekie—857
Specific heat of $He^3 - He^4$ solutions, P. J. Price and P. B. Linhart—243(A)
Superfluidity and heat transport in unsaturated He-II film, Earl Long and Lothar Meyer—1616
Superfluidity in liquid He^3, M. J. Buckingham—1855(L)
Surface tension of He^3, D. R. Lovejoy—1196(A)

Symmetry effects in gas kinetics. I. He isotopes, O. Halpern and R. A. Buckingham—1626
Thermodynamic properties of liquid He^3. I. Specific heat and entropy, Thomas R. Roberts and Stephen G. Sydoriak—1672

High-Voltage Tubes and Machines (see **Methods and Instruments**)

Hydrodynamics (see **Fluid Dynamics**)

Hyperfine Structure (see **Atomic Structure and Spectra; Molecular Structure and Spectra; Nuclear Moments and Spin**)

Imperfections in Solids (see also **Crystalline State; Electrical Conductivity and Resistance; Luminescence; Semiconductors**)
Ag halide phosphors, Frank Moser and Franz Urbach—1557(A)
Annealing kinetics of lattice defects in evaporated Cu films, Ned S. Rasor—1555(A)
Changes in KCl lattice dimensions by soft x-rays, Chester R. Berry—1540(A); 934
Conductivity of Teflon and polyethylene during γ irradiation, R. A. Meyer and F. L. Boquet—1531(A)
Creation of potential difference across NaCl crystals by deformation, D. B. Fischbach and A. S. Nowick—1543(A)
Detection of vacancies created in NaCl by x-rays, H. W. Etzel—1531(A)
Determination of dislocation densities with double crystal spectrometer, A. D. Kurtz, S. A. Julin, and B. L. Averbach—1543(A)
Diffusion of Cu and Zn in ordered and disordered CuZn, Alan B. Kuper and Carl T. Tomizuka—244(A)
Dislocation line energy and slip in NaCl and AgCl crystals, Robb Thomson—1171(A)
Dislocation model of liquids, Jerome Rothstein—1157(A)
Dislocation relaxations at low temperatures and determination of limiting shearing stress of metal, W. P. Mason—1136(L)
Disordering of polyatomic solids by neutrons, E. G. Harris—1151(A)
Donor impurities in graphite, G. Hennig and M. Dzurus—227(A)
Effect of Br on dark conductivity of AgBr and its relation to photoconductivity, George W. Luckey—1558(A)
Effect of cold work on local order, B. L. Averbach and P. S. Rudman—1554(A)
Effect of dislocations on recombination of holes and electrons in Ge and Si, S. A. Kulin, A. D. Kurtz, and B. L. Averbach—1566(A)
Effect of O_2 gas on photoconductivity of BaO, M. Sakamoto, S. Kobayashi, and S. Ishii—552(L)
Effect of plastic deformation on electrical conductivity of AgBr, William G. Johnston—1777
Effect of quench on structure of Au, Monroe S. Wechsler—245(A)
Effect of quenching and neutron irradiation on atomic mobility in Cu-Al alloy, Chi Yao Li and A. S. Nowick—1531(A)
Effect of vacancies and interstitials on electrical properties of Cu, F. J. Blatt—245(A)
Elastic modulus of x-irradiated rock salt, R. B. Gordon and A. S. Nowick—1540(A)
Electrical characteristics of grain boundaries, H. F. Matare, H. Kedesdy, A. MacDonald, and A. Petersen—1179(A)
Electrical properties of electron-bombarded Ge, E. E. Klontz, R. R. Pepper, and K. Lark-Horovitz—1535(A)
Electron spin resonance in irradiated alkali halides, A. M. Portis and D. Shaltiel—264(A)
Electron voltaic study of electron bombardment damage and its thresholds in Ge and Si, J. J. Loferski and P. Rappaport—1861(L)
Energy dependence of radiation effects in solids, E. Pearlstein, H. Ingham, and R. Smoluchowski—1530(A)
Energy requirement for *F*-center formation, R. S. Alger and R. D. Jordan—1550(A)
Expansion of Cu bombarded by 19-Mev deuterons, Henry A. Kierstead—245(A)
Expansion of Cu bombarded by 21-Mev deuterons, William R. McDonell and Henry A. Kierstead—1870(E)
Experimental evidence for thermal spikes in radiation damage, W. Primak—1854(L)
Fast-neutron bombardment of *n*-type Ge, J. W. Cleland, J. H. Crawford, Jr., and J. C. Pigg—1742
Formation energy of lattice vacancies in Au, J. W. Kauffman and J. S. Koehler—245(A)
Generation of electron traps by plastic flow, Werner Känzig and Masayasu Ueta—236(A)
Heat treatment of irradiated NaN_3, Russell W. Dreyfus and Paul W. Levy—1541(A)
Impurity-induced color centers in fused silica, Alvin J. Cohen—1550(A)
Internal friction as function of cold work of Cu reeds at low frequencies, J. J. Brady, M. B. Larson, and T. A. O'Halloran—271(A)
Interpretation of dimensional changes on dezincification of α brass, David D. Van Horn and William J. Cooley—245(A)
Isothermal anneal study of quenched and cold-worked Cu-Pd alloys, A. Sawatzky and F. E. Jaumot, Jr.—1555(A)
Lattice defects in Si, Sumner Mayburg—1177(A)
Lattice resistance to dislocation motion at high velocity, Edward W. Hart—1775
Long-wavelength neutron transmission as absolute method for determining concentration of lattice defects in crystals, J. J. Antal, R. J. Weiss, and G. J. Dienes—1541(A)
Magnetic susceptibility of fast neutron bombarded crystalline quartz, D. K. Stevens—1541(A)
Mechanism of grain boundary relaxation in metals and alloys, A. S. Nowick and Chi Yao Li—1556(A)
Model for luminescence and photoconductivity in sulfides, John Lambe and Clifford C. Klick—909
Model for room temperature bleaching of *F* centers by *F* light in x-rayed NaCl, Robert Herman and R. F. Wallis—1171(A)
Neutron irradiation effects in Cu and Al at 80°K, A. W. McReynolds, W. Augustyniak, Marilyn McKeown, and D. B. Rosenblatt—418
Optical absorption bands induced in γ-irradiated glass, K. R. Ferguson—1542(A)
Optical absorption measurements on Ag halide crystals, Nelson R. Nail, Frank Moser, Pliny E. Goddard, and Franz Urbach—1557(A)
Optical and electrical properties of LiF x-rayed at liquid nitrogen temperature, C. J. Delbecq, P. Pringsheim, and P. H. Yuster—237(A)
Order-disorder and ionic conductivity in Ag_2HgI_4, Jerome Rothstein—271(A)
Photoconductivity in KI, Nicolas Inchauspé—1550(A)
Photoconductivity of electron-bombarded Ge, F. Stoeckmann, E. Klontz, H. Y. Fan, and K. Lark-Horovitz—1535(A)
Photoelastic observation of expansion of alkali halides in irradiation, W. Primak, P. H. Yuster, and C. J. Delbecq—237(A); W. Primak, C. J. Delbecq, and P. H. Yuster—1708
Polytypism and dislocations, N. Cabrera and M. M. Levine—1543(A)

Imperfections in Solids (Continued)
Prismatic slip in crystals, J. W. Davisson, Elias Burstein, and P. L. Smith—1544(A)
Radiation effects in solids produced by nuclear disintegrations, R. Smoluchowski, E. Pearlstein, and H. Ingham —1530(A)
Radiation-induced coloring of NaN_3, Hyman Rosenwasser and Paul W. Levy—1541(A)
Reactor- and γ-ray-induced coloring in Corning fused silica, Paul W. Levy—1541(A)
Recombination of injected carriers at dislocation edges in semiconductors, J. P. McKelvey and R. L. Longini—1566(A)
Relationship between small-angle dislocation boundaries and creep, Betsy Ancker, Thomas H. Hazlett, and Earl R. Parker—1151(A)
Relaxation of monatomic crystal lattice around vacancy, Stefan Machlup—1556(A)
Resistivity due to point imperfections in Cu, F. J. Blatt, M. C. Huse, and R. A. Rubenstein—1553(A)
Ring diffusion as mechanism of self-diffusion in Ge, Sumner Mayburg—1134(L)
Shear modulus recovery of electron-irradiated Cu, H. Dieckamp—1531(A)
Smakula's equation in insulating solids, D. L. Dexter—1560(A)
Source of disordering of alloys during irradiation, F. Seitz —1530(A)
Spin resonance in neutron-irradiated Si, E. Schulz-DuBois, M. Nisenoff, H. Y. Fan, and K. Lark-Horovitz—1561(A)
Storage of energy in BeO, C. E. Mandeville and H. O. Albrecht—1546(A)
Susceptibility and entropy of *F*-centers, J. G. Daunt and J. Korringa—1550(A)
Theory of radiation damage, W. A. Harrison and Frederick Seitz—1530(A)
Theory of steady-state creep based on dislocation climb, J. Weertman—246(A)
Thermal bleaching of color centers, A. Halperin and A. Braner—1135(L)
Thermal formation of colloids from *F*-centers in KCl crystals, H. Pagnia and F. Stockman—236(A)
Thermal ionization of interstitials in cubic ZnS, H. D. Vasileff—237
X-ray measurements on low-temperature neutron-irradiated graphite, David T. Keating—1859(L)
X-ray scattering effects in irradiated boron carbide, C. W. Tucker, Jr., and P. Senio—1541(A)
Inelastic Scattering (see **Nuclear Reactions; Scattering**)
Instruments (see **Methods and Instruments**)
Internal Conversion (see **Nuclear Spectra**)
Ionization (see also **Electrical Discharges; Range and Energy Loss of Particles**)
Cumulative ionization processes in He positive column, L. S. Frost and A. V. Phelps—559(A)
Electron loss cross sections of moving He atoms, Sol Krasner and J. Cuevas—1149(A)
Energy required to produce one ion pair for several gases, J. Weiss and W. Bernstein—1828
High-frequency ionization coefficients in Ne-A mixtures, A. D. MacDonald and J. H. Matthews—1070
Ionization accompanying long-lived nitrogen afterglow, W. B. Kunkel and A. L. Gardner—558(A)
Ionization loss in nuclear emulsions, John R. Fleming and J. J. Lord—268(A)
Ionization of air by γ rays, E. L. Burkhard and J. H. Lewis—1154(A)
Measurement of absorption coefficients for photoionizing radiations in low-pressure gases with space charge detector, C. D. Maunsell—1831
Measurement of ionization yield of low-energy ions in gas, Ralph A. Lowry and Glenn H. Miller—243(A)
Method for observation of ionization profile behind explosive-produced shocks in air, Jacob Savitt—1158(A)
μ-meson ionization in argon at energies 10 to 100 Bev, Allan N. Wilson—268(A)
Photoionization by absorption in gas of radiations from discharge in same gas, C. D. Maunsell—263(A)
Photoionization cross sections of CO_2, A, H_2 and H_2O, N. Wainfan, W. C. Walker, and G. L. Weissler—561(A)
Redetermination of ionization coefficient n for hydrogen, D. J. Rose—558(A)
Specific ionization of high-energy electrons, W. C. Barber —276(A)
Theory of cavity ionization, L. V. Spencer and F. H. Attix—233(A)
Ionization Potentials of Atoms (see **Atomic Structure and Spectra**)
Ionization Potentials of Molecules (see **Molecular Structure and Spectra**)
Ionosphere (see **Geophysics**)
Ions (see also **Electrical Discharges**)
Analysis of electron stripping data, Robert L. Gluckstern —276(A)
Charge distributions of O and Ne ions passing through gases, Edward L. Hubbard and Eugene J. Lauer—1814
Charge states of H ions in gases, P. M. Stier, C. F. Barnett, R. A. Howard, and W. Bugg—1149(A)
Comparison of energy to make ion-pair in various gases for α and β particles, William P. Jesse and John Sadauskis—1150(A)
Cross section measurements for large angle collisions of He, Ne, and A ions with argon gas atoms at energies from 25–100 kev, Robert J. Carbone, Gerald Stone, and Edgar Everhart—1150(A)
Cross sections for electron capture and loss by 26-Mev N ions, A. Zucker, H. L. Reynolds, and L. D. Wyly—1150(A); 1825
Differential cross-section measurements for large-angle collisions of He, Ne, and A ions with A atoms at energies to 100 kev, Edgar Everhart, R. J. Carbone, and Gerald Stone—1045
Double electron capture by α particles in He, D. D. Betts and J. D. Jackson—1149(A)
Ejection of electrons from contaminated metals by positive ions, Homer D. Hagstrum—561(A)
Electron capture and loss by ions in gases, Robert L. Gluckstern—1817
Electron capture cross section for protons, C. F. Barnett and P. M. Stier—1537(A)
Equilibrium charge distribution of energetic N ions, H. L. Reynolds, L. D. Wyly, and A. Zucker—474; 242(A)
Experimental cross section for photodetachment of electrons from H^- and D^-, Lewis M. Branscomb and Stephen J. Smith—1028
Influence of space charge on potential distribution in mass spectrometer ion sources, W. M. Brubaker—563(A)
Measurement of ionization yield of low-energy ions in gas, Ralph A. Lowry and Glenn H. Miller—243(A)
Measurements and collision theory of high vacuum sputtering, Frank Keywell—561(A)
Microwave study of positive ion collection by probes, George J. Schulz and Sanborn C. Brown—559(A)
Negative ion formation using monoenergetic electrons, W. M. Hickam and R. E. Fox—557(A)
Results of limitations on space current densities in galactic and intergalactic space, W. F. G. Swann—871; 1546(A)
Self-focusing streams, Willard H. Bennett—1584
Stark fields from ions in plasma, Arthur Broyles—1166(A)

Stripping electrons from accelerated O and Ne ions, Edward L. Hubbard and Eugene J. Lauer—276(A)
Theory of magnetic self-focusing, Willard H. Bennett—1169(A)
Validity criteria for calculating differential cross section for collisions of kev ions with atoms, Gerald Stone, Robert Carbone, and Edgar Everhart—1150(A)
Ions and Electrons, Mobility (see also **Semiconductors**)
Attempt to detect high mobility holes in Ge using drift mobility technique, N. J. Harrick—1131(L)
Electron mobility in AgCl: Comparison of experiment with theory, Frederick C. Brown—263(A)
Mobility of holes in Si and Ge, H. Ehrenreich and A. W. Overhauser—1533(A)
Mobility of slow electrons in polar crystals, Francis E. Low and David Pines—414
Isobars (see **Atomic Mass and Abundance**)
Isomers, Molecular (see **Molecular Structure and Spectra**)
Isomers, Nuclear (see **Nuclear Spectra**)
Isotopes (see **Atomic Mass and Abundance; Radioactivity**)

Kerr Effect (see **Optical Properties**)
Kinetic Theory of Gases (see **Gases**)

Liquid Helium (see **Helium, Liquid**)
Liquids
Dislocation model of liquids, Jerome Rothstein—1157(A)
Electrical conductivity of liquid Te, V. A. Johnson—1567(A)
Physical theory for capillary flow, E. E. Miller—251(A)
Secondary recrystallization analogy in heterogeneous liquid system, John P. Nielsen—1157(A)
Structure of liquid Te, R. Buschert, I. G. Geib, and K. Lark-Horovitz—1157(A)
Luminescence
Ag halide phosphors, Frank Moser and Franz Urbach—1557(A)
Alternative explanation of Waymouth-Bitter experiments, Laurence Burns—1863(L)
Dielectric dispersion in ZnS phosphors, I. Ames, H. S. Sack, and R. M. Wood—1545(A)
Edge electroluminescence from CdS crystals at low dc fields, R. W. Smith—1169(A)
Effect of temperature upon scintillation efficiency of NaI(Tl), L. A. Webb and R. F. Johnson—234(A)
Effects of electric fields on uv excited ZnS phosphors, Sol Nudelman and Frank Matossi—1545(A)
Electroluminescence excited with short field pulses, F. Matossi and S. Nudelman—238(A)
Electroluminescence in ZnS single crystals, D. R. Frankl—238(A)
Field-enhanced solid-state luminescence, D. A. Cusano—1169(A)
Influence of electric field on thermoluminescence of ZnS crystals, Gertrude Neumark—1546(A)
Light output from dielectric-imbedded electroluminescent phosphors, F. A. Schwertz and J. J. Mazenko—1169(A)
Low-temperature luminescence and absorption of CdS, L. R. Furlong and C. F. Ravilious—954
Low-temperature luminescence in KCl:Tl, D. A. Patterson and C. C. Klick—1546(A)
Magnetic properties of ZnS and CdS phosphors, Simon Larach and John Turkevich—1015
Model for luminescence and photoconductivity in sulfides, John Lambe and Clifford C. Klick—909; 1545(A)
Origin of luminescence in Cu-activated ZnS phosphors, Nathan T. Melamed and Raymond Bowers—1545(A)
Paramagnetic resonance spectrum of some doubly activated phosphors, W. Low—426
Polarization effects on brightness waves of electroluminescence, Frank Matossi—434; 1545(A)
Possibility of nuclear radiation detector by means of electroluminescent phosphors, W. Low—556(L)
Radiation-controlled electroluminescence and light amplification in phosphor films, D. A. Cusano—546(L)
Recombination processes in CdS, John Lambe—985
Response of anthracene and stilbene to low-energy protons and x-rays, J. M. Fowler and C. E. Roos—996
Response of anthracene to low-energy protons and He ions, E. J. Zimmerman—1153(A)
Scintillation studies on activated alkali halides, T. H. Anderson—281(A)
Stacked barriers in electroluminescent ZnS crystal, E. E. Loebner and H. Freund—1545(A)
Storage of energy in BeO, H. O. Albrecht and C. E. Mandeville—1546(A)
Temperature dependence of electroluminescence, Claus H. Haake—1544(A)
Temperature sensitivities of sensitized fluorescence spectrum of Th, Robert E. Swanson and Robert H. McFarland—1063
Theoretical basis for light-amplifying phosphors, Ferd E. Williams—547(L)
Theory of electroluminescence, Brian T. Howard—1544(A)
Theory of electroluminescence, W. W. Piper and F. E. Williams—1809
Time-average light output from electroluminescent phosphors, S. Nudelman and F. Matossi—238(A)
Voltage-dependence of electroluminescent brightness. I. Dielectric-imbedded phosphors, F. A. Schwertz, J. J. Mazenko, and E. R. Michalik—1133(L); II. Chemically-deposited phosphor films, F. A. Schwertz and R. E. Freund—1134(L)
X-ray-induced luminescence from air, William E. Spicer—1061

Magnetic Fields (see **Electromagnetic Theory and Electrodynamics**)
Magnetic Properties
Antiferromagnetism in Cr_2O_3 crystal, T. R. McGuire, E. J. Scott, and F. H. Grannis—1562(A)
Antiferromagnetism of Yb_2O_3 at liquid He temperatures, Warren E. Henry—226(A)
Calculation of g-factor of metallic Li, P. N. Argyres and A. H. Kahn—226(A)
Classical theory of temperature dependence of magnetic crystalline energy, Clarence Zener—225(A)
Diffuse magnetic neutron diffraction, A. W. McReynolds—1200(A)
Direct observation of domain rotation in ferrites, Fielding Brown and Charles L. Gravel—442
Domain configuration and crystallographic orientation in grain-oriented Fe-Si alloy—T. G. Nilan and W. S. Paxton—1200(A)
Domain patterns on rolled single crystal of Ni_3Fe, Sōshin Chikazumi and Kenzō Suzuki—1130(L)
Ferromagnetic Hall effect of Ni alloys, Albert I. Schindler—1199(A)
Ferromagnetic resonance in Ferroxdure, M. T. Weiss and P. W. Anderson—925
Galvanomagnetic effects in InSb, W. R. Hosler and H. P. R. Frederikse—1532(A)
Hall effect and magnetoresistance oscillations of Sb single crystals in magnetic fields at liquid He temperatures, M. C. Steele—1180(A)
Interaction between spin waves and conduction electrons in ferromagnetic metals, Elihu Abrahams—387
Ionic distribution in Mg ferrite, C. J. Kriessman, S. E. Harrison, and H. B. Callen—1562(A)

Magnetic Properties (Continued)
Linear magnetostriction of some ternary Co-Fe-Ni alloys, H. E. Stauss and G. Sandoz—271(A)
Magnetic and thermal properties of $MnCl_3$ at liquid He temperatures, R. B. Murray and L. D. Roberts—1180(A)
Magnetic and thermal properties of UI_3 at liquid He temperatures, L. D. Roberts and R. B. Murray—1180(A)
Magnetic coercive force in alloys of Fe and N, J. Kerr and C. Wert—225(A)
Magnetic domain patterns observed by Kerr effect in BiMn alloy, B. W. Roberts and C. P. Bean—225(A)
Magnetic domains in single crystal of Co near 275°C by longitudinal Kerr effect, Edward M. Fryer and Charles A. Fowler, Jr.—270(A)
Magnetic moment of Fermi-Dirac gas, A. W. Saenz and R. C. O'Rourke—1166(A)
Magnetic moment of free electrons, D. J. Besdin and Joseph H. Robinson III—272(A)
Magnetic properties of ZnS and CdS phosphors, Simon Larach and John Turkevich—1015
Magnetic resonance in ferrimagnetic containing arbitrary number of sublattices, Roald K. Wangsness—1200(A)
Magnetic rotation phenomena in polycrystalline ferrite. II, David Park—438
Magnetic scattering of slow neutrons by gaseous oxygen, H. Palevsky and R. M. Eisberg—492
Magnetic susceptibility in InSb, J. H. Crawford, Jr., and D. K. Stevens—1532(A)
Magnetic susceptibility in Zn ferrite, A. Arrott and J. E. Goldman—1201(A)
Magnetic susceptibility measurements by nuclear magnetic resonance, M. P. Klein and B. E. Holder—265(A)
Magnetic susceptibility of α-Mn at low temperatures, A. Arrott, B. R. Coles, and J. E. Goldman—1864(L)
Magnetic susceptibility of fast-neutron-bombarded crystalline quartz, D. K. Stevens—1541(A)
Magnetic susceptibility of Hf and Mn, C. J. Kriessman and T. R. McGuire—936
Magnetic transformation in MnBi, R. R. Heikes—1199(A)
Magnetization reversal in thin films, R. L. Conger—1752
Multiple resonances in Co ferrite, P. E. Tannenwald and H. J. Zeiger—1562(A)
Multiple scattering of slow neutrons by flat specimens and magnetic scattering by Zn ferrite, B. N. Brockhouse, L. M. Corliss, and J. M. Hastings—1721
Oscillatory Hall effect and magnetoresistance of Bi, Jules A. Marcus—1540(A)
Oscillatory Hall effect, magnetoresistance, and magnetic susceptibility of graphite single crystal, Ted G. Berlincourt and M. C. Steele—227(A); 956
Oscillatory thermomagnetic properties of Bi single crystal at liquid He temperatures, M. C. Steele and J. Babiskin—359
Paramagnetism observed at superconducting transition, Yoshio Shibuya and Seichi Tanuma—938
Pressure dependence of de Haas-van Alphen parameters in Bi crystal at 4.2°K, William C. Overton, Jr., and Ted G. Berlincourt—1180(A)
Rapid remagnetization of thin Mo permalloy tapes, T. L. Gilbert, J. M. Kelly, and H. Ekstein—1200(A)
Relation of magnetic structure to electrical conductivity in NiO and related compounds, R. R. Heikes—225(A)
Saturation magnetization and remanence of β-UH_3, Warren E. Henry and Dieter M. Gruen—1200(A)
Slow-neutron spectrometry—New tool for study of energy levels in condensed systems, B. N. Brockhouse—1171(A)
Specific heats of Zn ferrite and Zn chromite at low temperatures, S. A. Friedberg and D. L. Burk—1200(A)
Susceptibility and entropy of *F*-centers, J. G. Daunt and J. Korringa—1550(A)
Temperature dependence of magnetic susceptibility of carbons and polycrystalline graphites, P. Kiive and H. T. Pinnick—1564(A)
Temperature effects in ferrites at microwave frequencies, B. J. Duncan and L. Swern—1201(A)
Theory of ionic ordering, crystal distortion, and magnetic exchange due to covalent forces in spinels, J. B. Goodenough and A. L. Loeb—391
Theory of paramagnetic effect in superconductors, Hans Meissner—1539(A)
Magnetic Resonance (see also **Nuclear Moments and Spin**)
As^{75} pure quadrupole resonance, P. J. Bray and R. G. Barnes—1182(A)
Boltzmann theory of cyclotron resonance for warped spherical energy surfaces, H. J. Zeiger—1560(A)
Calculation of *g*-factor of metallic Li, P. N. Argyres and A. H. Kahn—226(A)
Collision alignment of molecules, atoms, and nuclei, Norman F. Ramsey—1853(L)
Cyclotron and spin resonance in InSb, G. Dresselhaus, A. F. Kip, C. Kittel, and G. Wagoner—556(L)
Cyclotron resonance of electrons and holes in Si and Ge crystals, G. Dresselhaus, A. F. Kip, and C. Kittel—368
Cyclotron resonances in Ge at 1.4°K, R. C. Fletcher, F. R. Merritt, and W. A. Yager—1560(A)
Diamagnetic resonance in electronic conductors, R. B. Dingle—550(L)
Diffusion model for nuclear precession relaxation in solids, E. L. Hahn and B. Herzog—265(A)
Direct measurement of nuclear spin-lattice relaxation time, J. L. Walsh, A. G. Berger, J. V. Rogers, and W. D. Knight—265(A)
Effective mass of carriers and relaxation time in Ge, F. D'Altroy and H. Y. Fan—1561(A)
Electric quadrupole interaction and spin echoes in crystals, T. P. Das and A. K. Saha—516
Electron spin resonance absorption in metals. I. Experimental, George Feher and A. F. Kip—337; II. Theory of electron diffusion and skin effect, Freeman J. Dyson—349
Electron spin resonance in frozen metal-ammonia solutions, G. Feher and R. A. Levy—264(A)
Electron spin resonance in irradiated alkali halides, A. M. Portis and D. Shaltiel—264(A)
Electron spin resonance in liquid alkali metals, R. A. Levy—264(A)
Ferromagnetic resonance in Ferroxdure, M. T. Weiss and P. W. Anderson—925
g factor of electron in 2*S* state of hydrogen, L. D. White—1194(A)
Hfs in paramagnetic resonance of V ions in solution, G. E. Pake and R. H. Sands—266(A)
Impurity effects on nuclear quadrupole spectrum of Cl^{35}, S. L. Segel and B. C. Lutz—1183(A)
Interaction between spin waves and conduction electrons in ferromagnetic metals, Elihu Abrahams—387
Isotope abundance ratios by nuclear magnetic resonance, B. E. Holder and M. P. Klein—265(A)
K^{39} nuclear magnetic moment, L. Carlton Brown and Dudley Williams—1537(A)
Magnetic hyperfine effects and electronic structure of NO, G. C. Dousmanis—1160(A)
Magnetic resonance for arbitrary field strengths, Roald K. Wangsness—927
Magnetic resonance in ferrimagnetic containing arbitrary number of sublattices, Roald K. Wangsness—1200(A)
Magnetic resonance properties of raw cokes, J. G. Castle, Jr.—1564(A)
Magnetic susceptibility measurements by nuclear magnetic resonance, M. P. Klein and B. E. Holder—265(A)
Matrix treatment of nuclear induction, E. T. Jaynes—1099

Microwave spectrum of CS, Richard C. Mockler and George R. Bird—1837
Molecular constants and nuclear-molecular interactions of Li^7F^{19} by molecular beam electric resonance method, R. Braunstein and J. W. Trischka—1092
Multiple resonances in Co ferrite, P. E. Tannenwald and H. J. Zeiger—1562(A)
Nuclear electric quadrupole moment of Na^{23} by atomic beam resonance method, M. L. Perl, I. I. Rabi, and B. Senitzky—611
Nuclear induction in inhomogeneous fields, Arnold L. Bloom—1105
Nuclear magnetic moments of Rh^{103} and W^{183}, P. B. Sogo and C. D. Jeffries—265(A)
Nuclear magnetic relaxation in natural and synthetic rubbers, E. M. Banas, B. A. Mrowca, and E. Guth—265(A)
Nuclear magnetic relaxation of nonuniform systems, S. Broersma—1182(A)
Nuclear magnetic resonance in semiconductors: Exchange broadening and line shapes, R. G. Shulman, J. M. Mays, and D. W. McCall—1182(A)
Nuclear magnetic resonance in semiconductors: GaSb and InSb, J. M. Mays, R. G. Shulman, and D. W. McCall—1182(A)
Nuclear magnetic resonance relaxation times for polyisobutylene in CCl_4 solution, A. W. Nolle—1560(A)
Nuclear magnetic resonance saturation in solids, Alfred G. Redfield—1787
Nuclear magnetic resonance spectra of annular samples, C. A. Reilly, H. M. McConnell, and R. G. Meisenheimer—264(A)
Nuclear resonance saturation in solids, Alfred G. Redfield—1182(A)
Nuclear spin and hfs interaction in 3.1-hr Cs^{134m}, D. A. Gilbert and Victor W. Cohen—1194(A)
Nuclear spin relaxation in alkali metals, D. F. Holcomb and R. E. Norberg—1074
Nuclear spin relaxation in alkali metals near their melting points, R. E. Norberg and D. F. Holcomb—226(A)
Nuclear spin-spin relaxation time in polymers, E. M. Banas and B. A. Mrowca—1548(A)
Orientation and alignment of Na atoms by means of polarized resonance radiation, William Bruce Hawkins—478
Overhauser effect in nonmetals, A. Abragam—1729
Overhauser nuclear polarization effect, W. A. Barker and A. Mencher—1868(L)
Overhauser nuclear polarization effect and minimum entropy production, Martin J. Klein—1736
Paramagnetic resonance absorption in glass, R. H. Sands—266(A)
Paramagnetic resonance of atomic phosphorus, H. G. Dehmelt—1181(A)
Paramagnetic resonance spectrum of some doubly activated phosphors, W. Low—426
Proton magnetic resonance in polyamides, W. P. Slichter and J. M. Mays—1559(A)
Pure quadrupole resonances in Sb and Bi compounds, R. G. Barnes and P. J. Bray—1182(A)
Quadrupolar splitting of nuclear resonance lines in alums, W. G. Segelken and H. C. Torrey—1537(A)
Quantized spin paramagnetism in free radical near magnetic saturation, Warren E. Henry—252(A)
Quantum theory of cyclotron resonance for degenerate bands, J. M. Luttinger—1560(A)
Rb^{85} and Rb^{87} quadrupole moments, B. Senitzky, I. I. Rabi, and M. L. Perl—1537(A)
Relaxation time modification by double nuclear resonance, B. Herzog and E. L. Hahn—226(A)
Saturation of nuclear electric quadrupole energy levels by ultrasonic excitation, W. G. Proctor and W. H. Tanttila—1854(L)
Spin echo serial storage memory, A. G. Anderson, R. L. Garwin, E. L. Hahn, J. W. Horton, G. L. Tucker, and R. M. Walker—283(A)
Spin echoes with four pulses—extension to n pulses, T. P. Das and D. K. Roy—525
Spin-lattice relaxation time of Si^{29} nucleus in pure fused silica, G. R. Holzman, John H. Anderson, and W. Koth—542(L)
Spin resonance in neutron-irradiated Si, E. Schulz-DuBois, M. Nisenoff, H. Y. Fan, and K. Lark-Horovitz—1561(A)
Spin resonance widths of electrons in donor states in Si, W. Kohn—1178(A)
Strong crystal field theory of magnetic resonance for d^9 configurations, C. M. Herzfeld—226(A)
Temperature effect of paramagnetic line shape, E. P. Gross—1561(A)
Temperature effects in ferrites at microwave frequencies, B. J. Duncan and L. Swern—1201(A)
Third harmonic cyclotron resonance of holes in Ge, R. N. Dexter—1560(A)

Magneto-Optical Effects (see **Optical Properties**)
Magnetoresistance (see **Electrical Conductivity and Resistance; Semiconductors**)
Magnetostriction (see **Magnetic Properties**)
Mass Defects (see **Atomic Mass and Abundance**)
Mass Spectroscopy (see **Atomic Mass and Abundance; Methods and Instruments**)
Mathematical Methods
Decomposition of generalized Duffin-Kemmer algebra, K. M. Case—1189(A)
Determination of scattering potential from spectral weight function, I. Kay and H. E. Moses—1190(A)
Formulation of probability theory as physical theory, A. O. Barut—274(A)
Generation of Coulomb wave functions by means of recurrence relations, Irene A. Stegun and Milton Abramowitz—1851
Joint probabilities and transition probabilities in differential-space quantum theory, Norbert Wiener and Armand Siegel—1190(A)
Problem in shower theory—"Approximation A," R. C. O'Rourke—1190(A)
Random walk methods in statistical mechanics of one-dimensional systems, R. L. Sells, C. W. Harris, and E. Guth—272(A)

Measurements (see **Methods and Instruments**)
Mechanics
Dynamical friction, R. Riddell, Jr., M. Newman, and S. Gasiorowicz—257(A)
Force—its nature, structure, and generation (creation) (as disclosed by $f \times t = m$), Lucien V. Alexis, Sr.—1176(A)
Modified Holtzmark distribution, S. Gasiorowicz—257(A)
New extension of collective coordinates for many-body problem, Jerome K. Percus and George J. Yevick—1164(A)

Mechanics, Quantum—Atomic Structure and Spectra (see **Atomic Structure and Spectra**)
Mechanics, Quantum—General (see **Quantum Mechanics**)
Mechanics, Quantum—Molecular Structure and Spectra (see **Molecular Structure and Spectra**)
Mechanics, Quantum—Nuclear (see **Nuclear Structure Theory**)
Mechanics, Quantum—of Solid Bodies (see **Crystalline State**)
Mechanics, Statistical (see **Statistical Mechanics and Thermodynamics**)
Meson Field Theory (see **Field Theory**)

Mesons and Hyperons (see also **Cosmic Radiation; Elementary Particle Interactions; Nuclear Reactions Induced by Mesons; Scattering of Mesons**)

Analysis of charged V events, W. H. Arnold, J. Ballam, A. L. Hodson, R. Ronald Rau, George T. Reynolds, S. B. Treiman, and V. A. Van Lint—275(A); W. H. Arnold and J. Ballam—1204(A)

Angular distribution of pions from θ^0 decay, R. M. Sternheimer—205(L)

Capture of negative K mesons, J. Hornbostel and E. O. Salant—218(L)

Charged pion production in n-p collisions, Gaurang B. Yodh—268(A)

Charged V particle production in p-p collision, M. M. Block, E. M. Harth, W. B. Fowler, R. P. Shutt, A. M. Thorndike, and W. L. Whittemore—248(A)

Chi meson produced by 3-Bev protons, R. D. Hill, E. O. Salant, and M. Widgoff—247(A)

Conservation of parity and new particles, R. Utiyama and W. Tobocman—780

Correlation of planes in V-particle decay events, V. A. J. Van Lint, George T. Reynolds, S. B. Treiman, and F. H. Tenny—1203(A)

Cosmic-ray observations of $K^{\pm}$ mesons, N. Seeman, M. M. Shapiro, and B. Stiller—1202(A)

Delayed disintegration of nuclear fragments, W. F. Fry, J. Schneps, and M. S. Swami—247(A)

Diffusion cloud-chamber study of very slow mesons. I. Internal pair formation, C. P. Sargent, R. Cornelius, M. Rinehart, L. M. Lederman, and K. Rogers—1349

Effect of anomalous nucleon magnetic moment on π^0 lifetime, Stanley Cohen—749

Effect of extended size of nucleus on μ-meson pair photoproduction, George Rawitscher—272(A)

Elastic photoproduction of π^0 mesons for He, E. L. Goldwasser, L. J. Koester, and F. E. Mills—239(A)

Electron spectrum from muon decay, H. J. Bramson—1187(A)

Energy levels of π-mesonic atoms, K. A. Brueckner—769

Evidence for charge asymmetry of $V^{\pm}$ particles, Y. B. Kim, J. R. Burwell, R. W. Huggett, and R. W. Thompson—248(A)

Evidence for γ rays from hyperons or heavy mesons produced by cosmotron protons, S. L. Ridgway and George B. Collins—247(A)

Evidence for pion-pion interaction, W. G. Holladay and R. G. Sachs—1155(A)

Example of cascade decay of negative hyperon, W. H. Arnold, J. Ballam, G. K. Lindeberg, and V. A. J. Van Lint—838(L)

Heavy meson and hyperon production at Bevatron, Gerson Goldhaber, W. W. Shupp, S. J. Goldsack, J. Lannutti, and F. Webb—267(A)

Heavy mesons and hyperons from targets bombarded by 4.8- and 5.7-Bev protons, S. Goldhaber, Gerson Goldhaber, H. H. Heckman, and F. M. Smith—1203(A)

Heavy unstable particles from captured K^- mesons, J. Hornbostel and E. O. Salant—1202(A)

Identity of shower particles in stars in region 1–2 × minimum ionization, E. Pickup and A. Husain—247(A)

Internal pair production associated with emission of high-energy γ rays, Norman M. Kroll and Walter Wada—1355

K mesons produced by 2.2- and 3-Bev protons, G. G. Harris—1202(A)

$\Lambda^0 - \theta^0$ production in $\pi^- - p$ collisions at 1 Bev, W. D. Walker—1407

Low-energy photoproduction of π^0 mesons from H: Total cross section, F. E. Mills and L. J. Koester, Jr.—210(L)

Low-energy photoproduction of π^0 mesons in H: Differential cross sections at 135°, Louis J. Koester, Jr.—211(L)

Mass spectrum of shower particles from cosmic-ray interactions, A. Husain and E. Pickup—136

Measurement of Čerenkov radiation from positive and negative π mesons, J. R. Winckler, E. N. Mitchell, K. A. Anderson, and L. Peterson—1411

Measurements on K particles and their decay products, Gerson Goldhaber and Stephen J. Goldsack—1203(A)

Mesonic decay of ejected nuclear fragment, Herman Yagoda—153

μ-meson ionization in argon at energies 10 to 100 Bev, Allan N. Wilson—268(A)

Nature of neutral secondary particle produced in decay of $K_{\pi 2}$-meson, Herbert DeStaebler, Jr., and B. V. Sreekantan—1520(L)

Negative pions from neutron bombardment of deuterons, Myron W. Knapp and Wilson M. Powell—1188(A)

New evidence concerning specific identity of θ^0 decay fragments and statistics of θ^0 particle, J. R. Burwell, R. W. Huggett, and R. W. Thompson—247(A)

New examples of anomalous V^0 particles, R. W. Huggett, J. R. Burwell, and R. W. Thompson—248(A)

Nuclear absorption of fast charged hyperon, D. T. King and M. M. Block—1203(A)

Observations of K^+ mesons, Harry H. Heckman, S. Goldhaber, and F. M. Smith—1202(A)

Photomeson production from hydrogen, Bernard T. Feld—238(A)

Photomeson production from H, D, and C, Walter Dudziak, Ryokichi Sagane, and James Vedder—269(A)

Photoproduction of neutral mesons in H and D, H. H. Bingham, J. C. Keck, and A. V. Tollestrup—1187(A)

Photoproduction of π^+ mesons from H near threshold, J. E. Leiss, C. S. Robinson, and S. Penner—201(L); 1188(A)

Photoproduction of π^0 mesons in hydrogen, L. J. Koester—239(A)

π^- counting by delayed coincidence, K. M. Crowe, R. M. Friedman, and H. Motz—268(A)

π^+ photomeson production at 180°. Experimental arrangement, Gordon W. Repp, Mark J. Jakobson, and R. Stephen White—268(A); Experimental results, R. Stephen White, Mark J. Jakobson, and Gordon W. Repp—269(A)

π^0 photoproduction from protons and deuterium nucleons. I, R. M. Worlock and W. R. Smythe—269(A); II, W. R. Smythe and R. M. Worlock—269(A)

π^-/π^+ ratios in asymmetric nuclei, H. Motz, K. M. Crowe, and R. M. Friedman—268(A)

Pion-pair production in nuclear emulsion, Herman Yagoda—103; 1187(A)

Pion photoproduction ratios, D. C. Peaslee—239(A)

Pion production by electrons, W. K. H. Panofsky, C. M. Newton, and G. B. Yodh—751

Polarization effects in reaction $p + p \rightarrow \pi^+ + d$, L. Wolfenstein—766

Positron spectrum from decay of μ meson, Ryokichi Sagane, Walter Dudziak, and James Vedder—269(A)

Production of charged pions in n-p collisions, Gaurang B. Yodh—1330

Production of heavy unstable particles by 1.37-Bev pions, W. B. Fowler, R. P. Shutt, A. M. Thorndike, and W. L. Whittemore—121

Production of K mesons by protons of Cosmotron energy, Martin M. Block—1156(A)

Production of neutral V events in Pb by neutrons from Cosmotron, R. M. Walker, R. S. Preston, E. C. Fowler, and H. L. Kraybill—1203(A)

Production of unstable particles in C and Pb by 2-Bev pions, H. Blumenfeld, E. T. Booth, L. M. Lederman, and W. Chinowsky—1203(A)

Radiative corrections to muon decay, R. J. Finkelstein and R. E. Behrends—1155(A); 1870(E)
Reaction $H^3(p,t)\pi^0$ at 340-Mev proton energy, K. C. Bandtel, W. J. Frank, L. Higgins, and B. J. Moyer—269(A)
Results on heavy charged mesons, R. Armenteros, B. Gregory, P. Hendel, A. Lagarrigue, L. Leprince-Ringuet, F. Muller, and C. Peyrou—275(A)
Results on K particles, W. B. Fretter, E. W. Friesen, G. E. Kepler, and A. Lagarrigue—1202(A)
Search for improbable meson decays, S. Lokanathan and J. Steinberger—240(A)
Simple, empirical mass spectrum of fundamental particles, Leo Banet—1176(A)
Stars formed by protons of 3.2 Bev from Bevatron, Joseph Lannutti, Gerson Goldhaber, and Stephen J. Goldsack—258(A)
τ^+ decay in flight, J. R. Burwell, R. W. Huggett, and R. W. Thompson—101
Theory of pion photoproduction, M. Ross—1156(A)

Metals (see **Crystalline State**)

Metastable Atoms (see **Atomic Structure and Spectra**)

Metastable Molecules (see **Molecular Structure and Spectra**)

Meteorology (see **Geophysics**)

Methods and Instruments

Aberrations and fringing effects in modified Siegbahn-type magnetic spectrometer, S. A. Bludman and D. L. Judd—283(A)
Amplitude and frequency stabilized adjustable high-frequency oscillator, R. C. Mobley and B. R. Albritton, Jr.—232(A)
Analysis of angular distribution data by electronic computers, L. C. Biedenharn and A. Simon—1153(A)
Analysis of high-energy photons from cyclotron target, Harlan Shaw, David Cohen, Burton J. Moyer, and Charles Waddell—259(A)
Apparatus for making simultaneous stress and birefringence measurements on polymers, E. F. Gurnee, L. T. Patterson, and R. D. Andrews—1547(A)
Application of fixed field alternating gradient principle to betatrons and cyclotrons, K. M. Terwilliger, L. W. Jones, D. W. Kerst, and K. R. Symon—1153(A)
Background tracks in nuclear emulsions, S. Yamamoto and F. E. Steigert—1210(A)
Betatron orbit stability studies, G. C. Baldwin—1152(A)
Bilateral development of thick nuclear emulsions, Raymond Fox and R. W. Waniek—1153(A)
Calibration of linear amplifiers with Hg relay pulse generator, J. K. Major—1210(A)
Charge-exchange accelerator, J. R. Woodyard—284(A)
Cine-microscopy of sparks exploding wires, and fracture at framing rates $> 10^6$/second, L. Zernow and G. Hauver—1551(A)
Co^{60} field distributions using Ag activated phosphate glass, Herbert Rabin and William E. Price—1154(A)
Coupling of betatron and phase oscillations in synchrotron, E. A. Crosbie and M. Hamermesh—233(A)
Crystal technique for measuring cyclotron beam energies, Philip Yuster, Sol Rocklin, Warren Ramler, and Charles Delbecq—233(A)
Direct production of spectroscopic specimens from single crystals by controlled growth from vapor; infrared absorption anisotropy and induced molecular motion in single crystal of benzene, Solomon Zwerdling and Ralph S. Halford—243(A)
Effect of temperature upon scintillation efficiency of NaI(Tl), L. A. Webb and R. F. Johnson—234(A)
Electron beam extraction from X-band microtron, H. F. Kaiser, W. T. Mayes, and W. J. Willis—1538(A)
Evapor-ion pump developments, Melvin J. Bina, Igor Alexeff, and Richard M. Sanders—251(A)
Experimental ion source for 184-inch cyclotron, Warren Fenton Stubbins—274(A)
External proton beam at Cosmotron, O. Piccioni, D. Clark, R. Cool, G. Friedlander, and D. Kassner—275(A)
Fast coincidence system with amplitude discrimination, G. S. Stanford and G. F. Pieper—1154(A)
Fission fast counter using gas scintillation principle, A. E. Villaire and L. F. Wouters—280(A)
Fixed field alternating gradient accelerator with spirally ridged poles, D. W. Kerst, K. M. Terwilliger, K. R. Symon, and L. W. Jones—1153(A)
Fixed field alternating gradient accelerators, Keith R. Symon—1152(A)
Forty-channel pulse-height analyzer, E. J. Cook and G. F. Pieper—1154(A)
Four-inch diameter liquid hydrogen bubble chamber, D. Paramentier, A. J. Schwemin, L. W. Alvarez, F. S. Crawford, Jr., and M. L. Stevenson—284(A)
High-resolution magnetic spectrometer, Sylvan Rubin and D. C. Sachs—284(A)
High-sensitivity mass spectrometer, J. H. Reynolds—283(A)
Influence of space charge on potential distribution in mass spectrometer ion sources, W. M. Brubaker—563(A)
Intensity distribution among spectral orders in grazing incidence spectrograph, D. E. Bedo and D. H. Tomboulian—242(A)
Investigation of quantitative phase contrast method for examining nonhomogeneous media, G. C. Krueger—1157(A)
Ionization loss in nuclear emulsions, John R. Fleming and J. J. Lord—268(A)
Isotope abundance ratios by nuclear magnetic resonance, B. E. Holder and M. P. Klein—265(A)
Long-wavelength x-ray reflection microscope, J. F. McGee—282(A)
Magnetic analyzer for nuclear reactions, T. D. Hanscome and D. K. Willett—232(A)
Magnetic susceptibility measurements by nuclear magnetic resonance, M. P. Klein and B. E. Holder—265(A)
Magnification and resolution of field emission electron microscope, D. J. Rose—1169(A)
Magnistor, solid-state electronic valve, Milton Green—1169(A)
Measurement of ionizing radiation by frequency variation using ferroelectric material, Hans Kohn Richards and Eugene D. Denman—250(A)
Measurement of scattering constant in nuclear emulsion, Lyle W. Smith—100
Mechanism of termination of Geiger plateau region, H. L. Wiser and A. D. Krumbein—203
Metal vacuum joint suitable for field emitters, Howard H. Pattee, Jr.—283(A)
Metallic deposits and shock waves due to electrically "exploded" wires, Willi M. Conn—1551(A)
Method for observation of ionization profile behind explosive-produced shocks in air, Jacob Savitt—1158(A)
Monte Carlo methods in study of cell growth, Joseph G. Hoffman, N. Metropolis, and V. Gardiner—1195(A)
Multiple-scattering microscope for "constant sagitta" measurements, Stephen J. Goldsack and Gerson Goldhaber—284(A)
Neutron spectrometer for 100–500 kev region, G. J. Perlow—223(A)
Neutron transmission measurements at new Argonne reactor, *CP*-5, L. M. Bollinger, D. A. Dahlberg, R. E. Cote, H. E. Jackson, and G. E. Thomas—223(A)
New method for investigating hfs of metastable state, J. Heberle, H. Reich, and P. Kusch—1194(A)
New method in x-ray crystal structure determination in-

Methods and Instruments (Continued)
volving use of anomalous dispersion, Y. Okaya, Y. Saito, and R. Pepinsky—1857(L)
New method of microelectrophoresis, Alexander Kolin—1195(A)
New technique for observing cyclotron phase grouping, Stewart D. Bloom—233(A)
Nuclear interactions of cosmic rays in Al, W. W. Brown—275(A)
Open screen technique in electron microscopy, George A. Farrall and Charles R. Mingins—1211(A)
Orientation and alignment of Na atoms by means of polarized resonance radiation, William Bruce Hawkins—478
Performance characteristics of BNL research electrostatic accelerator, C. M. Turner—233(A)
Performance data for high-sensitivity mass spectrometer, J. Lipson and J. H. Reynolds—283(A)
Phase change on reflection from multilayer films, F. A. Jenkins and D. R. Speck—282(A)
Photographic amplification in α-particle autoradiography, K. H. Sun, P. R. Malmberg, and P. Szydlik—1154(A)
Photomultiplier transit time measurements, R. V. Smith—1170(A)
π^- counting by delayed coincidence, K. M. Crowe, R. M. Friedman, and H. Motz—268(A)
Possibility of nuclear radiation detector by means of electroluminescent phosphors, W. Low—556(L)
Preliminary studies with high-energy photon spectrometer, C. E. Swartz and J. W. DeWire—1164(A)
Proposed method for obtaining high-energy polarized proton beam, R. Tripp—1167(A)
Radiation-controlled electroluminescence and light amplification in phosphor films, D. A. Cusano—546(L)
Range straggling in nuclear track emulsion, Walter H. Barkas, Frances M. Smith, Wallace Birnbaum—605
Rapid remagnetization of thin Mo permalloy tapes, T. L. Gilbert, J. M. Kelly, and H. Ekstein—1200(A)
Recent mechanical improvements in Brookhaven fast chopper, F. G. P. Seidl—1161(A)
Reduction of Doppler width of microwave lines, R. H. Romer and R. H. Dicke—1160(A)
Relation between multiple Coulomb scattering and residual range in nuclear emulsion, R. G. Glasser—174
Response of anthracene and stilbene to low-energy protons and x-rays, J. M. Fowler and C. E. Roos—996
Response of anthracene to low-energy protons and He ions, E. J. Zimmerman—1153(A)
Scintillation studies on activated alkali halides, T. H. Anderson—281(A)
Sequence experiment for study of reciprocity law failure at low intensities, J. H. Enns, R. L. Martin, and E. Katz—1556(A)
Slow-neutron spectrometry—New tool for study of energy levels in condensed systems, B. N. Brockhouse—1171(A)
Slow-neutron velocity spectrometer using Nevis synchrocyclotron, G. Grimm, L. J. Rainwater, and W. W. Havens, Jr.—1161(A)
Spin echo serial storage memory, A. G. Anderson, R. L. Garwin, E. H. Hahn, J. W. Horton, G. L. Tucker, and R. M. Walker—283(A)
Superconducting winding for electromagnet, G. B. Yntema—1197(A)
Synchromicrotron, H. F. Kaiser—233(A)
Synchrotron application of reverse field types of fixed field alternating gradient magnets, L. W. Jones, K. R. Symon, K. M. Terwilliger, and D. W. Kerst—1153(A)
Theoretical basis for light-amplifying phosphors, Ferd E. Williams—547(L)
Theory of magnetic rectifier, Kurt Lehovec, Alma Marcus, and Kurt Schoeni—229(A)
Ultra-short light-and-voltage pulses applied to Ag-halide crystals by turbine-driven mirror and electrical contacts, J. H. Webb—1558(A)
Ultrasonic technique for nondestructive evaluation of metal to metal adhesive bonds, J. S. Arnold—283(A)
Vacuum deposition of magnetic alloy films, M. S. Blois, Jr.—281(A)

Microwaves (see also **Atomic Structure and Spectra; Magnetic Resonance; Molecular Structure and Spectra; Nuclear Moments and Spin**)
Penetration into rarer medium in total reflection of microwaves, R. O. Brick, J. J. Brady, and M. D. Pearson—282(A)
Reduction of Doppler width of microwave lines, R. H. Romer and R. H. Dicke—1160(A)
Secondary electron resonance discharge mechanism. I, R. K. Smither and C. W. Hoover, Jr.—1149(A); II, C. W. Hoover, Jr., and R. K. Smither—1149(A)
Spectroscopic study of discharge and afterglow produced in nitrogen by pulsed microwaves, Georges Dejardin, Joseph Janin, and Ivan Eyraud—1149(A)
Wide-range electronic tuning of microwave cavities in gas atmospheres, Frank R. Arams and Hans K. Jenny—562(A)

Miscellaneous
Fundamental research in United States, J. L. B. Blizard—1211(A)
Origins of papers presented at regular meetings of American Physical, Acoustical, and Optical Societies in 1954, J. A. Dillon, Jr., and M. L. Dillon—1211(A)

Mobility of Ions and Electrons (see **Ions and Electrons, Mobility**)

Molecular Aggregates
Apparatus for making simultaneous stress and birefringence measurements on polymers, E. F. Gurnee, L. T. Patterson, and R. D. Andrews—1547(A)
Behavior of nonpigmented rubber vulcanizates in tension, G. M. Martin, F. L. Roth, and R. D. Stiehler—1557(A)
Behavior of rubbers in simple shear, J. E. Ivory, F. B. Baldwin, and R. L. Anthony—1558(A)
Biaxial creep fracture of high polymers, Chester G. Bragaw, Jr.—1559(A)
Calculation of compressibility of polyethylene from energy of interaction between ($-CH_2-$) groups, Werner Brandt—243(A)
Conductivity of Teflon and polyethylene during γ irradiation, R. A. Meyer and F. L. Boquet—1531(A)
Determination of polydisperse aerosol size distributions from analysis of light scattering data, T. L. Gilbert—242(A)
Dynamic mechanical properties of concentrated cellulose trinitrate solutions, D. J. Plazek and John D. Ferry—1548(A)
Dynamic properties of glucose glass, W. Philippoff and J. Brodnyan—1549(A)
Electrical conduction in plastics, Raymond J. Munick—236(A)
Extension of Hertz theory of impact to viscoelastic case, Yoh-Han Pao—1548(A)
Glass transitions in polymer-plasticizer systems, Leo Breitman—1559(A)
Impurity induced color centers in fused silica, Alvin J. Cohen—1550(A)
Infrared spectrum and structure of polyvinylidene chloride, S. Krimm and C. Y. Liang—1547(A)
Light scattering from optical glass, R. D. Maurer—1544(A)
Mechanism of high-speed-waterdrop erosion of methyl methacrylate plastic, Olive G. Engel—236(A)

Microwave dielectric measurements on single fibers, J. J. Windle and T. M. Shaw—281(A)
Molecular orientation produced in polymethyl methacrylate by hot stretching, Mary J. Kramer—1170(A)
Molecular weight distributions of polymers: I. Speculations on polymerizations to equilibrium, John Lauren Lundberg—1559(A)
Nature of stark rubber, Donald E. Roberts and Leo Mandelkern—1559(A)
Normal vibrations and infrared spectrum of polytetrafluoroethylene, C. Y. Liang and S. Krimm—1548(A)
Nuclear magnetic relaxation in natural and synthetic rubbers, E. M. Banas, B. A. Mrowca, and E. Guth—265(A)
Nuclear magnetic resonance relaxation times for polyisobutylene in CCl_4 solution, A. W. Nolle—1560(A)
Nuclear spin-spin relaxation time in polymers, E. M. Banas and B. A. Mrowca—1548(A)
Optical absorption bands induced in γ irradiated glass, K. R. Ferguson—1542(A)
Paramagnetic resonance absorption in glass, R. H. Sands—266(A)
Proton magnetic resonance in polyamides, W. P. Slichter and J. M. Mays—1559(A)
Reactor- and γ-ray-induced coloring in Corning fused silica, Paul W. Levy—1541(A)
Retraction of oriented polystyrene monofilaments, R. D. Andrews—1547(A)
Spin-lattice relaxation time of Si^{29} nucleus in pure fused silica, G. R. Holzman, John H. Anderson, and W. Koth—542(L)
Temperature dependence of relaxation mechanisms in amorphous polymers and other glass-forming liquids, Malcolm L. Williams, Robert F. Landel, and John D. Ferry—1549(A)
Tensile strength of elastomers, G. R. Taylor and S. R. Darin—1558(A)
Unilateral compression of rubber, Michael J. Forster—1559(A)
Viscosity-molecular weight relationship for long chain polymers in bulk or in concentrated solution, T. F. Fox and S. Loshaek—1549(A)

Molecular Beams (see **Atomic and Molecular Beams**)

Molecular Structure and Spectra
Collision line widths and shapes in vibration-rotation bands of HCl, W. S. Benedict, G. E. Moore, and S. Silverman—1551(A)
Cosine interaction in CsF and RbF, G. Bemski, W. A. Nierenberg, and H. B. Silsbee—470
Diffusion and volume loss coefficients of He metastable atoms and molecules, A. V. Phelps—558(A)
Direct production of spectroscopic specimens from single crystals by controlled growth from vapor; infrared absorption anisotropy and induced molecular motion in single crystal of benzene, Solomon Zwerdling and Ralph S. Halford—243(A)
Effect of temperature on lifetime of metastable Hg molecules, C. G. Maitland and A. O. McCoubrey—558(A)
Emission spectra of some polyatomic molecules, G. W. Robinson—1550(A)
Extension of Hund's rule, G. F. Koster—514
Ideal gas thermodynamic properties of isotopic hydrides of group of diatomic free radicals, Lester Haar—1551(A)
Infrared absorption of liquid and solid hydrogen, Elizabeth J. Allin, W. F. J. Hare, and R. E. MacDonald—554(L)
Magnetic hyperfine effects and electronic structure of NO, G. C. Dousmanis—1160(A)
Microwave spectrum of CS, Richard C. Mockler and George R. Bird—1837
Microwave spectrum of methylamine, Koichi Shimoda, Tetsuji Nishikawa, and Takashi Itoh—1160(A)
Microwave spectrum of NO_2, George R. Bird—1160(A)
Microwave spectrum of NOBr, Quitman Williams and T. L. Weatherly—1159(A)
Microwave spectrum of $N^{15}O^{16}$, J. J. Gallagher, W. C. King, and C. M. Johnson—1551(A)
Molecular constants and nuclear-molecular interactions of Li^7F^{19} by molecular beam electric resonance method, R. Braunstein and J. W. Trischka—1092
Molecular distortion caused by hindered rotation, Henry T. Minden—1160(A)
Normal coordinate treatments and calculated thermodynamic properties of $POCl_3$, POF_3, $PSCl_3$, and PSF_3, Joseph S. Ziomek, Edward A. Piotrowski, and Edward N. Walsh—243(A)
Normal vibrations and infrared spectrum of polytetrafluoroethylene, C. Y. Liang and S. Krimm—1548(A)
One-electron energies of atoms, molecules, and solids, J. C. Slater—1039
Oxygen gas continuous absorption in extreme uv, William A. Rense and R. Mercure—1195(A)
Pure rotational spectra of Tl halides, M. Mandel and A. H. Barrett—1159(A)
Raman and fluorescence spectra of allyl diglycol carbonate, Myron A. Jeppesen—1211(A)
Reduction of Doppler width of microwave lines, R. H. Romer and R. H. Dicke—1160(A)
Rotational excitation by slow electrons. II, E. Gerjuoy and S. Stein—1848
Sparkling potential and molecular structure of hydrocarbon gases, R. W. Crowe and J. C. Devins—560(A)
Spin, quadrupole moment, and mass of Se^{75}, L. C. Aamodt and P. C. Fletcher—1224
Theoretical evaluation of binding energy of HeH, A. A. Evett—1191(A)
Vibration-rotation line intensities in HCl and DCl, R. Herman, G. E. Moore, S. Silverman, and R. F. Wallis—1550(A)
Zeeman effect in rotational spectrum of NO, Masataka Mizushima, J. T. Cox, and Walter Gordy—1159(A)

Moments, Nuclear (see **Nuclear Moments and Spin**)

Moments of Molecules (see **Molecular Structure and Spectra**)

Neutrino (see also **Nuclear Spectra; Radioactivity**)
Electron-neutrino angular correlation in β decay of Ne^{19}, D. R. Maxson, J. S. Allen, and W. K. Jentschke—230(A)
Magnetic and electric deflection spectrometry of neutrino recoils in A^{37}, Arthur H. Snell and Frances Pleasonton—1174(A)

Neutron Diffraction (see **Diffraction; Scattering of Neutrons**)

Neutrons (see **Elementary Particle Interactions**)

Noise
Excess noise and trapping in Ge, H. A. Gebbie—1567(A)
Fluctuation dissipation theorem, J. Weber—1165(A)
Noise in Si p-n junction photocells, G. L. Pearson, H. C. Montgomery, and W. L. Feldmann—1567(A)
Noise measurements in semiconductors at very low frequencies, T. E. Firle and H. Winston—1567(A)
Quantum correction to shot effect, Hans Ekstein and Norman Rostoker—222(A)
Quantum theory of noise, Norman Rostoker and Hans Ekstein—222(A)
Shot noise in CdS crystals, C. Y. Shulman—384
Surface traps and $1/f$ noise in Ge, A. L. McWhorter—1191(A)

Nuclear Fission
Angular distribution of fission fragments from 22-Mev proton-induced fission of U^{238}, U^{235}, U^{233}, Th^{232}, and Th^{230}, B. L. Cohen, B. L. Ferrell-Bryan, D. J. Coombe, and M. K. Hullings—685
Angular distribution of fragments from 450-Mev proton fission of Bi, R. L. Wolke—1199(A)
Excitation functions for some proton-induced reactions of Th, Howard A. Tewes—25
Fission fast counter using gas scintillation principle, A. E. Villaire and L. F. Wouters—280(A)
Fission of Bi by 22-Mev deuterons, A. W. Fairhall—276(A)
Fission-spallation competition in heavy elements, R. A. Glass, R. J. Carr, J. W. Cobble, and G. T. Seaborg—261(A)
γ rays accompanying spontaneous fission of Cf^{252}, Harry R. Bowman and Lloyd G. Mann—277(A)
High-energy proton spallation-fission of uranium, R. L. Folger, P. C. Stevenson, and G. T. Seaborg—107
Mendelevium, atomic number 101, A. Ghiorso, B. G. Harvey, G. R. Choppin, S. G. Thompson, and G. T. Seaborg—1518(L)
Model for asymmetric fission, R. D. Hill—1272
Neutron multiplicity spectrum from spontaneous fission, John Ise, Jr., Donald A. Hicks, and Robert V. Pyle—1199(A)
Nuclear properties of 100^{256}, G. R. Choppin, B. G. Harvey, S. G. Thompson, and A. Ghiorso—1519(L)
Spontaneous-fission neutrons of Cf^{252} and Cm^{244}, Donald A. Hicks, John Ise, Jr., and Robert V. Pyle—1521(L)
Ta spallation and fission induced by 340-Mev protons, Walter E. Nervik and Glenn T. Seaborg—261(A)
Thermodynamic theory of fission, J. K. Perring and J. S. Story—1525(L)
U^{236} thermal neutron fission yields at masses 90 and 91, George W. Reed—1327
Nuclear Forces (see **Elementary Particle Interactions; Field Theory; Nuclear Structure Theory**)
Nuclear Induction (see **Magnetic Resonance; Nuclear Moments and Spin**)
Nuclear Isomers (see **Nuclear Spectra; Radioactivity**)
Nuclear Moments and Spin
Ac^{227} nuclear moments, Mark Fred, Frank S. Tomkins, and William F. Meggers—1514(L)
"Brute force" polarization of In^{115} nuclei; angular momentum of 1458-ev neutron resonance, J. W. T. Dabbs, L. D. Roberts, and S. Bernstein—1512(L)
Ce^{140} and Sr^{88} spins and parities of excited states, G. R. Bishop and J. P. Perez Y Jorba—89
Cl^{36} magnetic moment and mass, L. C. Aamodt and P. C. Fletcher—1317
Collision alignment of molecules, atoms, and nuclei, Norman F. Ramsey—1853(L)
Effect of anomalous nucleon magnetic moment of π^0 lifetime, Stanley Cohen—749
Exchange current effects in two-nucleon system, J. Bernstein and Abraham Klein—1155(A)
Hfs of He^{3+} and He^3, A. M. Sessler and H. M. Foley—6
K^{39} nuclear magnetic moment, L. Carlton Brown and Dudley Williams—1537(A)
Magnetic moment of 0.247-Mev excited state of Cd^{111}, W. Zobel and R. M. Steffen—1186(A)
Molecular constants and nuclear-molecular interactions of Li^7F^{19} by molecular beam electric resonance method, R. Braunstein and J. W. Trischka—1092
Nb quadrupole moment, D. R. Speck and F. A. Jenkins—282(A)
Nuclear electric quadrupole moment of Na^{23} by atomic beam resonance method, M. L. Perl, I. I. Rabi, and B. Senitzky—611
Nuclear magnetic moments of Cl^{36}, Rh^{103}, and W^{183}, P. B. Sogo and C. D. Jeffries—1316
Nuclear magnetic moments of Rh^{103} and W^{183}, P. B. Sogo and C. D. Jeffries—265(A)
Nuclear moments of Nb^{93}, La^{139}, Os^{187}, and Hg^{201}, Kiyoshi Murakawa—1285
Nuclear spin and hfs interaction in 3.1-hr Cs^{134m}, D. A. Gilbert and Victor W. Cohen—1194(A)
Orientation and alignment of Na atoms by means of polarized resonance radiation, William Bruce Hawkins—478
Overhauser effect in nonmetals, A. Abragam—1729
Overhauser nuclear polarization effect, W. A. Barker and A. Mencher—1868(L)
Rb^{85} and Rb^{87} quadrupole moments, B. Senitzky, I. I. Rabi, and M. L. Perl—1537(A)
Saturation of nuclear electric quadrupole energy levels by ultrasonic excitation, W. G. Proctor and W. H. Tanttila—1854(L)
Spin and lifetime of 439-kev excited state of Hg^{209}, Franz R. Metzger—200(L)
Spin echoes with four pulses—extension to n pulses, T. P. Das and D. K. Roy—525
Spin, quadrupole moment, and mass of Se^{75}, L. C. Aamodt and P. C. Fletcher—1224
3-body exchange magnetic moments of H^3 and He^3, Andrew M. Lockett—1204(A)
Nuclear Photoeffects
$C^{12}(\gamma,n)C^{11}$ absolute cross section, W. C. Barber, W. D. George, and D. D. Reagan—73; W. George, W. Barber, and D. Reagan—276(A)
Deuteron model for π-meson and photon capture by complex nuclei, B. T. Feld—1155(A)
Effect of extended size of nucleus on μ-meson pair photoproduction, George Rawitscher—272(A)
Elastic photoproduction of π^0 mesons for He, E. L. Goldwasser, L. J. Koester, and F. E. Mills—239(A)
Energy dependence of photoyields of N^{17}, D. D. Reagan—258(A)
Energy spectrum of photoprotons from C, W. E. Stephens and A. K. Mann—241(A)
Exchange current effects in two-nucleon system, J. Bernstein and Abraham Klein—1155(A)
Fine structure in (γ,p) reaction in oxygen, W. E. Stephens, A. K. Mann, B. J. Patton, and E. J. Winhold—839(L)
(γ,n) cross sections in Mg^{24} and Mg^{25}, P. F. Yergin and R. Nathans—1198(A)
(γ,n) cross sections in Zr^{90} and Zr^{91}, R. Nathans and P. F. Yergin—1197(A)
Low-energy photoproduction of π^0 mesons from H: Total cross section, F. E. Mills and L. J. Koester, Jr.—210(L)
Low-energy photoproduction of π^0 mesons in H: Differential cross sections at 135°, Louis J. Koester, Jr.—211(L)
Neutrons in coincidence with photoprotons, A. C. Odian, W. Rankin, P. C. Stein, and A. Wattenberg—248(A)
Photodisintegration of C, O, and N in nuclear emulsions, Raymond D. Cooper and Dan J. Zaffarano—1199(A)
Photodisintegration of C^{12} by 330-Mev bremsstrahlung, Sheldon D. Softky—173
Photodisintegration of deuteron, Yoshio Yamaguchi and Yoriko Yamaguchi—69
Photodisintegration of deuteron by 95-Mev bremsstrahlung, Lew Allen, Jr.—705
Photodisintegration of deuterons by high-energy γ rays, Dwight R. Nixon and Kenneth C. Bandtel—259(A)
Photomeson production from hydrogen, Bernard T. Feld—238(A)
Photomeson production from H, D, and C, Walter Dudziak, Ryokichi Sagane, and James Vedder—269(A)

Photoneutron cross sections in Mg^{24}, Mg^{25}, Zr^{90}, Zr^{91}, Robert Nathans and Paul F. Yergin—1296
Photoproduction of neutral mesons in H and D, H. H. Bingham, J. C. Keck, and A. V. Tollestrup—1187(A)
Photoproduction of π^+ mesons from H near threshold, J. E. Leiss, C. S. Robinson, and S. Penner—201(L); 1188(A)
Photoproduction of π^0 mesons in hydrogen, L. J. Koester—239(A)
Photoprotons from Pb^{208} and Ta, M. Elaine Toms and William E. Stephens—626
π^+ photomeson production at 180°. Experimental arrangement, Gordon W. Repp, Mark J. Jakobson, and R. Stephen White—268(A); Experimental results, R. Stephen White, Mark J. Jakobson, and Gordon W. Repp—269(A)
π^0 photoproduction from protons and deuterium nucleons. I, R. M. Worlock and W. R. Smythe—269(A); II, W. R. Smythe and R. M. Worlock—269(A)
Pion photoproduction ratios, D. C. Peaslee—239(A)
π^-/π^+ ratios in asymmetric nuclei, H. Motz, K. M. Crowe, and R. M. Friedman—268(A)
Self-absorption or self-indication in nuclear elastic scattering experiment, E. G. Fuller and Evans Hayward—1537(A)
Theory of pion photoproduction, M. Ross—1156(A)
Velocity-dependent nuclear potential, J. S. Levinger—1205(A)

Nuclear Reactions, General (see also **Elementary Particle Interactions; Scattering**)
Anomalous dependence of F_p/F_n on bombarding energy, B. L. Cohen and E. Newman—1198(A)
Fission-spallation competition in heavy elements, R. A. Glass, R. J. Carr, J. W. Cobble, and G. T. Seaborg—261(A)
Giant resonance interpretation of nucleon-nucleus interaction, A. M. Lane, R. G. Thomas, and E. P. Wigner—693
High-energy reactions and evidence for correlations in nuclear ground state wave function, K. A. Brueckner, R. J. Eden, and N. C. Francis—1445
Importance of parentage of nuclear states for nuclear reaction phenomena, D. H. Wilkinson and A. M. Lane—235(A)
Inelastic electron scattering from C at 188 Mev, J. H. Fregeau and R. Hofstadter—1184(A)
Isotopic spin selection rule for electric dipole transitions, William M. MacDonald—60
Magnetic analyzer for nuclear reactions, T. D. Hanscome and D. K. Willett—232(A)
Polarization and cross section for inelastic scattering, M. A. Ruderman—267(A)
S matrix in terms of phenomenological collision parameters, R. M. Thaler and J. L. McHale—1189(A)
Scattering of polarized nucleon beams, Reinhard Oehme—147
7.68-Mev level in C^{12} and stellar energy production, E. E. Salpeter—1183(A)
Soluble problem in theory of Coulomb excitation, L. C. Biedenharn and C. M. Class—691
Spin polarization of deuteron, W. Lakin—139
Statistical model for high-energy events, Joseph V. Lepore and Maurice Neuman—1484
Theory of nuclear excitation in inelastic electron scattering, C. J. Mullin and E. Guth—277(A)
Upper limit to lifetime of compound nucleus, H. G. Graetzer and E. C. Pollard—1184(A)
Variational expressions for *N*-channel collision parameters, J. L. McHale and R. M. Thaler—1189(A)

Nuclear Reactions Induced by α Particles and He^3 (see also **Scattering of α Particles**)
(α,p) reaction studies, G. F. Pieper, G. S. Stanford, and P. von Herrmann—1185(A)
Assignment of energy levels by Coulomb excitation with 5.7-Mev α particles, N. P. Heydenburg and G. M. Temmer—1198(A)
Competition between (α,pn) and $(\alpha,2n)$ reactions on Cr^{50}, J. M. Miller, G. Friedlander, and S. Markowitz—1197(A)
Coulomb excitation of energy levels in Te and Ag, L. W. Fagg, E. A. Wolicki, R. O. Bondelid, K. L. Dunning, and S. Snyder—1538(A)
Energy levels in N^{14} by inelastic α scattering, D. W. Miller, U. C. Gupta, V. K. Rasmussen, and M. B. Sampson—1184(A)
F^{17} and Al^{30} energy levels, W. T. Doyle and A. B. Robbins—1185(A)
Fission-spallation competition in heavy elements, R. A. Glass, R. J. Carr, J. W. Cobble, and G. T. Seaborg—261(A)
γ radiation from Po neutron sources, R. J. Breen and M. R. Hertz—599
Interactions of 380-Mev α particles in Ilford G.5 emulsion, Dora F. Sherman—259(A)
Multipolarity of γ transitions in F^{19} and Na^{23} by Coulomb excitation, G. M. Temmer and N. P. Heydenburg—1198(A)
Neutron spectrum and absolute yield of Pu-Be source, Leona Stewart—740
Production of high-energy neutrons and deuterons from stripping of He, Warren Heckrotte—259(A)
Properties of excited states of Pd and Cd nuclei by Coulomb excitation, G. M. Temmer and N. P. Heydenburg—1308
7.68-Mev level in C^{12} and stellar energy production, E. E. Salpeter—1183(A)
Upper limit to lifetime of compound nucleus, H. G. Graetzer and E. C. Pollard—1184(A)

Nuclear Reactions Induced by Deuterons and Tritons (see also **Scattering of Deuterons**)
Analysis of disintegration products from reactions of 125-Mev deuterons with Li nuclei, F. C. Gilbert—275(A)
Angular distribution of disintegration products from $O^{16}(d,p)O^{17}$, $Be^9(d,p)Be^{10}$, and $Be^9(d,t)Be^8$ reactions, Mira K. Jurić—85
Angular distribution of neutrons from reaction $D(d,n)He^3$ at 100 kev, J. C. Fuller and D. C. Ralph—248(A)
Angular distributions and excitation functions of $C^{13}(d,p)$ reaction, K. W. Jones, M. T. McEllistrem, R. A. Douglas, D. F. Herring, and E. Silverstein—241(A)
Angular distributions of resolved neutron groups from $B^{11}(d,n)C^{12}$ reaction, J. R. Risser, J. Price, and C. M. Class—1183(A)
Angular momentum coupling in deuteron reactions, T. Auerbach and J. B. French—1276
Coulomb effects in (d,p) reaction R. W. Hockney and P. V. C. Hough—234(A)
$D(t,\alpha)n$ reaction at 1.5 Mev, A. Hemmendinger and H. V. Argo—70
Deuteron reactions and *j-j* coupling shell model, J. B. French and B. J. Raz—1523(L)
Experimental determination of absolute differential cross sections for $O^{16}(d,p)O^{17}$, $O^{16}(d,p)O^{17*}$, and $O^{18}(d,p)O^{19*}$ reactions, T. F. Stratton, J. M. Blair, K. F. Famularo, and R. V. Stuart—629
Fission of Bi by 22-Mev deuterons, A. W. Fairhall—276(A)
γ radiation from deuteron bombardment of N^{14}, R. D. Bent, T. W. Bonner, J. H. McCrary, and R. F. Sippel—1198(A)
γ-ray thresholds in $F^{19}(d,n\gamma)Ne^{20}$ reaction, J. W. Butler—241(A)

Nuclear Reactions Induced by Deuterons and Tritons (Continued)

γ-rays from deuteron bombardment of C^{13}, R. J. Mackin, Jr., W. B. Mims, and W. R. Mills, Jr.—43

$Li^7(d,n)Be^8$ neutron spectrum and differential cross section, C. C. Trail and C. H. Johnson—249(A)

Limitations of stripping theory in inelastic deuteron scattering, James W. Haffner—1156(A)

Low-energy protons from targets bombarded by 15-Mev deuterons, F. A. Aschenbrenner—657

Neutron yields as function of energy in reactions $Li^7(d,n)Be^8$ and $Be^9(d,n)B^{10}$, D. C. Ralph and F. E. Dunnam—249(A)

Nuclear energy levels of Be^8 from $Li^7(d,n)Be^8$, M. A. Ihsan—689

$O^{16}(t,n)F^{18}$ excitation function, Nelson Jarmie—41

Pair spectrometer measurements of radiations from excited states of light nuclei, R. D. Bent, T. W. Bonner, and R. F. Sippel—1237

Polarization measurement in $D(d,p)H^3$ reaction, R. E. Segel and S. S. Hanna—1538(A)

Q values for $O^{17}(d,p)O^{18}$ and $O^{18}(d,p)O^{19}$ reactions, H. D. Holmgren, T. D. Hanscome, and D. K. Willett—241(A)

Sc^{41} levels, H. S. Plendl and F. E. Steigert—1538(A)

Search for excited states of Be^8, R. E. Holland, D. R. Inglis, and F. P. Mooring—240(A)

Search for reaction $T(d,\gamma)He^5$, George A. Sawyer and Louis C. Burkhardt—1305

Nuclear Reactions Induced by Mesons (see also **Elementary Particle Interactions; Mesons; Scattering of Mesons**)

Absorption of pions in C and N, P. Ammiraju, M. Rinehart, K. C. Rogers, and L. M. Lederman—1188(A)

Deuteron model for π-meson and photon capture by complex nuclei, B. T. Feld—1155(A)

Diffusion cloud-chamber study of very slow mesons. I. Internal pair formation, C. P. Sargent, R. Cornelius, M. Rinehart, L. M. Lederman, and K. Rogers—1349

Interaction of 46-Mev π^+ mesons in deuterium, D. Bodansky and A. M. Sachs—240(A)

Interactions of 1.5-Bev π^- mesons, W. D. Walker and J. Crussard—240(A)

Internal pair production associated with emission of high-energy γ rays, Norman M. Kroll and Walter Wada—1355

$\Lambda^0 - \theta^0$ production in $\pi^- - p$ collisions at 1 Bev, W. D. Walker—1407

Nuclear absorption of fast charged hyperons, D. T. King and M. M. Block—1203(A)

π^--nucleon collisions at 1.5 Bev, W. D. Walker and J. Crussard—1416

Production of heavy unstable particles by 1.37-Bev pions, W. B. Fowler, R. P. Shutt, A. M. Thorndike, and W. L. Whittemore—121

Production of unstable particles in C and Pb by 2-Bev pions, H. Blumenfeld, E. T. Booth, L. M. Lederman, and W. Chinowsky—1203(A)

Scattering and absorption of 50-Mev π^+ mesons in Pb, G. Saphir—269(A)

Scattering of 195-Mev pions by deuterium, W. Skolnik—240(A)

Nuclear Reactions Induced by Neutrons (see also **Elementary Particle Interactions; Scattering of Neutrons**)

Anomalous absorption of neutrons in single crystals, J. W. Knowles—224(A)

$B^{11}(n,\alpha)Li^8(\beta)Be^{8*}(2\alpha)$ reaction from 12 to 20 Mev, G. M. Frye, Jr., A. H. Armstrong, and L. Rosen—241(A)

$Be^9(n,2n)Be^8$ reaction, J. M. Fowler, S. S. Hanna, and G. E. Owen—249(A)

"Brute force" polarization of In^{115} nuclei; angular momentum of 1458-ev neutron resonance, J. W. T. Dabbs, L. D. Roberts, and S. Bernstein—1512(L)

Cascade γ rays from 2.5-Mev neutron bombardment of Au, I, and Cr, V. E. Scherrer, W. R. Faust, and B. A. Allison—224(A)

Charged pion production in n-p collisions, Gaurang B. Yodh—268(A)

Correction to exponential dependence of neutron transmissions, R. G. Thomas—77

Determination of nuclear level density, S. E. Darden, A. Okazaki, and R. L. Becker—1147(A)

Disintegration of O by 300-Mev neutrons, Melvin Otis Fuller—274(A)

Experimental evidence for optical model for neutrons between 60 and 110 Mev, Vaughn Culler and R. W. Waniek—1148(A)

$\bar{\Gamma}_n^0/\bar{D}$ for slow neutron resonances, R. Cote and L. M. Bollinger—1162(A)

γ radiation from interaction of 4.4-Mev neutrons with Fe^{54} and Fe^{56}, Rolf M. Sinclair—1147(A)

γ radiation from neutron inelastic scattering, G. L. Griffith—579

γ rays from inelastic scattering of neutrons in Al, Mg, and Ag, L. A. Rayburn, D. L. Lafferty, and T. M. Hahn—701

γ-γ coincidences produced by inelastic scattering of 2.5-Mev neutrons, W. R. Faust, V. E. Scherrer, and B. A. Allison—224(A)

High-energy cross sections. I. Size of nucleus, Robert W. Williams—1387; II. Nucleon-nucleon cross section at cosmic-ray energies, Robert W. Williams—1393

Inelastic collision cross sections at 1.0-, 4.0-, and 4.5-Mev neutron energies, J. R. Beyster, R. L. Henkel, R. A. Nobles, and J. M. Kister—1216

Inelastic scattering of neutrons by Fe, F, Mn, and I, J. J. Van Loef and D. A. Lind—224(A)

Interaction of 4.1-Mev neutrons with nuclei, M. Walt and J. R. Beyster—279(A); 677

Interaction of high-energy neutrons with Mo, R. W. Waniek, R. Fox, L. Garrido, and E. G. Silver—1148(A)

Level spacings of heavy nuclei, John A. Harvey—1162(A)

Measurement of scattering cross sections for low-energy neutron resonances, C. Sheer and J. Moore—565

$Na^{23}(n,2n)$ cross section at 14.1 Mev, R. J. Prestwood—47

Negative pions from neutron bombardment of deuterons, Myron W. Knapp and Wilson M. Powell—1188(A)

Neutron cross sections for Zr, Janet B. Guernsey—1210(A)

Neutron cross sections in 4-Mev range, W. S. Emmerich—1148(A)

Neutron inelastic scattering, Janet B. Guernsey and A. Wattenberg—1147(A)

Neutron self-indication transmission cross sections, J. E. Monahan and A. Langsdorf, Jr.—1147(A)

Neutron transmission cross sections by self-indication technique, A. Langsdorf, J. E. Monahan, and F. Paul Mooring—1148(A)

Neutron transmission measurements at new Argonne reactor, CP-5, L. M. Bollinger, D. A. Dahlberg, R. E. Cote, H. E. Jackson, and G. E. Thomas—223(A)

Neutron widths of nuclear energy levels, D. J. Hughes—1161(A)

Nuclear cross sections for 1.4-Bev neutrons, T. Coor, D. A. Hill, W. F. Hornyak, L. W. Smith, and G. Snow—1369

Parameters for neutron resonance in Au, R. E. Wood, H. H. Landon, and V. L. Sailor—639
Polarized neutrons on Li^6, M. Peshkin, J. H. Roberts, and V. L. Telegdi—1204(A)
Problems in analysis of neutron resonance data, V. L. Sailor, H. H. Landon, H. L. Foote, Jr., and R. E. Wood —224(A)
Production of neutral V events in Pb by neutrons from Cosmotron, R. M. Walker, R. S. Preston, E. C. Fowler, and H. L. Kraybill—1203(A)
Radiation width variations in neutron resonances of Eu and In, H. H. Landon and V. L. Sailor—225(A)
Radiation width variations in slow-neutron resonances of Eu and In, H. H. Landon and V. L. Sailor—1267
Radiation widths of nuclear energy levels, J. S. Levin and D. J. Hughes—1161(A)
Resonance parameters in U^{238}, R. S. Carter—1161(A)
Scattering of 4.4-Mev neutrons by Fe and C, B. Jennings, J. Weddell, I. Alexeff, and R. L. Hellens—582
Total cross section of deuterium for neutrons from 0.2 to 22 Mev, John D. Seagrave and Richard L. Henkel—666
Total neutron cross section of Eu in 0.001 to 0.01 ev region, N. Holt—1162(A)
Total neutron cross sections in kev region: Be, B, C, F, Ti, Ni, and Bi, Carl T. Hibdon and Alexander Langsdorf, Jr.—223(A)
Total neutron cross sections in kev region: Sc, V, Mn, and Co, H. Marshak and H. W. Newson—1162(A)
Total neutron cross sections in kev region: Separated isotopes of Ni and Ce, R. C. Block and H. W. Newson —1162(A)
Zr^{90m} decay and fast neutron excitation, E. C. Campbell, R. W. Pelle, F. C. Maienschein, and P. H. Stelson—1172(A)

Nuclear Reactions Induced by Protons (see also **Elementary Particle Interactions; Scattering of Protons**)

Al^{26} energy levels, R. Sherr, R. W. Kavanagh, and W. R. Mills—1185(A)
α-α angular correlation in $B^{11}(p,\alpha\alpha)He^4$, E. H. Geer, E. B. Nelson, and E. J. Wolicki—241(A)
Angle and energy distributions of charged particles from cyclotron bombardment of Ni and Ag by 200-Mev protons, L. Evan Bailey—275(A)
Angular distribution of fission fragments from 22-Mev proton-induced fission of U^{238}, U^{235}, U^{233}, Th^{232}, and Th^{230}, B. L. Cohen, B. L. Ferrell Bryan, D. J. Coombe, and M. K. Hullings—685
Angular distribution of fragments from 450-Mev proton fission of Bi, R. L. Wolke—1199(A)
Angular distribution of γ rays from Coulomb excitation, P. H. Stelson and F. K. McGowan—249(A)
Angular distribution of pickup deuterons for 95-Mev protons on C, and implications as to internal interactions in carbon, W. Selove—208(L)
Angular distributions and yields of neutrons from (p,n) reactions, Bernard L. Cohen—49
Angular distributions of neutrons from (p,n) reactions, Bernard L. Cohen—1206(A)
Anomalous dependence of F_p/F_n on bombarding energy, B. L. Cohen and E. Newman—1198(A)
Asymmetry in deuteron pickup by high-energy polarized protons, B. J. Malenka—1156(A)
$C^{13}(p,\gamma)N^{14}$ reaction, H. B. Willard, J. D. Kington, and J. K. Bair—1184(A)
Coulomb excitation of energy levels in Te and Ag, L. W. Fagg, E. A. Wolicki, R. O. Bondelid, K. L. Dunning, and S. Snyder—1538(A)
Deuteron pickup by high-energy polarized protons, B. J. Malenka—843(L)
Differential cross sections for scattering of protons by C as function of incident proton energy, Robert Peelle—1184(A)
Electric excitation of certain medium-weight nuclei by protons, Hans Mark, Clyde McClelland, and Clark Goodman—1245
Electric excitation of heavy nuclei with protons, Clyde McClelland, Hans Mark, and Clark Goodman—249(A)
Electric excitation of nuclei near closed 50 proton and neutron shells, Hans Mark, Clyde McClelland, and Clark Goodman—249(A)
Energy levels in B^9 and Be^7 from reactions $C^{12}(p,\alpha)B^9$ and $B^{10}(p,\alpha)Be^7$, J. B. Reynolds—1289
Excitation curve of reaction $B^{10}(p,\gamma)C^{11}$, T. M. Hahn, Jr., B. D. Kern, and G. K. Farney—1183(A)
Excitation function of $C^{12}(p,pn)C^{11}$ reaction in Bev region, R. L. Wolfgang and G. Friedlander—1870(E)
Excitation functions for reactions of Cu with high-energy protons, J. A. Miskel, M. L. Perlman, G. Friedlander, and J. M. Miller—1197(A)
Excitation functions for some proton-induced reactions of Th, Howard A. Tewes—25
Excitation functions of radioactive products from interaction of high-energy protons with Pb, E. Baker, A. Caretto, J. Cumming, G. Friedlander, J. Hudis, and R. Wolfgang—242(A)
$F^{19}(p,p')F^{19*}$ absolute magnetic analysis, C. R. Gossett, G. C. Phillips, and J. T. Eisinger—724
γ rays from low-energy proton bombardment of Be, R. R. Carlson and E. B. Nelson—1310
γ rays from proton bombardment of Li^6, S. Bashkin and R. R. Carlson—230(A)
γ rays from proton capture in Li^7, C. P. Swann, M. A. Rothman, W. C. Porter, and C. E. Mandeville—1183(A)
High-energy proton spallation-fission of uranium, R. L. Folger, P. C. Stevenson, and G. T. Seaborg—107
Ho^{167}, T. H. Handley, W. S. Lyon, and E. L. Olson—688
Interaction of 95-Mev protons with He^4, J. M. Teem, W. Selove, and U. E. Kruse—259(A)
$Li^6(p,d)Li^5$ reaction, J. G. Likely—1538(A)
Mechanism of reaction $C^{12}+p\rightarrow p+3\alpha$ at 32 Mev, John Logan Need—1538(A)
Millisecond γ emitter from protons on Ta, Sheldon D. Softky—280(A); 736
Multipolarity of γ transitions in F^{19} and Na^{23} by Coulomb excitation, G. M. Temmer and N. P. Heydenburg—1198(A)
Neutrons from proton bombardment of P^{31}, A. Rubin, F. Ajzenberg, and J. B. Reynolds—1185(A)
Nuclear pairs from proton bombardment of Ca^{40}, T. W. Bonner, R. D. Bent, and J. H. McCrary—1198(A)
Nuclear pairs from 3.5-Mev state in Ca^{40}, R. D. Bent, T. W. Bonner, and J. H. McCrary—1325
(p,a) and (p,ab) reactions at 100 Mev, J. W. Meadows—744
Pair spectrometer measurements of radiations from excited states of light nuclei, R. D. Bent, T. W. Bonner, and R. F. Sippel—1237
Polarization effects in reaction $p+p\rightarrow\pi^++d$, L. Wolfenstein—766
Radiative capture of protons by N^{14}, S. Bashkin, R. R. Carlson, and E. B. Nelson—1184(A)
Reaction $H^2(p,t)\pi^0$ at 340-Mev proton energy, K. C. Bandtel, W. J. Frank, L. Higgins, B. J. Moyer—269(A)
Stars formed by protons of 3.2 Bev from Bevatron, Joseph Lannutti, Gerson Goldhaber, and Stephen J. Goldsack—258(A)
Survey of (p,n) reactions at 11.7 Mev, H. G. Blosser, T. H. Handley, and M. K. Hullings—1198(A)

Nuclear Reactions Induced by Protons (Continued)
Ta spallation and fission induced by 340-Mev protons, Walter E. Nervik and Glenn T. Seaborg—261(A)
Yield of high-energy γ rays from proton capture in Be^9, O. O. Lönsjö, O. Os, and R. Tangen—727
Nuclear Scattering (see **Scattering**)
Nuclear Spectra (see also **Nuclear Reactions; Radioactivity**)
Al^{26} energy levels, R. Sherr, R. W. Kavanagh, and W. R. Mills—1185(A)
Al^{26}, long-lived, J. R. Simanton, R. A. Rightmire, A. L. Long, and T. P. Kohman—260(A)
α decay of spheroidal nuclei, R. F. Christy—1205(A)
α-α angular correlation in $B^{11}(p,\alpha\alpha)He^4$, E. H. Geer, E. B. Nelson, and E. J. Wolicki—241(A)
Am^{243} α groups and angular correlation, F. Stephens, J. Hummel, F. Asaro, and I. Perlman—261(A)
Angular distribution of γ rays from Coulomb excitation, P. H. Stelson and F. K. McGowan—249(A)
Angular distribution of resonance fluorescence radiation from 411-kev level in Hg^{198}, Franz R. Metzger—1186(A)
Anisotropic γ radiation from aligned Nd^{147}, E. Ambler, R. P. Hudson, and G. M. Temmer—230(A)
Assignment of energy levels by Coulomb excitation with 5.7-Mev α particles, N. P. Heydenburg and G. M. Temmer—1198(A)
Attenuation of α-γ angular correlation of Am^{241} in liquid-film sources, S. Raboy, T. B. Novey, and V. E. Krohn—1187(A)
Ba^{128}–Cs^{128} radiations, J. M. Hollander and M. I. Kalkstein—260(A)
Be^8 nuclear energy levels from $Li^7(d,n)Be^8$, M. A. Ihsan—689
Bi^{207} decay, N. H. Lazar and E. D. Klema—710; 1186(A); D. E. Alburger and A. W. Sunyar—276(A)
Capture-positron branching ratios, P. F. Zweifel—1871(E)
Cascade γ rays from 2.5-Mev neutron bombardment of Au, I, and Cr, V. E. Scherrer, W. R. Faust, and B. A. Allison—224(A)
Ce^{140} and Sr^{88} spins and parities of excited states, G. R. Bishop and J. P. Perez Y Jorba—89
Cf^{246} α and γ spectra, J. P. Hummel, Frank S. Stephens, Jr., Frank Asaro, A. Chetham-Strode, Jr., and I. Perlman—22
Co^{60} decay angular correlation, J. P. Hurley, S. W. Rudman, and P. S. Jastram—1187(A)
Co^{56} decay polarization correlation, G. T. Wood and P. S. Jastram—1187(A)
Co^{57} decay, L. Madansky and F. Rasetti—1870(E)
Co^{57} radioactivity, Bernd Crasemann and D. L. Manley—66; 279(A)
Cr^{49} decay, R. van Lieshout, D. H. Greenberg, and C. S. Wu—1171(A)
Cs^{132} electromagnetic radiations, Berol L. Robinson and Richard W. Fink—231(A)
Direct evaluation of fractional parentage coefficients using Young operators: Normalization of four-particle wave functions, M. J. Englefield—1213
Electric excitation of certain medium-weight nuclei by protons, Hans Mark, Clyde McClelland, and Clark Goodman—1245
Electric excitation of heavy nuclei with protons, Clyde McClelland, Hans Mark, and Clark Goodman—249(A)
Electric excitation of nuclei near closed 50 proton and neutron shells, Hans Mark, Clyde McClelland, and Clark Goodman—249(A)
Electric monopole transitions in C^{12} and O^{16}, L. I. Shiff—1281
Electron-neutrino angular correlation in β decay of Ne^{19}, D. R. Maxson, J. S. Allen, and W. K. Jentschke—230(A)
Er^{166} γ-γ directional correlation, J. S. Fraser and J. C. D. Milton—1173(A)
Evidence for mixed $M3+M4$ isomeric transition, John W. Mihelich and M. Goldhaber—1185(A)
Evidence for 0+ first excited state in Zr^{90}, O. E. Johnson, R. G. Johnson, and L. M. Langer—1517(L)
Excited states of C^{12} and O^{16}, L. I. Schiff—235(A)
Extranuclear effects on directional correlation of Ta^{181} γ rays, H. Paul and R. M. Steffen—231(A)
Fast $E2$ transitions, A. W. Sunyar—653
γ radiation from deuteron bombardment of N^{14}, R. D. Bent, T. W. Bonner, J. H. McCrary, and R. F. Sippel—1198(A)
γ radiation from interaction of 4.4-Mev neutrons with Fe^{54} and Fe^{56}, Rolf M. Sinclair—1147(A)
γ radiation from neutron inelastic scattering, G. L. Griffith—579
γ radiation from Po neutron sources, R. J. Breen and M. R. Hertz—599
γ rays accompanying spontaneous fission of Cf^{252}, Harry R. Bowman and Lloyd G. Mann—277(A)
γ-rays from deuteron bombardment of C^{13}, R. J. Mackin, Jr., W. B. Mims, and W. R. Mills, Jr.—43
γ rays from inelastic scattering of neutrons in Al, Mg, and Ag, L. A. Rayburn, D. L. Lafferty, and T. M. Hahn—701
γ rays from low-energy proton bombardment of Be, R. R. Carlson and E. B. Nelson—1310
γ rays from proton bombardment of Li^6, S. Bashkin and R. R. Carlson—230(A)
γ rays from proton capture in Li^7, C. P. Swann, M. A. Rothman, W. C. Porter, and C. E. Mandeville—1183(A)
γ rays in α decay of 100^{254}, F. Asaro, F. Stephens, and I. Perlman—260(A)
γ-γ directional correlation in $Cl^{34}\rightarrow S^{34}$ decay, Harry E. Handler and J. Reginald Richardson—281(A)
Gyromagnetic ratio of 6×10^{-8} sec Np^{237} by angular-correlation techniques, V. E. Krohn, T. B. Novey, and S. Raboy—1187(A)
Hf^{177} energy levels, P. Marmier, F. Boehm, and J. W. M. DuMond—280(A)
Higher excited states of even-even nuclei, Gertrude Scharff-Goldhaber and Joseph Weneser—1186(A)
Ho^{166} disintegration (27-hr), R. L. Graham, J. L. Wolfson, and M. A. Clark—1173(A)
Ho^{166} long-lived isomer, J. C. D. Milton, J. S. Fraser, and G. M. Milton—1173(A)
Ho^{167}, T. H. Handley, W. S. Lyon, and E. L. Olson—688
I^{130} radiations, L. Koerts, P. Macklin, B. Farrelly, R. van Lieshout, and C. S. Wu—1172(A); 1230
In^{117} and Sb^{117} radioactivity, Carl L. McGinnis—1870(E)
Inner bremsstrahlung from A^{37}, Torsten Lindqvist and C. S. Wu—231(A)
Internal conversion in L and M subshells, E. L. Church and J. E. Monahan—718
Ir^{194}, C. E. Mandeville, Jagdish Varma, and Babulal Saraf—94; 1185(A)
Isomeric states in chain $Mo^{90}\rightarrow Nb^{90}\rightarrow Zr^{90}$, H. B. Mathur and E. K. Hyde—261(A)
Isotopic spin selection rule for electric dipole transitions, William M. MacDonald—60
K and L x-ray intensities in Cs^{131} decay, Richard W. Fink and Berol L. Robinson—1293
K-shell internal conversion coefficients, R. C. Rohr and R. D. Birkhoff—1266
L-conversion in pure $E2$ transitions, F. Boehm, P. Marmier, and J. W. M. DuMond—280(A)

Magnetic and electric deflection spectrometry of neutrino recoils in A^{37}, Arthur H. Snell and Frances Pleasonton—1174(A)
Magnetic moment of 0.247-Mev excited state of Cd^{111}, W. Zobel and R. M. Steffen—1186(A)
Millisecond γ emitter from protons on Ta, Sheldon D. Softky—280(A); 736
Mo^{90} radiations and Nb^{90} isomeric states, Hirdaya Mathur and Earl K. Hyde—79
Modification of one-particle model for nuclear radiative transitions, P. R. Wallace—1205(A)
Molecular excitation in β decay, Murray Cantwell—235(A)
Multipolarity of γ transitions in F^{19} and Na^{23} by Coulomb excitation, G. M. Temmer and N. P. Heydenburg—1198(A)
Na^{25} decay γ rays, John E. Iwersen and W. S. Koski—1307
Nb^{91} and Nb^{90} disintegration, R. W. Hayward, D. D. Hoppes, and H. Ernst—231(A)
Np^{235} positron emission, R. J. Prestwood, H. L. Smith, C. I. Browne, and D. C. Hoffman—1324
Np^{235} decay scheme, J. O. Rasmussen and H. Slätis—261(A)
Nuclear configuration interaction with singlet two-body forces, Carl A. Levinson—1205(A)
Nuclear pairs from 3.4-Mev state in Ca^{40}, R. D. Bent, T. W. Bonner, and J. H. McCrary—1325
100^{254} γ rays, Frank Asaro, Frank S. Stephens, Jr., S. G. Thompson, and I. Perlman—19
Pa^{231} α decay, John P. Hummel, F. Asaro, and I. Perlman—261(A)
Pair spectrometer measurements of radiations from excited states of light nuclei, R. D. Bent, T. W. Bonner, and R. F. Sippel—1237
Pb^{204m} γ-γ correlation, Sol Raboy and Victor E. Krohn—231(A)
Pb^{208} energy levels, G. E. Tauber—1204(A)
Pm^{151} and Nd^{147} disintegration, coincidence studies, H. S. Hans, Babulal Saraf, and C. E. Mandeville—1173(A)
Predicted 0+ level in $_{40}Zr^{90}$, Kenneth W. Ford—1516(L)
Properties of excited states of Pd and Cd nuclei by Coulomb excitation, G. M. Temmer and N. P. Heydenburg—1308
Ra^{225} and Tl^{200} γ rays, I. Perlman, F. Stephens, and F. Asaro—262(A)
Radioactive decay of 65-hr Sb^{122}, Michael J. Glaubman—645
Radionuclides Al^{24}, P^{32}, Cl^{32}, and Sc^{40}, Neel W. Glass and J. Reginald Richardson—1251
RaE β decay, L. Lidofsky, N. Benczer, P. Macklin, and C. S. Wu—1186(A)
Re^{186} first-forbidden nonunique β spectra, F. T. Porter, M. S. Freedman, T. B. Novey, and F. Wagner, Jr.—214(L)
Ru^{103} decay, H. H. Forster and A. Rosen—1172(A)
Sb^{120} disintegration (5.8-day), C. L. McGinnis—1172(A)
Sb^{122} decay of 3.5-min metastable state, J. M. LeBlanc, J. M. Cork, and S. B. Burson—39
Sb^{122} decay (65-hour), Michael J. Glaubman—1172(A)
Sb^{122} radiations, B. Farrelly, L. Koerts, R. van Lieshout, N. Benczer, and C. S. Wu—1172(A)
Sc^{41} levels, H. S. Plendl and F. E. Steigert—1538(A)
Se^{78} disintegration, R. W. Hayward and D. D. Hoppes—1172(A)
Se^{76} energy levels in disintegration of As^{76}, J. D. Kurbatov, B. B. Murray, and M. Sakai—674
Search for excited states of Be^{8}, R. E. Holland, D. R. Inglis, and F. P. Mooring—240(A)
Sn^{109} radioactivity, M. D. Petroff, S. W. Mead, and W. O. Doggett—279(A)
Soluble problem in theory of Coulomb excitation, L. C. Biedenharn and C. M. Class—691
Spin and lifetime of 439-kev excited state of Hg^{202}, Franz R. Metzger—200(L)
Supermultiplet structure and spin-dependent forces, R. W. King—235(A)
System of even-even nuclei, Gertrude Scharff-Goldhaber and J. Weneser—212(L)
Ta^{180} nuclear orbital assignments, P. F. Zweifel—1174(A)
Tabulation of F coefficients, M. Ferentz and N. Rosenzweig—222(A)
Tensor force interaction energies for configurations important in O^{18} and F^{18}, D. R. Bach, C. R. Lubitz, and P. V. C. Hough—235(A)
Th^{228} α-γ directional correlation, T. B. Novey—232(A)
Theorem on angular correlation, S. Raboy and V. E. Krohn—24
Threshold values of internal conversion coefficients for K-shell, B. I. Spinrad—1302
$_{22}Ti^{51}$ decay (5.8 min), S. B. Burson, W. C. Jordan, and J. M. LeBlanc—230(A)
Tl^{204} and Bi^{207} radioactivity, L. S. Cheng, Virginia C. Ridolfo, M. L. Pool, and D. N. Kundu—231(A)
U^{234} rotational states of excitation, E. L. Church and A. W. Sunyar—1186(A)
V^{48} nuclear levels, Joseph R. Wilkinson and Raymond K. Sheline—1538(A)
Y^{90}, Zr^{97}, Pr^{142}, and Pr^{143}, B. Saraf, J. Varma, and C. E. Mandeville—1206(A)
Y^{91} decay, B. Kahn and W. S. Lyon—58
Zr^{90m} decay and fast neutron excitation, E. C. Campbell, R. W. Peelle, F. C. Maienschein, and P. H. Stelson—1172(A)

Nuclear Structure Theory (see also **Nuclear Reactions; Nuclear Spectra**)

α decay of spheroidal nuclei, R. F. Christy—1205(A)
Angular momentum coupling in deuteron reactions, T. Auerbach and J. B. French—1276
Average nuclear potentials and densities, W. J. Swiatecki—204(L)
Cloudy crystal ball analysis of 14-Mev elastic neutron scattering data, W. R. Faust, R. C. O'Rourke, and J. O. Elliot—1147(A)
Determination of nuclear level density, S. E. Darden, A. Okazaki, and R. L. Becker—1147(A)
Deuteron model for π-meson and photon capture by complex nuclei, B. T. Feld—1155(A)
Deuteron reactions and j-j coupling shell model, J. B. French and B. J. Raz—1523(L)
Electric monopole transitions in C^{12} and O^{16}, L. I. Schiff—1281
Equivalent two-body method for triton, Herman Feshbach and S. I. Rubinow—188
Evaluation of imaginary part of nuclear complex potential, A. M. Lane and C. F. Wandel—1524(L)
Exchange current effects in two-nucleon system, J. Bernstein and Abraham Klein—1155(A)
Excited states of C^{12} and O^{16}, L. I. Schiff—235(A)
Experimental evidence for optical model for neutrons between 60 and 110 Mev, Vaughn Culler and R. W. Waniek—1148(A)
$\bar{\Gamma}_n^0/\bar{D}$ for slow neutron resonances, R. Cote and L. M. Bollinger—1162(A)
Giant resonance interpretation of nucleon-nucleus interaction, A. M. Lane, R. G. Thomas, and E. P. Wigner—693
High-energy cross sections. I. Size of nucleus, Robert W. Williams—1387

Nuclear Structure Theory (Continued)
High-energy reactions and evidence for correlations in nuclear ground-state wave function, K. A. Brueckner, R. J. Eden, and N. C. Francis—1445
Importance of parentage of nuclear states for nuclear reaction phenomena, D. H. Wilkinson and A. M. Lane —235(A)
Independent particle model mass surface, A. E. S. Green and Kiuck Lee—1205(A)
Intermediate coupling model of Li^6, R. H. Adkins and J. G. Brennan—235(A)
Isotopic spin impurity in light nuclei, W. M. MacDonald —234(A)
Isotopic spin selection rule for electric dipole transitions, William M. MacDonald—60
Level spacings of heavy nuclei, John A. Harvey—1162(A)
Many-body problem with strong forces, Robert Jastrow— 1479
Matrix elements of nuclear p^3 configuration, S. Meshkov and C. W. Ufford—1204(A)
Model for asymmetric fission, R. D. Hill—1272
Modification of one-particle model for nuclear radiative transitions, P. R. Wallace—1205(A)
Neutron widths of nuclear energy levels, D. J. Hughes— 1161(A)
Nuclear configuration interaction with singlet two-body forces, Carl A. Levinson—1205(A)
Nuclear models, R. J. Eden and N. C. Francis—1205(A)
Nuclear surface energy and diffuseness of nuclear surface, W. J. Swiatecki—203(L)
Optical model analysis of scattering of 14-Mev neutrons, N. Sherman, G. Culler, and S. Fernbach—273(A); II. Polarization effects, S. Fernbach, G. Culler, and N. Sherman—273(A)
Particle motion in anisotropic harmonic oscillator well, Martin L. Gursky—1205(A)
Pb^{208} energy levels, G. E. Tauber—1204(A)
Photodisintegration of deuteron, Yoshio Yamaguchi and Yoriko Yamaguchi—69
Polarization of deuteron, B. W. Downs—258(A)
Polarization of nucleons elastically scattered from nuclei, R. M. Sternheimer—1156(A); 1870(E)
Radiation widths of nuclear energy levels, J. S. Levin and D. J. Hughes—1161(A)
Scattering of high-energy neutrons and Johnson-Teller type nuclei, Yoshihiro Nakano—842(L)
Shell theory for nuclei with mass 19, Martin G. Redlich— 199(L)
Supermultiplet structure and spin-dependent forces, R. W. King—235(A)
System of even-even nuclei, Gertrude Scharff-Goldhaber and J. Weneser—212(L)
Tensor force interaction energies for configurations important in O^{18} and F^{18}, D. R. Bach, C. R. Lubitz, and P. V. C. Hough—235(A)
3-body exchange magnetic moments of H^3 and He^3, Andrew M. Lockett—1204(A)
Variation calculation of polarizability of deuteron, B. W. Downs—194
Velocity-dependent nuclear potential, J. S. Levinger— 1205(A)

Optical Instruments (see **Methods and Instruments**)
Optical Properties (see also **Luminescence**)
Absorption by free and bound holes in p-type Ge, S. Teitler, M. Lax, and E. Burstein—1561(A)
Absorption of radiation in vacuum uv by N atoms produced in discharge plasma in nitrogen, A. W. Ehler and G. L. Weissler—561(A)
Anomalous optical properties of ferroelectric $PbTiO_3$, Gen Shirane and Ray Pepinsky—1201(A)
Birefringence in Si, W. C. Dash—1536(A)
Detection of vacancies created in NaCl by x-rays, H. W. Etzel—1531(A)
Direct production of spectroscopic specimens from single crystals by controlled growth from vapor; infrared absorption anisotropy and induced molecular motion in single crystal of benzene, Solomon Zwerdling and Ralph S. Halford—243(A)
Displacement of latent image in photographic emulsion grains, J. F. Hamilton, F. A. Hamm, and J. W. Castle —1557(A)
Effect of O_2 gas on photoconductivity of BaO, M. Sakamoto, S. Kobayashi, and S. Ishii—552(L)
Effect of pressure on absorption edges of Te, L. J. Neuringer—1193(A)
Effect of pressure on optical absorption edge in Si and Ge, D. M. Warschauer, W. Paul, and H. Brooks—1193(A)
Electrical and optical properties of GaSb films, R. J. Collins, F. W. Reynolds, and G. R. Stilwell—227(A)
Energy requirement for F-center formation, R. S. Alger and R. D. Jordan—1550(A)
Extreme uv absorption spectrum of AgCl, Charles J. Koester and M. Parker Givens—1543(A)
Heat treatment of irradiated NaN_3, Russell W. Dreyfus and Paul W. Levy—1541(A)
Impurity-induced color centers in fused silica, Alvin J. Cohen—1550(A)
Infrared absorption in n-type Ge, W. Spitzer, R. J. Collins, and H. Y. Fan—1536(A)
Infrared absorption of InSb, W. Kaiser and H. Y. Fan —966
Infrared absorption of liquid and solid hydrogen, Elizabeth J. Allin, W. F. J. Hare, and R. E. MacDonald—554(L)
Infrared absorption of Si near lattice edge, G. G. Macfarlane and V. Roberts—1865(L)
Interpretation of donor state absorption lines in Si, Walter Kohn—1856(L)
Interpretation of optical properties of metal surfaces, S. Roberts—1151(A)
Investigation of quantitative phase contrast method for examining nonhomogeneous media, G. C. Krueger— 1157(A)
Light scattering from optical glass, R. D. Maurer— 1544(A)
Low-intensity reciprocity law failure for pure AgBr emulsions of different grain size, R. L. Martin, J. E. Enns, and E. Katz—1557(A)
Low-temperature luminescence and absorption of CdS, L. R. Furlong and C. F. Ravilious—954
Magnetic domain patterns observed by Kerr effect in BiMn alloy, B. W. Roberts and C. P. Bean—225(A)
Magnetic domains in single crystal of Co near 275°C by longitudinal Kerr effect, Edward M. Fryer and Charles A. Fowler, Jr.—270(A)
Model for room temperature bleaching of F centers by F light in x-rayed NaCl, Robert Herman and R. F. Wallis —1171(A)
New radiation due to recombination of holes and electrons in Ge, J. R. Haynes—1866(L)
Optical absorption bands induced in γ irradiated glass, K. R. Ferguson—1542(A)
Optical absorption in single crystals of Ge and Si, W. C. Dash, R. Newman, and E. A. Taft—1192(A)
Optical absorption measurements on Ag halide crystals, Nelson R. Nail, Frank Moser, Pliny E. Goddard, and Franz Urbach—1557(A)
Optical absorption spectra of ThO, J. H. Bodine and F. B. Thiess—1532(A)
Optical and electrical properties of LiF x-rayed at liquid nitrogen temperature, C. J. Delbecq, P. Pringsheim, and P. H. Yuster—237(A)

Optical effects in plastically deformed Ge, H. G. Lipson, E. Burstein, and P. L. Smith—1535(A)
Optical properties and twinning of $PbZrO_3$ single crystals, F. Jona, G. Shirane, and R. Pepinsky—1201(A)
Optical properties of group III elements in Si, E. Burstein, G. Picus, B. Henvis, and M. Lax—1536(A)
Oxygen gas continuous absorption in extreme uv, William A. Rense and R. Mercure—1195(A)
Phase change on reflection from multilayer films, F. A. Jenkins and D. R. Speck—282(A)
Photoconductivity and photodesorption in ZnO, David B. Medved—237(A)
Photoelastic observation of expansion of alkali halides in irradiation, W. Primak, P. H. Yuster, and C. J. Delbecq—237(A); W. Primak, C. J. Delbecq, and P. H. Yuster—1708
Photographic effects in single crystals of AgBr, W. West and V. I. Saunders—1557(A)
Photographic "order principle," E. Katz—1556(A)
Pressure dependence of absorption edge in Ge and Si, W. Spitzer, C. O. Bennett, and H. Y. Fan—228(A)
Properties of powdered Ge and effects of heat treatment, E. A. Kmetko—1535(A)
Radiation-induced coloring of NaN_3, Hyman Rosenwasser and Paul W. Levy—1541(A)
Reactor- and γ-ray-induced coloring in Corning fused silica, Paul W. Levy—1541(A)
Recombination processes in CdS, John Lambe—985
Sequence experiment for study of reciprocity law failure at low intensities, J. H. Enns, R. L. Martin, and E. Katz—1556(A)
Smakula's equation in insulating solids, D. L. Dexter—1533(A)
Storage of energy in BeO, H. O. Albrecht and C. E. Mandeville—1546(A)
Susceptibility and entropy of F centers, J. G. Daunt and J. Korringa—1550(A)
Theory of Ag-halide photolysis, Charles A. Duboc—1557(A)
Thermal bleaching of color centers, A. Halperin and A. Braner—1135(L)
Thermal formation of colloids from F centers in KCl crystals, H. Pagnia and F. Stockman—236(A)
Ultra-short light-and-voltage pulses applied to Ag-halide crystals by turbine-driven mirror and electrical contacts, J. H. Webb—1558(A)
Visible light from Si p-n junction, R. Newman, W. C. Dash, R. N. Hall, and W. E. Burch—1536(A)

Pair Production (see **Electrons and Positrons**)
Phosphors and Phosphorescence (see **Luminescence; Semiconductors**)
Photoconductivity (see **Electrical Conductivity and Resistance**)
Photodistintegration (see **Nuclear Photoeffects**)
Photoelasticity (see **Elasticity and Plasticity**)
Photoelectric Effect (see **Electrical Properties**)
Photography and Photographic Emulsions (see **Methods and Instruments; Optical Properties**)
Photometry (see **Methods and Instruments; Optical Properties**)
Photons (see **Radiation**)
Photovoltaic Effect (see **Electrical Properties; Semiconductors**)
Piezoelectric Effect (see **Dielectrics and Dielectric Properties**)
Plasticity (see **Elasticity and Plasticity**)
Polarization, Electrical (see **Dielectrics and Dielectric Properties**)
Polymers (see **Molecular Aggregates**)
Positrons (see **Electrons and Positrons**)
Probability (see **Mathematical Methods**)
Proceedings of the American Physical Society
Seventh Annual Gaseous Electronics Conference at New York, New York, on October 14–15–16, 1954—557
Meeting of the Division of Fluid Dynamics Held at Old Point Comfort and Langley Aeronautical Laboratory, Virginia, November 22–24, 1954—1139
Thanksgiving Meeting at Chicago, Illinois, November 26 and 27, 1954 [Bull. Am. Phys. Soc. **29**, No. 7 (1954)]—220
Winter Meeting on the Pacific Coast at University of California, Berkeley, California, December 28, 29, and 30, 1954 [Bull. Am. Phys. Soc. **29**, No. 8 (1954)]—254
Annual Meeting at New York City, New York, January 27–29, 1955 [Bull. Am. Phys. Soc. **30**, No. 1 (1955)]—1144
Meeting Held at Baltimore, Maryland, March 17–18–19, 1955 [Bull. Am. Phys. Soc. **30**, No. 2 (1955)]—1528
Spring Meeting of the New England Section at Brown University, Providence, Rhode Island on April 2, 1955—1210
Protons (see **Elementary Particle Interactions**)

Quantum Electrodynamics (see also **Field Theory**)
Derivation of Feynman-Dyson rules from time-independent theory, Saul T. Epstein—196
Effect of extended size of nucleus on μ-meson pair photoproduction, George Rawitscher—272(A)
Fourth-order radiative corrections to atomic energy levels. II, Robert L. Mills and Norman M. Kroll—1489
Hfs of He^{3+} and He^3, A. M. Sessler and H. M. Foley—6
Infrared divergence, F. Rohrlich and J. M. Jauch—222(A)
Infrared divergence in bound state problems, F. Rohrlich—181
Lamb shift of $1S$ level of deuterium, G. Herzberg—223(A)
Multiple-photon production in quantum electrodynamics, Suraj N. Gupta—1502
New relativistic two-body equation, Vladimir Glaser—840(L)
Possible convergence of mass renormalization, T. A. Welton—1175(A)
Quantum effects in interaction between electrons and high-frequency fields. II, I. R. Senitzky—875
Radiative correction to electron scattering, H. Suura—278(A)
Radiative corrections to electron scattering, Max Chrétien—1515(L); Roger G. Newton—1514(L)
Radiative corrections to muon decay, R. J. Finkelstein and R. E. Behrends—1155(A); 1870(E)
Vacuum polarization and p-p scattering, Leslie L. Foldy and Erik Eriksen—775; 1190(A)
Quantum Mechanics
Auxiliary conditions in Bohm-Pines theory of electron gas, E. N. Adams—1130(L)
Canonical invariance in Lagrangian quantum mechanics, W. K. Burton—555(L)
Collective description of electron gas, M. Dresden—1165(A)
Connection between recent theories of Bohm, De Broglie, Dirac, and Schrödinger, Hans Freistadt—1176(A)
Construction on noncentral potentials from S-matrix, Roger G. Newton and Res Jost—1189(A)
Decomposition of generalized Duffin-Kemmer algebra, K. M. Case—1189(A)
Determination of scattering potential from spectral weight function, I. Kay and H. E. Moses—1190(A)
Dirac bracket transformations in phase space, Peter G. Bergmann and Irwin Goldberg—531
Dirac's method using complex variables in quantum mechanics, Eugene Guth—273(A)

Quantum Mechanics (Continued)
Energies of ground states of He, Li^+, and O^{6+}, S. Chandrasekhar and G. Herzberg—1050
Existence of Dirac generating functions, Peter G. Bergmann—544(L)
Extension of Hund's rule, G. F. Koster—514
Formulation of probability theory as physical theory, A. O. Barut—274(A)
Foundation of wave-mechanical theory of electron, Walter Glaser—1176(A)
Generation of Coulomb wave functions by means of recurrence relations, Irene A. Stegun and Milton Abramowitz—1851
He wave equation, James H. Bartlett—1067
Joint probabilities and transition probabilities in differential-space quantum theory, Norbert Wiener and Armand Siegel—1190(A)
Many-body problem with strong forces, Robert Jastrow—1479
New extension of collective coordinates for many-body problem, Jerome K. Percus and George J. Yevick—1164(A)
New interpretation of Dirac equation, Ralph Schiller—1176(A)
New relativistic two-body equation, Vladimir Glaser—840(L)
Nonrelativistic limit of spin $(k+\frac{1}{2})$ particle wave equations, P. A. Moldauer and K. M. Case—1190(A)
One-electron energies of atoms, molecules, and solids, J. C. Slater—1039
Orthogonality of Furry-Sommerfeld-Maue wave functions and their use in perturbation theory, R. T. Sharp and J. David Jackson—1128(L)
Projection operator for Rarita-Schwinger equation, F. J. Milford—1488
Quantized linear theory of gravitation, F. J. Belinfante and J. C. Swihart—222(A)
Quantum effects in interaction between electrons and high-frequency fields. II, I. R. Senitzky—875
Quantum theory of noise, Norman Rostoker and Hans Ekstein—222(A)
Relativistic energy of two-electron atoms, Ta-You Wu and G. E. Tauber—222(A)
Relativistic wave equations, Herman Feshbach—801
Spin models, David Finkelstein—1175(A)
Tabulation of F coefficients, M. Ferentz and N. Rosenzweig—222(A)
Transformations in phase space and Dirac brackets, Peter G. Bergman and Irwin Goldberg—1175(A)
Variational principle for tensor forces, J. L. McHale and R. M. Thaler—273(A)
Wave functions and transition probabilities for light atoms, Huseyin Yilmaz—1190(A)
Quenching of Radiation (see **Radiation**)

Radar (see **Methods and Instruments; Radiation**)
Radiation (see also **Gamma Rays; Range and Energy Loss; X-Rays**)
Analysis of high-energy photons from cyclotron target, Harlan Shaw, David Cohen, Burton J. Moyer, and Charles Waddell—259(A)
Angular distribution of bremsstrahlung photons, John D. Anderson, Robert W. Kenney, and Charles A. McDonald, Jr.—258(A)
Cyclical variations in effective radiation temperature of ozone region, Arthur Adel—282(A)
Determination of bremsstrahlung spectrum produced by 18-Mev electrons, R. L. Stearns, J. W. Robson, and E. C. Gregg—232(A)
Determination of polydisperse aerosol size distributions from analysis of light scattering data, T. L. Gilbert—242(A)
Elastic scattering of 0.41 and 0.66 Mev γ rays by Sn and Pb, A. K. Mann—234(A)
Elastic scattering of 1.6-Mev γ rays from C, Luis W. Alvarez, Frank S. Crawford, Jr., and M. Lynn Stevenson—280(A)
Emergent electron distribution resulting from bremsstrahlung incident on thin scatterer, J. W. Robson, R. L. Stearns, and E. C. Gregg—233(A)
Entropy of radiation, Aadne Ore—887
Experimental cross section for photodetachment of electrons from H^- and D^-, Lewis M. Branscomb and Stephen J. Smith—1028
Inner bremsstrahlung from A^{37}, Torsten Lindqvist and C. S. Wu—231(A)
Light scattering from optical glass, R. D. Maurer—1544(A)
Measurement of absorption coefficients for photoionizing radiations in low-pressure gases with space charge detector, C. D. Maunsell—1831
Measurement of Čerenkov radiation from positive and negative π mesons, J. R. Winckler, E. N. Mitchell, K. A. Anderson, and L. Peterson—1411
Orientation and alignment of Na atoms by means of polarized resonance radiation, William Bruce Hawkins—478
Photoelectric mixing of incoherent light, A. Forrester, Richard A. Gudmundsen, and Philip O. Johnson—1169(A)
Preliminary studies with high-energy photon spectrometer, C. E. Swartz and J. W. DeWire—1164(A)
Proton bremsstrahlung, Hans Mark, Clyde McClelland, and Clark Goodman—279(A); Behram Kurşunoğlu—1156(A)
Resonance absorption of sunlight in twilight layers, T. M. Donahue and Robert Resnick—1622
Scattering of 100-Mev γ rays from C, D. M. Ritson, A. Pevsner, and R. L. Zimmerman—1168(A)
Self-absorption or self-indication in nuclear elastic scattering experiment, E. G. Fuller and Evans Hayward—1537(A)
Stark fields from ions in plasma, Arthur Broyles—1166(A)
Radio Waves (see **Radiation**)
Radioactivity (see also **Nuclear Spectra**)
Am^{243} α groups and angular correlation, F. Stephens, J. Hummel, F. Asaro, and I. Perlman—261(A)
Branching ratio of K^{40} and age of meteorites, G. J. Wasserburg and R. J. Hayden—250(A)
Cf^{246} α and γ spectra, J. P. Hummel, Frank S. Stephens, Jr., Frank Asaro, A. Chetham-Strode, Jr., and I. Perlman—22
Co^{60} field distributions using Ag activated phosphate glass, Herbert Rabin and William E. Price—1154(A)
γ rays accompanying spontaneous fission of Cf^{252}, Harry R. Bowman and Lloyd G. Mann—277(A)
γ rays in α decay of 100^{254}, F. Asaro, F. Stephens, and I. Perlman—260(A)
Gyromagnetic ratio of 6×10^{-8} sec Np^{237} by angular-correlation techniques, V. E. Krohn, T. B. Novey, and S. Raboy—1187(A)
Mendelevium, atomic number 101, A. Ghiorso, B. G. Harvey, G. R. Choppin, S. G. Thompson, and G. T. Seaborg—1518(L)
Neutron deficient chains of mass 187 through 191, W. G. Smith and J. M. Hollander—262(A)
Np^{234} positron emission, R. J. Prestwood, H. L. Smith, C. I. Browne, and D. C. Hoffman—1324
Np^{239} decay scheme, J. O. Rasmussen and H. Slätis—261(A)

Nuclear properties of 100^{256}, G. R. Choppin, B. G. Harvey, S. G. Thompson, and A. Ghiorso—1519(L)
Occurrence of Tc^{98} in nature, Edward A. Alperovitch and J. Malcolm Miller—262(A)
100^{254} γ rays, Frank Asaro, Frank S. Stephens, Jr., S. G. Thompson, and I. Perlman—19
Photographic amplification in α-particle autoradiography, K. H. Sun, P. R. Malmberg, and P. Szydlik—1154(A)
Potassium-argon ages of lepidolites, G. W. Wetherill, L. T. Aldrich, and G. L. Davis—250(A)
Ra^{225} and Tl^{209} γ rays, I. Perlman, F. Stephens, and F. Asaro—262(A)
Radiochemical study of neutron-deficient chains in noble metal region, W. G. Smith and J. M. Hollander—1258
RaE β decay, L. Lidofsky, N. Benczer, P. Macklin, and C. S. Wu—1186(A)
Rb^{86} half-life, James B. Niday—42
Ta^{180} nuclear orbital assignments, P. F. Zweifel—1174(A)
Th^{228} α-γ directional correlation, T. B. Novey—232(A)
Tl^{204} and Bi^{207} radioactivity, L. S. Cheng, Virginia C. Ridolfo, M. L. Pool, and D. N. Kundu—231(A)
U^{234} rotational states of excitation, E. L. Church and A. W. Sunyar—1186(A)
U^{238} disintegration constant, A. F. Kovarik and N. I. Adams, Jr.—46

Raman Spectra (see **Molecular Structure and Spectra**)

Range and Energy Loss of Particles (see also **Scattering**)
Comparison of energy to make ion-pair in various gases for α and β particles, William P. Jesse and John Sadauskis—1150(A)
Direct measurement of effect of polarization on energy loss, E. L. Goldwasser, F. E. Mills, and T. R. Robillard—1763
Electron capture and loss by ions in gases, Robert L. Gluckstern—1817
Energy loss by 8.86-Mev deuterons and 4.43-Mev protons, J. E. Brolley, Jr., and F. L. Ribe—1112
Energy required to produce one ion pair for several gases, J. Weiss and W. Bernstein—1828
Ionization loss in nuclear emulsions, John R. Fleming and J. J. Lord—268(A)
Ionization of air by γ rays, E. L. Burkhard and J. H. Lewis—1154(A)
μ-meson ionization in argon at energies 10 to 100 Bev, Allan N. Wilson—268(A)
New method for measuring α-particle range and straggling in liquids, Gunner Aniansson—300
Passage of charged particles through plasma, Jacob Neufeld and R. H. Ritchie—1632
Range straggling in nuclear track emulsion, Walter H. Barkas, Frances M. Smith, and Wallace Birnbaum—605
Relation between multiple Coulomb scattering and residual range in nuclear emulsion, R. G. Glasser—174
Relative stopping powers for 20-Mev protons, C. P. Sonett and K. R. MacKenzie—280(A)
Rotational excitation by slow electrons. II, E. Gerjuoy and S. Stein—1848
Specific ionization of high-energy electrons, W. C. Barber—276(A)
Stopping cross sections of metals for protons of energies from 400 to 100 kev, D. Wayne Green, John N. Cooper, and James C. Harris—466
Theory of electron penetration, L. V. Spencer—1597

Recombination (see **Molecular Structure and Spectra**)

Rectifiers (see **Electrical Conductivity and Resistance; Semiconductors**)

Relativity and Gravitation
Emission of negative-energy gravitons by matter, F. J. Belinfante—1175(A)
Freundlich red-shift formula, M. A. Melvin—884
New approximation method for gravitational field equations, J. N. Goldberg—1176(A)
Quantized linear theory of gravitation, F. J. Belinfante and J. C. Swihart—222(A)
Relativistic cosmology. I, Amalkumar Raychaudhuri—1123
Special-relativistic derivation of generally covariant gravitation theory, Robert H. Kraichnan—1118
Use of flat-space metric in Einstein's curved universe, and "Swiss-cheese" model of space, Frederik J. Belinfante—793

Resistance, Electrical (see **Electrical Conductivity and Resistance**)

Resonance Radiation (see **Radiation**)

Scattering, General (see also **Diffraction; Elementary Particle Interactions; Nuclear Reactions; Range and Energy Loss of Particles**)
Applications of causality to scattering, Robert Karplus and Malvin A. Ruderman—771
Collision alignment of molecules, atoms, and nuclei, Norman F. Ramsey—1853(L)
Construction of noncentral potentials from S-matrix, Roger G. Newton and Res Jost—1189(A)
Determination of scattering potential from spectral weight function, I. Kay and H. E. Moses—1190(A)
Differential cross-section measurements for large-angle collisions of He, Ne, and A ions with A atoms at energies to 100 kev, Edgar Everhart, R. J. Carbone, and Gerald Stone—1045
Lower limit for energy derivative of scattering phase shift, Eugene P. Wigner—145
Measurement of scattering constant in nuclear emulsion, Lyle W. Smith—100
Multiple-scattering microscope for "constant sagitta" measurements, Stephen J. Goldsack and Gerson Goldhaber—284(A)
Polarization and cross section for inelastic scattering, M. A. Ruderman—267(A)
Polarization of nucleons elastically scattered from nuclei, R. M. Sternheimer—1156(A); 1870(E)
Possible triple-scattering experiments, L. Wolfenstein—1870(E)
Relation between multiple Coulomb scattering and residual range in nuclear emulsion, R. G. Glasser—174
S-matrix in terms of phenomenological collision parameters, R. M. Thaler and J. L. McHale—1189(A)
Scattering of polarized nucleon beams, Reinhard Oehme—147
Structure of scattering matrix, Yoichiro Nambu—803
Time-dependent displacement correlations and inelastic scattering by crystals, R. J. Glauber—1692
Two-dimensional Coulomb scattering in quantum mechanics, Ming Chen Wang and Eugene Guth—274(A)
Variational expression for N-channel collision parameters, J. L. McHale and R. M. Thaler—1189(A)
Variational principle for scattering with tensor forces, S. I. Rubinow—183
Variational principle for tensor forces, J. L. McHale and R. M. Thaler—273(A)
Variational principle for total scattering amplitude, J. Mayo Greenberg—1189(A)

Scattering of α Particles (see also **Nuclear Reactions Induced by α Particles and He^3**)
Energy levels in N^{14} by inelastic α scattering, D. W. Miller, U. C. Gupta, V. K. Rasmussen, and M. B. Sampson—1184(A)
Multiple scattering of low-energy α particles in gas, G. Allen, R. Webeler, and S. Barile—1168(A)

Scattering of Atoms and Molecules (see **Atomic and Molecular Beams**)

Scattering of Deuterons (see also **Nuclear Reactions Induced by Deuterons and Tritons**)

d-He differential scattering cross sections, A. Galonsky, R. A. Douglas, W. Haeberli, M. T. McEllistrem, and H. T. Richards—586

Li^6 energy levels from *d*-He differential cross sections, A. Galonsky and M. T. McEllistrem—590

Spin polarization of deuteron, W. Lakin—139

Scattering of Electrons and Positrons (see also **Electrons and Positrons**)

Absolute cross sections for Coulomb scattering of 1.75-Mev electrons, T. F. Ruane, B. Waldman, and W. C. Miller —1166(A)

Effects of electron collisions on width of spectral lines, Henry Margenau and Bennett Kivel—1822

Electric quadrupole effects in scattering of high-energy electrons by heavy nuclei, B. W. Downs, D. G. Ravenhall, and D. R. Yennie—277(A)

Electrodisintegration of deuteron, V. Z. Jankus—278(A)

Electron impact broadening of spectral lines, B. Kivel, S. Bloom, and H. Margenau—495

Electron scattering from proton, Robert Hofstadter and Robert W. McAllister—217(L)

Energy required to produce one ion pair for several gases, J. Weiss and W. Bernstein—1828

High-energy electron scattering in Rh, Ta, W, and U, Beat Hahn and Robert Hofstadter—278(A)

Inelastic electron scattering from C at 188 Mev, J. H. Fregeau and R. Hofstadter—1184(A)

Modified Born approximation for electron scattering calculations, D. R. Yennie, D. G. Ravenhall, and B. W. Downs—277(A)

Multiple scattering of 2.5-Mev positrons by 0.1-mil Au foil, L. Grodzins—279(A)

Nuclear dispersion contribution to high-energy electron scattering, L. I. Schiff—278(A); 756

Phase shift analysis of high-energy electron scattering, D. G. Ravenhall and D. R. Yennie—277(A)

Radiative correction to electron scattering, H. Suura—278(A)

Radiative corrections to electron scattering, Max Chrétien —1515(L); Roger G. Newton—1514(L)

Rotational excitation by slow electrons, E. Gerjuoy and S. Stein—557(A); II, E. Gerjuoy and S. Stein—1848

Scattering of high-energy electrons by nuclei, A. E. Glassgold—1360

Scattering of 192-Mev electrons from deuterium, John A. McIntyre and Robert Hofstadter—158

Scattering of 20-kev electrons in thin films, H. Mendlowitz and L. Marton—1168(A)

Single scattering of 20-kev electrons in solids, L. Marton, J. Arol Simpson and T. F. McCraw—1168(A)

Theory of electron penetration, L. V. Spencer—1597

Theory of nuclear excitation in inelastic electron scattering, C. J. Mullin and E. Guth—277(A)

W.K.B. approximation to phase shifts, S. P. Heims, D. R. Yennie, and D. G. Ravenhall—278(A)

Scattering of Mesons (see also **Mesons; Nuclear Reactions Induced by Mesons**)

Applications of causality to scattering, Robert Karplus and Malvin A. Ruderman—771

Differential cross sections for pion-proton scattering at 150 and 170 Mev, F. Feiner, J. Ashkin, J. P. Blaser, and M. O. Stern—239(A)

D-wave solution to pion-proton scattering data, Jay Orear —1155(A)

Effect of renormalization on meson-nucleon *S*-scattering, Maurice M. Lévy—1470

Elastic scattering of π mesons from nuclei. I, Ross Williams, Winslow Baker, Aihud Pevsner, and James Rainwater—1188(A); II, W. F. Baker, R. E. Williams, and J. Rainwater—1188(A)

Interaction of 46-Mev π^+ mesons in deuterium, D. Bodansky and A. M. Sachs—240(A)

Interactions of 1.5-Bev π^- mesons, W. D. Walker and J. Crussard—240(A)

Lower limit for energy derivative of scattering phase shift, Eugene P. Wigner—145

Pion-nucleon *s*-wave phase shift from $ps-ps$ with cutoff, Charles J. Goebel—273(A)

Positive pion scattering by H at 189 Mev, U. Kruse, H. L. Anderson, W. C. Davidon, and M. Glicksman—1188(A)

Scattering and absorption of 50-Mev π^+ mesons in Pb, G. Saphir—269(A)

Scattering of mesons by light nuclei, L. S. Kisslinger—761

Scattering of π mesons by nuclei, Leonard S. Kisslinger—239(A)

Scattering of 23-Mev positive pions on hydrogen, Jay Orear—239(A)

Scattering of 165-Mev pions by protons, M. Glicksman and H. L. Anderson—239(A)

Scattering of 195-Mev pions by deuterium, W. Skolnik—240(A)

Self-energy effects on meson-nucleon scattering according to Tamm-Dancoff method, J. C. Taylor—201(L)

Scattering of Neutrons (see also **Nuclear Reactions Induced by Neutrons**)

Angular distribution of fast neutrons scattered from Pb, W. J. Rhein—1300

Cloudy crystal ball analysis of 14-Mev elastic neutron scattering data, W. R. Faust, R. C. O'Rourke, and J. O. Elliot—1147(A)

Correction to exponential dependence of neutron transmissions, R. G. Thomas—77

Differential elastic scattering cross section for neutrons on nitrogen, J. L. Fowler and C. H. Johnson—728

Differential elastic scattering of 14-Mev neutrons, J. O. Elliot—1147(A)

Diffuse magnetic neutron diffraction, A. W. McReynolds —1200(A)

Elastic and inelastic scattering of 90-Mev neutrons by deuterons, Leroy Kerth and Byron L. Youtz—259(A)

Elastic scattering angular distributions of fast neutrons on light nuclei, Harvey B. Willard, Joe K. Bair, and Joe D. Kington—669

Evaluation of imaginary part of nuclear complex potential, A. M. Lane and C. F. Wandel—1524(L)

γ radiation from neutron inelastic scattering, G. L. Griffith —579

γ rays from inelastic scattering of neutrons in Al, Mg, and Ag, L. A. Rayburn, D. L. Lafferty, and T. M. Hahn —701

γ-γ coincidences produced by inelastic scattering of 2.5-Mev neutrons, W. R. Faust, V. E. Scherrer, and B. A. Allison—224(A)

Inelastic scattering of cold neutrons by Al, R. L. Zimmerman and H. Palevsky—1162(A)

Inelastic scattering of neutrons by Fe, F, Mn, and I, J. J. Van Loef and D. A. Lind—224(A)

Interaction of 4.1-Mev neutrons with nuclei, M. Walt and J. R. Beyster—279(A); 677

Liquid scintillator measurements of angular elastic scattering of neutrons from C, Al, and S, R. N. Little, Jr., B. P. Leonard, Jr., J. T. Prud'homme, and L. C. Vincent—634

Long-wavelength neutron transmission as absolute method for determining concentration of lattice defects in crystals, J. J. Antal, R. J. Weiss, and G. J. Dienes—1541(A)
Magnetic scattering of slow neutrons by gaseous oxygen, H. Palevsky and R. M. Eisberg—492
Measurement of scattering cross sections for low-energy neutron resonances, C. Sheer and J. Moore—565
Multiple scattering of slow neutrons by flat specimens and magnetic scattering by Zn ferrite, B. N. Brockhouse, L. M. Corliss, and J. M. Hastings—1721
Neutron inelastic scattering, Janet B. Guernsey and A. Wattenberg—1147(A)
n-p scattering at 17.9 Mev, A. Galonsky and J. Judish—1168(A)
n-p scattering at 20 Mev, R. B. Day, R. L. Mills, J. E. Perry, Jr., and F. Scherb—279(A)
Optical model analysis of scattering of 14-Mev neutrons, N. Sherman, G. Culler, and S. Fernbach—273(A); II. Polarization effects, S. Fernbach, G. Culler, and N. Sherman—273(A)
Scattering of 4.4-Mev neutrons by Fe and C, B. Jennings, J. Weddell, I. Alexeff, and R. L. Hellens—582
Scattering of high-energy neutrons and Johnson-Teller type nuclei, Yoshihiro Nakano—842(L)
Slow neutron resonant scattering, H. L. Foote, Jr., and J. Moore—1161(A)
Slow neutron scattering by liquid He, D. G. Hurst and D. G. Henshaw—224(A)
Slow neutron spectrometry—New tool for study of energy levels in condensed systems, B. N. Brockhouse—1171(A)
Scattering of Protons (see also **Nuclear Reactions Induced by Protons**)
Analysis of triple scattering and correlation experiments, Henry P. Stapp—267(A)
Asymmetry in deuteron pickup by high-energy polarized protons, B. J. Malenka—1156(A)
Complete scattering matrix in proton-carbon collision, R. Tripp, C. Wiegand, T. Ypsilantis, O. Chamberlain, and E. Segrè—266(A)
Depolarization in scattering of polarized protons by H at 310 Mev, T. Ypsilantis, C. Wiegand, R. Tripp, E. Segrè, and O. Chamberlain—267(A)
Differential cross sections for scattering of protons by C as function of incident proton energy, Robert Peelle—1184(A)
Differential *p-p* scattering cross sections at 419 Mev, J. Marshall, L. Marshall, and V. A. Nedzel—1513(L)
Direction of proton spin polarization produced by elastic scattering, L. Marshall and J. Marshall—1398
Double-scattering experiment with 96-Mev protons, Karl Strauch—234(A)
Elastic *p-p* angular distributions from 440 to 1000 Mev, L. W. Smith, A. W. McReynolds, and G. A. Snow—1167(A)
Elastic scattering of 9.76-Mev protons by He, John H. Williams and Stanley W. Rasmussen—56
Elastic scattering of protons from Li^7, Philip R. Malmberg—1167(A)
Elastic scattering of 20.6-Mev protons by deuterons, David O. Caldwell and J. Reginald Richardson—28
Electron capture cross section for protons, C. F. Barnett and P. M. Stier—1537(A)
$F^{19}(p,p')F^{19*}$ absolute magnetic analysis, C. R. Gossett, G. C. Phillips, and J. T. Eisinger—724
Phase shift analysis of 240-Mev *p-p* scattering, L. Beretta, E. Clementel, and C. Villi—1526(L)
p-He^3 interaction, R. M. Frank and J. L. Gammel—1204(A)
Possible experiments to determine transition matrix for *p-p* scattering, Reinhard Oehme—216(L)
Possible triple-scattering experiments, L. Wolfenstein—1870(E)
p-p scattering at 900 Mev, T. W. Morris, J. D. Garrison, E. C. Fowler, W. B. Fowler, R. P. Shutt, A. M. Thorndike, and W. L. Whittemore—1167(A)
p-p scattering experiments at 170 and 260 Mev, Owen Chamberlain and John D. Garrison—1167(A)
Proposed method for obtaining high-energy polarized proton beam, R. Tripp—1167(A)
Proton bremsstrahlung, Hans Mark, Clyde McClelland, and Clark Goodman—279(A); Behram Kurşunoğlu—1156(A)
Proton scattering from N^{14}, G. W. Tautfest, J. R. Havill, and Sylvan Rubin—280(A)
Rotation of polarization vector and depolarization in *p-p* scattering, T. Ypsilantis, C. Wiegand, R. Tripp, E. Segrè, and O. Chamberlain—840(L)
Scattering of 9.76-Mev protons by He^4, John H. Williams and Stanley W. Rasmussen—1167(A)
Vacuum polarization and *p-p* scattering, Leslie L. Foldy and Erik Eriksen—775; 1190(A)
Scattering of Radiation (see **Gamma Rays; Radiation; X-Rays**)
Scintillation Counters (see **Methods and Instruments**)
Secondary Emission (see **Electrical Properties**)
Semiconductors
Absorption by free and bound holes in *p*-type Ge, S. Teitler, M. Lax, and E. Burstein—1561(A)
Adsorption of H_2 and O_2 on Ge, R. M. Burger, H. E. Farnsworth, and R. E. Schlier—1179(A)
Attempt to detect high mobility holes in Ge using drift mobility technique, N. J. Harrick—1131(L)
Au, an "amphoteric" impurity element in Ge, W. C. Dunlap, Jr.—1535(A)
Birefringence in Si, W. C. Dash—1536(A)
Boltzmann theory of cyclotron resonance for warped spherical energy surfaces, H. J. Zeiger—1560(A)
Bond dipoles and piezoelectricity in zincblende semiconductors, Joseph L. Birman—1567(A)
Carrier effective masses in Ge, James M. Goldey and Sanborn C. Brown—1192(A)
Conductance of *p*-type inversion layers on *n*-type Ge, G. deMars, H. Statz, and L. Davis, Jr.—1565(A)
Crystal growth, and electrical and optical properties of gray Sn, J. H. Becker—1192(A)
Crystal structure of InBi, W. P. Binnie—228(A)
Cyclotron and spin resonance in InSb, G. Dresselhaus, A. F. Kip, C. Kittel, and G. Wagoner—556(L)
Cyclotron resonance of electrons and holes in Si and Ge crystals, G. Dresselhaus, A. F. Kip, and C. Kittel—368
Cyclotron resonances in Ge at 1.4°K, R. C. Fletcher, F. R. Merritt, and W. A. Yager—1560(A)
Donor and acceptor ionization energies in Si and Ge, A. H. Mitchell and C. Kittel—271(A)
Effect of dislocations on recombination of holes and electrons in Ge and Si, S. A. Kulin, A. D. Kurtz, and B. L. Averbach—1566(A)
Effect of impurities on mobility in *n*-type InSb, T. C. Harman, R. K. Willardson, and A. C. Beer—1532(A)
Effect of ion-bombardment cleaning of Ge on point contact rectification, R. B. Allen and H. E. Farnsworth—1179(A)
Effect of pressure on electrical properties of InSb, Donald Long and Park H. Miller, Jr.—1192(A)
Effect of pressure on optical absorption edge in Si and Ge, D. M. Warschauer, W. Paul, and H. Brooks—1193(A)
Effective mass of carriers and relaxation time in Ge, F. D'Altroy and H. Y. Fan—1561(A)
Elastic strain energy stored in mechanically disturbed surfaces, R. L. Hopkins—1567(A)

Semiconductors (Continued)
Electrical and optical properties of GaSb films, R. J. Collins, F. W. Reynolds, and G. R. Stilwell—227(A)
Electrical breakdown in Ge at low temperatures, F. J. Darnell and S. A. Friedberg—1178(A); 1860(L)
Electrical conductivity of liquid Te, V. A. Johnson—1567(A)
Electrical properties of electron-bombarded Ge, E. E. Klontz, R. R. Pepper, and K. Lark-Horovitz—1535(A)
Electron capture probability of upper Cu acceptor level in Ge, R. M. Baum and J. F. Battey—923
Electron voltaic study of electron bombardment damage and its thresholds in Ge and Si, J. J. Loferski and P. Rappaport—1861(L)
Excess noise and trapping in Ge, H. A. Gebbie—1567(A)
Faraday effect in semiconductors at microwave frequencies, Richard Rau and P. H. Miller, Jr.—1533(A)
Fast-neutron bombardment of *n*-type Ge, J. W. Cleland, J. H. Crawford, Jr., and J. C. Pigg—1742
Field effect in Ge, H. C. Montgomery and W. L. Brown—1565(A)
Forward characteristic of point contact rectifier, Kurt Lehovec, Alma Marcus, and Kurt Schoeni—1179(A)
Galvanomagnetic effects in InSb, W. R. Hosler and H. P. R. Frederikse—1532(A)
Ge surface conductivity and effects of water vapor, Edward N. Clarke—1178(A)
Generalized deformation potential theory for *n*-type Ge, William P. Dumke—230(A)
Hall effect and resistivity of InSb at low temperatures, H. Fritzsche and K. Lark-Horovitz—1532(A)
Hall effect and resistivity of *p*-type Ge at low temperatures, K. Lark-Horovitz and H. Fritzsche—1536(A)
Hall effect in *p*-type Ge, Colman Goldberg and R. E. Davis—1192(A)
Hall mobility of optically excited carriers in Ge, W. W. Tyler and R. Newman—961; 1192(A)
Heat capacity measurements on pure and slightly reduced rutile (TiO_2) at very low temperatures, P. H. Keesom and N. Pearlman—1539(A)
Impurity band conduction in Ge and Si, E. M. Conwell—1178(A)
Infrared absorption in *n*-type Ge, W. Spitzer, R. J. Collins, and H. Y. Fan—1536(A)
Infrared absorption of InSb, W. Kaiser and H. Y. Fan—966
Infrared absorption of Si near lattice edge, G. G. Macfarlane and V. Roberts—1865(L)
Interpretation of donor state absorption lines in Si, Walter Kohn—1856(L)
Lattice defects in Si, Sumner Mayburg—1177(A)
Localized photoeffect in PbS photocells, E. S. Rittner and S. Fine—545(L)
Low-energy electron diffraction studies of Ge crystal surface, H. E. Farnsworth, R. E. Schlier, and R. M. Burger—250(A)
Low-temperature electrical conductivity of Ge, S. H. Koenig and G. R. Gunther-Mohr—228(A)
Magnetic susceptibility in InSb, J. H. Crawford, Jr., and D. K. Stevens—1532(A)
Magneto-electric effects in Ge in strong magnetic fields, Warren E. Henry—1534(A)
Measurement and interpretation of conductance of *p*-type inversion layers on Ge, G. A. deMars, H. Statz, and L. Davis, Jr.—539(L)
Microwave determination of average masses of electrons and holes in Ge, James M. Goldey and Sanborn C. Brown—1761
Minority carrier extraction in Ge, Ralph Bray—229(A)
Minority carrier lifetime as function of crystal growth variables, A. C. Sheckler and D. C. Jillson—229(A)
Mobility of holes in Si and Ge, H. Ehrenreich and A. W. Overhauser—1533(A)
New radiation due to recombination of holes and electrons in Ge, J. R. Haynes—1866(L)
Noise in Si *p-n* junction photocells, G. L. Pearson, H. C. Montgomery, and W. L. Feldmann—1567(A)
Noise measurements in semiconductors at very low frequencies, T. E. Firle and H. Winston—1567(A)
Nonsteady state conductance of inversion layers and structure of surface states on Ge, H. Statz, L. Davis, Jr., and G. deMars—1566(A)
Nuclear magnetic resonance in semiconductors: Exchange broadening and line shapes, R. G. Shulman, J. M. Mays, and D. W. McCall—1182(A)
Nuclear magnetic resonance in semiconductors: GaSb and InSb, J. M. Mays, R. G. Shulman, and D. W. McCall—1182(A)
Optical absorption in single crystals of Ge and Si, W. C. Dash, R. Newman, and E. A. Taft—1192(A)
Optical and impact recombination in impurity photoconductivity in Ge and Si, N. Sclar and E. Burstein—1178(A); 1757
Optical effects in plastically deformed Ge, H. G. Lipson, E. Burstein, and P. L. Smith—1535(A)
Optical properties of group III elements in Si, E. Burstein, G. Picus, B. Henvis, and M. Lax—1536(A)
Oxidation of clean surfaces of Ge below 25°C, Mino Green and J. A. Kafalas—1566(A)
Photoconductivity of electron-bombarded Ge, F. Stoeckmann, E. Klontz, H. Y. Fan, and K. Lark-Horovitz—1535(A)
Photomultiplication at surface of Ge, H. Bernstein and R. H. Kingston—1566(A)
Physical model of semiconductors, J. G. Barredo—229(A)
Pressure dependence of absorption edge in Ge and Si, W. Spitzer, C. O. Bennett, and H. Y. Fan—228(A)
Pressure dependence of resistivity, Hall effect, and magnetoresistance in Ge, G. B. Benedek, W. Paul, and H. Brooks—1193(A)
Pressure dependence of resistivity of Si, William Paul and G. L. Pearson—1755
Propagation and plasma oscillation in semiconductors with magnetic fields, Benjamin Lax and Laura M. Roth—548(L)
Properties of Ge doped with Mn, H. H. Woodbury and W. W. Tyler—1534(A)
Properties of Ge doped with Ni, W. W. Tyler, R. Newman, and H. H. Woodbury—461
Properties of Mg_2Sn, R. F. Blunt, H. P. R. Frederikse, and W. R. Hosler—1533(A)
Properties of powdered Ge and effects of heat treatment, E. A. Kmetko—1535(A)
Quantum theory of cyclotron resonance for degenerate bands, J. M. Luttinger—1560(A)
Recombination of injected carriers at dislocation edges in semiconductors, J. P. McKelvey and R. L. Longini—1566(A)
Rectification in thin films of PbS, M. Silver, R. S. Witte, and F. McCaffrey—270(A)
Relaxation effects in field-induced surface conductance, R. H. Kingston and A. L. McWhorter—1191(A)
Reverse current and carrier lifetime as function of temperature in Ge and Si junction diodes, E. M. Pell—1536(A)
Ring diffusion as mechanism of self-diffusion in Ge, Sumner Mayburg—1134(L)
Saturation Hall constant and magnetoresistance in semiconductors, John A. Swanson—1534(A)

Seebeck effect in Si, T. H. Geballe and G. W. Hull—940
Segregation coefficient of As in Ge as function of crystal growth variables, D. C. Jillson and A. C. Sheckler—229(A)
Self-diffusion in Ge, William M. Portnoy, Harry Letaw, Jr., and Lawrence Slifkin—1536(A)
Semiconducting diamond, W. J. Leivo and R. Smoluchowski—1532(A)
Semiconducting properties of FeO thermistor material, J. J. Brophy, N. Rostoker, and L. V. Azaroff—228(A)
Short-time polarization in ThO, W. E. Danforth—1177(A)
Shot noise in CdS crystals, C. I. Shulman—384
Single-crystal layers of Ge semiconductors, W. M. Becker and K. Lark-Horovitz—228(A)
Solution of Hartree-Fock-Slater equations for Si crystal by method of orthogonalized plane waves, Truman O. Woodruff—1741
Spin resonance in neutron irradiated Si, E. Schulz-DuBois, M. Nisenoff, H. Y. Fan, and K. Lark-Horovitz—1561(A)
Spin resonance widths of electrons in donor states in Si, W. Kohn—1561(A)
Structure of surface states at Ge-Ge oxide interface, H. Statz, L. Davis, Jr., and G. A. deMars—540(L)
Surface potential and surface charge distribution from semiconductor field effect measurements, W. L. Brown—1565(A)
Surface-recombination velocity and surface conductance of thin Ge slabs, Donald T. Stevenson—1566(A)
Surface traps and $1/f$ noise in Ge, A. L. McWhorter—1191(A)
Temperature dependence of width of band gap in several photoconductors, Richard H. Bube—431
Theory of donor states in Si, W. Kohn and J. M. Luttinger—915
Theory of energy levels of donor electrons in Si, W. Kohn and J. M. Luttinger—1178(A)
Theory of magnetic rectifier, Kurt Lehovec, Alma Marcus, and Kurt Schoeni—229(A)
Theory of photomagnetoelectric effect in semiconductors, W. Van Roosbroeck—1533(A)
Thermal conductivity of Ge at ambient temperatures, Kathryn A. McCarthy and Stanley S. Ballard—271(A)
Third harmonic cyclotron resonance of holes in Ge, R. N. Dexter—1560(A)
Ultraviolet light induced surface channel and carrier lifetime effects in Ge, H. Christensen—1178(A)
Usually large magnetoresistive effects in InSb for specialized boundary conditions, R. K. Willardson, T. C. Harman, P. F. Choquard, and A. C. Beer—227(A)
Verification of Bridgman relation for mixed semiconductor, G. M. Seidel and V. A. Johnson—230(A)
Visible light from Si p-n junction, R. Newman, W. C. Dash, R. N. Hall, and W. E. Burch—1536(A)
Water-vapor-induced n-type surface conductivity on p-type Ge, R. H. Kingston—1766

Shock Waves (see **Fluid Dynamics**)
Solid State (see **Crystalline State**)
Solutions (see **Liquids**)
Sound (see **Acoustics**)
Spallation (see **Nuclear Reactions**)
Spark Discharge (see **Electrical Discharges**)
Specific Heat (see **Thermal Properties**)
Spectra, Atomic (see **Atomic Structure and Spectra**)
Spectra, General

Absorption bands of Rb in presence of foreign gases, Shang-Yi Ch'en, Robert B. Bennett, and Oleg Jefimenko—281(A)
Effects of electron collisions on width of spectral lines, Henry Margenau and Bennett Kivel—1822
Electron impact broadening of spectral lines, B. Kivel, S. Bloom, and H. Margenau—495
Intensity distribution among spectral orders in grazing incidence spectrograph, D. E. Bedo and D. H. Tomboulian—242(A)
Photoelectric mixing of incoherent light, A. Theodore Forrester, Richard A. Gudmundsen, and Philip O. Johnson—1169(A)

Spectra, Molecular (see **Molecular Structure and Spectra**)
Spectra, Nuclear (see **Nuclear Spectra**)
Spectroscopy Technique (see **Methods and Instruments**)
Spinor Fields (see **Field Theory**)
Standards (see **Constants, Standards, Units**)
Stark Effect (see **Atomic Structure and Spectra**)
Statistical Mechanics and Thermodynamics

Bose-Einstein condensation of imperfect gas, M. H. Friedman and S. T. Butler—294
Collective description of electron gas, M. Dresden—1165(A)
Deformation of viscoelastic plates derived from thermodynamics, M. A. Biot—1869(L)
Dynamical friction, R. Riddell, Jr., M. Neuman, and S. Gasiorowicz—257(A)
Entropy of radiation, Aadne Ore—887
Fluctuation dissipation theorem, J. Weber—1165(A)
Ideal gas thermodynamic properties of isotopic hydrides of group of diatomic free radicals, Lester Haar—1551(A)
Invariant characteristics of one-dimensional binary lattices, Edward H. Kerner and Joseph G. Logan—1165(A)
Magnetic moment of Fermi-Dirac gas, A. W. Saenz and R. C. O'Rourke—1166(A)
Modified Holtzmark distribution, S. Gasiorowicz—257(A)
New extension of collective coordinates for many-body problem, Jerome K. Percus and George J. Yevick—1164(A)
Normal coordinate treatments and calculated thermodynamic properties of $POCl_3$, POF_3, $PSCl_3$, and PSF_3, Joseph S. Ziomek, Edward A. Piotrowski, and Edward N. Walsh—243(A)
Overhauser nuclear polarization effect and minimum entropy production, Martin J. Klein—1736
Partition function for system of interacting Bose-Einstein particles, S. T. Butler and M. H. Friedman—287
Random walk methods in statistical mechanics of one-dimensional systems, R. L. Sells, C. W. Harris, and E. Guth—272(A)
Role of coordination number in Lee-Yang lattice gas, C. W. Harris and E. Guth—272(A)
Rotational transition in solid hydrogen, K. Tomita—1197(A)
Stark fields from ions in plasma, Arthur Broyles—1166(A)
Statistical analog of second law of thermodynamics, John S. Thomsen—1625
Statistical ensemble representing stationary nonequilibrium states, Joel Lebowitz and Peter G. Bergmann—1165(A)
Statistical model for high-energy events, Joseph V. Lepore and Maurice Neuman—1484
Statistical thermodynamics of isotope effects. I. Theory of equilibrium processes, Irwin Oppenheim—258(A); II. Equation of state of H_2 isotopes at intermediate densities, Abraham S. Friedman and Irwin Oppenheim—258(A)
Susceptibility and entropy of F-centers, J. G. Daunt and J. Korringa—1550(A)
Symmetry effects in gas kinetics. I. He isotopes, O. Halpern and R. A. Buckingham—1626
Theory of successive orientational phase transitions in two- and three-dimensional systems, T. E. Lockary and E. Guth—274(A)
Variational principles in irreversible thermodynamics, Irwin Manning and Laszlo Tisza—1165(A)

Statistical Methods (see **Mathematical Methods**)
Superconductivity
Absorption of 10 Mc/sec sound pulses by superconducting polycrystalline Sn rod, L. Mackinnon—1181(A)
Contact resistance between superconductors and normal conductors, F. Bedard and H. Meissner—1539(A)
Effect of superconducting transition on internal friction of Sn, Benjamin Welber—1196(A)
Electron transfer mechanism for ultrasonic attenuation in metals, C. Kittel—1181(A)
Paramagnetism observed at superconducting transition, Yoshio Shibuya and Seichi Tanuma—938
Stability of phase boundary inside superconductor, F. Beck —852
Superconducting Re alloys and compounds, J. K. Hulm—1539(A)
Superconducting winding for electromagnet, G. B. Yntema —1197(A)
Theory of paramagnetic effect in superconductors, Hans Meissner—1539(A)
Supersonics (see **Fluid Dynamics**)

Thermal Conductivity (see **Thermal Properties**)
Thermal Diffusion (see **Diffusion**)
Thermal Expansion (see **Thermal Properties**)
Thermal Properties
Anomaly in low-temperature atomic heat of Ag, P. H. Keesom and N. Pearlman—548(L)
Atomic heat of graphite between 1° and 20°K, N. Pearlman and P. H. Keesom—1539(A)
Atomic heats of Cu, Ag, and Au from 1°K to 5°K, William S. Corak, M. P. Garfunkel, C. B. Satterthwaite, and Aaron Wexler—1699
Curie constant, spontaneous polarization, and latent heat in ferroelectric, S. Triebwasser and J. Halpern—1562 (A)
Dimensional changes during heat treatment thermal expansion of polycrystalline carbons and graphites, F. M. Collins—1564(A)
Elastic constants and specific heat of KCl at elevated temperatures, F. D. Enck and C. B. Cooper—237(A)
Electronic specific heat of α-Mn, G. Guthrie, S. A. Friedberg, and J. E. Goldman—1181(A)
Heat capacity measurements on pure and slightly reduced rutile (TiO_2) at very low temperatures, P. H. Keesom and N. Pearlman—1539(A)
Lattice thermal conductivity, J. S. Dugdale and D. K. C. MacDonald—1751
Magnetic and thermal properties of $MnCl_2$ at liquid He temperatures, R. B. Murray and L. D. Roberts—1180(A)
Magnetic and thermal properties of UI_3 at liquid He temperatures, L. D. Roberts and R. B. Murray—1180(A)
Specific heats of Zn ferrite and Zn chromite at low temperatures, S. A. Friedberg and D. L. Burk—1200(A)
Temperature dependence of heat capacity of molybdenite, Edgar F. Westrum, Jr., and John J. McBride—270(A)
Thermal conductivities of carbons and graphites, C. P. Jamieson—1564(A)
Thermal conductivity of Ge at ambient temperatures, Kathryn A. McCarthy and Stanley S. Ballard—271
Thermal magnetoresistance of Zn at liquid He temperatures, P. B. Alers—1180(A)
Two-medium theory of thermal conductivity of artificial graphite: Experimental, Alan W. Smith—1563(A); Interpretation, John E. Hove—1563(A)
Vibration spectra and specific heats of cubic metals. I. Theory and application to Na, A. B. Bhatia—245(A); II. Application to Ag, A. B. Bhatia and G. K. Horton —1181(A); 1715

Thermal Radiation (see **Radiation**)
Thermionic Emission (see **Electrical Properties**)
Thermodynamics (see **Statistical Mechanics and Thermodynamics**)
Thermoelectric Effect (see **Electrical Properties; Semiconductors**)
Thermoluminescence (see **Luminescence**)
Thermomagnetic Effect (see **Magnetic Properties**)
Total Cross Sections (see **Electrons and Positrons; Nuclear Reactions**)
Transmutation (see **Nuclear Reactions**)

Uncertainty Principle (see **Quantum Mechanics**)
Units (see **Constants, Standards, Units**)

Vacuum Tubes (see **Methods and Instruments**)
Van der Waals Forces (see **Molecular Structure and Spectra**)
Viscosity (see **Liquids**)

Wave Mechanics (see **Quantum Mechanics**)
Work Function (see **Electrical Properties**)

X-Rays
Change in KCl lattice by soft x-rays, Chester R. Berry —934
Computed transition probabilities for x-ray continua of K, Margaret N. Lewis, Louis C. Green, Marjorie M. Mulder, Paul C. Milner, and Eleanor K. Kolchin—1020; 1210(A)
Determination of dislocation densities with double crystal spectrometer, A. D. Kurtz, S. A. Kulin, and B. L. Averbach—1543(A)
Energy levels in metallic potassium, E. L. Jossem and L. G. Parratt—1151(A)
Intensity distribution among spectral orders in grazing incidence spectrograph, D. E. Bedo and D. H. Tomboulian—242(A)
Isotope shift in x-ray spectra of heavy elements, M. S. Wertheim and G. Igo—1
Localized energy states in crystalline alkali chlorides, C. F. Hempstead and L. G. Parratt—1170(A)
Long-wavelength x-ray reflection microscope, J. F. McGee —282(A)
Measurements of x-ray diffuse scattering from Co-Pt disordered solid solutions and of long-range order for alloy CoPt, P. S. Rudman and B. L. Averbach—1554(A)
New method in x-ray crystal structure determination involving use of anomalous dispersion, Y. Okaya, Y. Saito, and R. Pepinsky—1857(L)
Satellites in soft x-ray spectrum of Zr, J. Korringa—1556(A)
Small-angle scattering of x-rays by surface irregularities, W. H. Robinson and R. Smoluchowski—1555(A)
Small-angle x-ray scattering by system iso-octane-*n*-heptforane, T. E. Brackett, R. D. Dunlap, and J. Biscoe —1210(A)
Spatial distribution of atoms in liquid He^4, Louis Goldstein and James Reekie—857
U L_1 x-ray transition from separated isotopes, G. L. Rogosa and W. F. Peed—1173(A)
X-ray analysis of compressed KCl powder crystals, J. G. Kereiakes—553(L)
X-ray-induced luminescence from air, William E. Spicer —1061
X-ray measurements on low-temperature neutron-irradiated graphite, David T. Keating—1859(L)
X-ray scattering effects in irradiated boron carbide, C. W. Tucker, Jr., and P. Senio—1541(A)

CONTENTS—*continued*

Letters to the Editor:

Collision Alignment of Molecules, Atoms, and Nuclei . . . . . Norman F. Ramsey 1853

Saturation of Nuclear Electric Quadrupole Energy Levels by Ultrasonic Excitation . . . . . W. G. Proctor and W. H. Tanttila 1854

Experimental Evidence for Thermal Spike in Radiation Damage . . . . . W. Primak 1854

Superfluidity in Liquid He^3 . . . . . M. J. Buckingham 1855

Interpretation of Donor State Absorption Lines in Silicon . . . . . Walter Kohn 1856

New Method in X-Ray Crystal Structure Determination Involving the Use of Anomalous Dispersion . . . . . Y. Okaya, Y. Saito, and R. Pepinsky 1857

X-Ray Measurements on Low-Temperature Neutron-Irradiated Graphite . . . . . David T. Keating 1859

Electrical Breakdown in Germanium at Low Temperatures . . . . . F. J. Darnell and S. A. Friedberg 1860

Electron Voltaic Study of Electron Bombardment Damage and its Thresholds in Ge and Si . . . . . J. J. Loferski and P. Rappaport 1861

Alternative Explanation of the Waymouth-Bitter Experiments . . . . . Laurence Burns 1863

Average Crystal Potential . . . . . Joseph L. Birman 1863

Magnetic Susceptibility of a Manganese at Low Temperatures . . . . . A. Arrott, B. R. Coles, and J. E. Goldman 1864

Infrared Absorption of Silicon Near the Lattice Edge . . . G. G. Macfarlane and V. Roberts 1865

New Radiation Resulting from Recombination of Holes and Electrons in Germanium . . . . . J. R. Haynes 1866

Overhauser Nuclear-Polarization Effect . . . . . W. A. Barker and A. Mencher 1868

Deformation of Viscoelastic Plates Derived from Thermodynamics . . . . . M. A. Biot 1869

Errata 1870

Author Index to Volume 98 1872

Analytic Subject Index to Volume 98 1901

CONTENTS

THE PHYSICAL REVIEW SECOND SERIES, VOLUME 92, NO. 4 JUNE 15

Pressure-Volume Isotherms of He^3 between 1.5 and 3.0°K . . . . . William E. Keller 1
Retrograde Motion in Gas Discharge Plasmas . . . . . K. G. Hernqvist and E. O. Johnson 1
Self-Focusing Streams . . . . . Willard H. Bennett 1
Dissociation of Oxygen in the Upper Atmosphere . . . . . E. T. Byram, T. A. Chubb, and H. Friedman 1
Theory of Electron Penetration . . . . . L. V. Spencer 1
Superfluidity and Heat Transport in the Unsaturated Helium-II Film . . . Earl Long and Lothar Meyer 1
Resonance Absorption of Sunlight in Twilight Layers . . . . . T. M. Donahue and Robert Resnick 1
Statistical Analog of the Second Law . . . . . John S. Thomsen 1
Symmetry Effects in Gas Kinetics. I. The Helium Isotopes . . . . . O. Halpern and R. A. Buckingham 1
Passage of Charged Particles through Plasma . . . . . Jacob Neufeld and R. H. Ritchie 1
Microwave Study of Positive Ion Collection by Probes . . . . . George J. Schulz and Sanborn C. Brown 1
Field Measurements in Glow Discharges with a Refined Electron Beam Probe and Automatic Recording . . . . . Roger Warren 1
Interpretation of Field Measurements in the Cathode Region of Glow Discharges . . . . . Roger Warren 1
Motion and Spectrum of Arc Cathode Spot in a Magnetic Field . Robert M. St. John and J. G. Winans 1
Thermodynamic Properties of Liquid Helium Three. I. The Specific Heat and Entropy . . . . . Thomas R. Roberts and Stephen G. Sydoriak 1
Directional Breakdown in Alkali Halide Crystals . . . . . M. E. Caspari 1
Time-Dependent Displacement Correlations and Inelastic Scattering by Crystals . . . . . R. J. Glauber 1
Atomic Heats of Copper, Silver, and Gold from 1°K to 5°K . . . . . William S. Corak, M. P. Garfunkel, C. B. Satterthwaite, and Aaron Wexler 1
Photoelastic Observations of the Expansion of Alkali Halides on Irradiation . . . . . W. Primak, C. J. Delbecq, and P. H. Yuster 1
Vibration Spectra and Specific Heats of Cubic Metals. II. Application to Silver . . . . . A. B. Bhatia and G. K. Horton 1
Multiple Scattering of Slow Neutrons by Flat Specimens and Magnetic Scattering by Zinc Ferrite . . . . . B. N. Brockhouse, L. M. Corliss, and J. M. Hastings 1
Abnormal Increase in the Dielectric Constant of an Electret-Forming Material . . . . . S. D. Chatterjee and T. C. Bhadra 1
Overhauser Effect in Nonmetals . . . . . A. Abragam 1
Overhauser Nuclear Polarization Effect and Minimum Entropy Production . . . . . Martin J. Klein 1
Work Function of Cadmium . . . . . Paul A. Anderson 1
Solution of the Hartree-Fock-Slater Equations for Silicon Crystal by the Method of Orthogonalized Plane Waves . . . . . Truman O. Woodruff 1
Fast-Neutron Bombardment of n-Type Ge . . . . . J. W. Cleland, J. H. Crawford, Jr., and J. C. Pigg 1
Lattice Thermal Conductivity . . . . . J. S. Dugdale and D. K. C. MacDonald 1
Magnetization Reversal in Thin Films . . . . . R. L. Conger 1
Pressure Dependence of the Resistivity of Silicon . . . . . William Paul and G. L. Pearson 1
Optical and Impact Recombination in Impurity Photoconductivity in Germanium and Silicon . . . . . N. Sclar and E. Burstein 1
Microwave Determination of the Average Masses of Electrons and Holes in Germanium . . . . . James M. Goldey and Sanborn C. Brown 1
Direct Measurement of the Effect of Polarization on Energy Loss . . . . . E. L. Goldwasser, F. E. Mills, and T. R. Robillard 1
Water-Vapor-Induced n-Type Surface Conductivity on p-Type Germanium . . . . . R. H. Kingston 1
Lattice Resistance to Dislocation Motion at High Velocity . . . . . Edward W. Hart 1
Effect of Plastic Deformation on the Electrical Conductivity of Silver Bromide . . . William G. Johnson 1
Nuclear Magnetic Resonance Saturation and Rotary Saturation in Solids . . . . . Alfred G. Redfield 1
Theory of Electroluminescence . . . . . W. W. Piper and F. E. Williams 1
Charge Distributions of Oxygen and Neon Ions Passing through Gases . . . . . Edward L. Hubbard and Eugene J. Lauer 1
Electron Capture and Loss by Ions in Gases . . . . . Robert L. Gluckstern 1
Effects of Electron Collisions on the Width of Spectral Lines . . . Henry Margenau and Bennett Kivel 1
Cross Section for Electron Capture and Loss by 26-Mev Nitrogen Ions . . . . . H. L. Reynolds, L. D. Wyly, and A. Zucker 1
Energy Required to Produce One Ion Pair for Several Gases . . . . . J. Weiss and W. Bernstein 1
Measurement of Absorption Coefficients for Photoionizing Radiations in Low-Pressure Gases with a Space Charge Detector . . . . . C. D. Mansell 1
Microwave Spectrum of Carbon Monsulfide . . . . . Richard C. Mockler and George R. Bird 1
Static Magnetic Field Quenching of the Orthopositronium Decay: Angular Distribution Effect . . . . . V. W. Hughes, S. Marder, and C. S. Wu 1
Rotational Excitation by Slow Electrons. II . . . . . E. Gerjuoy and S. Stein 1
Generation of Coulomb Wave Functions by Means of Recurrence Relations . . . . . Irene A. Stegun and Milton Abramowitz 1

(Continued on cover three)

LANCASTER PRESS, INC., LANCASTER